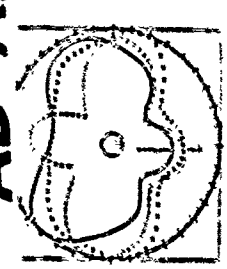
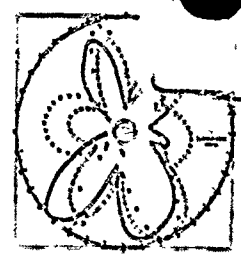
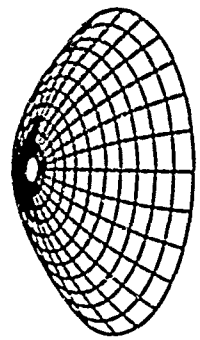
DTIC FILE COPY

AD-A217 994









DTIC
ELECTE
FEB 13 1990
S D
CD

8th Annual Review of Progress in

APPLIED COMPUTATIONAL ELECTROMAGNETICS

at the

Naval Postgraduate School

Monterey, CA

March 20-24, 1989

CONFERENCE PROCEEDINGS

DISTRIBUTION STATEMENT A
Approved for public release
Distribution Unlimited

90 02 09 0

CONFERENCE PROCEEDINGS

5th Annual Review of Progress in

APPLIED

COMPUTATIONAL

ELECTROMAGNETICS

at the

Naval Postgraduate School

Monterey, CA

March 20-24, 1989

SYMPOSIUM PROGRAM COMMITTEE CHAIRMAN

Michael Thorburn

Sponsored by

The Applied Computational Electromagnetics Society

and DOD/USA ECOM, USAISEC, NOSC, NPS, DOE/LLNL

THE NAVAL POSTGRADUATE SCHOOL

TABLE OF CONTENTS

SESSION 1: GENERAL PURPOSE ELECTROMAGNETIC CODES
Chairman: Constantine Balanis

"Comparison of Antenna and Scattering Patterns by the NEC and ESP Codes"
K Liu and C Balanis 1

"Electromagnetic Design Codes Maintained on the MFENET by the LAAGO"
T Barts, K Chan, R Cooper and M Browman 9

"A Comparison of the PATCH, JUNCTION and NEC Codes: Admittance and Near Fields for a Whip on a Box"
P Ellinadis, R Adler and J Breakall 22

"EMPACK: Building Block Subroutines for the Method of Moments"
D Wilton, S Yesantharao, C Cheng and R Sharpe 34

"JUNCTION: A Computer Code for the Computation of Radiation and Scattering by Arbitrary Conducting Wire/Surface Configurations"
D Wilton and S Hwu 43

SESSION 2: MICROWAVE CIRCUITS, Chairman: Vijai Tripathi

"Application of the TLM Method to Microwave Circuits"
R G Rancon 53

"Three-Dimensional Full Wave Analysis of Passive Microstrip Components Using the TLM Method"
F German, H Williams, L Figge and M Beginski 63

"The Field Theoretic MMIC Computation Enhanced by the Variational Principle"
Y Chow, G Howard and M Stubbs 78

"Accurate and Efficient Modeling of Dispersive MMIC Passive Discontinuity Components"
A Nakatani and J Castaneda 81

"Spectral Domain Technique and Finite Thickness Metallizations"
S Tedjini, N Daoud, E Pic and M Mabrouk 95

"The Dispersion Characteristics of the FD-TD Method in Cylindrical Waveguides"
D Choi 101

"Computational Electromagnetics Applied to Integrated Circuit Microlithography and Metrology"
G Wojcik and J J Mould, Jr. 107

"Transverse Resonance Analysis of Three Coupled Transmission Lines"
G Bartolucci, F Giannini, C Paoloni and V Tripathi 114

INVITED PAPER: "CAD Oriented Enhanced Models for Planar Subs"
F Giannini 121

SESSION 3: ELECTROMAGNETIC COMPATIBILITY AND INTERFERENCE; Chairman: Harold Sabbagh

"An Integrated Workstation for Cosmic EMI Analysis"
P Magie, J Holeman, P Alexander and D Tam 130

"Modeling Unintentional Sources of Electromagnetic Radiation"
T Hubing and J Kauffman 133

"Comparative Calculation of Basic EMC Configurations with NEC3 and NEC2-MBG"
F Heidler, K Muller and M Wurm 158

POSTER PAPERS: Chairman: David Stein

"An Implicit Three Dimensional Electromagnetic Field Code"
R Clemens, R Knight and R Chase 168

"Adaptive Algorithms for the Analysis of a Microstrip Discontinuity Inductance"
A Hill and V Tripathi 183

"A Finite Element Code for Solving 2-D Scattering Problems on IBM PC Compatible Computers"
A Castillo and A Peterson 189

"End Effect in Shielded Coplanar Lines"
G Bartolucci, F Giannini and C Paciori 195

"Wave Propagation on Infinite, Two Dimensional Structures"
R Speciale 200

"A MMP Program for Computation of 3-D Electromagnetic Fields on PCS"
L Bomholt and C Hafner 235

"Increasing Oil Production from a Well with Radio Waves"
E Siambar, F Vermeulen and F Chute 253

"Finite Element Analysis of Microstrip Systems in the Vicinity of an Edge"
M Baginski, L Figge, H Williams and F German 260

"Atmospheric Attenuation of Synthetic Aperture Radars and Real Radars"
R Au 281

"The Dual Mode Log Periodic Dipole Antenna"
E Wiseman and M Wheeler 292

"Numerical Solution to Scattering from 2-D Infinite Bodies in Finite Computational Domain"
A Mohammadian, W Hall and V Shankar 298

"A General UTD Diffraction Coefficient for Two Wedges"
R Luebbers and N Schneider 315

"Transient Response of Highly Conductive Materials Using a New FDTD Formulation"
R Luebbers, F Hunsberger and K Kunz 328

"Finite Difference Time-Domain Modeling of Electromagnetic Radiation from an Electron Beam"
S Pennock, R McLeod and H Hudson 360

"A Buried Antenna Analytic Modeling Program - PATB"
R Gilchrist, P Barrett, B Gross, K King and D Faust 373

SESSION 4 SCATTERING I Chairman: James Rogers

"UTD Scattering from Dihedrals"
R Marhefka and N Akhter 374

"A Magnetic Field Integral Equation Formulation for Electromagnetic Scattering from Inhomogeneous 3 D Dielectric Bodies"
A Peterson 387

"Scattering from Cylindrical Dielectric Slabs: A Method of Moments Approach"
K Clancy, S Pongerasian and R Hodges 404

"Radar Cross Section Calculation of Partially Coated Conducting Bodies"
G Bridges, M Aboutahra, A Kishk and L Shafai 411

"Calculation of Admittance of Slots on a Body of Revolution Using the Method of Moments"
J Rogers 421

SESSION 5 VALIDATION Chairman: J W Williams

"Validation of a Moment Method Code"
E Yip and E Sabetha 437

"Improving Moment Method Predictions with Measurements"
J Stoch 457

"Electromagnetic Code Validation by the Infrared Measurement Method"
J Norgard, R Sega, D Fromme, D Metzger and K Ianacone 461

"Large FORTRAN Program Structure, Maintenance, Reliability and Documentation"
J Janni et al 474

SESSION 6 FINITE DIFFERENCES AND FINITE ELEMENTS Chairman: Andrew Peterson

"A Novel Finite Element Formulation using Quintic Splines for Field Analysis in Closed Structures"
A Chan and C Chui 524

"A Time-Domain Numerical Algorithm for Scattering of E-M Wave by 2-D Anisotropic Objects"
Y Chen and X Zhong 532

"Representation and Implementation of Time Domain Scattering Information"
T Lowe and R Kochhar 538

"Solving 2-D Electrostatic Problems on the Connection Machine using the Finite Element Method"
S Hutchinson, S Castillo and E Hensel 550

"Efficient Modeling of Thin Dielectric Structures using the Finite-Difference Time-Domain Technique",
K Demarest, D Long and P Tirkas 558

SESSION 7 NEC: NUMERICAL ELECTROMAGNETICS CODE: Chairman: Robert Noel

"Intelligent Pre-Processor for NEC2"
O Girvel, A Clark and A Fourie 572

"Problems with Thin Wire Emulation of Thicker Wires using NEC2"
A Clark and A Fourie 584

"NEC-3 on a PC, Revisited: Three Years Later"
T O'Hara and R Adler 594

SESSION 8 ANTENNAS: Chairman: William Imbriale

"Multiband Off-Center-Fed HF Antenna"
W Wheless Jr and M Fanning 609

"Simple Method to Compute the Current Distribution, Input Impedance and Efficiency of Thick Unloaded and Loaded Dipole Antennas"
A Fourie 621

"Verifying the Relationships between AM Broadcast Fields and Tower Currents"
J Hatfield 636

"Four-Element Monopole Array",
C Vandement 649

"Modeling the Quadrifilar Helix (Volute) Antenna using the Method of Moments"
S Best 657

"Analysis of Microstrip Antennas using the TLM Method",
F German, L Figge, G Gothard and M Beginski 675

"Numerical and Experimental Results of Multi-Wire Junction Triaxt Knit Mesh Reflectors by Fourier Moment Methods"
W Imbriale, V Galindo-Israel and Y Rahmat-Samii 692

SESSION 9 COMPUTATIONAL ISSUES: Chairman: Francis Canning

"A Symptotic Evaluation of the Physical Optics Integral for Generalized Ellipsoidal"
R Crawey and C Cha 710

"A New Fast Fourier Integral Transform: Rediscovering the Significance of Lanczos Sigma Effect Multipliers as a Digital Finite Impulse Response Windows in the Frequency Domain",
E Dombroski 719

"Implementation and Performance of MMP Programs on Transputers"
C Hafner and L Bomholt 736

"Effect of Approximations of Accuracy and Convergence Rate in the Mixed Potential of Integral Equation"
A Ohlsson 742

"Exploitation of Structural Symmetries for the Solution of Huge Matrices"
E Miller, K Kalbasi and K Demarest 751

"How to Efficiently Calculate Matrix Condition Numbers and the 'Error Bounds' They Generate"
F Canning 783

SESSION 10 INPUT/OUTPUT AND INTERFACE ISSUES: Chairman: Frank Walker

"Triangulation of Arbitrarily Shaped Geometric Models for Methods of Moments Applications"
D Wilkes and C Cha 771

"Graphic Output Routines of the MMP Program Package on PC's and Sun Workstations"
P Pagé, C Hafner and N Kuster 786

"An Interactive Waveguide Program"
G Sewell 793

"Supertab Interface for NEC"
F Walker, E Sorensen and J Kenney 806

SESSION 11 COMPUTATIONAL ISSUES II: Chairman: Michael Thorburn

"A Mathematical Theory of Light Diffraction by Dielectric Wedges"
G Wojcik and J Mould, Jr. 819

SESSION 12 SCATTERING II: Chairman: E L Fritz Roetman

"A New FDTD Formulation for Materials with Frequency-Dependent Constitutive Properties"
R Luebbers, F Hunsberger and K Kunz 827

"Far Field Projection"
M Barth and R Zolikowski 845

Author Index 864

STATEMENT "A" per Professor R.W. Adler
NPS/Code 62
TELECON
2/12/90
CG

DTIC COPY INSPECTED

Accesion For
NTIS CRA&I
DTIC TAB
Unannounced
Justification
By per call
Distribution /
Availability Codes
Dist | Avail and / or Special
A-1

PAPERS AND POSTER SESSIONS PRESENTED BUT PAPERS NOT SUBMITTED OR PUBLISHED

"Radiation and Scattering from a Circular Wave Guide Terminated with a Plane Conducting Screen: Exact Solution/Moment Method Solution"
Y Cho

"An Anisotropic Two-Dimensional Scattering Code"
J Heaton

"Combined Field Formulation for Conducting Bodies with Thin Coatings"
J Putnam

"A Dual Normal Mode Representation for Electromagnetic Scattering"
T Lehman and E Miller

"A Multizone, Finite-Volume Approach to Computation of Scattering from Complex Internal/External Layered Media"
V Shankar and W Hall

"Comparison of Models for Aperture Coupling to a Wire Interior to a Conducting Cavity"
J Williams, G Panoor and R Balestri

"Near-Field Contour Analysis and Evaluation of Potential Radiation Hazards from High-Power LW, MW and SW Antennas"
R Anders

"Analysis of the High Altitude EMP (HEMP) Coupling to a Well-Shielded Satellite Terminal Complex"
F Gorman, L Riggs, P Hayes and B Balestri

"A Computational Framework for the Treatment of Thin Layers in Electromagnetics"
W Hall and V Shankar

"Computation of Phased Array Element Gain"
H Schuman, G Bright and S Barbour

"Application of the Singular Value Decomposition Method in Method-of-Moments Algorithms"
R Balestri

"Application of the Discrete Fourier Transform Method to Planar Structures"
C Shen

©1989, The Applied Computational Electromagnetics Society

SESSION 1 - "GENERAL PURPOSE ELECTROMAGNETIC CODES"

Chairman: Constantine Balanis

COMPARISON OF ANTENNA AND SCATTERING PATTERNS BY THE NEC AND ESP CODES

Kefeng Liu*, Constantine A. Balanis
Department of Electrical and Computer Engineering
Arizona State University
Tempe, Arizona 85287

ABSTRACT

In this paper, a comparison of the field computations with two of the most widely used computational electromagnetic codes, the user-friendly Numerical Electromagnetic Code (NEC)[1], and another user-oriented computer code the Electromagnetic Surface Patch code (the ESP code)[4] has been undertaken. The radiation patterns of antennas mounted on a scaled model helicopter and the monostatic Radar Cross-Section (RCS) of a 90-degree dihedral corner reflector have been computed the the two codes. Measurements of the monostatic RCS patterns have been performed in the Arizona State University's anechoic chamber. By comparison with the experimental data, the performance of the electromagnetic codes can be evaluated.

I. INTRODUCTION

Innovations in modern digital computers have made computational electromagnetics a more important tool in solving electromagnetic problems involving realistic complex structures[3]. The user-friendly nature of the NEC and ESP code has increased the availability of numerical solutions to electromagnetic problems involving complex structures. Since the two codes are based on two different integral equations(the line integral equation for the NEC and the surface integral equation for the ESP code), a comprehensive comparison of the performance of the two codes will be valuable to the users.

Radiation and scattering patterns have been computed with the codes. The ESP code is more suited to this type of modeling because the two structures analyzed are mostly composed of polygonal surfaces[5]. A wire-grid model is introduced to model the surfaces when NEC is used[6]. Since the results of the wire-grid model are sensitive to the wire radius, the approach of an equal surface-area with the rule of thumb[2] is adopted to determine the radius of the wires to model the surfaces. One restriction of the ESP code is that all surfaces are assumed to be of zero thickness. For those wire structures besides the surfaces, the ESP code requires that all those wires be of the same radius.

To perform the computations, an automated computer program has been developed to generate the input data for both the NEC and the ESP code. The program is based on a quadrilateral wire-griding method the authors developed to model the enclosed surface. Such a data-generating program is convenient in the modeling of complex structures. Furthermore, the quadrilateral wire-griding method can be a very general method in the modeling of complex structures.

II. COMPARISON OF RADIATION PATTERNS

Figure 1 shows the geometry of the scaled model helicopter along with the wire antenna while Figure 2 displays the coordinate system of the model. For the NEC, the maximum segment size is chosen to be 0.05 λ at an operating frequency of 60.0 MHz. This segment size generates 820 segments for the helicopter, 14 segments for the rotor and blades, and 11 segments for the wire antenna. The excitation is a one-volt source fed in the middle of the tail wire antenna. For the ESP code, the maximum patch size is set at 0.1875 λ, and it results in 170 sinusoidal surface patch modes and 27 sinusoidal wire modes for the rotor, blades, and the wire antenna (i.e., 29 segments; the same as in the NEC). The roll, yaw, and pitch patterns of the helicopter antenna are shown in Figures 3, 4, and 5, respectively. The roll pattern is the radiation pattern in the elevation plane where $\phi=0^\circ$, $0^\circ \leq \theta \leq 180^\circ$, and $\phi=180^\circ$, $0^\circ \leq \theta \leq 180^\circ$. The yaw pattern is the azimuth radiation pattern where $\theta=90^\circ$, $0^\circ \leq \phi \leq 360^\circ$. The pitch pattern is another elevation radiation pattern where $\phi=270^\circ$, $0^\circ \leq \theta \leq 180^\circ$, and $\phi=90^\circ$ $0^\circ \leq \theta \leq 180^\circ$. The patterns have been normalized to 0 dB relative to the maximum value of the most intense component. Notice that the E_ϕ component in the pitch pattern computed using both codes is far below -40 dB, and therefore it can not been seen in Figure 5. The results obtained from the two codes agree extremely well in most areas. However, divergence of the results for certain field patterns occurs. For example, the E_θ patterns in the yaw pattern (Figure 4) and in the pitch pattern (Figure 5) disagree. Unfortunately, measurements for these patterns are not available at this time to show which code gives better results. Since the ESP code gives the solutions to the actual solid surface structure, the possible reason for the disagreements may be that the wire-grid model does not represent very well surfaces with wedges that are electrically close. This will produce errors in regions where E_θ is primarily a result of surface reflections and wedge diffractions.

Other antenna patterns for antennas mounted in other locations has also been computed, but they are not shown here because of space limitations. The patterns in Figure 3, 4, and 5 are computed when the blades are aligned with the x and y axes. Patterns for different blade positions have also been computed to show the effect of the blade rotation on the antenna patterns. Efficiency of the two codes has also been examined.

III. COMPARISON OF SCATTERING PATTERNS

Figure 6 shows the geometry and the coordinate system of a 90-degree dihedral corner reflector. The maximum segment sizes are chosen as 0.125λ and 0.1λ for the ESP code and the NEC, respectively. With such a segment size, the automated program generates 1072 wire-grid segments for the NEC, while the ESP generates 742 surface patch modes for both polarizations(vertical and horizontal). The ESP is more suitable for computing scattering patterns while the NEC is configured to compute the bistatic RCS only. However, the NEC has been modified to compute the monostatic RCS so that it can be compared with the ESP code as well as with the measurements. Figures 7 and 8 show the comparisons of the

monostatic RCS of the corner reflector for both the vertical and the horizontal polarizations. The NEC agrees better with the experimental data because the wire-grid model with finite radius represents more accurately the structure of the object(the metallic plates for the corner reflector have a thickness of 0.82mm while the diameter of the wire in the wire-grid model is 0.853mm) which the measurements are performed. The ESP code gives excellent results except in the area where possibly the thickness of the corner reflector may play an important role to the RCS.

CONCLUSIONS

Comparisons of the field computations by the use of the NEC and the ESP code show that although the NEC is developed from a line integral formulation, it still works very well in modeling the surface with certain types of wire-grid techniques. It is even more accurate and efficient when it is used to model electrically small scattering objects. The ESP code performs extremely well for solid flat surfaces, except possibly in regions where the thickness may play an important role.

ACKNOWLEDGEMENT

The authors would like to thank George Barber, George Stech and Tom Campell for their interests and continuous supports of our research projects. This work was funded by NASA Langley Research Center under Grant NAG-1-562.

REFERRENCES

1. G. J. Burke and A. J. Poggio, "Numerical electromagnetic code (NEC)-Method of moments Parts I, II and III,". Naval Ocean Systems Center, San Diego, CA, NOSC TD 116 (revised), 1980.

2. Arthur C. Ludwig, " Wire grid modeling of surfaces," *IEEE Trans. Antennas Propagat.*, vol. AP-35, pp.1045-1048, September, 1987.

3. Edmund K. Miller, " A selective survey of computational Electromagnetics," *IEEE Trans. Antennas Propagat.*, vol. AP-36, pp.1281-1305, Sept., 1988.

4. E. H. Newman, " A user's manual for electromagnetic surface patch code (ESP)", Ohio State Univ. Electro Sci. Lab., Rep. 7134021-1, Dept. of Elect. Eng. prepared under Contract DAAG39-81-K-0020 for the Department of Army, U.S. Army Res. Office, Res. Triangle Park, NC. July, 1981.

5. E. H. Newman, "Polygonal plate modeling of realistic structures," *IEEE Trans. Antennas Propagat.*, vol. AP-32, pp.742-747, July, 1984.

6. J. H. Richmond, "A wire grid model for scattering by conducting bodies," *IEEE Trans. Antennas Propagat.*, vol. AP-14, pp.782-786, Nov., 1966.

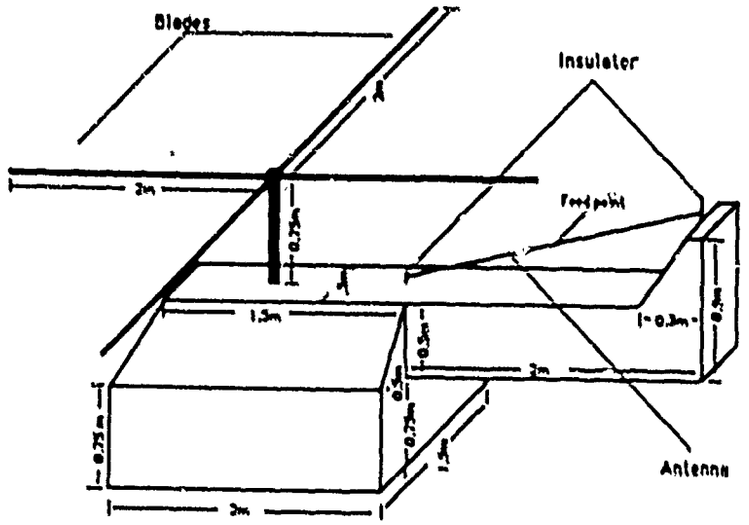


Figure 1. The scaled model of the helicopter.

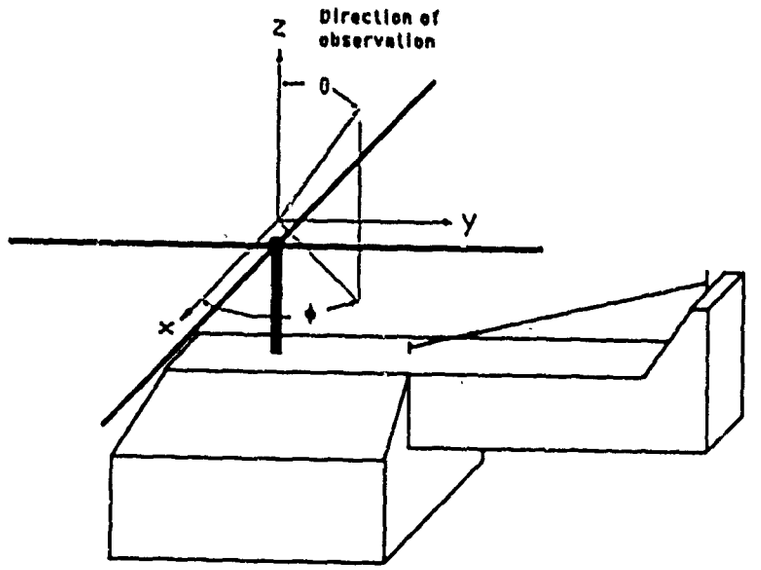


Figure 2. Coordintate system for the helicopter model.

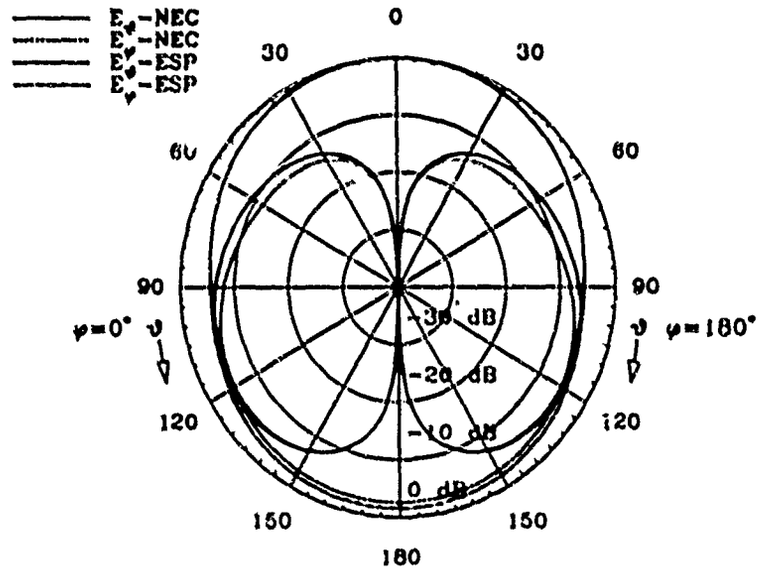


Figure 3. Comparison of roll plane radiation patterns for the helicopter antenna using the NEC and the ESP code. Frequency = 60 MHz.

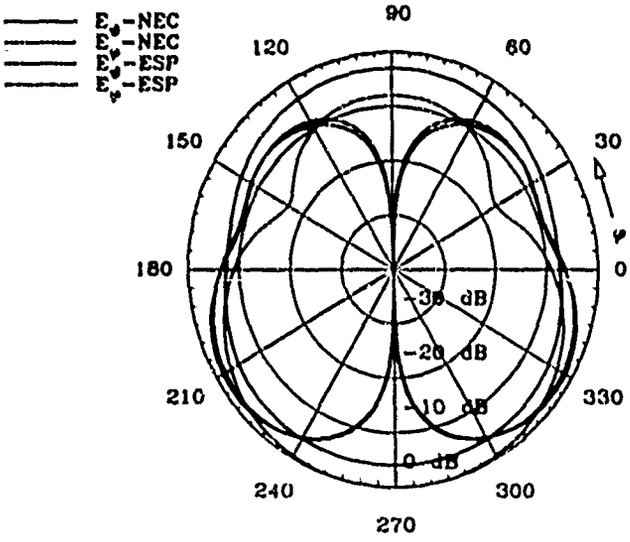


Figure 4. Comparison of yaw plane radiation patterns for the helicopter antenna using the NEC and the ESP code. Frequency = 60 MHz.

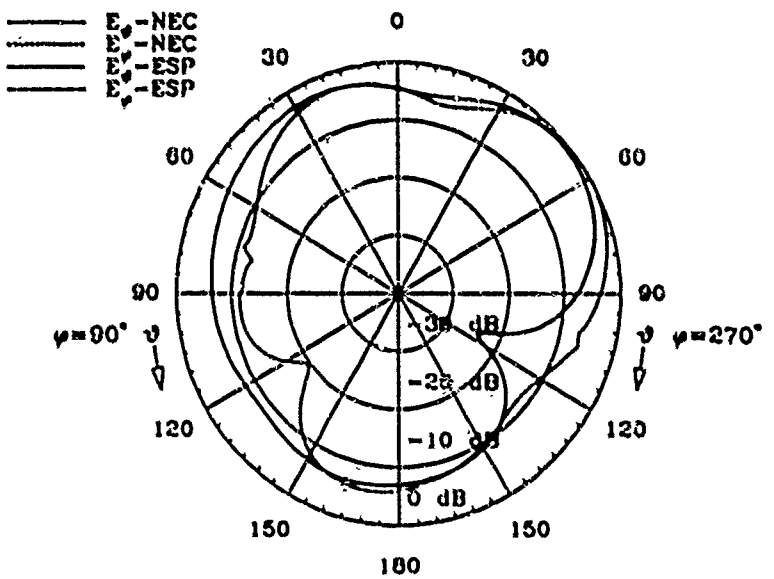


Figure 5. Comparison of pitch plane radiation patterns for the helicopter antenna using the NEC and the ESP code. Frequency=60 MHz.

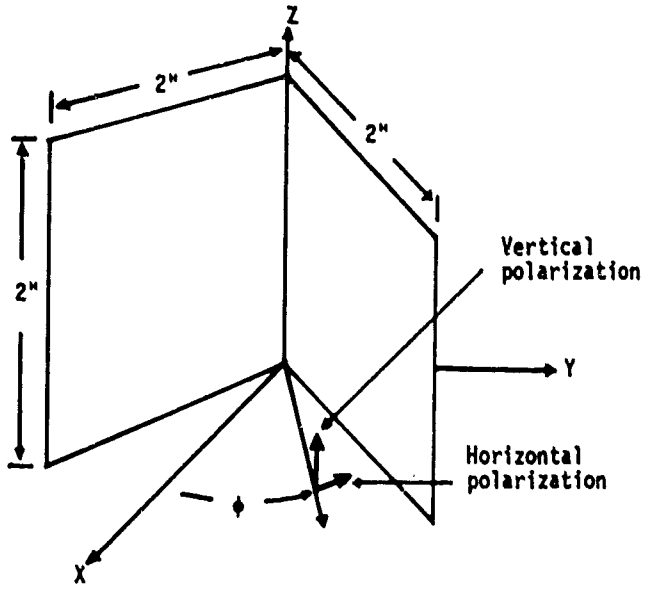


Figure 6. Geometry and coordinate system for a 90-degree dihedral corner reflector.

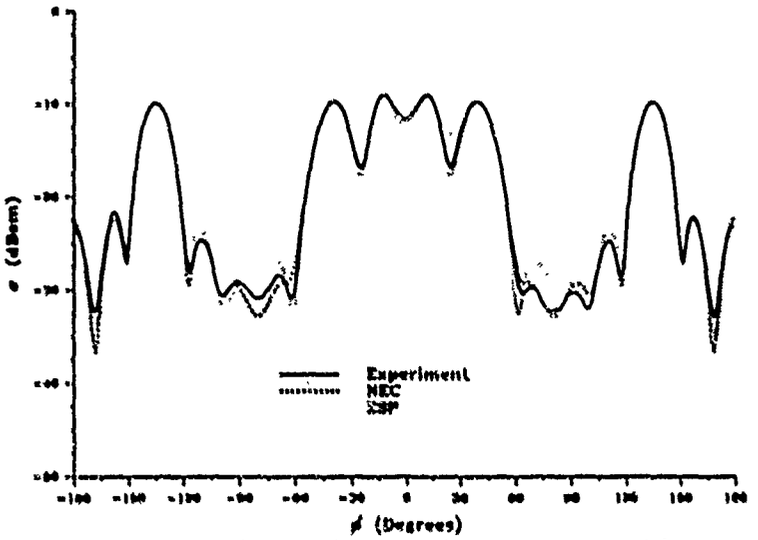


Figure 7. Vertical polarization. Monostatic RCS of a 90° dihedral corner reflector (Frequency = 10 GHz).

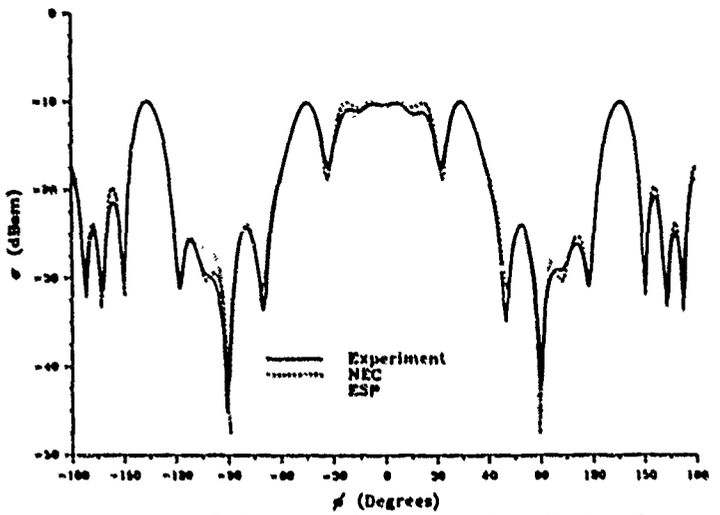


Figure 8. Horizontal polarization. Monostatic RCS of a 90° dihedral corner reflector (Frequency = 10 GHz).

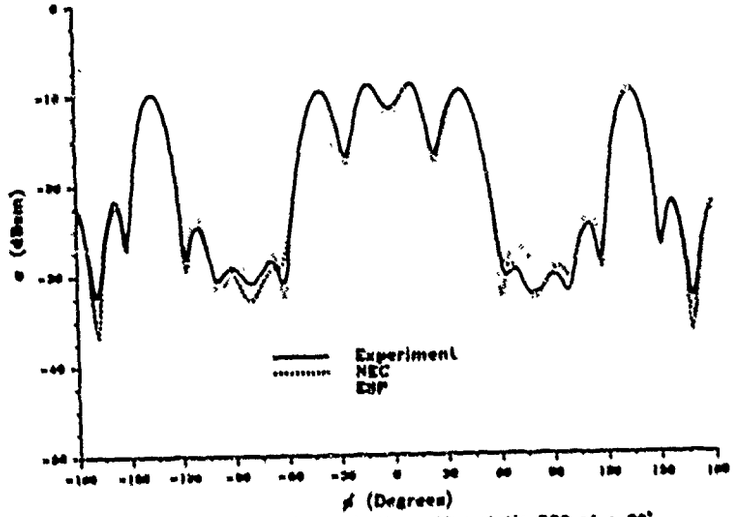


Figure 7. Vertical polarization. Monostatic RCS of a 90° dihedral corner reflector (Frequency = 10 GHz).

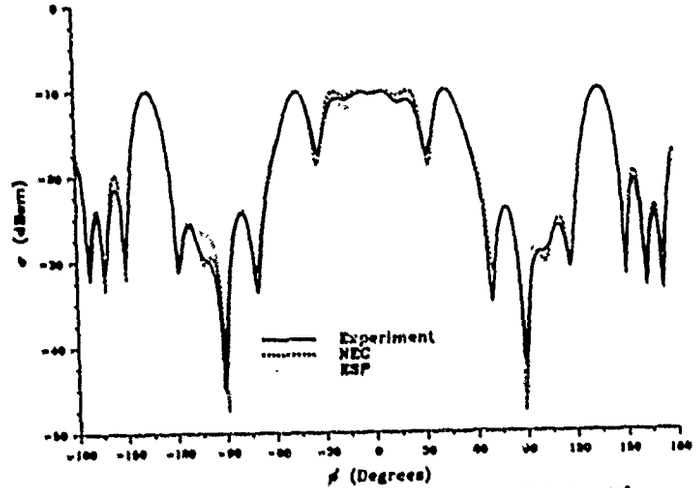


Figure 8. Horizontal polarization. Monostatic RCS of a 90° dihedral corner reflector (Frequency = 10 GHz).

ELECTROMAGNETIC DESIGN CODES MAINTAINED ON THE MFE NETWORK BY THE LAACG*

T. C. Barts, K. C. D. Chan, R. K. Cooper, and M. J. Browman
Los Alamos National Laboratory
Los Alamos, NM 87545

ABSTRACT

The Los Alamos Accelerator Code Group (LAACG) maintains the two- and three-dimensional (2-D, 3-D) MAFIA[1] codes and the POISSON/SUPERFISH codes at the National Magnetic Fusion Energy Computer Center (NMFECC). These codes, principally electromagnetic field solvers, are used for the analysis and design of electromagnetic components, e.g., magnets, radio-frequency (rf) structures, pickups, etc. We will give a brief description of all the codes and explain how they may be accessed via the Magnetic Fusion Energy Network (MFENET).

INTRODUCTION

Two sets of codes useful for the computer-aided analysis and design of 2-D and 3-D electromagnetic structures are installed at the NMFECC. The 2-D MAFIA codes in cylindrical and cartesian coordinates and the 3-D MAFIA codes in cartesian coordinates, written by Thomas Weiland and coworkers of the Deutsches Elektronen-Synchrotron (DESY), constitute the first group. The 2-D POISSON/SUPERFISH group for cartesian and cylindrical coordinates is the second installed group. Klaus Halbach of Lawrence Berkeley Laboratory (LBL) developed the theory and Ronald Holsinger working at LBL and Los Alamos National Laboratory (LANL) did the programming for the POISSON/SUPERFISH group.

NMFECC provides large-scale computational support to the magnetic fusion energy community and the larger energy research community. There are four CRAYs available for users at NMFECC (located at Lawrence Livermore National Laboratory).

Guidelines are given below for obtaining a computer account at NMFECC; for obtaining documentation; for accessing source codes, executable codes, and test problems; for compiling and executing the run-time modules.

Examples Using MAFIA and POISSON/SUPERFISH Codes

A representative use of the MAFIA codes is a study[2] to minimize the power loss density in the four-rod radio frequency quadrupole (RFQ) shown in Fig. 1.

Figure 2 is a plot of the MAFIA model. Only two cells are modeled because the structure is periodic.

The resonant frequency of 398.9 MHz calculated by MAFIA is within 2.1% of the measured value, 407.5 MHz. Figure 3 is a plot of the magnetic fields in the rod region just in front of the middle metal plate. The arrows show the amplitude and direction of the magnetic field in the plane of the plot surface. The size of the circles shows the magnitude of the magnetic field normal to the plot surface. A "·" in the circle shows the tip of the arrow coming towards the reader and the "×" in the circle shows the tail of the arrow

* Work supported by the US Department of Energy (DOE), Office of High Energy and Nuclear Physics.

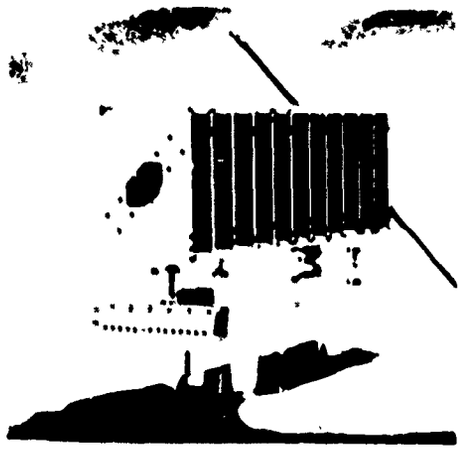


Fig. 1. The four-rod RFQ modeled by the MAFIA codes.

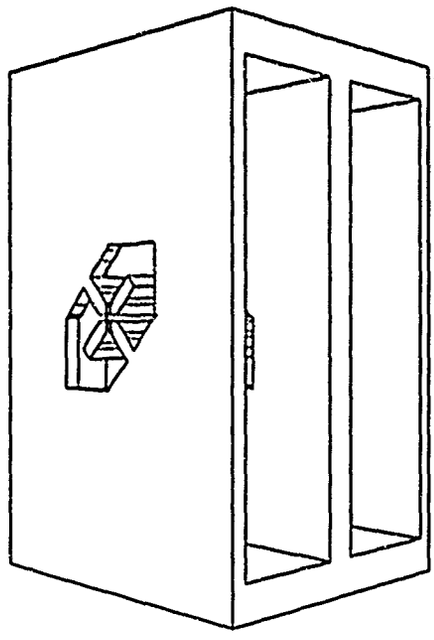


Fig. 2. A plot of the four-rod RFQ model produced by the MAFIA codes.

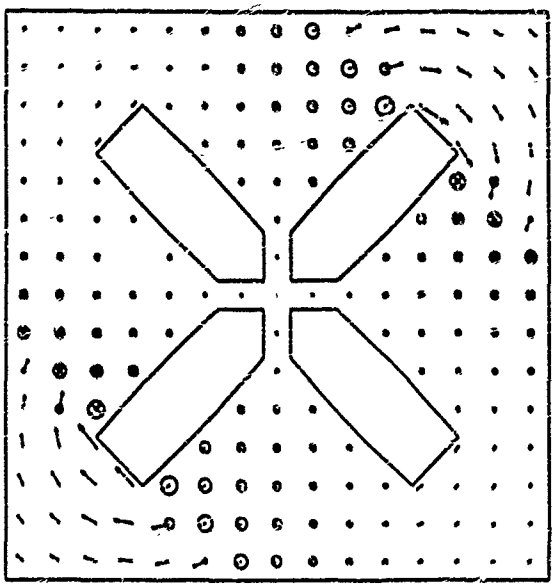


Fig. 3. A magnetic field plot of the rod region just in front of the middle metal plate.

going away from the reader. All of the following magnetic field plots were produced by the MAFIA post-processor.

Figure 4 is a plot of the magnetic field of the entire x-y plane at the middle metal plate of the modeled structure.

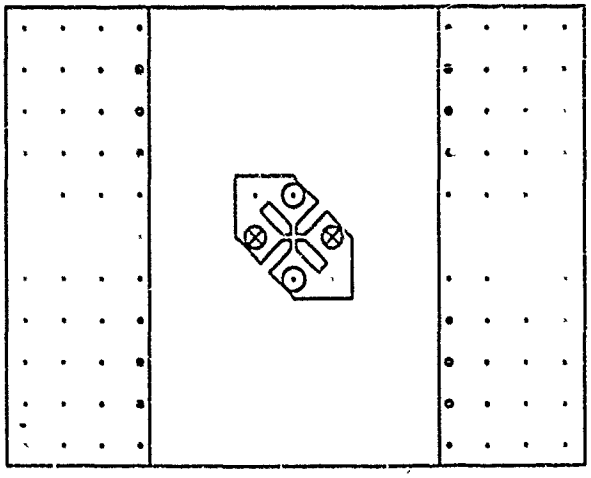


Fig. 4. A magnetic field plot of the entire x-y plane at the middle metal plate.

The enlarged view of the rod region in Fig. 5 shows the peak magnetic fields. From this plot it can be seen that the peak current flow and power loss is concentrated where the rods are connected to the metal plate.

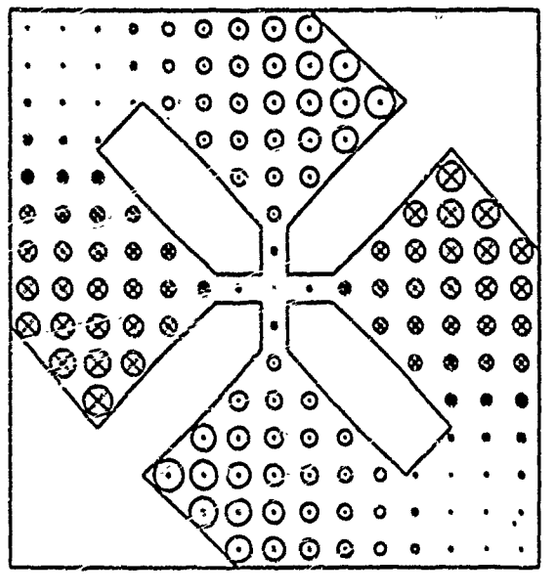


Fig. 6. A magnetic field plot of the rod region at the middle metal plate.

Further modeling showed that increasing the width of the base of the rods reduced the power loss density in that region.

A representative use of the POISSON/SUPERFISH codes is magnet design including H magnets, septum magnets, and quadrupoles. These codes have also been used to calculate electric fields between plates of fixed potential in an infinite pipe, and to calculate the fields at both the center and the fringe of a magnetic geometry. Figure 6 is a plot of the magnetic field lines for a quadrupole magnet calculated with POISSON.

Although it is possible to use only one-eighth of the total geometry because of the symmetry, in this case, one-fourth of the geometry was used.

The Magnetic Fusion Energy Network and Computer Center

The NMFECC, established in 1974, provides large-scale computational support to the magnetic fusion energy community and the larger energy research community. The center facilitates the sharing of information, codes, data, manpower, and computer power among American and Japanese energy researchers.

Currently, the NMFECC user community consists of about 4400 users at about 121 sites throughout the country and Japan. By means of a nationwide communications network MFENET, users may access the following large-scale computers at NMFECC: one CRAY-1 machine (to be phased out shortly), a CRAY XMP 24, and two CRAY-2 machines.

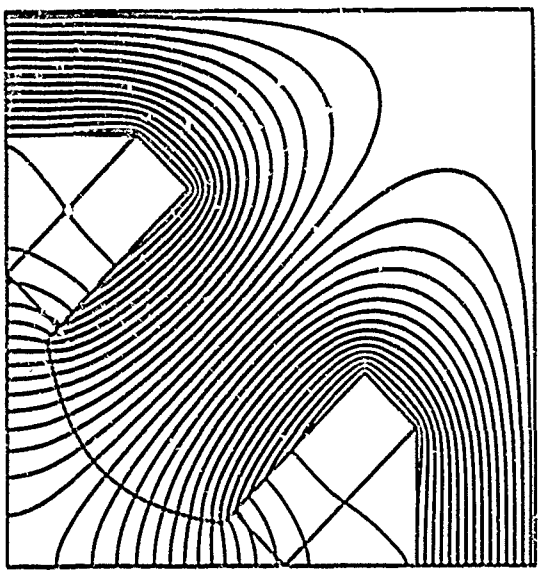


Fig. 6. A plot of the magnetic field lines of one-quarter of a quadrupole.

Machine b, a CRAY-2, has 40 Mwords of memory and 4 CPUs; Machine f, a CRAY-2, has 80 Mwords of memory and 4 CPUs; Machine e, the XMP24, has 1.3 Mwords of memory and 2 CPUs. These computers can be accessed via dial-up lines, TYMNET, INTERNET, Remote User Service Station (RUSS), and/or a VAX on MFENET.

Potential users with no access to an NMFECC account need to contact their DOE monitor to determine eligibility for an account. Those eligible then need to contact Dan Hitchcock at the Office of Energy Research at DOE in Washington, D.C.

New users can be added to existing accounts by having their Principal Investigator contact JoAnne Revelli at NMFECC, phone (415) 422-4228.

Overview of the 2-D and 3-D Mafia Code

The 2-D and 3-D MAFIA Systems

The 2-D and 3-D MAFIA systems are sets of computer programs used for the computer-aided analysis and design of three-dimensional electromagnetic structures including electrostatic and magnetostatic devices, rf cavities, bellows, etc. The programs are the result of an ongoing collaboration between the DESY Laboratory, the Los Alamos National Laboratory, and the Kernforschungs Anlage-Jülich. MAFIA is an acronym for the solution of MAxwell's equations using the Finite Integration Algorithm.[3] This algorithm reduces the integral representation for each of MAxwell's equations to a fully generalized matrix equivalent that is convenient for use in large-scale computers. Solutions can be obtained in either the frequency domain or the time domain. The theory behind the MAFIA codes is well documented.[4–7] The latest versions, 5.0+ for URMEL and TBCI, 2.0+ for URMEL-T and the 3-D MAFIA codes, are installed and maintained at NMFECC. Figure 7 shows a 3-D MAFIA system diagram.

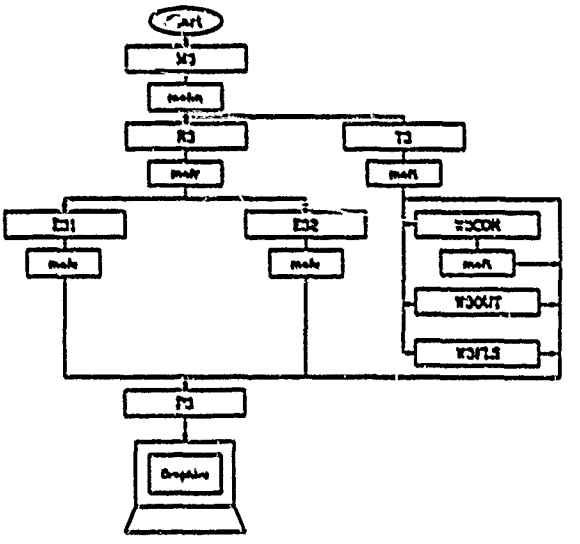


Fig. 7. The 3-D MAFIA system on the NMFECC CRAY computers.

The 2-D MAFIA Codes

URMEL — Version 5.02 calculates TM modes in cylindrically symmetric cavities and cutoff frequencies of waves in longitudinally invariant waveguides. The cavity electromagnetic fields may have any azimuthal dependence. The code uses a variable rectangular mesh, which may be subdivided into triangles. The semianalytic processor (SAP)[8] is used to find the eigensolutions. Plots of the geometry and electric and magnetic fields are available.

URMEL-T — Version 2.01 is similar to URMEL but uses a triangular mesh. It also provides for dielectric and for permeable materials; it calculates TE and TM modes and waveguide propagation constants.

TBCI — Version 5.02 calculates the time-dependent electric and magnetic fields in cylindrically symmetric structures in which charged-particle beams occur. The code also calculates the integrals of the forces acting back upon the particles of the beam as well as force integrals (wake potentials) for test particles accompanying or following the beam. The code uses a square mesh. Plots of the geometry, the electric and magnetic fields, and the wake potential are available.

The 2-D MAFIA Postprocessors

WAKCOR — Version 5.02 calculates the difference between the values of two separate TBCI solutions at identical mesh points. Plots of the resultant wake potential are available.

WAKFLS — Version 5.02 prints the wakefields and wake potentials saved at selected locations for every time step and optionally does a Fourier transform of the fields at selected points.

WAKOUT — Version 5.02 prints the wake potentials saved at selected time steps. Plots of the wake potential are available.

The 3-D MAFIA Preprocessor

M3 — Version 2.02 generates a rectangular variable mesh for the problem geometric data in cartesian coordinates on a direct access (da) file. At NMFECC, the da file is an absolute file. Selected rectangular mesh cells (bricks) can be subdivided into two triangular bricks. Color plots of the geometry, mesh, and materials used are available in 3-D and in 2-D cut planes.

The 3-D MAFIA Codes

R3 — Version 2.01 generates the equations and coefficients for the eigenvalue solvers E31 and E32 and appends them on a copied da file. The R3-E3 combination is the 3-D frequency-domain solver.

E31 — Version 2.02 solves for the eigenvalues and calculates the resonant frequencies and the electric and magnetic fields. The SAP is used to find the solutions. These solutions are appended on a copied da file.

E32 — Version 2.01 generates solutions as E31 but uses a multigrid technique.

T3 — Version 2.03 solves for the electric and magnetic fields in the time domain; it also calculates the integrals of the forces acting back upon the particles of the beam as well as force integrals (wake potentials) for test particles accompanying or following the beam. These solutions are appended on a copied da file.

The 3-D MAFIA Postprocessors

P3 — Version 2.03 analyzes and displays the electric and magnetic field solutions calculated by the main codes and stored on the da file. It provides printouts of the frequencies, field components, electric field energies, power losses, quality (Q) factors, integrals of the field, and net forces for particles with phases 0° and 90° . Color plots are available for the geometry and materials in 3-D and for the electromagnetic fields in 1-D, 2-D, and 3-D.

W3COR — Version 2.02 calculates the difference between the values of two wake potentials at identical mesh points from two separate T3 solutions stored on da files. Plots of the resultant wake potential are available. The calculated difference is appended on a copied da file.

W3FLS — Version 2.02 plots the fields and wake potentials saved at specified points at each time step from a T3 solution stored on a da file. This code optionally calculates a Fourier transform of the fields at selected points.

W3OUT — Version 2.02 prints and plots the scaling function $G(u,v,s)$ for every position s in the beam bunch; also, this code can plot the wake potentials from a T3 solution stored on a copied da file.

Overview of the Poisson/Superfish Group of Codes

The POISSON/SUPERFISH Group of Codes is used in the computer-aided design of magnets and rf structures. These codes provide the user with a choice between cartesian (x,y) coordinates and cylindrical (r,z) coordinates. POISSON calculates magnetostatic and electrostatic fields while SUPERFISH computes the resonant frequencies and fields of circularly-symmetric TM modes in cylindrically symmetric radio-frequency cavities. Dielectric materials and linear magnetic materials can be included in the calculations. These codes use a variable triangular mesh that distorts to fit the problem geometry; the codes are the original eleven programs, the standardized version for the accelerator

community. The latest version, 2.003, November 1, 1988, is installed at NMFECC. Changes include a corrected stored energy ca. . ion[9] in POISSON, PANDIRA, and MIRT; addition of the codes PANT and FORCE; addition of the DISSPLA-based[10] plotting program, DISPLOT, and numerous programming changes bringing the codes closer to FORTRAN77 standards.[11] Figure 8 shows a POISSON/SUPERFISH system diagram.

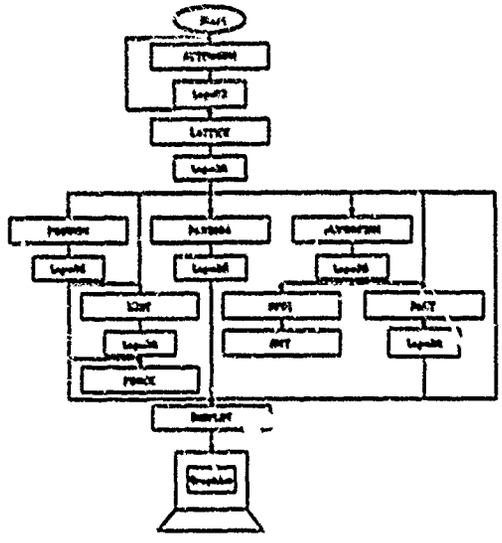


Fig. 8. The POISSON/SUPERFISH system on the CRAY Machine c at NMFECC.

POISSON/SUPERFISH Preprocessors

AUTOMESH generates an ASCII file for input to LATTICE from the problem geometric and material data.

LATTICE generates a binary file, describing the problem to be solved, for input to the main codes.

POISSON/SUPERFISH Codes

POISSON solves Poisson's (or Laplace's) equation for the vector (or scalar) potential for 2-D cartesian geometry or geometry with cylindrical symmetry using "successive point over-relaxation" (SPOR).

PANDIRA is similar to POISSON but uses a direct method of solution.

SUPERFISH solves for the TM resonant frequencies and field distributions in an rf cavity with three-dimensional cylindrical symmetry; it also solves for the cutoff frequencies and mode patterns for a waveguide. For the cylindrically symmetric cavities, the only modes found are azimuthally symmetric.

MIRT optimizes magnet profiles, coil shapes, and current densities based on a field specification defined by the user. The code can be used as a main code or it can use a POISSON or PANDIRA solution as a starting solution.

PANT calculates a thermal distribution in the walls of an rf cavity. The code can be used as a main code or to postprocess a SUPERFISH solution.

POISSON/SUPERFISH Postprocessors

MIRT and *PANT* see above.

FORCE calculates forces on coils and iron regions from a POISSON, PANDIRA, or MIRT solution.

SF01 calculates auxiliary quantities for the design of drift-tube linacs from a SUPERFISH solution.

SHY calculates H_ϕ and the E fields for a specified region from a SUPERFISH and SF01 solution.

TEKPLOT and *DISPLOT* plot the physical geometry and meshes from a LATTICE solution; plot the equipotential lines from a POISSON, PANDIRA, or MIRT solution; plot the field lines from a SUPERFISH solution; or plot the isothermal lines from a PANT solution.

Documentation of the LAACG NMFECC Codes

On-Line Documentation. NMFECC users logged on to any CRAY and wanting basic information on MAFIA and POISSON/SUPERFISH codes may type in

```
cfs get /laacc/info/readme
end
cat readme
```

for a brief description of each code, documentation available, code storage, and information on accessing, compiling, and executing the codes.

NMFECC users logged on to any CRAY may also read the up-to-date messages on the bulletin board, LAACG POISSON MAFIA, by typing

```
bulletin laacg
```

Hard Copy Documentation. MAFIA Documentation: URMEL and URMEL-T User Guide,[12] TBCI Short User Guide,[13] MAFIA User Guide.[14]

POISSON/SUPERFISH Documentation: POISSON/SUPERFISH User's Guide,[15] POISSON/SUPERFISH Reference Manual.[16]

Any of these manuals, code access permission, or a nine-track POISSON/SUPERFISH tape may be requested from the LAACG by messages sent as follows:

NMFECC users logged on to any computer on MFENET may type in

```
tell at6tcb@lmp
```

BITNET users may use the address:

```
at6tcb@lampf
```

U.S. mail requests may be sent to

```
LAACG
AT-6, MS H829
Los Alamos National Laboratory
Box 1663
Los Alamos, NM 87545
```

Storage of LAACG NMFECC Codes

Central File System (CFS). On the Central File System (CFS) there is a root node, `/lacc`. Under `/lacc` are three directory codes: `/info`, `/mafia`, and `/poicodes`. Under `/lacc/info` is the file `/readme`.

CFS MAFIA Storage. Only CRAY-executable MAFIA codes (controllees) are available to NMFECC users. Standard length versions named with an x concatenated to the source code name, for example `xm3`, are available for Machine e and the CRAY-2 machines. In addition, one million point versions are available for the CRAY-2 machines for all MAFIA codes except URMEL-T. URMEL-T is a 350,000 point version. These versions have a + as the last character of their names, for example `xm3+`. The controllees can be found under the node `/lacc/mafia/e` for Machine e and under the node `/lacc/mafia/2` for the CRAY-2 machines. Test problems are found under the latter nodes under the `tps` directory. The controllees are stored for execution at NMFECC.

CFS POISSON/SUPERFISH Storage. Both sources and controllees are stored for POISSON/SUPERFISH codes for the CRAY XMP (Machine e) and also for any VAX running under VMS. File names are identical to those cited in the POISSON/SUPERFISH User's Guide. The CRAY sources are stored under `/lacc/poicodes/cray/src` with names such as `autso`, `latso`, etc. and the CRAY controllees are stored under `/lacc/poicodes/cray/xeq` with names such as `automesh`, `lattice`, etc. Test examples are stored under `/lacc/poicodes/cray/examples` on separate files and in libraries with names such as `poisex` for a complete POISSON run. Output files in the `poisex` library have a `po` appended to their names for example `outautpo`. A cosmos `jci` file with a name such as `jcipo` that will execute the actual run is included in each example library. The source codes are stored for compiling at NMFECC or for file transfer, and the controllees are stored primarily for execution at NMFECC.

VAX sources are stored under `/lacc/poicodes/vax/src` with names such as `autso.for`, `latso.for`. The executables are stored under `/lacc/poicodes/vax/xeq` with names such as `automesh.exe`, `lattice.exe`. Test examples are stored under `/lacc/poicodes/vax/examples` on separate files and in libraries with names such as `poisex.tlb` for POISSON examples. These files are stored at NMFECC primarily for file transfer.

Access of LAACG NMFECC Codes

MAFIA Code Access. Source codes for the MAFIA systems are distributed solely by DESY, Notkestrasse 85, D2000 Hamburg, The Federal Republic of Germany. Requests for hard copies of release forms may be made to `at6tcb@lmp` via MFENET or to `at6tcb@lampf` via BITNET or to the mailing address included in the section on Documentation. Profit-making organizations should expect to negotiate a contract with DESY for use of the MAFIA codes.

POISSON/SUPERFISH Code Access. Anyone with an NMFECC account may have access to the POISSON/SUPERFISH codes. The LAACG requires that a request be made for permission to access either the source or executable codes, but this is only for the purpose of keeping an up-to-date data base of users. Requests may be made to the same network or mailing addresses listed under Hard Copy Documentation.

Execution and compilation of the LAACG—NMFECC Codes

MAFIA Execution. All controllees are stored on CFS as described in the section on storage. To get a controllee in a CRAY local file space type in (for example)

```
cfs get dir=/lacc/mafia/e xm3
end
```

All 2-D and 3-D codes except for P3 require an ASCII input file. The CRAY input files are always the name of the source code concatenated with `in`. For example, the input file for M3 is `m3in`. All the MAFIA codes except P3 (where it is optional) produce an ASCII output (print) file. The output file name is again the source code name concatenated with `out`. URMEL-T is the exception; its ASCII output file is named `urmeltou`. The 3-D MAFIA codes use a da absolute file for intercommunication. That file name is `maf` concatenated with the first letter of the 3-D code name. M3 produces `mafm`, which is used for communication with R3. R3 in turn produces `mafr`, etc. For large problems familying will place on the da files. The scheme used at NMFECC is that if the first file is named `mafm`, for example, then the second is `mafm01`, etc., but the last file has a name ending in x, such as `mafm1x`. Libraries of test examples are in `/lacc/mafia/tps`. For 3-D MAFIA, the file `m3r3e31` contains inputs and outputs for a complete 3-D frequency-domain calculation.

In codes where plots are available, a menu will request that the user select one option from 20 plot options. Some options will be followed by queries for baud rate and box number. The experienced user may select the file substitution option available and freely substitute file names for expected file names and also may type in `po=` for plot option, `baud=` for baud rate, `xob=` for box number right on the execution line. For example, typing in

```
xm3 po=2 xob=q36 mafm=maftest
```

results in `xm3` executing with plot option 2, box number q36; the da file produced will be named `maftest`. File substitution is not available for plot file names.

Input files for test problems can be obtained by typing in (for example)

```
cfs get /lacc/mafia/tps/m3r3e31
end
lib m3r3e31
x
end
```

All input and output files will be in the local file space. Output files will have a 1 appended or substituted for the last character in file names over seven characters long so that comparisons can be made.

POISSON/SUPERFISH Execution. All controllees are stored on CFS as described in the section on storage. To get a controllee in a CRAY local file space type in (for example)

```
cfs get dir=/lacc/poicodes/cray/xeq automesh
end
```

For each test example library included in CFS under `/lacc/poicodes/cray/examples`, there is a `jci` file that will execute with COSMOS. This `jci` file will get all the necessary files from CFS, extract all files from the library, and execute the problem with a running log displayed at the terminal. A log file is also produced for later viewing. Each test example library also has a `readme` file with a more detailed explanation of how the codes run. For example, to run the POISSON test example, type in example, type in

```
cfs get /lacc/poicodes/cray/examples/jcipo
end
cosmos jcipo
```

At NMFECC, all plots are made with the code DISPLOT. A menu similar to the MAFIA initial plotting menu will be displayed and will request that the user select one of the 20 plot options presented. Some options will be followed by queries for baud rate and box number. The experienced user may type in `po=` for the plot option, `baud=` for the baud rate and `xob=` for the box number right on the execution line. For example, typing in

```
displot po=3 baud=9600
```

will result in DISPLOT executing the plot option 3 at 9600 baud. Please note that TEKPLOT based on PLOT10[17] stored in CFS node `/lacc/poicodes/cray/xeq` will not execute at NMFECC and is stored in CFS for file transfer convenience only.

POISSON/SUPERFISH Compilation. All POISSON/SUPERFISH CRAY source codes in local disk space can be compiled on Machine c by typing in (for example)

```
trixgl o(libso) run end
```

The library source code `libso` must be compiled first followed by `poiso`, then the remaining source codes may be compiled in any order.

Up-to-date instructions for compiling on the CRAYs or VAXes will always be available in the `readme` files stored in

```
/lacc/poicodes/cray/info/readme.c
```

or

```
/lacc/poicodes/vax/info/readme.v
```

To transfer files to an MFNET computer type in (for example) `netout libso.for site=lmp user=at6tcb binary`. Use the `binary` option for all file types. If the transfer site is a VAX-VMS, there must be a directory with all world privileges named `user.net`; for the above example: `at6tcb.net`.

References

[1] R. Klatt, F. Krawczyk, W. R. Novender, C. Palm, T. Weiland, B. Steffen, T. Barts, M. J. Browman, R. Cooper, C. T. Mottershead, G. Rodenz, and S. G. Wipf, "MAFIA—A Three-Dimensional Electromagnetic CAD System for Magnets, RF Structures, and Transient Wake-Field Calculations," Proc. 1986 Linear Accelerator Conference, Stanford Linear Accelerator Center report SLAC-303 (June 1986), pp. 276-278.

[2] M. J. Browman, G. Spalek, P. B. Friedrichs, T. C. Barts, "Studies of the Four-Rod RFQ using the MAFIA Codes," Los Alamos National report LA-UR-88-3263, Proceedings of the 1988 Linear Accelerator Conference (October 1988), to be published.

[3] T. Weiland, "On the Numerical Solution of Maxwell's Equations and Applications in the Field of Accelerator Physics," *Particle Accelerators* 15 (4), 245-292 (1984).

[4] T. Weiland, "Numerical Solution of Maxwell's Equation for Static, Resonant and Transient Problems," in *U.R.S.I. International Symposium on Electromagnetic Theory*, Akademiai Kiado, Ed. (Budapest, Hungary, 1986), Part B., pp. 537-542.

[5] T. Weiland, "On the Unique Numerical Solution of Maxwellian Eigenvalue Problems in Three Dimensions," *Particle Accelerators* 17(3-4), 117-242 (1985).

[6] T. Weiland, "Transverse Beam Cavity Interaction, Part I: Short Range Forces," *Nuclear Instruments and Methods* (NIM) 212, 13-34 (1983).

[7] R. Klatt and T. Weiland, "Wake Field Calculations with Three-Dimensional BCI Code," in *Proceedings of the 1986 Linear Accelerator Conference*, Stanford Linear Accelerator Center report SLAC-303 (June 1986), pp.282-285.

[8] J. Tückmantel, "Application of SAP in URMEL," CERN report EF/RF 85-4 (September 1985).

[9] J. Liu and H. A. Thiessen, "A Correction of the Magnetic Stored Energy Calculation for the POISSON Computer Code," (AHF Technical Note 88-008), (Los Alamos, March 1988).

[10] Computer Associates International, "DISSPLA 10.0 User's Manual," (Garden City, New York, 1988).

[11] American National Standards Institute, Inc., "American National Standard Programming Language FORTRAN," (NewYork, 1978).

[12] U. Laustroer, U. van Rienen, T. Weiland, "URMEL and URMEL-T User Guide," DESY-M-87-03 (February 1987).

[13] R. Klatt and T. Weiland, "TBCI Short User Guide," (unpublished) (January 1, 1988).

[14] The Mafia Collaboration, "MAFIA User Guide," Los Alamos National Laboratory (in process).

[15] M. T. Menzel, H. K. Stokes, "User's Guide for the POISSON/SUPERFISH Group of Codes," Los Alamos National Laboratory report LA-UR-87-115 (January 1987).
[16] Los Alamos Accelerator Code Group, "POISSON/SUPERFISH Reference Manual," Los Alamos National Laboratory report LA-UR-87-126 (January 1987).
[17] Tektronix Incorporated, "PLOT 10 Terminal Control System User's Manual," (Beaverton, Oregon, 1979)

A COMPARISON OF THE PATCH, JUCTION AND NEC CODES : ADMITTANCE AND NEAR FIELDS FOR A WHIP-ON-A-BOX

PANAGIOTIS ELLINIADIS
Hellenic Navy
RICHARD W. ADLER
and
JAMES K. BREAKALL
Naval Postgraduate School

ABSTRACT

Recently, the measured and calculated input impedances were presented for a monopole attached at various locations to a conducting box over perfect ground. The PATCH code (featuring an electric field integral equation surface patch formulation) produced the calculated values. This provide us a benchmark for a comparison study of wire grid and magnetic field integral equation surface patch modeling via NEC. The near field capability of NEC was exercised for gaining experience in predicting RADHAZ conditions for Navy HF shipboard antennas.

Early indications for whips-on-boxes suggested three things :

(1) Surface patch models were preferable from a computational efficiency standpoint when the whip was mounted a quarter wavelength away from edges.

(2) Wire grid models required more computational resources but were necessary for edge- and corner-mounted whips, and

(3) The coarseness of the uniform patch current model and the discretely distributed currents of the wire grid model gave cause for apprehension concerning the correctness of the near fields they produced. In this exercise, however, the NEC-produced near electric fields turned out to be quite credible when modeling parameters were carefully selected.

A developmental version of JUNCTION (a new wire-patch code) was exercised for near fields and the results compared to those of NEC.

INTRODUCTION

The admittance and the electric near fields of a monopole antenna ($\lambda/5$) mounted on a cubical box ($\lambda/3$ per side) over a perfectly conducting ground plane as shown in Figures 1a and 1b were evaluated using the Numerical Electromagnetics Code (NEC) [1,2]. Surface patch and wire grid models of the box were employed. The monopole was positioned at the center, the edge, and at a corner of the box top surface. The results from NEC were obtained and compared with experimental data and results from PATCH another independent electromagnetic modeling code [3]. Contour and 3-D amplitude and phase plots of the near electric fields are presented for the surface patch and wire

grid models and conclusions are presented. Efficiency and computational resource demands are discussed for both approaches and guidelines are presented. A new version of the PATCH code, JUCTION, is discussed with some comparative preliminary results.

BACKGROUND

Monopoles are often used as antennas on the Navy shipboard topside and are located near edges and corners of the super-structure. Measurements and PATCH code results have been previously reported for the admittance characteristics of a monopole antenna mounted on a simple conducting cubical box over a ground plane which simulates the topside environment of a ship [4]. This approach can therefore be realistically extended to predict RADHAZ conditions on actual ship models. This paper presents NEC admittance comparisons as well as further NEC results of near fields using both surface patch and wire grid models. Additionally JUNCTION code results are presented and compared using some very recent modeling exercises.

RESULTS

To find the optimum density of patches, the number on the top of the box was varied until convergence was obtained. For each position of the monopole a frequency sweep of 40% (initial frequency = 1 GHz) was used. In Figures 2, 3, and 4 NEC results versus measurements and the PATCH code for

admittance for the monopole at the center, the edge, and the corner are presented. For the three different mounting geometries optimum NEC models were found to be :
CENTER : 9 by 9 or 81 total patches on the top of the box ($0.0013\lambda^2$ patch area), EDGE and CORNER : 11 by 11 or 121 patches on the top ($0.0009\lambda^2$ patch area).

To plot the magnitude and phase of the near electric field for the three different mounting geometries FORTRAN algorithms were developed using NEC output data. The contour plot of magnitude of the total electric field is presented in Figure 5 for the monopole at the center. The main lobe starts to develop at a distance 2λ (0.6 meters) from the antenna along the x axis with a maximum occurring at an elevation angle of 60°. Box re-radiation and diffraction causes a deep null to occur at an elevation angle of 27° from the box surface. A 3-dimensional plot is presented in Figure 6 in order to give better insight about the electric near field variations. The phase variation of the z-component of the electric field shown in Figure 7 displays a spherical wavefront pattern except for the region of the null. Wire grid modeling of these geometries gave essentially identical results to those above using surface patches. This attests to the equivalence of the two numerical techniques in NEC (less than 2 dB differences).

The computer time required for the wire grid solutions took six times the CPU time as that of the surface patch solution for similar convergence.

An opportunity to test a new electric field integral equation surface patch code arose. JUNCTION, a code based on PATCH but with the addition of wires, was being extended to include near electric field calculations [5,6]. A preliminary version was provided by Professor D. R. Wilton of the University of Houston. The initial problem input to JUNCTION was the monopole center-mounted on the conducting box as shown in Figure 8. The near field results were totally unrealistic compared with those of NEC. Input admittance values were also in error as seen in Figure 9.

Utilizing more basic geometries produced very good agreement with NEC and MININEC for simple dipoles and monopoles as shown in Figures 10 and 11. As can be observed from this figure JUNCTION needs 20 segments to obtain convergence similar to MININEC for the same geometry. An example of a whip on a flat plate in free space from the JUNCTION Manual [6] yielded excellent results, as seen in Figures 12 and 13 for conductance and susceptance. Retrying the input data sequence for the whip on the box (increasing the patch and segment density) did not help the initial problem. A careful check of the input geometry and the output listing did not reveal any errors.

CONCLUSIONS

Surface patch and wire grid modeling techniques using NEC can both be applied to accurate near field prediction of antennas in complex environments as demonstrated in the

present study. Guidelines for both models have been developed in this paper, as well as the results of the near field behavior of the monopole on the conducting box. This information can be used for future investigations on "ship-like" structures [2].

Although this initial test of the JUNCTION (near field version) code was not successful, the basic JUNCTION code has been shown to perform as well as the PATCH code [3].
Once the explanation and correction of errors is found, JUNCTION (near field version) should be most useful for cases such as open structures which NEC's surface patch model cannot handle. The JUNCTION code seems to require more unknowns per square wavelength. For example, the conducting box/monopole model of a 6x6 patch top surface, four 4x6 patch sides, and a 15 segment monopole required 424 edges (unknowns) compared to 265 for NEC [2].

REFERENCES

1. Burke, G.J. and Poggio, A.J., Naval Ocean Systems Center Technical Document 116, Numerical Electromagnetics Code (NEC) - Method of Moments, January 1981.

2. Elliniadis, P., An Investigation of Near Fields for HF Shipboard Antennas - Surface Patch and Wire Grid Modeling Using the Numerical Electromagnetics Code, Master's Thesis, Naval Postgraduate School, Monterey, California, December 1988.

3. Johnson, W.A., Wilton, D.R., and Sharpe, R.M., Sandia National Laboratories Report SAND87-2991, Patch Code User's Manual, May 1988.

4. Bhattacharya, S., Long, S.A., and Wilton, D.R., The Input Impedance of a Monopole Antenna Mounted on a Cubical Conducting Box, IEEE Transactions on Antennas and Propagation, Vol. AP-35, No. 7, pp. 756-761, July 1987.

5. Wilton, D.R., and Hwu, S.U., Naval Ocean Systems Center Technical Document 1324, Junction Code User's Manual, August 1988.

6. Wilton, D.R., and Hwu, S.U., Naval Ocean Systems Center Technical Document 1325, Electromagnetic Scattering and Radiation by Arbitrary Configurations of Conducting Bodies and Wires, August 1988.

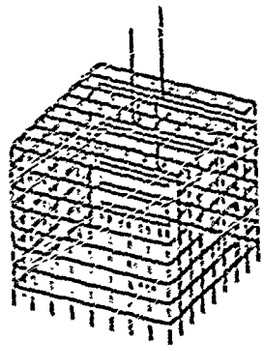


Fig. 1a. Monopole at Center, Edge and Corner of the Cubical Box. NEC, Wire Grid Model.

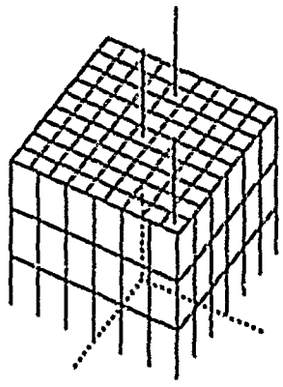


Fig. 1b. Monopole at Center, Edge and Corner of the Cubical Box. NEC, Surface Path Model.

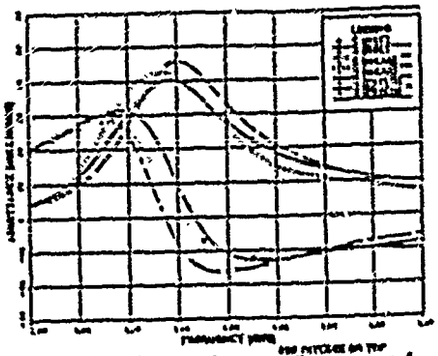


Fig. 2. Monopole at Center of Patch Box.

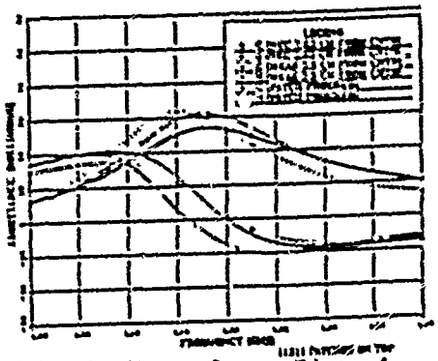


Fig. 3. Monopole at Edge of Patch Box.

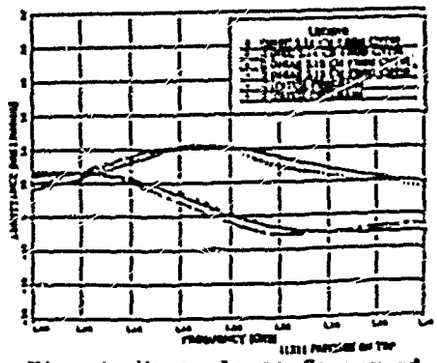


Fig. 4. Monopole at Corner of Patch Box.

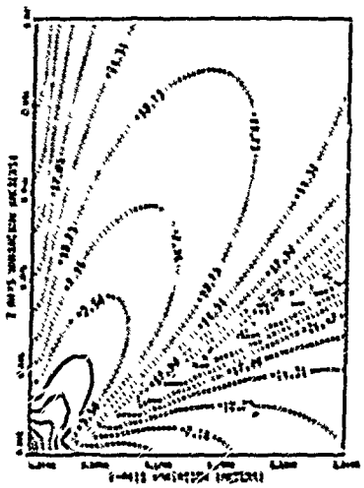


Fig. 5. Total E-Field Contours
(dB Ref. to 1 V/m)
Monopole at Box Center.

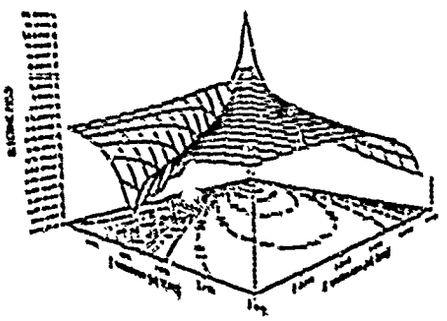


Fig. 6. Total E-Field 3-D Plot
(dB Ref. to 1 V/m)
Monopole at Box Center.

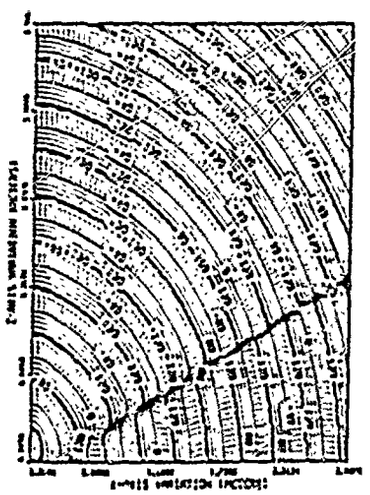


Fig. 7. Z-Component, E-Field
Phase Contours
Monopole at Box Center.

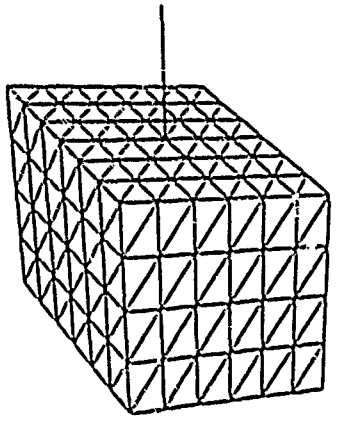


Figure 8. Monopole at Center of the Cubical Box. JUNCTION Code Model.

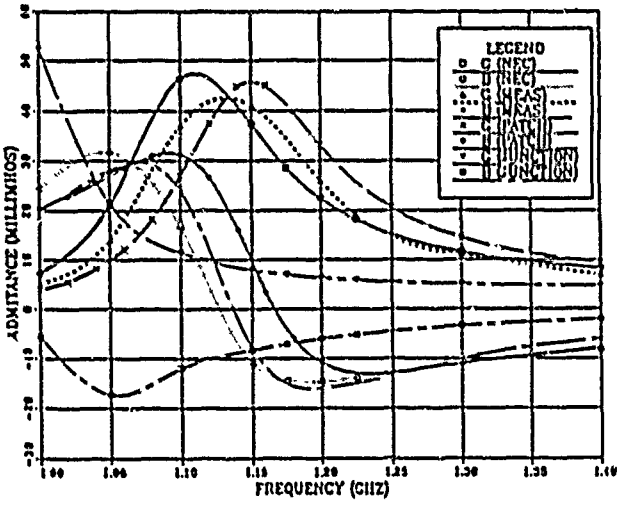


Figure 9. Monopole at Center of the Cubical Box. Admittance Comparison Between: Measurements; and NEC, PATCH, and JUNCTION Codes.

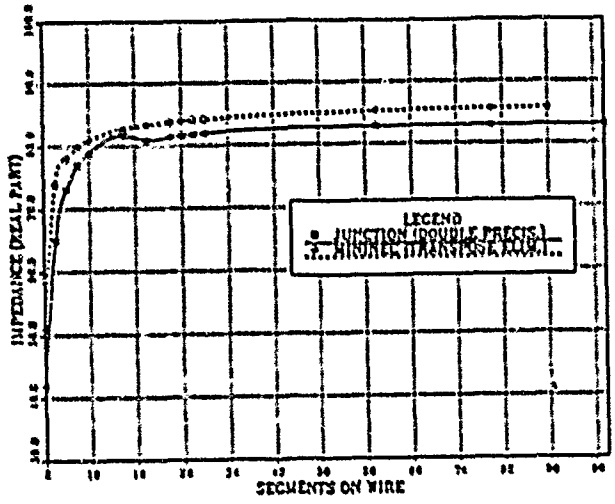


Figure 10. Half-wave Dipole in Free Space. Convergence of JUNCTION vs. MININEC for Impedance (Real Part).

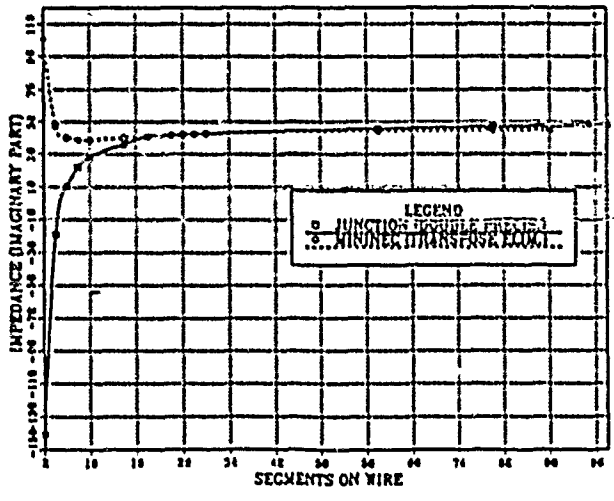
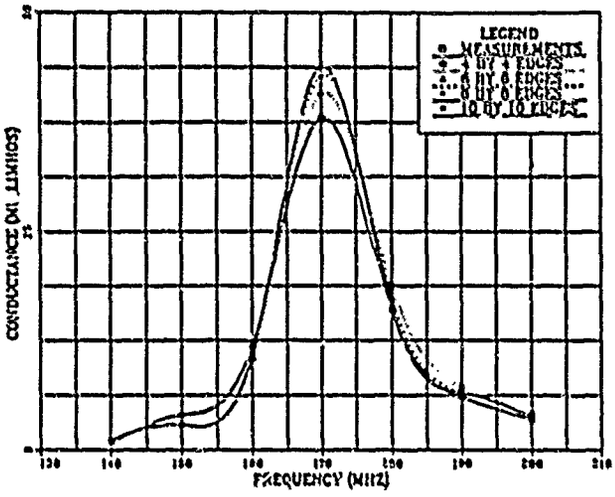


Figure 11. Half-wave Dipole in Free Space. Convergence of JUNCTION vs. MININEC for Impedance (Imaginary Part).



Figfure 12. Monopole at the Center of a Flat Plate in Free Space. JUNCTION Results for Conductance as the Patch Density Varies.

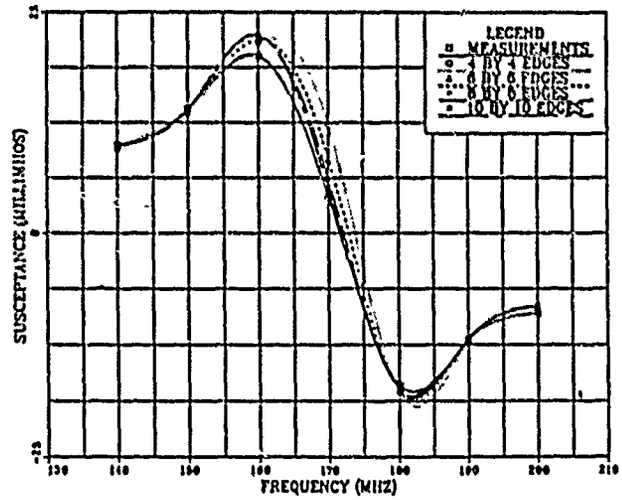


Figure 13. Monopole at the Center of a Flat Plate in Free Space. JUNCTION Results for Susceptance as the Patch Density Varies.

EMPACK: Building Block Subroutines for the Method of Moments

D. R. Wilton*, S. V. Yesantharao,
C. M. Cheng, and R. M. Sharpe
Dept. of Electrical Engineering, University of Houston
University Park, Houston TX 77004

1. Abstract. The basic steps in the solution of electromagnetic field problems by the method of moments are the following:

- Reading in the problem geometry information and other problem parameters, and setting up any auxiliary tables needed to fill the moment matrix.
- Assembling the moment matrix.
- Assembling the right hand side forcing function
- Solving the resulting system of equations for actual or equivalent sources.
- Computing desired quantities from the sources.
- Writing out problem input and computed data.

EMPACK is a library of FORTRAN subprograms currently being developed to perform most of these tasks. For example, it contains a set of subroutines to read in data describing discretized contours, surfaces, and volumes in a standardized format. For contours, provisions are made for simultaneously specifying several segment attributes (e.g., wire radii, segment radius of curvature, or surface impedance), and node attributes (e.g., voltage sources or lumped loading impedances). Similar provisions are made for specifying vertex, edge, face, and cell attributes for surfaces and volumes. To aid in the matrix assembly, subprograms are being developed to identify and tag contour and surface junctions, and to set up tables mapping potential integral contributions from source and observation point pairs defined on nodes, edges, faces, or cells, to appropriate moment matrix locations. Other mapping tables, such as for defining trees and loops for the decomposition of basis functions into divergence- and curl-free parts, are planned.

A set of subprograms has already been developed to evaluate potential integrals and their gradients for uniform and linearly varying source distributions defined on simply shaped domains. Such domains include linear wire and cylinder segments, planar triangular and rectangular surfaces, conical segments with $\exp(jm\phi)$ phase variation, triangular prisms of infinite and finite extent, and rectangular and tetrahedral cells. Practically all electromagnetic field quantities can be expressed in terms of these integrals.

Since EMPACK can perform many of the subtasks required in the method of moments, it frees the code developer from being overly concerned with the details of the task, leaving him to concentrate on the analytical and numerical formulation of a problem. Its flexibility also allows him to experiment with alternative numerical approaches. And while the resulting code cannot be optimum for a specific problem, it can serve as a developmental platform and a validation tool for a more problem-specific code.

2. Numerical Representation of Electromagnetic Fields. Electric and magnetic fields can be represented in a standardized form that requires only the computation of scalar potentials and their gradients due to piecewise-linear and piecewise constant source distributions on simply shaped domains. The expressions obtained are valid everywhere, including in source regions.

We first define the symbol $\mathcal{D}$ to represent a domain which may be either a curve ($\mathcal{C}$), a surface ($\mathcal{S}$), or a volume ($\mathcal{V}$). For numerical purposes, we presume that $\mathcal{C}$ is approximated by piecewise linear segments; that $\mathcal{S}$ is approximated by planar triangular or rectangular patches, conical frusta, or tubular segments; or that $\mathcal{V}$ is approximated by rectangular, tetrahedral, or right triangular prismatic cells. The segments, patches, frusta, or cells into which $\mathcal{D}$ is divided are called *elements*. Fig. 1. attempts to depict a pair of adjacent elements with a common element subboundary $\mathcal{C}_n$. If $\mathcal{D} \equiv \mathcal{S}$, the figure might represent adjacent rectangular and triangular elements, or possibly adjacent tubular and conical elements. If $\mathcal{D} \equiv \mathcal{V}$, it might represent the side view of a rectangular cube or a prism adjacent to a second prism. Stretching the free vertices of these elements to infinity in directions either transverse or normal to $\mathcal{C}_n$ results in infinite strips or in infinite prisms of triangular or rectangular cross section which are used to model cylindrical structures. If $\mathcal{D} \equiv \mathcal{C}$, we shrink $\mathcal{C}_n$ to a point and view the figure as representing two adjacent line segments.

In a homogeneous, isotropic, source free material region, all fields may be computed from equivalent electric and/or magnetic surface currents on the region's boundaries. Inhomogeneous regions may be represented in terms of volume electric and magnetic polarization currents. If these currents are known, the electromagnetic problem can be reduced to the computation of fields from these currents. In a solution by the Method of Moments (MoM), however, these sources are equivalent sources which become the unknowns in an integral equation formulation. The computation of electric and magnetic fields due to these equivalent currents is most conveniently performed by using electromagnetic potentials. Hence we are led to consider the fields due to electric currents $J_{\mathcal{D}}$ and magnetic currents $M_{\mathcal{D}}$ representing line, surface, or volume currents for $\mathcal{D} \equiv \mathcal{C}, \mathcal{S}$, or $\mathcal{V}$, respectively. The fields are given in terms of magnetic vector, electric scalar, electric vector, and magnetic scalar potentials A, Φ, F, and Ψ, respectively, as

$$E = -j\omega A - \nabla\Phi - \frac{1}{\epsilon}\nabla \times F \tag{1}$$

$$H = -j\omega F - \nabla\Psi + \frac{1}{\mu}\nabla \times A \tag{2}$$

where

$$A(\mathbf{r}) = \mu \int_{\mathcal{D}} J_{\mathcal{D}}(\mathbf{r}') \frac{e^{-jkR}}{4\pi R} d\mathcal{D}' \tag{3}$$

$$F(\mathbf{r}) = \epsilon \int_{\mathcal{D}} M_{\mathcal{D}}(\mathbf{r}') \frac{e^{-jkR}}{4\pi R} d\mathcal{D}' \tag{4}$$

$$\Phi(\mathbf{r}) = \frac{1}{\epsilon} \int_{\mathcal{D}} q_{\mathcal{D}}(\mathbf{r}') \frac{e^{-jkR}}{4\pi R} d\mathcal{D}' \tag{5}$$

$$\Psi(\mathbf{r}) = \frac{1}{\mu} \int_{\mathcal{D}} m_{\mathcal{D}}(\mathbf{r}') \frac{e^{-jkR}}{4\pi R} d\mathcal{D}'. \tag{6}$$

The charge densities $q_{\mathcal{D}}, m_{\mathcal{D}}$ are related to $J_{\mathcal{D}}$ and $M_{\mathcal{D}}$ through the equation of continuity,

$$q_{\mathcal{D}} = -\frac{1}{j\omega}\nabla_{\mathcal{D}} \cdot J_{\mathcal{D}} \tag{7}$$

$$m_{\mathcal{D}} = -\frac{1}{j\omega}\nabla_{\mathcal{D}} \cdot M_{\mathcal{D}}, \tag{8}$$

with a suitable interpretation of the divergence operator. Any electric or magnetic currents present may be approximated by means of a linear combination of known functions $A_n^{\mathcal{D}}$ (basis functions or expansion functions). For the electric current, for example,

$$J_{\mathcal{D}}(r) = \sum_{n=1}^{N} J_n \Lambda_n^{\mathcal{D}}(r) \tag{9}$$

where the constants J_n represent the current crossing the boundary $\mathcal{E}_n$ between and directed from the element $\Delta\mathcal{D}_{n+}$ to $\Delta\mathcal{D}_{n-}$ of Fig. 1. A basic function $\Lambda_n^{\mathcal{D}}$ is associated with each $\mathcal{E}_n$ and is defined as follows:

$$\Lambda_n^{\mathcal{D}}(r) = \begin{cases} \frac{\rho_{n\pm}}{h_{n\pm}} & , r \text{ in } \Delta\mathcal{D}_{n\pm} \\ 0 & \text{otherwise.} \end{cases} \tag{10}$$

It can be shown that $\Lambda_n^{\mathcal{D}}$ can be represented as a linear combination of vectors of constant direction and linearly varying amplitude as,

$$\frac{\rho_{n\pm}}{h_{n\pm}} = \frac{1}{h_{n\pm}} \sum_{i=1}^{l_{n\pm}} \sigma_{n\pm}^{i} \xi_{n\pm}^{i} \zeta_{n\pm}^{i} \tag{11}$$

where $\zeta_{n\pm}^{i}$ are linear vectors associated with the edges of $\Delta\mathcal{D}_{n\pm}$ not belonging to $\mathcal{E}_n$ as shown in the Fig. 1, and the $\xi_{n\pm}^{i}$ are normalized coordinates which vary linearly across $\Delta\mathcal{D}_{n\pm}$. Substituting $J_{\mathcal{D}}$ from (9) in (3) to obtain

$$A(r) = \mu \sum_{n=1}^{N} J_n \int_{\Delta\mathcal{D}} \Lambda_n^{\mathcal{D}}(r') \frac{e^{-jkR}}{4\pi R} d\mathcal{D}' \tag{12}$$

Substituting $\Lambda_n^{\mathcal{D}}$ from (10) and (11) in (12), we obtain

$$A(r) = \mu \sum_{n=1}^{N} J_n \left[\sum_{i=1}^{l_{n+}} \frac{\sigma_{n+}^{i} \zeta_{n+}^{i}}{h_{n+}} \psi_i^{\Delta\mathcal{D}_{n+}}(r) + \sum_{i=1}^{l_{n-}} \frac{\sigma_{n-}^{i} \zeta_{n-}^{i}}{h_{n-}} \psi_i^{\Delta\mathcal{D}_{n-}}(r) \right] \tag{13}$$

where $\psi_i^{\Delta\mathcal{D}_{n\pm}}$ is defined below. Since

$$\nabla_{\mathcal{D}} \cdot \Lambda_n^{\mathcal{D}} = \begin{cases} \pm \frac{\rho_{n\pm}}{h_{n\pm}} & , r \text{ in } \Delta\mathcal{D}_{n\pm} \\ 0 & \text{otherwise} \end{cases}$$

$$= \frac{\sigma_{n+}}{h_{n+}} \Pi_{n+}^{\mathcal{D}}(r) - \frac{\sigma_{n-}}{h_{n-}} \Pi_{n-}^{\mathcal{D}}(r) \tag{14}$$

where $\Pi_{n\pm}^{\mathcal{D}}(r)$ is a unit pulse function in $\Delta\mathcal{D}_{n\pm}$, the quantity $\sigma_{n\pm}$ is defined as

$$\sigma_{n\pm} = \begin{cases} \dim(\Delta\mathcal{D}_{n\pm}), \text{ on simplex domains,} \\ 1 \text{ on rectangular or cubical domains,} \end{cases} \tag{15}$$

and $\dim(\Delta\mathcal{D}_{n\pm})$ is the spatial dimension of $\Delta\mathcal{D}_{n\pm}$ (= 1, 2, or 3 for $\mathcal{D} = \mathcal{C}, \mathcal{S}$, or $\mathcal{V}$, respectively). Thus charge distributions are approximated as piecewise constant. We have from (5), (7), (9), and (14)

$$\Phi(r) = \frac{-1}{j\omega\epsilon} \sum_{n=1}^{N} J_n \left[\frac{\sigma_{n+}}{h_{n+}} \psi^{\Delta\mathcal{D}_{n+}}(r) - \frac{\sigma_{n-}}{h_{n-}} \psi^{\Delta\mathcal{D}_{n-}}(r) \right] \tag{16}$$

where $\psi^{\Delta\mathcal{D}_{n\pm}}$ is defined below. From (13) we obtain

$$\nabla \times A(r) = \mu \sum_{i=1}^{N} J_n \left[\sum_{i=1}^{l_{n+}} \frac{\sigma_{n+}^{i}}{h_{n+}} \nabla\psi_i^{\Delta\mathcal{D}_{n+}}(r) \times \zeta_{n+}^{i} + \sum_{i=1}^{l_{n-}} \frac{\sigma_{n-}^{i}}{h_{n-}} \nabla\psi_i^{\Delta\mathcal{D}_{n-}}(r) \times \zeta_{n-}^{i} \right] \tag{17}$$

and from (16),

$$\nabla\Phi(r) = \frac{-1}{j\omega\epsilon}\sum_{n=1}^{N} J_n\left[\frac{\sigma_{n+}}{h_{n+}}\nabla\psi^{\Delta D_{n+}} - \frac{\sigma_{n-}}{h_{n-}}\nabla\psi^{\Delta D_{n-}}\right]. \tag{18}$$

Using (13), (17), and (18) in (1) and (2), we can compute E, H for electric sources. Similar expressions for the contributions to these fields from any magnetic sources present can be obtained by duality. A key observation is that *the problem of computing the fields is thus reduced to the evaluation of scalar potential integrals due to linear and constant source density distributions,*

$$\psi_l^{\Delta D_{n\pm}}(r) = \int_{\Delta D} \xi_{n\pm}^l \frac{e^{-jkR}}{4\pi R} dD' \tag{19}$$

and

$$\psi^{\Delta D_{n\pm}}(r) = \int_{\Delta D} \frac{e^{-jkR}}{4\pi R} dD', \tag{20}$$

and their gradients. For efficiency, $\psi_l^{\Delta D_{n\pm}}$, $\psi^{\Delta D_{n\pm}}$, and their gradients are evaluated simultaneously.

EMPACK currently includes FORTRAN subprograms to compute static and dynamic scalar potential integrals for linear and constant source densities over the following domains:

- Wire segments
- Strip segments
- Conical frusta with $e^{jm\phi}$ circumferential variation
- Rectangular patches
- Triangular patches
- Tetrahedra
- Rectangular cubes
- Triangular prisms

In order to model surface vertex junctions, the potential due to a $1/\rho$ distribution on a triangular patch is also available. The static form of most of the above integrals may be written in closed form [2].

3. Examples.

In the following sections we show how the results of the previous section may be specialized to treat several specific cases.

3.1 Electrostatics—Conducting Body Charged to a Constant Potential. The equations of electrostatics follow from the previous section by setting all currents and the frequency to zero. Thus, we have,

$$E = -\nabla\Phi \tag{21}$$

where

$$\Phi(r) = \frac{1}{\epsilon}\int_D q_D(r')\frac{1}{4\pi R} dD'. \tag{22}$$

As implied by (14), a piecewise linear approximation to the charge may be represented in terms of the pulse functions $\Pi_n^D(r)$. Hence,

$$q_D(r) = \sum_{n=1}^{N} q_n \Pi_n^D(r), \tag{23}$$

where q_n is the charge density in $\Delta\mathcal{D}_n$ and

$$\Pi_n^{\mathcal{D}}(\mathbf{r}) = \begin{cases} 1 & , \mathbf{r} \text{ in } \Delta\mathcal{D}_n \\ 0 & \text{otherwise.} \end{cases} \tag{24}$$

In terms of q_n, the potential in (22) becomes

$$\Phi(\mathbf{r}) = \frac{1}{\epsilon}\sum_{n=1}^{N} q_n \psi^{\Delta\mathcal{D}_n}(\mathbf{r}), \tag{25}$$

where

$$\psi^{\Delta\mathcal{D}_n}(\mathbf{r}) = \int_{\Delta\mathcal{D}_n} \frac{1}{4\pi R} dD'. \tag{26}$$

Hence E can be computed from

$$\nabla\Phi(\mathbf{r}) = \frac{1}{\epsilon}\sum_{n=1}^{N} q_n \nabla\psi^{\Delta\mathcal{D}_n}(\mathbf{r}). \tag{27}$$

An integral equation for unknown charge density induced on the surface S of a perfect electric conductor (PEC) charged to a specified potential V is now easily obtained. Since the tangential electric field must vanish on S, the scalar potential Φ must be constant there. Hence,

$$\Phi(\mathbf{r}) = V. \tag{28}$$

Enforcing this condition at the centroid $\mathbf{r}_m$ of each element and employing (25), and (28), we have

$$\frac{1}{\epsilon}\sum_{n=1}^{N} q_n \psi^{\Delta\mathcal{D}_n}(\mathbf{r}_m) = V. \tag{29}$$

Figs. 2 and 3 show charge density distributions on a flat strip and on a T-shaped strip obtained by solving (29). For this case $\psi^{\Delta\mathcal{D}_n}$ reduces to

$$\psi^{\Delta\mathcal{C}_n}(\rho_m) = -\frac{1}{2\pi}\int_{\Delta\mathcal{C}_n} \ln|\rho_m - \rho'| d\mathcal{C}'. \tag{30}$$

3.2 Electric Field Integral Equation for TM Illumination of an Infinite Conducting Cylinder. Consider the specialization of (10) to the case of scattering by a PEC cylinder illuminated by a field incident normal to the cylinder axis and polarized TM with respect to the cylinder axis, taken to be the z-axis. The cylinder cross section in the $z = 0$ plane is described by the contour C, approximated by a series of piecewise linear segments, ΔC_n. With the excitation and polarization specified, current induced on the infinite cylinder is directed only parallel to the z-axis. The contour segment ΔC_n may now be taken as the boundary between two rectangular cells extending from $z = -h$ to $z = 0$ and from $z = 0$ to $z = +h$, respectively, and the infinite cylinder is obtained by allowing h to approach infinity. The basis function defined with respect to the element boundary ΔC_n thus becomes

$$\begin{aligned} A_n^s(\mathbf{r}) &= \begin{cases} \hat{z}\,\frac{\Delta}{h} \xrightarrow{h\to\infty} \hat{z}, & \rho \text{ in } \Delta C_n, \\ 0 & \text{otherwise,} \end{cases} \\ &= \hat{z}\Pi_n(\rho), \end{aligned} \tag{31}$$

where ρ is the projection of $\mathbf{r}$ onto the plane $z = 0$, and $\Pi_n(\rho)$ is the unit pulse function defined on ΔC_n. Since

$$\nabla_s \cdot A_n^s = \begin{cases} \pm\frac{1}{h} \xrightarrow{h\to\infty} 0, & \rho \text{ in } \Delta C_n, \\ 0 & \text{otherwise,} \end{cases} \tag{32}$$

clearly no surface charge density is present in the TM polarization and hence the scalar potential Φ vanishes. Substitution of the expansion (31) for the surface current density induced on C into (12) and use of the identity

$$\int_{-\infty}^{\infty} \frac{e^{-jkR}}{4\pi R} dz' = \frac{1}{4j} H_0^{(2)}(k|\rho - \rho'|) \tag{33}$$

yields for the vector potential of the scattered field,

$$A(r) = \hat{z}\mu \sum_{n=1}^{N} J_n \psi^{\Delta C_n}(\rho), \tag{34}$$

where

$$\psi^{\Delta C_n}(\rho) = \frac{1}{4j} \int_{\Delta C_n} H_0^{(2)}(k|\rho - \rho'|) dC'. \tag{35}$$

Hence the electric field scattered by the current induced on the cylinder is

$$E^s(\rho) = -j\omega\mu\hat{z} \sum_{n=1}^{N} J_n \psi^{\Delta C_n}(\rho). \tag{36}$$

An integral equation for TM cylinder scattering is obtained by enforcing the boundary condition that the scattered field exactly cancel the incident field on the cylinder at the centroid ρ_m of each segment ΔC_m:

$$j\omega\mu \sum_{n=1}^{N} J_n \psi^{\Delta C_n}(\rho_m) = E_z^i(\rho_m), \quad m = 1, 2, \ldots, N. \tag{37}$$

4.2 Electric Field Integral Equation for TE Illumination of an Infinite Cylinder. For a conducting cylinder illuminated by a TE polarized incident field, the current can be expanded in terms of triangular basis functions:

$$J(\rho) = \sum_{n=1}^{N} J_n \Lambda_n(\rho)$$

where

$$\Lambda(\rho) = \begin{cases} \frac{\rho_{n\pm}}{h_{n\pm}}, & \rho \text{ in } \Delta C_{n\pm}, \\ 0, & \text{otherwise.} \end{cases}$$

In terms of local coordinates $\zeta_{n\pm}$, however,

$$\frac{\rho_{n\pm}}{h_{n\pm}} = \frac{1}{h_{n\pm}} \zeta_{n\pm} \ell_{n\pm},$$

an hence the vector and scalar potentials of the scattered field are given by

$$A(\rho) = \mu \sum_{n=1}^{N} J_n \left[\frac{\ell_{n+}}{h_{n+}} \psi_+^{\Delta C_{n+}}(\rho) + \frac{\ell_{n-}}{h_{n-}} \psi_-^{\Delta C_{n-}}(\rho) \right]$$

and

$$\Phi(\rho) = \frac{-1}{j\omega\epsilon} \sum_{n=1}^{N} J_n \left[\frac{1}{h_{n+}} \psi^{\Delta C_{n+}}(\rho) - \frac{1}{h_{n-}} \psi^{\Delta C_{n-}}(\rho) \right]$$

where

$$\psi_{\pm}^{\Delta C_{n\pm}}(\rho) = \frac{1}{4j} \int_{\Delta C_{n\pm}} \zeta_{n\pm} H_0^{(2)}(k|\rho - \rho'|) dC'$$

and

$$\psi^{\Delta C_n}(\rho) = \frac{1}{4j}\int_{\Delta C_n} H_0^{(2)}(k|\rho-\rho'|)dC'.$$

Upon substitution of the current representation into the EFIE, and integration of the result between the centroids of adjacent elements, we obtain an $N \times N$ system of linear equations:

$$[Z_{mn}][I_n] = [V_m],$$

where the matrix elements Z_{mn} are given by

$$\begin{aligned} Z_{mn} = {} & j\omega\mu\left[\frac{\ell_{m+}\cdot\ell_{n+}}{2k_{n+}}\psi_+^{\Delta C_{n+}}(\rho_{m+}^c)+\frac{\ell_{m+}\cdot\ell_{n-}}{2k_{n-}}\psi_-^{\Delta C_{n-}}(\rho_{m+}^c)\right. \\ & \left.+\frac{\ell_{m-}\cdot\ell_{n+}}{2k_{n+}}\psi_+^{\Delta C_{n+}}(\rho_{m-}^c)+\frac{\ell_{m-}\cdot\ell_{n-}}{2k_{n-}}\psi_-^{\Delta C_{n-}}(\rho_{m-}^c)\right] \\ & +\frac{j}{\omega\epsilon}\left[\frac{1}{k_{n+}}\psi^{\Delta C_{n+}}(\rho_{m-}^c)-\frac{1}{k_{n-}}\psi^{\Delta C_{n-}}(\rho_{m-}^c)\right. \\ & \left.-\frac{1}{k_{n+}}\psi^{\Delta C_{n+}}(\rho_{m+}^c)+\frac{1}{k_{n-}}\psi^{\Delta C_{n-}}(\rho_{m+}^c)\right]. \end{aligned}$$

A similar result holds for surfaces and wires; for scattering by wires of radius $a(r)$, for example, we merely replace ρ_{ms}^c by r_{ms}^c and the potentials are replaced by

$$\psi_A^{\Delta C_n}(r) = \frac{1}{2\pi a(r)}\int_{\Delta C_n}\ell_n\left[\int_0^{2\pi}\frac{e^{-jkR}}{4\pi R}d\phi'\right]dC'$$

and

$$\psi^{\Delta C_n}(r) = \frac{1}{2\pi a(r)}\int_{\Delta C_n}\left[\int_0^{2\pi}\frac{e^{-jkR}}{4\pi R}d\phi'\right]dC'.$$

4.3 Magnetic Field Integral Equation for TM Illumination of an Infinite Cylinder. The MFIE is derived from the condition that the total tangential magnetic field just inside the surface S of the scatterer is zero. Thus, for the TM case,

$$\hat{z}\cdot\left[H^i+H^s\right] = 0. \tag{38}$$

Point-matching yields

$$\hat{\ell}_m\cdot H^s(\rho_m^-) = -H_z^i(\rho_m^-), \quad \rho_m^- \in \Delta C_m^- \text{ (just } \textit{inside}\ \Delta C_m). \tag{39}$$

For this case we can express the magnetic vector potential A as

$$A(\rho) = \hat{z}\sum_{n=1}^{N}\mu J_n\psi^{\Delta C_n}(\rho) \tag{40}$$

and hence we have

$$\nabla\times A(\rho) = -\hat{z}\times\sum_{n=1}^{N}\mu J_n\nabla\psi^{\Delta C_n}(\rho), \tag{41}$$

From (39) and (41) we thus have

$$\sum_{n=1}^{N}J_n\hat{n}_m\cdot\nabla\psi^{\Delta C_n}(\rho_m^-) = H_z^i(\rho_m^-) \tag{42}$$

since

$$\hat{z}\cdot(\hat{s}\times\nabla\psi) = (\hat{z}\times\hat{s})\cdot\nabla\psi = \hat{n}\cdot\nabla\psi = \frac{\partial\psi}{\partial n}. \tag{43}$$

Fig. 4 illustrates the induced currents on a square cylinder illuminated by a TM incident field obtained by solving (42).

4.4 Magnetic Field Integral Equation for TE Illumination of an Infinite Cylinder. In the case of TE illumination, the induced surface current has only a circumferential component and hence the scattered magnetic field field is entirely z-directed. Setting the magnetic field to zero just inside the cylinder cross section yields the magnetic field integral equation,

$$\hat{z}\cdot\left[H^i + H^s\right] = 0. \tag{44}$$

For this case we have

$$A(\rho) = \sum_{n=1}^{N} J_n \hat{z}\mu\psi^{\Delta C_n}(\rho), \tag{45}$$

and

$$\nabla\times A(\rho) = -\sum_{n=1}^{N} J_n\mu\hat{z}\times\nabla\psi^{\Delta C_n}(\rho) \tag{46}$$

from which the magnetic field is found from

$$H = \frac{1}{\mu}\nabla\times A. \tag{47}$$

Recognizing that

$$\hat{s}\cdot\hat{l}_n\times\nabla\psi = \hat{s}\times\hat{l}_n\cdot\nabla\psi = -\hat{n}\cdot\nabla\psi. \tag{48}$$

Point-matching in the resulting integral equation yields

$$\sum_{n=1}^{N} J_n\hat{n}_n\cdot\nabla\psi^{\Delta C_n}(\rho_m^-) = -H_z^i(\rho_m^-) \quad \rho_m^- \in \Delta C_m^- \text{ (just } \textit{inside}\ \Delta C_m). \tag{49}$$

Fig. 5 shows currents induced on a square cylinder illuminated by TE incident field obtained by solving (49).

References

[1] J. E. Akin, *Application and Implementation of Finite Element Methods*. Orlando: Academic Press, 1984.

[2] D. R. Wilton, S. M. Rao, A. W. Glisson, D. H. Schaubert, O. M. Al-Bundak, and C. M. Butler, "Potential Integrals for Uniform and Linear Source Distributions on Polygonal and Polyhedral Domains," *IEEE Transactions on Antennas and Propagation*, Vol. AP-32, No. 3, pp. 276-281, March 1984.

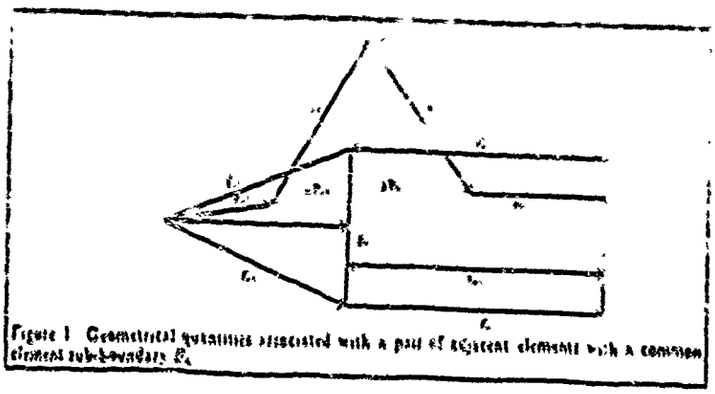


Figure 1 Geometrical quantities associated with a pair of adjacent elements with a common element sub-boundary B_n

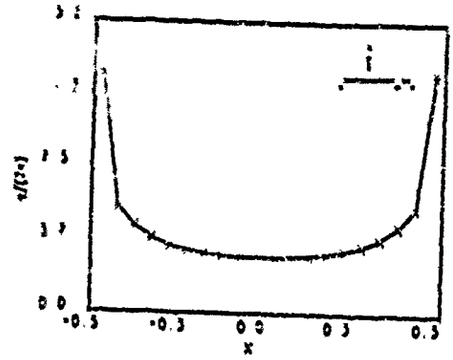


Figure 2: Charge density on a PEC strip (1 m1 volt, 2=m1 m.)

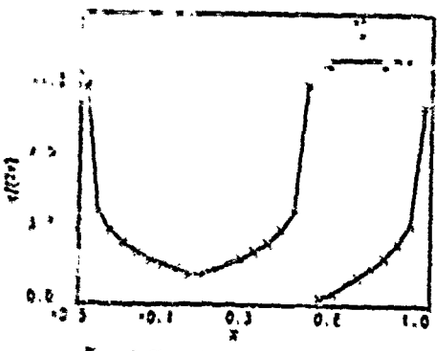


Figure 3: Charge density on a junction of PEC strips (Vm1 volt, 2=m1 m.)

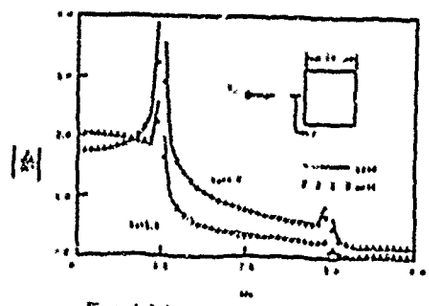


Figure 4: Induced current on a square cylinder illuminated by TM incident field.

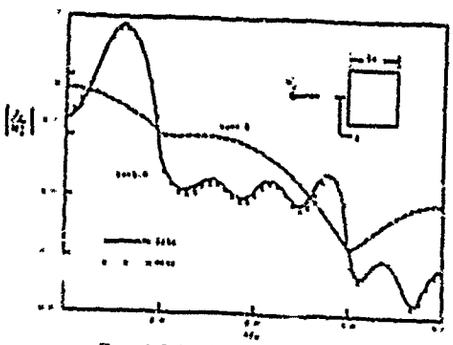


Figure 5: Induced current on a square cylinder illuminated by TE incident field.

JUNCTION: A Computer Code for the Computation of Radiation and Scattering by Arbitrary Conducting Wire/Surface Configurations

D. R. Wilton*, and S. U. Hwu
Dept. of Electrical Engineering, University of Houston
University Park, Houston TX 77004

1. Introduction. JUNCTION, a computer code, results from the application of numerical procedures described in this paper which invoke the method of moments to solve a coupled electric field integral equation for the currents induced on an arbitrary configuration of perfectly conducting bodies and wires. An important feature of the code is its ability to treat wire-to-wire, surface-to-surface, and wire-to-surface junctions. Wires may be connected to surfaces at essentially arbitrary angles and may be attached to surface edges or vertices. Results obtained using this algorithm are in the form of electric current and charge densities and far- and near-field patterns. Fig. 1 depicts a typical conducting wire and body configuration which might be treated by JUNCTION.

2. Formulation. Let S denote a configuration of perfectly conducting surfaces immersed in an incident electromagnetic field. In general, S may consist of a collection of conducting bodies (S_B)and wires (S_W). An electric field E^i, defined to be the field due to an impressed source in the absence of S, is incident on and induces surface current J and total current I on S_B and S_W respectively. A pair of coupled integral equations for the configuration of wires and bodies may be derived by requiring the tangential component of the electric field to vanish on each surface. Thus we have

$$E^i_{tan} = (j\omega A + \nabla\Phi)_{tan}, \quad \mathbf{r} \text{ on } S \tag{1}$$

where

$$A = \frac{\mu}{4\pi}\left[\int_{S_B} J\frac{e^{-jkR}}{R}dS' + \int_{S_W}\frac{I'}{2\pi a(s')}\frac{e^{-jkR}}{R}dS'\right] \tag{2}$$

$$\Phi = -\frac{1}{j4\pi\omega\epsilon}\left[\int_{S_B}\nabla'\cdot J\frac{e^{-jkR}}{R}dS' + \int_{S_W}\frac{1}{2\pi a(s')}\frac{dI}{ds'}\frac{e^{-jkR}}{R}dS'\right] \tag{3}$$

and $R = |\mathbf{r}-\mathbf{r}'|$ is the distance between an arbitrarily located observation point $\mathbf{r}$ and a source point $\mathbf{r}'$ on S. In (2) and (3), $k = \frac{2\pi}{\lambda}$, where λ is the wavelength, μ and ϵ are the permittivity and permeability, respectively, of the surrounding medium, s' is the arc length along the wire axis, and a is the radius of the wire.

3. Basis Functions. A triangular patch model of S_B and a linear tubular segment model of S_W is assumed (c.f. Figs. 2 and 3). Basis functions suitable for representing currents induced on S_B and S_W are given by

$$A^\gamma_n(\mathbf{r}) = \begin{cases} \dfrac{\rho^{\gamma\pm}}{h^{\gamma\pm}_n} & ,\mathbf{r} \text{ in } S^{\gamma\pm}_n \\ 0 & ,\text{otherwise} \end{cases} \tag{4}$$

where, as illustrated in Figs. 4 and 5, $S^{\gamma\pm}_n$, $\gamma = B$ or W, is the $\pm$ reference triangle or segment attached to the nth edge or node of a body or wire, respectively. The height (length) of $S^{\gamma\pm}_n$ relative to the nth edge (node) of S_n, $\gamma = B$ (W) is $h^{\gamma\pm}_n$, and $\rho^{\gamma\pm}$ is ($\pm$1)x(vector from the free node of $S^{\gamma\pm}_n$ to $\mathbf{r}$). A wire-to-surface junction is assumed to exist only at a triangle vertex. The surface divergence of $A^\gamma_n(\mathbf{r})$, which is proportional to the surface charge density associated with this basis function, is

$$\nabla_s \cdot \Lambda_n^\gamma(\mathbf{r}) = \begin{cases} \pm\dfrac{2}{h_m^{B\pm}}, & \gamma \equiv B \quad ,\mathbf{r} \text{ in } S_m^{B\pm} \\ \pm\dfrac{1}{h_m^{W\pm}}, & \gamma \equiv W \quad \mathbf{r} \text{ in } S_m^{W\pm} \\ 0 & ,\text{otherwise.} \end{cases} \tag{5}$$

Referring to Fig. 6, the vector basis function associated with the nth junction is

$$\Lambda_n^J(\mathbf{r}) = \begin{cases} K_{nl}\left[1 - \dfrac{(h_{nl}^{J\pm})^2}{(\rho^{\pm} \cdot \hat{h}_{nl}^{J\pm})^2}\right] \Lambda_{nl}^B(\mathbf{r}) & ,\mathbf{r} \text{ in } S_{nl}^{J\pm} \\ \Lambda_n^W(\mathbf{r}) & ,\mathbf{r} \text{ in } S_n^{J-} \\ 0 & ,\text{otherwise} \end{cases} \tag{6}$$

where the double index nl refers to the lth triangle, $S_{nl}^{J\pm}$, at the nth junction. $\Lambda_{nl}^B(\mathbf{r})$ and $h_{nl}^{J\pm}$ are the body basis function and vector height, respectively, associated with the edge opposite the junction vertex in $S_{nl}^{J\pm}$. The total flux from the junction triangles into the wire is normalized to unity if we choose

$$K_{nl} \equiv \frac{\sigma_{nl}}{\ell_{nl}\sum_{l=1}^{N_{J_n}} \sigma_{nl}} \equiv \frac{\sigma_{nl}}{\ell_{nl}\sigma_n^t} \tag{7}$$

where σ_{nl} is the angle between the two edges of $S_{nl}^{J\pm}$ common to the nth junction vertex, and σ_n^t is the sum of the nth junction vertex angles. N_{J_n} is the number of patches attached to the nth junction. The surface divergence of $\Lambda_n^J(\mathbf{r})$, which is proportional to the surface charge density, is given by

$$\nabla_s \cdot \Lambda_n^J(\mathbf{r}) = \begin{cases} \dfrac{2K_{nl}}{h_{nl}^{J\pm}} & ,\mathbf{r} \text{ in } S_{nl}^{J\pm} \\ -\dfrac{1}{h_n^{J-}} & ,\mathbf{r} \text{ in } S_n^{J-} \\ 0 & ,\text{otherwise.} \end{cases} \tag{8}$$

The current on the surfaces S_B may now be represented as

$$J(\mathbf{r}) \approx \sum_{n=1}^{N_B} I_n^B \Lambda_n^B(\mathbf{r}) + \sum_{n=1}^{N_J} I_n^J \Lambda_n^J(\mathbf{r}), \quad \mathbf{r} \text{ on } S_B, \tag{9}$$

and the total axial current on the wire may be represented as

$$I(\mathbf{r})\hat{z} \approx \sum_{n=1}^{N_W} I_n^W \Lambda_n^W(\mathbf{r}) + \sum_{n=1}^{N_J} I_n^J \Lambda_n^J(\mathbf{r}), \quad \mathbf{r} \text{ on } S_W, \tag{10}$$

where N_β, $\beta \equiv B, W$, or J is the unknown number of bodies, wires, or junctions, respectively. Note that according to (5) and (8), the surface divergence, and hence the charge, is constant on all body, wire, and junction subdomains.

4. **Testing.** To enforce the integral equation on S_B, one may integrate the vector component of (1) parallel to the path from the centroid of S_m^{B+} to the middle of the edge ℓ_m^B and thence to the centroid of S_m^{B-}. A similar path is used on wires between the centers of adjacent wire segments. At a junction, we first integrate the tangential electric field along a path from the centroid of each junction triangle to the junction and then along the wire axis to the center of the attached wire segment. The resulting equations are then combined into a single equation

for the junction by weighting each with the associated triangle vertex angle, and summing the results for each junction patch. E^i and A are approximated along each portion of the path by their respective values at the centroids. The integral on $\nabla\Phi$ reduces to a difference of the scalar potentials at the path endpoints. With $\mathcal{L}_m^k$, $\gamma \equiv B, W$, or J, as the vector path segment, we thus have

$$j\omega\left[A(r_m^{\gamma,+})\cdot\mathcal{L}_m^{+}+A(r_m^{\gamma,-})\cdot\mathcal{L}_m^{-}\right]+\left[\Phi(r_m^{\gamma,-})-\Phi(r_m^{\gamma,+})\right]$$
$$=\left[E^i(r_m^{\gamma,+})\cdot\mathcal{L}_m^{+}+E^i(r_m^{\gamma,-})\cdot\mathcal{L}_m^{-}\right], \tag{11}$$

$m=1,2,\ldots,N_\gamma,\quad \gamma \equiv B \text{ or } W$

and

$$\frac{1}{\alpha_m^{+}}\sum_{l=1}^{N_J}\alpha_{ml}\left[j\omega A(r_{ml}^{J,+})\cdot\mathcal{L}_{ml}^{J,+}-\Phi(r_{ml}^{J,+})\right]+j\omega A(r_m^{J,-})\cdot\mathcal{L}_m^{J,-}+\Phi(r_m^{J,-})$$
$$=\frac{1}{\alpha_m^{+}}\sum_{l=1}^{N_J}\alpha_{ml}E^i(r_{ml}^{J,+})\cdot\mathcal{L}_{ml}^{J,+}+E^i(r_m^{J,-})\cdot\mathcal{L}_m^{J,-}, \tag{12}$$

$m=1,2,\ldots,N_J$

Using the source expansion defined in (4) and (6), we obtain from (11)-(12) a set of linear equations whose solution yields the unknown current coefficients. A detailed derivation and computation of the system equations can be found in [1].

5. Calculation of Near Fields. Since the near electric field is dominated by the contribution of the scalar potential, the computed result is sensitive to the basis function representing charge density. To demonstrate this point, two different basis functions are used to represent the charge density and their computational properties are illustrated.

5.1 Charge Representation. The constant charge density on the nth triangular patch q_n^B (or wire segment q_n^W) is computed from the total surface current out of a triangular patch (or wire segment) by utilizing the continuity equation as

$$q_n^B = \frac{-1}{j\omega}\nabla\cdot J \approx \frac{-1}{j\omega}\frac{\sum_i\left[\ell_i J_i + k_i J_i^t\right]}{A}, \text{ and} \tag{13}$$

$$q_n^W = \frac{-1}{j\omega}\nabla\cdot I\hat{\ell} \approx \frac{-1}{j\omega}\frac{\sum_i I_i}{h}, \tag{14}$$

where J_i is the outwardly directed current density across the ith edge (with length of ℓ_i) of the nth triangle and A is the area of the triangular patch, J_i^t is the outwardly directed current through the ith vertex (with vertex angle α_i) of the triangle, $k_i = \frac{\alpha_i}{\alpha^t}$, α^t is the sum of the vertex angles at a junction, and I_i is the outwardly directed current from the nth wire segment of length h. To establish a linear charge representation, one can obtain the charge on the nth patch vertex or wire node by averaging the charges in the adjacent cells as

$$q^{B_n} = \frac{\sum_j A_j\, q_j^B}{\sum_j A_j}, \text{ and } q^{W_n} = \frac{\sum_j h_j\, q_j^W}{\sum_j h_j}. \tag{15}$$

where $q_j^{(p)}$ ($q_j^{(w)}$) is the constant charge density on the jth patch with area A_j (wire segment with length h_j) attached to the nth body vertex (wire node). A linear representation of the charge density on a triangular patch (wire segment) is then obtained as a linear combination of the charge values at three triangular vertices (two wire nodes):

$$q^{(p)}(r') = \sum_{i=1}^{3} f_i q^{(p)}_i, \quad \text{and} \quad q^{(w)}(r') = \sum_{i=1}^{2} f_i q^{(w)}_i, \quad \text{where} \quad f_i = 1 - \frac{\rho_i}{h_i}, \; h_i. \tag{16}$$

The scalar potential of (3) thus becomes

$$\Phi = \frac{1}{4\pi\epsilon}\left[\sum_{p=1}^{N_p}\int_{S_p} q^{(p)}(r')\frac{e^{-jkR}}{R}dS' + \sum_{n=1}^{N_w}\int_{S_w}\frac{1}{2\pi a(r')}q^{(w)}(r')\frac{e^{-jkR}}{R}dS'\right],$$

$$= \frac{1}{4\pi\epsilon}\left[\sum_{n=1}^{N_p}\sum_{i=1}^{3} q^{(p)}_i\int_{S_p} f_i\frac{e^{-jkR}}{R}dS' + \sum_{n=1}^{N_w}\sum_{i=1}^{2} q^{(w)}_i\int_{S_w}\frac{f_i}{2\pi a(r')}\frac{e^{-jkR}}{R}dS'\right]. \tag{17}$$

Since the magnitude of the normal electric field is proportional to the surface charge density, the constant charge representation will cause a step discontinuity in the normal electric field directly at the surface, whereas the linear charge representation produces a smooth (linear) variation of the normal component. The disadvantage of the numerical smoothing is that it takes place even when the charge should not be smooth, such as at edges or near sources. In addition, the smoothing provided by the linear charge representation tends to lower the peaks and elevate the valleys in the charge distribution when the sampling density is low. In these cases, if one ignores the step discontinuities, the constant charge representation may provide more reasonable results, and for this reason the constant charge representation is made an option in the code.[1]

The numerically computed tangential electric field at a surface is even poorer behaved than the normal component. The computed tangential field is theoretically infinite at discontinuities either in the charge or in its slope—only charge basis functions with continuous derivatives can produce a smooth tangential field; unfortunately, such basis functions would demand that the current have second derivative continuity. The tangential field computed from linear charge distributions, however, does *appear* to be considerably smoother than that of piecewise constant representations. And the infinities can be eliminated if finite differences are used to approximate the gradient of the scalar potential; since the scalar potential is smooth, its differences are guaranteed to be finite. For this reason, the finite difference approach described in the following section is used in the code.

5.2 Near Fields Representation. The vector and scalar potentials A and Φ may be calculated at any point in space according the formulas of the previous section. Finite differences may then be used to approximate the gradient and curl operating on scalar and vector potentials, and hence to determine the near electric and magnetic fields at a given point. For example, the x- component of electric field can be approximated as

$$E_x = -j\omega A_x + \frac{\partial\Phi}{\partial x} \approx -j\omega A_x + \frac{\Delta\Phi}{\Delta x}$$

$$\approx -\frac{j\omega}{2}\left\{[A_x(x+\Delta x, y, z) + A_x(x-\Delta x, y, z)]\right.$$

$$\left. + \frac{1}{2\omega\epsilon\Delta x}[\Phi(x+\Delta x, y, z) - \Phi(x-\Delta x, y, z)]\right\}, \tag{18}$$

and similarly for the z- component of magnetic field,

[1] Neither the piecewise constant nor the piecewise linear representation can provide much information in the near neighborhood of an edge since the normal electric field is infinite there and a singular basis function is required to reproduce this behavior correctly.

$$H_z = \hat{z} \cdot \frac{1}{\mu} \nabla \times A = \frac{1}{\mu}\left(\frac{\partial A_z}{\partial y} - \frac{\partial A_y}{\partial z}\right) \approx \frac{1}{\mu}\left(\frac{\Delta A_z}{\Delta y} - \frac{\Delta A_y}{\Delta z}\right)$$

$$\approx \frac{1}{\mu}\left\{\frac{1}{2\Delta y}[A_z(x, y+\Delta y, z) - A_z(x, y-\Delta y, z)]\right.$$

$$\left. - \frac{1}{2\Delta z}[A_y(x, y, z+\Delta z) - A_y(x, y, z-\Delta z)]\right\}. \tag{19}$$

JUNCTION always computes scalar and vector potentials simultaneously, and hence to avoid excessive computation when only the vector potential at (x, y, z) is needed, it is approximated by its average at the neighboring points $(x \pm \Delta x, y \pm \Delta y, z \pm \Delta z)$.

6.1 Current and charge distributions. Fig. 7 illustrates the current distribution near the junction of a circular disk and a monopole attached at the center and inclined at an angle of 30° to the disk axis. The length of the monopole, and the radius of the disk are $a = 0.333\lambda$. The radius of the monopole is $r = 0.001a$. The result is compared with the current distribution obtained by solving a magnetostatic field integral equation for an infinite disk with a similarly inclined semi-infinite filamentary current attached to its center [4]. Since the magnetostatic result gives the shape but not the magnitude of the current distribution, a complex normalizing constant is chosen so that the magnetostatic current interpolates the dynamic result at one point. Also shown is the uniform distribution that would result from taking the current in the wire and distributing it uniformly about the disk. Figs. 8 and 9 show the computed current distributions on a circular cylinder with monopoles attached to the center of each endcap and driven at the attachment point. Measured results by Cooper [5] are shown for comparison. The diameter and the height of the cylinder are 0.25λ or 0.5λ. The wire radius is 0.007λ and the lengths are 0.125λ or 0.25λ. Charge distributions corresponding to these similar cases are shown in Figs. 10-12.

6.2 Input Impedance. Fig. 13 shows the input admittance as a function of frequency for a monopole attached to the center of a flat plate and fed at the attachment point. The length of the monopole is 0.421 m, its radius is 0.0008 m, and it is oriented normal to the 0.914 m square plate. The results are compared with those calculated and measured by Newman and Pozar [6]. In Fig. 14 is illustrated the input impedance versus frequency of a monopole inclined at an angle of 60° from normal and attached off-axis on a circular disk. The results are compared with measurements by Marin and Catedra[7].

6.3 Far Field. Fig. 15 shows a 0.25λ monopole mounted on a sphere with radius 0.2λ. The compared results are computed by Tesche [8]. Fig. 16 shows the radiation pattern of a wire of length 0.5λ and radius 0.007λ attached to a circular cylinder with diameter and height 0.25λ. The measured results shown for comparison are by Cooper [5].

6.4 Near Field. Figs. 17 and 18 present numerical results for normal electric and tangential magnetic fields along a circular cylinder on a perfectly conducting ground plane with a monopole attached to the center of its endcap. A unit voltage source drives the monopole at the attachment point. The cylinder radius and height are both 0.0617λ; the radius of the wire is 0.001λ and its length is 0.218λ. Results computed by Tsai [9] based on a Fourier transform approach for treating the wire and the use of a set of equivalent currents for the body are shown for comparison.

Fig. 19 illustrates the geometrical parameters for a circular coaxial resonator, the resonant fields for which are considered in Figs. 20-24. The inner conductor of the coaxial line is a thin wire. The cavity radius is 1 m, the length of the wire is 2 m, its radius is 0.001 m, and it is attached to the centers of the top and bottom plates of the circular cavity. This problem serves as a rigorous test of the near-field computational capabilities of the code since a closed form solution for the cavity fields exists and since the geometry includes a thin wire, a curved surface, and a wire-to-surface junction. Questions of solution accuracy and difficulties with the large matrices needed to very accurately model the geometry can be eliminated since the cavity

currents are known in closed form and can be given as input values to the subroutines used to compute the near fields. Thus any inaccuracies in this computation are due solely to errors in geometry modeling and in approximating the current with basis functions.

Fig. 20 shows the ϕ-component of the magnetic field, H_ϕ, for TM_{020} modes of the coaxial line cavity, along the dashed line from point C to point D of Fig. 19. To illustrate the dependence of the electric field near a conducter on the charge expansion functions, the axial component of the electric field, E_z, just above the conductor plate, has been computed along the dashed line from point A to point B. The radial component of the electric field near the inner conductor has also been computed along the dashed line from A to C. In Figs. 21-24, we see that since the magnitude of the normal electric field is proportional to the surface charge density, the constant charge representation produces a step discontinuity in the normal electric field, whereas the linear charge representation produces an averaging effect which tends to smooth out the step discontinuity. As with any smoothing process, however, the peaks and valleys in the charge distribution will not be faithfully reproduced if the spatial resolution is not sufficiently great. The accuracy can, of course, be improved by subdividing the region into smaller subdivisions.

References

[1] S. U. Hwu and D. R. Wilton, "Electromagnetic Scattering and Radiation by Arbitrary configurations of Conducting Bodies and Wires," Technical Report No. 87-17, Applied Electromagnetics Laboratory, Department of Electrical Engineering, University of Houston, December 1987.

[2] D. R. Wilton and S. U. Hwu, "JUNCTION CODE USER'S MANUAL ," Technical Report No. 87-18, Applied Electromagnetics Laboratory, Department of Electrical Engineering, University of Houston, December 1987.

[3] S. U. Hwu and D. R. Wilton, "Electromagnetic Near-Field Computation for Arbitrary configurations of Conducting Bodies and Wires," Technical Report No. 88-13, Applied Electromagnetics Laboratory, Department of Electrical Engineering, University of Houston, December 1988.

[4] Qinglun Chen and D. R. Wilton, "Computation of Magnetostatic Current Distributions Near Wire-To-Surface Junctions," National Radio Science Meeting Digest, Syracuse, NY, June 1988.

[5] Lee J. Cooper and Ronold W. P. King, "Monopole Antennas on Electrically Thick Conducting Cylinders," Technical Report No. 660, Division of Engineering and Applied Physics, Harvard University, 1975.

[6] E. H. Newman and D. M. Pozar, "Electromagnetic Modeling of Composite Wire and Surface Geometries," *IEEE Transactions on Antennas and Propagation*, Vol. AP-26, No. 6, pp. 784-789, November 1978.

[7] M. Marin and M. F. Catedra, " A Study of a Monopole Arbitrarily Located on a Disk Using Hybrid MM/GTD Techniques," *IEEE Transactions on Antennas and Propagation*, Vol. AP-35, No. 3, pp. 287-292, March 1987.

[8] F. M. Tesche and A. R. Neureuther, "The Analysis of Monopole Antennas Located on a Spherical Vehicle: Part 1 and Part 2," *IEEE Transactions on Electromagnetic Compatibility*, Vol. EMC-18, No. 1, pp. 2-15, Feb. 1976.

[9] Leonard L. Tsai, "Analysis and Measurement of A Dipole Antenna Mounted Symmetrically on A Conducting Sphere or Cylinder," Technical Report No. 2648-3, ElectroScience Laboratory, Ohio State University, 1970.

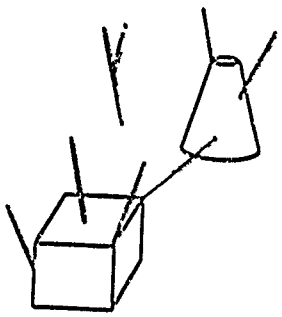


Fig. 1

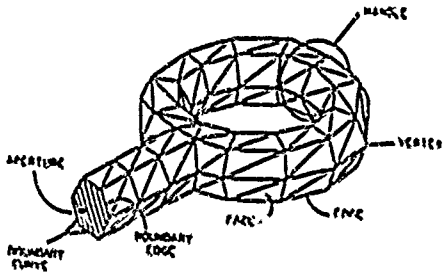


Fig. 2

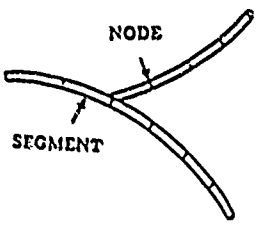


Fig. 3

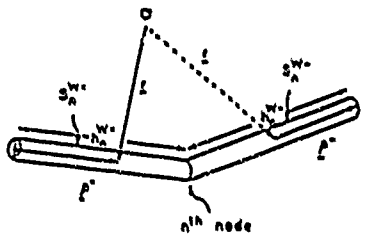


Fig. 4

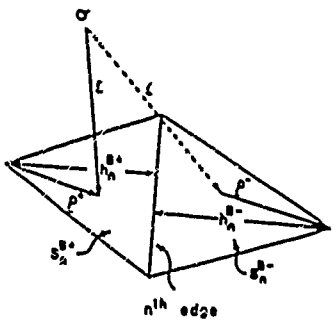


Fig. 5

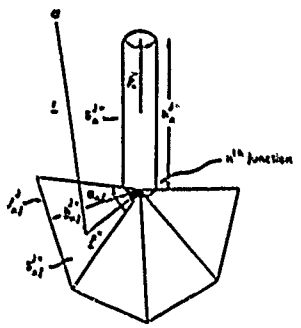


Fig. 6

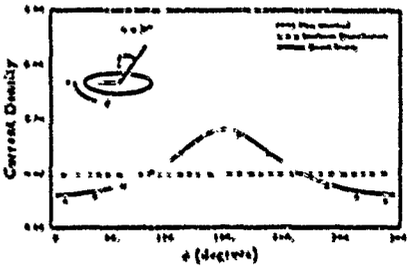


Fig. 7

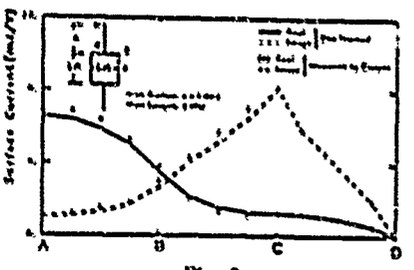


Fig. 8

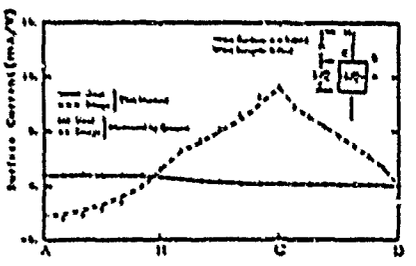


Fig. 9

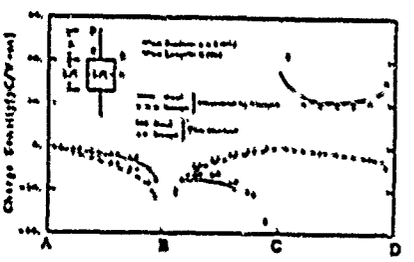


Fig. 10

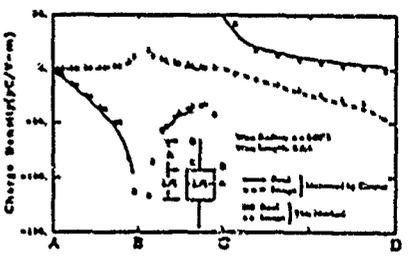


Fig. 11

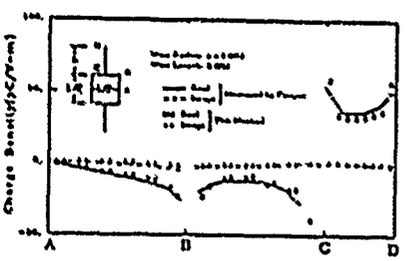


Fig. 12

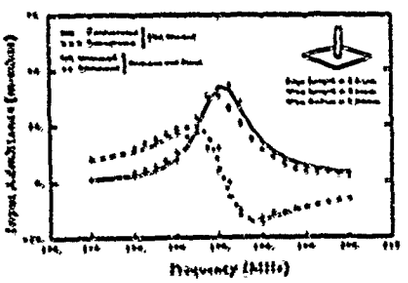


Fig. 13

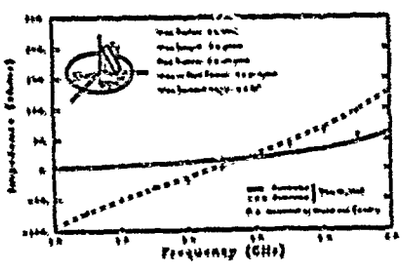


Fig. 14

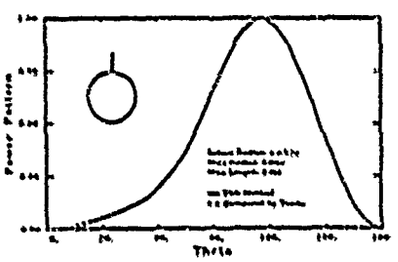


Fig. 15

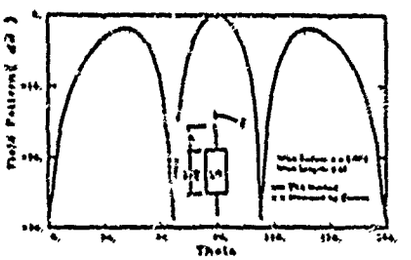


Fig. 16

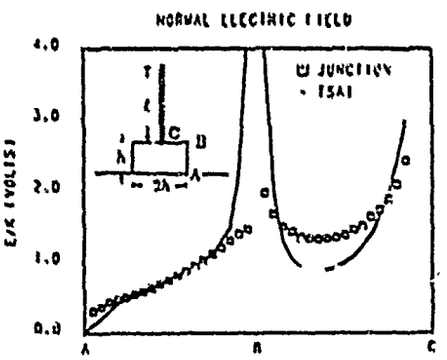


Fig. 17

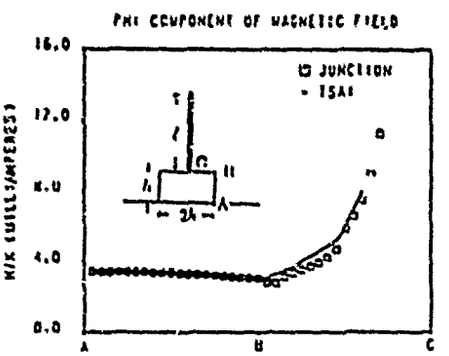


Fig. 18

SESSION 2 - "MICROWAVE CIRCUITS"

Chairman: Vijai Tripathi

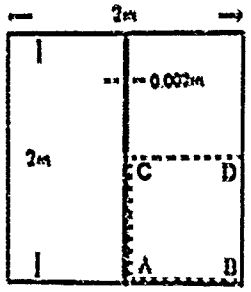


Fig. 19

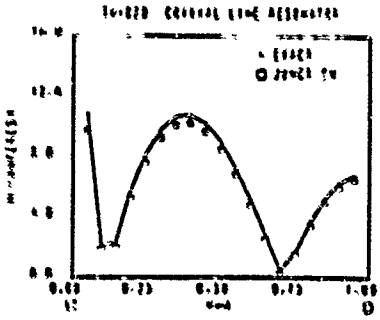


Fig. 20

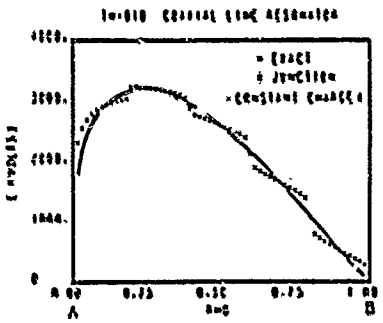


Fig. 21

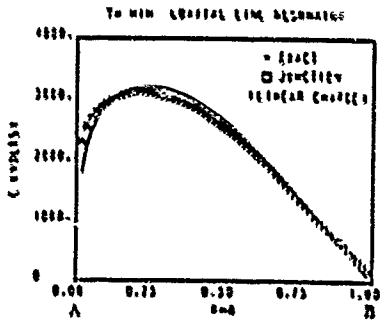


Fig. 22

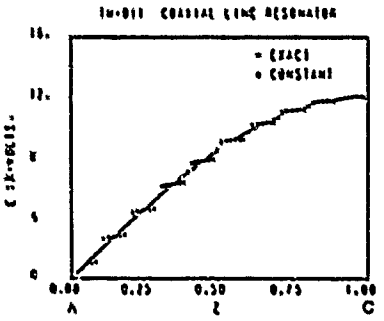


Fig. 23

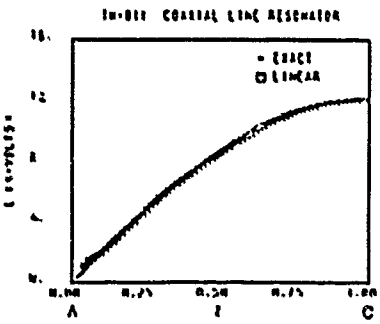


Fig. 24

APPLICATIONS OF THE TLM METHOD TO MICROWAVE CIRCUITS

Dr R.G. Hanson
Watkins Johnson Company
3333 Hillview Avenue
Palo Alt CA 94304

Abstract

The modelling of multiaxial discontinuities is one of the most challenging problems in microwave circuit analysis. Recent advances in computers and numerical techniques have made solutions to basic field structures possible and these have great potential for solving microwave circuit problems. Of the several methods available the Transmission Line Matrix is attractive because it offers a highly flexible, mathematically straightforward method of solving the general three dimensional bounded structure that is common in microwave circuits. The purpose of this paper is to illustrate the practicality of the TLM method with a realistic microstrip problem. Then to show the most recent improvements to the basic algorithm and to discuss the potential applications of this method taking into account future improvements in CPU power.

TLM Basics

The Transmission Line Matrix (TLM) method can be categorized as a finite difference, time domain, modelling technique. It uses a network analogue approach to solving Maxwell's Equations in time and space. This analogue is based on the commonly known equivalence between the inter-relationship of propagating electromagnetic fields and that of voltages and currents along transmission lines [1,2]. The method employs a mesh of nodes interconnected with uniform transmission lines that model the electro-magnetic properties of the original structure. This leads to a general, elegant algorithm that tracks the time domain propagation of impulse functions through the network. Thus, the equivalence of voltages and currents in the network to electric and magnetic field quantities produces the desired field solution.

The correspondence between circuit and field parameters can be illustrated by considering the TLM node structure as originally proposed by Johns [3]. Each point in space is approximated by a small cube as shown in figure 1a. In turn each cube consists of 3 series and 3 shunt nodes connected by transmission lines (figure 1b). The two types of nodes are shown in more detail in figures 2 and 3. In each case the short interconnecting transmission lines are approximated by LC equivalent circuits. Application of Kirchoff's laws at these two junctions yields differential equations relating the voltages and currents. Comparison of the equations in figure 2 shows a direct analogy of voltages and currents in the network with electric and magnetic fields as described by

Maxwell's equations. The same can be seen in the equations for figure 3. Note also that even though each node is 2 dimensional, the interconnection pattern shown in figure 1b provides 6 nodes for each basic cube which are oriented in a way that completly describe the 6 E and H field components in 3 dimensions. Furthermore, local permeability, permittivity and boundary conditions can be added to each node by the extra terms Zxx and Gyy in figures 2 and 3 [4]. A more comprehensive explanation of these concepts can be found in two excellent review papers [4,5].

The TLM algorithm simulates time variation by computing the propagation of impulse functions through the 3D network at successive time intervals. Starting from an approximate excitation, the algorithm computes how incident pulses are reflected at each series node. Mathematically this is a scattering computation which takes into account the local permeability, permittivity and boundary conditions [6]. Since the series and shunt nodes alternate through the mesh, these reflected pulses automatically become the incident pulses to the shunt nodes. The time step is completed by computing the scattering at the shunt nodes in a manner similar to the series case. These two scattering procedures represent the core of the TLM algorithm and it is because these are so very simple that this can be an efficient numerical method.

Output data from the simulation can be applied in a variety of ways. All 6 E and H field quantities can be computed at each node and for each time step. So the question is not what data is available but rather what data is the most useful.

An Example Circuit

The microstrip cavity shown in figure 4 is used to illustrate applications of the TLM method in microwave circuit analysis. This structure was chosen because it has been analysed before [7], so it is relevant for comparative purposes and is realistic without being unduly complex. The problem is broken down into a uniform mesh that contains 7x7x10 nodes in the (x,y,z) directions. A magnetic wall is used in the y,z plane to exploit the plane of symmetry through the centre of the microstrip line. This is particularly helpful as it reduces the number of nodes needed by one half.

The model is stimulated with unity value impulse functions for Ey on all nodes in the dielectric and beneath the microstrip line. Then the time stepping algorithm is allowed to run for 400 iterations. Table 1 shows a summary of the memory requirements for this problem.

Table 1

	Quantity	Reals	Total
Space nodes	640	26	16,640
Time iterations	400	1	400
Total Real Data			17,040

Summary of Data Storage for the Example Circuit

The output is tabulated at each time step for Ey at the node 2,5,6 under the microstrip. Then this data, which is a time sequence of the impulses that travelled through that node, is Fourier transformed into the frequency domain (figure 5).

The results show a resonance at a normalized frequency of 0.085 which compares favorably with the results of other computations [7] and measurements [8]. The frequency normalization factor is dL/v where dL is the spatial step size and v is the propagation velocity in the TLM mesh structure. For most applications this is a simple linear factor but care must be taken as this can be non-linear in cases where the dispersion of the TLM mesh is significant [5].

There are other computations possible with the abundance of field information that is available with this method. A simple extension of the procedure above forms a practical method of characterizing one port discontinuities [9]. The length of the cavity is increased; then Ey field data is extracted from a line of nodes parallel to the axis of propagation. After Fourier transformation this data is analagous to the standard VSWR measurement using a slotted line.

The calculation of circuit parameters for 2 port structures is also possible though more complicated [10,11]. The first reference uses a contour integral of the H field and a line integral of the E field to compute the circuit voltages and currents. The second uses a Poynting vector approach to compute power waves and hence the scattering parameters. Both methods are subject to some approximation concerning non-TEM modes.

Finally table 2 shows a comparison of run times for the example circuit on different machines. Computer power has increased by more than ten times in the last fifteen years and thus these types of computations have become practical on a personal computer.

Table 2

CPU	Time mins:secs	Vintage year
Main Frame		
ICL 1908A	15:00	1976
IBM 370	1:30	1982
PC		
IBM PC	13:09	1982
IBM Model 80	1:49	1988

Summary of Computation Times for the Example Circuit

Enhancements to the Algorithm

The TLM algorithm is very simple and in its most basic form is available in less than 200 lines of Fortran [10]. Enhancements fall into two basic areas. First the input and output capabilities of the research oriented programs are very limited and so pre- and post-processor arrangements are valuable extensions. Second (and more fundamental) are the improvements to the algorithm itself which lead to greater accuracy or speed or both. Two important schemes follow which deserve further discussion:

In any finite difference approximation, accuracy can be improved by reducing the step size of the mesh. Unfortunately, this is usually not very practical because as the step size decreases the number of nodes increases dramatically with a corresponding increase in CPU and memory requirements. However, it is common that high accuracy is only needed in certain regions of a problem where the boundary structure is complicated or where the field gradients are large. In this case a more practical approach is to employ a graded mesh scheme that provides for high resolution in only some areas. Such a scheme has been applied to the TLM method and is surprisingly easy to implement [13]. The cross section shown in figure 6 illustrates how this technique can be applied to microstrip circuits. The grading scheme there represents a 40% reduction in the number of nodes when compared with a comparable linear grading.

A new symmetric condensed node has recently been developed by Johns [14]. It is shown in figure 7 and consists of a single rather complex junction of the 6 interconnecting lines, which are organized as pairs of balanced transmission lines orthogonal to each other. In one sense this model is more abstract than the earlier expanded node model but it has several advantages. In the expanded node (figure 1) the separation of the series and shunt nodes means that some boundary conditions are misaligned because they are controlled by nodes that are on opposite sides of the cube. The new node condenses all the field components into

one point in space to avoid such difficulties and is superior to previous condensed node formulations which were asymmetric.

Finally it should be noted that the core of the TLM method is the scattering computations that occur at each node and in each time step. This amounts to a mere 60 line of Fortran in Akhtarzad's original program [12] and so could be carefully optimized for use on a particular computer. More significantly though, is the possibility of implementing this algorithm on a large parallel computer. The scattering at each node depends exclusively on local data and can be handled in parallel with a small overhead for communicating the impulses between adjacent nodes at the end of each time step.

Summary of Strengths and Weaknesses

It is true that the TLM method is attractive to microwave engineers because the circuit analogue is rather familiar. In addition, the general nature of the field computations and the guaranteed stability are very important attributes. Other important strengths of this technique are the ability to identify electrical network parameters which can be utilized in more traditional CAD procedures and the ability to simulate a range of frequencies.

The main weakness of the TLM method is the necessity of choosing some initial condition and the uncertainty associated with the number of steps needed to reach a required accuracy. However, in practice these are not as limiting as might first be expected for two reasons. First, most problems have a known dominant mode which can be used as a good initial condition. Second the method is absolutely stable so iteration time can be made very large to start with and reduced as required.

Accurate solutions to microwave discontinuity problems may now be possible with modern numerical techniques. Furthermore the trend towards more powerful computers means that general purpose models which retain physical interpretation, such as the TLM method, will become more attractive as the computational overhead factor decreases.

References

1. E.C. Jordan,"Electromagnetic waves and radiating systems" Prentice Hall, 2nd Edition, 1968, Section 5.5, p 155.

2. G. Kron,"Equivalent circuit of the field equations of Maxwell", Proc IRE, vol 32, May 1944, pp 360-367.

3. S. Akhtarzad P.B. Johns,"Solution of Maxwell's equations in three space dimensions and time by the TLM method of numerical analysis", Proc. Inst. Elec. Eng. vol 122, no 12 Dec 1975, pp 1344-1348.

4. Alexopoulos, "Integrated circuit Structures on Anistropic Substrates", IEEE MTT, vol 33, no 10, Oct 1985, pp 8xx-881.

5. W.J.R Hoefer,"The transmission line matrix - Therory and application", IEEE MTT, vol 33, no 10, Oct 1985, pp 882-893.

6. G.E. Mariki C. Yeh,"Dynamic Three Dimensional TLM Analysis of Microstrip Lines on Anisotropic Substrate" IEEE MTT, vol33, no 9, Sept 1985, pp 789-799.

7. S. Akhtarzad P.B. Johns,"The dispersion characteristic of a microstrip line with a step discontinuity" Electron Lett., vol 11, July 1975, pp310-311.

8. A. Farrar, A.T. Adams,"Matrix methods for microstrip three dimensional problems", IEEE MTT, vol 20, no 8, Aug 1972, pp 497- 540.

9. P. Saguet W.J.R Hoefer,"The modelling of multiaxial discontinuities in quasi-planar structures with the modified TLM method", Int. J. of Numerical Modelling, vol 1, no 1, Mar 1988, pp 7-17.

10. S. Akhtarzad J.B. Johns,"The TLMRES computer program for the analysis of Microstrip resonators", ASIS/NAPS Doc no NAPS 02862.

11. X. Zhang et al.,"Calculations of the dispersive characteristics of microstrips by the time-domain finite difference method", IEEE MTT, vol 36, no 2, Feb 1988, pp 263-267.

12. W. McKenzie et al.,"3-D TLM analysis of E plane transitions for MM wave networks" Proc. 18th European Microwave Conf. 1988, pp 156-161.

13. D.A. Al-Mukhtar et al,"Transmission Line Matrix method with irregularly graded space" IEE Proc, Vol 128, Pt H, No 6 Dec 1981, pp 299-305.

14. P.B. Johns,"A symmetrical Condensed Node for the TLM method", IEEE Trans MTT, vol 35, no 4, April 1987, pp 370-377.

THREE DIMENSIONAL
NODE STRUCTURE

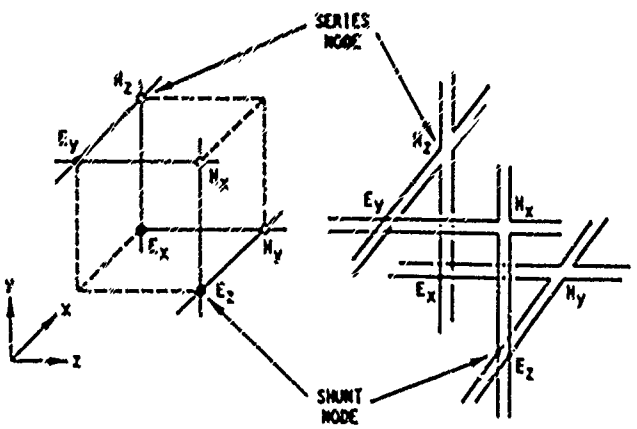
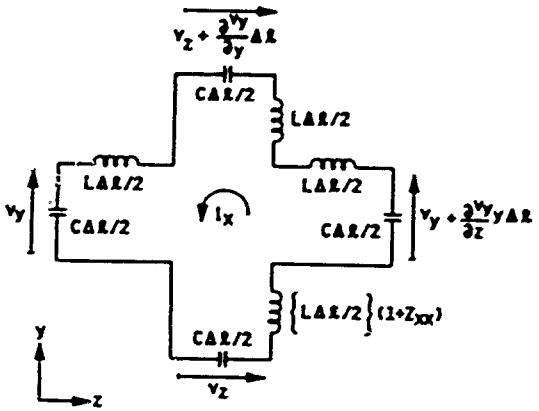


Figure 1

DETAIL OF SERIES MODE



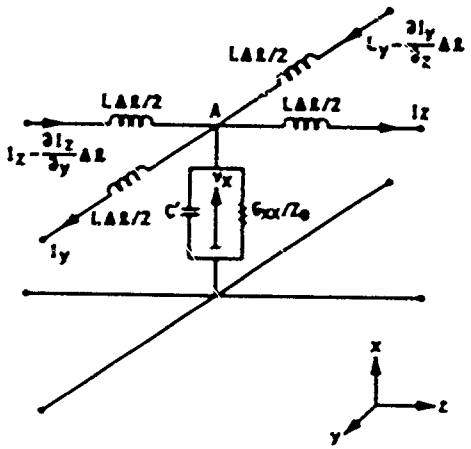
$$\nabla \times E = -\frac{\partial B}{dt}$$

$$\frac{\partial V_z}{\partial y} - \frac{\partial V_y}{\partial z} = -2L\left(1 + \frac{Z_m}{4}\right)\frac{\partial i_x}{\partial t}$$

$$\frac{\partial E_x}{\partial y} - \frac{\partial E_y}{\partial z} = -\mu_0\mu_m \frac{\partial H_x}{\partial t}$$

Figure 2

DETAIL OF SHUNT MODE



$$\nabla \times H = J + \frac{\partial D}{\partial t}$$

$$\frac{\partial i_x}{\partial y} - \frac{\partial i_y}{\partial z} = \frac{G_m V_x}{Z_0 \Delta l} + 2C\left(1 + \frac{Y_m}{4}\right)\frac{\partial V_x}{\partial t}$$

$$\frac{\partial H_x}{\partial y} - \frac{\partial H_y}{\partial z} = \sigma_m E_x + \epsilon_0\epsilon_m \frac{\partial E_x}{\partial t}$$

Figure 3

THREE DIMENSIONAL
MICROSTRIP CAVITY

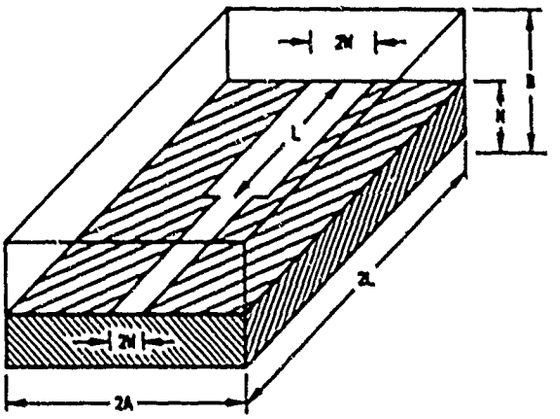
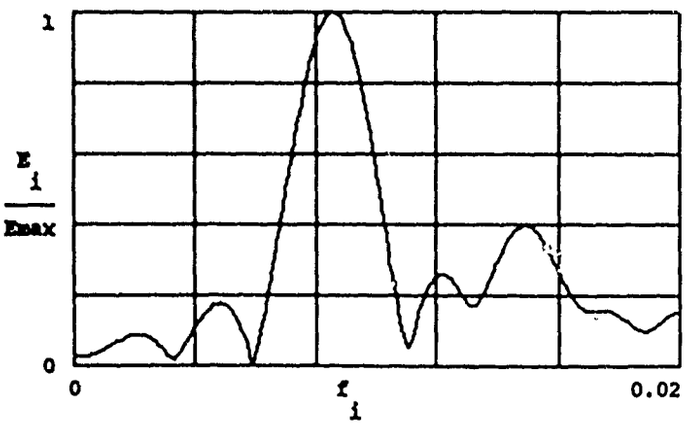


Figure 4

Frequency Response of Microstrip Cavity



Normalized Frequency dL/v

Figure 5

EXAMPLE OF MESH GRADING
FOR A MICROSTRIP PROBLEM

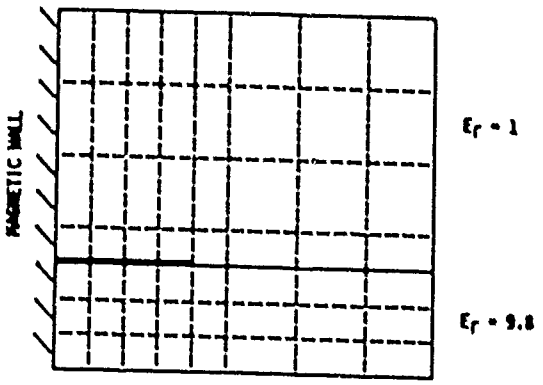


Figure 6

THE SYMMETRICAL
CONDENSED NODE

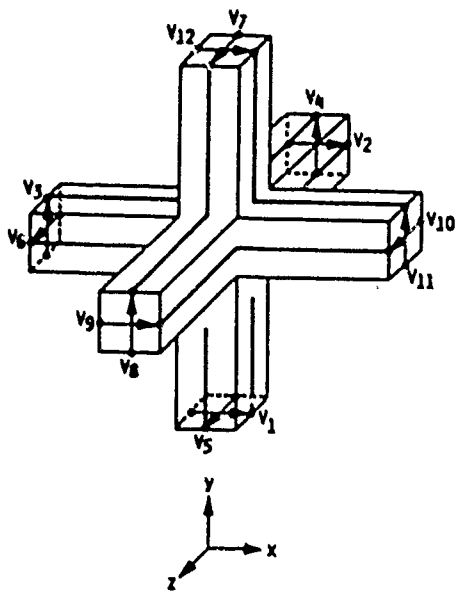


Figure 7

THREE-DIMENSIONAL FULL-WAVE ANALYSIS OF PASSIVE MICROSTRIP COMPONENTS USING THE TLM METHOD

F.J. German, H.D. Williams, L.S. Riggs, M.E. Bagiraki
Department of Electrical Engineering
200 Broun Hall
Auburn University, AL 36849

In this paper we apply the TLM method to the problem of determining the frequency characteristics of passive microstrip circuit elements. A pulse excitation is used to excite the structure. The frequency domain information is then obtained via the FFT of the input pulse and the output. From this data the frequency dependence of the structure can be determined over a broad frequency range. There are several advantages to this technique. The first being that a single analysis using a pulsed excitation yields frequency information over a broad bandwidth. Secondly, since the method is completely three dimensional and material parameters can be specified arbitrarily through the mesh, complex structures can be analyzed. In addition, there is no need to know a Green's function for the specific problem at hand. The method is also very general and efficient--no reformulation is required for different geometries; only the input data requires modification.

INTRODUCTION

The ever increasing use of microstrip and stripline type transmission lines in microwave and hybrid circuits at higher frequencies and switching speeds has led to the need for a full wave electromagnetic analysis of these structures for the prediction of their electrical properties. The costly procedure of building and testing such structures on an iterative basis has led to the need for efficient computer algorithms for use in the design stages of these devices.

At lower operating frequencies, quasi-static analyses often give results that are quite satisfactory [1]. However, as the frequency increases, the non-TEM nature of the structures becomes more pronounced and the quasi-static techniques begin to break down. Since it is not exactly clear at what frequency this occurs, great caution must be exercised so as not to use these methods when they are not valid.

In order to overcome this problem, a full wave three dimensional solution of Maxwell's equations becomes necessary. The method chosen should be efficient and general enough to adapt to different geometries. We have applied the transmission line matrix (TLM) method to the analysis of these structures. Preliminary investigations have shown that the TLM method is capable of predicting dispersion in microstrip type transmission lines as well as the characteristics of discontinuities and coupled systems [2]. In this paper, we present further results on the TLM analysis of passive microstrip components.

THE TLM METHOD

The TLM method works by modeling a portion of space with a mesh of

interconnected transmission lines. Voltages and currents on the transmission lines are used to calculate the electric and magnetic field quantities via well known equivalences. A three dimensional TLM cell is shown in Figure 1. An area of space is discretized using many of these cells. Boundaries and material parameters are modeled by the addition of inductance, capacitance, and resistance to the transmission lines in each cell. The time domain impulse response of the three dimensional transmission line mesh is calculated by stepping in time with all six electromagnetic field components available at the center of each cell at each time step. This time domain transfer function can then be convolved with a desired excitation function or Fourier transformed to yield the desired electromagnetic field data. [4]

MICROSTRIP LINES

The basic geometry of a simple microstrip transmission line is shown in Figure 2. Because the fields occupy both the dielectric and the air above the strip, the microstrip line displays dispersive behavior. Also, although at low frequencies the propagating mode can be approximated by a TEM field distribution, the actual propagating mode is a TE mode. In order to accurately model a microstrip line, the modeling technique must be able to account for the dispersive properties of the line as well as the non-TEM propagating mode.

To demonstrate the TLM modeling of microstrip lines, a single microstrip with w = 25 mils, h = 25 mils, and ϵ_r = 10 was modeled with our three dimensional TLM program. In order to terminate the finite TLM mesh without introducing non-physical reflections we have developed a perfectly absorbing boundary condition which works for inhomogeneous anisotropic spaces. Figure 3 shows the time domain response for the y directed electric field component directly beneath the strip at several points along the microstrip line. The dispersive behavior of the

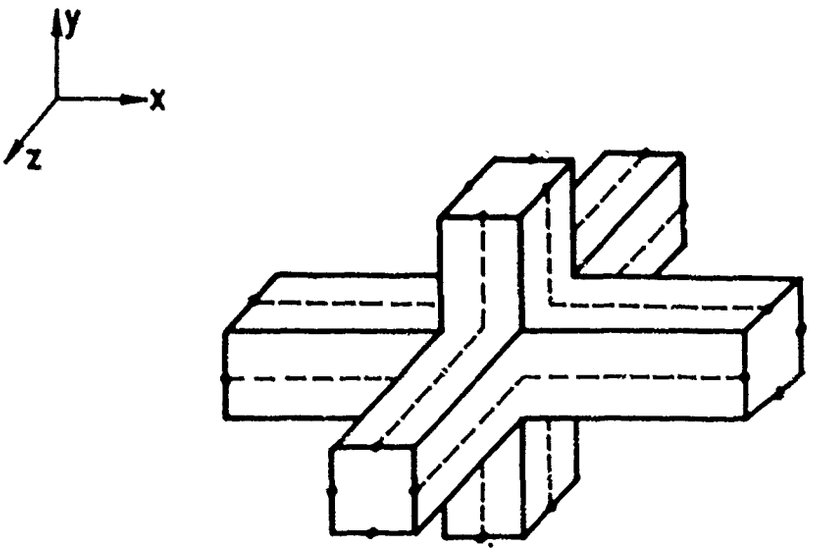


Fig. 1. Symmetrical Condensed TLM Node.

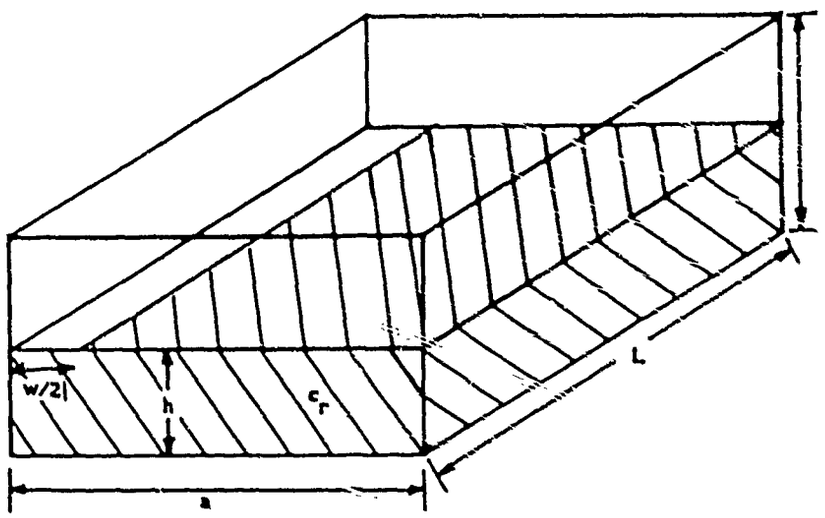


Fig. 2. Geometry of Microstrip.

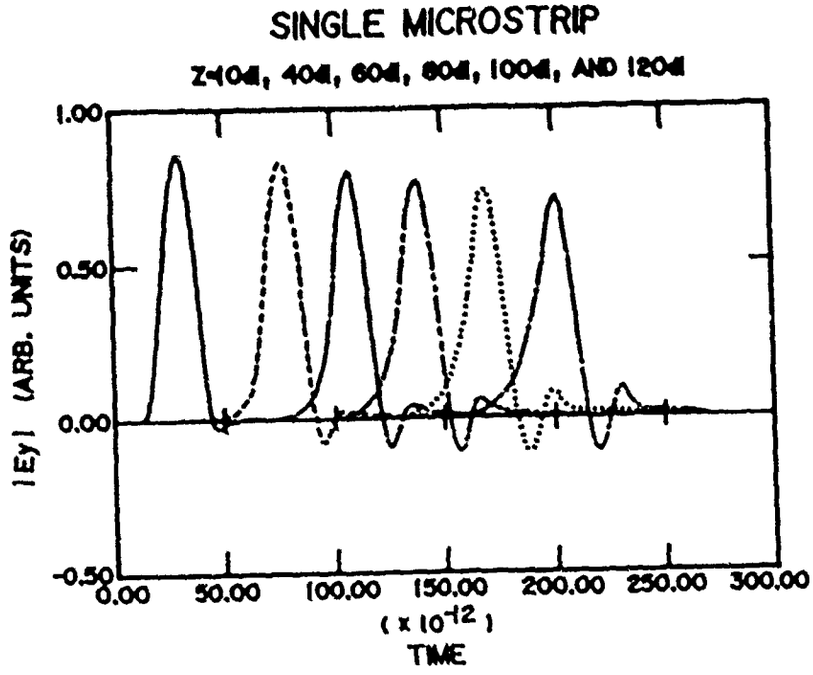


Fig. 3. Time-Domain Pulse Propagation along Microstrip.

microstrip line causes the pulse to distort as it propagates along the line and clearly the TLM method has modeled this behavior.

In order to investigate the propagating mode characteristics, we have examined the x component of the electric and magnetic fields midway between the strip and ground plane as a function of frequency. These results are given in Figure 4 and it is evident that the propagating mode is mainly TE, becoming more so with increasing frequency.

The time domain data in Figure 3 demonstrates, in a qualitative way, the dispersive characteristics of microstrip transmission lines. In order to produce useful design data, however, it is often useful to examine frequency domain data. For this reason, we have calculated the propagation constant β ($=2\pi/\lambda_g$) versus frequency for a microstrip line of w/h = 1.0, h = 1.27 mm. The results are shown in Figure 5 along with data presented in [5] for substrate permittivities of $4.2\varepsilon_o$ and $20\varepsilon_o$. The values for normalized guide wavelength agree within a couple of percent. This agreement is very good considering that a very coarse TLM mesh was used for the analysis (the dielectric was only 6 cells deep). It is interesting to note that these curves were calculated using a stepped impedance boundary technique [6] which allows an arbitrary length of microstrip line to be modeled using only two cells in the propagation direction.

Next we investigated the calculation of the characteristic impedance of microstrip lines with the TLM method. We have defined the characteristic impedance of the microstrip as follows:

$$Z_0 = |V|/|I|$$

where V is the voltage between the center of the strip and the ground plane, and I is the current in the strip. The voltage is calculated by integrating the TLM calculated electric field along a line between the

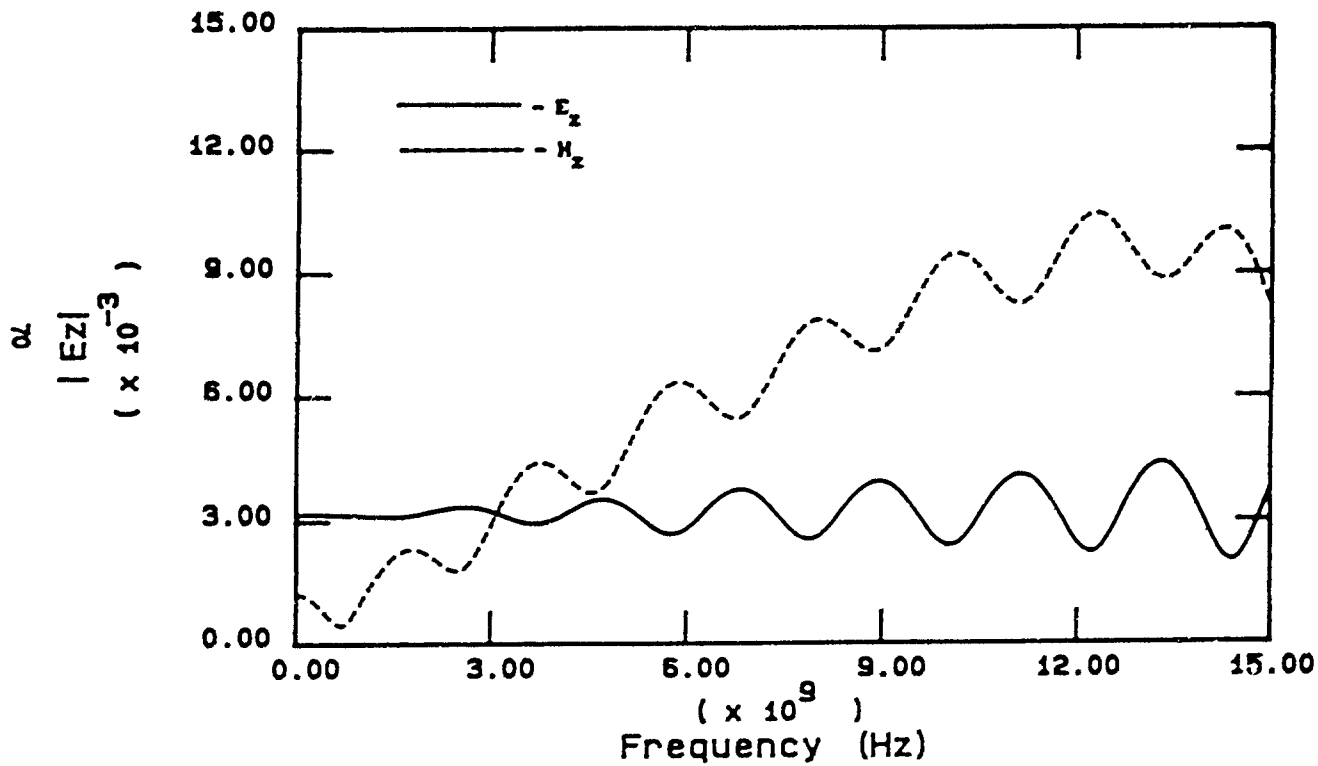


Fig. 4. Magnitude of the Z-directed Fields vs. Frequency.

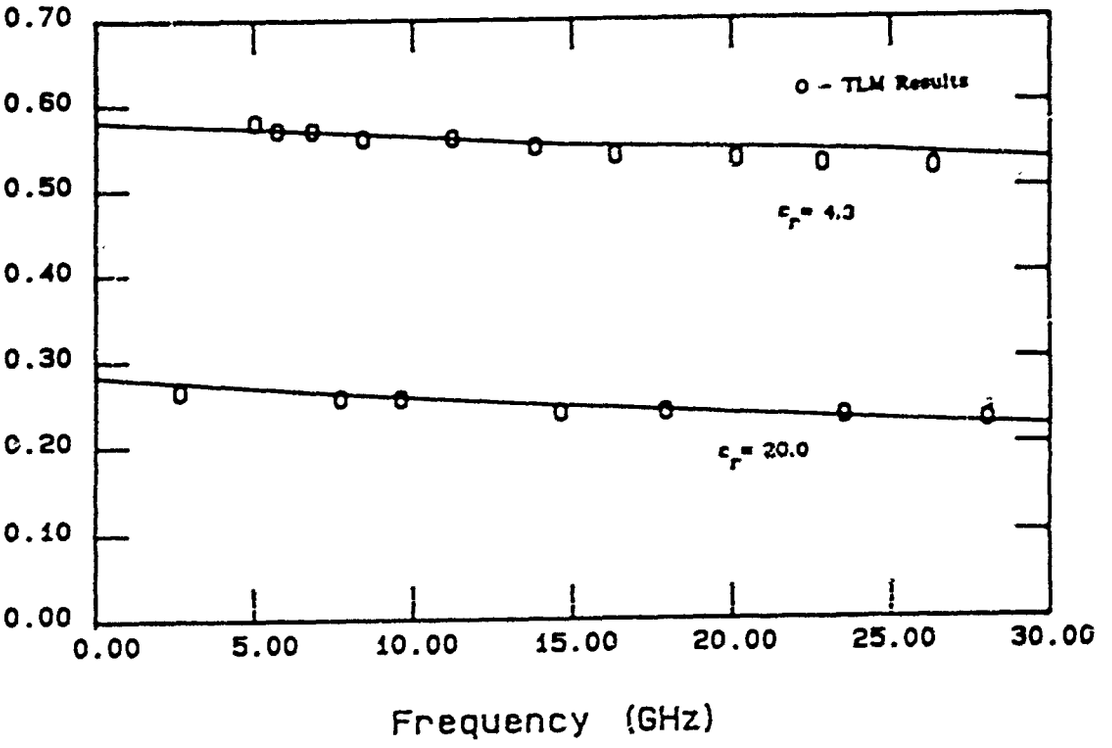


Fig. 5. Normalized Microstrip Wavelength. (w/h = 1.0)

strip and ground. I is calculated by integrating the magnetic field about a path enclosing the strip. Results for several W/H ratios for a substrate of $\epsilon_r = 2.6$ are shown in Figure 6. These are plotted on a curve given by Yoshida and Fukai in [7].

In order to compare our results with the results of measurements, we have examined the buried microstrip line shown in Figure 7. This geometry was analyzed, and measured results were presented in [1]. The results for the characteristic impedance from a moment analysis yielded 39.47 Ω. Integration of the TLM calculated field using a voltage/current definition for the characteristic impedance yielded a value of 39.55 Ω. These results, and values for the static capacitance of the structure are shown in Table I.

TABLE I

Method	C (pF/cm)	Z_o(Ω)
MOM	2.62	39.43
TLM	2.61	39.55
Measured	2.48	-

FUTURE DEVELOPMENTS

In order to get the full benefits of the full wave three dimensional analysis techniques such as TLM, they must be incorporated into user friendly CAD circuit packages. Many of the CAD packages available today, GREENFIELD, for example, use quasi-static techniques for the analysis of transmission lines and discontinuities which have been shown to lose validity at higher frequencies. Thus, we are working on implementing the TLM analysis of these structures into already existing CAD packages.

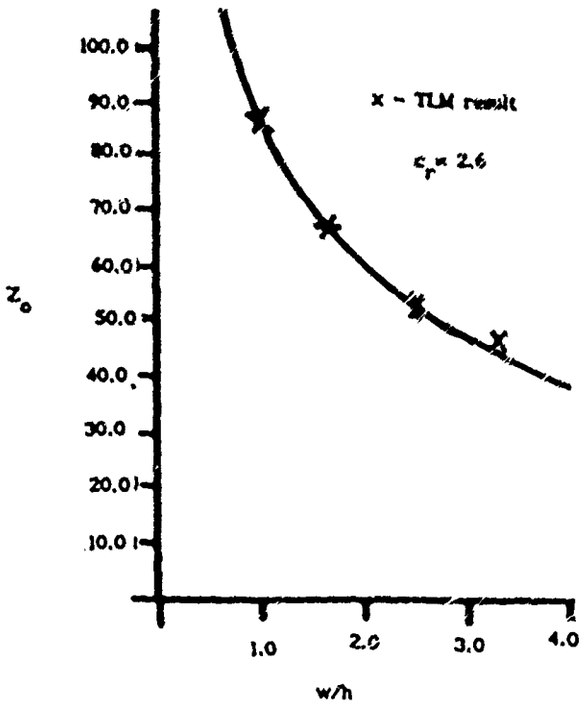


Fig. 6. Caracteristic Impedance (Z_o) of Microstrip.

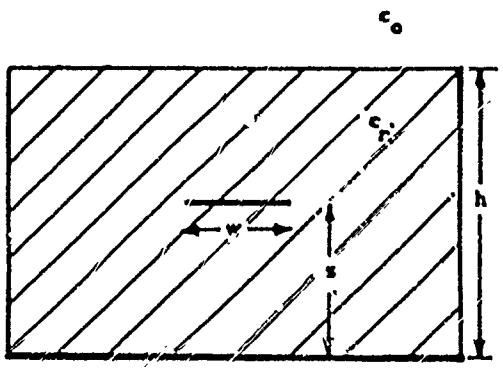


Fig. 7. Buried Microstrip Geometry.

Of the presently available CAD packages that do not use utilize quasi-static analyses for the electromagnetic analysis, many are restricted in the type of passive components that they can model. One of the main advantages of TLM is that the geometry of the device under consideration can be quite arbitrary. For example, layered lines in layered media are easily modeled. Also, three dimensional discontinuities such as wire bonds or vias can be modeled rather easily. As an example of a three dimensional discontinuity, a wire bond, is shown in Figure 8. Figure 9 shows the response at the input port to a 35ps rise time voltage step. Comparison of this waveform with preliminary data measured with a time domain reflectometer (TDR) shows reasonable agreement. We are currently making more refined measurements of several structures for comparison with TLM calculated data.

CONCLUSIONS

We have presented our results for the analysis of passive microwave devices using the TLM method of electromagnetic analysis. Comparison with other methods and measurements where available has been very favorable. The advantages of the TLM method lie in the fact that the method produces a full wave three dimensional solution to Maxwell's equations. In addition, the method is simple, general (the TLM program used for the results in this paper has been used, without modification, to predict the EMP response of aircraft and buildings simply by changing the input data), and efficient. The simplicity and generality of the method has led us to work on incorporating the TLM method into existing CAD packages for microwave and hybrid circuits.

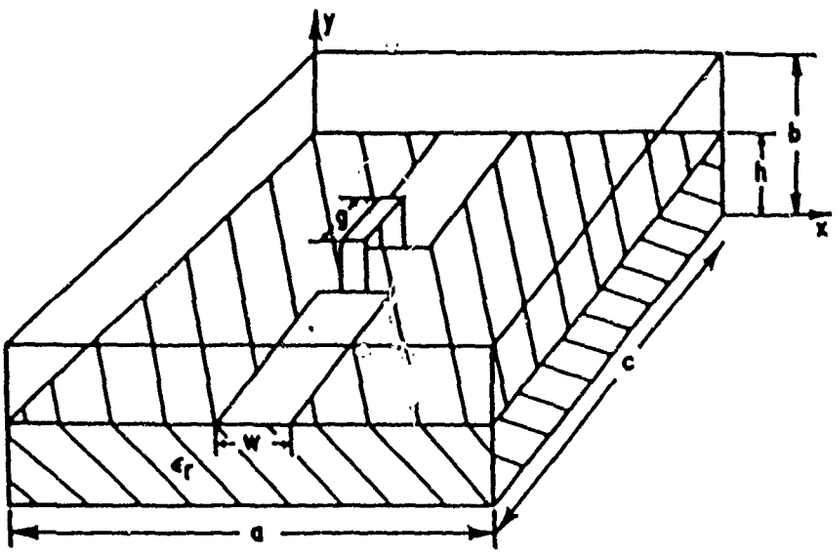


Fig. 8. Geometry of Wire Bond.

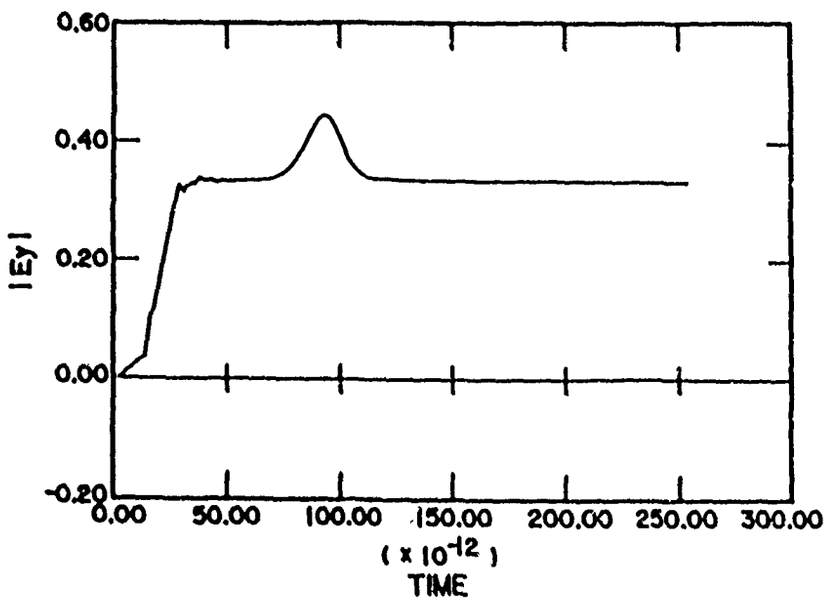


Fig. 9. Time Domain Response of Wire Bond Geometry at Input Port.

REFERENCES

[1] M.R. Scheinfein, J.C. Liao, O.A. Palusinski, and J.L. Prince, "Electrical Performance of High-Speed Interconnect Systems," IEEE Trans. Components, Hybrids, and Manuf. Tech, Vol. CHMT-10, no. 3, Sept. 1987, 303-309.

[2] F.J. German, B. Dillard, L.S. Riggs, and R.W. Johnson, "Transmission Line Matrix Method for Modelling the Electrical Performance of Interconnections," Proceedings of the 1988 International symposium on Microelectronics," Oct. 1988, Seattle, WA, 402-409.

[3] G. Kron, "Equivalent Circuit of the Field Equations of Maxwell - I," Proceedings of the IRE, May 1944, 289-299.

[4] P.B. Johns, A Symmetrical Condensed Node for the TLM Method," IEEE Trans. Microwave Theory Tech., Vol. MTT-35, no. 2, April 1987, 370-377.

[5] T. Itoh and R. Mittra, "Spectral-Domain Approach for Calculating the Dispersion Characteristics of Microstrip Lines," IEEE Trans. Microwave Theory Tech, Vol. MTT-21, July 1973, 496-499.

[6] J.E. Sitch and P.B. Johns, "Transmission-line Matrix Method Analysis of Continuous Waveguiding Structures Using Stepped-Impedance Cavities," Proceedings IEE: Microwaves, Optics, and Acoustics, Vol. 1, no. 5, Sept. 1977, 181-184.

[7] N. Yoshida and I. Fukai, "Transient Analysis of a Stripline Having a Corner in Three-Dimensional Space," IEEE Trans. Microwave Theory Tech., Vol. MTT-32, no. 5, 491-498.

The Field Theoretic MMIC Computation Enhanced by the Variational Principle

by
Y.L. Chow, G.E. Howard and M.G. Stubbs
University of Waterloo and Communications Research Centre, Canada

Abstract

The field theoretic software MATHIC - EMsim [1] has been shown to give accurate results for MIC and MMIC circuits, eg. [2]. It is a modification of the moment method for linear antennas [3] and requires the solution of a matrix equation.

For large circuits, eg. large couplers and spiral transformers, the matrix size can be up to 500 X 500 and takes up substantial amounts of computer time, especially if many frequency points are required.

A simple way to enhance the computing speed is to select a few frequency points for an accurate solution by the matrix equation. The frequency points not computed with such solution are solved by interpolation through the variational principle.

The variational principle for two linear antennas a and b is the well known formula [4],

$$Z_{ab} = \frac{-1}{I_a I_b} \int_{\ell_b} \bar{E}^a \cdot \bar{I}^b \, d\ell_b \qquad (1)$$

The variational formula for MIC-MMIC circuits is the same except that a and b represent ports of the circuits. The variational formula gives accurate results provided that the currents $\bar{I}^b$ and $\bar{I}^a$ (generating $\bar{E}^a$) are approximately known. With the selected frequency points accurately computed, as mentioned in the last paragraph, it is a simple matter to find the approximate currents $\bar{I}^b$ and $\bar{I}^a$ at the intermediate frequencies, by a linear interpolation.

Equation (1) is quite accurate because of the nature of the variational principle, but it requires no solution of the matrix equation and thus the computing speed is greatly enhanced.

An MMIC spiral transformer, shown in figure 1 is computed using matrix solution every fourth frequency point. The result as shown in figure 2 is just as accurate as the all matrix solution, but only taking 1/3 the computer time.

The paper ends with a discussion on the interdependance of the computer time, the variational solutions and the matrix solutions of the moment method MATHIC-EMsim.

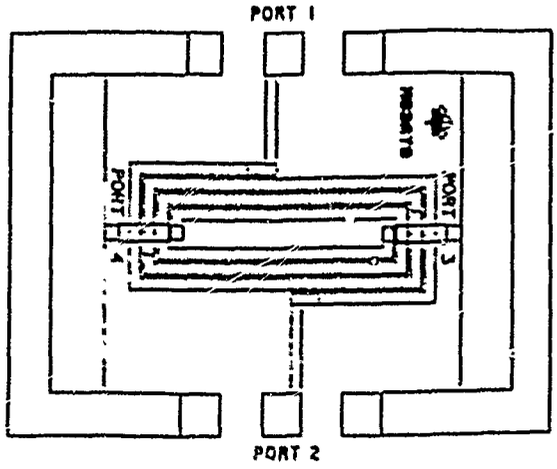
References

[1] EMsim: MIC software of EEsof Inc. Westlake Village Ca. 1988. WATMIC: field theoretic software from Univ. of Waterloo, Waterloo, Ont., Canada 1987. WATMIC is embedded in EMsim.

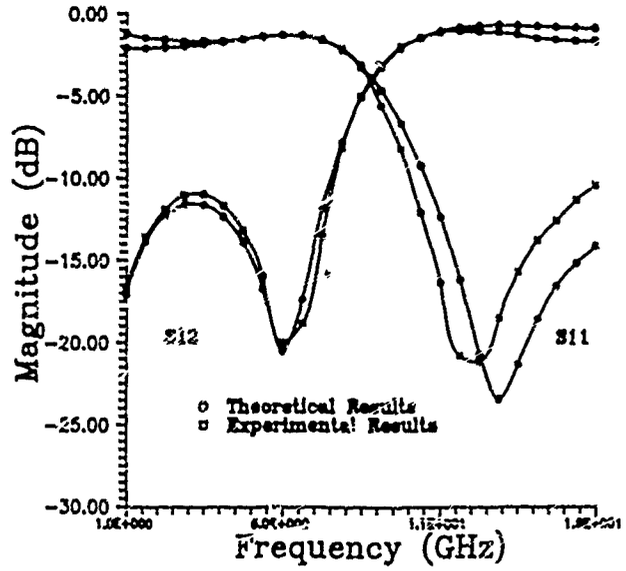
[2] M.G. Stubbs, Y.L. Chow and G.E. Howard, "Use of a Spatial Field Technique for the Analysis of Active MMICs", Proc. 17th European Microwave Conference, Rome, Sept 1987.

[3] R.F. Harrington, "Field Computation by Moment Methods", R.E. Krieger Publishing Co., Malabar, Florida. Reprinted Edition 1982, Chapter 4.

[4] R.F. Harrington, "Time Harmonic Electromagnetic Fields", McGraw-Hill Book Company Inc. New York, 1961, pp 349.



The spiral transformer example.



The $|S_{21}|$ and $|S_{11}|$ responses of the two port configuration of the transformer in Fig. 1.

ACCURATE AND EFFICIENT MODELING OF DISPERSIVE MMIC PASSIVE DISCONTINUITY COMPONENTS

Akifumi Nakatani and Jesse Castaneda

Phraxos Research & Development Inc.
2716 Ocean Park Blvd., Suite 1020
Santa Monica, California 90405

Abstract

The fullwave Green's-function-and-Method-of-Moments approach is recognized as the most general and accurate solution method to the problem of high frequency modeling of MMIC passive circuit components. However, the computer codes derived on the basis of this method are usually computationally intensive. Several numerical techniques that significantly improve both the accuracy and efficiency of this method are presented. The numerical technique is described as it has been applied to the problem of the waveguide shielded microstrip structure.

This research was supported by the U.S. Army under research contract DAAL 01-88-C-0513 and the Air Force contract F19628-88-C-0059.

1 Introduction

Recently, significant attention has been paid to the characterization of high frequency microstrip discontinuities, since ultimately the accuracy of a MMIC design depends on the accuracy of the individual junction models. The high frequency information, such as the equivalent circuit or scattering matrix parameters of the junctions, can be extracted by many different ways. A method has been described by Katehi and Alexopoulos [2] where the discontinuity characteristics are deduced from the standing wave pattern of current on the microstrip line. In that method the line (or lines) are excited by a delta-gap voltage source. R.W. Jackson [3,5] and Pozar [3], on the other hand, used an incident traveling wave (on the microstrip line) as the excitation in their moment method solution. Chu and Itoh [7] analyzed the step discontinuity using waveguide models with magnetic sidewalls for the lines. A spectral domain analysis in an enclosed structure has been used by Jansen [1,6] and Koster [6] extensively. This work addresses the characterization of waveguide shielded lines and discontinuities. It is a complete dynamic solution and all the effects associated with the waveguide enclosure (shield) are included. In the application of the moment method procedure, an expansion of the surface current density on the microstrip line or of the electric field on the slot line is made. The basis functions include *dominant traveling wave* functions and *roof-top* subdomain basis functions. A special modification of the traveling wave functions has been introduced which increases the accuracy of the characterization in the quasi-static limit. The roof-top basis functions are used in the immediate vicinity of the junction to represent any possible current/field disturbance.

The focus of this work is on the application of the modified traveling wave functions to the general problem of shielded MMIC structures [4], and on the use of an interpolation technique which significantly reduces computational times in the characterization of general discontinuity structures.

2 Green's Function Approach

Figure 1 depicts the cross section of the multilayer substrate structure within the surrounding waveguide shield. Microstrip currents and/or slot fields can be represented by:

$$\bar{\Psi}(x,y,z) = \sum_{n=-\infty}^{\infty} \int_{-\infty}^{+\infty} \bar{\bar{\Psi}}(k_{zn},y,k_z)\, e^{jk_z z} e^{jk_{zn}x} dk_z \ , \tag{1}$$

or

$$\bar{\Psi}(x,y,z) = \sum_{n=0}^{\infty} \int_{-\infty}^{+\infty} \bar{\bar{\Psi}}(k_{zn},y,k_z)\, e^{jk_z z} cs(k_{zn}x) dk_z \ , \tag{2}$$

where $\bar{\bar{\Psi}}(k_{zn},y,k_z)$ can be represented as

$$\bar{\bar{\Psi}}(k_{zn},y,k_z) = \Omega(k_{zn},y,k_z) \cdot \bar{\bar{\Phi}}(k_{zn},s_1,k_z) \ . \tag{3}$$

The quantities, $\bar{\bar{\Phi}}(k_{zn},s_1,k_z)$ and $\bar{\bar{\Psi}}(k_{zn},y,k_z)$, refer to the transforms of $\vec{E}$ or $\vec{J}$. $\Omega(k_{zn},y,k_z)$ is the dyadic which relates the electric fields and current distributions. In the above definition, $sc(k_{zn})$ is defined either as *sine* or *cosine* functions where the center and side wall

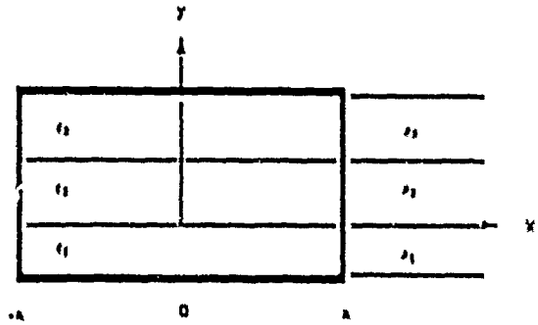


Figure 1: Geometry of Interest

conditions (electric or magnetic) are included in the transform. The first form is the complex finite Fourier transform and the second form is the *sine* or *cosine* Fourier transform. When the second form is taken, the appropriate transform must be selected, depending on the side wall boundary conditions and the field or current component. These component relations are given in reference 4. When $\bar{\bar{\Phi}}(k_{xn}, s_1, k_z)$ is expanded in terms of known basis functions as

$$\bar{\bar{\Phi}}(x, s_1, z) = \sum_{m=1}^{\infty} c_m \cdot \bar{\bar{\Phi}}_m(x, s_1, z) = \sum_{m=1}^{\infty} \bar{\bar{\Phi}}_m(x, s_1, z) \cdot c_m \ , \tag{4}$$

then the substitution of above equation yields

$$\bar{\bar{\Psi}}(x, y, z) = \sum_{m=1}^{\infty} \left\{ \sum_{n=0}^{\infty} \int_{-\infty}^{+\infty} \Omega(k_{xn}, y, k_z) \cdot \bar{\bar{\Phi}}_m(k_{xn}, s_1, k_z) e^{jk_z z} \, sc(k_{xn} x) dk_z \right\} \cdot c_m \ . \tag{5}$$

When the inner product of the basis function is taken for the left and right hand sides of Equation (5), the following linear equation is obtained:

$$\bar{V}_{m'} = \sum_{m=1}^{\infty} \bar{Z}_{m'm} \cdot c_m \tag{6}$$

When the same number of testing functions are used in the above equations, a set of linear equations is obtained.

$$\left[\bar{V}_{m'}\right] = \left[\bar{Z}_{m'm}\right] \cdot \left[c_m\right] \tag{7}$$

The unknown dyadic coefficients are numerically obtained. In the above equation, $\bar{V}_{m'}$ and $\bar{Z}_{m'm}$ are defined as

$$\bar{V}_{m'} = \langle \bar{u}_{m'}(k_{xn}, s_1, k_z), \bar{\bar{\Psi}}(k_{xn}, s_1, k_z) \rangle = \int_{z=0}^{a} \int_{x=-\infty}^{\infty} \bar{u}_{m'}(x, s_1, z) \cdot \bar{\bar{\Psi}}(x, s_1, z) dx \, dz \tag{8}$$

and

$$\bar{Z}_{m'm} = \sum_{n=0}^{\infty} \int_{-\infty}^{\infty} \langle \bar{u}_{i,m'}(z, s_1, z), e^{jk_z z} \, sc(k_{xn} x) \rangle \cdot \Omega(k_{xn}, s_1, k_z) \cdot \bar{\bar{\Phi}}_m(k_{xn}, s_1, k_z) \, dk_z \ . \tag{9}$$

The last expression can also be written as:

$$\bar{\bar{Z}}_{m'm} = \sum_{n=0}^{\infty} \int_{-\infty}^{\infty} \bar{\bar{u}}^{*}_{m'}(k_{zn}, s_1, k_z) \cdot \Omega(k_{zn}, s_1, k_z) \cdot \bar{\bar{\Phi}}_m(k_{zn}, s_1, k_z)\, dk_z \ , \qquad (10)$$

where $\bar{\bar{u}}^{*}_{m}(k_{zn}, s_1, k_z)$ is the conjugate operation. When there is no source, then the problem is an eigenvalue problem. $\bar{\bar{\Phi}}(k_{zn}, s_1, k_z)$ is the Fourier transform of the basis expansion function defined as

$$\bar{\bar{\Phi}}(k_{zn}, s_1, k_z) = \frac{\epsilon_{zn}}{2\pi a} \int_{-\infty}^{\infty} \int_{-a}^{a} \bar{\Phi}(x, s_1, z)\, e^{-jk_z z}\, sc(k_{zn} x)\, dx\, dz \qquad (11)$$

where $\epsilon_{zn} = 1/2$ only if $k_{zn} = 0$, otherwise $\epsilon_{zn} = 1$. [1] When the basis function is separable, Equation (10) can be expressed as

$$\bar{\bar{Z}}_{m'm} = \int_{-\infty}^{\infty} \bar{\bar{u}}^{*}(k_z) \cdot S(k_z) \cdot \bar{\bar{\Phi}}_i(k_z) dk_z \ , \qquad (12)$$

where $S(k_z)$ is defined as

$$S(k_z) = \sum_{n=0}^{\infty} \bar{\bar{u}}^{*}(k_{zn})\, \Omega_{ij}(k_{zn}, k_z) \bar{\bar{\Phi}}_i(k_{zn}) \qquad (13)$$

with $\Omega_{ij}(k_{zn}, k_z)$ as the dyadic component for $i, j = x, z$. In the above definition, $\bar{\Phi}(x, z)$ is the basis function and the quantities of $\bar{\bar{\Phi}}_i(k_{zn})$ and $\bar{\bar{\Phi}}_i(k_z)$ are defined as the x and z dependent terms of the basis functions. Since the electric field or current distribution at an arbitrary position can be constructed by linearly superimposing all the components caused by the segmental basis functions, the total interaction $\bar{\Psi}^{total}$ can be expressed as

$$\bar{\Psi}^{total} = \bar{\Psi}^{drv} + \sum \bar{\Psi}^{jnc} + \sum \bar{\Psi}^{rct} \qquad (14)$$

where "*drv*" identifies the driving function, "*jnc*" the junction field/current functions, and "*rct*" the reaction field/current functions. In general, the number of reaction functions must be equal to N for the N-port network.

3 Algorithm Description

A general algorithm to approach the discontinuity problem is described in Figure 2.

3.1 Matrix Management

A solution of a discontinuity problem by the present method involves the partition of the junction into rectangular subsections. In effect, a rectangular grid is overlaid on the junction. This is depicted in the drawing in Figure 3 for the asymmetric step discontinuity. In the procedure the circuit component one wishes to analyze is drawn on the grid, following

[1] In reference [4], the summation must start from n = 0 and ϵ_{zn} must be added.

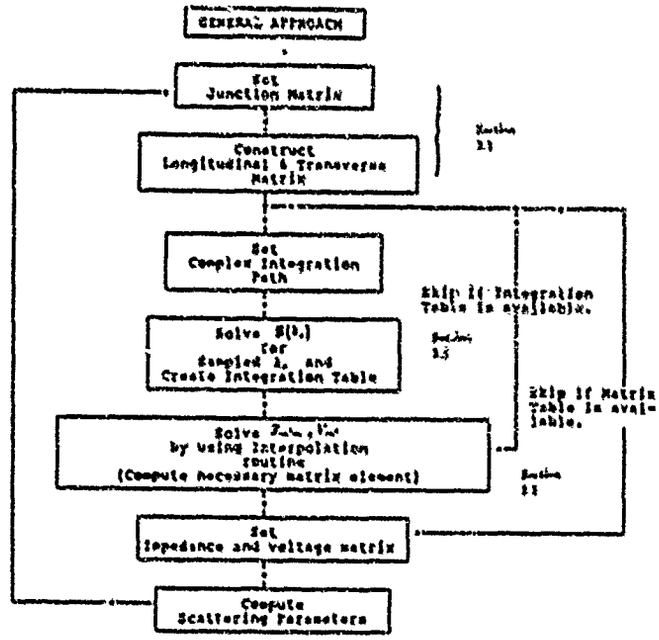


Figure 2: General Algorithm for Discontinuity Problem

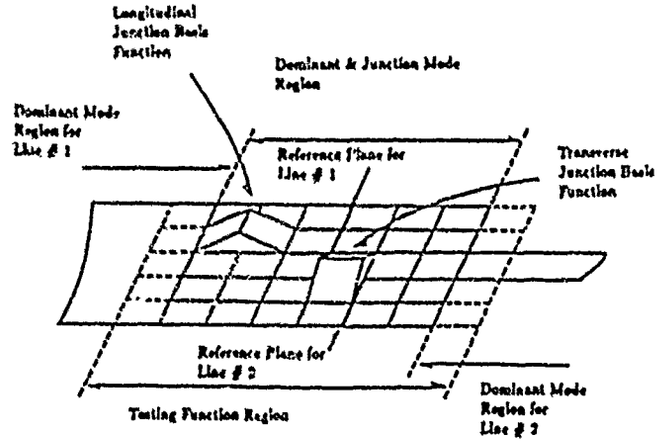
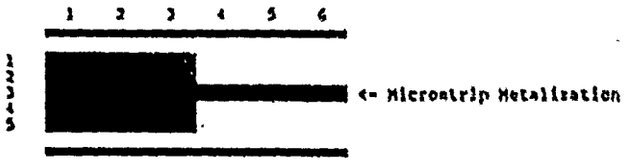


Figure 3: Grid Partitioning in the Vicinity of Junction



. Longitudinal Geometry Matrix

$$\begin{bmatrix} 1 & 1 & 0 & 0 & 0 \\ 1 & 1 & 0 & 0 & 0 \\ 1 & 1 & 1 & 1 & 1 \\ 1 & 1 & 0 & 0 & 0 \\ 1 & 1 & 0 & 0 & 0 \end{bmatrix}$$

. Transverse Geometry Matrix

$$\begin{bmatrix} 1 & 1 & 1 & 0 & 0 & 0 \\ 1 & 1 & 1 & 0 & 0 & 0 \\ 1 & 1 & 1 & 0 & 0 & 0 \\ 1 & 1 & 1 & 0 & 0 & 0 \end{bmatrix}$$

Figure 4: Geometry Cell and Longitudinal/Transverse Basis Matrixes

the grid lines. This identifies the subdomain segments that must be used in the moment method. One, or both, longitudinal and transverse basis functions may be required in each of the subdomain regions. In the solution, impedance matrix elements (of the method of moments) are found for the complete rectangular grid, that is for all subsections or cells of the grid regardless of whether the component of interest requires it or not. We start, therefore, with the impedance matrix to a rectangular patch. Geometry matrices are then introduced that, in effect, select the subdomain terms appropriate to the component. This identification is completed in terms of three geometry matrices that are defined as follows: $g(i,j)$ describes, exactly, the topology of the component. A value of one indicating that the associated cell is part of the conductor (for microstrip), and a value of zero indicating there is no conductor in that cell region. This is the matrix that the user will specify to describe his component. Because of the nature of the basis functions the matrices that identify the location of the basis functions are shifted. This is reflected in their definitions. For the transverse-current-basis-geometry-matrix we have

$$g^t(i,j) = g(i,j) \cdot g(i+1,j) \ , \tag{15}$$

while for the longitudinal-basis-functions-geometry-matrix, we write

$$g^\ell(i,j) = g(i,j) \cdot g(i,j+1) \ . \tag{16}$$

When operated on by $g^t(i,j)$ and $g^\ell(i,j)$, the full-rectangular grid impedance matrix is reduced to that appropriate to the component under consideration. An inversion of the reduced matrix then results in the solution to the desired problem. An example is shown in Figure 4 where the number of cells is 30, and after operating with the geometry matrices the resulting longitudinal and transverse basis functions are reduced to 13 and 12 respectively. This methodology can be easily extended to address other irregular shaped junctions.

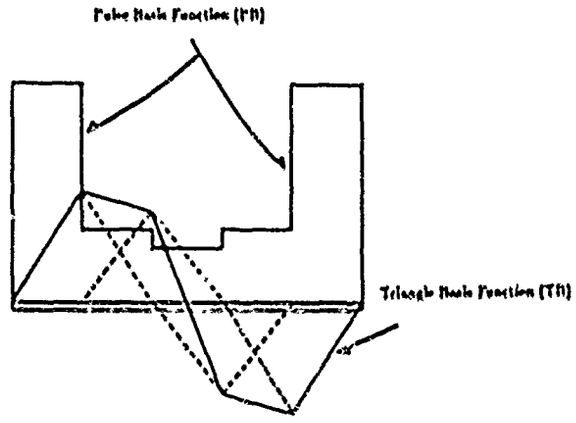


Figure 5: Basis Functions for Computing $S(k_z)$

3.2 Computation of $S(k_z)$

When the traveling waves (in-coming and out-going waves from the junction) have the same transverse dependence (x-dependence) as the roof-top basis functions, $S(k_z)$ can be computed independently of the longitudinal dependence (z-dependence) of the function. The longitudinal and transverse current distribution can be placed as shown in the Figure 5, where the longitudinal basis has a pulse shape (PB), while the transverse basis shows the triangle shape (TB).

With this choice of basis functions, $S(k_z)$ is expressed in a closed form where both the accuracy and the efficiency can be drastically improved. The asymptotic form of the dyadic Green's function can be expressed as

$$\lim_{k_{zn}\to\infty} \Omega(k_{zn}, z_1, k_z) = \Omega^{asy}(k_{zn}, z_1, k_z) = \begin{bmatrix} C_{zz}^{\infty}(k_z)k_{zn} & C_{xz}^{\infty}(k_z) \\ C_{zx}^{\infty}(k_z) & C_{xx}^{\infty}(k_z)/k_{zn} \end{bmatrix} . \qquad (17)$$

The k_z and k_{zn} dependences of the dyadic Green's function are separated. The transform of the normalized PB is obtained as $\tilde{\Phi}_{lm}^{PL} = sinc(k_{zn}\frac{\Delta}{2})sc(k_{zn}S_m)$ and the transform of the normalized TB is the convolution of PB so that the transform is obtained as $\tilde{\Phi}_{lm}^{TR} = sinc^2(k_{zn}\frac{\Delta}{2})sc(k_{zn}S_m)$. When the Galerkin's method is used, $S(k_z)$ can be written as

$$\begin{aligned} S(k_z) &= \sum_{n=0}^{\infty} \bar{\bar{\Phi}}_{lm'}^{*}(k_{zn})\, \Omega(k_{zn}, z_1, k_z) \bar{\bar{\Phi}}_{lm}(k_{zn}) \\ &= \sum_{n=0}^{\infty} \bar{\bar{\Phi}}_{lm'}^{*}(k_{zn})\, \Omega^{asy}(k_{zn}, z_1, k_z) \bar{\bar{\Phi}}_{lm}(k_{zn}) - \\ &\sum_{n=0}^{\infty} \bar{\bar{\Phi}}_{lm'}^{*}(k_{zn})\, [\Omega(k_{zn}, z_1, k_z) - \Omega^{asy}(k_{zn}, z_1, k_z)]\, \bar{\bar{\Phi}}_{lm}(k_{zn}) \end{aligned} \qquad (18)$$

where the summation of the first term can be easily converted to a closed form expression, which is easily evaluated. The factor in brackets of the second sum accelerates the convergence as compared to the original sum form, since the sum is evaluated as the difference

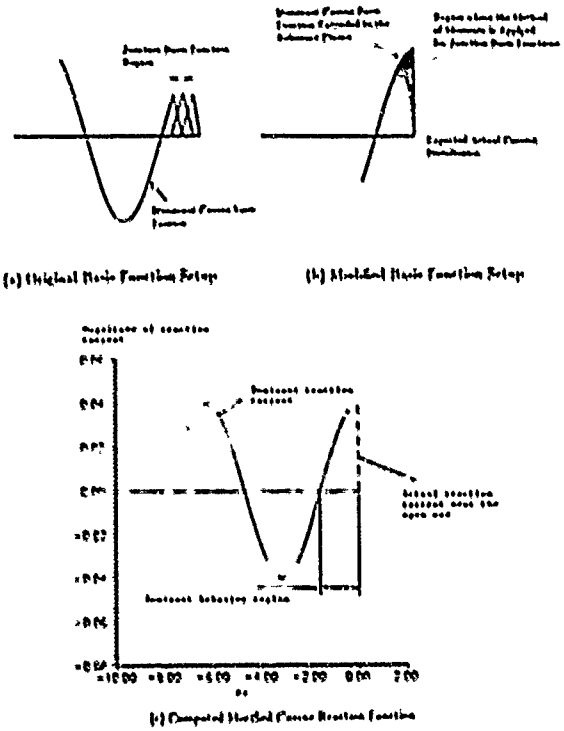


Figure 6: Modified *Cosine* Basis Function Behavior in the Vicinity of the Junction.

of the Green's function and its asymptotic form. The convergence of the bracket term, however, is relatively slow when the argument k_z is large; nonetheless, when the enclosure is large and the side walls are at a large distance from the circuit, the bracket term represents the principal convergence factor. With the adopted forms, 7-8 digit accuracy for the computation of the infinite sum can be easily obtained. Note that the function $S(k_z)$ is monotonic for $k_z \to \infty$. Therefore, once the integration table for a sampled k_z is created, the integration can be evaluated from interpolated values of $S(k_z)$.

3.3 Computation of $V_{m'}$ and $Z_{m'm}$

Once $S(k_z)$ is computed, the impedance matrix elements $Z_{m'm}$, and voltages, $V_{m'}$, can be computed. The junction basis functions (roof-top basis functions) can be expressed as *sinc* and *sinc*^{2} functions similar to PB and TB in the previous section. A traveling wave, given by $e^{\pm\beta z}$, is the expected functional form except right at the discontinuity. The functional behavior must be modified in such a way as to correctly represent the conduction current (for real current system) or the aperture field (for slot system). One modification was proposed by R.W. Jackson [3] and applied to the open-end and gap

microstrip discontinuities. The traveling wave form $e^{-j\beta z}$ was written as

$$e^{-j\beta z} = \cos(\beta z) - j\sin(\beta z) \tag{19}$$

The cosine function was truncated at $\lambda_g/4$ away from the discontinuity. Piece-wise basis functions were then overlaid in the junction region. This situation is illustrated in Figure 6 (a). To reproduce the actual current distribution in the immediate vicinity of the junction, the size of junction current basis functions must be small. Thus the necessary number of junction basis functions becomes huge, especially for low frequency (thin substrate) modeling.

A variation of the previously referenced method is adopted here:
For the longitudinal *cosine* basis function we use

$$\cos^{long}(\beta z) = \begin{cases} \cos(\beta z) & -\infty < \beta z < -\Delta \\ -(z/\Delta)\cos(\beta\Delta) & -\Delta \le \beta z \le 0 \end{cases}, \tag{20}$$

while for the transverse *cosine* basis function we use

$$\cos^{tran}(\beta z) = \begin{cases} \cos(\beta z) & -\infty < \beta z < -\Delta \\ \cos(\beta\Delta) & -\Delta \le \beta z \le 0 \end{cases}. \tag{21}$$

The use of the above forms of *cosine* basis functions focus the method of moments solution on the difference between the ideal transmission line current behavior and the actual current behavior instead of modeling the entire $\lambda_g/4$ region from the discontinuity. The situation is illustrated in Figure 6 (b). The overlap region of junction basis functions can be reduced to the immediate vicinity of the junction where the current disturbance is expected. The computed modified *cosine* basis function is shown in Figure 6 (c) for relatively low frequency. While a total of 48 longitudinal subdomain basis functions (PB) were needed for the original procedure, with the proposed modified *cosine* basis, the number of basis functions is reduced to about 12. This can also be applied to slot type lines in the vicinity of discontinuities.

Once the junction and traveling wave functions are determined, the integration can be performed. The path of integration is deformed to avoid poles associated with the waveguide modes. In Figure 7, the behavior of $S_{zz}(k_z)$ is shown for a real axis integration path, and for a modified (complex integration) path. The use of modified (complex) integration contour is equivalent to the introduction of loss into the system. With the modified contour an interpolation technique using tabulated values of $S(k_z)$ for sampled k_z can be used without degrading the accuracy of the integration.

4 Numerical Examples

The first example (Figure 8) shows the eigenvalue solution derived from $S(k_z)$. When the waveguide side walls are chosen to be magnetic walls, the boundary conditions at the side walls electrically separate the top and bottom walls. A slotline mode is then supported. The configuration approximates the open structure slotline. In Figure 8, the normalized

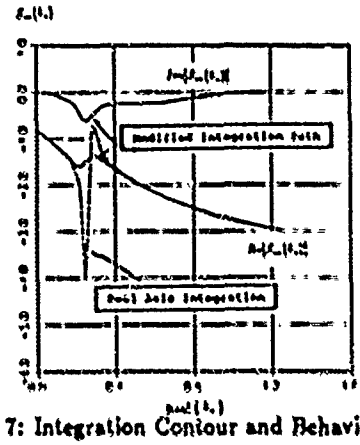


Figure 7: Integration Contour and Behavior of $S_{xx}(k_x)$.

effective wavelength of the slot mode is computed. Two sets of data are plotted. The dashed line indicates the case where the side walls are separated by $a = 10.0$, while the solid line is for $a = 40$. In both cases, the slotline is placed at the center of the waveguide. The circled data is that of Cohn [9] using the transverse resonant method. When the magnetic side walls are separated enough from the slotline, the open geometry can be modeled by using the present method. When the side walls are close to the slotline (given by dashed line), the effective wavelength diverges from that of the open geometry model.

The open-end microstripline is the simplest discontinuity. It is also fundamental in that it involves all the significant phenomena associated with the more complex components, in particular, the phenomena of coupling with the waveguide modes of the boxed structure at high frequencies. The first example in Figure 9 shows how the excess length is affected by the external structure. With an external waveguide shield, the open-end discontinuity may behave as an antenna element which excites or couples to the waveguide modes (both evanescent and propagating modes.) In the two cases that follow the microstrip line is placed at the center of the waveguide structure where the most significant effect is expected for TE_y mode. The substrate material is $\epsilon_r = 9.6$, and the dimensions of the microstrip are $w = 1.0$ and $h = 1.0$. The solid line shows the case where the waveguide mode turns on around $k_o h = 0.21$ for a waveguide dimension of $a = 20$. The dashed line shows the case with a waveguide dimension $a = 10$, where there are no propagating waveguide modes excited in the range of interest.

Anisotropy of materials can cause some change in open-end excess length. In figure 10, the excess length is computed for isotropic and anisotropic cases.

The characterization of gaps in microstrip is useful in the design of dc blocks, end coupled filters, coupling elements to resonators, etc. The microstrip gap is treated as a numerical example.

When the coupling to the waveguide modes is strong, then the parasitic conductance elements exist in parallel with the equivalent capacitance. The equivalent capacitance C_p is due to the field fringing to the ground plane, and the equivalent capacitance C_g is the gap capacitance due to the coupling to the second conductor. It is common practice to

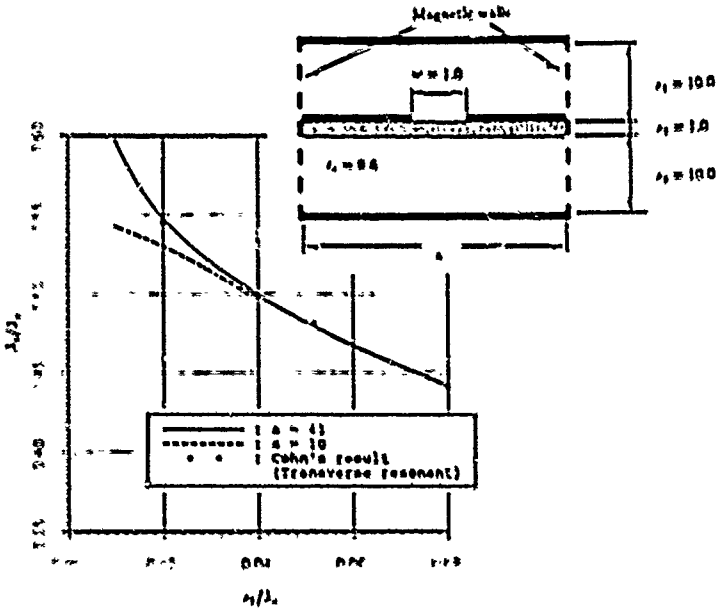


Figure 8: Normalized Effective Wavelength of the Slotline

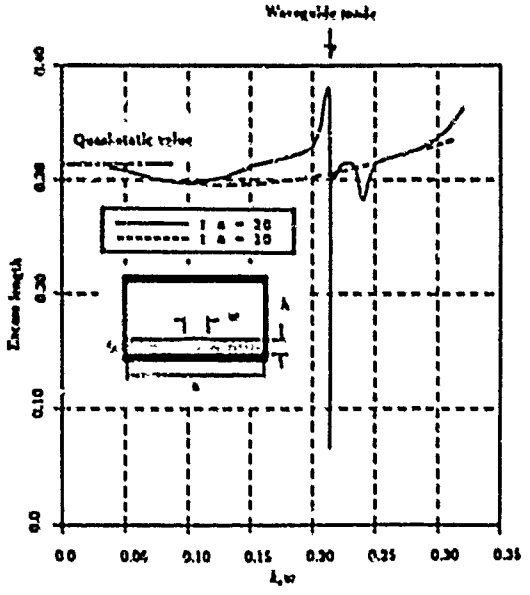


Figure 9: Excess length and Waveguide Mode Coupling

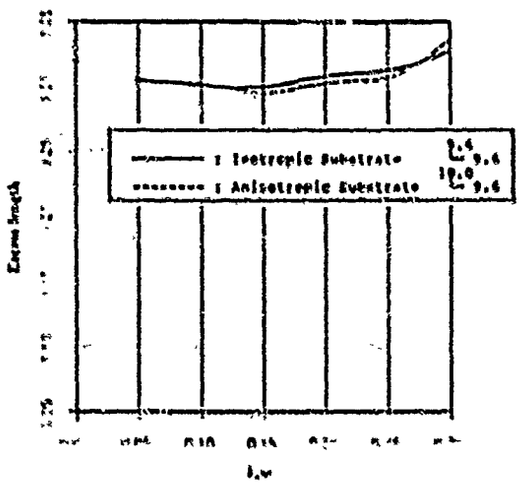


Figure 10: Excess Length of Isotropic and Anisotropic Substrate

represent the gap characteristics using C_{even} and C_{odd}. These quantities are related to C_f and C_g as follows:

$$C_{even} = 2\,C_f \tag{22}$$

and

$$C_{odd} = 2\,C_f + C_g\ . \tag{23}$$

The code for the gap discontinuity is similar to the open-end code except that transmission coefficient matrix elements are included. Since the primary and secondary line is symmetric, the gaps can be efficiently characterised by considering all the symmetric properties of the method of moments solutions. The code is modified in such a way as to generate various gap separations while computing the matrix elements once. The resonance nature of the problem due to the enclosure is avoided in this example by selecting the enclosure appropriately. An example of computed data for these even and odd capacitances is plotted in Figure 11. As the separation of the two lines is increased, both the even and odd capacitances approach asymptotically the open-end case, i.e. the gap capacitance decreases.

5 Conclusion

A numerical approach for the high frequency characterization of waveguide-shielded microstrip and slot line structures has been presented. The algorithms were developed for use on desktop computers. The formulation and methods described briefly here, such as the closed form expression [8] or the interpolation routine, reduced CPU time drastically. The open-end or gap discontinuities can be characterized within five to six minutes on a 386/387 computer. The Green's function approach included all the physical phenomena,

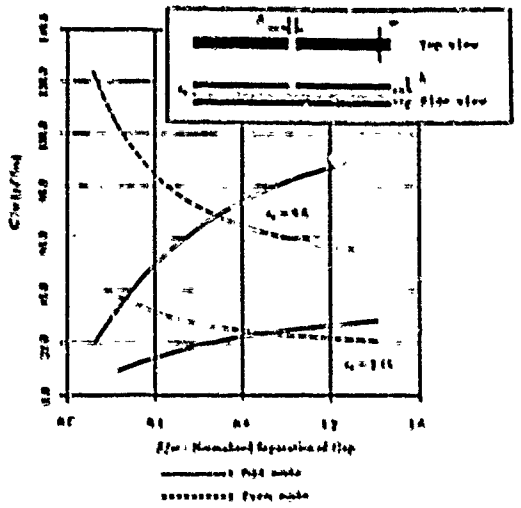


Figure 11: Even and Odd Capacitance versus Gap Spacing

such as coupling to waveguide modes and complex waves, and so on. The obtained results can be applied at high frequencies. The extension of this method to an irregular shaped discontinuity topology has also been established in this paper.

6 Reference

1 R.H. Jansen "Hybrid Mode Analysis of End Effects of Planar Microwave and Millimeterwave Transmission Lines," *IEE Proceedings*, vol. 128, Pt. H, no.2, pp. 77-86, April 1981.

2 P.B. Katehi and N.G. Alexopoulos, "Frequency Dependent Characteristics of Microstrip Discontinuities in Millimeter-Wave Integrated Circuits," *IEEE Trans, Microwave Theory Tech.*, vol. MTT-33, no. 10, pp. 1029-1035, October 1985.

3 R.W. Jackson and D.M. Pozar, "Full-Wave Analysis of Microwave Open-End and Gap Discontinuities," *IEEE Trans, Microwave Theory Tech.*, vol. MTT-33, no. 10, pp. 1036-1042, October 1985.

4 A. Nakatani and N.G. Alexopoulos, "Toward a Generalized Algorithm for the Modeling of the Dispersive Properties of Integrated Circuit Structure on Anisotropic Substrate," *IEEE Trans, Microwave Theory Tech.*, vol. MTT-33, no. 12, pp. 1436-1441, December 1985.

5 R.W. Jackson, "Considerations in the Use of Coplanar Waveguide for Millimeter-Wave Integrated Circuits," *IEEE Trans, Microwave Theory Tech.*, vol. MTT-34, no. 12, pp. 1450-1456, December 1986.

6 N.H.L. Koster and R.H. Jansen, "The Microstrip Discontinuity: A Revised Description," *IEEE Trans, Microwave Theory Tech.*, vol. MTT-34, no. 2, pp. 213-223, February 1986.

7 T.S. Chu and T. Itoh, "Generalized Scattering Matrix Method for Analysis of Cascaded and Offset Microstrip Step Discontinuities," *IEEE Trans, Microwave Theory Tech.*, vol. MTT-34, no. 2, pp. 280-284, February 1986.

8 N.G. Alexopoulus and A. Nakatani, "Cylindrical Substrate Microstrip Line Characterization," *IEEE Trans, Microwave Theory Tech.*, vol. MTT-35, no. 9, pp. 843-849, September 1987.

9 S.B. Cohn, "Slotline on a Dielectric Substrate," *IEEE Trans, Microwave Theory Tech.*, vol. MTT-17, pp. 768-778, 1969.

The Spectral Domain Technique for the MMICs

Smail TEDJINI IEEE Member, Nahla DAOUD , Etienne PIC IEEE Member & Mohamed MABROUK

LEMO URA CNRS 833 23 Avenue des Martyrs B.P. 257
38016 Grenoble Cédex FRANCE.
Phone (33) 76 87 69 76 Fax (33) 76 43 37 96

The Spectral Domain technique is modified in order to take into account both finite thickness and conductivity of metallizations in planar monolithic integrated transmission lines.The proposed method is applied to a GaAs monolithic microstrip. The theoretical and experimental results which are presented and discussed in this abstract are in very good agreement.

1. Introduction

In the last decade, several approaches have been developped for the analysis and the study of Microwave and Millimeterwave Hybrid Integrated Circuits (MMHIC).Today the most popular method in this area is the well known Spectral Domain Technique. The SDT was first introduced in 1971 by Mittra & Itoh [1] to calculate the dispersion characteristics of microstrip lines. Other authors have extended the method to the different planar microwave lines commonly used in MMHIC's. The method is suitable for the analysis of multilayer planar structures and two unified formulations of the SDT are found in the litterature [2,3].

Because one assumes a zero thickness and infinite conductivity of the metallization, the SDT can't be considered as a realistic method for the prediction of the performances of monolithic microwave integrated lines. Indeed, in monolithic circuits the thickness of the metallization becomes comparable with the width of the strips and then the strips cannot be considered as ideal conductors.The differences between a Hybrid and a Monolithic microstrip lines are summarized figure 1. To overcome this difficulty we adress, in this paper, an extension of the SDT in order to analyse the monolithic integrated circuits.

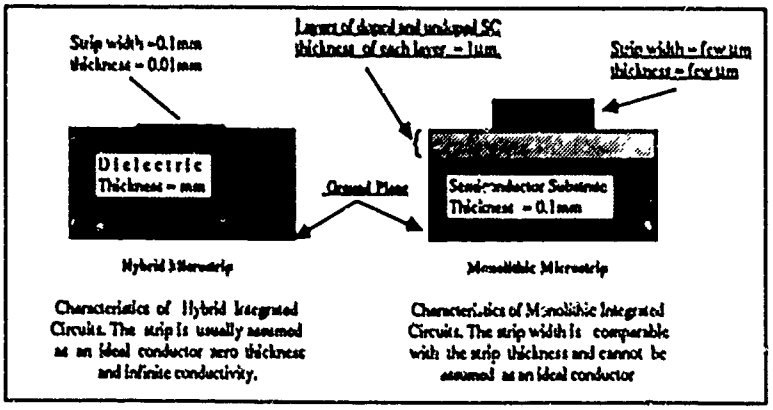


Figure 1. The characteristic dimensions of Hybrid and Monolithic Microstrip Lines.

2. The Modified Spectral Domain Technique

In the classical formulation of the Spectral Domain Technique, one writes the fundamental equation of the SDT which is a relation between the Fourier component of the current densities (J_y & J_z) and the tangential electric fields (E_y & E_z) in the plane of the metallization (i.e. the plane x = 0 on the figure 2).

This fundamental equation reads :

$$\begin{bmatrix} E_y(u,\gamma) \\ E_z(u,\gamma) \end{bmatrix} = \begin{bmatrix} G_{11}(u,\gamma) & G_{12}(u,\gamma) \\ G_{21}(u,\gamma) & G_{22}(u,\gamma) \end{bmatrix} \begin{bmatrix} J_y(u,\gamma) \\ J_z(u,\gamma) \end{bmatrix}$$

where u is the Fourier variable, γ the propagation constant. The $G_{ij}(u,\gamma)$ are known functions and depend on the electric and geometric parameters of the different layers of the structure.

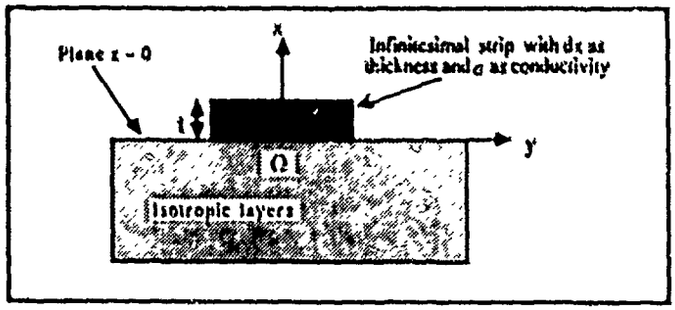


Figure 2. Basic structure and the subdivision in infinitesimal strips

The fundamental equation is usually solved by using the classical Moment method. To this end, one projects the current densities on a realistic basis of functions. The solution is obtained by writing the inner product of the current densities and the electric fields. This inner product is zero because the current and the electric field are defined in complementary spaces.

$$\int_{-\infty}^{+\infty} J_y(u,\gamma)\, E_y(u,\gamma)\, du = 0 \qquad \int_{-\infty}^{+\infty} J_z(u,\gamma)\, E_z(u,\gamma)\, du = 0$$

Let us now transform the fundamental equation of the SDT in order to take into account the thickness and the conductivity of the strip. The structure considered is depicted figure 2. The strip of non zero thickness is subdivided in infinitesimal strips. Each strip located at "x" supports an infinitesimal current density dJ (u,γ,x) and is related to the electric field dE (u,γ) in the plane x = 0 by the following relation

$$dE(u,\gamma) = G(u,\gamma) \exp(-\gamma_0 x)\, dJ(u,\gamma,x)$$

where γ_0 is given by $\gamma_0 = (u^2 + \gamma^2 - \omega^2 \varepsilon_0 \mu_0)^{1/2}$

The dJ (u,γ,x) is related to the total current J (u,γ) on the strip by :

$$dJ(u,\gamma,x) = J(u,\gamma)\, f(x)\, dx,$$

where f(x) is a normalized distribution i.e.

$$\int_0^t f(x)\, dx = 1$$

Combining the previous relations, it is easy to arrive to the new fundamental relation of the SDT

$$E(u,\gamma) = \int_0^t dE(u,\gamma) = \int_0^t G(u,\gamma) \exp(-\gamma_0 x)\, f(x)\, J(u,\gamma)\, dx = G(u,\gamma)\, S(u)\, J(u,\gamma)$$

This equation is quite similar to the first one. The difference between the two fundamental equations lies in the term S(u) which depend on the thickness of the strip and the f(x) distribution along the ox direction. The resolution of this new equation is also done using the Moment Method and Ohm law's. The conductivity of the strip is taken into account when we write the inner product of E and J which is non zero because the conductivity of the conductor is finite.

3. Determination of the distribution f(x).

In an ideal conductor one assumes that the total current is located on the surface of the conductor and is zero inside the conductor. These assumptions are not correct in reality due to the finite conductivity of the material. In fact the current inside the conductor depends on the conductivity and the frequency as well as on the boundary. The current is governed by the classical equation :

$$\nabla^2 J(x,y) = ((1+j)^2/\delta) J(x,y)$$

where δ is the skin depth of the conductor given by $\delta = (2/\omega\mu_0\sigma)^{1/2}$

Solving the previous equation one obtains the following expression of the current density

$$J(x, y) = A \operatorname{ch}\left(\frac{1+j}{\delta}\right) x . \operatorname{ch}\left(\frac{1+j}{\delta}\right) y$$

Finally, the expression of the distribution f(x) is given by :

$$f(s) = \frac{1}{\operatorname{ch}\dfrac{t}{2\delta}} . \operatorname{ch}\left(\frac{s - t/2}{\delta}\right)$$

4. Applications

This method has been used to analyze the GaAs microstrip line with Schottky contact shown figure 3. The calulated data are the slow-wave factor and the propgation losses in the structure. The microwave model used in the calculation is given below (figure 4).

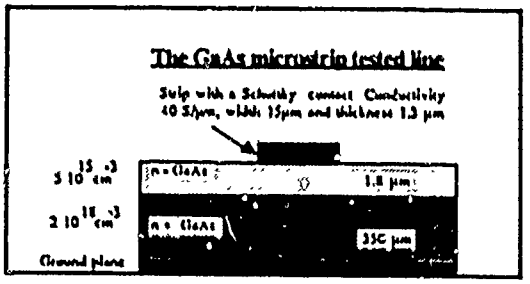


Figure 3. The GaAs microstrip analyzed line.

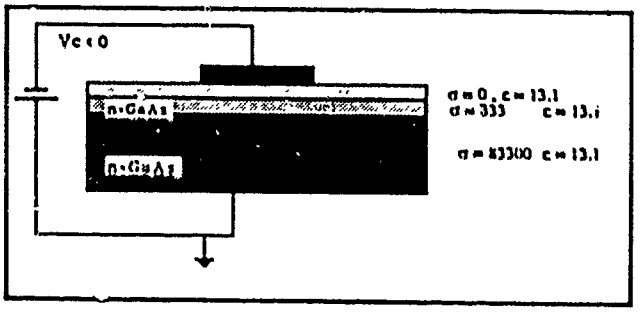


Figure 4. Microwave model used in the calculation

where e, the thickness of the depleted layer, is determined from the Schottky relation [4] :

$$e = \left[\frac{2 . \varepsilon_r . \varepsilon_0}{q . N_D} (0{,}74 - V_C) \right]^{1/2} \quad \text{with } V_C < 0$$

Figure 5 shows the microstrip line (D.U.T.) that was tested on a chip carrier. The test configuration is shown in Figure 6.The parameter of interest is the scattering parameter S_{21} of the de-embedded D.U.T. :

$$S_{21} = \exp[-\gamma(\omega).l] \qquad \text{where } \gamma(\omega) = \alpha(\omega) + j\beta(\omega)$$

The slow-wave factor of structure is given by the imaginary part (phase of S_{21}) and the attenuation constant is given by :

$$\alpha_{(dB/cm)} = \left[\frac{1}{L_{(cm)}}\right] 20 \cdot \log_{10} |S_{21}|$$

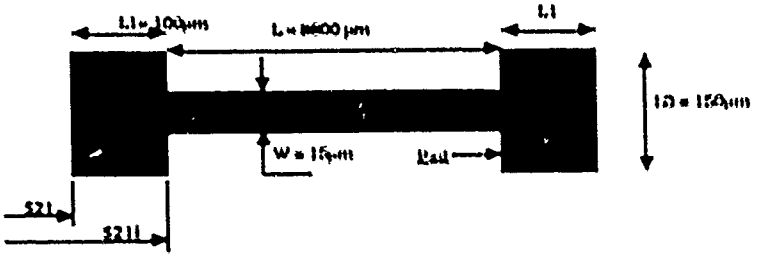


Figure 5. Geometry of the metallization.

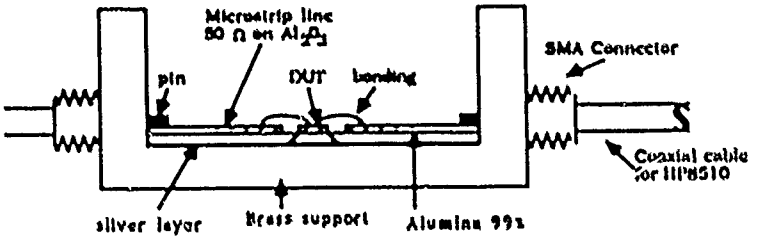


Figure 4. Chip carrier configuration.

After an evaluation of the pad phases, the phase of the intrinsic S_{21} is calculated. S_{21} measurements were carried out using the HP 8510 vectoriel Automatic Network Analysed (VANA), connected to on HP 216 computer, and applying the TRL [5] method. The necessary calibration standards were realised on Al_2O_3 substrate.

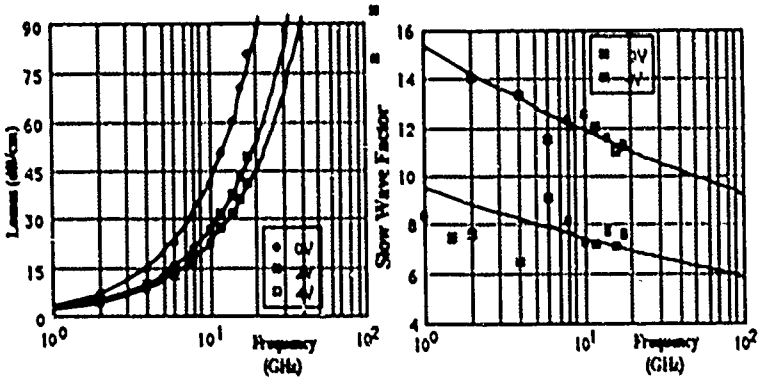


Figure 7. A comparison between experimental and theoretical results concerning a GaAs microstrip line.

The comparison between experimental and theoretical data is shown in figure 7. The continuous lines represent the results obtained by the proposed method and the points are the experimental data for several polarisations of the Schottky contact. One notices the excellent agreement between our theory and the experiments.

5. Conclusion.

A modification of the well known Spectral Domain Technique has been developped and presented. This modification allows the use of the SDT to analyze the monolithic microwave integrated line taking into account both conductivity and thickness of the metallization. It consists of the subdivision of the strip in elementary strips. The method has been applied to a GaAs microstrip line with a Schottky contact. The same line has been characterized experimentally using the Thru-Reflect-Line procedure. The slow-wave factor and the propagation losses given by the present theory are compared to the experimental data. An excellent agreement is pointed out. Finally the same method has been extended to analyse structures with several strips such as coupled microstrips. The experimental data concerning the coupled lines are now going on and will be presented elsewhere.

References.

[1] R.MITTRA, T.ITOH
A new technique for the analysis of the dispersion characteristics of microstrip lines.
IEEE MTT, vol 19, n°1, pp 47-56 (Jan 1971)

[2] R.H. JANSEN
Unified user-oriented computation of shielded, covered and open planar microwave and millimeterwave transmission line characteristics
IEE proc. part H, MOA 3, pp 14-22 (1979)

[3] S.TEDJINI, D.RAULY & P.SAGUET
Generalized Spectral Domain Technique Theory and Applications
16th Eu.M.C proc Dublin (sept 1986)

[3] S.M. SZE
Physics of semiconductor devices
2nd edition A Willey publication 1981.

[2] G.F. ENGEN , C.A. HOER
Thru-Reflect-Line : An improved technique for calibration the dual six-port automatic network analyzer.
IEEE MTT , vol 27, n° 12 pp 987-993 (Dec 1979)

THE DISPERSION CHARACTERISTICS OF THE FD-TD METHOD IN CYLINDRICAL WAVEGUIDES

Dennis H. Choi and Elmer H. Hara
Faculty of Engineering, University of Regina
Regina, Saskatchewan, Canada, S4S 0A2

Abstract

The numerical phase and group velocity characteristics of the FD-TD algorithm are presented for wave propagation in TEM, and TE or TM modes. In the numerical simulation of waveguide modal solutions, it is found that there is an optimum value of s and optimum frequencies at which least errors in group and phase velocities occur. From these, a procedure to find a maximum frequency which provides least error for modal solutions of cylindrical waveguides is proposed. This will provide guidance for applications of the FD-TD method to a wide variety of guided wave problems.

Introduction

The Finite Difference Time Domain (FD-TD) method based on Yee's algorithm has been used recently to solve the problems of waveguiding structures such as cut-off frequencies of finlines[1] or scattering parameters of microstrip discontinuities[2]-[3]. Even though the FD-TD technique has been applied quite successfully in the past(see for example [4]), the numerical mesh network of the algorithm causes errors in the phase and group velocities of the propagating wave. This is caused by the dispersive nature of the FD-TD method[5].

In order to assess the numerical errors caused by the dispersion for solutions of a TEM, and TE or TM wave, an explicit expression of the phase and group velocities of the three-dimensional FD-TD algorithm is derived from the following dispersion relation[4].

$$\sin^2(\omega\Delta t/2) = s^2[\sin^2(k_x\Delta x/2) + \sin^2(k_y\Delta y/2) + \sin^2(k_z\Delta z/2)] \quad (1)$$

where s is the stability factor given as $s = v\Delta t/\Delta l$.

Formulation

For a wave with propagation directions α, β and γ as shown in Fig. 1.a, the following relations exist: $k_x = k\cos\alpha$, $k_y = k\cos\beta$, $k_z = k\cos\gamma$, $k\Delta x = k\Delta y = k\Delta z = k\Delta l = \theta$. It can be shown that the group and phase velocities in free space are given as

$$v_g = [s\sqrt{\sin^2(\theta\cos\alpha) + \sin^2(\theta\cos\beta) + \sin^2(\theta\cos\gamma)}]/\sin(\omega\Delta t) \quad (2)$$

$$v_p = \omega\Delta t/s\theta \quad (3)$$

where v_g and v_p are normalized by the velocity of light v in the medium.

For $\theta << 1$, equations (2) and (3) reduce to:

$$v_g = 1-(R-s^2)\theta^2/8+O(\theta^4)+\cdots \quad (4)$$

$$v_p = 1-(R-s^2)\theta^2/24+O(\theta^4)+\cdots \quad (5)$$

where $R = \cos^4\alpha+\cos^4\beta+\cos^4\gamma$. Note that the second term of v_g is larger than that of v_p by a factor of three[5].

Expressions (2) and (3) are mixed forms which show the separate effects of ω and k on the propagating wave. Depending upon the problem or initial conditions, it is sometimes convenient to express Eqs. (2) and (3) in terms of only ω or only k. However, this is possible only for the cases where propagation occurs in the axial direction(A), in the diagonal direction(B) of a plane, and in the diagonal direction(C) of a cubic cell in free space(See Fig. 1. b). For other directions of propagation, the dispersion relation (1) and either Eq. (2) or (3) are required. For example, the phase and group velocities in the A direction in terms of ω are:

$$v_g = \sqrt{1-W^2}/\cos(\omega\Delta t/2) \quad (6)$$

$$v_p = \frac{\omega\Delta t/2s}{\sin^{-1}(W)} \quad (7)$$

where W is given by $W = \sin(s\pi\Delta l/\lambda)/s$. Note that $\Delta l/\lambda$ is used as a normalized frequency such that $\omega\Delta t = 2s\pi\Delta l/\lambda$.

Fig. 2 shows the velocities v_g and v_p as a fuction of $\Delta l/\lambda$ with the maximum stability factor of $1/\sqrt{3}$. From Eqs.(6) and (7) we can see that as s is reduced from the maximum value $1/\sqrt{3}$, all the velocities experience further dispersion that results in smaller magnitudes of v_g and v_p. However, it is found that the cut-off frequencies do not change significantly with variations in s.

A wave that is propagating in a closed-boundary waveguiding system experiences further dispersion in the longitudinal direction of the waveguide. This is the so-called modal dispersion which can be calculated numerically by the procedure similar to that used for the unbounded medium.

Let the z coordinate be the axial direction of a waveguide. At cut-off frequencies, the propagating wave number β or k_z in the dispersion relation of Eq. (1) becomes 0. Then Eq. (1) becomes:

$$\sin^2(\omega_c\Delta t/2) = s^2[\sin^2(k_{xc}\Delta x/2)+\sin^2(k_{yc}\Delta y/2)] \quad (8)$$

where ω_c is the cut-off frequency and k_{xc} and k_{yc} are cut-off wave numbers in the x, y coordinates respectively. As the operating frequency ω increases, starting from ω_c,

the transverse wave numbers k_x and k_y do not change from k_{xc} and k_{yc}. Therefore, substitution of (8) into Eq. (1) gives:

$$\sin^2(\omega\Delta t/2) = s^2\sin^2(k_x\Delta l/2) + \sin^2(\omega_c\Delta t/2) \tag{9}$$

The phase and group velocities of cylindrical waveguides are therefore,

$$v_g = \frac{s[\sin(2s\sin^{-1}\sqrt{W^2 - W_c^2})]}{\sin(\omega\Delta t)} \tag{10}$$

$$v_p = \frac{\omega\Delta t}{2s[s\sin^{-1}\sqrt{W^2 - W_c^2}]} \tag{11}$$

and

$$v_g v_p = \frac{\omega\Delta t\sin(2s\sin^{-1}\sqrt{W^2 - W_c^2})}{2s\sin^{-1}(\sqrt{W^2 - W_c^2})\sin(\omega\Delta t)} \tag{12}$$

where W_c is given by $W_c = \sin(s\pi\Delta l/\lambda_c)/s$ and λ_c is the cutoff wavelength.

Equations (10) and (11) hold for cylindrical waveguides with different cross-sections, provided that the cut-off frequency W_c is properly replaced by the appropriate value. W_c can be calculated readily by employing the two-dimensional FD-TD algorithm. For illustrative purposes, the phase and group velocities of a simple waveguide with a rectangular cross-section were calculated and the results are shown in Figs. 3 and 4. The Figs. 3 and 4 also show results from theoretical calculations for comparison.

From the Fig. 3, we can observe that the theoretical and numerical curves cross over each other at a certain frequency. At this frequency the numerical group velocity coincides with the theoretical group velocity. It is known that at this frequency, the composite TEM wave of the modal solution propagates at an angle of 45° to the axial direction. As discussed in Ref[4], at this angle, the propagation direction of the physical wave and numerical wave coincide.

The relative cross-over frequency $F_o = f/f_c$ depends on the stability factor s and has a slight dependency on the mesh size Δl. The characteristics of this normalized frequency F_o with respect to mesh size are illustrated in Fig. 5. Based on Fig. 5., an optimum value for the stability factor s can be chosen.

Starting from the maximum cross-over frequency ($F_o = 1.33$ at $s = 1/\sqrt{3}$), a reduction of s generates smaller values of F_o. As seen in the Fig.4, the numerical errors are small below the cross-over frequency F_o. Detailed numerical comparison shows that the numerical error increases uniformly as the frequency moves away from the cross-over frequency(F_o). Therefore, at frequencies below F_o, the numerical error is maximum at the cut-off frequency. Let the tolerable numerical error of the group velocity be half of the maximum error. Then the acceptable highest frequency can be extended up to the frequency F_{max} defined as

$$F_{max} = F_o + (F_o - F_c)/2 \tag{13}$$

Therefore, the best numerical simulation of information transmission in a cylindrical waveguide, is obtained by choosing the stability factor s according to the operating frequency. Fig. 5 shows examples of values of s for which optimum frequencies can be identified. Corresponding F_0 and F_c are substituted into Eq. (13) to obtain F_{max}. It is found that F_{max} is about $1.5f_c$. The operating frequencies for the most practical applications fall withinthis range. The application of the FD-TD method beyond this range may cause larger error.

The characteristics of phase velocity are different from those of group velocity. Because the numerical phase velocity is always less than theoretical values there is no cross-over frequency. However, there is a minimum error frequency which is slightly different from the cross-over frequency of the group velocity. For the best simulation to obtain phase information, such as the guided wavelength or resonant frequency, a similar procedure to that applied to the group velocity can be used and F_{max} can be employed in this procedure as well.

Conclusion

The numerical phase and group velocity characteristics of the FD-TD algorithm are derived from the dispersion relation for wave propagation in TEM, and TE or TM modes.

In the numerical simulation of waveguide modal solutions, there is an optimum value of s and optimum frequencies at which least errors in group or phase velocities occur. These optimum frequencies can be used to obtain a frequency range in which the numerical error is minimized. The algorithm described here will provide guidance for applications of the FD-TD method to a wide variety of guided wave engineering problems.

References

1. D.H. Choi and W.J.R. Hoefer,"The Finite Difference Time Domain Method and Its Application to Eigenvalue Problems", IEEE Trans., Microwave Theory Tech., vol MTT-34, pp.1464-1470, Dec. 1986.
2. X. Zhang, J. Fang, K.K. Mei and Y. Liu,"Calculation of the Dispersive Characteristics of Microstrips by the Time-Domain Finite Difference Method", IEEE Trans. Microwave Theory Tech. vol. MTT-36, No.2, pp 263-267, Feb. 1988.
3. X. Zhang and K.K. Mei,"Time Domain Finite Difference Approach for the Calculation of Microstrip Open-Circuit End Effect", IEEE MTT-S International Microwave Symposium Digest pp 363-366, June 1988.
4. A. Taflove and A. R. Umashankar, "Finite Difference Time Domain Modeling of Electromagnetic Wave Scattering and Interaction Problems", IEEE Antenas and Propagation Society Newsletter, pp 5-20, April 1988.
5. L. N. Trefethen,"Group velocity in Finite Difference Schemes", Siam Review vol. 24, No.2, pp 113-135, April 1982.

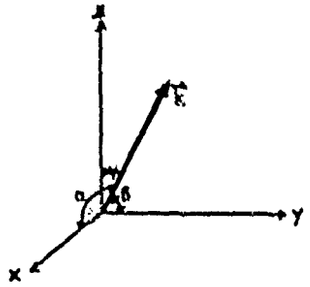


Fig. 1 a) Wave Propagating Angles with respect to the coordinates.

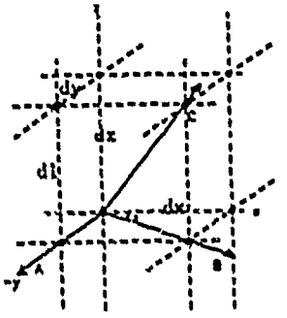


Fig. 1 b) Three Fundamental Direccions of TEM Wave Propagation

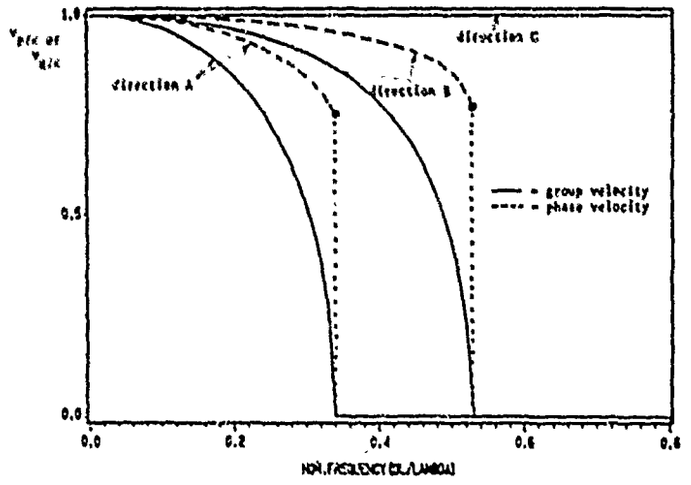


Fig. 2 Group and Phase velocities of TEM wave propagating to the three fundamental directions

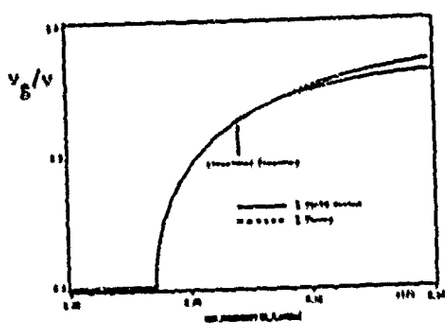


Fig. 3 Group Velocity Characteristics of a rectangular W/G.

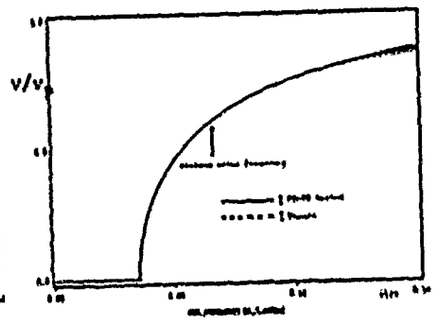
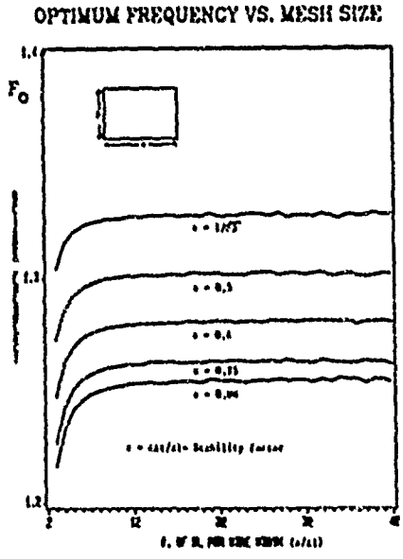
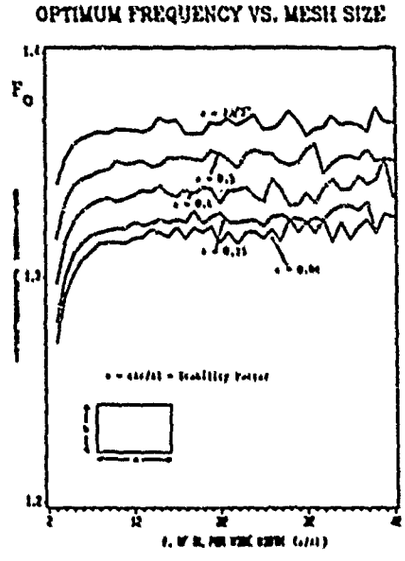


Fig. 4 Phase Velocity Characteristics of a rectangular W/G.



a)



b)

Fig. 5 Optimum frequency (F_o) vs. relative mesh size
a) for group velocity
b) for phase velocity

ABSTRACT

COMPUTATIONAL ELECTROMAGNETICS APPLIED TO INTEGRATED CIRCUIT MICROLITHOGRAPHY AND METROLOGY

John C. Mould Jr. & Gregory L. Wojcik
Weidlinger Associates, 4410 El Camino Real, Los Altos, Ca. 94022

It is recognized that as average feature size and spacing on integrated circuits (ICs) continue to decrease for reasons of speed and density, the manufacturing (microlithography) and inspection (metrology) problems naturally increase. Analytical tools are necessary to understand the resulting problems. One difficulty with the analysis of optically printed ICs is that feature dimensions and the wavelengths used to produce and measure them are of comparable size. Therefore, the patterns of light projected onto photoresist, and optical microscope images of the developed features are diffraction dominated, hence, not amenable to asymptotic methods of analysis. Another difficulty is the geometrical complexity of the IC features. Therefore, discrete solvers using finite element or finite difference techniques are necessary to simulate and interpret some of the problems encountered in IC manufacturing.

For microlithography, we explore the principal issues concerning quantitative numerical simulation of positive photoresist exposure dynamics.

To address the metrology problem, we discuss an algorithm based on the inverse scattering formalism in an effort to augment current optical inspection techniques. The objective here is to systematically determine a feature cross-section that minimizes in a least-squares sense, the error between observations and calculations at a discrete set of field points.

COMPUTATIONAL ELECTROMAGNETICS APPLIED TO INTEGRATED CIRCUIT MICROLITHOGRAPHY AND METROLOGY

John C. Mould Jr. & Gregory L. Wojcik
Weidlinger Associates, 4410 El Camino Real, Los Altos, Ca. 94022

1. Photoresist Exposure dynamics in Microlithography

We explore the principal issues concerning quantitative numerical simulation of positive photoresist exposure dynamics. This class of electromagnetic wave simulation problems is motivated by a need to model the macroscopic physics of optical lithography using commercial resists at the submicron scales necessary for modern integrated circuit manufacturing. The modeling issues are presented here in the context of an explicit finite difference time domain algorithm for the nonlinear photoresist exposure problem in 2-D.

The constitutive model of Dill, et al (1975) for the evolution of optical parameters, the so-called ABC model, is combined with Maxwell's equations governing electromagnetic wave propagation to obtain the nonlinear partial differential equations describing the exposure of positive photoresist. These equations are discretized in space and time using classical finite differences and combined with inhomogeneous radiation boundary conditions to model general 2-D submicron features on or in the photoresist. The present problems involve a uniform, plane, layered model of air, positive photoresist, and a silicon substrate, illuminated from above by monochromatic, transversely polarized (TM) light at normal incidence. The approach is readily generalized to less restrictive conditions including non-normal incidence and other polarizations, as well as axisymmetric and 3-D geometric idealizations.

Prevailing techniques for microlithography simulation are currently based on classical thin film (1-D) models, and even in 2-D often assume 1-D wave propagation in uniformly layered geometries. The numerical approach described here can be used to verify these simplifying assumptions, but more importantly, it can solve completely general problems, both in geometry and constitutive properties, albeit at a higher cost in computer resources. The numerical simulations of nonlinear exposure processes are readily coupled with Fourier optics techniques to economically include the lense systems.

Electromagnetic wave propagation is described in macroscopic terms by Maxwell's equations. If we restrict our attention to nonmagnetic materials and further assume that the magnetic permeability is a constant (μ_0) for all materials of interest, the equations may be written for the transverse magnetic (TM) polarization as:

$$\frac{\partial(\epsilon E_z)}{\partial t} = \frac{\partial H_y}{\partial x} - \frac{\partial H_x}{\partial y} - \sigma E_z \qquad (1.1a)$$

$$\mu_0 \frac{\partial H_x}{\partial t} = \frac{\partial E_z}{\partial y} \qquad (1.1b)$$

$$\mu_0 \frac{\partial H_y}{\partial t} = \frac{\partial E_z}{\partial x} \qquad (1.1c)$$

If we further assume time-harmonic fields, and that $\mathrm{Im}(\chi) = 0$ (*ie*: all absorption is associated with free charges), then ϵ and σ can be related to the refractive index ($N = n + ik$) used in classical optics, where $i = \sqrt{-1}$.

$$\varepsilon = \varepsilon_0 (n^2 - k^2) \qquad (1.2a)$$

$$\sigma = 2 \omega \varepsilon_0 n k \qquad (1.2b)$$

Here ω denotes the angular frequency. Note that σ is frequency dependent. For illustration purposes, we restrict our discussion to the exposure of positive photoresist. The photoresist is assumed to have an initial inhibitor concentration (M_0) which is not necessarily uniform. This inhibitor concentration decays with exposure to light. During the subsequent development process, the resist is etched away at a rate which is inversely proportional to the remaining inhibitor. Thus, an imposed light pattern will result in valleys or holes where the exposure was greatest.

The exposure of positive photoresist is described mathematically by the ABC model. Here, the relative inhibitor concentration at a given time (t) is defined as :

$$m(t) = M(t) / M_0 \qquad (1.3)$$

where $M_0 = M(0)$. m is assumed to decay with exposure as:

$$m = \exp(-c I t) \qquad (1.4)$$

where (c) is an experimentally measured rate constant and (I) is the time averaged electric energy density:

$$I = < 0.5 \varepsilon E^2 > \qquad (1.5)$$

where the brackets denote a time average over time large relative to one period. The model further specifies that the absorption coefficient (α) is a linear function of m:

$$\alpha = A m + B \qquad (1.6)$$

where A and B are experimentally measured constants. If we assume time-harmonic fields, α is related to the complex part of the refractive index by (1.7).

$$\alpha = 4 \pi k / \lambda \qquad (1.7)$$

This in turn is related to the dielectric constant and conductivity, so:

$$\varepsilon = \varepsilon_0 (n^2 - (\alpha \lambda / 4 \pi)^2) \qquad (1.8)$$

$$\sigma = \varepsilon_0 \alpha n c \qquad (1.9)$$

Substitution of (1.8) and (1.9) into (1.1) give the nonlinear partial differential equations governing photoresist exposure for the 2-D, transverse magnetic polarization, monochromatic idealization.

We wish to construct solutions to (1.1) for arbitrary configurations of scattering features. To accomodate general non-seperable geometries, we consider discrete approximations in space. Due to the large number of unknowns in the discrete spatial model, and to the nonlinearity, we are lead also to time domain numerical discretization. For large problems, explicit techniques employing single point integration have proven most efficient. For the 2-D problem considered here, we adopt central differences in time as proposed by Yee (1966). This finite difference technique is more efficient than the corresponding finite element formulation. However, the staggered mesh becomes very unwieldy for nonlinear problems in

3-D, so finite elements become more attractive. One of the primary reasons is that the nonlinear constitutive relations require all components of the E field, but these are not all defined at any one location in the staggered mesh.

The destruction of inhibitor occurs on a time scale which is extremely slow relative to the electromagnetic wave propagation. Fortunately, the exposure process may be accelerated (corresponding physically to a higher intensity incident light) and for practical purposes, the same residual distribution of inhibitor will be observed.

2. Optical Inversion for Submicron Features

For steady-state, coherent, monochromatic, TM illumination, Maxwell's equations reduce to the scalar Helmholtz equation. A finite element formulation of this equation has been nested in an outer optimization loop to study the feasibility of inverting far-field optical backscatter measurements for sub-micron line features on a substrate. The combination of feature size and illuminating wavelength is in the diffraction-dominated regime, so that full wave solvers (as opposed to asymptotic methods) are required. Numerical experiments indicate that such inversions are indeed possible, provided that a reasonable estimate of feature size and sufficient backscatter information are available.

Numerical experiments indicate that inversions based on amplitude measurements alone are feasible only for perfectly reflecting features (if we restrict ourselves to single frequency illumination). For more general dielectrics, both amplitude and phase measurements, in conjunction with multiple illumination angles are required.

For the examples considered, local minimization methods such as Gauss-Newton and Levenberg-Marquardt performed well, even in the presence of realistic random and systematic noise levels. The fundamental inversion algorithm is straightforward. First, the scattering feature's geometry is estimated and parameterized, using vertex coordinates for example, as shown in Fig.1. This first estimate is usually the design shape. Second, synthetic backscatter is calculated at the observation points from a finite element model of the estimated domain. In addition, the Jacobian, (*i.e.* the derivative of field variables with respect to shape parameters) is calculated. Third, field residuals (measurements minus synthetics) are found at the observation points, combined with the Jacobians in a minimization equation, and solved to give an incremental change in the feature shape parameters that minimizes the residual. The algorithm finally returns to the second step and iterates until a suitable convergence criterion is satisfied. Fig. 2 shows the iteration sequence for a perfectly conducting 1 micron feature on a perfectly conducting substrate. Fig. 3 shows the sequence for a 1 micron photoresist feature on a silicon substrate. Both simulations employ helium-neon laser illumination at a wavelength of 0.6328 microns.

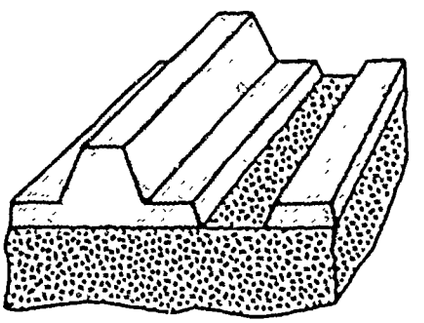
The primary expense in the algorithm is the solution of large systems of linear equations arising from finite element forward solves, and Jacobian calculations. These systems are complex, banded, sparse, non-hermitian and indefinite. Preliminary evaluations indicate that iterative methods will be the most cost-effective means of solving these systems. In conjunction with iterative solvers, bounds on required solution accuracy at any given iteration have been derived, but not yet implemented.

Application related issues still to be addressed include: the effects of differing layers and substrates, resolution limits *i.e.*, in terms of corner rounding, etc., and the incorporation of optical systems (as opposed to simple far-field extrapolation) in the inversion loop. A large amount of work is also required to improve processing speed. Possible improvements include alternative iterative solvers or preconditioners, holding the Jacobian fixed over a number of iterations or using a quasi-Newton method to update it instead of recomputing at each iteration. Another possibility is partitioning the problem since only a region about the feature changes at each iteration, with most of the grid remaining invariant.

3. References

Dill, F.H., Optical Lithography, IEEE Transactions on Electron Devices, Vol.ED-22, No.7, July 1975.

Yee, K.S., Numerical Solution of Initial Boundary Value Problems Involving Maxwell's Equations in Isotropic Media, IEEE Transactions on Antennas and Propagation, Vol.AP-14, No.3, May 1966.



• Fixed Region Corners
⊙ Free Region Corners

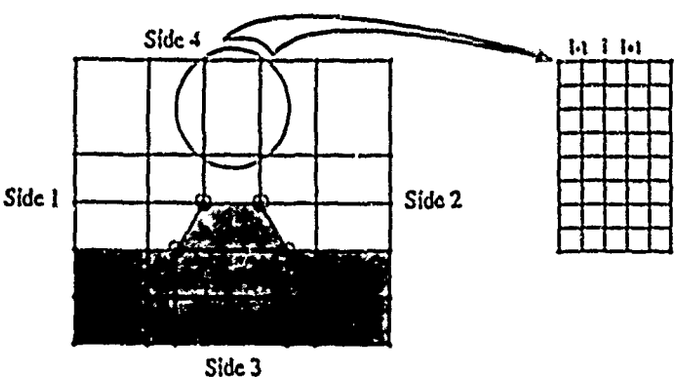


Fig.1 - Parameterization of I.C. line features

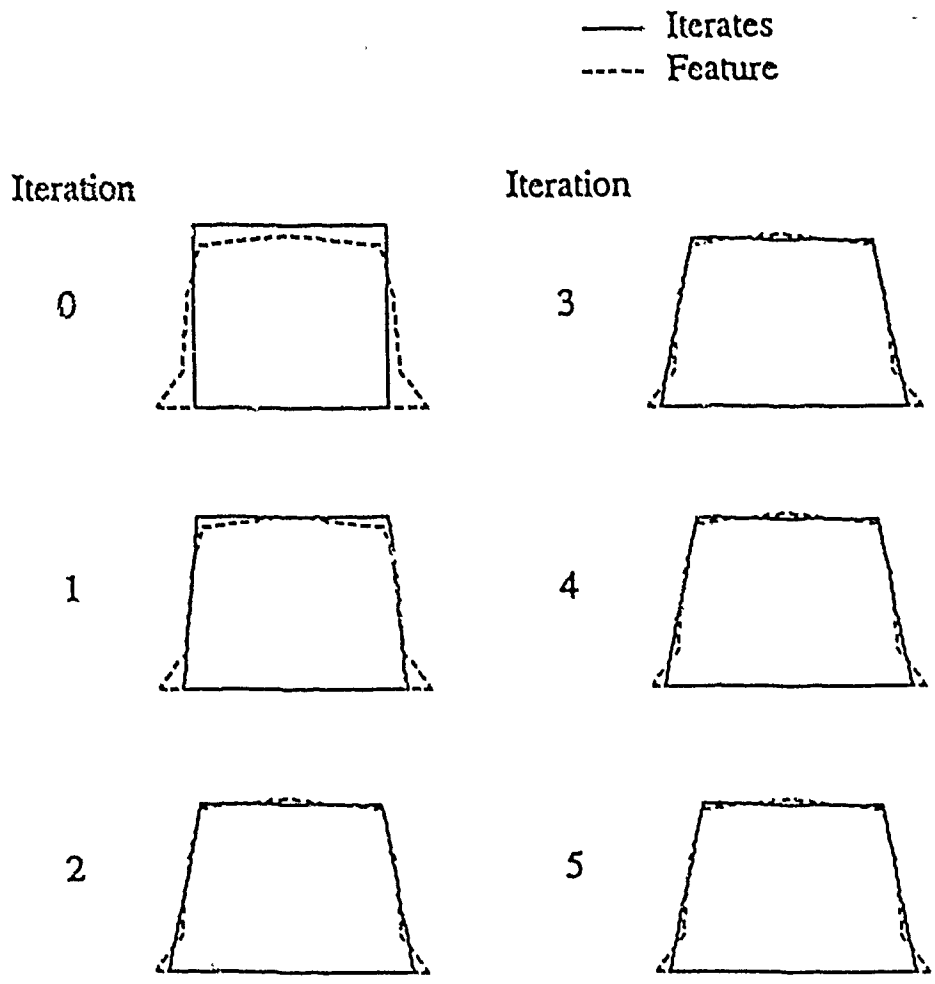


Fig.2 - Inversion sequence for perfectly conducting feature on perfectly conducting substrate, amplitude and phase, ±45° incident illumination

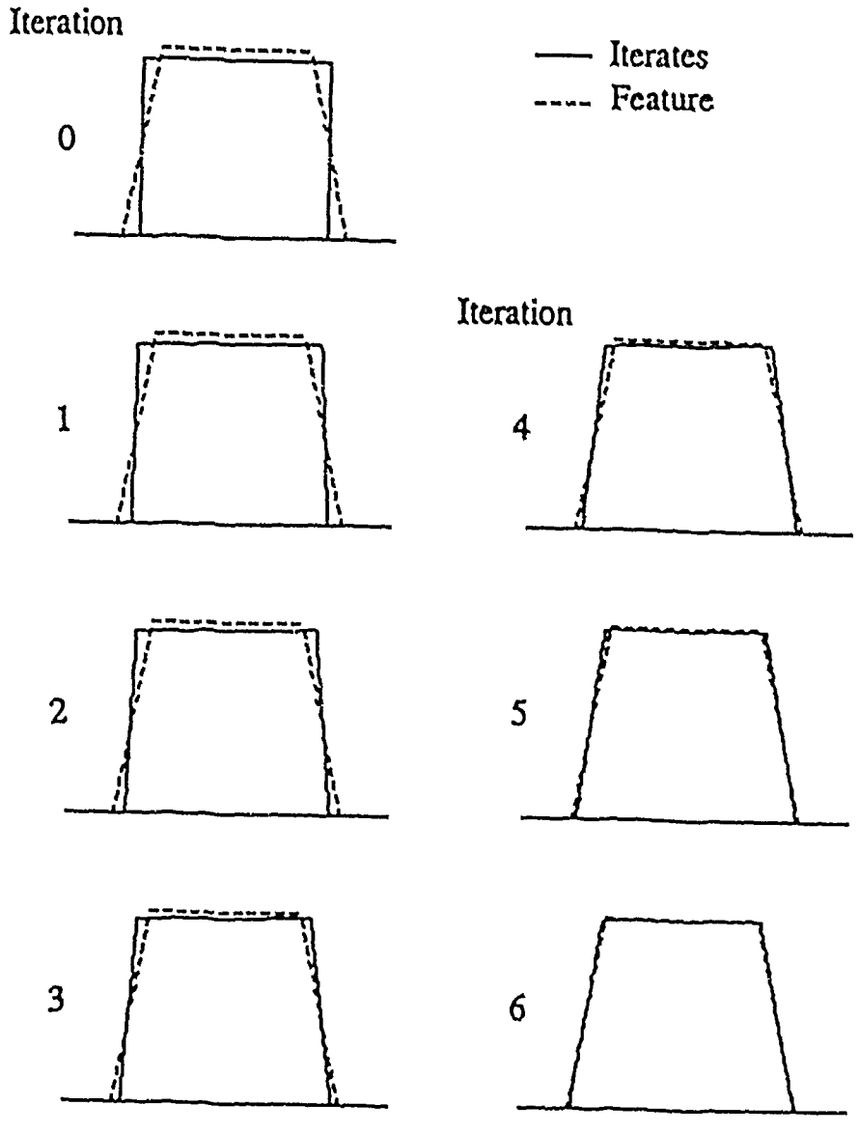


Fig.3 - Inversion sequence for photoresist feature on silicon substrate, amplitude and phase, ±45° incident illumination

TRANSVERSE RESONANCE ANALYSIS

OF

THREE COUPLED TRANSMISSION LINES

G.Bartolucci, F.Giannini, C.Paoloni
University of Rome "Tor Vergata", Italy

V.K.Tripathi
Oregon State University, Corvallis, Oregon

ABSTRACT

A numerical analysis has been developed in order to characterize a three coupled microstrip transmission lines structure. The method utilized is based on the transverse resonance technique applied to the analysis of a resonator obtained by inserting two electric walls transversally to the direction of propagation of the transmission lines.

INTRODUCTION

Multicoupled microstrip transmission lines have been investigated recently by many authors [1,2,3]. The most common approaches utilized to analyze this structure are the quasi- static method or the spectral domain technique. The obtained results are suitable for a good characterization of the structure but normally in the case of zero thickness metallization.

In this paper the structure in fig.1 has been taken into consideration. The transverse resonace approach is proposed in order to extend the analysis at the case of finite metal thickness. In order to study the

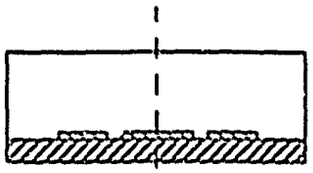


Fig.1

structure two electric walls are inserted orthogonally to the propagation direction obtaining a rectangular resonant cavity [4]. The electromagnetic field is expanded in terms of TE and TM modes in the transverse direction. Assuming a fixed frequency value is possible to obtain the resonator length that is equal to half wavelength of this particular mode.

The dielectric effective constant is reported for the three fundamental modes as function of the frequency and of the thickness metallization.

TRANSVERSE RESONANCE ANALYSIS

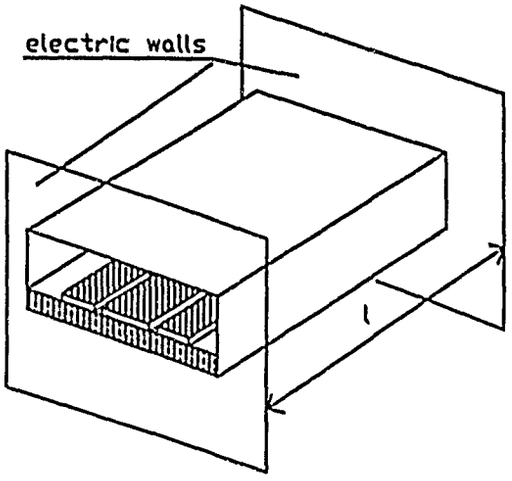


Fig.2

In this section the transverse resonance technique is applied to analyze the resonant cavity shown in figure 2. Because the structure presents a longitudinal symmetry plane, it is possible to replace this plane with an electric or a magnetic wall obtaining the two resonators of fig. 3 and 4. For sake of brevity the method will be discussed only for the cavity with the electric walls.

This resonator can be viewed in the Z-direction as two rectangular waveguides separated by a septum with two slots.

The electromagnetic field in regions 3 and 4 can be expressed in series of TE and TM modes:

$$\bar{E}_t^{(l)} = \sum_m F_m^{(l)}(z)\bar{z}_o \times \nabla_t \Psi_m + \sum_m G_m^{(l)}(z)\,\nabla_t \Phi_m$$

$$\bar{H}_t^{(l)} = \sum_m T_m^{(l)}(z)\,\nabla_t \Psi_m + \sum_m W_m^{(l)}(z)\,\nabla_t \Phi_m \times \bar{z}_o$$

with l=3,4

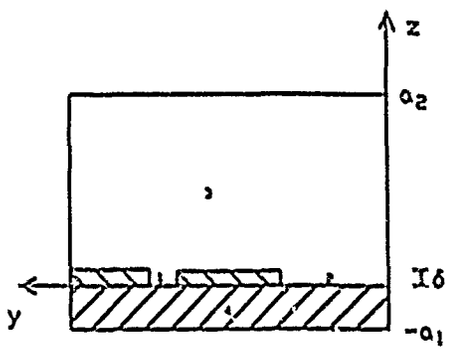


Fig.3

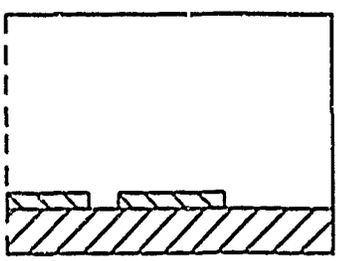


Fig.4

where Ψ_m and Φ_m are the potential functions for the TE and TM modes. The coefficients $F_m(z)$, $G_m(z)$, $T_m(z)$, $W_m(z)$ satisfy the boundary conditions for $Z = -a_1$ and $Z = a_2$. Also in region 1 and 2 in the two slots the electromagnetic field is expanded in series of TE and TM modes:

$$\bar{E}_t^{(j)} = \sum_q \left(A_q^{(j)} \sin \beta_q^{(j)} x + B_q^{(j)} \cos \beta_q^{(j)} x\right) \bar{z}_0 \times \nabla_t U_q^{(j)} -$$

$$- \sum_q \left(C_q^{(j)} \sin \tilde{\beta}_q^{(j)} x - D_q^{(j)} \cos \tilde{\beta}_q^{(j)} x\right) \nabla_t V_q^{(j)}$$

$$\bar{H}_t^{(j)} = \sum_q \frac{\beta_q^{(j)}}{j\omega\mu} \left(A_q^{(j)} \cos \beta_q^{(j)} x - B_q^{(j)} \sin \beta_q^{(j)} x\right) \nabla_t U_q^{(j)} +$$

$$+ \sum_q \left(C_q^{(j)} \cos \tilde{\beta}_q^{(j)} x + D_q^{(j)} \sin \tilde{\beta}_q^{(j)} x\right) \frac{j\omega\epsilon_0}{\tilde{\beta}_q^{(j)}} \nabla_t V_q^{(j)} \times \bar{z}_0$$

with $j = 1,2$.

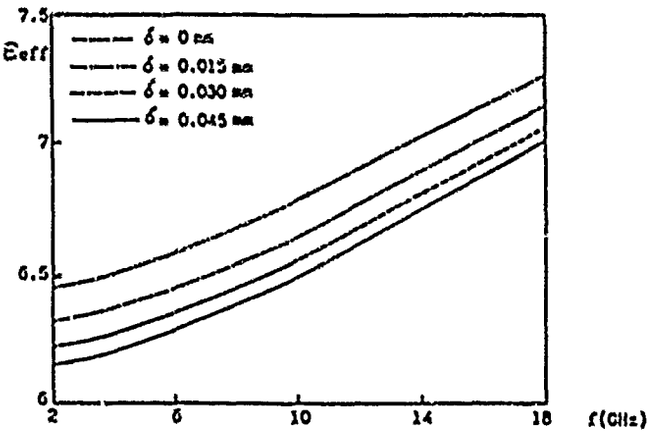


Fig.5a

The quantity $\beta_q^{(j)}, U_q^{(j)}$ and $\tilde{\beta}_q^{(j)}, V_q^{(j)}$ are respectively the propagation constants the potentials functions for TE and TM modes of rectangular waveguides with the same transversal sections of the two slots. By imposing the continuity of the tangential electric and magnetic fields in the two planes $Z = 0$ and $Z = \delta$ it is possible to obtain a homogenous linear system of equations.

The unknowns are the expansion coefficients $A_q^{(j)}$, $B_q^{(j)}, C_q^{(j)}$ and $D_q^{(j)}$ in the slots.

The condition for non trivial solutions is a function of the resonator length l and of the frequency equated to zero. Therefore, for a fixed frequency value it is possible to obtain the resonator length, that is

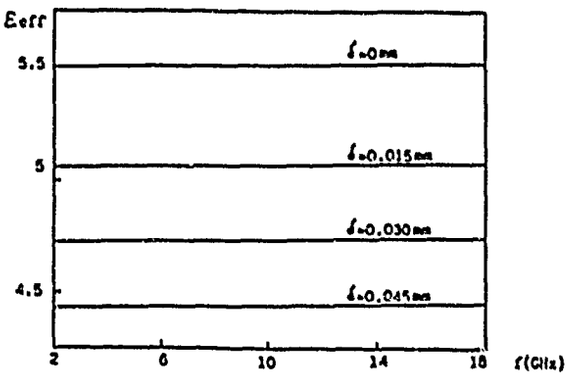


Fig.5b

related to the propagation constant of the mode by the following formula:

$$\beta = \pi / l$$

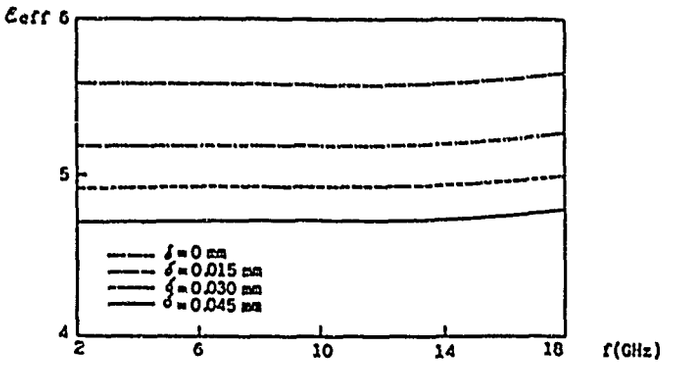


Fig.6

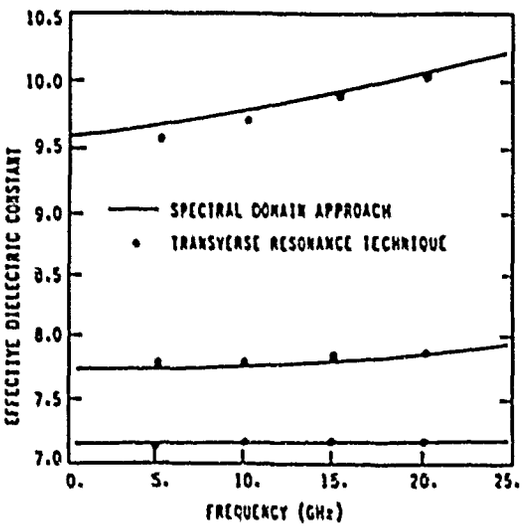


Fig.7

RESULTS

The presented technique is now applied to the study of a particular case. The three coupled microstrip transmission lines are considered on Alumina substrate .635 mm thick ($\varepsilon_r = 10$).

The width of the central conductor is 150 μm, the width of the lateral conductor is 100 μm. The slot between the central conductor and the lateral conductor is 150 μm. Besides the case of zero thickness metallization ($\delta = 0$) three other figures have been considered ($\delta = 15, 30, 45$ μm).

The effective dielectric constant computed for the two modes corresponding to the magnetic central plane of symmetry is shown as function of the frequency in figs. 5a and 5b.

The results relative to the case of the electric central plane of symmetry are reported function of the frequency in fig.6.

Moreover a comparison has been performed with other results obtained using the Spectral Domain approach [5] to evaluate the reliability of the achieved results. As it is shown in fig.7 good agreement has been obtained.

CONCLUSIONS

Three coupled microstrip transmission lines have been characterized in terms of dielectric effective constant for the three fundamental modes. A transverse resonant technique has been utilized in order to take into account the finite metal thickness.

A series of results for different metal thickness have been presented.

Moreover good agreement with previous data presented in literature has been obtained.

REFERENCES

[1] E.G.Farr and R.Mittra, "Frequency dependent coupled mode analysis of multiconductor microstrip lines, VLSI interconnection problem", IEEE Trans. on MTT, pp.307-310, Feb.1986

[2] T.C.Mu, H.Ogawa, T.Itoh, "Characteristics of multiconductor asymmetric slow-wave microstrip transmission lines", IEEE Trans. on MTT, pp.1471-1477, Dec.1986

[3] T.Kitazawa and Y.Hayashi, "Asymmetrical three line coupled strip lines with anisotropic substrates", IEEE trans. on MTT, pp.767-772, July 1980

[4] S.B.Cohn, "Slot line on a dielectric substrate", IEEE Trans. on MTT, pp.768-778, Oct.1969

[5] V.K.Tripathi and H.Lee, "Spectral domain computation of characteristic impedances and multiport parameters of multiple coupled microstrip lines", IEEE Trans. on MTT, Jan.1989

CAD ORIENTED ENHANCED MODELS FOR PLANAR STUBS

F. Giannini University of Roma 'Tor Vergata'
Dpt. Electronics Engineering

ABSTRACT

The effectiveness of the use of a planar approach to fully characterize some commonly used matching elements, like straight and radial stubs, is demonstrated.

Quasi frequency-independent wide-band equivalent models, easy to be implemented in the available CAD packages, are derived and their superiority with respect to the presently achievable ones is theoretically and experimentally pointed out.

A physical insight into the e.m. properties of such structures is also given, and the resulting external frequency behaviour, is depicted.

I. INTRODUCTION

Low impedance elements are widely used in a large variety of circuital solutions, including matching, filtering and biasing networks.

Nevertheless, the low-impedance requirement represents a critical issue, due to the fact that the geometry of the corresponding solution involves electromagnetic phenomena, that cannot be properly taken into account through the simple and well-known line, i.e. mono-dimensional, theory.

Two are the main approaches to face a low impedance issue.

Firstly, straight stubs can be used: in this case the inadequacy of the mono-dimensional approach can be overcome by adopting a complete modal theory [1], developed to fully

characterize the electromagnetic features deriving from the "planarity"of the structure.

Secondly, a different geometry can be considered, able both to provide the required low impedance values and to minimize simply and effectively the drawbacks deriving from the use of the wide rectangular matching elements.

With this respect, radial stubs can represent the proper solution to the mentioned requirements [2]. The features of those structures, in fact, mainly consist in a broadband behaviour together with a well defined "low-impedance" insertion point [3,4].

Moreover, the complete e.m. characterization of such structures can be carried out on the basis of the same modal theory usable in the case of straight stubs [5,6]. Finally, the effective substitution of straight stubs with "equivalent" radial ones, can be easily achieved through the settlement of a tight correspondance between the two proposed structures [7,8].

Therefore a powerful e.m. characterization of the planar elements, through, for instance, the above mentioned modal theory represents the only viable solution to address the issue of a more accurate modelling of both straight and radial stubs [9,10].

Moreover, a development of lumped models based on this methodology [11] can represent a proper merging of the required accuracy with the availability of friendly tools easy to be implemented in the presently commercial CAD packages, and so

effectively usable in practical circuit design [12,13,14].

II THEORETICAL CHARACTERIZATION

A. General approach

The electromagnetic behaviour of both straight and radial stubs can be derived from the application of a previously developed [1] analysis technique for planar circuits, based on the theory of resonant cavities and performed in the specific case of a two-port network of a generic geometrical shape.

The use of this method is particularly advantageous as it results in:

- the introduction of frequency dependent effective parameters for each resonant mode of the structure so achieving an accurate description of its frequency behaviour;
- a physical insight into the filtering properties of the structure, resulting in a dependable basis of accurate synthesis tools;
- the evaluation of the structure impedance matrix, which represents a flexible tool for the analysis and a key point for an effective lumped modelling and a resulting synthesis procedure.

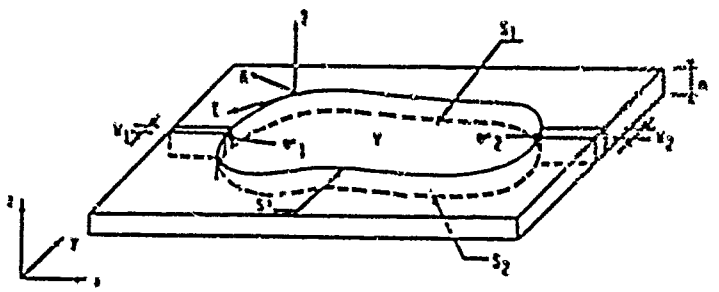


Fig.1

The analysis of a generic two-port microwave planar network (Fig. 1) can be performed by firstly evaluating, in the S domain of the xy plane, the orthonormalized set of eingenfunctions of the bi-dimensional Helmholtz equation:

$$\nabla^2\phi_m + K_m^2\phi_m = 0 \qquad (1)$$

with homogeneous Neumann's boundary conditions.

The confortable terminal description of the structure as a two-port network is obtained by evaluating the impedance (Z) matrix, related to the dominant TEM modes of the lines.

Under the hypotheses of negligible losses, evanescent higher order modes on the connecting lines, and line widths much smaller than the structure dimensions, the network impedance matrix is given by:

$$[Z] = \sum_{m=0}^{\infty} [Z_m] \qquad (2)$$

with:

$$[Z_m] = \frac{j\omega}{\omega_m^2-\omega^2}\cdot\frac{h}{\varepsilon_m}\begin{bmatrix} R_{m1}^2 & R_{m1}R_{m2} \\ R_{m1}R_{m2} & R_{m2}^2 \end{bmatrix} \qquad (2')$$

where $\omega_m = K_m/\sqrt{\mu\varepsilon_m}$ is the mth structure resonant frequency and:

$$R_{mi} = \frac{1}{W_{iff}}\int_{l_i}\phi_{mi}\,dl \qquad i=1,2 \qquad (2'')$$

is the coupling coefficient between the mth resonant mode and the TEM wave travelling on the ith line; l_i is the portion on the planar structure contour corresponding to the ith port; K_m^2 and

ϕ_m are the mth eigevalue and eigenfunction of eq. (1) respectively; ε_m is the effective permittivity of the mth resonant mode; h is the substrate thickness; Wi,eff is the effective width of the ith line.

B. The straight stub.

The modal approach can be specialized considering, as a particular two-port network, two straight open lines shunt connected to a feeding line (Fig. 2). The structure has a separable geometry in rectangular coordinates, and the corresponding [Z] matrix can be analytically derived.

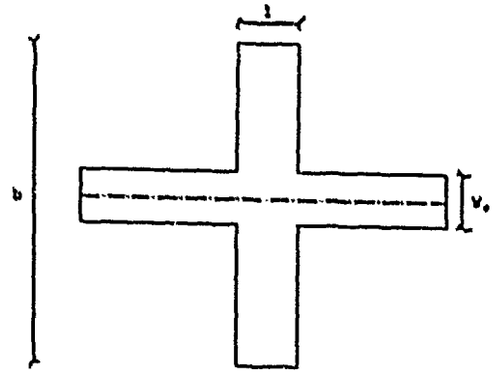


Fig.2

Under the assumption of a double simmetrical structure, the eqs. (2) can be specialized to give:

$$Z_{11}=Z_{22}=\frac{j\omega\mu h}{b\ell}\sum_{m=0}^{\infty}\sum_{n=0}^{\infty}\frac{\delta_n\delta_m q_n^2}{k_{x_n}^2-\omega^2\mu\varepsilon_{m,n}} \qquad (3)$$

$$Z_{12} = Z_{21} = \frac{j\omega\mu h}{b\ell} \sum_{m=0}^{\infty} \sum_{n=0}^{\infty} (-1)^n \frac{\delta_m \varepsilon_n g_n^2}{k^2_{m,n} - \omega^2 \mu \varepsilon_{m,n}} \qquad (3')$$

where

$$\delta_{m,n} = \begin{cases} 1 & m,n = 0 \\ 2 & m,n \neq 0 \end{cases} \quad ; \quad g_n = \sin\left(\frac{n\pi W_0}{2b}\right) \Big/ \left(\frac{n\pi W_0}{2b}\right)$$

$$K^2_{m,n} = \pi^2 \left[(m/\ell)^2 + (n/b)^2 \right]$$

C. <u>The radial stub.</u>

In the case of a radial stub (Fig.3a, Fig.3b) the general theory can be simplified and reduced to the calculation of the

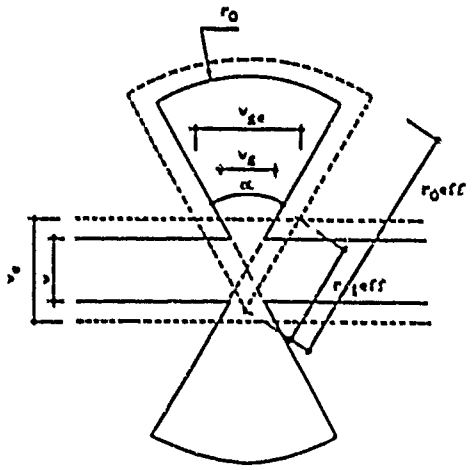


Fig.3a

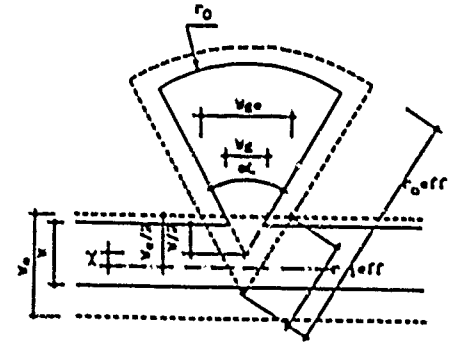


Fig.3b

input impedance of the structure in Fig. 3c, taking into account, with proper equivalent geometries [15], the e.m. differencies related to the asymmetrical (i.e. "fan") or symmetrical (i.e."butterfly") configuration.

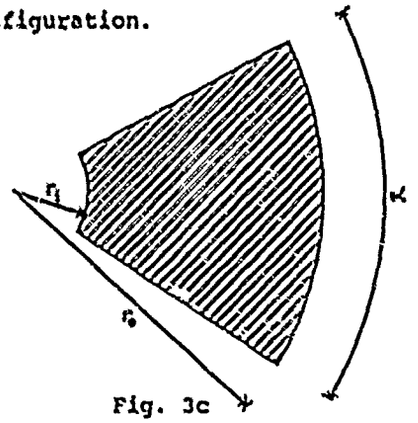


Fig. 3c

Moreover, assuming the input port to be a non-significant fraction of the wavelength and consequently that only TMon radial modes are excited, the terminal description of the radial line can be done in terms of the following input impedance:

$$Z_{in} = -j\frac{k_g \rho_{00}^2}{k_0^2 \varepsilon_{d,0}} + j k_g \sum_{n=1}^{\infty} \frac{\rho_{on}^2}{K_{on}^2 - k^2 \varepsilon_{d,n}} \qquad (4)$$

where Pon is the coupling coefficient between the TEM mode on the feeding line and the Tmon mode excited in the radial structure; Kg is the wavenumber of the feeding line, $K_0 = \omega\sqrt{\mu\varepsilon_0}$ is the free-space wavenumber; ε_{dn} and Kon are the dynamic effective permittivity and the eigenvalue of the TMon mode respectively.

III. LUMPED MODELS

A. Planar equivalent circuits

The effectiveness of the above described approach for the analysis of planar structures, fully results if it can be translated in CAD-oriented models usable in broadband applications and comprehensive of almost all the e.m. phenomena occurring in a planar structure.

In the past, equivalent circuits have been derived and proposed, but with limited applicability in frequency, accuracy and possible geometries of planar structures [16, 17].

On the contrary, a circuit was proposed , whose elements are frequency dependent practically only because of dispersion [11].

As a consequence the equivalent model can be assumed to be constant with frequency in a wide frequency range and its applicability in broadband applications is straightforward.

For a generic, symmetric two-port planar structure, the general equivalent circuit in Fig. 4 can be derived [11].

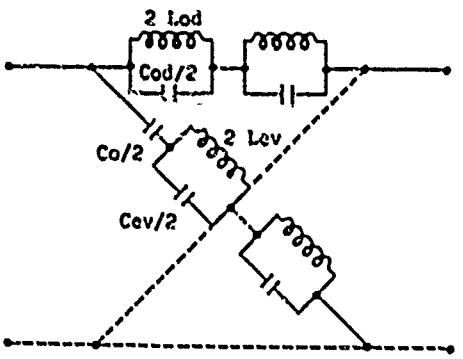


Fig.4

The circuit is composed of antiresonant LC cells (with the exception of the electrostatic term, corresponding to a pure capacitor). Each LC cell represents a resonant mode sustained by the <u>effective</u> planar structure, i.e. by a structure derived from the actual one having effective dimensions and permittivity, which are, in general, both dependent on the field configuration of the resonant mode.

Only a finite number of such cells has to be considered in particular applications, depending on both the frequency range of interest and the accuracy to be reached.

8. <u>One-port model for radial stub.</u>

The above theoretical characterization of a lossless radial stub, can be put into the form of a CAD-oriented equivalent circuit starting from the eq. (4). The equivalent lumped elements can be easily derived, in fact, settling:

$$jX_{in} = -j\frac{1}{\omega C_{00}} + j\omega \sum_{n=1}^{\infty} \frac{L_{0n}}{1-\omega^2 L_{0n} C_{0n}} \qquad (5)$$

where

$$C_{00} = \sqrt{\frac{\mu}{\varepsilon_g}}\, \varepsilon_0 E_{d,0} / P_{00}^2$$

$$L_{0n} = P_{0n}^2 \sqrt{\mu \varepsilon_g} / K_{0n}^2$$

$$C_{0n} = \sqrt{\frac{\mu}{\varepsilon_g}}\, \varepsilon_0 E_{d,n} / P_{0n}^2$$

Moreover, noting that the useful working frequency range for a radial line is normally limited up to the frequency of its first infinite reactance, the simplified model of fig. 5 can be

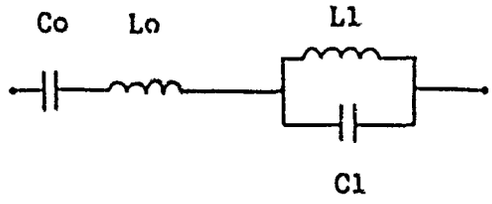


Fig.5

used, where :

$$C_0 = C_{00} \quad ; \quad C_1 = C_{01}$$

$$L_1 = L_{01} \quad ; \quad L_0 = \sum_{n=2}^{n} L_{0n}$$

C. Two-port model for straight stub.

A different approach has demonstrated to be more appropriate in the development of an equivalent model for the electrical behaviour of a two-port rectangular structure. The usefulness of the equivalent circuit of fig. 4, in the analysis and the design of a microwave integrated circuit, in fact, is practically limited being quite apart from the typical microwave designer, who is used to treat the circuits in terms of trasmission lines and to add as lumped elements only the results of the so called "parasitic" effects.

Moreover, the presently available CAD packages are mostly structured to be aligned with this kind of approach.

For this reason eq. (3) can be re-written as:

$$Z_{11} = Z_{22} = Z_s + Z_d - Z_\gamma$$
$$Z_{12} = Z_{21} = Z_s + Z_\beta - Z_\gamma \qquad (6)$$

where

$$Z_s = \frac{j\omega\mu h}{b\ell} \sum_{n=0}^{\infty} \frac{\delta_{1n}}{k_{0,1n}^2 - \omega^2\mu\varepsilon_{0,1n}} = -j\frac{Z_{0s}}{2}\cot g\frac{\omega b}{2c} \quad \text{with } Z_{0s} = \sqrt{\mu/\varepsilon}\,(h/\ell)$$

$$Z_d = \frac{j\omega\mu h}{b\ell}\left[\sum_{m=1}^{\infty}\sum_{n=0}^{\infty} \frac{2\delta_{1n}q_{1n}^2}{k_{1m,1n}^2 - \omega^2\mu\varepsilon_{1m,1n}} + \sum_{m=1}^{\infty}\sum_{n=0}^{\infty} \frac{2\delta_{1n}q_{1n}^2}{k_{1m-1,1n}^2 - \omega^2\mu\varepsilon_{1m-1,1n}}\right] = Z'_{ev} + Z'_{od}$$

$$Z_\beta = \frac{j\omega\mu h}{b\ell}\left[\sum_{m=1}^{\infty}\sum_{n=0}^{\infty} \frac{2\delta_{1n}q_{1n}^2}{k_{1m,1n}^2 - \omega^2\mu\varepsilon_{1m,1n}} - \sum_{m=1}^{\infty}\sum_{n=0}^{\infty} \frac{2\delta_{1n}q_{1n}^2}{k_{1m-1,1n}^2 - \omega^2\mu\varepsilon_{1m-1,1n}}\right] = Z'_{ev} - Z'_{od} \qquad (7)$$

$$Z_\gamma = \frac{j\omega\mu h}{b\ell} \sum_{n=0}^{\infty} \frac{(1-q_{1n}^2)\delta_{1n}}{k_{a1n}^2 - \omega^2\mu\varepsilon_{a,1n}} = \frac{j\omega\mu h}{b\ell} \sum_{n=1}^{\infty} \frac{2(1-q_{1n}^2)}{k_{0,1n}^2 - \omega^2\mu\varepsilon_{0,1n}}$$

with b,l and Wo effective dimensions, $\varepsilon_{m,n}$ the effective permittivity of the (m,n)th resonant mode; h the substrate thickness. The Z-parameters expressed through eqs. (6) and (7) represnt the structure in fig. 2, as a sum of different contributions.

More exactly Z'ev and Z'od are summations of all the terms having an even or an odd "m" index respectively; Z_γ takes into account the finite width of the input and output ports; Zs is the input impedance of two shunt stubs having a width l and a length b/2.

The described representations can be translated into the equivalent circuit of fig. 6a and 6b, which fully describes the

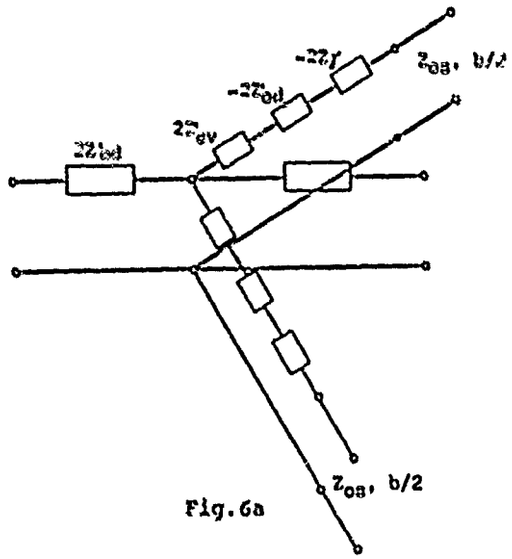


Fig.6a

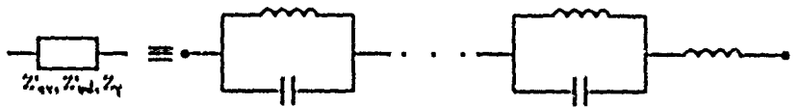


Fig.6b

frequency behaviour of a so called "Cross-Junction" discontinuity.

IV DISCUSSION

A. The fan and the butterfly cases

The accuracy of the modal approach and the usefulness of the proposed equivalent model have been checked through the development of pratical circuits [7,10].

In particular, the insertion- dependency of the equivalent

model has been stressed and experimentally demostrated [13,15].

As an example, the comparisons between the results obtained from the above described equivalent models and the corresponding available commercial CAD simulations are reported in fig. 7a and 7b [10]. Both figures show the percentage displacement, derived from different approaches, in the radial stub induced trasmission zero frequency, with respect to a reference case evaluated through the proposed equivalent circuit.

In fig. 7a the comparison for the single radial stub in shunt configuration (i.e. the "fan" stub) is shown, while 7b reports the comparison for the double radial stub in shunt connection (i.e. the "butterfly" stub).

As it can be observed, both the proposed model and the experimental results point out the quite different frequency behaviour of the "fan" and the "butterfly" insertions.

It means that a successful simulation of radial stubs requires the use of an equivalent geometry properly related to the particular insertion [15]. Moreover, the presently available CAD packages seem to provide a quite good agreement only in the case of the "fan" stub, but demostrate a poor accuracy for the "butterfly" configuration.

B. The "mcross" element

The symmetric cross-junction is a widely encountered discontinuity element. In many CAD packages, the simulation is limited up to some particular shape ratios, because the

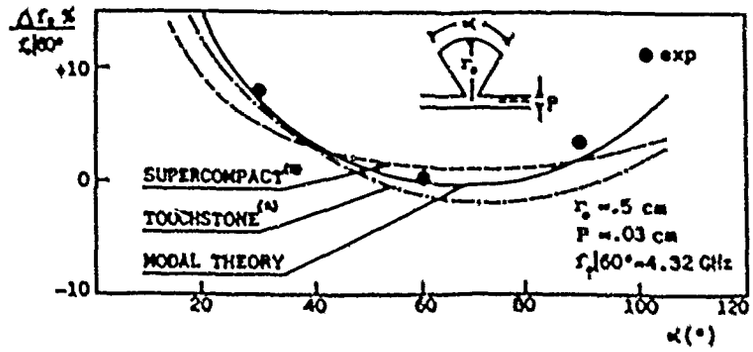

+10
0
-10
20
40
60
80
100
120
α(°)
● exp
SUPERCOMPACT
TOUCHSTONE
MODAL THEORY
r₀ =.5 cm
P =.03 cm
f₀|60°=4.32 GHz

Fig. 7a

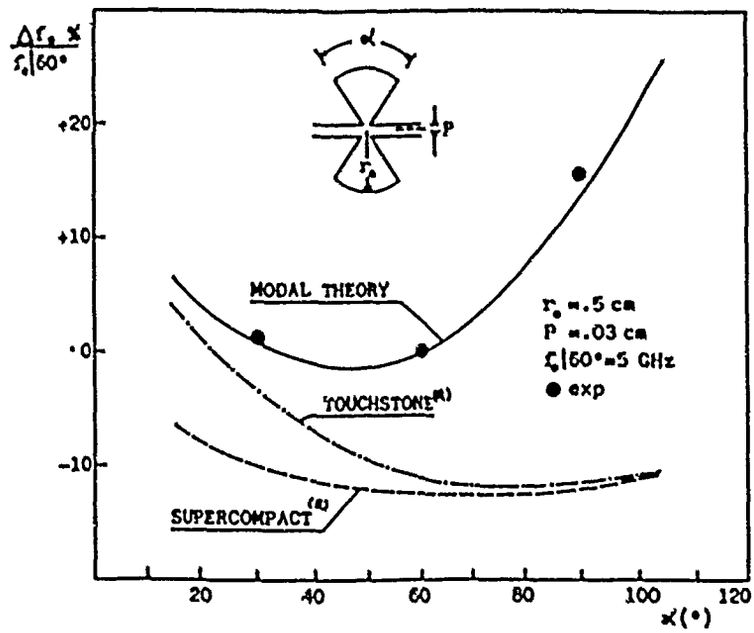

+20
+10
0
-10
20
40
60
80
100
120
α(°)
MODAL THEORY
TOUCHSTONE
SUPERCOMPACT
r₀ =.5 cm
P =.03 cm
f₀|60°=5 GHz
● exp

Fig. 7b

equivalent circuits do not take into the proper account the excitation of trasversal modes, whose importance becomes relevant with the increasing of frequency and/or the lowering of the stub impedance.

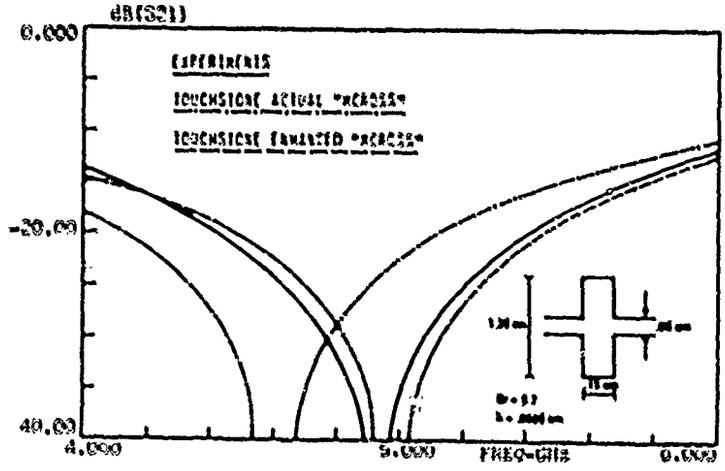


Fig.8a

The modal theory and the related equivalent circuit do not suffer from these limitations and give effective tools for properly simulating all the possible geometries independently from their shape ratios, so widening the range of validity of the existing equivalent models.

A comparison between experiments and simulations achieved from the mode based models and widespread commercial CAD packages is presented in fig. 8a and 8b for two specific geometries.

The accuracy of the commercial code is acceptable only for rectangular stubs having a quite narrow width, where it becomes extremely poor for wide transversal dimensions. On the

contrary, the planar approach and the related equivalent circuit on fig. 6 fit the experiments whatever the structure size.

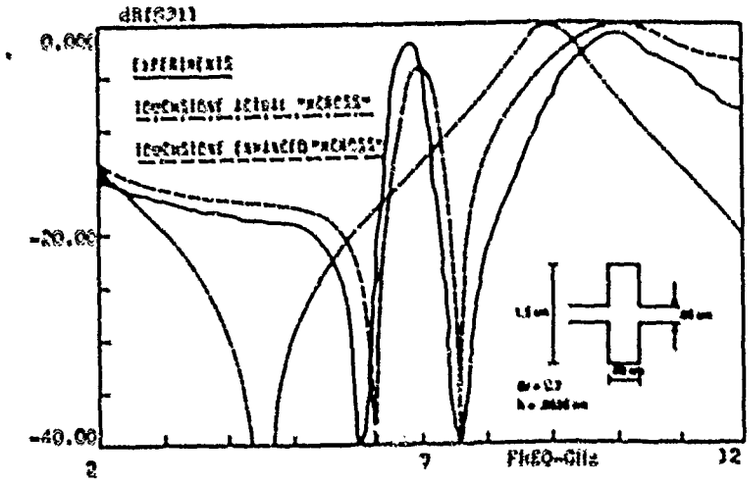


Fig.8b

V CONCLUSIONS

Planar stubs, both in the straight and radial shape, are a proper solution for the low-impedance issue. Moreover, a modal theory represents a powerful approach to fully characterize their electromagnetic features and it can be easily translated in very effective lumped equivalent circuits, easy to be implemented in the presently available commercial packages. The proposed models, based on a dynamic approach, fully describe the frequency behaviour of the structure, so overcoming the limits of the previously proposed quasi-static approximations.

The values of the equivalent components are pratically not frequency dependent, with the exception for the very moderate dispersion effect, so enhancing the effectiveness of already proposed frequency-dependent elements.

The frequency range of validity of the equivalent circuit is much broader with respect to the existing ones and it is intrinsically potential of a further broadening by adding further lumped-element cells.

References

[1] G. D'Inzeo, F. Giannini, C. M. Sodi, R. Sorrentino: "Method of analysis and filtering properties of microwave planar networks", IEEE Trans. MTT, vol. 26, pp. 462-471, July 1978.

[2] J. P. Vinding: "Radial line stubs as elements in stripline circuits", NEREM Record, 1967, pp. 108-109.

[3] H. A. Atwater: "Microstrip reactive circuit elements", IEEE Trans. MTT, vol. 233-239, June 1988.

[4] B. A. Syrett "A Broad-Band element for microstrip bias or tuning circuits", IEEE Trans. on MTT, vol. 28, pp. 925-927, August 1980.

[5] F. Giannini, R. Sorrentino, J. Vrba: "Planar circuit analysis of microstrip radial stub", IEEE Trans. MTT, vol.32, pp. 1652-1655, December 1984.

[6] F. Giannini, M. Ruggieri, J. Vrba: "Shunt-connected microstrip radial stub", IEEE Trans. MTT, vol. 34, pp.363-366, March 1986.

[7] F. Giannini, M. Salerno, R. Sorrentino: " Two-octave stopband microstrip low-pass filter design using butterfly stubs", Proc. of 16th Eu.M.C., Dublin 1986, pp. 292-297.

[8] F. Giannini, G. Bartolucci, M. Ruggieri: "Design Charts for low impedance radial line matching", Proceed. of MIOP'89, Sindelfingen, 28-February 2-March 1989.

[9] F. Giannini, G. Bartolucci, M. Ruggieri: "Low-impedance matching: the straight stub solution", to appear on Microwave and Optical Technology letters, March 1989.

[10] F. Giannini, M. Ruggieri. G. Bartolucci, C. Paoloni: "Low-impedance matching: the radial stub solution", to appear on Microwave and Optical technology letters.

[11] G. D'Inzeo, F. Giannini, R. Sorrentino: "Wide-band equivalent circuit of microwave planar networks", IEEE Trans. MTT, vol. 28, pp. 1107-1113, October 1980.

[12] F. Giannini, C. Paoloni: "Broadband lumped equivalent circuit of shunt-connected radial stub", Electronic Letters vol. 22, pp. 485-486, April 1986.

[13] F. Giannini, C. Paoloni, M. Ruggieri: "CAD-oriented lossy models for radial stubs", IEEE Trans. MTT, vol. 36, pp. 305-313, February 1988.

[14] F. Giannini, G. Bartolucci, M. Ruggieri: "Enhanced model for interacting step-discontinuities", 1989 IEEE MTT-S Int. Microwave Symposium Digest, Long Beach CA, June 1989.

[15] F. Giannini, C. Paoloni, "Modelling of Shunt Connected Single Radial Stub for CAD Applications", Alta Frequenza, vol. LVII n.5, June 1988, pp. 227-232.

[16] B. Bianco, M. Granara, S. Ridella, "Filtering Properties of Two-Dimensional Lines Discontinuities", Alta Frequenza, vol. XLII, July 1973, pp. 140E-140E.

[17] W. Menzel, I. Wolff, "A Method for Calculating the Frequency Dependent Properties of Microstrip Discontinuities", IEEE Trans. on MTT, MTT-25, n.2, pp. 107-112, Febr. 1977.

SESSION 3 - "ELECTROMAGNETIC COMPATIBILITY AND INTERFERENCE"

Chairman: Harold Sabbagh

AN INTEGRATED WORKSTATION FOR COSITE EMI ANALYSIS

P. Magis, J. Holtzman, P. Alexander
Telecommunications and Information Sciences Lab
The University of Kansas
2291 Irving Hill Road
Lawrence, KS 66045

D. Tam
Naval Oceans Systems Center
271 Catalina Blvd.
San Diego, CA 92152

Sponsored by NOSC and The Department of The Army

ABSTRACT

The Communications Engineering Design System (COEDS) developed at the University of Kansas is a Computer Aided Analysis and Design (CAAD) tool for Electromagnetic Interference/Electromagnetic Compatibility (EMI/EMC) analysis of colocated communications equipment. COEDS has been designed as a shell or wrapper around codes previously implemented, providing intelligent user interfaces for data entry, a smart postprocessor to display data in a "thought enhancing" manner, and all data management functions. The COEDS shell can also be applied to other EMI/EMC codes and can be adapted to other large programs. COEDS permits the EMI/EMC engineer to determine the interference between communication systems where the principle coupling results from the antenna to antenna interactions causing multiple unwanted signals to enter sensitive receivers.

Introduction

The design of communication systems generally follows well developed methodologies which have been successfully extended to distributed networks with many nodes. When nodes for different networks are colocated in a relatively confined area such as is found aboard ships, communication "huts" and so forth, interference occurs between the networks because of mutual coupling between antennas. There are other mechanisms that cause Electromagnetic Interference (EMI), however, most of the effort at achieving Electromagnetic Compatibility (EMC) has focused on analysis and methods of overcoming the antenna coupling effects.

Over the past ten years, under sponsorship of the Naval Ocean Systems Center (NOSC), several computer programs have been created by the Electromagnetic Compatibility and Analysis Center (ECAC) to perform EMI/EMC analyses for situations such as those described above. The methodologies employed for analysis have been sufficient but laborious [Rockway78]. The programs developed require

extensive data preparation and careful control of data management and produce large volumes of tabular data which are difficult to interpret and even more difficult to use in an iterative design procedure. The Communications Engineering Design System (COEDS) was conceived, designed and implemented as a shell or wrapper around these codes to provide an intelligent user interface, data flow and program control, and a postprocessor that would present the data to the design engineer in a "thought enhancing" manner. COEDS can also serve as a model for similar shells that may be developed to interface to other EMI/EMC programs such as the Numerical Electromagnetic (NEC) codes. Thus, COEDS is a prime example of reuseable software which can be adapted to other EMI/EMC codes.

Systems Analysis Using COEDS

The present design procedure for communication systems involves an iterative process. A candidate design is analyzed in terms of the amount of interference caused by colocated equipment. If the degree of cosite interference is greater than the ambient noise level, then the EMC requirements have not been satisfied and an alternative design must be formulated. The approach used in producing an alternative design may exercise one of the following options: change equipment; add filtering on the transmit or receive side of the system; change the location of the antenna(s); provide for frequency management by increasing the frequency separation between the transmitter and receiver, and/or assigning intermodulation free frequency sets; support power management by reducing transmitter power; provide for time management by monitoring the number of simultaneous transmissions or duty cycles; or reduce design goals and accept interference interaction [Li88].

COEDS can be used to analyze and synthesize the effects of most of the above design improvement methods. In this paper, we will discuss the COEDS structure and provide some typical examples of system use. Specifically, COEDS uses existing code for communication systems analysis when determining the degree of interference at a receiver caused by colocated transmitters. A number of interference sources are considered including simple broadband noise, spurious transmitter emissions and spurious receiver responses, transmitter and receiver intermodulation, and coupler harmonics. Once data are obtained regarding the amount of interference present at the receiver from as many as forty neighboring transmitters, COEDS can be used to determine the frequency separation required for the system to be ambient noise-limited rather than interference-limited, or to investigate other interference mitigation techniques. Successive analyses of the communications system are based on test plan structures which allow the user to choose the frequency intervals at which a transmitter is tuned with respect to a victim receiver in the system. Various test plan types can be specified depending on the classifications of interference interactions to be considered.

COEDS Architecture

COEDS was developed as an interactive CAAD/CAE workstation tool. The system, shown in Figure 1, is based on four functional modules which illustrate the range of functionality provided by COEDS: (1) Platform Database Operations; (2) Platform Viewer; (3) Configuration Viewer; and (4) EPF (Equipment Parameter File) Viewer.

Platform Database Manipulations

The iterative nature of the design process requires the capability for freedom of movement through the space of alternative designs. In order to achieve an optimal configuration, the engineer must be able to view the alternatives in an efficient manner. The Platform Database stores the user's design instantiations (referred to as configurations in the COEDS system) as well as analysis results for each design. Platform Database operations allow the user to review the steps that he or she has taken in the process in order to compare alternative designs and analysis results.

Platform Viewer

The Platform Viewer allows the user to create and/or open a platform for communications system design. A particular platform may have several configurations associated with it, each of which represents an alternative design. One of the functions provided in the viewer is the capability to input antenna to antenna coupling for the platform.

Antenna to antenna coupling, the chief mechanism allowing the mixing of interfering signals, is input to COEDS in one of several ways. External files of coupling data obtained from measurements or calculated from NEC codes may be used. Coupling data can be input using a point curve input module that permits the engineer to place the antenna coupling versus frequency points on a curve using the mouse or keyboard. Alternatively, simplified equations incorporated in the analysis engines may be used to calculate the coupling from the physical locations of the various antennas.

Antennas are modeled as ideal elements in so far as impedances are concerned. COEDS has the capability of placing a coupler or filter in series with the antenna representing the power transmission loss versus frequency arising from the actual antenna impedance. A antenna impedance matching program developed at NOSC is also included that calculates matching networks.

Configuration Viewer

Once a platform has been selected with the Platform Viewer, a configuration can be built using the block diagram editor, analyzed by specifying a test plan and running the appropriate analysis engines, and evaluated by viewing graphical ouput with the COEDS postprocessor.

Block Diagram Editor

An engineer normally thinks in terms of block diagrams. Therefore, the user interface to COEDS was designed to allow the engineer to build a block diagram for the communications system on the screen using equipment "black boxes". Available equipment is displayed via pop up menus and can be selected by pointing and clicking with a mouse. Using a mouse and menu-driven approach for data and command entry minimizes the requirements for error checking and reduces the possibility of the user entering erroneous data.

A communications suite is constructed using the block diagram editor. Operations which are available to the user include adding and deleting blocks, changing the connectivity between blocks, adjusting equipment parameters, and moving the blocks around on the screen. The blocks are specified as transmitters, receivers, couplers (filters), decouplers and antennas. The engineer selects the various blocks, interconnects them and sets key parameters such as the physical location of antennas, the range of frequencies, modulation types, power transmitted and so forth. After a system is built with the block diagram editor and configured with the desired parameters, it is saved in the platform data base with any other configurations instantiated for the current platform. Once the configuration is saved, the engineer does not have to enter any further equipment parameters or values. All data are automatically passed to the appropriate modules. At this time the communications engineer can create a desired test plan for specific or generic compatibility analyses. COEDS will then generate the equipment connectivity, extract the appropriate data, and run the analysis engines for interference computations.

System Analysis

Predicting cosite interference, performance degradation, and link performance is accomplished using batch programs integrated into COEDS. The batch programs used are COSAM II [Clubb87] for interference and degradation and LINCAL [Roder79] for link analysis.

COSAM II operates in two different modes, a System Performance Score (SPS) mode and a Necessary Desired Power (NDP) mode. In the SPS mode, the engineer sets or uses predetermined levels of received sensitivity. The system then calculates, as one output product, the probability of successful communications for ambient noise limited and interference limited conditions. In the NDP mode, target performance indices are set by the engineer and the system calculates the required receiver input signal power to achieve these goals for both ambient noise limited and interference limited situations.

While these output products are satisfactory for a comprehensive final report, they do not lend themselves to the needs of an engineer in an iterative design process. One of the interim calculated products is the equivalent on tune power (PINO) for

each interaction at each receiver. Given the PINO at a receiver, the Excess Interference Level (EIL) is defined as the amount by which the PINO exceeds the ambient noise power at the receiver [Rockway78]. This EIL value represents the additional isolation needed between systems. Since the communications system under analysis will always suffer the effects of ambient noise, an EIL value of zero denotes the elimination of cosite interference and thus, the achievement of EMC requirements. A frequency management plan which maintains compatibility can be specified by determining the frequency separation required to achieve zero EIL for each equipment. Alternatively, additional filtering can be inserted, selected transmitter powers reduced, antenna isolation increased by repositioning the antennas and so forth.

LINCAL calculates groundwave and skywave propagation losses, as well as received signal statistics based on transmit frequency, power, and distance. Once a frequency plan has been determined and the required signal to noise plus interference levels established, LINCAL can be used to determine the achieved quality of service for specified circuits between remote nodes when the nodes are in a complex interference environment.

The COEDS interface to these batch programs is the test plan generator. The test plan generator allows the user to specify sets of parameters based on the type of test plan chosen. The various types are as follows: isolation study; intermodulation study; spurious emissions/response study; compatibility analysis; and link analysis.

An isolation study in the COEDS system will perform adjacent signal and broadband interference analysis automatically to determine minimum transmitter-receiver frequency spacing. This test will show how close each transmitter can operate to each receiver for the most efficient use of the frequency spectrum. The minimum separation between each receiver and transmitter is determined by calculating the performance degradation from adjacent signal interference and broadband transmitter noise as a function of transmitter-receiver frequency spacing.

An intermodulation study in COEDS will evaluate the effect of intermodulation products, harmonic products and cross modulation products which may be generated in transmitters, couplers or receivers. The interfering effect of these products does not depend on frequency spacing but on the ratio (f1/f2) between emitter, oscillators and intermediate frequencies. Slight changes in an emitter frequency, reduction in power, addition of filters or denying particular operating frequencies to a transmitter or receiver will eliminate product effects. The results of the product study can be used either to confirm that a given frequency plan may be used, or to show which discrete frequencies in a band should not be used to achieve EMC.

A spurious emissions/response study will consider exclusively the interference generated by spurious emission and spurious response interactions. Compatibility studies take into account all possible interactions including intermodulation

products, harmonic products, cross modulation products, adjacent signal analysis and spurious emissions/spurious response.

Link analyses predict the link range between a system receiver and a remote transmitter. Typically the link range is limited by cosite interference, ambient noise and receiver intrinsic noise. The objective in cosite analysis is to reduce cosite interference to a level whereby it does not limit link range. The goal is to balance the interferers and other noise so that the link is limited only by ambient noise and intrinsic noise.

Postprocessor

One of the strengths of the COEDS system is the Postprocessor subsystem. It manages the data generated during the various analyses, presenting essential information needed by the engineer for the various tasks at hand. Interference and performance prediction results are arranged hierarchically in graphical and pictorial format from the most general view to more specific views. This allows the engineer to look at the overall performance, quickly select the most damaging interference and focus on the specific devices which cause the problem. Various graphical aids are included to help the engineer select appropriate mitigation techniques.

Equipment Parameter File Viewer

The Equipment Parameter File Viewer allows for access to the communications equipment contained in the equipment data bases. The data bases store the equipment operating parameters and performance degradation curves required by the analyses engines. When building a block diagram, the user chooses equipment for the communications system from these data bases. The Viewer included in COEDS is used to set values in the block diagram, search the data base for alternative items or to check the range of values for the selected items. In addition to the equipment contained in the inventory, COEDS has the provision to add equipment, modify equipment or alter key parameter values.

System Example

An example of EMC analysis, using COEDS, is explained in the following section. Figure 2 shows an example HF system with three transmitters, a coupler and decoupler, one receiver, and two antennas. The purpose of the example is to demonstrate: the steps used to divide the cosite problem; the methods of displaying interference interactions, performance degradation, and link performance; and the iterative approach used to identify and reduce the most damaging interference. The example illustrates analysis and prediction methods only and is not intended to represent an actual system.

The example analysis follows four steps: (1) Adjacent signal analysis to determine minimum transmitter/receiver frequency spacing; (2) Intermodulation analysis to

determine undesirable frequency combinations and maximum allowable transmitter power; (3) Frequency selection and system connectivity adjustments in order to mitigate problems found in steps 1 and 2; (4) Receiver performance degradation and link performance prediction in the presence of all known cosite interferers. Because of the ease in changing the system and automatically updating the system data base, the system may be changed at any time during the analysis. This allows for an iterative approach to reduce interference to a level whereby EMC is achieved.

Analysis Example

In step one of the analysis we investigate the effects of transmitter/receiver frequency spacing on receiver performance. For the most efficient use of the spectrum and to be able to have the maximum number of frequencies available, we want to know how close each transmitter can operate to each receiver. Figures 3a and 3b show the results of adjacent signal analysis by the frequency of the interferers and the relative interfering power. The frequency of the receiver being analyzed is denoted by the dashed line to draw attention to the main area of interest. We are concerned with the effect of the transmitters on an individual receiver. The relative power of each interferer is shown as the amount by which the interference power exceeds a certain threshold. This value, the Excess Interference Level (EIL), is calculated such that an EIL value of 0 dB represents the threshold. A level above 0 dB will not meet EMC requirements. A level below 0 dB and the receiver performance will meet or exceed EMC requirements.

In Figures 3a and 3b, receiver 1 is shown as being tuned at 3.12 MHz. The interfering signals and their interfering effects (EIL) are shown as icons on the graph, at frequency spacings of 2.5, 5, and 10 percent away from the operating frequency of receiver 1. These figures show that transmitters 1 and 2 interfere with receiver 1 at frequency separations of 10 percent or less. Regardless of intermodulation, spurious emission and harmonic products, the system is fundamentally limited by adjacent signal noise. To reduce the effect of adjacent signal noise to an EIL of 0 dB without resorting to extremely large frequency separations, either the system connectivity can be changed or the equipment can be changed. As it is usually very difficult to increase the antenna isolation we have changed the method of coupling transmitter 1 and receiver 1 to antenna 1 by adding two additional couplers. The revised system, shown in Figure 4, was entered into the COEDS adjacent signal analysis model with the results shown in Figures 5a and 5b. The result of changing the coupling was to reduce the adjacent signal noise in receiver 1. Figures 5a and 5b show that if transmitters 2 and 3 operate at 1.5 percent spacing or greater, then broadband noise will not limit system performance. By establishing this minimum transmitter/receiver frequency spacing, the frequency requirements for EMC have be determined.

In step two of the analysis, we investigate the effects of intermodulation products, harmonic products, and cross modulation products which may be generated in

transmitters, couplers or receivers. Due to the fact that these effects are nonlinear, results cannot be derived for a band of frequencies. Instead, the user must evaluate the system at discrete frequency values and repeat the process until a satisfactory level of performance is achieved. An advantages of using COEDS in this step of the design is the ease of changing frequency values for evaluation. The results of an example intermodulation study are shown in Figures 6a and 6b by the frequency of the interferer and the relative interfering power of the intermodulation product term (EIL). The results of the study are shown for receiver 1 and all the products from transmitters 1, 2, and 3. The figures show that, for receiver 1, all frequency products produce an EIL value less than 0 when the interfering transmitters are tuned at a frequency spacing of 10 percent. Figure 6a demonstrates the effects with transmitters 1 and 2 tuned 10 percent below the receiver operating frequency while Figure 6b shows a separation 10 percent above the receiver frequency. Additional analyses must be evaluated in order to determine if a smaller frequency spacing can be used. The point of this example is to show the capabilities of COEDS when evaluating various frequency plans for a system.

The final step in the analysis is to predict link range between the system shown in Figure 4 and a remote transmitter. Figure 7 shows the difference between noise-limited service and interference-limited service. The top curve in Figure 7 shows link range when receiver 1 is limited only by ambient and intrinsic noise. The bottom curve in Figure 7 shows the link range when receiver 1 is primarily limited by interference interactions. For the example shown, the effect of cosite interference is to reduce maximum link range by approximately 30 km. Thus, the meeting of EMC requirements for colocated equipment by the reduction of cosite interference provides the additional benefit of improved link performance.

Future Work

COEDS was designed to permit the inclusion of additional analysis engines in future versions or for the replacement of the engines with other communications systems analysis tools. The control structure of COEDS is written in LISP and can operate with auxiliary code in any major programming language. Planned future enhancements include the addition of an antenna data base, a frequency hopping and spread spectrum model for interference, a PC-based system, and a knowledge-based version for automated design.

Summary

COEDS is an interactive CAAD/CAE workstation tool to be used as an aid in predicting interference, performance degradation and link performance when determining the degree of EMC for cosite communications systems. An example was shown which demonstrated the block diagram interface, automated program operation, generation of graphical output, and ease of use in changing the design to meet performance criteria. Key features of COEDS are the block diagram editor,

configuration data base, the test plan/frequency plan generator, use of a mouse to point and select for all input and execution, and a postprocessor for output displays.

References

[Clubb87] Clubb, K. et al, "The COSAM II (DECAL/PECAL) Wideband and Narrowband RF Architecture Analysis Program User's Manual," Consulting Report, ECAC-CR-86-112, ECAC, Annapolis, Maryland, February 1987.

[Li88] Li, S.T., J. C. Logan, and J. W. Rockway, "Ship EM Design Technology," Naval Engineers Journal, May 1988, pp. 154-165.

[Rockway78] Rockway, J. W., S. T. Li, D. E. Baran, W. Kowalyshyn, "Design Communication Algorithm (DECA)," IEEE International Symposium on Electromagnetic Compatibility, June 1978.

[Roder79] Roder, C. et al, "A Method for Evaluating the Received Signal Statistics of a Communications Link Termination on a Naval Ship," Consulting Report, ECAC-CR-79-126, ECAC, Annapolis, Maryland, November 1979.

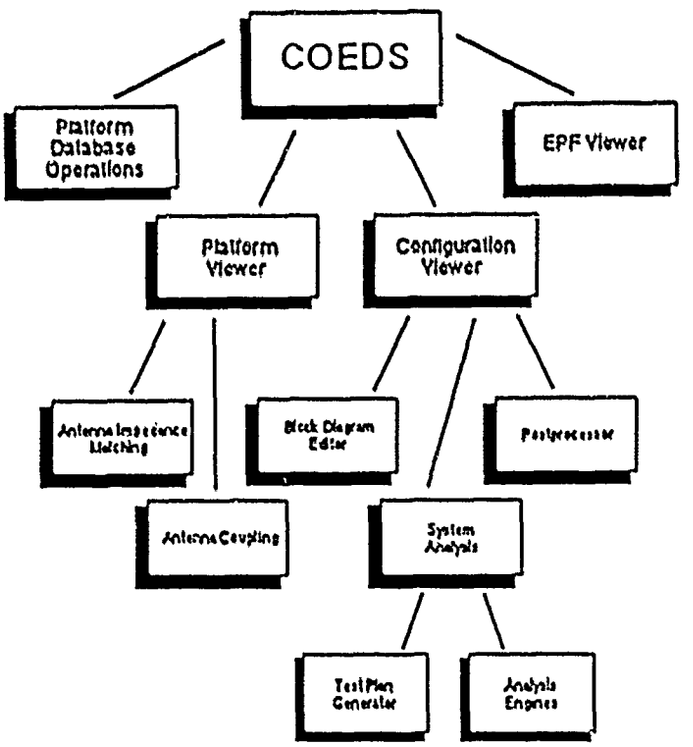


Figure 1. COEDS Architecture.

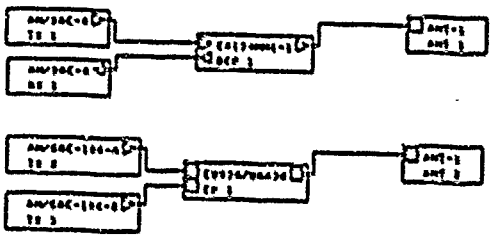
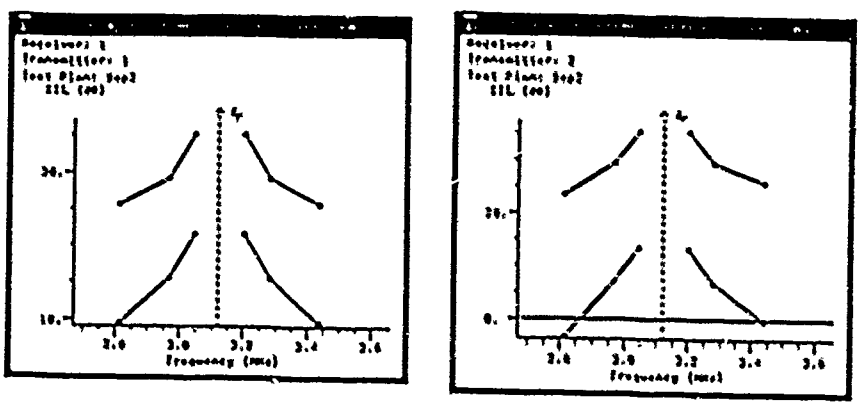


Figure 2. HF Example System



SIL Values for receiver 1

Trans	Freq.(mhz)	Type	SIL(db)	Diag(deg)	St.dv.(deg)	Prb
1	2.81	VAS	-5.21	-56.35	10.00	0.356
1	2.44	VAS	-3.25	-56.35	10.00	0.356
1	2.50	VAS	11.28	-56.82	10.00	0.337
1	2.38	VAS	11.28	-56.82	10.00	0.337
1	2.81	VAS	11.31	-56.82	10.00	0.337
1	2.44	VAS	11.31	-56.82	10.00	0.337
1	2.50	VAS	11.31	-56.82	10.00	0.337
1	2.38	VAS	11.31	-56.82	10.00	0.337
1	2.81	AAS1	11.34	-56.36	0.03	0.000
1	2.44	AAS1	11.34	-56.36	0.03	0.000
1	2.50	AAS1	11.34	-56.36	0.03	0.000
1	2.38	AAS1	11.34	-56.36	0.03	0.000
1	2.81	AAS1	11.34	-56.36	0.03	0.000
1	2.44	AAS1	11.34	-56.36	0.03	0.000
1	2.50	AAS1	11.34	-56.36	0.03	0.000
1	2.38	AAS1	11.34	-56.36	0.03	0.000
2	2.81	VAS	-3.23	-56.83	10.00	0.333
2	2.44	VAS	+0.16	-56.83	10.00	0.333
2	2.50	VAS	5.31	-56.82	10.00	0.333
2	2.38	VAS	5.03	-56.82	10.00	0.333
2	2.81	VAS	11.30	-56.36	10.00	0.333
2	2.44	VAS	11.30	-56.36	10.00	0.333
2	2.50	AAS1	11.31	-56.82	0.03	0.000
2	2.38	AAS1	11.31	-56.82	0.03	0.000
2	2.81	AAS1	11.34	-56.36	0.03	0.000
2	2.44	AAS1	11.34	-56.36	0.03	0.000
2	2.50	AAS1	11.34	-56.36	0.03	0.000
2	2.38	AAS1	11.34	-56.36	0.03	0.000

Figures 3a and 3b. Adjacent Signal Analysis for Transmitters 1 and 2 vs. Receiver 1

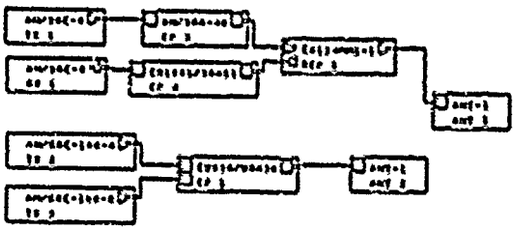
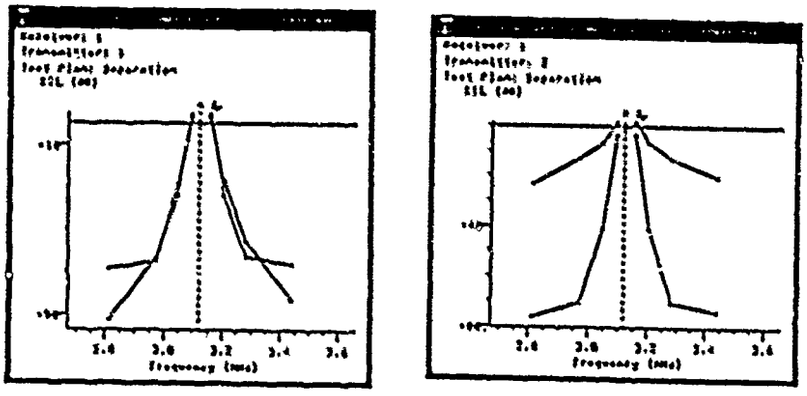
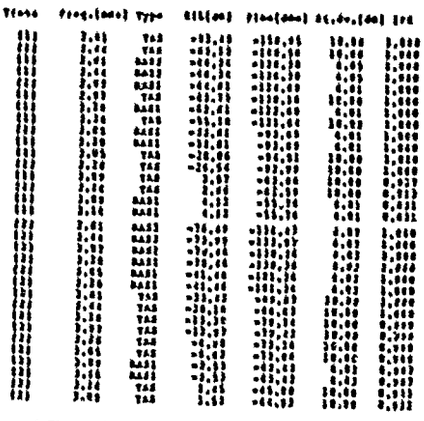


Figure 4. Alternative Design





Figures 5a and 5b. Adjacent Signal Interference for Alternative Design

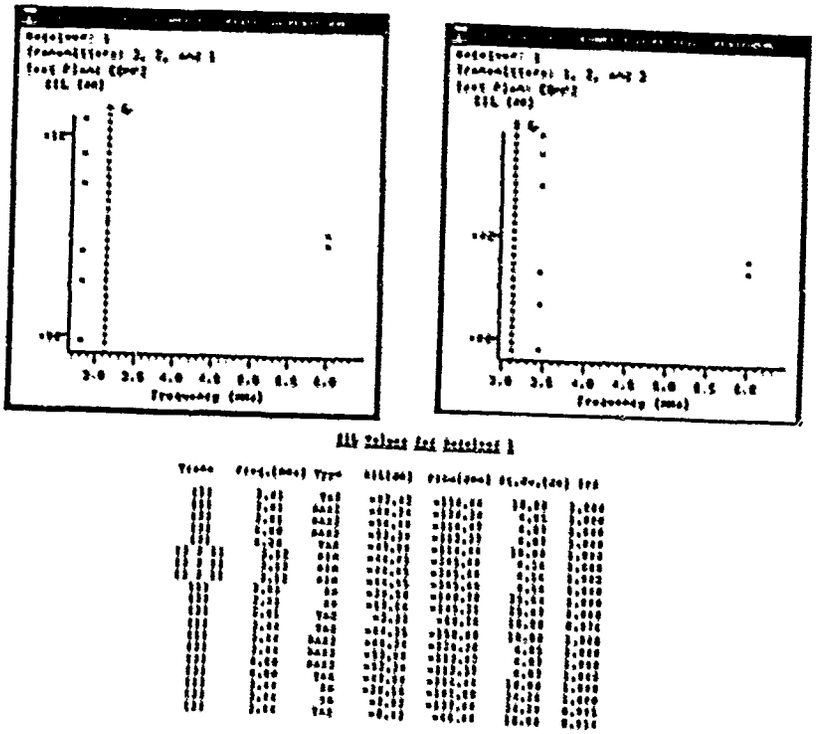


Figure 6a and 6b. Results of Frequency Product Study

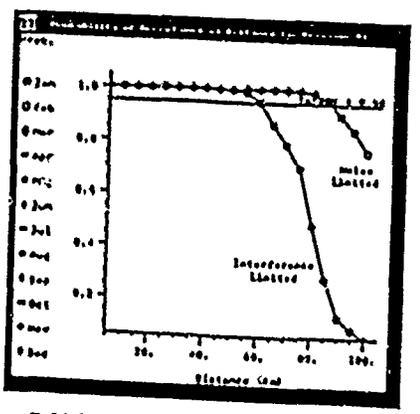


Figure 7. Link Range Analysis for Alternative System

Modeling Unintentional Sources of Electromagnetic Radiation

Todd H. Hubing
IBM Communication Systems
Research Triangle Park, NC 27709

J. Frank Kauffman
North Carolina State University
Raleigh, NC 27695-7911

Abstract - Suppressing the electromagnetic emanations from unintentional radiation sources is a growing concern. A variety of simple radiation models are used by electronic circuit and systems designers to help them locate and evaluate potential sources of radiation. However, the powerful numerical modeling techniques that are widely used to analyze antenna designs, are rarely applied to unintentional radiation sources. Numerical EM analysis codes that work well for modeling antennas are not readily applied to devices that are not designed to radiate. The analysis of unintentional radiation sources presents a unique set of problems. This paper investigates some of these problems and illustrates them using simple models for a video display terminal. Approaches to the analysis of this model using existing moment-method algorithms are investigated. This investigation reveals some of the weaknesses of the existing techniques and makes it clear that a new approach is needed. Although this approach is yet to be defined, essential features of such an approach and the incorporation of these features in a computer modeling code are discussed.

Introduction

Unintentional sources of electromagnetic radiation have been the object of an increasing amount of concern. Many countries, including the U.S., regulate the electromagnetic emissions from unintentional sources such as computers and computer peripherals. The trend towards faster, more sophisticated, but less expensive computing devices has made it much more difficult for computer manufacturers to meet these requirements using traditional methods. There is an increasing need for EM modeling algorithms that can be applied to unintentional radiation sources.

Unfortunately, most unintentional radiation sources are very complex. It is not usually clear which parameters of the source are critical to its analysis. For example, a video display terminal may contain several high-frequency circuit cards, internal wires, and external power and signal cables. Modeling every circuit and wire using numerical modeling techniques is not usually practical. Excessive amounts of computation would be required and existing numerical techniques are unable to model this type of highly-complex source. It would be much better to eliminate those wires and circuits that do not have a significant effect on the radiation prior to the application of a numerical technique.

When modeling sources that are designed to radiate, it is relatively easy to determine which parameters are important enough to be included in the model. However, the radiation mechanism of unintentional sources is not usually well-understood. The high-frequency coupling between circuits makes it difficult to determine one specific source and there are often several possible radiating elements.

Example

Consider the video display terminal (VDT) illustrated in Figure 1. Rather than attempting to model all of the significant parameters immediately, it is often useful to start with a simple model of a primary radiation mechanism. Once the behavior and limitations of the simple model are well understood, other parameters of the VDT can be included in the model. In this way, the potential significance of these parameters can be evaluated.

If the VDT is small relative to a wavelength at the frequencies of interest, it is reasonable to expect

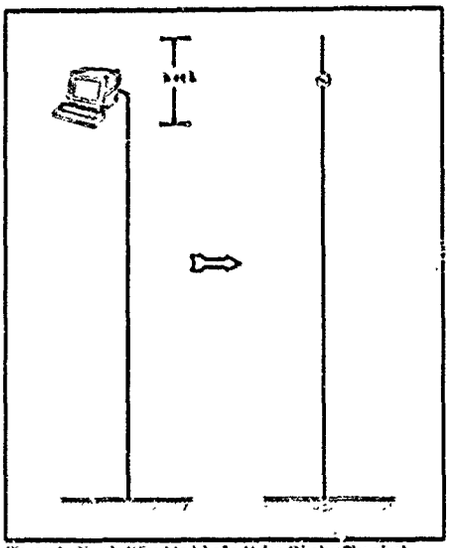


Figure 1. Simple Wire Model of a Video Display Terminal

[1,2] that the common-mode[1] currents induced on the attached cables are the most significant electromagnetic radiation source. The simplest possible model of the VDT therefore consists of a cable and a source that puts current on the cable. Since only common-mode currents are being considered, the cable can be modeled with a solid wire. A source on the end of the wire supplies the current and an undetermined length of wire on the opposite side of the source models the parts of the VDT that are *driven* relative to the cable.

Although Figure 1 represents a very crude model of a complex device, it is readily analyzed and can tell us many important things about the way this device radiates. For example, the current distribution (though not the amplitude) on the cable can be calculated for various cable positions, terminations and frequencies. By setting bounds on the length of the wire segment above the source (based on the dimensions of the VDT), useful information pertaining to the input impedance and possible resonant frequencies can be obtained [2].

This model can be improved somewhat by modeling the source with greater detail. Comparisons with actual measurements or experience with VDT testing are useful for estimating a voltage level and source impedance to use in the model. Filters, ferrites, or shields that are designed to reduce common-mode currents on the cable can be added to the model to predict their effectiveness. For example, a source model for a 50-ohm circuit above a ground plane in a VDT with a ferrite choke on the power cable might be modeled as shown in Figure 2. This type of model is more accurate than the single wire model and can provide useful information about the effect that the ground plane, circuit resistance and ferrite impedance have on the radiation from the VDT.

Numerical Techniques

Models such as the one in Figure 2 consisting of three-dimensional circuit layouts in the presence of nearby metal plates and cables are very useful for analyzing a variety of electromagnetic compatibility problems. Unfortunately, this type of configuration

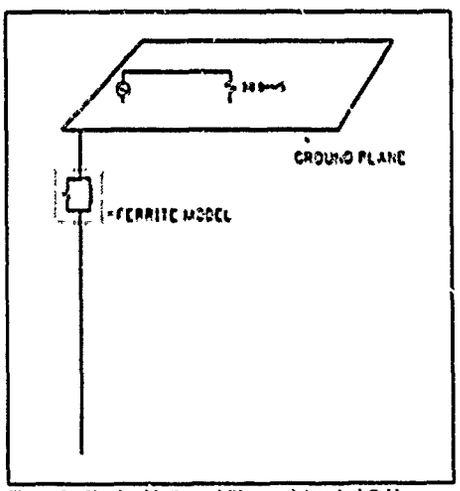


Figure 2. Circuit with Ground Plane and Attached Cable

[1] Common-mode current is the component of the cable current that flows in the same direction on all conductors as opposed to differential or normal-mode current which flows in opposite directions using different conductors in the same cable.

is not readily analyzed using existing numerical EM analysis techniques.

A finite-element technique would appear to be appropriate for modeling electrically small circuits and metal plates, however most practical unintentional source models have relatively long attached wires [2]. For this reason, a moment-method technique is preferred. Unfortunately, a survey of existing moment-method algorithms did not turn up any readily-available codes capable of modeling this type of configuration.

Two of the codes that were evaluated did come close however. The ESPII code [3] developed at Ohio State University models wires and conductive surfaces and can accurately calculate the input impedance of a source near a wire attachment. It does not model wire attachments near the edge of a plate however (prohibiting wire attachments to electrically small plates) and it could not analyze wire attachments to opposite sides of a thin plate. The Numerical Electromagnetics Code (NEC) [4] developed at Lawrence Livermore National Laboratories models wire attachments near the edge of a surface and on both sides of a surface. It does not however, model thin surfaces very well and calculations of the input impedance of a source near a wire attachment point are not always accurate. Modifications to the NEC code were attempted in an effort to use this algorithm for modeling unintentional sources [5]. These modifications improved the detail and accuracy of the wire attachment calculations at the expense of additional computer time and memory. The result was a relatively inefficient code that accurately calculated the input impedance of sources near a wire attachment, but could still not model thin surfaces. The inability of NEC to model thin surfaces is due in part to properties of the magnetic field integral equation (MFIE), which it uses to solve for the currents on conductive surfaces. This limitation can be overcome by modeling the surface with smaller patches so that the length and width of each patch are comparable to the thickness of the metal plate. This requires a large number of patches however, and the computing resource required to model the conductive surfaces found in most unintentional sources is prohibitive.

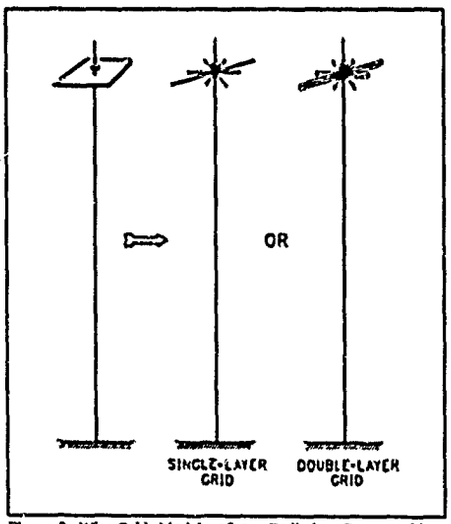


Figure 3. Wire-Grid Models of an Radiation Source with a Metal Plate

Wire Grid Modeling

Another possible approach to the analysis of this type of configuration is wire-grid modeling. Conductive surfaces are often modeled by a *grid* of wires, which facilitates their analysis using one of many moment-method codes that accurately model wire configurations.

Two techniques for modeling electrically small, thin plates with a wire grid were investigated. They are illustrated in Figure 3. The first technique (single-layer grid) represents the entire plate with one grid. The second technique (double-layer grid) uses a separate grid to model each side of the plate.

Various wire-plate structures were built and tested in order to obtain measured data to compare with wire-grid model results. In general, the wire-grid models were capable of modeling the plate very well except at frequencies near the system resonance. The results were relatively insensitive to the diameter of the wires in the grid, which was surprising since the wire diameter is a critical parameter in the analysis of electrically large or resonant surfaces [6]. For these electrically small plates, it was only necessary to choose wire diameters within the constraints of the algorithm and to insure that the sum of the wire diameters at an attachment point was on the order of the diameter of the attaching wire.

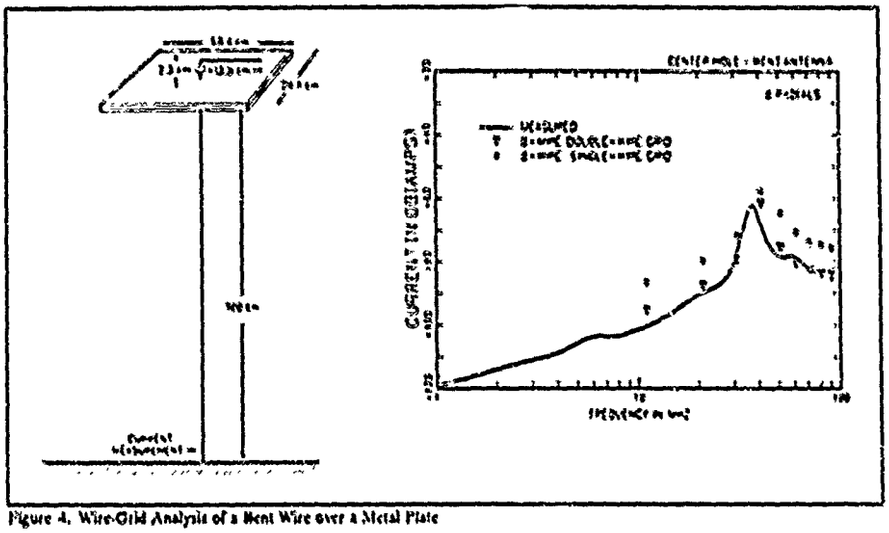


Figure 4. Wire-Grid Analysis of a Bent Wire over a Metal Plate

Figures 4-7 show the results obtained when single and double-layer grids were used to model four different configurations. The source amplitude was 1 volt and the current was measured at the base of the long wire just above the ground plane. Details of the measurement procedure and additional results are presented in [5].

The double-layer grid did a good job of modeling the metal plate in a variety of configurations. The single-layer grid worked well in some configura-

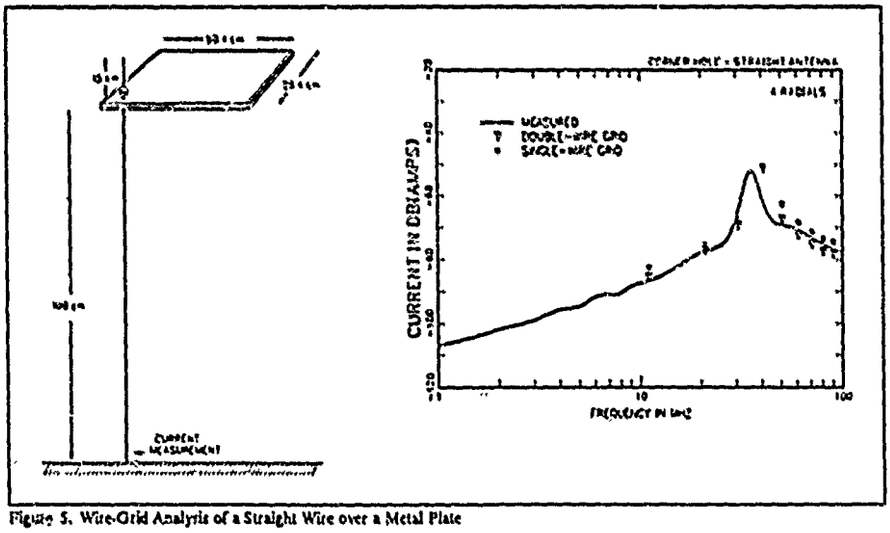


Figure 5. Wire-Grid Analysis of a Straight Wire over a Metal Plate

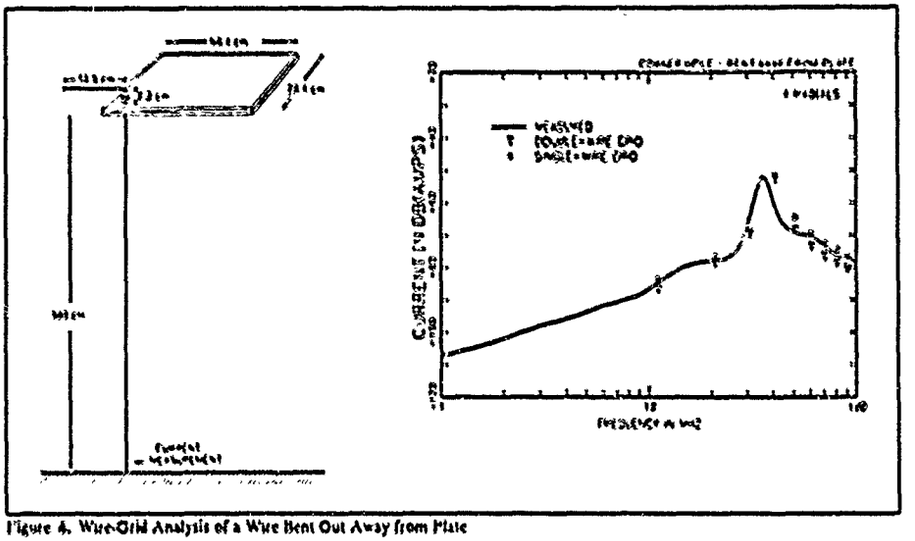


Figure 6. Wire-Grid Analysis of a Wire Bent Out Away from Plate

tions, but did not generally perform well when the attached wire was bent over the plate.

Wire grid models are a convenient and relatively accurate way of modeling the conductive surfaces in a variety of unintentional source configurations. They are not the ultimate solution, however. Although they do a good job of modeling the far-field effects of a metal plate, the fields calculated near a wire grid do not approximate the fields near a smooth conductive surface. This makes it

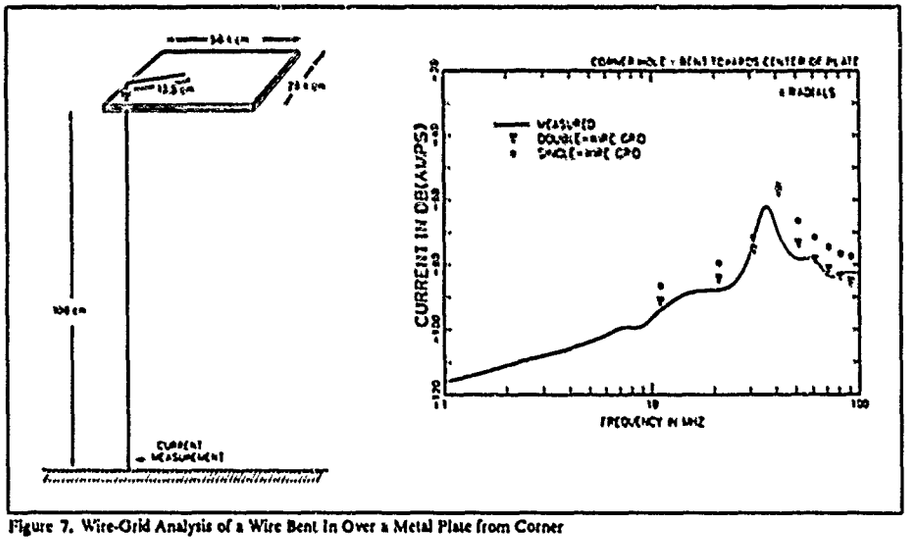


Figure 7. Wire-Grid Analysis of a Wire Bent In Over a Metal Plate from Corner

very difficult to model the details of a circuit or component near a metal surface accurately.

Conclusions

Even simple models of an unintentional radiation source are likely to contain electrically thin plates with attached wires. Existing numerical EM modeling techniques generally cannot model these configurations effectively. Wire models can be used in some cases, and in fact, wire models have been used by the authors to analyze a variety of unintentional source configurations. However, the fields near a conductive surface are not modeled accurately by wires or wire grids and thus wire models cannot be used to analyze the effect of subtle changes in a circuit's design or layout.

A new technique is needed before numerical modeling of unintentional sources can become as useful and routine as intentional source modeling. This new technique should be able to analyze circuit card configurations with a relatively high degree of detail and then analyze the entire system, which may contain several circuit cards, shields and cables. One possible approach would be to use a hybrid technique. For example, a finite element method might be used to analyze the cards and define boundary conditions to be used in a moment method analysis of the whole system.

Radiation from unintentional sources has become a critical concern of electronic device manufacturers and developers. Stringent military and nonmilitary requirements are becoming more difficult to meet as operating speeds of electronic systems increase. A numerical EM modeling technique that could be applied to digital circuits and systems would find a large number of potential users. The availability of such a technique could make EM radiation modeling an integral part of the development process for state-of-the-art electronic systems.

References

[1] C. R. Paul and D. R. Bush, *Radiated Emissions from Common-Mode Currents*, Proceedings, 1987 IEEE International Symposium on Electromagnetic Compatibility, Atlanta, GA, August 1987.

[2] T. H. Hubing and J. F. Kauffman, *Modeling the Electromagnetic Radiation from Electrically Small Table-Top Products*, IEEE Transactions on Electromagnetic Compatibility, Vol. 31, Feb. 1989, pp. 74-84.

[3] E. H. Newman and D. M. Pozar, "Electromagnetic Modeling of Composite Wire and Surface Geometries," *IEEE Transactions on Antennas and Propagation*, vol. AP-26, Nov 1978, pp. 784-789.

[4] G. J. Burke and A. J. Poggio, *Numerical Electromagnetics Code (NEC) - Method of Moments*, Naval Ocean Syst. Center, San Diego, CA, NOSC Tech. Document 116, Jan. 1981.

[5] T. H. Hubing, *Modeling the Electromagnetic Radiation from Electrically Small Sources with Attached Wires*, Ph.D. Dissertation, North Carolina State University, May 1988.

[6] A. C. Ludwig, "Wire-Grid Modeling of Surfaces," *IEEE Transactions on Antennas and Propagation*, vol. AP-35, Sep 1987, pp. 1045-1048.

Comparative Calculations of Basic EMC Configurations with NEEOS and NEC2-IABG

M. Wurm, F. Heidler, K. Müller
Industrieanlagen-Betriebsgesellschaft mbH (IABG)
Department SOE
Einsteinstraße 20
D-8012 Ottobrunn/Germany
Phone: (089) 6088-3250 or -2820

Abstract:

Comparative calculations on six basic EMC configurations were performed with several versions of the Numerical Electromagnetics Code (NEC2-IABG, NEC2-PC, NEC81, MININEC3, NEC2DPC) to check the accuracy and validity of the different codes, especially with respect to their built-in arithmetics. In the simulations the coupling characteristics between transmitting and receiving antennas and the input impedance of the transmitting antenna were examined primarily. Generally it was found that there is a sufficient agreement between all codes as long as the segmentation condition $1/1000 \leq l/\lambda \leq 1/10$ is fulfilled. Especially the recently developed NEC81 code shows the same degree of accuracy as the double precision version NEC2-IABG when analysing regular problems. For the simulation of low frequency problems double precision arithmetics is absolutely necessary to obtain reliable results. Therefore IABG has developed NEC2DPC, a double precision NEC2 version for Personal Computers under MS-DOS. Applying NEC2DPC on basic EMC configurations has shown that this NEC2 version can successfully be used to analyse problems with small segment to wavelength ratio.

1. Introduction

In connection with German activities to establish a standardized software tool for computerized EMC analysis extensive comparative calculations were performed using NEC2-IABG (a double precision version of NEC2 /1/ installed on IABG's vector processor mainframe VP 200) and the

single precision codes NEC2-PC and MININEC3, both part of the NEEDS version 1.0 software package /2/ and installed under MS-DOS 3.3 on a TANDON PCA. Furthermore some calculations were performed with NEC81, an improved version of NEC2-PC, which will be part of the NEEDS system version 2. The authors greatfully acknowledge the advance release of NEC81 to IABG by ACES /3/ to support this effort.

In the simulations the coupling characteristics between transmitting and receiving antennas and the input impedance of the transmitting antenna were examined primarily. For this purpose typical basic configurations of rod and loop antennas were defined. The investigations were performed for different frequencies. A point of particular interest was the analysis of the different computer codes nearby the resonance frequency and for low frequencies.

2. Basic configurations for the EMC-analysis

Fig. 1 shows the 6 defined basic antenna configurations for the EMC-analysis. The corresponding geometrical dimensions of the antenna system structures are listed in fig. 2a. The antennas are connected to an ideal conducting plain surface and they are assumed to be ideal conductors. In the configurations 1-3 the transmitting antennas are rod antennas, in the configurations 4-6 loop antennas excited by a voltage source.

Configuration 1 (fig. 1a) simulates the coupling characteristics between two rod antennas. The configurations 2 and 3 (fig. 1b, c) analyse the short circuit currents of closed loops excited by the field radiation of rod antennas with respect to different loop area orientations (relative to the location of the rod antenna). Configuration 4 (fig. 1d) represents the coupling features of a transmitting loop antenna and a receiving loop antenna terminated with a resistance R = 50 ohms. In configuration 5 and 6 the loops are of small altitude relative to their length. Therefore these configurations especially deal with coupling aspects between two shorted cables. With this type of configurations the EMC-behaviour of crossed lines (fig. 1e) and parallel lines (fig. 1f) was simulated. Fig. 2b shows the chosen segmentation datas for the antenna configurations. For all computer codes the same segmentation was applied to enable a suitable comparison between the simulations.

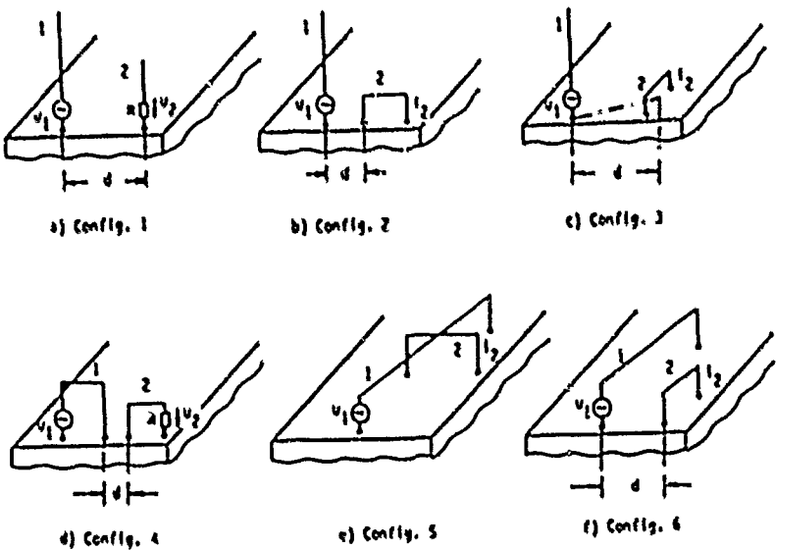


Fig. 1: Basic antenna configurations for the EMC-analysis

Config.	d	antenna 1	antenna 2
1	10 m	rod: h=12 m, r= 1.5 cm	rod: h=7 m, r=1.5 cm
2	5 m	rod: h=12 m, r= 1.5 cm	loop: l=2 m, h=10 m, r=5 mm
3	5 m	rod: h=12 m, r= 1.5 cm	loop: l=2 m, h=10 m, r=5 mm
4	2 m	loop: l= 2 m, h= 2 m, r=1 cm	loop: l=1 m, h= 1 m, r=1 cm
5	-	loop: l=10 m, h=12 cm, r=5 mm	loop: l=8 m, h=10 cm, r=5 mm
6	20 cm	loop: l=10 m, h=10 cm, r=5 mm	loop: l=8 m, h=10 cm, r=5 mm

a) Geometrical dimensions of the antennas

Config.	antenna 1,	antenna 2
1	40	24
2	38	1 + 35 + 1
3	38	1 + 35 + 1
4	12 + 16 + 12	6 + 6 + 6
5	1 + 35 + 1	1 + 28 + 1
6	1 + 30 + 1	1 + 24 + 1

b) Segmentations of the antennas

Fig. 2: Geometrical input data for the computer analysis

The configurations 1-5 were analysed only at one frequency. It was found that especially in the case of loop configurations the simulation results are more sensitive compared to rod configurations. Therefore configuration 6 was analysed more in detail at various frequencies nearby a resonance frequency as well as for low frequencies. The code comparisons were performed for the complex antenna impedance $Z_1(\omega)$ of the transmitting antenna and the short circuit current i_2 induced in the receiving antenna resp. voltage u_2 for an ohmic antenna termination.

3. Computed results for the configurations 1-5

Fig. 3 shows the results of the computer analysis. For the configurations 1-4 the source voltage u_1 of the transmitting antennas was chosen such, that the radiation power amounts to P_1 = 1W. Analogous a current amplitude I_1 = 1A was chosen for configuration 5.

In configuration 1 the results of NEC2-IABG, NEC2-PC and MININEC-3 agree satisfactorily (fig. 3a). According to the chosen frequency of f = 2 MHz the wavelength λ is 150 m. The segment-wavelength ratio is approx. $1/\lambda$=0.002. For the configurations 2 and 3 the computer results of the antenna impedance calculations with NEC2-IABG and NEC2-PC are identical (fig. 3b,c). The impedances calculated with MININEC3 agree with these results sufficiently, although the real parts differ about 20 percent. The computed results for the loop current i_2 between NEC2-IABG and MININEC3 show only small differences, whereas the corresponding NEC2-PC based values deviate more extensively. The analysis was performed with a frequency f = 21 MHz corresponding to $0.005 \leq 1/\lambda \leq 0.025$. The results for configuration 4 again show satisfactory agreement.

In configuration 5 the antenna impedances are in a good agreement between MININEC3 and NEC2-IABG, whereas a significant higher difference was found for NEC2-PC. The computed results for the current amplitude i_2 differ about 20 percent and more between the different computer codes. The antennas were excited with a frequency f=10 MHz, which corresponds to $0.001 \leq 1/\lambda \leq 0.012$.

For all analysed configurations the NEC81 version of NEC2 shows excellent agreement with the double precision version NEC2-IABG.

Configuration		NEC2-IABG	NEC81	NEC2-PC	MININEC3
1 (f = 2 MHz, P = 1 W)	Impedance (Ω)	2,53 + j620	2,53 + j620	2,57 + j620	2,43 + j605
	U_2 (V)	0,445	0,459	0,442	0,457
2 (f = 21 MHz, P = 1 W)	Impedance (Ω)	173 + j217	173 + j217	173 + j217	210 + j219
	I_2 (mA)	0,897	0,897	1,363	0,936
3 (f = 21 MHz, P = 1 W)	Impedance (Ω)	173 + j217	173 + j217	173 + j217	210 + j219
	I_2 (mA)	0,347	0,347	0,306	0,343
4 (f = 15 MHz P = 1 W)	Impedance (Ω)	68,8 + j504	68,8 + j504	68,8 + j501	57,7 + j463
	U_2 (V)	0,353	0,353	0,363	0,362
5 (f = 15 MHz I = 1A)	Impedance (Ω)	0,111 + j365	0,110 + j365	0,186 + j516	0,107 + j359
	I_2 (mA)	45,9	45,9	53,6	33,8

Fig. 3: Computed results for configuration 1-5

4. Computed results of configuration 6

For configuration 6 simulations were performed in the frequency interval between f_1 = 15 MHz and f_2 = 16 MHz to examine the behaviour of the computer codes nearby a resonance frequency. Fig. 4 shows the frequency dependence of the impedance Z_1 of the transmitting antenna. In the calculations with NEC2-IABG and MININEC3 the real parts R_1 agree very well and the deviation is about 1 percent. The frequency dependence of the imaginary part X_1 is approximately linear in this frequency range (fig. 4b). For this configuration resonance frequencies of $f_r \approx 14.8$ MHz (NEC2-IABG/NEC81) and $f_r \approx 15.0$ MHz (MININEC3) can be figured out, the results shift about 0.2 MHz.

The results obtained by NEC2-PC show insufficient accuracy. For example, at f = 14.4 MHz the imaginary part X_1 is 123 ohms, at f = 14.6 MHz X_1 is 628 ohms and at f = 14.8 MHz X_1 is -360 ohms. For this reason the results of NEC2-PC are not included in the diagrams. The NEC81 based results are in excellent agreement with NEC2-IABG again. The computed antenna input impedances are nearly identical as indicated in fig. 4.

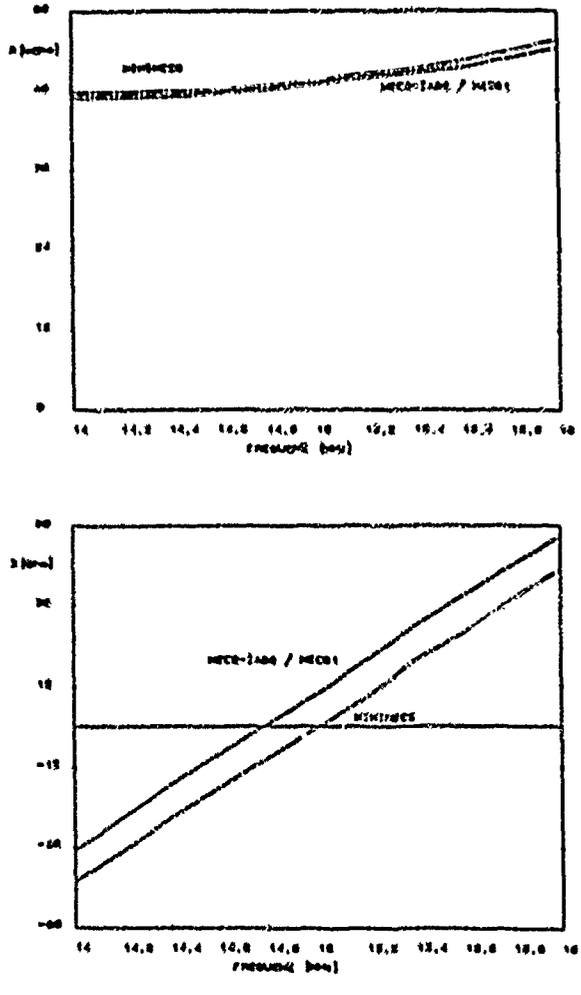


Fig. 4: Frequency dependence of the antenna input impedance $Z_1 = R_1 + jX_1$ nearby a resonance frequency (config. 6)

Fig. 5 shows the computed results of the current amplitude i_2 with i_1 assumed to be 1 A. The calculations with NEC2-IABG and NEC81 agree excellently, while there is only a moderate agreement between the NEC2-PC and MININEC3 generated results.

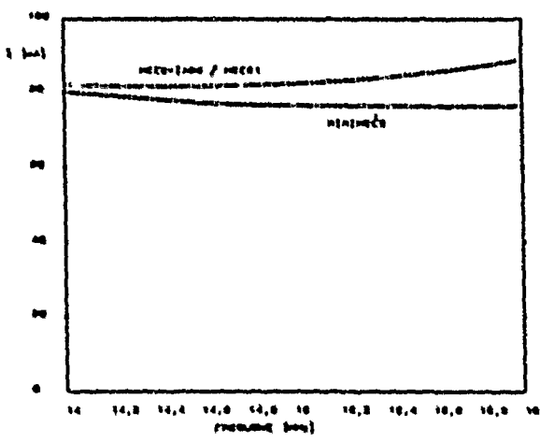


Fig. 5: Computed results of the current amplitude I_2
(Config. 6)

Furthermore some investigations with varying frequencies were performed to test configuration 6 for large wavelength, starting with f = 10 MHz and decreasing in decades down to f = 0.01 MHz. Fig. 6 shows the results of the calculations.

While at f = 10 MHz the computed results agree satisfactorily, the NEC2-PC calculated values show greater deviations at f = 1 MHz compared to the other codes. For frequencies f 0.1 MHz greater differences between NEC2-IABG and the other codes occur as well in respect to antenna input impedance as to current amplitude.

To examine and to validate the accuracy of NEC2-IABG the computed results were compared with an analytical approximation for low frequencies. At f = 0.01 MHz this approximation provides as antenna input impedance Z_1 = j 0.47 ohms and as current I_2 = 94 mA. The NEC2-IABG calculations are in a good agreement with regard to the assessed antenna impedance as well as to the current amplitude.

f (MHz)		NEC2-IABG	NEC2-PC	NEC81	MININEC3
10.000	Z (Ω) I (mA)	$9.82 \cdot 10^{-2} + j361$ 155	$1.02 \cdot 10^{-1} + j342$ 164	$9.82 \cdot 10^{-2} + j361$ 155	$9.65 \cdot 10^{-2} + j361$ 164
1.00	Z (Ω) I (mA)	$6.94 \cdot 10^{-6} + j18.3$ 97.4	$2.33 \cdot 10^{-2} + j1227$ 135	$6.20 \cdot 10^{-6} + j18.3$ 97.6	$3.22 \cdot 10^{-4} + j16.1$ 97.6
0.10	Z (Ω) I (mA)	$6.23 \cdot 10^{-10} + j0.3$ 85.5	$+2.00 + j31.809$ -	$+6.6 \cdot 10^{-8} + j1.11$ 97.3	$3.76 \cdot 10^{-4} + j1.49$ 55.5
0.01	Z (Ω) I (mA)	$6.66 \cdot 10^{-14} + j0.03$ 97.3	- -	- -	$2.50 \cdot 10^{-4} + j0.3$ 7.11

Fig. 6: Frequency dependent results of configuration 6

5. Conclusion

Generally the performed investigations have demonstrated that there is a sufficient agreement between the results of the computer codes NEC2-IABG, NEC2-PC and MININEC3 as long as the segmentation condition $0.001 \leq l/\lambda \leq 0.1$ is fulfilled. But especially at resonance frequencies the results of NEC2-PC may be not satisfying. For lower frequencies MININEC3 seems to provide better results than NEC2-PC.

The inclusion of NEC81 instead of NEC2-PC into the NEEDS version 2 release will significantly improve the EMC-analysis capability and accuracy of the NEEDS-software tool. For the analysis of regular problems NEC81 provides almost the same accuracy as a double precision NEC2 version. The main advantage of a double precision version like NEC2-IABG is the capability to analyse low frequency problems with sufficient reliability. To achieve this capability also on PC systems, IABG has developed a double precision version NEC2DPC, which was derived from the NEC2-PC version as distributed within the NEEDS system version 1.
From fig. 7, which shows the imaginary part of the antenna input impedances for low frequencies on the example of configuration 6, it can be concluded that NEC2DPC can successfully be used to analyse problems with small segment to wavelength ratios on personal computers under MS-DOS.

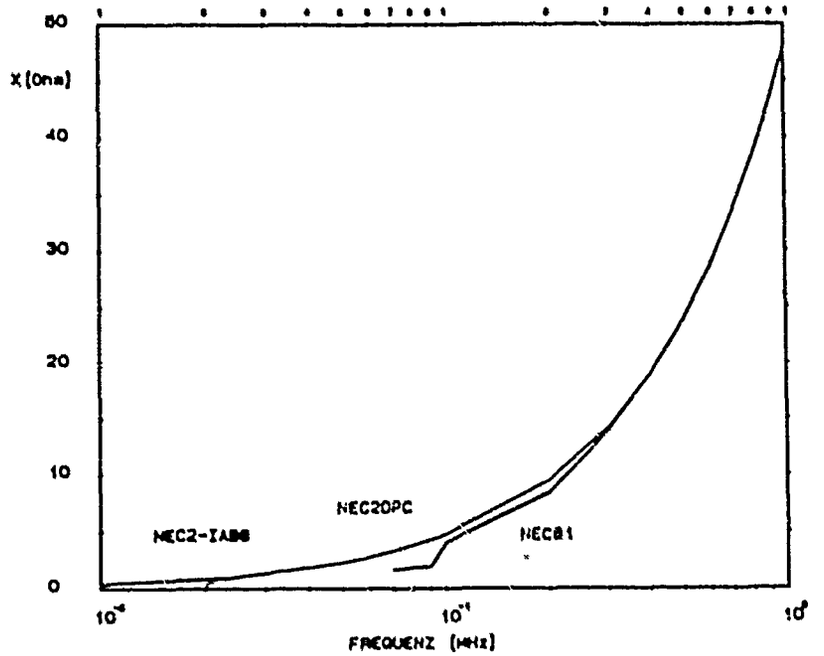


Fig. 7: Computed imaginary part X_1 of config. 6 for low frequencies

References

/1/ Burke G., Poggio A.: Numerical Electromagnetics Code - Method of Moments, Navel Ocean System Center, San Diego, Cal., Technical Doc. 116, 1980/81.

/2/ Adler, R.W.: NEEDS - The Numerical Electromagnetic Engineering Design System. ACES, Code 62 AB, Monterey 1988.

/3/ N.E.C. Program NEC-81 v. 2.00
(c) Davin J. Pinion
Private communication with R. Adler, March 1989

POSTER PAPERS

Chairman: David Stein

AN IMPLICIT THREE DIMENSIONAL ELECTROMAGNETIC FIELD CODE

Reginald W. Clemens
Richard L. Knight
Applied Physics, Inc.
5353 Wyoming Blvd., NE, Suite 3
Albuquerque, NM 87109

Ronald Chase
Harry Diamond Laboratories
End of Dawson Beach Road
Woodbridge, VA 22191

A fully implicit, three-dimensional, finite difference Electromagnetic Field code has been developed to solve Maxwell's equations in nonlinear media. The code is designed to couple fields from nuclear weapons (EMP) to military systems in the source region of the weapon. At early retarded time of the burst point, the time step in such a problem is determined by the rise time of the γ-ray pulse emitted from the weapon. At later retarded times, the γ-ray pulse is slowly varying and the time step in an explicit finite difference code is determined by the Courant condition. The implicit code discussed in this paper is unconditionally stable and excells on late time or low frequency problems in which the physics allows large time steps. The code is set up to allow the time step to increase as time increases. A typical 3-D coupling problem can be run to .1 sec of problem time in about 3 hours of Cray 2 time.

The matrix resulting from the implicit code is solved using an Incomplete Cholesky Conjugate Gradient itterative matrix solver. This scheme is far superior for this problem to the many others that were investigated.

WHY USE NSLT3D?

- Consider a coupling problem with millisecond rise times. For example, coupling of rail currents to Rail Garrison cars.
- Assume that 1. m^3 cells are used in the problem.
- The Courant condition limits the time step in explicit codes such as ISM and THREDE to 3.33×10^{-9} sec.
- To calculate to the peak of the pulse at 10^{-3} sec would then require 3×10^5 time steps.
- NSLT3D has no Courant condition and would require less than 100 time steps to resolve the pulse.

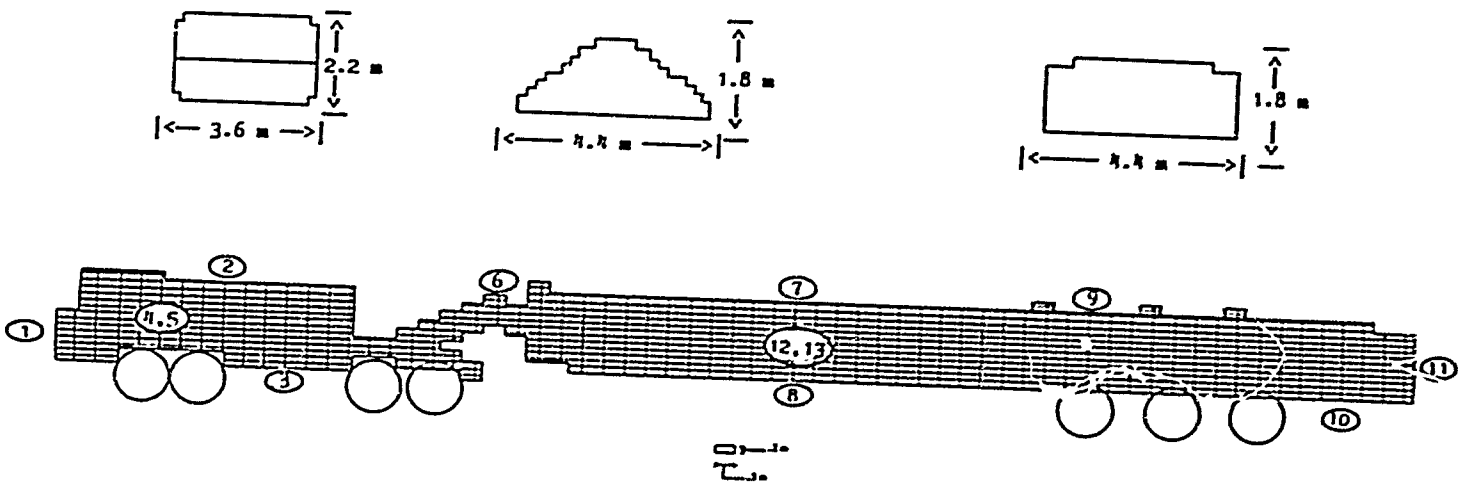


Figure 6. Finite-difference model of the tractor and launcher.

NSLT3D

THE DIFFERENCING

- Solves Maxwell Equations in 3 Dimensions
- Uses Cartesian Coordinates
- Is an Implicit Code

Maxwell's Equations

We assume the constitutive equations

$$\vec{D} = \epsilon \vec{E}$$

$$\vec{B} = \mu \vec{H}$$

and that the total current is the sum of the real current and the conduction current

$$\vec{J}' = \vec{J} + \sigma \vec{E}$$

Maxwell's Equations

Giving (for ϵ and μ constant in space and time)

$$\nabla \cdot \vec{E} = \rho/\epsilon$$

$$\nabla \cdot \vec{H} = 0$$

$$\mu \frac{\partial \vec{H}}{\partial t} = -\nabla \times \vec{E}$$

$$\epsilon \frac{\partial \vec{E}}{\partial t} + \sigma \vec{E} = -\vec{J} + \nabla \times \vec{H}$$

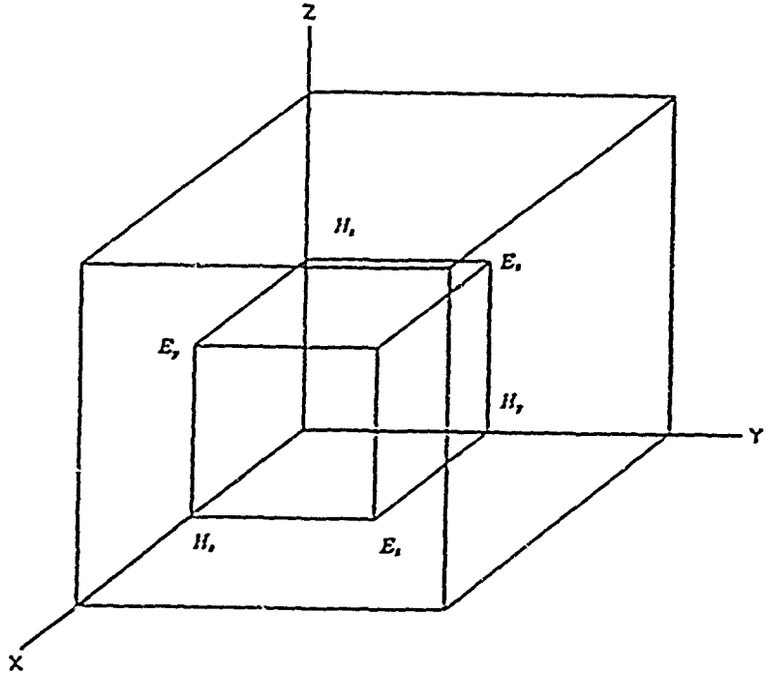
The first two equations are initial conditions.

The last two equations describe the time development of the fields.

Maxwell's Equations

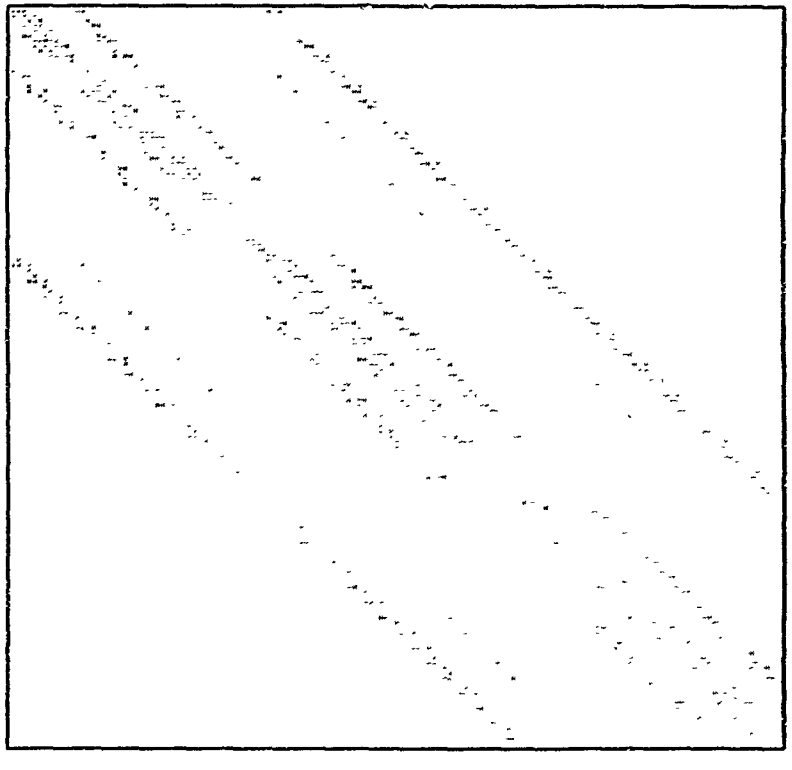
- We Would like to do an Algebraic substitution to eliminate either $\vec{E}$ or $\vec{H}$, giving 3 equations in 3 unknowns.
- This is impossible.
- If we Time Difference the equations, then the Algebraic substitution becomes possible.
- We Time Difference, Substitute, and then Difference Spatially.

NSLT3D
The DIFFERENCE MESH



NSLT3D

The MATRIX WE MUST SOLVE



NSLT3D

MATRIX SOLVERS

- Gaussian Elimination
- SOR (Sucessive Over Relaxation)
- ICCG (Incomplete Cholesky Conjugate Gradient)
- MultiGrid Methods
  (— in the future?)

NSLT3D

The ICCG MATRIX SOLVER

Assume you want to solve

$$Ax = b$$

If someone gave you A^{-1}, then premultiplying gives

$$A^{-1}Ax = Ix = x = A^{-1}b$$

What if they only gave you $\bar{A} \approx A^{-1}$?

NSLT3D

RESULTS

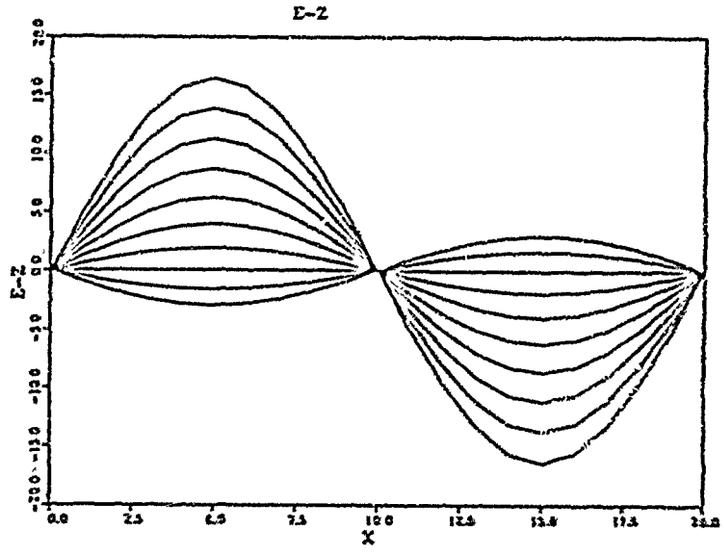


Figure 2. Ez along line (i,5,5) for 10 cycles.

RESULTS

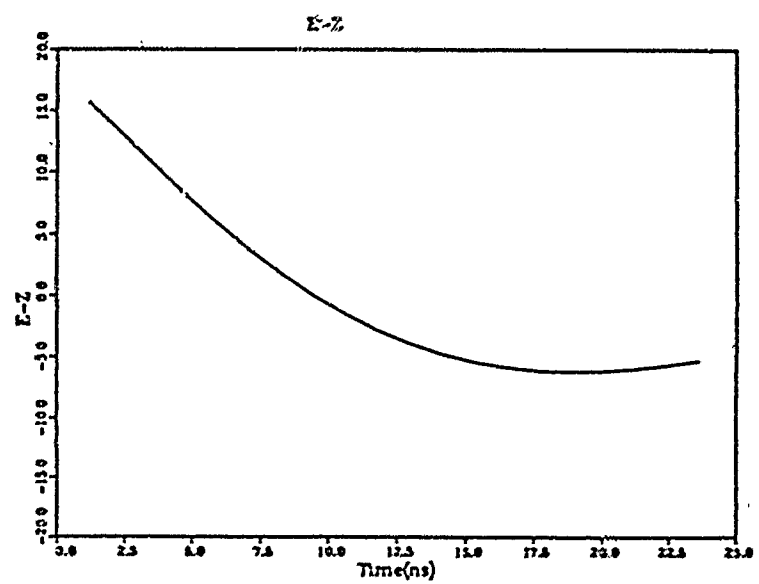


figure 3. Ez vs time at point (5,5,5).

NSLT3D

RESULTS

Timing Summary NSLT3D							
Run	Size	Machine	Other	Reported CPU (sec)	True CPU (sec)	Cycles	Time /cell (μsec)
1	21**3	CRAY1	Jr w/ output	23.977	25.871	10	374
2	21**3	CRAY1	Jr w/o output	14.733	18.416	10	230
3	11**3	CRAY1	Jr w/ output	3.714	4.643	10	464
4	11**3	CRAY1	Jr w/o output	1.586	1.983	10	198
5	11**3	CRAY1	Jr w/o output	1.663	2.079	10	208
6	11**3	CRAY1	Jr w/o output	1.695	2.119	10	212
7	21x11x11	CRAY2	cavity w/ output	72		100	360
8	21x11x11	CRAY2	cavity min output	48		100	240
9	21x11x11	CRAY2	cavity min output	38		100	190

Table 1. Timing Summary NSLT3D

Timing Summary NSLT2D							
Run	Size	Machine	Other	Reported CPU (sec)	True CPU (sec)	Cycles	Time /cell (μsec)
1	60x90	CRAY1	Jr w/o output	26.571	33.214	100	62
2	60x90	CRAY1	LN w/o output	53.408	66.760	100	124

Table 2. Timing Summary NSLT2D

NSLT3D

RESULTS

Timing Breakdown (μs/cell)			
Routines	NSLT3D	NSLT2D equivalent	NSLT2D realistic
Differencing	16	27	28
Source	13	5	24
Matrix Solver	156	13	8
Trig & Exp		16	50
Conductivity			8

Table 3. Timing Breakdown

ADAPTIVE ALGORITHM FOR THE ANALYSIS OF A MICROSTRIP DISCONTINUITY INDUCTANCE

A. Hill and V.K. Tripathi
Department of Electrical and Computer Engineering
Oregon State University
Corvallis, OR 97331

Abstract

An algorithm is presented for the evaluation of a microstrip right angle bend discontinuity inductance. The moment method in conjunction with an adaptive set of basis functions is employed to solve for the excess current distribution in the corner region. These basis functions are defined over an error dependent triangular region which leads to an optimum element size and reduces the system's matrix dimension.

Introduction

In the past, several authors have characterized a microstrip right angle bend discontinuity in terms of equivalent excess inductance and capacitance which are associated with the corner region.[1-6]. Inductance calculation requires the determination of the current distribution in the discontinuity region. Instead of calculating the total current it is numerically more efficient to set up the governing magnetic field intergral equation in terms of excess currents. These currents represent the perturbation of the current distribution from the distribution that exists on the respective uniform microstrip line. The current perturbation is strong in the discontinuity region and decays away from it. In previous formulations the unknown current has been expanded in terms of basis elements over a rectangular region. In this paper we employ triangular basis functions that adapt to the characteristics of the solution. Their size is determined from a local error criterion. In [8] use is made of complementary variational principles to asses the error in a finite element method for the purpose of grid optimization. In the present method evaluation of fields is performed only on the boundary which favors the derivation of the error criterion from the boundary condition. An optimum shape of the triangles is maintained through additional post processing [7].

Moment Method Formulation

The excess current distribution is found by computing the vector potential on the strip surface due to all currents and utilizing the boundary conditions that the normal magnetic field be zero on the strip. The procedure is similar to the evaluation of the via excess inductance in [10]. The integral equation for the excess current J_e can be formulated as

$$m \cdot \nabla \times A(J_e) = - m \cdot \nabla \times A(J) \qquad (1)$$

where A represents the magnetic field integral operator and n is the unitvector normal to the stripsurface. On the microstrip lines J is defined such that it corresponds to the current distribution on the respective uniform line. In the corner region the current J assures continuous current flow through the discontinuity. The source currents in (1) can be decomposed and after applying stokes theorem for the integration over the strip region a numerically more efficient formulation can be found such that on the striplines no evaluation of the self elements is necessary:

$$n \cdot \nabla \times A(J_e) = - n \cdot \nabla \times A(J^*) \qquad (2)$$

J^* is decomposed as

$$J^* = J_a + J_b + J_c \qquad (3)$$

J_b corresponds to the source current J in region b (fig.1). J_a and J_c represent the current distribution on the uniform stripline. The extension of the decomposed currents J_a and J_c depends on the region where (2) is evaluated. If (2) is computed on region a then J_a extends from $z=z_a$ to $z=$ and J_c extends from $x=x_a$ to $x=$. If (2) is evaluated on region b J_a is defined from $z=-$ to $z=z_a$ and J_c is defined from $x=x_a$ to $x=$. If (2) is evaluated on region c then J_a is defined from $z=-$ to $z=z_a$ and J_c is defined from $x=-$ to $x=x_a$. Once the excess current is determined the excess inductance can be found from

$$L_e = \frac{1}{I^2} \int A(J^*, J_e)\, J \, dS \qquad (4)$$

Adaptive Algorithm

The basis functions in the moment method formulation of (1) are surface currents defined over a triangular region [10]. One such element corresponds to a current which circulates around an interior node. Each basis element is associated with an interior node of the triangulated microstrip region. An optimum triangular grid is established in an iterative manner. Matrix solutions are computed by means of a conjugate gradient algorithm [11] which uses the moment solution for excess current of the previous step as initial guess for the new current distribution. Starting with an initial set of surface current elements as is shown in figure 2, the excess currents are evaluated by enforcing the normal magnetic field at the interior nodes of the defined triangular grid to be zero. In a next step the local element error is found by computing the residual flux through each triangular element. Those elements with a flux density greater than some threshold are refined by introducing an additional node at their center point which forces the local error to zero. An optimum triangular grid is maintained in the sense of maximizing the minimum interior angle of each triangle [7] with the constraint of maintaining the border regions of areas a, b and c. This can be accomplished by applying the circle criterion to neighboring triangles as is illustrated in figure 3. Consider two

triangles A and B. Let a circle pass through three of the vertices of the quadrilateral which is formed by the triangles A and B. If the fourth vertex of the quadrilateral is interior to the circle, swap the common triangle side. If the fourth vertex is exterior to the circle do not swap the common triangle side. If the fourth vertex is on the circle either triangulation can be used.
Suppose node C is introduced for refinement purpose then the optimizing scheme can be summarized as follows:
1. delete the triangle that contains node C and create three new triangles.
2. consider sucessively each new created triangle and all its neighbors and apply the circle test to their common side if it is not a boundary of region a b or c.
3. repeat step two to all new created triangles and their neighbors until no diagonal swap is performed.
Triangles for which one side falls on a border region require special treatment. If the side on the border region is the maximum lenth of the particular triangle then step one is modified as follows:
delete the triangle that contains node C and create two new triangles by uniformly deviding the side which falls on the border line.
Figure 4 shows the final grid for the exces current of a rectangular microstrip discontinuity. Note that the deviation of the assumed current from the actual current distribution is largest in the corner region. Results for the excess inductance are shown in figure 5, normalized with respect to the inductance of a uniform stripline and substrate height. For comparison results obtained from [12,13] are included.

Summary

An adaptive algorithm in conjunction with an excess formulation for the evaluation of a microstrip right angle bend discontinuity has been presented. The algorithm establishes an error dependent grid size and therefore reduces the matrix size of the problem. Due to the triangular surface currents in the moment method formulation the algorithm is suitable for application to arbitrary discontinuity regions such as chamfered microstrip bends with variable bend angle.

References

[1] Farrar A. and Adams A.T.,"Matrix Methods for Microstrip Three-Dimensional Problems", IEEE Trans.on Microwave Theory Tech., vol. MTT-20, pp 497-504, August 1972.

[2] Thompson A.F. and Gopinath A.,"Calculation of a Microstrip Discontinuity Inductance", IEEE Trans. on Microwave Theory Tech, vol. MTT-23, pp 497-504., May 1975.

[3] Silvester P. and Benedek P., "Microstrip Discontinuity Capacitance for Right-Angle Bends, T Junction, and Crossings", IEEE Trans. on Microwave Theort Tech. MTT-21, pp 341-346, May, 1973.

[4] Gopinath A.and Easter B., "Moment Method of Calculating Inductance of Microstrip Right-Angle Bends", IEEE Trans. on Microwave Theory Tech. pp 880-883, October, 1974.

[5] Gopinath A. and Gupta C., "Capacitance Parameters of Discontinuities in Microstriplines", IEEE Trans.on Microwave Theory Tech. vol MTT-26, pp 831-836, October, 1978.

[6] Neale B.M. and Gopinath A., "Microstrip Discontinuity Inductances", IEEE Trans. on Microwave Theory Tech. Vol MTT-26, pp 827-831, October, 1978.

[7] Lawson C.L., "Software for C1 Surface Interpolation", Mathematical Software 3, edited by Rice J.R., 1977.

[8] Thatcher R.W., "Assessing the Error in a Finite Element Solution", IEEE Trans. on Microwave Theory and Technique, vol MTT-30, pp 911-911, June 1982.

[9] Mautz J.R. and Harrington R.F., "Calculation of the Excess Capacitance of a Microstrip Discontinuity", Technical Report, February, 1984.

[10] Rao S.M. et. al, "Electromagnetic Scattering by Surface of Arbitrary Shape", IEEE Trans. on Microwave Theory Tech., vol MTT-20, pp 409-418, May 1982.

[11] Sarkar T.K. et al. ,"Survey of Numerical Methods for Solution of Large Systems of Linear Equations for Electromagnetic Field Problems", IEEE Trans. on Antennas and Propagation ,vol AP-29, pp 847-856, Nov. 1981.

[12] Kirschning et. al "Measurement and Computer Aided Modelling of Microstrip Discontinuites by an Improved Resonator Method", IEEE MTT-S Digest, 1983.

[13] B.Neale and A. Gopinath, "Microstrip Discontinuity Inductance", IEEE Trans. Microwave Theory Tech., vol MTT-26, pp. 827-831, October 1978.

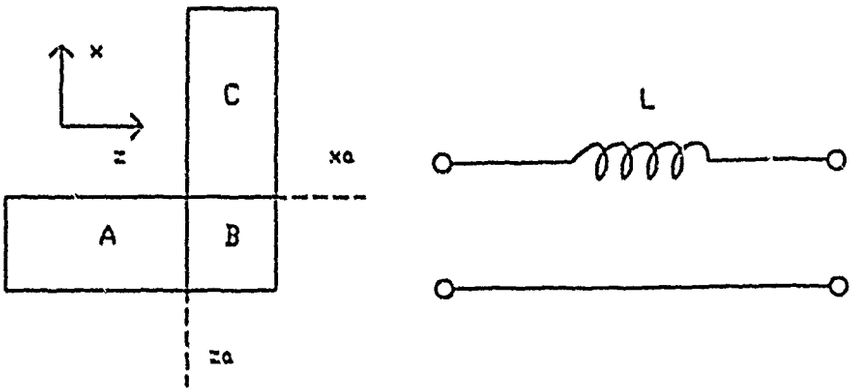


Figure 1: Microstrip right angle bend and equivalent circuit for the excess inductance.

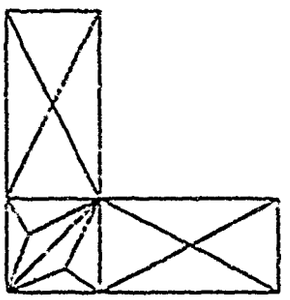


Figure 2: Initial grid for excess currents.

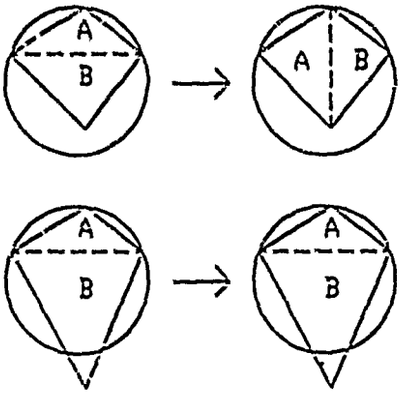


Figure 3: Circle criterion: Diagonal of quadrilateral is swapped if fourth vertex is inside of circle.

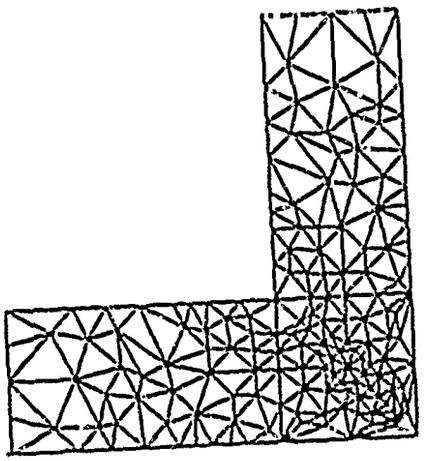


Figure 4: Final grid for evaluation of excess currents.

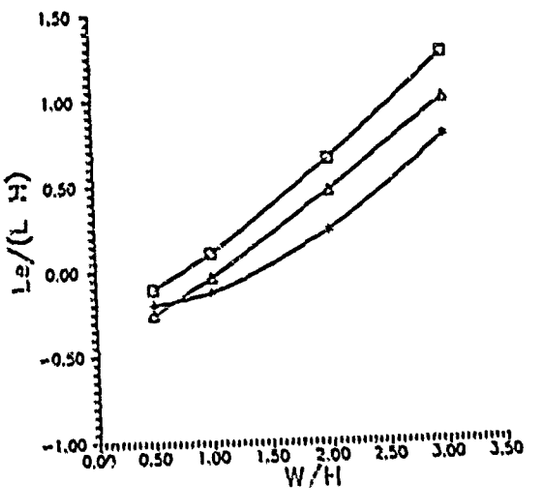


Figure 5: Normalized excess inductance versus width to height ratio.
△ ...this method. ✳...[12], □...[13].

A FINITE ELEMENT CODE FOR SOLVING 2-D SCATTERING PROBLEMS ON IBM PC COMPATIBLE COMPUTERS

Steven P. Castillo

Electrical and Computer Engineering Department
New Mexico State University
Box 3-O
Las Cruces, NM 88003

Andrew F. Peterson

Electromagnetic Communications Laboratory
University of Illinois
1406 West Green Street
Urbana, Illinois 61801

ABSTRACT

The increasing power and speed of today's most advanced IBM pc compatible workstations are allowing engineers in many of the physical sciences to solve problems at their desks that required a large mainframe only five years ago. In computational electromagnetics, the use of partial differential equation solution methods in conjunction with absorbing boundary conditions (ABC) has opened the door to a new class of scattering problems not previously considered to be solvable using traditional integral equation techniques.

A finite element code for solving two-dimensional TM and TE scattering problems has been written to run on a 386 based pc computer. The scatterer must be described in a piecewise homogeneous manner with each homogeneous section being either a conductor or a dielectric of constant permeability and permitivity. Mesh generation can either be done using simple mesh generation codes for simple scatterers, or using PDA's Patran on a separate graphics workstation. A frontal solution technique is used which takes advantage of the large disk size available on most advanced workstations.

A short development of the code will be presented followed by some results for some representative scattering problems. Run times for various size scatterers will also be given as well as some of the limitations of the code.

Introduction

Traditionally, the user of an electromagnetics scattering code such as NEC was confined to using some large mainframe computer to solve a given scattering problem. Constraints on the amount of memory and cpu time available for a given user limited the size of the problem that could be numerically solved. With the advent of the vector supercomputer in the early 1980's, the size of the scattering problems that could be considered was increased by several orders of magnitude. However, a vector supercomputer was and still is a resource available only to a small portion of the scientific community.

The advent of the IBM pc computer has brought significant computing power at low cost to the scientific user. The newest generation of IBM pc compatible computers which use the Intel 80386 processor allows the user to solve medium to large problems on the user's desktop.

In this paper, we discuss the feasibility of using the finite element method to solve two-dimensional (2-D) open-region scattering problems on a 386 IBM pc compatible computer. A short discussion of the finite element method as applied to the wave equation is discussed. The radiating boundary is given and integrated into the finite element equations. Finally, some results and timings for some simple scattering problems are given.

Formulation of the Problem

The differential equations to be solved for the TM and TE scattering problems are given as

$$\nabla\cdot\frac{1}{\mu_r}\nabla E_z^{tot} + k_0^2\epsilon_r E_z^{tot} = 0$$

and

$$\nabla\cdot\frac{1}{\epsilon_r}\nabla H_z^{tot} + k_0^2\mu_r H_z^{tot} = 0$$

where E_z^{tot} and H_z^{tot} represent the unknown z-directed electric and magnetic fields respectively (Figure 1). Applying the weighted residual method over the domain, Γ, we arrive at the following equations:

$$\int_\Gamma \frac{1}{\mu_r}\nabla T\cdot\nabla E_z^{tot} - k_0^2\epsilon_r T E_z^{tot}\,dxdy = \int_{\partial\Gamma} T\frac{\partial E_z^{tot}}{\partial n}\,dl$$

$$\int_\Gamma \frac{1}{\epsilon_r}\nabla T\cdot\nabla H_z^{tot} - k_0^2\mu_r T H_z^{tot}\,dxdy = \int_{\partial\Gamma} T\frac{\partial H_z^{tot}}{\partial n}\,dl$$

In the finite element method, the domain is broken up into several subdomains, Γ_e so that

$$\Gamma = \Sigma\,\Gamma_e.$$

Over each domain, the approximation that

$$E_z^{tot}(x,y) = \sum_{n=1}^{N} e_n B_n(x,y)$$

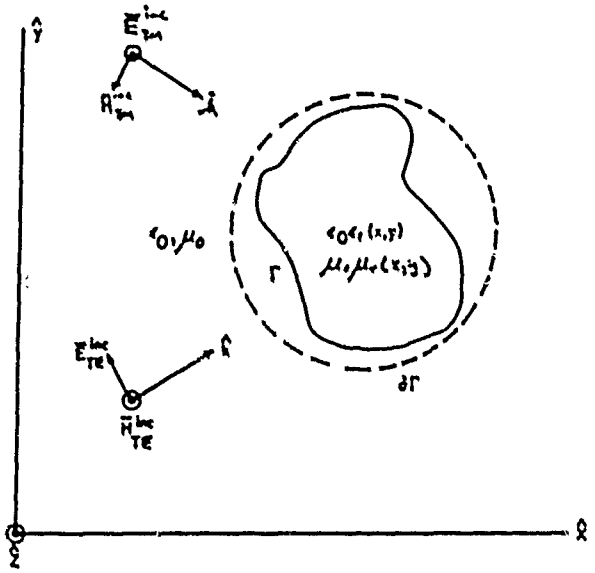


Figure 1. Cross section of the cylindrical geometry under consideration.

for the TM polarization and

$$H_z^{tot}(x,y) = \sum_{n=1}^{N} h_n B_n(x,y)$$

where B represents a Lagrange polynomial basis function so that e and h represent the unknown field at a discrete set of points over the element. To arrive at an algebraic set of equations for each element, the Galerkin technique is used. The resulting matrix equation has the form

$$A_e x = b_e.$$

The global set of equations is assembled by requiring the fields to be continuous at the nodes that are common between the elements. Thus over Γ

$$A = \Sigma A_e$$

where the summation is over all the elements. The global set of equations is then given by

$$Ax = b.$$

The coefficient matrix A is sparse. Therefore, the system of equations can be solved using a sparse matrix equation solver such as sparsepak.

Absorbing Boundary Condition

Theoretically, an infinite amount of time and memory would be needed to solve an open-region scattering problem with the finite element method. Therefore, it becomes necessary to truncate the region of interest. The Bayliss-Turkill absorbing boundary condition (ABC) approximates an infinite region over the artificial boundary surrounding the scatterer. The boundary condition is given by

$$\frac{\partial E_z^s}{\partial \rho} = \alpha(\rho) E_z^s + \beta(\rho) \frac{\partial^2 E_z^s}{\partial \varphi^2}$$

where α and β are functions of ρ and k and the artificial boundary is been taken to be circular[1]. A similar boundary condition for H is also used in the TE case. The boundary condition is incorporated into the right-hand side of the finite element equations. Since the ABC is an approximation, the distance at which the boundary condition should should be applied for a given scatterer cannot be readily deduced.

Equation Solution

Most users of a pc are currently using the MS-DOS operating system. Therefore, the user is severely restricted by the amount of memory provided by DOS. The frontal equation solver was used for the developed codes[2]. The frontal method is essentially an element by element approach to performing Gaussian elimination. The system of equations is simultaneously assembled and solved so that only a fraction of the amount of memory used for direct in-core solutions is needed. If multiple right-hand sides are given as forcing functions, a secondary storage device can be used to store some of the intermediate results needed for each of the solutions.

Results

A code was written using the above formulations and techniques. A Compaq 386 pc was used for all of the solutions. The simple circular meshes were done on the pc while the more complicated meshes were done with PATRAN on a microVAX. A variety of different scatterers were analyzed with the code to get a feeling for the accuracy of the FEM using the ABC. Provided that the Bayliss-Turkel condition is applied at a sufficient distance from the scatterer, the accuracy appears comparable to that of integral equation formulations for a given mesh density. Figures 2 and 3 show the E produced by a perfect conducting cylinder of radius 5λ on a circle of radius 5.55λ by a TM incident plane wave. The comparison is done with a numerical eigenfunction solution. The

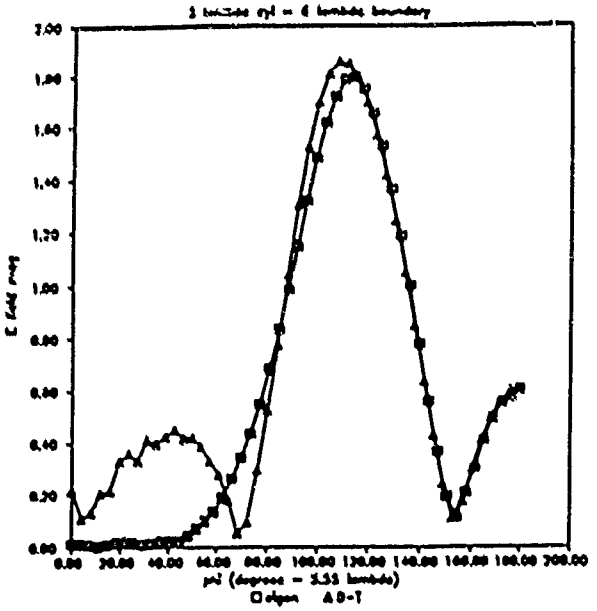


Figure 2. The total E-field produced at ρ=5.55λ surrounding a perfectly conducting cylinder of radius 5.0λ illuminated by a TM plane wave. The Bayliss–Turkel boundary condition is applied at ρ=6.0λ. The exact eigenfunction solution is shown for comparison.

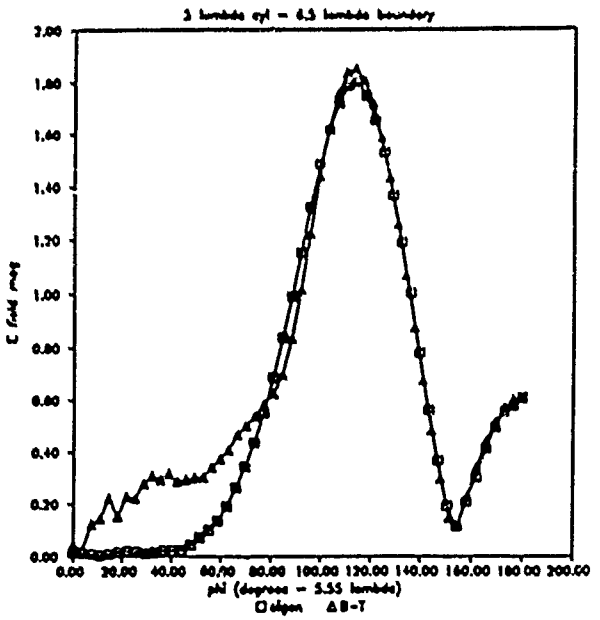


Figure 3. Same as Figure 2, except with the absorbing boundary condition applied at ρ=6.5λ.

cylinder model for the case where the ABC is at $\rho = 0.5\lambda$ contained 5712 nodes and 10650 first-order elements. The results show the dependency on the location of the ABC on the accuracy of the results.

Number of nodes	Execution time (minutes)
1599	13
2480	28
3760	61
4092	126
5712	133
5928	145

Table 1. Execution times as a function of the number of nodes. These were obtained on the Compaq 386 personal computer running the Microsoft Fortran 4.01 compiler under MS-DOS.

Table 1 gives run-times for some various problems. Although the user will not get immediate answers for larger problems, a dedicated 386 based pc can be expected to solve even large 2-D problems in reasonable time.

Conclusions

A powerful 386 based pc can be used to solve large 2-D scattering problems using FEM in conjunction with the Bayliss-Turkill ABC. The user may have to take an iterative approach to using the code since the solution accuracy is dependant on the location of the outer boundary for a given scatterer. As desktop pcs become more powerful, the need for having a supercomputer on hand will shrink. However, for the largest 2-D problems and 3-D problems, MS-DOS will be the limiting factor. Manufacturers such as SUN and DEC are now producing workstations that rival IBM compatible pcs in cost and power without the storage constraints associated with pcs.

REFERENCES

[1] A. Bayliss and E. Turkel, "Radiation boundary conditions for wave-like equations," Comm. Pure Appl. Math., vol. 33, pp. 707-725, 1980.

[2] B. M. Irons, "A frontal solution program for finite element analysis," Int. J. Num. Methods Eng., vol 2, pp. 5-32, 1970.

END-EFFECT IN SHIELDED COPLANAR LINE

G.Bartolucci, F.Giannini, C.Paoloni
II University of Rome "Tor Vergata" Dept. Electrical Engineering
Via Orazio Raimondo, 00173 Rome Italy

ABSTRACT

The end-effect in shielded short circuited coplanar lines is investigated and is characterized in terms of an equivalent normalized reactance. The structure consists of a shielded coplanar line in which the central conductor and the coplanar ground planes are short circuited by a metal septum. The electromagnetic analysis is performed using the transverse resonant technique applied to a resonant cavity obtained by inserting the discontinuity in a resonator. The results show in particular both the importance of the modeling of this kind of discontinuity and its effectiveness in the design of the filtering structures.

INTRODUCTION

The applications of coplanar lines are becoming larger in both hybrid and monolithic integrated circuits , principally because of their interesting features in terms of low mechanical complexity and reduced radiation losses. On the other hand, a very accurate characterization of various kinds of discontinuities improves the effectiveness of the use of coplanar structures, that are utilized in the realization of many subsystems.

The purpose of this paper is to perform an accurate analysis of one of these discontinuities, giving an effective characterization of the end-effect in a shielded short circuited coplanar line, in terms of an equivalent normalized reactance.

The coplanar discontinuity is inserted in a resonator that is analyzed by using the transverse resonance method. With this technique is possible to evaluate the effect of the normalized reactance associated with the discontinuity, reducing the computational effort.

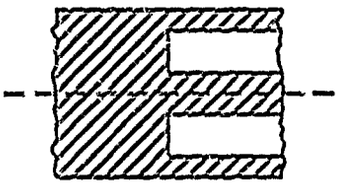


Fig.1a

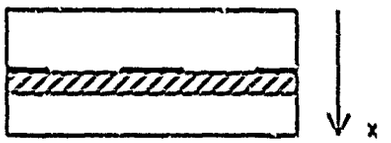


Fig.1b

ANALYSIS METHOD

In fig.1a a shielded coplanar line in which the central conductor and the coplanar ground planes are short circuited by a metal septum is shown. The transversal section of a uniform shielded coplanar line is sketched in fig.1b.

A resonant cavity (fig.2) is obtained by placing two auxiliary electric walls at some distance from the discontinuity. The presence of a symmetry plane allows the possibility to analyze only half structure by replacing this plane with a magnetic wall (fig.3). If the distance a is large enough, the auxiliary wall on the left do not perturb the field near the edge of the septum.

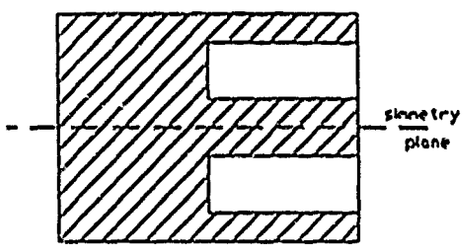


Fig.2

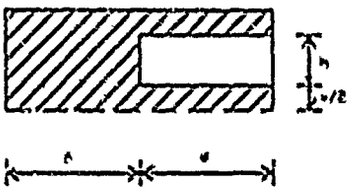


Fig.3

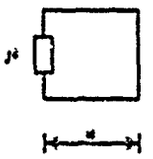


Fig.4

The equivalent circuit of the structure is shown in fig.4 , where the normalized reactance $\overline{X}$ takes into account the effect of the discontinuity. If $d+s$ is the total length of the resonator at a given frequency, the value of $\overline{X}$ can be obtained from the following equation:

$$\overline{X} = -\operatorname{tg}(2\pi/\lambda_g\, d) \qquad (1)$$

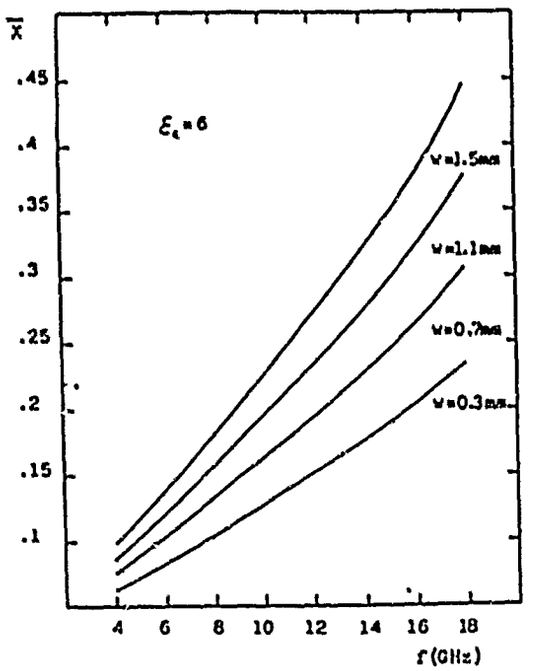


Fig.5

where λ_g is the wavelength of the fundamental mode.

So the problem is to compute the resonant length d at a given frequency and with a fixed s. To solve this problem a transverse resonance technique is applied. Looking into the x- direction the resonator can be viewed as two rectangular waveguides separated by a slotted diaphragm (the thickness metallization is supposed to be zero). In each one of this two waveguides the electromagnetic field is expanded in terms of TE-to-x (LSE) and TM-to-x (LSM) modes. In the slot, the electromagnetic field is expanded in series of the modal functions of a rectangular waveguide with the same transversal section of the slot aperture. By imposing the boundary conditions in the plane of the slot a homogeneous system of equations can be obtained.

The condition for non trivial solutions determines the characteristic equation of the given structure. This equation can be considered as a function of the frequency and of the quantity d equated to zero. Therefore, for any given frequency value the solution of this equation gives the corresponding length d.

The same approach can be also applied to compute the wavelength λ_g, that is required in (1) to obtain the equivalent normalized reactance $\bar{X}$. In fact, in the particular case of $s=0$, the resonator length d is equal to half wavelength.

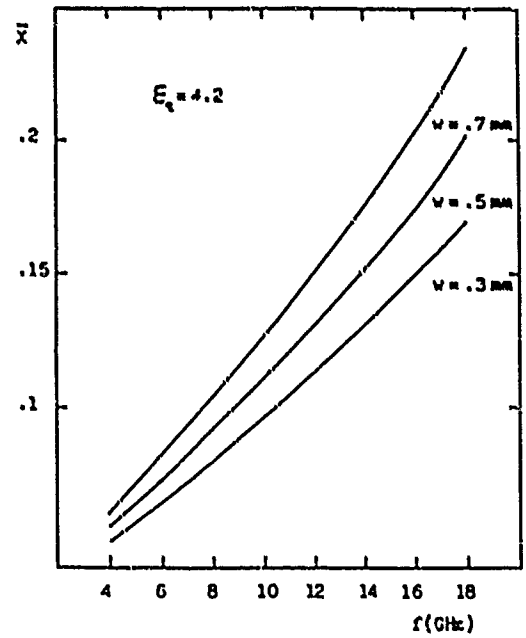


Fig.6

RESULTS

The end-effect equivalent normalized reactance $\bar{X}$ is reported in fig.5 as function of the frequency. The dielectric thickness is 254 μm ($\varepsilon_r = 6$) and the slot width is 700 μm.

As it is possible to see, the reactance is positive (i.e. of inductive type) and increases with the frequency. In this figure is also possible to see the behavior of the end effect reactance for difference values of the width of the central conductor. Another possible structure with dielectric constant ($\varepsilon_r = 4.2$) and the slot width equal to 1 mm, has been analyzed and the values of the normalized reactance are plotted in fig.6.

CONCLUSIONS

A transverse resonant approach is used to characterize a short circuit end-effect for shielded coplanar lines. An equivalent normalized reactance is computed. Simulation results are discussed for different values of the physical parametersof the structure and reported in meaningful diagrams.

REFERENCES

[1] Cohn S.B., "Slot line on a dielectric substrate", IEEE MTT, Vol. MTT-17, Oct.1969, pp.768-778

[2] Sorrentino R., Leuzzi G., Silbermann A., "Characteristics of metal-insulator-semiconductor coplanar waveguides for monolithic microwaves circuits", IEEE MTT, Vol. MTT-32, pp.410-416, April 1984

[3] Jackson R.W., "Considerations in the use of coplanar waveguide for millimeter-wave integrated circuits", IEEE MTT, Vol. MTT-34, pp.1450-1456, Dec. 1986

[4] Jackson R.W., Pozar D.M., "Surface wave losses at discontinuities in millimeter wave integrated transmission lines", IEEE MTT-S Digest, June 1985, pp.563-565

[5] Riazat M., Zubeck I., Bandy S., Zdasiuk G., "Coplanar waveguides used in 2-18 Ghz distributed amplifier", IEEE MTT-S Symp. Digest, pp.337-338, Baltimore 1986

[6] Williams D.F., Schwarz S.E., "Design and performance of coplanar waveguide bandpass filters", IEEE MTT, Vol. MTT-31, July 1983, pp.558-566

[7] Stegens R.E., D.N.Alliss, "Coplanar microwave integrated circuit for integrated subsystems", MSN, Octob 1987, pp.84-96

Wave Propagation on Infinite, Two-Dimensional Structures

Ross A. Speciale
General Dynamics, Ontario, CA

ABSTRACT

A general theory has been developed to analyze wave-propagation processes on infinite, two-dimensional structures. The considered structures are represented as infinite, doubly-periodic or quasi-doubly-periodic clusters of elementary, unit-cell, microwave multiport networks. The theory has been used to analyze models of element-to-element, electromagnetic proximity coupling in planar- and non-planar-phased-arrays and array feed-networks.

APERTURE-SURFACE WAVES

The process of excitation of aperture-surface waves, that propagate through element-to-element, electromagnetic proximity-coupling, across the radiating aperture of a two-dimensional, planar phased-array, is qualitatively illustrated in Figure 1, where the array is shown in a receive-mode and illuminated by an off-boresight planar wave. Constructive and destructive interference between the creeping surface-wave and the incoming planar space-wave is known to cause 'Blind Spots' in the array receiving pattern. A similar process takes place, in reverse sequence, when the array is in transmit-mode.

A qualitative illustration of surface-wave excitation across the aperture of a conformal, cylindrical array is shown in Figure 2, again with the array in a receive-mode.

The qualitative illustration of the process of aperture-surface-wave excitation, shown in Figures 1 and 2, also qualitatively shows the process of sub-surface-wave excitation, that takes place when the element-to-element, electromagnetic coupling is not just an uncontrolled, geometry-dependent proximity-coupling, but is intentionally introduced and controlled, behind the array aperture-surface.

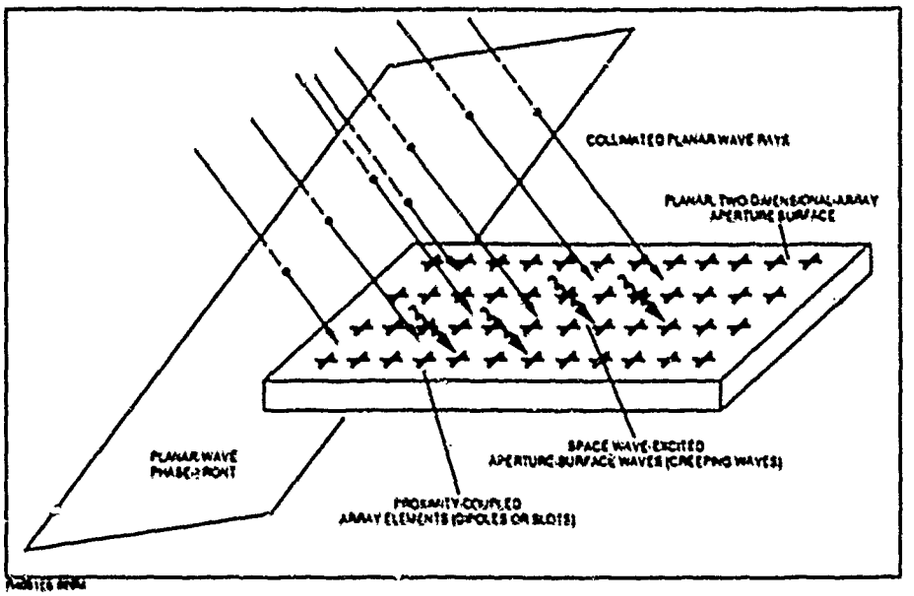


Figure 1. Space-Excitation of Aperture-Surface Waves by Off-Boresight Planar Waves, Incident on a Planar Phased-Array.

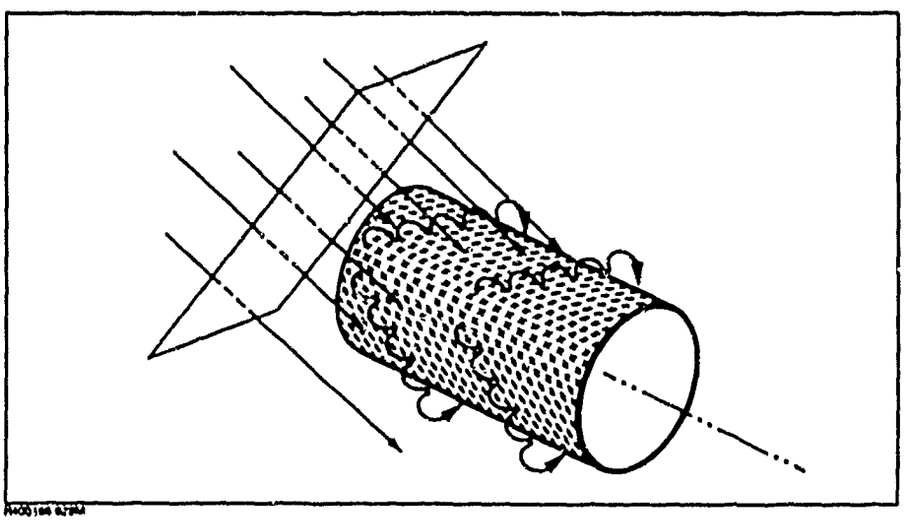


Figure 2. Space-Excitation of Aperture-Surface Waves by Off-Boresight Planar Waves, Incident on a Cylindrical, Conformal Array.

APPLICATION EXAMPLES

Figures 3A and 3B shows a fundamental one-dimensional cluster of cascaded four-port networks referred to as 'the fishbone network'. Such a one-dimensional chain may include any number n of unit-cells, although only four are shown as an example. The fundamental interest of this cluster is represented by the free ports, aligned along the top and bottom interfaces and available for further interconnection to additional 'fishbone networks', extending parallel to the first.

Figure 4 shows a finite patch of a prototype, infinite, two-dimensional microwave network, composed of multiple, parallel fishbone networks, mutually interconnected along the common horizontal interfaces.

Practically relevant examples of infinite, strictly doubly-periodic, two-dimensional microwave structures are given in Figures 5 through 9, that represent infinite, two-dimensional clusters of mutually coupled, TEM ring-resonators. Such structures have been analyzed in substantial detail, and used to model element-to-element, electromagnetic proximity-coupling in planar- and non-planar-phased-arrays, as well as in array-feed-networks.

Figure 5 shows a particular case of a rectangular-lattice two-dimensional structure as in Figure 4, where the unit cells are mutually identical pairs of coupled transmission lines. The multiple paths, created by the interconnection of many fishbone networks, generate here an infinite two-dimensional cluster of mutually-coupled TEM ring-resonators.

The same two-dimensional structure of Figure 5 is shown redrawn in Figure 6, with the dashed interfaces tilted at 45 degrees and the coupled-line pairs running horizontally and vertically.

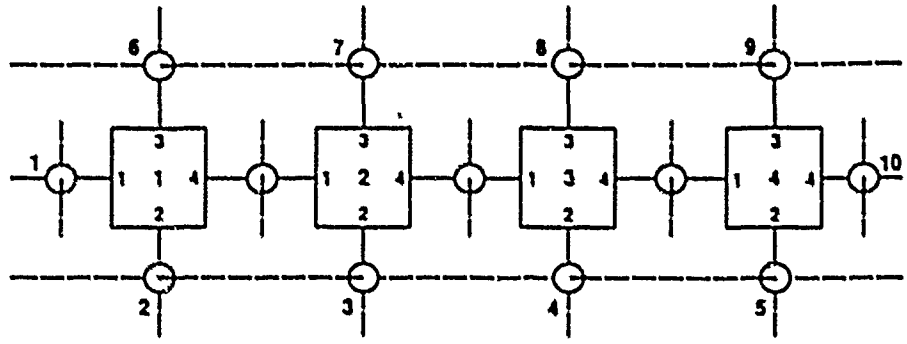
The same infinite, two-dimensional cluster of mutually-coupled ring-resonators of Figures 5 and 6 is redrawn in Figures 7 through 9. In Figure 7 the dashed interface lines, cutting halfway across each coupled-line pair both horizontally and vertically, isolate mutually identical, composite, eight-port unit-cells, each including four coupled-line pairs in a doubly-symmetric four-arm configuration.

This composite, eight-port unit-cell, isolated in Figure 10, resembles a four-atom 'monomer-molecule' of a 'cross-linked polymer', and has been analyzed in substantial detail to model element-to-element, electromagnetic proximity-coupling effects in planar- and non-planar-phased-arrays.

Figures 11, 12 and 13 represent various entries of the 8 x 8 Z-matrix, computed numerically with a microwave CAD program, for an amount of line-coupling equivalent to that of a 3 dB single-section coupler.

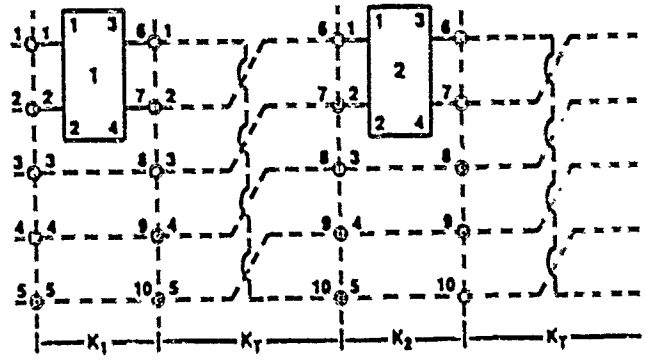
Closed-form, analytical expressions of the 8 x 8 Z-matrix, Y-matrix, and ABCD-matrix and of the 4 x 4 image-impedance- and image-transfer-function matrices have also been derived and physically interpreted. The image-impedance-matrix of this unit-cell is purely resistive and frequency-independent, and this proves that, contrary to expectations, the unit-cell has no stop-bands, under image-match conditions (Table I).

Finally, Figure 14 shows a variant of the structure in Figures 5 through 9, where the mutually-coupled TEM ring-resonators are arranged in an hexagonal lattice, as required to model element-to-element, electromagnetic proximity-coupling effects in phased-array with hexagonal element distributions. The dashed interface lines at zero and ±60 degrees orientation show that even this rather sophisticated structure-configuration can be decomposed in mutually-interconnected fishbone networks. Alternatively a three-arm 'monomer-molecule' could be isolated.



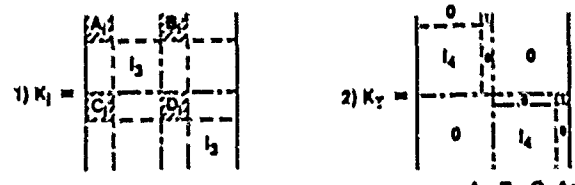
$K_1 = 4 \times 4$; $K = 10 \times 10$

Figure 3A. A Typical "Fishbone" Network.



$K = K_1 \cdot K_T \cdot K_2 \cdot K_T \cdot K_3 \cdot K_T \cdot K_4$

K, K_1 And $K_T = 10 \times 10$



A_1, B_1, C_1 And $D_1 = 2 \times 2$

Figure 3B. Alternate Computation Scheme for the "Fishbone" Network.

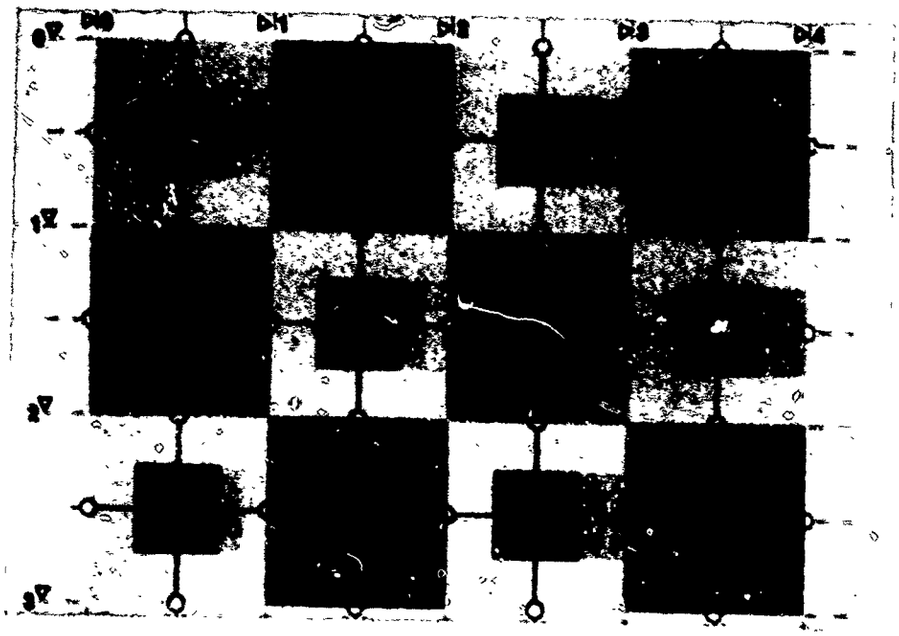


Figure 4. A Prototype Two-Dimensional Network; ($n = 3$; $m = 4$).

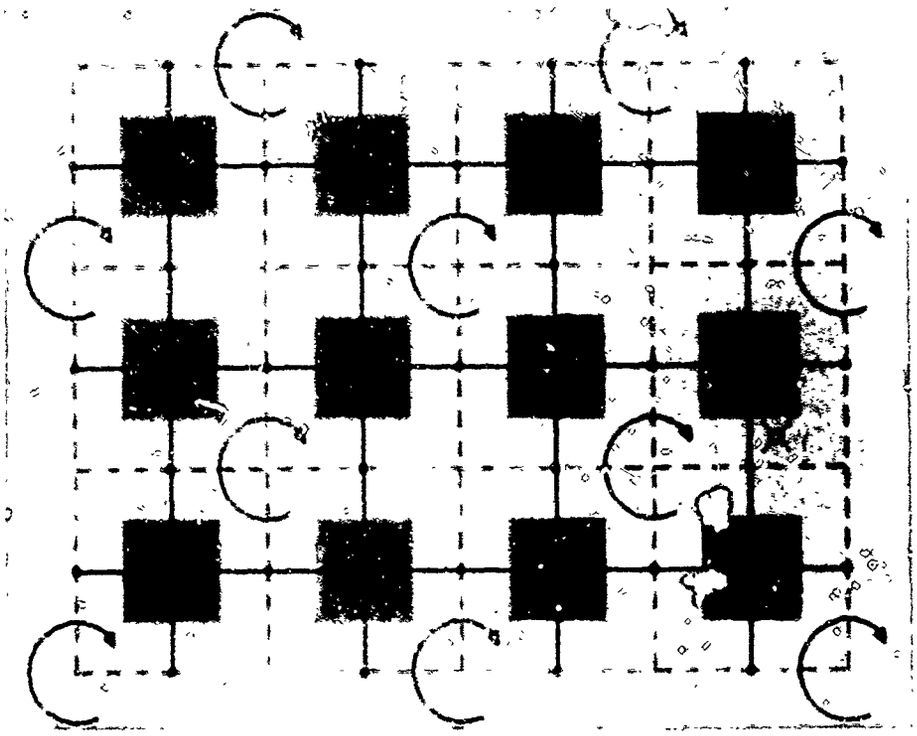


Figure 5. Two-Dimensional Cluster of Ring-Resonators.

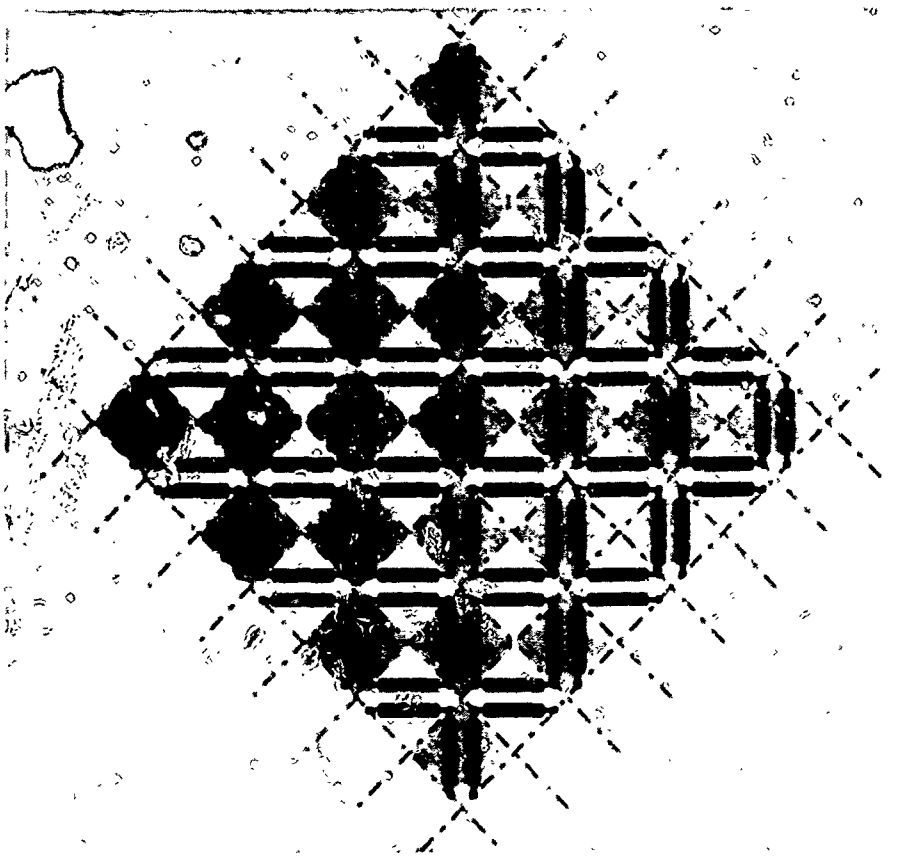


Figure 6. Rectangular Lattice of Ring-Resonators.

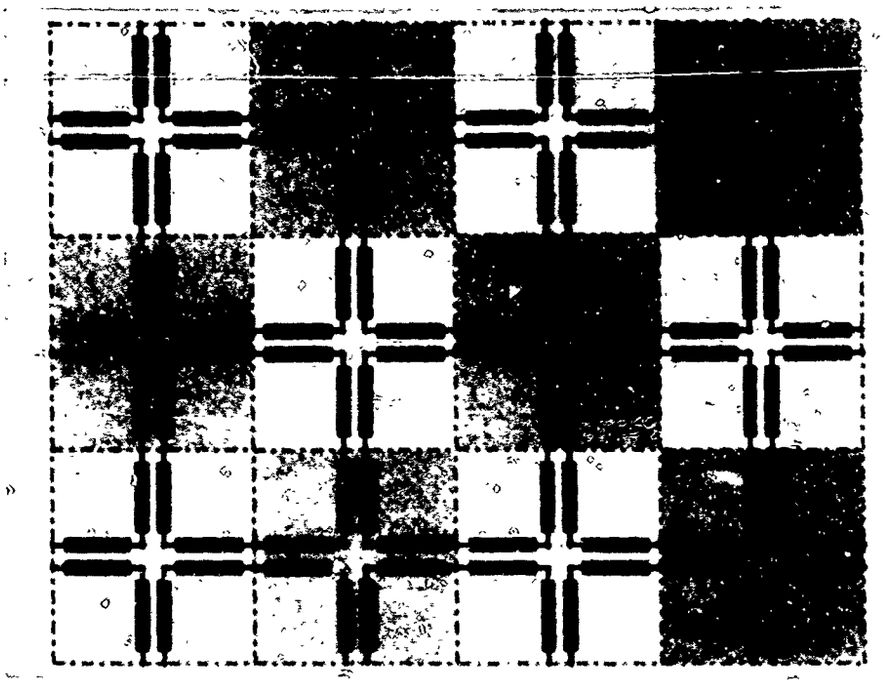


Figure 7. Rectangular Lattice of TEM Ring-Resonators.

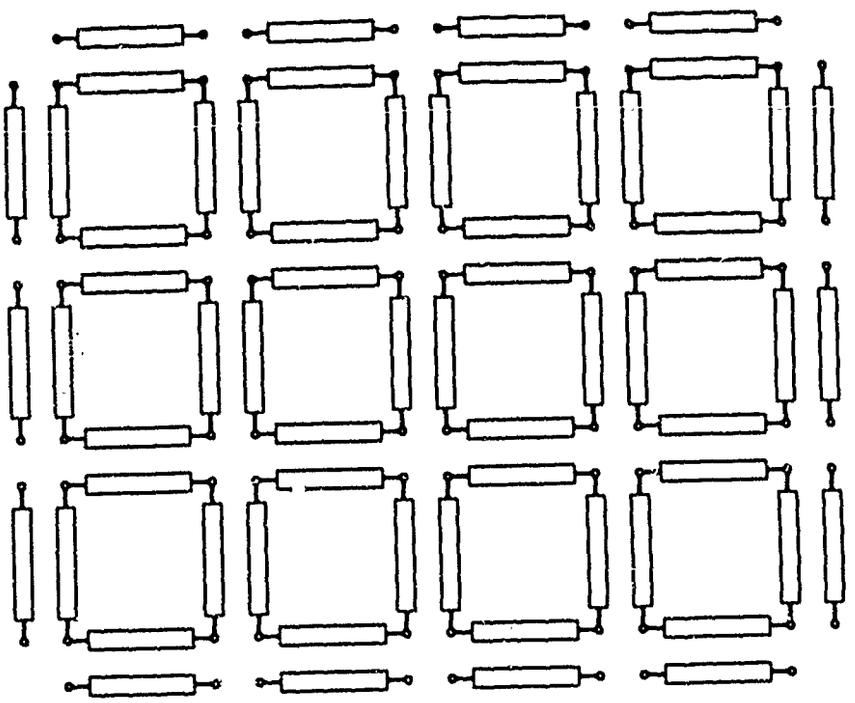


Figure 8. Two-Dimensional Cluster of Coupled Ring-Resonators.

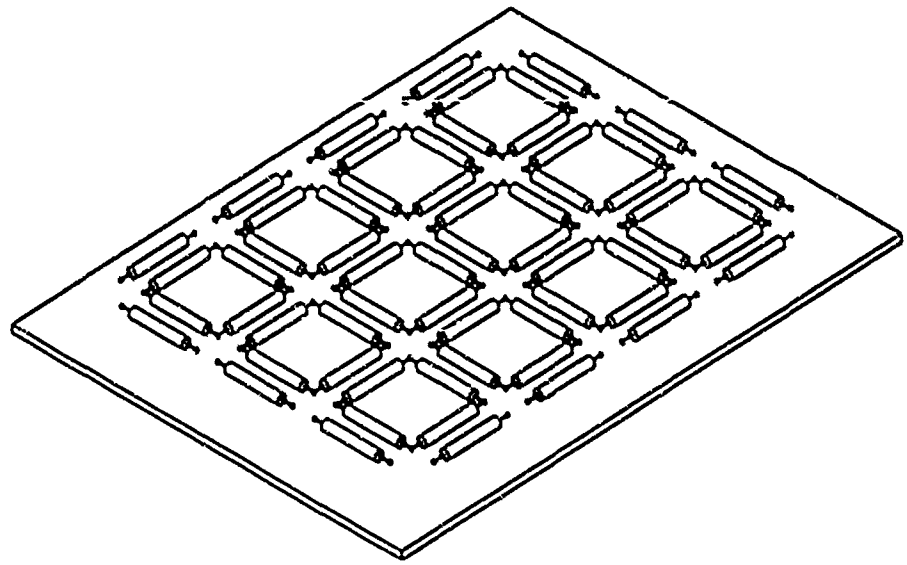


Figure 9. Two-Dimensional Cluster of Coupled Ring-Resonators.

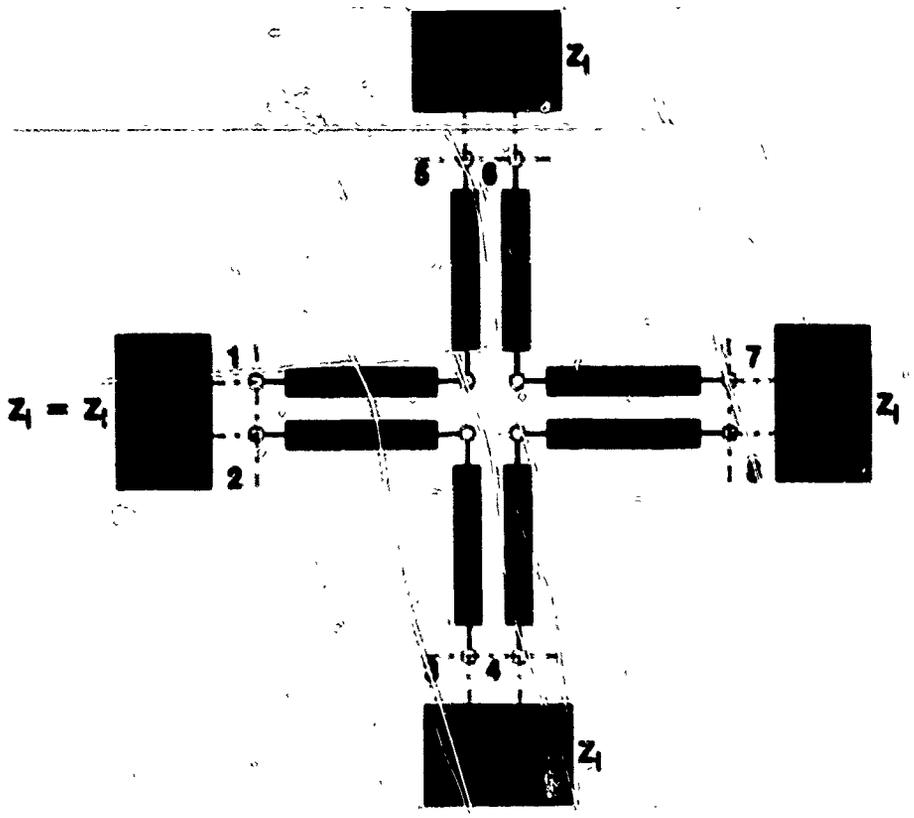


Figure 10. The Four-Arm Unit-Cell Network.

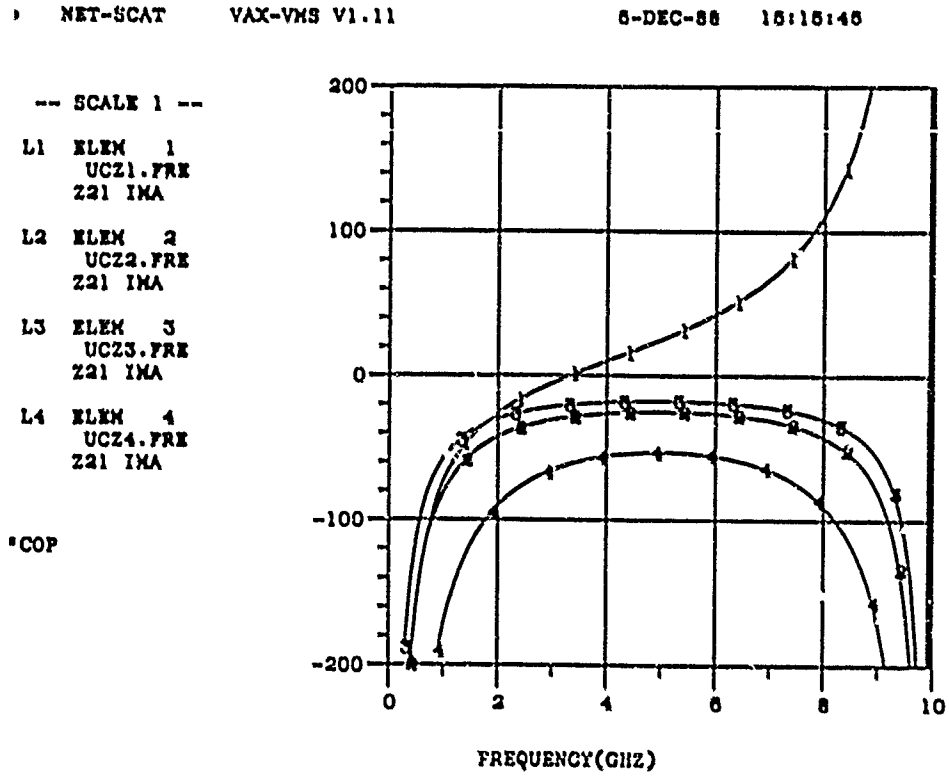


Figure 11. Open-Circuit Impedances of the Four-Arm Unit-Cell of the Rectangular Lattice of TEM Ring-Resonators; Curve 1 = Z12, Curve 2 = Z13, Curve 3 = Z14, Curve 4 = Z15.

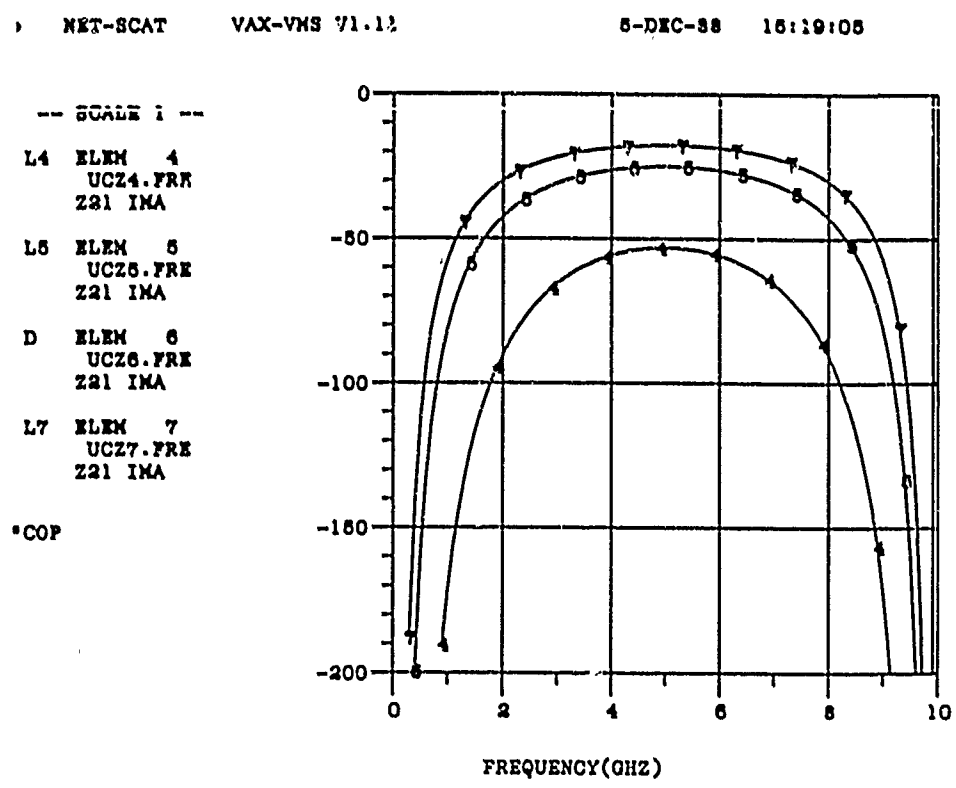


Figure 12. Open-Circuit Impedances of the Four-Arm Unit-Cell of the Rectangular Lattice of TEM Ring-Resonators; Curve 4 = Z15, Curve 5 = Z16, Curve 6 = Z17, Curve 7 = Z18 (Z16 = Z17).

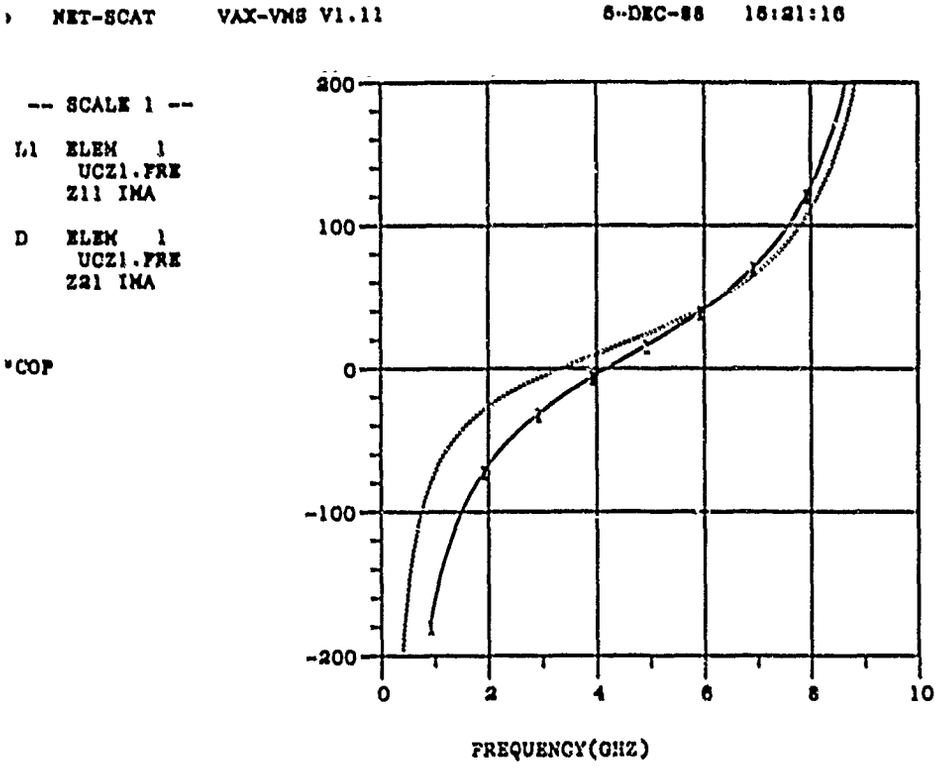


Figure 13. Open-Circuit Impedances of the Four-Arm Unit-Cell of the Rectangular Lattice of TEM Ring-Resonators; Curve 1 = Z11, Curve 2 = Z12 (Dashed).

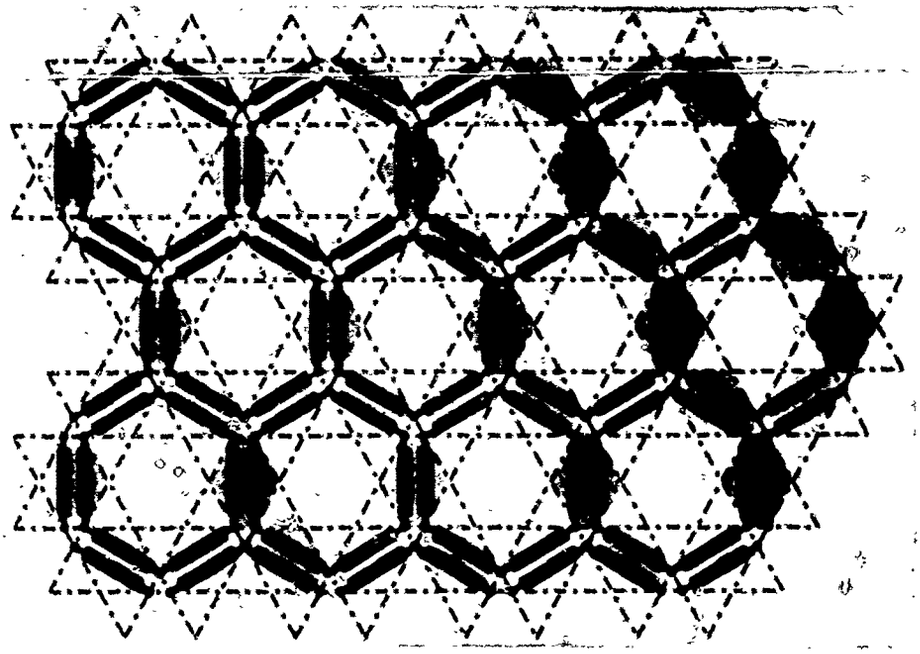
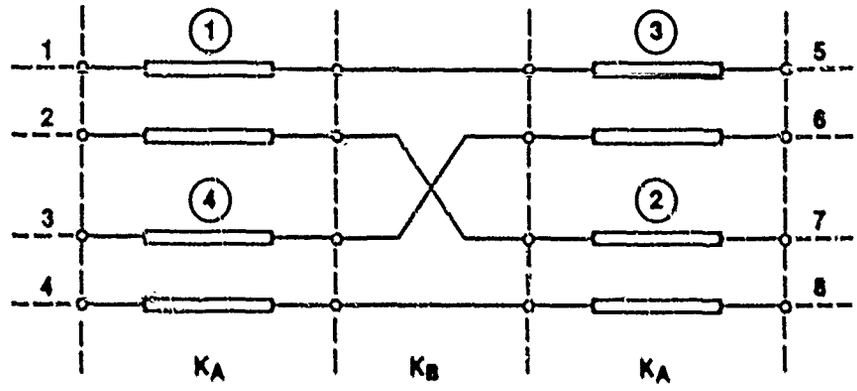


Figure 14. Hexagonal Lattice of TEM Ring-Resonators.



$$1)\quad K = K_A \bullet K_B \bullet K_A$$

Table IA. The ABCD Matrix of the Unit-Cell of the Two-Dimensional Cluster of Ring Resonators (In Its "Twisted Form").

$$2)\quad \begin{vmatrix} V_1 \\ V_2 \\ V_3 \\ V_4 \\ \hline I_1 \\ I_2 \\ I_3 \\ I_4 \end{vmatrix} = K \bullet \begin{vmatrix} V_5 \\ V_6 \\ V_7 \\ V_8 \\ \hline -I_5 \\ -I_6 \\ -I_7 \\ -I_8 \end{vmatrix} = \left[\begin{array}{cc:cc} A_1 & A_2 & B_1 & B_2 \\ A_3 & A_4 & B_3 & B_4 \\ \hdashline C_1 & C_2 & D_1 & D_2 \\ C_3 & C_4 & D_3 & D_4 \end{array}\right] \bullet \begin{vmatrix} V_5 \\ V_6 \\ V_7 \\ V_8 \\ \hline -I_5 \\ -I_6 \\ -I_7 \\ -I_8 \end{vmatrix}$$

Table IB. The ABCD Matrix of the Unit-Cell of the Two-Dimensional Cluster of Ring Resonators (In Its "Twisted Form").

3) $K =$

$a^2+b_1c_1$	b_1c_2	b_2c_1	b_2c_2	$2ab_1$	ab_2	ab_2	0
b_2c_1	b_2c_2	$a^2+b_1c_1$	b_1c_2	ab_2	0	$2ab_1$	ab_2
b_1c_2	$a^2+b_1c_1$	b_2c_2	b_2c_1	ab_2	$2ab_1$	0	ab_2
b_2c_2	b_2c_1	b_1c_2	$a^2+b_1c_1$	0	ab_2	ab_2	$2ab_1$
$2ac_1$	ac_2	ac_2	0	$a^2+b_1c_1$	b_2c_1	b_1c_2	b_2c_2
ac_2	0	$2ac_1$	ac_2	b_1c_2	b_2c_2	$a^2+b_1c_1$	b_2c_1
ac_2	$2ac_1$	0	ac_2	b_2c_1	$a^2+b_1c_1$	b_2c_2	b_1c_2
0	ac_2	ac_2	$2ac_1$	b_2c_2	b_1c_2	b_2c_1	$a^2+b_1c_1$

Table IC. The ABCD Matrix of the Unit-Cell of the Two-Dimensional Cluster of Ring Resonators (In Its "Twisted Form").

1) $a = \cos\theta$

2) $b_1 = j\sqrt{Z_{OE}Z_{OO}}\ \dfrac{R_Z+1}{2\sqrt{R_Z}}\ \sin\theta$

3) $b_2 = j\sqrt{Z_{OE}Z_{OO}}\ \dfrac{R_Z-1}{2\sqrt{R_Z}}\ \sin\theta$

4) $C_1 = \dfrac{j}{\sqrt{Z_{OE}Z_{OO}}}\ \dfrac{R_Z+1}{2\sqrt{R_Z}}\ \sin\theta$

5) $C_2 = -\dfrac{j}{\sqrt{Z_{OE}Z_{OO}}}\ \dfrac{R_Z-1}{2\sqrt{R_Z}}\ \sin\theta$

6) $R_Z = \dfrac{Z_{OE}}{Z_{OO}} = \dfrac{1+C}{1-C}$

7) $C = 10^{\frac{C_{dB}}{20}}$

Table ID. The Closed-Form Expressions of the Parameters of the ABCD Matrix K.

MATHEMATICAL FOUNDATIONS

The new theory of wave-propagation on infinite, two-dimensional structures, represented as clusters of unit-cell, multiport microwave networks, is based on fundamental extensions of the classical concepts of image-impedance and of image-transfer-function of two-port networks, to the domain of multiport microwave networks.

In the domain of 2n-port microwave networks, the familiar complex, scalar image-impedances and image-transfer-functions become complex n x n matrices. The image-impedance-matrices and the image-transfer-function-matrices are defined, however, in total analogy to the familiar scalar image-parameters of two-port networks, and may be expressed in closed-form as non-linear matrix-functions of the four n x n blocks A, B, C and D of the generalized 2n x 2n ABCD-matrices of the considered unit-cell networks.

The non-linear expressions of the image-matrices of a linear, 2n-port microwave network, given here, have been derived by systematic exploitation of the generalized, multidimensional fractional-linear-transformation that was previously found [1] to quantitatively describe the electrical transformation of n-port loads, from one structural interface to another, through a 2n-port unit-cell network.

The so-defined and expressed image-impedance-matrices represent the multiport loads required to obtain bilateral, multiport impedance-match, in two-dimensions, at all the interfaces of a unit-cell multiport network.

In the most general case, the multiport unit-cells of an infinite, two-dimensional structure need not be all mutually identical, as long as the image-match condition is satisfied at each internal interface, and the validity of the general theory extends to infinite, quasi-doubly-periodic structures.

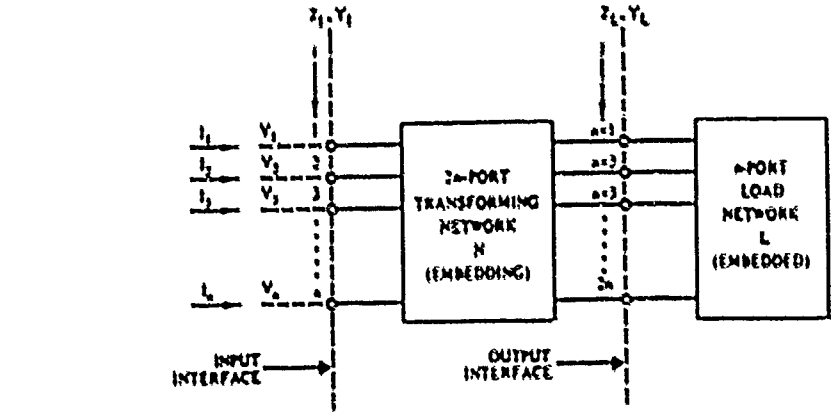
Conversely, strictly doubly-periodic structures are represented by infinite two-dimensional clusters of mutually identical and doubly-symmetric unit-cell multiport networks.

Further, the so-defined and expressed image-transfer-function-matrices quantitatively describe the propagation of arbitrary voltage- and/or current-vectors, between the interfaces of a unit-cell multiport network, under bilateral, multiport impedance-match.

The fundamental, normal modes of such a strictly doubly-periodic two-dimensional structure are then identified and defined by the eigenvectors of the image-transfer-function matrices of the unique unit-cell-network that is the fundamental building-block of the whole infinite, two-dimensional structure, and are then constant, up to a complex scaling factor, through the whole system. Further, the wave-number of each normal mode is directly related to the corresponding eigenvalue of the image-transfer-function-matrix of the multiport unit-cell.

The modal eigenvectors constitute a vector-base that may be used to represent arbitrary voltage- and/or current-patterns at any interface, as vector-linear-combinations of the normal modes with known complex weights.

The eigenvalues of the image-impedance-matrix of the unit-cell network represent complex, scalar load-impedance values that will bilaterally match the unit-cell network, under a single-normal-mode excitation, when connected to all its ports. These eigenvalues are the 'Modal Impedances' of the unit-cell network, and are biunivocally associated to the corresponding normal modes, exactly as the even- and odd-mode impedances of a coupled-line pair are associated to the corresponding even and odd modes.



$$\begin{vmatrix} V_i \\ I_i \end{vmatrix} = \begin{vmatrix} A & B \\ C & D \end{vmatrix} \cdot \begin{vmatrix} V_j \\ -I_j \end{vmatrix} \qquad \begin{vmatrix} V_1 \\ \vdots \\ V_n \end{vmatrix} = Z_i \cdot \begin{vmatrix} I_1 \\ \vdots \\ I_n \end{vmatrix} \qquad \begin{vmatrix} V_{n+1} \\ \vdots \\ V_{2n} \end{vmatrix} = Z_L \cdot \begin{vmatrix} -I_{n+1} \\ \vdots \\ -I_{2n} \end{vmatrix} \qquad i = 1,2, \ldots n$$

$$\begin{vmatrix} I_1 \\ \vdots \\ I_n \end{vmatrix} = Y_i \cdot \begin{vmatrix} V_1 \\ \vdots \\ V_n \end{vmatrix} \qquad \begin{vmatrix} -I_{n+1} \\ \vdots \\ -I_{2n} \end{vmatrix} = Y_L \cdot \begin{vmatrix} V_{n+1} \\ \vdots \\ V_{2n} \end{vmatrix} \qquad j = n+1, n+2, \ldots 2n$$

$$Z_i = (A \cdot Z_L + B)(C \cdot Z_L + D)^{-1} \qquad Y_i = (D \cdot Y_L + C)(B \cdot Y_L + A)^{-1}$$

Figure 15. Transformation of an n x n, Complex, Impedance Matrix Z_L, (and of the Corresponding Admittance Matrix Y_L).

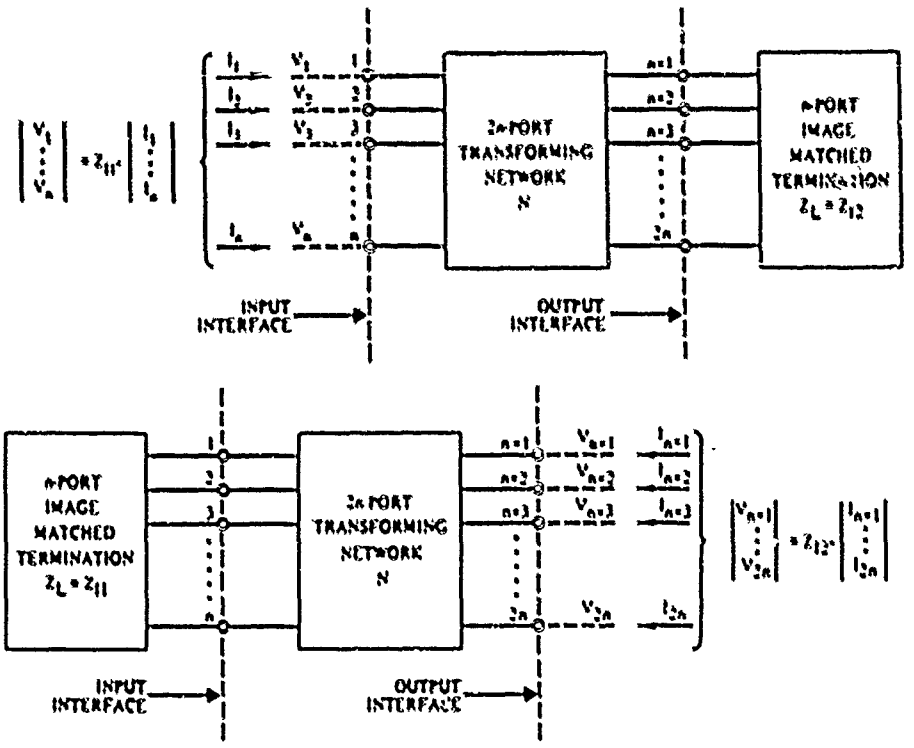


Figure 16. Illustration of the Basic Concept of Image-Impedance Matrix.

$$\left|\begin{array}{c} V_i \\ \hline I_i \end{array}\right| = K_F \cdot \left|\begin{array}{c} V_j \\ \hline -i_j \end{array}\right| = \left|\begin{array}{c|c} A_F & B_F \\ \hline C_F & D_F \end{array}\right| \cdot \left|\begin{array}{c} V_j \\ \hline -I_j \end{array}\right| \qquad (1)$$

$$\left|\begin{array}{c} V_j \\ \hline I_j \end{array}\right| = K_B \cdot \left|\begin{array}{c} V_i \\ \hline -I_i \end{array}\right| = \left|\begin{array}{c|c} A_B & B_B \\ \hline C_B & D_B \end{array}\right| \cdot \left|\begin{array}{c} V_i \\ \hline -I_i \end{array}\right| \qquad (2)$$

Figure 17. The Forward- and Backward-ABCD Matrices.

$$Z_{I1} = \left(A_F \cdot Z_{I2} + B_F\right)\left(C_F \cdot Z_{I2} + D_F\right)^{-1}$$

$$Z_{I2} = \left(A_B \cdot Z_{I1} + B_B\right)\left(C_B \cdot Z_{I1} + D_B\right)^{-1}$$

$$Y_{I1} = \left(D_F \cdot Y_{I2} + C_F\right)\left(B_F \cdot Y_{I2} + A_F\right)^{-1}$$

$$Y_{I2} = \left(D_B \cdot Y_{I1} + C_B\right)\left(B_B \cdot Y_{I1} + A_B\right)^{-1}$$

Figure 18. Definition of the Image-Matrices.

$$Z_{11} = (BD^{-1}) \cdot (DB^{-1}AC^{-1})^{1/2} = (BD^{-1}) \cdot (CA^{-1}BD^{-1})^{-1/2}$$

$$= (AC^{-1}) \cdot (CA^{-1}BD^{-1})^{1/2} = (AC^{-1}) \cdot (DB^{-1}AC^{-1})^{-1/2}$$

$$Z_{12} = (A^{-1}B) \cdot (B^{-1}AC^{-1}D)^{1/2} = (A^{-1}B) \cdot (D^{-1}CA^{-1}B)^{-1/2}$$

$$= (C^{-1}D) \cdot (D^{-1}CA^{-1}B)^{1/2} = (C^{-1}D) \cdot (B^{-1}AC^{-1}D)^{-1/2}$$

Figure 19. The Image-Impedance Matrices.

$$K_B = \left|\begin{array}{c|c} 1 & 0 \\ \hline 0 & -1 \end{array}\right| \cdot K_F^{-1} \cdot \left|\begin{array}{c|c} 1 & 0 \\ \hline 0 & -1 \end{array}\right| \qquad (3)$$

Symmetry Condition: $K_F = K_B$

$$K_F = \left|\begin{array}{c|c} (1 + B_F C_F)^{1/2} & B \\ \hline C & (1 + C_F B_F)^{1/2} \end{array}\right| \qquad (4)$$

$$A_F = (1 + B_F C_F)^{1/2} \qquad D_F = (1 + C_F B_F)^{1/2}$$

Figure 20. The Matrix Relation Between ABCD Matrices.

$$Z_{11} = Z_{12} = Z_I = C^{-1}\ (CB)^{1/2} = B \cdot (CB)^{-1/2} = (BC)^{1/2} C^{-1} = (BC)^{-1/2} \cdot B$$

For $K_F = K_B$ Or:

$$A = (I + BC)^{1/2} \qquad \text{And} \quad D = (I + CB)^{1/2}$$

Figure 21. The Image-Impedance Matrices of a Symmetric Network.

$$T_{IVF} = \left[I + (A^{-1}BD^{-1}C)^{1/2}\right]^{-1} \cdot A^{-1} \qquad \text{Voltage Forward}$$

$$T_{IVB} = A \cdot \left[I - (A^{-1}BD^{-1}C)^{1/2}\right] \qquad \text{Voltage Backward}$$

$$T_{IIF} = \left[I + (D^{-1}CA^{-1}B)^{1/2}\right]^{-1} \cdot D^{-1} \qquad \text{Current Forward}$$

$$T_{IIB} = D \cdot \left[I - (D^{-1}CA^{-1}B)^{1/2}\right] \qquad \text{Current Backward}$$

Figure 22. The Image-Transfer-Function Matrices.

$$T_{IVF} = \left[(I + BC)^{1/2} + (BC)^{1/2} \right]^{-1}$$

$$T_{IVB} = (I + BC)^{1/2} - (BC)^{1/2}$$

$$A = (I + BC)^{1/2} \qquad D = (I + CB)^{1/2}$$

Figure 23. The Voltage Image-Transfer-Function Matrices of a Symmetric 2n-Port Network.

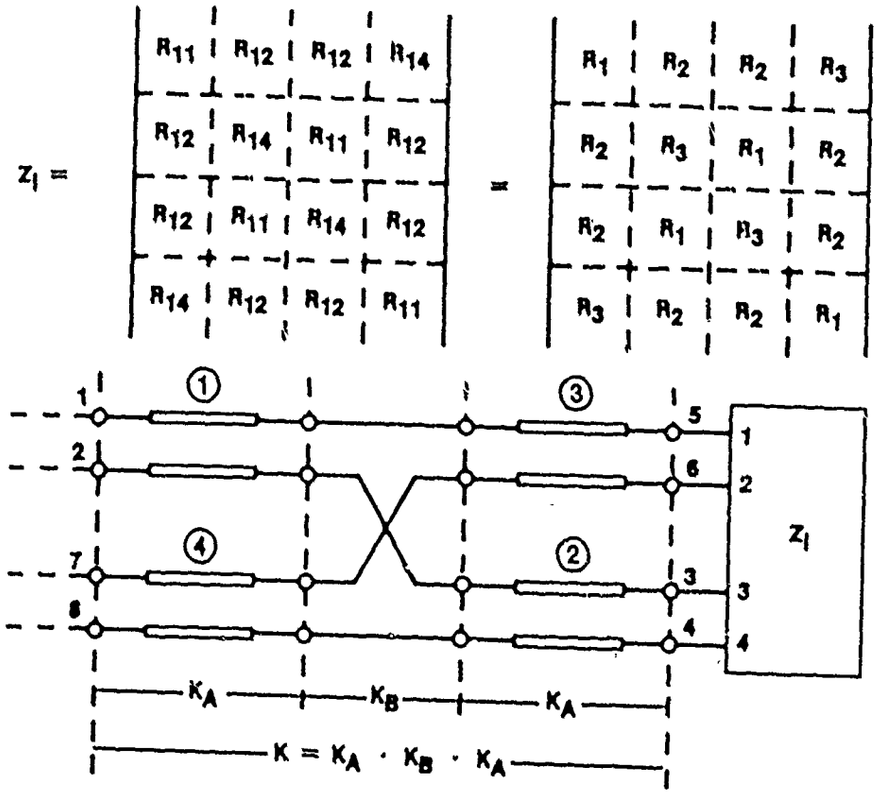


Figure 24. The Symmetry Structure of the Image-Impedance-Matrix Z_L of the Four-Arm Unit-Cell (All 16 Blocks R_{ij} are 2 x 2).

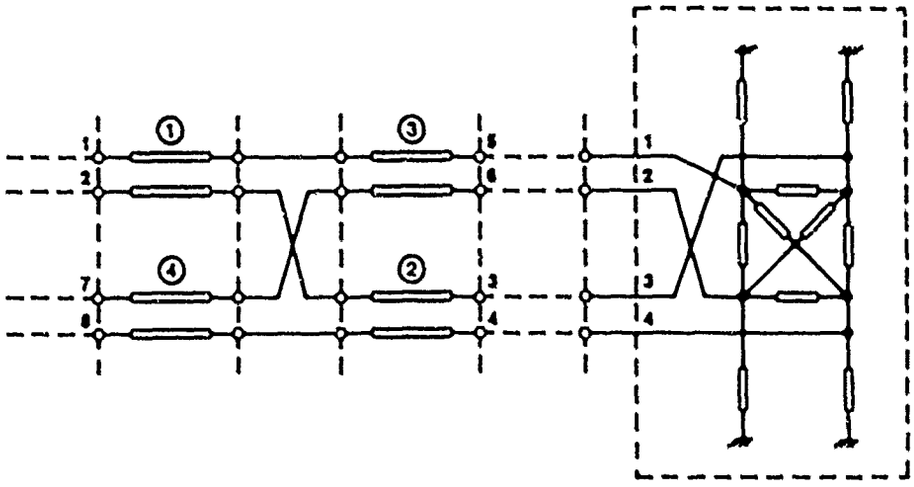


Figure 25. Resistance-Only, Four-Port Network Equivalent to the Frequency-Independent Image-Impedance-Matrix Z_L of the Four-Arm Unit-Cell (Synthesized Without Ideal Transformers).

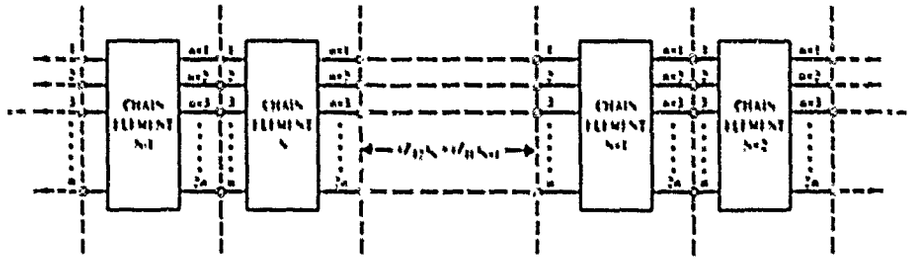
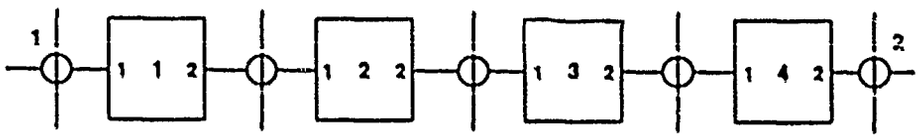


Figure 26. Illustration of the Fundamental Concept of Image-Matched Chain of 2n-Port Networks.

CONCLUSIONS

Extensive preliminary results of the new theory of wave propagation on infinite, two-dimensional structures, as applied to two-dimensional clusters of mutually-coupled microwave resonators, show that: a) The usable bandwidth of such a structure largely increases with increasing mutual coupling between adjacent unit-cell resonators, and can attain values vastly in excess of the intrinsic bandwidth of each isolated array-element, b) The center-frequency of the usable bandwidth of the structure is controlled by the common, nominal resonant frequency of all the unit-cell resonators, and c) The adverse effects of the natural, uncontrolled, element-to-element proximity-coupling can be countered by intentionally introducing a controlled amount of sub-aperture-surface coupling, between adjacent array-elements.

Some of the described results, that relate to simple one-dimensional chains of mutually-coupled resonators, are shown in Figures 27 to 47. The dispersion characteristics in Figures 29, 30, 37, and 43 represent 'image-phase-rotations per unit-cell' or, equivalently, arguments of the corresponding complex voltage-transfer-functions. The image-impedances in Figures 31 and 32 are normalized to the square-root of the ratio L/C, while those in Figures 38, 44 and 45 are expressed in ohm, under the assumption that the square-root of the product $Z_{oe} \cdot Z_{oo}$ equals 50 ohm. Similarly, the group delays in Figures 33 and 34 are normalized to the period of the unit-cell resonant frequency -- that equals $2\pi\sqrt{LC}$ --, while the group delays in Figures 39 and 46 are normalized to the periods of the half-wave, shorted-line resonance (Figure 36) or of the full-wave ring-resonance (Figure 42), at which frequencies the couplers in the unit-cells are a quarter-wave long (Theta = 90 degrees). Finally, the attenuations in Figures 35, 40, 41 and 47 are expressed in 'dB per unit-cell' outside the passbands, while being zero dB within the passband, as would be expected of a chain of cascaded, lossless unit-cell networks.



$$K = K_1 \cdot K_2 \cdot K_3 \cdot K_4$$

K And K_i = 2 X 2

Figure 27. A Chain of Cascaded Two-Ports.

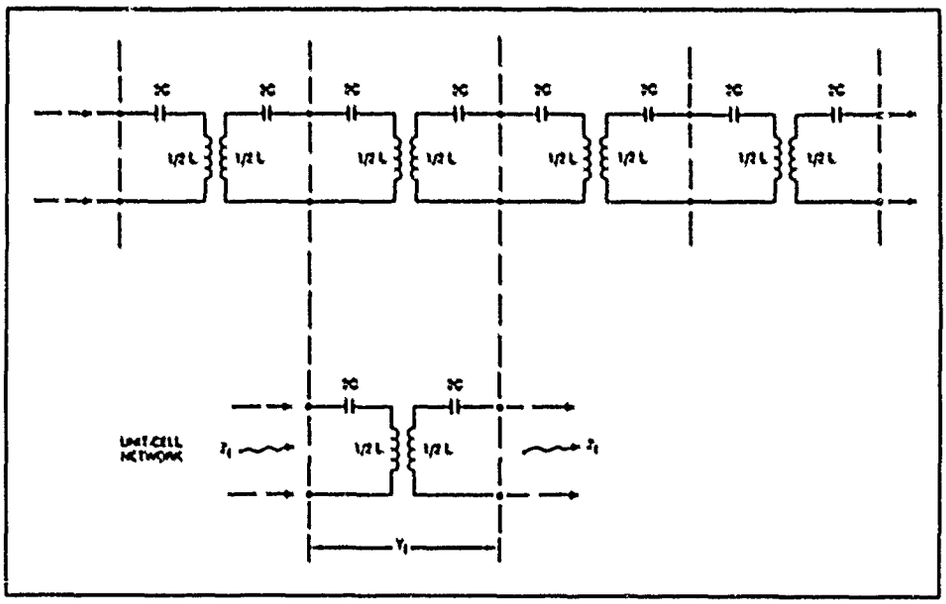


Figure 28. The One-Dimensional Chain of Lumped Resonators.

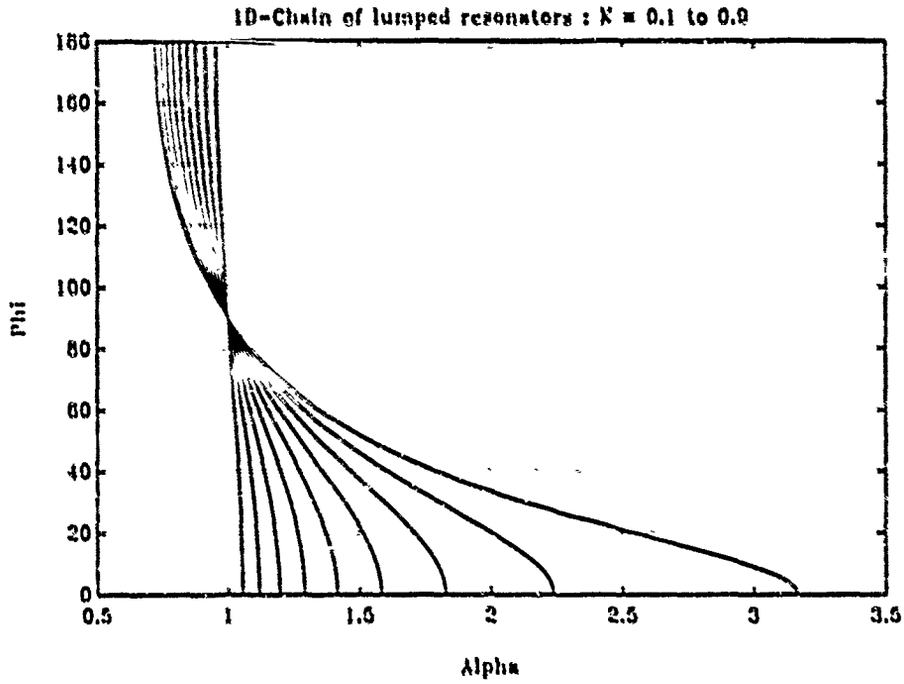


Figure 29. One-Dimensional Chain of Lumped Resonators; Dispersion Characteristics in the Passband.

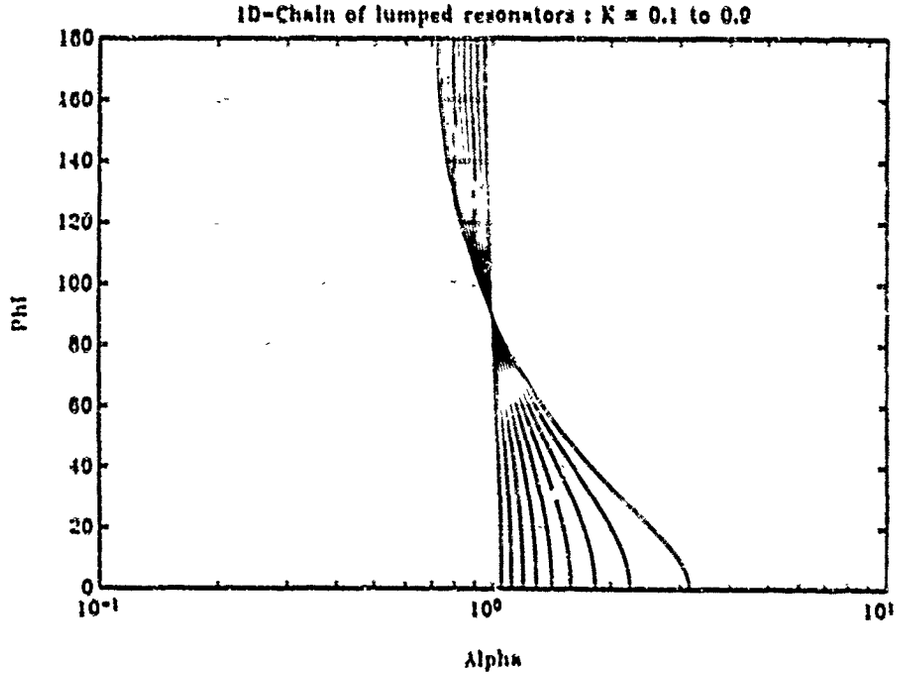


Figure 30. One-Dimensional Chain of Lumped Resonators; Dispersion Characteristics in the Passband.

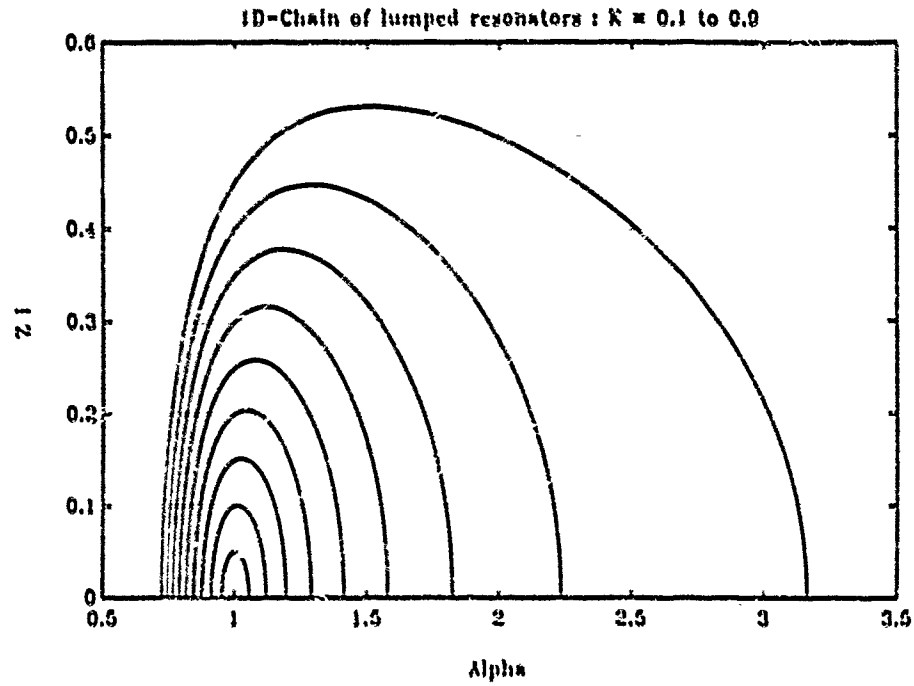


Figure 31. One-Dimensional Chain of Lumped Resonators; Real Image-Impedance in the Passband.

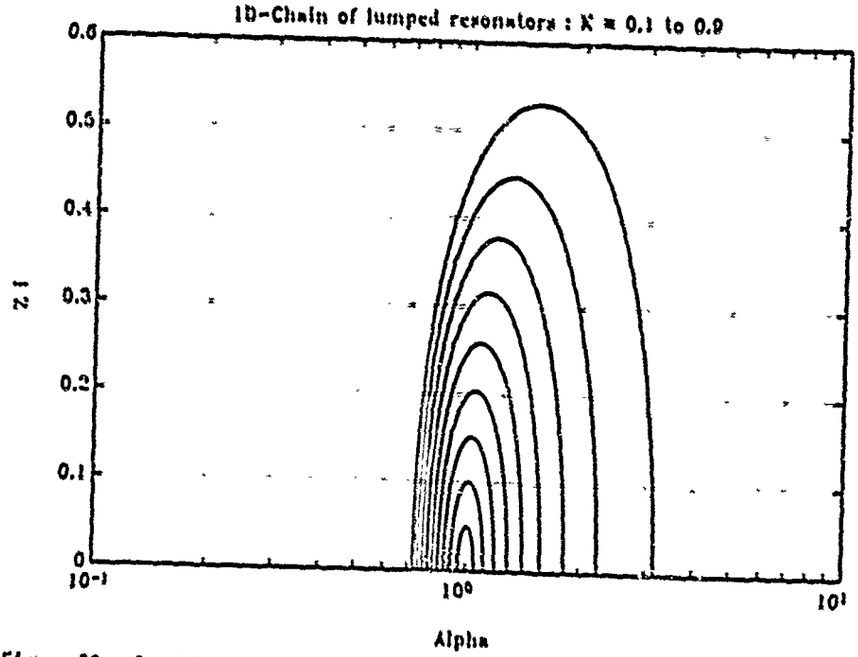


Figure 32. One-Dimensional Chain of Lumped Resonators; Real Image-Impedance in the Passband.

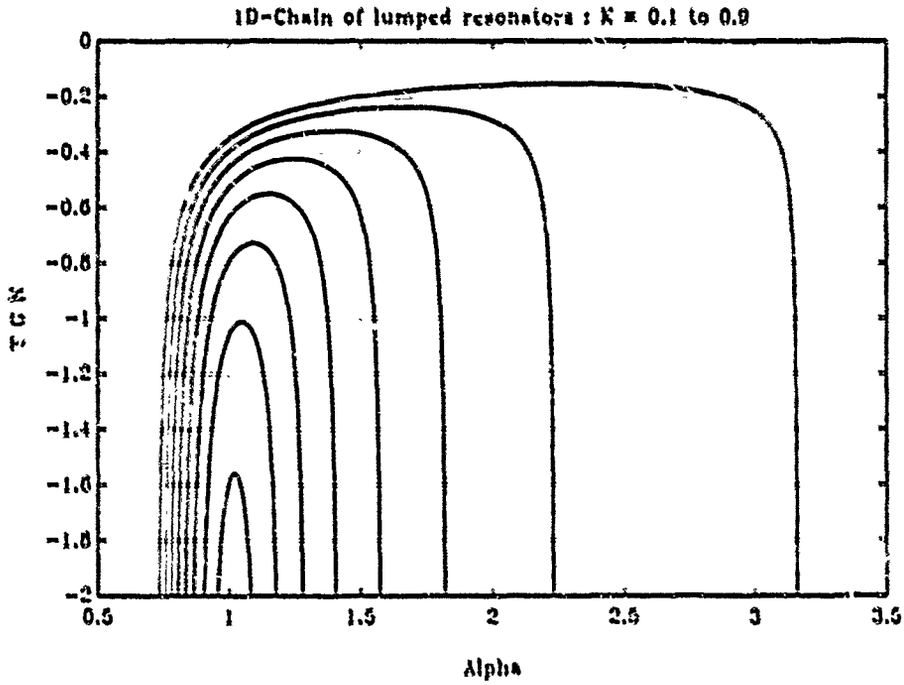


Figure 33. One-Dimensional Chain of Lumped Resonators; Normalized Group Delay.

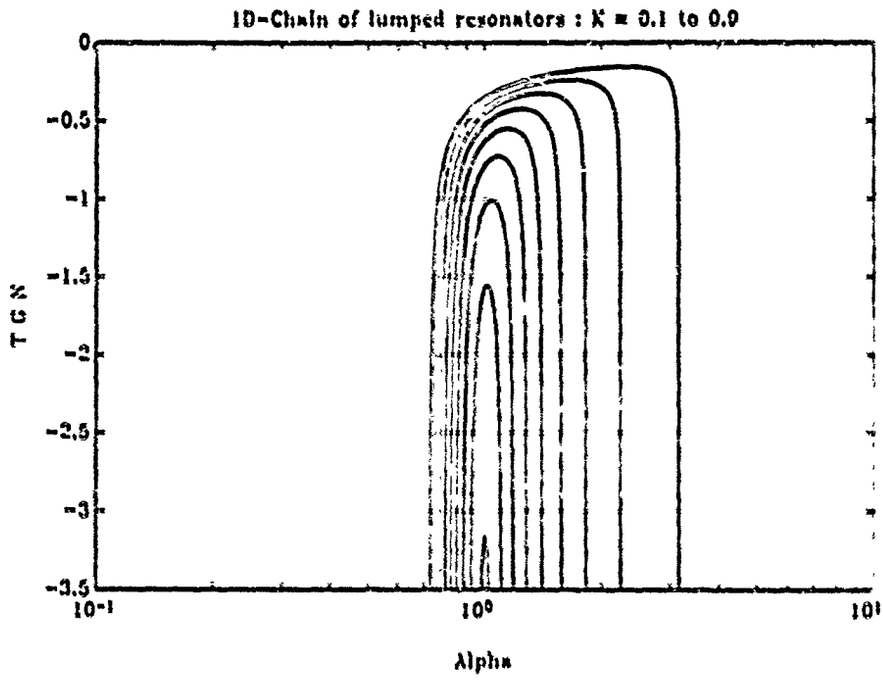


Figure 34. One-Dimensional Chain of Lumped Resonators; Normalized Group Delay.

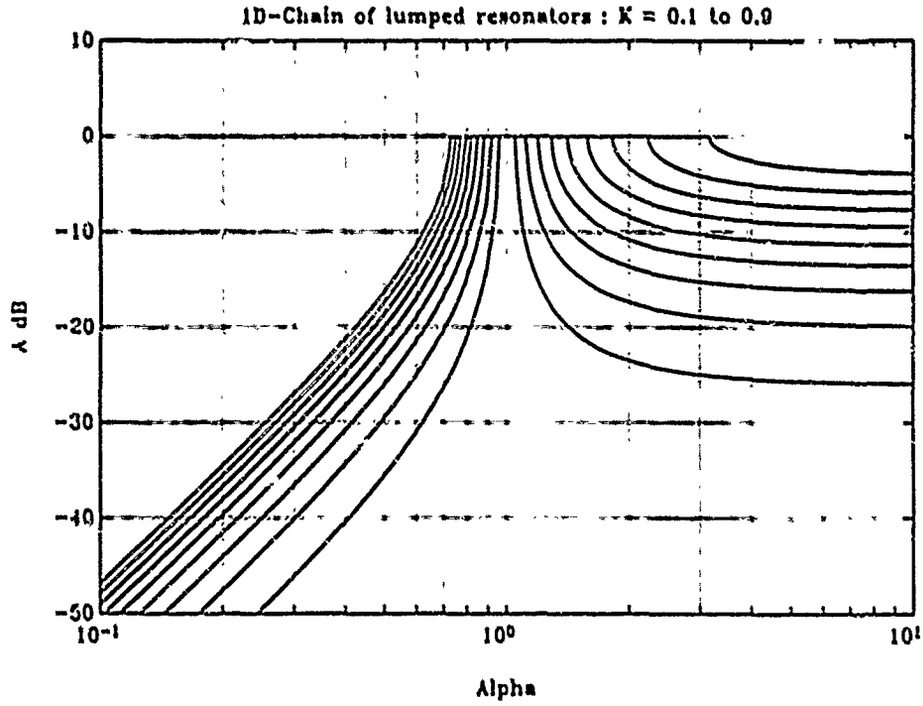


Figure 35. One-Dimensional Chain of Lumped Resonators; Attenuation per Unit-Cell Around and Across the Passband.

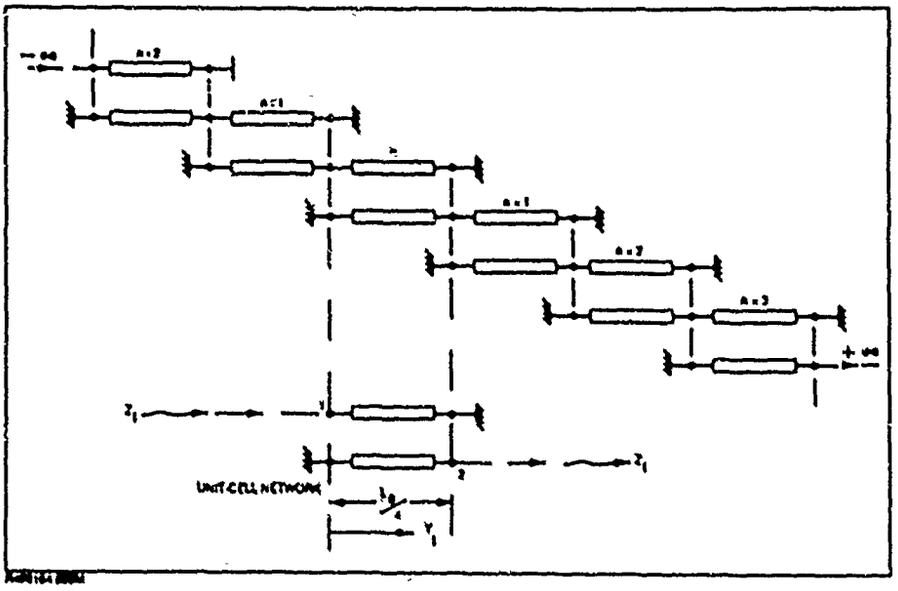


Figure 36. The One-Dimensional Chain of Coupled, Half-Wave Resonators.

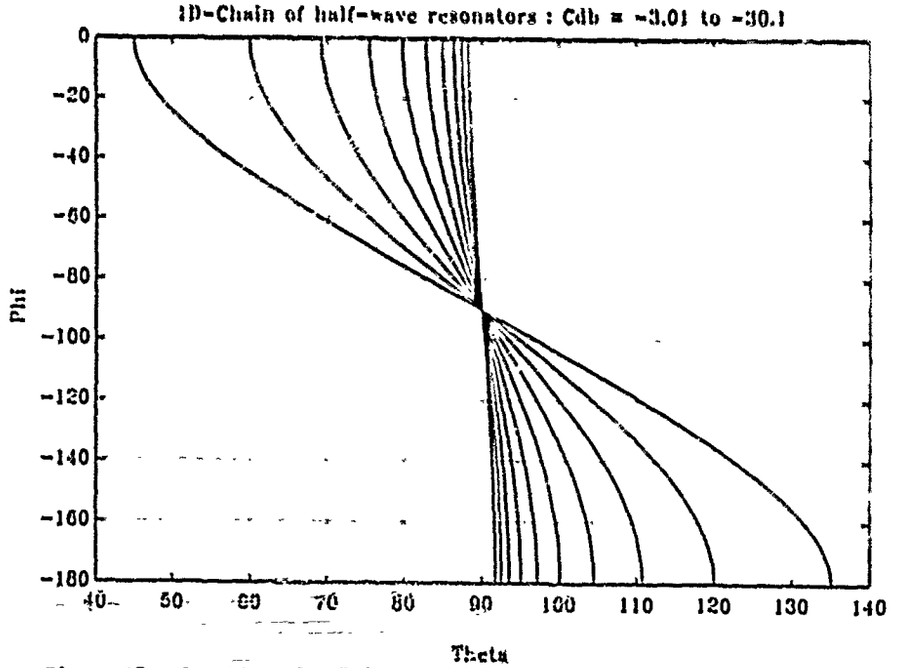


Figure 37. One-Dimensional Chain of Half-Wave Resonators; Dispersion Characteristic in the First Passband.

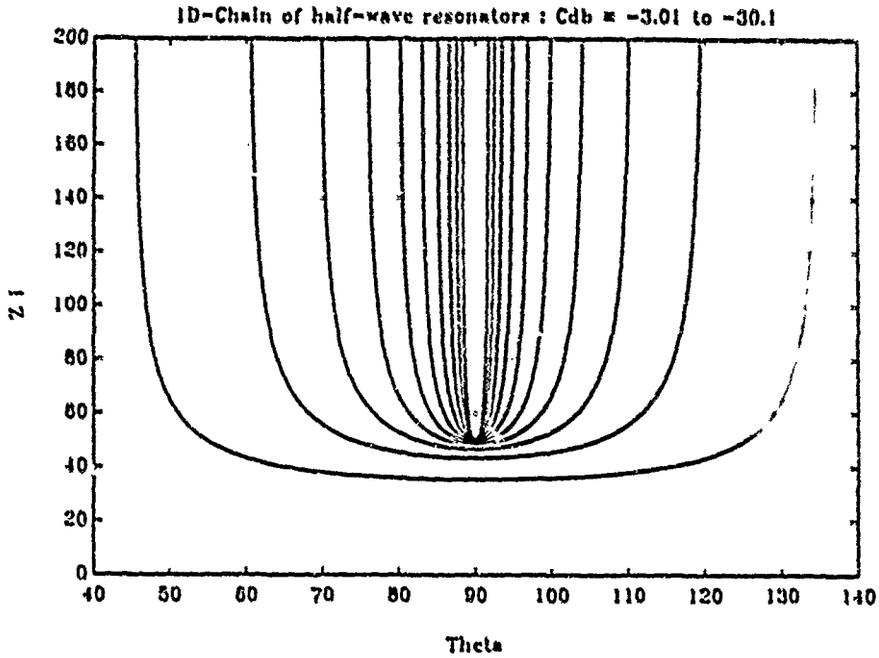


Figure 38. One-Dimensional Chain of Half-Wave Resonators; Real Image-Impedance in the First Passband.

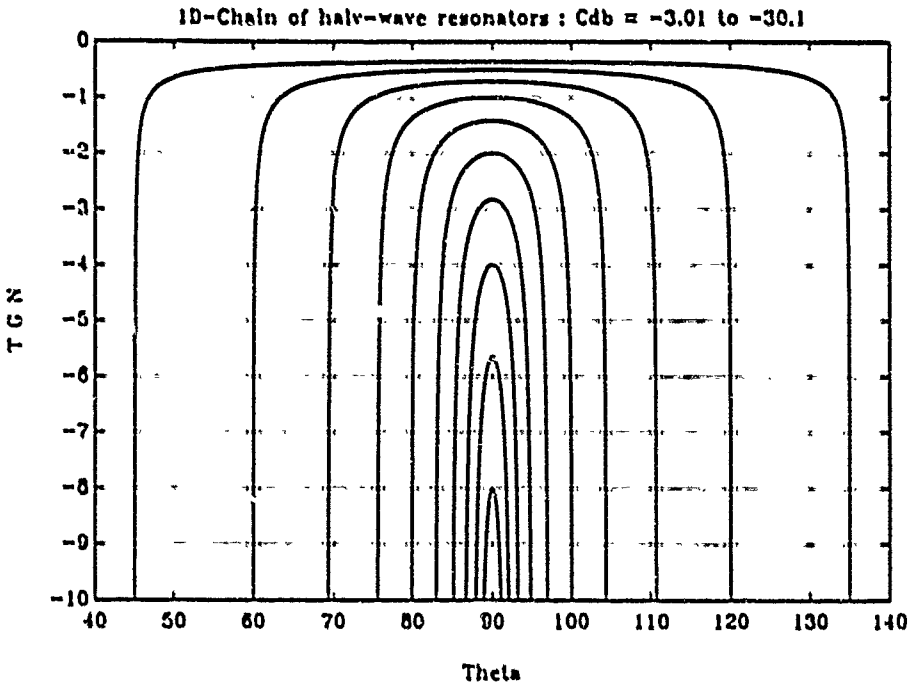


Figure 39. One-Dimensional Chain of Half-Wave Resonators; Normalized Group Delay.

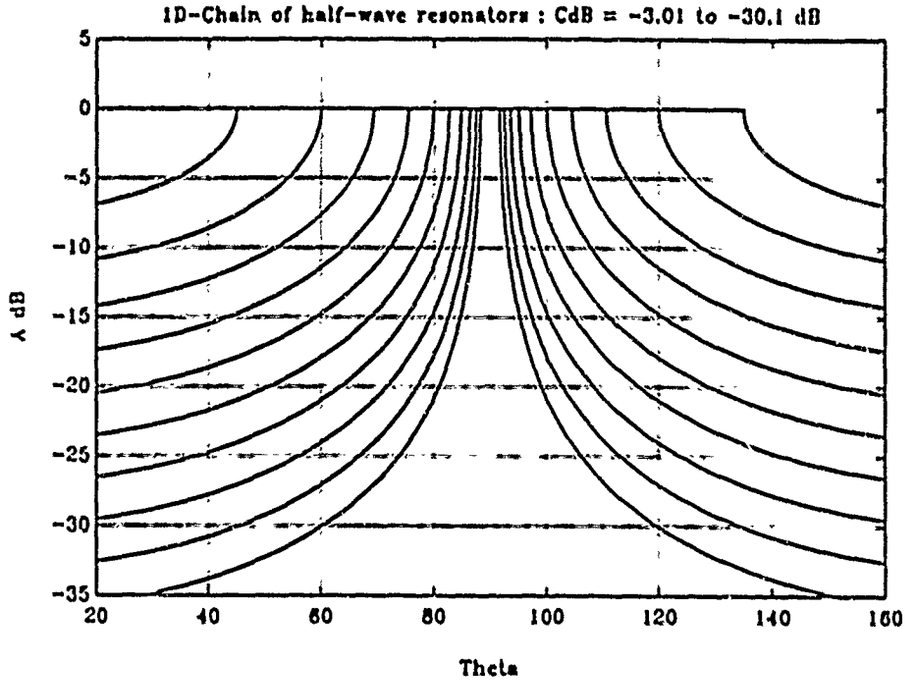


Figure 40. One-Dimensional Chain of Half-Wave Resonators; Attenuation per Unit-Cell Around and Across the First Passband.

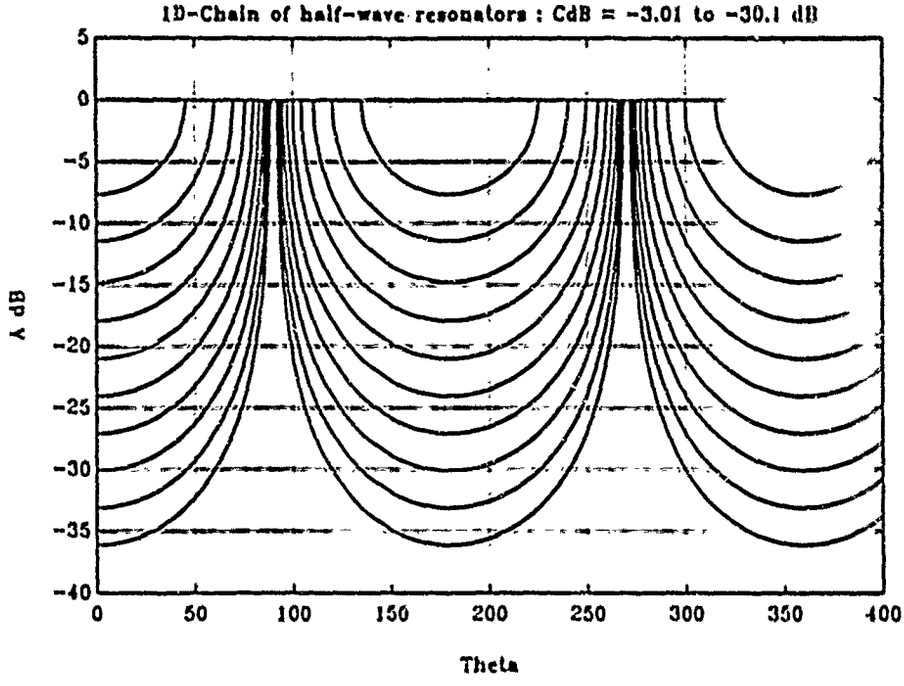


Figure 41. One-Dimensional Chain of Half-Wave Resonators; Attenuation per Unit-Cell Around and Across the First Two Passbands.

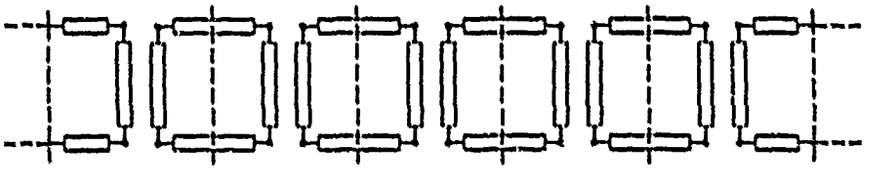


Figure 42. One-Dimensional Chain of Ring-Resonators.

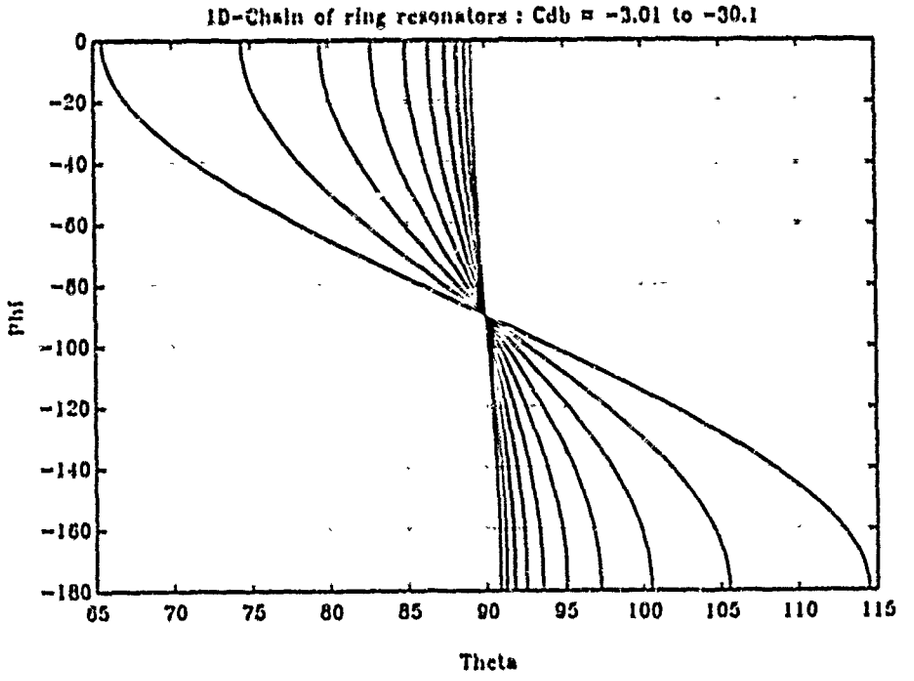


Figure 43. One-Dimensional Chain of Ring-Resonators; Dispersion Characteristics in the First Passband.

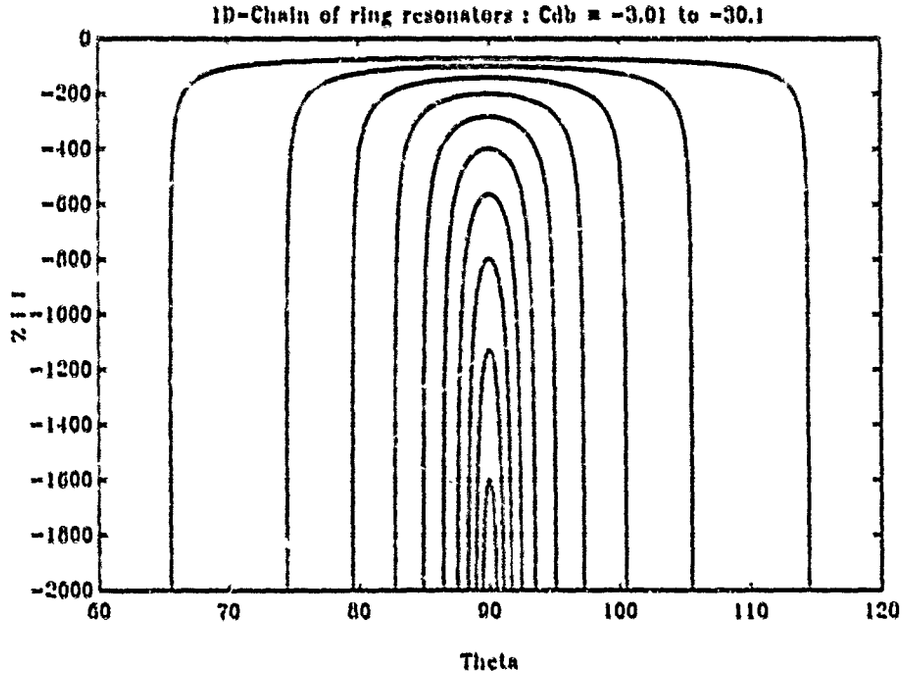


Figure 44. One-Dimensional Chain of Ring-Resonators; Real Diagonal-Entry of the Image-Impedance-Matrix.

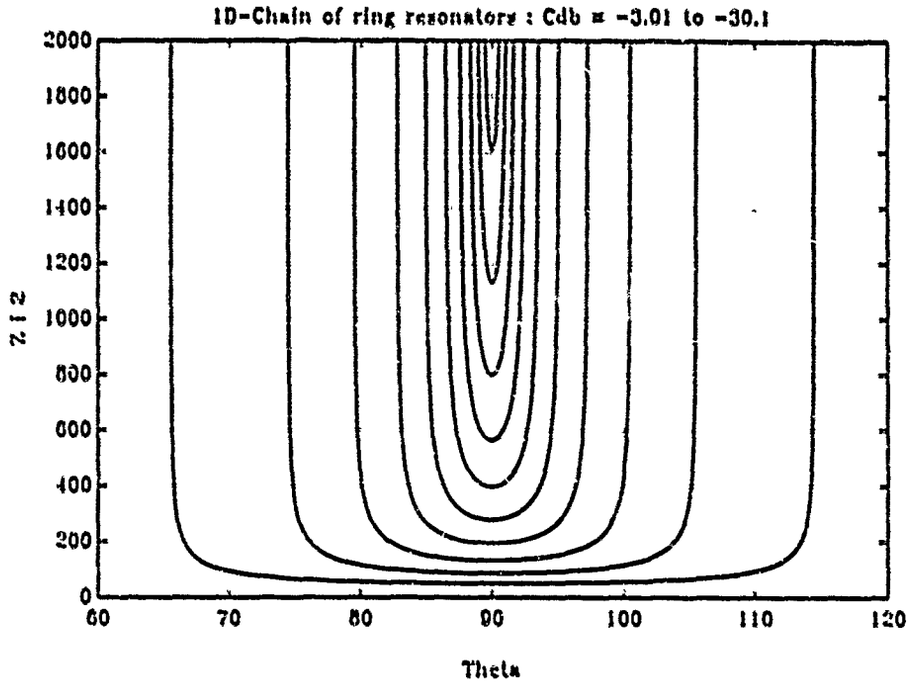


Figure 45. One-Dimensional Chain of Ring-Resonators; Real Off-Diagonal-Entry of the Image-Impedance-Matrix.

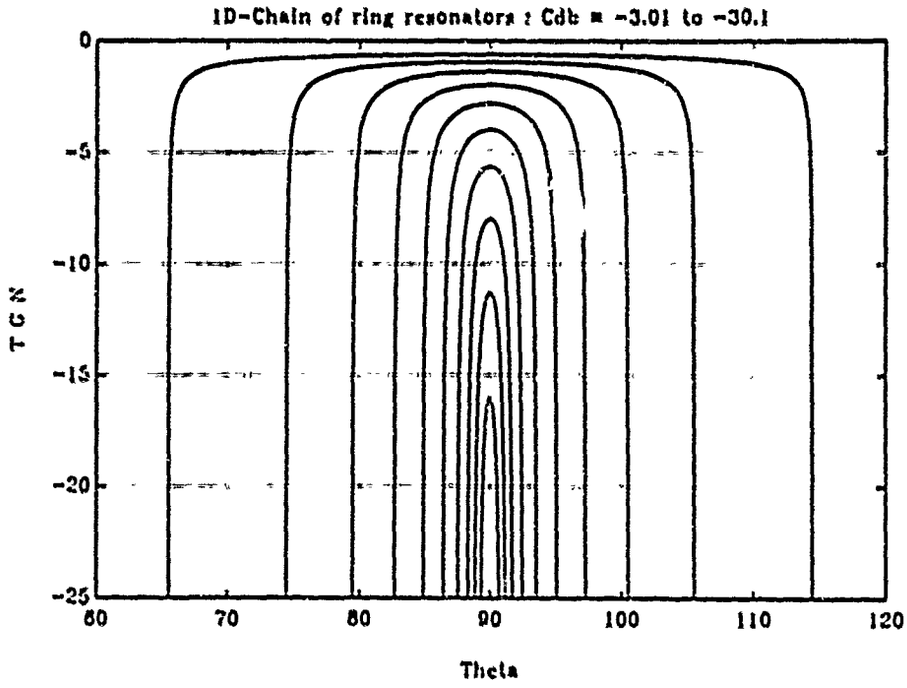


Figure 46. One-Dimensional Chain of Ring-Resonators; Normalized Group Delay.

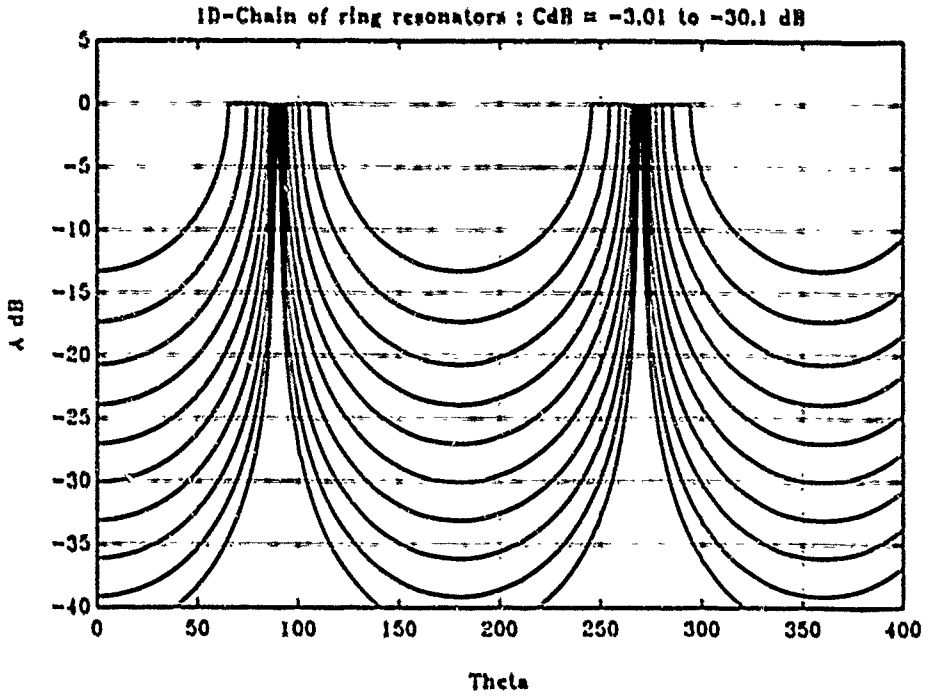


Figure 47. One-Dimensional Chain of Ring-Resonators; Attenuation per Unit-Cell Around and Across the First Two Passbands.

A MMP PROGRAM FOR COMPUTATIONS OF 3D ELECTROMAGNETIC FIELDS ON PCs

Lars Bomholt, Christian Hafner

Electromagnetics Group
Swiss Federal Institute of Technology
8092 Zurich, Switzerland

Abstract
The MMP (Multiple MultiPole) programs are based on the Generalized Multipole Technique (GMT). They offer fast and efficient computations of time harmonic electrodynamic problems with piecewise linear, homogeneuous and isotropic materials.
A new implementation for 3D problems has just been completed. It runs on PCs, workstations and T800 transputer networks. We present an outline of the method and implementation along with some examples.

Outline of the Method

MMP (Multiple MultiPole) programs are an implementation of the GMT (Generalized Multipole Technique). GMT covers several methods some of which have come from MoM. The MMP programs have evolved from an extension of the PM (Point Matching) technique. In GMT time harmonic analytic solutions of the field equations are used to model a field. Most important are multipole expansions which have a very local behaviour and are therefore easy to use. Several multipoles of finite order located outside the domain are used. Because the singularities of the expansions are away from the boundary, nearfield behaviour is very good. The method works for piecewise linear, homogenuous and isotropic materials in the time harmonic case. Lossy materials require no discretisation of the domains as in the MoM.

Field Expansions

In the MMP programs, the field inside a domain is expanded directly as a field of several multipole expansions:

$$F = \sum_{j=1}^{P} F_j \qquad \text{where} \qquad F_j = \sum_{l=1}^{N_j} a_{lj} f_{lj}$$

The f_{lj} are exact solutions of the Helmholtz Equations and can be written in two or in three dimensions be written as

$$f_{lj} = H_n^{(1)}(\kappa\varrho_j)\begin{matrix}\cos\\ \sin\end{matrix}(n\varphi_j)e^{(\gamma z_j)} \qquad \text{resp.} \qquad f_{lj} = h_n^{(1)}(kr_j)P_n^m(\cos\vartheta_j)\begin{matrix}\cos\\ \sin\end{matrix}(m\varphi_j)$$

$H_n^{(1)}$ and $h_n^{(1)}$ are Hankel functions; the origins (r=0) of the expansions are located outside the domain. Placing the expansions according to the shape of the domain, certain rules must be followed in order to avoid "almost" linear dependencies among the expansion functions.
The program supports also other solutions of the field equations like Bessel expansions, TEM expansions, plane waves and waveguide modes for rectangular and circular waveguides.

Matching

The expansions for the field in the various domains are matched in discrete matching points on the boundary of the domains. Normally all 6 boundary conditions for the normal and transversal electric and magnetic field are used. This makes it necessary to use overdetermined systems of equations, but improves the numerical behaviour significantly. Usually we have 3 to 10 times more equations than unknowns. To get accurate solutions the weighting of the equations is very important. The weighting factors used in the MMP programs have been derived by comparison of the extended PM with the Error Method and with the Projection Technique (PT). This allows to get as good results as the PT with Galerkin's choice of testing functions, but in a much easier way [1].

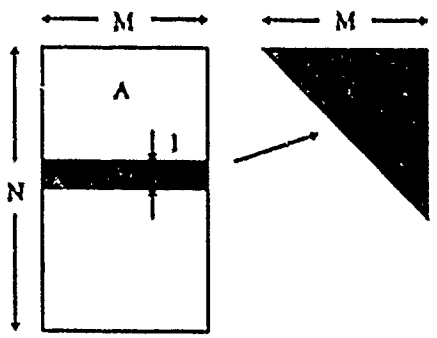
Solving the System of Equations

Solving the overdetermined system of equations in the least squares sense by a Cholesky procedure leads practically to the same results as a projection method with Galerkin's choice of testing functions without the need of solving integrals. Therefore it is much faster. The Cholesky procedure needs the matrix A^TA where A is the system matrix. Instead of this we use an updating technique which transforms A directly into a triangular matrix T using Given's plane rotations [2]. The triangular matrix is then solved by backsubstitution.

This algorithm is numerically better than the Cholesky procedure and also very memory efficient because it needs only the rows being updated and the triangular matrix. The original matrix A does not have to be stored. Since the condition of the matrix A is usually good this procedure is useful even for large matrices.

Another advantage is the easy implementation on parallel processors [3].

The quality of the calculation is estimated by the sum of the squares of the residues, which can be directly obtained from the triangular matrix, and by calculating the residues in the single matching points.



Updating of rows of an overdetermined system of equations A into a triangular matrix using Given's Plane Rotations. The algorithm is very memory efficient as only the shaded parts need to be stored. After the rows have been updated, they can be discarded.

Plotting and Zooming

After the unknowns have been determined the computation of the field in the different regions is a very fast procedure. Zooming in the field in details can be done very quickly and is a good procedure to get an impression of the quality of the solution.

Symmetries

Many objects being modeled have geometric symmetries. Considering symmetries can greatly reduce the number of matching points and unknowns needed. This is especially valuable in 3D modelling. One symmetry plane reduces M and N by a factor of 2. The smaller problem has to be solved twice: for even and odd symmetry about the plane. However often one of these parts can be excluded in advance.

The program supports rotational symmetries with one possible symmetry plane perpendicular to the symmetry axis, and for full 3D calculations arbitrary combinations of symmetries about the planes x=0, y=0 and z=0.

Implementation

The program is written in standard FORTRAN 77. It has a size of around 200 Kbytes, depending of the compiler used. For a problem with about 1000 unknowns about 9Mbytes of memory is required. This makes it possible to run the program on PCs and other small machines. It is currently installed on SUN workstations (SUN Fortran), PCs with 80x87 coprocessor or Weitek 1167 floating point accelerator (Ryan McFarland and NDP Fortran)and on IMS T800 transputer networks (3L Parallel Fortran).

Input and Output

The program communicates to the outside world via ASCII files. The input file contains all information about the problem: frequency, symmetries used, the coefficients of dielectricity, permeability and conduction of the various domains, kind, location and orientation of the expansions, the matching points, integrals to evaluate and the area in which the field will be plotted.

A mouse supported graphic input output editor for SUN workstations already exists [4]. Furthermore we also plan to write one for PCs.

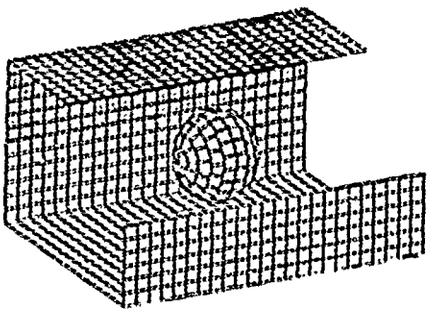
Range of Application

The program is designed for 2D and 3D scattering. Its strengths lie in nearfield calculations and in calculations involving lossy media [5]. In our group it is currently used for scattering on biological bodies, on metallic bodies, for calculation of aperture coupling and scattering and for waveguide problems.

Two easy examples which may further point out the use of the MMP programs in 3D scattering are shown in the appendix.

Future

Our group concentrates its research on MMP and its applications. The method and the programs are continuously improved. Planned are the combination with Laplace Transformation to allow time domain calculations and with techniques having other strengths, like FEM for nonlinear materials or MoM (NEC) for wire antennas.

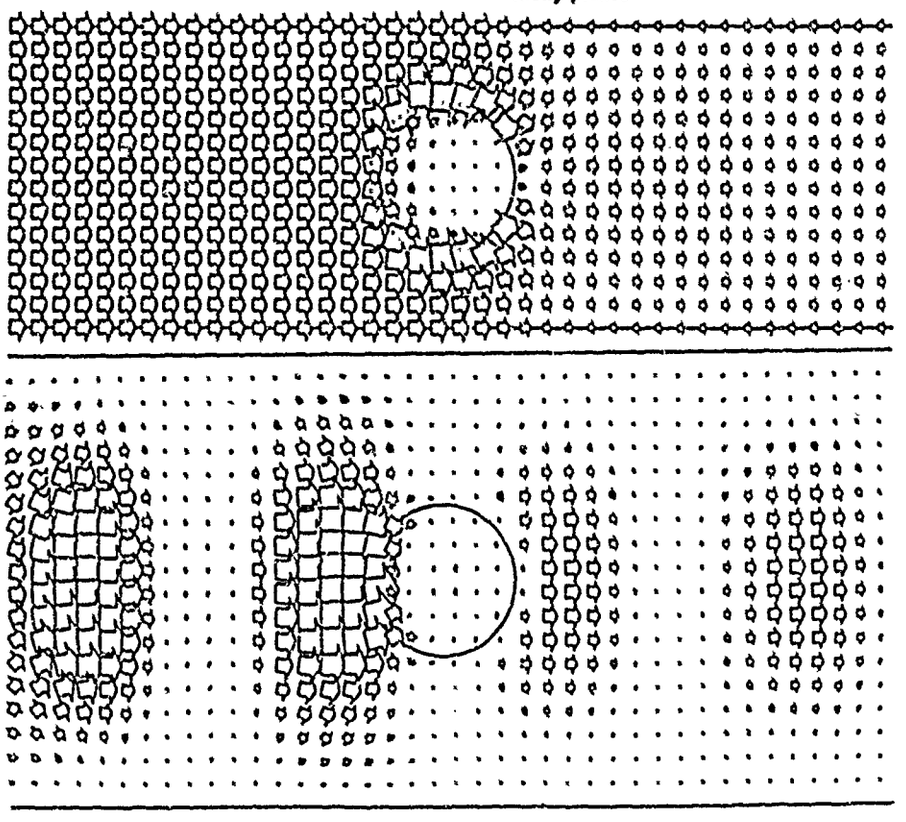


Rectangular waveguide with lossy dielectric sphere

A dielectric lossy sphere in a rectangular waveguide, in which only the H01 mode can propagate. The wave guide has a cross section of 3 by 2 units and is modeled in full 3D over a length of 4 units; the sphere has a diameter of 1 unit.

right: View of a section of the wave guide with the sphere inside. Only a quarter of the geometry (shaded) has to be discretized.

below and bottom: Poynting time average and Poynting field in the two symmetry planes

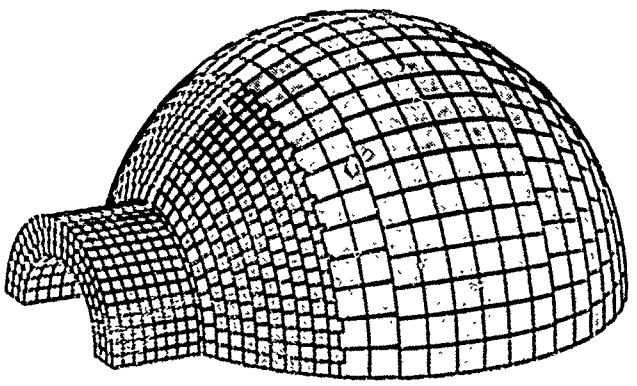


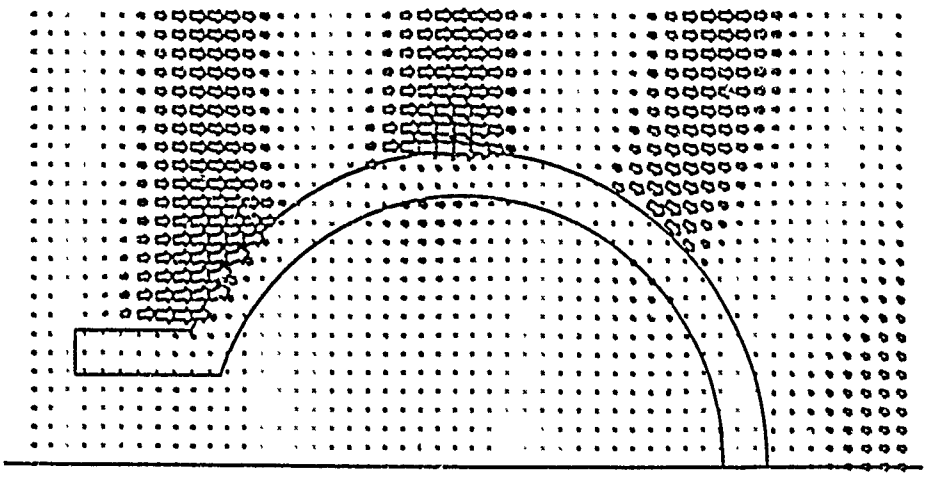
Igloo standing on a perfectly conducting plane with an incident plane wave

The igloo is modeled of dielectric conducting material. The dome is 3.5 units high, the entrance tunnel 1.5 units. The "snow" is 0.5 units thick. Only half of the igloo (shaded) has to be modelled, because a symmetry plane is used. The perfectly conducting plane on which the igloo is standing is brought into the model by another symmetry consideration. Each square corresponds to a matching point.

In this example the plane wave is polarized with E perpendicular to the plane and is incident horizontally towards the entrance. The model can also be used for waves incident from other directions.

The Poynting field in a plane standing perpendicular on the ground along the direction of propagation is shown.





Literature

[1] Ch. Hafner, "Numerische Berechnung elektromagnetischer Felder", *Springer, Berlin, 1987*

[2] J.J. Dongarra, C.B. Moler, J.R. Bunch, G.W. Stewart, "LINPACK User's Guide", *SIAM, Philadelphia, 1979*

[3] Ch. Hafner, L. Bomholt, "Implementation and Performance of MMP Programs on Transputers", *5th Annual Review of Progress in Applied Computational Electromagnetics (ACES), Conference Proceedings, March 1989*

[4] P. Regli, N. Kuster, "Graphic Output Routines of the MMP Program Package on PCs and Sun Workstations", *5th Annual Review of Progress in Applied Computational Electromagnetics (ACES), Conference Proceedings, March 1989*

[5] N. Kuster, R. Ballisti, "MMP-Method-Simulation of Antennae with Scattering Objects in the Closer Nearfield", *IEEE Trans. Magn., Vol MAG-25, July 1989*

Increasing Oil Production From A Well With Radio Waves

E. Sumbar, F.E. Vermeulen, and F.S. Chute

Applied Electromagnetics Laboratory
Department of Electrical Engineering
University of Alberta
Edmonton, Alberta, Canada, T6G 2G7
(403) 492-3332

Abstract

A novel technique for enhancing the recovery of heavy oil from deep wells is being studied. The technique involves the propagation of high frequency electromagnetic energy through the lossy (loss tangent about 3) oil-bearing formation and takes advantage of the heat generated by the dissipation of the wave. An antenna structure installed at the bottom of a well and radiating 5 to 50 kW of power at frequencies in the range 100 kHz to 5 MHz can raise the temperature of the surrounding strata by more than 100 Celsius degrees above *in situ* conditions within several months. This increase in temperature causes a dramatic reduction in oil viscosity in the vicinity of the well which in turn lowers flow resistance and allows the production rates to be significantly higher than would otherwise be expected.

A two-dimensional finite element code called FEAST (**F**inite **E**lement **A**nalysis of **S**ubterranean Radio **T**ransmission) is being developed to model this system. FEAST provides an azimuthally symmetric solution to Maxwell's equations in cylindrical coordinates for arbitrary lossy materials. The program uses the resultant internal heating rates to solve the transient heat flow equation. As the thermal solution advances in time, the electromagnetic fields and the electrical heating terms are reevaluated at specified intervals in order to account for the changes in the electrical properties of the formation with temperature.

FEAST has been successfully used to replicate many theoretical and experimental results for antennas operating in various media at constant temperature. Encouraged by this, we have examined several antenna heating-schemes of practical interest to us. We present here an overview of FEAST and an analysis of a typical *in situ* heating arrangement.

Introduction

To model the temperature rise near a transmitting antenna operating in a lossy medium, the program FEAST sequentially evaluates Maxwell's equations and the transient heat conduction equation.

For the case of axisymmetric cylindrical antennas, Maxwell's equations can be

written as

$$\nabla \times \mathbf{H} = -\frac{\partial H_\phi}{\partial z}\hat{\mathbf{a}}_r + \frac{1}{r}\frac{\partial r H_\phi}{\partial r}\hat{\mathbf{a}}_z = (\sigma + j\omega\epsilon)\,\mathbf{E}$$

$$\nabla \times \mathbf{E} = -j\omega\mu\, H_\phi\, \hat{\mathbf{a}}_\phi.$$

These equations can be manipulated to give an expression for rH_ϕ:

$$-\frac{\partial}{\partial r}\left(\frac{1}{r(\sigma + j\omega\epsilon)}\frac{\partial r H_\phi}{\partial r}\right) - \frac{\partial}{\partial z}\left(\frac{1}{r(\sigma + j\omega\epsilon)}\frac{\partial r H_\phi}{\partial z}\right) + \frac{j\omega\mu}{r} r H_\phi = 0$$

from which the E-fields may be derived.

$$E_z = \left(\frac{1}{r(\sigma + j\omega\epsilon)}\frac{\partial r H_\phi}{\partial r}\right), \text{ and}$$

$$E_r = \left(\frac{-1}{r(\sigma + j\omega\epsilon)}\frac{\partial r H_\phi}{\partial z}\right).$$

Knowing the E-fields, the rate of energy dissipation in the medium may be evaluated from

$$\sigma |\mathbf{E}|^2.$$

This quantity represents the internal heating rate which drives the transient heat conduction equation.

$$\rho c r \frac{\partial T}{\partial t} - \frac{\partial}{\partial r}\left(kr\frac{\partial T}{\partial r}\right) - \frac{\partial}{\partial z}\left(kr\frac{\partial T}{\partial z}\right) = r\sigma|\mathbf{E}|^2.$$

The volumetric heat capacity ρc has units of J/m³-°C; the thermal conductivity k is given in units of W/m-°C; and T is the temperature in °C.

Implementation

FEAST is structured around the solution of the transient heat conduction equation. At the beginning of the calculation sequence and as the solution steps in time, the program evaluates the electromagnetic fields and the electrical heating rates. These electrical parameters are updated only when the temperature dependent electrical conductivity of the medium has changed by a user specified amount. (The other electrical and thermal properties of the material are assumed to remain constant with temperature.) A typical temperature profile for the electrical conductivity of oil sand is (Chute *et al.*, 1988)

$$\sigma(T) = 10\,(\,0.0263\Delta T + 17.05\times10^{-5}\Delta T^2 - 9.77\times10^{-7}\Delta T^3\,),$$

with T in °C, $\Delta T = T - 24$, and σ in mS/m.

The numerical techniques in FEAST are based on those found in a teaching program called UNAFEM. UNAFEM is a finite element code written in FORTRAN by W. John Denkmann and David S. Burnett of AT&T Bell Laboratories which uses the Galerkin method in its approach to the solution of partial differential equations. David Burnett has written a book to

support UNAFEM called *Finite Element Analysis: From Concepts to Applications*.

To model the domain for the finite element analysis of Maxwell's equations, a normalized mesh was constructed made up of 424 C^0-quadratic isoparametric elements comprising 943 nodes. A subset of this mesh was used to define the thermal domain with 119 C^0-linear elements and 84 nodes. A schematic representation of the mesh is given in Fig. 1.

Antennas of various heights can be accommodated by scaling all of the coordinates of the normalized mesh. The scale factor can not be too much greater than the wavelength, expressed in meters, however as the node density may become too low to accurately represent the undulations of the wave solution. On the other hand, the scale factor can not be too small because the far boundary on which the radiation boundary condition is imposed will be too close to the point of excitation. In a small region surrounding the antenna, groups of nodes can be translated independently of the larger mesh to allow a range of antenna diameters and coating thicknesses. The meshes for both thermal and electrical parts of the problem are scaled identically.

FEAST's solution of the transient heat conduction equation was validated by analyzing a hypothetical problem and comparing the results to those obtained with a second independent computer code (Hiebert *et al.*, 1983). As well, solutions to a variety of antenna propagation problems were obtained with FEAST and compared to theory and experiment. Both thermal and electrical solvers performed satisfactorily. Verification of FEAST's output is continually checked as new validation possibilities comes to light.

Simulation Results

One possible configuration for a practical antenna heater was designed and tested with FEAST. A diagram of the apparatus appears in Fig. 2. The following simulation parameters were used.

frequency ..... 3 MHz

power ..... 5 kWrms (constant)

initial temperature ..... 15°C

elapsed heating time ..... 90 days

oil sand electrical conductivity, $\sigma(T)$ ..... (as given earlier)

oil sand ϵ_r 20

oil sand μ_r 1

oil sand thermal conductivity, k ..... 1.8 W/m-°C

oil sand volumetric heat capacity, ρc ..... 2 MJ/m³-°C

air thermal conductivity ..... 0.001 W/m-°C

air volumetric heat capacity ..... 1 kJ/m³-°C

Given these parameters, the electrical characteristics in the oil sand are

wavelength, λ = 15.5 m

skin depth, δ = 3.4 m

loss tangent = 3.0.

Using a time step size of 500 seconds, 15553 loops of the thermal solver were executed. A total of 28 electrical solutions were required to update the electrical heating terms using a 10% $\Delta\sigma$ threshold. Total program run time was approximately 8 hours on a Macintosh II computer.

On the basis of the predicted initial input impedance of the antenna, 5 kW of power could be generated with a driving point voltage and current of 617 Vrms and 8.5 Arms, respectively.

Some results from the run are presented in Figs. 3 and 4, showing in one, the change in antenna impedance as time progresses and temperatures rise, and in the other, the temperature distribution near the antenna at the end of the 90-day heating period. This last figure shows a significant temperature rise along the entire antenna length (which would also serve as the oil collector in a practical application). The higher temperatures are seen to extend about 3 meters into the oil bearing region as well.

Conclusions

A finite element FORTRAN code called FEAST has been developed for studying the thermal and electrical phenomena of cylindrical antennas radiating into lossy materials. It is being used to evaluate alternative techniques for enhancing the recovery of oil from heavy-oil wells. Results of practical significance have been obtained for the preliminary antenna designs which were tested.

References

Burnett, David S., *Finite Element Analysis: From Concepts to Applications*, Addison-Weseley, 1987.

Chute, F.S., F.E. Vermeulen, and E. Sumbar, "Update of Electrical Conductivity Measurements and an Introduction to FEAST", AOSTRA Interim report, June 1988.

Hiebert, A.D., C.E. Capjack, F.S. Chute, F.E. Vermeulen, "A simulation code for investigating 2D heating of material bodies by low frequency electric fields", *Appl Math Modelling* 7, 366 (1983).

Figure Captions

FIG. 1 The finite element mesh used by the thermal and electrical solvers within FEAST. Boundary conditions are also indicated.

FIG. 2 A schematic representation of a proposed antenna heating arrangement.

FIG. 3 Antenna driving point impedance as a function of time.

FIG. 4 Distribution of temperatures in °C for the upper half of the domain at the end of the 90-day heating period.

Figure 1

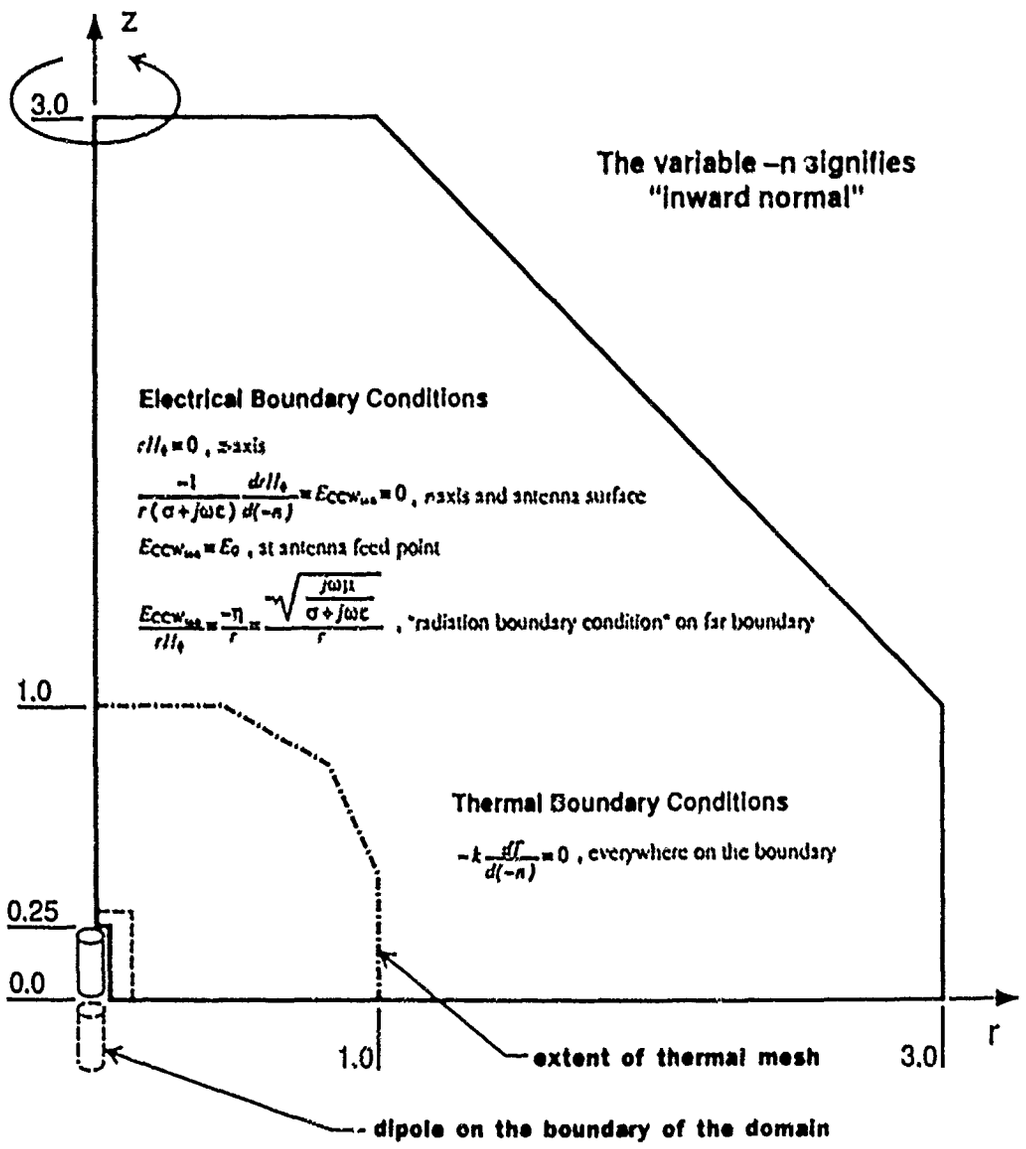
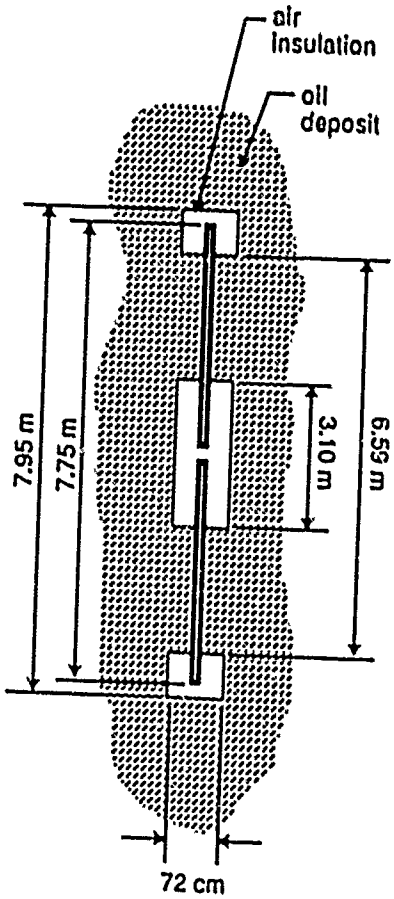

z
3.0
The variable –n signifies "inward normal"
Electrical Boundary Conditions
$rH_\phi = 0$, z-axis
$\frac{-1}{r(\sigma+j\omega\varepsilon)}\frac{drH_\phi}{d(-n)} = E_{ccw_{ss}} = 0$, r-axis and antenna surface
$E_{ccw_{ss}} = E_0$, at antenna feed point
$\frac{E_{ccw_{ss}}}{rH_\phi} = \frac{-\eta}{r} = \frac{-\sqrt{\frac{j\omega\mu}{\sigma+j\omega\varepsilon}}}{r}$, "radiation boundary condition" on far boundary
1.0
Thermal Boundary Conditions
$-k\frac{dT}{d(-n)} = 0$, everywhere on the boundary
0.25
0.0
1.0
extent of thermal mesh
3.0
r
dipole on the boundary of the domain

Figure 2



15.5 cm
antenna
diameter
and a
3 cm gap

Figure 3

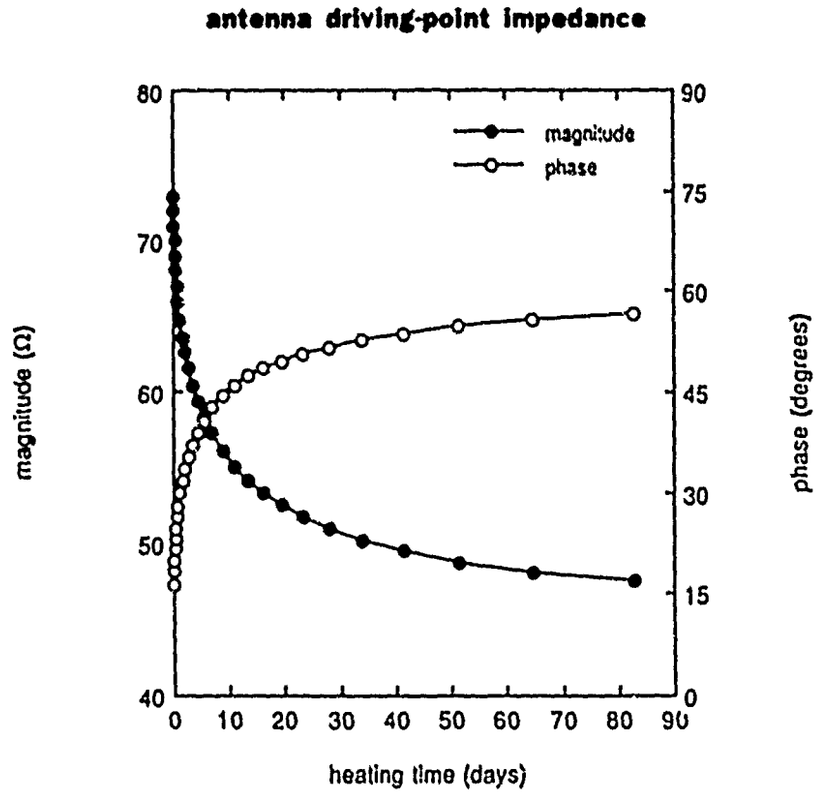
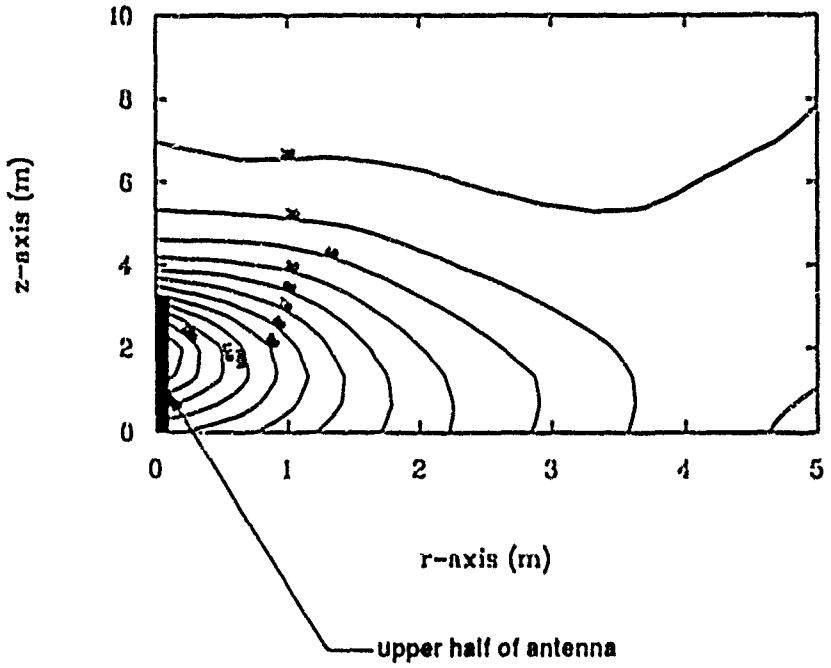

antenna driving-point impedance
magnitude
phase
magnitude (Ω)
phase (degrees)
heating time (days)
80
70
60
50
40
90
75
60
45
30
15
0
0
10
20
30
40
50
60
70
80
90

Figure 4



FINITE ELEMENT ANALYSIS OF MICROSTRIP SYSTEMS IN THE VICINITY OF AN EDGE

Michael E. Baginski, Lloyd S. Riggs, Hugh D. Williams, Fred J. German
Department of Electrical Engineering
Auburn University
Auburn, AL. 36849-3501

March 1989

FINITE ELEMENT ANALYSIS OF MICROSTRIP SYSTEMS IN THE VICINITY OF AN EDGE

ABSTRACT

TEM ELECTRICAL CHARACTERISTICS OF AN INFINITELY LONG MICROSTRIP STRUCTURE IN THE VICINITY OF AN EDGE ARE INVESTIGATED VIA A SERIES OF NUMERICAL SIMULATIONS. A FINITE ELEMENT ROUTINE IS USED AS THE BASIS FOR THE SIMULATIONS THAT SOLVE THE QUASI-STATIC MAXWELL EQUATIONS ($\nabla \cdot D = \rho_f$) SUBJECT TO THE APPROPRIATE ELECTROMAGNETIC BOUNDARY CONDITIONS. THE GEOMETRIC AND ELECTRICAL PARAMETERS USED IN THE SIMULATIONS ARE SELECTED TO BE REPRESENTATIVE OF THOSE TYPICALLY ENCOUNTERED IN PRINTED CIRCUIT BOARD FABRICATIONS (MICROSTRIP FEATURES ~ 10 - 30 MILS). SEVERAL PLOTS OF THE VECTOR ELECTRIC FIELD INTENSITY AND CONTOURS OF EQUAL ELECTRIC POTENTIAL IN THE VICINITY OF THE DIELECTRIC'S EDGE ARE PRESENTED. THESE PLOTS IDENTIFY THE GENERAL PERTURBATION IN THE FIELD MAPPING CAUSED BY THE PRESENCE OF THE EDGE; THERE BY PROVIDING THE DESIGN ENGINEER WITH INSIGHT INTO THE CHARACTER OF THE FRINGING EFFECTS. BASED ON THE SIMULATIONS, AN ANALYTIC EXPRESSION FOR THE MICROSTRIP-TO-GROUND CAPACITANCE IS ALSO DEVELOPED. THE FORMULATION SHOWS GOOD OVERALL AGREEMENT WHEN COMPARED TO THE SIMULATED RESULTS (MAXIMUM DIFFERENCE OF 10%) FOR THE RANGE OF PARAMETERS USED.

INTRODUCTION

MICROSTRIP CIRCUITRY IS USED EXTENSIVELY IN BOTH THE FABRICATION OF MICROELECTRONIC AND PRINTED CIRCUIT BOARD SYSTEMS. THERE EXISTS A LARGE VOLUME OF TABULATED DATA AND APPROXIMATE ANALYTIC EXPRESSIONS FOR THE ELECTRICAL CHARACTERISTICS OF THESE STRUCTURES IN THE VICINITY OF INFINITE PLANER SURFACES, [1-2]. HOWEVER, THE DESIGN ENGINEER IN MANY CASES MUST LOCATE CONDUCTING LINES IN THE PROXIMITY OF AN EDGE AND THUS FACES THE PROBLEM OF ESTIMATING THE CORRESPONDING CHANGE IN THE MICROSTRIP'S ELECTRICAL PROPERTIES. THIS IS OFTEN DIFFICULT AND FORCES SEVERAL TRIAL AND ERROR DESIGNS BEFORE CORRECT OPERATION OF THE SYSTEM IS ACHIEVED. THIS TYPE OF EDGE EFFECT PROBLEM WILL MOST LIKELY WORSEN AS THE PACKING DENSITY AND SPEED OF LOGIC DEVICES INCREASE.

AN OBVIOUS SOLUTION TO THIS DESIGN PROBLEM IS TO PROVIDE A CHARACTERIZATION OF THE ELECTRICAL PROPERTIES OF MICROSTRIP STRUCTURES INCLUDING EDGE EFFECTS; THIS BEING THE FOCUS OF THE RESEARCH PRESENTED HERE. A FINITE ELEMENT ROUTINE SERVES AS THE BASIS FOR A COMPUTER SOLUTION OF THE TEM ELECTRICAL CHARACTERISTICS OF THE MICROSTRIP SYSTEM IN THE VICINITY OF AN EDGE [3-4]. THE MICROSTRIP-TO-GROUND CAPACITANCE (PER UNIT LENGTH) IS DEPICTED AS A FUNCTION OF DIELECTRIC THICKNESS, DIELECTRIC PERMITTIVITY, MICROSTRIP SEPARATION DISTANCE FROM THE EDGE, MICROSTRIP LINE WIDTH AND THICKNESS. THE CATALOGUED DATA IS PRESENTED IN A FORMAT THAT FACILITATES INTERPOLATION BETWEEN CURVES AND GENERAL GEOMETRIC SCALING OF DIMENSIONS. AN APPROXIMATE ANALYTIC EXPRESSION OF THE MICROSTRIP'S ELECTRICAL PROPERTIES FOR SEVERAL OF THE CASES CONSIDERED IS ALSO GIVEN.

TEM NUMERICAL ANALYSIS

GEOMETRY OF REGION

FIGURE 1 IDENTIFIES THE RELATIVE CROSS SECTIONAL DIMENSIONS OF THE MICROSTRIP SYSTEM. THE MICROSTRIP LINE AND INFINITE GROUND PLANE ARE ASSUMED PERFECTLY CONDUCTING; ONLY THE ELECTRICAL PARAMETERS ASSOCIATED WITH THE TEM MODE OF OPERATION ARE CONSIDERED. THE SUBSTRATE LAYER HAS THICKNESS H AND PERMITTIVITY ϵ. IT INTERFACES WITH THE MICROSTRIP AS SHOWN, WITH THE SURROUNDING REGION ASSUMED TO BE FREE SPACE. THE MICROSTRIP HAS THICKNESS T AND WIDTH W SEPARATED FROM THE EDGE BY DISTANCE X. THE LENGTH OF THE LINE IS ASSUMED INFINITE AND CROSS SECTION INVARIANT WITH LENGTH.

NUMERICAL MODEL

IN THIS ANALYSIS THE GOVERNING SET OF ELECTROMAGNETIC EQUATIONS REDUCES TO THE QUASI-ELECTROSTATIC EQUATIONS:

$$\nabla \cdot D = \rho_F \tag{1}$$

$$D = \epsilon E \tag{2}$$

$$E = -\nabla \phi \tag{3}$$

WHERE

ρ_F = FREE CHARGE DENSITY

D = ELECTRIC FLUX DENSITY

E = ELECTRIC FIELD INTENSITY

ϕ = ELECTRIC POTENTIAL

THE CLASSIC ELECTROSTATIC BOUNDARY CONDITIONS ARE ASSUMED: THE TANGENTIAL COMPONENT OF THE ELECTRIC FIELD ACROSS A DIELECTRIC INTERFACE IS CONTINUOUS ($E_{T1} = E_{T2}$) AND THE NORMAL COMPONENT OF THE ELECTRIC FLUX DENSITY IS CONTINUOUS AT THE INTERFACE ($D_{N1} = D_{N2}$) [5]. THE PER UNIT LENGTH MICROSTRIP TO GROUND PLANE CAPACITANCE IS DETERMINED BASED ON THE FUNDAMENTAL DEFINITION OF CAPACITANCE:

$$C = (1/V)(1/2)\int E^2 d(vol) \qquad (4)$$

WHERE

C = CAPACITANCE IN FARADS

V = POTENTIAL DIFFERENCE BETWEEN THE SURFACES (PLATES) WHERE THE CAPACITANCE IS DETERMINED

IN THE MODELING, THE MICROSTRIP'S ELECTROSTATIC POTENTIAL IS SET AT 1 VOLT AND THE INFINITE CONDUCTING GROUND PLANE AT 0 VOLTS. CAPACITANCE IS DETERMINED NUMERICALLY ACCORDING TO THE ABOVE EQUATION.

GENERALLY, WHEN NUMERICAL METHODS ARE USED TO SOLVE A TIME INDEPENDENT LINEAR DIFFERENTIAL EQUATION, THE ERROR CAN BE REDUCED TO ANY NECESSARY LEVEL [6]. FOR THE RESEARCH DISCUSSED HERE, THE WORST CASE ESTIMATE OF THE NUMERICAL ERROR IS APPROXIMATELY 0.01 PERCENT BASED ON STANDARD ERROR ESTIMATION TECHNIQUES (TECHNIQUES FOR DETERMINING NUMERICAL ERROR ARE DISCUSSED IN DETAIL IN [7]). THE SPECIFIC FINITE ELEMENT COMPUTER SOLUTION USES THE METHOD OF TRIANGULATION (TRIANGLE PATCH METHOD). A COMPLETE DESCRIPTION OF THE FINITE ELEMENT CODE USED AS THE BASIS OF THE SIMULATIONS IS GIVEN BY BAGINSKI [3]. FOR THE MICROSTRIP TO GROUND CAPACITANCE'S DESCRIBED HERE, THE FINAL TRIANGULAR GRID IS COMPOSED OF 1000 TRIANGLES WITH MESH DENSITY GRADED TO BE LARGEST IN THE VICINITY OF GREATEST CHANGE IN THE ELECTROSTATIC POTENTIAL'S SOLUTION.

THE SECOND SOURCE OF ERROR IS INHERENT WHENEVER INFINITE BOUNDARIES ARE TRUNCATED. FOR THE MICROSTRIP STRUCTURE CONSIDERED, IT IS NECESSARY TO LIMIT BOTH THE VERTICAL AND HORIZONTAL DIMENSIONS. THE DIMENSIONS USED ARE SELECTED BY SIMULTANEOUSLY INCREASING EACH UNTIL THE REGIONS TOTAL STORED ELECTROSTATIC ENERGY IS APPROXIMATELY INVARIANT (REGION'S VERTICAL AND HORIZONTAL EXTENT SET AT 100 MILS AND 1500 MILS RESPECTIVELY). ALSO, AS A PRECAUTIONARY MEASURE TO ENSURE THE CODE'S CORRECT OPERATION, THE CLASSICAL PROBLEM OF DETERMINING THE CAPACITANCE OF A THIN WIRE ABOVE A INFINITE GROUND PLANE IS SOLVED NUMERICALLY WITH NEGLIGIBLE DIFFERENCE IN THE SOLUTION WHEN COMPARED TO THE CANONICAL ANALYTIC SOLUTION [8].

RESULTS

FIGURE 2 AND 3 DEPICT THE VECTOR ELECTRIC FIELD INTENSITY (D) AND ELECTRICAL POTENTIAL MAPPING THAT OCCURS AS THE EDGE SEPARATION DISTANCE IS INCREASED FOR W = 10 MILS, H = 10 MILS, T = 0.7 MILS AND ϵ_r = 2, 10. ONE OF THE MOST OBVIOUS RESULTS THAT CAN BE GLEANED FROM A QUALITATIVE COMPARISON OF THE TWO FIELD PLOTS IS THAT THE INCREASE IN THE DIELECTRIC'S RELATIVE PERMITTIVITY CAUSES A GREATER PERCENTAGE OF THE ELECTRIC FLUX TO BE FOCUSED BETWEEN THE ELECTRIFIED EQUAL POTENTIAL SURFACES. THIS BEHAVIOR IS EXPECTED INTUITIVELY. THE EDGE EFFECT PERTURBATIONS IN THE CONTOURS OF EQUAL ELECTRIC POTENTIAL ARE MORE PRONOUNCED AS THE RELATIVE PERMITTIVITY IS INCREASED. THIS OBSERVATION SUGGESTS THAT EITHER FREE OR BOUND CHARGE DENSITIES ARE LIKELY TO BE INDUCED IN THE PROXIMITY OF THE EDGE IF THE MICROSTRIP SYSTEM IS FABRICATED. EDGE CHARGING OF THIS TYPE IS HIGHLY SENSITIVE TO ELECTROMAGNETIC INTERFERENCE FROM STRAY SOURCES AND, BECAUSE OF THE DIRECT CAPACITIVE COUPLING TO THE MICROSTRIP SYSTEM, SHOULD BE MINIMIZED.

THE ELECTRICAL AND GEOMETRIC PARAMETERS USED IN THE CAPACITIVE CHARACTERIZATION PRESENTED BELOW ARE REPRESENTATIVE OF THOSE TYPICALLY ENCOUNTERED IN PRINTED CIRCUIT BOARD DESIGN [10]. THESE CURVES MAY BE SCALED TO ACCOMMODATE INTEGRATED CIRCUIT GEOMETRIES AS WELL.

FIGURE 4 IDENTIFIES CAPACITANCE VERSUS THE MICROSTRIP DISTANCE FROM THE DIELECTRIC EDGE FOR RELATIVE PERMITTIVITIES OF 1 - 10 AND DIELECTRIC THICKNESSES OF 10 AND 20 MILS. (HORIZONTAL AXIS IS SHOWN IN METERS NOT MILS). THERE ARE SEVERAL INTERESTING CHARACTERISTICS TO NOTE. THE MOST OBVIOUS IS THAT AS THE RELATIVE PERMITTIVITY INCREASES THE OVERALL CAPACITANCE INCREASES. FIGURE 5 IDENTIFIES THE CHANGE IN MICROSTRIP-TO-GROUND PLANE CAPACITANCE AS THE DIELECTRIC THICKNESS (H) IS INCREASED AND RELATIVE PERMITTIVITY HELD CONSTANT AT 10. THE CAPACITIVE CHARACTERISTIC CURVES FOR THE ABOVE CASES SHOW NO UNEXPECTED TRAITS. IN EVERY CASE THE MICROSTRIP'S RELATIVE CAPACITANCE IS A MINIMUM WHEN X = 0 (MICROSTRIP LOCATED AT EDGE) AND MONOTONICALLY INCREASES AS DISTANCE X IS INCREASED UNTIL A RELATIVE MAXIMUM VALUE IS REACHED. THE POINT AT WHICH THE THE RELATIVE MAXIMUM IS REACHED IS DEPENDENT ON ALL THE VARIABLES CONSIDERED. IN GENERAL THIS DISTANCE IS PROPORTIONAL TO DIELECTRIC THICKNESS (H) AND THE MICROSTRIP'S WIDTH (W).

THE NATURE OF THE MICROSTRIP'S CHARACTERISTIC CURVES SUGGESTS THAT A RELATIVELY SIMPLISTIC ANALYTIC DESCRIPTION IS AT LEAST POSSIBLE FOR THE RANGE OF PARAMETERS CONSIDERED IN THE SIMULATIONS. AN ANALYTIC EXPRESSION THAT INCLUDES EDGE EFFECTS WAS DEVELOPED BY FIRST COMPARING SEVERAL OF THE ACCEPTED FORMULATIONS FOR MICROSTRIP CAPACITANCE [11] TO THE SIMULATED RESULTS. THE VALUES OF SIMULATED CAPACITANCE FAR FROM THE EDGE (CAPACITANCE AT A RELATIVE MAXIMUM) WERE FOUND TO BE IN GOOD AGREEMENT WITH THE APPROXIMATE FORMULATIONS GIVEN BY CANRIGHT [12] FOR ϵ_r RANGING FROM 1-5. CANRIGHT'S FORMULATION FOR MICROSTRIP-TO-GROUND PLANE CAPACITANCE IS GIVEN AS:

$$Z_0 = (60/(\epsilon_{r1})^{0.5})\text{LN}(5.97H/(0.8W+T)) \quad (5)$$

$$\epsilon_{r1} = (\epsilon_r + 1)/2 + (\epsilon_r - 1)/2(1 + 10H/W)^{-0.5} \quad (6)$$

$$C = (\mu\epsilon)^{0.5}/Z_0 \quad (7)$$

AN ANALYTIC SOLUTION FOR AN INFINITE MICROSTRIP'S ELECTRIC FIELD AND POTENTIAL HAS BEEN PRESENTED BY BAUM [13]. BAUM EMPLOYED THE METHOD OF SEPARATION OF VARIABLES TO SOLVE THE LAPLACE EQUATION (IN TWO DIMENSIONS) AND A HYPERBOLIC GENERATING FUNCTION TO CONFORMALLY MAP (TRANSFORM) THE CROSS SECTIONAL POTENTIAL VARIATION FOR AN INFINITE PLANAR STRUCTURE. AFTER QUALITATIVELY CONSIDERING THE INFLUENCE OF THE MICROSTRIP'S EDGE ON THE SOLUTION DEDUCED BY BAUM A SERIES OF MODELS USING A MODIFIED HYPERBOLIC TANGENT FUNCTION AS THE BASIS WERE COMPARED TO THE SIMULATED RESULTS RELATIVELY GOOD AGREEMENT WAS FOUND (MAXIMUM VARIANCE ~10%) FOR THE CAPACITANCE DESCRIBED BY EQUATION 8 AND THE SIMULATED RESULTS. (FIGURE 6).

$$C = C_0(1 - \text{TANH}(U))/2 + C_1(1 + \text{TANH}(U))/2 \quad (8)$$

$$C_0 = (3\times10^8)/(60\text{LN}(5.97H/(0.8W+T))) \quad (9)$$

$$C_1 = (3\times10^8)(\epsilon_{r1})^{0.5}/(60\text{LN}(5.97H/(0.8W+T))) \quad (10)$$

$$U = \text{TAN}((W/2 + X)/H) \quad (11)$$

FIGURE 68. CONTRASTS THE CAPACITANCE RESULTING FROM THE SIMULATIONS TO THE ABOVE FORMULATION FOR THE PARAMETER VALUES LISTED. THE CAPACITANCE DESCRIBED BY THE ANALYTIC SOLUTION IS EASILY ADAPTED TO COMPUTER AIDED DESIGN CODES TYPICALLY USED IN THE INITIAL PHASES OF CIRCUIT BOARD DESIGN. EVEN THOUGH THE FORMULATION HAS BEEN DEVELOPED TO DEPICT THE SIMULATED CAPACITANCE VALUES FOR A LIMITED PARAMETER RANGE, IT AFFORDS THE DESIGN ENGINEER THE ABILITY TO SET LIMITS ON THE MICROSTRIP'S PROBABLE CHARACTERISTIC IMPEDANCE.

IT SHOULD BE NOTED THAT THIS MODEL HAS ONLY BEEN COMPARED TO RESULTS FOR A RELATIVELY SMALL RANGE OF VALUES AND MAY NOT BE ACCURATE GENERALLY. THE POSSIBILITY OF DEVELOPING A MORE COMPLETE ANALYTIC FORMULATION OF THE MICROSTRIP TO GROUND CAPACITANCE WILL BE INVESTIGATED IN THE FUTURE.

THE SIMULATED AND ANALYTIC FAMILY OF CURVES DESCRIBING THE PER UNIT LENGTH MICROSTRIP-TO-GROUND CAPACITANCE MAY BE USED TO INFER THE CAPACITANCE OF MICROSTRIP STRUCTURES THAT HAVE CROSS SECTIONAL GEOMETRIES OUT OF THE SIMULATED PARAMETRIC RANGE. THIS IS ALLOWABLE IF THE GEOMETRIC RATIOS OF H,W,T,X, AND ϵ_r IN THE MICROSTRIP CONSIDERED ARE IDENTICAL TO THE RELATIVE RATIO OF THESE PARAMETERS IN A GIVEN SIMULATION. IF THIS CONDITION IS MET, THE PER UNIT LENGTH CAPACITANCE OF THE STRUCTURE CONSIDERED IS IDENTICAL TO THAT IDENTIFIED IN THE SIMULATED CHARACTERISTIC CURVE OF EQUAL GEOMETRIC RATIOS AND IDENTICAL PERMITTIVITY.

THE FUNDAMENTAL REASON THE ABOVE INFERENCE IS POSSIBLE STEMS FROM THE FACT THAT CAPACITANCE IN ALL CANONICAL CASES IS A FUNCTION OF THE RATIO OF THE GEOMETRIC PARAMETERS AND PERMITTIVITY (PERMITTIVITY NOT A FUNCTION OF FIELD STRENGTH) ALONE.

CONCLUSIONS

IN THE PRECEDING SECTIONS THE MICROSTRIP-TO-GROUND CAPACITANCE WAS CHARACTERIZED AS A FUNCTION OF CROSS SECTIONAL GEOMETRY, MICROSTRIP'S SEPARATION DISTANCE FROM THE DIELECTRIC'S EDGE AND RELATIVE PERMITTIVITY (ϵ_r). AN ANALYTIC FORMULATION OF THIS CAPACITANCE WAS DEVELOPED AND FOUND TO BE IN GOOD OVERALL AGREEMENT WITH THE SIMULATED VALUES. THE CAPACITIVE CHARACTERISTIC CURVES WERE ALSO SHOWN TO BE USEFUL IN DETERMINING PER UNIT LENGTH CAPACITANCE FOR MICROSTRIP GEOMETRIES OUTSIDE THE RANGE CONSIDERED PROVIDING THAT THE GEOMETRIC RATIOS OF THE STRUCTURE CONSIDERED ARE EQUAL TO THAT OF THE CHARACTERISTIC CURVE CONSIDERED AND THE RELATIVE PERMITTIVITIES IDENTICAL.

References

[1] H.R. Kaupp, "Characteristics of microstrip transmission lines," IEEE Trans. Electronic Comp., Vol. EC-16, No.2, April 1967

[2] S.Y. Poh, W.C. Chew, and J.A. Kong, "Approximate formulas for line capacitance and characteristic impedance of microstrip line," IEEE Trans. Microwave Theory Tech, vol. MTT-29, pp. 135-142, Feb. 1981

[3] M.E. Baginski, "Finite element simulation of the atmosphere's electromagnetic response to charge perturbations associated with lightning," Ph.D. thesis, The Pennsylvania State University, 111 pp 1987

[4] M.E. Baginski, L.S. Riggs, F.J. German, "Electrical berakdown of soil about earthed conductors resulting from late time EMP effects," IEEE Trans. Electrogn. Compat., Vol. 30, No. 3, August 1988

[5] J.D. Jackson, "Classical Electrodynamics," John Wiley & Sons, Inc., 1975

[6] K.S. Kunz, et. al., "Lawrence Livermore National Laboratory Electromagnetic Measurement Facility," IEEE Trans. Electromagn. Compat., vol. EMC-29, no.2, pp. 93-103, May 1987

[7] P.P. Silvester and R.L. Ferrari, "Finite Elements for Electrical Engineers," Cambridge University Press, 1986

[8] W.R. Smythe, "Static and dynamic electricity," 3rd edition, McGraw-Hill, New York, 1969

[9] J. Van Bladel, "Electromagnetic Fields," Hemisphere Publishing Corporation, 1985

[10] R. Senthinathan, J.L. Prince, and M.R. Scheinfein, "Characteristics of coupled buried microstrip lines be modeling and simulation," IEEE Trans. Components, Hybrids, Manuf. Technol., vol. CHMT-12, no. 4, pp. 604-611, December 1987

[11] C.J. Bartlett, J.M. Segelken, and N.A. Teneketges, "Multi-chip packaging design for VLSI-based systems," in Proc. 37 Electronic Components Conf., 1987, pp. 518-521

[12] R.E. Canright, Jr., "High speed electrical effects", presented to the IEEE MTT/AP chapter Orlando, FL., Martin Marietta, 1988

[13] C.E. Baum, "Impedances and field distributions for parallel plate transmission line simulators," AFWL EMP 1-1, vol 1, note 21, pp. 1-36, June 1970

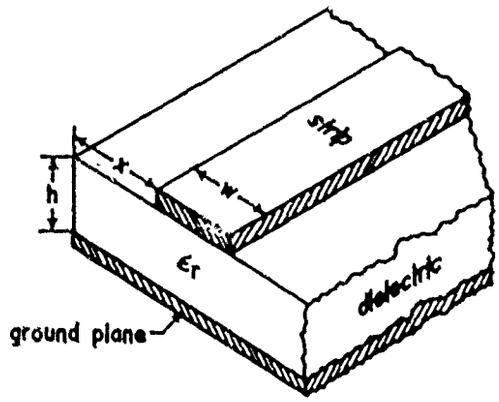


FIG. 1. CROSS-SECTIONAL GEOMETRY OF MICROSTRIP USED IN THE SIMULATIONS.

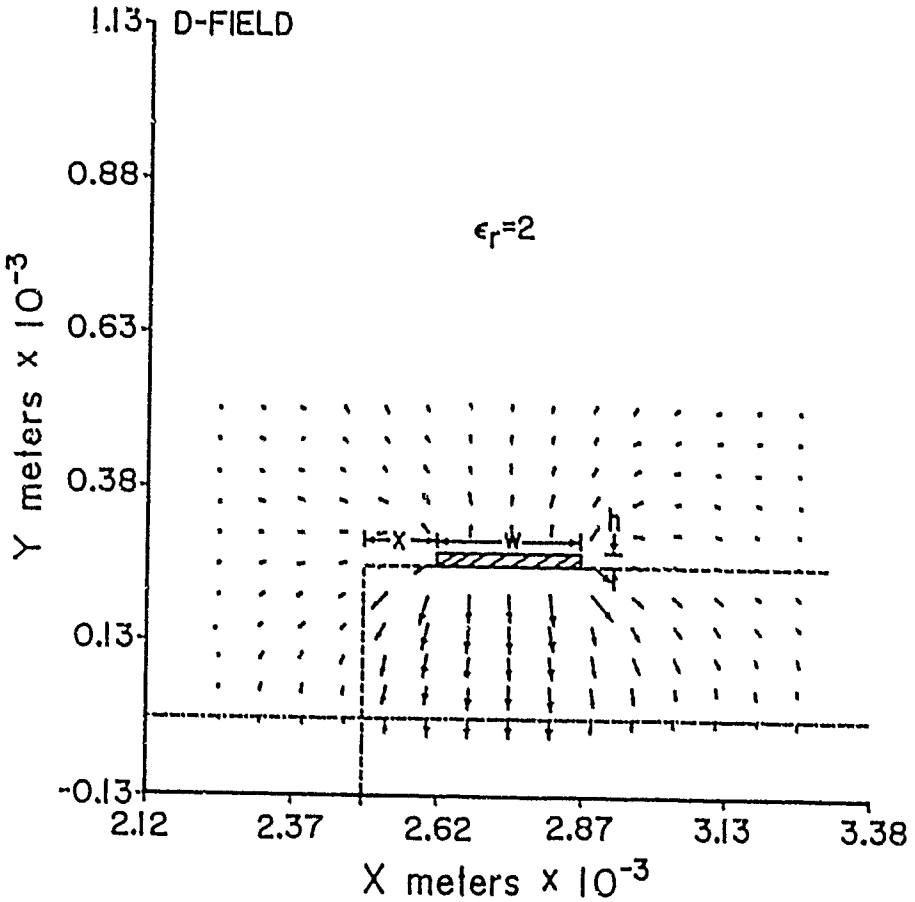


FIG. 2-a

NORMALIZED VECTOR ELECTRIC FIELD INTENSITY MAPPING FOR W = 10 MILS, H = 10 MILS, T = 0.7 MILS, X = .12 MM.

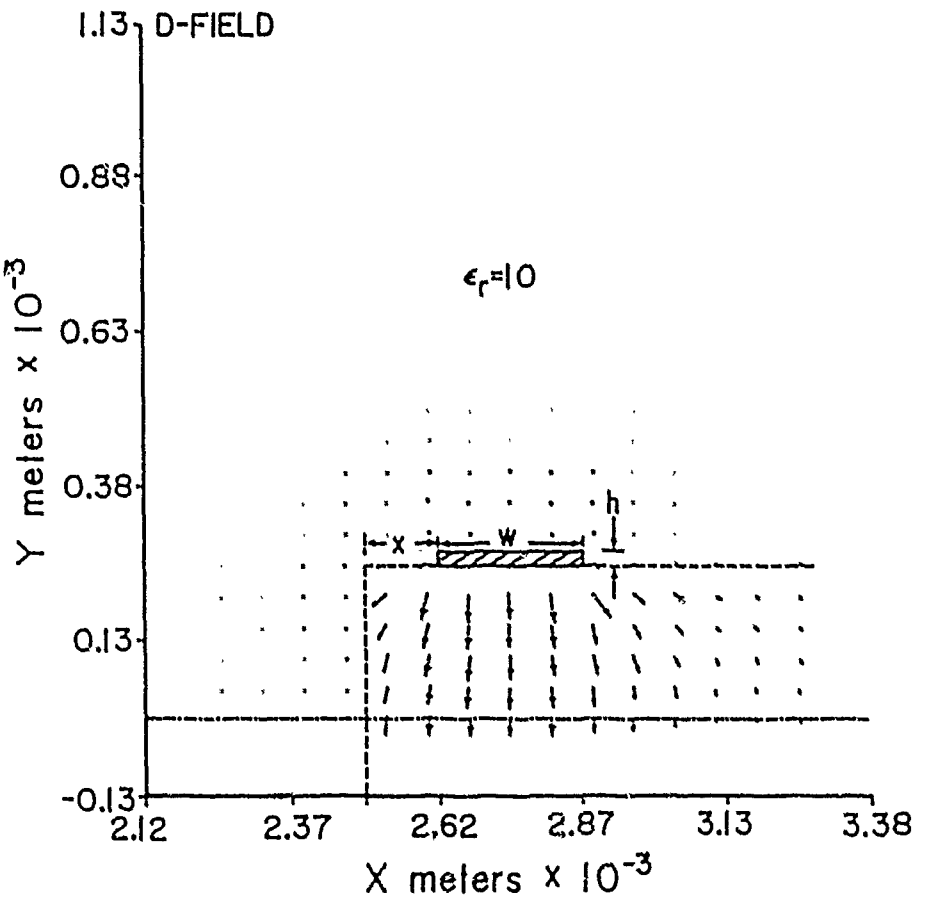


FIG. 2-b

NORMALIZED VECTOR ELECTRIC FIELD INTENSITY MAPPING FOR W = 10 MILS, H = 10 MILS, T = 0.7 MILS, X = .12 MM.

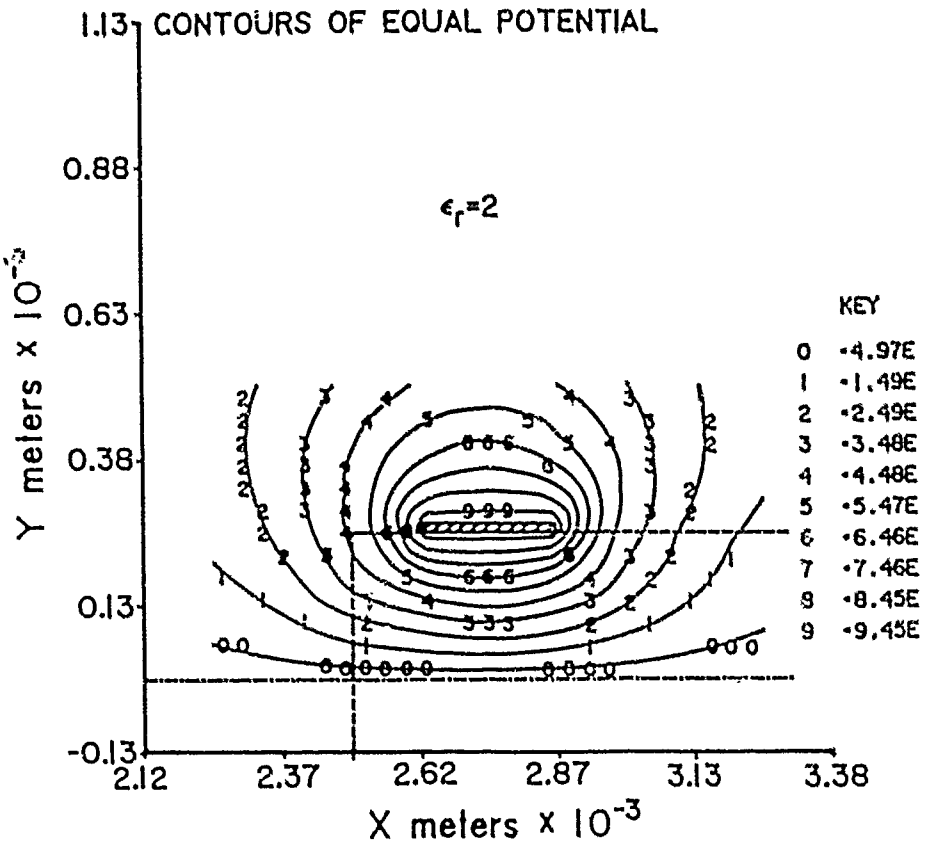


FIG. 3-a

CONTOURS OF EQUAL ELECTRIC POTENTIAL FOR W = 10 MILS, H = 10 MILS, T = 0.7 MILS, X = .12 MM.

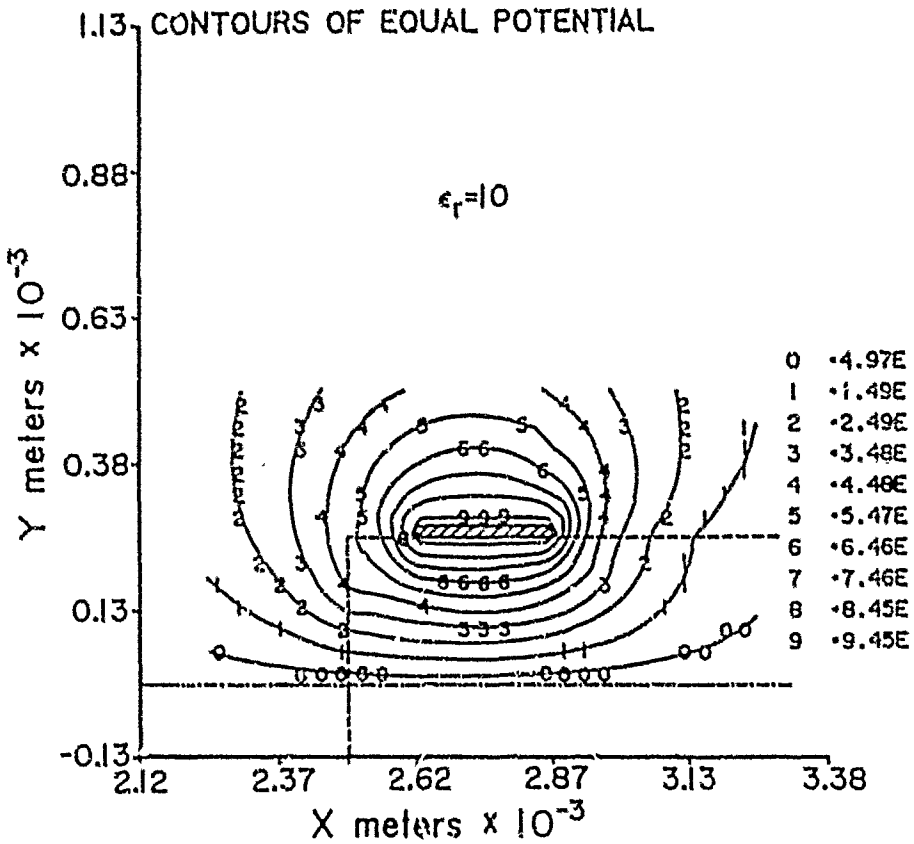


FIG. 3-b

CONTOURS OF EQUAL ELECTRIC POTENTIAL FOR W = 10 MILS, H = 10 MILS, T = 0.7 MILS, X = .12 MM.

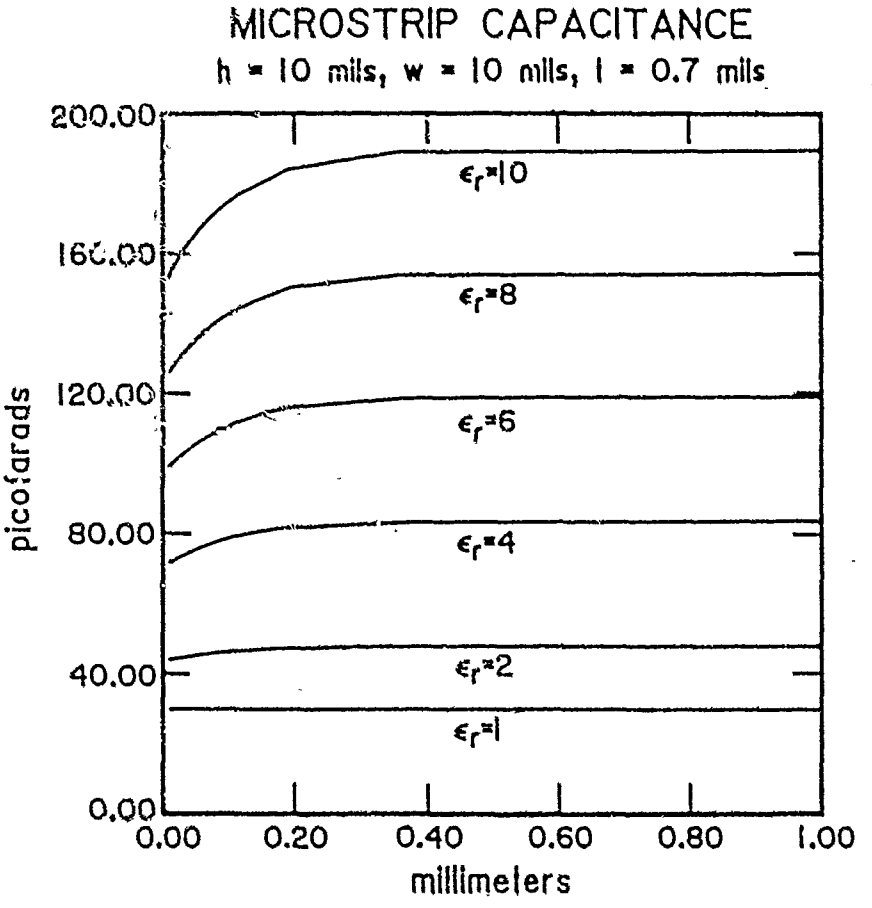


FIG. 4-a

SIMULATED CAPACITANCE VS. MICROSTRIP DISTANCE FROM EDGE (X).

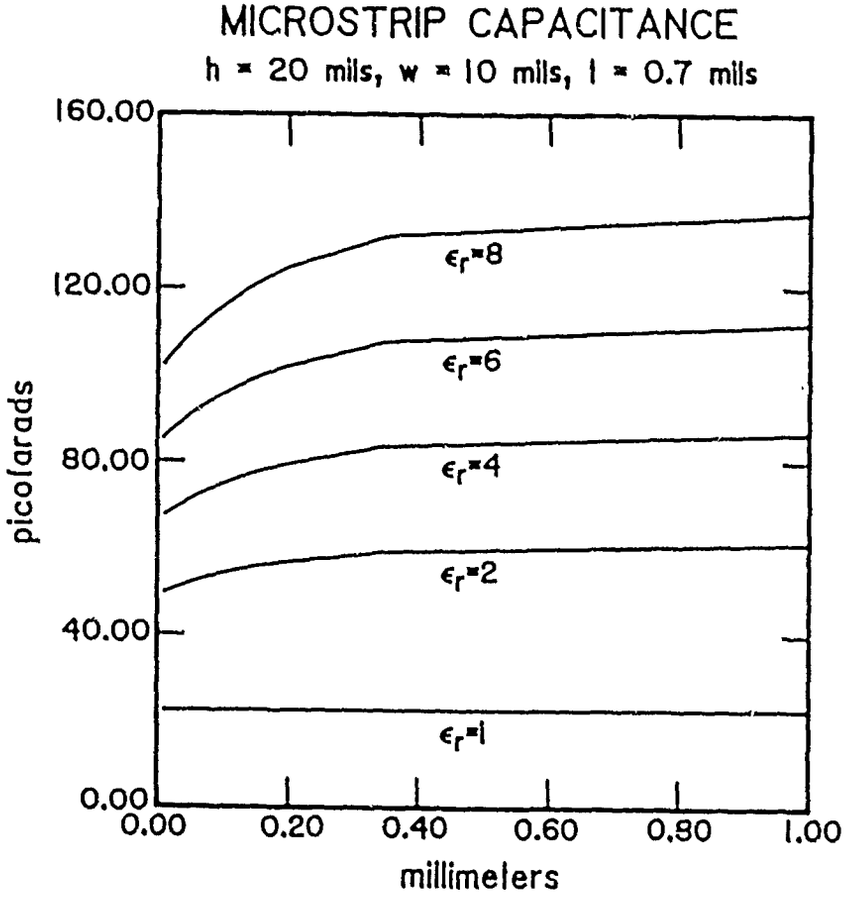


FIG. 4-b

SIMULATED CAPACITANCE VS. MICROSTRIP DISTANCE FROM EDGE (X).

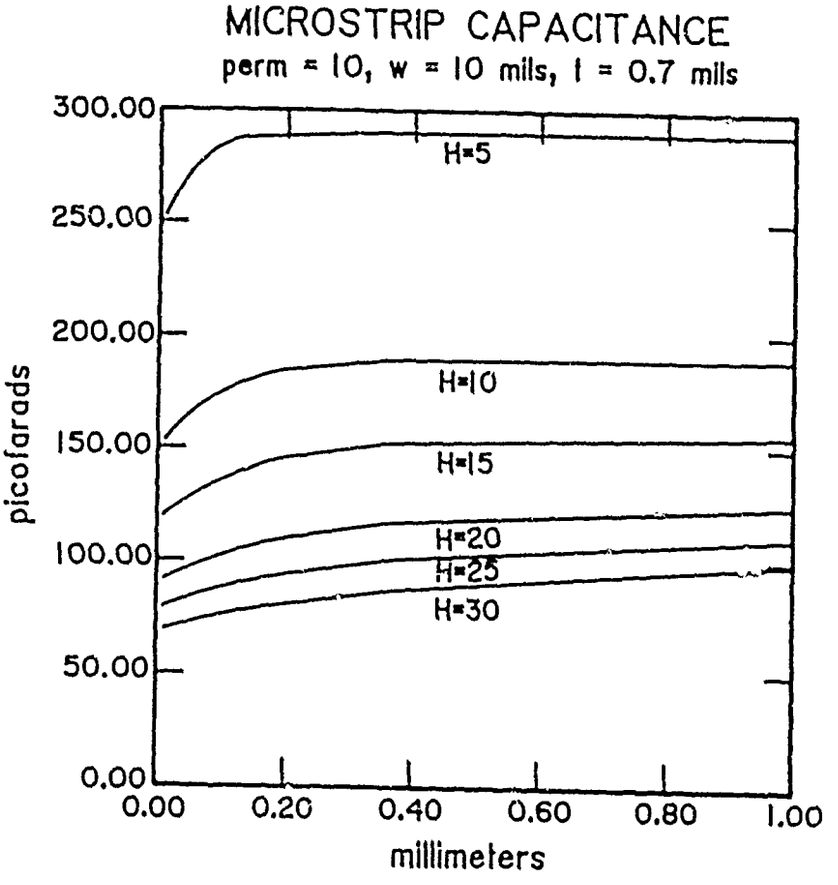


FIG. 5

SIMULATED CAPACITANCE VS. MICROSTRIP DISTANCE FROM EDGE (X) FOR W = 10 MILS, ϵ_r = 10, H VARIED FROM 5 - 30 MILS.

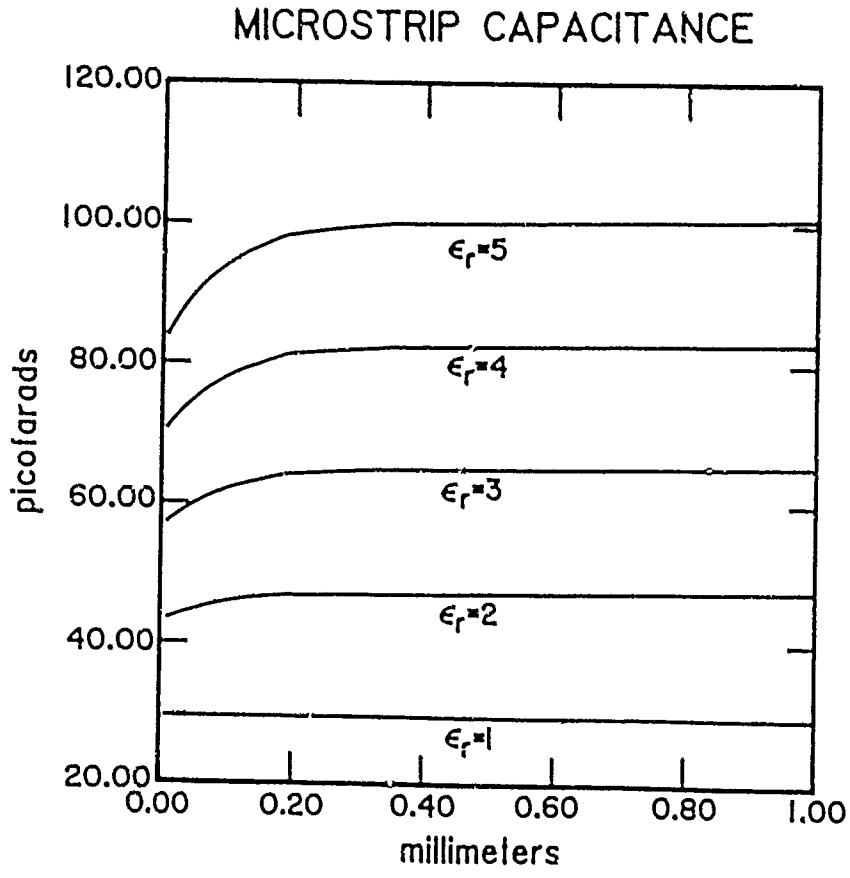


FIG. 6-a

CAPACITANCE VS. MICROSTRIP DISTANCE FROM EDGE (X) PREDICTED BY FORMULATION (EQUATION 8).

W = 10 MILS, H = 10 MILS, T = .7 MILS, ϵ_r = 1 - 5.

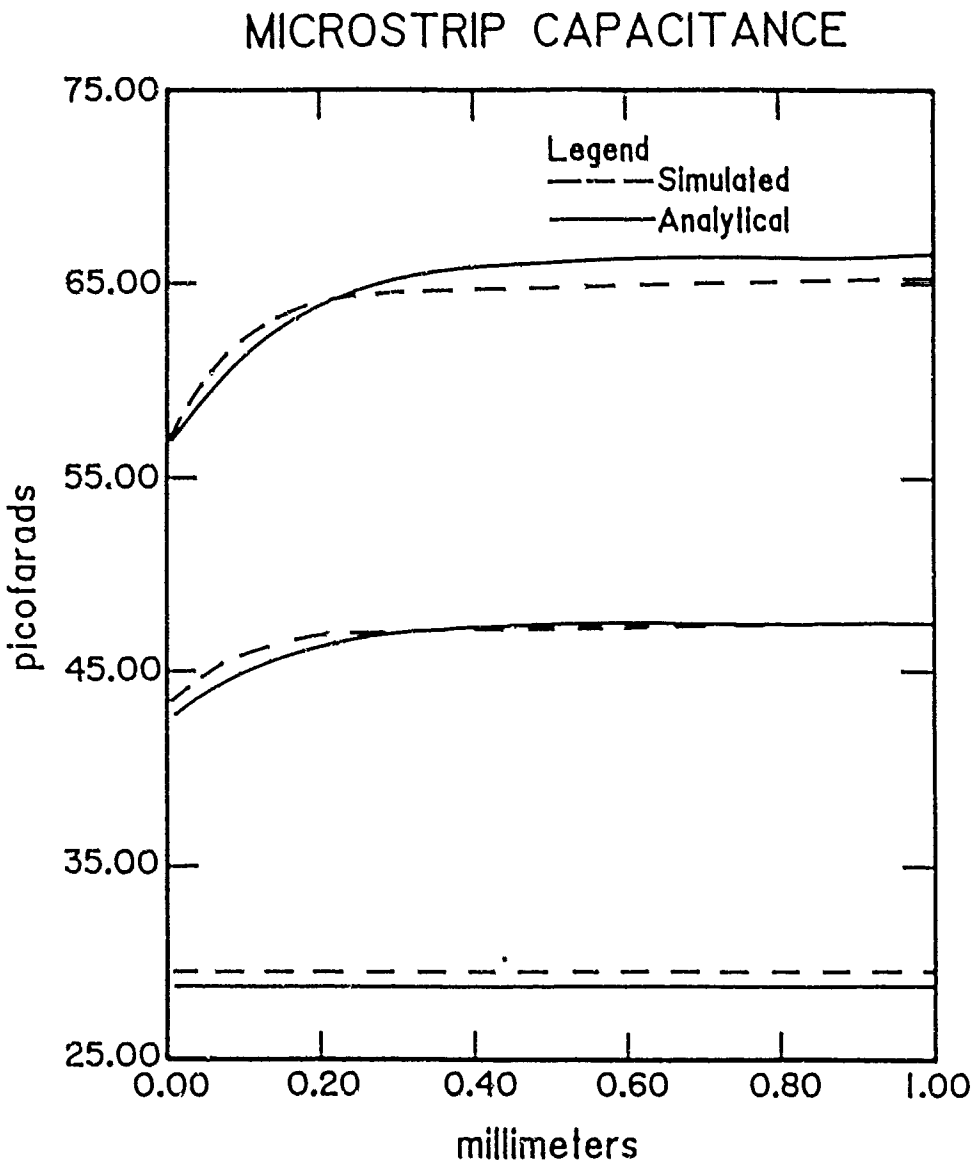


FIG. 6-b

COMPARISON OF SIMULATED VS. FORMULATED (EQUATION 8) MICROSTRIP CAPACITANCE FOR W = 10 MILS, H = 10 MILS, T = 0.7 MILS, ϵ_r VARIED FROM 1 - 3

ATMOSPHERIC ATTENUATION OF SYNTHETIC APERTURE RADARS AND REAL RADARS

Robert H. Au
Astronautics Division
Lockheed Missiles and Space Co., Inc.
Sunnyvale, California, 94089

1. INTRODUCTION

A comparison of the atmospheric attenuation between a Synthetic Aperture Radar (SAR) and a real radar operating in an air-to-ground mode at 50, 22 and 10 Ghz has been made. The atmosphere is clear air and fog. Expressions for the atmospheric attenuation factor of two-way propagation for clear air and for the combined clear air and fog are given.

The comparison shows that the attenuation depends on the angle between the local horizontal and the radar line of sight and the radar frequency. The attenuation at 55 Ghz is significant and at 10 Ghz comparatively small. The attenuation at low incident angles are significantly higher than looking vertically downward because of the longer slant ranges in the fog region. The fog was assumed to extend from sea level to an altitude of 2 km with clear air up to 50 km altitude. The calculations were performed using Lotus 123 and the Personal Computer (Reference 1).

2. ATMOSPHERIC ATTENUATION AND COEFFICIENTS

The expressions for the atmospheric attenuation factor and coefficients were obtained for the geometry shown in Figure 1. The air-borne SAR or real radar looks downward at a depression angle, D, with the slant range R and propagates the signal through clear air and fog. The attenuation of the electromagnetic energy due to absorption by primarily the oxygen and the water vapor can be modelled using the data shown in Figure 2, (Reference 2). The data show the variation for winter and summer and the trend reversal at 22 and 32.5 GHz which is attributed to the water resonance line at 22.3 GHz. Since the absorption depends on the air constituents and the constituents vary with altitude, better estimates for absorption as a function of radar operating altitude can be made. The coefficients used in this analysis were obtained from Figure 2.

The atmospheric attenuation factor for two-way propagation is given by (Reference 3):

$$F = e^{-.4605\int \alpha(R)dR} \qquad (1)$$

where the one way attenuation coefficient is

$$\alpha = e^{-(a+bR)} \tag{2}$$

and the slant range R,

$$R = h/\sin D \tag{3}$$

The integration yields the following atmospheric attenuation factor for clear air attenuation:

$$F_{ca} = e^{-.4605\, e^{-a}/_{b}\,(1-e^{-bh/\sin D})} \tag{4}$$

The atmospheric attenuation factor for fog is given by:

$$F_{fog} = e^{-.4605\, \alpha_f\, h_f/\sin D}$$

and the atmospheric attenuation factor for both clear air and the fog is given by:

$$F_a = F_{ca}\ F_{fog}$$

or

$$F_a = e^{-.4605\, e^{-a}/_{b}\,(1-e^{-bh/\sin D})} \times e^{-.4605\, \alpha_f\, h_f/\sin D} \tag{5}$$

The coefficients a and b are obtained by the linear estimate of the absorption curves for 10, 22 and 50 GHz contained in Figure 2. The higher absorption value of the winter and summer was used in the curve fitting of a the intercept and b, the slope of the line. The one way attenuation coefficient can be written as the functional relationship shown in Equation 2. This form allows one to determine the values of a and b because when h, the altitude is zero, then α is 1.4 x 10^-2 db/km and the coefficient a, becomes 4.268 for the case of 10 GHz. Similarly, when h is 40.6 km, α is 10^-6 and one can solve for the second coefficient, b which is 0.2352. Then the form for the 10 GHz case becomes:

$$\alpha = e^{-4.268 + .2352h} \tag{6}$$

The coefficients a and b for the 22 and 50 GHz cases are 1.05 and .511 (coefficients a), and .002 and .188 (coefficients b) respectively.

The atmospheric factors and coefficients described above apply to both the SAR and the real radar.

3. COMPARISON OF THE SAR AND REAL RADAR

The comparison of the atmospheric attenuation for the SAR and the real radar can be made because of the difference between the exponents in the range equation: the real radar is written to the fourth power while the SAR is to the third power.

The expression for calculating the reduction of the SAR detection range is based on the equality of the signal to noise for free space with the signal to noise for the attenuation through weather. The SAR or the real radar looking downward from an altitude towards the earth will propagate its signal through the atmosphere and will be attenuated by an amount depending on the frequency of the radars. The equations for assessing the attenuation are written in terms of the third and fourth power of the freespace range, Rfs and the attenuated range, Ra:

SAR
$$R_{fs}^{3} = \frac{R_a^{3}}{F_a} \tag{7}$$

Real Radar
$$R_{fs}^{4} = \frac{R_a^{4}}{F_a} \tag{8}$$

These expressions have been written on Lotus 123 and have been solved assuming a flat earth. The use of a spreadsheet software requires no programming knowledge and is convenient to the user with a personal computer. The technique used for solving Equations (7) and (8) is very similar to the numerical hand-solutions of the past using accounting paper, a set of trigonometry, natural and common logarithm tables, pencils and a hand-cranked or electric calculator. This capability is contained in a half ounce diskette using the power and speed of the personal computer. An example of the expression for the SAR free space range written for Lotus 123 is,

```
@EXP((3*@LN($A14)+0.4605*@EXP(-J$11)/
J$12*(1-@EXP(-J$12*$A14))+0.4605*$F$9*$B14)/3)        (9)
```

The corresponding term for the real radar would have the same form and terms with the exception that the exponent in the range equation is changed from 3 to 4.

4. RESULTS OF THE COMPARISON

The results of the calculations are shown on Tables 1 and 2 and Figures 3, 4, and 5. The Equation (9) is the solution written in the Lotus 123 "language" and are contained in each of the cell or entry under the free space range of Tables 1 and 2. The columns to the right and left represent the altitude, slant range and angle conditions which each cell must use. The @ symbol calls the specific mathematical function such as the natural lograrithm, LN. The mixed cell address, $A14, represents that value in the cell contained in the A column and 14th row. The $ symbol fixes the Ath column and varies the row values over a range of altitude. The mixed address cell $A14 represents the altitude of the radar which is used in computing one of the cells for computing the free space range. The mixed address J$11 represents the values for the coefficient a, and fixes the 11th row and varies across the columns J, K and L at the computation cells.

The results show that the atmospheric attenuation for the Synthetic Aperture Radar is greater than the real radar.The Figures 3, 4, and 5 show the ratio of the attenuated to the free space range and a function of the depression angle of 90, 30, and 20. The values represent the two-way attenuation of the signal. The attenuation in general decreases with increasing depression angle, D. The reason is that as the depression angle decreases, the slant range in the fog region increases which increases the total attenuation.

The SAR has the advantage of decreased power requirements over the real radar since power for the SAR is proportional to the cube of the range. One must recognize that this advantage comes from the efficient integration of the signals returned from the ground which are coherently added to effectively have a zero integration loss. The range is introduced when one considers the number of pulses to be integrated which is the product of the radar PRF and the time to fly a SAR. This range cancels out one of the range factors in the equation.

5. CONCLUSIONS

The results of the calculations show that the atmospheric attenuation of the SAR operating at 10 GHz is small compared with the values at 22 and 50 GHz. In addition, the atmospheric attenuation of the SAR is greater than the real radar.

REFERENCES

1. LOTUS 123 Reference Manual, Release 2, Lotus Development Corporation, Cambridge, MA.

2. Class Notes.

3. S.A. Hovanessian, "Radar Detection and Tracking Systems," Artech House, Inc, 1973.

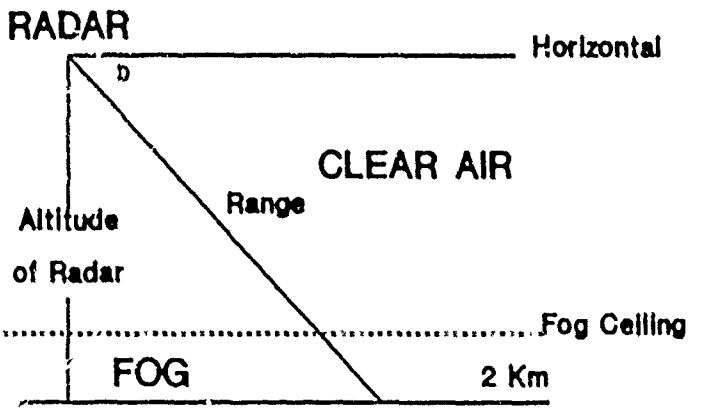


Figure 1. Radar Geometry

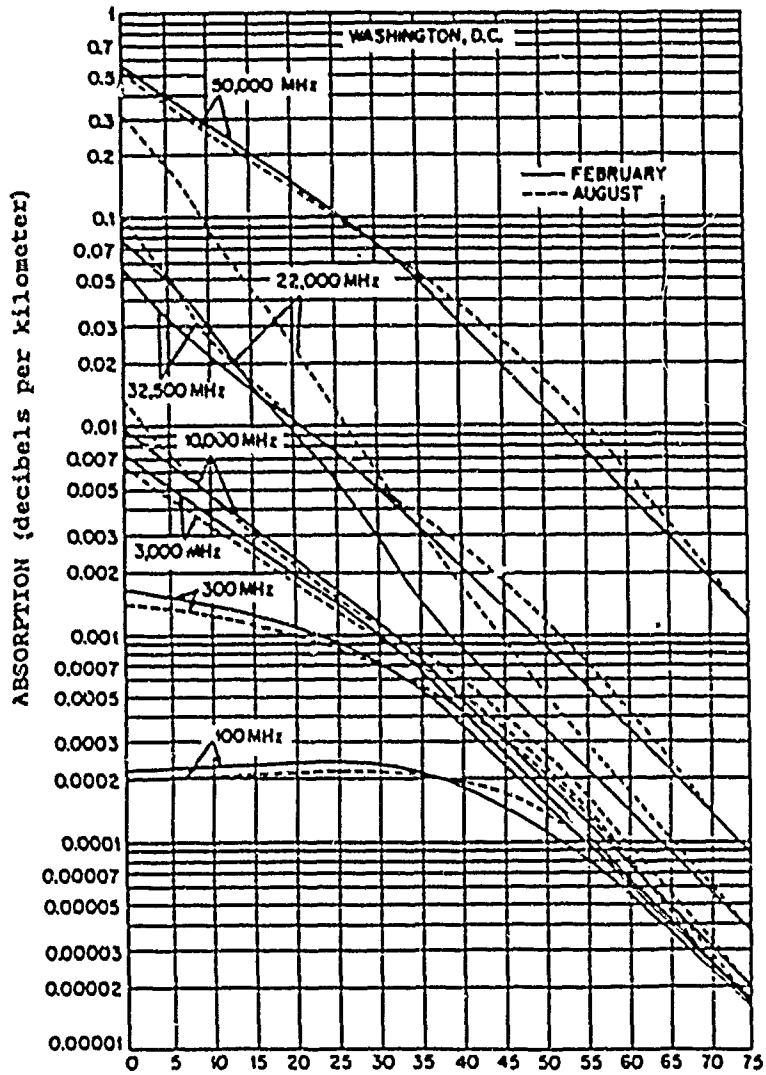


Figure 2. Atmospheric Absorption (Washington D. C.)

Table 1. Attenuation Calculations for a Real Radar

ALTITUDE		Att Coef	FREE SPACE RANGE			ATTENUATED RN SLANT RANGE	
		f =GHz	1.52 50	0.54 22	0.11 10	Rc	Rfog
h,radar km	h,fog km	a = b =	0.511 0.188	1.050 0.402	4.268 0.235	km	km
0.10	0.10		0.1	0.1	0.1	0.1	0.1
1.00	1.00		1.3	1.1	1.0	1.0	1
2.00	2.00		3.3	2.4	2.1	2.0	2
6.00			11.2	7.4	6.2	6.0	2
8.00	(90 degrees)		15.5	10,0	8.3	8.0	2
10.00			19.8	12.5	10.3	10.0	2
15.00			30.8	18.8	15.5	15.0	2
20.00			41.6	25.0	20.7	20.0	2
25.00			52.2	31.3	25.8	25.0	2
30.00			62.8	37.6	31.0	30.0	2
40.00			83.9	50.1	41.3	40.0	2
50.00			104.8	62.6	51.6	50.0	2
0.10	0.10		0.2	0.2	0.2	0.2	0.2
1.00	1.00		3.3	2.4	2.1	2.0	2.0
2.00	2.00		10.2	5.6	4.2	4.0	4.0
6.00			35.2	17.0	12.7	12.0	4.0
8.00	(30 degrees)		47.8	22.7	16.9	16.0	4.0
10.00			60.4	28.3	21.2	20.0	4.0
15.00			91.2	42.5	31.8	30.0	4.0
20.00			121.8	56.7	42.4	40.0	4.0
25.00			152.2	70.9	53.0	50.0	4.0
30.00			182.7	85.0	63.6	60.0	4.0
40.00			243.6	113.4	84.7	80.0	4.0
50.00			304.5	141.7	105.9	100.0	4.0
0.10	0.10		0.3	0.3	0.3	0.3	0.3
1.00	1.00		5.9	3.8	3.0	2.9	2.9
2.00	2.00		22.2	9.2	6.3	5.8	5.8
6.00			74.4	27.9	19.0	17.5	5.8
8,00	(20 degrees)		100.1	37.2	25.4	23.4	5.8
10.00			125.5	46.5	31.7	29.2	5.8
15.00			188.4	69.7	47.6	43.9	5.8
20.00			251.3	93.0	63.4	58.5	5.8
25.00			314.1	116.2	79.3	73.1	5.8
30.00			376.9	139.5	95.1	87.7	5.8
40.00			502.6	186.0	126.8	117.0	5.8
50.00			628.2	232.4	158.5	146.2	5.8

Table 2. Attenuation Calculations for a SAR

ALTITUDE		Att Coef	FREE SPACE RANGE			ATTENUATED RN SLANT RANGE	
		f =GHz	1.62	0.54	0.11	Rc	Rfog
h,radar km	h,fog km	a = b =	50 0.511 0.188	22 1.050 0.402	10 4.268 0.235	km	km
0.10	0.10		0.1	0.1	0.1	0.1	0.1
1.00	1.00		1.4	1.1	1.0	1.0	1
2.00	2.00		3.8	2.5	2.1	2.0	2
6.00			13.7	8.0	6.2	6.0	2
8.00	(90 degrees)		19.3	10.7	8.3	8.0	2
10.00			24.9	13.5	10.4	10.0	2
15.00			39.1	20.2	15.7	15.0	2
20.00			53.1	27.0	20.9	20.0	2
25.00			66.8	33.7	26.1	25.0	2
30.00			80.4	40.5	31.3	30.0	2
40.00			107.3	54.0	41.8	40.0	2
50.00			134.2	67.5	52.2	50.0	2
0.10	0.10		0.2	0.2	0.2	0.2	0.2
1.00	1.00		3.8	2.5	2.1	2.0	2.0
2.00	2.00		14.0	6.2	4.3	4.0	4.0
6.00			50.3	19.1	12.9	12.0	4.0
8.00	(30 degrees)		68.9	25.5	17.3	16.0	4.0
10.00			87.3	31.8	21.6	20.0	4.0
15.00			132.2	47.8	32.4	30.0	4.0
20.00			176.5	63.7	43.2	40.0	4.0
25.00			220.6	79.6	54.0	50.0	4.0
30.00			264.8	95.5	64.8	60.0	4.0
40.00			353.0	127.4	86.4	80.0	4.0
50.00			441.3	159.2	108.0	100.0	4.0
0.10	0.10		0.3	0.3	0.3	0.3	0.3
1.00	1.00		7.4	4.1	3.1	2.9	2.9
2.00	2.00		34.7	10.7	6.5	5.8	5.8
6.00			120.4	32.6	19.5	17.5	5.8
8.00	(20 degrees)		162.4	43.4	26.1	23.4	5.8
10.00			203.9	54.3	32.6	29.2	5.8
15.00			306.4	81.4	48.9	43.9	5.8
20.00			408.5	108.5	65.1	58.5	5.8
25.00			510.7	135.7	81.4	73.1	5.8
30.00			612.8	162.8	97.7	87.7	5.8
40.00			817.0	217.0	130.3	117.0	5.8
50.00			1021.3	271.3	162.8	146.2	5.8

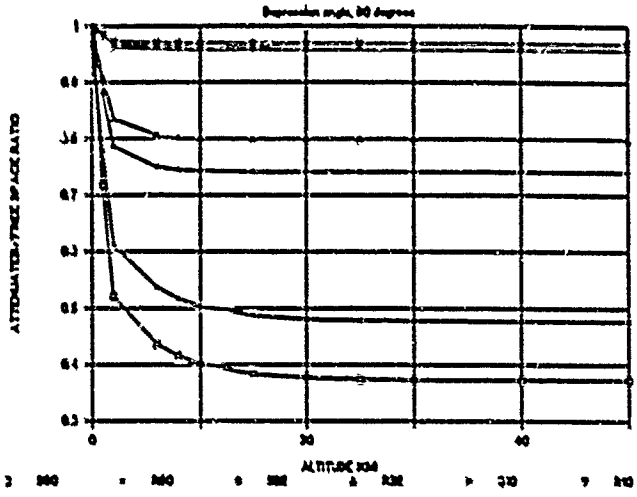


Figure 3. Comparison of SAR and Real Radar (D=90 Deg)

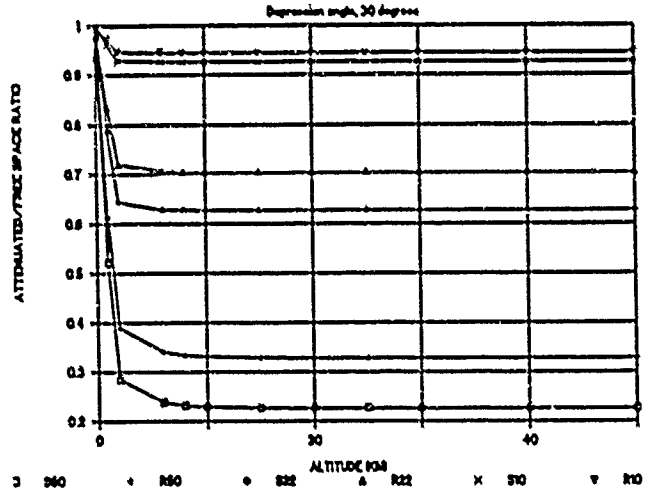


Figure 4. Comparison of SAR and Real Radar (D=30 Deg)

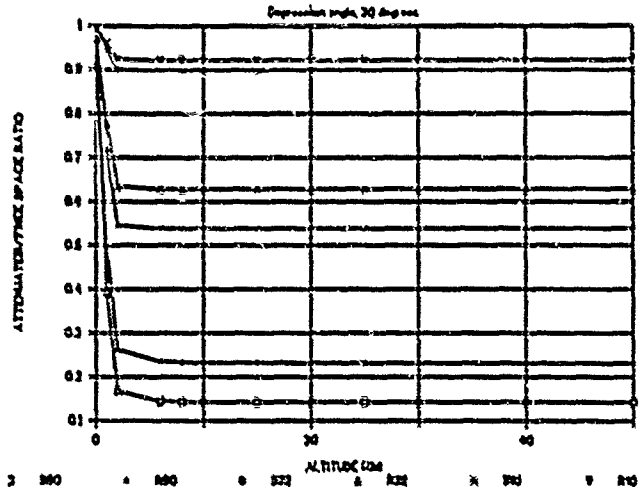


Figure 5. Comparison of SAR and Real Radar (D=20 Deg)

THE DUAL MODE LOG PERIODIC DIPOLE ANTENNA*

Eduardo H. Villaseca and Mark Wheeler
P.O. Box 3310, Bldg. 600/B135
Hughes Aircraft Company, Ground Systems Group, Fullerton, CA 92634

Abstract - A novel variation of the log periodic antenna is presented. This new design employs a dual feed scheme that can produce dipole sum and difference patterns depending on the method of excitation. The input impedance and radiation characteristics still maintain a broadband response that is characteristic of the conventional log periodic antenna. The performance of the design was determined using the NEC3 method of moments computer code.

Introduction

The dual mode log periodic dipole antenna was designed as part of a RF mobile antenna project. The project required that an antenna be designed that could determine the direction of the source of any incident radio transmission. This antenna type is commonly known as a direction finding or DF antenna. In addition, it was required that the antenna produce a directional pattern when used as a transmitter. The antenna was to operate over a 7.5:1 frequency band that was contained in the HF and VHF regions of the spectrum. Conventionally, two separate antennas are used to comprise a DF system. The dual mode LPD design would enable direction finding to be implemented using one antenna structure. As a result the DF system would be lighter, easier to deploy, and more cost efficient; while still retaining the desired radiation characteristics.

Theory and Design Description

The radiation response of the dual mode log periodic dipole is an extension of the response produced when a single dipole is excited by two separate feeds. The two feeds are placed equidistant from the ends of the element and from each other. In other words one feed is located at L/3 and the second feed is located at 2L/3, where L is the length of the dipole. If both feeds are fed in phase the dipole will resonate at $L = \lambda/2$ and produce a current distribution characteristic of the common center fed $\lambda/2$ dipole. However, if both feeds are fed 180° out of phase with each other the dipole will resonate at $L = \lambda$ and produce a current distribution characteristic of a center fed λ dipole. These characteristic current distributions will produce a sum pattern for the in phase case and a difference pattern for the out of phase case. In addition, the input impedance match is less than 2:1 (referenced to 50 ohms) for both feed configurations.

A log periodic dipole configuration was the logical choice for expanding the single element dual mode concept into a broadband antenna design. The log periodic structure was introduced by DuHamel and Isbell and its theory and design are well documented in the open literature [1]-[3]. The basic log periodic dipole

*Hughes Aircraft Company Patent Pending Number PD-87372.

array design consists of an array of parallel wire dipoles of successively increasing lengths extending outward from the feed point at the apex. The array is fed in series at the center of each element. The geometrical dimensions of the design increase logarithmetically and are defined by the inverse of the geometric ratio τ. That is,

$$\frac{1}{\tau} = \frac{L_{n+1}}{L_n} = \frac{R_{n+1}}{R_n} = \frac{d_{n+1}}{d_n} = \frac{D_{n+1}}{d_n} = \frac{D_{N+1}}{D_n} \tag{1}$$

where: L = element length
R = distance, along the array, of the element from the apex
d = spacing between elements
D = diameter of elements
n = n'th element

In addition to τ, there are two other important design parameters; the spacing factor σ and the apex angle α. The spacing factor is defined as

$$\sigma = \frac{d_n}{2L_n} \tag{2}$$

From equation (2) the apex angle can be found and expressed as

$$\alpha = 2 \tan^{-1}\left(\frac{1-\tau}{4\sigma}\right) \tag{3}$$

Also, it should be noted that the standard log periodic design calls for a crisscrossing or transposing of the feed lines between adjacent elements. This 180° phase shift between elements produces a phase progression that allows the energy to be directed endfire in the direction of the shorter elements. The dual mode design deviates from the standard design by having two separate feed points and two independent sets of crisscrossing transmission lines.

Mostly, the design parameters for this specific dual mode log periodic design were chosen as a response to the severe antenna size limitations required for the system's application. As a result a variable τ design was implemented [4]. Initial design parameters were chosen to be $\tau = 0.87$, $\sigma = 0.06$, and $\alpha = 56.9°$. The design consisted of 20 elements with the three longest elements mechanically shortened and inductively loaded. In an effort to "squeeze" one more low frequency element in the same fixed array length, a second increased τ of 0.97 was chosen for the seven longest elements. This increased τ applied only to the element spacing and not the length. This allowed the effective α angle to remain constant. Thus, the final design consisted of 21 elements with the four electrically longest elements shortened and inductively loaded (see Figure 1). In addition, the lowest frequency element had to be loaded resistively for impedance matching purposes; at a cost to low frequency difference mode gain.

Performance Characteristics

The NEC3 computer code was used to predict the performance characteristics of the dual mode design. The configuration was modeled in free space with a vertical polarization. Figure 2 shows a typical midband E-plane sum pattern. The maximum gain, at boresight, is 6.1 dBi. The pattern has a 3-dB beamwidth of 70.0° and a front-to-back ratio of 20.4 dB. The corresponding H-plane pattern is shown in Figure 3. This pattern has a 3-dB beamwidth of 132.0°. Figure 4 shows a typical E-plane difference pattern. The maximum gain is 5.49 dBi located at 33.0° off boresight. All patterns are power patterns calibrated in dBi.

The sum mode VSWR and gain over the entire band are shown in Figure 5. The VSWR is less than 2.0:1 over the entire band and a gain of 6.0 dBi or higher is typical over most of the band. Figure 6 shows the difference pattern VSWR and gain. Again, VSWR is less than 2.0:1 except at the very low end of the frequency band. Gain over the upper half of the band is 6.0 dBi or greater. However, the gain drops off sharply at the low end due to the resistive loading of the back element. The resistive loading was necessary only because of the antenna size limitations required for this particular project. In general, the gain at the low end of the band for a non-loaded array will be similar to high end gain values.

Conclusion

A new variation of the log-periodic antenna has been designed and the impedance and radiation characteristics investigated. It has been shown that this new design can produce sum and difference patterns over a broad band while maintaining a low input impedance. An antenna of this type has direct application in any DF system that operates in the HF, VHF, or UHF regions of the spectrum. Further investigations into the effects of feed placement along an element are recommended.

References

[1] R.H. DuHamel and D.E. Isbell, "Broadband Logarithmically Periodic Antenna Structures," 1957 IRE National Convention Record, Pt. 1, pp.119-128.

[2] D.E. Isbell, "Log Periodic Dipole Arrays," IRE Trans. Antennas Propag., Vol. AP-8. pp,260-267, May 1960.

[3] R.L. Carrel, "Analysis and Design of the Log-Periodic Dipole Antenna," Ph.D. Dissertation, Elec. Eng. Dept., University of Illinois, 1961, University Microfilms, Inc., Ann Arbor, Michigan.

[4] Daniel F. Difonzo, "Reduced Size Log Periodic Antennas," The Microwave Journal, Vol. VII, No. 12, pp.37-42, Dec. 1964.

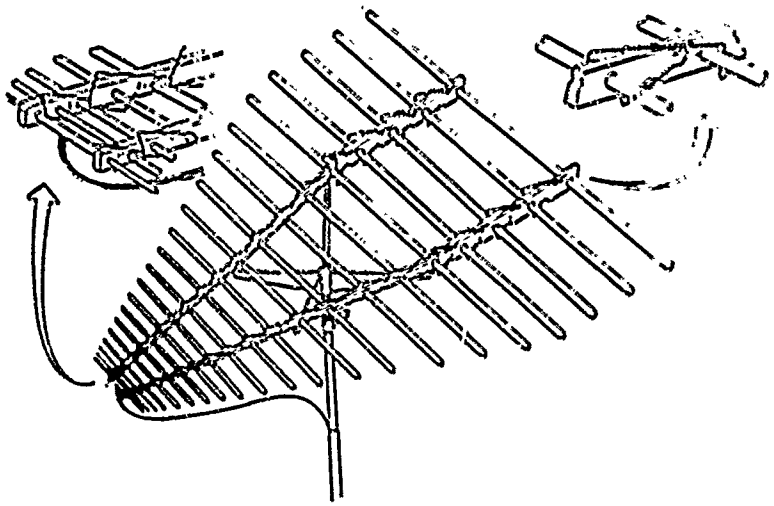


Fig. 1. Dual mode log periodic dipole.

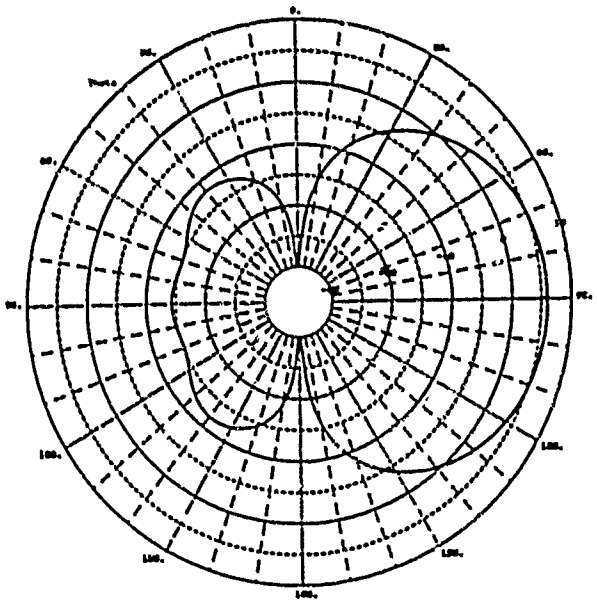


Fig. 2. E-plane sum pattern.

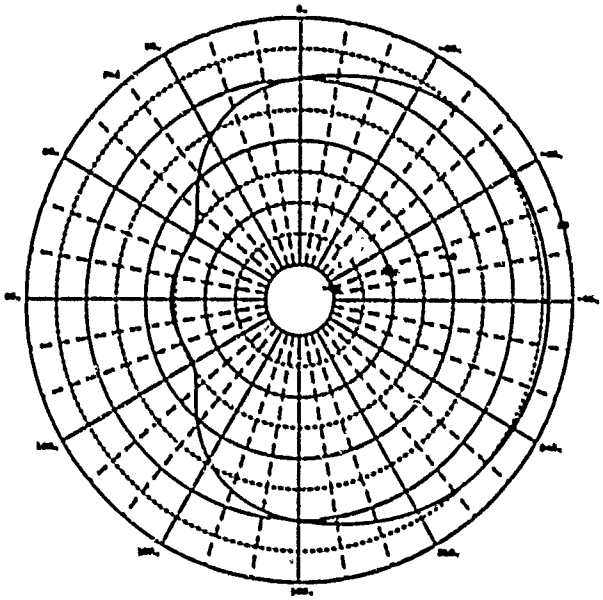


Fig. 3. H-plane sum pattern.

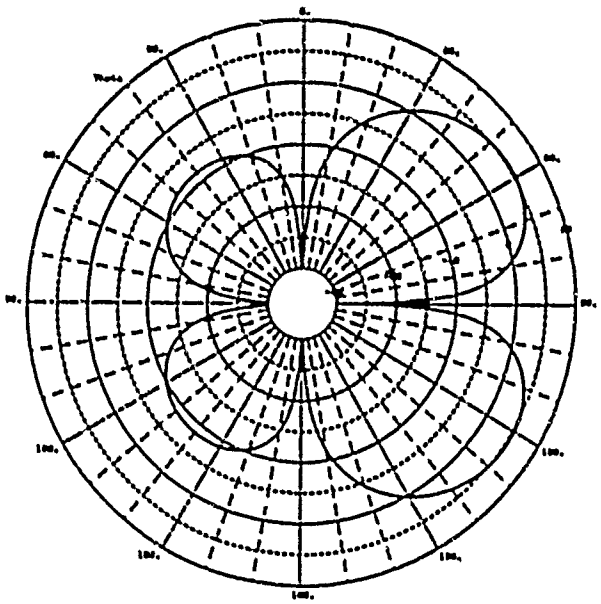


Fig. 4. E-plane difference pattern.

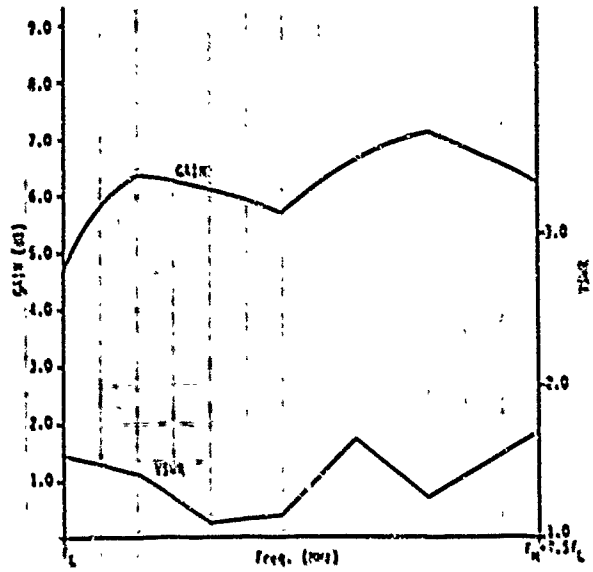


Fig. 5. Sum mode gain and VSWR.

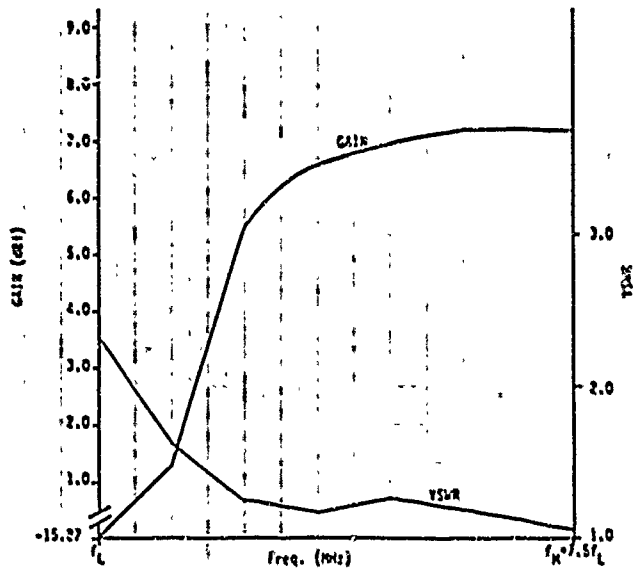


Fig. 6. Difference mode gain and VSWR.

NUMERICAL SOLUTION TO SCATTERING FROM 2-D INFINITE BODIES IN FINITE COMPUTATIONAL DOMAIN

A.H. Mohammadian, W.F. Hall, and V. Shankar
Science Center
Rockwell International Corporation
P.O. Box 1085
Thousand Oaks, CA 91360

ABSTRACT

A methodology is proposed and implemented to solve for scattering from arbitrary objects over a ground plane, cavities in a ground plane, half planes, and conducting wedges using the computational fluid dynamic (CFD)-based finite volume scheme for solving Maxwell's equations . The computational domain used in these problems is a finite portion of the infinite domain of the problem with appropriate outer boundary conditions to simulate this infinite domain. For the problems involving an infinite ground plane, the "diffracted field" formulation has been adopted so that, where advantageous, a non-rectangular grid can be used. In other cases the "scattered field" formulation has been used. Both the near and far field quantities for some canonical geometries are studied and compared to the exact or other known solutions.

INTRODUCTION

In spite of major advances in numerical solution of partial differential equations in the last two decades and exploitation of them in computational fluid dynamics for solving Euler and Navier-Stokes equations, the electromagnetic community at large has been ignorant about the partial differential equation (PDE) approach for solving Maxwell's equations. As examples of some exceptions in this area, the readers are referred to the works reported in [1] and [2]. More recently, however, efforts to take advantage of the proven CFD techniques have led to the formulation of a very comprehensive numerical technique for solving electromagnetic scattering and radiation problems involving complex objects [3]-[5]. This technique has been successfully applied to a diverse range of problems involving electrically large scatterers, inhomogeneous and layered dielectrics, cavities, and frequency-dependent materials to name just a few. Some of the results are reported in [6], [7].

It should be mentioned that both [2] and the CFD-based approach are explicit time-domain techniques. However, while [2] is based on Yee's algorithm [8] the present method is based on the Riemann integration method [9] and recent advances in numerical solution of PDEs in CFD. Unlike [2], the CFD-based technique uses body-fitted coordinates and is not confined to Cartesian grids. It consequently does not suffer from inaccuracies or inconveniences in implementing the boundary condition on the object. Also, Maxwell's equations are solved for the "scattered field", i.e. the difference between the field in presence and in the absence of the scatterer, and unlike [2] one does not have to propagate the incident field from the outer boundary (or from some other boundary enclosing the scatterer)to the object. Some salient features of the CFD-based method may be summarized as follows

1) Maxwell's equations are solved for the scattered wave and the incident wave is introduced only as a boundary condition on the conducting portions of the object. This way the propagation of the incident wave through the computational grid is avoided.

2)Multizone partitioning particularly reduces the geometrical complexity of the problems.

3)Use of the elliptic grid-solving techniques results in a grid with a prescribed variable resolution in different portions of the computational domain.

4)Application of the characteristic theory of signal propagation contributes to the stability and accuracy of the computation.

5)Utilization of the Lax-Wendroff explicit scheme provides second-order accuracy in both space and time..

6)Fast Fourier transforms (FFT) generate the frequency-domain quantities over a range of frequencies from their time-domain counterparts, which are obtained in a single computation.

In this paper after a brief review of the CFD-based approach for solving Maxwell's equations, the cases involving infinite ground planes and half planes will be elaborated. Throughout the text, boldface letters represent vectors and small letters bearing a caret represent unit vectors.

DESCRIPTION OF FORMULATION

a) Scattered and Diffracted Field Formulations

Maxwell's equations in an inhomogeneous medium with constitutive parameters σ, μ, and ε may be presented as follows

$$\nabla \times \mathbf{E} = -\frac{\partial \mathbf{B}}{\partial t} - \frac{\partial}{\partial t}[(\mu - \mu_0)\mathbf{H}],$$
$$\nabla \times \mathbf{H} = \frac{\partial \mathbf{D}}{\partial t} + \sigma \mathbf{E} + \frac{\partial}{\partial t}[(\varepsilon - \varepsilon_0)\mathbf{E}]. \qquad (1)$$

$\mathbf{D} = \varepsilon_0 \mathbf{E}$ and $\mathbf{B} = \mu_0 \mathbf{H}$ are respectively, electric displacement and magnetic flux density. All the vector quantities in (1) are total fields in free space, while the inhomogenity of the medium is presented as conduction and polarization sources. However, it is more logical to formulate the problem in terms of the scattered field (i.e. the difference between the field in presence and absence of the scatterers) since the incident field satisfies Maxwell's equations in free space and moreover, is analytically known everywhere.The equations for the scattered field are

$$\nabla \times \mathbf{E}^s = -\frac{\partial \mathbf{B}^s}{\partial t} - \frac{\partial}{\partial t}[(\mu - \mu_0)(\mathbf{H}^s + \mathbf{H}^i)],$$

$$\nabla \times \mathbf{H}^s = \frac{\partial \mathbf{D}^s}{\partial t} + \sigma(\mathbf{E}^s + \mathbf{E}^i) + \frac{\partial}{\partial t}[(\epsilon - \epsilon_0)(\mathbf{E}^s + \mathbf{E}^i)]. \tag{2}$$

Then, the boundary condition for the scattered field on the surface of a perfect conductor becomes

$$\hat{n} \times \mathbf{E}^s = -\hat{n} \times \mathbf{E}^i$$

In problems involving an infinite ground plane, since the specular reflection from the ground plane is known it is possible and advantageous to solve Maxwell's equations for the diffracted wave,i.e. scattered minus specular reflection from the ground plane

$$\nabla \times \mathbf{E}^d = -\frac{\partial \mathbf{B}^d}{\partial t} - \frac{\partial}{\partial t}[(\mu - \mu_0)(\mathbf{H}^d + \mathbf{H}^r + \mathbf{H}^i)],$$

$$\nabla \times \mathbf{H}^d = \frac{\partial \mathbf{D}^d}{\partial t} + \sigma(\mathbf{E}^d + \mathbf{E}^r + \mathbf{E}^i) + \frac{\partial}{\partial t}[(\epsilon - \epsilon_0)(\mathbf{E}^d + \mathbf{E}^r + \mathbf{E}^i)]. \tag{3}$$

Also the boundary condition for the diffracted field on a perfectly conducting surface is

$$\hat{n} \times \mathbf{E}^d = -\hat{n} \times (\mathbf{E}^i + \mathbf{E}^r)$$

For the outer boundary of the computational domain a first order Sommerfeld-type condition is used. This will be discussed later on.

b) Conservation Form of Maxwell's Equations

Attention will be confined to the 2-D formulation of the problem here. Also, the scattered field formulation will be elaborated only. The diffracted field formulation may be treated in a similar manner. In a cartesian coordinate system, (2) may be represented as follows

$$\frac{\partial Q}{\partial t} + \frac{\partial R}{\partial x} + \frac{\partial S}{\partial y} = -J_{eq}, \tag{4}$$

where $Q = \begin{bmatrix} p \\ q_1 \\ q_2 \end{bmatrix}$; $R = -\begin{bmatrix} v_2 \\ 0 \\ u \end{bmatrix}$; $S = \begin{bmatrix} v_1 \\ u \\ 0 \end{bmatrix}$.

In CFD nomenclature Q is referred to as the solution vector and R and S are called the flux vectors in the directions x and y, respectively. These flux vectors are mathematical entities and should not be confused with the electric and magnetic fluxes in electromagnetics. As a matter of fact, the components of these fluxes represent the tangential electric and magnetic fields along the constant coordinate curves. For TM polarization

$p = D_z^s$; $u = E_z^s$,

$q = q_1 \hat{x} + q_2 \hat{y} = B^s$; $v = v_1 \hat{x} + v_2 \hat{y} = H^s$;

$$J_{eq} = \begin{bmatrix} \left(\sigma + \alpha \frac{\partial}{\partial t}\right)(u + u^i) \\ \beta\,(v_1 + v_1^i) \\ \beta\,(v_2 + v_2^i) \end{bmatrix}; \quad \alpha = \epsilon - \epsilon_0;\ \beta = \mu - \mu_0$$

and for TE polarization

$$p = B_z^s;\ u = H_z^s;\ q = D^s;\ v = E^s;\ J_{eq} = \begin{bmatrix} \alpha \frac{\partial}{\partial t}(u + u^i) \\ \left(\sigma + \beta \frac{\partial}{\partial t}\right)(v_1 + v_1^i) \\ \left(\sigma + \beta \frac{\partial}{\partial t}\right)(v_2 + v_2^i) \end{bmatrix}.$$

$\alpha = \mu - \mu_0$; $\beta = \epsilon - \epsilon_0$.

In the above expressions u^i, v^i_1, and v^i_2 are the components of the incident field. Following the CFD nomenclature (4) is referred to as the conservation form of Maxwell's equations. They constitute a hyperbolic system of PDEs and as a result amenable to an explicit method of solution by marching in time till the desired solution is reached.

c) Multi-zoning and Body-fitted Coordinate Transformation

The object and its surrounding space is divided into a number of zones and in each zone a local system of body-fitted coordinates is established. If the problem

involves an infinite plane, a half plane, or a wedge, only a finite portion of the structure will lie in the computational domain. However, with proper boundary conditions on the outer boundary, the true geometry can be simulated. This will be discussed further in conjunction with the outer boundary conditions. Fig. 1 shows a simple example, namely a cylindrical cavity in a ground plane, where the whole space is divided into six zones. However, the method is quite flexible and the same geometry may be partitioned in many other ways. Fig.2 illustrates a 4-zone rectangular grid for a rectangular cavity in a ground plane. In each zone a local system of griding is sketched.

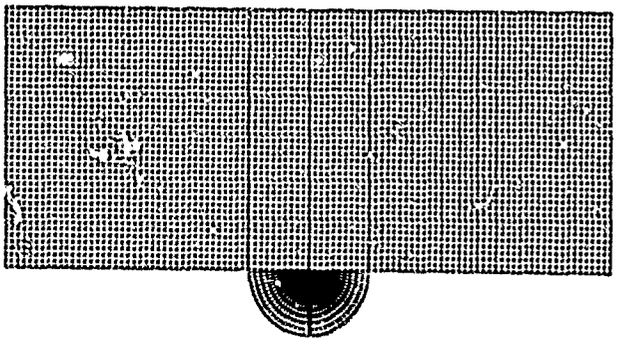


Fig. 1. A choice of griding for a cylindrical cavity in an infinite ground plane

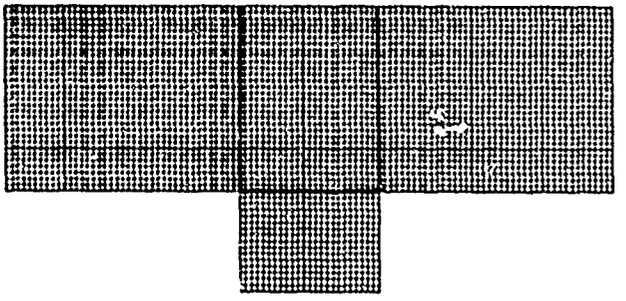


Fig. 2. A choice of griding for a rectangular cavity in an infinite ground plane

For arbitrary objects the grids can be obtained from the solution of the following set of elliptic PDE's [10]:

$$\begin{cases} \xi_{\bar{x}\bar{x}} + \xi_{\bar{y}\bar{y}} = P(\xi,\eta) \\ \eta_{xx} + \eta_{yy} = Q(\xi,\eta) \end{cases} \tag{5}$$

where subscripts denote differentiation. P and Q are prescribed to obtain the desired resolution in different parts of each zone. This is in fact a transformation of the coordinate system from Cartesian (x, y) to the body-fitted (ξ, η), i.e.

$$\begin{cases} x = x(\xi,\eta), \\ y = y(\xi,\eta). \end{cases} \tag{6}$$

Fig.3 schematically shows a body-fitted grid in (ξ, η) coordinates.

d) Maxwell's Equations in (ξ,t_f) Space

The Maxwell's equations are going to be solved in (ξ, η) space. Therefore, the transformation given by (6) is applied to the conservation form of these equations as expressed in (4). In order not to disturb the conservation form of (4), new solution vector and flux vectors are to be introduced. It may be shown that in (ξ, η) space, Maxwell's equations may be presented as

$$\frac{\partial \bar{Q}}{\partial t} + \frac{\partial \bar{R}}{\partial \xi} + \frac{\partial \bar{S}}{\partial \eta} = -\frac{J_{eq}}{J}, \tag{7}$$

where

$$\bar{Q} = Q/J \; ; \; \bar{R} = \left(\frac{1}{J}\, \bar{\xi} \times \nu \cdot \hat{z}, x_\eta u, y_\eta u \right);$$

$$\bar{S} = \left(-\frac{1}{J}\, \bar{\eta} \times \nu \cdot \hat{z}, x_\xi u, y_\xi u \right);$$

$$\bar{\xi} = \nabla\xi, \bar{\eta} = \nabla\eta; \; J = \partial(\xi,\eta)/\partial(x,y).$$

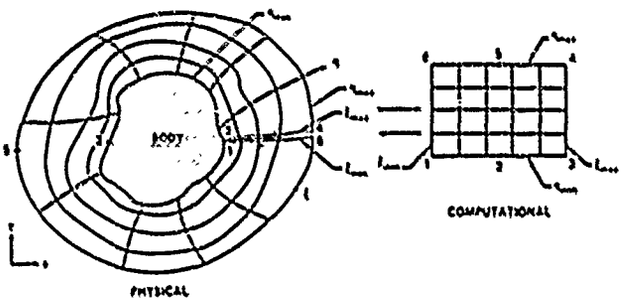


Fig. 3. Schematic of a body-fitted system

The current-like vector quantities $\bar{\xi} \times \nu$ and $\bar{\eta} \times \nu$ are in the z direction and may be regarded to be flowing over the walls of all computational cells. It should be noted that after the transformation from (x, y) to (ξ, η), the fields are still expressed in terms of their Cartesian components.

In each zone the grid divides the object and the surrounding space into a number cells with finite area (volume in 3-D problems). The material property within each cell is assumed to remain homogeneous and constant, but it may vary from one cell to the other. Across the four boundaries of each cell the tangential components of the electric and magnetic fields must satisfy the appropriate boundary conditions. These are simply

$$\hat{n} \times (E_1 - E_2) = 0 \quad ; \quad \hat{n} \times (H_1 - H_2) = 0$$

except where a cell neighbors a perfect conductor, in which case the only required condition is that $n \times E = 0$.

According to the characteristic theory of signal propagation the waves may be resolved into left and right traveling components along the coordinate directions ξ and η. This is analogous to the waves traveling back and forth on an unmatched transmission line [12]. The characteristic speeds for (7) may be obtained from the determinants

$$|\lambda I - A_R| = 0 \quad ; \quad |\lambda I - A_S| = 0,$$

where I is the identity matrix, $A_R = \frac{\partial \bar{R}}{\partial \bar{Q}}$, and $A_S = \frac{\partial \bar{S}}{\partial \bar{Q}}$.

When the right and left running signal components cross their corresponding characteristic directions (λ^- and λ^+) a jump occurs in their value. For computation since a discrete model is used these jumps are taken into account at the boundary between every two cells in both ξ and η directions. These jumps (denoted by vertical bars around the discontinuous quantities) are obtained from

$$\begin{cases} -\lambda \,|\, \bar{Q} \,|\, + \,|\, \bar{R} \,|\, = 0 \\ -\lambda \,|\, \bar{Q} \,|\, + \,|\, \bar{S} \,|\, = 0 \end{cases} \tag{8}$$

along ξ and η directions, respectively. Across the characteristic direction λ^0, the conditions to be satisfied are actually the continuity of the tangential components of the electric and magnetic fields. They are as follows

$$\begin{cases} u^* = u^{**} \\ \bar{\eta} \times (v^* - v^{**}) = 0 \\ \bar{\xi} \times (v^* - v^{**}) = 0 \end{cases} \tag{9}$$

Star and double star quantities are the values of the fields in each two neighboring cells right across the boundaries between them as shown in Fig. 4. In this figure two neighboring cells are presented. Solving (6) and making use of (9) produces the following expressions

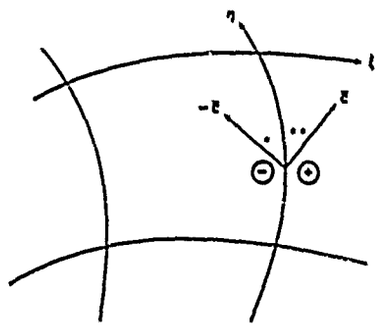


Fig. 4. One dimensional treatment for interface flux

$$\begin{cases} u^{*} = \dfrac{\gamma^{-}u^{-} + \bar{\xi} \times v^{-} \cdot \hat{z} + \gamma^{+}u^{+} - \bar{\xi} \times v^{+} \cdot \hat{z}}{\gamma^{-} + \gamma^{+}}, \\ \bar{\xi} \times v^{*} = \bar{\xi} \times v^{-} - \gamma^{-}(u^{*} - u^{-})\hat{z}, \end{cases} \tag{10}$$

along η direction, and

$$\begin{cases} u^{*} = \dfrac{\gamma^{-}u^{-} - \bar{\eta} \times v^{-} \cdot \hat{z} + \gamma^{+}u^{+} + \bar{\eta} \times v^{+} \cdot \hat{z}}{\gamma^{-} + \gamma^{+}}, \\ \bar{\eta} \times v^{*} = \bar{\eta} \times v^{-} + \gamma^{-}(u^{*} - u^{-})\hat{z}, \end{cases} \tag{11}$$

along ξ direction. In (10) and (11), $\gamma = 1/Z$ for TM-pol, and $\gamma = Z$ for TE-pol where $Z = \sqrt{\epsilon/\mu}$ is the intrinsic impedance of the material. Also field quantities with plus and minus superscripts represent the fields at the center of two neighboring cells.

e) Boundary Conditions at the Outer Boundary of the Computational Domain

Numerical solution to (7) at the center of each cell in the computational domain requires knowledge of the field quantities on the four walls of that cell. For cells neighboring the outer boundary of the computational domain, this information is not available for those walls residing on the boundary. Therefore, in general some approximate values have to be used. For scatterers of finite size, as a first order approximation one may use the Sommerfeld boundary condition. This would result in $u = 0$, $v_1 = 0$, and $v_2 = 0$ on the outer boundary. Higher order approximations also have been discussed in the literature [13], [14]. They generally reduce the size of the computational domain, and result in less computational time and storage requirement for a given problem.

The value of the field at the boundary of the computational domain may be specified so that some infinite size objects can be simulated in a finite domain. In this paper, this has been shown for an infinite plane, cavities in a ground plane and the half-plane problem. It may also be readily extended to the wedge.

The problem of reflection from an infinite plane can serve as a good tutorial example and will be considered first. Fig. 5 shows an infinite conducting plane

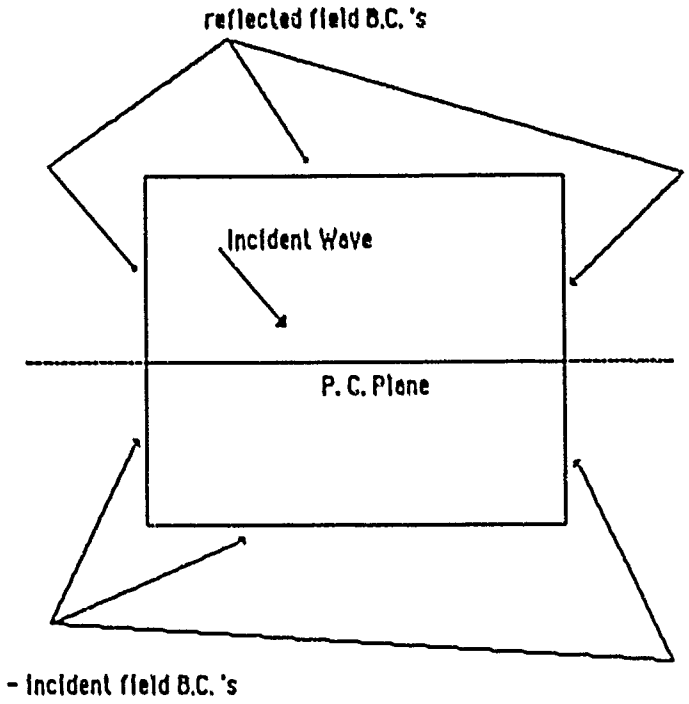


Fig. 5. Outer boundary condition for scattering from an infinite plane

dividing the space into two semi-infinite regions. For this problem the diffracted field formulation results in a trivial solution. Thus, the scattered field formulation will be discussed. The solution to the scattered field is, of course, known. It is simply a reflected field in region 1 and the negative of the incident field in region 2. To simulate the infinite plane, the exact value of the field on the outer boundary of the computational domain may be used in the computation. These are $u = u^r$, $v_1 = v^r_1$, and $v_2 = v^r_2$ in region 1, and $u = -u^i$, $v_1 = -v^i_1$, and $v_2 = -v^i_2$ in region 2.

The problem of a cavity in a ground plane may also be solved with either the scattered or diffracted field formulations. In the latter, the boundary condition will be similar to a finite body, i.e. no reflection from the outer computational boundary. In the former case, however, in addition to the scattering from the cavity a field reflected from the ground plane is also present everywhere in the space. Therefore, it is necessary to include the reflected field in the outer boundary condition. For the first order condition previously mentioned, one would now have $u = u^r$, $v_1 = v^r_1$, and $v_2 = v^r_2$. Fig. 6 depicts the geometry and the boundary field values.

The half-plane problem is more delicate. In this case, the reflected field is not present in the whole space. Therefore, it has to be determined where on the outer boundary it is present. Fig. 7 schematically shows that for for an arbitrary outer boundary.

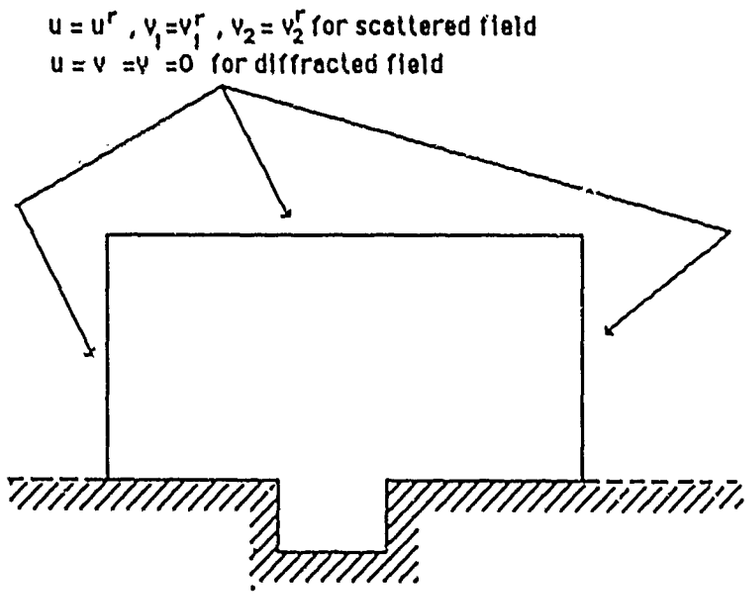


Fig. 6. Outer boundary condition for the rectangular cavity in a ground plane

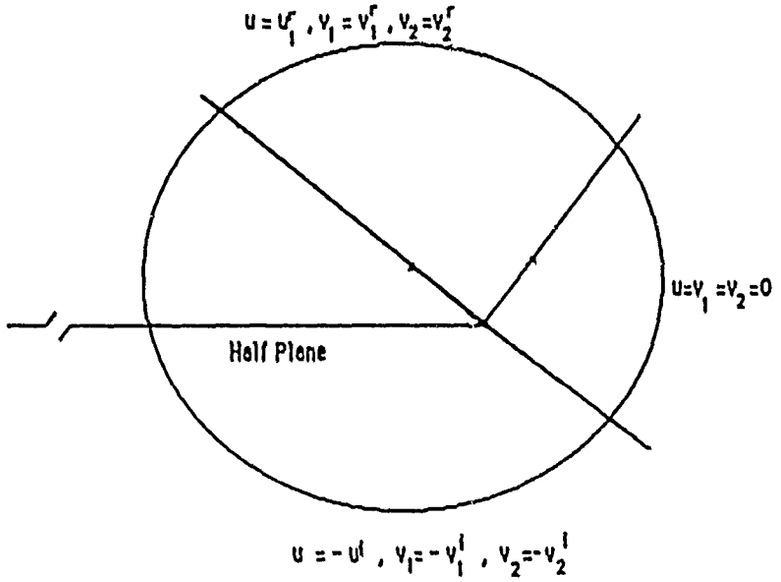


Fig. 7. Outer boundary condition for the half-plane problem

LAX-WENDROFF UPWIND NUMERICAL ALGORITHM

PDEs in (7) are now discretized and solved while making use of (10) and (11) which were derived based on the characteristic theory of signal propagation. The numerical algorithm used here is known as Lax-Wendroff upwind scheme [15], and is composed of two parts called predictor and corrector steps. A brief description of these steps is given in this section.

a) Predictor Step

The predictor will be explained when one of the coordinate variables in (4) is constant. In the ξ direction where η remains constant, (7) reduces to

$$\frac{\partial \tilde{Q}}{\partial t} + \frac{\partial \tilde{R}}{\partial \xi} = 0, \tag{12}$$

For simplicity assume that $J_{eq} = 0$. In (12) $\tilde{R}$ may be decomposed into plus and minus portions, corresponding to the characteristic combination of u and v which propagate toward increasing and decreasing ξ, respectively:

$$\frac{\partial \tilde{Q}}{\partial t} + \frac{\partial \tilde{R}^+}{\partial \xi} + \frac{\partial \tilde{R}^-}{\partial \xi} = 0. \tag{13}$$

For computational purposes, the time and space are discretized in (13), and the first order upwind scheme is applied to obtain the following algorithm

$$\tilde{Q}_j^{\overline{n+1}} = \tilde{Q}_j^n - \frac{\Delta t}{\Delta \xi}\left(\tilde{R}^-_{j+\frac{1}{2}} + d\tilde{R}^-_{j+\frac{1}{2}} - \tilde{R}^+_{j-\frac{1}{2}} + d\tilde{R}^+_{j-\frac{1}{2}} \right)^n \tag{14}$$

where dR^+ and dR^- are jumps in the fields across the positive and negative characteristic directions, respectively. Q, which is computed numerically at the spatial location j and time level n+1, is accurate to the first order.

b) Corrector Step

The solution from the previous step can be refined by accounting for second order terms. The upwind scheme that does this is expressed as follows

$$\begin{aligned} \tilde{Q}_j^{n+1} = \frac{1}{2}\Big\{ & \tilde{Q}_j^n + \tilde{Q}_j^{\overline{n+1}} \\ & - \frac{\Delta t}{\Delta \xi}\left[\tilde{R}^-_{j+\frac{1}{2}} + d\tilde{R}^-_{j+\frac{1}{2}} - \tilde{R}^+_{j-\frac{1}{2}} + d\tilde{R}^+_{j-\frac{1}{2}} \right]^n \\ & - \frac{\Delta t}{\Delta \xi}\left(d\tilde{R}^+_{j-\frac{1}{2}} - d\tilde{R}^+_{j-\frac{3}{2}} \right)^n + \frac{\Delta t}{\Delta \xi}\left(d\tilde{R}^-_{j+\frac{3}{2}} - d\tilde{R}^-_{j+\frac{1}{2}} \right)^n \Big\} \end{aligned} \tag{15}$$

Here dR^+ and dR^- are second order correction terms. From this algorithm Q is obtained at the time level n+1.

COMPUTATION OF THE FAR FIELD

Once Q is computed from (12), in principle electric and magnetic fields everywhere in the computational domain are known. In practice the grid is clustered near the object and is gradually declustered away from the object and toward the far-field boundary of the computational domain. This way a very accurate value can be obtained for the near field. The near field over a path enclosing the object is converted to the frequency domain using a FFT algorithm. The free-space Green's function is then used to obtain the field everywhere in space, including the far zone. The technique is a standard practice in electromagnetic theory and will not be discussed here.

NUMERICAL RESULTS

Some numerical results for scattering by an infinite plane, a cavity in a ground plane, and a half-plane will be presented here. Fig. 8 shows the scattered and total field contours for the infinite plane problem. These results show excellent agreement with the exact solution. Fig. 9 shows diffracted field contours for a 0.8 λ by 1.2 λ rectangular cavity in a ground plane and a cylindrical cavity with 0.5 λ radius in a ground plane. Fig. 10 shows some preliminary results for the RCS of the rectangular cavity. The far field, used to compute the RCS, is obtained by excluding the surface current on the portions of the ground plane which lie outside the computational domain. As a result the computed RCS values are to be regarded as approximations to the exact values. Better ways of computing the RCS are currently being considered.Fig. 11 shows the scattered and total fields for the half-plane problem. Finally, Fig. 12 shows the H_z (TE incidence) around the half plane at a distance of about λ /40 from the half-plane. The agreement between the numerical and the exact solutions appears to be very good.

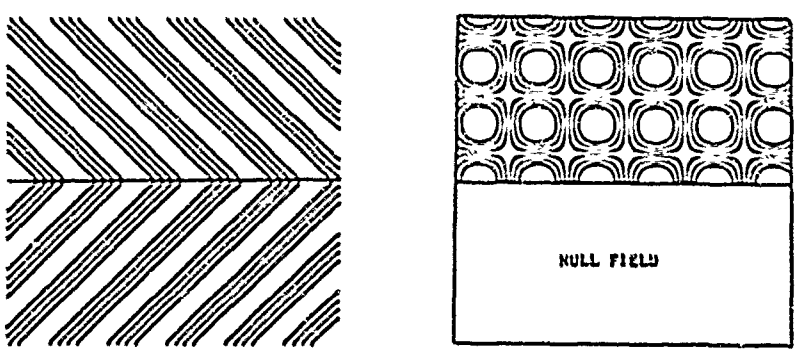


Fig. 8. Field contours for an infinite plane: scattered(left), total (right)

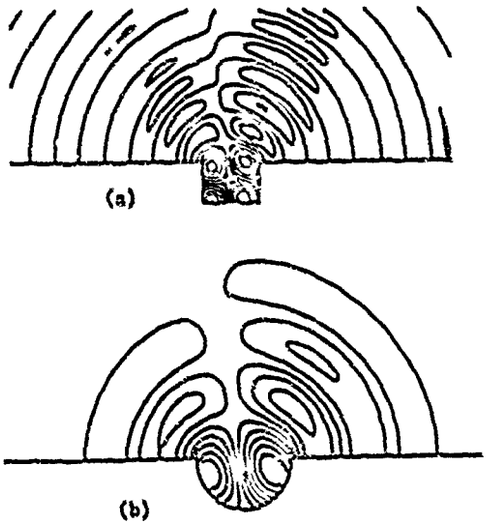


Fig. 9. Diffracted field contours for a cavity in a ground plane (a) rectangular (b) cylindrical.

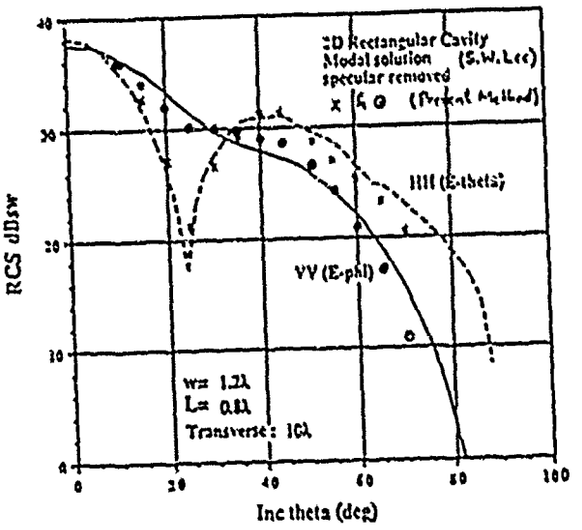


Fig. 10 . RCS for a rectangular cavity in a ground plane (specular removed)

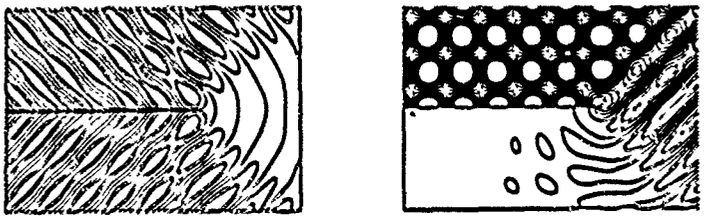


Fig. 11. Contours of the scattered field (left) and total field (right) for the half-plane problem

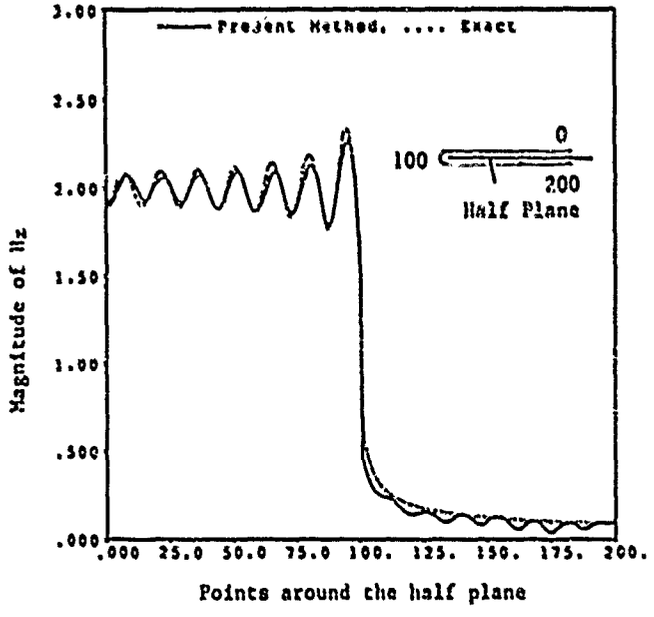


Fig. 12. Near field for the half-plane problem

REFERENCES

[1] K.K. Mei, M.E. Morgan, and S-K Chang," Finite methods in electromagnetic scattering," In *Electromagnetic Scattering* Edited by P.L.E. Uslenghi, New York: Academic Press, 1978.

[2] A. Taflove,"Application of the finite-difference time-domain method to sinusoidal steady-state electromagnetic penetration problems,"*IEEE Trans. Electromagnetic Compatibility*, vol. EMC-22, no.3, August 1980.

[3] V.S. Shankar and W.F. Hall," A time-domain differential solver for electromagnetic scattering," *URSI Meeting* , Boulder, January 1988.

[4] V. Shankar and W.F. Hall," A three-dimensional Maxwell's equations solver for computation of scattering from layered media," *Proc. of The Third Biennial Conference on Electromagnetic Field Computation*, Washington D.C., December 1988.

[5] V. Shankar, W.F. Hall, and A.H. Mohammadian," A time-domain differential solver for electromagnetic scattering problems," To appear in a special issue of the *Proc. of IEEE* in Mid-1989.

[6] A.H. Mohammadian, V. Shankar, and W.F. Hall," Application of the time-domain differential solver to 2-D electromagnetic penetration problems," *Proc. of The Third Biennial Conference on Electromagnetic Field Computation*, Washington D.C., December 1988.

[7] A.H. Mohammadian, W.F. Hall, and V. Shankar," Time-domain solution of Maxwell's equations in frequency-dependent media," *National Radio Science Meeting*, Boulder, Colorado, January 1989.

[8] K.S. Yee, " Numerical solution of initial boundary value problems involving Maxwell's equations in isotropic media," *IEEE Trans. Antennas Propagat.*, vol. AP-14, pp.302- 307, 1966.

[9] A. Sommerfeld, *Partial Differential Equations in Physics* (English translation). New York: Academic Press, 1949.

[10] J.F. Thompson, F.C. Thames, and C.W. Mastin," Automatic numerical generation of body-fitted curvilinear coordinate system for field containing any number of arbitrary two-dimensional bodies," *J. of Computational Physics*, vol. 15, no. 3, pp. 299-319, July 1974.

[11] J.L. Steger and R.L. Sorenson," Automatic Mesh-point clustering near a boundary in grid generation with elliptic partial differential equations," *J. of Computational Physics*, vol. 33, no. 3, pp.405-410, December 1979.

[12] F.H. Branin, Jr." Transient analysis of lossless transmission lines," *Proc. IEEE*, vol.55, pp. 2012-2013, Nov. 1967.

[13] B. Engquist and A. Majda, " Absorbing boundary conditions for the numerical solution of waves," *Mathematics of Computation* , vol. 31, no. 139, pp. 629-651, July 1977.

[14] G. Mur, " Absorbing boundary conditions for the finite-difference approximation of the time-domain electromagnetic-field equations," *IEEE Trans. Electromagnetic Compatibility*, vol. EMC-23, no.4, November 1981.

[15] R.F. Warming and R.M. Beam," Upwind second-order difference schemes and applications in Aerodynamic Flows," *AIAA J.*, vol. 14, no. 9, Sept. 1976.

A General UTD Diffraction Coefficient for Two Wedges

Raymond Luebbers
Michael Schneider

Communications and Space Sciences Laboratory
The Pennsylvania State University
University Park, PA 16802

ABSTRACT

The Uniform Theory of Diffraction has been extended to include double diffraction by an arbitrary configuration of two wedges. The resulting double diffraction coefficient D^2 is expressed as a sum of two double Fresnel integrals which can be rapidly evaluated.

INTRODUCTION

The Geometrical Theory of Diffraction has traditionally been used to compute scattering by perfectly conducting wedges. GTD[1] has subsequently been improved in the Uniform Theory of Diffraction[2] to remove singularities around optical boundaries. UTD itself has been extended in 1974 to include higher order terms of the asymptotic expansion to allow for slope diffraction which is involved in diffraction by thick edges. UTD, however, is not capable of handling double wedge diffraction as has been pointed out by many researchers. Previous solutions[3] were not general, putting restrictions on the geometry involved. In addition to geometrical generality, the new double diffraction coefficient D^2 is directly related to the product of two single diffraction coefficients. This greatly simplifies implementation in existing computer codes and incorporating it into a general UTD formulation combining direct, singly diffracted and doubly diffracted rays.

FORMULATION

The geometry of the double wedge configuration is shown in Fig. 1. The field is incident from source 0 with soft or hard polarization on the first edge and the consequently diffracted to reach observation point P. Respective distances are denoted by ρ, ρ', ρ''. Normal incidence to the edge (two-dimensional scattering) has been assumed while for oblique incidence (three-dimensional) the distances need to be multiplied by $\sin\beta_0$ where β_0 is the angle of the incident field with the first edge. The wedges are perfectly conducting. The exterior wedge angles are given by $n\pi$ and $n\pi$, where n,n need not be integers.

The complete diffraction coefficient D^2 and all variables needed for a numerical evaluation have been summarized in Table 1 of [6]. All variables used are defined in Table 2 of [6]. After the uniform double diffraction coefficient D^2 has been computed from Table 1, the doubly diffracted electric field becomes

$$E_{dd} = E_i \, D^2 \, A_{dd}(\rho, \rho', \rho'') e^{-jk\rho}$$

where E_i is the incident electric field at the first edge and A_{dd} is the ray spreading factor for double diffraction[4] given by

$$A_{dd}(s) = \begin{cases} \dfrac{1}{\sqrt{\rho\rho'\rho''}} & \text{for plane, cylindrical, and conical wave incidence} \\[2ex] \dfrac{\sqrt{\rho' + \rho''}}{\sqrt{\rho(\rho + \rho' + \rho'')}} & \text{for spherical wave incidence} \end{cases}$$

Outside of transition regions, where rays emanate from the diffracting edge with a cylindrical phase front, the Uniform Theory of Diffraction

provides correct answers[4]. With UTD diffraction coefficients D_1 for the first edge and D_2 for the second edge, the doubly diffracted electric field is then given by

$$E_{dd} = E_i \, D_1 \, D_2 \, A_{dd}(\rho,\rho',\rho'')e^{-jk\rho}$$

It has been shown[5],[6] that outside of transition D^2 reduces to $D_1 D_2$ such that numerical evaluations can be speeded up significantly.

The total field scattered by the geometrical structure of Fig. 1 is generally decomposed into different type of rays. These are the geometrical optics or direct ray, singly diffracted rays by the first and second edge and a doubly diffracted ray. Mathematically this can be formulated as

$$E(P) = E_i(P) + E_{d1}(P) + E_{d2}(P) + E_{dd}(P)$$

where P is the observation or field point.

If rays can not exist due to blockage, they don't contribute to the total field and their corresponding term must be removed from the summation. The direct ray reaching the observation point $E_i(P)$ is to be computed with a plane, cylindrical or spherical spread while singly diffracted rays $E_{d1}(P)$ and $E_{d2}(P)$ are computed using conventional UTD.

REFERENCES:

1. Keller, J. B.: Geometrical theory of diffraction, J. Opt. Soc. of America, Vol. 52, No. 2, pp. 116-130, 1962.

2. Kouyoumjian, R. G., Pathak, P. H.: A uniform geometrical theory of diffraction for an edge in a perfectly conducting surface, Proc. IEEE, Vol. 62, pp. 1448-1461, 1974.

3. Tiberio, R., Kouyoumjian, R. G.: An analysis of diffraction at edges illuminated by transition region fields, Radio Science, Vol. 17, No. 2, pp. 323-336, 1982.

4. Luebbers, R. J.: Propagation prediction for hilly terrain using GTD wedge diffraction, IEEE Trans. Antennas and Propagation, Vol. AP-32, No. 9, pp. 951-955, 1984.

5. Schneider, M.: A uniform solution of double wedge diffraction, Ph.D. Thesis, The Pennsylvania State University, December 1988.

6. Schneider, M., Luebbers, R.: A general uniform double wedge diffraction coefficient, submitted to IEEE Trans. Antennas and Propagation.

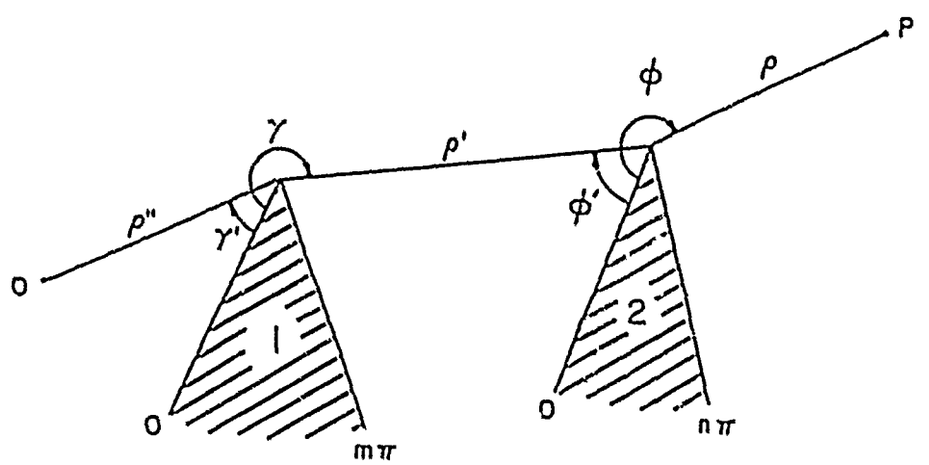


Figure 1. Geometry of double wedge configuration showing two perfectly conducting wedges, source point O and diffraction points at tip of wedges.

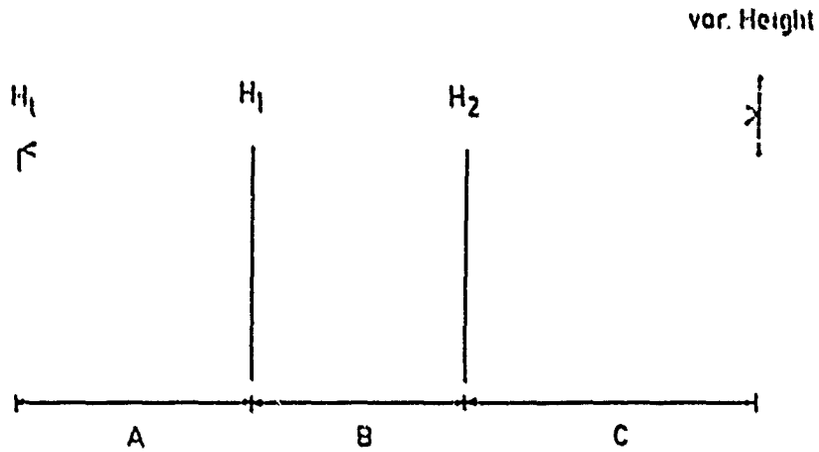


Figure 2. Geometry showing perfectly conducting knife-edges at heights H_1 = 50.0 m, H_2 = 50.0 m and a source at height H_t = 50.0 m. The spacings are A = 8000 m, B = 2000 m, C = 10000 m.

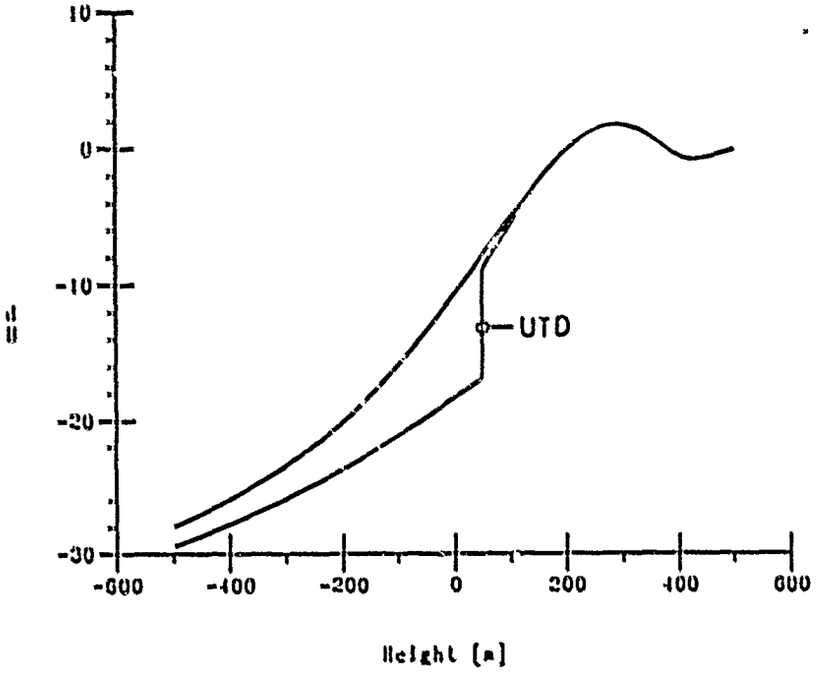


Figure 3. Graph corresponding to geometry of Fig. 2 showing path-loss in dB normalized to free space for the soft boundary condition and variable receiver height, compared to a mechanical application of UTD. The wavelength, λ, is 3.0 m. Transition region illumination of second edge results in large UTD error and illustrates improvement of new solution.

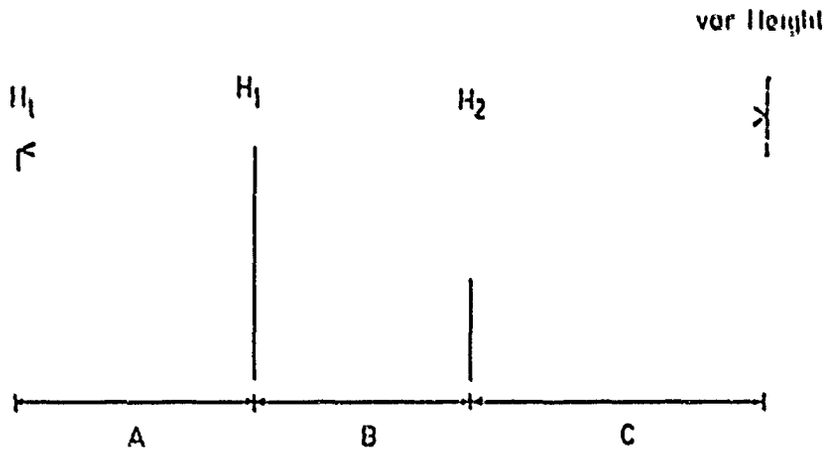


Figure 4. Geometry showing two perfectly conducting knife-edges at heights H_1 = 50.0 m, H_2 = 100.0 m and a source at height H_t = 50.0 m. The spacings are A = 8000 m, B = 2000 m, C = 10000 m. H_2 is now completely outside the transition region.

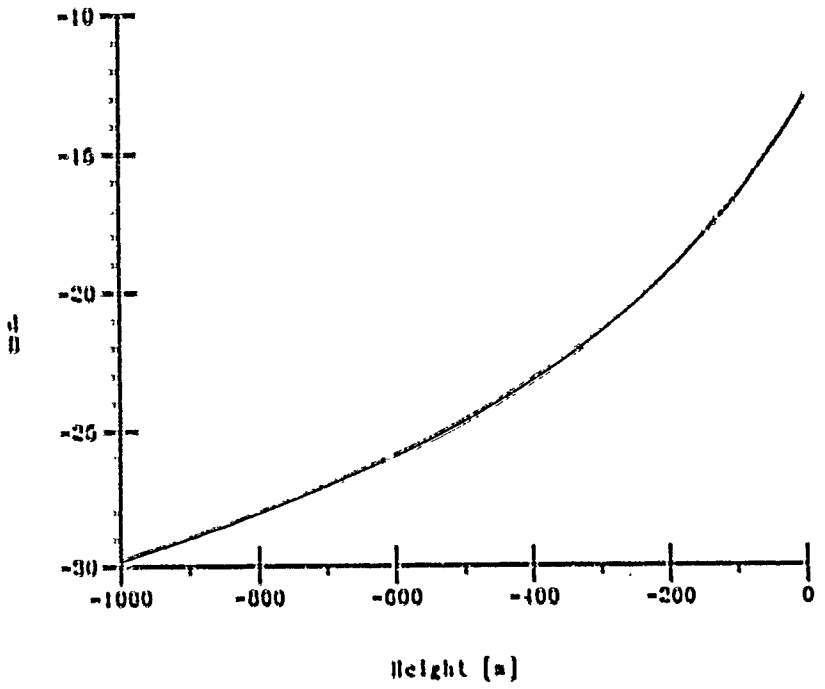


Figure 5. Graph corresponding to geometry of Fig. 4 showing path-loss in dB normalized to free space for the soft boundary condition and variable receiver height, compared to a mechanical application of UTD. The wavelength, λ, is 3.0 m. Lowering second edge completely outside of transition region eliminates UTD error and illustrates agreement of both solutions outside of transition regions.

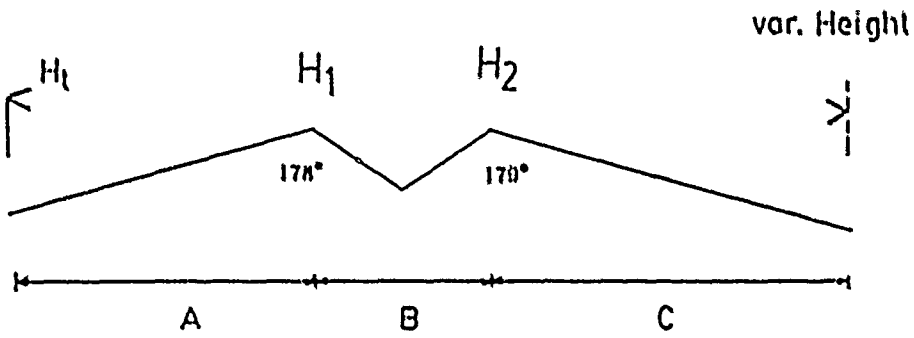


Figure 6. Geometry showing two perfectly conducting wedges at heights H_1 = 50.0 m, H_2 = 50.0 m and a source at height H_t = 50.0 m. The spacings are A = 8000 m, B = 2000 m, C = 10000 m.

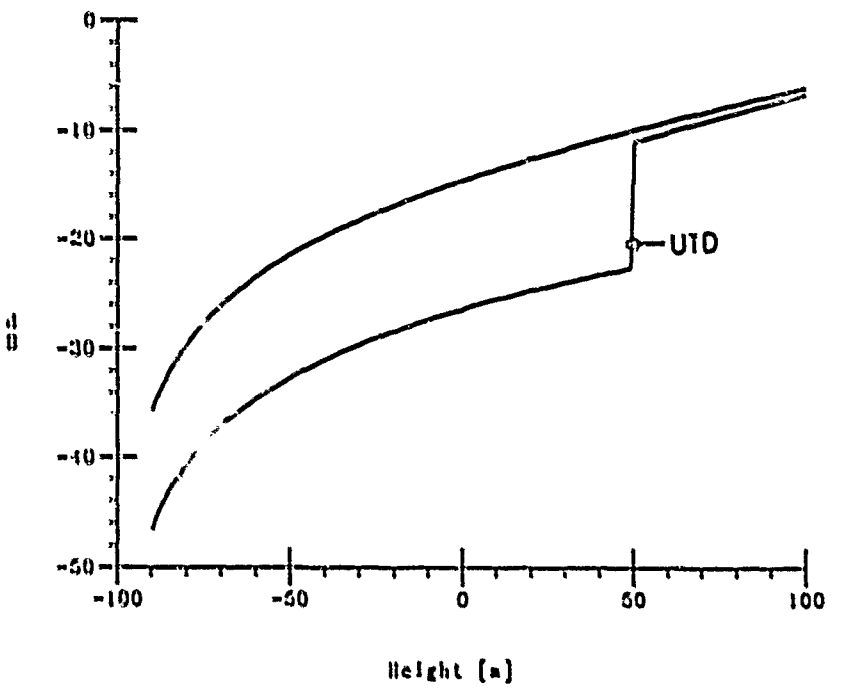


Figure 7. Graph corresponding to geometry of Fig. 6 showing path-loss in dB normalized to free space for the soft boundary condition and variable receiver height, compared to a mechanical application of UTD. The wavelength, λ, is 3.0 m. New solution gives smooth, continuous result for wedges with large interior angles.

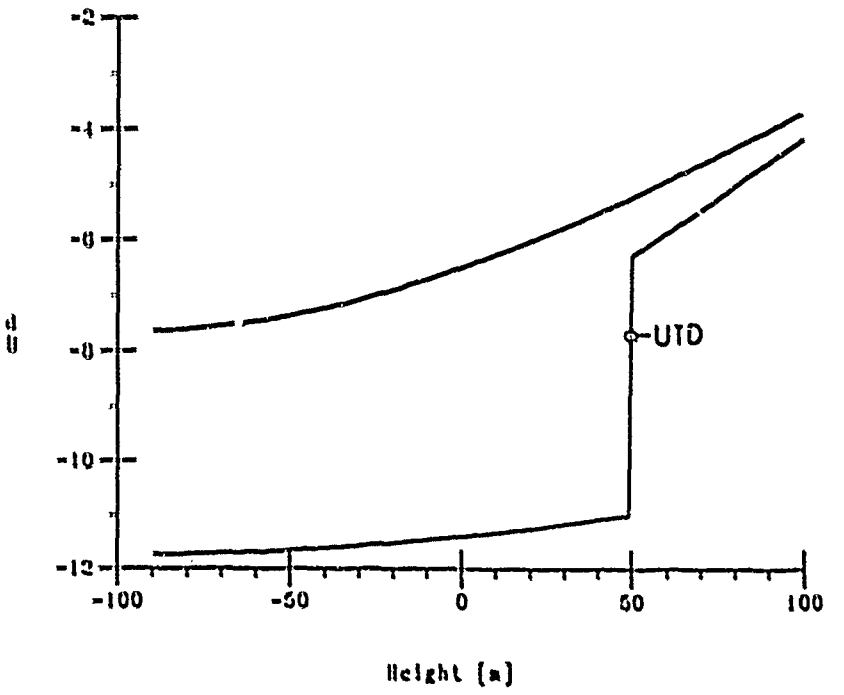


Figure 8. Graph corresponding to geometry of Fig. 6 showing path-loss in dB normalized to free space for the hard boundary condition and variable receiver height, compared to a mechanical application of UTD. The wavelength, λ, is 3.0 m. New solution gives smooth, continuous result for wedges with large interior angles.

Transient Response of Highly Conductive Materials Using a New FDTD Formulation

R. J. Luebbers
F. P. Hunsberger
K. S. Kunz

Communications and Space Science Laboratory
Electrical Engineering Department
The Pennsylvania State University
University Park, PA 16802

March 1989

ABSTRACT

Present Finite Difference Time Domain (FDTD) formulations use non-dispersive constitutive parameters to model materials, thereby reducing the accuracy of results obtained with wide-band transient excitation. The temporally-dispersive electric permittivity of a dielectric material has been incorporated by the authors into a frequency-dependent FDTD formulation, or $(FD)^2TD$, which includes discrete convolution of the time-domain electric susceptibility function with previous electric field values.

Results are presented here for application of $(FD)^2TD$ to materials with high conductivities which, because of their non-negligible zero frequency conductivity, exhibit a time-domain susceptibility function much different from polar dielectrics like water. For plasma applications where the frequency content of the excitation pulse may include the plasma frequency, the effective frequency-domain permittivity passes through zero and precludes the use of traditional FDTD algorithms. $(FD)^2TD$ has no difficulty with this situation, as will be shown. For very good conductors, the $(FD)^2TD$ formulation reduces to another form that exhibits a very different physical interpretation than that of other FDTD approximations.

INTRODUCTION

Traditional Finite Difference Time Domain (FDTD) formulations require the material permittivity, permeability, and conductivity be constant [1,2,3,4,5]. However, these parameters may vary significantly with frequency in dispersive materials. The effects of constitutive parameters which vary with frequency are included in a frequency-dependent FDTD formulation, $(FD)^2TD$, by extending the traditional Yee formulation to include discrete convolution of time-domain constitutive functions and previous field values. The accuracy of $(FD)^2TD$ has been demonstrated by computing the reflection coefficient at an air-water interface over a wide frequency band including the effects of the frequency-dependent permittivity of water [6].

While the results for water are encouraging, application of $(FD)^2TD$ to other materials, specifically conductors and plasmas, requires further investigation. This is because polar dielectrics such as water exhibit frequency- and time-domain electric permittivity functions very different from materials like conductors, which have large conductivities (and free electrons) at zero frequency. In fact, for plasmas the value of the complex frequency-domain permittivity is zero at the plasma frequency, while the time-domain permittivity function remains non-zero.

Having obtained the appropriate susceptibility functions, we have investigated the capability of $(FD)^2TD$ to compute electromagnetic interactions with conductive materials. Preliminary results indicate that $(FD)^2TD$ performs well, and furthermore is not subject to the same limitation ($\sigma \Delta t / \varepsilon < 1$) on highly conductive materials that applies to some other formulations [2,3,4].

FREQUENCY-DEPENDENT FDTD

The relation between the present electric polarization P of a material and the local electric field E is [7]

$$\vec{D}(t) = \varepsilon_{\infty}\varepsilon_{0}\vec{E}(t) + \varepsilon_{0}\int_{0}^{t}\vec{E}(t-\tau)\chi(\tau)d\tau \tag{1}$$

where ε_0 is the permittivity of free space, ε_∞ is the relative permittivity of the material as $\omega\to\infty$, and where $\chi(\tau)$ is the electric susceptibility. For polar dielectrics the frequency-domain relative permittivity is of the form

$$\varepsilon_r(\omega) - \varepsilon_\infty = \frac{\varepsilon_s - \varepsilon_\infty}{1 + j\omega t_0} \tag{2}$$

where t_0 is the relaxation time of the material [8]. The corresponding time-domain relative susceptibility function is

$$\chi(\tau) = \left(\frac{\varepsilon_s - \varepsilon_\infty}{t_0}\right)\cdot\exp(-\tau/t_0) \qquad \text{for } \tau>0 \tag{3}$$

Equations (1) and (3) can be substituted into the finite difference equations given by Yee [1] to find the appropriate relations between present and previous field values. For a one-dimensional propagation problem (in the $+x$ direction) the $(FD)^2TD$ equation for Maxwell's $\nabla\times\vec{H}$ equation is

$$E_y^{n+1}(i) = \frac{\varepsilon_\infty(i)}{\varepsilon_\infty(i)+\chi_0(i)}E_y^n(i) + \frac{1}{\varepsilon_\infty(i)+\chi_0(i)}\sum_{m=0}^{n-1}E_y^{n-m}(i)\Delta\chi_m(i)$$

$$-\frac{\Delta t}{(\varepsilon_\infty(i)+\chi_0(i))\varepsilon_0\Delta x}\left[H_z^{n+\frac{1}{2}}(i+\tfrac{1}{2}) - H_z^{n+\frac{1}{2}}(i-\tfrac{1}{2})\right] \tag{4}$$

(Refer to [6] for a description of the notation and variables.) Note that if we assume the relative permittivity, ε_r, is independent of frequency (the usual FDTD assumption) then $\chi(\tau)=0$, $\varepsilon_\infty=\varepsilon_r$, $\chi_m=0$ for all m, and the above reduces to the Yee formulation. The Yee equation for H will be unchanged for nonmagnetic media,

$$H_z^{n+\frac{1}{2}}(i+\tfrac{1}{2}) = H_z^{n-\frac{1}{2}}(i+\tfrac{1}{2}) - \frac{\Delta t}{\mu \Delta x}\left[E_y^n(i+1) - E_y^n(i)\right] \tag{5}$$

As mentioned above, the expression for the complex permittivity of conducting materials is different from dielectrics because conductors are characterized by a free electron density. Instead of (2), the frequency-domain relative permittivity for plasmas and conductors is [7]

$$\varepsilon^*(\omega) = \varepsilon_0\left(1 + \frac{\omega_p^2}{\omega(j\nu_c - \omega)}\right) \tag{6}$$

where ν_c is the collision frequency and ω_p is the radian plasma frequency. Transformation of (6) into a causal time-domain susceptibility function results in

$$\chi(\tau) = \frac{\omega_p^2}{\nu_c}\left[1 - \exp(-\nu_c \tau)\right] \cdot U(\tau) \tag{7}$$

where $U(\tau)$ is the unit step function. Following the method described in [6], equation (7) can be substituted into (4) to modify $(FD)^2TD$ for plasma and conductor propagation problems.

DEMONSTRATION

To demonstrate the validity of $(FD)^2TD$ for electromagnetic interactions with a plasma, the reflection and transmission coefficients from a cold plasma slab were calculated. The one-dimensional problem space consisted of 800 cells each 75 μm thick with plasma occupying cells 300 through 500. The time step was 0.125 ps. The plasma frequency was 28.7 GHz and the collision frequency was 2.0×10^{10}. From (6) one can see that below the plasma frequency the real part of the complex permittivity is negative and at the plasma frequency it passes through zero. This fact precludes the use of some traditional FDTD algorithms when applied to problems where significant signal content is located near the plasma frequency.

Calculations were made by propagating a Gaussian-derivative pulse through a plasma slab. The spectrum of the pulse is shown in Figure 1 and the electric field vs. position at

every 200 time steps is shown in Figure 2 through Figure 5. As can be seen, the plasma acts as a high-pass filter and rejects the slowly-varying part of the pulse. Figure 9 through Figure 12 show the magnitude and phase of the reflection and transmission coefficients measured just in front of, and just in back of, the plasma slab. The excellent agreement with the exact results is evident.

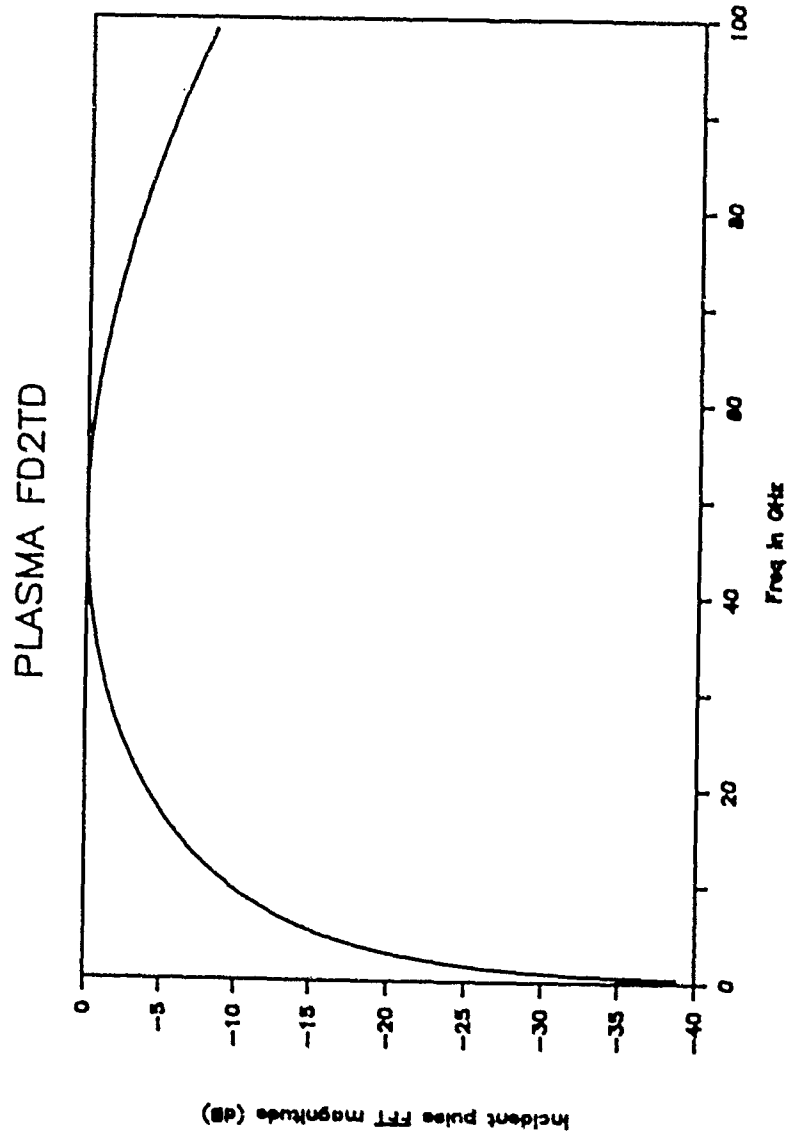


Figure 1: Incident Pulse Spectrum

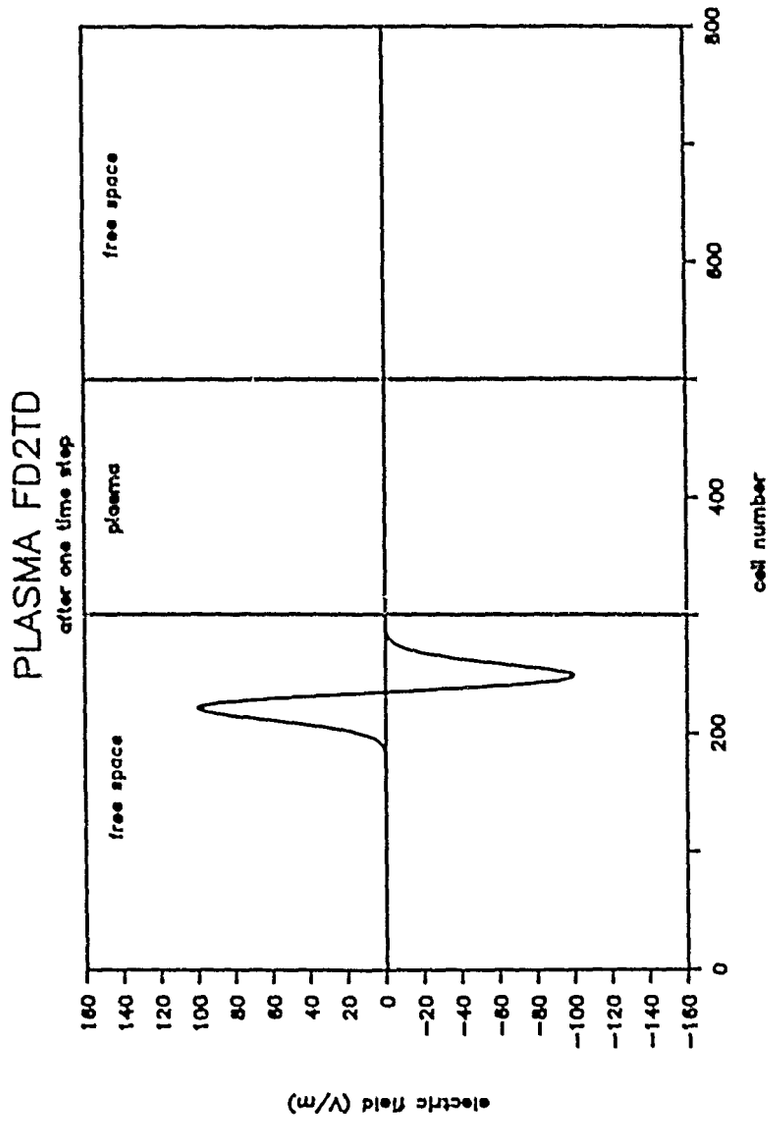


Figure 2: Initial Pulse

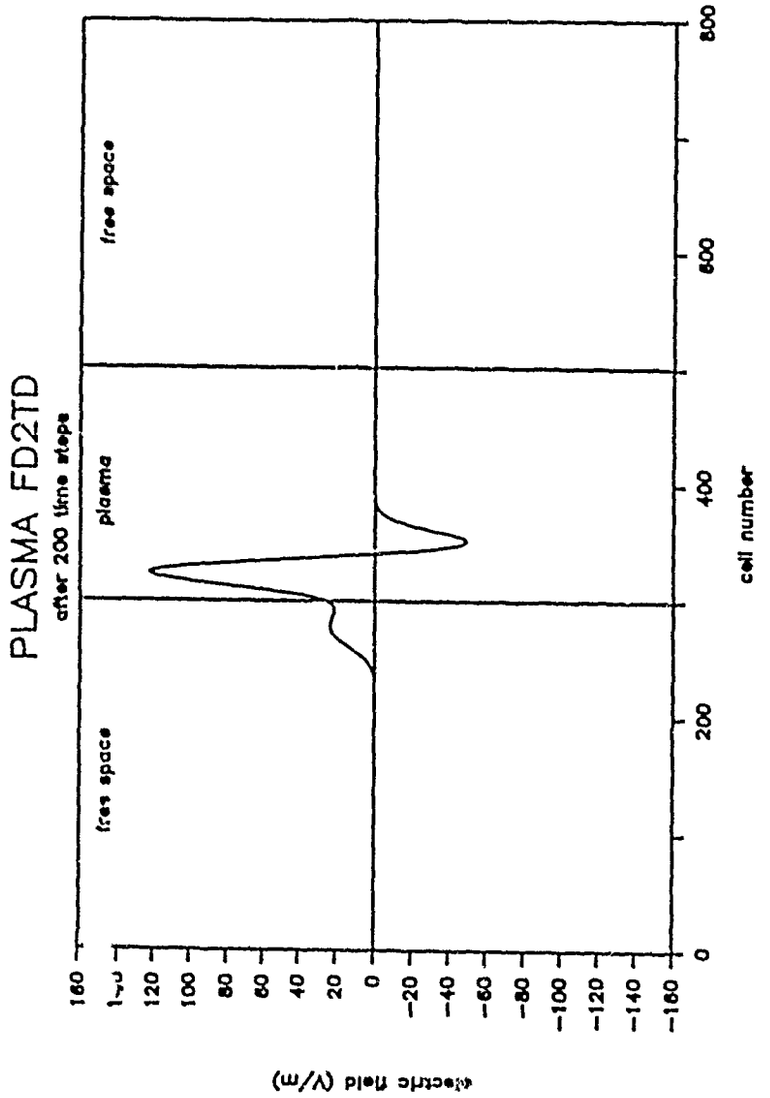


Figure 3: (FD)^{2}TD Pulse After 200 Time Steps

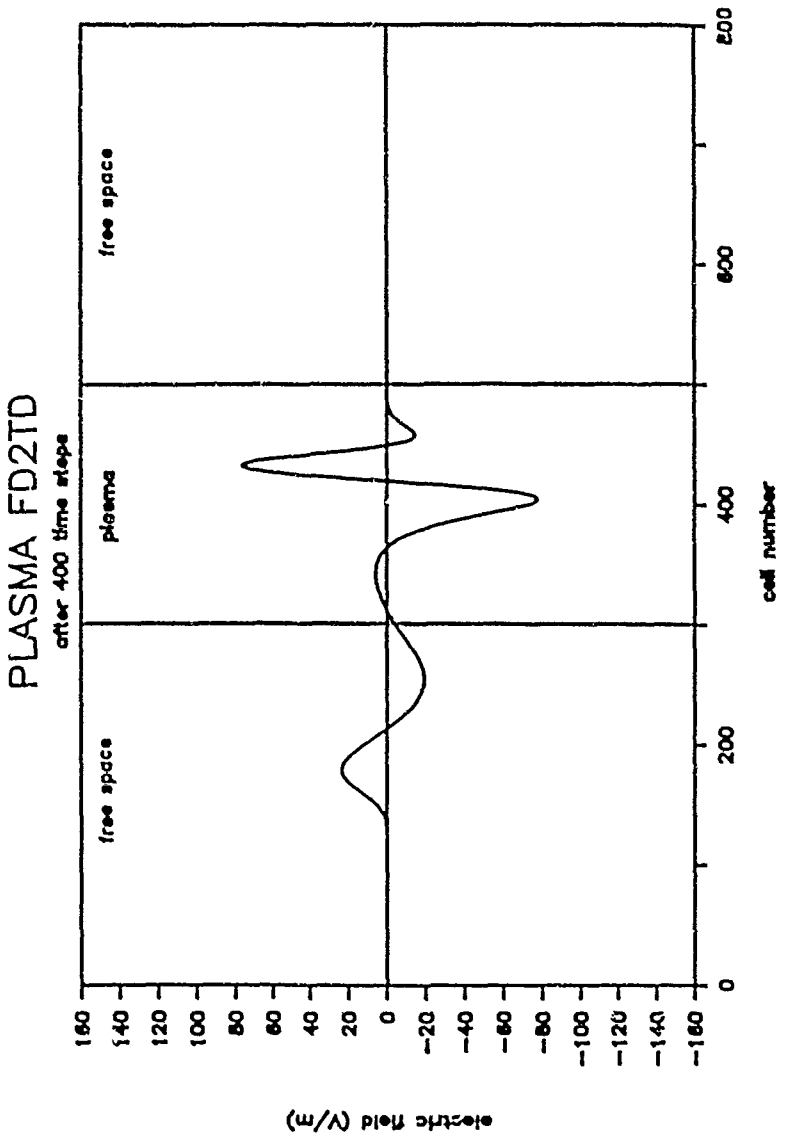


Figure 4: (FD)^{2}TD Pulse After 400 Time Steps

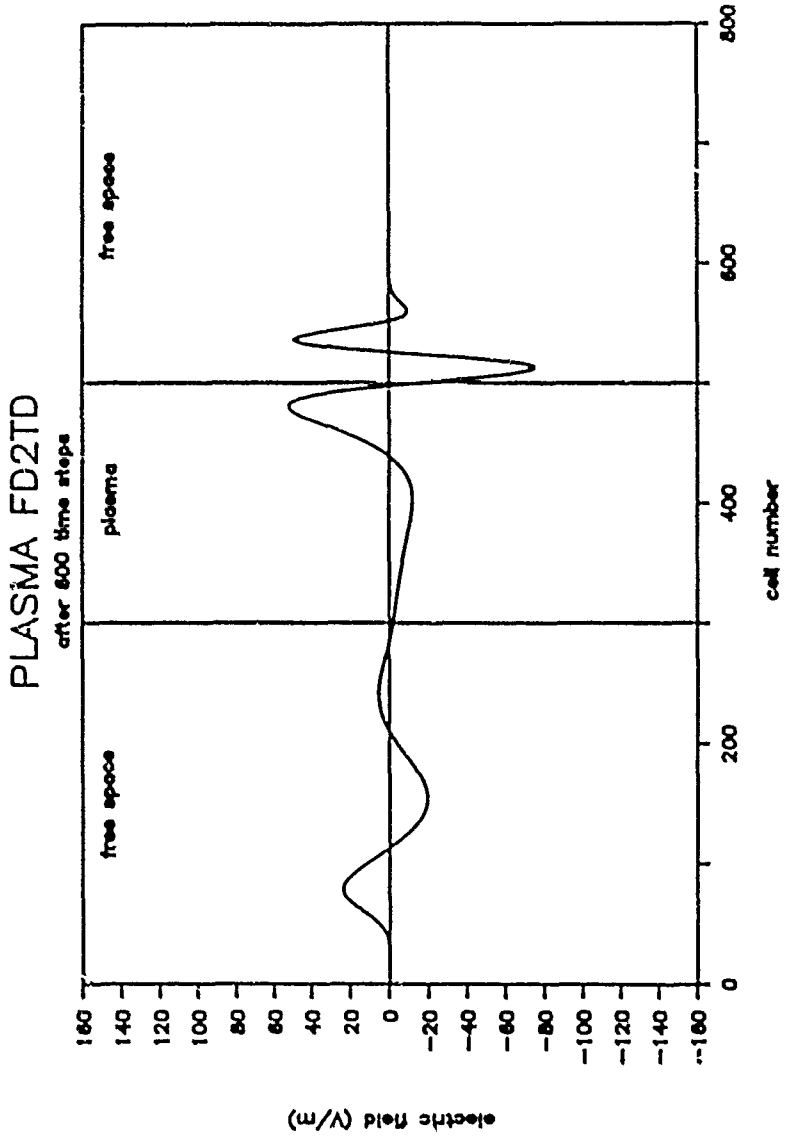


Figure 5: (FD)^{2}TD Pulse After 600 Time Steps

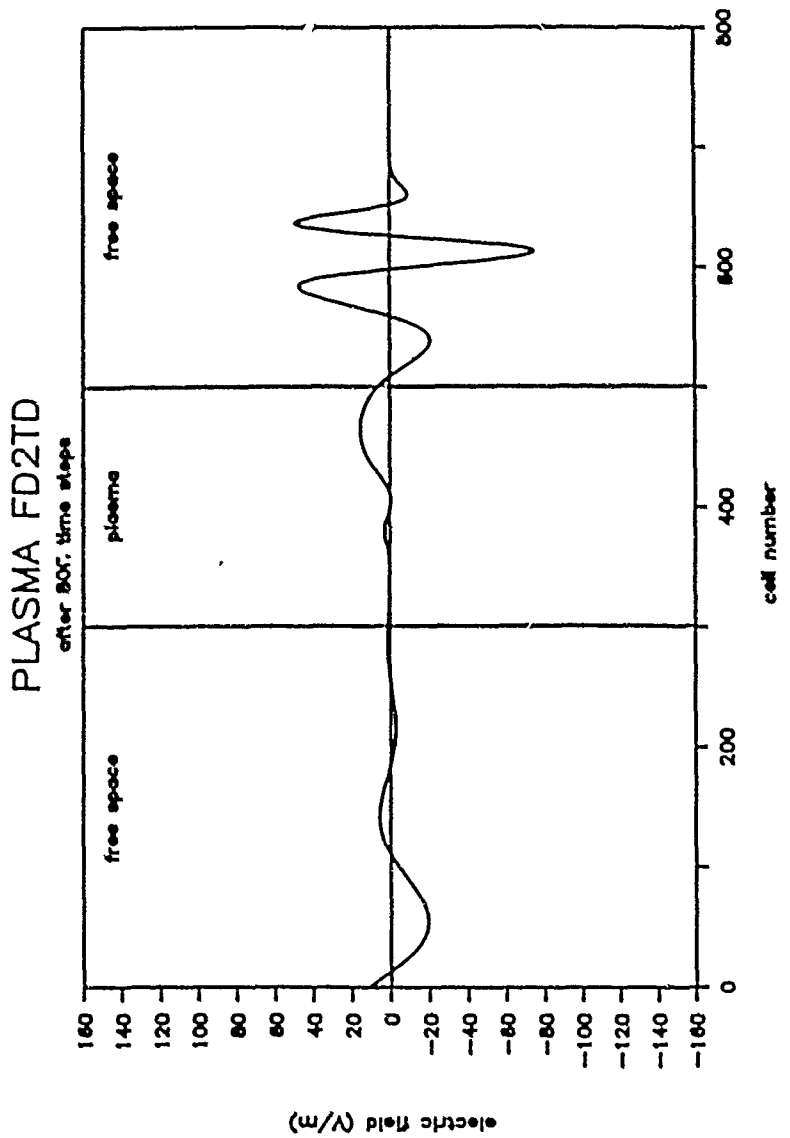


Figure 6: (FD)^{2}TD Pulse After 800 Time Steps

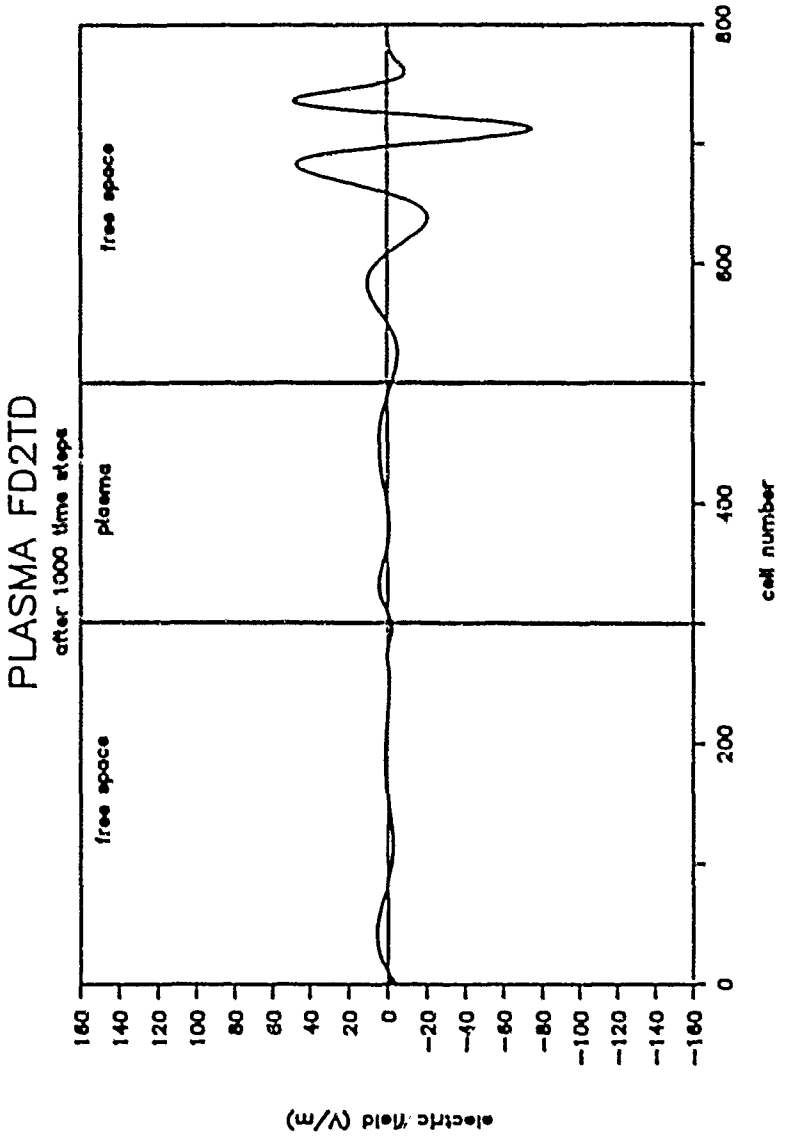


Figure 7: (FD)^{2}TD Pulse After 1000 Time Steps

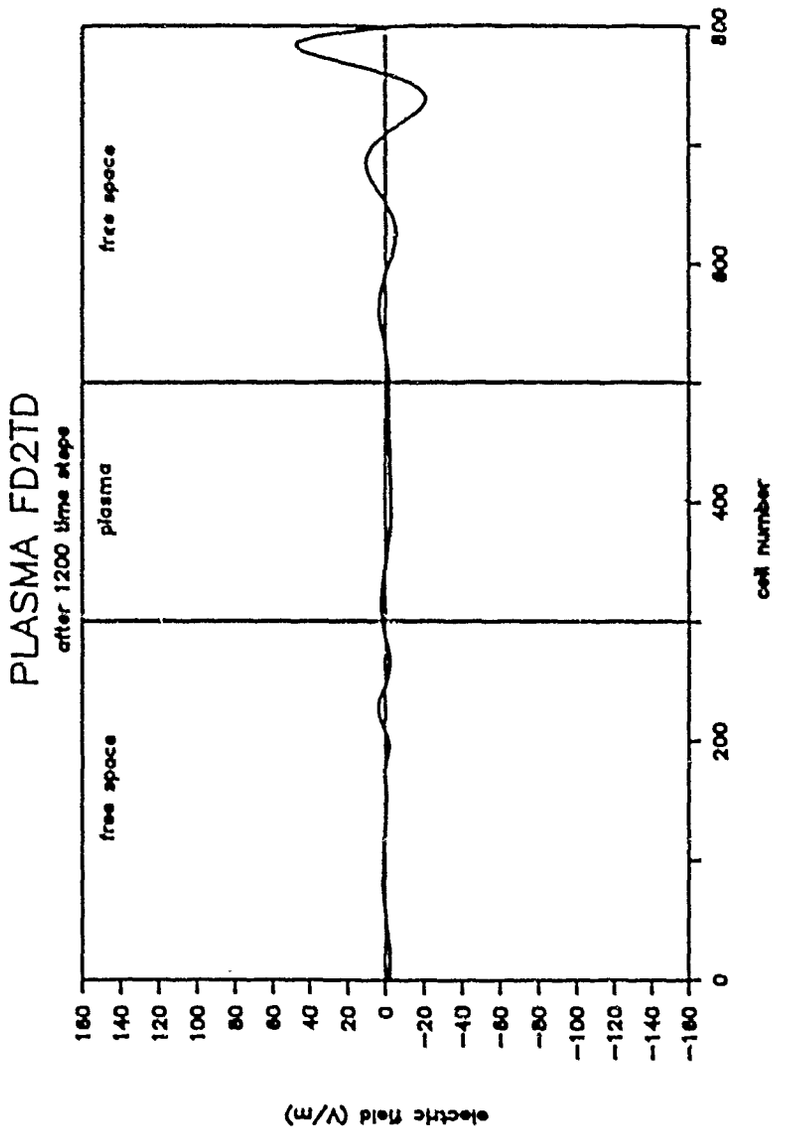


Figure 8: (FD)^{2}TD Pulse After 1200 Time Steps

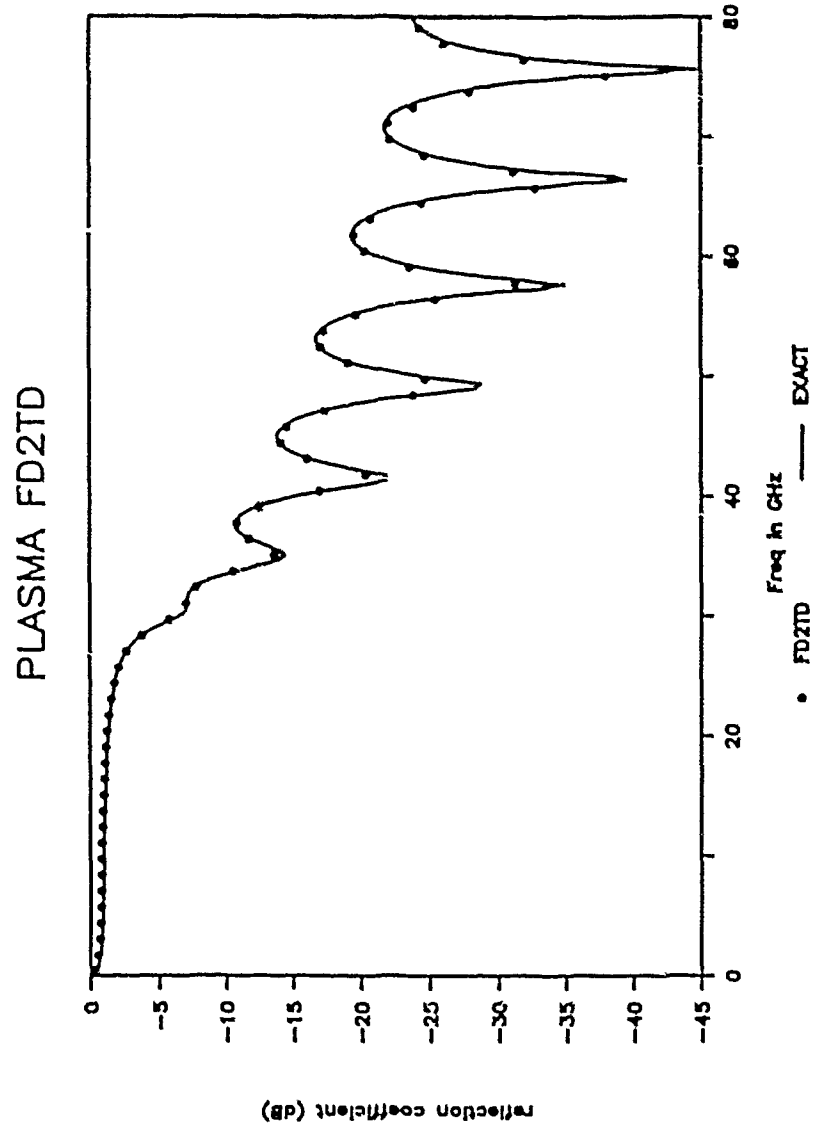


Figure 9: (FD)^{2}TD Reflection Coefficient Magnitude

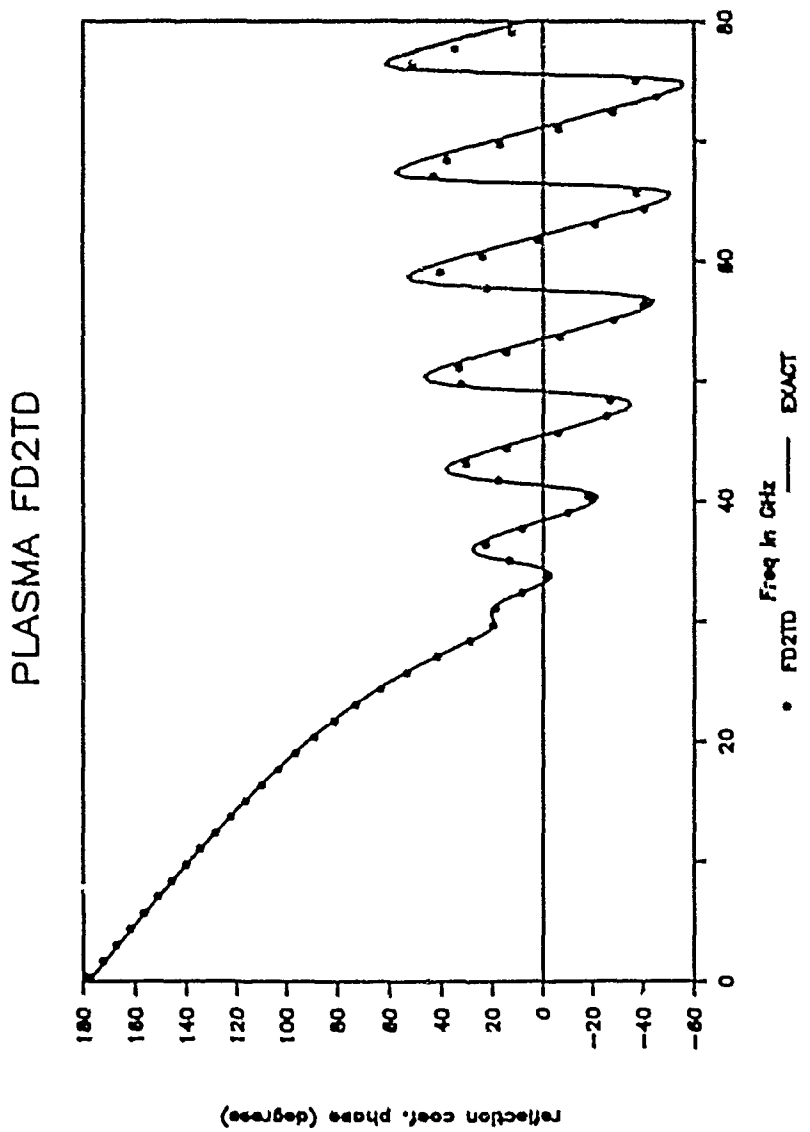


Figure 10: (FD)^{2}TD Reflection Coefficient Phase

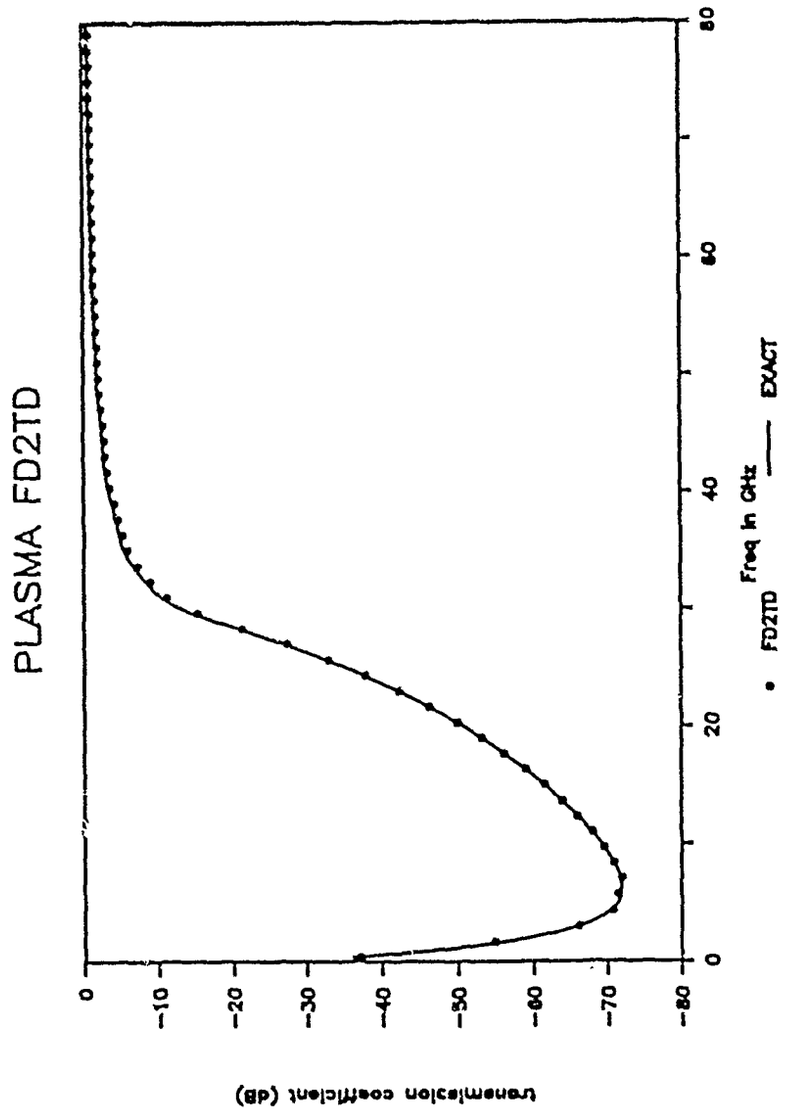


Figure 11: (FD)^{2}TD Transmission Coefficient Magnitude

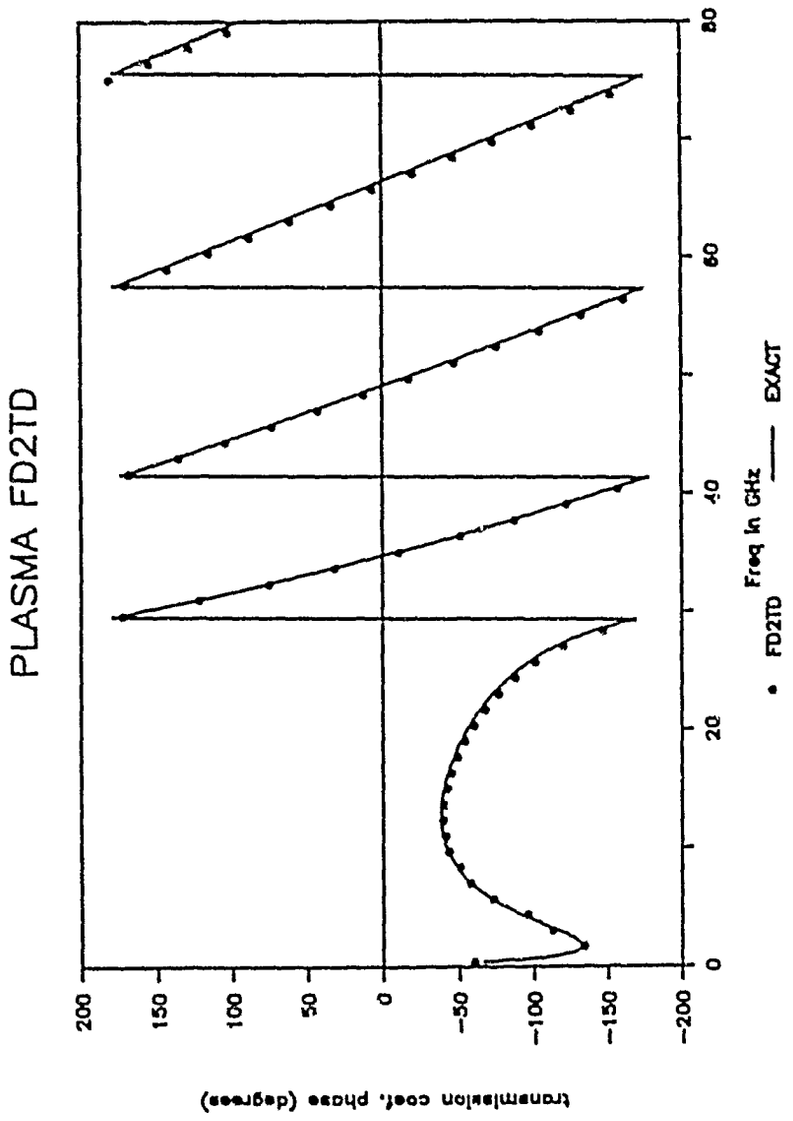


Figure 12: $(FD)^2TD$ Transmission Coefficient Phase

For extremely good conductors, the collision frequency ν_c approaches infinity (for copper $\nu_c \approx 3\times10^{11}$) [7]. In this limit, the $(FD)^2TD$ equation in (4) becomes

$$E_y^{n+1}(l) = \left[\frac{\varepsilon_\infty}{\varepsilon_\infty + \frac{\sigma\Delta t}{\varepsilon_0}}\right] E_y^n(l) - \frac{\Delta t}{\left(\varepsilon_\infty + \frac{\sigma\Delta t}{\varepsilon_0}\right)\varepsilon_0 \Delta x}\left[H_z^{n+\frac{1}{2}}(l+\tfrac{1}{2}) - H_z^{n+\frac{1}{2}}(l-\tfrac{1}{2})\right] \quad (8)$$

where the spatial dependence of ε_∞ has been omitted.

To demonstrate this modified form of $(FD)^2TD$ a Gaussian derivative pulse is propagated into a thin conductor slab. The spectrum of this pulse is shown in Figure 13. The one-dimensional cell space is 500 cells long (each measuring 10.62 μm) with a conductor (σ=1000) occupying cells 300 through 320. The time step is 1.77×10^{-14} so that $\sigma\Delta t/\varepsilon \approx 2$. The pulse's electric field amplitude vs. position at 100 time step increments is shown in Figure 14 through Figure 19. The strong reflection from the conductor is evident.

As a comparison, FDTD algorithms from other papers were also used with the parameters (cell size, conductivity, etc.) of this problem. Figure 20 shows the instability of the algorithm by Taflove and Brodwin [2,3] for propagation inside the conductor. (Shortly after this electric field profile was stored, the computer run aborted due to overflow errors.) Examination of their equations shows that when the conductivity (or the time step) is too large ($\sigma\Delta t/\varepsilon \to \infty$) computational errors arise. The equations by Ziolkowski, Madsen, and Carpenter's [4] are slightly different, but become unstable for the same reason as shown in Figure 21.

Figure 22 shows the stability of the algorithm by Sullivan, Borup, and Gandhi [5]. In fact, comparison of Figure 22 with Figure 23 (the modified $(FD)^2TD$ formulation result at the same time step) shows little difference. This agreement is surprising given the fact that

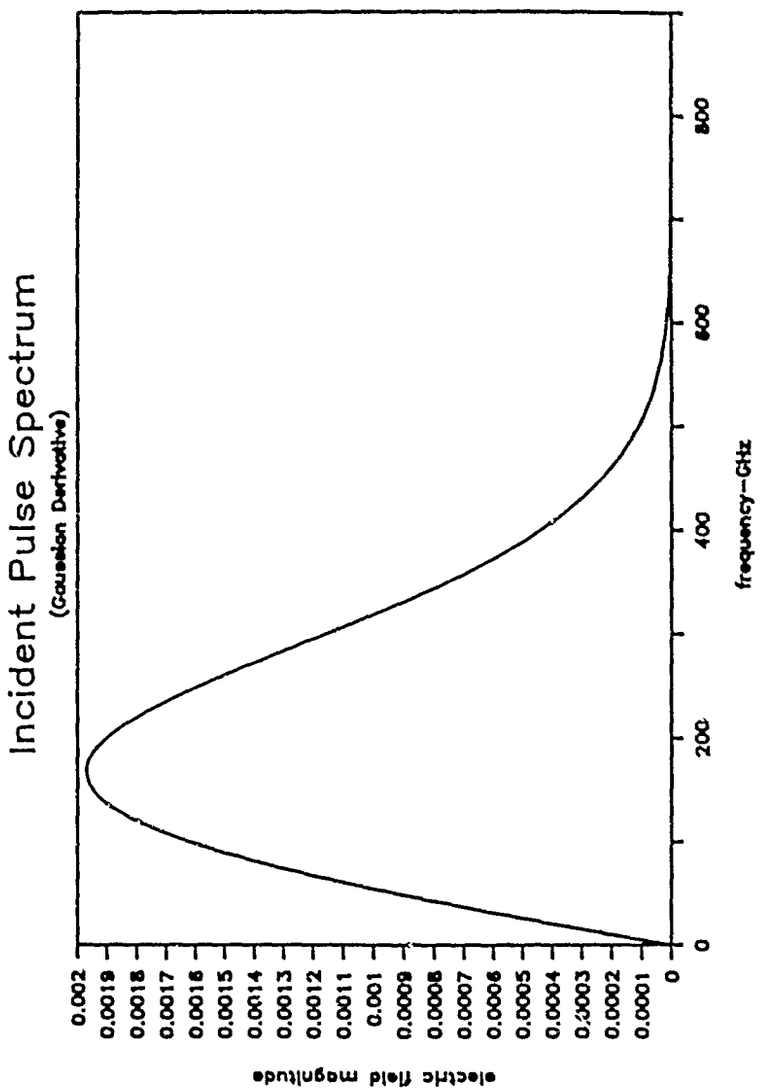


Figure 13: Incident Pulse Spectrum

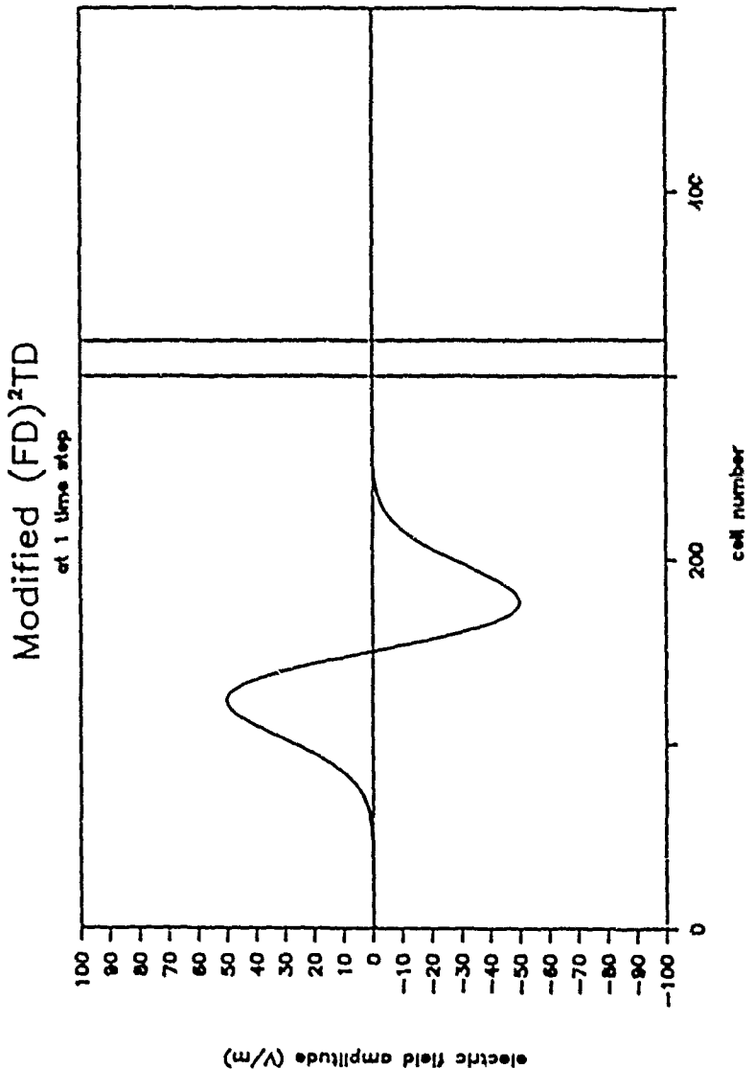


Figure 14: Initial Pulse

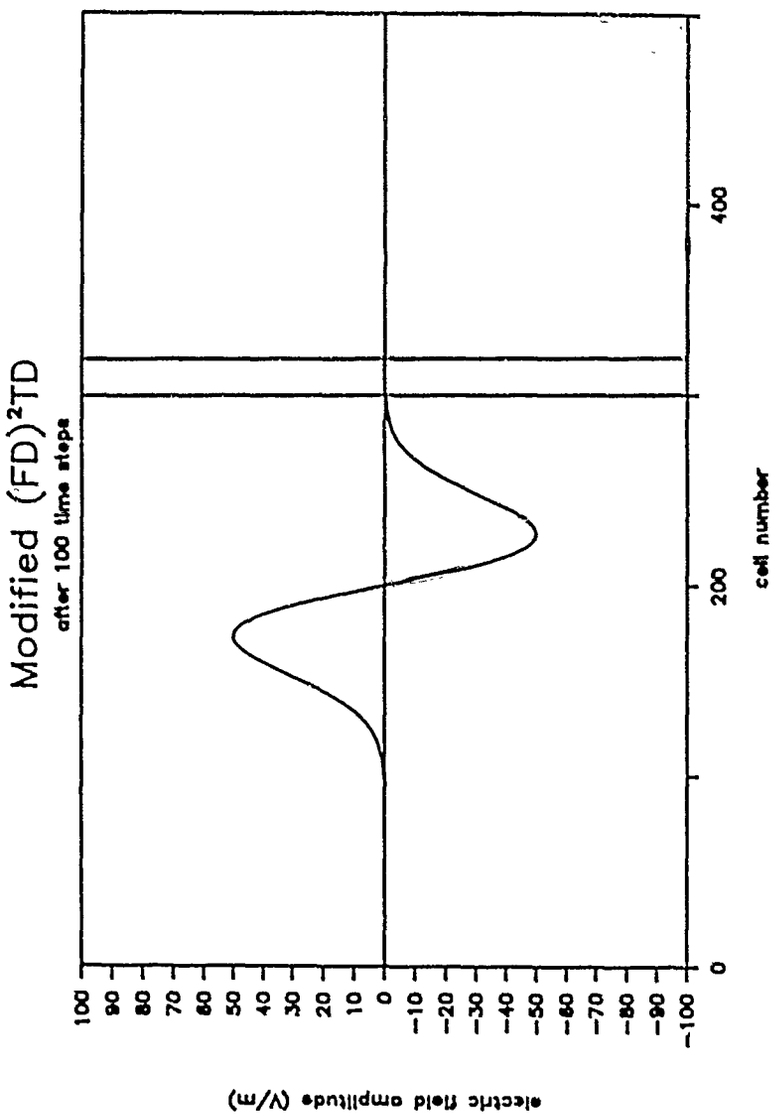


Figure 15: Pulse After 100 Time Steps

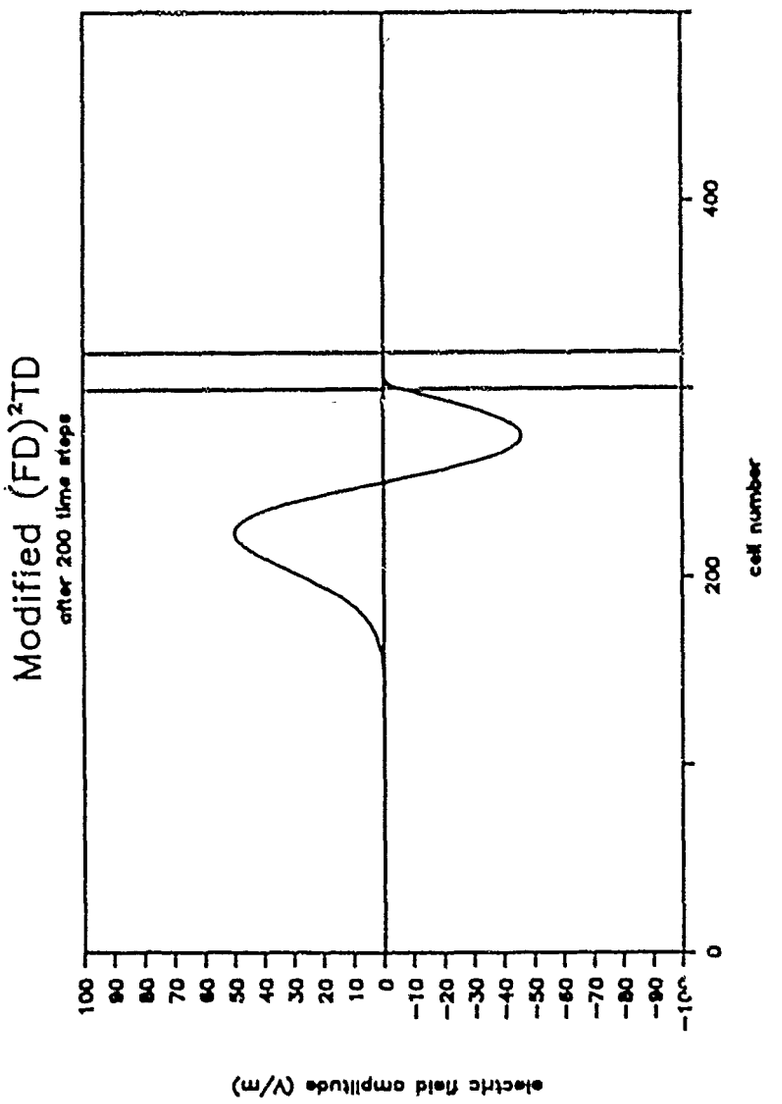


Figure 16: Pulse After 200 Time Steps

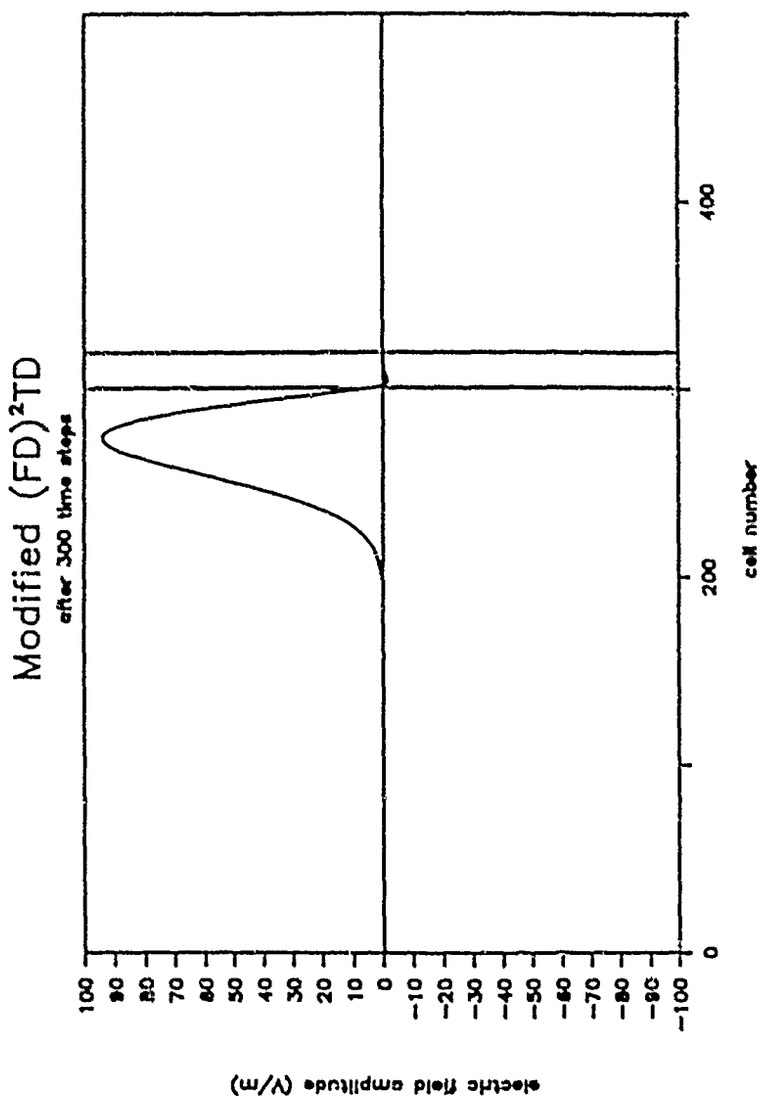


Figure 17: Pulse After 300 Time Steps

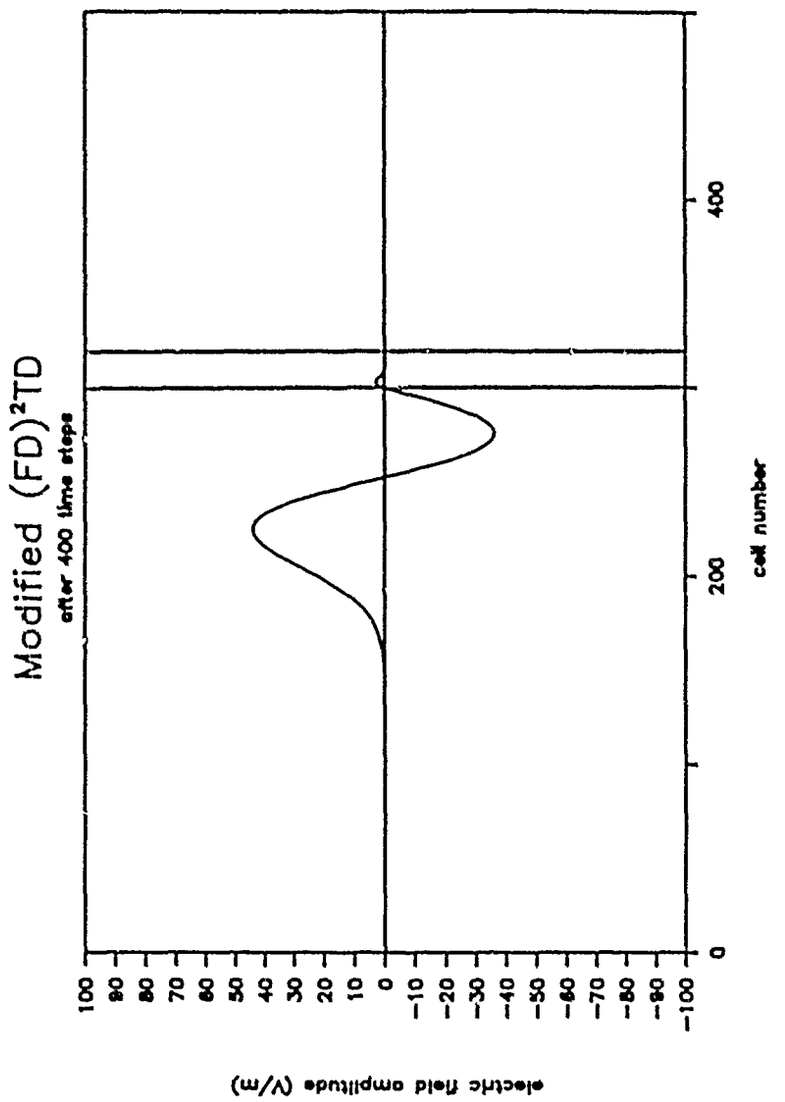


Figure 18: Pulse After 400 Time Steps

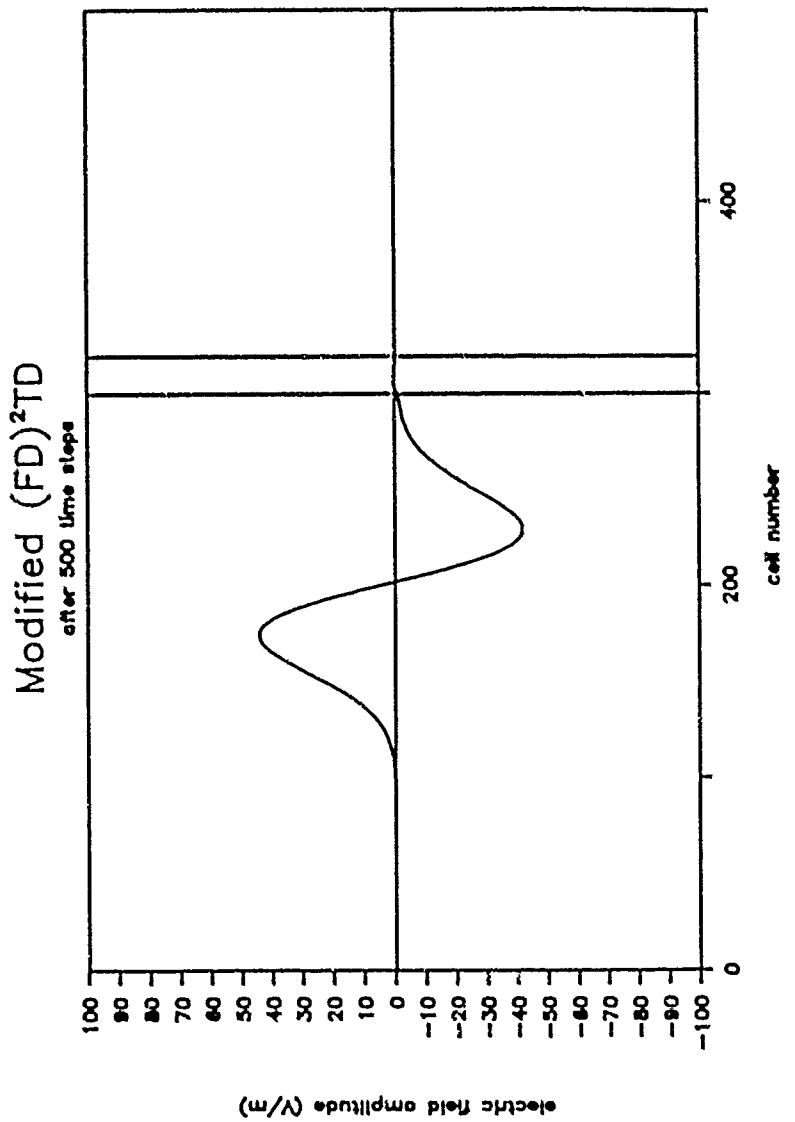


Figure 19: Pulse After 500 Time Steps

when both finite difference equations (equation (8) and that found in [5]) are solved, it is seen that the modified (FI)^{2}TI formulation considers the current density term J a function of the present E field value

$$\frac{D^n - D^{n-1}}{\Delta t} = \nabla \times H^{n-\frac{1}{2}} - \sigma E^n \tag{9}$$

while Sullivan's form assumes the current density is an average of the previous and present E field values:

$$\frac{D^n - D^{n-1}}{\Delta t} = \nabla \times H^{n-\frac{1}{2}} - \frac{1}{2}(\sigma E^n + \sigma E^{n-1}) \tag{10}$$

The formulations given in [2] and [4] give more significance to the E^{n-1} term and this apparently leads to the resulting instability.

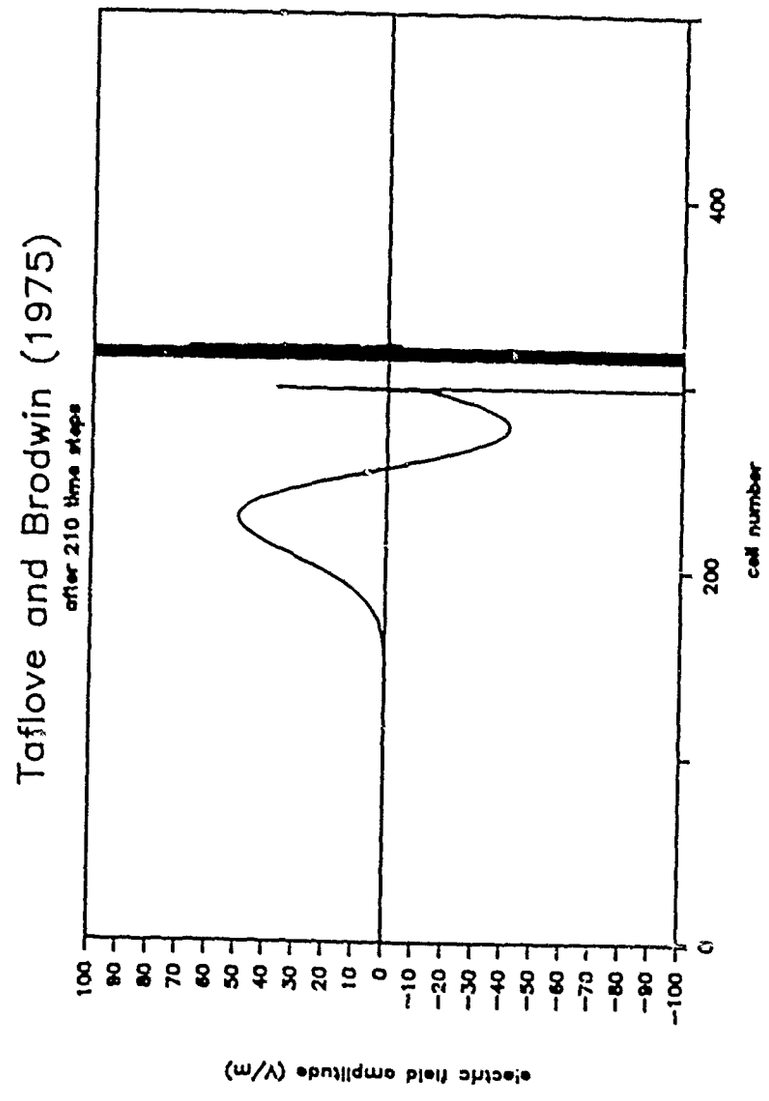


Figure 20: Taflove and Brodwin FDTD

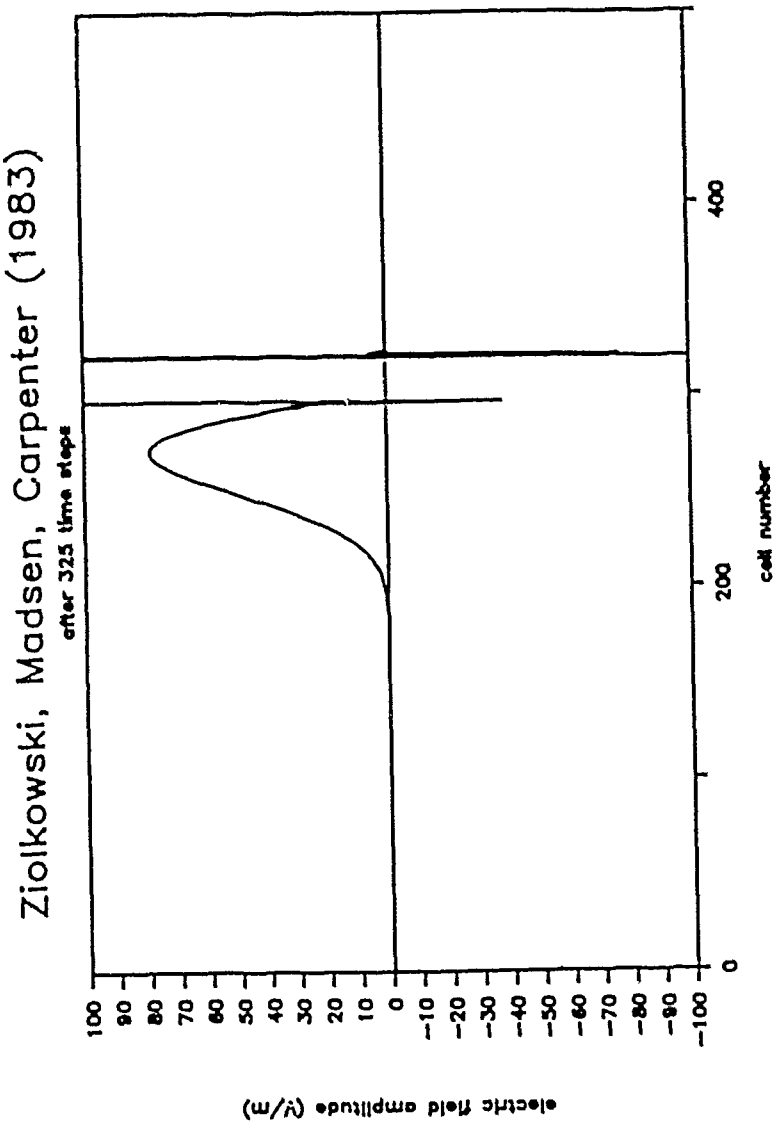


Figure 21: Ziolkowski, Madsen, and Carpenter FDTD

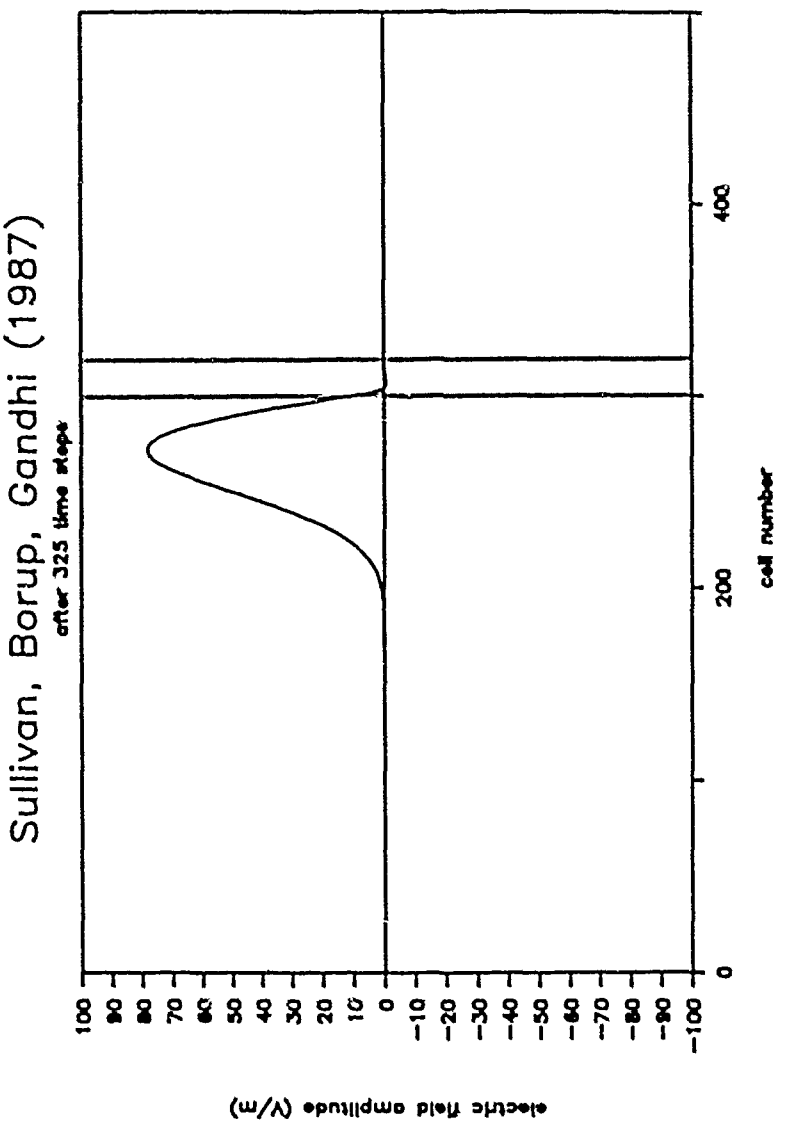


Figure 22: Sullivan, Borup, and Gandhi FDTD

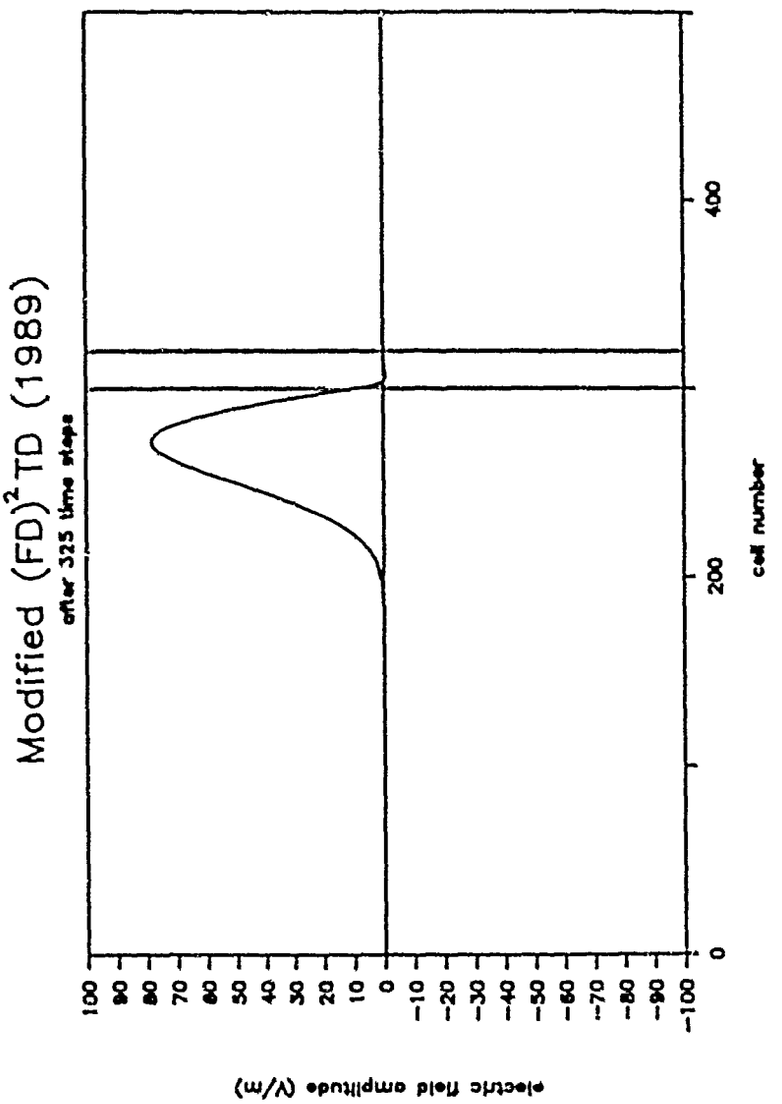


Figure 23: Modified (FD)^{2}TD

CONCLUSIONS

Extension of the basic $(FD)^2TD$ formulation to include electromagnetic wave interactions with materials characterized by free electrons has been presented. Validity was established with the computation of reflection and transmission coefficients through a plasma slab.

It was also shown that for plasmas and conductors characterized by a large collision frequency $(FD)^2TD$ reduces to a modified form that differs from other approaches in the interpretation of the current density term. This modified form was compared to other FDTD algorithms found in the literature in an example problem.

BIBLIOGRAPHY

1. K. Yee, "Numerical Solution of Initial Boundary Value Problems Involving Maxwell's Equations in Isotropic Media", *IEEE Transactions on Antennas and Propagation*, vol. AP-14, no. 3, pp.302-307, 1966.
2. A. Taflove and M. Brodwin, "Numerical Solution of Steady-State Electromagnetic Scattering Problems Using the Time-Dependent Maxwell's Equations", *IEEE Transactions on Microwave Theory and Techniques*, vol. MTT-23, no. 8, pp. 623-630, 1975.
3. A.Taflove and M. Brodwin, "Computation of the Electromagnetic Fields and Induced Temperatures Within a Model of the Microwave-Irradiated Human Eye", *IEEE Transactions on Microwave Theory and Techniques*, vol. MTT-23, no. 11, pp. 888-896, 1975.
4. R. Ziolkowski, N. Madsen, and R. Carpenter, "Three-Dimensional Computer Modelling of Electromagnetic Fields: A Global Lookback Lattice Truncation Scheme", *Journal of Computational Physics*, vol. 50, pp. 360-408, 1983.
5. D. Sullivan, D. Borup, and O. Gandhi, "Use of the Finite-Difference Time-Domain Method in Calculating EM Absorption in Human Tissues", *IEEE Transactions on Biomedical Engineering*, vol. BME-34, no. 2, pp.148-157, 1987.
6. R. Luebbers, F. Hunsberger, and K. Kunz, "A New FDTD Formulation for Materials with Frequency-Dependent Constitutive Parameters", presented at *The Fifth Annual Review of Progress in Applied Computational Electromagnetics.*
7. J. Jackson, *Classical Electrodynamics, 2nd ed.*. Wiley: New York, 1975.
8. K. Cole and R. Cole, "Dispersion and Absorption in Dielectrics", *J. Chemical Physics*, vol. 9, pp.341, 1941.

FINITE-DIFFERENCE TIME-DOMAIN MODELING OF ELECTROMAGNETIC RADIATION FROM AN ELECTRON BEAM *

S.T. Pennock, R.R. McLeod, H.G. Hudson
P.O. Box 808, L-156
Engineering Research Division
Lawrence Livermore National Laboratory
Livermore, CA 94550

Finite difference time domain codes have been used for a variety of propagation and scattering work in the past. Some recent work has been done in attempting to represent the electromagnetic radiation from a relativistic electron beam propagating in the atmosphere, in the presence of ground and metallic structures. Several methods of launching the electromagnetic waves from such a source have been tried, with results compared to both a scale-model representation and to time-domain measurements taken at a beam facility. Early time comparisons with the measurements show good agreement, and the code was used to try to determine which parts of the facility were causing specific structure in the measured time record. Examples of the data comparisons will be presented, and the current best method for representing the electron beam in the TSAR finite difference code will be explained.

* Work performed under the auspices of the U. S. Department of Energy by the Lawrence Livermore National Laboratory under Contract No. W-7405-ENG-48. Funding provided by the Combined Community Measurement Program.

THE 3-D FDTD CODE TSAR (Temporal Scattering And Response) WAS USED TO MODEL THE E-BEAM



- Central differencing of Maxwell's Curl Equations
- Produces a time record of the E or H field at selected points
- Written at Livermore, based on codes by Yee, Kunz, Taflove and others
- Model generation, model display and post-processing capabilities are part of the package

TSAR PROVIDES SEVERAL OPTIONS FOR LAUNCHING WAVES-



- Plane waves from any direction.
- Direct stimulation of E-field values at specified points.
- Time delays between source points.
- Time history is also specified; a Gaussian shape was used for these calculations.

SEVERAL METHODS WERE TRIED USING TSAR

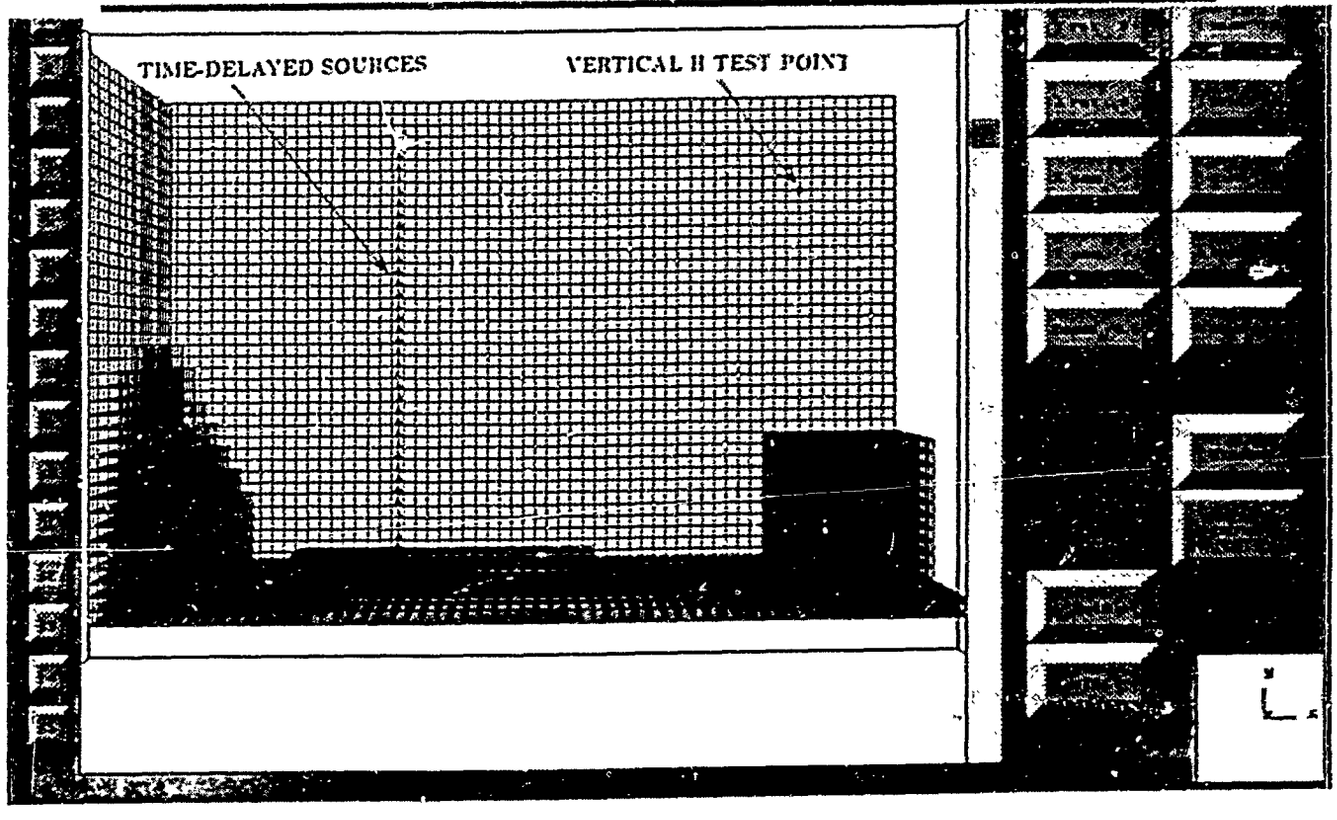


- Directly specifying the horizontal E-field time history at the beam exit point.

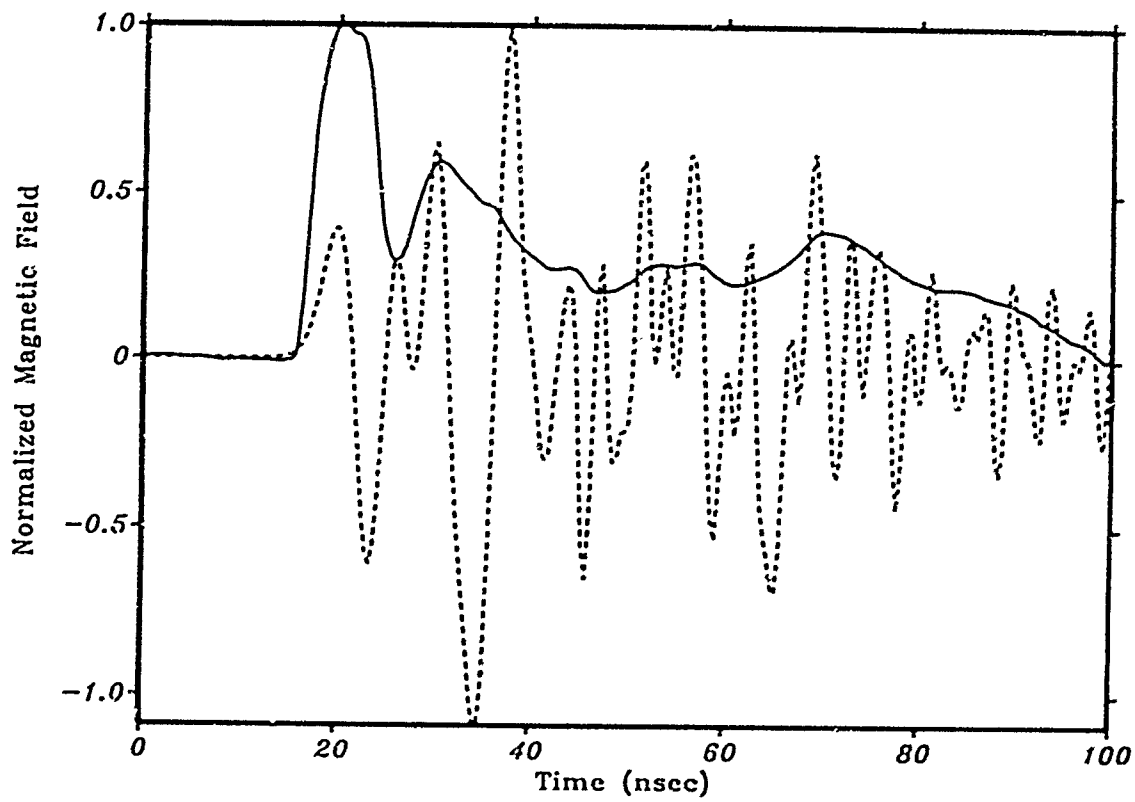
- Specifying the horizontal E-field time history at the beam exit point, with the continuation of the beam represented by a line of perfect conductors.

- Specifying a line of sources, with each source time-delayed by $\Delta t = \Delta x/c$

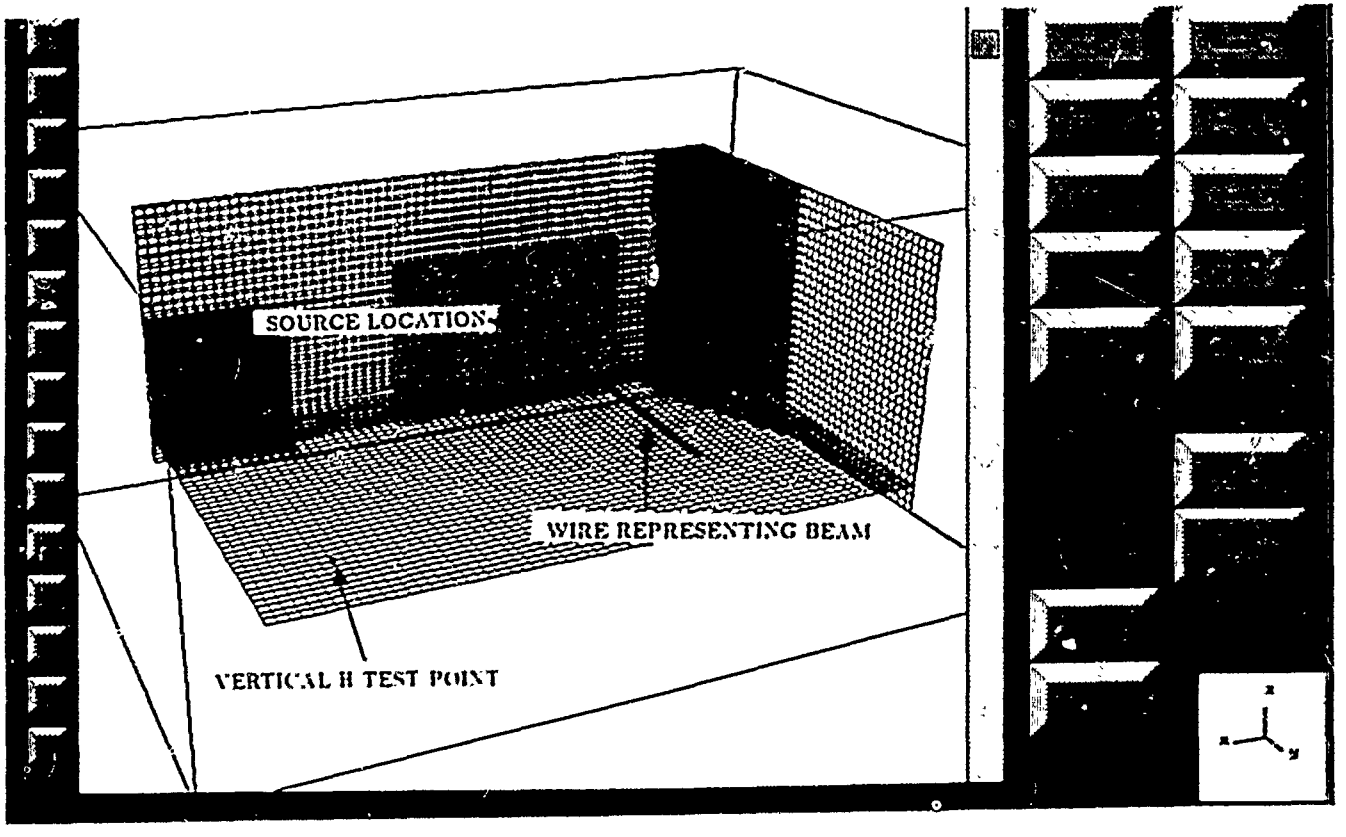
TOP VIEW OF BEAM EXIT AREA, SHOWING LINE OF SOURCES ALONG BEAM PATH



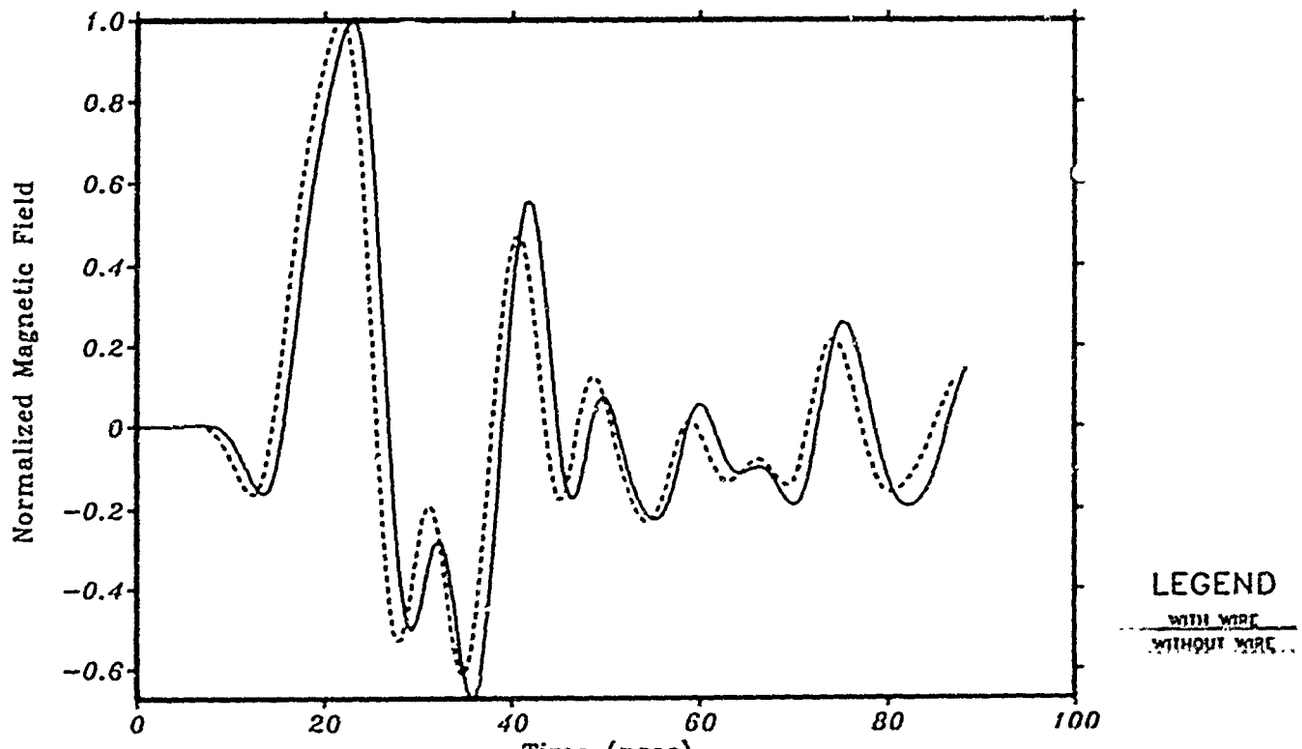
A LINE OF SOURCES DOESN'T SEEM TO ACCURATELY MODEL THE SITUATION



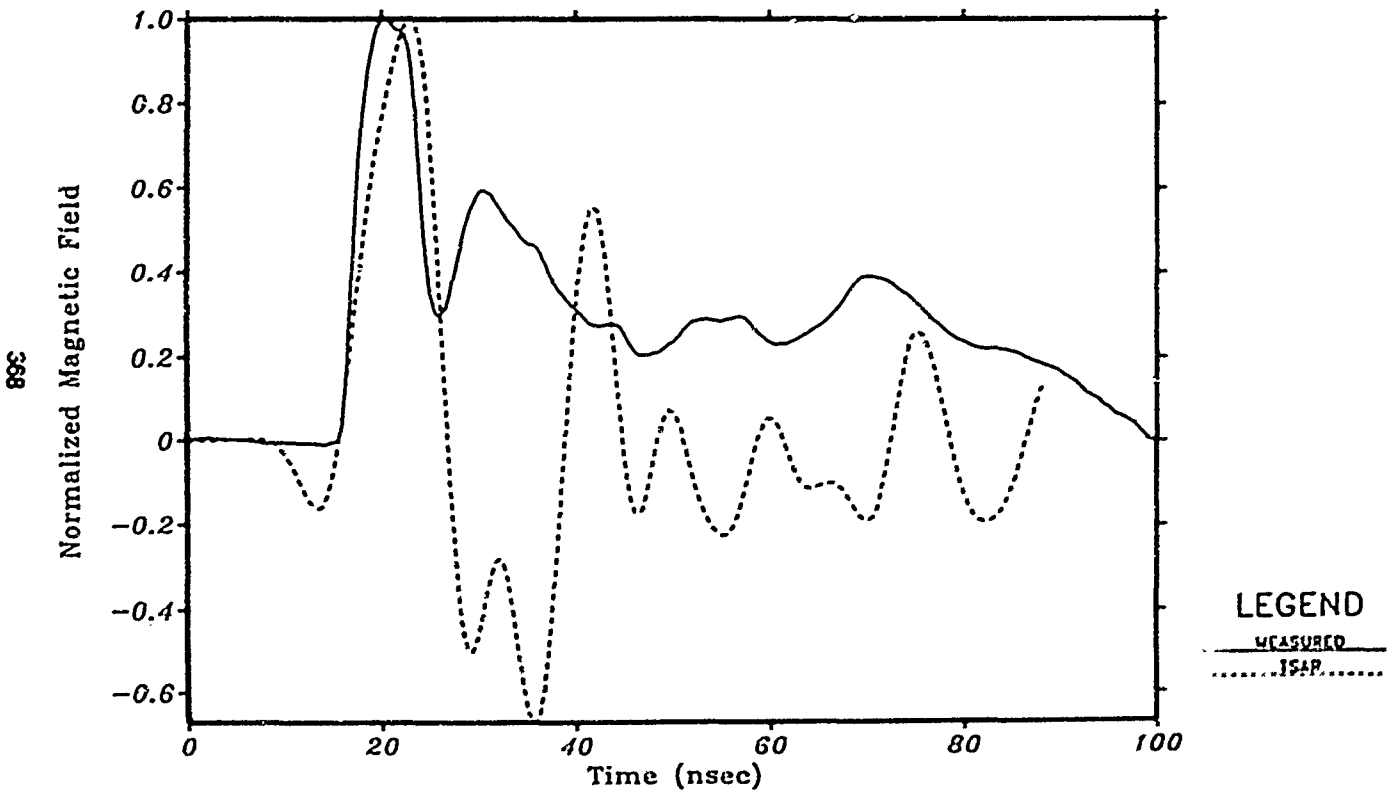
VIEW OF BEAM EXIT AREA, SHOWING LINE OF PERFECT CONDUCTORS WHICH REPRESENT BEAM



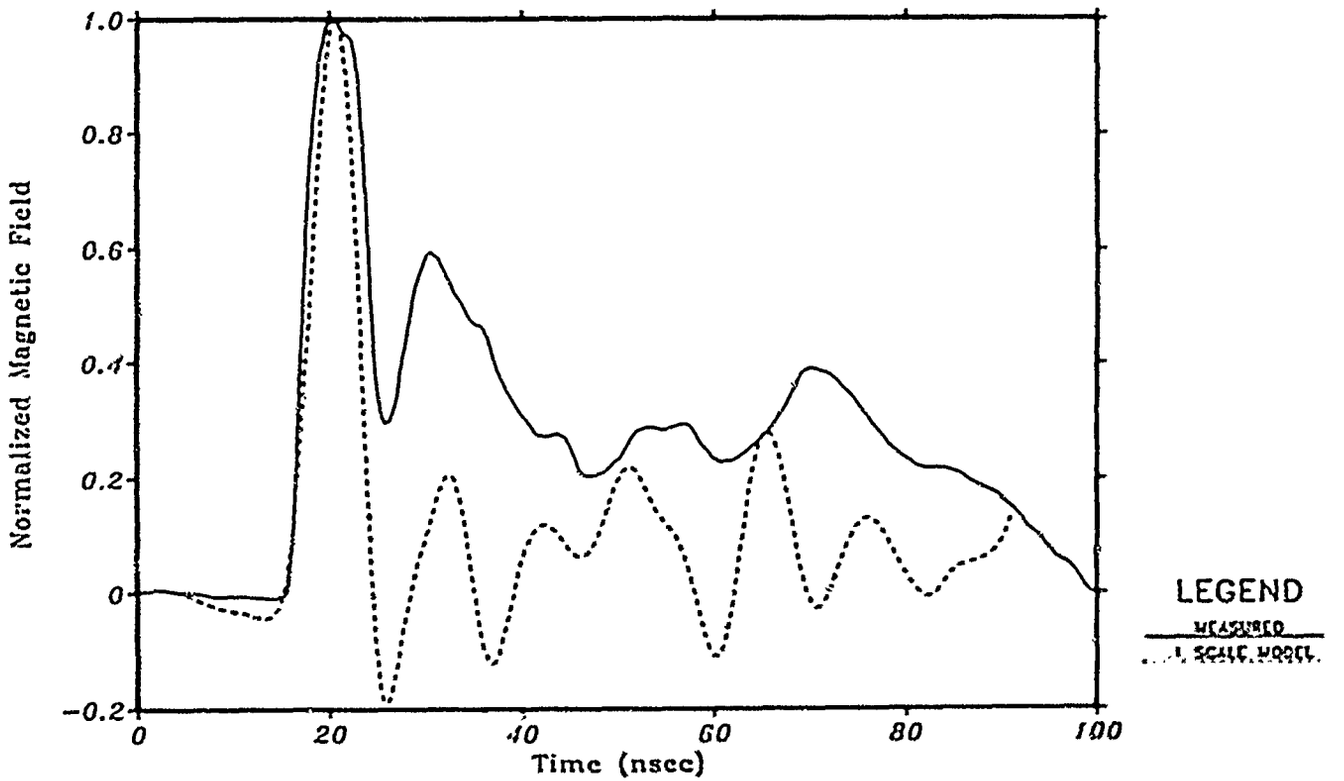
USING A WIRE FOR THE BEAM SEEMS UNNECESSARY



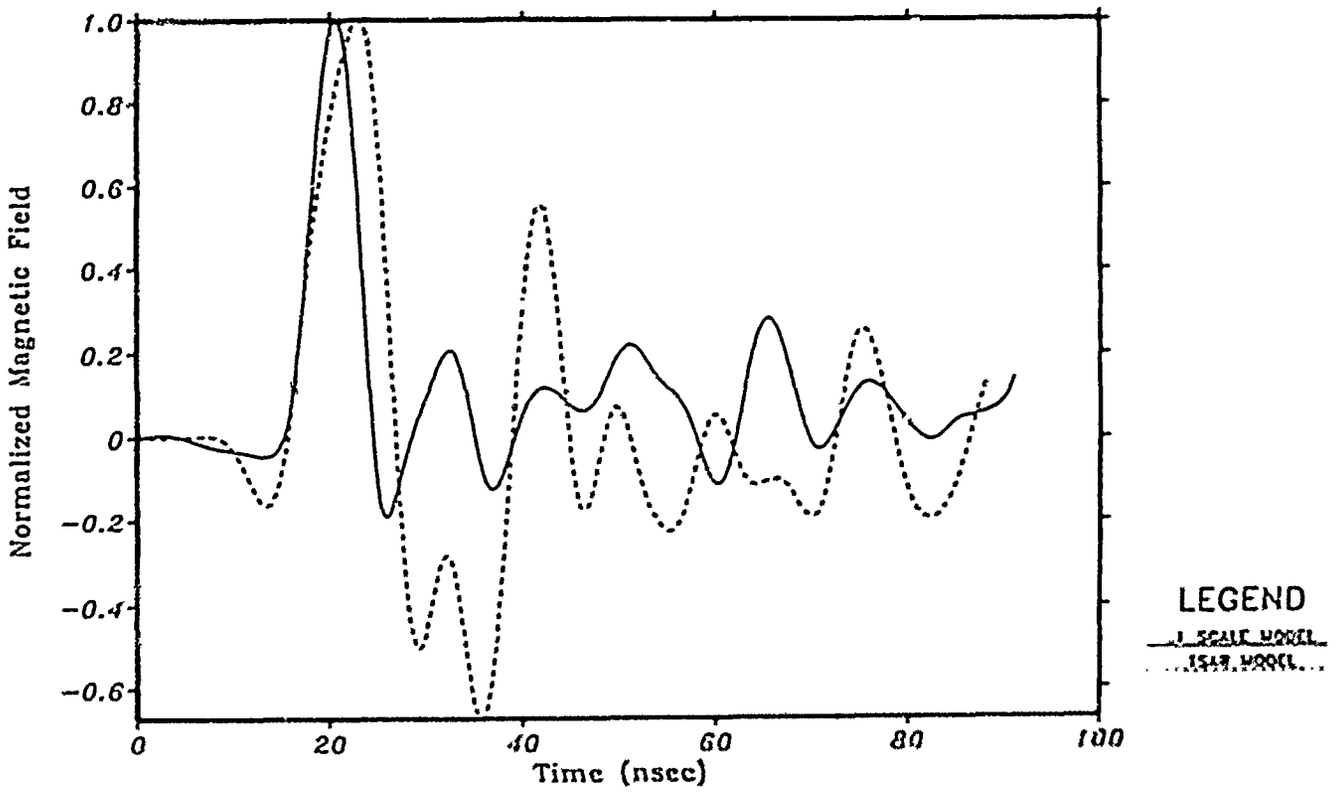
TSAR AND MEASURED DATA DON'T COMPARE WELL



SCALE MODEL AND MEASURED DATA ALSO DON'T COMPARE TOO WELL



TSAR WITH SINGLE SOURCE SHOWS SOME AGREEMENT WITH SCALE MODEL



FURTHER EXAMINATION OF MEASURED DATA REVEALED DIFFICULTIES



- After the completion of our modeling efforts, more measured data was released. Processing this data revealed some interesting information-
  - Coherence function showed no linear relationship between beam current and measured H-field above 70 MHz.
  - Since both TSAR and scale models depend on linear relationships, differences from measured data should be expected.

- Possibly a future experiment will produce more usable data, with a better relationship between input and output.

SUMMARY

- Several methods of modeling the EM radiation from an E-beam, using the FDTD code TSAR, were tried.
- The simplest method, using a single point source, seemed to work best.
- Comparison with data from a 0.1 scale model is acceptable.
- Better data from a future open-air experiment may allow refinements to be made to the TSAR model.

A Buried Antenna Analytic Modeling Program - PAT6

R. Bruce Gilchrist
Paul O. Berrett
Brian Grose
Moray B. King
David L. Faust

Eyring Inc.
Communications Systems Division
1455 West 820 North
Provo, Utah 84601
(801) 375-2434

PAT6 is an analytic modeling program designed to model the performance of buried and near-earth antennas. The program has been developed over the past five years to assist in the investigation of buried antenna structures operating in the 100 KHz to 100 MHz frequency range. The model is based on equations developed by the Russian text **Near Earth and Buried Antennas** by G. A. Lavrov and A. S. Knyazev (1965, translation 1967) and the American Text **Antennas in Matter** by R. W. P. King and G. S. Smith (1981). The original PAT4J modeling program is a companion program to the **Antenna Engineering Design Handbook For Buried Linear Arrays**, produced by Eyring under contract* to Rome Air Development Center, Griffiss AFB, New York, April 1988.

PAT6 is currently a versatile antenna design investigation tool with an N x M multi-element array modeling capability. The program tabulates and plots both pattern and feedpoint characteristics for models in real earth environments. Ground conductivity and dielectric constants as a function of frequency are used to characterize the burial or underlying environment of the modeled antenna elements. Antenna patterns are described as a function of elevation, azimuth and polarization. Groundwave patterns are described in terms of field strength at a specific far field distance over real ground conditions (these can differ from the ground conditions at the antenna).

PAT6 capabilities are currently going into a Beta test stage. Validation of the code has been provided to date by comparisons to NEC-3I numerically modeled data as well and full scale testing of 11 elementary 1-element buried antenna configurations and four multi-element buried array configurations. The program supports Hercules, CGA and EGA graphics, requires a math coprocessor and runs on IBM PCs and compatiables with 256K of memory. The final program is expected to be available in late 1989.

The demonstration used a Tandy 1400LT Laptop with a CGA display and an 8087 coprocessor option.

---

* Hardened Antenna Technology Program Contract No. F30602-85-C-0282.

SESSION 4 - "SCATTERING I"

Chairman: James Rogers

UTD SCATTERING FROM DIHEDRALS

R. J. Marhefka and N. Akhter
The Ohio State University
ElectroScience Laboratory
1320 Kinnear Road
Columbus, Ohio 43212-1156

March 17, 1989

Abstract

The monostatic and bistatic scattering from dihedrals of arbitrary angles is presented. The Uniform Geometrical Theory of Diffraction (UTD) is used to analyse the problem. The near zone (non-parallel ray) and the far zone (parallel ray) cases are discussed.

The NEC-BSC is a near zone code. It has arbitrary plates that can be placed together to form dihedrals. It includes multiple plate UTD interaction terms up to second order. It gives good results for most situations. When the source and receiver distances are large and the dihedral angle is near 90°, however, the present version of the NEC-BSC can deviate from the correct answer in the peak region. Improvements of the UTD corner theory are under investigation to correct this problem.

In order to study the parallel ray case, a two dimensional computer code has been written. Arbitrary dihedral angles and bistatic angles can be used. This code contains all UTD interaction terms up to third order along with a few fourth order interactions. Excellent results are obtained for dihedrals as small as a wavelength on a side and dihedral angles as small as 60°. The code is validated against method of moments (MM) results.

1 Introduction

The scattering from dihedrals has been studied for a long time. Interest in the subject has renewed and several papers have been recently reported.

Physical optics solutions have traditionally been used to study the dihedral. Papers by Michaeli [1], Blejer [2], and Griesser and Balanis [3] are recent examples.

Analysis of interaction between plates have been studied by Aberegg and Marhefka [4] and specifically the corner reflector by Akhter and Marhefka [5] completely using the Geometrical Theory of Diffraction (GTD) [6] and its uniform verion (UTD) [7] techniques including the latest double diffraction coefficients [8]. In addition, recently Griesser and Balanis [9] have analyzed the dihedral using UTD and imposed edge approximations.

This paper is motivated by some engineers use of the NEC-BSC [10] code for analyzing dihedrals which presently has some numerical and theoretical limitations for large distances and 90° dihedrals. In addition, it will point out improvements to a previous ACES paper [11] based on Reference [4] where bugs in the code caused unexpected poor results for one of the polarizations not actually in the theory. It should be noted that most all of the above references have solved the dihedral problem in two dimensions and mostly in the far zone. The NEC-BSC is a near zone code in three dimensions. A discussion comparing the differences in near and far zone UTD implementations is given in Reference [12]. This paper also touchs on this point.

The results in this paper are compared with two dimensional method of moments (MM) solutions [13,14]. This is so large sized dihedrals could be studied without worrying about excessive computer times or memory requirements.

2 NEC-BSC Results

The NEC-BSC is a general purpose user oriented computer code. It has multiple sided flat plates that can be used in such a way as to form arbitrary shapes. It has the first and second order UTD interaction terms between plates, that is, it includes incident, reflected, edge and corner diffraction, double reflected, reflected - diffracted, and diffracted - reflected fields. These terms have been shown to be sufficient for most antenna placement problems for which the NEC-BSC was originally designed.

The plates can be put together to form a dihedral. By using a source and receiver that both move with respect to the dihedral, the non-parallel ray UTD solution to the dihedral can be calculated. The scattered field from a structure can be found by calculating the total field and subtracting the incident field (actually the negative of the incident field need only be added

in the shadow region of the structure). Since this is a near zone code, the results need to be normalized so as to be relative to a square meter. This can be accomplished by comparing the coupling formulas with the known result for a sphere as would be done in a spherical range measurement.

A dihedral with 9 inch length sides is considered. The width is 4.82 inches and the frequency is 10 GHz. This width is chosen so that the results can be directly compared with the far zone two dimensional results below, since at that frequency and width the results with respect to a square meters in 3-D and meters in 2-D will be the same. The backscatter from a 90° dihedral for horizontal polarization is shown in Figure 1. The peak should be at approximately 13.4 dB as given by PO (actually around 12.5 dB as given by MM as given in Figure 5). Obviously the result given by the NEC-BSC is considerably off in the peak region. The pattern is actually taken at 864 inches which is well within the far zone of the dihedral and with a 0.5° bistatic angle to help stability. Instabilities can be see as the sharp spikes through out the pattern. These are due to the large distances for the source and receiver involved. The seven digit accuracy of the VAX is not enough to keep track of the small differences. The peak region is bad because of the inaccuracies of the present near zone corner diffraction coefficient. It is very accurate except right at specular [15]. For the dihedral, however, this specular region is spread out all over the main beam region.

To test this theory, the dihedral angle is open to 90.5°. The pattern is shown in Figure 2. The result is only off by around 3 dB as can be seen by comparing it with MM results in Figure 5. Again this is due to the near zone corner diffraction coefficient. The pattern for the dihedral opened to 95° is shown in Figure 3. This result shows numerical jitter but the result is now within less than 1 dB of the exact result (see Figure 7).

3 Far Zone Results

In order to understand what needs to be included in more detail for dihedral situations in a UTD sense, a two dimensional code has been written. It is based on far zone parallel ray UTD concepts. The details of the developed is given in Reference [5]. This code includes up to and including all third order interactions between two plates. In addition, some fourth order interaction terms have been added. The terms included are illustrated in Figure 4. This code is ideal for analyzing dihedral configurations. It is necessary to include only the diffraction from the edges and their reflection in the other plate. In

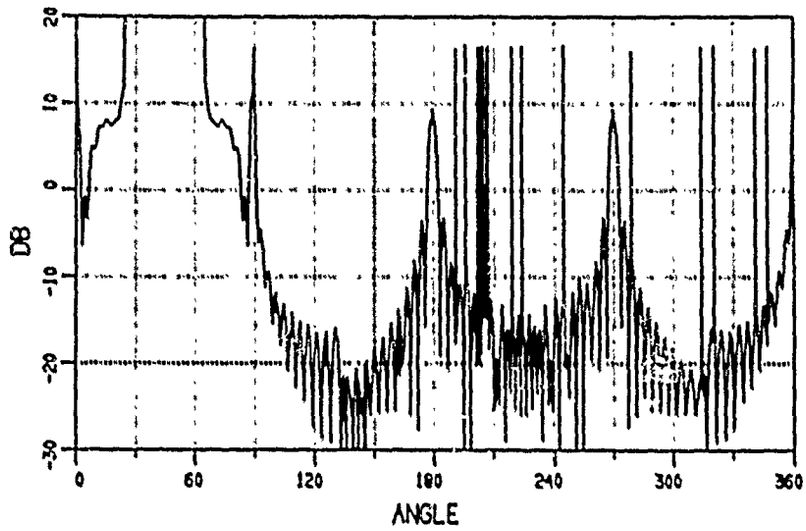


Figure 1: The backscatter from a 9 × 4.82 inch 90° dihedral for horizontal polarization using the NEC-BSC.

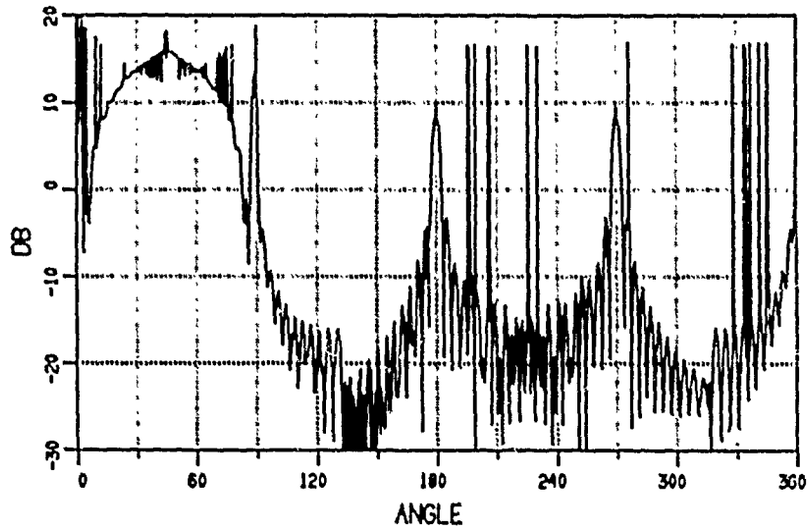


Figure 2: The backscatter from a 9 × 4.82 inch 90.5° dihedral for horizontal polarization using the NEC-BSC.

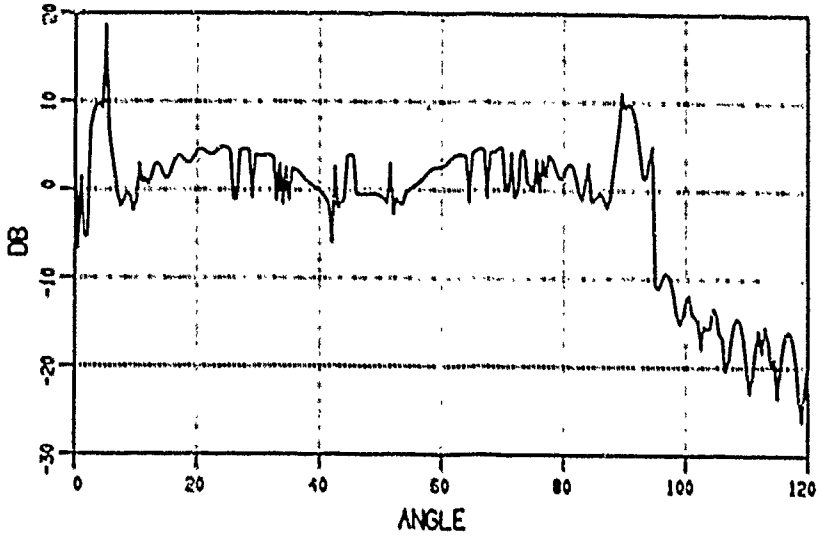


Figure 3: The backscatter from a 9 × 4.82 inch 95° dihedral for horizontal polarization using the NEC-BSC.

addition, double diffraction between edges with possible intervening reflections have been included. The newly developed far zone double diffraction coefficients [8] are used. With this formulation for double, it is not necessary to use false edges or imposed edges as some people call them.

As an example, a 9-inch two dimensional dihedral has been analyzed for horizontal polarization for the 90° dihedral as shown in Figure 5 at 10 GHz. Note the excellent agreement. To illustrate the importance of the double diffraction type terms, the combination of diffracted, reflected - diffracted, and diffracted - reflected fields, is shown as the solid line in Figure 6. The long dashes show the double diffracted field contribution and the short dashes the diffract - reflected - diffracted fields. Note that the peak value is refined using double diffracted fields.

For comparison purposes the backscatter for a 95° dihedral is shown in Figure 7. The backscatter for a 60° dihedral is also shown in Figure 8. Notice that nearly all the terms mentioned above are needed to get this good of an accuracy. If the angle is made smaller even more terms are needed. In addition, as the dihedral becomes smaller it becomes necessary to use these higher order UTD terms to get as good of accuracy. The result for a 9 inch

90° dihedral at 2 GHz for horizontal and vertical polarizations are shown in Figures 9 and 10. These results illustrated that a UTD solution of a dihedral can in fact show polarization differences. A result with a 90° bistatic angle at 10 GHz for a 90° dihedral and vertical polarization is shown in Figure 11 to complete the verification of the method.

4 Conclusions

The present version of the NEC-BSC can be used to find the near zone scattering from plates. The example of the dihedral presented in this paper represents one the most challenging problems. If the angle is not too near 90° reasonable results are obtained. Research on a better near zone corner diffraction coefficient is being conducted to improve this situation.

A dihedral has also been studied using the latest UTD techniques for the far zone in two dimensions. The results are excellent as compared with MM for both large and small sizes and angles.

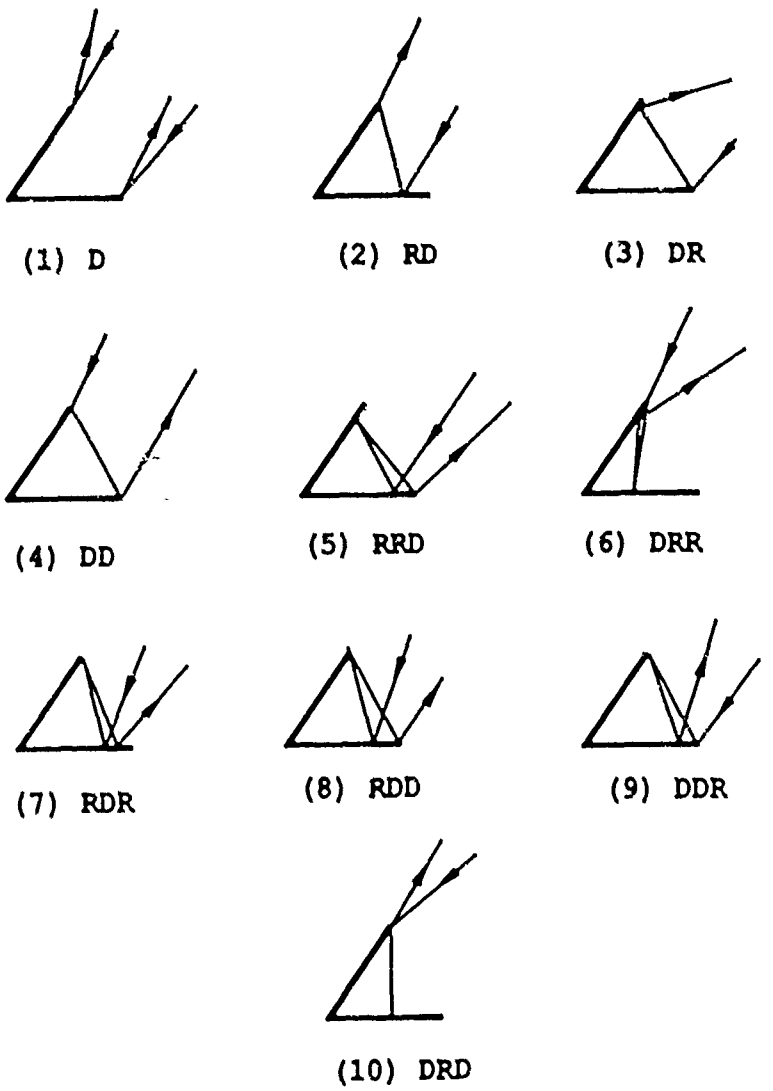


Figure 4: Illustration of the UTD terms included in two dimensional far zone dihedral code.

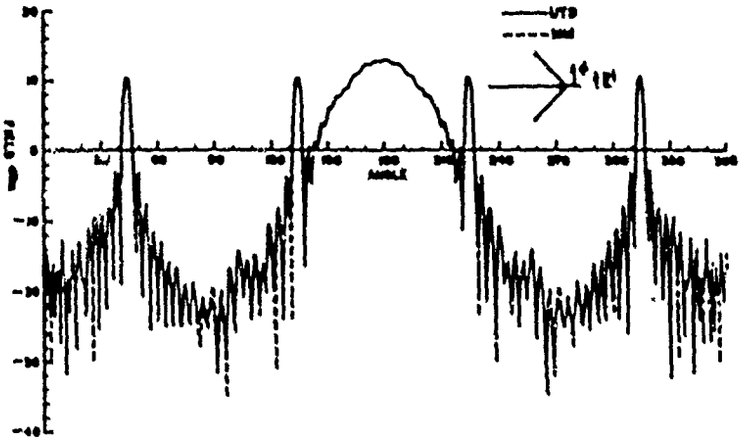


Figure 5: The backscatter from a 9 inch 2-D 90° dihedral for horizontal polarization.

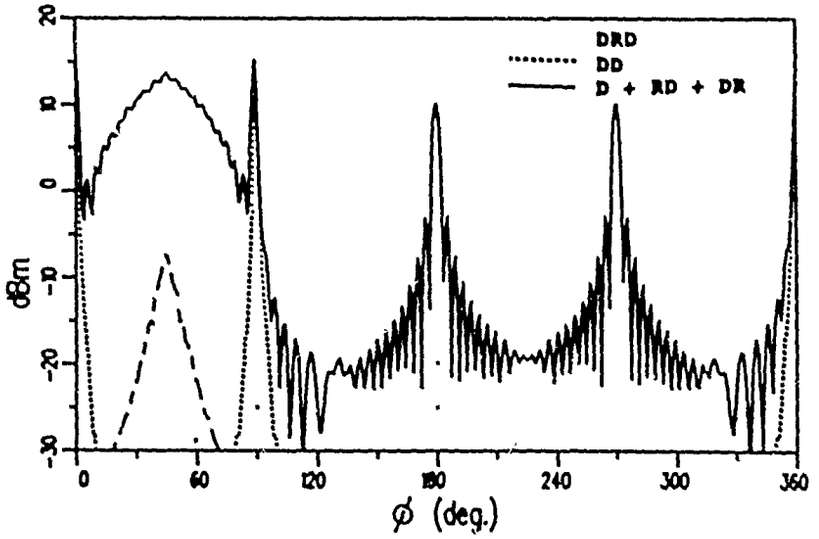


Figure 6: The backscatter from a 9 inch 2-D 90° dihedral for horizontal polarization comparing contribution of various UTD terms.

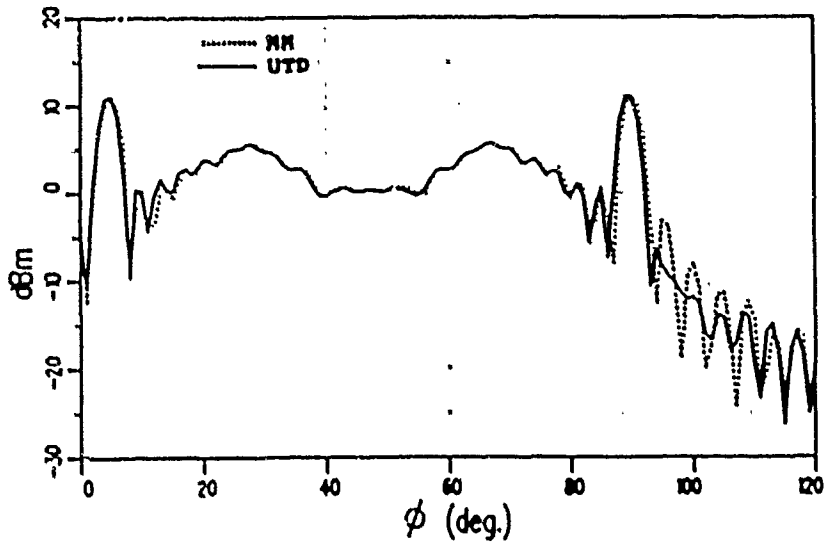


Figure 7: The backscatter from a 9 inch 2-D 95° dihedral for horizontal polarization.

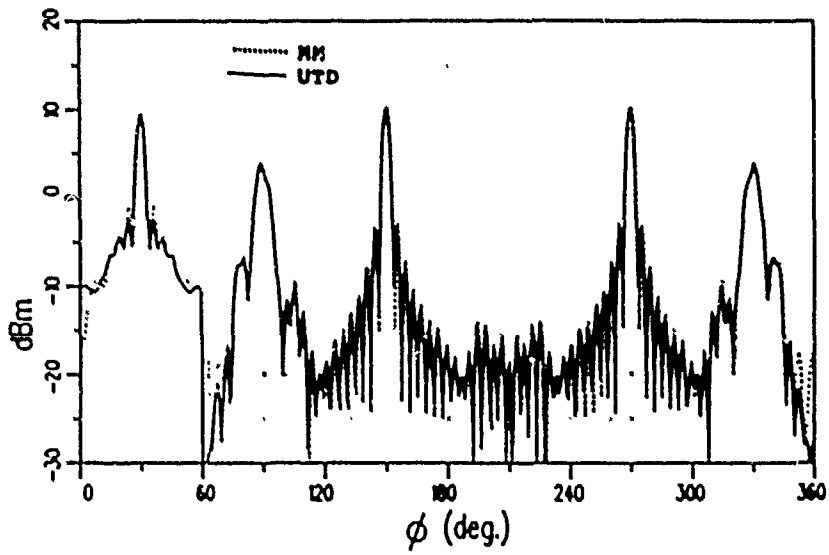


Figure 8: The backscatter from a 9 inch 2-D 60° dihedral for horizontal polarization.

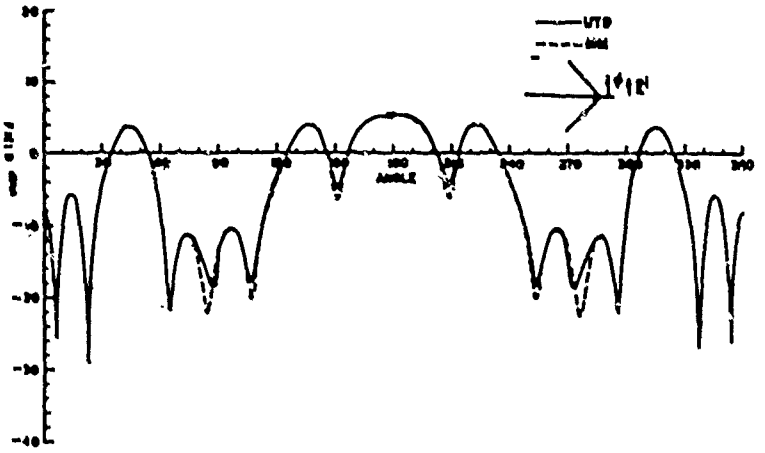


Figure 9: The backscatter from a 9 inch 2-D 90° dihedral for horizontal polarization at 2 GHz.

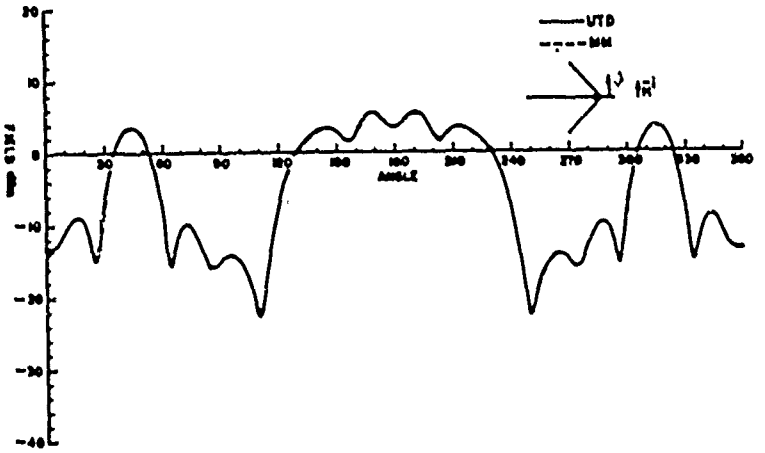


Figure 10: The backscatter from a 9 inch 2-D 90° dihedral for vertical polarization at 2 GHz.

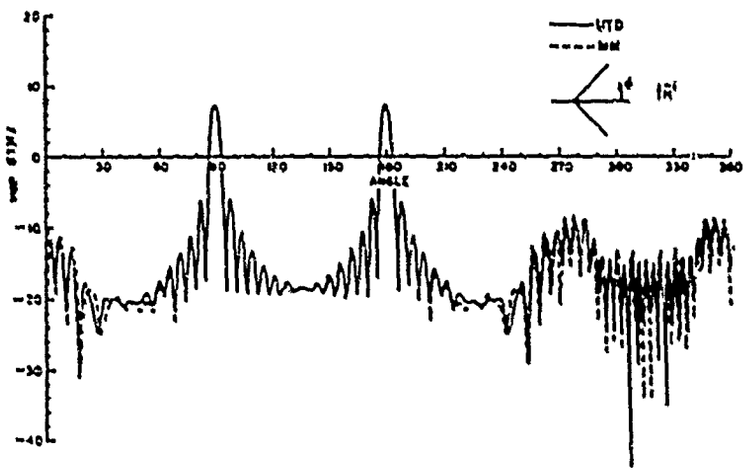


Figure 11: The bistatic scatter with a 90° angle from a 9 inch 2-D 90° dihedral for vertical polarization.

References

[1] A. Michaeli, "A closed form physical theory of diffraction solution for the electromagnetic scattering by stripe and 90° dihedrals," *Radio Science*, vol. 19, pp. 609-616, 1984.

[2] D. J. Blejer, "Physical optics polarization scattering matrix and impulse response of a right dihedral corner reflector," ADT Project Memorandum 47PM-ADT-0052, MIT, Lincoln Laboratory, Dec. 1986.

[3] T. Griesser and C. A. Balanis, "Analysis of dihedral corner reflectors using physical optics and the physical theory of diffraction," *IEEE Trans. Antennas Propagat.*, vol. AP-35, pp. 1137-1147, Oct. 1987.

[4] K. R. Aberegg and R. J. Marhefka, "UTD interaction between plates for backscatter," Technical Report 71573-1, The Ohio State University ElectroScience Laboratory, Department of Electrical Engineering, Aug. 1986. Prepared under Contract No. DAAH01-83-C-1075 for U. S. Army Missile Command.

[5] N. Akhter and R. J. Marhefka, "Far zone scattering from rectangular and triangular dihedrals in the principal plane," Technical Report 721198-1, The Ohio State University ElectroScience Laboratory, Department of Electrical Engineering, March 1989.

[6] J. B. Keller, "Geometrical theory of diffraction," *J. Opt. Soc. of America*, vol. 52, pp. 116-130, Feb. 1962.

[7] R. G. Kouyoumjian and P. H. Pathak, "A uniform geometrical theory of diffraction for an edge in a perfectly conducting surface," *Proc. IEEE*, vol. 62, pp. 1448-1461, 1974.

[8] R. Tiberio, M. Giuliano, G. Pelosi, and R. G. Kouyoumjian, "High-frequency electromagnetic scattering of plane waves from double wedges," in *International Symposium Digest*, (Vancouver, Canada), IEEE/APS, June 17-21 1985.

[9] T. Griesser and C. A. Balanis, "Dihedral corner reflector backscatter using higher order reflections and diffractions," *IEEE Trans. Antennas Propagat.*, vol. APS-35, pp. 1235-1247, Nov. 1987.

[10] R. J. Marhefka and J. W. Silvestro, "Near zone - basic scattering code, user's manual with space station applications," Technical Report 718422-13, The Ohio State University ElectroScience Laboratory,

Department of Electrical Engineering, March 1988. Prepared under Grant No. NSG 1613 for National Aeronautics and Space Administration.

[11] J. L. Fath, A. J. Terzuoli, and E. G. Zelnio, "UTD-MOM model comparison for a dihedral corner reflector," in *Conference Proceedings*, (Naval Postgraduate School, Monterey, CA), Applied Computational Electromagnetics Society, March 24-26 1987.

[12] E. H. Newman and R. J. Marhefka, "An overview of MM and UTD methods at The Ohio State University," *Proc. IEEE*, May 1989. Also to be published in IEEE Press book on RCS of Complex Objects.

[13] J. H. Richmond, "An integral - equation solution for TE radiation and scattering from conducting cylinders," Technical Report 2902-7, The Ohio State University ElectroScience Laboratory, Department of Electrical Engineering, Oct. 1972. Prepared under Grant No. NGL 36-008-138 for National Aeronautics and Space Administration.

[14] N. N. Wang, "Reaction formulation for radiation and scattering from plates corner reflectors and dielectric coated cylinders," Technical Report 2902-15, The Ohio State University ElectroScience Laboratory, Department of Electrical Engineering, Apr. 1974. Prepared under Grant No. NGL 36-008-138 for National Aeronautics and Space Administration.

[15] R. J. Marhefka and T. J. Brinkley, "Comparison of methods for far zone scattering from a flat plate and cube," *Applied Computational Electromagnetics Society Journal and Newsletter*, vol. 3, pp. 57–78, Fall 1988.

A MAGNETIC FIELD INTEGRAL EQUATION FORMULATION FOR ELECTROMAGNETIC SCATTERING FROM INHOMOGENEOUS 3D DIELECTRIC BODIES

Andrew F. Peterson
Electromagnetic Communication Laboratory
Department of Electrical and Computer Engineering
University of Illinois
1406 W. Green St.
Urbana, IL 61801

ABSTRACT: A method-of-moments formulation involving the magnetic field integral equation (MFIE) is presented for the analysis of inhomogeneous 3D dielectric scatterers. The approach involves the use of tetrahedral cells, a piecewise linear expansion for the total magnetic field, and point matching at the nodal points of the tetrahedral-cell model. Preliminary numerical results are presented and compared to exact solutions for spherical scatterers.

I. INTRODUCTION

Numerous applications require accurate electromagnetic modeling of finite, 3D dielectric bodies. Because volume discretizations necessitate a large number of unknowns, relatively few techniques have been developed for inhomogeneous scatterers. In the time domain, explicit "marching on in time" algorithms are under study and are attractive because they require no matrix solution. In the frequency domain, two types of formulation are being employed: those based on the electric-field integral equation (EFIE)[1-3] and those based on the vector wave equation [4]. To augment these approaches and provide an alternative method for validation purposes, this paper presents a new formulation for modeling 3D inhomogeneous dielectric bodies based on the magnetic field integral equation (MFIE). The approach is an extension of a 2D formulation developed by Peterson and Klock [5].

The MFIE is discretized over piecewise homogeneous tetrahedral cells using a linear representation for the magnetic field components and point-matching. The expansion functions employed enforce the continuity of all three components of the vector $\bar{H}$-field. Despite the volume discretization, the matrix "fill" requires only two-dimensional numerical

integration over the faces of the cells. Preliminary numerical results for homogeneous spherical scatterers are presented to illustrate the accuracy of the MFIE formulation.

2. FORMULATION

Consider a region of infinite space containing a dielectric scatterer characterized by a complex-valued relative permittivity $\varepsilon_r(x,y,z)$. Suppose that the scatterer is illuminated by a time-harmonic electromagnetic field with time dependence $e^{j\omega t}$. In the absence of the scatterer, the illuminating magnetic field is given by $\bar{H}^{inc}$. It is desired to find the total magnetic field $\bar{H}$. To cast the problem into one directly amenable to numerical solution, we replace the dielectric material by the equivalent polarization current density

$$\bar{J}(x,y,z) = \frac{\varepsilon_r(x,y,z) - 1}{\varepsilon_r(x,y,z)} \nabla \times \bar{H}(x,y,z) \tag{1}$$

radiating in free space. The internal fields and radar cross section can be determined from knowledge of the current density of Equation (1), which in turn can be found from the magnetic field. The magnetic field must satisfy the MFIE

$$\bar{H}^{inc}(x,y,z) = \bar{H}(x,y,z) - \nabla \times \left\{ \bar{J}(x,y,z) * \frac{e^{-jkr}}{4\pi r} \right\} \tag{2}$$

where k is the free-space wavenumber. The asterisk operator (*) denotes three-dimensional convolution, i.e., each scalar component has the form

$$a(x,y,z) * b(x,y,z) = \int_{-\infty}^{\infty} \int_{-\infty}^{\infty} \int_{-\infty}^{\infty} a(x',y',z')\, b(x-x',y-y',z-z')\, dx'dy'dz' \tag{3}$$

Because convolution and differentiation operators commute, Equation (2) can be written in the form

$$\bar{H}^{inc}(x,y,z) = \bar{H}(x,y,z) - \{\nabla \times \bar{J}\} * \frac{e^{-jkr}}{4\pi r} \tag{4}$$

Below, the explicit form of Equation (4) is shown to be preferable to Equation (2) in the context of the present formulation.

In order to effect a numerical solution to Equation (4), the dielectric scatterer can be modeled by a superposition of homogeneous tetrahedral cells. Within each cell, the magnetic field can be represented by a linear function

$$\bar{H}(x,y,z) = \bar{\alpha} + \bar{\beta}x + \bar{\gamma}y + \bar{\delta}z \tag{5}$$

where the vectors $\bar{\alpha}$, $\bar{\beta}$, $\bar{\gamma}$ and $\bar{\delta}$ are constants of the form

$$\bar{\alpha} = \hat{x}\,\alpha_x + \hat{y}\,\alpha_y + \hat{z}\,\alpha_z \tag{6}$$

Since the representation for $\bar{H}$ is linear, it follows from Equation (1) that the current density $\bar{J}$ will be a constant in each cell. Furthermore, since Equation (4) requires the differentiation of the current density, the quantity $\nabla x \bar{J}$ will collapse to a Dirac delta function with constant support over the face between any two cells. In order to describe the resulting function, it is convenient to work within a local coordinate system comprised of the normal and tangential variables at a given face. The normal vector to face "i" can be defined in terms of the spherical angle (θ_i,ϕ_i) into which it points, i.e.,

$$\hat{n} = \hat{x}\sin\theta_i\cos\phi_i + \hat{y}\sin\theta_i\sin\phi_i + \hat{z}\cos\theta_i \tag{7}$$

Tangential vectors to face "i" are uniquely defined by

$$\hat{t}_1 = -\hat{x}\sin\phi_i + \hat{y}\cos\phi_i \tag{8}$$

and

$$\hat{t}_2 = -\hat{x}\cos\theta_i\cos\phi_i - \hat{y}\cos\theta_i\sin\phi_i + \hat{z}\sin\theta_i \tag{9}$$

Note that these unit vectors are mutually perpendicular and satisfy

$$\hat{t}_1 \times \hat{t}_2 = \hat{n} \tag{10}$$

Using this local description, $\nabla \times \bar{J}$ can be written in the vicinity of a face as

$$\nabla \times \bar{J} = \hat{t}_2 \frac{\partial J_{t1}}{\partial n} - \hat{t}_1 \frac{\partial J_{t2}}{\partial n} \tag{11}$$

Because $\bar{J}$ is constant within each cell, Equation (11) can be expressed at face i as

$$\nabla \times \bar{J} = \delta_i(n)\, p_i(t_1,t_2) \{ [\hat{t}_2 J_{t1} - \hat{t}_1 J_{t2}]_{i+} - [\hat{t}_2 J_{t1} - \hat{t}_1 J_{t2}]_{i-} \} \tag{12}$$

where "i+" and "i-" refer to the two cells adjacent to face i (the normal vector points into the "+" cell). In Equation (12), $\delta_i(n)$ denotes a Dirac delta function that vanishes except on face i, and $p_i(t_1,t_2)$ is a step function having constant support over face i and vanishing off of face i in the transverse direction. Using the representation of $\bar{H}$ from Equation (5), the vector components of $\nabla \times \bar{J}$ at face i are

$$\hat{x} \cdot \nabla \times \bar{J} = \delta_i(n)\, p_i(t_1,t_2) \left\{ \frac{\varepsilon_r^+ - 1}{\varepsilon_r^+} \left[\sin\theta_i \sin\phi_i \, (\beta_y^+ - \gamma_x^+) + \cos\theta_i \, (\beta_z^+ - \delta_x^+) \right] \right.$$
$$\left. - \frac{\varepsilon_r^- - 1}{\varepsilon_r^-} \left[\sin\theta_i \sin\phi_i \, (\beta_y^- - \gamma_x^-) + \cos\theta_i \, (\beta_z^- - \delta_x^-) \right] \right\} \tag{13}$$

$$\hat{y} \cdot \nabla \times \bar{J} = \delta_i(n)\, p_i(t_1,t_2) \left\{ \frac{\varepsilon_r^+ - 1}{\varepsilon_r^+} \left[\sin\theta_i \cos\phi_i \, (\gamma_x^+ - \beta_y^+) + \cos\theta_i \, (\gamma_z^+ - \delta_y^+) \right] \right.$$
$$\left. - \frac{\varepsilon_r^- - 1}{\varepsilon_r^-} \left[\sin\theta_i \cos\phi_i \, (\gamma_x^- - \beta_y^-) + \cos\theta_i \, (\gamma_z^- - \delta_y^-) \right] \right\} \tag{14}$$

and

$$\hat{z}\cdot\nabla\times\bar{J} = \delta_i(n)\, p_i(t_1,t_2)\left\{ \frac{\epsilon_r^+ - 1}{\epsilon_r^+}\sin\theta_i\left[\cos\phi_i\,(\delta_x^+ - \beta_z^+) + \sin\phi_i\,(\delta_y^+ - \gamma_z^+)\right]\right.$$

$$\left. - \frac{\epsilon_r^- - 1}{\epsilon_r^-}\sin\theta_i\left[\cos\phi_i\,(\delta_x^- - \beta_z^-) + \sin\phi_i\,(\delta_y^- - \gamma_z^-)\right]\right\} \qquad (15)$$

In Equations (13)-(15), the "+" and "-" superscripts denote the parameter values in the "+" and "-" cell adjacent to face i, respectively.

3. EXPANSION AND TESTING FUNCTIONS

Although we have prescribed a linear dependence for $\bar{H}$, freedom remains in the selection of specific basis functions. Consider the expansion of the three Cartesian components of $\bar{H}$ in linear interpolation functions between the nodes of the tetrahedral-cell mesh [6]. This expansion ensures the continuity of all three components of $\bar{H}$ at cell interfaces, which is desirable since the actual magnetic field is a continuous function throughout a piecewise-homogeneous dielectric region. The unknowns associated with this approach are the three components of $\bar{H}$ at each node of the scatterer model.

The constants associated with the expansion of Equation (5) can be readily determined within a given cell. Consider a tetrahedron having vertices at (x_1,y_1,z_1), (x_2,y_2,z_2), (x_3,y_3,z_3), and (x_4,y_4,z_4). The coefficients representing the x-component of $\bar{H}$ within this tetrahedron can be found from

$$\begin{bmatrix}\alpha_x\\ \beta_x\\ \gamma_x\\ \delta_x\end{bmatrix} = \begin{bmatrix}1 & x_1 & y_1 & z_1\\ 1 & x_2 & y_2 & z_2\\ 1 & x_3 & y_3 & z_3\\ 1 & x_4 & y_4 & z_4\end{bmatrix}^{-1}\begin{bmatrix}H_{x1}\\ H_{x2}\\ H_{x3}\\ H_{x4}\end{bmatrix} \qquad (16)$$

where H_{x1}, etc. are the values of the x-component of $\bar{H}$ at the corresponding vertices. The coefficients of the expansions for H_y and H_z can be found from similar equations.

In order to generate a linear system of equations that can be solved for the unknown coefficients of $\bar{H}$, it is necessary to select a set of testing functions and approximately enforce the MFIE by way of an inner product between the testing function and Equation (4). In this case, the representation of the current density ensures the continuity of the magnetic field. Thus, it is sufficient to employ Dirac delta functions as testing functions. In other words, each component of the MFIE can be enforced by "point matching" at the nodes of the model. This procedure produces a 3Nx3N matrix equation, where N is the number of nodes in the tetrahedral-cell mesh representing the scatterer.

The entries of the matrix equation involve the integral appearing in Equation (4). Since this operation is a convolution between $\nabla x\bar{J}$ and the free-space Green's function, and since $\nabla x\bar{J}$ has Dirac delta function support over cell faces, the required integrals collapse to surface integrals over the faces of the tetrahedral cells. Thus, only two-dimensional numerical integration is required to calculate the matrix elements. This simplification is possible because the form of the MFIE appearing in Equation (4) permits the explicit use of $\nabla x\bar{J}$.

Each entry in the 3Nx3N matrix corresponds to the interaction between an observation and source node in the scatterer model. Rather than constructing the matrix entries sequentially on a node-by-node basis, it is more convenient to indirectly compute the matrix entries in terms of the contribution from a given face. At each face within the model, 45 coefficients relate the three components of $\nabla x\bar{J}$ to the 15 components of $\bar{H}$ (3 at each of the 5 nodes surrounding the face, unless the face is located on an exterior surface of the scatterer). These coefficients can be determined from Equations (13)-(16). Once the 45 coefficients are calculated for a given face, the contribution from that source term to each observation point (node) in the model can be computed (one numerical integration over the face is required for each observation point). This process is repeated for each face in the scatterer model. When the observation point happens to coincide with one of the three nodes of the source face, the resulting singularity can be extracted from the integrand,

integrated analytically, and combined with the numerical residual. The right-hand side of the system consists of the sampled values of the x, y, and z-components of the incident magnetic field at the node points.

4. NUMERICAL RESULTS

The MFIE formulation described above is directly applicable to arbitrarily shaped, inhomogeneous scatterers. To test the accuracy of the approach, exact solutions for homogeneous spherical scatterers illuminated by uniform plane waves [7] were compared with numerical results. Tetrahedral-cell models were constructed using the PATRAN preprocessor [8]. In the examples presented below, scaling was used to equate the volume of the scatterer model with that of the desired sphere. For initial validation purposes, numerical results were obtained using an AT&T 6300 personal computer running single precision FORTRAN under DOS at about 20 KFlops. Because the matrix order was restricted to approximately 210 on this machine, the results presented below are limited to electrically small scatterers.

Table 1 presents numerical and exact solutions for the magnetic field at various node points for a sphere of radius "a" having ε_r=2.5921 and ka=1. In this case, the model consisted of 48 tetrahedral cells, 27 node points, and 120 faces. Although the cells were not all identical in size, an average cell density of 681 cells per cubical dielectric wavelength was provided by this model. The resulting matrix equation was of order 81. Similar numerical results are presented in Table 2 for a refined model of the same sphere containing 176 cells, 53 nodes, and 376 faces. The average cell density in the refined model was 2497 cells per cubical dielectric wavelength. Note that the agreement between the numerical and exact solutions for the dominant component of the magnetic field is excellent in both cases.

Table 3 presents data for a 27-node, 48-cell model of a sphere with ka=0.1 and ε_r=2.5. In this case, the average cell density in the model is 719000 cells per cubical dielectric wavelength. This extremely high cell density was employed in order to study the convergence of the numerical solutions for the magnetic field. Approximately 4 or 5 decimal places of accuracy is observed in the magnitude of the numerical results (the phase is accurate to 4 decimal places, if normalized to a possible ±180 degrees).

Table 4 presents similar data for a lossy sphere having ka=0.2 and ε_r=4-j4. A 43-node, 80-cell model was employed with an average cell density of 44000 cells per cubical dielectric wavelength. Although the cell density is high, this model consisted of 42 nodes on the surface of the sphere, and only one additional node at the center. Interestingly, a large phase error is observed at the center of the sphere (node 34). It is apparent that additional internal nodes would better resolve the field data in this example.

Although the magnetic field exhibits excellent agreement with exact data, the electric fields computed within the scatterer models were not as accurate. Electric field components within each cell of the model were calculated by taking the curl of the linear representation for $\bar{\Pi}$ appearing in Equation (5). Even for the electrically small example of ka=0.1 and ε_r=2.5, the dominant component of the electric field computed using the 27 node model was in error by about 10 percent at the center of each cell (the numerical result for the magnitude of E_x was approximately 225 in every cell, as compared with the exact result of approximately 252). This trend was observed in every scatterer model studied to date. To further investigate this behavior, numerical solutions for the magnetic field at nodes of the mesh were replaced by exact data obtained from the Mie series solution. Even when the exact data was employed, the electric fields computed from the linear representation of Equation (5) exhibited significant error. For illustration, Table 5 presents E-field data for the 53-node, 176-cell model of the sphere with ka=1.0 and ε_r=2.5921.

The error observed in the electric field is believed to be related to the specific shape of the tetrahedral cells used to model the scatterer. It is expected that the best accuracy in the electric fields would be obtained by using equilateral tetrahedra whenever possible. (We note that in the two-dimensional modeling employed in reference [5], very accurate electric field components were computed from the magnetic field at the corners of equilateral triangles using a similar interpolation scheme.) This preliminary study did not employ equilateral cells, and in general it is difficult to do so in three dimensional models. An additional source of error in the preliminary data may be due to the resolution associated with the surface of the scatterer. For electrically small scatterers, the scattered fields are a strong function of the induced surface charge density. Although the models were scaled to obtain the same volume as the desired sphere, it is likely that the polygonal approximation to the spherical surface employed too few cells to accurately model the spherical surface.

Assuming that the incident field is scaled so that the $\bar{H}^{inc}$ field has unity magnitude, the scattering cross section can be computed according to

$$\sigma(\theta,\phi) = \lim_{r\to\infty} 4\pi r^2 \left| \bar{H}^s(r,\theta,\phi) \right|^2 \tag{17}$$

For numerical purposes, the far-zone magnetic field can be calculated by approximating the integral of the source function $\nabla x \bar{J}$ over each face within the model, with the observation point in the far field. Results for scattering cross section as a function of far-zone spherical angle (θ,ϕ) are presented in Tables 6, 7, and 8 for the three spherical scatterers previously considered. The incident plane wave consisted of E_x and H_y components propagating into the z direction. Observe that the numerical results improve as a function of the number of nodes in the scatterer model.

5. CONCLUSION

A new formulation is presented for the analysis of 3D inhomogeneous dielectric scatterers based on the numerical solution of the MFIE. Preliminary results suggest that the numerical solutions for the magnetic field exhibit good agreement with exact solutions. Additional study is necessary to validate the approach, especially with regard to the accuracy of the electric fields computed from the numerical solutions and the sensitivity of the results to the shape of the cells employed within the scatterer models. The procedure requires the solution of a fully-populated complex matrix equation, with order equal to three times the number of nodes in the scatterer model. Although this formulation may not prove as efficient as others based on the solution of differential equations, it remains an alternative that might be employed to help validate more efficient schemes for rather arbitrary scatterers.

REFERENCES

[1] D. E. Livesay and K. M. Chen, "Electromagnetic fields induced inside arbitrarily shaped biological bodies," *IEEE Trans. Microwave Theory Tech.*, vol. MTT-22, pp. 1273-1280, Dec. 1974.

[2] D. H. Schaubert, D. R. Wilton, and A. W. Glisson, "A tetrahedral modeling method for electromagnetic scattering by arbitrarily shaped inhomogeneous dielectric bodies," *IEEE Trans. Antennas Propagat.*, vol. AP-32, pp. 77-85, Jan. 1984.

[3] C. T. Tsai, H. Massoudi, C. H. Durney, and M. F. Iskander, "A procedure for calculating fields inside arbitrarily shaped, inhomogeneous dielectric bodies using linear basis functions with the moment method," *IEEE Trans. Microwave Theory Tech.*, vol. MTT-34, pp. 1131-1139, Nov. 1986.

[4] S. P. Castillo and A. F. Peterson, "An investigation of three-dimensional electromagnetic scattering problems using the finite element method," *Abstracts of the 1988 URSI Radio Science Meeting*, Syracuse, NY, p. 32' June 1988.

[5] A. F. Peterson and P. W. Klock, "An improved MFIE formulation for TE-wave scattering from lossy, inhomogeneous dielectric cylinders," *IEEE Trans. Antennas Propagat.*, vol. AP-36, pp. 45-49, Jan. 1988.

[6] P. P. Silvester and R. L. Ferrari, *Finite Elements for Electrical Engineers*. Cambridge: Cambridge University Press, 1983.

[7] R. F. Harrington, *Time-Harmonic Electromagnetic Fields*. New York: McGraw-Hill, 1961.

[8] *PATRAN User's Guide*. Santa Ana, CA: PDA Engineering, 1984.

Table 1

The magnitude and phase of the H_y-field at various node points within a 27-node model of a homogeneous dielectric sphere with ka=1.0 and ε_r=2.5921. The numerical solutions are compared to exact solutions. For this scatterer model, all the nodes except node 19 were located on the surface of the sphere (node 19 was at the center of the sphere).

(magnitude of H_y)

node	numerical	exact
1	1.0443	1.0487
2	1.0724	1.0873
3	1.1199	1.1249
19	1.3723	1.3878
27	1.3034	1.3249

(phase of H_y)

node	numerical	exact
1	-1.15°	-1.70°
2	-1.21	-1.83
3	-59.10	-61.37
19	-1.43	-2.17
27	66.53	66.11

Table 2

The magnitude and phase of the H_y-field at various node points within a 53-node model of a homogeneous dielectric sphere with ka=1.0 and ϵ_r=2.5921. The numerical solutions are compared to exact solutions. For this scatterer model, node 33 was at the center of the sphere.

(magnitude of H_y)

node	numerical	exact
1	1.0776	1.0873
2	1.0422	1.0487
3	1.1219	1.1239
4	1.2998	1.3158
7	1.3355	1.3685
22	1.3753	1.3893
24	1.4032	1.4443
33	1.3826	1.3878
37	1.2670	1.2783
44	1.3805	1.4044
53	1.0776	1.0873

(phase of H_y)

node	numerical	exact
1	-1.49°	-1.83°
2	-1.40	-1.70
3	-1.59	-1.95
4	-1.73	-2.12
7	18.12	17.17
22	26.43	24.81
24	36.36	34.78
33	-1.78	-2.17
37	-32.85	-31.94
44	26.35	24.57
53	-1.49	-1.83

Table 3

The magnitude and phase of the H_y-field at various node points within a 27-node model of a homogeneous dielectric sphere with ka=0.1 and ϵ_r=2.5. The numerical solutions are compared to exact solutions. For this scatterer model, node 19 was at the center of the sphere and all other nodes were located on the surface.

(magnitude of H_y)

node	numerical	exact
1	1.00035	1.00034
2	1.00052	1.00056
3	1.00138	1.00134
5	1.00099	1.00106
8	1.00240	1.00235
9	1.00072	1.00078
18	1.00140	1.00137
19	1.00287	1.00251
20	1.00101	1.00108
27	1.00243	1.00238

(phase of H_y)

node	numerical	exact
1	0.000	0.000
2	0.000	0.000
3	-5.527	-5.561
5	-3.955	-3.932
8	-7.814	-7.861
9	0.000	0.000
18	5.527	5.560
19	0.000	0.000
20	3.955	3.932
27	7.814	7.860

Table 4

The magnitude and phase of the H_y-field at various node points within a 43-node model of a lossy homogeneous dielectric sphere with ka=0.2 and ε_r=4-j4. The numerical solutions are compared to exact solutions. For this scatterer model, node 34 was at the center of the sphere and all other nodes were located on the surface.

(magnitude of H_y)

node	numerical	exact
1	1.0055	1.0057
2	1.0214	1.0234
3	0.9945	0.9932
5	1.0324	1.0382
8	1.0485	1.0564
10	0.9885	0.9846
19	0.9871	0.9816
34	1.0273	1.0403
41	0.9944	0.9932
43	1.0070	1.0068

(phase of H_y)

node	numerical	exact
1	-0.23°	-0.36°
2	6.46	6.26
3	-7.05	-7.13
5	11.18	11.33
8	15.67	15.85
10	-11.60	-11.83
19	-16.45	-16.81
34	-1.40	9.70
41	-7.04	-7.13
43	-0.35	-0.53

Table 5

The magnitude and phase of the E_x-field at the center of various cells within a 53-node model of a homogeneous dielectric sphere with ka=1.0 and ε_r=2.5921. The numerical solutions are compared with exact solutions.

(magnitude of E_x)

cell	numerical	exact
1	324.2	330.0
2	316.3	323.8
3	324.8	314.5
4	230.0	285.3
20	264.6	293.1
21	202.6	262.9
22	268.5	283.0
23	316.3	323.8
50	281.0	296.6
51	217.9	276.4
52	230.0	285.3
53	272.1	296.5
100	268.1	343.6
101	311.9	343.5
102	275.1	351.0
103	334.9	338.4

(phase of E_x)

cell	numerical	exact
1	-0.90°	-6.51°
2	1.41	-1.76
3	1.16	-6.20
4	8.71	-2.26
20	7.72	9.34
21	20.48	21.11
22	6.30	5.39
23	1.41	-1.76
50	6.87	8.83
51	20.44	18.41
52	8.71	-2.26
53	7.32	3.79
100	-55.0	-56.0
101	-37.5	-37.7
102	-55.1	-50.1
103	-18.8	-17.2

Table 6

The bistatic scattering cross section for a homogeneous dielectric sphere with ka=1.0 and ε_r=2.5921. The numerical solutions obtained with 27 and 43 node models are compared to exact solutions.

SCS (dB λ_0^2)

θ	ϕ	27-node	43-node	exact
0	0	-14.32	-13.80	-12.335
45	0	-17.67	-17.09	-15.523
45	45	-16.05	-15.52	-14.036
45	90	-14.89	-14.40	-12.930
90	0	-47.24	-43.28	-36.487
180	0	-18.22	-17.34	-16.749

Table 7

The bistatic scattering cross section for a homogeneous dielectric sphere with ka=0.1 and ε_r=2.5. The numerical solutions obtained with 27, 33, and 43 node models are compared to exact solutions.

SCS (dB λ_0^2)

θ	ϕ	27-node	33-node	43-node	exact
0	0	-75.39	-75.37	-75.09	-74.487
45	0	-78.40	-78.37	-78.10	-77.500
45	45	-76.64	-76.62	-76.34	-75.741
45	90	-75.40	-75.38	-75.10	-74.493
90	0	-135.23	-130.02	-136.62	-139.500
180	0	-75.43	-75.41	-75.13	-74.529

Table 8

The scattering cross section for a homogeneous dielectric sphere with ka=0.2 and ε_r=4-j4. The numerical solutions obtained with 27 and 43 node models are compared to exact solutions.

SCS (dB λ_0^2)

θ	ϕ	27-node	43-node	exact
0	0	-51.64	-51.08	-49.892
45	0	-54.66	-54.09	-52.904
45	45	-52.91	-52.35	-51.161
45	90	-51.67	-51.11	-49.921
90	0	-101.17	-96.32	-92.984
180	0	-51.81	-51.25	-50.090

SCATTERING FROM CYLINDRICAL DIELECTRIC SLABS: A METHOD OF MOMENTS APPROACH*

Kevin C. Clancy, Semblam R. Rengarajan, Richard E. Hodges
Department of Electrical and Computer Engineering
California State University, Northridge
Northridge, CA 91330

Abstract

Schelkunoff's equivalence principle is employed to solve the problem of scattering from a cylindrical dielectric structure in terms of equivalent electric and magnetic currents on the surface of the dielectric. A pair of coupled integro-differential equations are derived for the equivalent currents and are solved by the method of moments (MOM). Source of excitation in the form of electric or magnetic line current with e^{jwt} time dependence is assumed. The MOM computer code is validated by generating test cases for scattering from a conducting structure in place of the dielectric. Numerical results are presented for the surface equivalent currents and scattered fields and MOM results are compared to physical optics results.

I. INTRODUCTION

The scattering of electromagnetic waves by a dielectric structure is a problem of interest in radome applications. Recently results of an investigation of various asymptotic approximations employed in radome analysis were presented [1]. In that study, a method-of-moments (MOM) type solution for volume polarization current was obtained in a manner similar to that of Richmond [2]. Scattered fields computed from polarization current were compared to similar results obtained from asymptotic solutions in order to investigate their approximations. The MOM technique for scattered fields computed from a solution of polarization current is limited to thin structures. In this paper, the problem of scattering from a cylindrical dielectric is formulated in terms of surface integral equations and applied specifically to determine the scattering characteristics of a dielectric ogival structure.

II. ANALYSIS

The cross-section of a curved dielectric cylinder of thickness t is shown in Figure 1. The dielectric is assumed to be linear homogeneous isotropic material of constitutive parameters

*This work was supported in part by the Hughes Aircraft Company, Missile Systems Group, Canoga Park, CA.

μ_0, ϵ. The source of excitation is assumed to be a z-directed infinite electric or magnetic line current with an $e^{j\omega t}$ time dependence. Because of z-invariance, the analysis becomes a two-dimensional problem. Schelkunoff's equivalence principle [3] is invoked to divide the domain of this problem into two regions; region 1 is the dielectric bounded by curve C and region 2 is the free space outside. For the purpose of solving the problem in region 2, electric and magnetic equivalent surface currents are placed on C. Scattered fields in region 2 are obtained from the fields radiated by these equivalent currents in a homogeneous free space medium. Similarly the total field in region 1 is determined from the fields radiated by negative of the above mentioned equivalent currents in a homogeneous medium of constitutive parameters, μ_0, ϵ.

The boundary conditions are then applied; i.e., the continuity of the tangential components of the electric and magnetic fields across the boundary C. This results in a pair of coupled integro-differential equations for the electric line source (TM) as shown below.

$$\frac{\omega\mu_0}{4}\oint_C J_z(\bar{r}')\left[H_0^{(2)}(k_0\rho)+H_0^{(2)}(k\rho)\right]dl' + \frac{1}{4j}\oint_C M_t(\bar{r}')\frac{\partial}{\partial n'}\left[H_0^{(2)}(k_0\rho)+H_0^{(2)}(k\rho)\right]dl' = E_z^{inc}(\bar{r}) \tag{2.1a}$$

$$\frac{\omega\epsilon_0}{4}\oint_C (\hat{n}\times\hat{t}')M_t(\bar{r}')\left[H_0^{(2)}(k_0\rho)+\epsilon_r H_0^{(2)}(k\rho)\right]dl' + \frac{1}{4\omega\mu_0}\frac{\partial}{\partial t}\oint_C \frac{\partial}{\partial t'}M_t(\bar{r}')\left[H_0^{(2)}(k_0\rho)+H_0^{(2)}(k\rho)\right]dl' + \frac{1}{4j}\oint_C J_z(\bar{r}')\frac{\partial}{\partial n}\left[H_0^{(2)}(k_0\rho)+H_0^{(2)}(k\rho)\right]dl' = H_t^{inc}(\bar{r}) \tag{2.1b}$$

For the magnetic line source (TE) a similar set of equations can be obtained from duality.

III. METHOD-OF-MOMENTS SOLUTION

The integro-differential equations have been solved by the method of moments (MOM). Sub-sectional expansion functions and testing functions have been chosen to produce matrix equations. For the TM case, pulse expansions for the electric currents and triangle functions for the magnetic currents were employed. Testing functions in the form of Dirac delta functions and pulse functions were used for equations (2.1a) and (2.1b) respectively. A similar approach was employed for the dual problem (TE). The resulting matrix equation for the TM case has been expressed in the form

$$\begin{pmatrix} [Z] & [\alpha] \\ [\beta] & [Y] \end{pmatrix}\begin{pmatrix} [a] \\ [b] \end{pmatrix} = \begin{pmatrix} [V] \\ [I] \end{pmatrix} \qquad (3.1)$$

The submatrices and the source matrix are given by

$$Z_{ij} = \frac{\omega\mu_0}{4}\int_{C_i-\frac{\Delta C}{2}}^{C_i+\frac{\Delta C}{2}}\left\{H_0^{(2)}(k_0\rho_j) + H_0^{(2)}(k\rho_j)\right\}dt' \qquad (3.2)$$

$$\alpha_{ij} = \frac{k_0}{4j}\int_{C_i-\Delta C}^{C_i+\Delta C} T_i(t')\cos\theta'\left[H_1^{(2)}(k_0\rho_j) + \sqrt{\epsilon_r}H_1^{(2)}(k\rho_j)\right]dt' \qquad (3.3)$$

$$\beta_{ij} = -\frac{k_0}{4j}\int_{C_j-\frac{\Delta C}{2}}^{C_j+\frac{\Delta C}{2}}\int_{C_i-\frac{\Delta C}{2}}^{C_i+\frac{\Delta C}{2}}\cos\theta\left[H_1^{(2)}(k_0\rho) + \sqrt{\epsilon_r}H_1^{(2)}(k\rho)\right]dt'dt \qquad (3.4)$$

$$\begin{aligned} Y_{ij} &= \frac{\omega\epsilon_0}{4}\Delta C_j\int_{C_i-\Delta\frac{C}{2}}^{C_i+\Delta\frac{C}{2}}\cos p\left[H_0^{(2)}(k_0\rho_{ij}) + \epsilon_r H_0^{(2)}(k\rho_{ij})\right]dt' \\ &- \frac{1}{4\omega\mu_0\Delta C_i}\int_{C_i-\Delta C}^{C_i+\Delta C}\mathrm{sgn}_i(t')\left[H_0^{(2)}\left(k_0\rho_{j-\frac{1}{2}}\right) + H_0^{(2)}\left(k\rho_{j-\frac{1}{2}}\right)\right]dt' \\ &+ \frac{1}{4\omega\mu_0\Delta C_i}\int_{C_i-\Delta C}^{C_i+\Delta C}\mathrm{sgn}_i(t')\left[H_0^{(2)}\left(k_0\rho_{j-\frac{1}{2}}\right) + H_0^{(2)}\left(k\rho_{j-\frac{1}{2}}\right)\right]dt' \end{aligned} \qquad (3.5)$$

where

$$\mathrm{sgn}_i(t') = 1 \ , \ t' > C_i$$
$$= -1 \ , \ t' < C_i$$

$$\rho_j = |\vec{r}_j - \vec{r}'| = \sqrt{(x_j - x')^2 + (y_j - y')^2}$$

$$V_j = E_z^{inc}(C_j) \qquad (3.6)$$

$$I_j = \int_{C_j-\frac{\Delta C}{2}}^{C_j+\frac{\Delta C}{2}} H_t^{inc}dt \qquad (3.6)$$

Each of the sub-matrices given by equations (3.2) through (3.5) with a minor modification becomes the MOM matrices for the electric field integral equation (EFIE) of a conductor in place of the dielectric for TM, the magnetic field integral equation (MFIE) for TM, the MFIE for TE, and the EFIE for TE respectively.

IV. NUMERICAL RESULTS AND DISCUSSION

The four conductor test cases were used to independently validate the four sub-matrices given by equations (3.2) through (3.5).

The MOM solution was compared to the PO solution for various shaped structures to determine the limits of applicability of PO. The PO solution shows insignificant degradation for structures with radius of curvature greater than 10 wavelengths, a length greater than 6 wavelengths, and for a source-scatterer seperation greater than 2 wavelengths. Outside of these limits, the PO solution was poorer.

Figures 2 through 6 are graphs of the surface currents and the scattered field for curved dielectrics. Both PO (+'s) and MOM (solid line) solutions are shown. The x-axis is cell or sub-domain number. A 5 wavelength by 0.2 wavelength slab with a radius of curvature of 200 wavelengths was first tested. The source is an electric line current that is 10 wavelengths away from the center of the inner broad wall. The dielectric constant is 2 and the loss tangent is zero. The cell size is approximately .1 wavelength over the entire surface. As was expected with these parameters, the PO solution is very close to the MOM solution.

PO results show significant deviation from MOM results for structures with a small radius of curvature. A radius of 10 wavelengths exhibits a boresight error of the order of 1.5°. The boresight error is the angle between the peaks of the scattered fields for the two solutions.

There are significant differences between the PO and MOM solutions when the source is within 2 λ from the dielectric. There is a slight boresight error at the peaks, and much more deviation away from the peaks.

Similar results were obtained for the magnetic line source excitation.

CONCLUSION

The problem of scattering from cylindrical dielectric structures has been formulated in the form of a pair of coupled integro-differential equations involving the equivalent electric and magnetic surface currents. Numerical results have been obtained by a method-of-moments (MOM) solution. The MOM computer code has been validated by recognizing that the MOM

matrix for the dielectric can be modified to generate the MOM matrix for the problem of scattering from a conductor in place of the dielectric. A comparison of MOM solutions for the equivalent currents and the scattered field with similar results obtained by the physical optics technique showed that the latter is less accurate for radius of curvature less than 10 λ, lengths less than 6 λ and a source to scatterer separation less than 2 λ. Also the P.O. currents have substantial errors near the edges.

REFERENCES

[1] S.R. Rengarajan and E.S. Gillespie, Jr., "Asymptotic Approximations in Radome Analysis", IEEE Trans. on Antennas and Propagation, vol. AP-36, pp. 405-414, March 1988.

[2] J.H. Richmond, "Scattering by a Dielectric Cylinder of Arbitrary Cross-Section Shape", IEEE Trans. on Antennas and Propagation, vol. AP-13, pp. 334-341, May 1965.

[3] S.A. Schelkunoff, "Some Equivalence Theorems of Electromagnetics and Their Application to Radiation Problems", Bell System Technical Journal, vol. 15, pp. 92-112, 1936.

[4] K.C. Clancy, "Method of Moments Analysis of a Dielectric Cylinder", Master's Thesis, California State University, Northridge, August 1988.

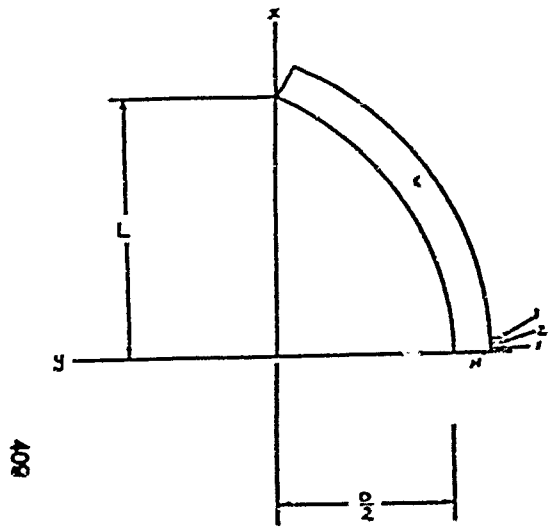


Figure 1 Geometry of a curved scatterer

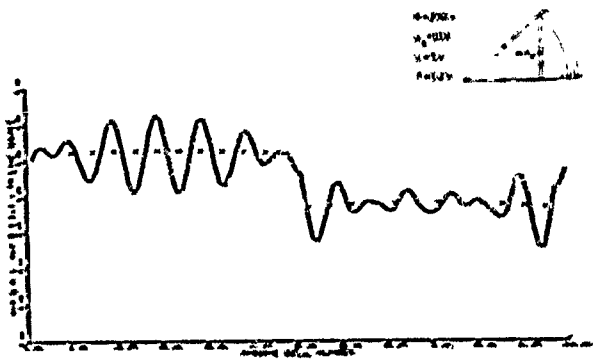


Figure 2 Magnitude of the magnetic surface current

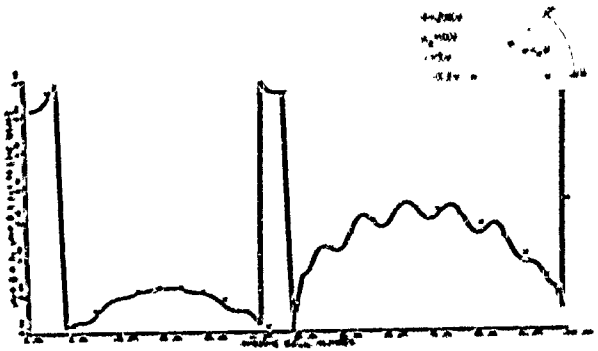


Figure 3 Phase of the magnetic surface current

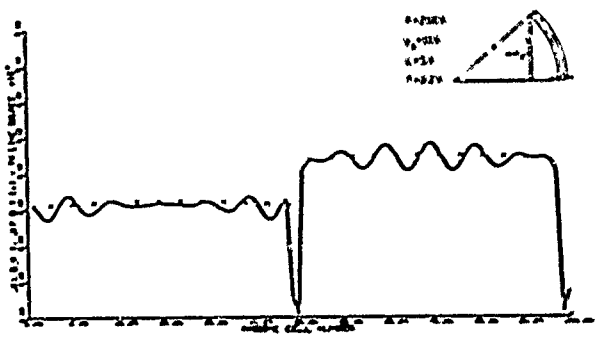


Figure 4 Magnitude of the electric surface current

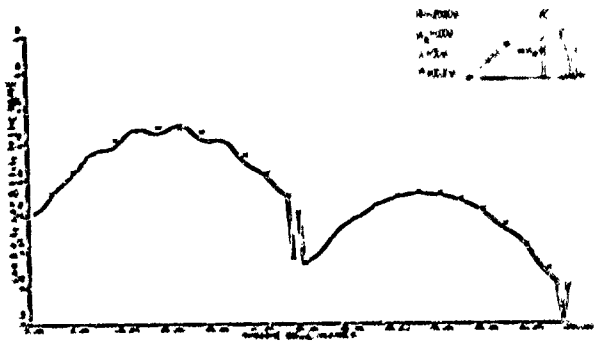


Figure 5 Phase of the electric surface current

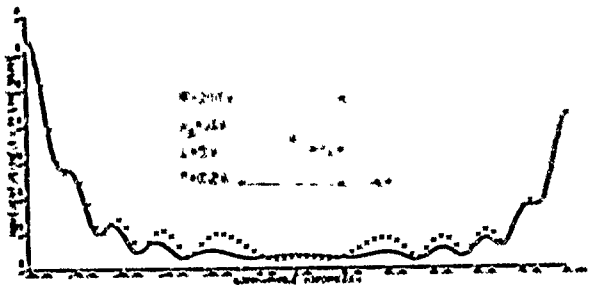


Figure 6 Magnitude of the scattered electric field

RADAR CROSS SECTION CALCULATION OF PARTIALLY COATED CONDUCTING BODIES

G. Bridges[1], M. Abouzahra[2], A. Kishk[3] and L. Shafai[4]

[1]CANCAD Technology Inc., P.O. Box 546, Winnipeg MB, Canada R3C 2J3
[2]MIT Lincoln Laboratory, P.O. Box 73, Lexington MA 02173-0073
[3]Dept. of Electrical Engineering, University of Mississippi MS 38677
[4]Dept. of Electrical Engineering, University of Manitoba, Canada R3T 2N2

Abstract

Many Problems in radar scattering and antenna design involve complex material objects made of conductors, dielectrics and their combination. Analytical solutions are available for only a few special geometries and almost always a numerical method must be employed. For the solution of conducting or dielectric bodies, numerous publications are available in the literature. The solution of their combination however, has only recently received attention, and the validation of these techniques is an important topic. In this paper, experimental verification of a method of moments program (MBES) for radar cross section calculation and antenna analysis is presented. The electromagnetic simulation code being examined is a program for the calculation of scattering or radiation from bodies of revolution, which can consist of conducting or lossy dielectric materials. A numerical solution is obtained using an integral-equation formulation, for which several different forms can be selected. Numerical and experimental results for the mono-static radar cross section calculation of conducting objects partially coated with a dielectric material will be presented, these including cases where the dielectric coating is lossy. As well, results calculated using the impedance boundary condition to model the dielectric coated surface will be examined.

1. INTRODUCTION

Most scattering and antenna problems involve material objects made of conductors, dielectrics and their combinations. When the object shape is complex, an analytic solution is not usually available and a numerical method must be used. Problems involving either conducting or dielectric bodies have been studied extensively and numerous publications are available in the literature. However, many important antenna and scattering problems involve combinations of conductors and dielectrics, such as dielectric loaded structures, microstrip antennas, or coated objects. For conducting bodies of revolution Mautz and Harrington [1] have provided three different moment method formulations, called E-field, H-field and Combined-field, and investigated their solution accuracies. Wu and Tsai [2] used the moment method to solve the scattering from arbitrarily shaped and lossy dielectric bodies of revolution. Shortly after, Mautz and Harrington [3] solved the problem of homogeneous lossy bodies using the Wu and Tsai formula, which they named PMCHW, and a formulation due to Müller. More recently, the solutions of scattering from inhomogeneous penetrable bodies of revolution, dielectric coated conductors, and multiple bodies of revolution have been reported [4,5]. The case of conductors with partial dielectric coatings was investigated by Mautz and Harrington [6] in investigating electromagnetic coupling problems. Using the equivalence principle, they have suggested different formulations and in [7] have solved numerically the electromagnetic coupling

This work was sponsored in part by the Department of the Air Force. The views expressed are those of the authors and do not reflect the official policy or position of the U.S. Government.

problems for bodies of revolutions by a formulation called E-PMCHW. Based on these results, Kishk and Shafai [8], presented various formulations for the solution of multiple bodies of revolution, which consisted an arbitrary combination of conducting and/or dielectric regions.

The multiple body electromagnetic scattering code (MBES) presented in this paper is a method of moments program for the scattering and radiation analysis of single or multiple objects made of conductors, lossy dielectrics, or their combination. The code is specialized for the analysis of rotationally symmetric geometries, making solutions computationally economical, and thus enabling the study of larger and more complex problems. Both multiple dipole and plane wave excitation can be used to specify incident fields. The former allows the solution of antenna problems, where the dipole excitation can be placed either inside or outside the dielectric region. The latter allows the calculation of the mono-static or bi-static radar cross section of an object. The code is based on the results of [8], where by applying the equivalence principle, several different integral equation formulation types are possible. This allows the selection of the most suitable formulation for the specific problem being studied. A comparison of these formulations for the solution of various scattering problems has been examined [8,9]. The MBES code has been used for the analysis of many antenna geometries, these including dielectric rod antennas [10], circular waveguide feeds [11], and microstrip antennas [8], as well as for the solution of scattering problems. This paper will concentrate on the experimental verification of the code for the mono-static radar cross section calculation for conducting bodies partially coated with lossless or lossy dielectric materials. The ability to model a surface using the impedance boundary condition will also be examined and compared to the experimental results.

2. PROBLEM FORMULATION

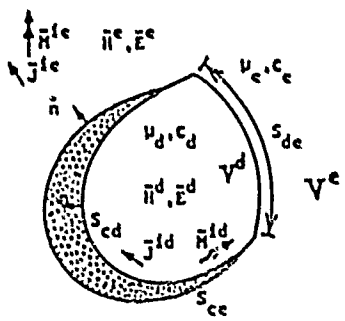


Figure 1: Scattering geometry with conducting and dielectric regions.

Figure 1 shows the general electromagnetic problem under consideration, where the object consists of both conducting and dielectric regions. The surfaces S_{ce}, S_{cd} and S_{de} refer, respectively to the boundaries between the conductor and the exterior region, conductor and dielectric, and dielectric and exterior region, respectively. V^d is a finite volume filled with a homogeneous material of permittivity ϵ_d and permeability μ_d and bounded by the two surfaces S_{de} and S_{cd}. The surface S_{cd} may consist of several sub-surfaces, to represent multiple dielectric and conducting interfaces as well as conducting bodies inside the dielectric. V^e represents the external region, with permittivity of ϵ_e and permeability of μ_e, and is bounded by two surfaces S_{de} and S_{ce}. Again, the surface S_{ce} may consist of several sub-surfaces for the modeling of multiple conducting bodies. Also, $\bar{E}^d$, $\bar{H}^d$ and $\bar{E}^e$, $\bar{H}^e$ refer to the field vectors within the dielectric and the exterior region. The sources of the electromagnetic excitation are provided by the impressed electric and magnetic currents $\bar{J}^{ie}$ and $\bar{M}^{ie}$ in V^e and $\bar{J}^{id}$ and $\bar{M}^{id}$ in V^d. The problem of Figure 1 is a general one since it can be used to represent both conducting and dielectric problems. In particular, it reduces to the case of; scattering from a dielectric body, when S_{cd} and S_{ce} vanish and S_{de} becomes a closed surface; scattering from a perfect

conductor, when S_{cd} and $S_{\mu\epsilon}$ vanish and $S_{c\epsilon}$ becomes a closed surface; scattering from a dielectric clad body, when $S_{c\epsilon}$ vanishes and S_{cd} and $S_{\mu\epsilon}$ become closed surfaces. The MBES program assumes all surfaces are rotationally symmetric, thus representing bodies of revolution.

The integral formulation of the problem is developed by specifying the boundary conditions and equivalent surface currents at the conducting and dielectric surfaces as

$$\hat{n} \times \bar{E}^d = 0 \qquad \bar{J}_{cd} = \hat{n} \times \bar{H}^d \qquad \text{on } S_{cd}$$

$$\hat{n} \times \bar{E}^\epsilon = 0 \qquad \bar{J}_{c\epsilon} = \hat{n} \times \bar{H}^\epsilon \qquad \text{on } S_{c\epsilon} \tag{1}$$

$$\left.\begin{aligned} \hat{n} \times \bar{E}^d &= \hat{n} \times \bar{E}^\epsilon \\ \hat{n} \times \bar{H}^d &= \hat{n} \times \bar{H}^\epsilon \end{aligned}\right\} \qquad \left.\begin{aligned} \bar{J}_{\mu\epsilon} &= \hat{n} \times \bar{H}^\epsilon \\ \bar{M} &= -\hat{n} \times \bar{E}^\epsilon \end{aligned}\right\} \qquad \text{on } S_{\mu\epsilon}$$

where $\hat{n}$ is the outward normal on each surface considered. The currents $\bar{J}_{cd}$, $\bar{J}_{c\epsilon}$ and $\bar{J}_{\mu\epsilon}$ are the equivalent electric currents on each respective surface and $\bar{M}$ is the magnetic current on the interface surface between the dielectric and the exterior region. From the above conditions, the following set of equations can be written

$$\hat{n} \times \bar{E}^d\,(\bar{J}_{cd} + \bar{J}_{\mu\epsilon}, \bar{M}) = \hat{n} \times \bar{E}^d\,(\bar{J}^d, \bar{M}^d) \qquad \text{just outside } S_{cd} \tag{2}$$

$$\hat{n} \times \bar{E}^d\,(\bar{J}_{cd} + \bar{J}_{\mu\epsilon}, \bar{M}) = \hat{n} \times \bar{E}^d\,(\bar{J}^d, \bar{M}^d) \qquad \text{just outside } S_{\mu\epsilon} \tag{3}$$

$$-\hat{n} \times \bar{E}^\epsilon\,(\bar{J}_{c\epsilon} + \bar{J}_{\mu\epsilon}, \bar{M}) = \hat{n} \times \bar{E}^\epsilon\,(\bar{J}^\epsilon, \bar{M}^\epsilon) \qquad \text{just inside } S_{c\epsilon} \tag{4}$$

$$-\hat{n} \times \bar{E}^\epsilon\,(\bar{J}_{c\epsilon} + \bar{J}_{\mu\epsilon}, \bar{M}) = \hat{n} \times \bar{E}^\epsilon\,(\bar{J}^\epsilon, \bar{M}^\epsilon) \qquad \text{just inside } S_{\mu\epsilon} \tag{5}$$

$$\hat{n} \times \bar{H}^d\,(\bar{J}_{cd} + \bar{J}_{\mu\epsilon}, \bar{M}) = \hat{n} \times \bar{H}^d\,(\bar{J}^d, \bar{M}^d) \qquad \text{just outside } S_{cd} \tag{6}$$

$$\hat{n} \times \bar{H}^d\,(\bar{J}_{cd} + \bar{J}_{\mu\epsilon}, \bar{M}) = \hat{n} \times \bar{H}^d\,(\bar{J}^d, \bar{M}^d) \qquad \text{just outside } S_{\mu\epsilon} \tag{7}$$

$$-\hat{n} \times \bar{H}^\epsilon\,(\bar{J}_{c\epsilon} + \bar{J}_{\mu\epsilon}, \bar{M}) = \hat{n} \times \bar{H}^\epsilon\,(\bar{J}^\epsilon, \bar{M}^\epsilon) \qquad \text{just inside } S_{c\epsilon} \tag{8}$$

$$-\hat{n} \times \bar{H}^\epsilon\,(\bar{J}_{c\epsilon} + \bar{J}_{\mu\epsilon}, \bar{M}) = \hat{n} \times \bar{H}^\epsilon\,(\bar{J}^\epsilon, \bar{M}^\epsilon) \qquad \text{just inside } S_{\mu\epsilon} \tag{9}$$

where $\bar{E}^\epsilon(\bar{J}, \bar{M})$ and $\bar{E}^d(\bar{J}, \bar{M})$ are the electric fields due to currents $\bar{J}$ and $\bar{M}$, radiating in the media characterized by ϵ_ϵ, μ_ϵ and ϵ_d, μ_d, respectively. $\bar{H}^\epsilon(\bar{J}, \bar{M})$ and $\bar{H}^d(\bar{J}, \bar{M})$ are the associated magnetic fields.

The dielectric region V^d is defined by specifying the relative dielectric constant $\epsilon_{cd} = \epsilon_{rd} - j\epsilon_{id}$, where ϵ_{rd} is the relative permittivity and $\epsilon_{id} = \sigma_d/w\epsilon_0$ where σ_d is the conductivity of the dielectric region. The MBES analysis program also has the option of specifying the surface impedance $\bar{Z}$ for a surface in the exterior region $S_{c\epsilon}$. This allows the modeling of lossy conductors, as well as the ability to model lossy dielectric coatings using the impedance boundary condition. Two components of the surface impedance can be specified, $\bar{Z} = Z_t\hat{t} + Z_\phi\hat{\phi}$, where Z_t is the axial surface impedance and Z_ϕ is the azimuthal surface impedance as $Z_{t,\phi} = [j\omega\mu_c/(\sigma_c + j\omega\epsilon_c)]^{1/2}$ (for lossy conductors).

Observing that equations (2-9) are 8 equations with 4 unknown field vectors, many different solution formulations can be developed by considering various combinations to determine the unknown currents. Seven different combinations are available in the MBES analysis code, these being denoted as: E-Field, H-Field, C-Field, E-PMCHW, E-Müller, H-PMCHW, and H-Müller. The development of these formulations is discussed in [8,9]. For perfectly conducting objects the above sets can be reduced to three formulations, namely, E-field, H-field and C-field. For dielectric objects five formulations can be used; the E-field, H-field, C-field, PMCHW, and the Müller formulations. For combinations of dielectric and conducting bodies, and aperture coupling problems, all seven formulations may be used. The user has the option of choosing any one of these possible formulation types in the MBES program. For most applications the E-PMCHW formulation usually gives the most reliable results. However, other formulations are better suited when the dielectric constant is very large or small [8].

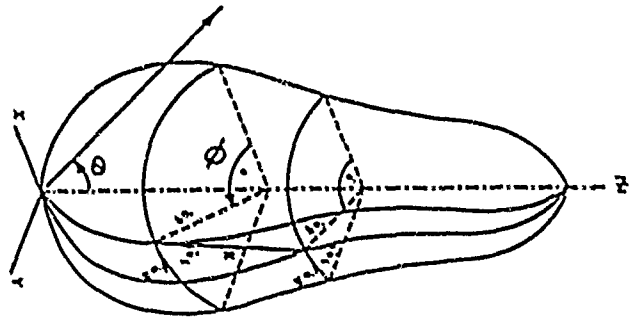


Figure 2: Rotationally symmetric body geometry.

A moment method solution of the above formulations will be applied to rotationally symmetric bodies with a geometry as shown in Figure 2. The reduction of integral equations to matrix equations involving unknown surface currents follows the procedure well known for bodies of revolution. Here, both electric and magnetic surface currents are decomposed into tangential components as

$$\bar{J}(\bar{r}) = \hat{t}\, I^t(t,\phi) + \hat{\phi}\, I^\phi(t,\phi) \tag{10}$$

$$\bar{M}(\bar{r}) = \hat{t}\, M^t(t,\phi) + \hat{\phi}\, M^\phi(t,\phi) \tag{11}$$

where $\hat{t}$ and $\hat{\phi}$ are the unit tangents to the body and I^t, I^ϕ and M^t, M^ϕ are the current components. The electric current $\bar{J}$ exists on both conducting and dielectric surfaces, but $\bar{M}$ exists only on the dielectric. The surface current is then expanded using a discrete Fourier basis in the azimuthal dimension and a triangle function basis along the generating contour for the body. To this extent, the total generating curve of all bodies is sub-divided into Nc segments and that of dielectrics into Nd segments, so that the surface currents can be represented as

$$\bar{J}(\bar{r}) = \sum_{n=M1}^{M2} \sum_{j=1}^{Nc} I^t_{nj} J^t_{nj}(t,\phi)\,\hat{t} + I^\phi_{nj} J^\phi_{nj}(t,\phi)\,\hat{\phi} \tag{12}$$

$$\bar{M}(\bar{r}) = \eta_\epsilon \sum_{n=M1}^{M2} \sum_{j=Nc+1}^{Nc+Nd} K^t_{nj} M^t_{nj}(t,\phi)\,\hat{t} + K^\phi_{nj} M^\phi_{nj}(t,\phi)\,\hat{\phi} \tag{13}$$

where J^t_{nj}, J^ϕ_{nj}, K^t_{nj}, K^ϕ_{nj} are expansion functions defined as

$$J^t_{nj} = J^\phi_{nj} = K^t_{nj} = K^\phi_{nj} = f_j(t)\, e^{jn\phi} \tag{14}$$

Azimuthal modes in the range $M1 \le n \le M2$ are used to represent the surface currents in the azimuthal dimension. The number of modes can be specified in the code. The unknown current coefficients I^t_{nj}, I^ϕ_{nj}, M^t_{nj}, M^ϕ_{nj} are determined by choosing an appropriate inner product and a set of testing functions $\bar{W}^t_{ii}$ and $\bar{W}^\phi_{ii}$ defined as

$$\bar{W}^t_{ii} = \hat{t}\, f_i(t)\, e^{-jn\phi} \quad , \quad \bar{W}^\phi_{ii} = \hat{\phi}\, f_i(t)\, e^{-jn\phi} \tag{15}$$

By applying the moment method, with the chosen expansion (12,13) to the desired integral equation formulation, the current coefficients can be determined in the general matrix form

$$[\bar{T}_n]\,[\bar{I}_n] = [\bar{V}_n]\,, \; n = 0, \pm 1, \pm 2, \cdots \tag{16}$$

where $\bar{T}_n$ is a square matrix representing the impedance and the admittance sub-matrices, $\bar{I}_n$ is a column matrix for the unknown expansion coefficients of $\bar{J}$ and $\bar{M}$, and $\bar{V}_n$ is the excitation column matrix.

The MBES code allows two types of excitations; plane wave or multiple dipole. The excitation matrix for plane wave incidence can easily be determined. For an electric dipole in the region q, the excitation matrix can be determined from the vector potentials

$$\bar{E}^{inc,i} = -j\omega \bar{A}^i - \nabla\Phi^i \quad , \quad \bar{A}^i = \frac{-jk_i\mu_i}{4\pi r}\,\bar{\Pi}\, h_0^{(2)}(k_i\,|\bar{r}-\bar{r}'|) \tag{17}$$

$$\bar{\Pi}^{inc,i} = \frac{1}{\mu_i}\nabla\times\bar{A}^i \quad , \quad \Phi^i = \frac{\eta_i}{4\pi r}\,\bar{\Pi}\cdot\nabla h_0^{(2)}(k_i\,|\bar{r}-\bar{r}'|) \tag{18}$$

and $h_0^{(2)}$ is the spherical Hankel function of the second kind and zero order and $\bar{\Pi}$ is the dipole moment with an arbitrary orientation. The inner products of $\bar{E}^{inc}$ and $\bar{\Pi}^{inc}$ with testing functions $\bar{W}_k$ provide the elements of the excitation matrix $[\bar{V}_n]$ for each formulation.

After filling the impedance matrices $[\bar{T}_n]$ and the excitation matrices $[\bar{V}_n]$ of equation (16) for each of the desired modes, the currents $\bar{J}$ and $\bar{M}$ on the surfaces of the conducting and dielectric regions can be solved for. Once the induced currents $\bar{J}$ and $\bar{M}$ are determined, the far field components E_θ^{scat} and E_ϕ^{scat} at the point (r_o, θ_o, ϕ_o) can be calculated as

$$E_\theta^{scat} = \frac{-j\omega\mu_i}{4\pi r_o}e^{-jkr_o}\,F_1(\theta_o,\phi_o) \quad , \quad F_1(\theta_o,\phi_o) = \int_s (\bar{J}\cdot\hat{a}_\theta + \frac{1}{\eta_i}\bar{M}\cdot\hat{a}_\phi)\,e^{+jk\hat{\rho}_o\cdot\bar{r}'}\,ds \tag{19}$$

$$E_\phi^{scat} = \frac{-j\omega\mu_i}{4\pi r_o}e^{-jkr_o}\,F_2(\theta_o,\phi_o) \quad , \quad F_2(\theta_o,\phi_o) = \int_s (\bar{J}\cdot\hat{a}_\phi - \frac{1}{\eta_i}\bar{M}\cdot\hat{a}_\theta)\,e^{+jk\hat{\rho}_o\cdot\bar{r}'}\,ds \tag{20}$$

where S is the surface of the object, $\hat{\rho}_o$ is a unit vector in the direction from the origin of the coordinates to the field point, $\bar{r}'$ is the positional vector of the source point (x',y',z') on the body and, $\hat{a}_\theta$ and $\hat{a}_\phi$ are unit vectors in the direction of θ and ϕ, respectively. Note that, E_θ^{scat} and E_ϕ^{scat} are the scattered fields if the excitation source is in the exterior region, and are the total fields if the source is located in the interior region. The bi-static radar cross section can be determined form the scattered fields as

$$\frac{\sigma_{\theta\theta}(\theta,\phi)}{\lambda^2} = \frac{1}{4\pi r_0^2}\left|\frac{E_\theta^{scat}(\theta,\phi)}{2\pi\eta_0}\right|^2 \quad , \quad \frac{\sigma_{\phi\theta}(\theta,\phi)}{\lambda^2} = \frac{1}{4\pi r_0^2}\left|\frac{E_\phi^{scat}(\theta,\phi)}{2\pi\eta_0}\right|^2 \quad \text{for } E_\theta^{inc}(\theta_{inc},\phi=0) \tag{21}$$

$$\frac{\sigma_{\theta\phi}(\theta,\phi)}{\lambda^2} = \frac{1}{4\pi r_0^2}\left|\frac{E_\theta^{scat}(\theta,\phi)}{2\pi\eta_0}\right|^2 \quad , \quad \frac{\sigma_{\phi\phi}(\theta,\phi)}{\lambda^2} = \frac{1}{4\pi r_0^2}\left|\frac{E_\phi^{scat}(\theta,\phi)}{2\pi\eta_0}\right|^2 \quad \text{for } E_\phi^{inc}(\theta_{inc},\phi=0) \tag{22}$$

Note that for the mono-static backscattering case, $\sigma_{\theta\phi}(\theta=\theta_{inc},\phi=0) = \sigma_{\phi\theta}(\theta=\theta_{inc},\phi=0) = 0$. The near fields E_θ^{scat} and E_ϕ^{scat}, can also be determined by the MBES analysis program by direct integration of the the surface currents on the exterior bodies.

3. PROGRAM DESCRIPTION

The MBES analysis code is divided into three distinct programs; one performs the geometry entry function, one performs the numerical simulation, and one displays the computed results [12]. The geometry entry program is a two-dimensional editor allowing the graphical entry of the scattering structure geometry as shown in figure 3a). Since only rotationally symmetric bodies are considered, the generating contour for the structure is adequate to completely specify the object. A variety of mouse and menu options are used to enter geometrical data as well as excitation information, such as the number of azimuthal modes desired and the formulation type to be used. Segmentation of the generating contour for the triangle basis expansion is also performed graphically. Once the object is created, a three-dimensional plot of the completed structure can be made as shown in figure 3b). The output of the editor produces an ascii data file (similar to the form used by NEC) describing the structure geometry and desired excitation. The simulation program accepts the geometry input data, checks its validity, and then implements the moment method solution of the problem as described in the previous section. Resulting radiated/scattered fields as well as induced surface currents on the scattering object can be produced for examination. These computed results can be displayed in a variety of graphical ways. The radiated fields (or radar cross section results) can be examined using a two-dimensional cartesian or polar display, or using a three-dimensional cartesian or spherical display as shown in figures 3c,d). The electric or magnetic

surface currents ($\overline{J}, \overline{M}$) induced on the surface of the object can also be examined using a three-dimensional cartesian display, where one axis is the azimuthal angle ϕ and the other is the position along the generating contour, or by using the three-dimensional display of the object as was shown in figure 3b), where the degree of shading indicates the magnitude of the current. Total or individual mode results are available for observation.

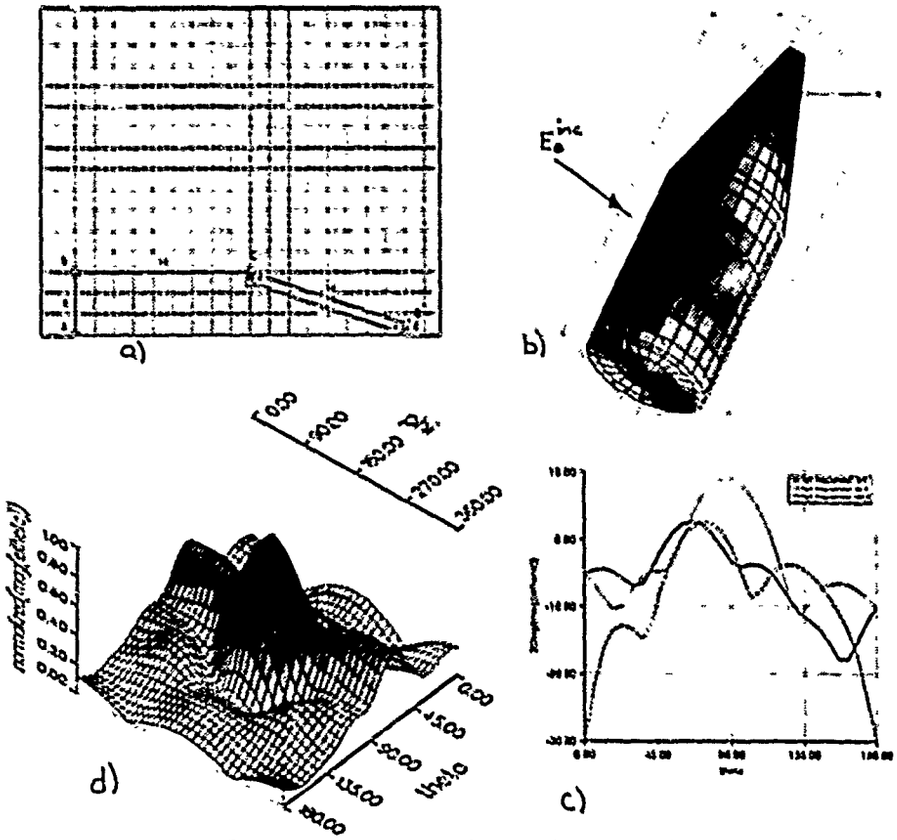


Figure 3: Geometry entry and output display method.

4. NUMERICAL AND EXPERIMENTAL VERIFICATION

The MBES analysis code has previously been verified to some degree by comparison to various special geometries for which analytical solutions exist, these specifically being conducting sphere and coated sphere type structures [8,9]. Results presented in this paper will concentrate on the comparison of the numerical and experimentally generated results for the radar cross section analysis of various conducting objects coated with lossless and lossy dielectric materials. Experimental work was performed at MIT Lincoln Laboratory. In all cases the mono-static radar cross section $\sigma_{\theta,\theta}(0)/\lambda^2$ and $\sigma_{\phi,\phi}(0)/\lambda^2$ was measured. The experimental and numerical results for four test objects are given in figures 4-7. These cases include two lossless and two lossy dielectric coated configurations.

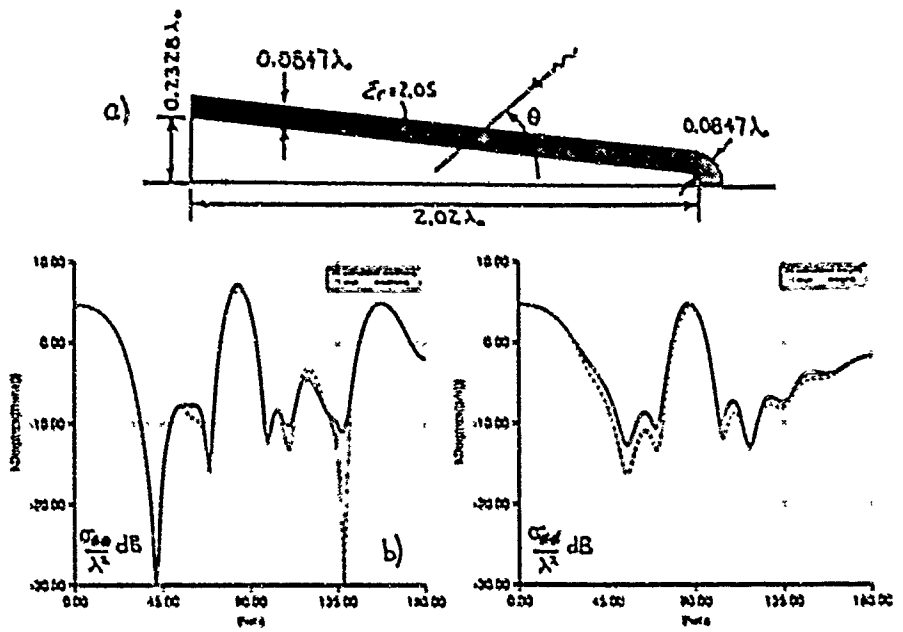


Figure 4: Teflon coated conducting cone (ε_r=2.05).

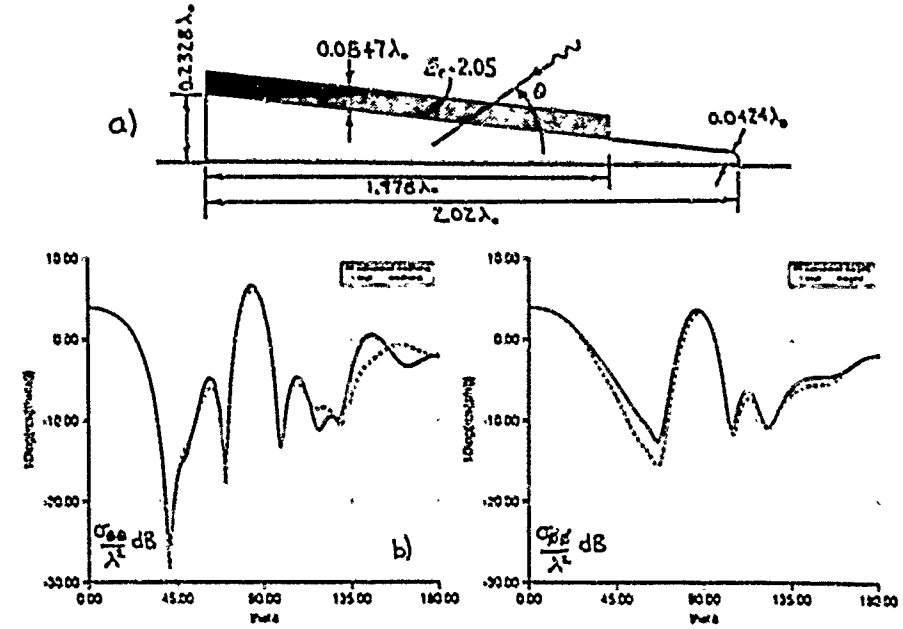


Figure 5: Teflon coated conducting cone with the tip exposed.

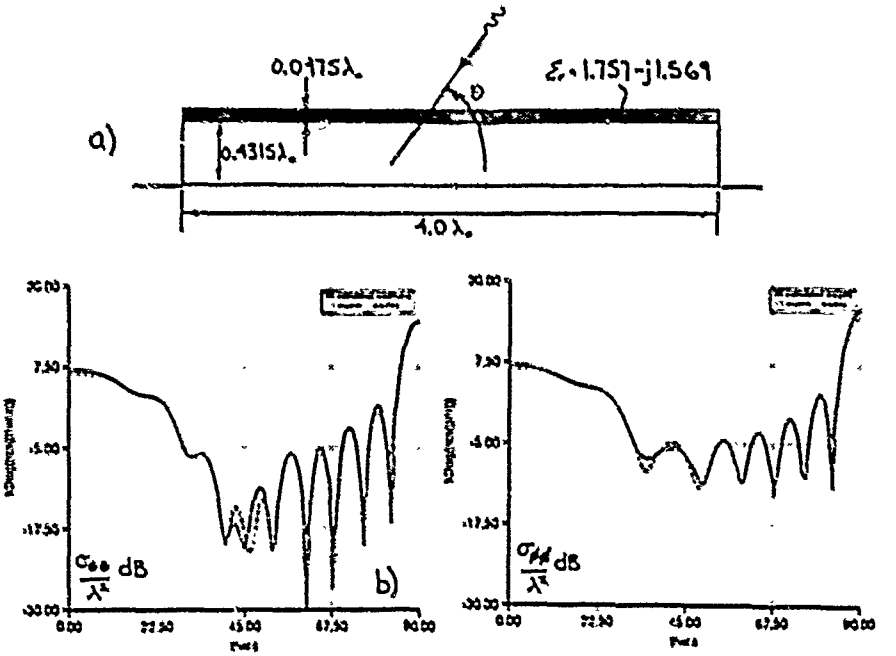


Figure 6: Dielectric coated conducting cylinder ($\epsilon_r = 1.757 - j\,1.569$).

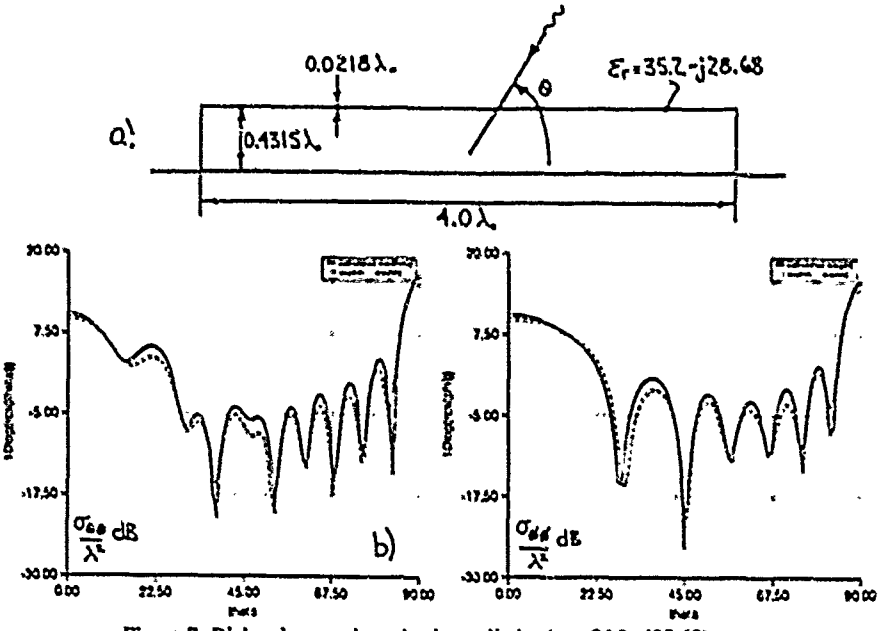


Figure 7: Dielectric coated conducting cylinder ($\epsilon_r = 35.2 - j\,28.68$).

The first geometry considered is that of a sphere tipped conducting cone partially covered with a teflon coating as shown in figures 4a), 5a). The teflon coating ($\epsilon_r = 2.05$) is assumed to be lossless at the chosen operating frequency of *4GHz*. To study the effect of the coating on the radar cross section, two configurations were examined; one case with the tip of the cone coated, and one case with the tip of the cone left uncoated. The numerical results generated using the MBES simulation program utilized the E-PMCHW formulation in all cases and the number of azimuthal modes were chosen as the sum of $n = 0, 1, 2, 3, 4$. Selected experimental and numerical results are shown in figures 4b) and 5b). The figures indicate a good agreement at all angles of incidence, with the largest discrepancies occurring for the $\sigma_{\theta\theta}$ results.

To examine the validity of the simulation code when lossy dielectric materials are considered, the case of a conducting cylinder with its sides coated by a lossy dielectric was studied as shown in figures 6a), 7a). Two different material types and thicknesses were considered; a 6.8mm coating with $\epsilon_r = 1.757 - j1.569$ (Emerson and Cummings Echosorb LF-22), and a 1.5mm coating with $\epsilon_r = 35.2 - j28.68$ (Echosorb VF-60), at the operating frequency of *1.5GHz*. Again the E-PMCHW formulation was used and the number of azimuthal modes chosen as $n = 0, 1, 2, 3, 4$. Selected experimental and numerical results are shown in figures 6b) and 7b). The results show a good agreement for both polarizations, with the best results for the lower loss (thicker dielectric) case. Discrepancies for scattering angles near $0 \rightarrow 0^\circ$ in figure 7 may be due to errors at the interface between the conductor and dielectric regions, as well as the modeling of the cylinder edge.

In many cases, such as when lossy conductors or very lossy dielectric materials are present, an impedance boundary condition (IBC) approach can be utilized to model the scattering structure. The approach greatly simplifies the computational complexity of the problem since the fields inside the dielectric region do not have to be directly solved for. Figure 8a) compares the results of the IBC approach to the experimental results for the coated cylinder case of figure 7. The surface impedance along the side of the cylinder was determined using a transmission line assumption as $Z_{\theta,\theta} = 15.76 + j62.4$. The surface impedance at the perfectly conducting ends was specified as $Z_{\theta,\theta} = 0.0 + j0.0$. There is a large difference between the results except for scattering angles near $\theta = 90^\circ$ (perpendicular to the cylinder). Much of this error may be caused by the modeling of the interface between the lossy and perfectly conducting regions at the conductor edge. To examine this possibility, figure 8b) compares results of the IBC approach to those calculated numerically for the case when the cylinder is *completely* coated by the lossy dielectric (sides plus ends are coated). These results show a large improvement in the validity of the IBC method, even though there are still discrepancies for scattering angles incident at the cylinder edge $\theta = 45^\circ$.

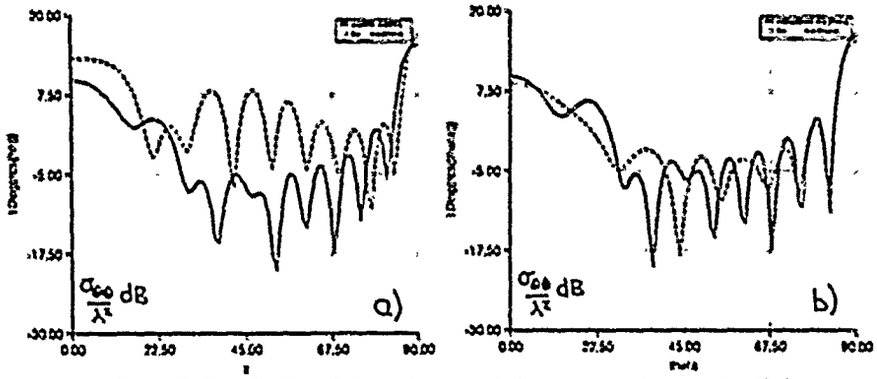


Figure 8: Examination of the IBC approach for a) a partially coated cylinder and b) a completely coated cylinder.

5. CONCLUSIONS

The experimental and numerical results presented showed that the moment method approach was accurate for the analysis of partially coated conducting objects even when the dielectric material was lossy. The impedance boundary condition approach was shown to give fair results when very lossy materials are used, but had difficulty modeling sharp transitions in the impedance along the structure surface.

6. REFERENCES

[1] Mautz, J.R. and Harrington, R.F., "H-field, E-field, and combined field solutions for conducting bodies of revolution," AEU, vol. 32, pp. 157-164, 1978.

[2] Wu, T., and Tsai, L.L., "Scattering from arbitrarily-shape lossy dielectric bodies of revolution," Radio Science, vol. 12, pp. 709-718, 1977.

[3] Mautz, J.R. and Harrington, R.F., "Electromagnetic scattering from a homogeneous material body of revolution," AEU, vol. 33, pp. 71-80, 1979.

[4] Govind, S., Wilton, D.R., and Glisson, A.W., "Scattering from inhomogeneous penetrable bodies of revolution," IEEE Trans. Anten. Prop., vol. AP-32, pp. 1163-1173, 1984.

[5] Hunka, J.F. and Mei, K.K., "Electromagnetic scattering by two bodies of revolutions," Electromagnetics, vol. 1, pp. 329-349, 1981.

[6] Mautz, J.R. and Harrington, R.F., "Boundary formulation for aperture coupling problem," AEU, vol. 34, pp. 377-384, 1980.

[7] Mautz, J.R. and Harrington, R.F., "Electromagnetic coupling to a conducting body of revolution with a homogeneous material region," Electromagnetics, vol. 2, pp. 257-308, 1982.

[8] Kishk, A.A. and Shafai, L., "Different formulations for numerical solution of single or multibodies of revolution with mixed boundary conditions," IEEE Trans. Anten. Prop., vol. AP-34, pp. 666-673, 1986.

[9] Kishk, A.A. and Shafai, L., "Numerical solution of scattering from coated bodies of revolution using different integral equation formulations," Proc. IEE, vol. 133, Pt. H, pp. 227-232, 1986.

[10] Kishk, A.A. and Shafai, L., "Radiation characteristics of the short dielectric rod antenna: a numerical solution," IEEE Trans. Anten. Prop., vol. AP-35, pp. 139-146, 1987.

[11] Shafai, L. and Kishk, A.A., "Phase centre of small primary feeds and its effect on the feed performance," Proc. IEE, vol. 132, Pt. H, pp. 207-214, 1985.

[12] R. Schneider, C. Schneider, D. Burek, G. Bridges, W. Pries, "MBES: Multi-Body Electromagnetic Scattering Package, Users Manual and Technical Documentation," CANCAD Technology Inc., Tech. Rep. CMP86-01, 1987.

Calculation of Admittance of Slots on a Body of Revolution Using the Method of Moments

James R. Rogers
Atlantic Aerospace Electronics Corporation
6404 Ivy Lane, Suite 300
Greenbelt, Maryland 20770-1406

Abstract: Self and mutual admittances of rectangular apertures on a body of revolution (BOR) are calculated using different surface integral equation formulations, solved by the method of moments. The CFIE, CSIE and pseudo-image/CSIE formulations are compared as to their abilities to accurately calculate admittance. For self admittance, and admittance of closely-spaced slots, the pseudo-image formulation proved most accurate.

1.0 Introduction

Radiation and scattering solutions involving slots (apertures) on a general body can be formulated using a network approach (Harrington, 1976). The region outside the apertures is electrically isolated from the region inside by covering each aperture with an unknown magnetic current backed by a perfect conductor. The boundary condition on tangential magnetic field through the aperture leads to an operator equation for the ultimate solution for the magnetic current. A key part of this formulation is the calculation of admittances between the basis functions of the unknown magnetic currents as they radiate into either electrically-isolated region. Accuracy in the admittances, especially in the self-admittances, is very important in obtaining a meaningful solution for the unknown aperture magnetic currents.

This paper investigates the calculation of admittance between aperture magnetic currents (m) on a body of revolution (BOR). Our general approach to the calculation of admittance is as follows. Because the generality of the BOR does not allow an analytical (separable) solution, we use surface integral equations to formulate either a scattering problem (m is a known source) or an aperture radiation problem ($E = n \times m$ is a known boundary condition). The method of moments is then used to accomplish the calculation of admittance. The focus of this paper is to compare admittances calculated with the following different integral equation formulations:

(1) combined-field integral equation (CFIE) (Mautz, 1977),
(2) combined-source integral equation (CSIE) (Mautz, 1979), and
(3) pseudo-image/combined-source integral equation (PI/CSIE) (Harrington, 1985).

Section 2.0 will describe the geometry of the problem considered in this paper and Section 3.0 will define each of the above integral equation formulations as to how they are used for the calculation of admittance. Numerical results are presented in Section 4.0.

By the discussion of the formulations and the numerical results, we hope to demonstrate the following main points. The CFIE and CSIE formulations, as defined here, produce identical results for admittance and have identical mathematical complexity in their solutions. Thus, there is no inherent advantage of one versus the other. The pseudo-image formulation is more complex since it requires an additional numerical integration of a separate operator. All three formulations were equivalently accurate for mutual admittance of widely-spaced slots. However, the pseudo-image/CSIE formulation produces superior results for self admittance and mutual admittance of closely-spaced slots, both in terms of accuracy and in solution convergence behavior. These conclusions about the pseudo-image formulation are consistent with those discussed previously by Harrington (1985).

2.0 Geometry and Formula for Admittance

Figure 1 illustrates the basic geometry of the slot/BOR problem, considered for the results of this paper. The slot magnetic currents reside on a perfectly-conducting BOR surface which is defined by an arbitrary generating contour. All solutions are time harmonic ($e^{j\omega t}$ dependence).

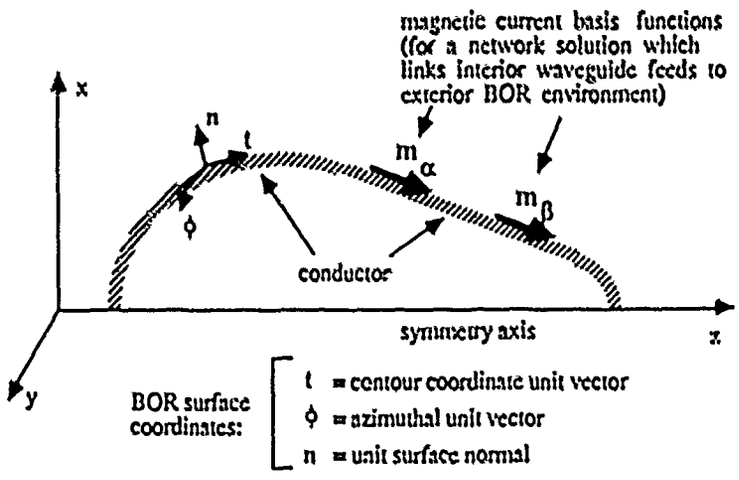


Figure 1. Aperture magnetic currents on a conducting BOR.

Figure 2 illustrates the definition of a conformal slot aperture on a BOR surface. The apertures are defined in a plane and then the points are projected down along lines parallel to the unit normal at the BOR slot location. Slot basis functions are also defined in the plane and projected down onto the BOR surface.

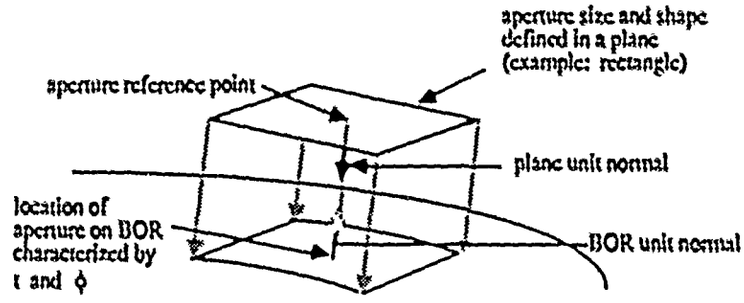


Figure 2. Definition of a rectangular aperture on a surface of revolution.

Let m_α and m_β be two different (or the same) known magnetic currents on the BOR surface. The admittance can be expressed as a reaction integral:

$$Y^r_{\alpha\beta} = -\langle m_\alpha, H^r(m_\beta)\rangle \qquad (1)$$

where $\langle a,b\rangle$ denotes the surface integral of $a\cdot b$, and $H^r(m_\beta)$ denotes the H-field operator for m_β radiating into region r in the presence of its boundaries and materials. Thus, for our problem, region r represents the entire region outside the BOR conducting body. Our choice of m is related to the normal mode electric field, E, of a waveguide having the same shape as the aperture by $m = E \times n$, where n is the outward unit surface normal.

3.0 Surface Integral Equation Formulations for Slot Admittance Calculation

In this section we briefly describe the three surface-integral-equation approaches which will be compared for their calculation of admittance. Figure 3 illustrates the formulations considered in this paper in terms of the equivalence principle. In each case illustrated in Fig. 3, the inhomogeneous scattering problem is cast in terms of an equivalent problem having known (m_β and/or m_β^{im}) and unknown (J,M) sources radiating into an infinite, homogeneous medium.

Note that J and/or M in each formulation is different from those of the others.

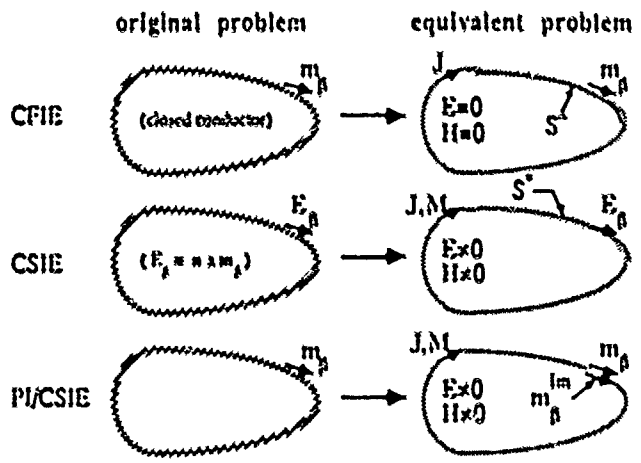


Figure 3. Formulations in terms of the equivalence principle.

Table 1, below, summarizes the boundary conditions, equivalent currents and sources for the three integral equation formulations used in this paper to calculate admittance.

Table 1. Three boundary-condition formulations for the admittance problem.

	formulation, type source	boundary condition (on total fields)	equivalent currents (electric,magnetic)
CFIE	scattering m_β	$[1-\zeta]E_{tan} + \zeta\eta\, n \times H = 0$ on S^-	$(J,0)$
CSIE	aperture radiation $E_\beta = n \times m_\beta$	$E_{tan} = E_\beta$ on S^+	$([1-\zeta]J, \zeta\eta\, n \times J)$
PI/CSIE	scattering m_β	$E_{tan} = 0$ on S^+	$([1-\zeta]J, \zeta\eta\, n \times J) + (0, m_\beta^{im})$

ζ = scalar weighting coefficient

η = wave impedance of homogeneous medium outside conductor

As defined in Table 1, the CSIE and CFIE operators are adjoints of each other (Hewitt, 1984 and Mautz, 1979). The CFIE is the typically-used null-field formulation which, for perfect conductors, uses only an equivalent electric source (J) to formulate the integral equation. Boundary conditions on a combination of electric (E) and magnetic (H) fields are enforced just inside the conducting surface (outside the region of interest for field evaluation), denoted as S^-. Here, we define the weighting coefficient ζ such that it is varied from 0 (EFIE) to 1 (MFIE). The CSIE uses a combination of equivalent electric and magnetic (M) sources with the boundary condition on E being enforced just outside the conductor (just inside the region for field evaluation), denoted as S^+. Again, we define the weighting coefficient ζ such that it is varied from 0 (ESIE) to 1 (MSIE). The CSIE can be used as either a scattering formulation (m is a known source) or an aperture radiation formulation ($E = n \times m$ is a known boundary condition). For this paper, we use the aperture radiation formulation for calculation of admittance, except when a pseudo-image is used as part of the CSIE equivalent-current set.

The pseudo-image/CSIE (PI/CSIE) is a variation of the CSIE. The pseudo-image (denoted as m^{im}) is a magnetic current identical to the source magnetic current, and is placed just on the other side of the conducting surface upon which the source resides (Harrington, 1985). m^{im} is part of the equivalent current set of the BOR problem, the remaining part being the unknown BOR equivalent currents that are solved for using the method-of-moments. Since m^{im} is known, it forms part of the source vector in the operator equation. Thus the PI/CSIE operator is the same as the CSIE operator.

We can now specialize our formula for admittance (Eq. 1) in terms of the equivalent currents of the above described integral equation formulations:

$$\text{CFIE} \qquad Y^r_{\alpha\beta} = - < m_\alpha , J \times n > \qquad (2a)$$

$$\text{CSIE} \qquad Y^r_{\alpha\beta} = - < m_\alpha , H(J,M) > \qquad (2b)$$

$$\text{PI/CSIE} \qquad Y^r_{\alpha\beta} = - < m_\alpha , H(J,M) > - < m_\alpha , H(m_\beta , m^{im}_\beta) > \qquad (2c)$$

where the H() operators are infinite-medium operators. Again note that J and/or M in each of the above formulations are different from each other. To evaluate admittance in Eqs. 2, the method of moments is used to obtain an approximate solution for the unknown equivalent currents, (J,M). For our BOR solutions, we use refined versions of the Mautz (1977) codes.

Some comments about Eqs. 2 are in order. The CFIE (Eq. 2a) appears to be the simplest formulation since one directly tests the equivalent electric current while in the CSIE (Eq. 2b), the testing vectors are determined from integral operators on the equivalent currents. However, since the source vectors to the CFIE are adjoints of the CSIE testing vectors and the source vectors to the CSIE are adjoints of the CFIE testing vectors, the two formulations actually have identical computational complexity for the calculation of admittance. Owing to the adjoint relationship of the operators and that the same moment-method matrix operators are used to construct each solution, we expect that the CFIE and CSIE formulations should give identical results for calculated admittances. This does indeed turn out to be the case.

The formula for admittance using the PI/CSIE formulation (Eq. 2c) is fundamentally different from the other two. The admittance is the sum of two parts, one part being calculated from the method-of-moments-derived equivalent currents (J,M) and the other part being due to m and m^{im} radiating into infinite medium. This latter part is a direct numerical integration which is inherently more accurate than the moment-method-derived equivalent currents. Generally, the slots are placed on a smooth, convex surface having radii of curvature large compared to the slot dimensions. When the radii of curvature become larger and larger, the source vector to the PI/CSIE moment-method problem (due to m and m^{im}) gets smaller and smaller. This tends to allow the second term of the right-hand side of Eq. 2c to dominate the solution. Eventually, as the radii of curvature approach infinity, the complete solution for admittance is given by the second term on the right-hand side of 2c which reduces to the infinite-ground-plane formula.

One can now see why the pseudo-image formulation is expected to give superior results for self admittance and admittance of closely-spaced slots over either the CFIE or CSIE formulations. Moment-method-derived equivalent currents have their own inherent degree of accuracy which is complicated by testing in the near-field of the source excitation. This is especially true for calculating slot self-admittance. m^{im} removes the singular nature of the near-fields due to m , the true source to the moment-method problem. Thus, when the slot "sees" a locally flat or nearly-flat surface, the direct numerical integration part of admittance will dominate the solution, improving accuracy.

4.0 Numerical Results

In this section we present numerical results for admittance of rectangular slots on a conducting BOR. We will compare the CSIE (aperture radiation formulation) to the PI/CSIE (scattering formulation). When viewing the results, keep in mind that the CPIE results are always identical to the CSIE results when the weighting coefficients and moment-method parameters are chosen to be the same. In one of the examples, a short table is included which demonstrates this point.

The following geometries are considered:

1. rectangular slots on a "simulated cylinder" - a section of a conducting cylinder with large-radius spherical end caps.
2. rectangular slots on a "simulated ground plane" - a flat, thick, circular disk with a large-radius (1-wavelength) end termination.

The above-described geometries are chosen for two reasons. First, there are many solutions for admittance of slots on conducting cylinders, both of large and relatively small radii of curvature and for slots on an infinite ground plane. Thus these geometries allow independent comparisons for our moment-method-derived admittances. Secondly, it will be shown that the solution behavior of the two cases, when using the BOR CSIE to calculate admittance, is strikingly different -- the admittance solutions for slots on a cylinder will be shown to be much less sensitive than for slots on the flat part of the simulated ground plane.

The magnetic current basis and testing function, m, for all numerical examples is that associated with the TE_{10} normal-mode E-field of a rectangular waveguide having the same shape as the slot. $m = n \times E$, where n is the outward unit surface normal. The m's satisfy the normalization:

$$\int_{slot} m_\alpha \cdot m_\beta \, da = \delta_{\alpha\beta} \tag{3}$$

Although our computer codes have been written to allow multiple normal modes in each slot, it has not been investigated as to whether this method-of-moments approach to calculating admittance is practical for the higher-order modes. It probably is not, due to the rapid spatial variation of the higher-order modes.

The geometry of the simulated cylinder is indicated below in Figure 4. The end cap terminations are greater than 1 wavelength from any slot.

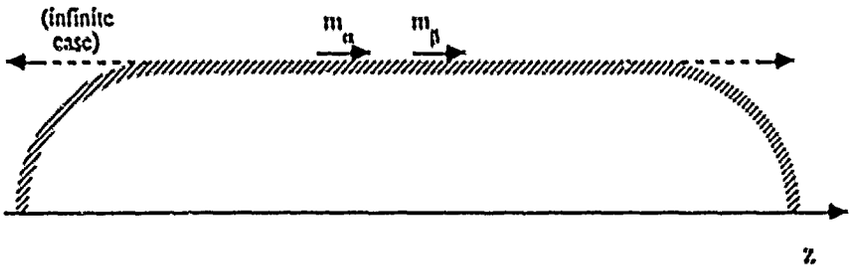


Figure 4. Geometry of the "simulated cylinder".

Figure 5 compares mutual admittance solutions of our integral equation formulations to an exact modal solution for an infinite cylinder from the Conformal Array Handbook (1981). The dashed line indicates the modal solution and the dots represent either the CSIE or the PI/CSIE which, for this example, always agreed to within 1% of each other when the ζ, the moment-method segmentation and number of Fourier modes used in each solution was the same (ζ=0.5, 10 triangles/λ and 20 Fourier modes for Fig. 5). For this geometry, the solutions were not particularly sensitive to ζ -- any value from 0 to 1 gave results within a couple percent of each other (although using values associated with the ESIE and MSIE are risky for large bodies since spurious interior resonances can contaminate the solutions). For our applications, the accuracy indicated in Fig. 5 is adequate for mutual admittances. Thus, there is no advantage of the PI/CSIE formulation for this case and the extra complications in the formulation actually make it a disadvantage.

Figure 6 compares PI/CSIE solutions (calculated with 10 triangles/wavelength, ζ=0.9) for self-admittance to published data (Bird, 1988) for a rectangular slot on a cylinder oriented at various angles with respect to the cylinder axis. The dots represent the published data, which were picked off the curves of the paper. Generally the results compare very well and the minor variations could be due to a number of reasons, such as: (1) differences in the definition of the slot on the conformal surface, (2) a slight effect of the simulated cylinder end cap, or (3) approximations in the published data due to the use of GTD for the solutions.

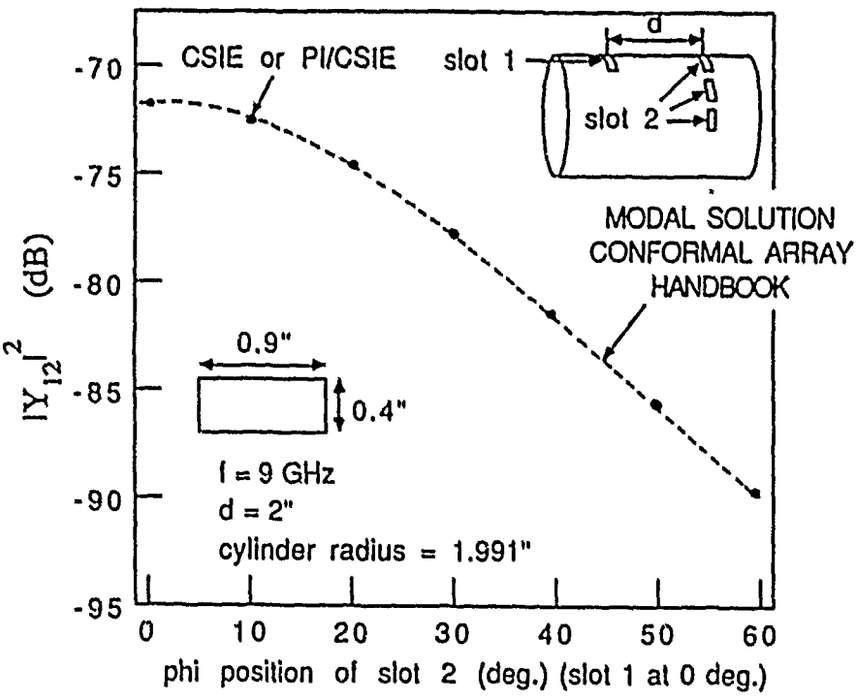


Figure 5. Mutual admittance of widely-spaced rectangular slots on cylinder: Comparison of moment method solutions to cylinder modal solution.

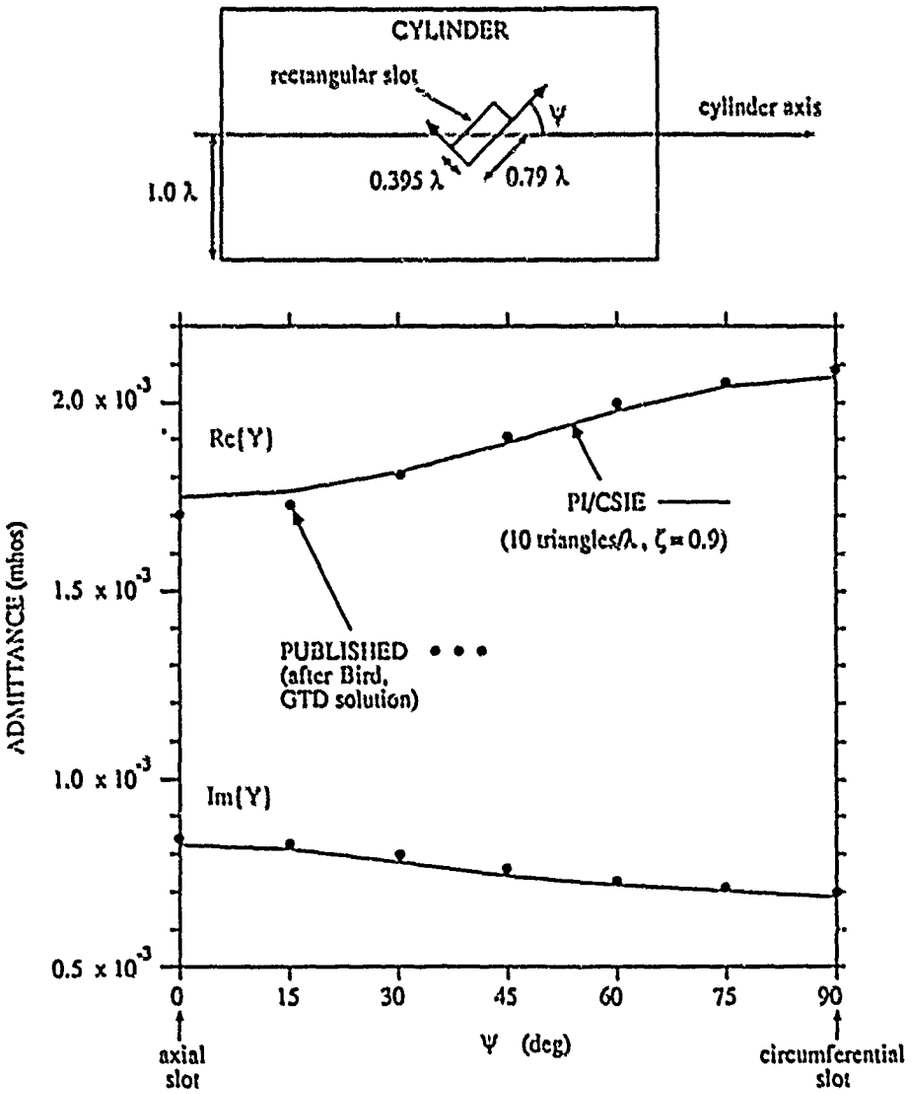


Figure 6. Comparison of PI/CSIE solutions to published data for self admittance of rectangular slot on cylinder.

Table 2, below, lists results from the two formulations for a longitudinal slot and a circumferential slot on a cylinder (same geometry as in Figure 6). Also included are results from the PI/CSIE formulation. All calculations used 10 triangles per wavelength and 21 Fourier modes (more than enough Fourier modes needed for convergence).

Table 2. Self Admittance (Y) of Rectangular Slot on Cylinder, Calculated Using Different Formulations

slot length = 0.79 slot width = 0.395
wavelength = 1.0 cylinder radius = 1.0

ζ	CFIE		CSIE		PI/CSIE	
	Re(Y)	Im(Y)	Re(Y)	Im(Y)	Re(Y)	Im(Y)
			(axial slot)			
0.0	.1734E-02	.8329E-03	.1734E-02	.8329E-03	.1748E-02	.8302E-03
0.5	.1759E-02	.8191E-03	.1759E-02	.8191E-03	.1739E-02	.8203E-03
0.9	.1749E-02	.7980E-03	.1749E-02	.7980E-03	.1746E-02	.8230E-03
1.0	.1750E-02	.8025E-03	.1750E-02	.8025E-03	.1749E-02	.8313E-03
			(circumferential slot)			
0.0	.2055E-02	.7252E-03	.2055E-02	.7252E-03	.2087E-02	.7012E-03
0.5	.2087E-02	.7099E-03	.2087E-02	.7099E-03	.2054E-02	.6959E-03
0.9	.2076E-02	.6825E-03	.2076E-02	.6825E-03	.2068E-02	.6880E-03
1.0	.2076E-02	.6828E-03	.2076E-02	.6828E-03	.2073E-02	.6938E-03

The data above demonstrate earlier assertions that the CFIE and CSIE give identical results for admittance, when ζ and other parameters (such as moment-method segmentation) are the same. This occurred for all cases compared. Also, the PI/CSIE results exhibit smaller variations with ζ, especially in the reactive part of admittance. This is probably a consequence of faster convergence of solution, as will be demonstrated in the next two figures.

Relative to the PI/CSIE results of Fig. 6, convergence of the moment-method solutions is examined in Figures 7 and 8. In Fig. 7, the number of triangles per wavelength is varied from 2 to 10 and the average percent deviation from the converged solution is plotted (seven slot tilt angles from 0 to 90 degrees was used for this average). The convergence behavior of the PI/CSIE is seen to be superior to the CSIE, especially in the reactive part of admittance.

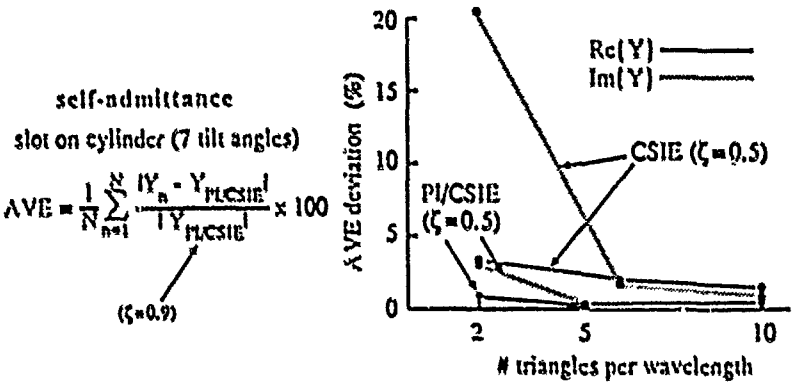


Figure 7. Convergence with increasing triangle functions

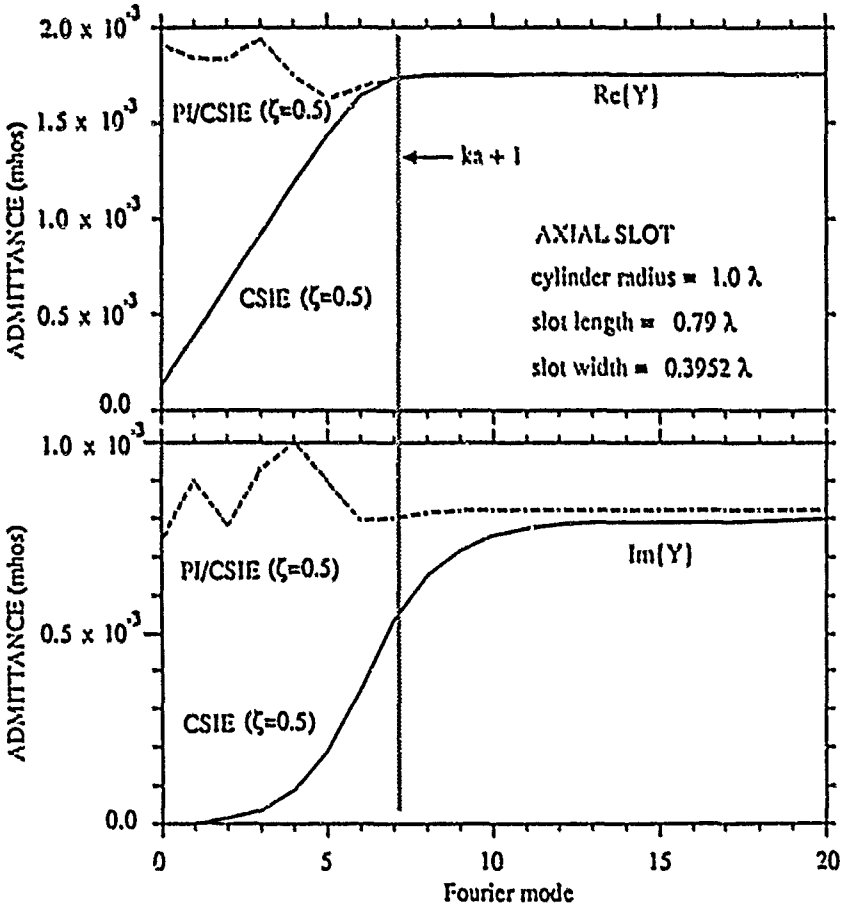


Figure 8. Convergence with increasing Fourier mode

In Fig. 8, the real part of admittance in both solutions converges after the ka+1st Fourier mode -- which is similar to convergence behavior for planewave scattering from a BOR. The convergence behavior for the reactive part of self admittance is very different for the two solutions. The PI/CSIE solution appears to converge at nearly the same rate as in the real part of admittance while the CSIE solution is much slower to converge. This behavior represents a very big computational advantage for using the PI/CSIE formulation; i.e., limiting the number of Fourier modes needed in the solution.

Figure 9 illustrates the geometry for slots on the simulated ground plane. The slots are located on the flat portion of the circular disk and the termination of the disk is smooth, minimizing effects of scattering off the edge of the disk in the solutions.

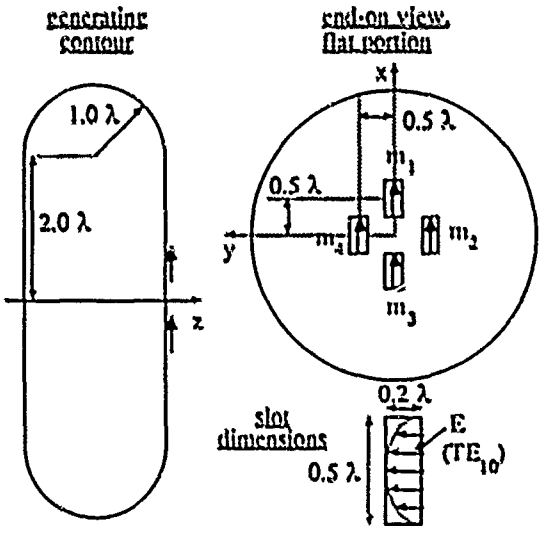


Figure 9. Geometry for slots on simulated ground plane.

Table 3 on the next page compares the PI/CSIE and CSIE results to the infinite ground plane solution (Rogers, 1988). As expected, the PI/CSIE results compare quite well, especially for self admittance. The very small deviations are those that might be expected due to scattering off the rounded edges of the disk. Since the PI/CSIE solutions converged very fast and were very stable, those deviations indicated are probably the real influences of the disk termination. The CSIE result for self admittance, however, is not particularly close to the infinite ground plane solution. Figure 10 shows that the solution using 10 triangles/wavelength is not converged.

Table 3. Comparison of PI/CSIE and CSIE solutions to Infinite Ground Plane Solution for Admittances of Slots on the Simulated Ground Plane of Figure 9.

	Infinite ground plane		PI/CSIE (10 tri./λ, ζ=0.5)		CSIE (10 tri./λ, ζ=0.5)	
	Re{Y}	Im{Y}	Re{Y}	Im{Y}	Re{Y}	Im{Y}
$Y_{11} \times 10^4$	7.809	2.175	7.810	2.176	8.355	2.559
$Y_{12} \times 10^4$	-1.162	-0.794	-1.155	-0.795	-1.139	-0.795
$Y_{13} \times 10^4$	-0.463	-0.058	-0.477	-0.051	-0.479	-0.061
$Y_{24} \times 10^4$	0.335	1.787	0.319	1.788	0.305	1.780

Figures 10 and 11 demonstrate the strong sensitivity of the CSIE solutions for self admittance to changes in moment-method segmentation and/or ζ. The PI/CSIE solutions, in contrast, exhibit very little sensitivity. The simulated ground plane (a flat portion of a BOR) is and ideal case for the PI/CSIE. The slow convergence and and high sensitivity to ζ of the CSIE solutions indicates that it is unsuitable for geometries such as that in Fig. 9. The mutual admittance results of the CSIE (not shown in the figures) also exhibited slower convergence and greater sensitivity to ζ than the PI/CSIE solutions.

5.0 Summary

This paper has investigated the calculation of admittances of slots on a body of revolution using surface integral equations, which are solved by the method of moments. Three formulations were compared: (1) combined-field integral equation (CFIE), (2) combined-source integral equation (CSIE), and (3) pseudo-image/combined-source integral equation (PI/CSIE).

The discussion of the formulations and the numerical results demonstrate that the CFIE and CSIE formulations are equivalent, both in terms of computational complexity and in terms of their solutions. For mutual admittance of widely-spaced slots, these two formulations appear adequate. For self admittance and mutual admittance of closely-spaced slots, the PI/CSIE formulation is superior, both in terms of accuracy of the solutions and in terms of convergence behavior. Because of the improved solution convergence behavior for self admittance, we found the PI/CSIE solution to be faster in total computational time even though it included an additional numerical integration that the CSIE or CFIE do not require.

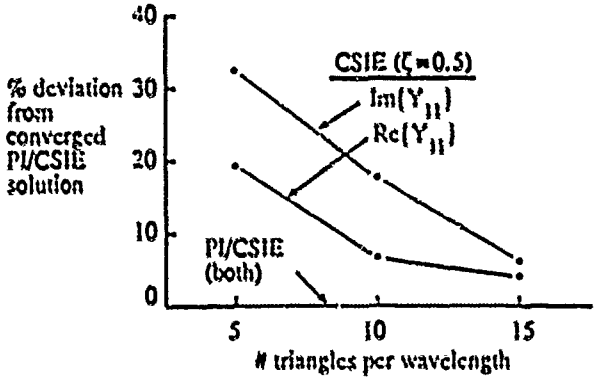


Figure 10. Convergence of solutions with increasing moment-method segmentation (self admittance, slot 1 on disk of Fig. 9)

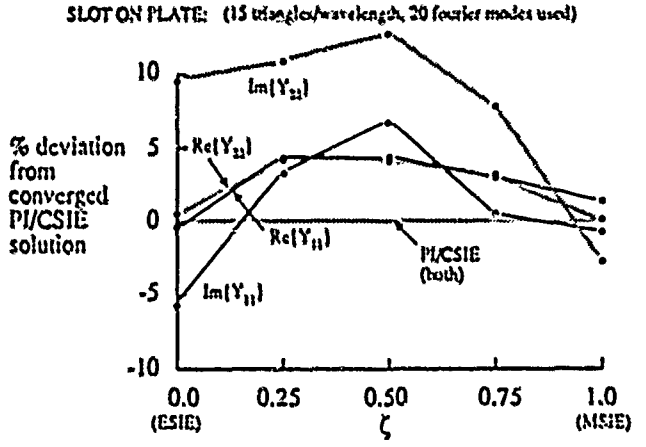


Figure 11. Sensitivity of CSIE solutions to choice of weighting coefficient (self admittance, slots 1 and 2 on disk of Figure 9)

References

1. Bird, T.S., "Admittance of Rectangular Waveguide Radiating from a Conducting Cylinder" IEEE Transaction on Antennas and Propagation 36(9), 1217, September, 1988.

2. Hansen, R.C., ed., Conformal Array Handbook, 1981.

3. Harrington, R. F., "Admittance of Apertures in Bodies of Finite Extent", paper B-15-3, 1985 North American Radio Science Meeting, Vancouver, Canada, June 17-21, 1985.

4. Harrington, R. F., and J. R. Mautz," A Generalized Network Formulation for Aperture Problems", IEEE Transactions on Antennas and Propagation, November, 1976.

5. Heath, G. E. "Impedance Boundary Condition Integral Equations", 1984 IEEE AP-S International Symposium, paper APS-18-2, Boston, Massachusetts, June 25-29, 1984.

6. Mautz, J. R. and R. F. Harrington, "H-Field, E-Field, and Combined Field Solutions for Bodies of Revolution", Department of Electrical and Computer Engineering, Technical Report TR-77-2, Syracuse University, Syracuse, New York, 13210, February 1977.

7. Mautz, J. R. and R. F. Harrington, "H-Field, E-Field, and Combined Field Solutions for Conducting Bodies of Revolution", AEU (Germany), 32 (1), 157, 1978.

8. Mautz, J. R. and R. F. Harrington, "A Combined-Source Solution for Radiation and Scattering from a Perfectly Conducting Body", IEEE Trans. on Antennas and Propagation, AP-27 (4), 445, July, 1979.

9. Rogers, J. R., et.al., "Rigorous Analysis of Slot Antenna Arrays Using the Network Approach", The Antenna Development Group Report, Atlantic Aerospace Electronics Corp., May 1988.

SESSION 5 - "VALIDATION"

Chairman: J W Williams

VALIDATION OF A MOMENT METHOD CODE

ELIZABETH YIP

EDWARD SABATKA

Boeing Advanced Systems,

P.O. Box 3707, M.S. 4C-01,

Seattle, Wa. 98124-2207

We are beta-testing a 2D moment method code called RAMZ. Our experience leads us to establish a list of basic tasks which we think are necessary in the beta-testing of any moment method codes in electromagnetic scattering. These tasks usually reveal subtle and unexpected weaknesses either in the code, the documentation, or the code developer's assumptions. These tasks also infer a set of guide lines for the usage of the code. We shall report on our experience with RAMZ.

The purpose of this paper is to illustrate a procedure of testing a moment method code. Before a package of software is released for usage, two sets of standard tests are performed. These two sets are termed α-tests and β-tests. α-tests are performed by the code developers to ensure the code is "bug-free"; β-tests are performed by potential users of the code to determine the code's usefulness, its ease of use, and whether the code does everything the developers intended. A code's usefulness and ease of use are largely determined by the need and background of the majority of the users. We do not discuss these two matters in this paper. Instead, we shall present our experience in the validation and determination of accuracy of the developer's assumptions of RAMZ, a 2 dimensional (2D) moment method code in the "public domain".

RAMZ is a modified version of RAMVS which was written by Liepa, Knott and Senior [2] in 1974. Yip [4] corrected some minor errors, changed the input/output and renamed the program RAMZ. The program computes the far field scattering pattern of a 2D cylindrical body (or bodies) treated with absorbing materials. The program admits two types of profiles: closed body surfaces, which an impedance boundary condition is imposed, and open resistive sheets, which may consist of several disjoint parts. Closed body surfaces have one variable per cell, namely, the surface current. Open resistive sheets have two variables per cell, namely, the equivalent electric and magnetic currents. Although all bodies with closed surfaces can be modeled with open resistive sheets, it is more efficient to use the closed surface models. However, Knott and Senior [1] warned that solution of the closed surface model will deteriorate as the thickness of the body decreased with its length.

The purpose of the tests reported in this paper are two fold: to validate the code with measured and known data and to "stretch" some of the code developers' assumptions as "far" as possible. We will limit our tests to perfectly conducting bodies. These tests answer the following questions:

1. How does RAMZ output compare with measured and analytical data?
2. How does the quality of the solution deteriorate as we decrease the thickness of closed body in comparison with its length?
3. How does the code handle decreasing gaps between disjoint open re-

sistive sheets and closed surfaces?

To demonstrate the consistency and accuracy of the code, a comparative study between analysis, experimental results, and known solutions are illustrated in figures 4 through 7. In these figures, RAMZ's results are compared with an exact analytical solution of the bistatic RCS of a circular cylinder as well as experimental backscattering RCS of an ogival cylinder (See Figure 1 for geometry description). Both the closed surface and the open sheet models are used in this set of tests and the computed answers of both models are in exact agreement with one another.

Figure 4 is a plot comparing Richmond's solution [3] (the solid curve) and the moment method results of RAMZ (the square symbol) for a circular cylinder. Take note that the minimums and the maximums occur at precisely equal aspects and magnitudes for both polarizations. The maximum backscattering of a circular cylinder is equal to:

$$\sigma = \pi n$$

where, n , is the radius in wavelengths. The RCS for our circular cylinder is calculated as 5 dB and is equal to the magnitude values at 0 degrees.

Figures 5 through 7 are backscattering comparisons of an ogival cylinder between RAMZ and experimental data (the darker lines) at frequencies of 8, 10, and 16 GHz. The dimensions are specified as 10" (the major axis) by 1.25" (the minor axis) with a length of 30". The high frequency conversion factor from three to two dimensional RCS is calculated to be 0.65 dB and is neglected . The RAMZ model consists of a perfectly conducting closed surface with segmentation resolution of 1/20 th of a wavelength at 18 GHz.

In Figures 5 through 7 there is excellent agreement for the E-polarization case , the incident electric vector field parallel to the cylindrical axis. Also, the edge-on RCS at both 0 and 180 degrees are independent of frequency as expected. For the H-polarization case, the electric vector field perpendicular to the cylindrical axis, differences between experimental and RAMZ data at aspect angles from 0 and 45 degrees are small (± 3.0 dB). The RCS at these angles represent positions where surface traveling wave and edge diffraction mechanisms dominate and is very important for some applications. Note that the moment method solution represents the total RCS

and not individual scattering mechanisms. The plots indicate that large variations in magnitude throughout the pattern match well between measured and calculated data. Futhermore, the RAMZ signatures are evenly symmetric as expected for our geometry.

Our next set of tests evaluate the limitation of the closed surface model. Figures 8 through 13 are RAMZ plots of various rectangular strips, which we first modeled as closed surfaces then as resistive sheets, with various thicknesses. The length of the strips are all 6 wavelengths long and the thicknesses are 1/10, 1/15, 1/20, 1/25 wavelengths.

From figures 9 and 11, it is clear that the H-polarization results are independent of thickness when the geometry is modeled as a closed surface. Note that for values beyond 63 degrees in azimuth, the closed surface RCS converge to that of the open sheet (each side of the rectangular strip is one open sheet). In figures 8 and 10, the open sheet modeling requires only one impedance input specification whereas the closed surface model requires two. The curves for the open sheet model RCS tend toward that of the infinitely thin strip as expected. The absolute minimum near 0 degrees increases as the edge thicknesses decreases. For the E-polarization case of figures 12 and 13, the closed surface model solutions are also independent of thickness. The diffraction levels are slightly higher for greater thicknesses for the open sheets.

The third set of tests are examples of RAMZ backscattering data at 8 GHz of the 10" by 1.25" ogival cylinder with various gap sizes located at the edge discontinuity. The RCS pattern of these ogives are illustrated in figures 14, 15 and 16. Because the small gap forms two edges, it is interesting to compare the changes in diffraction levels and patterns between gap sizes.

Figure 16 is a plot comparison between various gaps for the E-polarization case. The Figure indicates an increase in RCS for greater gap sizes from aspects between 0 to 45 degrees. An increase in diffraction levels at 0 and 180 degrees is consistent with greater gaps for the H-polarization case in figures 14 and 15. Our interpretation for the closed surface ogive with various gaps are as follows:

1. The gaped ogival patterns tend toward the no gap case as gap size decreases.

2. The diffraction levels at 0 degrees increase as gap sizes increase.

3. Most of the incident energy is either trapped inside or guided through the gap at aspects near 0 degrees.

4. There exists a cut off gap size where energy no longer propagate through the gap to the trailing side.

5. The over prediction of the 1/50 th gap size to the no gap case is due to the fact the size is less than the cutoff gap size, therefore no energy propagates through the gap. However, there is reradiated power backscattered from the exposed corner and the flat surface due to the geometry.

The β–tests revealed interesting results in RAMZ's calculations. Besides code evaluation, they provided us an insight into interpreting electromagnetic scattering behavior. These three sets of tests allow us to draw the following conclusions:

1. The first set of tests indicates that the computed data of RAMZ are in excellent agreement with measured data.

2. From the ogive data on our first set of tests, the closed surface model can be used to model closed bodies with aspect ratio (which we define as thickness over length) about 1/10. The second set of tests indicates that the closed surface model breaks down for closed bodies with aspect ratio less than or equal to 1/60.

3. The third set of tests indicates that RAMZ is able to detect the existence of gaps as small as 1/50 wavelength between disjoint resistive sheets and closed surfaces.

The tests reported in this paper validates the code and provides quantitative guide lines regarding the code developers' assumptions. These guide lines would be included in our user manual.

References

[1] E.F. Knott and T.B.A. Senior, *Non-Specular Radar Cross Section Study*, Technical Report AFAL-TR-73-422, University of Michigan, January, 1974.

[2] V.V. Liepa, E.F, Knott and T.B.A. Senior, *Scattering from Two-Dimensional Bodies with Absorber Sheets*, Technical Report AFAL-TR-74-119, University of Michigan, May, 1974.

[3] J.H. Richmond, *Efficient Recursive Solutions for Plane and Cylindrical Multilayers*, Report No. 1968-1, Ohio State University, August, 1965.

[4] E.L. Yip *Final Report: Non-metallic Radar Cross Section Analysis, Vol. 2 - Computer Program Specification*, Document No. D180-31151-2, The Boeing Company, July, 1988

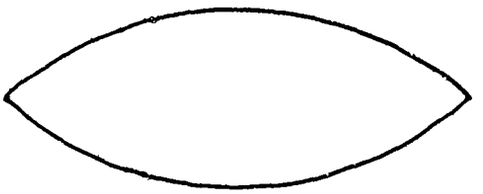


Fig. 1 Geometry of Ogive

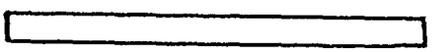


Fig. 2 Geometry of Rectangular Slab

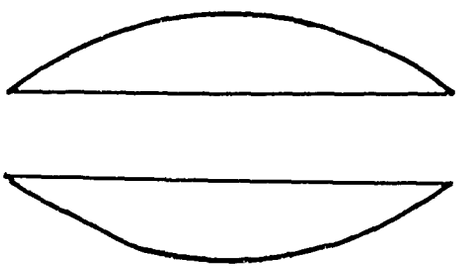


Fig. 3 Geometry of "Ogive" with Gaps

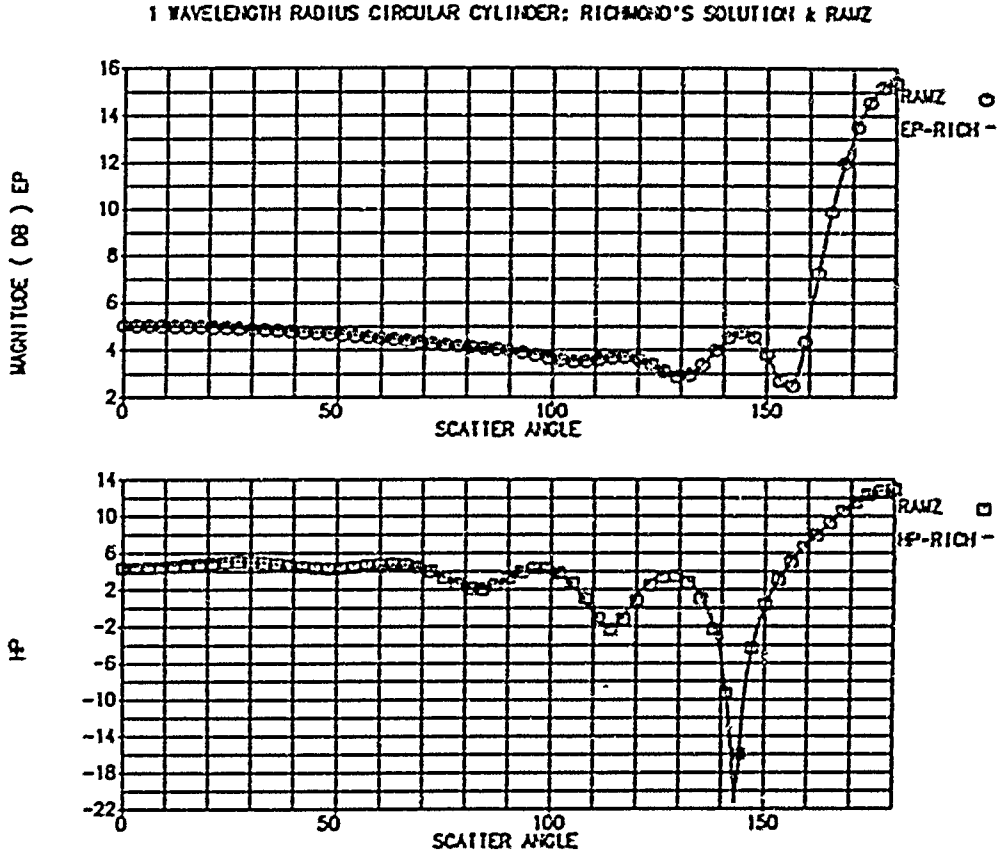
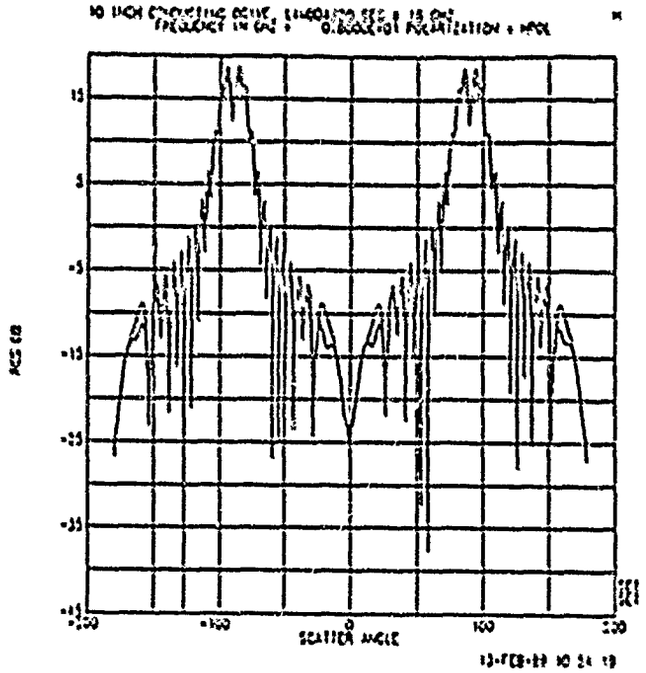


Fig. 4 1 λ Radius Circular Cylinder: Richmond v/s RAMZ



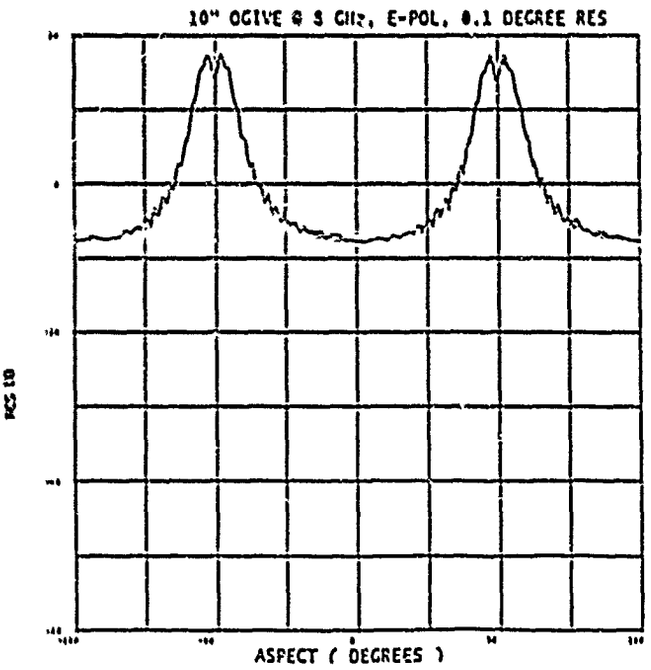
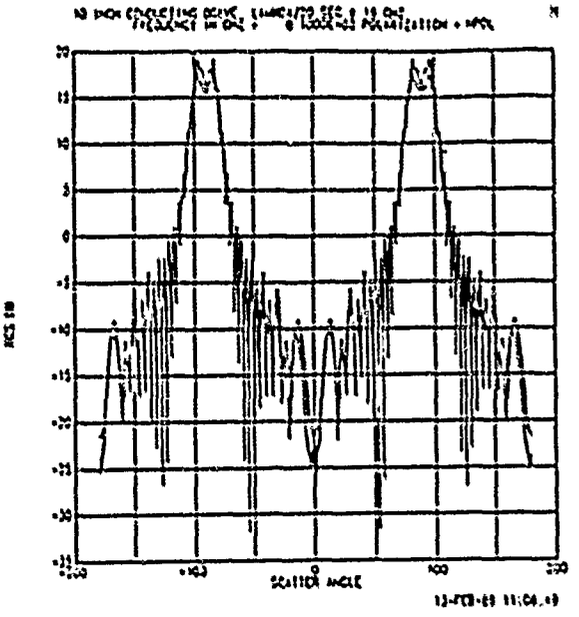


Fig. 5 10 in. Ogive at 8 GHz: Measurement v/s RAMZ



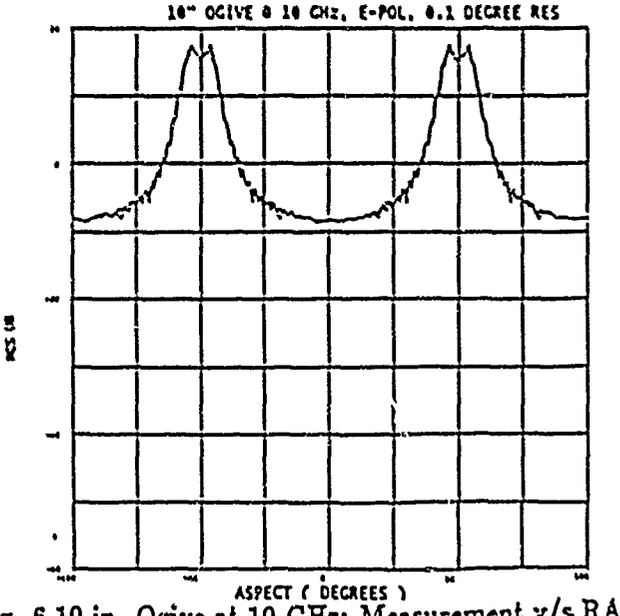
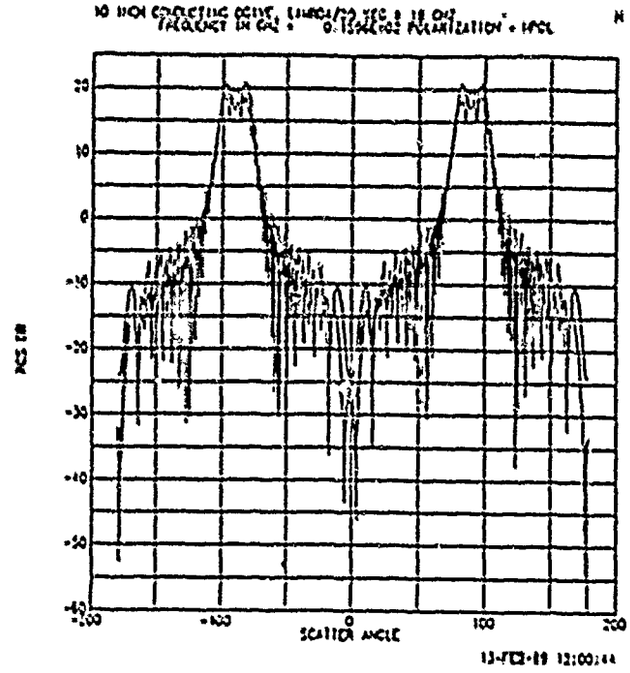


Fig. 6 10 in. Ogive at 10 GHz: Measurement v/s RAMZ



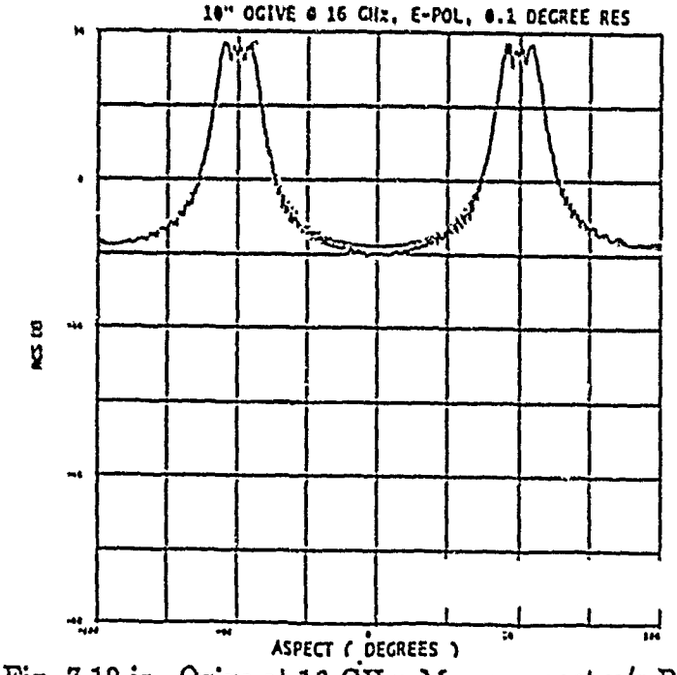


Fig. 7 10 in. Ogive at 16 GHz: Measurement v/s RAMZ

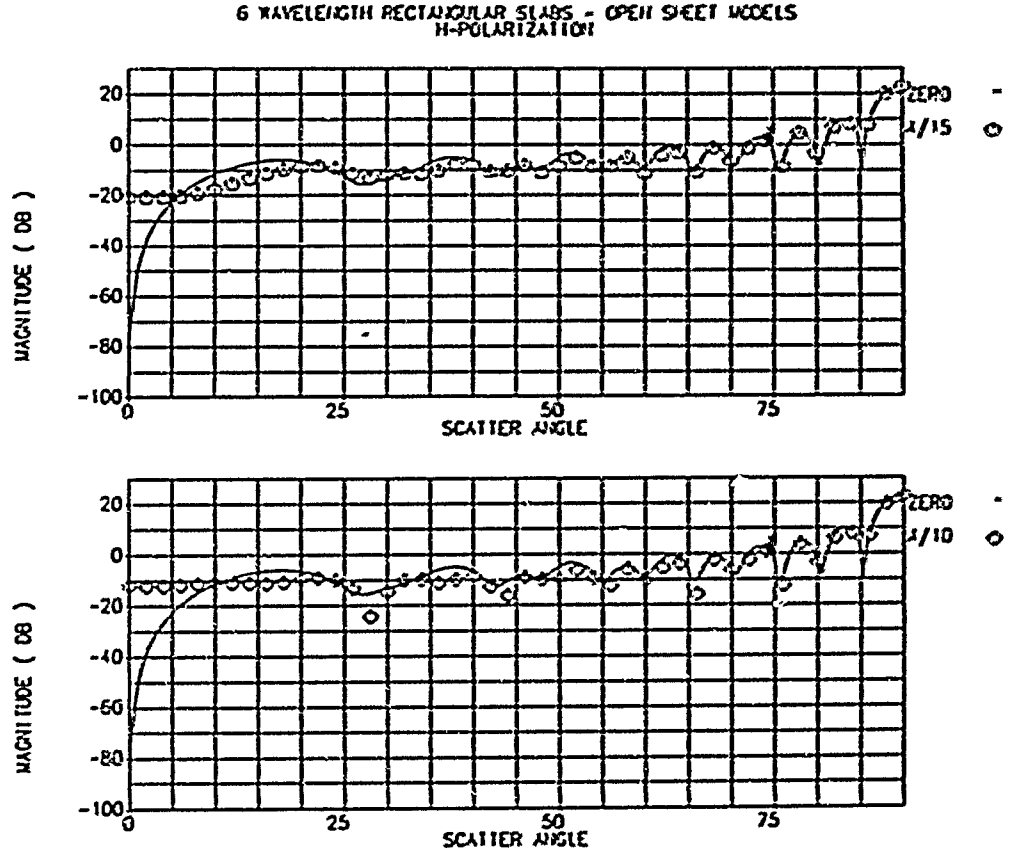


Fig. 8 6 λ Slab - (Th $= \frac{\lambda}{15}, \frac{\lambda}{10}$) H-pol Open Sheet

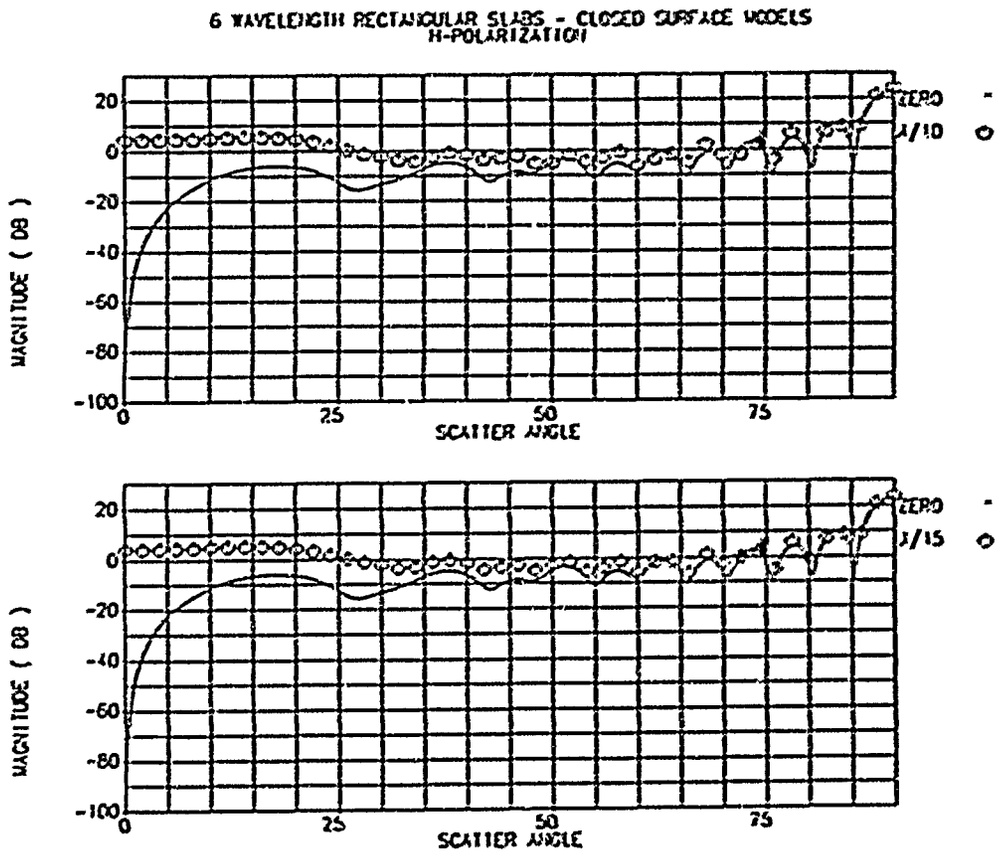


Fig. 9 6 λ Slab - (Th = $\frac{\lambda}{15}, \frac{\lambda}{10}$) H-pol Closed Surface

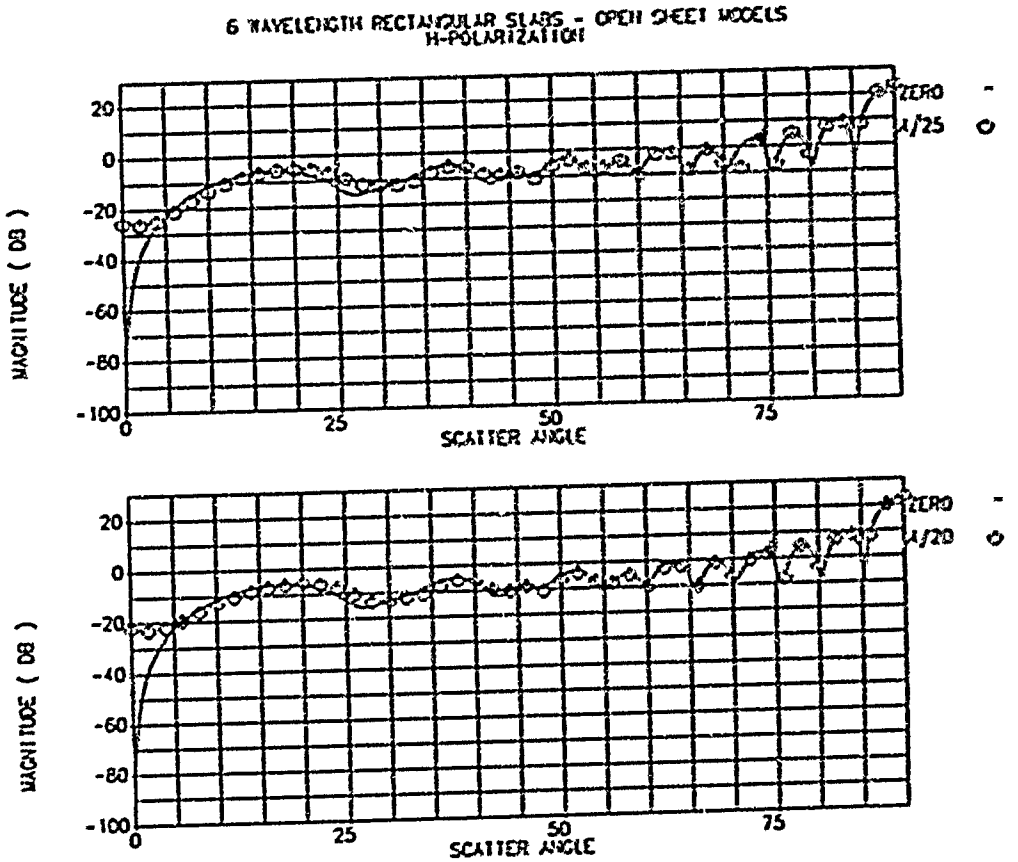


Fig. 10 6 λ Slab - (Th $= \frac{\lambda}{25}, \frac{\lambda}{20}$) H-pol Open Sheet

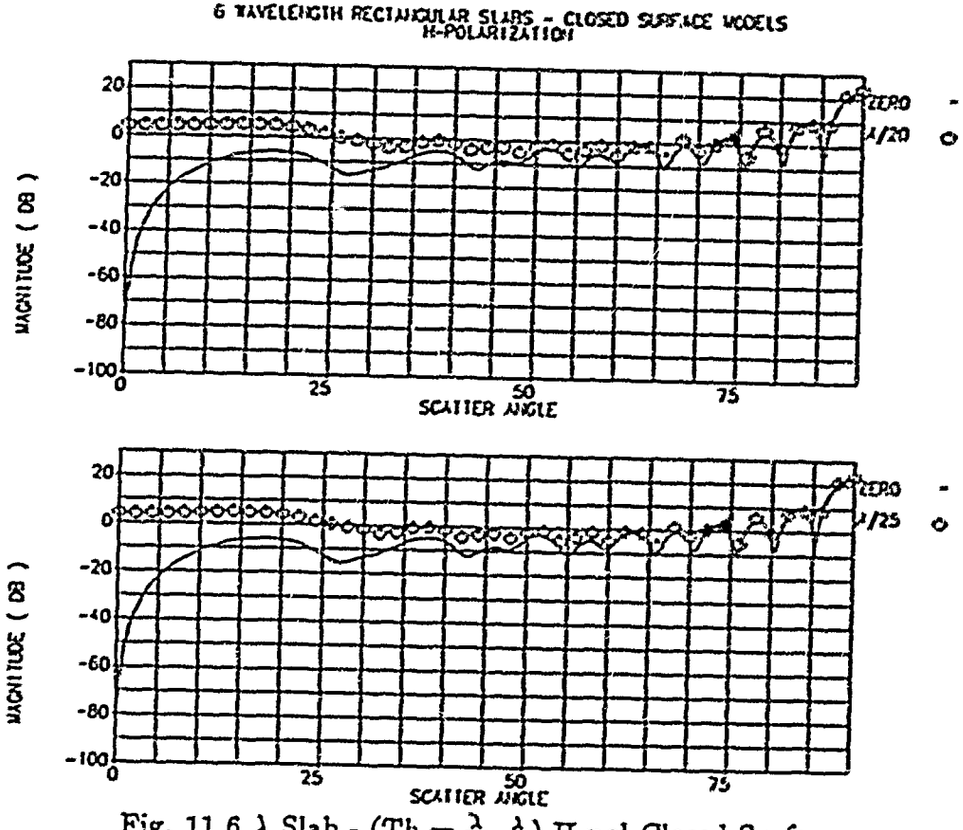


Fig. 11 6 λ Slab - (Th $= \frac{\lambda}{18}, \frac{\lambda}{10}$) H-pol Closed Surface

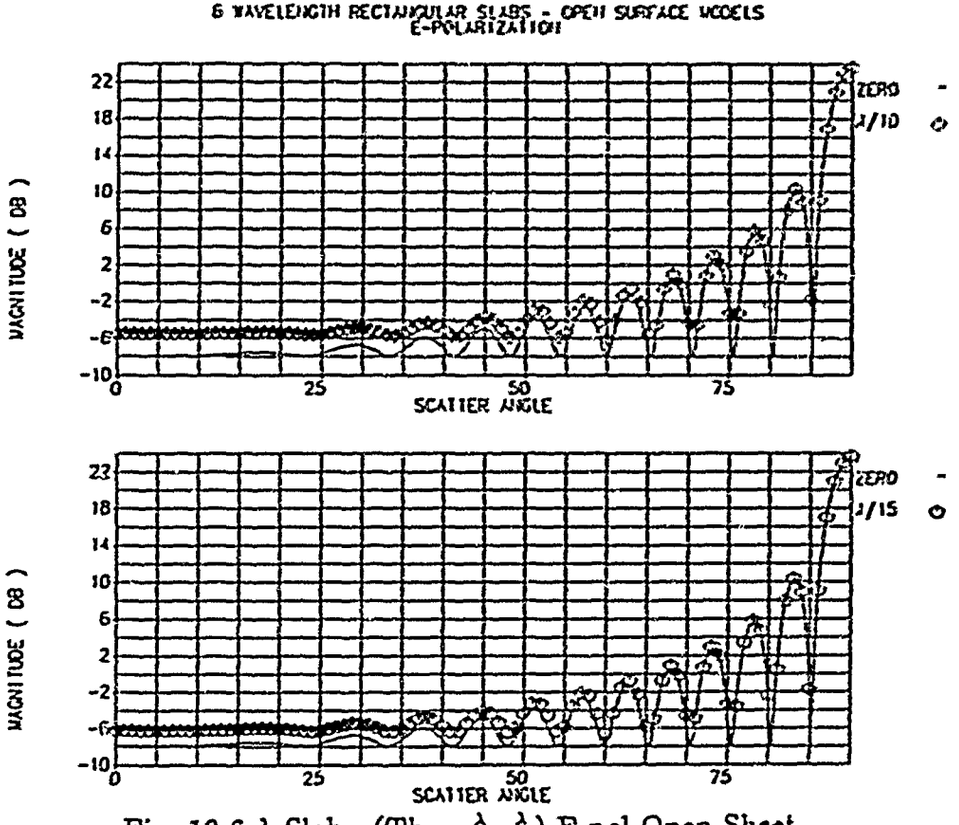


Fig. 12 6 λ Slab - (Th $= \frac{\lambda}{15}, \frac{\lambda}{10}$) E-pol Open Sheet

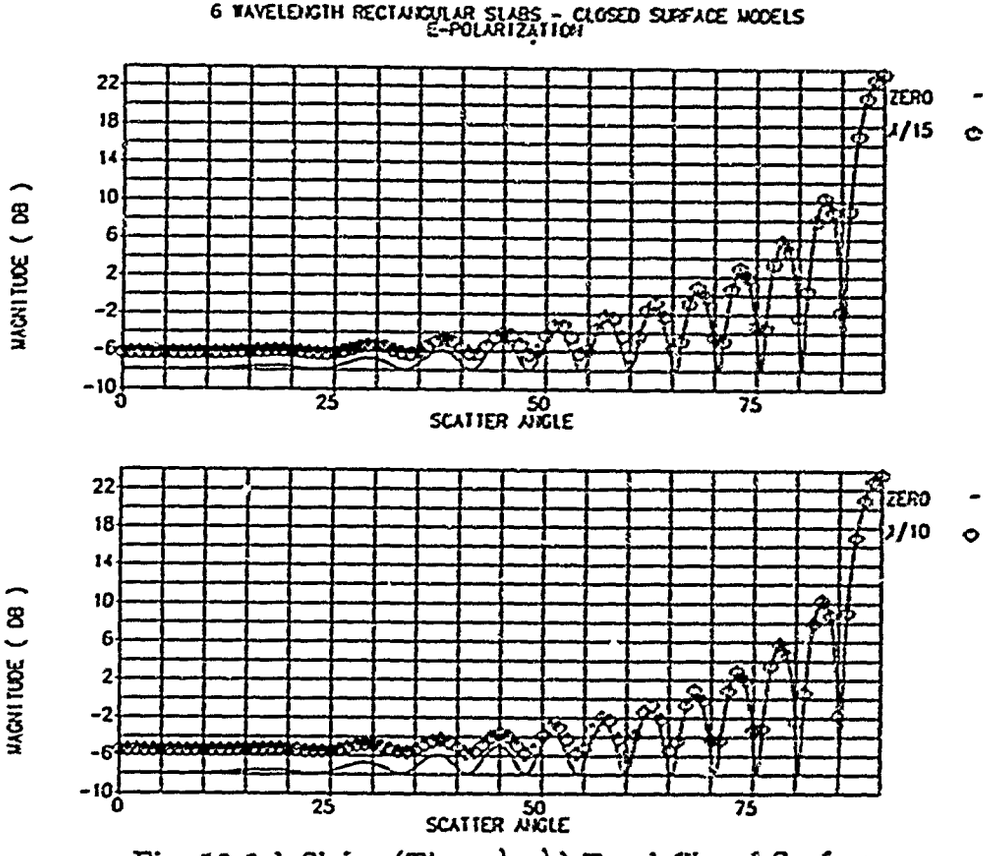


Fig. 13 6 λ Slab - (Th $= \frac{\lambda}{15}, \frac{\lambda}{10}$) E-pol Closed Surface

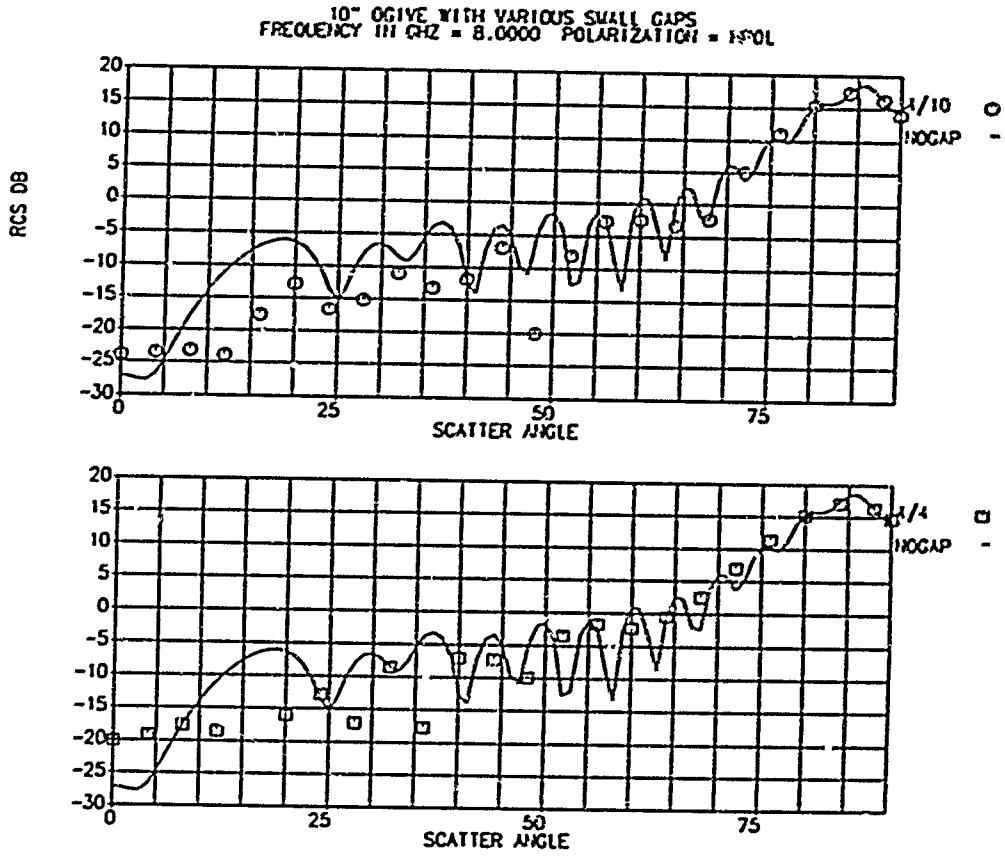


Fig. 14 10 in "Ogive" with (gap $= \frac{\lambda}{10}, \frac{\lambda}{4}$) 8 gHz H-pol

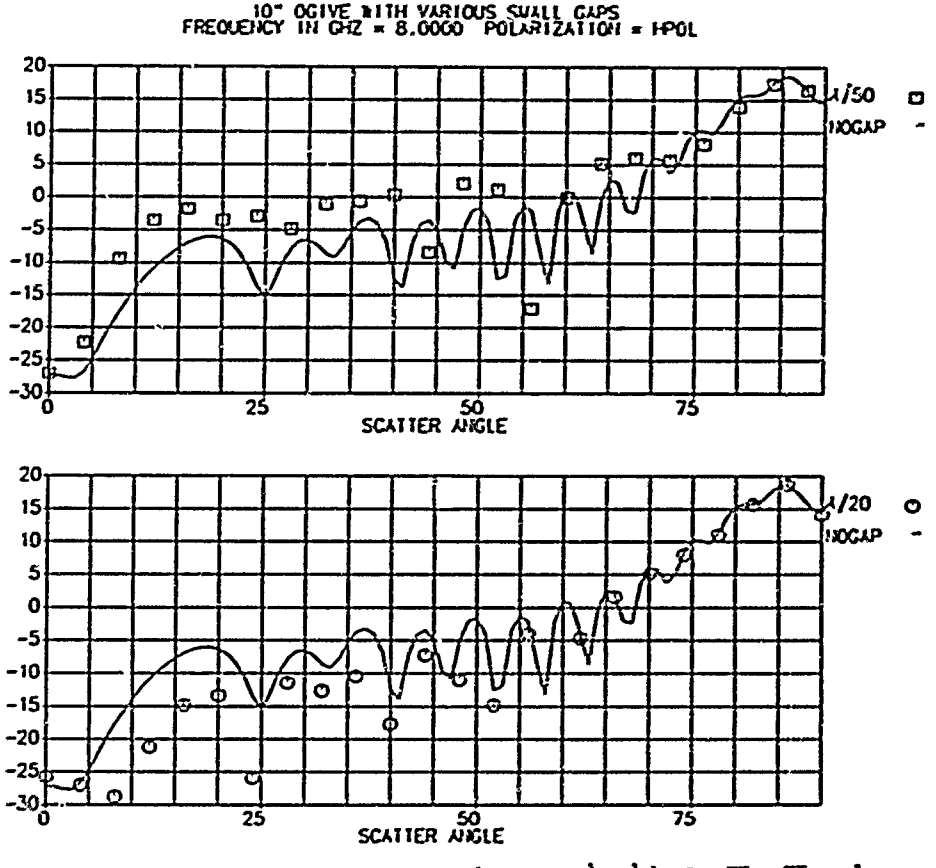


Fig. 15 10 in "Ogive" with (gap = $\frac{\lambda}{50}, \frac{\lambda}{20}$), 8 gHz, H-pol

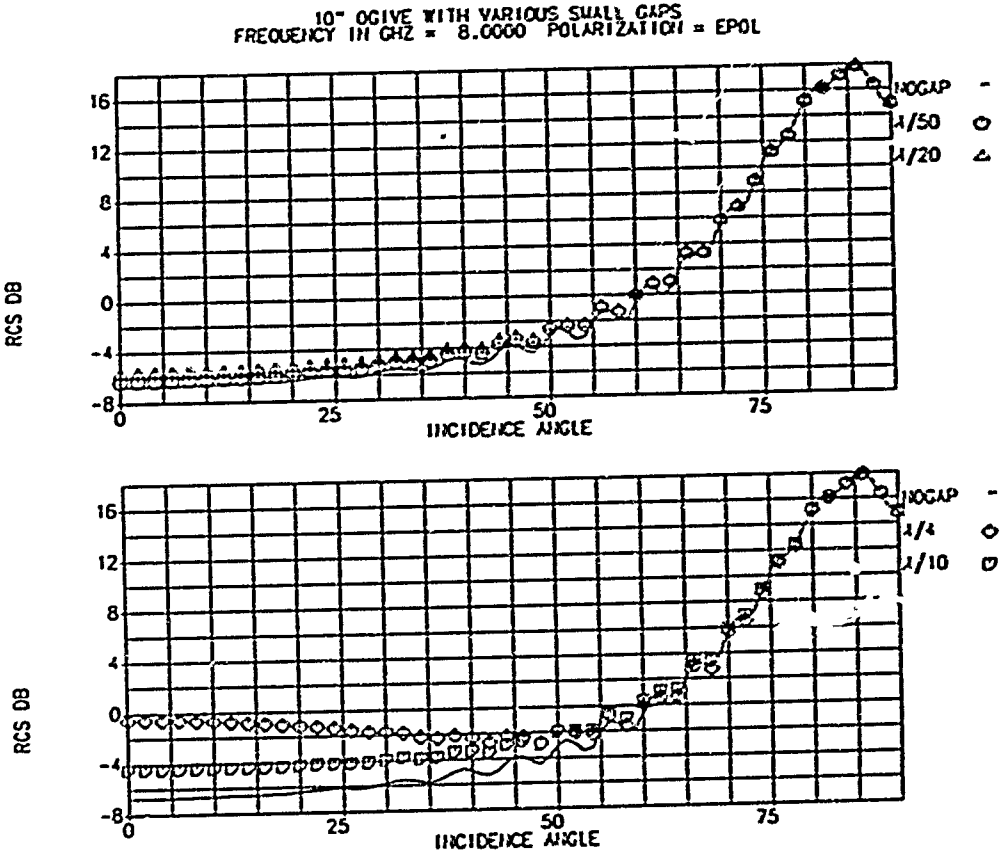


Fig. 16 10 in "Ogive" with Various Gaps, 8 gHz, E-pol

IMPROVING MOMENT-METHOD PREDICTIONS WITH MEASUREMENTS

John F. Stach
SRI International
Remote Measurements Laboratory
Menlo Park, California 94025

INTRODUCTION

In comparing measured and simulated data, one often alternates between modifying the measurement and modifying the simulation in order to improve their agreement. This procedure is necessary and useful for many applications. However, there are also applications where the goal is to predict measured data with the greatest possible accuracy without extensive theoretical analysis. Performance analysis, measurement extrapolation, and feedback models are examples. For these applications and others, a parametric model is what may be required. Ideally, such a model could be calibrated by a few measurements to enable it to predict other measurements with a high degree of accuracy.

In this paper, we will show that it is possible to treat the moment-method (MM) model as a parametric model to be used for predicting measured data accurately. The process is done in two steps and takes advantage of whatever existing MM code and measurements are available. Once a reasonably accurate geometry is created for the MM code, the code is run to define some key parameters. Then the MM admittance matrix is adjusted to account for differences between a set of calibration predicted and measured data. Measured data at new angles can then be predicted by using the adjusted admittance matrix.

The advantages of using MM codes over other parametric models are the excitation-independent admittance matrix, which allows arbitrary measurements to be used in the calibration, and the physical nature of the MM models, which makes the model more robust than simple data-fitting models. The physical nature of the model also provides a way to analyze the calibration itself in order to improve the theoretical model.

LEAST-SQUARES CALIBRATION

The approach taken in this paper is to modify the form of the MM equations so that a least-squares (LS) solution can be applied to the admittance matrix. The MM equation for the prediction of a scattered field, $\hat{s}$, is shown below.

$$\hat{s} = [g_1 \cdots g_n \cdots g_N] \begin{bmatrix} y_{11} & \cdots & y_{1N} \\ \vdots & \cdots & \vdots \\ y_{N1} & \cdots & y_{NN} \end{bmatrix} \begin{bmatrix} v_1 \\ \vdots \\ v_N \end{bmatrix} , \quad (1)$$

where n is the MM element index, v_i is the incident field term at the ith wire, g_i is the radiated field term from the ith wire at the receiver, and y is an element of the admittance matrix. Equation (1) can also be written in a form where the admittance matrix is a vector:

$$\hat{s} = [g_1 \cdots g_N] \otimes [v_1 \cdots v_N] \begin{bmatrix} y_{11} \\ \vdots \\ y_{1N} \\ \vdots \\ y_{N1} \\ \vdots \\ y_{NN} \end{bmatrix} , \quad (2)$$

where $\otimes$ represents the Kronecker product of two vectors. The Kronecker product substitutes each element of the first vector with the product of that element multiplied by the second vector. The length of the new vector is therefore the product of the original vector lengths. The predicted field, $\hat{s}$, and the Kronecker vector can be augmented with as many scattering geometries as desired for a calibration. The admittance matrix remains unchanged as shown below.

$$\begin{bmatrix} e_1 \\ e_2 \\ \vdots \\ e_M \end{bmatrix} = \begin{bmatrix} [g_{11}\cdots g_{N1}] \otimes [v_{11}\cdots v_{N1}] \\ [g_{12}\cdots g_{N2}] \otimes [v_{12}\cdots v_{N2}] \\ \vdots \\ [g_{1M}\cdots g_{NM}] \otimes [v_{1M}\cdots v_{NM}] \end{bmatrix} \begin{bmatrix} y_{11} \\ \vdots \\ y_{1N} \\ \vdots \\ y_{N1} \\ \vdots \\ y_{NN} \end{bmatrix} \quad (3)$$

where m represents the scattering geometry index. The $b = Ax$ form of this equation makes it straightforward to modify the admittance matrix. Assume a modification of the admittance matrix, δy, that will adjust the predicted fields, e, closer to the measured data:

$$e_{meas} = A(y + \delta y) \quad , \quad (4)$$

where A represents the Kronecker matrix and e_{meas} is a vector of measured data at the chosen angles.

$$\delta y = A^H(AA^H + \lambda Q^{-1})^{-1}(e_{meas} - Ay) \quad , \quad (5)$$

is then the LS solution for δy. A^H is the Hermitian conjugate of A, λ is a regularization diagonal matrix, and Q is the error covariance matrix for the measurements. The λQ^{-1} term is a constraint on the accuracy of the solution which can be used when A is singular or when the measurement error can be estimated.

AN EXAMPLE USING NEC

An example of the above procedure was run using the NEC code to illustrate how to apply it to a code and some characteristics of the method. The example is a 1.5λ-long cylinder with a 1.5λ-long wire attached at the center, as shown in Figure 1. A measurement was made of the scattering from a brass cylinder and wire in this configuration. A NEC mesh geometry was also designed as shown in Figure 1. A 10.6° bistatic angle due to the separation of transmit and receive horns was also included in the model. The example used transmit and receive polarizations parallel to the wire. The pattern data was taken over 360° around the cylinder with the wire vertical.

In order to apply the method to NEC, the terms v_i, g_i, and y had to be found. The admittance matrix is never explicitly determined in NEC, so the impedance matrix was extracted and inverted. Since the NEC currents are readily available, the product of the currents and the impedance matrix was used to find the incident terms, v_i. Finally, due to integrations within the code, it was simpler to find the individual contributions to the receiver than to find g_i. However, these contributions include the currents. Therefore g_i was found simply by dividing the individual field contributions by the currents.

The first example in Figure 2 shows a 12-point calibration with no regularization. At each of the 12 uniformly distributed points, an exact match to the measured V-pol data is enforced. It is clear that the calibrated model agrees well with the measured magnitude and phase over the entire range. Figure 3 shows that the LS calibration did not affect the H-pol NEC prediction at all. This is a property of the LS algorithm. The algorithm finds the minimum δy that will match the measurments. In doing so, it affects the the elements of the admittance matrix in proportion to their contribution to the calibration angles. Figure 4 shows this as well. Only half of the calibration points were used. Even though the target is symmetric, the LS calibration left the uncalibrated angles mostly unchanged.

SUMMARY

This method can be useful to create an accurate parametric model of measured data. However, the extent to which it can extrapolate data when calibrated at a few angles has yet to be determined. It is possible that all polarizations and many calibration angles will be required for a robust model. An interesting byproduct of the method is a determination of the contribution of each MM element to the scattering at a given set of angles. This may be useful in scattering analysis.

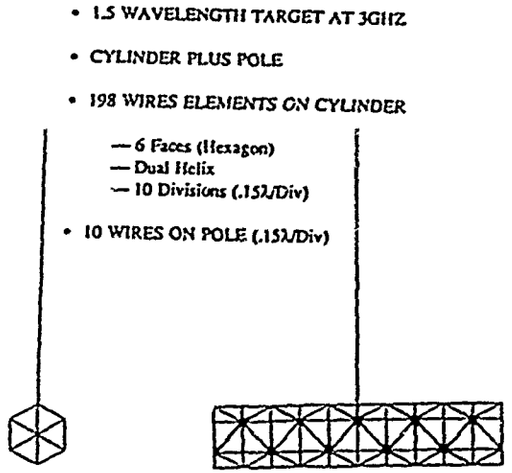


Fig 1. NEC wire grid model

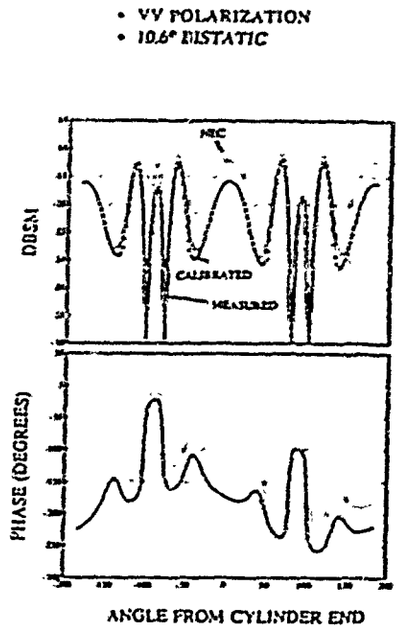


Fig 2. 12 point vertical polarization calibration

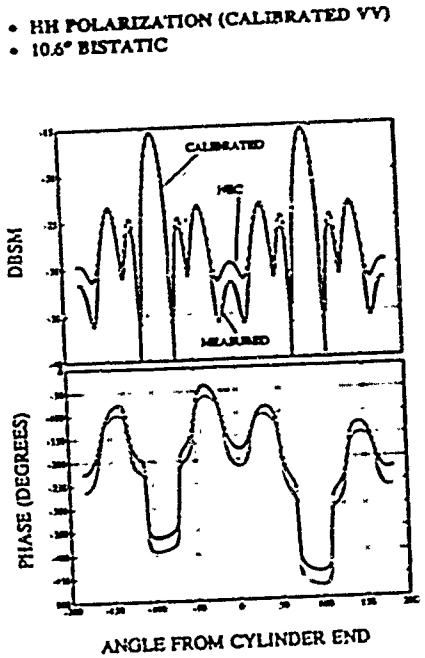


Fig 3. Vertical calibration effect on horizontal polarization

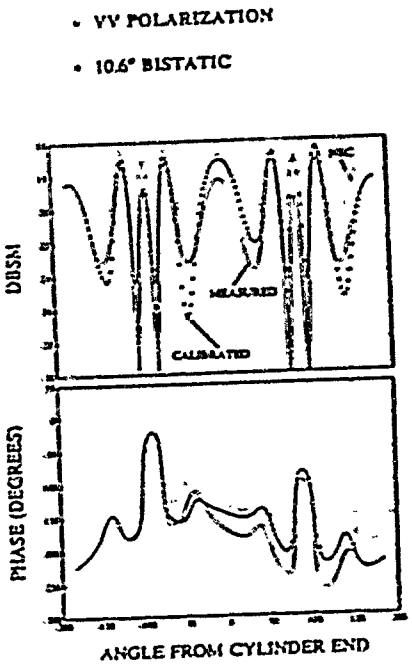


Fig 4. 6 point vertical calibration

ELECTROMAGNETIC CODE VALIDATION BY THE INFRARED MEASUREMENT METHOD

J.D. Norgard, R.M. Sega, D.C. Fromme and K.J. Ianacone
Department of Electrical and Computer Engineering
University of Colorado
Colorado Springs, Colorado 80933–7150

ABSTRACT

An experimental technique for determining the two and three dimensional electromagnetic (EM) field distributions that are predicted by various EM codes is presented. The experimental technique is based on infrared (IR) measurements of Joule heating induced when electromagnetic energy is absorbed by lossy dielectric and resistive materials. An infrared scanning system records the thermal radiation from a calibrated detection screen and the actual field strengths are then related to the surface temperature variations. The detection screen material is of planar construction and thus provides a two–dimensional field mapping. By moving the screen, the three dimensional field is obtained. This experimental approach has been applied to antenna radiation patterns and several scattering and coupling problems. Comparisons are made between the theoretical and experimental approaches for various hollow and loaded slit cylinder configurations, and near and far field antenna patterns for frequencies from 1 to 18 GHz. The advantages and limitations for validation of theoretical work are discussed.

I. INTRODUCTION

The ability to obtain an experimentally determined field mapping for a given situation can be used by the EM modeling and computations community in several ways. First, if a visual presentation is provided at the outset of code development, insight into the physics of the interaction mechanisms can provide assistance for the initial approach to the problem. Second, a number of actual physical systems, sufficiently complex with respect to structure or loss mechanism, may require a hybid approach where theory and experiment are used to determine appropriate coefficients. Finally, a code that is developed independent of experimental results can be validated by a method such as the infrared (IR) technique. This technique provides a rapid two or three dimensional mapping of the test environment but is limited with respect to dynamic range and phase information.

CW measurements by the IR measurement technique have been demonstrated and reported over the past several years[1-4]. While the technique requires a minimum energy deposition for sufficient heating, the electrical parameters of the detection screen can be selected such that the thermal mass of the screen is reduced, allowing for a fast response. IR data acquisition by a high-speed memory system is used to store approximately 500,000 pixels of a two-dimensional IR image in less than three seconds[5]. This corresponds to thirty 128 pixel × 128 pixel frames of data with each pixel element represented as an 8-bit word, which, after calibration of the detection screen material, is correlated to the electric or magnetic field intensity at that location.

This is a non-destructive, relatively non-perturbing IR measurement technique that has been developed to observe EM fields. This paper will discuss the IR technique used to detect and measure EM fields from horn antennas and

EM coupling inside cylinders. It will be shown that this measurement procedure avoids some of the problems associated with electric and magnetic field probes[2], since it produces a quick, accurate picture of the field distribution. The application presented includes feasibility demonstrations for mode determination in a open ended cylinder with an axial slot aperture while also determining the external field distribution. The demonstrations were carried out at 1–4 GHz using IR detection ranges of 2–5.6μ and 8–14μ.

2. INFRARED DETECTION OF ELECTROMAGNETIC FIELDS

The IR detection technique is based on heating that occurs when EM energy is absorbed by an object. When the surface temperature rises to 0.1 K or higher above ambient, the induced temperature distribution at the surface (which corresponds to field intensities in that surface) can be detected by an IR scanning system via emitted thermal radiation. By Poynting's Theorem, the absorbed power in a given volume is a function of the electric (E) and magnetic (H) field magnitudes as shown by the equation[4]

$$P_{abs} = \int_v (\sigma E^2 + \omega \epsilon'' E^2 + \omega \mu'' H^2) dv \qquad (1)$$

where σ is the conductivity, ϵ'' is the imaginary permittivity, μ'' is the imaginary permeability of the detector, and ω is the angular frequency of the incident microwave radiation. Thus, it becomes possible to relate surface temperature variations to E and H field intensities. As shown by the above equation, a material can absorb power via E and/or H field coupling.

The heat transfer problem to predict temperature increases in a microwave heated homogeneous material involves solving a non–linear second–order

differential equation in both space and time, while considering radiative and convective heat losses from the material surface, conductive heat transfer within the material, and the power absorbed as a function of distance into the material[4-6].

For electric field detection, a detection screen is selected which has a large conductivity σ or imaginary permittivity ϵ'' compared to its imaginary permeability μ'' (e.g., carbon paper). The electric field absorption problem is solved as a function of screen thickness, conductivity and imaginary permittivity for an incident plane wave, and an approximate solution of the thermal problem relating surface temperature to absorbed microwave power is then obtained[8].

For detection of fields internal to the test structure or in cavities, the material is optimized so as to allow only sufficient absorbed power for IR observation, while minimizing reflection and the perturbation of the field distribution being measured.

For the detection of the electric field scattered from an object, a requirement exists for a material with the properly selected σ and/or ϵ'' such that sufficient energy is absorbed for a given temperature rise. IR detection of scattered electric fields was accomplished using a screen of carbon paper (σ = 8 mhos/m) mounted on styrofoam and placed in the plane of interest. A method of calibrating a material screen for the incident field strength as a function of temperature rise has been developed and has previously been presented[9].

3. EXPERIMEMTAL SET-UP

The experiments described below in this paper are performed in the anechoic chamber in the Electromagnetics Laboratory at the University of Colorado at Colorado Springs. The experimental equipment includes the following items: a signal generator, an amplifier, a microwave antenna, a scattering object, a detection screen (whose characteristics were explained above), an IR scanner, and

an IR monitor and a digital recording system. The detection screen used is a carbon based paper with a conductivity of 8 mhos per meter, a thickness of approximately 80 microns, and a power transmission coefficient of 0.87.

The placement of the screen from the camera and the lens selection will determine the pixel size that is observed, and hence, the spatial resolution. The lenses that are available include 3.5°, 7° and 20° fields of view with extension rings providing additional flexibility in observation area and resolution.

4. RESULTS

The following laboratory experiments demonstrate the flexibility of this technique for measuring radiated field distributions and for testing and analysis of electromagnetic coupling into various structures. The data recieved from this scanning system is graphically depicted by a thermogram, (on a pixel by pixel basis) or by equal contours (plots of the intensity of the field distribution). Three examples are now presented:

4.1 Near field of a horn antenna.

Results previously presented[12] are shown in figures 1 and 2. Figure 1 shows the thermogram of the near field region of a standard gain horn, in band at 2.5 GHz. Results are shown for the E–plane. Figure 2 shows the results of a numerical prediction of the field structure in this region.

4.2 Mode Determination of a Cylindrical Cavity

Grey–scale images of IR experimental measurements, performed in an anechoic chamber with computer aided analysis, are shown in figure 3. A cylinder with an axial aperture is illuminated with E–field perpendicular to the cylinder axis. A thin resistive screen (disk shaped) is placed in a given plane in the

cylinder and the electric field distribution is recorded. Several planes are selected along the axis of the cylinder and perpendicular to it such that the field distribution can be reconstructed in the vicinity of the aperture. Figure 4 is the theoretical distribution of the dominant mode of figure 3.

4.3 Coupling to a long Cylinder with an Axial slot Aperture

A thermogram taken at the mid-point of the aperture with the screen perpendicular to the aperture axis (giving E plane distributions) is shown in figure 5. Figure 6 shows a theoretical solution at 2.9 GHz. Figure 5 shows only the interior of the cylinder, while figure 6 includes some exterior regions. The agreement between the experimental and theoretical results is good. The theoretical results are from Ziolkowski[9]. This technique is based on the generalized dual series solution method which yields precise edge effects.

5. CONCLUSION

In this paper, techniques were reviewed for IR detection and computer analysis for the purpose of determining microwave interactions from planar and cylindrical structures, with and without apertures and antennas. The interference is observed on a screen that absorbs microwave energy from which an image is recorded with an infrared scanner. The images are sampled, digitized and recorded on magnetic tape. A system of computer procedures and programs were developed for each experiment in the laboratory series for organizing, accessing, analyzing and calibrating the IR images.

The IR technique, with computer aided analysis, is complementary to probe methods, which give increased dynamic range at points of interest, for studying the interaction of microwave fields. The standard techniques for detecting microwave fields, e.g., electric and magnetic field probes, are generally complex, time

consuming, and costly. The utility of the IR technique is demonstrated in the study of wide fields of view and where minimum perturbation of the measured quantity is necessary.

REFERENCES

1. Sega R.M., Martin, V.M., Warmuth, D.B. and Burton, R.W., "An Infrared Application to the Detection of Induced Surface Currents," Modern Utilization of Infrared Technology VII, Vol. 304, SPIE – The International Society for Optical Engineering, pp. 84–91, August 1981.
2. Sega R.M., and Genello, G.J., "Infrared Thermography Techniques for EMI/EMC Measurements," Proceedings of Electromagnetic Compatability '83, Arlington, VA, pp. 29–33, August 1983.
3. Sega R.M. and Norgard, J.D., "An Infrared MEasurement Technique for the Assessment fo ELecttromagnetic Coupling," IEEE Transactions on Nuclear Science, Vol. NS–32, No. 6, pp. 4330–4332, December 1985.
4. Sega R.M. and Norgard, J.D., "Infrared Measurement of Scattering and Electromagnetic Penetrations Through Apertures", IEEE Transactions on Nuclear Science, Vol. NS–33, No. 6, pp. 1658–1663, December 1986.
5. Fredal, D., Bussey, P., Sega R.M. and Norgard, J.D., "Hardware and Software Advancement for Infrared Detection of Microwave Fields," SPIE Proceedings, Infrared Image Processing and Enhancement, Orlando, FL, May 1987, (in publication).
6. Ramo, S., Whinnery, R.R., and Van Duzer, T., Fields and Waves in Communication Electronics, 2nd ed. New York: John Wiley & Sons, 1984, pp. 137–143.
7. Siegel, R. and Howell, J.R., Thermal Radiation Heat Transfer, 2nd ed. New York: McGraw–Hill, 1972, pp. 384–145, 679–711.
8. Wetlaufer, G.D., "Optimization of Thin–Screen Material Used in Infrared Detection of Microwave Induced Surface Currents at 2–3 GHz," M.S. Thesis, 1985.
9. J.D. Norgard and R.M. Sega, "Microwave Fields Determined from Thermal Patterns", SPIE Proceedings, Thermal InfraredSensing for Diagnostic Control; Thermosense IX, Orlando, FL., May 1987.
10. R.E. Ziolkowski and J.B. Grant, IEEE Transactions of Antennas and Propogation, AP–35, 504–528, 1987.
11. W.A. Johnson and R.W. Ziolkowski, Radio Sci. 19 275–291, 1984.
12. Metzger, D.W., "Numerical Computation and Experimental Verification of Near fields from Horns," ACES Proceedings 1987.

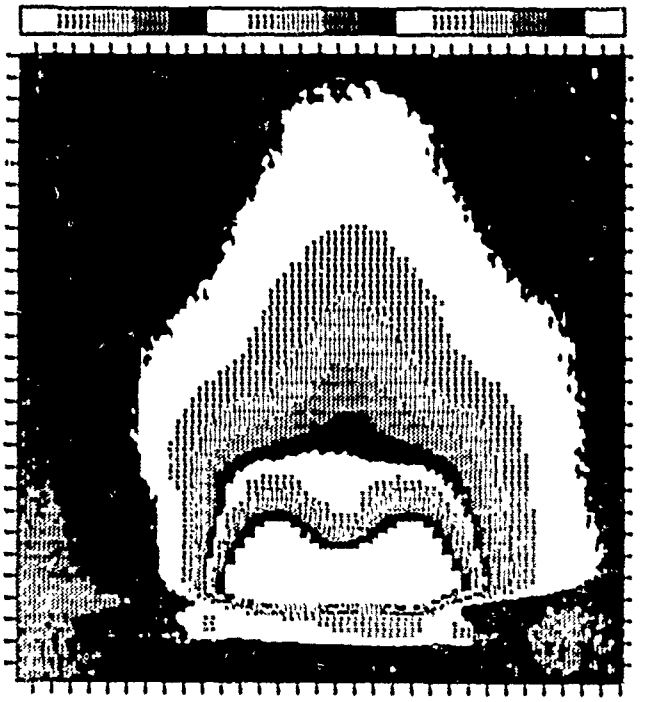


Fig. 1 Thermogram of the E–plane of an in–band horn at 2.5 GHz.

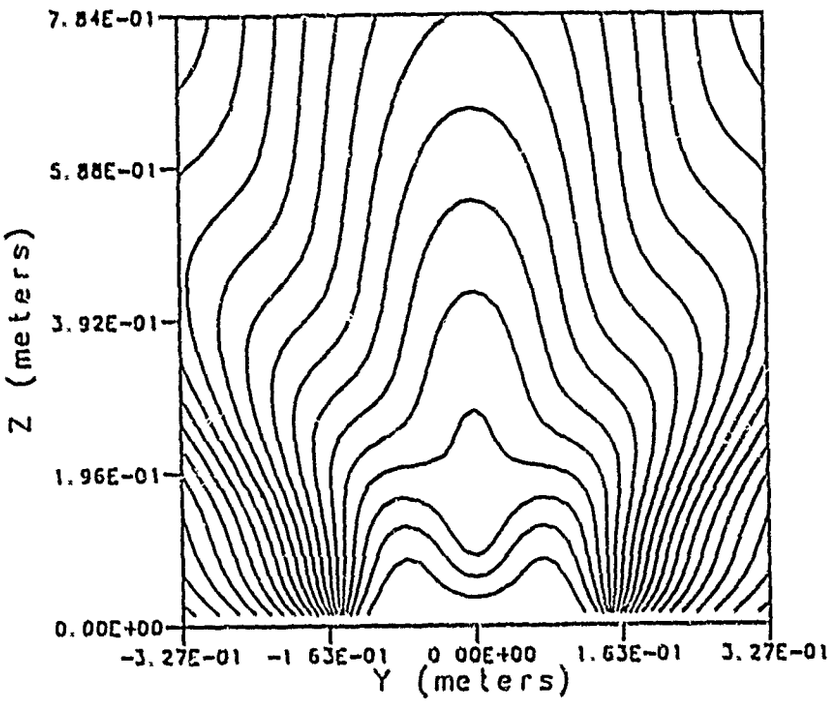
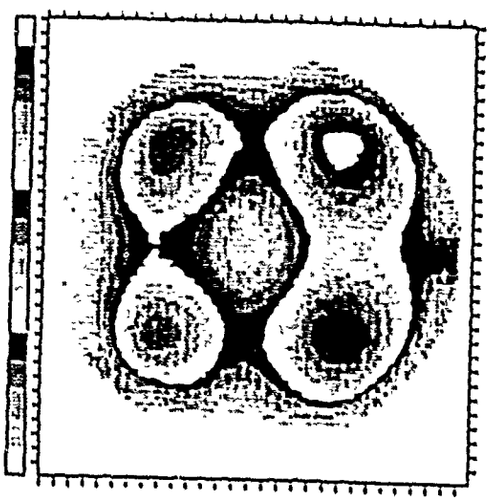


Fig. 2 Numerical prediction of field structure for the same region of the horn as in figure 1.



Thermogram (Top View)

Surface and Contour Plots

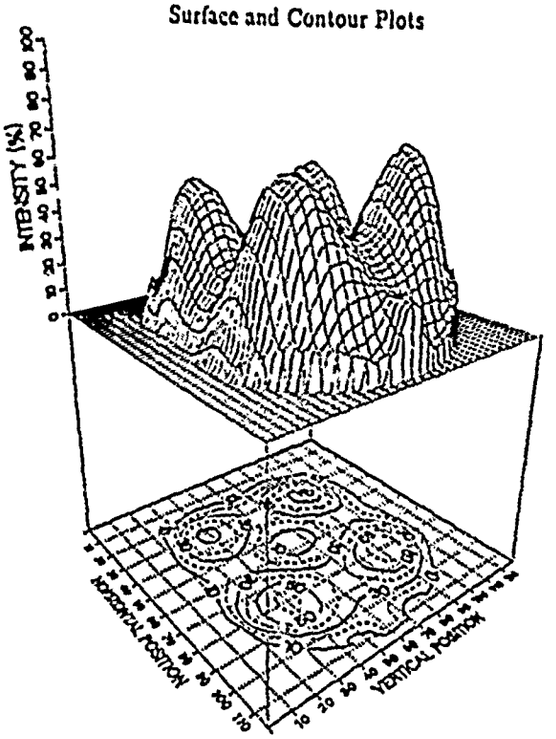
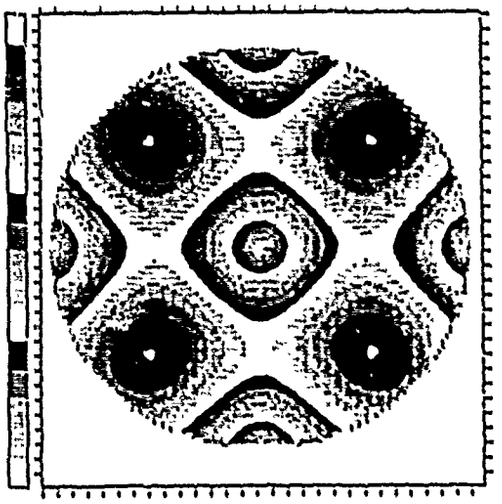
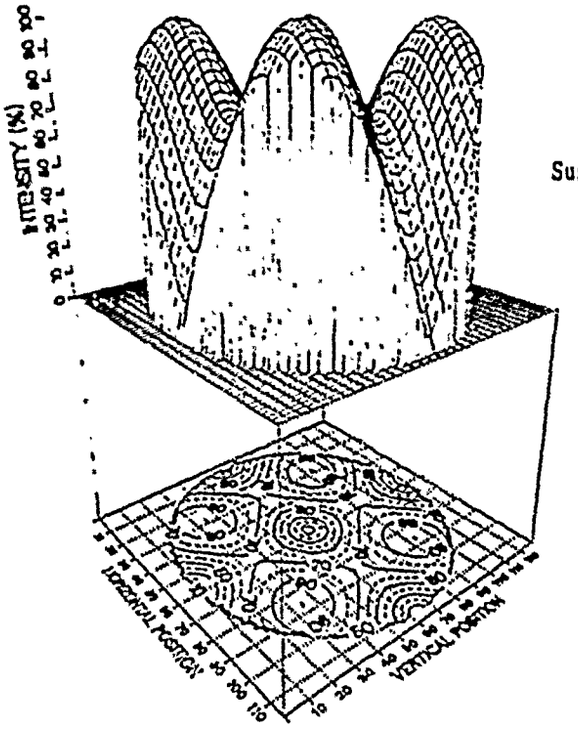


Fig. 3 Thermogram of the modes inside a cylinder with a short axial slot aperture.



Grey Scale Image (Top View)



Surface and Contour Plots

Fig. 4 Theoretical prediction of the modal structure for the geometry of figure 3.

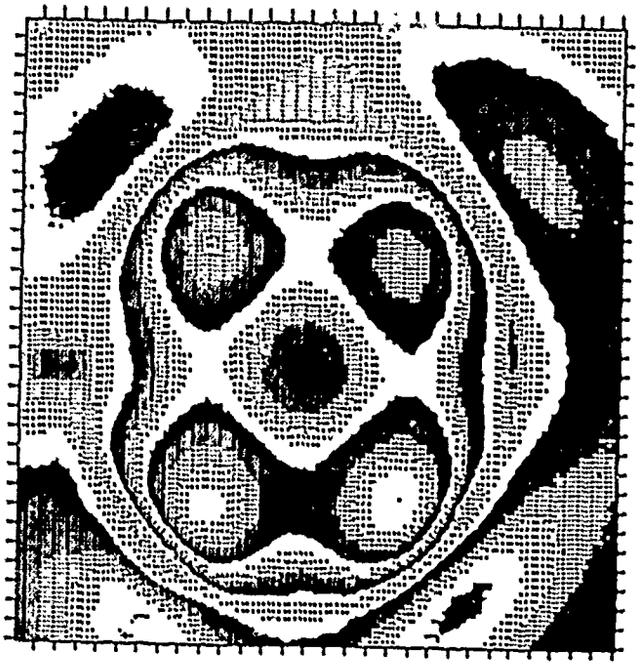


Fig. 5 Thermogram of the field structure inside a cylinder with a long axial slot aperture.

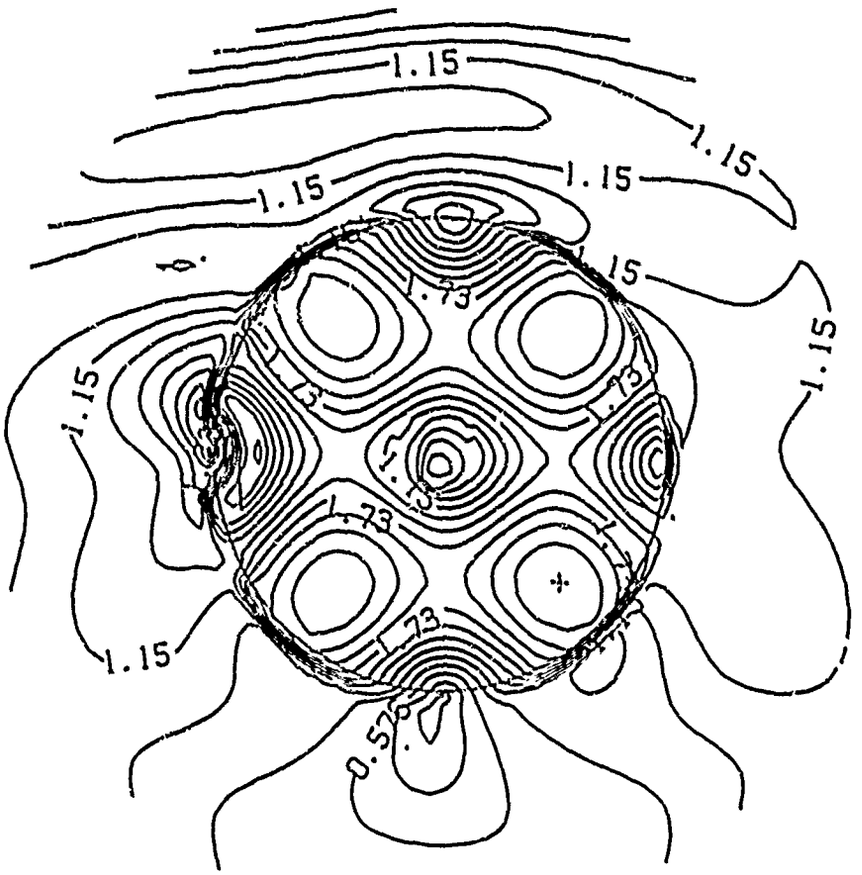


Fig. 6 Theoretical prediction of the fields for the geometry of figure 5.

LARGE FORTRAN PROGRAM STRUCTURE, MAINTENANCE, RELIABILITY, AND DOCUMENTATION

Dr Joseph F. Janni - Principal Author
USAF Space Technology Center
Kirtland AFB NM 87117-6008

Contributors: Major R. Berry, Mr J. Burgio, Dr G. Cable*, Mr R. Conley, Jr., Captain H. Happ, III, Ms D. Janni*, Major L. Lutz, Mr H. Murphy, Mr N. Phillíber**, Mr G. Radke, Jr., Captain J. Spear

An improved approach to programming has been developed in the last decade which produces reliable, efficient computer programs using fewer labor hours and far fewer maintenance hours than other coding approaches. This approach uses a disciplined style and is usually referred to as structured programming. This standard applies the concepts of structured programming to FORTRAN-77 (ANSI X3.9-1978) and contains procedures which result in better, more reliable computer programs. It is based on many actual experiences, careful research, and documented studies. Literature citations are provided for those who wish to verify the published research that supports this document. This standard classifies coding practices into five categories: mandatory, recommended, permitted, discouraged, and forbidden.

The objectives of this standard in directing the use of disciplined programming practices are:

(a) To apply an architectural and syntactical method to the FORTRAN-77 language that greatly reduces the probability of errors.

(b) To produce code that is modified easily, rapidly, and reliably by applying the principles of modular, structured, and machine interchangeable FORTRAN-77.

(c) To improve code clarity, simplicity, robustness, and reliability.

(d) To prohibit convoluted logic.

(e) To produce well-documented code.

* Dr Cable and Ms Janni are at Sandia National Laboratories
** Mr Phillíber is at Computer Sciences Corporation

FOREWORD

These standards are dedicated to all the programmers who have to modify someone else's code.

The standards were born out of frustration and developed out of necessity. The situation that initiated their development occured at 3 o'clock in the morning on a Sunday. We had been working all weekend trying to get answers from large FORTRAN programs designed to calculate a wide range of complex radiation effects. We had worked on the project for several months and had encountered so many problems with these programs that we had been forced into a 24 hour-a-day dedicated effort in order to meet the impending deadline. The codes failed during execution every few hours. As I debugged each code failure, I found the same poor programming that I had been finding repeatedly in prior months. It was on this Sunday in the early morning hours that I decided to produce a set of standards that would resolve these problems and prevent them in the future.

The radiation effects programs were almost impossible to understand. They also proved to be very unreliable. The programs contained convoluted logic full of GO TO statements and confusing structure. Whenever one "bug" was found and patched, the program was resubmitted but another problem would soon occur. These programs evolved over a 10 year period and were written by dozens of programmers at several different facilities. All of the programmers who had written these codes said that they understood and applied good programming practices. Although they may have believed it themselves, only a few actually implemented good programming practices. Most of the programming was a disaster.

It took over a year to develop the standards in this document. In addition to drawing on our many years of combined experience for background material, the modern literature was carefully reviewed. Recent well-documented and well-researched studies have been used extensively. Appropriate literature citations are provided for those who wish to verify the published research that supports this document. These standards are now solving the overwhelming majority of our programming problems. I believe they can do the same for others.

These standards are, of necessity, mechanical in nature. In some cases, recommendations are made but specific programming decisions are left to the programmer. In many cases the programming approach is mandated. Adherence to this standard is a necessary but not sufficient condition to produce large high-quality FORTRAN programs. These standards must be used with a positive and constructive attitude if they are to be successful.

The team of contributors to this document all share two crucial attributes: (1) they are excellent FORTRAN programmers (many are also proficient in other languages), and (2) they all have had painful experiences with junk code which didn't work reliably and which wasn't documented. The entire team contributed to this document and the members abide by it themselves.

After this document was released for an initial review by other programmers, two inter-

eating trends were observed in their reaction. Programmers who routinely had to modify code provided by someone else were strongly in favor of the standards. Programmers who wrote original codes and who didn't have to use or modify other codes frequently did not like the standards. They claimed too many constraints were placed on their judgement, unduly inhibiting their full capabilities as superior programmers. My sympathies are primarily with the first group. Although I understand the attitude of the second group, I do not agree with it. Large FORTRAN programs must be written in a consistent form that maximizes the probability of success and simultaneously minimizes the introduction of "bugs" through poor programming practices. Undisciplined programming with clever methods and tricky algorithms is contrary to this objective. Undisciplined programming also tends to be imbued with a programmer's idiosyncracies and is very difficult to verify and modify.

The most controversial aspect of this document is the tight control on the utilization and structure of COMMON blocks. Our position on COMMON blocks is well-founded. Another controversial issue is the mandatory application of FORTRAN implicit declarations for variable and PARAMETER names. Again, the programmers who use and debug programs written by others have supported both restrictions; the programmers who write code for their own use or for use by others usually disagree with our position.

This standard discusses three general aspects of programs: structural content, documentation, and cosmetic appearance. The latter characteristics include the format of statement label fields, the columns and form of the comments, indentation rules, and other similar features. They are mandated primarily to produce a uniformity of style and appearance that is highly desirable in large FORTRAN programs written by many individuals who would otherwise use widely different styles.

The standard is intended to be read from start to finish. It is written in a direct style for easy reading, but as a result is not organized as a reference manual. For this reason, a cross-reference index is included to help locate specific topics.

In order to keep this document as short as possible, the rationale for most of the individual features of this standard is usually omitted. Exceptions are made for particularly controversial features or for specific issues meriting a textual explanation. When possible, citations to references are provided for those readers desiring supporting information.

Implementation of these standards will produce less expensive programs over the long term because the resulting coding will be more reliable, will contain fewer bugs, will be easier to modify, and will require far fewer maintenance hours than alternate FORTRAN coding approaches. Over the short term, adherence to these standards will not substantially increase the development time of a new program because the improved reliability, organization, modularity, and understandability will offset the extra effort required for documentation, testing, and peer review.

Joseph F. Janni

Albuquerque, New Mexico
December 9, 1985

1 BACKGROUND

An improved approach to programming has been developed in the last decade which produces reliable, efficient computer programs using fewer labor hours and far fewer maintenance hours than other coding approaches. This new approach uses a disciplined style and is usually referred to as structured programming. This standard applies the concepts of structured programming to FORTRAN-77 (ANSI X3.9-1978) and contains procedures which result in better, more reliable computer programs (Ref. 1). It is based on many actual experiences, careful research, and documented studies (Refs. 2-31).

This standard classifies coding practices into five categories: mandatory, recommended, permitted, discouraged, and forbidden. A mandatory coding practice must always be implemented. A recommended coding practice should usually be used, but the programmer can apply prudent judgement and occasionally deviate in a specific situation. A permitted coding practice may be used. A discouraged coding practice should not be used except on rare occasions and only if extraordinary care is taken. A forbidden coding practice is never permitted. The boldface words in this paragraph clarify the intent of practices discussed in this standard.

2 OBJECTIVES

The objectives of this standard in directing the use of disciplined-programming practices are:

- To apply an architectural and syntactical method to the FORTRAN-77 language that greatly reduces the probability of errors. Poor use of the language creates many problems (Ref. 18).
- To produce code that is modified easily, rapidly, and reliably by applying the principles of modular, structured, and machine interchangeable FORTRAN-77 that adheres to top-down design.
- To improve code clarity, simplicity, robustness, and reliability.
- To prohibit convoluted logic.
- To minimize the dependence of one module on the internal details of another. A module should have limited access to the data structures used by other modules.
- To produce well-documented code.
- To avoid the seemingly endless series of patches and repairs whose implementation requires explicit changes in many places throughout the program.

3 CONCEPTS, DEFINITIONS, AND RELATED RESTRICTIONS

3.1 PROGRAMMING LANGUAGE

The programming language is ANSI FORTRAN-77, which is hereby made a part of this standard. If there is a conflict between this standard and ANSI FORTRAN-77, the provisions of this standard apply.*

3.2 CODE

Code is a term for instructions in a computer programming language.

3.3 PROGRAM

A program is an organized set of code tailored to perform specific tasks. The intent of a FORTRAN-77 computer program is to solve a mathematical, logical, physical, technical, or engineering problem. Although programs—including those written to solve apparently simple problems—can be quite complex, the program should have a simple organization and structure. A program should be partitioned into sections of code to perform specific tasks. These sections of code are composed of subprograms and modules consisting of closely related subprograms:

EXECUTIVE (Master Control).

INPUT SECTION.

Subprograms.

COMPUTATIONAL SECTION.

Subprograms and Modules.

OUTPUT SECTION.

Subprograms.

ERROR EXIT SECTION.

Subprograms.

DATA STRUCTURE DEFINITION.

BLOCK DATA Subprograms.

*An extension to the FORTRAN-77 standard is the required use of the INCLUDE statement or its equivalent (Ref. 20). Other limited exceptions are permitted only when specified explicitly by this standard (refer to Section 9, page 30).

3.4 SUBPROGRAM

A. A subprogram is a SUBROUTINE, FUNCTION, or BLOCK DATA and is limited to a single purpose. A subprogram can reference (call) other subprograms, or it can be referenced by the executive or other subprograms.

1. A directly subordinate subprogram is referenced by an executive or subprogram. Specifically, a subprogram is directly subordinate to an executive (or another subprogram) if it is explicitly referenced by the executive (or other subprogram).
2. An indirectly subordinate subprogram is referenced by a directly subordinate subprogram or another indirectly subordinate subprogram. Specifically, a subprogram is indirectly subordinate to an executive (or another subprogram) if it can be reached from the executive (or other subprogram) only through at least one intervening subprogram.
3. A basic subprogram does not reference any subordinate subprogram.

B. A subprogram must perform correctly the process claimed for it for all valid combinations of arguments, and it must detect and take defensive action for all invalid arguments.

C. A subprogram should be written so that a typical programmer can determine that it works correctly by careful inspection, logic verification, and execution tests.

D. Access to arrays and variables should be limited to those arrays and variables actually needed in the subprogram (e.g., limit COMMON blocks and subprogram arguments to those actually needed) (Refs. 18 and 31).

1. The primary method of providing access to arrays and variables is through argument lists.
2. The secondary method of providing access is through labeled COMMON blocks, whose usage is severely restricted (Ref. 6).
3. COMMON blocks may be either local or global.
   a. A local COMMON block may be used only within a module. Once a value is set in a COMMON block it may not be changed unless it is a local COMMON block confined to a module, as defined in Section 3.5.
   b. A global COMMON block may be used anywhere in a program but only within specified constraints.
      (1) Globally applied COMMON blocks are permitted to carry only unchanging quantities into subprograms. Global COMMON blocks must not transfer variables out of a subprogram that have been modified or altered in that subprogram, except for the initialization of the COMMON block. Data stored in a globally applied COMMON block must not be subsequently modified.

(2) Globally applied COMMON blocks must be loaded by means of either DATA statements in BLOCK DATA, by reading a data file at the beginning of program execution, or by a one-time calculation.

3.5 MODULE

A module (colloquially referred to as a package of tightly knit subprograms) consists of closely related subprograms which share an execution and interface environment (refer to Appendix A).

A. A module must have a well-defined objective of limited scope.

B. A module must manipulate a single conceptually related data structure. This data structure is isolated from the external environment. No subprogram outside of the module has access to, or information about, the data structure.

C. A module consists of one or more interface subprograms and subordinate subprograms.

D. A module must have a minimal external interface. Variables and arrays may be passed to and from a module only via arguments of interface subprograms.

E. Within a module, arrays and variables may be transferred vertically via arguments, or transferred laterally between subprograms of the module via a single labeled COMMON block (containing conceptually related variables). This labeled COMMON block is local and can be used only within the module.

F. A module must be thoroughly documented.

1. All subprograms in a module must be identified in their internal documentation as belonging to the module.
2. Each interface subprogram must be explicitly identified as such in its internal documentation.
3. Each interface subprogram must contain a master list showing the identities and purposes of every subprogram in the module.
4. Each interface subprogram must be named in the internal documentation of every subprogram in the module.

G. Examples of modules include:

1. An input subprogram and its subordinate subprograms.
2. The subprograms comprising a consolidated phenomenological model.
3. A data manipulation subprogram, with subordinate subprograms performing calculations of data on the grid.

H. Subprograms and modules are fundamentally different; what is central to one may be inappropriate to the other. A subprogram performs a single task, whereas a module collects several tasks together which share the support of a data structure, and which hide the data structure from the external environment. While a single interface is good structure for a subprogram, it does not necessarily promote sound programming for a module. A module should have a separate subprogram interface for each operation on the data structure; each interface subprogram should have an argument list that corresponds to the information needed to perform the task on the data structure.

3.6 STRUCTURED STYLE

One of the fundamental elements of well-written code is the application of a structured style to the complete program, to each subprogram, and to each module (Ref. 31).

A. Structured style applies to the complete program.

1. Good structure is the key to both a well-organized program and a program that can be easily adapted to solve new problems (Ref. 31). Changes to a program should only require modifications to the executive and the addition of new subprograms and modules. It is widely agreed that logically partitioned FORTRAN programs minimize code errors and execution failures (Refs. 4 and 6).
2. The schematic of a program is illustrated in Fig. 1. Each computer program must be organized into separate sections:
   a. executive,
   b. input,
   c. computations,
   d. output,
   e. error exit if needed, and
   f. data structure definition, if needed.
3. This overall structure consolidates related tasks. Modifications and incorporation of new computational models are readily integrated into these sections.

B. Structured style applies to each subprogram.

1. Good structure allows a subprogram to be written independently of other subprograms, and allows subprograms to be modified or replaced quickly, easily, and reliably (Ref. 2).
2. Each subprogram must have a single purpose so that program modifications are usually limited to changes in the executive and to the replacement or addition of individual subprograms.

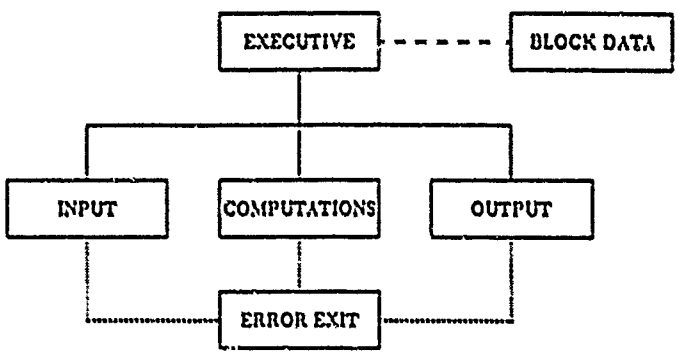


Figure 1. Schematic of a computer program. Error exit subprograms may be called as necessary from any subprogram.

3. The inputs and outputs of each subprogram must be well-defined with clear and specific interfaces (Refs. 17–19).

C. Structured style applies to each module.

1. A module should be written independently of other modules, and should be written so that it can be modified or replaced quickly, easily, and reliably (Ref. 2).
2. Each module must have a primary purpose so that program modifications are usually limited to changes in the executive and to the replacement or addition of modules.
3. The inputs and outputs of each module must be well-defined with clear and specific interfaces through one or more interface subprograms (Refs. 17–19).
4. Data structures within a module must be isolated from the external environment.

4 PROGRAM ORGANIZATION

4.1 EXECUTIVE CONTROL

A. The executive is the program controller. The executive is a logic and flow director only.

B. It writes the program name, version number, version date, current time, and date to the primary output text file.

C. It directs the reading of the input, directs the computations, writes appropriate periodic progress messages, and directs the writing of the final output.

D. The primary purpose of the executive is to orchestrate the logic. All nontrivial computations are done in subordinate subprograms. The executive is limited to administrative computations necessary for orchestration.

4.2 INPUT PRACTICES

A. The reading of user-specified data from any source must be controlled by an input subprogram or module.

1. It may read all the user-defined data directly or be an input master subprogram that directs other subordinate subprograms to read or process input data.
2. Input data must be read only in input subprograms, not anywhere else in the program.

B. Keyword-driven input is encouraged (Ref. 21). (Keyword-driven input is similar to table-driven (Ref. 19) and name-directed (Ref. 21) input. This input form is substantively different from NAMELIST, which is forbidden.

1. Keyword-driven input increases readability of input files, and minimizes order-of-input errors (Ref. 21).
2. The objectives for keyword-driven input are (Ref. 21):

   Clarity: minimize user confusion,

   Conciseness: minimize useless verbiage,

   Organization: maximize proximity of related information,

   Flexibility: minimize artificial limitations, and

   Ease of Use/Learning: minimize inconvenience or time to learn.

C. Fixed-field input is acceptable. Human engineering of all formatted input data files is critically important. Fields of five or multiples of five must be used. Such formatting improves readability.

D. Completely free-field input is discouraged except to implement keyword-driven input. Free-field means the input stream has no predefined column positions where information is to be placed.

E. Specification of input options with numbers is forbidden; use mnemonic keywords.

F. Nonsensical or out-of-range values are forbidden as input options or control flags. Example: Do not use the negative component of −10 as a control option for a variable that must be nonnegative to be correct.

G. Each user-defined input record must be written to an appropriate output file (echo printed) immediately following the READ statement for that record. This echo print must identify the record and all the data fields on the record (Refs. 7 and 19). A string of markers above or beneath an output line or page should be used to assist in determining the columns of each field.

H. Default values should be assigned whenever possible by the input subprograms to user-defined input variables when a value is not specified by the user (Ref. 7). Where it is reasonable to assign default values, blank fields must be used to set them. Default values must be identified and written out to the output file with the echo print immediately following the READ statement for that record.

I. Input values which are critical (have no reasonable default) must be explicitly checked as specified in the following paragraph. Such values must be identified in the internal and external documentation. Nonentry of a critical value must be treated as bad input data.

J. All input data must be checked for unreasonableness, inconsistencies, and out-of-range values (Refs. 7, 19, 27, and 31). As a minimum, exhaustive error checking of all input data against the entire permissible range of values is mandatory. If bad input data are discovered, descriptive error messages must be written in sufficient detail to locate and identify the problem.

K. If one or more fatal input errors are detected, scanning of input data should continue as far as possible, issuing error messages as problems are detected. After scanning of input data for errors has proceeded as far as practical, execution must stop or be aborted.

L. Entering the same datum more than once is forbidden (e.g., the density of aluminum must not be entered more than once).

M. Conceptually similar input data should be grouped together.

N. Changes of engineering units (e.g., inches to centimeters) should be made in input subprograms, and should be done as soon as practical after associated READ statements.

O. The reading of input should be terminated by an end-of-file or a marker (Refs. 7 and 19). Termination by predetermined count is discouraged (Ref. 19).

P. The END option in a READ statement must be used to preclude an abort due to a premature end-of-file on the input data stream (Ref. 19). The ERR option in a READ statement must be used to detect bad data (but this check alone is not sufficient input validation). The IOSTAT= read option may be used in lieu of the END= and ERR= options in cases where it is desirable to do error checking after the read, rather than to execute a simple branch.

4.3 COMPUTATIONAL SUBPROGRAMS

A. The computational subprograms (FUNCTIONs and SUBROUTINEs) must perform all nontrivial calculations.

B. Each computational subprogram must either initialize or define at first use all variables internal to the subprogram (Ref. 7).

C. Temporary scratch files may be written and used as necessary in any computational subprogram.

4.4 OUTPUT SUBPROGRAMS

A. All final, summary output must be written in output SUBROUTINEs. Intermediate printing in computational subprograms is permitted only when necessary for diagnostic output.

B. Interim, diagnostic output may be written as needed as specified in Section 4.1, Standards B and C on page 7, and Section 4.2, Standard G on page 8.

C. All output text and graphical data must be clearly defined and explicitly labeled. The output pages should each provide sufficient explanation of their content. When necessary for full understanding, output must be preceded by a page which explains in detail the output appearing on the following page or pages. Engineering units must be associated with all output numbers and graph axes.

D. A scale factor of 1 must be used with all printed output which uses the "Ew.d" format field descriptor (i.e., the digit printed to the left of the decimal point must be nonzero as in "1.2345E+12," rather than "0.1234E+13"). Note that a scale factor applies to all subsequent fields in the FORMAT statement. If a "1PEw.d" precedes a "Fw.d" specification, the "F" specification must be changed to "0PFw.d" to obtain the desired "F" specification output.

4.5 ERROR EXIT SUBPROGRAMS

A. Error exit subprograms are not required, but may be used to perform error analysis, error reporting, and final cleanup prior to abnormal program termination.

B. When used, error exit subprograms must immediately precede any BLOCK DATA subprograms, or must be the last subprograms if BLOCK DATA subprograms are not used.

4.6 BLOCK DATA PLACEMENT

When used, BLOCK DATA must be at the end of a module or program. All BLOCK DATA must be named.

5 DOCUMENTATION

5.1 EXTERNAL DOCUMENTATION

Each program must be fully documented. Documentation equivalent to the *American National Standard Guidelines for the Documentation of Digital Computer Programs* is recommended (Ref. 12). Documentation must include: (1) the computer program abstract; (2) application information (user's manual); (3) problem or function definition; (4) program design information; and (5) sample problems (refer to Section 6.13, Standard G on page 28).

5.2 INTERNAL DOCUMENTATION

The following internal documentation requirements apply to the executive and all subprograms. In addition to external documentation, complete and detailed comments must

be interspersed within the code itself (Refs. 14 and 31). Subprograms using nonANSI FORTRAN-77 must be specifically identified in their preamble (refer to Section 0, page 30).

5.2.1 Preamble documentation – The beginning of the executive and each subprogram must have a standard comment section that fully describes the coding and specifies all information that passes into or out of it (Ref. 19). This preamble begins with the first line below the name and ends with the line just prior to the first noncomment statement (normally a PARAMETER statement). The following general rules apply to all preambles:

A. Correct grammatical style and punctuation will be used throughout the preamble.

B. Abbreviations will be limited to those defined within the preamble except for the standard units abbreviations.

C. Every line of the preamble will have a 'C' in column 1, except blank comment lines.

D. The major headings Purpose, Input, Output, etc., will start in column five and all additional indentations are moved to the right at multiples of 5 spaces.

The order and format of the preamble is specified to insure uniformity of content and appearance. The content and order of the information in the preamble changes slightly for the program executive, an ordinary subprogram, or an input subprogram.

5.2.1.1 Executive preamble – The following information in the sequence specified will appear in each program executive:

A. The description of the program. Included in the description will be a statement of purpose, an outline of the method used, a description of the known limitations of the program, and a brief summary of the input and output data.

B. The version number and its date.

C. The name, organization, address and phone number of the programmer.

D. A list of all files used by the program. The list will include a brief description of the file type, structure, and contents.

E. A list and one line description of each subprogram called by the executive.

F. An alphabetized list with full descriptions (including units) of all local variables used in the executive.

G. A list of references used in the program.

See Appendix B for an example of an executive preamble.

5.2.1.2 Subprogram preamble – The following information in the sequence specified will appear in each subprogram:

A. A statement of subprogram purpose.

B. The version number and its date. Revisions to the initial version must include a brief summary of each change, who modified the subprogram, and the date of modification.

C. The name, organization, address, and phone number of the programmer.

D. A list of files used and a brief description of the file type, structure, and contents.

E. A list and one line description of each subprogram required by the subprogram.

F. An alphabetized list and full descriptions (including units) of all local variables.

G. A list of references used to develop the subprogram.

H. An alphabetized list and full descriptions (including units) of all input variables from all sources.

I. An alphabetized list and full descriptions (including units) of all output variables.

J. If a commercial software or system utility is used, a statement warning the user of its use is placed here. Identify the I/O units used by the package or utility, if known.

K. An alphabetized list and full description of all special constants.

Optional information that can be included in the preamble is a statement of method which would be placed immediately after the purpose. Notes may be placed anywhere if they are needed to highlight some unusual feature or provide additional information. See Appendix C for an example of a subprogram preamble.

5.2.1.3 Input subprogram preamble – Input subprograms have some documentation requirements in addition to the requirements in Section 5.2.1.2. The following information must appear in the places specified:

A. A description of each input record must be given after the output variable list. The information must include the variable name, the columns or field location, the format and full description. The description must include the input engineering units, range of allowable values, and program default values, if any.

B. If more than one record is read by the subprogram, then the number and types of records that can be read must be summarized. This information will be placed just following the description of the input records.

See Appendix D for a brief example of an input subprogram preamble.

5.2.2 Comment form, style, and placement – Commenting uniformity eases the tasks of reading and understanding the code.

A. Comments must provide additional information not easily found in the code itself (Ref. 7). Describe the intent of a segment of code; do not merely restate the code (Ref. 19).

B. Comments containing information (i.e., other than blank separater lines) must equal at least twenty percent of the total number of executable statements in the subprogram. Each subprogram must meet this requirement. This minimum percentage is intended to insure that the internal code documentation is adequate to explain the variables, clarify the logic, and summarize what the code is trying to accomplish.

C. More than 15 consecutive FORTRAN executable statements are forbidden without at least one informative comment. Meaningful sections of code should be shorter than 10 to 15 executable statements (Ref. 19).

D. Comments must be written simultaneously with the code, not after coding has been completed. When coding is changed, the comments must be modified simultaneously. Simultaneous commenting has been shown to produce more complete and accurate internal documentation (Refs. 9, 23, and 28).

E. Comments must always precede, not follow, the code being described. All comments must appear between the PROGRAM, BLOCK DATA, FUNCTION or SUBROUTINE statement, and the associated END statement.

F. Comments which appear before the executable portion of each subprogram must begin in column 5. Comments which follow the preamble and are interspersed with executable code must be indented; these indented comments must begin in column 20 (Ref. 19). Further indenting is permitted occasionally when it improves clarity.

G. To improve visual clarity, blank lines must preceed and follow a block of one or more informative comments.

H. Comments must not be bordered in any way by lines or columns of characters. Drawing boxes around comments is forbidden.

I. Inserting comments between the continuation lines of nonexecutable or executable statements is forbidden.

J. Identical comments which describe the contents of a COMMON block must immediately precede that block every time it appears. Each COMMON block variable must be described in order of appearance. (Refer to Section 6.10, Standard H on page 26.)

K. Identical comments which describe the contents of a PARAMETER statement must immediately precede that statement every time it appears.

L. Comments must use mixed upper- and lower-case letters.

1. Only printable US ASCII characters (refer to Appendix E) may be used in comments and CHARACTER strings.
2. Correct sentence structure and grammatical style should be used.
3. The imperative form of a sentence may be used.
4. Phrases may be used only when their meaning is absolutely clear (sentences are preferred).

6 ROBUST PRINCIPLES AND IMPLEMENTATION

All subprograms must be written employing robust principles. A robust subprogram does not fail under any circumstances. Defensive coding must always be used because it helps achieve this objective (Ref. 7). Many proven techniques that lessen the probability of a failure are summarized below.

6.1 CODE STRUCTURE

A. A PROGRAM statement must be the first statement in an executive, and therefore must be the first statement in any program.

B. Each subprogram must have a single entry located only at the first executable statement.

C. Each subprogram should have only a single exit located at the end of its executable statements (Ref. 6). Exceptions are permitted only to eliminate a branch to the exit and improve clarity. However, when a subprogram needs statements which are guaranteed to execute whenever the subprogram exits, then a single exit is mandatory.

D. A subprogram should be short, consistent with the process being performed. Subprograms with more than 100 executable statements are discouraged (Ref. 6). More than 200 executable statements are forbidden. (Comments, FORMATs, and DATA definitions are automatically excluded because they are not executable statements. COMMON blocks and type, PARAMETER, and DIMENSION declarations are not executable and are excluded as well.) Long subprograms tend to be disproportionately more complex (Ref. 17).

E. Decisions made at one level of a software structure frequently have an effect on other levels (Ref. 6).

1. If a subprogram references a subordinate subprogram, then the subordinate subprogram is within the span-of-control of the first.

2. If a decision made within the first subprogram directly affects a process within the second, then the second subprogram is within the scope-of-effect of the first (Ref. 6).
3. The direct span-of-control of a subprogram is itself and all directly subordinate subprograms.
   a. In Fig. 2, Subprograms D, G, and H are in the direct span-of-control of Subprogram D.
   b. Subprogram K is within the indirect span-of-control of Subprogram D, and in the direct span-of-control of Subprogram G.
   c. Subprograms I, J, and K are basic subprograms.
   d. Subprogram J is a general purpose subprogram which may be called from any hierarchical level.
   e. Subprograms D, G, H, and K constitute a module, with Subprogram D as the interface.
   f. Coupling between modules employing local COMMON blocks is forbidden. For example, Subprogram G is within a module; it must not be linked laterally to Subprogram F by a local COMMON block (refer to Appendix A).
4. Subprograms should be designed so that their indirect span-of-control is minimized. A strictly-linear deeply-descending hierarchy of subprograms is generally poor. A shallow parallel structure is recommended.
5. A subprogram must not directly reference more than nine different subordinate subprograms; thus, the direct span-of-control must not exceed nine (excluding intrinsic FUNCTIONs and general-purpose system library subprograms) (Ref. 13).

F. The general flow of any subprogram must be downward from the entry to an exit (Ref. 6), except for the DO, and the equivalent FORTRAN implementation of DO WHILE (Ref. 20), REPEAT UNTIL, and LOOP LEAVE AGAIN (Ref. 22) constructs (see Appendix F).

G. The action clauses of any control structure (looping constructs, CASE structures,* and IF-THEN-ELSE statements) must be indented to provide better readability (Refs. 6 and 19).
   1. The code must be indented to reflect the nesting levels.
   2. Each nest must be indented three columns to the right of those at the previous nesting level.
   3. All code within the same level of nesting must start in the same column.

H. The END statement must not be used in lieu of a RETURN statement. A RETURN statement is always required.

*Refer to Appendix G for additional information on the CASE structure and repetitive ELSEIF use.

I. If a statement does not need a label, it is forbidden to have one. A statement needs a label only when it is referenced by another statement.

J. All [illegible]cation statements must appear before the first executable statement and must [illegible]e any statement FUNCTION definitions.

K. All statement FUNCTIONs must immediately precede the first executable statement in each subprogram and must be preceded by comments which describe the purpose of the statement FUNCTION, the arguments accepted and the results produced.

L. All statement labels must begin with at least the number 10 and be left justified in column 2. These numbers must be in ascending order within each subprogram (Ref. 6).

M. FORMAT statements must be grouped at the end of each subprogram immediately preceding the END statement. FORMAT statement labels must begin with at least 100, must be in ascending order (Ref. 6), and must be larger than the preceding executable statement label.

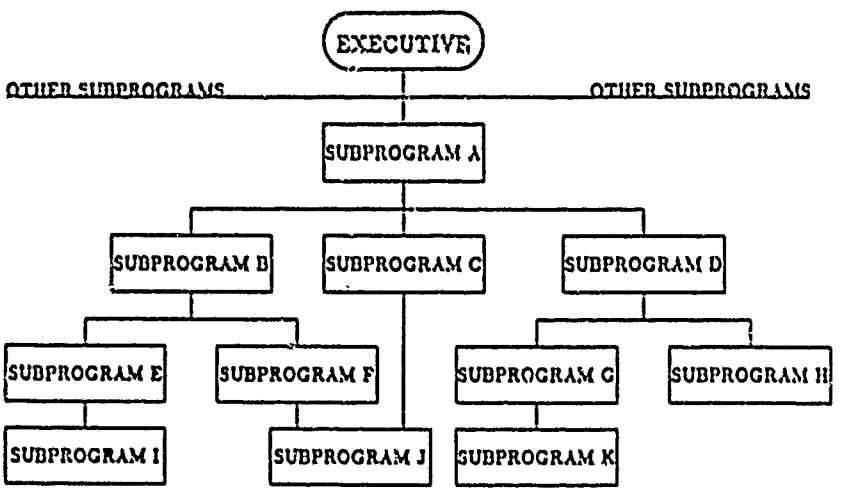


Figure 2. Subprogram hierarchy example (Ref. 6).

N. Continuation lines are permitted.

1. The maximum number of continuation lines for an executable FORTRAN statement is nine (Ref. 6).
2. Continuation lines for executable statements must be sequentially numbered in column 6 with integers sequenced from 1 through 9.
3. Continuation lines for nonexecutable statements must be sequentially numbered in column 6 with integers sequenced from 1 through 9, then with sequential letters of the alphabet beginning with A in column 6 for continuations longer than nine lines.
4. All continuations must have a blank in column 7, with the sole exception of FORMAT statements.

O. Long statements should be organized into short and easily understood sections. Statements with more than five simple sections are generally difficult to understand, and increase the probability of introducing misplaced parentheses and unintended operations (Ref. 19).

6.2 GENERAL RULES

A. Logical correctness, functional reliability, and good architecture are much more important than execution speed.

1. Coding must not be made complex to increase speed. Such efforts frequently introduce errors while also producing coding which is incomprehensible to other programmers (Refs. 7, 9, and 19).
2. Efficiency is usually determined by the algorithm chosen rather than by how compactly it is coded (Ref. 7).

B. Deeply nested statements produce obscure code. Multiple nesting should be used with great care, and only when multiple nesting will produce well-structured code.

1. Triply or deeper nested "IF-THEN-ELSE" statements are discouraged (Ref. 6).
2. Many repetitive ELSEIF clauses with lengthy blocks and inadequate comments produce obscure code and are discouraged.
3. A few well-documented repetitive ELSEIF clauses with short blocks (simulating the Pascal language CASE statement) produce understandable code and are encouraged. Each ELSEIF clause must be preceded by informative comments.

C. Error checking code must be permanently incorporated (Ref. 19). All error messages must be descriptive, grammatically correct, and concisely written.

D. Each program must be written to minimize requirements on the computer operator such as punched card handling, magnetic tape mounting and dismounting, restarting after programmed PAUSE, and so forth (Ref. 21).

E. The PAUSE statement may not be used unless it is absolutely essential for the correct operation of the program (Refs. 6 and 21). All such PAUSE statements must be fully documented with complete operating instructions.

F. All FORTRAN code must be in upper-case letters (Ref. 1), except for CHARACTER data and comments.

G. CHARACTER data may contain mixed upper and lower case (Ref. 3), and upper and lower case use is recommended for general text output.

H. Engineering units must be the same throughout the program, and are permitted to be changed *only* immediately after input or immediately before output. This consistency minimizes the probability of inadvertently using incorrect units in a computation.

I. Unsatisfied externals are not permitted in executable code. Stub subprograms (dummy subprograms which merely return sample values rather than calculated results) may be used, if necessary, to satisfy externals during code development.

6.3 DATA INITIALIZATION

A. Floating point and integer constants which have physical, mathematical, or engineering significance (e.g., Avogadro's number "N" and the speed of light "c") should not appear explicitly in the executable code (Ref. 6).

   1. These constants should be defined using PARAMETER names and their description provided in comments prior to the PARAMETER statement. Names for these constants must be descriptive.
   2. Unitless, simple mathematical floating point values (such as 0.5, 2.0, 3.5, 10.0, 50.0, etc.) usually do not require any additional description and should appear directly in the executable code.
   3. Integer values should appear directly in the executable code rather than in a defined constant (refer to Standard C of this section and Standard A of Section 6.5, page 21).
   4. Any irrational number (e.g., "π" and the base of natural logarithms "e") must be defined with at least 10 significant digits using a PARAMETER statement. Computer system constraints rather than the programmer should limit precision.

B. When a scalar variable represents a nonchanging value, the variable must be preset in a PARAMETER statement rather than by executable code (Ref. 7).

1. Other variables should be initialized through the use of executable code (Refs. 7 and 9); however, reasonable exceptions exist (such as the initialization of counters).
2. Only one version of a PARAMETER statement may be maintained. Each PARAMETER statement and the associated comments used in more than one subprogram must be inserted automatically into each applicable subprogram (Ref. 6). This capability exists on many computer systems using features such as UPDATE, HISTORIAN, or the INCLUDE statement (Ref. 20). PARAMETER statements used only in a single subprogram may be defined explicitly in that subprogram.

C. PARAMETER names must be used to set all array dimensions. When arrays are in COMMON blocks, explicit PARAMETER statements must be used. All references to array bounds must use the PARAMETER name and not a literal constant. This requirement does not extend to object-time dimensioning. Using the same PARAMETER name to set more than one dimension is forbidden unless the dimensions are logically related and will always be identical.

6.4 ARITHMETIC OPERATIONS

A. Parenthesize to avoid ambiguity (Refs. 7 and 19). Do not rely on an assumed evaluation order for arithmetic expressions. In all arithmetic expressions, parentheses must be used to define the proper order of evaluation. For example, the following ambiguous statement: A=B/C/D should be either A=(B/C)/D or A=B/(C/D). A better form would replace one of the divisions by a multiplication.

B. Expressions involving successive exponentiations (such as A**B**C) must be explicitly parenthesized to show order of evaluation (Ref. 19). The evaluation order is clarified by parentheses (e.g., A**(B**C)).

C. Whole numbers used as exponents should be integer constants or integer variables (Ref. 6).

D. Mixed mode arithmetic statements are discouraged (Ref. 6). Mixed mode assignments or arithmetic expressions are allowed only with the explicit use of type conversion FUNCTIONs (e.g., INT(X), FLOAT(N), DBLE(X)) (Ref. 6). Integer exponentiation is not considered mixed mode arithmetic.

E. When an operation is performed that has a restricted domain, the validity of the operation must be checked before the operation is executed (Ref. 19). Some operations with restricted domains are:

1. Division – Check every denominator for a zero or near-zero value.
2. Square Root – Make sure the argument is nonnegative.

3. Log or Ln FUNCTIONs – Make sure the argument is greater than zero.

4. Arcsine or Arccosine – Make sure the absolute value of the argument is less than or equal to one.

5. Arctan2 – Make sure that the arguments are not both zero.

However, identical redundant checking is not necessary. If an invalid argument is detected, an error message must be printed out.

F. Testing whether one computed floating point value is exactly equal to another is very risky (Ref. 7). All floating point tests for equality of computed variables must incorporate a test accuracy tolerance whose value is limited by the unit roundoff of the target computer.

G. Subtraction of nearly equal floating point numbers should be avoided. Restructure the computations or use double-precision coding in this situation. Quite often the problem can be avoided by finding an alternate expression for the desired quantity. For example, the expression for the floating point quantity

$$A = 1.0 - \mathrm{COS}(X)$$

is given in better computational form by

$$A = 2.0 * (\mathrm{SIN}(0.5 * X)) * *2$$

The two expressions are identical in a mathematical sense, but if X is close to zero the second expression is better suited for use on a computer. Another example is

$$A = \sqrt{1.0 + X} - \sqrt{1.0 - X}$$

which is very unstable as X approaches zero, but

$$A = \frac{2.0 * X}{\sqrt{1.0 + X} + \sqrt{1.0 - X}}$$

is mathematically equivalent and avoids the numerical problem as X approaches zero. In both examples the prefered expression is more complex in appearance than the original expression. Therefore, the reason for using the more complex expression must be carefully explained in comments.

H. When using an intrinsic function, use its generic name. Generic names simplify the referencing of intrinsic functions, because the same function name may be used with more than one type of argument. For example, DSQRT(X) requires the argument X to be a double precision number. If, however, SQRT(X) is used (the generic form of the square root function) the argument may be either single or double precision and the result will be the same type as the argument.

6.5 GENERAL INPUT/OUTPUT GUIDANCE

A. Unit numbers for input, output, and scratch files should be designated by a PARAMETER constant (Ref. 6); however, an integer variable is permitted if more prudent. An integer constant must not be used.

B. All files must be explicitly opened and closed.

1. A list of files with a brief description of the exact structure and contents of each file must be included in the comments section at the beginning of the executive.
2. An OPEN statement allows the programmer to explicitly define the status of a file when it is opened and to take action if an expected file does not exist. A file should not be opened at the beginning of the program and left open until the end of the program. A file should be closed immediately when no more data are to be read from or written to it.

C. All input/output statements must be coded using READ and WRITE statements.

1. All READ or WRITE statements must contain unit numbers. The unit to be read from or written to must not be expressed as a numeric integer constant, but must use the same PARAMETER constant or integer variable which opened that unit.
2. Each READ and WRITE statement must be internally documented and explained; the documentation must summarize the purpose of the READ or WRITE statement.

D. Unformatted input or output is encouraged for very large data files, all scratch files, and restart files (refer to Section 8.2, page 29); it is prohibited for all other files. The FORMAT translation that takes place in writing and reading formatted scratch files can needlessly consume significant amounts of computer time. In addition, some accuracy is always lost in the formatting process which is not lost in unformatted input or output.

6.6 DO LOOPS

A. Each DO loop must end solely on a unique CONTINUE statement used only for that loop. Unique CONTINUE statements must be used as terminal statements for DO loops to clearly mark the end of the loop (in a manner identical to the nonstandard END DO construct) (Refs. 19 and 20).

B. The initial and terminal parameters of a DO loop must be explicitly checked or coded to assure that array dimensions will not be exceeded if an array is referenced within the loop.

6.7 BRANCHING

A. Programming logic should be straightforward, orderly, and should use simple logic.

B. Branching should be held to a minimum (Ref. 31).

1. Particular care must be paid to the necessity and appropriateness of each branching statement.
2. Each branching statement must be internally documented and explained; the documentation must summarize the purpose of the branch.
3. It is sufficient to group a conditional statement with the executable statements it controls and document the combined code segment once. The conditional test and branch statement does not need to be documented separately from the code which it controls.

C. Branching into any loop or control structure is forbidden.

D. Backward transfers are restricted to the equivalent FORTRAN implementation of DO WHILE (Ref. 20), and REPEAT UNTIL and LOOP LEAVE AGAIN constructs (Ref. 22) (refer to Appendix F). All other backwards branching is forbidden.

E. GO TO statements are discouraged; if used, the jump must be downward (Ref. 19), with the exceptions of the DO WHILE, REPEAT UNTIL, and LOOP LEAVE AGAIN constructs. GO TO branching statements usually produce obscure code (Refs. 7, 14, 18, and 19).

F. Every computed GO TO statement must be followed immediately by an unconditional STOP that locates and identifies the computed GO TO statement and prints the index value for which the computed GO TO failed.

G. The logical IF should be used instead of the arithmetic IF (Refs. 7, 19, and 21). The logical IF is understood more quickly and easily than the arithmetic IF.

H. Parenthesize to avoid ambiguity (Refs. 7 and 19). Do not rely on an assumed evaluation order for logical expressions.

6.8 VARIABLE NAMES, TYPES, AND USE

A. Variable names convey useful information when carefully selected (Refs. 10, 14, and 19).

1. The names of all variables, PARAMETERs, and COMMON blocks should be words or obvious truncations of words that mnemonically relate to the primary purpose of the variable, parameter, and common block. For example, an appropriate variable name for the speed of a moving object could be "SPEED." Inappropriate names would be "XYZ" or "EED" or "SP" because these examples have no obvious and apparent mnemonic relationship to speed.

2. Long (6-character maximum) variable names should be used.

3. Using the first letter of each word in a phrase to form a variable name is forbidden unless it constitutes an accepted acronym.

4. Using the numerals 0 (zero) or 1 (one) in variable names is discouraged. These numerals are easily confused with the alphabetic characters "O" and "I" in upper case on many output devices (Refs. 10 and 18).

5. FORTRAN-77 symbolic names must be different from FORTRAN-77 keywords.

B. Only one type declaration is allowed for any constant or variable name (Ref. 6).

C. The FORTRAN-77 default implicit declaration for REAL and INTEGER variable names, PARAMETER names, and nongeneric FUNCTION names must be used.

1. FORTRAN-77 implicitly assigns integer values to such names beginning with I through N; otherwise real values are assigned. Adhering to this convention greatly facilitates debugging and decreases the probability of confusing REAL and INTEGER types.

2. Meaningful variable names can usually be found within the FORTRAN implicit declaration constraint. Otherwise the leading letter "I" (for integer) or "R" (for real) is recommended as a prefix.

3. The flexibility of explicitly declaring variable names does not outweigh the subsequent disadvantages. Several modern high-level languages require that all variables be declared explicitly, but this flexibility requires a programmer to remember a large number of variable declarations or repeatedly search out the declaration of each variable in every subprogram. This unnecessarily complicates modification and debugging tasks by seriously hampering immediate understanding of a variable declaration. Constantly looking up variable declarations is usually unrelated to the immediate programming task and has a detrimental effect. Using the FORTRAN implicit declaration makes it much easier to remember those variables that are explicitly declared since they are usually few in number.

4. Adherence to the FORTRAN-77 implicit declaration is required by this standard. Explicit declaration of variables (and PARAMETERS) within the convention is needlessly redundant and is forbidden. Unlike FORTRAN, most modern procedural languages (including Ada, Jovial-J73, Pascal, and Modula-2) require explicit declaration of entities before they may be used. This mandatory declaration produces reliable code in other languages by allowing the compiler to perform extensive error checking at compile time and catch some programming errors that otherwise are often obscure. These concepts are recognized as useful in other languages, but are not to be applied because of the advantage provided by FORTRAN in this situation. This class of error will be minimized by adherence to Section 6.4, Standard A, page 19; Section 6.9, Standards B

and C, page 24; Section 6.10, Standards D, E and C, page 26; Section 6.13, Standards B, C, D, and G, pages 27 and 28; and Section 8.1, page 29.

D. The integer variable names I, J, K, L, M, and N must be used only as loop indices, counters, or subscripts.

E. A flag is a variable which can have only two possible values (e.g., 0 or 1). It is used to direct the flow of control.

1. INTEGER or REAL flags are discouraged. Use true or false LOGICAL variables with mnemonically meaningful names instead. The mnemonic content of the name should assert the meaning of the "true" logical value.
2. Multiple flags should only be used in a subprogram to clarify and consolidate the logic which controls the computation into clearly defined conditions. The number of flags is an indicator of the number of logical conditions significant to the computation.

F. Temporary variables are discouraged (Ref. 7). They are usually unnecessary and complicate the code (Ref. 19). Most modern optimizing compilers recognize common subexpressions and optimize them automatically.

1. Using a temporary variable to increase execution speed while simultaneously obscuring the coding is forbidden.
2. When temporary variables are used, they should express physical or mathematical relations and should be meaningful quantities having a mnemonic name or a name reflecting standard notation.
3. All temporary variables must be commented.
4. Temporary variables must be assigned before, and in close proximity to, the coding which first uses them.

6.9 COMMUNICATIONS VIA ARGUMENTS

A. A subprogram must always be called with the full set of arguments (Refs. 18 and 19).

B. Variable names must be identical when passed to or from subprograms (Refs. 19 and 31), with the exception of variable names in statement FUNCTIONs and general-purpose or library subprograms. Exempted general-purpose subprograms include but are not limited to interpolation, root-finding, numerical integration, equation-solving, and graphics subprograms.

C. Arguments (also called actual parameters) must be variable names, FUNCTIONs, or simple expressions.

1. Explicit numeric constants must not appear as arguments (Ref. 19). This constraint defends against inadvertently changing the value of a literal constant. Errors in which subprogram values are changed improperly can be detected more easily when numeric constants are names which can be examined by ordinary debugging techniques.
2. If an expression is used as an argument, it must be simple. A simple argument must not contain more than four arithmetic, logical, relational, or character operators (Ref. 6).

D. FUNCTION names appearing as arguments must be listed in an EXTERNAL or INTRINSIC statement (Ref. 19).

E. With one exception, FUNCTIONs must return results only through the normal value of the FUNCTION. A FUNCTION which alters the values of the calling arguments is forbidden; SUBROUTINEs must be used for that purpose (Ref. 19). The exception is a FUNCTION used solely to implement keyword-driven input.

6.10 COMMON BLOCKS

A. COMMON blocks must be carefully defined and strictly controlled to reduce coupling between subprograms (Ref. 6), and to minimize span-of-control/scope-of-effect conflicts (Ref. 18) (refer to Section 6.1, Standard E, page 14).

1. The primary method of providing access to arrays and variables is through argument lists.
2. The secondary method of providing access is through labeled COMMON blocks, whose scope is severely restricted (Ref. 6).
3. COMMON blocks may be either local or global.
   a. A local COMMON block may be used only within a module. Once a value is set in a COMMON block it may not be changed unless it is a local COMMON block confined to a module, as defined in Section 3.5, page 4.
   b. A global COMMON block may be used anywhere in a program but only within specified constraints.
      (1) Globally applied COMMON blocks are permitted to carry only unchanging quantities into subprograms. Global COMMON blocks must not transfer variables out of a subprogram that have been modified or altered in that subprogram, except for the initialization of the COMMON block. Data stored in a globally applied COMMON block must not be subsequently modified.
      (2) Globally applied COMMON blocks must be loaded by means of either DATA statements in BLOCK DATA, by reading a data file at the beginning of program execution, or by a one-time calculation.

B. Undisciplined COMMON usage makes a program hard to understand (Ref. 10). Variables should be transferred to subprograms primarily via argument lists, not COMMON blocks.

C. Blank (unlabeled) COMMON is forbidden (Ref. 6), with the two rare exceptions in Section 10, Standard G, page 31.

D. COMMON blocks should not introduce extraneous variables into a subprogram (Ref. 18). The fact that a variable exists in a COMMON block does not justify including the entire COMMON block in a subprogram to access the individual variable.

E. COMMON blocks must be short and contain only information that is conceptually similar or related (Refs. 6 and 31).

F. All subscripted arrays in COMMON blocks must have their dimensions declared in the COMMON statement, rather than in another specification statement.

G. A COMMON block must be identical in each subprogram in which it appears (Refs. 15 and 19). This consistency must be assured by using the INCLUDE procedure explained below.

H. Only one version of a COMMON block may be maintained. Each COMMON block and the associated comments must be inserted automatically into each applicable subprogram (Ref. 6). This capability exists on many computer systems using features such as UPDATE, HISTORIAN, or the INCLUDE statement (Ref. 20).

I. The INCLUDE file defining a COMMON block loaded by BLOCK DATA must contain an "EXTERNAL name" statement, where "name" is the name of the BLOCK DATA subprogram. This declaration insures that if the COMMON block becomes part of a library, the BLOCK DATA subprogram is included in the program linkage if the COMMON block is referenced.

J. Variables in COMMON blocks should have at least three-letter names. I, J, K, L, M, and N are forbidden as COMMON block variables.

6.11 ARRAYS

A. Whenever array indices are used outside a region of strict index control (e.g., a DO LOOP with a fixed number of loops is a region of strict index control) the indices must be checked to verify that the maximum array bounds have not been exceeded. If the array bounds have been exceeded, the program must stop or abort with an abnormal termination message.

B. An array should have the same dimensions in all subprograms in which it is included. Changing the number or bounds of array dimensions between a subprogram and its subordinate subprograms is discouraged (Refs. 6 and 18).

C. When an array and its dimensions are passed to a subordinate subprogram as arguments, the array dimension must be checked prior to the call if the dimension has been obtained from a calculation. It should be validated again in the directly subordinate subprogram.

6.12 PROGRAM TERMINATION

A. Program terminations must use STOP statements or an abort subprogram.

1. CALL EXIT and END statements will not be used in lieu of STOP statements.
2. There must be only one normal STOP in any program. Normal termination must be in the executive and should say "NORMAL TERMINATION." All other terminations will be abnormal stops or aborts and must provide:
   a. where the error condition occurred, and
   b. the variable or condition that caused the termination.

B. An abort subprogram may be a system-specific subprogram used solely for the purpose of terminating abnormal program execution, such that a controlling job or command procedure is also aborted properly.

C. Failure of calculations not needed for essential computations, such as those being performed for auxiliary output, should not cause termination of the primary calculation if it can proceed legitimately. However, an error of this type must be diagnosed and an appropriate error message issued.

6.13 DEVELOPMENT PRACTICES AND PROGRAM TESTING

A. Well-tested, defensively-coded, machine-portable, documented library FUNCTIONs and general-purpose subprograms should be used (Refs. 7 and 31). Do not "reinvent the wheel."

B. Each subprogram must be meticulously checked by peer review (Refs. 15, 16, 19, 27, 28, and 31).

C. Each subprogram must be compiled and tested independently during development. Errors can then be traced quickly to specific subprograms (Ref. 3).

D. Each subprogram must be exhaustively tested by constructing driver programs that provide input and write the output from the subprogram being tested.

1. The driver program must construct sample input data sets for the subprogram being tested such that all paths are taken and all boundaries (geometrical, physical, or numerical) are used (Ref. 27).

2. Software tools such as static analyzers, test-case generators, and coverage analyzers must be used for this purpose (Ref. 25-27, and 29).

3. Plausible results are encouraging but do not by themselves constitute sufficient evidence of correctness.

E. Using supporting external and internal documentation, a typical programmer should be able to understand the logic and verify with execution tests that a subprogram works correctly for many representative test cases after evaluating it for less than one day.

F. After subprogram development, all subprograms in a module should be combined into a single file and compiled as a module. This procedure simplifies subprogram management by reducing the number of files, and allows global compiler optimization.

G. Each program must be tested (Refs. 27 and 31).

1. Test problems must include a complete set of input data, a complete listing of the output produced by the program when run with the test data, and a compiler listing and cross-reference map of the program itself.

2. These test problems serve to detect blatantly incorrect programs, but do not assure the general correctness of the program nor can they constitute a complete verification.

3. At least three different typical test problems must be run.

H. In order to demonstrate satisfactory machine compatibility performance of a developed program, test problems and the associated results must be furnished so that identical tests can be made on the target computer to demonstrate that the program operates successfully.

7 LISTING ORGANIZATION

The program may be listed in either of two formats. The first format is recommended.

A. The first listing format must be in the following order: executive, followed by all subprograms (except error exit SUBROUTINEs and BLOCK DATA) in alphabetical order, followed by error exit SUBROUTINEs, followed by BLOCK DATA.

B. The second listing format uses an order determined by considerations of logical coherence. In this case, the executive must still be listed first, and a list of all subprograms and modules in their order of appearance must be included in the comments at the beginning of the executive. Subprograms of a module should be listed together.

8 SYSTEM DEPENDENT CONSIDERATIONS

8.1 PROGRAM EXECUTION PRESET

Prior to program execution, the computer memory should be preset to a value which represents extreme conditions and which will terminate execution if the value is encountered during a calculation. For example, a preset of negative indefinite should be used on Control Data Corporation (CDC) systems.

A. Preset values of zero or unity do not meet this criterion and may not be used unless the computer system provides no suitable alternative.

B. Relying on a machine preset (such as zero) for variable initialization is forbidden. All variables requiring initialization must be preset in the FORTRAN program before they are referenced.

8.2 PROGRAM RESTART

A. Programs which typically run for many hours on the target machine should have a restart capability. These programs should periodically dump all essential data in some semi-permanent form for restarting the program, should a restart be necessary (refer to Section 6.5, Standard D, page 21).

B. Restartable programs must be capable of terminating and dumping all essential data using a method which minimizes, and if possible eliminates, interactions with the computer operator.

1. This method may be nonANSI standard and computer system dependent. For example, in the CDC environment, the sense switch is such a method.
2. In programs using extensive computations involving complex cycles or iterations, dumping of restart data may be deferred until the current cycle or iteration is complete.

8.3 COMPILER OPTIONS

A. When available, program flow error traceback should be activated.

B. If run-time array-bounds checking is available from the compiler, it must be used but is not a substitute for index checking.

9 NONSTANDARD PROGRAMMING

A. Computer code not in ANSI FORTRAN-77 may be used only when such coding is essential to the successful operation of the program, and either

1. no means whatever exist to write equivalent code in ANSI FORTRAN-77, or
2. nonstandard FORTRAN-77 code is specifically required by this standard.

B. Any nonstandard source code except for the INCLUDE (or its equivalent) must be isolated in separate subprograms. The subprogram interfaces must be built so that the nonstandard subprogram can be removed and replaced easily when the program is moved to another processor.

C. The INCLUDE (Ref. 20) or its equivalent is restricted to PARAMETER statements or COMMON block insertions with associated EXTERNAL statements, and to their associated and preamble documentation.

1. An example of required nonstandard coding is the mandatory use of the INCLUDE (or its equivalent) to standardize COMMON blocks and their associated documentation.
2. On a computer system without this capability, a FORTRAN preprocessor which accomplishes this task using the VAX FORTRAN INCLUDE statement format should be provided to support programs containing PARAMETER statements and COMMON blocks.
3. Compiled listings should be used for code development and debugging, rather than uncompiled source code. This procedure permits the effects of the INCLUDE or its equivalent to be evaluated easily by the programmer.

10 RESTRICTIONS ON FORTRAN-77

A. ASSIGN statements are forbidden (Ref. 21).

B. ENTRY statements are forbidden (Ref. 21).

C. EQUIVALENCE statements are forbidden (Refs. 6, 21, and 24).

1. EQUIVALENCE statements increase coupling between subprograms and increase the possibility of a span-of-control/scope-of-effect conflict (Ref. 18).
2. The primary application of EQUIVALENCE statements was to save memory by allowing multiple uses of the same space, but the storage benefit does not offset the increased risk of error.

D. RETURN statements which contain an argument are forbidden. This prohibition assures that a subprogram always returns control to the statement immediately following the CALL or FUNCTION reference which invoked that subprogram (Refs. 6 and 21).

E. PRINT statements are forbidden.

F. REAL and INTEGER statements are forbidden. Refer to Section 6.3, Standard C on page 23 for supporting rationale. This prohibition is recognized as different from the recommendation in Ref. 21; unfortunately, the trend toward mandatory strong declarations is in conflict with an inherent advantage of the FORTRAN-77 language.

G. BLANK COMMON is permitted only in two rare situations.

1. Some computer systems have the capability to adjust dynamically a program's main memory usage during execution. Sometimes this capability uses unique system methods in conjunction with BLANK COMMON. This nonstandard approach is discouraged and may be used only when absolutely necessary. This is one of only two times BLANK COMMON may ever be used.
2. The only other situation where BLANK COMMON may be used is when it is imbedded in a commercial software module.

H. CHARACTER variables, PARAMETERS, and comments should contain only printable US ASCII characters (refer to Appendix E).

REFERENCES

1. American National Standard Programming Language FORTRAN, ANSI X3.9-1978, American National Standards Institute, Inc., NY, 3 April 1978.

2. D. Parnas, "On the Criteria to be Used in Decomposing Systems Into Modules," Communications of the ACM, 15, p1053, 1972.

3. R. Gauthier, and S. Pont, Designing Systems Programs, Prentice-Hall, Englewood Cliffs, NJ, 1970.

4. R. House, "Comments on Program Specification and Testing," Communications of the ACM, 23, p324, 1980.

5. R. Smith, "Validation and Verification Study," in Structured Programming Series, Volume XV, produced under USAF contract F30602-74-C-0180, RADC, Griffiss AFB, NY, by the IBM Federal Systems Center, 1975.

6. Radar Set AN/FPS-118, Software Standards and Procedures Manual, produced under USAF contract F19628-82-C-0114, P.D.B. No. 316, Revision O, HQ ESD, Hanscom AFB, MA, by General Electric, Syracuse, NY, 31 March 1983. (This manual is very strict, and in many cases is more stringent than the standards of this report.)

7. B. Kernighan, and P. Plauger, The Elements of Programming Style, Second Edition, McGraw-Hill Book Company, NY, 1978. (This book is an exceptionally fine exposition of good programming practices.)

8. M. Jackson, Principles of Program Design, Academic Press, London, 1975.

9. E. Yourdon, Techniques of Program Structure and Design, Prentice-Hall, Inc., Englewood Cliffs, NJ, 1975. (Pages 292-294 contain an excellent summary of the most common programming bugs.)

10. ANS Standard Recommended Programming Practices to Facilitate the Interchange of Digital Computer Programs, ANS Standard 3-1971, American Nuclear Society, Hinsdale, IL, 1971.

11. Guidelines for Considering User Needs in Computer Program Development, AND-10, National Standards Association, Inc., Washington, DC, 1978.

12. American National Standard Guidelines for the Documentation of Digital Computer Programs, ANSI N413-1974, American National Standards Institute, Inc., NY, 1974.

13. N. Chapin, "Structure Analysis and Structured Design: An Overview," in Systems Analysis and Design, A Foundation for the 1980's, W. Cotterman, et al., eds., North Holland Publishing Company, NY, 1981.

14. N. Enger, "Classical and Structured Systems Life Cycle Phases and Documentation," in Systems Analysis and Design, A Foundation for the 1980's, W. Cotterman, et al., eds., North Holland Publishing Company, NY, 1981.

15. M. Connor, "Structured Analysis and Design Technique," in Systems Analysis and Design, A Foundation for the 1980's, W. Cotterman, et al., eds., North Holland Publishing Company, NY, 1981.

16. F. Baker, "Software Design or What Stands Between Requirements and Programs?" in Systems Analysis and Design, A Foundation for the 1980's, W. Cotterman, et al., eds., North Holland Publishing Company, NY, 1981.

17. V. Basili and B. Perricon, "Software Errors and Complexity: An Empirical Investigation," Communications of the ACM, 27, p42, 1984.

18. G. Berns, "Assessing Software Maintainability," Communications of the ACM, 27, p14, 1984.

19. C. Hughes, C. Pfleeger, and L. Rose, Advanced Programming Techniques—A Second Course in Programming Using FORTRAN, John Wiley & Sons, NY, 1978. (The first three chapters are particularly relevant to good programming style.)

20. Military Standard—FORTRAN, DOD Supplement to American National Standard X3.9-1978, MIL-STD-1753, 9 November 1978. (This supplement to FORTRAN-77 has been approved by the Department of Defense and contains recommended extensions to FORTRAN-77. It has not been made a part of this standard nor is any of it automatically incorporated into this standard.)

21. J. Wagener, "Status of Work Toward Revision of Programming Language FORTRAN," FORTEC Forum SigPlan Technical Committee on FORTRAN, Number 2, Ser. No. 8, June 1984.

22. E. Solonay, J. Bonar, and K. Ehrlich, "Cognitive Strategies and Looping Constructs: An Empirical Study," Communications of the ACM, 26, p853, 1983.

23. E. Horowitz, and S. Sahni, Fundamentals of Data Structures, Computer Science Press, Inc., Rockville, MD, 1983.

24. M. Metcalf, "Has FORTRAN a Future?," ACM FORTRAN Forum, 3, No. 3, p21, December 1984.

25. G. Berns, "MAT, A Static Analyzer of FORTRAN PROGRAMS and the Most Common FORTRAN Reliability Problems," Proceedings of the Digital Equipment Computer Users Society, p309, December 1984.

26. L. Gaby, II, ANALYZE, FORTRAN Program Analyzer Users Guide, Computer Sciences Corporation Report H&T-C-7021, Albuquerque, NM, May 1985.

27. S. Saib, "RXVP — Today and Tommorrow," in Software Validation, H. Hausen, ed., North Holland Publishing Company, NY, 1984.

28. A. Ackerman, "Software Inspections and the Industrial Production of Software," in Software Validation, H. Hausen, ed., North Holland Publishing Company, NY, 1984.

29. R. Buck, and J. Dobbins, "Application of Software Inspection Methodology in Design and Code," in Software Validation, H. Hausen, ed., North Holland Publishing Company, NY, 1984.

30. L. Osterweil, "Integrating the Testing, Analysis and Debugging of Programs," in Software Validation, H. Hausen, ed., North Holland Publishing Company, NY, 1984.

31. T. Bowen, G. Wigle, and J. Tsai, "Specification of Software Quality Attributes," RADC-TR-85-37, Vol. I, Vol. II., and Vol. III, RADC, Griffiss AFB, NY, February 1985.

APPENDIX A
MODULES AND COMMON BLOCK RESTRICTIONS

A primary consideration of this report is the treatment of structural content. Structural content limits or promotes good programming methodology and governs the ultimate form that programs are allowed to assume. This appendix discusses the problem with regard to COMMON blocks.

A powerful construct in the organization of programs is a modularity intermediate between the subprogram and the entire program. The separation of a large computational process into internally-related subprograms with a minimal external interface is recognized in this report. One condition of separability is the manipulation of a single data structure. Typically the subprograms outside of the module need interface only at the highest level and have no need to know any of the particulars of the data structure or how it is manipulated.

In general, the data structure may involve one or more arrays, indices into the arrays, status values, and other variables. The external environment never needs access to any of the particulars of the data structure in order to use it; all the outside process needs is a functional interface. This leads to grouping the related subprograms, variables, and arrays into a module. As perceived by the external environment, the programming elements which implement the data structure are local to the module and hidden from the external environment. As perceived from within the module, these programming elements are global only within the module and access may be shared only within the module. The external environment has access only through the arguments of the interface subprogram(s) of the module.

High level languages support modules in various ways, but FORTRAN-77 does not provide direct support to a module. Indirect support is available by using a labeled COMMON statement. Its local use in a module can avoid needless vertical coupling via argument lists between the subprograms within a module. However, the wanton misuse of COMMON statements introduces increased coupling between modules and is forbidden.

Quite often COMMON blocks are used to avoid passing variables through intermediate subprograms which do not use them directly in any computations. Artificially passing parameters unrelated to the immediate process being performed is not good programming methodology. The resulting proliferation of parameters can degrade the reliability and readability of a program and increase the coupling of the subprogram to the environment. This situation is frequently caused by bad program architecture. Widespread use of COMMON blocks to pass variables laterally is not a good programming solution. Instead, tightly controlled modules with limited lateral coupling should be used in conjunction with good overall program architecture.

APPENDIX B
EXECUTIVE PREAMBLE EXAMPLE

```
      PROGRAM ORBIT

C     Program Description -
C          Program ORBIT is an ephemeris program to compute satellite
C          orbits.  The program is based upon Vinti's (Refs. 1, 2, 3, 4,
C          5) Theory of Accurate Intermediary Orbits. The treatment to
C          account for the atmospheric drag perturbations is based upon
C          a paper by Watson, et al. (Ref. 6).  Vinti found a closed form
C          gravitational potential about an axially symmetric planet in
C          oblate spheroidal coordinates.  This solution accounts for all
C          the effects of the second and third zonal harmonics and about
C          two-thirds of the fourth harmonic. This potential, which
C          simultaneously satisfies Laplace's equation and separates the
C          Hamilton-Jacobi equation, succeeds in reducing the problem of
C          satellite motion to quadratures.  Watson, et al., provided an
C          analytical method to account for the drag starting with the
C          orbital elements defined by the Vinti theory (in the program
C          they are referred to as the Vinti elements).  The atmospheric
C          model of the thermosphere was developed by Jacchia (Ref. 7).

C                    V E R S I O N   1        7 MAY 1985

C     Questions or comments should be addressed to

C          John P. Doe
C          XYZ Corporation
C          Albuquerque, NM 12345
C          Com. Phone (505) 123-4567

C     Files Used -
C          IUNIT     Currently unit number 14. Associated with file name
C                    INPUT. Coded sequential, input file. Contents are the
C                    user defined input data.
C          MSG       Currently unit number 6. Associated with file name
C                    MESAGE. Coded sequential, output file. Contents are
C                    error and warning messages.
C          MUNIT     Currently unit number 17. Associated with file name
C                    OUTPUT. Coded sequential, output file. Contents are
```

```
C               the normal printed output, the orbit specification.

C   Subroutines Required -
C        DRAG      Changes the Vinti elements due to drag effects.
C        EPHINP    Reads all the program input.
C        EPHOUT    Writes all the program output.
C        INFORM    Computes all the orbital point information.
C        INITAL    Initializes the starting conditions.
C        POSITN    Computes the satellite position in inertial space.

C   Local Variables -
C        DRGFLG    A logical control flag. If true, atmospheric drag
C                  calculations are to be included in the ephemeris.
C        LAST      A logical control flag. If true, the last ephemeris
C                  point calculation has been completed.
C        TIMFLG    A logical control flag. If true, the step increment
C                  between each ephemeris calculation is in equal steps
C                  of time. Otherwise, the step increment is in equal
C                  steps of true anomaly angle.

C   References -
C        1. J. P. Vinti, ''New Method of Solution for Unretarded
C           Satellite Orbits'', Journal of Research of the National
C           Bureau of Standards B. Mathematics and Mathematical Physics
C           Vol. 62B, No. 2, 105-116 (1959).
C        2. J. P. Vinti, ''Theory of an Accurate Intermediary Orbit
C           for Satellite Astronomy'', Journal of Research of the
C           National Bureau of Standards B. Mathematics and Mathematical
C           Physics, Vol 65B, No. 3, 169-201 (1961).
C        3. J. P. Vinti, ''Intermediary Equatorial Orbits of an
C           Artificial Satellite'', Journal of Research of the National
C           Bureau of Standards B. Mathematics and Mathematical Physics
C           Vol. 66B, No. 1, 5-13 (1962).
C        4. J. P. Vinti, ''Inclusion of the Third Zonal Harmonic in an
C           Accurate Reference Orbit of an Artifical Satellite'',
C           Journal of Research of the National Bureau of Standards B,
C           Mathematics and Mathematical Physics, Vol. 70B, No. 1, 17-46
C           (1966).
C        5. J. P. Vinti, ''Improvement of the Spheroidal Method for
C           Artifical Satellites'', The Astronomical Journal, Vol. 71,
C           No. 1, 25-34 (1969).
C        6. J.S. Watson, G.D. Mistretta, and M.L. Bonavito, ''An
C           Analytical Method to Account for Drag in the Vinti
```

C Satellite Theory'', Celestial Mechanics, Vol. 11, 145-176
C (1975).
C 7. L.G. Jacchia, ''Revised Static Models of the Thermosphere
C Exosphere with Empirical Temperature Profiles'', SAO
C Special Report No. 332, May 1971.

APPENDIX C
SUBPROGRAM PREAMBLE EXAMPLE

```
      SUBROUTINE SEMIAX(ARRAY,AXIS,BALIST,CHANGE,ECCENT,NUMBER,SMALLD)

C  Purpose -
C       To calculate the change of the semimajor axis of the orbit due
C       to drag.

C  VERSION 1, 19 OCT 83

C  Programmer -  John P. Doe
C                XYZ Corporation
C                Albuquerque, NM  12345
C                Phone (505) 123-4567

C  Files Used -  None

C  Subroutines Required -
C       FACTOR    Calculates the atmospheric fitting factors.
C       PACKS     Packs ARRAY with atmospheric fitting data.

C  Local Variables -
C       COEFF3    An array of three integration coefficients that are
C                 interval dependent, in kilometers.
C       COEFF7    An array of seven integration coefficients that
C                 are constant over the entire integration interval,
C                 unitless.
C       SMALLB    The small b in the King-Hele expression for the
C                 atmospheric density, unitless.

C  References -
C       1.  J.S. Watson, G.D. Mistretta, and M.L. Bonavito, ''An
C           Analytic Method to Account for Drag in the Vinti Satellite
C           Theory'', Journal of Celestial Mechanics, Vol. 11, 145-177
C           (1975).
C       2.  T. E. Sterne, ''An Introduction to Celestial
C           Mechanics'', Interscience Publishers, Inc., New York, 165
C           (1960).

C  Input -
```

```
C       ARRAY     An array that contains the integrals of the form
C                 EXP(TB2*E)*COS(E)**I, I=0,1,....13 (unitless).
C       AXIS      The semimajor axis of the orbit in kilometers.
C       BALIST    The ballistic coefficient of the satellite in
C                 kilograms per kilometer**2.
C       ECCENT    The eccentricity of the orbit, unitless.
C       NUMBER    The number of integration intervals, unitless.
C       SMALLD    The small d is the King-Hele expression for the
C                 velocity of the satellite relative to the atmosphere
C                 (Ref. 2), unitless.

C   Output -
C       CHANGE    The change of the semimajor axis of the orbit due to
C                 the atmospheric drag, in kilometers.

C   Special Constants -
C       CONST     The gravitational constant for the earth in
C                 kilometers**3/second**2.
C       ROTATE    The rotational rate of the earth in radians per
C                 second.
```

APPENDIX D
INPUT SUBPROGRAM PREAMBLE EXAMPLE

```
      SUBROUTINE READIT(ERROR,HEIGHT,LAT,LONG,NCARD)

C   Purpose - To read, verify and write an echo check of the observer's
C             location information required for look angle computation.

C   VERSION 1, 13 FEB 83

C   Programmer -   John P. Doe
C                  XYZ Corporation
C                  Albuquerque, NM  12345
C                  Phone (505) 123-4567

C   Files Used -
C        IUNIT     Currently unit number 14. Associated with file name
C                  INPUT. Coded sequential, input file. Contents are the
C                  user defined input data.
C        MUNIT     Currently unit number 17. Associated with file name
C                  OUTPUT. Coded sequential, output file. Contents are
C                  the normal printed output, the ephemeris.

C   Subroutines Required - None.

C   Local Variables - None.

C   Input -
C        NCARD     The number of records that have been read.

C   Output -
C        ERROR     A logical control flag.  If true, a nonrecoverable
C                  error has occured.
C        HEIGHT    The height of the observer's location above the
C                  reference geoid in kilometers.
C        LAT       The latitude of the observer's location in radians.
C        LONG      The longitude of the observer's location in radians.

C   Record Format -
C   VARIABLE  CARD
```

```
C   NAME      COLS.    FORMAT    VARIABLE DESCRIPTION
C   HEIGHT     1-10    F10.2     The height of the observer in kilometers.
C                                Value must be greater than zero.
C   LAT       11-20    F10.2     The latitude of the observer in degrees
C                                Value must be in the range of -90. to 90.
C   LONG      21-30    F10.2     The longitude of the observer in degrees.
C                                Value must be less than the absolute
C                                value of 360.0 degrees.
```

APPENDIX E
PRINTABLE US ASCII CHARACTERS

The printable US ASCII characters in Table E-1 are the only characters that may appear in comments or as literal character strings (e.g., ' 7' , 2H<>). In rare situations, the CHAR intrinsic function may be used to assign CHARACTER variables and PARAMETERS to characters that are not shown in Table E-1. The use of other characters must be isolated in a small number of subprograms and carefully documented as machine-dependent code. These restrictions are motivated by the ideas that a printed program listing should accurately represent the program, and that programs should not depend on a particular collating sequence, but only that the collating sequence has the properties specified in the FORTRAN-77 standard.

TABLE E-1. PRINTABLE US ASCII CHARACTERS

Decimal	Octal	Character	Decimal	Octal	Character	Decimal	Octal	Character
32	40		64	100	@	96	140	`
33	41	!	65	101	A	97	141	a
34	42	"	66	102	B	98	142	b
35	43	#	67	103	C	99	143	c
36	44	$	68	104	D	100	144	d
37	45	%	69	105	E	101	145	e
38	46	&	70	106	F	102	146	f
39	47	'	71	107	G	103	147	g
40	50	(	72	110	H	104	150	h
41	51	)	73	111	I	105	151	i
42	52	*	74	112	J	106	152	j
43	53	+	75	113	K	107	153	k
44	54	,	76	114	L	108	154	l
45	55	-	77	115	M	109	155	m
46	56	.	78	116	N	110	156	n
47	57	/	79	117	O	111	157	o
48	60	0	80	120	P	112	160	p
49	61	1	81	121	Q	113	161	q
50	62	2	82	122	R	114	162	r
51	63	3	83	123	S	115	163	s
52	64	4	84	124	T	116	164	t
53	65	5	85	125	U	117	165	u
54	66	6	86	126	V	118	166	v
55	67	7	87	127	W	119	167	w
56	70	8	88	130	X	120	170	x
57	71	9	89	131	Y	121	171	y
58	72	:	90	132	Z	122	172	z
59	73	;	91	133	[	123	173	{
60	74	<	92	134	\	124	174	|
61	75	=	93	135	]	125	175	}
62	76	>	94	136	^	126	176	~
63	77	?	95	137	_			

APPENDIX F
LOOP LEAVE AGAIN CONSTRUCT

Several loop constructs other than FORTRAN-77 DO loops are allowed. They are the DO WHILE, REPEAT UNTIL, and LOOP LEAVE AGAIN constructs. The preferred order of implementation of these three constructs is: (1) DO WHILE, (2) REPEAT UNTIL, and (3) LOOP LEAVE AGAIN.

When implemented in FORTRAN-77, the DO WHILE loop takes the form:

```
1 IF ( <condition> ) GO TO 2

    <statements>

    GO TO 1

2 <next statement>
```

The REPEAT UNTIL implementation is:

```
1 <statements>

    IF ( <condition> ) GO TO 1
```

These two constructs include a statement label on the first executable statement of a block, a body of statements, and a terminal branching statement. The two forms are distinguished by the location of the IF statement, which causes an exit from the loop based on the value of a condition. The DO WHILE requires the IF to be the first executable statement of the construct. The REPEAT UNTIL requires the IF to be the last executable statement.

Since the FORTRAN-77 forms of these constructs differ only in the location of the loop exit statement, a more general form can be introduced that includes both forms as special cases:

```
1 <statements>

    IF ( <condition> ) GO TO 2

    <statements>

    GO TO 1

2 <next statement>
```

The generality is obtained by allowing the loop exit statement to fall anywhere within the body of the loop. This generalization is the LOOP LEAVE AGAIN construct. In certain circumstances the LOOP LEAVE AGAIN construct expresses the action of the loop without being error-prone.* This standard acknowledges the general LOOP LEAVE AGAIN construct as acceptable.

*E. Soloway, J. Bonar, and K. Ehrlich, "Cognitive Strategies and Looping Constructs: An Empirical Study," Communication of the ACM, 26, p853, 1983.

APPENDIX G
CASE STRUCTURE AND REPEATED ELSEIF CONSTRUCTS

The CASE structure applies to situations where at most one of a mutually exclusive set of conditions can exist at some point in a computation. The CASE statement does not exist in FORTRAN-77, but a CASE structure can provide a multipath switch to select the course of computation based on the specific value of the condition which is in effect. A CASE structure can be implemented in FORTRAN-77. It can increase the clarity of code because, if used in a consistent way, one can immediately recognize that a decision is being made among a mutually exclusive set of options.

When such a situation presents itself to a FORTRAN-77 programmer, two choices are available. A computed GO TO can be used if the set of options is determined by an integer value in the range 1...N. The other choice is the repeated ELSEIF construct. The repeated ELSEIF construct is preferred over the computed GO TO statement.

The repeated ELSEIF construct has the following desirable features:

- No GO TO statements are used. GO TO statements usually obscure the code.
- Entry to a repeated ELSEIF is at the top of the construct, flow of control is linear, and exit is at the bottom. Within the flow of control, each block is either executed or bypassed, based upon a condition tested at the start of the block.
- Control exits the repeated ELSEIF structure following the execution of the first code segment which follows a successful test. Frequently the mathematics of a computation favors one condition over the others; placing this condition first optimizes average performance while maintaining sound programming methodology. Other FORTRAN-77 programming methods force best case, average case, and worst case performance to be the same (equal to the worst case); this can be computationally expensive if there are several paths.
- The trapping of unexpected errors, which occur when none of the anticipated conditions hold, is automatic with the use of an ELSE block following the final ELSEIF block. If the repeated ELSEIF construct is not used, then special testing of the error condition is forced into a separate statement. Since such a separate test must be coded explicitly, and must redundantly test the mutual exclusion of all the other tests, there is potential for introducing errors. Any change in a disjunctive test must be reflected in the separate exclusion test, which makes the code more error prone and modification more difficult.

☆ U.S. GOVERNMENT PRINTING OFFICE: 1986—476-134:40006

SESSION 6 - "FINITE DIFFERENCES AND FINITE ELEMENTS"

Chairman: Andrew Peterson

A Novel Finite Element Formulation using Quintic Vertex Splines for Field Analysis in Closed Structures

Andrew K. Chan and Charles K. Chui
Department of Electrical Engineering
Texas A&M University
College Station, Texas 77843

Abstract

A new Finite Element formulation using *quintic vertex splines* is presented in this paper. The support of such a basic spline function is a polygon with at most one single interior vertex and on each triangle it is represented as a finite sum of the Bézier polynomial basis. Consequently, Bézier net representation on triangular arrays of the spline functions can be easily implemented. Certain characteristics of the vertex splines and their advantages in FEM are discussed. Some examples of this formulation and its advantages are shown.

1. Introduction

In the approximate solution of a boundary value problem by the finite element method (FEM), shape functions defined over individual subdividing triangles in the region of interest are used as approximants. The choice of the shape functions is usually among bivariate polynomials of an appropriate total degree. Polynomials of total degrees from 1 to 5 have been used in the literature [1,2]. Shape functions defined over triangular elements are joined together at the element boundary to form the approximate solution. In general, the approximate solution is guaranteed to be continuous over the region of interest but the first partial derivatives of the approximating field are usually discontinuous. Such an

Research partially supported by NSF CDR-8721512 Off-shore Technology, Naval Research Lab. Contract No. N 00014-86-K-2025, Texas Higher Education Coordinating Board No. 32123-70030, and by SDIO/IST managed by the U.S. Army Research Office under Contract No. DAAL 03-87-K-0025.

approximate solution does not fit the nature of the field solution and consequently often yields unsatisfactory results.

In this paper, we present a new formulation of the finite element equation using quintic vertex splines as the shape functions, but in contrast to the traditional FEM formulation, the field components satisfying the wave equation are represented as a finite series of continuously differentiable vertex splines. Upon substituting into the energy functional and using the boundary conditions for the field at the physical boundaries of the region, the wave equation is described by an eigenmatrix equation with the eigenvalue being the propagation constants of the modes.

2. Bézier Polynomial basis and Bézier nets

A bivariate polynomial basis of total degree n is the collection $x^\ell y^m$ where ℓ and m run over all non-negative integers with $\ell + m \leq n$. Using this traditional representation in finite element formulation is very inconvenient when the supporting triangles are of arbitrary shape. One usually formulates the problem in terms of a standard right triangle and uses a linear mapping to transform the results to an arbitrary triangle. This problem can be avoided if one uses the Barycentric coordinates (or simplex coordinates).

Let (r,s,t) be the Barycentric coordinates of a point (x,y) relative to a given triangle with vertices $(x_1,y_1),(x_2,y_2)$, and (x_3,y_3) defined by

$$r = \frac{1}{\Delta}\begin{vmatrix} 1 & x & y \\ 1 & x_2 & y_2 \\ 1 & x_3 & y_3 \end{vmatrix} \quad s = \frac{1}{\Delta}\begin{vmatrix} 1 & x_1 & y_1 \\ 1 & x & y \\ 1 & x_3 & y_3 \end{vmatrix} \quad t = \frac{1}{\Delta}\begin{vmatrix} 1 & x_1 & y_1 \\ 1 & x_2 & y_2 \\ 1 & x & y \end{vmatrix} \tag{1}$$

where $\Delta = (x_2y_3 - x_3y_2) + (x_3y_1 - x_1y_3) + (x_1y_2 - x_2y_1)$. Just as the Bernstein polynomials are used as a basis to represent polynomials on $[0,1]$ in the univariate case, the most useful basis for the space of polynomials of total degree less than or equal to n on this triangle is the set of polynomials:

$$\phi^n_{ijk}(r,s,t) = \frac{n!}{i!j!k!} r^i s^j t^k \tag{2}$$

where i,j, and k run over all non-negative integers with $i + j + k = n$. For instance, there are 21 different combinations of the indices i,j, and k for $n = 5$, and so any quintic

polynomial $p(x,y)$ can be expressed uniquely as a linear combination of ϕ^3_{ijk} as

$$p(x,y) = \sum_{i+j+k=3} a_{ijk}\phi^3_{ijk}(r,s,t). \tag{3}$$

This is called the Bézier representation of the polynomial function $p(x,y)$ on the given triangle. It is customary to arrange the coefficients on a triangular array called the Bézier net, as shown in Figure 1. We emphasize that the coefficients a_{ijk} uniquely determine the polynomial $p(x,y)$ and are invariant relative to the location and shape of the triangle.

Bézier nets are used to represent the restriction on each triangle of the vertex splines. There are seven types of bivariate quintic vertex splines. They are contructed based on different criteria. For example, the $V(0,0)$ spline requires the value at one of the vertices to be unity and zero at all the other vertices while the first and second order derivatives and the normal derivatives along the edges are all zero. $V(0,2)$ means that all function values and derivatives are zero at all vertices except that $\partial^2 V/\partial y^2$ equals to unity at one of the vertices. Their Bézier net representations are completely given in Chui [3]. The graph of $V(0,0)$ and $V(0,2)$ are shown in Figures 2 and 3 respectively.

One should note that the support of any one of the quintic vertex splines is not a single triangular element. Instead, it is a polygon which includes all the triangles joined together at a common vertex. The value of the spline is zero everywhere outside this polygon. This local characteristic makes the vertex splines uniquely suitable for FEM analysis. In addition, since the splines are expressed in terms of the Bézier polynomials in Barycentric coordinates, the triangular partition of the region can be completely arbitrary. Hence, the Finite Element formulation can be directly applied to the partitioning triangles without the need of a linear map.

3. Formulations for field analysis in guiding structures

Assuming that a waveguide of an arbitrary cross section is filled with homogeneous dielectric material. A scalar formulation (E_z or H_z) is adequate to determine the modal propagation constants and the field distributions. The energy functional for the TE modes is given by

$$I(H_z) = \frac{1}{2}\int\int((\nabla H_z)^2 - k_t^2 H_z^2)dxdy. \tag{4}$$

We express the function H_z as a linear combination of the vertex splines, namely:

$$H_z(x,y) = \sum_{i}^{M} f_i V_i(x,y), \tag{5}$$

where M is the total number of basis spline functions in the region. Depending on the number of subdividing triangles, the number M is 0× (number of vertices) + (number of edges). For example, let the cross-section of a rectangular waveguide be as shown in Figure 4. There are 9 vertices and 16 edges, so that $M = 70$. If H_z in (5) is substituted into (4), minimizing the functional leads to an eigenmatrix equation of the form

$$[\phi^T A\phi] = k_t^2[\phi^T B\phi] \tag{6}$$

which can be solved using any standard eigenvalue package. The vector ϕ^T is a row vector containing all the unknown coefficients $f_i, i = 1,\ldots,M$. The dimension of the matrices A and B is $M \times M$ when the physical boundary conditions are ignored. When the boundary condition are included in the formulation, the size of the matrix is slightly reduced.

If the waveguide is filled with a layered dielectric similar to the substrate of a microstrip circuit, the scalar formulation is not adequate to solve the problem. Following the formulation of Angkaew et al. [4], the transverse electric and magnetic fields can be represented by the four spline series

$$\begin{cases} E_x = \sum_{i}^{M} f_{1i}V_i & H_x = \sum_{i}^{M} g_{1i}V_i \\ E_y = \sum_{i}^{M} f_{2i}V_i & H_y = \sum_{i}^{M} g_{2i}V_i. \end{cases} \tag{7}$$

A matrix equation similar to (5) can be obtained. We note that the elements in A and B contain inner products of any two vertex splines from two adjacent vertices and the appropriate value of the dielectric constant within the range of integration. This operation

involves multiplying the basis of the two splines together and integrating over the overlapping triangular region. There are at most two overlapping triangular regions between any two vertices. Since the integral $\iint V_i V_j dxdy$ can be computed and stored the inner products can be obtained easily.

4. Examples and Conclusions

As a preliminary test of this approach, we calculate the cutoff wavelength of a rectangular waveguide. The results are compared with the exact solutions and other known solutions in Israel and Miniowitz [2]. They are tabulated in Tables I and II. In another example, we follow the formulation given by Koshiba et al. [5] using all three components of the H field to compute the modal propagation constants of a rectangular waveguide filled with two dielectrics. Our results compared favorably with other published data. They are listed in Table III.

We conclude by pointing out several advantages in using this method. These include: (1) There is no need to map an arbitrary triangle into the standard triangle in order to conform to a given coordinate system. This formulation depends only on the locations of the vertices within the region. (2) The continuity of the function values and the first partial derivatives are built-in in the Bézier representation of the vertex splines. The resulting approximated function is everywhere smooth. (3) The order of approximation is full which is higher than the ordinary FEM. (4) The number of subdividing triangles required to achieve a given degree of accuracy is smaller and the speed of computation is increased.

References

[1] Silvester, P.P. and R.L. Ferrari, *Finite elements for electrical engineers*, Cambridge University Press, Cambridge, London, 1983.

[2] Israel, M., and R. Miniowitz, "An Efficient Finite Element Method for Nonconvex Waveguide Based on Hermitian Polynomials" IEEE Trans. on Micro. Theory and Tech. Vol. MIT-35, No. 11, 1987, pp. 1019-1026.

[3] Chui, C.K. *Multivariate Splines*, CBMS-NSF Series in Applied Mathematics #54, SIAM Publications, Philadelphia, Pa., 1988.

[4] Angkaew, T., M. Matsuhara, and N.K. Kumagai, "Finite Element Analysis of waveguide Modes: A novel Approach That Eliminates Spurious Modes", IEEE Trans. Microwave Theory and Tech. MIT-35, No. 2, 1987 pp. 117-123.

[5] Koshiba, M., K. Hayata, and M. Suzuki, "Improved Finite-Element Formulation in terms of the Magnetic Field Vector for Dielectric Waveguides", IEEE Trans. MIT-33, No. 3, 1985, pp. 227-233.

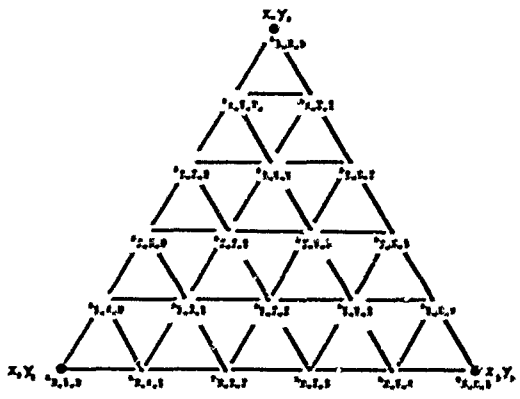


Figure 1

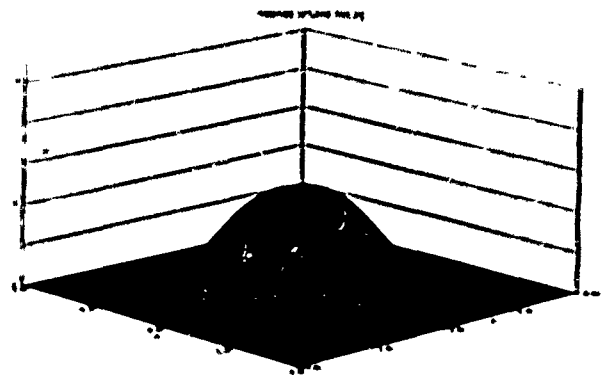


Figure 2

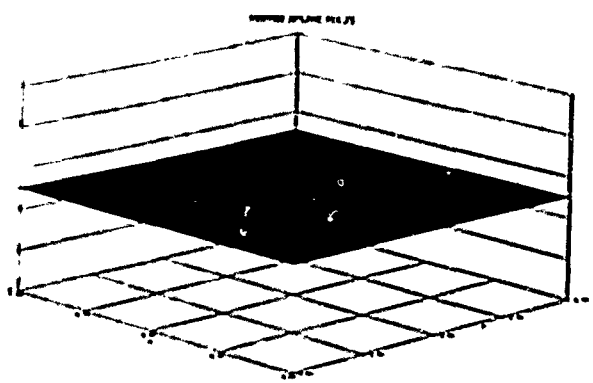


Figure 3

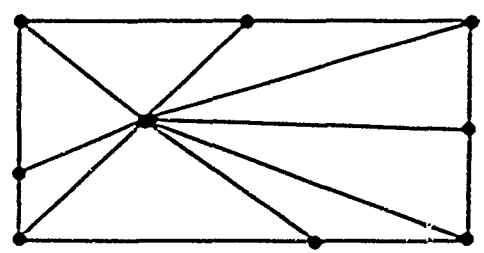


Figure 4

Table I TE_{10} mode cutoff wavelength in a rectangular waveguide with free boundary condition using vertex splines

m	n	$\log \lvert\lambda_m - \lambda_{ex}\rvert$
2	29	-6.277
4	35	-6.4256
8	70	-7.4208
16	82	-7.6046
18	129	-8.6495
32	206	-9.3092

Table II TE_{10} mode cutoff wavelength in a rectangular waveguide with free boundary condition using Hermite polynomials

m	n	$\log \lvert\lambda_{HI} - \lambda_{ex}\rvert$
8	54	-5.2
18	96	-6.3
32	150	-7.2

m is the number of partition triangles
n is the dimension of the mass and stiffness matrices

Table III Comparison of the propagation constants in a dielectric loaded wave guide ($k_0 w$)

Three Component H Field Method	Penalty Function Method	Vertex Spline Method
8.8093 (64,153)	8.8095	8.8101 (4,105)
10.2752	10.2765	10.2755
11.2677	11.2736	11.2355

A TIME-DOMAIN NUMERICAL ALGORITHM FOR SCATTERING OF EM WAVES BY 2-D ANISOTROPIC OBJECTS

Y. M. Chen and X. X. Zhang
Department of Applied Mathematics and Statistics
State University of New York at Stony Brook
Stony Brook, New York 11794-3600

ABSTRACT

An efficient and versatile numerical algorithm for calculating the scattered electromagnetic waves by two-dimensional objects with complex geometry and anisotropic material property in the time-domain has been developed. This is achieved by using a special finite difference method based upon a natural spatial discretization of the integral form of Maxwell's equations on a non-orthogonal grid-system and the leap-frog finite difference in the time-domain. It has the advantages of being (a) very efficient, (b) highly accurate due to the body-fitted grid system, and (c) very easy to implement boundary conditions. The capability and feasibility of this computer code are tested by performing numerical simulations on few realistic examples, e.g., cylindrical objects with cross sections of a metallic jet and an anisotropic composite airfoil. It has been found that its performance is quite good.

INTRODUCTION

An efficient finite difference method for solving E-M scattering problems in the space-time domain was first introduced by Yee [1] for the two-dimensional case and later applied to the three-dimensional case by Taflove and Brodwin [2], Holland [3], and Kunz and Lee [4]. This finite difference method requires a uniformly rectangular/cubical grid system and it is the most efficient numerical method (see the review by Chen [5]). Unfortunately, for scatterers with curved boundaries, one needs extra ordinarily large amount of uniform rectangular/cubical grid zones to approximate the curved boundaries and to minimize the undesirable "staircasing phenomenon", and thus it renders this numerical method inefficient in general.

Later, Mei, Cangellaris, Angelakos and Lin [6], [7] have presented the "Point-matched Time Domain Finite Element Method", a combination of the basic features of the standard Yee's finite difference method and the finite element method. Its efficiency is an improvement over the standard Yee's finite difference method due to its ability to compute on a body-fitted non-orthogonal grid system, but it pays a price for the additional interpolation and extrapolation in the non-orthogonal grid zones.

Recently, Yee [8] has made an improvement of his method by applying his finite difference discretization in the most natural way to the integral form of Maxwell's equations on a general non-

orthogonal grid system which makes the implementation of boundary conditions extremely easy. It can be shown [3] that it is the most efficient numerical method by performing the standard computational complexity analysis, i.e., to count the total floating point arithmetic operations needed in a typical calculation. Most recently, Taflove [9] and Madsen and Ziolkowski [10] have modified and extended Yee's non-orthogonal grid method. Here Yee's non-orthogonal grid method is generalized for solving the two-dimensional scattering problems of E-M waves by targets with complex geometry and anisotropic material property. Recently, MOM technique has been used to solve the corresponding time-harmonic scattering problems by Umashankar [11].

The whole space domain Ω is divided into three connected but non-overlapping sub-domains, the interior region Ω_1 representing the target and possessing a non-orthogonal cylindrical grid system, the intermediate region Ω_2 representing the free space just outside of the target and possessing the same non-orthogonal cylindrical grid system, and the large exterior region Ω_3 representing the far-field free space but truncated at a large distance away from the target and possessing the standard orthogonal cylindrical grid system. Now E-M waves must satisfy the following initial-boundary value problem of the integral form of Maxwell's equations,

$$\oint E_k \cdot dl = -\iint \mu_k \partial H_k/\partial t \cdot ds, \qquad t > 0, \qquad x \in \Omega_k,$$

$$\oint H_k \cdot dl = \iint (J_k + \underline{\sigma}_k E_k + \underline{\epsilon}_k \partial E_k/\partial t) \cdot ds, \qquad k = 1, 2, 3, \tag{1}$$

the initial conditions $E_k(x,0) = H_k(x,0) = 0, \quad x \in \Omega_k, \quad k = 1, 2, 3,$ (2)

the boundary conditions (no surface charges and currents),

$$\begin{aligned} &n \times E_2 = n \times E_1, \quad n \times H_2 = n \times H_1, \quad \epsilon_0 E_2 \cdot n = \underline{\epsilon}_1 E_1 \cdot n, \quad \mu_0 H_2 \cdot n = \underline{\mu}_1 H_1 \cdot n, \quad x \in \partial\Omega_{12}, \\ &n \times E_3 = n \times E_2, \quad n \times H_3 = n \times H_2, \quad E_3 \cdot n = E_2 \cdot n, \quad H_3 \cdot n = H_2 \cdot n, \quad x \in \partial\Omega_{23}, \end{aligned} \tag{3}$$

and the asymptotic terminating condition,

$$n \times E_3 = (\mu_0/\epsilon_0)^{1/2} (n \times H_3), \qquad x \in \partial\Omega_3, \tag{4}$$

where n is the unit outer normal vector at the interfaces, $\partial\Omega_{12}$ is the interface between Ω_1 and Ω_2, $\partial\Omega_{23}$ is the interface between Ω_2 and Ω_3, $\partial\Omega_3$ is the outer boundary of Ω_3, $J_1 = J_2 = 0$ and $J_3 = J(x)$ are the source distributions, $\underline{\epsilon}_3 = \underline{\epsilon}_2 = \epsilon_0 I$, $\underline{\mu}_3 = \underline{\mu}_2 = \mu_0 I$ and $\underline{\sigma}_3 = \underline{\sigma}_2 = \sigma_0 I$ are the free space permittivity, permeability and conductivity respectively, and $\underline{\epsilon}_1$, $\underline{\mu}_1$, and $\underline{\sigma}_1$ are the 3×3 real positive symmetric permittivity, permeability and conductivity matrices of the target respectively.

Here for simplicity, the scattering of normal incident TEM electromagnetic waves by a cylindrical target with its axis along z-axis is considered, e.g., $\underline{E} = E_x\underline{l}_x + E_y\underline{l}_y$ and $\underline{H} = H_z\underline{l}_z$, where $\underline{l}_n$ is the unit vector in the n-direction.

NUMERICAL CONSIDERATION

To discretize (1)-(4), the rectangle rule is used to approximate both the line and area integrals with the values of $\underline{E}$ and $\underline{H}$ fields to be calculated on two different but staggered grid systems, and the leap-frog finite difference scheme is used to approximate the first order time derivative. For example, the $\underline{E}$ fields are evaluated at the mid-points of the four edges of the quadrilaterals (Fig. 1) and at the integer time increments, and the $\underline{H}$ fields are evaluated at the centers of the quadrilaterals and at the half time increments.

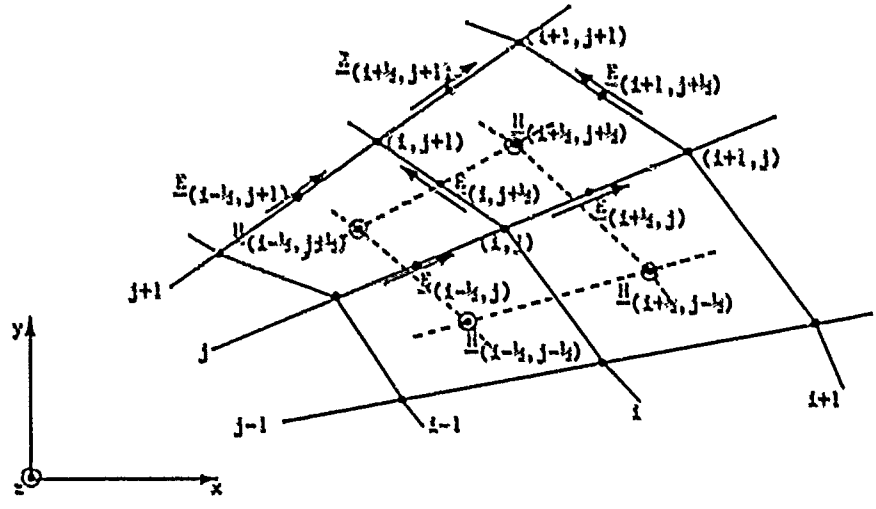


Fig. 1

Theoretically, the boundary conditions (3) must be imposed at the interface of two different materials. But here, there is no need to impose the boundary conditions explicitly in programming this numerical algorithm, because the boundary condition for the tangential component of $\underline{E}$ is satisfied automatically, and the other three boundary conditions are also automatically satisfied in the approximate sense if the differences of the material properties spread linearly across a complete grid zone instead of just across the interface. In this way, there is no cumbersome programming instruction at the interface to slow down the calculation; the application of boundary conditions is replaced by the process of assigning the material parameters into the grid zones. In particular, the programming instruction is extremely simple if the material interface is located either at a constant i-

line or at a constant j-line.

Finally, to achieve a stable computation for this explicit finite difference scheme, one must impose the well known Courant, Friedrichs, and Lewy stability condition.

RADAR CROSS SECTION

The definition of the radar cross section for the time-harmonic E-M fields is generalized to cases with C-W pulse as :

$$\Sigma(\psi) = \lim_{r\to\infty} r \int_{T_s}^{T_s+\Delta T_s} |E_s|^2 \, dt \Big/ \int_{T_{in}}^{T_{in}+\Delta T_{in}} |E_{in}^0|^2 \, dt, \tag{5}$$

where r equals to $2\pi r$ for 2-D problems and to $4\pi r^2$ for 3-D problems, r is the distance between the transmitter and the scatterer, E_{in}^0 is the incident E-field C-W pulse at the target, E_s is the scattered far field E-field, ψ is the angle between the transmitter and the zero angle axis, $E_{in}^0 = 0$ for $t < T_{in}$, $t > T_{in} + \Delta T_{in}$, and $E_s = 0$ for $t < T_s$, $t > T_s + \Delta T_s$.

NUMERICAL EXAMPLES

Example 1: A jet consisting of perfectly conducting material with the characteristic dimension of $\sim$ 10m is considered. A short C-W pulse of E-M fields with frequency $\sim$ 40 MHz is used as the source. The radar back-scattering cross section as a function of θ is plotted in Fig. 2. The CPU time on Silicon Graphics IRIS 4D 120/GTX for this example is 264s.

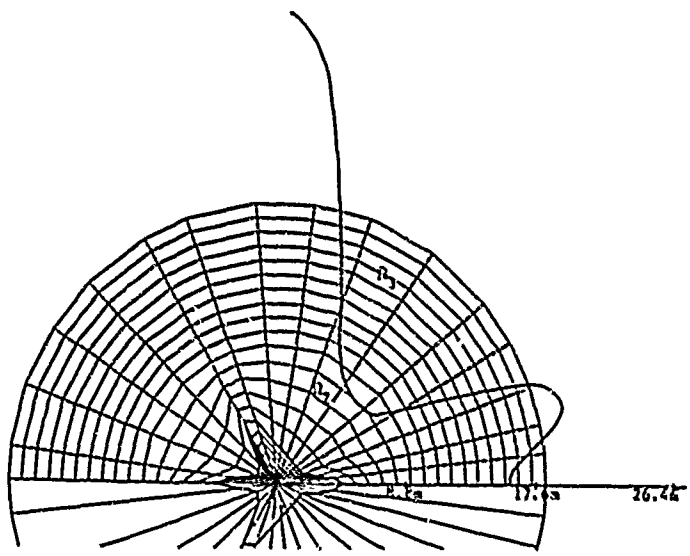


Fig. 2

Example 2: A composite airfoil with the leading edge consisting of anisotropic lossy dielectric, $\epsilon_{xx} = 23 \times 10^{-12}$farad/m, $\epsilon_{yy} = 44.2 \times 10^{-12}$farad/m, $\epsilon_{xy} = 0$, and $\underline{\sigma} = \sigma\underline{I}$, $\sigma = 5 \times 10^{-3}$ mho/m, and the trailing edge consisting of perfectly conducting material is used as the target. The characteristic length of the airfoil is 10m. A short C-W pulse of E-M fields with frequency ~ 238 MHz is used as the source. The radar back-scattering cross section as a function of θ is plotted in Fig. 3.

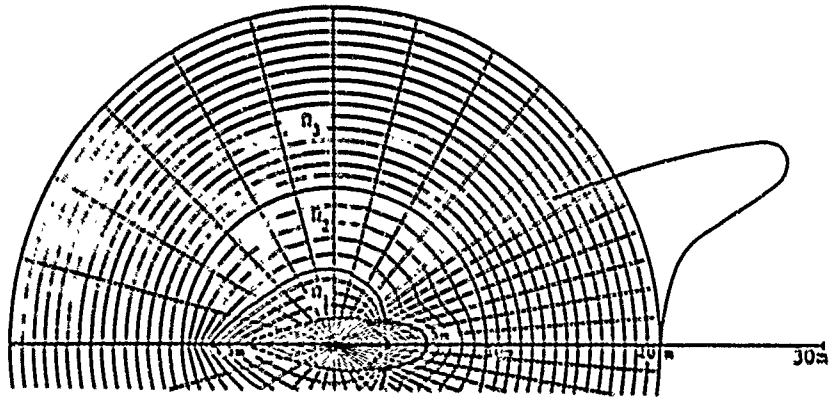


Fig. 3

REFERENCES

[1] K. S. Yee, Numerical solution of initial boundary value problems involving Maxwell's equation in isotropic media, IEEE Trans. Ant. Prop., AP-14, pp.302-307, 1966.

[2] A. Taflove and M. E. Brodwin, Numerical solution of steady-state electromagnetic scattering problems using the time dependent Maxwell's equations, IEEE Trans. Microwave Theo. Tech., MTT-23, pp.623-630, 1975.

[3] R. Holland, THEDE: a free-filed EMP coupling and scattering code, IEEE Trans. Nucl. Sci., NS-24, pp.2416-2421, 1977.

[4] K. S. Kunz and K. M. Lee, A three-dimensional finite-difference solution of the external response of an aircraft to a complex transient EM environment: Part I - The method and its implementation, IEEE Trans. E-M Comp., EMC-20, pp.328-333, 1978.

[5] Y. M. Chen, Efficiency of numerical methods for solving Maxwell's equations in space-time domain, SGEMP Note #8, Lawrence Livermore National Lab., Livermore, California, July 1986.

[6] K. K. Mei, A. Cangellaris and D. J. Angelakos, Conformal time domain finite difference method, Radio Science, 19, pp.1145-1147, 1984.

[7] A. C. Cangellaris, C. C. Lin and K. K. Mei, Point-matched time domain finite element methods for electromagnetic radiation and scattering, Mem. #UCB/ERL M85/25, Electronic Research Lab., University of California, Berkeley, April, 1985.

[8] K. S. Yee, Numerical solution to Maxwell's equations with non-orthogonal grids, SGEMP Note #4, Lawrence Livermore National Lab., Livermore, California, January 1985.

[9] A. Taflove, Review of formulation and applications of the finite-difference time-domain method for numerical modeling of electromagnetic wave interactions with arbitrary structures, Wave Motion, 10, pp.547-582, 1988.

[10] N. K. Madsen and R. W. Ziolkowski, Numerical solution of Maxwell's equations in the time domain using irregular nonorthogonal grids, Wave Motion, 10, pp.583-596, 1988.

[11] K. R. Umashankar, Numerical analysis of electromagnetic wave scattering and interaction based on frequency-domain integral equation and method of moments techniques, Wave Motion, 10, pp.493-525, 1988.

REPRESENTATION AND IMPLEMENTATION OF TIME DOMAIN SCATTERING INFORMATION

Timothy M. Lowe and Ram P. Kochhar
Boeing Advanced Systems
P.O. Box 3707 MS 4C-01
Seattle Wa. 98124-2207

Results from solving Maxwell's Equations as a system of first order differential equations with magnetic and electric losses are studied. This includes, in part, the postprocessing of the near fields to acheive frequency domain solutions and a more understanding of time domain scattering. Solutions are carried out to steady state where a frequency domain conversion may be performed on various parts of the result. Results include the total fields, scattered fields, and the surface and volume currents of 2-D geometry from which the RCS can be computed. It will also be shown that the RCS can be computed from equivalent current sheets around the geometry described by the near scattered fields, and the Equivalence Principle.

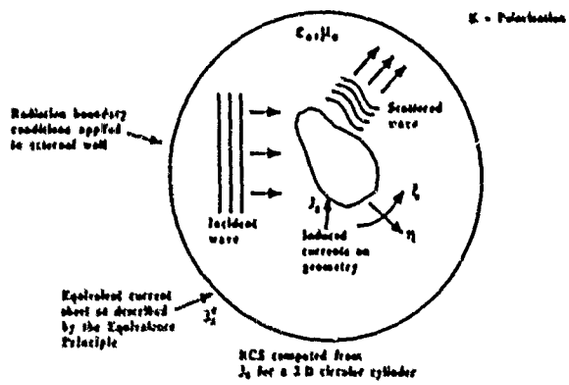
Results from wide bandwidth and modulated Gaussian pulses will be presented, where several frequencies contribute to the time domain solution. Fourier transforms will be computed on 2-D space-time data and converted to space-frequency data, where the desired sloution at a particular frequency is picked out. Performing a Fourier transform on truncated signals vs windowed signals in time is investigated.

Various techniques and formats for graphical representation will be presented for ease of understanding the 'big picture' in the time domain medium.

Approach

- Maxwell's Equations are specialized into a system of 2-D scaler ordinary differential equations
- Predictor corrector time stepping algorithm
- Radiation boundary conditions developed by Engquist and Majda
- Form fitted grid used to describe geometry
- Output field values at every grid point, including surface and volume currents as a function of time
- Signal processing techniques used to convert signal into frequency domain
- Display frequency domain and time domain data

Geometry and Procedure



2-D Maxwell's Equations

$$\frac{\partial E_z}{\partial t} - \frac{\sigma}{\epsilon} E_z = \frac{1}{\epsilon}\left[\frac{\partial H_y}{\partial \xi}\frac{\partial \xi}{\partial x} + \frac{\partial H_y}{\partial \eta}\frac{\partial \eta}{\partial x} - \frac{\partial H_x}{\partial \xi}\frac{\partial \xi}{\partial y} - \frac{\partial H_x}{\partial \eta}\frac{\partial \eta}{\partial y}\right]$$

$$\frac{\partial H_x}{\partial t} - \frac{\sigma}{\mu} H_x = \frac{1}{\mu}\left[\frac{\partial E_z}{\partial \xi}\frac{\partial \xi}{\partial y} + \frac{\partial E_z}{\partial \eta}\frac{\partial \eta}{\partial y}\right]$$

$$\frac{\partial H_y}{\partial t} - \frac{\sigma}{\mu} H_y = \frac{1}{\mu}\left[\frac{\partial E_z}{\partial \xi}\frac{\partial \xi}{\partial x} + \frac{\partial E_z}{\partial \eta}\frac{\partial \eta}{\partial x}\right]$$

The derivatives $\xi_x, \eta_x, \xi_y, \eta_y$ must be numerically calculated from the given x, y coordinate on the grid system, by the metric identities.

Metric Identities

$$\frac{\partial \xi}{\partial x} = \xi_x = \frac{y_\eta}{\sqrt{g}} \qquad \eta_x = \frac{-y_\xi}{\sqrt{g}}$$

$$\xi_y = \frac{-x_\eta}{\sqrt{g}} \qquad \eta_y = \frac{x_\xi}{\sqrt{g}}$$

where $\sqrt{g} = x_\xi y_\eta - y_\xi x_\eta$ = Jacobian

assume $\xi_t = \eta_t = 0$

Predictor Corrector Algorithm

$$\bar{u} = u_n + \alpha \Delta t\, f(u_n, t_n)$$

$$\bar{\bar{u}} = u_n + A \Delta t\, f(u_n, t_n)$$

$$\hat{u} = \bar{u} + \beta \Delta t\, f(\bar{\bar{u}}, t_n + A\Delta t)$$

$$\hat{\hat{u}} = \hat{u} + B \Delta t\, f(\bar{\bar{u}}, t_n + A\Delta t)$$

$$u_{n+1} = \hat{\hat{u}} + \gamma \Delta t\, f(\bar{\bar{u}}, t_n + (\alpha + B)\Delta t)$$

Note: Requires two memory locations per time step

where

$$\alpha + \beta + \gamma = 1$$
$$(\alpha + B)\gamma + A\beta = 1/2$$
$$(\alpha + B)^2\gamma + A^2\beta = 1/3$$
$$AB\gamma = 1/6$$

$\Rightarrow$

$\alpha = 1/4$
$A = 8/15$
$\beta = 0$
$B = 5/12$
$\gamma = 3/4$

This is one particular solution

* T. J. North, H. Lomax, NASA (Ames Research Center)

TEM

Absorbing Radiation Boundary Condition

Physical Basis

The operation

$$\left(\frac{\partial}{\partial z} - M\sqrt{\nabla^2 - \omega^2}\right)_{z=0} = 0$$

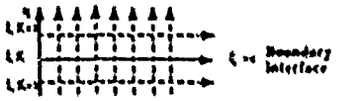
annihilates the plane wave

$$w = w_0 \exp\left(iM\sqrt{\nabla^2 - \omega^2}\, z + \omega t + \Omega\right)$$

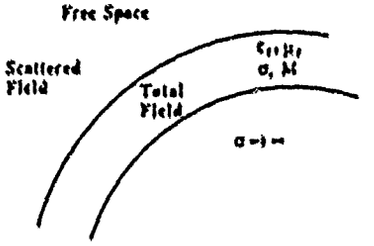
Boundary Conditions

$\hat{n} \times \vec{E} = 0$ on conductor

$\hat{n} \times \vec{E}$ continuance across dielectric interface
$\hat{n} \times \vec{H}$



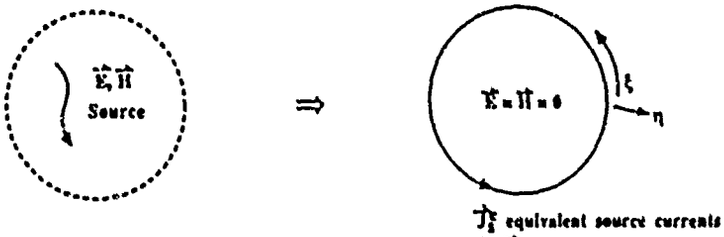
E^I and H^I are defined for all x, y, & t.



$$\left.\frac{\partial E^T}{\partial \eta}\right|_{I,K} = \frac{[E^I(I, K+1) + E^S(I, K+1)] - E^T(I, K-1)}{2\Delta\eta}$$

$$\left.\frac{\partial E^S}{\partial \eta}\right|_{I,K} = \frac{E^S(I, K+1) - [E^T(I, K-1) - E^I(I, K-1)]}{2\Delta\eta}$$

Equivalence Principle



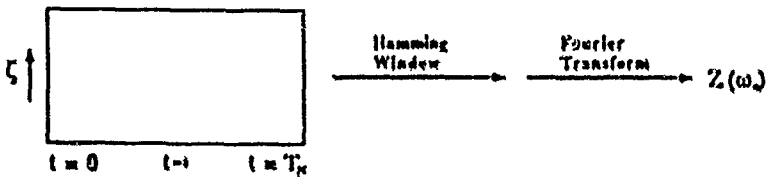
$\vec{J}_s$ equivalent source currents
$\hat{n} \times \vec{H}$ for E-polarization

$\sigma(\varphi) =$ 2-D RCS is computed for new boundary.

$\vec{J}_s$ on surface of geometry and $\vec{J}_f$ is computed

$J_T = \vec{J}_s + J_f$ for volume currents

Time Domain ⇒ Frequency Domain



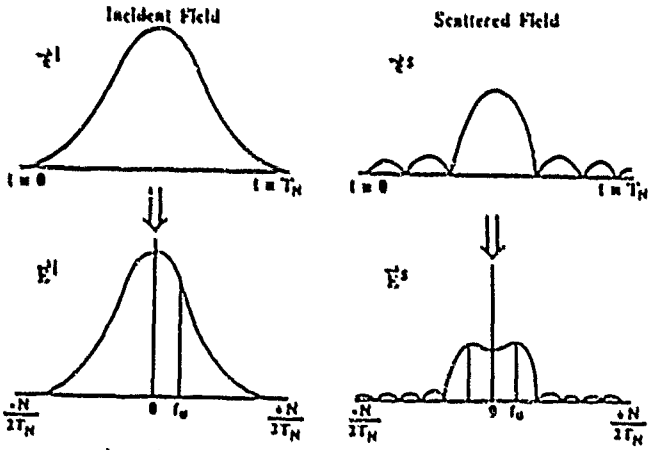
$$Z(\omega_n) = \frac{1}{N}\sum_{n=0}^{N-1} x_n(t)e^{-j\omega_n \Delta t\, n}$$

$Z(\omega)$ may be found for any ω, and $x_n(t)$ is discrete.

ω may be for any value within the bandwidth of the signal.

Note: Hamming window reduces any aliasing caused by truncating the signal in time.

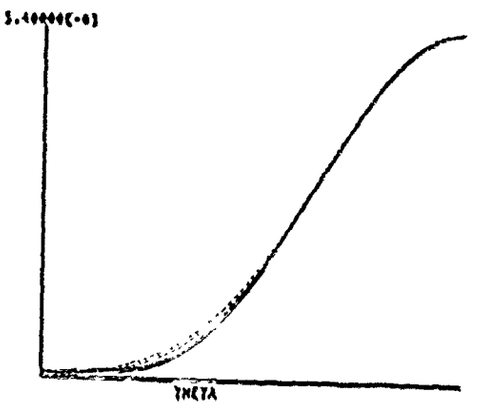
Frequency Scaling



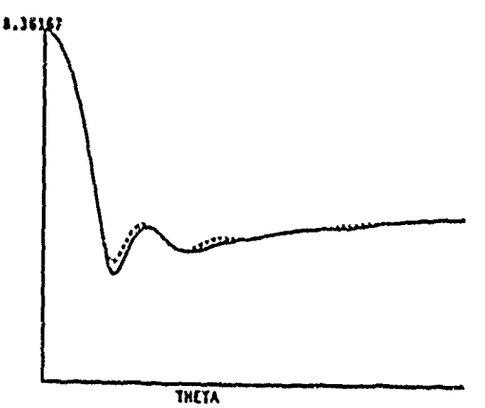
$\vec{E}^I(\eta,\xi)\Big|_{F=f_0}$ must be completed as a normalizing factor

i.e. $\vec{E}^S(\eta,\xi)\Big|_{F=f_0}$ due to an incident $|\vec{e}^I| = 1 \Rightarrow \left.\dfrac{\vec{E}^S(\eta,\xi)}{\vec{E}^I(\eta,\xi)}\right|_{F=f_0}$

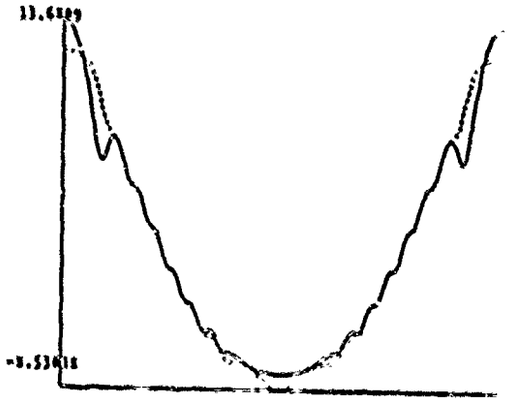
CYLINDER, ka = 5.13; --- = EXACT

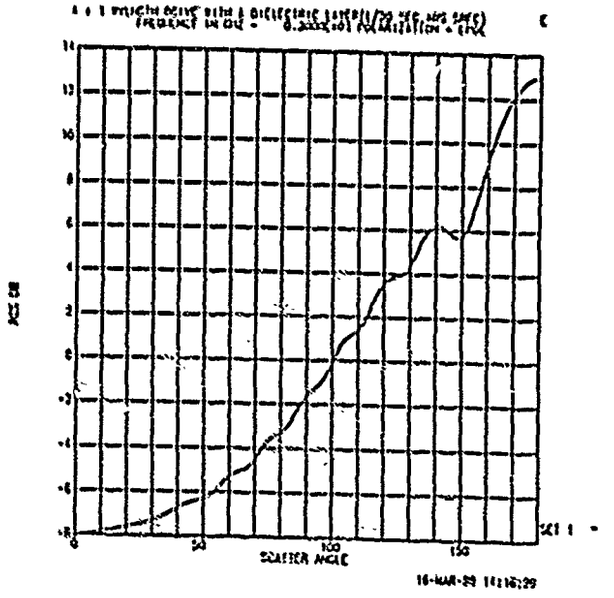


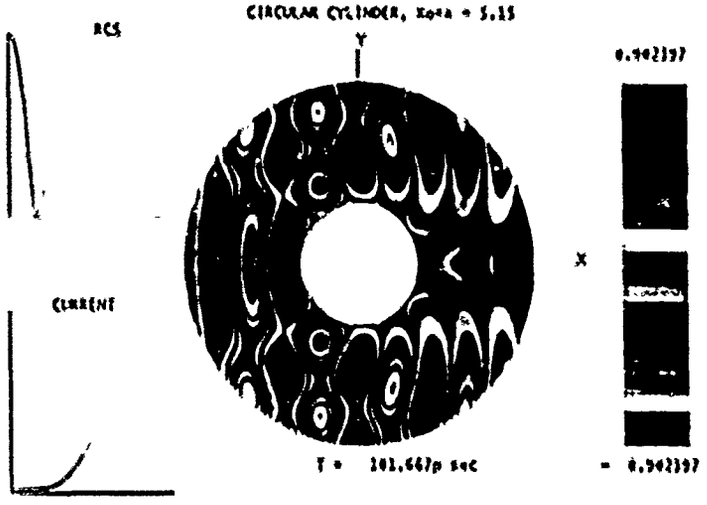
RCS, ka = 5.15, --- = EXACT

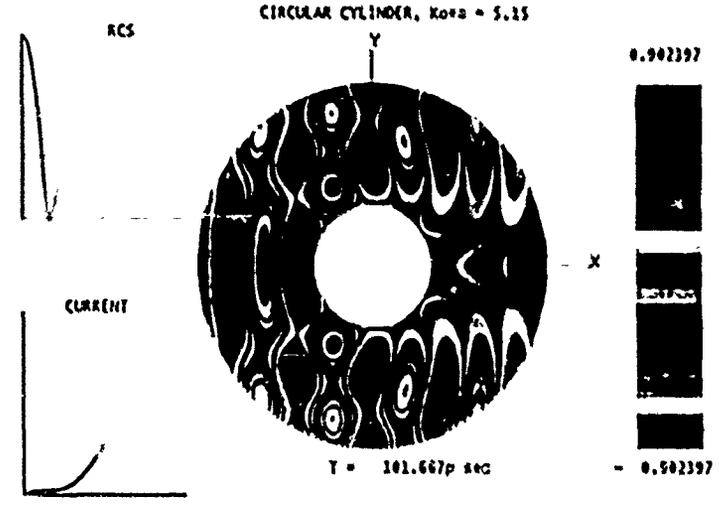


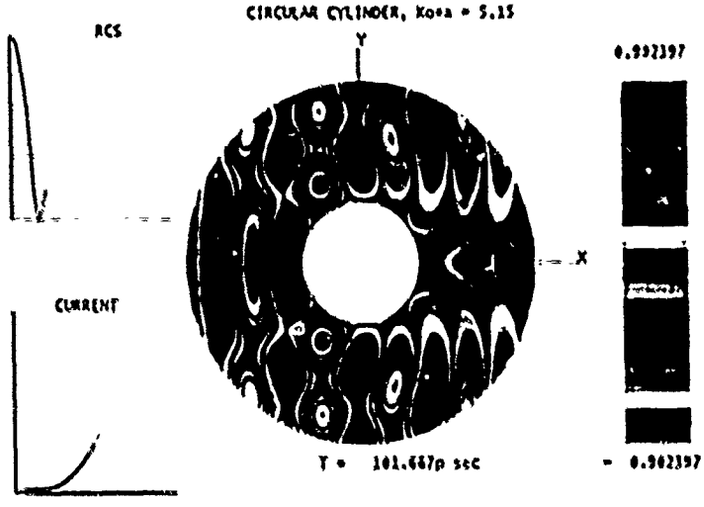
RCS FROM SURFACE CURRENT, --- FROM EQUIV BODY

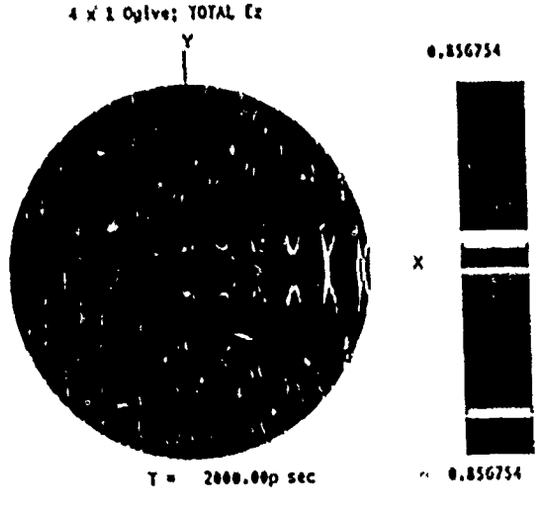


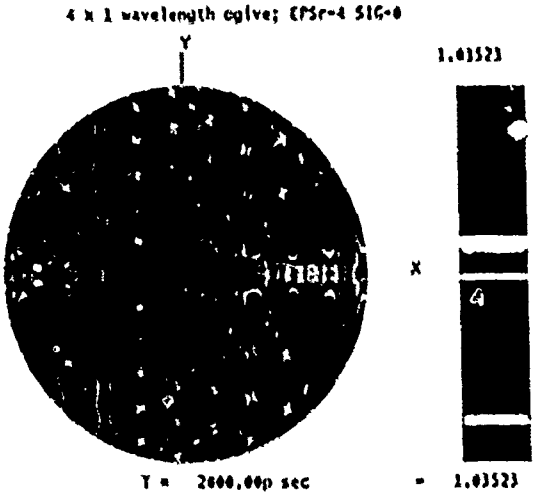


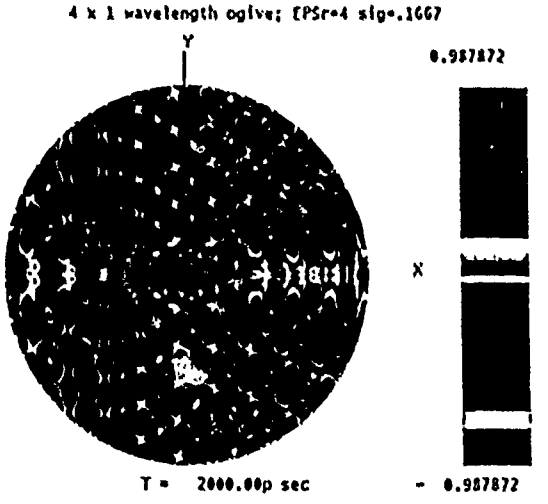

CIRCULAR CYLINDER, Ka=a = 5.15
RCS
CURRENT
Y
X
0.902397
T = 101.667p sec
= 0.902397

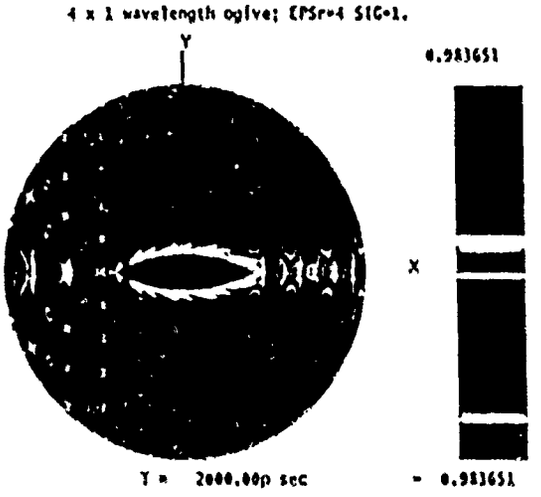

CIRCULAR CYLINDER, Ka=a = 5.15
RCS
CURRENT
Y
X
0.902397
T = 101.667p sec
= 0.902397

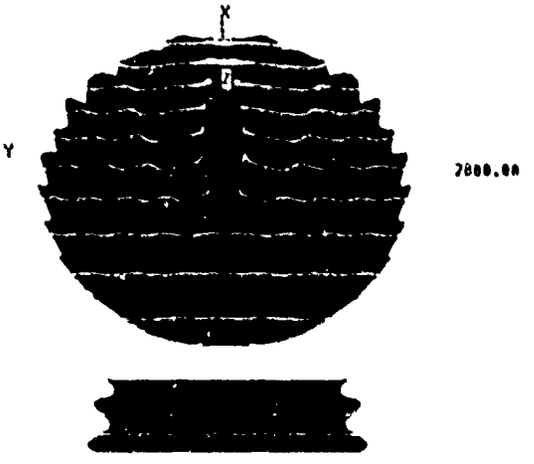

CIRCULAR CYLINDER, Koa = 5.15
RCS
CURRENT
Y
X
0.992397
T = 101.667p sec
= 0.992397


4 x 1 Ogive; TOTAL Ex
Y
X
0.856754
T = 2000.00p sec
= 0.856754


4 x 1 wavelength ogive; EPSr=4 SIG=0
Y
1.03523
X
4
T = 2000.00p sec
= 1.03523


4 x 1 wavelength ogive; EPSr=4 sig=.1667
Y
0.987872
X
T = 2000.00p sec
= 0.987872


4 x λ wavelength ogive; EPSr=4 SIG=1.
Y
0.983651
X
T = 2000.00p sec
= 0.983651


X
Y
2000.00

SOLVING 2-D ELECTROSTATIC PROBLEMS ON THE CONNECTION MACHINE USING THE FINITE ELEMENT METHOD

Scott Hutchinson
Steven Castillo
Dept. of Electrical and Computer Engineering

Edward Hensel
Dept. of Mechanical Engineering

New Mexico State University
Box 3-O
Las Cruces, New Mexico 88003

ABSTRACT

A development of a parallel computer Finite Element model for the potential distribution between conductors in a multi-conductor transmission line is considered. The parallel modeling is done on Thinking Machine's *Connection Machine*, a massively parallel computer employing up to 64k processors. The finite element methods employed are basic but illustrate the CM's performance when solving FEM problems using an element-by-element solution technique with conjugate gradients. Results and future research interests are given.

INTRODUCTION

Computationally, many aspects of the Finite Element Method (FEM) of modeling partial differential equations may be viewed as operations on a large number of data items. Thus, it is thought that the *Connection Machine* (CM) may yield significant advantages in FEM modeling. Although the literature contains much on parallel FEM modeling, work on the CM has been rare[1].

A simple illustration of the computational factors of FEM modeling is given. Next, the methods chosen are presented along with preliminary results using several simple problems. Finally, areas of current research on this subject are given.

FINITE ELEMENTS

One method of finite element analysis involves the solution of PDE's using the *method of weighted residuals* over some discretized domain. An approximation to the solution is calculated on a finite number of nodes by using a polynomial approximation of the field variable across a subdomain or element. Each element contributes independently to a global set of

linear algebraic equations representing the discrete solution (for a further description, see[2]). It is the parallel construction and solution of the system that is considered.

Without delving into the mathematics of the FEM, suffice it to say that the boundary-value problem

$$Lu = f \qquad (1)$$

in some domain Ω with appropriate boundary conditions is approximated with the linear system

$$Au = b \qquad (2)$$

for u the desired solution. In terms of elemental contributions, (2) may be written as an *assembly* of contributions due to individual elements

$$\left[\Sigma A_e\right]u = \left[\Sigma b_e\right] . \qquad (3)$$

CONJUGATE GRADIENT SOLUTION

Normally, the assembly, (3), is carried out and the system is solved using known techniques. For parallel solution, a somewhat different approach has come into use. Using an element-by-element scheme, each elemental contribution (A_e and b_e) is calculated independently. The A_e's are stored while the right-hand side is assembled into the global vector, b. As will be seen, this is a convenient method for parallel solution using the Conjugate Gradient method[3].

Conjugate Gradient (CG) solution methods are preferred in parallel environments because they are a collection of vector-matrix products, vector dot-products, scaler-vector products and vector additions - all operations with inherent parallel features[4]. The basic CG method is[5]

Initialize:

$$p_0 = r_0 = b - Au_0, \qquad (4a)$$

Iterate:

$$a_i = \frac{|r_i|^2}{(p_i, Ap_i)}, \qquad (4b)$$

$$u_{i+1} = u_i + a_i p_i, \qquad (4c)$$

$$r_{i+1} = r_i - a_i Ap_i, \qquad (4d)$$

$$b_i = \frac{|r_{i+1}|^2}{|r_i|^2}, \qquad (4e)$$

$$p_{i+1} = r_{i+1} + b_i p_i, \qquad (4f)$$

for u_e arbitrary. Thus, as stated, equations (4) are a set of many independent operations and well suited for parallelization.

SOLUTION IN PARALLEL

Since the machine in question is the CM, a basic understanding of its operation is needed. The CM is best described as a SIMD or data parallel machine containing up to 64k processors, each with local memory. It is configured in a hypercube format and attached to a front-end VAX, SUN or Symbolics computer. Among its tasks, the front-end serves to compile code, distribute instructions and data to the processors, and handle any non-parallel operations in a given program. Within the CM, processors may be allocated as needed to run certain instructions on a specified data set. Also, each physical processor may be configured into more than one virtual processor where the physical processor's memory and access is divided among the virtual processors. This allows the CM to effectively operate as a machine with up to 2048k virtual processors. For a more complete description, see[6].

Above, it was noted that the calculation of the elemental contributions is an independent process and may therefore be done in parallel. In the algorithm described here, a number of processors on the CM, each corresponding to an element, calculates its elemental contribution, both for the global system (A_e) and for the right hand side (b_e). Additionally, a different set of processors is allocated corresponding to the number of unknowns in the system, N. This array of processors contains all the vector quantities given in (4), each processor having one of the entries in each vector. This is the mapping of the problem onto the CM used here.

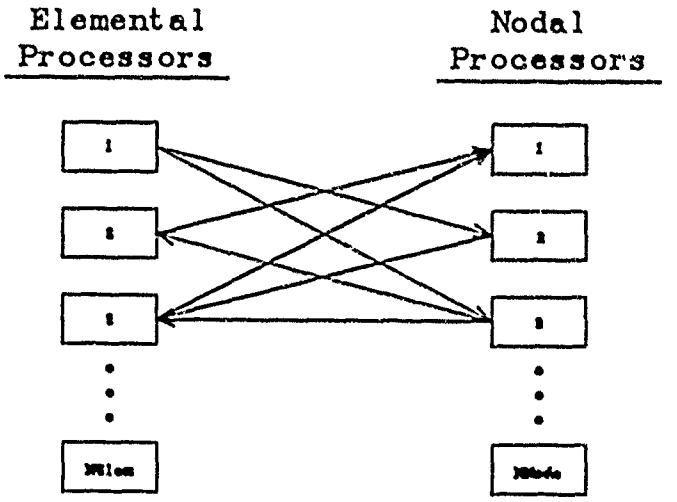


Figure 1. Processor Mapping on the CM for Solution Phase.

Once the elemental contributions have been computed, the b_e's are assembled into their proper locations in the b vector. Next, during the CG solution, a matrix-vector product must be computed

$$Ag = n \qquad (5)$$

where A is our global NxN matrix and g and n may represent any vector of length N. In the element-by-element method, each elemental contribution to A (A_e) is stored in its processor. When a product as in (5) is needed, each elemental processor multiplies its non-zero members by the corresponding values in g as required by matrix-vector multiplication. As they are calculated, each elemental processor sums its contributions into the proper processor corresponding to an entry in the vector n. Thus, the vectors needed in the CG solution technique are obtained. Note that in this process, many of the multiplications are done in parallel and, although interprocessor communication is needed, much of it is also parallel.

To carry out the rest of the solution in parallel is almost a trivial task on the CM. With one processor handling one entry in each of the vectors in (4), the CM acts as a huge vector processor, performing multiplications and additions for N unknowns concurrently. Where scaler values are used, they are either summed to the front end or broadcast to the N processors as required in the CG solution algorithm. As will be shown, this technique yields very fast solutions for which one iteration is almost independent of the number of unknowns.

RESULTS

For illustrative purposes, several two-dimensional quasi-static problems were solved using first-order, linear isoparametric elements. Specifically, the problems all involved the solution of Laplace's equation

$$\nabla \cdot \varepsilon(x,y) \nabla u = 0 \qquad (6)$$

in a cross sectional region with multiple conductors as in Figures (2) and (3). The problems are considered *quasi-static* since a inhomogeneous region will not support a true TEM wave. The conductors each possess a

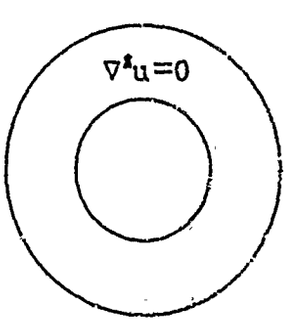


Figure 2. Coax Problem Solved.

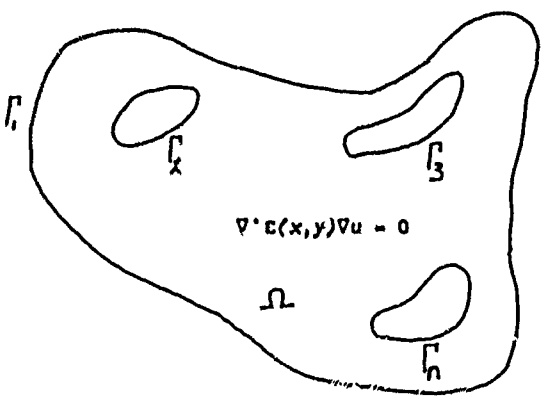


Figure 3. Multiconductor Problems.

Dirichlet boundary condition . The region is discretized in a preprocessor program and the mesh data is then read and transformed to the CM as needed.

The programming was done in C*, the data-parallel C++ type language for the CM, and executed on a machine with 32k processors. Both single precision (hardware) and double precision (software) floating point calculations were used. The results taken were run using a virtual processor ratio of one.

Figure (4) shows a comparison of the actual solution times for the coax problem. Although not strictly problem independent (the concurrency of the matrix-vector product computation is dependent on the number of elements in the problem) these results show the relative speed of the CM as compared to a known serial system (VAX 8800). Table 1 shows the results for several microstrip problems. Results were taken using the convergence criteria

$$1.0e\text{-}02 > \frac{|r_i|}{|b|},$$

with software, double-precision floating point calculations for the coax problem and hardware, single-precision floating point calculations for the microstrip results.

Referring to Figure (4), solution time on the CM-2 appears to be a nearly linear function of the number of unknowns. This increase in solution time is due almost entirely to the increase in the number of iterations required for the system to meet the convergence criteria. Time per iteration increased only slightly with the increase in unknowns - from 0.308 sec. to 0.382 sec. over an increase of 9100 unknowns.

Looking at the results for the microstrip problems in Table 1., times for both the Fill and the Solve portions of the program remain relatively constant over a range of elements and nodes. The Fill times seem comparatively long for the simple elements that were used. This is due to an un-optimized Fill routine which contains a fair amount of communication. Note that during the solution, the time per iteration (- 0.14 sec.) is approximately half that obtained using software, floating point calculations (- 0.34 sec.).

There are several points which should be made concerning these results. First, the problem was one for which the system of equations was symmetric and positive definite. This allowed the usage of the basic CG routine. A preconditioned CG algorithm may be used for systems which do not meet this criteria at the cost of solution time. Second, the algorithm has not been "tweaked" for the fastest communication pattern. That is, communication with the front end computer in the solution routine is not an absolute necessity and accumulation on the CM itself may yield faster results. Third, this mapping of the solution algorithm onto the CM results in a very inefficient use of processors. The processors associated with the elements remain unused during the solution phase except when calculating the matrix-vector multiply. Lastly, although the calculation of the element matrices was parallelized, times were relatively slow due to a communication bottleneck with the front end. Communicating the mesh data for finely discretized systems from the front-end to the CM is quite time consuming.

Although not conclusive, these results are promising. Results obtained by Johnsson and Mathur[7] using a slightly different mapping and a regular mechanical engineering problem indicate computational power on the order of a gigaflop for both the fill and solution portions of the FEM algorithm. With this type of power possible, the CM's relatively low cost compared with known supercomputers makes it a very viable alternative.

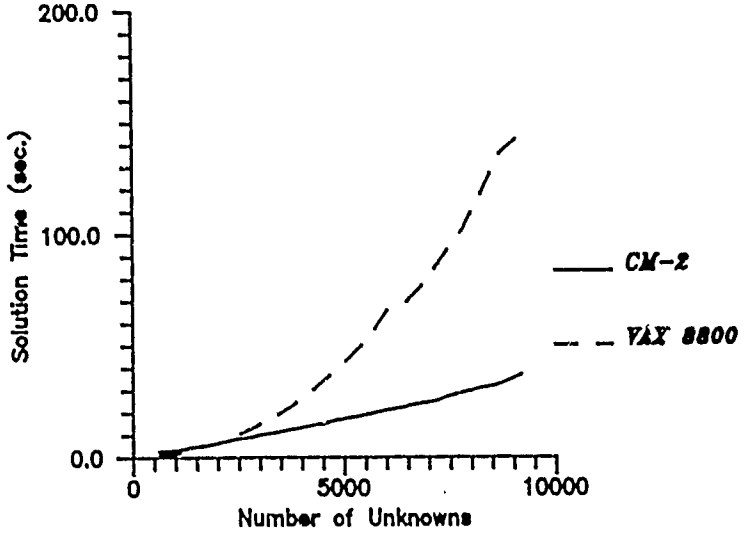


Figure 4. Coax Solution Comparison.

#Elem.	#Nodes	#Cond.	Fill Time (s)	Solve Time (s)	Time/Iter. (s)
724	399	2	8.17	3.12	0.13
966	532	3	7.98	2.43	0.13
3876	2037	3	8.00	4.59	0.14
2775	1481	6	7.99	2.59	0.14

Table 1. Results For Different Microstrip Problems.

CURRENT RESEARCH

Research into FEM analysis on the *Connection Machine* is ongoing at NMSU. Current activities include the implementation of a more efficient mapping of the solution algorithm, a Preconditioned Conjugate Gradient (PCG) solution algorithm, results with higher order elements, multigrid methods and parallel mesh generation.

A PCG algorithm would allow the solution of systems which are not symmetric-positive definite such as those which arise in the solution of the 2-d and 3-d wave equations. Plans for remapping the solution phase of the FEM algorithm will allow solution of much larger systems of equations with more efficient use of the processors. With regard to mesh generation, transferring large amounts of data (mesh) to the CM seems to be a bottleneck to the overall FEM solution times. It is hoped that the small amount of data needed to describe a mesh may be communicated and the mesh generated in parallel using a multigrid solution technique. The mesh data can then simply be used by the FEM program minimizing communication with the front end.

ACKNOWLEDGMENT

This work was conducted using the computational resources of the Northeast Parallel Architectures Center (NPAC) at Syracuse University, which is funded by and operates under contract to, DARPA, and the Air Force Systems command, Rome Air Development Center (RADC), Griffiss AFB, NY, under contract #F30602-88-C-0031.

Additionally, work on this project was supported by grant #EET-8812958 from the National Science Foundation.

REFERENCES

1. C.H. Farey, C.A. Felippa and K.C. Park, "Implementation Aspects of Concurrent Finite Element Computations", *Parallel Computations and Their Impact on Mechanics*, AMD-Vol.86, ASME, 1987, pp. 311.

2. P.P. Silvester and R.L. Ferrari, *Finite Elements for Electrical Engineers*, Cambridge, 1983.

3. E. Barragy and G.F. Carey, "A Parallel Element-By-Element Solution Scheme", *Int. J. Numer. Meth. Eng.*, Vol. 26, 1988, pp. 2367-2382.

4. G. Fox, et al, *Solving Problems on Concurrent Processors, Vol. I*, Prentice-Hall, 1988, pp. 139-147.

5. M.R. Hestenes and E. Stiefel, "Methods of Conjugate Gradients for Solving Linear Systems", *J. Research N.B.S.*, Vol. 49, Dec. 1952, pp.409-436.

6. W. Daniel Hillis, *The Connection Machine*, MIT Press, Cambridge, MA, 1985.

7. S. Lennart Johnsson and Kapil Mathur, *Data Structures and Algorithms for the Finite Element Method on a Data Parallel Supercomputer*, Thinking Machines Technical Report No. CS89-1, Thinking Machines Corp, 1988.

Efficient Modeling of Thin Dielectric Structures Using the Finite-Difference Time-Domain Technique

Kenneth R. Demarest* Daniel Long Panayiotis Tirkas

Electrical and Computer Engineering Department
University of Kansas
Lawrence, Kansas 66045

The Finite-Difference Time-Domain technique (FDTD) is a proven modeling technique and has been used successfully to model complex scatterers in both the time and frequency domains. The technique is very flexible in that it can model both conducting and dielectric media, configured as open or closed geometries.

In spite of the great success of this technique, it is, of course, not without its weaknesses. One such weakness is its relative inability to model geometries that are both electrically large, and yet contain fine detail; such detail could include sharp points, small apertures, and thin dielectric sheets. Small substructures such as these cause problems with the FDTD technique because the fields in the vicinity of these objects exhibit rapid spatial variations.

Although fine detail can be accommodated by using a finer spatial grid, this can also be a source of problems. First, if the cells small enough to resolve the fine detail are used throughout the problem space, the total number of cells may be enormous. Fine subgrid models can also be used, but there can be problems of numerical noise being transferred across the fine/coarse grid boundaries.

An attractive method of dealing with the problem of fine detail in FDTD codes is to build the near field physics of the fine detail in question into those cells that contain them, thus allowing the cell size in the solution space to be uniform and relatively large. The reasoning behind this technique is that, while the "normal" FDTD field advance equations assume a smooth linear variation of the fields in each cell, "smart" cells can have a specified nonlinearity built in and still be large. This approach has been used with success in the modeling of thin cracks, apertures, and wires.

In this paper we describe a technique for modeling dielectric sheets that are much smaller than the FTDT cell size. A simple model of the near field physics is developed and implemented in a FDTD code. Results are shown that compare the calculated plane wave scattering of thin dielectric plates, and are compared with both physical optics and "brute force" FDTD calculations.

INTRODUCTION

The Finite-Difference Time-Domain (FDTD) technique has become one of the standard numerical analysis tools of the electromagnetic community, taking its place next to techniques such as the Method of Moments and Finite Elements. The basics of FDTD were demonstrated in the mid 1960's, and has been progressively refined since then. It has many attractive characteristics, among which are its relative simplicity, versatility, and accuracy.

In many respects, FDTD can be considered to be a mature technique. Indeed, the basics of the method have been extensively studied and characterized. Thus, much is known about the characteristics of solutions produced from this technique, including the number of unknowns necessary to produce accurate solutions and the dynamic range and noise floor of the numerical grids. This has enabled a broad range of users to use these codes to solve important engineering problems.

In spite of the relative maturity and usefulness the FDTD technique, there are still many aspects of it that are the subject of ongoing research to improve it. An example of this is the effort to allow the analysis of large structures that contain fine detail using FDTD. The challenge here is to develop augmentations of FDTD that do not require the use of extremely large numbers of unknowns in order to resolve these details.

A geometry that is becoming increasingly important in electromagnetic analysis is that of thin dielectric sheets or slabs. This, of course, has arisen largely as a result of the recent use of dielectrics aircraft. These sheets may appear either free standing, or adhered to conductors. Also, these sheets may contain cracks, either due to their construction or to aging. These sheets pose new problems in electromagnetic modeling.

In this paper we describe methods of modeling thin dielectric sheets, possibly backed by conductors and containing cracks, using FDTD. The techniques discussed here are "course grid" techniques that allow the modeling of these thin structures without the need to use a fine grid throughout the problem space, which encumbers the model with far more unknowns than is truly necessary.

The Integral Equation View of FDTD

The name Finite-Difference Time-Domain is an accurate name for this technique, but it is not always the best view of what it actually does. Although there is no doubt that when Yee announced the technique to the electromagnetic community in 1966 [1] it was thought of as being solely a differential equation technique, it was later shown [2] that an integral equation view produced exactly the same field advance equations for situations where the fields are varying linearly with respect to position. For situations, however, where the fields within a cell are varying nonlinearly with respect to position, the integral equation viewpoint allows added insight into how to most accurately model the fields.

Figure 1 shows a representative situation where small scatterers are present in a numerical grid that is too course to resolve them. Due to the boundary conditions imposed by these scatterers, the electric and magnetic fields in their vicinities are likely to be nonlinearly distributed. Thus, the "normal" FDTD algorithms for advancing the fields in these

cells will fail since they depend on linear distributions of both E and H within a cell. But when FDTD is viewed from the perspective of the integral form of Maxwell's equations, it becomes apparent that if the spatial distribution (i.e., shape) of the field within these cells can be determined (possibly from quasi-static models), these distributions can be built into the contour and surface integrals of Ampere's and Faraday's laws that are used to advance these fields. Thus, only the field advance equations in those cells where the fields are nonlinearly distributed need to be modified to model these scatterers.

Using this philosophy, the standard FDTD technique can be augmented for a great number of situations where small parts of a scatterer would normally demand very small cells, and thus the need for using far more unknowns than is necessary to model the gross aspects of the scatterer. Building the near field physics of a difficult portion of a scatterer into only those cells that encounter allow the grid size to remain uniform across the problem space without sacrificing the ability to model these structural details.

Modifications For Thin Dielectric Slabs

Figures 2 and 3 summarize the changes that need to be made in the field advance equations in cells containing thin dielectric slabs. Here, a dielectric slab that is smaller than the cell dimensions is centered along a lattice line (a standard Yee type spatial lattice is assumed in all cases to follow).

Since the slab is electrically thin, all components of the magnetic field and the tangential component of the electric field can be considered to be linearly distributed within the cells containing the dielectric, but the normal component of E will, of course, exhibit a discontinuity across the dielectric interfaces. As a result, the calculations of the tangential electric field along the lattice line inside the slab and the tangential magnetic fields adjacent to the slab have to be modified. In the case of using Ampere's law to advance the electric field, only the step discontinuity in the permitivity needs to be addressed in the surface integral of E. As for modifying Faraday's law to advance the magnetic field, the discontinuity in the normal electric field must be addressed in the line integral of E.

The field advance equations developed in these two figures actually become more accurate as the electrical thickness of the slab becomes thinner since the tangential electric field within the cells containing the slab becomes more and more linear. Also, they are both applicable for both two and three dimensional codes.

Conductor Backed Dielectrics

The general philosophy for advancing the fields of a thin conductor backed dielectric is shown in figure 4. Here, the air/dielectric interface has been placed along a normal grid axis, and the conductor backing is placed a distance d below the axis.

As a result of this placement of the geometry within the FDTD grid, the only cells that will contain nonlinearly distributed field components are the ones that straddle the sheet. Due to the boundary conditions at the conductor, the tangential electric and normal magnetic fields will decrease linearly throughout these cells to zero values on the conductor surface.

A subtle part of this formalism is that the contour used in the integrals is not square and demands a value of the tangential magnetic field just above the conductor surface along a line not coinciding with a standard H field evaluation point. This can be circumvented, however, by evaluating Faraday's law over the s[illegible]d contour indicated within the dielectric to calculate this magnetic field component. Du[illegible]g this evaluation, the normal electric field component can be found from the field just outside the dielectric, subject to its known discontinuity across the interface.

As in the case of the dielectric slab without the conductor backing, these simple assumptions of the behaviors of E and H near the dielectric yield field advance equations that are no more difficult than the "standard" equations, but take into account the correct near field physics of these geometries. Notice also that although the contours used are not square, they retain the accuracy of central differencing because the correct near field physics have been build into the integrals.

Modeling of Thin Cracks

The presence of a crack in a thin dielectric structure poses an even greater challenge for the FDTD since the fields in the vicinity of the crack are highly nonlinear- particularly the electric field. This is because the dominant effect of the crack is the separation of polarization charge across the gap of the crack.

Figure 5 depicts a thin crack in a thin conductor backed dielectric, embedded in an FDTD grid. A "brute force" FDTD calculation (i.e.,using cells small enough to directly model the dielectric and the crack) of the electric field along the air/dielectric interface for such a geometry is shown in this figure. The nonlinear dipole nature of the fields generated by the polarization charge is clearly seen, giving rise to the given equation that describes the electric field in the vicinity of the crack.

This assumed tangential electric field distribution equation incorporates linear terms along both the x and z directions, as well as a nonlinear function f(x,z) that represents the fields of the dipole charge distribution of the crack. It can further be noted that the linear term in z drops out of the Ampere's law surface integral, and the constants E_{xL} and E_{xxL} are actually linked by the continuity of bound charge at crack edges. Thus, a unique E field distribution is predicted by this formula as a function of the slab and crack dimensions and can be used to model small cracks in relatively large cells. The substitution of this distribution into Ampere's law yields a simple field advance equation, applicable in both two and three dimensional FDTD codes.

Example Calculations

Figures 6 and 7 show time and frequency domain comparisons of plane wave scattering by square dielectric slabs, calculated by the "course grid" FDTD method described above and physical optics. Figure 8 shows a Comparison of "fine grid" and "course grid" FDTD formulations of a 2D slab. Excellent agreement is seen in all cases.

Figure 9 compares "course grid" and "fine grid" FDTD scattered field calculations for a 2D conductor backed dielectric slab. Although the far field RCS calculations of the

"course grid" formulation is almost point for point equal to the "fine grid" calculations, this is somewhat due to the fact that the thin dielectric has little to do with the far field scattering. More importantly, the plot of the near fields of this geometry calculated by both techniques shows excellent agreement, and significant differences with the fields of the conductor without the dielectric. This agreement is important since if shows how well the fields within the dielectric can be predicted with the "course grid" model. This kind of accuracy in the near field is mandatory in order for a "course grid" formulation of cracks in these structures to be possible.

Summary

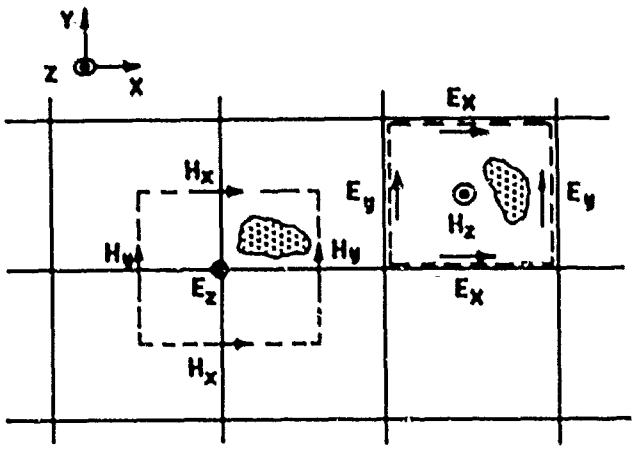
In this paper, we have demonstrated that thin dielectric structures can be modeled in FDTD codes by simply changing the field advance equations in only those cells that contain these structures. The agreement with both physical optics and "fine grid" FDTD formulations show that it is not necessary to use a spatial grid whose dimensions are small with respect to these features.

References

[1] Yee, K.S., "Numerical Solution of Initial Boundary Value Problems Involving Maxwell's Equations in Isotropic Media," IEEE Transactions on Antennas and Propagation, Vol. AP-14, May 1966, pp. 302-307

[2] Taflove, A., K.R. Umashankar, B. Becker, F. Harfoush, and K.S. Yee, "Detailed FD-TD Analysis of Electromagnetic Fields Penetrating Narrow Slots and Lapped Joints in Thick Conducting Screens," IEEE Transactions on Antennas and Propagation, Vol. 36, No. 2, February 1988, pp. 247-257.

Integral Equation View of FDTD



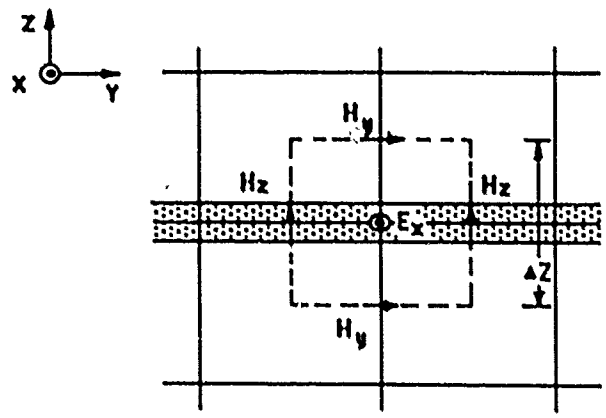
$$\oint \bar{H} \cdot d\bar{l} = \frac{\partial}{\partial t} \int_s \epsilon \bar{E} \cdot d\bar{S} \approx \frac{\partial}{\partial t} \epsilon E_z \Delta S$$

$$-\frac{\partial}{\partial t} \int_s \mu \bar{H} \cdot d\bar{S} \approx \oint E \cdot d\bar{l} \approx \Delta E_x \Delta y - \Delta E_y \Delta x$$

If the near field physics of the obstacle can be predicted, this field behavior can be used to evaluate the field at the cell center given its integral over the cell.

Figure 1

Advancing E Fields Within A Dielectric Slab



$$\oint \bar{H} \cdot d\bar{l} = -\frac{\partial}{\partial t} \int_s \epsilon \bar{E} \cdot d\bar{S}$$

Since the slab is centered with respect to the contour and E_x varies linearly throughout the contour, then

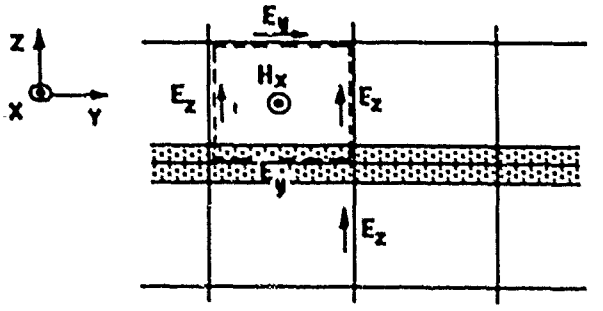
$$-\frac{\partial}{\partial t} \int_s \epsilon \bar{E} \cdot d\bar{S} = -\frac{\partial}{\partial t} \epsilon_{Ave} E_x \Delta S$$

Central differencing in time yields:

$$E_x^{n+1} = E_x^n - \frac{\Delta Z}{\epsilon_{Ave} \Delta S} \oint H \cdot d\bar{l}$$

Figure 2

Advancing H Fields Adjacent to A Dielectric Slab

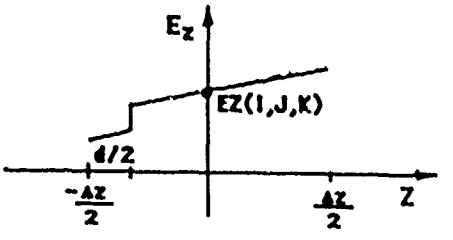


$$\oint \bar{E} \cdot d\bar{l} = -\frac{\partial}{\partial t} \int_s \mu \bar{H} \cdot d\bar{S}$$

Since μ is uniform and H_x is linear,

$$\oint \bar{E} \cdot d\bar{l} = -\frac{\mu \Delta S}{\Delta t} [H_x^{n+1/2} - H_x^{n-1/2}]$$

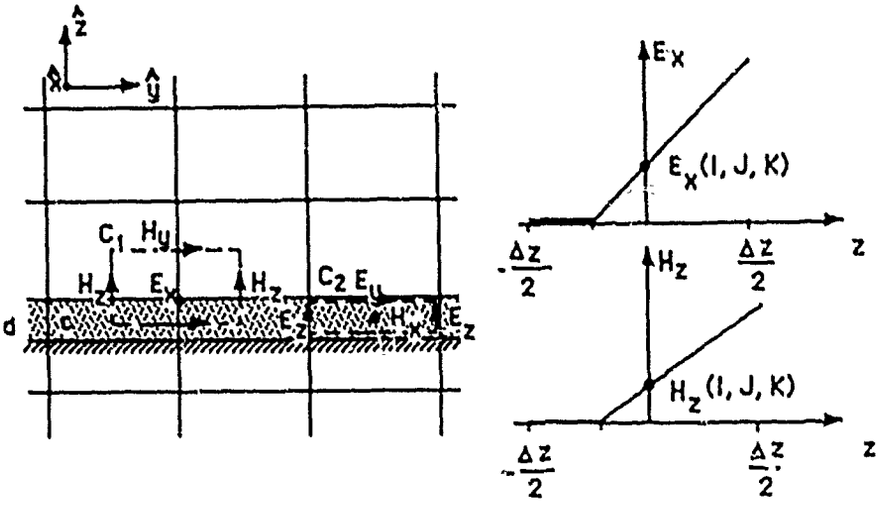
The problem with the contour integral is the discontinuity in E_z.



Using this assumed behavior of E_z yields a finite difference expression for $H_x^{n+1/2}$

Figure 3

Advancing the Fields of Conductor-backed Dielectrics



- E_x at the interface is found by applying Ampere's law around the "deformed" contour C_1:

$$\oint_{c_1} \bar{H} \cdot d\bar{l} = \frac{\partial}{\partial t} \int_s \varepsilon \bar{E} \cdot d\bar{S}$$

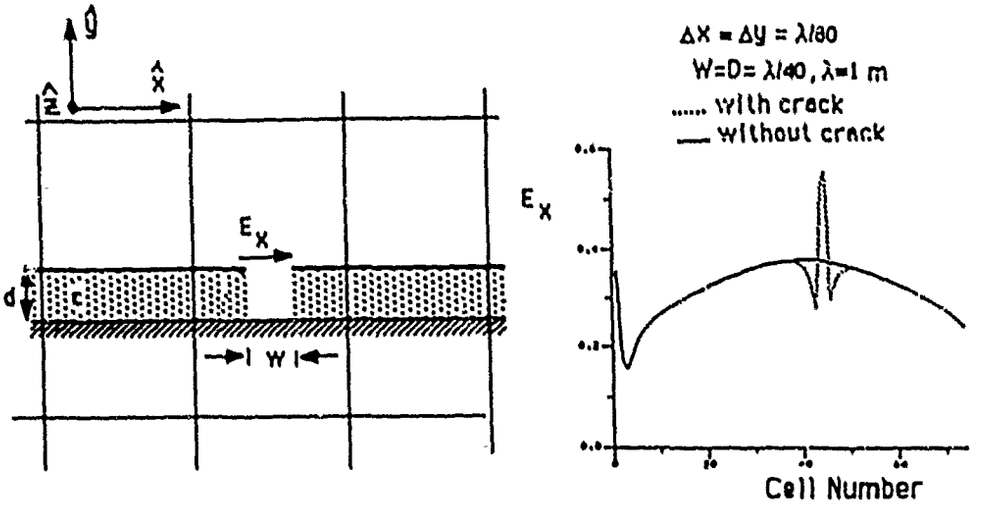
- Inside the dielectric, H_{tan} is found using the subcell within the dielectric and Faraday's law around contour C_2:

$$\oint_{c_2} \bar{E} \cdot d\bar{l} = \frac{-\partial}{\partial t} \int_s \mu \bar{H} \cdot d\bar{S}$$

- Central difference accuracy is retained because E_{tan} & H_{norm} become zero at the conductor surface.

Figure 4

Thin Crack Modeling



- The crack radically changes the distribution of tangential E fields, but not the H fields.

- $E_X = E_{XL} \bullet (1+y/d) + E_{XNL} \bullet f(x,y) + Const \bullet x$
  where, f(x,y) is the pattern function due to charge distribution on the crack walls.

- E_{XL} & E_{XNL} are dependent because ρ_S is proportional to E at the walls.

The E_X field above the crack can be evaluated using modified FDTD equations that utilize these assumptions.

Figure 5

TRANSIENT BACKSCATTER

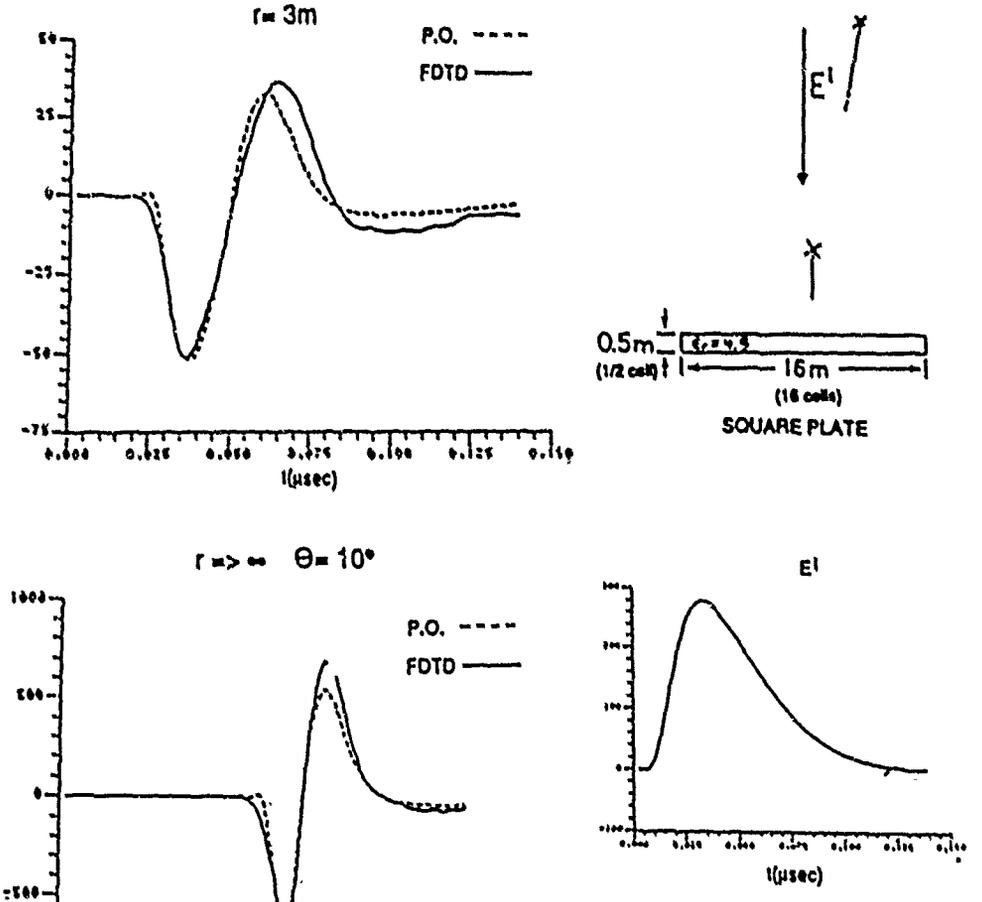


Figure 6

MONOSTATIC BACKSCATTER

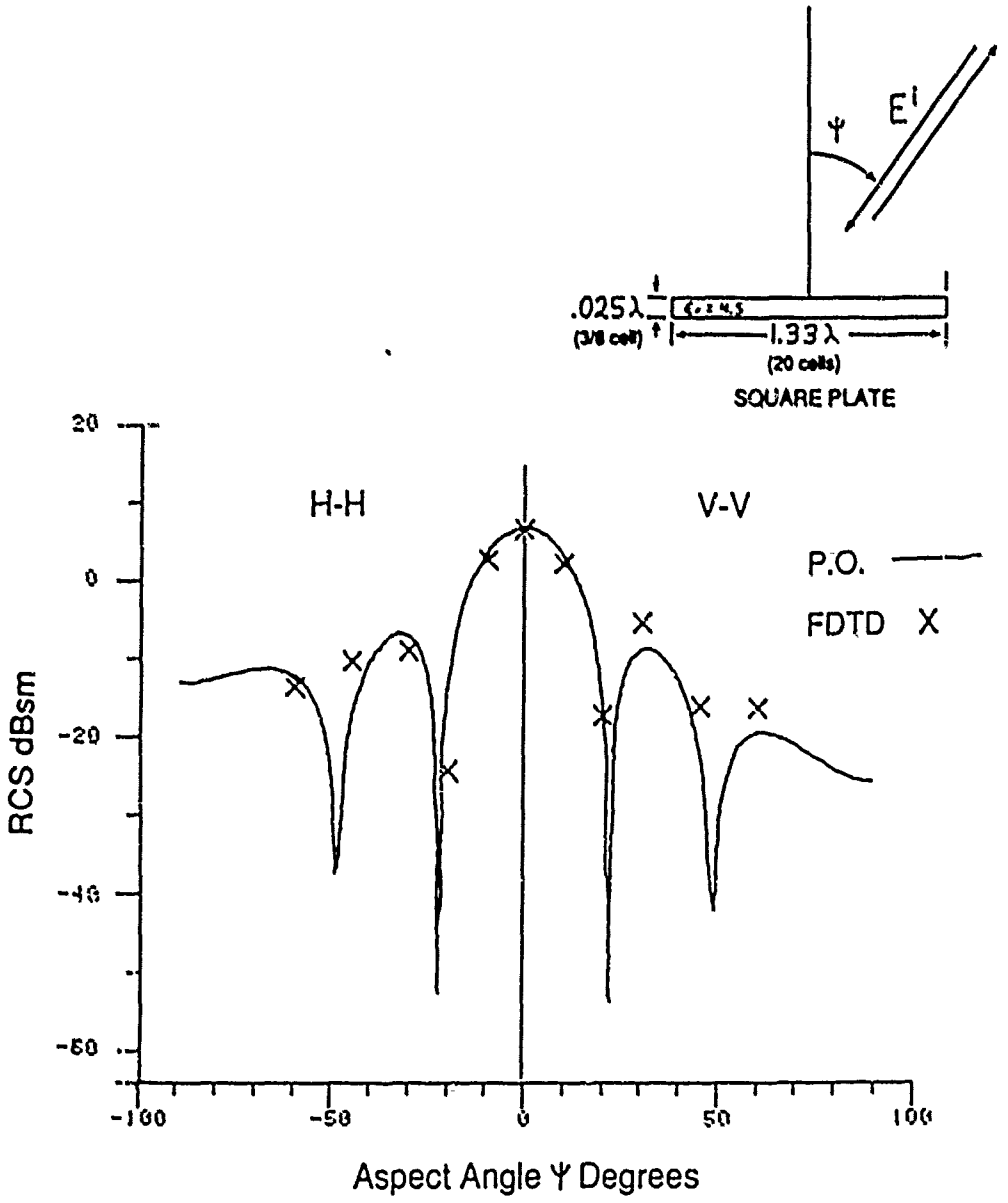


Figure 7

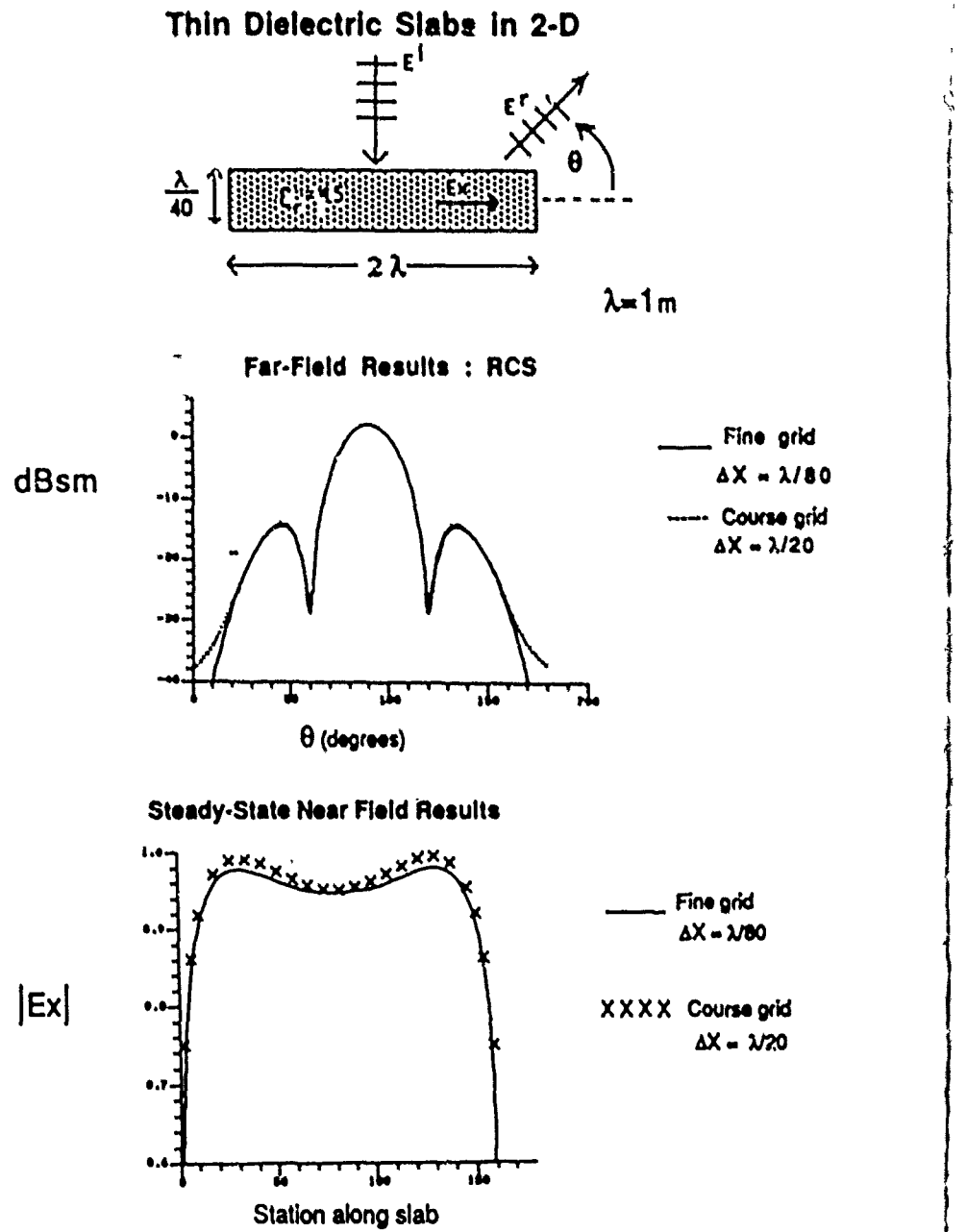
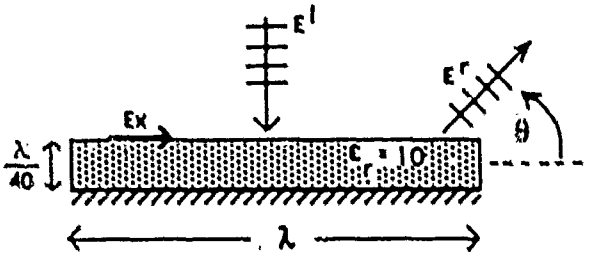

Thin Dielectric Slabs in 2-D
E^i
E^r
θ
λ/40
Er=4.5
Ex
2λ
λ=1m
Far-Field Results : RCS
dBsm
Fine grid
ΔX = λ/80
Course grid
ΔX = λ/20
θ (degrees)
Steady-State Near Field Results
|Ex|
Fine grid
ΔX = λ/80
XXXX Course grid
ΔX = λ/20
Station along slab

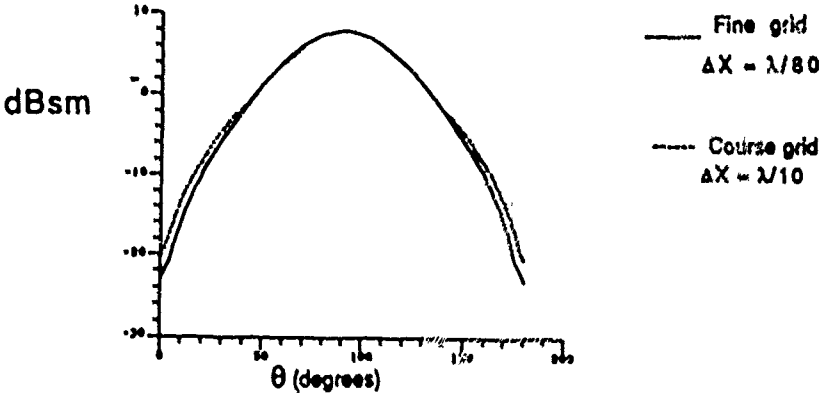
Figure 8

Conductor-Backed Dielectric Slabs in 2-D



λ = 1 m

Far-Field Results : RCS



Steady-State Near Field Results

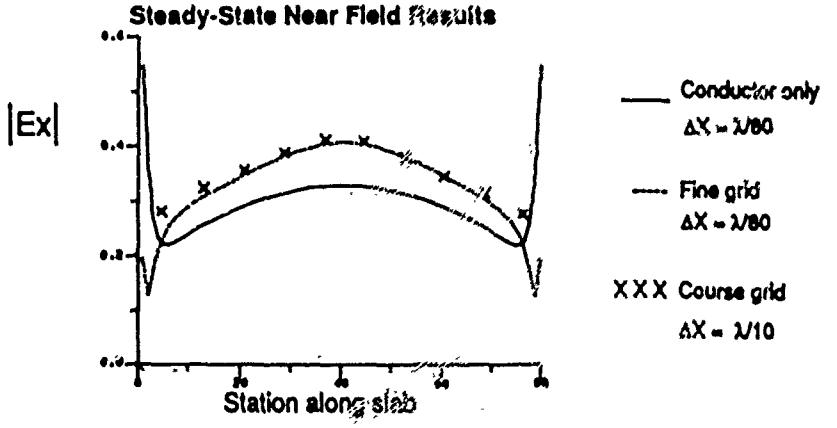


Figure 9

SESSION 7 - 'NEC: NUMERICAL ELECTROMAGNETICS CODE'

Chairman: Robert Noel

INTELLIGENT PRE-PROCESSOR FOR NEC ANTENNA DESIGN SOFTWARE

O. Givati
A.R Clark
A.P.C. Fourie
Department of Electrical Engineering
University of the Witwatersrand, Johannesburg
P.O. WITS 2050
R.S.A.

ABSTRACT

The Numerical Electromagnetic Code version 2, NEC2, is a well known Method of Moments program. NEC2 demands expertise for its use to ensure that results of the evaluation are valid. In addition, the input data file to the NEC2 code is column and row dependent which presents an unfriendly user interface. The Intelligent NEC2 Pre-processor, INP, was written in a modular fashion, using the Turbo Pascal language. It constitutes the framework of a pre-processor which has some built-in expertise required to use the NEC2 code. It may be concluded that the INP package provides a suitable environment to model structures by a user who is unfamiliar with the peculiarities of NEC2.

INTRODUCTION

The Numerical Electromagnetic Code, Version 2, NEC2 [1] is the well known Method of Moments code which analyses the electromagnetic response of metal structures. In order to obtain valid results, the numerical and mathematical modelling of structures must obey a rigid set of rules imposed by the NEC2 code. In addition, the input file which interfaces the NEC2 code is row and column dependent. This constitutes a user unfriendly interface which demands a high level of expertise to use.

The problem therefore, calls for the creation of a pre-processor which has the built-in expertise required for the construction of an input file to NEC2. The intent of this Intelligent NEC2 Pre-processor, INP, software is to keep the user isolated from the various constraints and limitations imposed by the NEC2 code as well as the automatic creation of the input data fi:.

Many antenna engineers with years of practical experience in the design of antennas would now be able to obtain valid evaluation results of performance without having to master the NEC2 manual [1]. This novice use of NEC2 will permit these users to concentrate on what they do best.

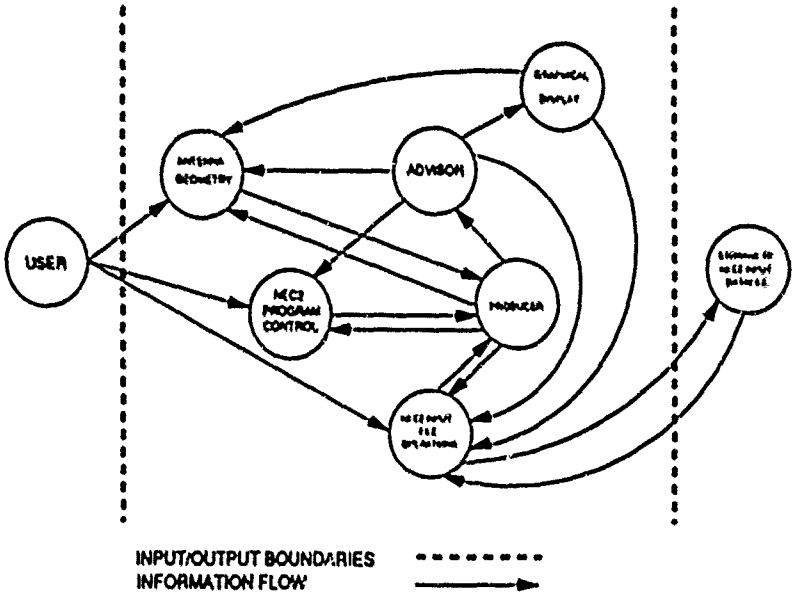


FIGURE 1: A conceptual model of the INP software package

INP is a complete menu driven software package comprising of:

- An input module which caters for the data capture of antenna geometry, NEC2 program control and NEC2 input file operations.
- Graphical display of structures.

- Producer module which coordinates and processes input data in accordance with NEC2 rules and constraints.
- Advisor module to provide the user with program state specific advice at any point in time.

The inter-relations between these modules, as shown in the conceptual model in figure 1, presents a scope for the adequate solution of the problem.

IMPLEMENTATION OF THE INP SOFTWARE PACKAGE

Essentially, the INP software package enables the user to model structures and generate a 'fault free' input data file to interface to the NEC2 code. 'Fault free' in this instance implies both for logical faults (data entry format) as well as modelling faults (violation of NEC2 constraint and rules of thumb). In order to facilitate a user friendly interface, a Screen Management Package [2] was utilized to create the environment within which the INP program executes. For the INP software package to be useful, the input facilities are supported by the presence of the following modules:

Graphical display:	To enable graphical display of the structure.
Producer:	To keep the user isolated from indirectly related computations concerning the structure being modelled and to construct the input data file which is to interface the NEC2 code.
Advisor:	To advise the user, upon request, at any point in time, providing general information concerning the NEC manual as well as past event dependent advice.

The purpose of the input routines is to facilitate data capture of the different specifications of the structure to be evaluated. This is carried out in a user friendly manner where the user is presented with menu options and is prompted for input. The input is then processed by the Producer where transformation of this information into the input data file to NEC2 is performed.

In this section the concepts of the graphical display, the Producer, and the Advisor are discussed and the hierarchical implementation of the INP software package is outlined.

The Graphical Display:

An effective way to present a structure is in graphical form. The motivation of the need of a graphical display emerges from the recognition of the need to reassure the user that the structure geometry

being modelled for simulation, using the NEC2 code, is in fact correctly specified. Ideally, it would be desirable to view the top, side and front views of the structure as well as its three dimensional representation.

Currently, the graphical display facility is able to present top, front and side views of straight wires and their associated loads specified by the user. However, due to the modular fashion with which this software is implemented, an improved visual representation of structures can be realized without effecting the program performance.

The Producer:

The basic devices for modelling structures with the NEC2 code are few and simple, namely straight segments and patches. Nevertheless, it is the proper choice of these devices which determine the accuracy of simulation results. Wire and surface modelling involves both geometrical and electrical factors, to comply with the NEC2 code numerical techniques and algorithm dependent constraints.

As previously stated, the primary objectives of the INP software package are to enable structure modelling and to produce an input data file to interface the NEC2 code. This must be achieved in such a way as to keep the user completely detached from the complexity involved with modelling. The user may therefore be confined to the coordinate system only. At first, this may be seen as an extraction of the power possessed by the NEC2 code. Nonetheless, this modelling power is retained by the editing facilities.

The objectives of the Producer module are therefore:

- To automatically perform segmentation of wires and allocate them with a tag number for identification purposes, as required by the NEC2 code.
- To convert coordinate specifications to their corresponding segments and patches.
- To check for violation of any of the modelling constraints wether these are NEC2 constraints or other rule found by users.
- To produce and maintain the input data file to NEC2, which comprises the deck of cards, subject to the various modelling constraints imposed.

In effect, the Producer is the principle coordinator of the INP software package, and any input made by the user is processed by this module.

The Advisor:

The user function is to describe an antenna and its environment and to request computation of antenna characteristics. The INP software package is configured in such a way as to allow free

access to all menu options at all times. Each menu option has a specific intent in specifying the model features. The process of specifying the different parameters demands some background knowledge which the user may not have. In addition, the unfamiliar user may attempt to specify parameters in an irrational manner or order. For example, specifying a request for radiation pattern before any geometry is specified is analogous to an attempt to place an item on a table which does not exist. In such event, the Producer will detect and resolve the misdeed but without a comprehensive elaboration on the nature of the blunder.

The objective of the Advisor module is therefore to cater for on-line help files. These help files provide general information concerning the various features of the program and modelling specifications which are program position dependent. Also, in the event of erroneous proceedings a comprehensive explanation of the nature of the oversight is made available. This feature is program state dependent (context sensitive) which also account for previous inputs.

The INP Program Hierarchy:

A descriptive manner in which the project hierarchy can be presented is by means of a block diagram representation, as shown in figure 2. This outlines the main menu options indicating the various modelling features provided by the NEC2 code to be utilized by the antenna engineer. These, together with input and output file handling for storage purposes, as well as editing facilities, graphical display and the presence of the Advisor and the Producer as illustrated in figure 1 above, provide inclusive categorisation of the INP software package as a whole.

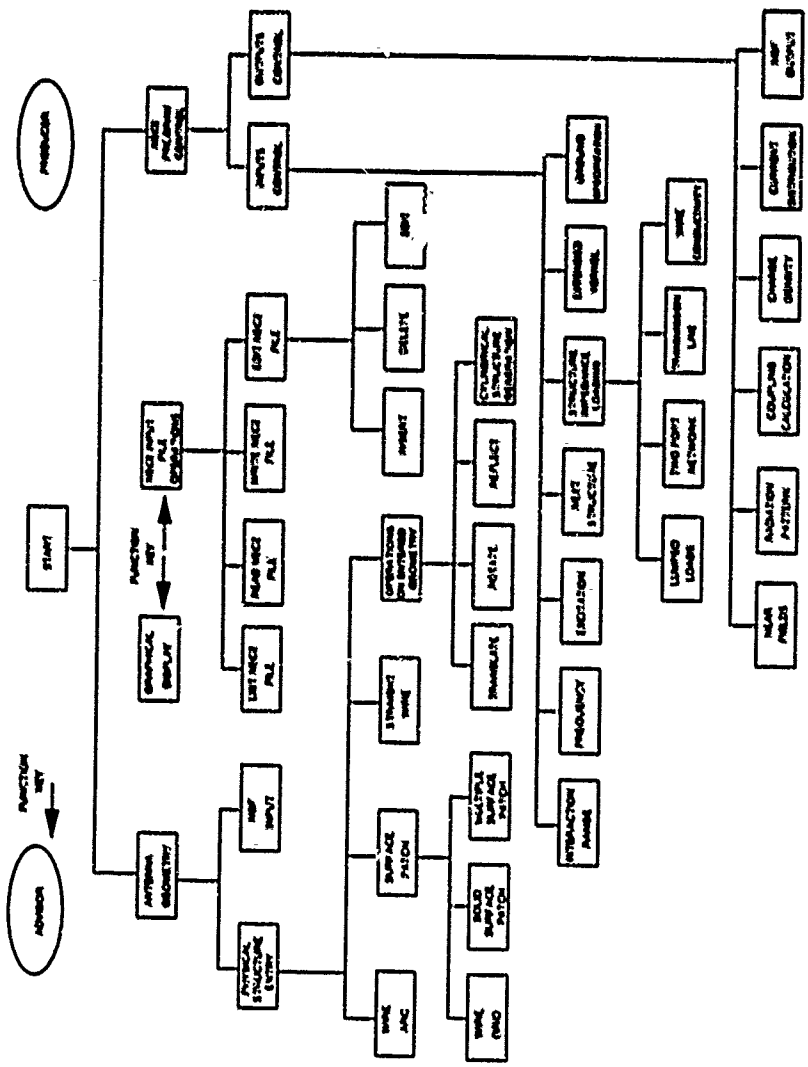


FIGURE 2: The input module hierarchy

THE CHOICE OF PROGRAMMING LANGUAGE AND THE SCOPE FOR BUILT-IN INTELLIGENCE

The Choice Of Programming Language

The amount of data storage requirements throughout the execution of the INP program is not fixed. This calls for dynamic data structures which change in size during the program execution. These provide an elegant and efficient means to insert and delete components without worrying about where new components fit or what happens to the empty space left by a deletion.

A versatile graphics library is the Turbo Graphix Toolbox [3], which was used for the development of graphical displays implemented in this project. In addition, the Screen Management Package [2] which constitutes the menu driven outer shell within which the INP program executes was also written in Turbo Pascal.

These considerations led to the choice of using Turbo Pascal [4] as a programming language.

Why Not Expert System?

The expert system consists of a knowledge base and an inference engine. The knowledge base contains facts and rules indicating how the facts are inter-related. The inference engine is a control mechanism inferring information from the knowledge base by selection of the rule to be used and at which point in time it should be used. Unlike conventional computer programs, the expert systems have no algorithmic solutions and often a conclusion is based upon uncertainty or incomplete information [5].

The power behind expert systems is that they provide a regimen for expert knowledge to be codified, and in that knowledge lies the power. Domain knowledge is processed in a strict order of deductive inference and execution occurs once only. Expert systems can have both deep and surface (also termed shallow) representation of knowledge. Deep representations are casual models, categories, abstractions and analogies, where an understanding of structures and their functions is represented. Surface representations are empirical associations of rules and facts [5].

A prerequisite for employing an expert system for this purpose is its capabilities to couple numeric and symbolic computation in an iterative fashion. This would require an intelligent front end system for numerical processes, which is required to be a deep coupled system [6] and this is unfortunately not yet available.

Numerical Modelling Constraints And Limitations

In this section, constraints associated with the use of the NEC2 code are highlighted [1]. It is not the purpose of this paper to cover all the modelling constraints which are imposed by the NEC2 code but only to highlight a cross section of them. This is carried out in the hope of conveying the complexity which is involved with structure modelling. The Producer in INP checks for these constraints, informs the Advisor, and either corrects or rejects input accordingly.

In NEC2, a segment length should be less than 0.1 of a wavelength and greater than 0.001 of a wavelength at the desired frequency of analysis. The built-in expertise of the pre-processor Producer module will therefore divide the wire into segments according to this 10:1 rule.

The Method of Moments technique used considers only current flow in the axial direction on a segment. The acceptability of these approximations is dependent on the wire radius such that unless the ratio of wire radius to wavelength is much less than 1-2, the validity of these approximations is questionable.

The accuracy of the numerical solution for axial currents is also dependent on the ratio of segment length to wire radius. This ratio must be greater than 8 in order to achieve errors of less than 1 percent, using the standard thin wire kernel, and may be as small as 2, if the extended thin wire kernel is used.

Segments are treated as connected when the separation of their ends is less than 0.001 times the length of the shortest segment.

Maintenance of current continuity across wire junction presents another limitation since antennas with short sections of wire coupled to long ones require exceedingly large number of segments to be analyzed [7]. Kubina's rule of thumb states that "The restriction on the relative length of segments that form a junction, require that these lengths be comparable within a factor of five" [8]. Furthermore, the number of wires joined at a single junction cannot exceed 30 due to a dimension limitation in the NEC2 code.

A conducting surface is modelled by means of multiple, small flat surface patches corresponding to segments used to model wires. The patches are specified such that they cover the entire surface to be modelled. The parameters defining a surface patch are the cartesian coordinates of the patch centre, the component of the outward directed unit normal vector and the patch area.

For accuracy of results, a minimum of 25 patches per square wavelength of surface area should be used and the maximum size of an individual patch should not exceed 0.04 square wavelengths.

Since the division of current between two overlapping segments or patches is indeterminate, segments or patches may not overlap.

The radius of tapered wires may not change drastically since a large radius change between connected segments may decrease accuracy. This rule particularly applies where the ratio of segment length to radius is small.

A segment must exist at each point where a network connection or voltage source will be positioned. This constraint is imposed so that voltage drop can be specified as a boundary condition.

Finally, the order in which the various cards are specified must obey some rules which are imperative for a successful run of the NEC2 code. Generally, the card deck begins with cards containing comments made by the user. These are followed by geometry data cards specifying the geometry of the antenna and thereafter the program control cards, specifying electrical parameters and requests for the computation of antenna characteristics.

New rules of thumb are emerging all the time and should be implemented as they come forth. Generally, modelling of structures subject to the various constraints will be coordinated by the Producer which at worst will reject the user specification and thereafter the Advisor will provide an explanation and advice.

AN EXAMPLE OF USE

In order to illustrate the manner in which the INP program should be used to produce the input file to NEC2, consider the High Frequency (HF) broadband antenna due to Givati and Clark [9]. This antenna is shown in figure 3 below.

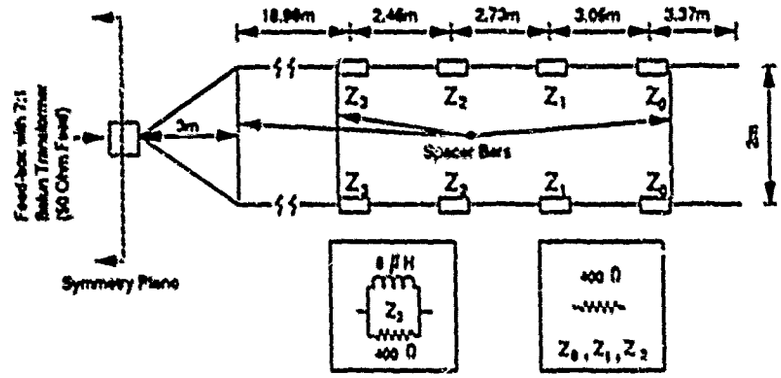


FIGURE 3: The HF broadband antenna due to Givati and Clark

In general, structures should be modelled, according to figure 2, by firstly specifying the Antenna Geometry, then the Inputs Control options and finally the specification of Outputs Control. The above antenna was modelled using the INP program as follows:

- Straight wires were specified in terms of cartesian coordinates as shown in figure 3 above.
- The various loads were specified on all arms using the Lumped Loads menu option. These loads are placed, by the Producer, in the closest segment to its specified location.
- A Ground plane was stipulated.
- Frequency sweep at 5MHz, 10MHz and 15MHZ was specified. The Producer then generates three differently segmented models for the different frequency bands. This enable the simulation of the antenna over the High Frequency band (2Mhz to 30MHz) and saves on computer time since the optimum number of segments are used at each frequency.
- The type of excitation and its magnitude was then stipulated using the Excitation menu option
- Finally, a request for Radiation Pattern was specified.

The output is the input data file to interface the NEC2 code. This output file has a normal ASCII format and can be used to execute NEC2. In addition, a second file is created in a different format for storage purposes.

CONCLUSION

An attempt has been made to create yet another interface to the NEC2 code which is so widely used today. This pre-processor to NEC2 caters for the antenna engineer who is unfamiliar with the various constraints and limitations imposed by the NEC2 code.

Even for a user who is familiar with the NEC2 code, the INP software package may prove to be a convenient tool for complex structures generation and perhaps partial isolation from the crude form of interface which is the input file to NEC2.

The INP software, to-date, is by no means finalized and perhaps will never be, as more expertise for the use of NEC2 are acquired all the time. There is room for all these to be built into the INP code. More suggestions for further work include the development of a higher level antenna design module which is able to interface the INP software. This module should include a library of design algorithms of known antenna structures which would then be transformed by the INP code into a file suitable for the execution of NEC2. These, together with the NEC2 code and a post-processing package possess a potential for a complete computer aided design tool for antennas.

REFERENCES

[1]. Burke, GJ. and Poggio, AJ. "Numerical Electromagnetic Code (NEC) - Method of Moments" Parts I, II, III. NOSC Tech Doc 116, Naval Ocean Systems Centre, San Diego, CA., July 1977 (NEC1); Revised Jan. 1980 (NEC2).

[2]. Walker, AJ. "Screen Management Library" University of the Witwatersrand, Johannesburg, 1986

[3]. -----,TURBO GRAPHIX TOOLBOX Version 1.0 Borland International Inc. California, USA. 1985.

[4]. -----,TURBO PASCAL, Version 3.0 Borland International Inc. California, USA. 1985.

[5]. Michaelsen, RH., Michie, D., and Boulanger, A. "The Technology of Expert Systems" Byte April 1985. pp 304-312.

[6]. Kutzmiller, CJ. and Kowalik, JS. "Coupling Symbolic and Numerical Computing in Expert Systems", Papers from workshop on coupling symbolic and numerical computing in expert systems, Bellevue, Washington, editor Kowalik, JS, 27-29 August 1985. Elsevier Science Publishers, Amsterdam pp 3-17.

[7]. Austin, BA. and Fourie, APC. "Numerical Modelling and Design of Loaded Broadband Wire Antennas" IEE Fourth International Conference on HF Radio Systems and Techniques, April 1988, pp 125-129.

[8]. Kubina, SJ. "Numerical Modelling Methods for Predicting Antenna Performance on Aircraft" AGARD lecture series No 131. Sept 1983. pp 9-1 to 9-38.

[9]. Givati O. and Clark, AR. "Computer Aided Design of an High Frequency Broadband Antenna" Chapter 3, Final Year Design Report, Department of Electrical Engineering, University of the Witwatersrand, Johannesburg. P.O WITS 2050. RSA. December 1987.

PROBLEMS WITH THIN WIRE EMULATION OF THICKER WIRES USING NEC2

A.R.Clark
A.P.C.Fourie
Department of Electrical Engineering
University of the Witwatersrand, Johannesburg
P.O.Wits
2050 South Africa

1 Abstract

The concept of emulating an electrically thick structure by thin wire vestigial emulation is well known. It is often useful, however, to investigate the properties of a simpler, thicker, structure model in preference to a thin wire cage model as this is typically less computationally intensive. The validity of adopting this simplified approach to antenna design was tested using the Method of Moments Code NEC2. Applying the method of the Geometric Mean Radius, a thick single wire model, a 2 wire flat model and a 4 wire cage model of the same antenna were designed and evaluated with NEC2. These models were excited by the current slope discontinuity, and the applied E-Field source. It is shown that the emulation approach outlined is valid for both source types, with a resultant significant reduction in computation time. However, the applied E-Field source model produces results that correlate to measured results, whereas the current slope discontinuity source model does not. It is also shown that the wire length of the thick wire model must include the length of any bends in the thin wire structure.

2 Background

Evaluating typical broadband HF antennas using NEC2 [1] presents a unique set of problems, as these antennas often operate over a 15:1 frequency bandwidth (2-30 MHz). Thus they are electrically short at the low frequencies (about a half wavelength long), and electrically long at the higher frequencies (about 6 wavelengths long).

To assist in achieving such a wide bandwidth, these antennas are made to be electrically thick, as it is well known that a thicker structure is more inherently broadband than a thin structure (as a result of a lower Q), and that this is usually implemented as a cage structure of thin wires, spaced apart to emulate a thicker structure. [2]

Unfortunately the length of computational time required to evaluate an antenna in NEC2 is essentially proportional to the square of the number of wavelengths of wire in the antenna (or even cubed if the antenna is large enough for the impedance matrix solution term to take precedence over the matrix fill term).

It is therefore desirable to be able to reduce the structure to a single thicker wire NEC2 model, as this will clearly greatly reduce computational effort. Once the trends have been noted, and the antenna optimized for a certain set of criteria, a full NEC2 thin wire emulated model can be used for the final results.

It is this approach that is discussed and validated in this paper. There are essentially two main aspects to be considered, namely:

- what the wire length of the single thick wire should be, if the original thin wire antenna contains bends, and
- which source model should be used.

3 Wire Length

The problem can be illustrated by considering the ubiquitous Australian Dipole [3], illustrated below.

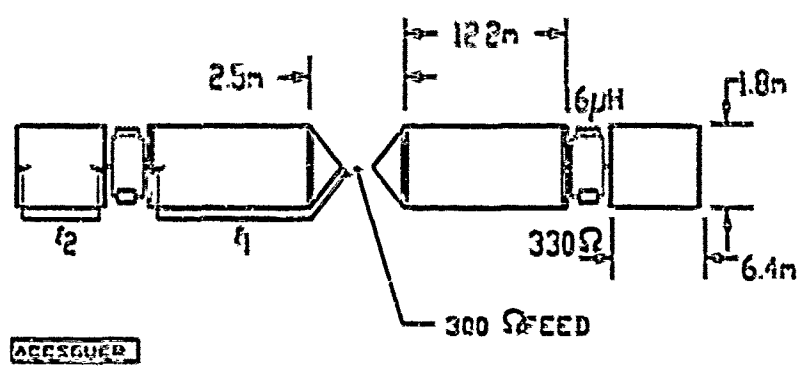


Figure 1: The Australian Dipole.

It can be seen that the wire length l_1, from the feed point to the load connection point is significantly longer than the linear length 12.2 m, as l_1 includes the length of the bends in the wire, and similarly with l_2, the length of wire from the load to the end of the antenna. Considering the section of wire

from the feed to the load, the question is whether to make that wire in the single thick wire model as long as the linear length (12.2m) or the wire length (l_1) in order to achieve accurate results. A useful experiment has been conducted by Austin & Fourie [4] in this regard, and whose results are shown in figure 2 below.

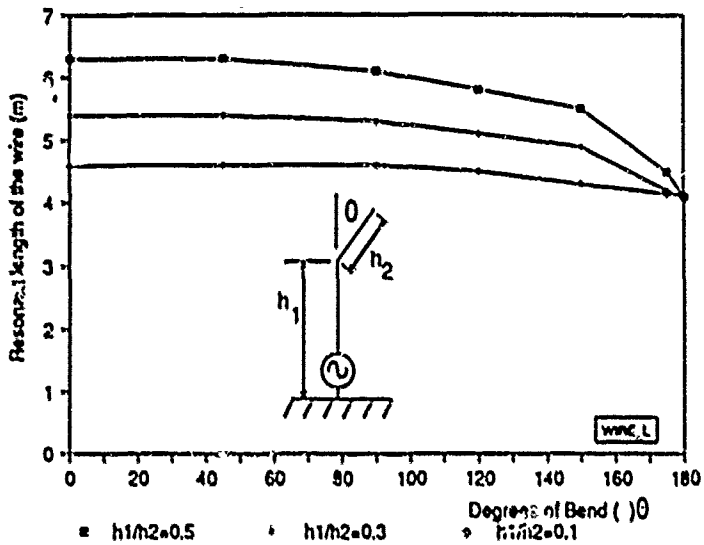


Figure 2: The effect of a bend on the resonant length of a wire.

The experiment was performed with NEC2, and involved examining the resonant length of a piece of wire if the top section was bent. Here h_1 is a fixed length of 1m, and the angle θ is varied from 0 to 180°. The top section's length is stepped through 0.1m, 0.3m, and 0.5m. The results show that the length at which the bent wire resonates is that at which the sum of the two lengths resonate (h_1+h_2). This holds for up to a 90° bend in the wire, and for length ratios (h_1/h_2) shown. As the angle increases, the resonant length tends to h_1.

Thus the correct value to use for the feed-to-load section of the Australian Dipole shown in Figure 1, is l_1(= 14.64m) and not 12.2m, which is a significant difference in the frequency at which this wire will resonate.

4 Source Type

Most HF dipole antennas are symmetrical in nature, and this is often exploited in their evaluations by the symmetry plane feature offered in NEC2. This feature reduces computation time by a significant amount and is, as a rule, employed wherever possible.

There are two source models in NEC2 that are of interest, the Current Slope Discontinuity model (source type 5), and the Applied E-Field model (source type 0).

The excitation produced by the Current Slope Discontinuity model is located at the first end of the segment in which it is specified, and hence the excitation is ideal for use at a plane of symmetry. The conditions for the application of this source model state that the abutting segment should be of the same length and radius, which is obviously met in a symmetry plane.

The excitation produced by an applied E-Field source model (type 0), however, excites the centre of the segment in which it is specified, and should this model be used in a segment abutting on a symmetry plane (but not penetrating the plane), the excitation on the structure will be offset by a half segment length, and thus will not be correctly placed at the symmetry plane.

The following investigation shows, however, that the better source model to use is, in fact, the applied E-field model (type 0), assuming, of course that the half segment offset is not too large. A single thick wire model of a multiple loaded antenna [5] was used in this investigation, each dipole arm being 33.75m long, with a 0.13m radius. Ie a thickness factor (Ω) of 12.5, where

$$\Omega = 2\ln\left(\frac{2h}{a}\right) \qquad (1)$$

where: a is the radius of the wire, and

h is the length of one dipole arm.

The physical antenna, in its two wire emulated form, is shown in Figure 3.

The NEC2 results of a single, thick wire model, excited by the two different source models are shown in Figure 4, together with a set of measured results for comparison. The measured results used in the investigations were obtained with an HP 4815A RF Vector Impedance Meter, on the two wire implementation of this antenna shown in Figure 3, configured in a sloping vee on a 12m mast.

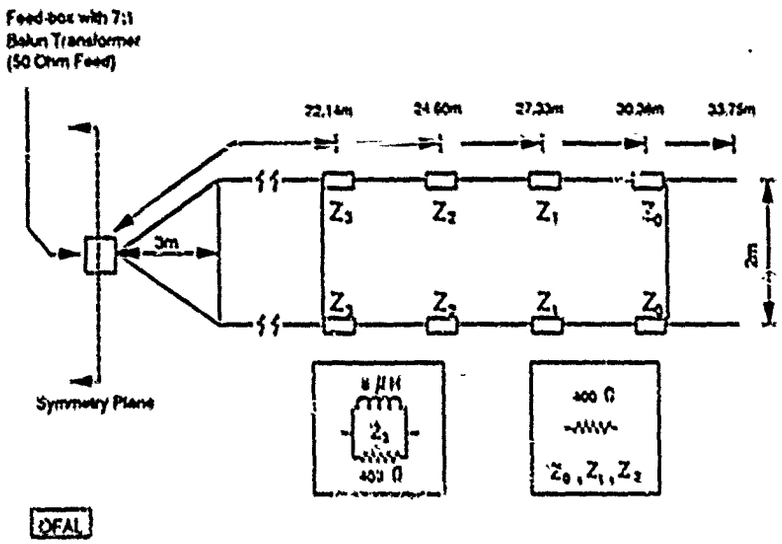


Figure 3: An HF Broadband Antenna, after Clark & Givati. [5]

From Figure 4 it is clear that the applied E-Field source VSWR results (the source 0 legend) are far closer to the measured results than the current slope discontinuity source results (the source 5 legend). One must therefore conclude that it is imperative to use the applied E-Field source model in this application.

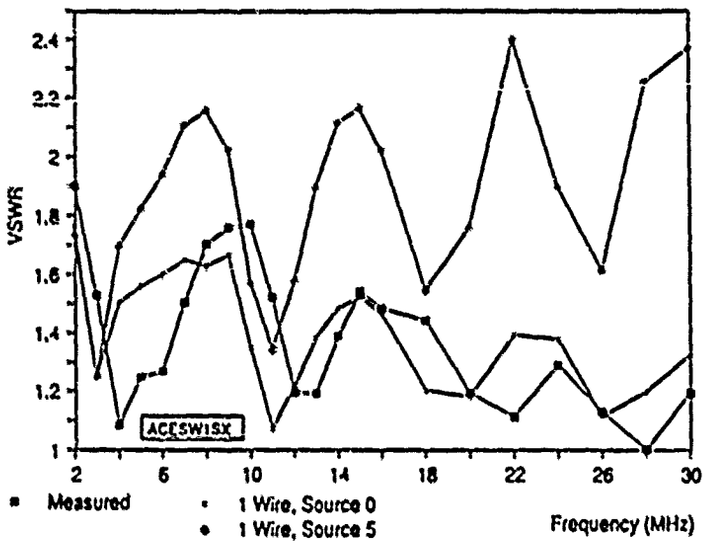


Figure 4: Thick wire model VSWR results, measured vs source 0 and source 5.

5 Emulation Method Verification

This investigation shows that results can be produced from a single thick wire structure which correlate well with those obtained by the 2 and 4 wire structures. The correct dimensions for the multiple wire structures were derived by the theory of the Geometric Mean Radius (GMR) [6], which states that the GMR of a bundle of n identical conductors, spaced symmetrically, is given by:

$$GMR = \sqrt[n]{r_m \left(\prod_{i=1}^{n} s_i \right)} \qquad (2)$$

$$r_m = e^{-\pi/4} a \qquad (3)$$

where: $\prod_{i=1}^{n} s_i$ is the product of all distances from one conductor in the group to all the others in the group. (Since we have made the simplifying assumption that symmetry exists)

r_m is the geometric mean radius of a single conductor

μ_r is the relative permeability of the conductor

a is the actual radius of a conductor.

Assuming non ferrous conductors, the $e^{-\mu_r/4}$ term in Equation (3) has been shown to have little effect on the final emulation results, and the r_m can be taken to be the actual radius of the conductor. As n increases, the effect becomes even less.

Using this method, a two wire flat model, and a four wire cage model were designed, and run on NEC2. In the case of the 4 wire model, the results are obtained up to 16 MHz only as higher frequencies demand too much space (and time) on a personal computer. The NEC2 results are shown in the figures below.

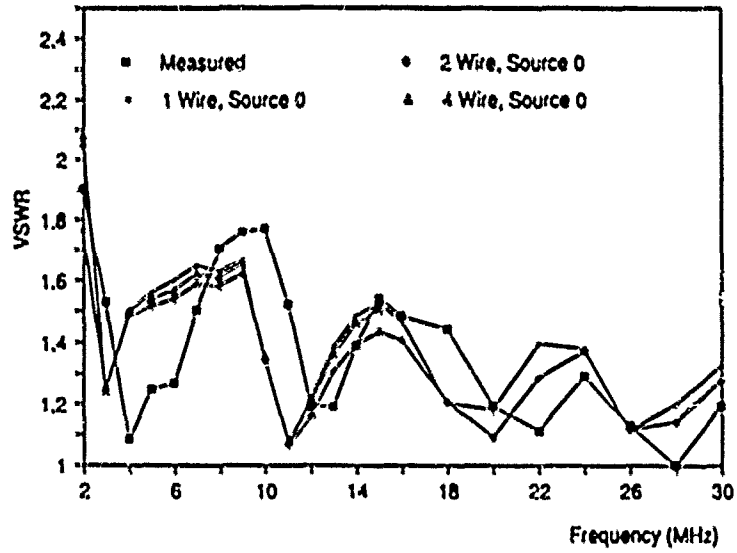


Figure 5: Source 0 results for 1, 2, and 4 wire models of the antenna, and the measured results.

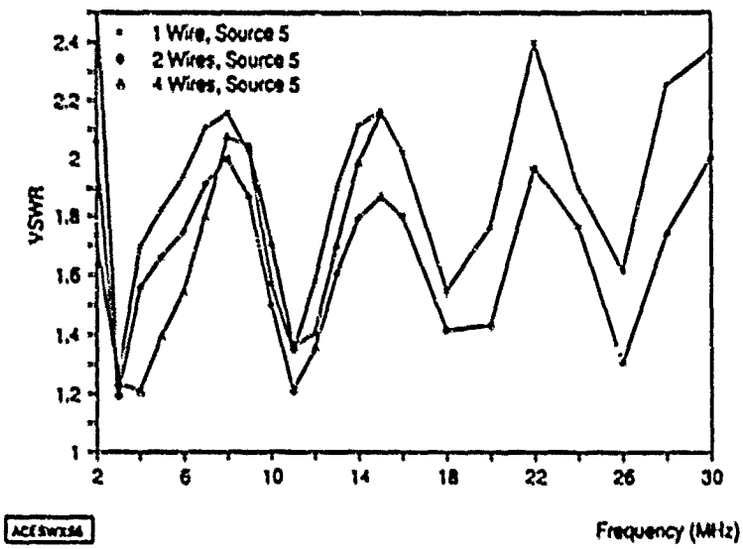


Figure 6: Source 5 results for 1, 2, and 4 wire models of the antenna.

Figure 5 and 6 show that the 1, 2, and 4 wire emulations of the antenna have very reasonable VSWR correlation for both source models, and thus the evaluation method outlined can be employed. It can also be seen that the two source models do not produce similar results and as is clear from Figure 5, the source 0 results track favourably with the measured results for this antenna, whereas the source 5 results do not.

Figure 7 shows the efficiency results produced by NEC for all emulations of the antenna, and both source types. It can be seen that the results all tend to bunch together, except the trace above and below the bunch. It should be noted that both of these errant traces are produced by the source type 5.

Thus again it is seen that the emulation method can be applied with a reasonable degree of accuracy, but that source 0 must be used if realistic results are to be achieved.

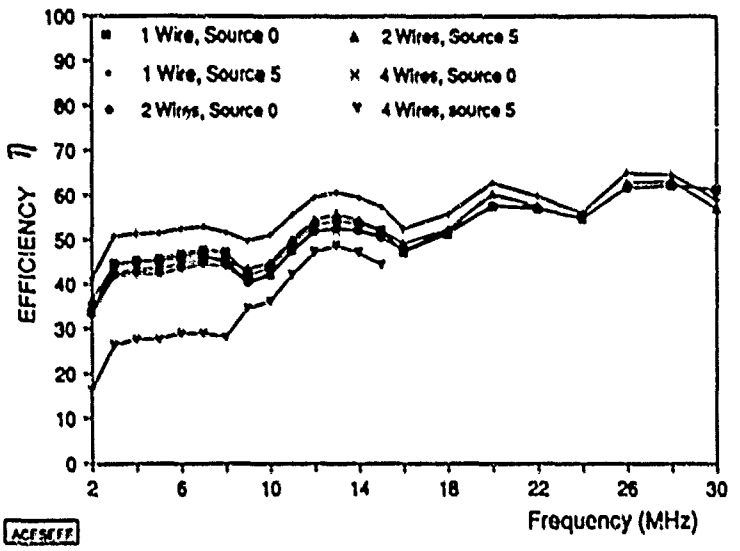


Figure 7: Efficiency results: All emulations and source types.

6 Conclusions

- A method of evaluating a multiple thin wire antenna using a simpler single thick wire model in NEC2 has been discussed, and validated. The results of the various emulations of the antenna are sufficiently similar to warrant its use, as the advantage to be gained by using this method is a major computational time saving, especially in optimization investigations.
- The NEC2 source type 5, the current slope discontinuity source model, seems to produce erroneous results. This was investigated only when placed at a plane of symmetry. It has been shown that the simple substitution of source type 0, the applied E-Field source, in its place, even though this does not result in an exact placement of the source, produces results which correlate to the measured results.
- The resonant length of a bent wire is that of the actual length of wire. This holds up to an angle of 90°, and for a bent section of up to half the length of the unbent section. It is important to use this length in the thick wire models for NEC2.

7 References

[1] Burke G.J, Poggio A.J "Numerical Electromagnetics Code (NEC) - Method of Moments" Naval Oceans Systems Centre, San Diego, CA Tech Doc 116 1981

[2] Treharne R.F "Multipurpose Whole-Band HF Antenna Architecture" Jrnl of Electrical & Electronics Engineering, Australia vol.33 no.2 pp.141 - 152 1983

[3] Guertler R.J.F, Collyer G.E "Improvements in Travelling Wave Dipoles" Proc. IREE Convention, Melborne August pp.70 - 71 1973

[4] Austin B.A, Fourie A.P.C "Numerical Modelling and Design of Loaded Broadband Wire Antennas" IEE Fourth International Conference on HF Communication Systems and Techniques. Conference Pulication 284 pp.125 - 128 1988

[5] Clark A.R., Givati, O "Computer Aided Design of an HF Broadband Antenna" Final year design report, Department of Electrical Enginnering, University of the Witwatersrand, Johannesburg. September 1987.

[6] Guile, A.E, Patterson, W. "Electrical Power Systems" Vol 1, Pergamon Press, Oxford, pp 72 - 98 1977

NEC-3 ON A PC, RE-VISITED: THREE YEARS LATER

Timothy M. O'Hara

and

Richard W. Adler

Code 62AB
Naval Postgraduate School
Monterey, CA 93943

ABSTRACT

The purpose of this study was to determine if recent improvements in the computing power of Personal Computers (PCs) have made them a viable alternative to the larger, multi-user oriented computers, better known as mainframes. The Numerical Electromagnetics Code (NEC3), a 10,000 line Fortran program, was down-loaded from the Naval Postgraduate School's IBM 3033AP mainframe and implemented on various PC systems. The systems considered were the IBM RT PC (using IBM RT PC VS FORTRAN), a Definicon DSI-780 Coprocessor Board (using SVS FORTRAN), and a Compaq Deskpro 386/20 AT PC (using NDP FORTRAN-386). Using NEC3 example problems, comparisions of speed and accuracy were made between the PCs and the mainframe.

Results show that the Compaq Deskpro 386/20, with a Weitek 1167 math coprocessor, using MicroWay's NDP FORTRAN-386 (32 bit Fortran compiler), can be used to implement NEC3 on a PC. Performance times for the Deskpro (w/1167) were only 20% to 25% slower than the mainframe's. Due to the Weitek's internal accuracy (single precision), solutions of the NEC3 examples were comparable to the mainframe's only for simple problems. As the complexity of the NEC3 problems increased, the error due to the Weitek's single precision calculations also increased.

I. INTRODUCTION

Within the last few years, the scientific, industrial, and educational communities have become increasingly dependent on the use of Personal Computers (PCs). Although word processing, data base management, and other utility programs have fueled this PC explosion, recent increased in CPU (Central Processing Unit) clock speeds and the improvement of math coprocessors have increased the computational capabilities of PCs to impressive levels. These improvements now make the PCs capable of handling numerically intensive programs usually reserved for larger computer systems, often referred to as mainframes.

The objective of the study was to determine whether or not a large mainframe dependent program, specifically the Numerical Electromagentics Code (NEC3), can be implemented on a PC. The PC systems to be considered are an IBM RT PC (work station), a Definicon DSI-780 Coprocessor Board (mounted in an IBM compatible AT/386), and a Compaq Deskpro 386/20 AT PC (with Intel 80387 and Weitek 1167 math coprocessors).

NEC was originally developed at Lawrence Livermore National Laboratory, Livermore, California, under the sponsorship of the Naval Ocean System Center and Air Force Weapons Laboratory. This program is an offspring of the Antenna Modeling Program (AMP) written in the early 1970's by MBAssociates for the Naval Research Laboratory, Naval Ships Engineering Center, U.S. Army ECOM/Communication Systems, U.S. Army Strategic Communications Command, and Rome Air Development under the Naval Research Contract N00014-71-C-0187. NEC3, the current version of NEC, was developed by G. J. Burke of Lawrence Livermore Laboratory.

NEC3 is an antenna modeling program designed to handle a wide range of antenna structures. This makes it ideal for use in the military due to the numerous structures (e.g., ships and vehicles) used to

support antennas. The code itself is heavily dependent on numerical integration and often pushes the computer's ability to calculate accurate data. NEC3, written in standard Fortran 77, is approximately 10,000 lines long and incorporates over 80 subroutines.

NEC was previously converted to a PC by Stephen P. Lamont. Each subroutine had to be separately compiled, and modifications to the code were made in order for NEC to run in the PC DOS (Disk Operating System) environment. Due to the limited in-core memory (640K), execution times were not fast enough to justify running NEC3 on a PC. However, recent advances in both hardware and software now make it worthwhile to investigate using a PC as an alternative to the mainframe.

II. SYSTEM HARDWARE AND SOFTWARE CONFIGURATIONS

The computer systems used in this experiment include an IBM RT PC, a Definicon DSI-780 Coprocessor Board, a Compaq Deskpro 386/20 PC, and the Naval Postgraduate School's IBM 3033AP Mainframe. The IBM RT PC, Compaq Deskpro 386/20, and IBM 3033AP are fully independent computer systems. The DSI-780 however, does require the power supply and input/output (I/O) capabilities of an IBM AT PC compatible host. Each of these systems requires unique software in order to compile and execute Fortran programs such as NEC3 and SOMNTX.

Since the focus of this research is on the PC world, the hardware and software descriptions of the IBM 3033AP Mainframe will not be included. Performance times of the mainframe compared to the other systems will be detailed in Section IV.

A. IBM RT PC

The IBM RT PC is an advanced computing system. Operating under a version of UNIX, the IBM Advanced Interactive Executive Operating System (AIX), the RT PC is a multi-user and multi-tasking capable computer. It uses a 32 bit RISC (Reduced Instruction Set Chip) processor and a 40 bit virtual memory manager. The RT PC is available in various configurations; the system used for this research is a Model 125. It comes standard with an Advanced Processor Card, a NS32081 Floating Point Accelerator Card, 4 Mbytes of 32 bit memory, a 1.2 Mbyte floppy disk drive, and a 70 Mbyte fixed disk drive. Installed options include a second 70 Mbyte fixed disk drive, and a 360 Kbyte floppy disk drive. The monitor used is an IBM 6154 Advanced Color Graphics Display.

IBM RT PC VS FORTRAN is a powerful and rather extensive programming package. Some of the most important features include.

- Source compatibility with ANSI Standard FORTRAN 77.
- Optimized executable code.
- No significant limit on program or data size.
- Variety of compile time options.

The most important features required to compile and run NEC3 are standard Fortran 77 compatibility and the ability for virtually unlimited program or data size. The limiting factor for the program or data size is simply the amount of memory installed in the system. Because VS FORTRAN operates in the UNIX environment, the 640 Kbyte addressable memory limit that is encountered on most IBM PCs and compatibles does not occur. The larger available memory allows a program the size of NEC3, which has over 10,000 lines of source code and over 80 subroutines, to be compiled in one large program. The single program eliminates the need to individually compile and link each of the subroutines, thereby making the code more efficient.

B. DEFINICON DSI-780 COPROCESSOR BOARD

The Definicon Coprocessor is an accelerator board for the IBM PCs and compatibles. Available in various configurations, the model DSI-780 is used for this research. The significance of this model number is directly related to the board's computational performance. The 780 in the model number signifies that the DSI-780 emulates the capabilities of a VAX-780 computer. The DSI-780 is built around Motorola's MC68020 32 bit CPU, a 32 bit data bus, an MC68881 Floating Point Math Coprocessor, and 4 Mbytes of 32

bit dynamic RAM. The memory can be expanded to a maximum of 16 Mbytes with an upgrade to higher density chips. The DSI-780 system clock is a crystal oscillator running at 20 MHz with one wait state. To make the DSI-780 operational, the board must be installed in an IBM PC AT compatible expansion slot. Switch settings located on the DSI-780 must be set depending on the host PC's hardware configuration. The manual for the DSI-780 clearly describes the proper settings for the more common IBM PC compatibles.

The software required to compile and run a Fortran program on the DSI-780 Coprocessor includes a compiler, code generator, linker, MS/DOS program loader, and Fortran and Pascal runtime library routines (intrinsic functions).

The compiler, SVS FORTRAN (written by Silicon Valley Software, Cupertino, CA), was originally written for a UNIX operating system. SVS FORTRAN is a single pass compiler (i.e., only reads source code once) that compiles in two phases. During the first phase the code is broken into procedure-by-procedure parcels, and then the compiler writes the parcel's tree representation. This allows the compiler, during the second phase, to optimize each parcel separately, thereby resulting in code so efficient it cannot be further hand-optimized. These optimized parcels are combined with their tree information which results in machine code ready for conversion into an object file necessary for linking.

JCODE.E20 is the code generator (assembler) for the previously compiled Fortran machine code. Running the machine code through the JCODE generator results in object code ready for linking with the necessary libraries of separate subroutines. The code generated by JCODE.E20, taken from the Motorola 68020 CPU instruction set, is in the final form necessary to execute on the DSI-780.

LINK20.E20 is the DSI linker that resolves all external calls and links the object modules with the required libraries. After linking, the original program can be loaded and executed using the DSI loader (LOAD.EXE).

LOAD.EXE is the PC DOS program loader which initializes and runs programs that have been compiled, assembled, and linked for the DSI-780. This loader does not physically load the program into the DSI-780 memory, but instead provides the address pointer of the program and initializes the DSI-780. Once initialized, the DSI-780 finds the program to be executed and uses its internal memory as needed. LOAD.EXE does provide the interface between the Host PC and the DSI-780 so I/O transfers can be accomplished.

C. COMPAQ DESKPRO 386/20

The Compaq Deskpro 386/20 (20MHz clock) is one of the fastest and most powerful PCs available on the market today. Surpassed only by the Deskpro 386/25 (25 MHz clock), the Deskpro 386/20 is an IBM AT PC compatible system that uses an Intel 80386 32 bit CPU and Compaq's Flex Architecture for handling memory access. Available in various configurations, the Deskpro used in this research is a Model 60, and comes standrd with an 80386-20 CPU, 1 Mbyte 32 bit memory, a 32 Kbyte cache memory, a 60 Mbyte fixed disk drive, a 1.2 Mbyte floppy disk drive, and accommodates both the Intel 80387 and the Weitek 1167 Math Coprocessors. Both coprocessors were installed for this research. Additional upgrade options installed include an additional 3 Mbytes of memory (total of 4 Mbytes), a Compaq VGA monitor, and a 1.4 Mbyte floppy disk drive. Memory can be expanded to a maximum of 16 Mbytes with appropriate hardware (higher density DRAMs).

Designed with 1 wait state for direct memory access, the Deskpro uses the Compaq Flexible Advanced Systems Architecture to reduce the delay caused by the wait state. Under normal operating conditions, Compaq claims that the 1 wait state is reduce to a 0 wait state 95% of the time. It accomplishes this by using a cache memory system in which the CPU gets its instructions from a small (32 Kbyte) area of high speed (35 nsec) memory (cache). As long as the data needed by the CPU is in the cache, the processor will run with 0 wait states. If the data is not available, the CPU waits for the data to be retrieved from the slower system memory (DRAM). Installed math coprocessors also execute instructions from the cache memory.

The Intel 80387 is an 80 bit Math Coprocessor designed to support the 80386 CPU. It provides the CPU with the floating point performance necessary for numerically intensive applications. The Weitek 1167

is a set of three chips mounted on a single PC board. It is designed to work with the 80386 CPU and provide floating point performance superior to that of the 80387. The Weitek board designed for use with the Compaq Deskpro PC includes a socket for the installation of the 80387, thereby allowing software to be compiled with either the 80387 or Weitek instructions. This convienent software option prompted the dual compilation and evaluation of NEC3 utilizing both the 80387 and the 1167 Math Coprocessors.

The software system used to compile, assemble, link, and run NEC3 on the Deskpro is a combination of two software packages: MicruWay's NDP FORTRAN-386 compiler (version 1.4e), and Phar Lap's Tools, containing the 386/ASM assembler (version 2.0), the 386/LINK linker (version 2.0), and the RUN386 DOS extender (version 2.0). NDP FORTRAN-386 is a UNIX based 32-bit Fortran compiler that generates assembly language code for the 80386 machines and supports the 80287, 80387, and Weitek 1167 Math Coprocessors. It requires a version of MSDOS 3.2 or higher, and at least 2 Mbytes of system memory. Although NDP does not require a coprocessor to compile source code, it does require one at run time. This compiler supports standard Fortran 77 and has a complete and thorough set of libraries.

III. BENCHMARKS

The two benchmarks presented are the Whetstone and a Complex Matrix Inverter. Both of these programs were choosen to test the computational ability of the various computer systems being considered. The Whetstone was used because of its popularity throughout the PC community and the Complex Matrix Inverter was choosen because it closely emulates the calculation requirements found in NEC3.

For each of the benchmarks, performance ratings will be described in terms of percentages. This percentage will relate the PC's performance to the mainframe's. For example, a 50% performance rating would indicate that the PC was running at half the mainframe capability. In this manner, the PC systems being evaluated can easily be compared to each other and to the mainframe.

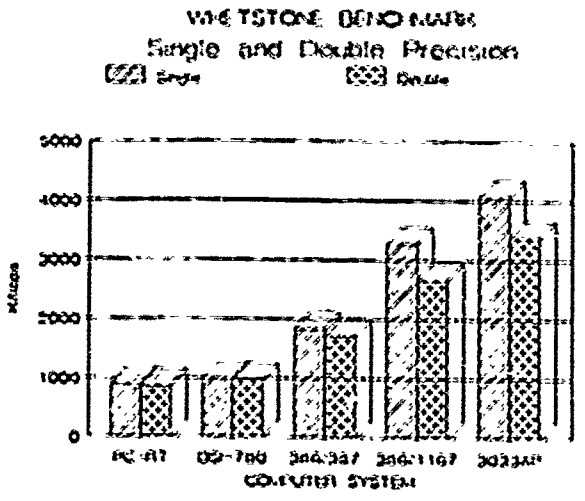
A. WHETSTONE

The WHETSTONE benchmark can best be thought of as a program that measures the time required to do an average simple operation in the simplest manner. There are two versions of WHETSTONE used in this research, one in single precision and one in double precision. The output is presented in units of a thousand WHETSTONE operations per second (Kflops) and has been compiled in Table 1 and displayed in Graph 1.

Performance ratings of the RT PC and DSI-780 range between 22% to 29%, indicating that the 3033AP runs approximately 4 times faster. The Deskpro 386/20 (w/80387) tested 45% to 51%, while the Deskpro (w/1167) showed the best performance with an 80% performance rating.

Table 1 WHETSTONE BENCHMARK: WHETSTONE Single and Double Precision Results (Kflop)

System	Single Whetstone (Kflop)	Double Whetstone (Kflop)
IBM RT PC	909	570
DSI-780	1000	973
Deskpro 386 20 (w 80387)	1838	1725
Deskpro 386 20 (w 1167)	3280	2677
IBM 3033AP (mainframe)	4076	3386



GRAPH 1

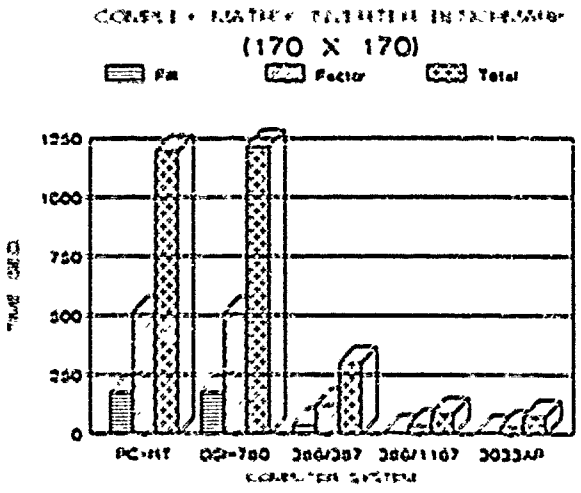
B. COMPLEX MATRIX INVERTER (CMATVRT)

CMATVRT is a Fortran program written by Prof. M. Morgan of the Naval Postgraduate School; it initializes and inverts a complex matrix of selectable size. This benchmark reflects the degree of matrix computations used in NEC3 and SOMNTX.

The results show significantly higher ratings for the Deskpro systems, 27% for the 80387 and 86% for the Weitek 1167, compared to the RT PC's and the DSI-780's ratings of 6%. Due to NEC3's dependence on matrix calculations, these results indicate that, of the PC systems being evaluated, the Deskpro's system will implement NEC3 more efficiently. Results are compiled in Table 2 and displayed in Graph 2.

Table 2 CMATVRT BENCHMARK: Complex Matrix Inverter

System	Fill Time (Seconds)	Inversion Time (Seconds)	Total Time (Seconds)
IBM RT PC	176	513	1196
DSI-780	173.95	510.50	1217.97
Deskpro 386 20 (w 80387)	39.76	123.53	300.45
Deskpro 386 20 (w 1167)	12.36	34.88	85.41
IBM 3033AP (mainframe)	10.58	30.03	73.70



GRAPH 2

IV. PERFORMANCE RESULTS OF NEC3 SAMPLE RUNS

The examples used to evaluate NEC3 are by no means a complete representation of the types of antenna design problems that can be solved on NEC3. However, these examples do represent a wide range of antenna problems and are considered a good test bed in the evaluation of NEC3.

It should be noted that the input impedances generated on NEC3 using the Deskpro 386/20 (w/80387) and NDP FORTRAN-386 appear to be pseudo-random. Although this randomness in not seen in example G2.NEC (monopole antenna), it does become apparent in S5.NEC (log-periodic antenna), RHOMBIC.NEC, and all the Halfwave Dipole examples. The more complex the design problem, and the more the code is stressed the more randomness appears in the solutions. Either through faults in the software or the 80387 or both, the solutions of the dipoles' input impedances do vary from run to run. These example problems were repeated on an identically configured Deskpro 386/20 with the same results. Although the answers appear to approximate the 3033AP results, the solutions can not be validated. The numbers that appear in the following tables and graphs for the Deskpro (w/80387) are averages of several runs.

A. S5.NEC - 12 ELEMENT LOG-PERIODIC ANTENNA IN FREE SPACE.

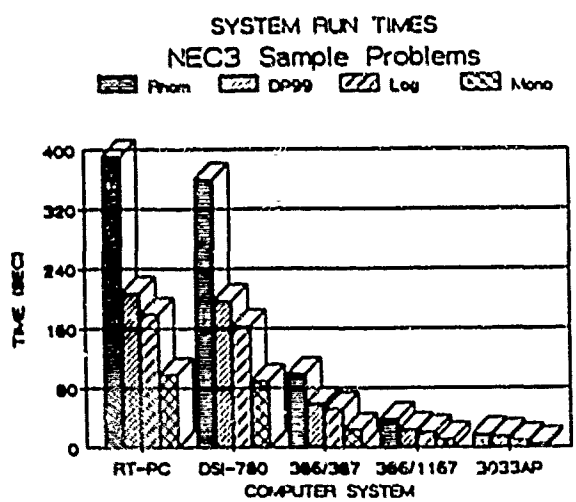
Results of this example show that the Deskpro (w/1167), with a rating of 47%, has the best performance. Input impedances for all PC systems are equal and closely approximate the 3033AP's solution. Results are listed in Table 3 with run times displayed in graph 3.

Table 3 EXAMPLE S5.NEC: Log-Periodic Antenna

System	Fill Time (Seconds)	Factor Time (Seconds)	Total Time (Seconds)
IBM RT PC	89	24	179
DSI-780	82.42	24.7	163.00
Deskpro 386/20 (w/80387)	27.95	4.73	51.90
Deskpro 386/20 (w/1167)	11.42	1.65	20.55
IBM 3033AP (mainframe)	5.34	1.06	9.62

System	Input Impedance (Ohms)	Gain (dB)
IBM RT PC	42.33 - j0.45	9.75
DSI-780	42.33 - j0.45	9.75
* Deskpro 386/20 (w/80387)	42.33 - j0.45	9.75
Deskpro 386/20 (w/1167)	42.33 - j0.45	9.75
IBM 3033AP (mainframe)	42.45 - j0.80	9.76

* Because of the randomness of the system, the reported results are the averages of several solutions.



GRA 3

B. G2.NEC - MONOPOLE ANTENNA (REQUIRES SOMNTX DATA)

Performance ratings for this example again indicate the superior speed of the Deskpro (w/Weitek). However, the input impedance could not be calculated for the Weitek due to a precision related run time error. All other input impedances closely resemble the 3033AP's solution. Results are listed in Table 4 with run times displayed in Graph 3.

Table 4 EXAMPLE G2.NEC: Monopole on a ground stake (requires SOMNTX data)

System	Fill Time (Seconds)	Factor Time (Seconds)	Total Time (Seconds)
IBM RT PC	60	< 1	98
DSI-780	56.30	0.33	88.56
Deskpro 386/20 (w/80387)	13.62	0.11	23.50
Deskpro 386/20 (w/1167)	6.02	0.02	11.21
IBM 3033AP (mainframe)	3.25	0.003	4.99

System	Input Impedance (Ohms)	Gain (dB)
IBM RT PC	96.78 + j38.35	0.32
DSI-780	96.55 + j38.71	0.32
Deskpro 386/20 (w/80387)	96.78 + j38.36	0.32
Deskpro 386/20 (w/1167)	Note	0.32
IBM 3033AP (mainframe)	94.88 + j39.01	0.33

C. RHOMBIC.NEC - RHOMBIC ANTENNA HORIZONTALLY POLARIZED

Results from the Rhombic example closely correspond to the previous examples of NEC3. Again, the Deskpro systems displayed superior speed while maintaining good solutions for the input impedances. With a performance ratio of 47%, the Deskpro (w/1167), is consistently twice as slow as the 3033AP mainframe. Results are listed in Table 5 with run times displayed in Graph 3.

Table 5 EXAMPLE RHOMBIC.NEC: Rhombic Antenna Horizontally Polarized

System	Fill Time (Seconds)	Factor Time (Seconds)	Total Time (Seconds)
IBM RT PC	260	51	391
DSI-780	244.91	53.23	359.88
Deskpro 386/20 (w/80387)	65.03	10.17	99.15
Deskpro 386/20 (w/1167)	25.54	3.62	38.34
IBM 3033AP (mainframe)	11.87	2.42	17.98

System	Input Impedance (Ohms)	Gain (dB)
IBM RT PC	352.05 + j172.06	17.95
DSI-780	352.06 + j172.06	17.95
* Deskpro 386/20 (w/80387)	352.32 + j172.14	17.95
Deskpro 386/20 (w/1167)	352.05 + j172.00	17.95
IBM 3033AP (mainframe)	352.05 + j172.04	17.95

* Because of the randomness of the system, the reported results are the averages of several solutions.

D. DIP49.NEC - HALFWAVE DIPOLE (USING 49 SEGMENTS)

Performance result range from 7% for the PC RT to 59% for the Deskpro (w/1167). All solutions for the input impedance closely resemble the 3033AP solutions. Results are listed in Table 6. Input impedances are displayed in Graphs 4,5, and 6

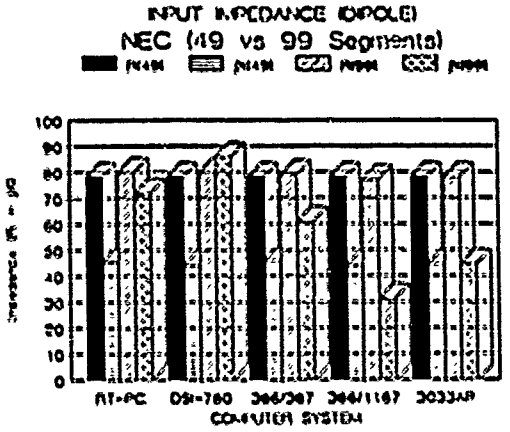
Table 6

EXAMPLE DIP49.NEC: Dipole Evaluated with 49 Segments

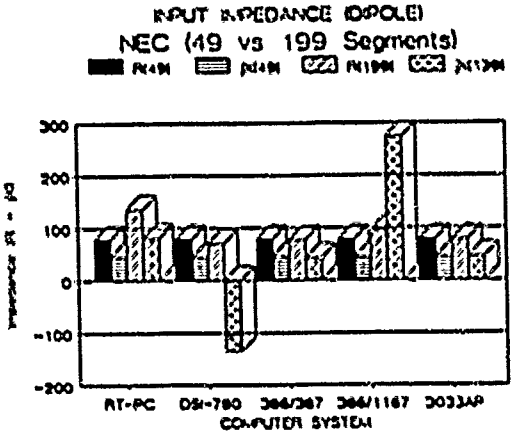
System	Fill Time (Seconds)	Factor Time (Seconds)	Total Time (Seconds)
IBM RT PC	40	6	50
DSI-780	36.91	6.15	44.60
Deskpro 386/20 (w/80387)	12.41	1.04	14.11
Deskpro 386/20 (w/1167)	5.08	0.45	5.88
IBM 3033AP (mainframe)	3.01	0.24	3.46

System	Input Impedance (Ohms)	Power (Watts)
IBM RT PC	78.01 + j45.52	4.78E-02
DSI-780	77.90 + j44.36	4.85E-02
* Deskpro 386/20 (w/80387)	78.02 + j45.87	4.76E-03
Deskpro 386/20 (w/1167)	77.91 + j43.66	4.88E-03
IBM 3033AP (mainframe)	77.90 + j44.48	4.84E-03

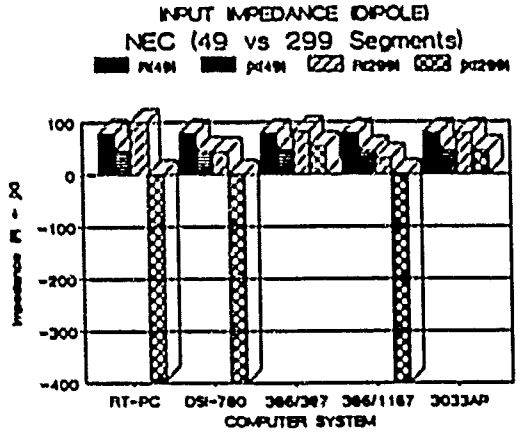
* Because of the randomness of the system, the reported results are the averages of several solutions.



GRAPH 4



GRAPH 5



GRAPH 6

E. DIP99.NEC - HALFWAVE DIPOLE (USING 99 SEGMENTS)

Results of this example begin to show the effect of the Weitek's 23 bit mantissa. Although the performance rating for the Deskpro (w/1167) is excellent (67%), the solution of the dipole's input impedance is beginning to deviate from that of the 3033AP's. The Deskpro using the 80387 has a 63 bit mantissa and performance rating of 27%. Results are listed in Table 7 with run times displayed in Graph 3. Input impedances are displayed in Graph 4.

Table 7 EXAMPLE DIP99.NEC: Dipole Evaluated with 99 Segments

System	Fill Time (Seconds)	Factor Time (Seconds)	Total Time (Seconds)
IBM RT PC	154	48	207
DSI-750	142.50	50.67	197.07
Deskpro 386/20 (w/80387)	48.23	9.72	59.43
Deskpro 386/20 (w/1167)	19.72	3.57	23.95
IBM 3033AP (mainframe)	12.25	2.24	14.81

System	Input Impedance (Ohms)	Power (watts)
IBM RT PC	79.625 + j71.703	3.47E-03
DSI-750	80.169 + j86.23	2.89E-03
* Deskpro 386/20 (w/80387)	79.03 + j60.65	3.98E-03
Deskpro 386/20 (w/1167)	77.38 + j31.51	5.54E-03
IBM 3033AP (mainframe)	78.00 + j44.61	4.83E-03

* Because of the randomness of the system, the reported results are the averages of several solutions.

F. DIP199.NEC - HALFWAVE DIPOLE (USING 199 SEGMENTS)

Although the performance ratings are consistent with the other examples, only the Deskpro with the 80387 is still maintaining an input impedance solution resembling that of the 3033AP's. The Weitek input impedance solution is no longer valid. Results are listed in Table 8. Input impedances are displayed in Graph 5.

Table 8 EXAMPLE DIP199.NEC: Dipole Evaluated with 199 Segments

System	Fill Time (Seconds)	Factor Time (Seconds)	Total Time (Seconds)
IBM RT PC	600	389	1005
DSI-750	556.00	619.81	1190.03
* Deskpro 386 20 (w/80387)	155.60	78.92	269.03
Deskpro 386 20 (w/1167)	75.74	28.95	106.28
IBM 3033AP (mainframe)	51.82	19.00	71.68

System	Input Impedance (Ohms)	Power (Watts)
IBM RT PC	134.85 + j80.941	1.00E-03
DSI-750	69.63 - j135.12	1.50E-03
* Deskpro 386 20 (w/80387)	77.00 + j42.54	5.18E-03
Deskpro 386 20 (w/1167)	94.99 + j273.73	5.66E-04
IBM 3033AP (mainframe)	78.05 + j44.69	4.82E-03

* Because of the randomness of the system, the reported results are the averages of several solutions.

G. DIP299.NEC - HALFWAVE DIPOLE (USING 299 SEGMENTS)

The evaluation of a 299 segment dipole clearly shows the high precision requirements of the NEC3 code. Only the Deskpro (w/80387) system can maintain a solution comparable with that of the 3033AP's. With a performance rating of 28%, the Deskpro (w/80387) is almost 4 times slower than the mainframe (3033AP). Results are listed in Table 9. Input impedances are displayed in Graph 6.

Table 9 EXAMPLE DIP299.NEC: Dipole Evaluated with 299 Segments

System	Fill Time (Seconds)	Factor Time (Seconds)	Total Time (Seconds)
IBM RT PC	1338	1319	2689
DSI-780	1239.72	1380.40	2644.50
* Deskpro 386 20 (w/80387)	411.28	269.13	689.48
Deskpro 386/20 (w/1167)	168.29	97.34	269.68
IBM 3033AP (mainframe)	121.69	67.36	190.73

System	Input Impedance (Ohms)	Power (Watts)
IBM RT PC	143.68 - j394.42	4.60E-06
DSI-780	42.75 - j2152.3	4.60E-06
* Deskpro 386 20 (w/80387)	81.95 + j52.95	3.33E-05
Deskpro 386 20 (w/1167)	30.165 - j1923.5	4.10E-06
IBM 3033AP (mainframe)	78.08 + j44.72	4.82E-03

* Because of the randomness of the system, the reported results are the averages of several solutions.

V. CONCLUSIONS

The results of the testing clearly show that the PC is now a viable option to the mainframe when implementing large engineering programs. Of the three systems reviewed, it is clear that the Compaq Deskpro 386/20 was the fastest and most powerful machine.

The Deskpro, when using the Weitek 1167 math coprocessor, was approximately 50% to 75% faster than all other systems. The Whetstone benchmark results indicate that only 20% of the Weitek's speed advantage is lost when calculations are made in double precision. The Deskpro 386/20 and 1167 combination rated between 75% and 80% of the IBM 3033AP mainframe. The disadvantage for the Weitek is its 23 bit mantissa instead of the 80387's 63 bit mantissa. This loss of accuracy was evident in the dipole examples of the previous chapter. As the number of segments increase, the amount of accuracy required by NEC3 also increases, requiring increased resolution in the NEC3 generated output. NEC3, converted to double precision, should improve the Weitek solution while still allowing a speed advantage over the 80387.

The Deskpro when using the 80387 math coprocessor, rated between 20% and 25% of the IBM 3033AP mainframe. The accuracy of the 80387 is much better than the Weitek's, and thereby better suited for NEC3 problems. This accuracy is overshadowed by the fact that the NDP FORTRAN-386/80387 combination results in unstable code giving pseudo-random solutions to complex antenna problems. These shortcomings must be further investigated to uncover and correct NDP FORTRAN bugs and to determine if the 80387 and/or NDP FORTRAN is flawed.

It should also be noted that due to the unstable results of the Deskpro (w/80387), separate test of the dipole examples were run on using a version of NEC3 that was compiled for an IBM AT using a 80287 Math Coprocessor with MS FORTRAN 4.01. These tests resulted in input impedances which closely correlate with those calculated with the IBM 3033AP. Due to these good results using a 16 bit Fortran compiler, it would seem that the 32 bit UNIX based FORTRANs still need some refinement. The results of this research indicate that the true potential for these 32 bit compilers in implementing large numerically intensive programs is excellent. Additional implementations of NEC3 with other 32 bit Fortran compilers, such as Silicon Valley Software's SVS FORTRAN 386 and Lahey Computer Systems' F77L-EM/32 will be attempted.

Of the three PC systems evaluated, only the Deskpro 386/20 provided enough speed and accuracy to challenge the mainframe. The Deskpro (w/Weitek 1167) is the fastest, but modifications to NEC3 must be made to minimize the Weitek's loss of accuracy. The Deskpro (w/80387) is slower, but provides increased accuracy. This conclusion assumes that the bug that is causing the 80387 pseudo-random solutions is correctable.

SESSION 8 - "ANTENNAS"

Chairman: William Imbriale

MULTIBAND OFF-CENTER-FED HF WIRE ANTENNA

By

W.P. Wheless, Jr. and M.D. Fanning
Department of Electrical Engineering
University of Alabama
P.O. Box 870286
Tuscaloosa, AL 35487-0286

ABSTRACT

Impedance characteristics of a horizontal off-center-fed hf wire antenna, operating close to real ground, are investigated both experimentally and with the aid of NEC2-PC. This antenna serves effectively for communications in bands about the discrete frequencies 1.9, 3.8, 7.2, 10.1, 14.2, 18.15, 21.3, 24.95, and 28.5 MHz. Impedances well suited to the tuning capabilities of commercially available three-reactance (Tee network) matching units are obtained. A dual coax feed, with 4:1 balun located at the transmitter end, is found to be feasible. Experimental antenna impedances, obtained with a laboratory grade rf impedance analyzer, are compared to theoretically predicted values for two feed/measurement circuits at the numerous frequencies of interest. A set of predicted values based on free-space impedance calculations is also presented.

I. Introduction

The wire antenna under study is illustrated in Figure 1. This configuration is a variation of the so-called "Windom" which is no longer referenced in the contemporary texts, but may be found in older handbooks [1]. To operate effectively about 3.9, 7.2, 14.2, and 28.5 MHz, the original Windom was made approximately 120 feet (36.6 meters) long overall (length L), with a *single-wire* feeder connected at the point 0.36L from one end. Of course, the wire feeder was part of the antenna, and brought considerable rf levels to the transmitter location. One variation, seen in [1], has a length L = 136 feet (41.4 meters) with a 300-Ohm twin-lead feed at 44 feet, 4 inches (13.5 meters) from the end. Similar problems with rf at the transmitter occur with the twin-lead feed. When the dual coax feed and transmitter-end balun illustrated in Figure 2 are employed, negligible rf currents on the outer coax conductors are observed at the transmitter site. The feed lines run away from the antenna at right angles for the greatest distance possible.

For this study, the length has been increased to 46.9 meters in an attempt improve utility at 1.9 MHz. Using the

original rule-of-thumb of 0.36L, the feed point would separate the antenna into dimensions of 16.9 and 30.0 meters. For the sake of inquiry, the feed point has been shifted slightly so that the actual lengths are 18.9 and 28.0 meters, as indicated in Figure 1.

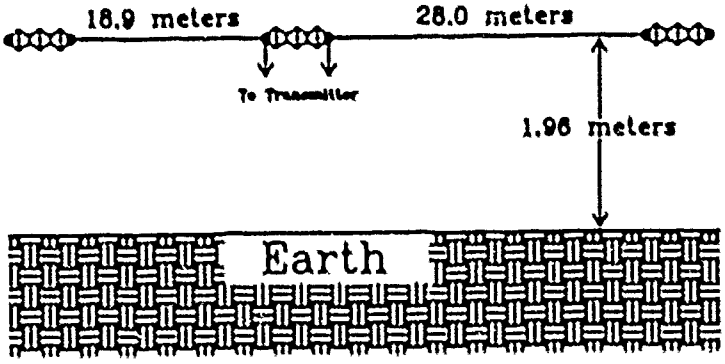


Figure 1. Unsymmetrical HF multiband wire antenna.

The present hf band allocations for amateur radio use are 1.8 - 2.0, 3.5 - 4.0, 7.0 - 7.3, 10.10 - 10.15, 14.0 - 14.35, 18.068 - 18.168, 21.0 - 21.45, 24.89 - 24.99, and 28.0 - 29.7 MHz. Within these bands, the nine design frequencies enumerated in the Abstract have been identified. At this time, there are over 300,000 licensed radio amateurs in the United States. Many, like the authors, live with limited space and/or restrictive covenants with regard to antennas. A single wire antenna capable of effective performance on all the currently allocated hf bands is an item of popular interest.

II. Predicted Impedances

For this application, the impedance of paramount importance is that at the transmitter end of the feed line(s) rather than directly at the antenna terminals. Consequently, in this study, circuit analysis will be applied to transform antenna impedances into impedances seen at the transmitter end. The objective is to discern if a commonly available three-reactance matching network, placed at the 50-Ohm transmitter output, can effectively match the impedances seen at that point, and thus efficiently export rf energy toward the antenna.

Calculations of the various antenna feed-point impedances

have been made with the assistance of the NEEDS package [2] on an IBM Model 70 personal computer. Special interest here is in calculations which take into account the presence of non-ideal ground, as the antenna is shown by Figure 1 to be operating only 1.96 meters above earth. For these calculations, the wire radius is 0.00343 meters.

The Norton/Sommerfeld method is employed for the modeling of this antenna over ground. Radiation patterns are not reported in this particular study, as no means of experimental validation was available, and only impedances are considered here. Of course, NEC2-PC requires for this method the input file generated by running the separate program SOMNEC in the NEEDS package, prior to the NEC run. SOMNEC, in turn, requires input of the effective ground conductivity and effective ground dielectric constant at each frequency.

The selected test site has a water table well below the surface, so a one-layer slab model should be sufficient for the ground. Proof-of-performance measurements on AM broadcast antennas in the area show the effective conductivity σ to be close to 2 mS/m over a widespread area of western Alabama, at frequencies to approximately 1.6 MHz. Without equipment to measure σ as a function of frequency to 30 MHz, or to directly measure effective dielectric constant ϵ_r, previous soil studies in the literature were consulted. Hagn [3] includes the necessary relevant data in his Figures 6.1 and 6.2. The soil in the test site vicinity closely resembles the Ft. Monmouth, NJ, type. Generally following the Ft. Monmouth curves, the values of σ and ϵ_r employed with SOMNEC are documented in Table 1.

For convenient comparison, the corresponding antenna feed-point impedances calculated for a free-space environment are presented in Table 2.

Standard circuit analysis is applied to transform the antenna impedances to those at the transmitter location. Both the transmission line(s) and the cables used to fabricate the coaxial 4:1 baluns are lossy. The relevant loss figures, in dB per hundred feet, are as follows:

Freq.	Line	Balun
1.90	0.305	0.55
3.80	0.41	0.80
7.20	0.56	1.20
10.10	0.68	1.50
14.20	0.77	1.70
18.15	0.88	2.00
21.30	0.98	2.20
24.95	1.02	2.35
28.50	1.20	2.50

TABLE_1

Impedances Computed by NEC2-PC
Ground Present

Freq. MHz	σ mS/m	ϵ_r	Impedance Z_a Ω
1.90	2	23	40.7 - j 629.
1.90	.5	10	47.9 - j 632.
3.80	2.3	19	181. + j 437.
7.20	3	15	1324. + j1257.
10.10	3.8	15	1291. + j 473.
14.20	4.8	14	557. + j 893.
18.15	5.5	13	177. - j 366.
21.30	6.0	13	1154. - j 642.
24.95	6.5	13	377. - j 395.
28.50	7.0	13	198. - j 52.8

TABLE_2

Comparison of NEC2-PC Calculated
Antenna Impedances

Freq. MHz	Ground Present	Ground Absent
1.90	40.7 - j 629.	21.1 - j 744.
3.80	181. + j 437.	198. + j 441.
7.20	1324. + j1257.	1371. + j1147.
10.10	1291. + j 473.	1207. + j 642.
14.20	557. + j 893.	619. + j 852.
18.15	177. - j 366.	137. - j 402.
21.30	1154. - j 642.	1185. - j 778.
24.95	377. - j 395.	328. - j 419.
28.50	198. - j 52.8	157. - j 58.9

The nominal velocity factor for the RG-213 transmission line(s) is 0.655. The $\lambda/2$ coaxial balun lengths were cut in the field, and later analysis indicated that four electrical lengths deviated sufficiently from 180° to be noted here, namely 174° at 1.9 MHz, 186° at 7.2 MHz, 189° at 14.2 MHz, and 185° at 18.15 MHz.

The circuit analysis problem, with lossy lines, is sufficiently tedious that computer assistance is helpful. For this study, all circuit analysis work was done with the program TAME (4).

III. Measured Impedances

All measured impedances were observed with a Hewlett-Packard model 4191A rf impedance analyzer. This is a current-production piece of equipment, with performance specifications which can be seen in Hewlett-Packard equipment catalogs of recent years. The single measurement port on this instrument is an (unbalanced) coaxial connector input.

IV. Theoretical and Experimental Results

The predicted antenna impedances from NEC2-PC calculation, both for cases of ground present and ground absent, are in Table 2. All impedances hereafter are at the remote (transmitter) end.

Figure 2 depicts the preferred mode of antenna feed/operation. In practice, the balun will be a commercial "broadband 4:1" toroidal balun. However, such baluns are not well characterized and it was deemed more appropriate, for experimental study, to use a well-known coaxial $\lambda/2$ balun which is more conducive to reliable circuit analysis. To illustrate the discrepancies, measured Z_{in} with the coax balun is compared in Table 3 to Z_{in} measured at the unbalanced input side to the balun contained in our MFJ Model MFJ-941D antenna tuner. The differences at 14.2 and 24.95 MHz are particularly conspicuous.

In Tables 4 through 6, theoretical Z_{in} values for three circumstances are compared to measured Z_{in}. To quantify agreement (or lack of it) between theory and experiment, it is useful to define the error function U by

$$U = \sum_{i=1}^{9} \left[\left[R^i_{theory} - R^i_{meas.} \right]^2 + \left[X^i_{theory} - X^i_{meas.} \right]^2 \right] \quad (1)$$

TABLE 3

Comparison of Measured Z_{in} for
Single-band Coaxial Balun versus a
Commercial "Broadband 4:1" Balun

Freq. MHz	Coaxial Balun Z_{in} Ω	Broadband Balun Z_{in} Ω
1.90	3.4 - j 14.9	1.3 - j 6.9
3.80	9.8 + j 4.8	2.7 + j 12.3
7.20	37.2 - j 53.7	11.5 - j 23.3
10.10	4.3 + j 22.1	3.3 + j 25.8
14.20	7.2 - j 27.3	64.2 - j 80.3
18.15	48.2 + j 39.2	71.7 + j 24.4
21.30	5.3 - j 2.1	5.7 + j 5.8
24.95	35.8 + j 73.1	150. + j 1.3
28.50	7.9 + j 10.2	13.1 + j 32.8

TABLE 4

Predicted vs. Measured Impedances
Measurement Circuit of Figure 2
Ground Absent

Freq. MHz	Theoretical Z_{in} Ω	Measured Z_{in} Ω
1.90	2.2 - j 16.8	3.4 - j 14.9
3.80	3.6 + j 0.9	9.8 + j 4.8
7.20	23.8 - j 70.2	37.2 - j 53.7
10.10	3.2 + j 0.9	4.3 + j 22.1
14.20	14.2 - j 46.2	7.2 - j 27.3
18.15	11.9 + j 37.7	48.2 + j 39.2
21.30	8.8 - j 28.4	5.3 - j 2.1
24.95	12.9 + j 33.3	35.8 + j 73.1
28.50	15.8 - j 5.8	7.9 + j 10.2
Error function U = 5,818		

which is a fundamental indicator of difference between the two. The basis for Table 4 is predicted impedances for the antenna in a free-space environment. Table 5 is similar, but with antenna impedances those in the presence of non-ideal ground. Tables 4 and 5 both employ the network of Figure 2.

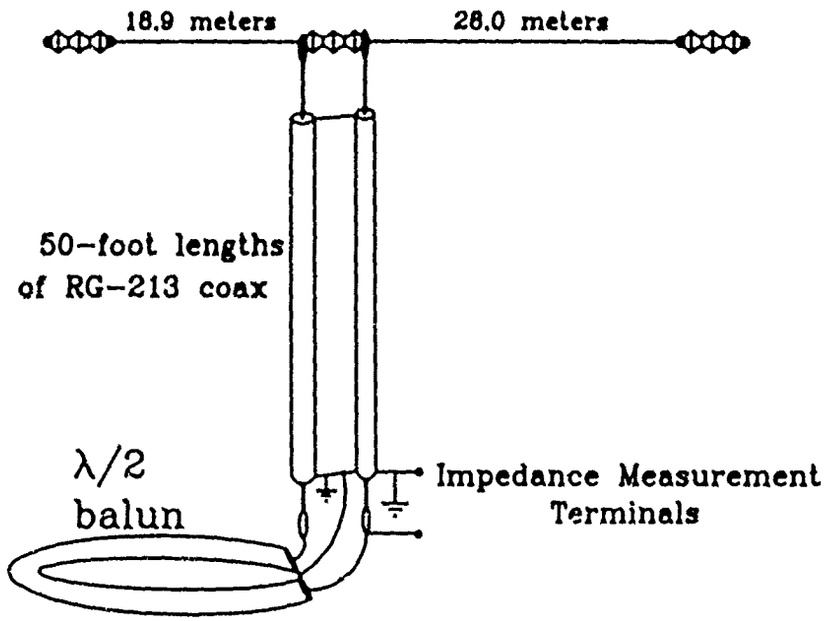


Figure 2. Principal measurement circuit.

Table 6 addresses two points of natural curiosity. It has been proposed that the balun be situated at the antenna terminals rather than at the transmitter, as illustrated in Figure 3. This reduces the transmission line requirement to one coaxial cable, and hopefully serves to minimize rf currents flowing on the outer conductor of that single cable. On the

other hand, one suspects that addition of the balun at the feed point will alter the original current distribution (and feed impedance) so that the already available NEC2-PC analysis is suspect. The data of Table 6 verifies that concern, as the error function value zooms.

TABLE_5

Predicted vs. Measured Impedances
Measurement Circuit of Figure 2
Ground Present

Freq. MHz	Theoretical Z_{in} Ω	Measured Z_{in} Ω
1.90	2.3 - j 16.0	3.4 - j 14.9
3.80	3.4 + j 0.9	9.8 + j 4.8
7.20	23.4 - j 71.0	37.2 - j 53.7
10.10	3.3 + j 1.1	4.3 + j 22.1
14.20	13.8 - j 46.6	7.2 - j 27.3
18.15	14.1 + j 36.6	48.2 + j 39.2
21.30	9.2 - j 28.4	5.3 - j 2.1
24.95	13.1 + j 32.0	35.8 + j 73.1
28.50	15.5 - j 8.8	7.9 + j 10.2
Error function U = 5,906		

Illustration of the relative effect of ground presence is also provided in Table 6 by a one-line addition. Note that 1.90 MHz appears twice. The values of σ = 2 mS/m and ϵ_r = 23 are in accord with [3], while the second line is based on σ = 0.5 mS/m and ϵ_r = 10 as an estimated lower bound on conceivable ground conditions in the area. The resultant change in theoretical Z_{in} is modest.

Finally, a reasonable inquiry is made into the feasibility of measuring the antenna impedance directly at its terminals. It is generally documented, for example in (5), that such measurement on an unsymmetrical antenna is not reliable. Accurate measured antenna impedances would, of course, lead to theoretical Z_{in} values in full agreement with those measured, resulting in an error function of zero.

For this procedure, the impedance analyzer is mounted in immediate proximity to the feed points on a wooden support. Because the impedance analyzer only has an unbalanced measurement port, it is necessary to connect one antenna feed point to instrument ground. It is observed immediately that the "polarity" of instrument connection affects the observed impedance value. Thus, the impedance is actually measured twice as shown in Figure 4 and the average of these two numbers is taken as the antenna impedance. The results of this exercise are summarized in Table 7 which shows, indeed, an impedance-disturbing effect arising from attempted direct observation at the antenna terminals.

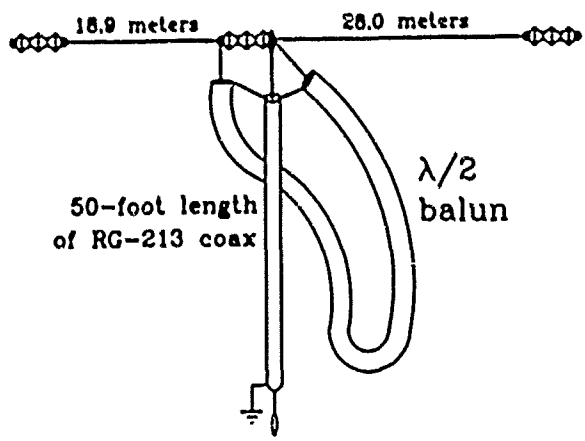


Figure 3. Secondary measurement circuit.

TABLE 6

Predicted vs. Measured Impedances
Measurement Circuit of Figure 3
Ground Present

Freq. MHz	Theoretical Z_{in} Ω	Measured Z_{in} Ω
1.90*	5.8 - j 27.7	13.7 - j 23.8
1.90**	7.0 - j 29.5	13.7 - j 23.8
3.80	2.6 - j 20.9	19.9 - j 15.1
7.20	58.1 - j 114.	83.8 - j 52.1
10.10	9.9 - j 0.7	12.1 + j 17.4
14.20	40.4 - j 84.6	32.3 - j 96.4
18.15	88.1 + j 95.0	85.7 + j 31.9
21.30	21.5 - j 53.4	12.0 - j 29.0
24.95	50.6 + j 65.0	103. + j 127.
28.50	40.6 + j 1.3	18.8 - j 8.4

Error function U = 17,272

*$\epsilon_r = 23$, $\sigma = 2$ **$\epsilon_r = 10$, $\sigma = 0.5$

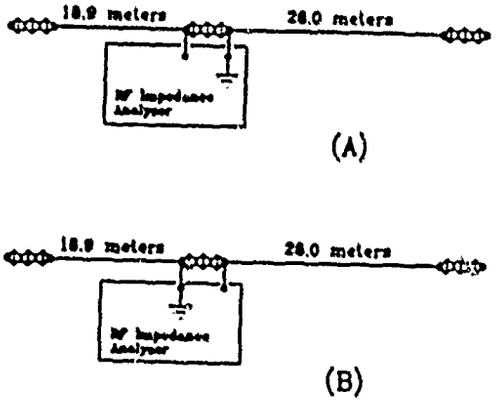


Figure 4. Impedance measurement directly at antenna terminals.

TABLE 7

Predicted Z_{in} Based on Impedances
Measured at the Antenna Terminals
(generally not reliable)

Freq. MHz	Measured Z_a Ω	Predicted* Z_{in} Ω
1.90	92.8 - j 308.	4.3 - j 11.3
3.80	237. + j 376.	4.6 + j 0.8
7.20	639. - j 840.	15.7 - j 51.6
10.10	404. - j 653.	3.3 + j 4.5
14.20	676. - j 595.	10.7 - j 33.0
18.15	94. - j 118.	50.2 + j 25.9
21.30	344. - j 261.	12.3 - j 21.2
24.95	231. - j 347.	15.8 + j 36.1
28.50	290. - j 197.	9.3 - j 11.3
	Error function U = 3,675	

*circuit of Figure 2.

V. Conclusions

The exercise described by Table 7's data indicates that impedance measurement on unsymmetrical antennas should be conducted remotely, through a section of transmission line, and then properly interpreted.

Actual operation of a similar antenna over a period of some months, as well as this study, suggests that the feed line/balun configuration of Figure 2 is preferable over that of Figure 3. Although the outer conductor of the coaxial lines is, in theory, a part of the antenna, it has been found that its involvement is negligible when the coax is run away from the antenna feed point at right angles.

For prediction of matching network component requirements at the transmitter, it turns out that the results from Tables 4 and 5 are equally acceptable. In this particular case, the

extra time and effort to include non-ideal ground effects were unnecessary. However, once the antenna system is matched and driven, radiation patterns become of interest. Operational experience makes it clear that ground presence has a profound effect on the radiation patterns, and accounting for imperfect ground will be a significant factor in future characterization of the antenna's radiation properties.

The antenna is badly mismatched at all the target operating frequencies. At the same time, it provides impedances which were easily matched with two different commercial tuners, the MFJ models MFJ-941D and the MFJ-989B. Its communications effectiveness is surprisingly competitive. Because its size is small compared to $\lambda/2$ at 1.9 MHz, its performance is somewhat less than desired at that particular frequency. Communications effectiveness may be described as excellent from 3.9 through 14.2 MHz, except 10.1 Mhz. It is quite effective at 10.1 and 18.15 through 28.5 MHz, although comparisons to a vertical antenna with 16 ground radials generally favor the vertical. A future investigation will consider the radiation patterns, in particular the potential benefits at 10.1 and 18.15 through 28.5 MHz from operating this multiband antenna at greater elevations above ground.

References

[1] American Radio Relay League, *The Radio Amateur's Handbook, 38th Edition*. Newington, Conn.: ARRL, 1961, p. 364.

[2] *NEEDS (Numerical Electromagnetic Engineering Design System)*, distributed by the Applied Computational Electromagnetics Society.

[3] G.H. Hagn, "HF ground constant measurements at the Lawrence Livermore National Laboratory (LLNL) field site," *Applied Computational Electromagnetics Society Journal and Newsletter*, vol. 3, no. 2, Fall 1988.

[4] *TANE (Top Algorithms for Microwave Engineering)*, Dr. Stephen E. Sussman-Fort, Department of Electrical Engineering, State University of New York at Stony Brook.

[5] R.W.P. King, H.R. Mimno, and A.H. Wing, *Transmission Lines, Antennas and Waveguides*. New York: Dover Publications, 1965, p. 146.

SIMPLE METHOD TO COMPUTE THE CURRENT DISTRIBUTION, INPUT IMPEDANCE AND EFFICIENCY OF THICK UNLOADED AND LOADED DIPOLE ANTENNAS.

A.P.C. Fourie
Dept of Electrical Engineering
University of the Witwatersrand
P O WITS
2050
Republic of South Africa

Abstract

The often used analogy between dipole antennas and transmission lines has been exploited for the analysis of unloaded and loaded dipole antennas. The dipole is modelled as a non-uniform, lossy transmission line using short segments of line. The empirically determined line series resistance component is used to take radiation effects into account. The length of the transmission line is also adjusted slightly to compensate for the different fields generated by dipole antennas in comparison to transmission lines.

The theory at the moment allows the analysis of dipoles with thickness factors between 12.5 and 20. The impedance and efficiency of two loaded antennas are presented given in comparison to NEC2 results. The accuracy obtaine are quite sufficient for initial evaluation and especially optimization. The method is also orders of magnitude faster than method of moment techniques since computer time is proportional to number of segments.

Keyword index

Cylindrical dipoles, loaded dipoles, loaded dipole impedance, loaded dipole efficiency, transmission line method

1 Introduction

Loaded antennas are of considerable interest since suitable loading may result in broadband performance for simple wire antennas. A particular frequency band where broad band performance is of importance is the HF band (3 - 30 MHz) where ionospheric variations and other channel selection criteria dictate frequency variations for effective communication links. Usually broadband antennas are also made electrically thick to exploit the inherent increased bandwidth of thicker antennas. This is often achieved using two or more parallel thin wires to

emulated a thicker structure but for analysis purposes a single thick wire produces the same results (*Clark&Fourie*[1]). Loading are also often used to produce multi-band antennas and for applications where the designer attempts to modify the current distribution to his benefit.

In order to design and optimize these antennas a large number of different loads as well as their position on simple dipole antennas have to be experimented with. Each of these configurations must then be evaluated over the full frequency range. Usually such dipole antennas are approximately half a wavelength long at the lowest frequency implying an electrical length of 5 wavelengths at the highest frequency. Using the method of moments programs which are suitable for the analysis of wire antennas the time taken to obtain a solution at one frequency is proportional to the wire length in terms of wavelength squared and cubed. This clearly results in a very time consuming evaluation cycle for these antennas since matrix fill and inversion is necessary for every frequency.

In this paper the frequently used analogy between dipole antennas and transmission lines are examined with the view to develop a fast method for evaluating loaded dipoles. The absolute accuracy of such a method is not of ultimate importance since the intention is to use it to speed up the iterative design cycle. A method of moments technique may still be used to accurately evaluate the final design. The aim was thus to obtain reasonable accuracy and faithfully reproduce trends.

2 Model Formulation

The loaded dipoles of interest in practical situations are usually cylindrical, or the cylindrical equivalents of other configurations.

Schelkunoff[2,3] derived the theory for cylindrical antennas by starting with the the conical dipole. This antenna is equivalent to a transmission line with constant characteristic impedance. The effect of radiation is clearly not accounted for when considering the antenna as a uniform transmission line but Schelkunoff lumped these effects together in a terminal impedance to the intuitively open circuited line. To obtain a method suitable for cylindrical dipoles, where the transmission line parameters is clearly not constant, Schelkunoff used average values for these parameters. With the aid of modern computational aids it is more elegant to treat the cylindrical antenna as an incremental conical antenna ; that is one in which Z_o changes gradually with distance from the feed. This local $Z_o(h)$ could then be used for small increments along the wire over which it could be assumed constant.

In this model the radiation effects are lumped into the real part of the terminating impedance, which is sufficient for the evaluation of unloaded dipoles but will clearly be invalid the loaded case. Schelkunoff indicated that the antenna could be considered as multiple transmission lines with the radiation represented as series resistance in the line but never developed the theory for this case. A novel method of doing so will now be developed using the non-uniform, lossy transmission line shown in Fig 1.

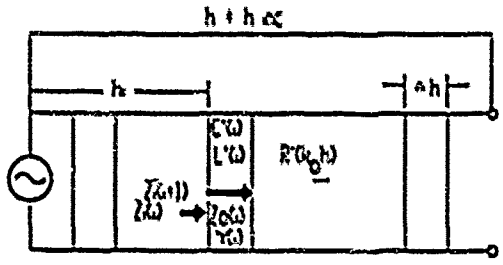


Fig 1 The non-uniform lossy transmission line model of a dipole antenna of length l = 2h

Clearly this model requires the use of the general lossy transmission line equation with the steps indicated below :

$$Z_i(l) = Z_o(l)\left[\frac{Z_i(1+l) + Z_o(l)\tanh[\gamma(i)\Delta h]}{Z_o(l) + Z_i(l+1)\tanh[\gamma(i)\Delta h]}\right]$$

This equation solved N times (for i = N .. 1) yields $Z_i(1)$ - the input impedance where N is the number of segments. It should be noted that the terminating impedance is a open circuit and the line length is adjusted by h_{ec} to take into account the fringing at the dipole end points. The radiation that takes place is taken into account by the series resistance incorporated into this

transmission line model. This series resistance, $R'(k_o h)$ is constant for the line at any one frequency but is a function of $k_o h = 2\pi h/\lambda$ and therefore varies with line electrical length and hence frequency.

If loads are present in the dipole these are added to the line impedance at the segment in which they occur. For instance a load, Z_l in segment, k from the feed will modify $Z_c(k)$ to become $Z_c(k)+2 \cdot Z_l$.

The value of the variable characteristic impedance, $Z_o(l)$, is calculated from first principles to be :

$$Z_o(l) = \sqrt{\frac{Z'(l)}{Y'(l)}}$$

Similarly the propagation coefficient, $\gamma(l)$, is given by :

$$\gamma(l) = \sqrt{Z'(l)Y'(l)}$$

with impedance per unit length, Z'(l) and admittance per unit length, Y'(l), given by:

$$Z'(l) = R'(k_o h) + j\omega L'(l) \qquad \Omega/m$$

$$Y'(l) = j\omega C'(l) \qquad S/m$$

assuming cross conductance G' to be zero.

where :

$$L'(l) = \frac{\mu_o}{\pi} \ln\left[\frac{2h(l)}{a}\right] \qquad H/m$$

$$C'(l) = \mu_o \frac{\epsilon_o}{L'(l)} \qquad F/m$$

Values for $R'(k_o h)$ as well as for h_{wr} is required to use the model above. These parameters were determined empirically for different thickness dipoles using the reputable *King – Harrison*[4] data. The values thus found graphically shown in Figs 2 and 3.

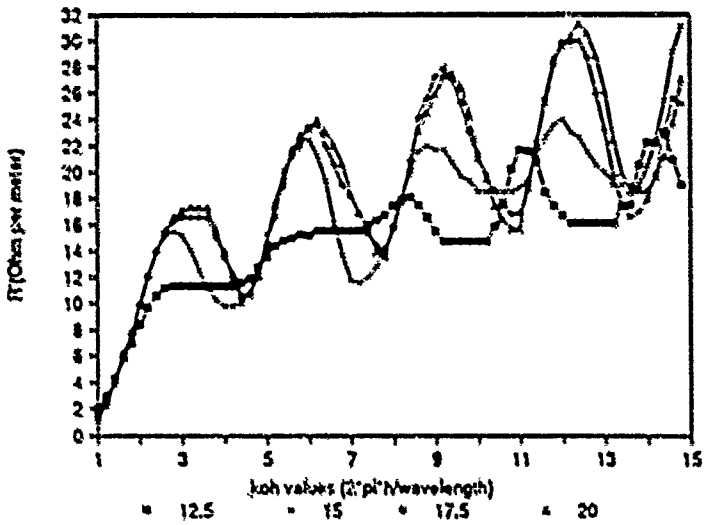


Fig 2 The $R'(k_0h)$ values for different thickness dipoles

The $R'(k_0h)$ results shown are for h = 23.2 m and must be modified to the actual halflength h in order to use for different length antennas. The equation to do so is :

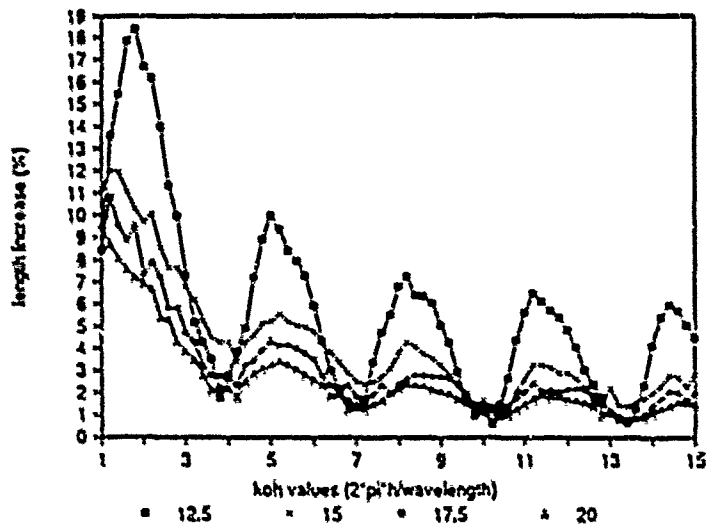


Fig 3 The h_{eq} values for different thickness dipoles

$$R'(koh)_{eq} = R'(koh) \cdot 23.2/h_{eq}$$

These empirically determined parameters are quite "noisy" due to the fairly sensitive iterative procedure used to determine them. This does not present serious problems however and still ensures reasonable results. An obvious solution to this problem is to smooth these curves using digital filtering techniques which will certainly give them a better appearance.

Once the transmission line parameters are known for a non-uniform line the current distribution could be calculated using standard transmission line equations on a segment by segment basis. This allows for the efficiency to be calculated if all losses are assumed to occur in the lumped loads (see Appendix A). Skin effect losses due to finite conductivity of the dipole elements may also be taken into account by considering them to be discrete loads at every segment. The results presented in this document assumed perfect conductors however.

3 Results

To indicate the accuracy of results for unloaded dipoles impedance values of a dipole with thickness factor, $\Omega = 2 \cdot \ln(2h/a) = 15$ are shown in figs 4 and 5 below in comparison to the King-Harrison results.

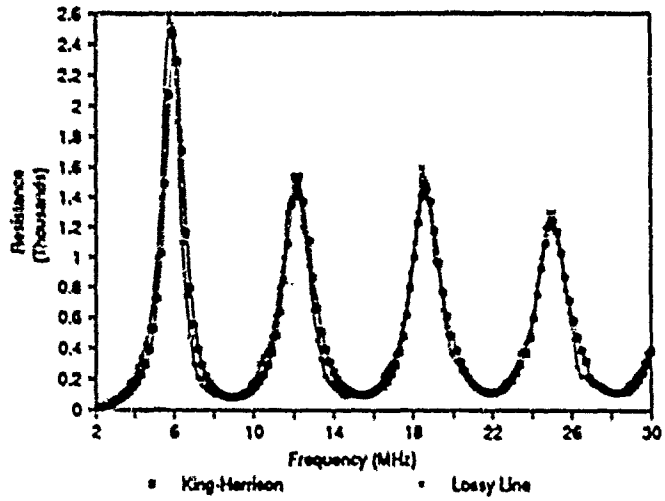


Fig 4 The resistance of a dipole with thickness factor of 15 as determined by the Lossy Line method compared to King-Harrison results

These curves show good correlation between the lossy line method and other theoretical results. Loaded dipoles, however of more interest and the well known *Altshuler*[4] type antenna of thickness factor 12.5 will be considered next. This antenna was scaled to a total length of 46 m with 330 Ohm loads placed 15.5 m from the feed as shown in Fig 6.

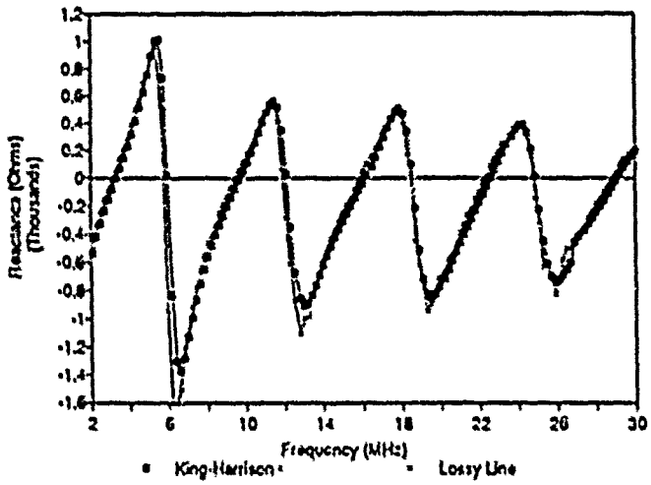


Fig 5 The reactance of a dipole with thickness factor of 15 as determined by the Lossy Line method compared to King-Harrison results

The input impedance and efficiency results for this antenna are shown in Figs 7, 8 and 9 with NEC results included for comparison.

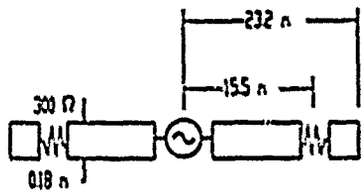


Fig 6 Altshuler type antenna used for tests

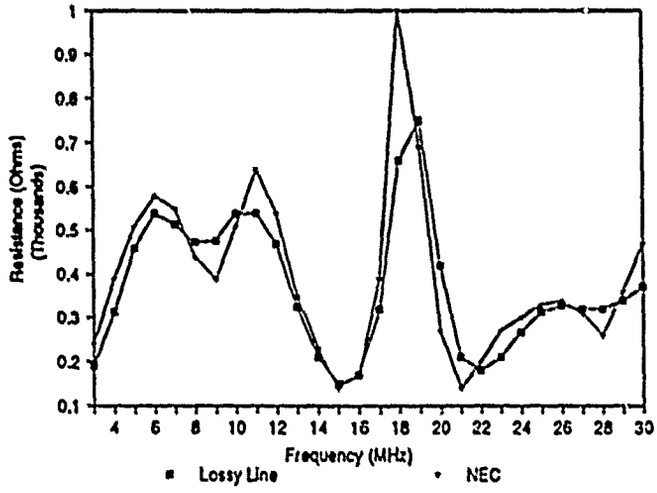


Fig 7 Input resistance of the Altshuler type antenna in comparison to NEC2 results

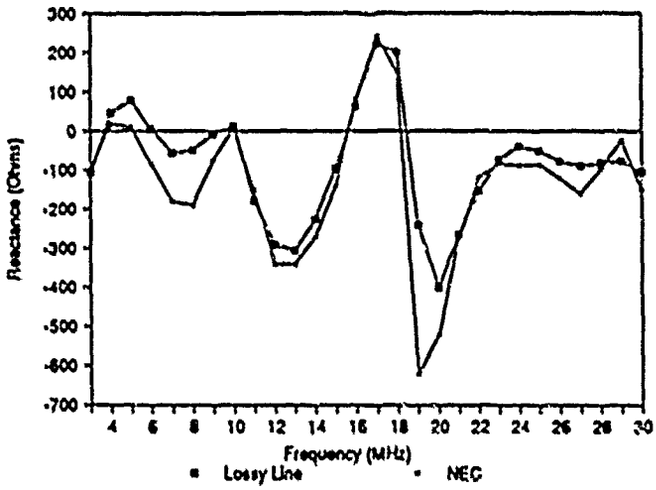


Fig 8 Input reactance of the Altshuler type antenna in comparison to NEC2 results

A previous attempt at a Lossy Line model (*Fourie*[4]) caused problems when a number of loads are included in a structure, especially if these included reactive components. The antenna in Fig 10 (*Clark Fourie*[1]) was therefore analyzed as a single thick dipole in accordance with the thick wire emulation theory. For the wire spacings shown an equivalent radius of 0.13 m is appropriate.

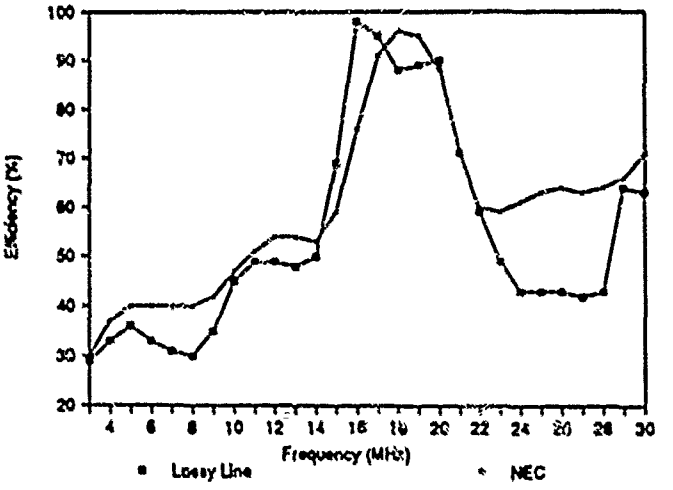


Fig 9 Efficiency of the Altshuler type antenna in comparison to NEC2 results

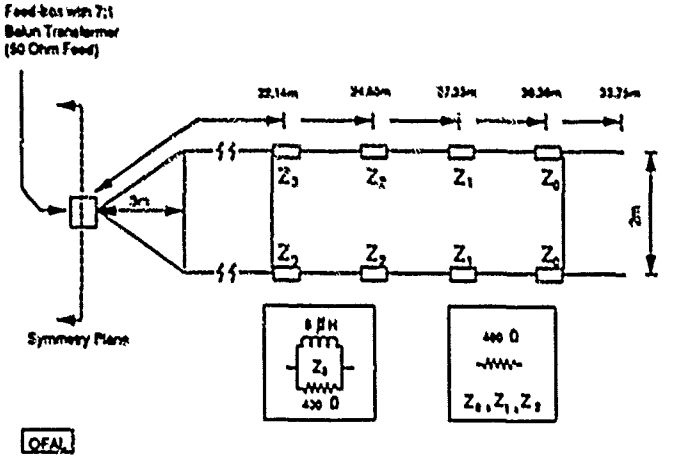


Fig 10 A multi-loaded antenna used to evaluate the Lossy Line method.

VSWR and efficiency results for this antenna is shown in Figs 11 and 12.

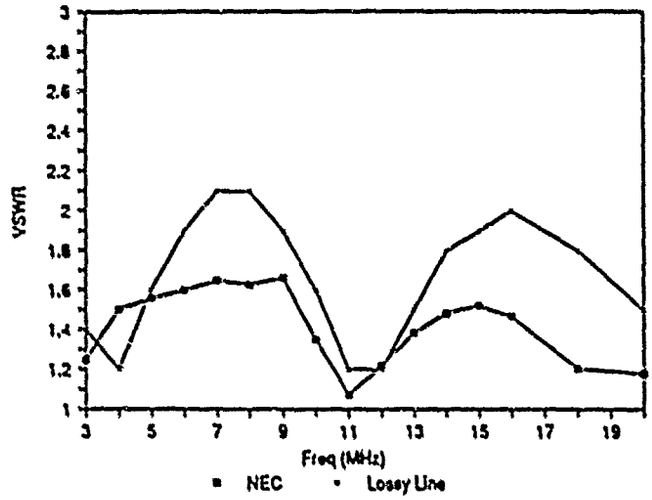


Fig 11 The VSWR of the multi-load antenna in comparison to NEC results

These results indicate the Lossy Line Model to be very successful and even the absolute values in most cases are a good approximations to the referenced results. Efficiency results gives an indication of the accuracy of the current distribution obtained using the Lossy Line method.

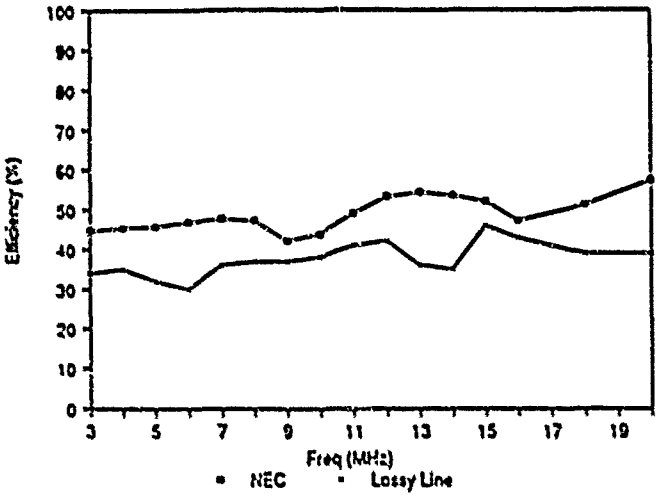


Fig 12 The Efficiency of the multi-load antenna in comparison to NEC results

4 Conclusion

The exploitation of the analogy between transmission lines and dipole antennas resulted in a suitable method for fast analysis of loaded dipole antennas. The computer time required to obtain a solution is proportional to the number of segments the wire is divided into. 6 segments per wavelength of dipole produced converged results for the cases shown above. This compares very favourably with method of moment codes where more segments per wavelength are normally required and the processor time is proportional to the number of segments squared and cubed. An evaluation of a loaded antenna such as the ones considered here requires 56 minutes to evaluate over the HF range whereas the Lossy line method accomplishes the same evaluation in about 0.5 minutes on an IBM PC AT running at 10 MHz. This is clearly significant for design and optimization purposes.

Appendix A Current distribution and efficiency

The current at a distance from the generator, x, on a uniform lossy transmission line of length, l, and terminated in a load, Z_L, is given by the equation :

$$I(x) = I(0)\left[\frac{Z_0\cosh(\gamma(l-x)) + Z_L\sinh(\gamma(l-x))}{Z_0\cosh(\gamma l) + Z_L\sinh(\gamma l)}\right]$$

This equation could then be used incrementally to solve for the current distribution on the more general non-uniform line.

If the current at the feed, I(0), is taken for convenience to be 1 A, then the current at any point, I, on the line could be determined by applying the above equation to each incremental piece of transmission line with :

$l = x = \Delta h$

This yields :

$$I(l+1) = \frac{I(l)Z_0(l)}{Z_0(l)\cosh(\gamma(l)\Delta h) + Z_t(l+1)\sinh(\gamma(l)\Delta h)}$$

The determination of Z_t is discussed in the main part of this text. When loads are present in the transmission line Z_t is modified as discussed before. After this process has been repeated for all segments 1 to N the complete current distribution is known. The efficiency could then simply be calculated by calcuting the input power, P_{in}, and the power dissipated in the loads, P_L :

$$P_{in} = \frac{R_{in}|I(0)|^2}{2}$$

$$P_L = 2 \times \frac{R_L|I(k)|^2}{2}$$

where k is the segment containing a load, $Z_L = R_L + jX_L$ in

each wire. The efficiency, η , is then given by the equation :

$$\eta = \frac{(P_{in} - P_L)}{P_{in}}$$

6 References

1. Clark, AR and Fourie, APC. "Problems with thin wire emulation of thicker wires using NEC2" The Fifth Annual Review of Progress in Applied Computational Electromagnetics, March 21-23 1989.

2. Schelkunoff, SA. " Theory of antennas of arbitrary size and shape." Proceedings of the IRE, Vol. 29, Sept. 1941, pp 493 - 521. Reprinted in the Proceedings of the IEEE, Vol. 72, No. 9, Sept. 1984, pp 1165 -1190.

3. Schelkunoff, SA. " Advanced Antenna Theory." John Wiley and Sons, 1952, Chaps. 2 and 5.

4. King, RWP and Harrison, CW. " Antennas and waves - A modern approach." The MIT Press, Mass. Appendix 4, Tables of Impedance and Admittance of electrically long antennas, 1969.

5. Altshuler, EE. "The traveling-wave linear antenna." IRE Transactions on Antennas and Propagation, Vol. AP-9, No. 4, July 1961, pp 324 - 329.

6. Fourie, APC. "Simple techniques for analysing and optimizing loaded broadband antennas". SAIEE Second Joint symposium on Antennas & Propagation and Microwave Theory an Techniques, 17 - 19 August, 1988, pp 21.1 - 21.10

VERIFYING THE RELATIONSHIPS BETWEEN AM BROADCAST FIELDS AND TOWER CURRENTS

James B. Hatfield

Hatfield and Dawson Consulting Engineers

4226 - 6th Avenue Northwest

Seattle, WA 98107

Abstract

The relative fields from the individual towers of an AM broadcast directional antenna array can be related to the voltages at the bases of the towers that are necessary to create those fields. The base voltages are used as sources for a modified version of Nininec III. The tower base currents computed by Nininec III for those tower base voltages are used to adjust the array of towers so that the correct far field pattern is achieved.

In the past, patterns for AM directional arrays have been brought into adjustment by a process of trial and error. The Nininec calculation procedure can reduce the amount of field work that is required to produce a properly functioning AM directional antenna system.

We have used the technique to adjust a variety of AM arrays in the past year. Adjustments are made so that the relative base currents of the towers are at the computed values, transmission lines are properly terminated, and field measurements are conducted without any further adjustments. In all cases so far, where re-radiating objects are not present, the resulting measured patterns have been within the tolerances of the FCC.

INTRODUCTION

AM (Amplitude Modulation) standard broadcast stations operate in the U.S. in the medium frequency band between 540 and 1600 kiloHertz. They frequently use directional antennas consisting of arrays of vertical radiators (towers) to allow operation without violating the interference rules of the FCC (Federal Communications Commission). Simplified mathematical expressions have been used since the 1930's to calculate the directional patterns for the electric fields radiated from these arrays. There have not been mathematical expressions that could accurately relate the drive voltages at the bases of the towers, or the tower currents, to the far field radiation pattern. The only practical way to calculate far field pattern shape has been to add the contributions to the far field of the radiation from the individual towers.

FCC DIRECTIONAL ANTENNA PATTERN FORMULA

Parallel ray geometry combined with the orientation and spacing of the towers is used to compute AM directional antenna pattern shape. The electrical constants used for calculating the pattern shape are the relative magnitudes and phases of the far field contribution of the radiation leaving each tower and a factor used to specify pattern size. The electrical and physical array constants that are used in the expression for calculating AM direction antenna pattern shapes from parallel ray geometrical assumptions are called "Field Parameters". The FCC requires that the DA (Directional Antenna) horizontal plane pattern be computed according to

$$E_{th} = k\left[f_1 \angle \underline{S_1 \cos(\phi_1 - \phi) + \Psi_1} \; + \ldots \; f_N \angle \underline{S_n \cos(\phi_n - \phi) + \Psi_n}\right]$$

where:

- E_{th} Inverse distance far field at one kilometer
- k Pattern size constant
- f_n Field ratio of tower "n"
- S_n Spacing of tower "n" in degrees from reference point
- ϕ_n Orientation of nth tower from reference point
- ϕ Orientation of observation point
- Ψ_n Phase angle of tower "n" (See Figure One)

Operating impedances and pattern size are calculated using "Loop Currents". Currents flowing in the towers are assumed to have sinusoidal distributions. The "Loop" is located at the point of maximum current on the tower. The relative magnitudes (ratios) and phases of the Loop Currents of the various towers were assumed to be the same as those of the fields of the towers. (The FCC DA pattern formula uses the relative magnitude of the field from the tower and the phase angle of the current "Loop" of the tower as though the tower currents and fields were synonymous.)

The magnitudes and phases of the loop currents are measured by the antenna monitor and sample system that are installed at AM directional arrays by requirement of the FCC. A substantial percentage of AM directional arrays in the U.S.A. use towers that are a quarter wave or less in physical height with the current loop at the base of the tower.

HOW DA ARRAYS HAVE BEEN ADJUSTED

All AM directional antennas in the U.S. must be adjusted so that the field intensities of their measured patterns are less than the field intensities of the Standard Pattern at all azimuths. Interference and protection from interference are determined using the Standard Pattern. The Standard Pattern is calculated from the Theoretical Pattern (described above) according to

$$E_{std} = 1.05\ [(E_{th})^2 + (Q)^2]^{\frac{1}{2}}$$

where E_{std} = Standard Pattern Field
E_{th} = Theo. Pattern Field
Q = Tolerance Factor

When adjustments are made to the phasing, power division and matching networks that are used to control the station's Directional Antenna pattern, the currents measured by the antenna monitor are set to the field parameter ratios and phases. In most cases this is just the starting point in the procedure that is used to create the correct pattern for the directional array. The correct pattern is not usually achieved when the antenna currents are set to the field parameters because the field contribution of each radiator is not exactly proportional to the loop current. Great emphasis is placed on pattern minima since they are used to supress radiation in those directions where interference could be created. The radiated field intensity is monitored in the direction of the minima (frequently called "Nulls" even though the theoretical pattern field does not go to zero) while adjustments are made to the DA array. This trial and error procedure continues until the field intensities in the nulls are within the Standard Pattern.

USING MININEC TO RELATE TOWER FIELDS TO TOWER CURRENTS

The trial and error procedure that is used for the adjustment of AM directional arrays can be greatly reduced or eliminated in many cases. The current or voltage at the base of a tower can be linearly related to the field from that tower by using the familiar "N" port admittance and impedance parameters. For base currents a matrix can be formed from

$$E_1/k_1 = V_1 = I_1(Z_{11}) + I_2(Z_{12})\ldots$$

For the base voltages we have

$$E_1/k_2 = I_1 = V_1(Y_{11}) + V_2(Y_{12})$$

Where E_1 is the field from tower one, the Y's are the self and mutual admittances and the k's are the constants of proportionality between the fields and base currents and voltages of the towers. For Mininec we want the base drive voltages so we will limit ourselves to the admittance parameters.

For Mininec the Far Zone E-Field is:

$$\bar{E}|\bar{R}| = \frac{jkn}{4\pi}\,\frac{e^{-jk|\bar{R}|}}{R}\,\bar{F}(\bar{R})$$

where

$$\bar{F}|\bar{R}| = \int_L \bar{I}(s)e^{+jk\,R\cdot\bar{r}(s)}ds$$

where

$$R = \bar{R}/|\bar{R}|$$

For an array of vertical radiators the "Z" component of the far zone E field in the horizontal or X/Y plane can be approximated as

$$E_1 = K_a \int_L I(s)\, ds$$

(where L is over the length of the vertical radiator)

since the terms in the more complete expression are approximately the same for all the towers in the array for great distances in the horizontal plane. This says that the far field from a tower in a vertical array is proportional to the summation of the current moments for that tower. And for Mininec this would be

$$E_1 = K_a \Sigma I(\Delta s).$$

Where Δs is the segment length and I is the current associated with segment length (Δs).

The expression used to form the matrix is

$$E_1/k_2 = K_a/k_2\, \Sigma I(\Delta s) = V_1(Y_{11}) + V_2(Y_{12}).$$

If we define $Y_{11}(k_2/K_a) = T_{11}$ and $Y_{12}(k_2/K_a) = T_{12}$ we have

$$E_1/k_a = \Sigma I(\Delta s) = V_1(T_{11}) + V_2(T_{12}).$$

Since we are interested in the field parameters relative to a reference tower we have

$$F_2 = E_2/E_1 = \frac{\Sigma I_2(\Delta s_2)}{\Sigma I_1(\Delta s_1)}$$

Where F_2 = Field ratio and Phase of tower #2

PRACTICAL IMPLEMENTATION OF THE TECHNIQUE

Mariabeth Silkey has modified the Mininec program to list the sums of the current moments for each wire and the field parameters as their complex ratios relative to tower (wire) one. (See Figure Two) To compute the "T" transfer parameters the towers are driven one at a time with one volt at the base segment. The "T" parameters in the matrix column with non-zero voltage are then equal to the respective tower current moment summation. The matrix that is formed from the equations relating the field parameters to the base segment drive voltages [$F_1 = 1 = V_1(T_{11}) + V_2(T_{12})\ldots$, $F_2 = V_1(T_{21}) + V_2(T_{22})\ldots$etc.]

is inverted to find the base drive voltages for Mininec that give the correct pattern. The current pulses (taken from the listed Mininec output currents) for the wire segments closest to the tower height where the antenna current is sampled give the correct relative adjustment parameters. The array is then adjusted so that the antenna monitor indicates those ratios and phases.

MEASURED RESULTS

We have adjusted several directional antennas using this technique without having to resort to trial and error field adjustment. I will discuss three examples. In all three examples antenna currents were monitored at the bases of the towers. Figures 3, 4, and 5 show the measured and standard horizontal plane patterns of the three stations.

A two tower array with unequal height towers (0.36λ and 0.18λ) that had inductive loading at the center of the taller tower was modeled using Mininec III. After computing the correct base current parameters it was necessary to apply a correction to account for the interaction of the tower base impedance with the base insulator capacitance. The impedance of the tall tower was quite high while the impedance of the short tower was almost two orders of magnitude lower than the capacitive reactance of the base insulator. Therefore a correction had to be applied only to the taller tower.

Neither the inductance of the coil at the center of the tall tower nor the capacitance of the base insulator were known or easily measurable. Measured impedances on both towers were available that were made with the inductive loading and the bases of the towers in a variety of open and short circuit configurations. The load inductance at the center of the tall tower and the capacitance of the base insulator at the tall towers were adjusted in the model until the computed Mininec values matched the measured values. When the array was adjusted to the computed base current parameters (the field ratio and phase angle of the tall tower were 0.83 and -94 degrees while the antenna monitor ratio and phase angle for this tower were 0.11 and -9.5 degrees) the measured operating base impedances were close to the predicted values and the measured fields were within the Standard Pattern (Figure Three).

An equal height 0.24λ three tower "dog leg" (not in a line) array was adjusted to the base current parameters computed from the Mininec procedure. The field ratios and phases of the end towers were 0.87 and -82.2 degrees and 0.348 and +88.4 degrees while the computed antenna monitor parameters were 0.85 and -77.3 degrees and 0.358 and +96 degrees respectively. The results are shown in Figure Four.

An unequal height (two towers 0.25λ and two towers 0.21λ) four tower parallelogram array (towers located at the corners of a parallelogram in the horizontal plane) was adjusted according to the Mininec

procedure. The non-reference tall tower had computed monitor ratio and phase that were 3% and 2 degrees higher than the field parameters. One of the shorter towers had antenna monitor ratio and phase that were 39% and 6.6 degrees higher, respectively, than the field ratio and phase. The other short tower had computed monitor ratio and phase that were 25% higher and 3.7 degrees more negative, respectively, than the field ratio and phase for that tower. The measured and Standard Pattern for this array are shown in Figure Five.

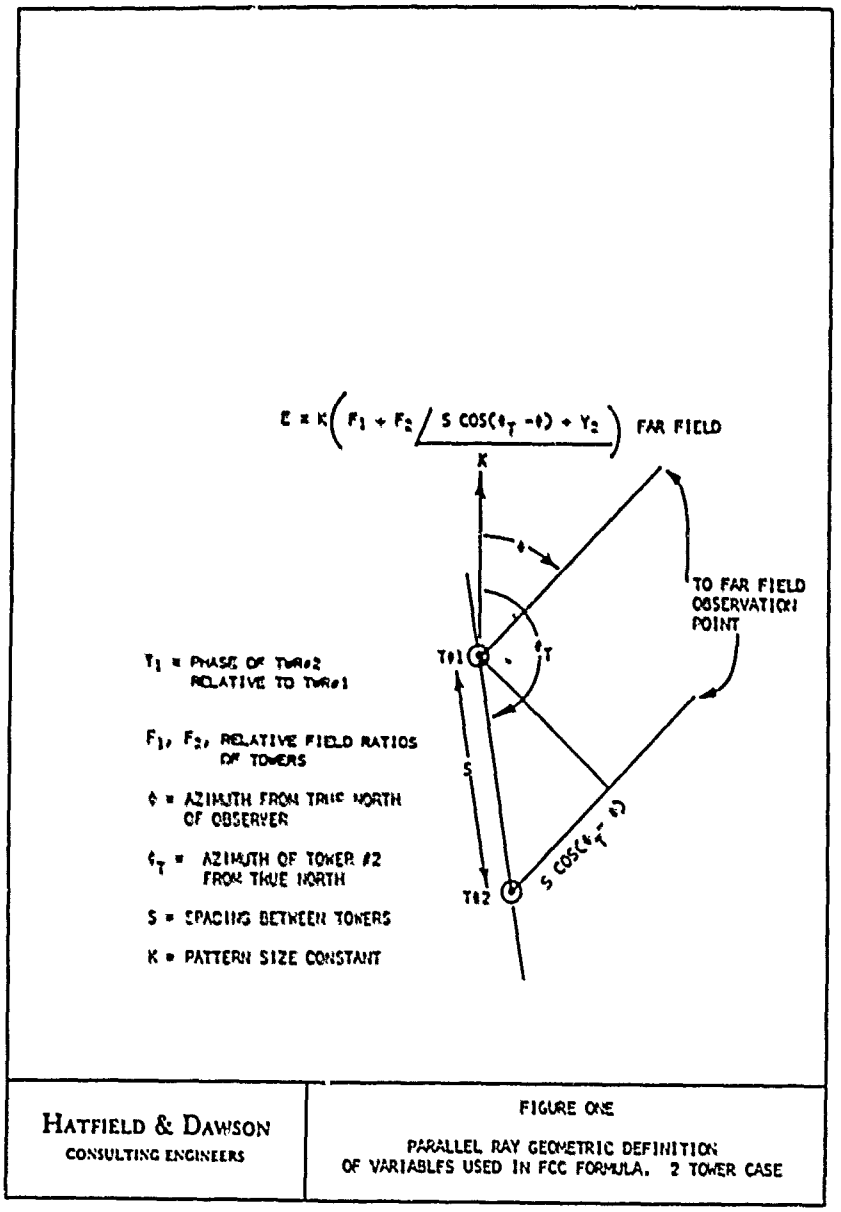
DETUNING TOWERS

Our success in adjusting AM directional arrays using tower base current parameters computed from the Mininec III current moment summations and the field parameters has led us to use the procedure for all of our AM directional antenna work. In those cases where nearby conducting objects such as buildings or power transmission towers and lines cause scattering and re-radiation of the incident fields we have had some success in pattern adjustment using the procedure. When we have been able to realistically model the towers and re-radiating objects pattern minima have been brought below the standard pattern. In two specific cases the pattern minimas were brought within tolerance when the arrays were adjusted to the computed base current parameters. In two other situations we were not able to define the situation well enough to make an adequate model.

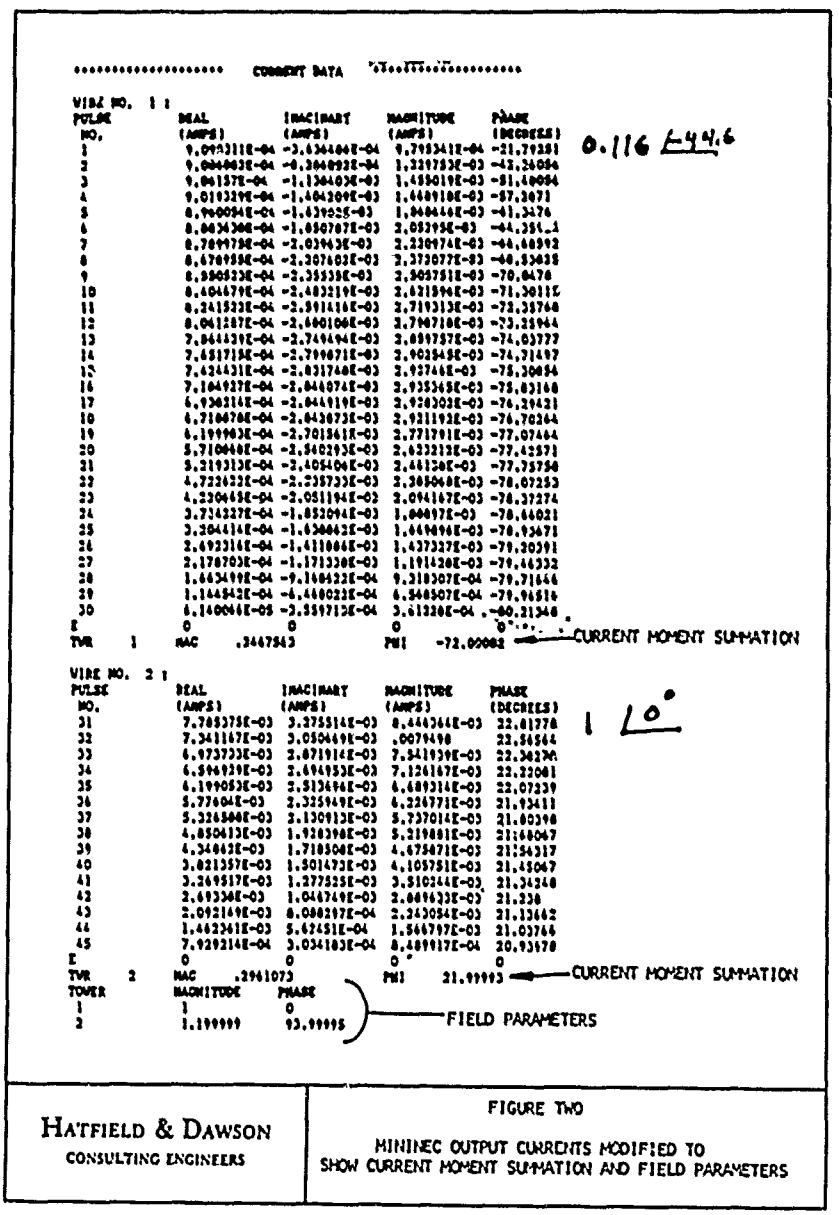
We have successfully detuned two towers in an AM array to allow omni-directional operation from a third tower. The magnitudes of the field parameters of the towers to be de-tuned were set at 10^{-6} and the computed base drive voltages that produced these fields were applied to the Mininec model of the array. The impedances of the de-tuned towers in the driven array were computed by Mininec. The real part of the impedance was typically two orders of magnitude lower than the imaginary part. Therefore the towers can be detuned by applying the conjugate of the reactive component of the operating impedance obtained from Mininec between the bases of the towers and ground (when towers are driven by base voltages that cause the fields of the de-tuned towers to be 10^{-6} of the field from the tower that is not de-tuned). When the model is run on Mininec with the grounded segments loaded with the de-tuning reactances some degredation of the de-tuning effect is observed (compared to the case where de-tuning is achieved by applying base drives), however, the scattered fields from the de-tuned towers are still several orders of magnitude below the fields from the tower that is not de-tuned.

CONCLUSION

Field parameters were devised so that AM directional antenna patterns could be computed. A realistic method to relate the field parameters to tower currents and tower base drives only became possible with the advent of numerical computer techniques. Method of moments procedures are not perfect for all AM antenna problems but they are more realistic than basing one's computation on assumed sinusoidal current distributions. By using programs like NEC-3 and Mininec III AM design engineers can compute base current parameters for AM directional antennas that produce measured patterns that are close to the calculated patterns and are within the limits of the FCC standard pattern. These results take much longer to achieve using trial and error in the field.



HATFIELD & DAWSON CONSULTING ENGINEERS	FIGURE ONE PARALLEL RAY GEOMETRIC DEFINITION OF VARIABLES USED IN FCC FORMULA. 2 TOWER CASE



```
********************    CURRENT DATA    ********************

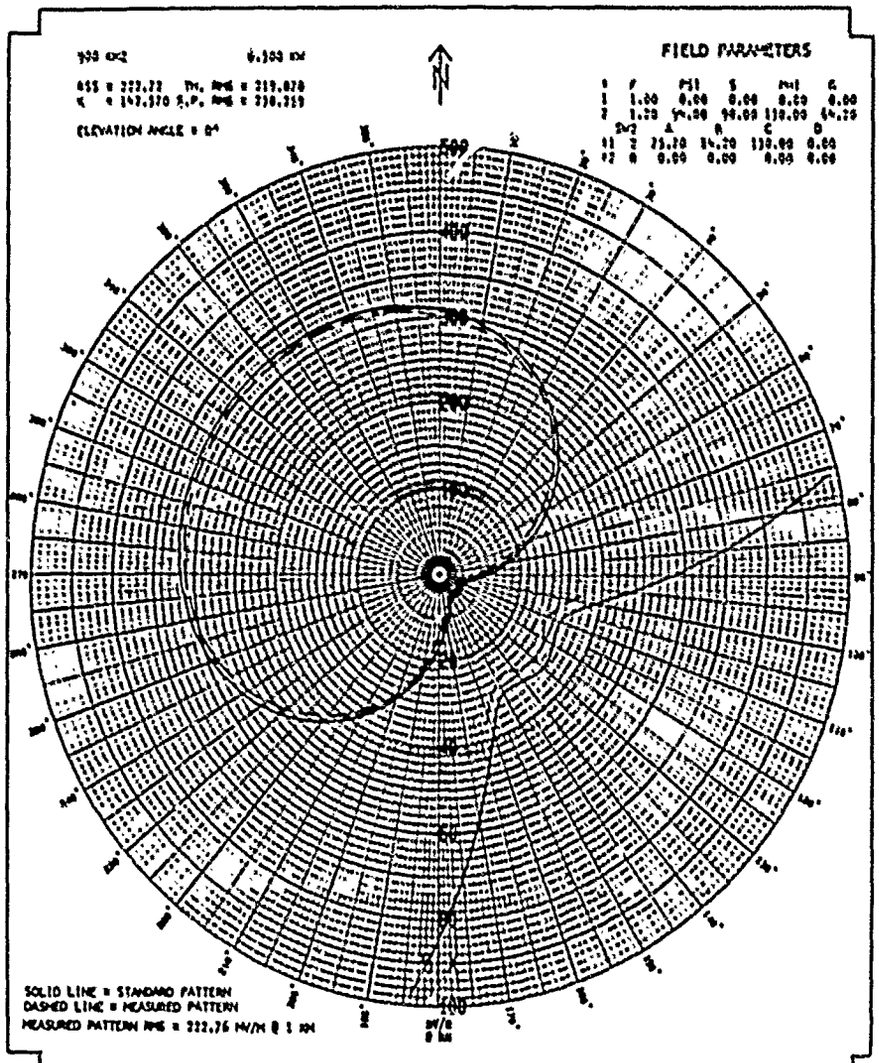
WIRE NO.  1 1
PULSE        REAL          IMACINARY     MAGNITUDE     PHASE
 NO.         (AMPS)        (AMPS)        (AMPS)        (DEGREES)
  1        9.095311E-04 -3.636406E-04  9.793541E-04 -21.79381
  2        9.044063E-04 -8.384892E-04  1.233783E-03 -42.36084
  3        9.041357E-04 -1.134403E-03  1.450019E-03 -51.48084
  4        9.013329E-04 -1.484209E-03  1.448918E-03 -57.3871
  5        8.990094E-04 -1.639525E-03  1.868646E-03 -61.3476
  6        8.843630E-04 -1.850707E-03  2.052795E-03 -64.351.1
  7        8.709978E-04 -2.03943E-03   2.220974E-03 -66.68992
  8        8.678958E-04 -2.207602E-03  2.372077E-03 -68.53628
  9        8.590522E-04 -2.355539E-03  2.5057511E-03 -70.0478
 10        8.404679E-04 -2.483219E-03  2.621594E-03 -71.30111
 11        8.241522E-04 -2.591411E-03  2.719313E-03 -72.33768
 12        8.061287E-04 -2.680106E-03  2.796710E-03 -73.25944
 13        7.844439E-04 -2.744494E-03  2.851757E-03 -74.03777
 14        7.651715E-04 -2.799671E-03  2.902345E-03 -74.71497
 15        7.424431E-04 -2.831746E-03  2.927466E-03 -75.30854
 16        7.184927E-04 -2.848074E-03  2.935365E-03 -75.83168
 17        6.936214E-04 -2.844119E-03  2.930303E-03 -76.29421
 18        6.718670E-04 -2.843673E-03  2.931193E-03 -76.70244
 19        6.499903E-04 -2.701361E-03  2.771791E-03 -77.07464
 20        5.710046E-04 -2.540293E-03  2.623213E-03 -77.42571
 21        5.219313E-04 -2.405406E-03  2.461126E-03  -77.75758
 22        4.722632E-04 -2.235733E-03  2.305068E-03 -78.07253
 23        4.220645E-04 -2.051194E-03  2.094167E-03 -78.37274
 24        3.734227E-04 -1.852094E-03  1.888917E-03  -78.66021
 25        3.204414E-04 -1.636643E-03  1.668946E-03 -78.93471
 26        2.692314E-04 -1.411884E-03  1.437327E-03 -79.20591
 27        2.178703E-04 -1.171330E-03  1.191428E-03 -79.46332
 28        1.663499E-04 -9.168422E-04  9.318307E-04 -79.71644
 29        1.144542E-04 -6.448022E-04  6.548507E-04 -79.96514
 30        6.140064E-05 -3.559713E-04  3.613226E-04 -80.21348
E          0             0             0             0
TWR    1   MAG    .3447543            PHI    -72.09082  <-- CURRENT MOMENT SUMMATION

WIRE NO.  2 1
PULSE        REAL          IMACINARY     MAGNITUDE     PHASE
 NO.         (AMPS)        (AMPS)        (AMPS)        (DEGREES)
 31        7.783378E-03  3.275514E-03  8.444364E-03  22.81778
 32        7.341167E-03  3.050469E-03  .0079498      22.56564
 33        6.973733E-03  2.871914E-03  7.541939E-03  22.36234
 34        6.596939E-03  2.694153E-03  7.126167E-03  22.22081
 35        6.199053E-03  2.513494E-03  6.689314E-03  22.07239
 36        5.77604E-03   2.325949E-03  6.226771E-03  21.93411
 37        5.326508E-03  2.130913E-03  5.737014E-03  21.80298
 38        4.850413E-03  1.928398E-03  5.219881E-03  21.68047
 39        4.34863E-03   1.718506E-03  4.675871E-03  21.54317
 40        3.821357E-03  1.501473E-03  4.105751E-03  21.45067
 41        3.269517E-03  1.277525E-03  3.510244E-03  21.34248
 42        2.693361E-03  1.046749E-03  2.889633E-03  21.238
 43        2.092169E-03  8.098297E-04  2.243084E-03  21.13442
 44        1.462361E-03  5.62451E-04   1.566797E-03  21.03766
 45        7.929214E-04  3.034183E-04  8.489917E-04  20.93678
E          0             0             0             0
TWR    2   MAG    .2961073            PHI    21.99993   <-- CURRENT MOMENT SUMMATION
TOWER      MAGNITUDE     PHASE
  1        1             0
  2        1.199999      93.99995     <-- FIELD PARAMETERS
```

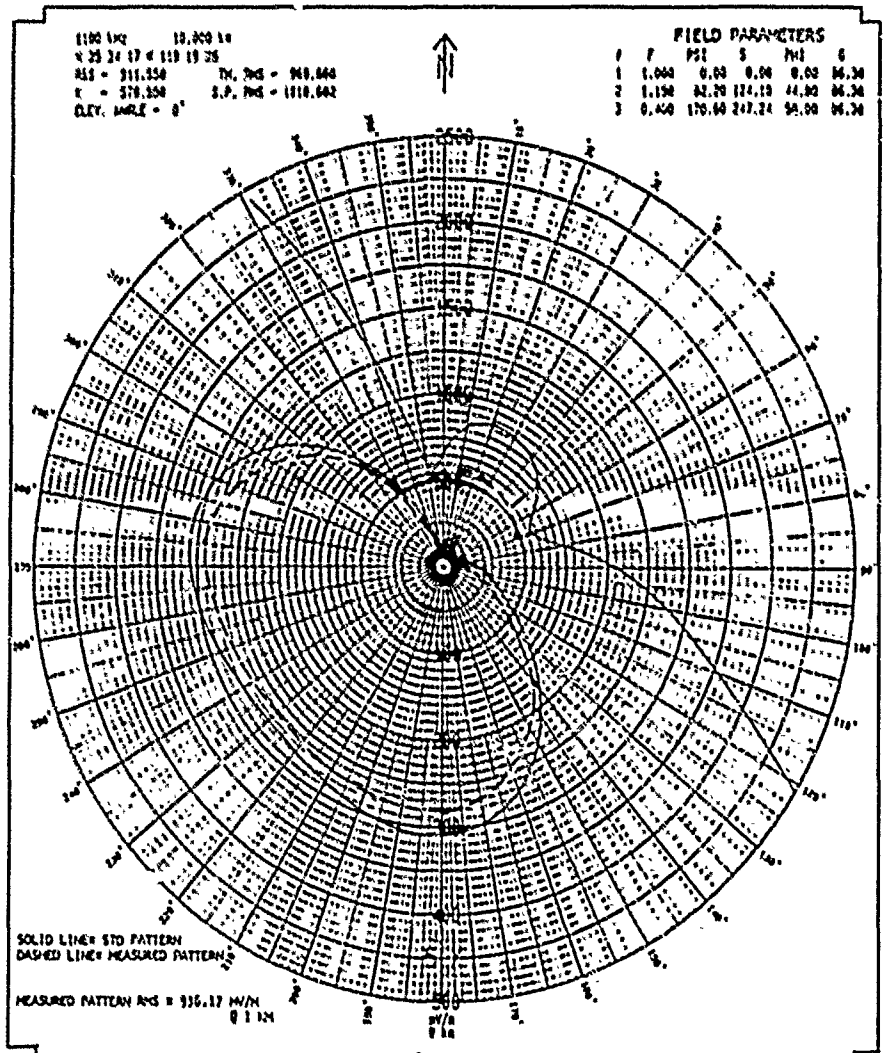
0.116 ∠44.6

1 10°

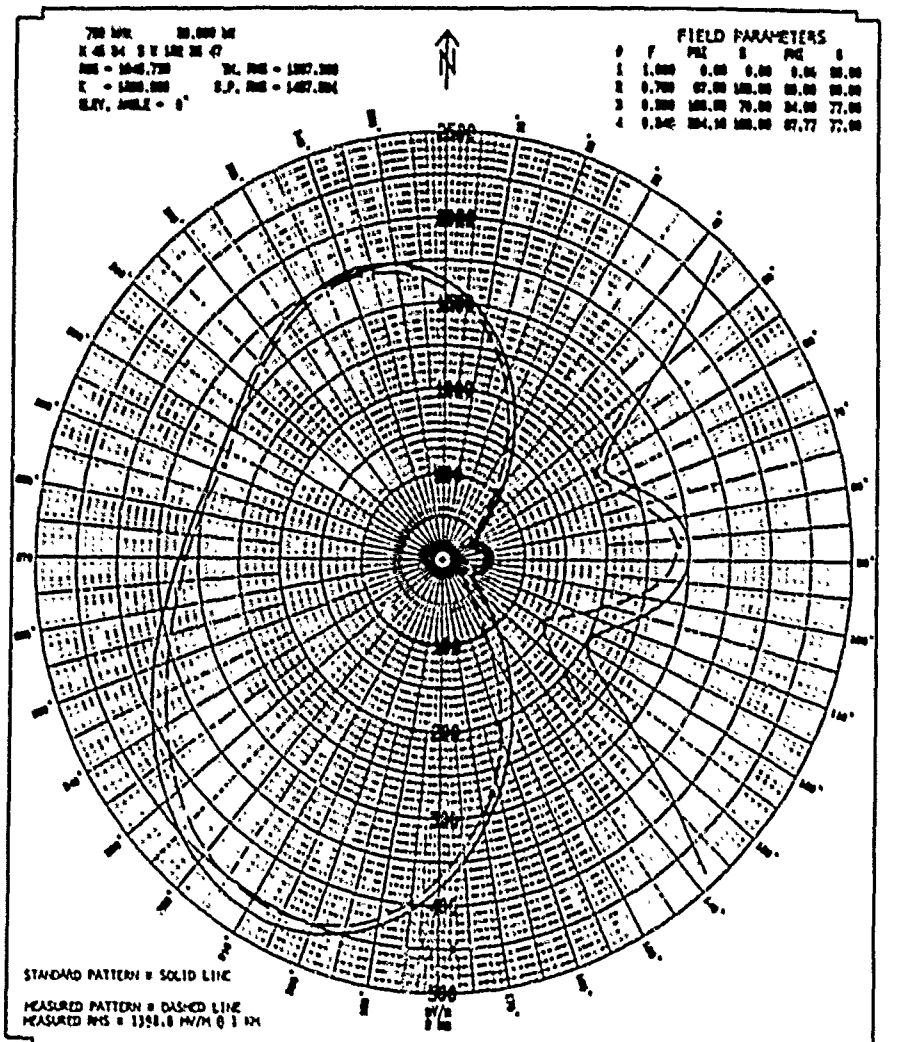
HATFIELD & DAWSON CONSULTING ENGINEERS	FIGURE TWO MININEC OUTPUT CURRENTS MODIFIED TO SHOW CURRENT MOMENT SUMMATION AND FIELD PARAMETERS



HATFIELD & DAWSON CONSULTING ENGINEERS	FIGURE THREE TWO TOWER ARRAY. UNEQUAL HEIGHT WITH CENTER OF TALL TOWER INDUCTIVELY LOADED



HATFIELD & DAWSON CONSULTING ENGINEERS	FIGURE FOUR THREE TOWER "DOG LEG" ARRAY



HATFIELD & DAWSON CONSULTING ENGINEERS	FIGURE FIVE FOUR TOWER PARALLELOGRAM ARRAY TOWER PAIRS DIFFERENT HEIGHTS

FOUR-ELEMENT MONOPOLE ARRAY

Charles H. "Chuck" Vardaman
Rockwell International, Collins Defense Communications
Advanced Technology and Engineering
3200 E. Renner Rd., Richardson, Texas 75080

An electrically short, closely spaced monopole array has been modeled experimentally and numerically. The goal of this experiment was to see if calculations could be used to economically obtain the spacings needed to achieve specified antenna beamwidths with an established feed system . The numerical model used a combination of NEC-3(MOM)[1] and NEC-BSC[2]. The size of the array was restricted by the requirement that it had to fit in an existing radome. The four elements were arranged in a square, as shown in figure 1, and fed in a manner to produce a "unidirectional" beam in the direction of one of the diagonals of the square. The antenna was to be used in a direction finder, switching the beam for rotation in ninety-degree steps.

The frequency was near one-gigahertz. The sides of the square were 0.31 wavelengths, and the height of the monopoles was 0.095 wavelengths. The array was mounted on a 4.0 wavelength diameter circular counterpoise. Round, flat disks were used as top-hats on each of the monopoles to tune them to resonance. The tuning procedure was an iterative "cut and try" operation. The impedance of one antenna was measured with the other three terminated in resistive loads. The size of the top-hats and the resistance of the loads were repetitively adjusted until the measured resistance of each element at resonance was equal to the termination resistance of the other three. The final top-hat radius was nearly the same as the monopole height. Tapered line transformers on printed circuit material brought the feedpoints to four fifty-ohm micro-coax connectors at the center.

A schematic of the feed system is shown in figure 2. The power- splitters were purchased items, but the delay lines were made in the laboratory. The coax lengths were adjusted until they provided four signals: one at 0 degrees, two at 90 degrees, and one at 180 degrees when all four leads were terminated in 50-ohm loads. It was understood that this phasing would not hold true after the leads were connected to the antennas due to the mutual impedance effects in the array.

The patterns of the array were measured for comparison to calculations which would come later. One THETA-cut was measured with PHI = 0-180 degrees. Several conical cuts were made with PHI variable, THETA being held constant at several angles between 65 degrees and 105 degrees.

The computer modeling was performed by "art imitating life", within the limits of the computer codes. The four monopoles were modeled in NEC-3 to get the source data for the BSC code. Both programs were installed on a CDC-CYBER 175 computer, a large fast mainframe. An infinite, perfectly conducting ground plane was used in

NEC-3. Each monopole was cut into seven segments and eight six-segment radials were used as top-hats. The top-hat radials were tuned to resonance following the same iterative technique as the experimental model. The experimental model used transformers to get the impedance back to the 50-ohm reference value of the test equipment and the prepared feedlines. That was not necessary in the numerical model; we simply established a 14-ohm reference system.

Feeding the phased array in NEC-MOM was not just a matter of putting in four excitation cards with equal voltages of the proper phases. Remember that the antenna impedances were tuned to some resistive value while the other elements were terminated in the same value. When the array is fed with different phases on the four elements, the mutual impedances change the input impedances and the currents are modified from the equal amplitude, equal phase conditions. However, in this case, we are imitating an experimental model so the feed technique was relatively straightforward. A Thevinen equivalent source was created by placing a resistive load in series with the feed-point at the base (center of bottom segment) of each of the four monopoles. The value of the resistor was that of the reference system, 14-ohms.

A short FORTRAN code was used to read a NEC-3 print file and extract the "SM" data for entry into the NEC-BSC code. The "SM" data consists of the total input power level (watts). And for each segment, it requires the x-y-z location of the segment center, its length, the direction of the segment measured in azimuth and elevation angles, and the amplitude and phase of the current in that segment. The BSC code was designed to take these values in a format readily available from the older MOM code.

Poets are allowed to use poetic license, and in that sense, engineering license was used on the model at this point. Only thirty "SM" sources are permitted in the unmodified BSC code. As modeled in NEC-3 (MOM), 220 segments were used. The choice was to cut out a lot of segments or modify the BSC code (increase the dimensions on several variables). Wanting to keep the code as "original" as possible, it was decided to delete segments. Since the top hats are not supposed to radiate, they were simply deleted for input to the BSC model. It was recognized that at the close spacing in this four-element array, the currents in the top hat radials might not fit the nonradiating condition that they be equal in amplitude and phase and also flow in the opposite direction from their counterparts in the center point symmetry. In fact, the currents within a single top hat varied by 0.12 dB. Symmetry did exist about the center of the array; top hat currents going forward from the front element matched the currents going aft of the rear element. The current amplitudes and phases on the monopoles were set (in NEC-3), so the source currents as used in the BSC model did not go to zero at the tops of the monopoles.

The only "adjustment" to the data was that the measured pattern gains were normalized to fit the maximum gain point on the counterpart calculated pattern. We did not make an absolute gain calibration of the pattern range, so the measured patterns are consistent only within each pattern.

The nine patterns presented in figures 3 - 5 show that the calculated and measured patterns match quite well. Note that the first pattern is a great-circle (elevation, or THETA) cut and the rest are conical (azimuth, or PHI) cuts at different THETA angles. The major lobes of the patterns fit within a few tenths of a dB between the -10 dB to -15 dB points. The maxima of the side/backlobes fit reasonably well, but there seems to be a systematic right-left asymmetry in the backlobes of the measured patterns (dashed lines).

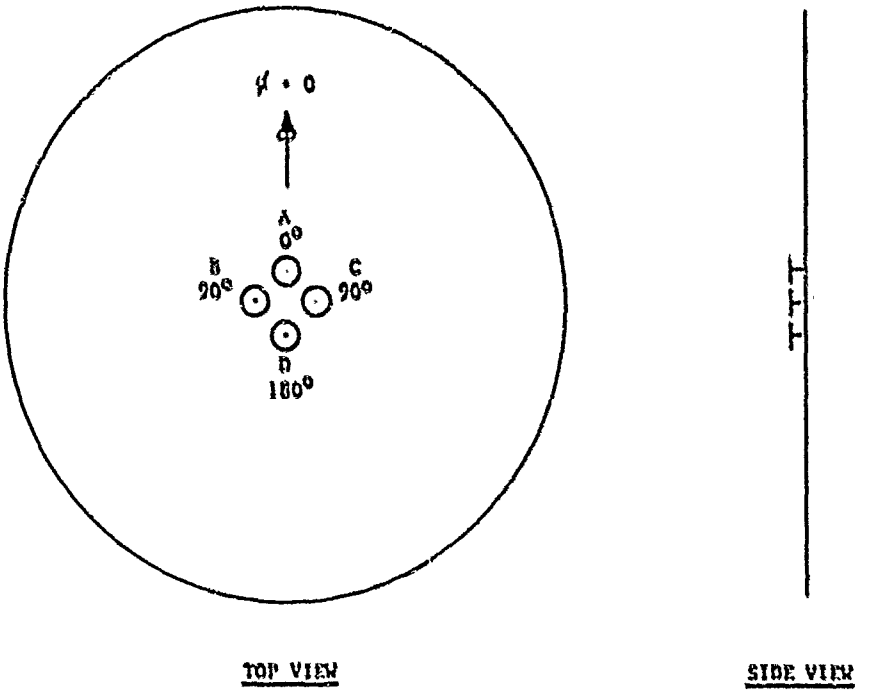
The conclusion was that numerical modeling could be used to predict the measured results in the significant area of the main beam, and that iterations could be performed in much less time than would be required for an experimental model.

I must say a hearty "thank-you" to Gilbert Smoak who constructed the antenna and the feedlines, Mark Montgomery who measured the patterns, and my wife Betsy who digitized the measured data.

REFERENCES

[1] Burke, G.J. and Poggio, A.J. "Numerical Electromagnetic Code (NEC) - Method Of Moments" Naval Oceans Systems Center, (NOSC) San Diego, CA., Technical Document 116, July 1977 rev Jan 1980.

[2] Marhefka, R.J. and Burnside, W.D. "Numerical Electromagnetic Code - Basic Scattering Code" The Ohio State University Electroscience Laboratory, Technical Report 712242-14 December, 1982.



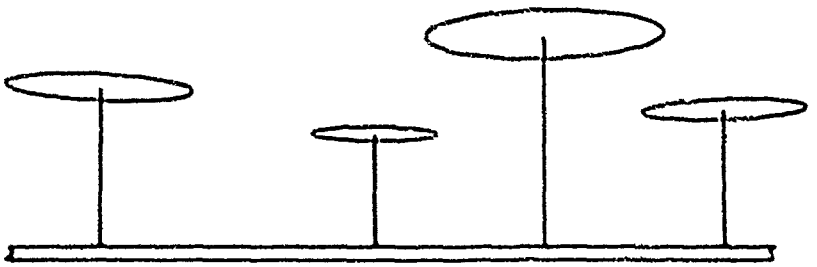


FIGURE 1. FOUR-ELEMENT MONOPOLE ARRAY
ON TWO-WAVELENGTH RADIUS COUNTERPOISE

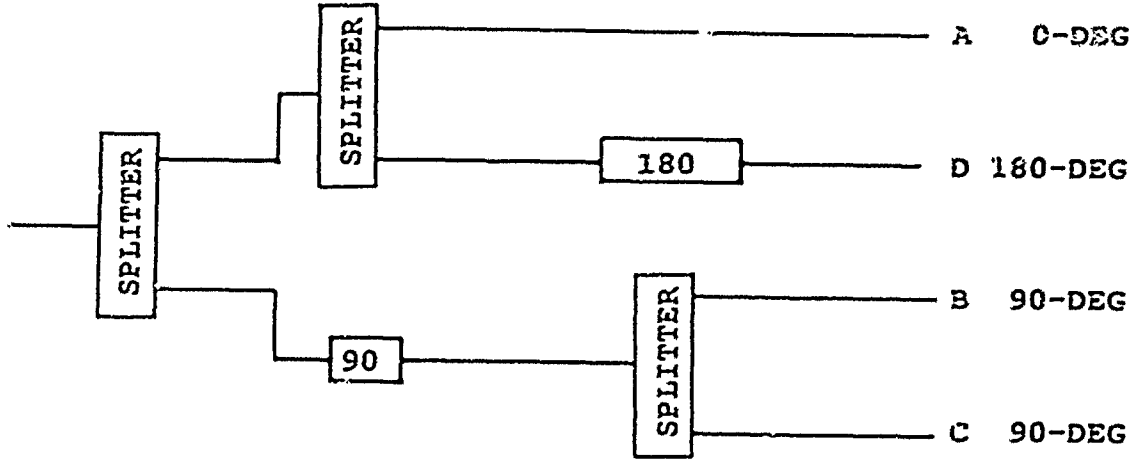


Figure 2. PHASING LINES FOR FOUR-ELEMENT ARRAY

CM FOUR-MONOPOLES ON 1.2 METER DIA. COUNTERPOISE
CE

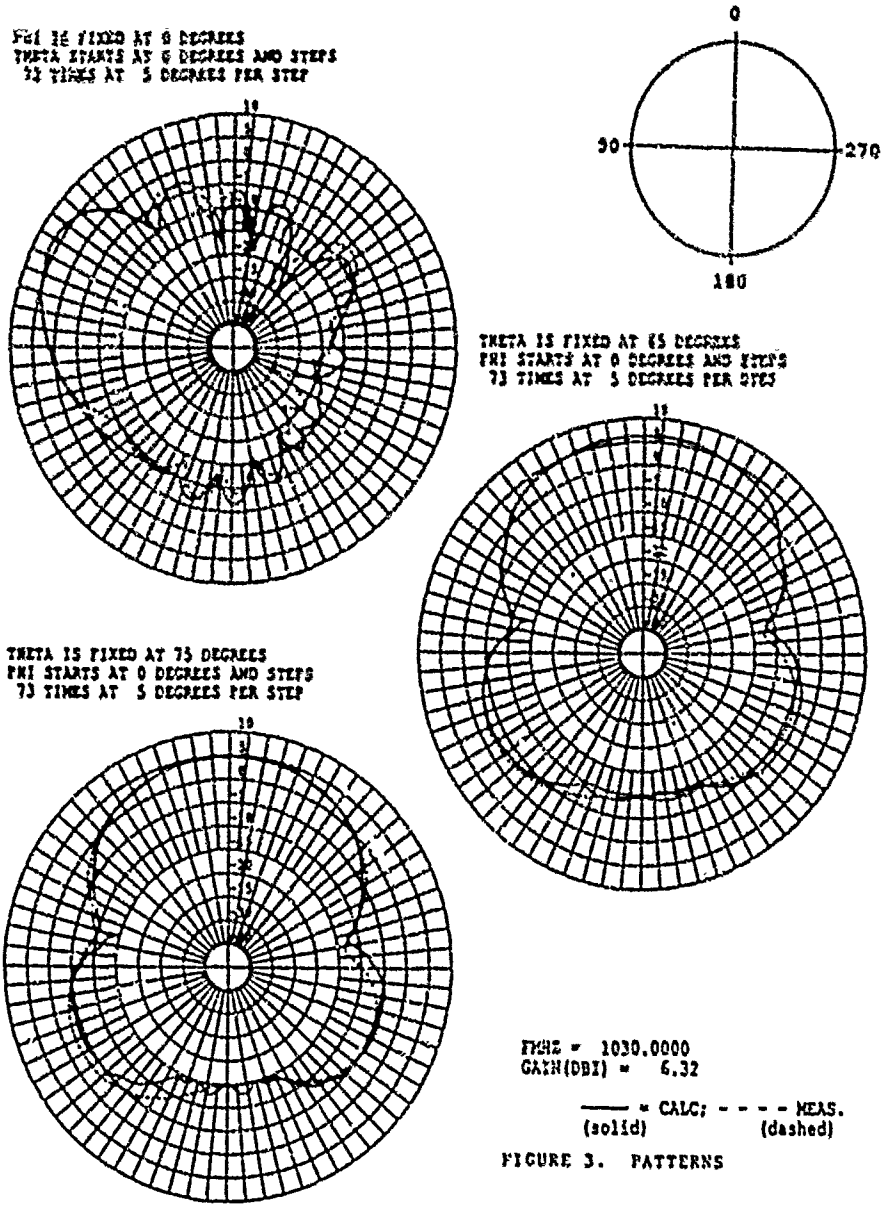


FIGURE 3. PATTERNS

CH FOUR MONOPOLES ON 1.2 METER DIA. COUNTERPOISE
CE

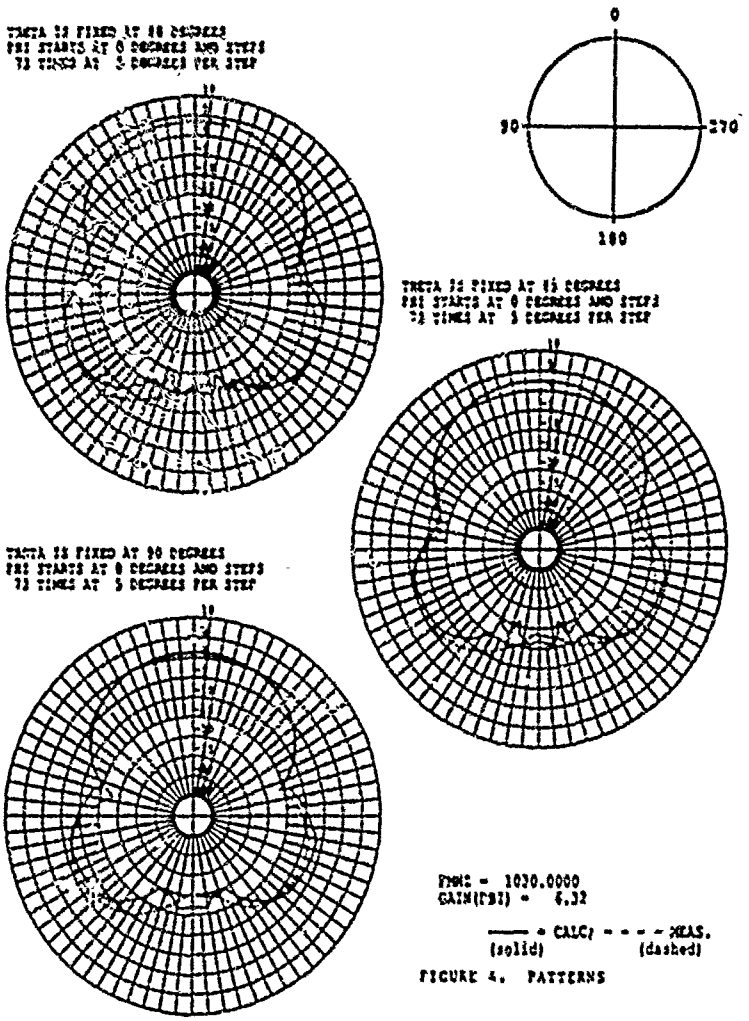


FIGURE 4. PATTERNS

CH FOUR MONOPOLES ON 1.2 METER DIA. COUNTERPOISE
CE

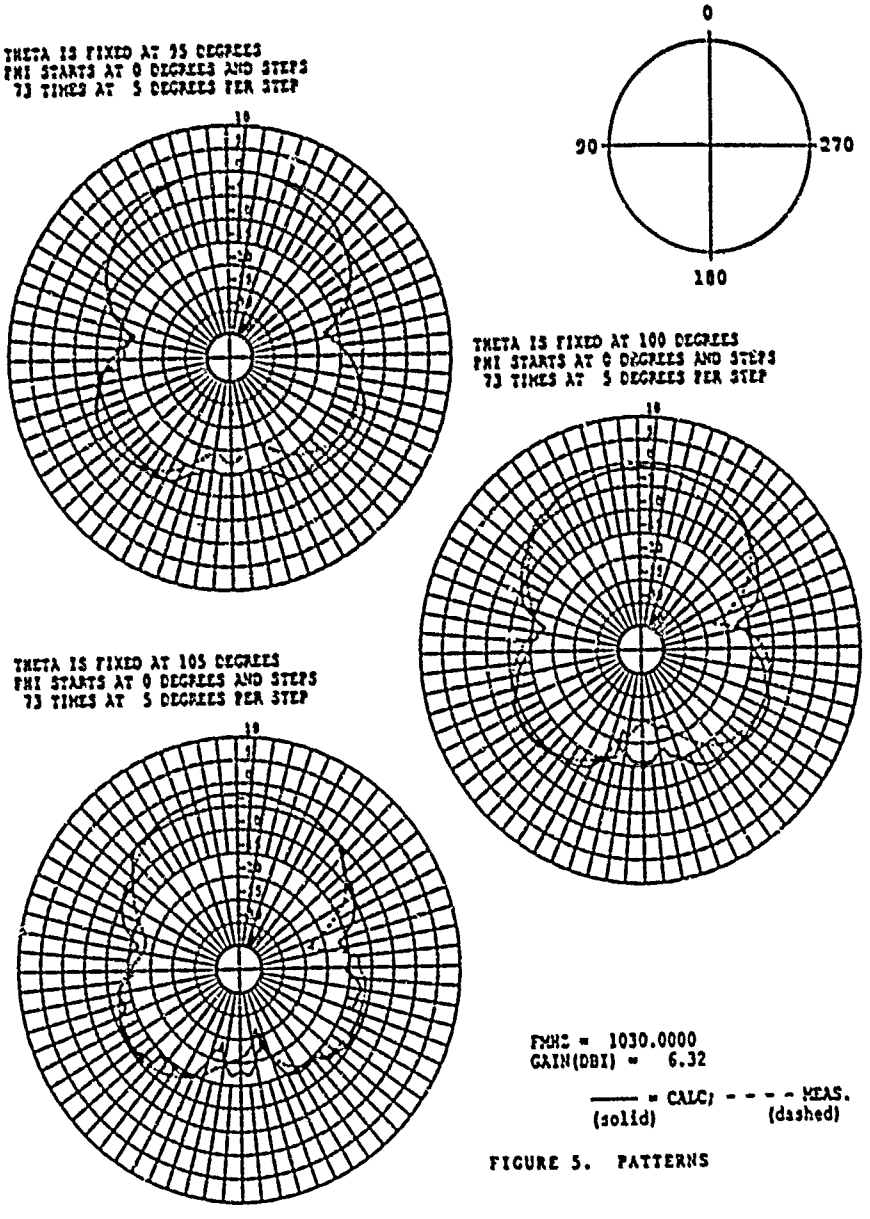


FIGURE 5. PATTERNS

MODELLING THE QUADRIFILAR HELIX (VOLUTE) ANTENNA USING THE METHOD OF MOMENTS

BY

STEVEN R. BEST
CHU ASSOCIATES INC.
800 FESLER STREET
EL CAJON, CA 92020
(619) 442-9459

ABSTRACT

One of the most commonly used antennas for Global Positioning System (GPS) applications is the quadrifilar helix antenna. Since the positioning accuracy required by many GPS users is at the sub-centimeter or millimeter level, it has become increasingly important to be able to accurately model the amplitude, phase and phase center characteristics of this and other GPS antennas.

The purpose of this paper is to present a moment method model for the quadrifilar helix antenna and to discuss some of the problems encountered implementing the model.

Finally, a comparison of modelling results for the quadrifilar helix antenna from different method of moments programs will be presented and discussed.

I INTRODUCTION

The quadrifilar helix (volute) antenna, shown in Figure 1, is one of the most commonly used antennas for Global Positioning applications owing to its small size, light weight and its circularly polarized, cardioid shaped radiation patterns. This antenna consists of four equally spaced helical conducting arms wound in air or on a cylindrical dielectric support member. The antenna feed point can be located at either the top or the bottom of the conducting arms. Opposite ends of the conducting arms are short-circuited or open-circuited, depending upon the operating mode. In order to obtain omnidirectional, hemispheric, circularly polarized radiation from this antenna, the four conducting arms must be fed with equal amplitude sources in phase quadrature.

The geometry of the quadrifilar helix can be described by

$$L = N\sqrt{\frac{1}{N^2}(E - 2R)^2 - 4\pi^2R^2} \qquad (1)$$

where L is the axial length of the helix, E is the element length, R is the helix radius and N is the number of turns.

The quadrifilar helix antenna has been studied in depth experimentally by Kilgus [1,2] who has presented detailed design curves and information for both fractional-turn and multi-turn volutes. Although Kilgus' data provides useful design information, it is both costly and time consuming to build experimental antenna models to determine amplitude and phase pattern characteristics for different designs. With the use of computer modelling, the determination of the antenna characteristics is both fast and cost-effective.

It is the purpose of this paper to present moment method modelling results for the quadrifilar helix and to discuss some problems encountered implementing the models. Measured and computed amplitude characteristics for a 1/2-turn a 1-turn quadrifilar helix antenna will be presented. Phase data for the 1/2-turn volute will also be presented.

II MODELLING TECHNIQUES

The two method of moments programs used to model the quadrifilar helix in this paper are the Numerical Electromagnetics Code (NEC) [3] developed by G. J. Burke and A. J. Poggio and the method of moments code developed by J. H. Richmond [4]. Details regarding the exact techniques used in each of these programs to determine antenna current distribution and radiation patterns will not be discussed in this work. These details can be found in the appropriate reference.

The above moment method programs were implemented and run on a IBM-PC compatible computer. The PC version of NEC was the NEC2-PC code distributed by ACES and the PC version of the Richmond code was implemented as an interactive PC program by the author.

The antenna structure input to each of the programs requires division of the antenna into small wire segments joined by defined junction points. Accurate modelling

results were obtained for the quadrifilar helix when 3 or 4 segments were used for each of the radial wire sections and 12 segments were used per turn for each of the four helical arms.

III. THE 1/2-turn QUADRIFILAR HELIX

The 1/2-turn quadrifilar helix modelled here has an axial length of 3.053 inches (.317 wavelengths at GPS frequency L2, 1227.6 MHz) and a radius of .5225 inches (.054 wavelengths at L2). This antenna was designed to produce a hemispheric radiation pattern typical of 1/2-turn volute antennas [1].

The first attempt at modelling this antenna was performed using the Richmond code where each helical arm had 6 wire segments and each radial arm had 4 wire segments. The antenna feed point was located at the center of the top radial arms while the bottom radial arms were short circuited at their central connection point. Since the antenna feed network requires two equal amplitude sources in phase quadrature the top radial sections were separated by 1 millimeter to accommodate two feed locations.

A comparison of measured and computed amplitude patterns at 1227.6 MHz is shown in Figure 2a. Although the comparison is good in the upper hemisphere, the computed pattern is not symmetrical and the results are not accurate for modelling of the antenna's radiation pattern. Since the computed and measured results did not agree when using the Richmond code, an attempt was made to model the same wire configuration using NEC. These results are presented in Figure 2b and it can be seen that the computed and measured patterns are in very good agreement except for the backlobe characteristics. The differences between the backlobe structures will be discussed shortly.

Since the Richmond moment method program did not properly model the above wire configuration, it was decided that a simpler configuration, such as a bifilar helix antenna should be modelled. The bifilar helix antenna consists of 2 helical arms joined at the top and bottom by radial arms. Fed at the top or bottom, this antenna produces a circularly polarized dipole shaped radiation pattern [1]. Computed results using Richmond's code are shown in Figure 3. As can be seen, the computed results correctly predict the amplitude pattern for the bifilar helix.

Since the computed pattern for the bifilar helix was accurate, another attempt was made to model the quadrifilar helix using Richmond's code. This time, however, the two orthogonal bifilar helices in the quadrifilar helix were left physically unconnected. The only difference between this wire configuration and the previous configuration was that the two bottom radial arms of each bifilar helix are not short-circuited at their central connection point.

A comparison of computed and measured results for the modified wire configuration using Richmond's code, is shown in Figure 4a. From these results it can be seen that there is excellent agreement between the computed and measured amplitude patterns. In fact, these results show much better agreement between computed and measured patterns than the NEC code. The same wire configuration was then modelled using NEC and these results are presented in Figure 4b. Using this wire configuration, there is a significant improvement in the accuracy of the computed results.

The only difference between the computed and measured data, for both NEC and Richmond's code, is in the antenna backlobe characteristics. The measured pattern has a deep null at an observation angle of 270 degrees, while the computed patterns have an amplitude lobe. Experimental data from Kilgus [2] and the computed output from NEC, indicate that the radiation in the backlobe is of opposite polarization sense than that of the front lobe, ie. RHCP is predominant over most observation angles while LHCP is predominant in the backlobe. Since the experimental measurements were made with a RHCP source the presence of a back lobe was undetected. Further experiments with both RHCP and LHCP sources show the presence of a LHCP backlobe (Figure 5). This level of circularly polarized backlobe radiation is consistant with the computed results.

In many GPS applications, knowledge of the antenna amplitude characteristics is insufficient in determining the effects of antenna performance on system accuracy. Knowledge of antenna phase and phase center characteristics is critical in determining final system performance [5,6,7]. Since the antenna phase center location is a function of the antenna far-field phase characteristics [5], this paper will limit the discussion of quadrifilar helix phase performance to its phase patterns.

Figures 6a and 6b present measured and computed - using NEC and Richmond's code - phase data for the 1/2-turn

quadrifilar helix. Results are shown for orthogonal linear polarizations (E_θ and E_ϕ) as defined in Figure 1. It can be seen that both programs accurately predict the antenna's phase characteristics.

IV THE 1-turn QUADRIFILAR HELIX

The quadrifilar helix antennas's design parameters include the axial length, the radius and the number of helical turns. To further validate the moment method model predictions of volute radiation characteristics, a 1-turn helix was modelled. The 1-turn quadrifilar helix has an axial length of 6.45 inches and a radius of .7425 inches. This antenna was designed for dual frequency (L1, 1575.42 MHz and L2, 1227.6 MHz) GPS applications, however, it was not designed to have optimum GPS pattern coverage at either L1 or L2 but rather to have drastically different patterns at each frequency in order to demonstrate the model capabilities. A comparison of measured and computed (NEC and Richmond codes) radiation patterns are shown in Figures 7 and 8 for L2 and L1 respectively. Again it can be seen that there is excellent agreement between the computed and the measured results for the NEC code with the exception of the backlobe characteristics which are a result of a change in the sense of circular polarization.

The results obtained using Richmond's code are acceptable at L2, however, there is a significant difference between the computed and measured patterns at L1. Several different modifications of the wire configuration were modelled, such as increasing the number of segments per turn and decreasing the bifilar separation and wire radius. However, there was no significant improvement in the computed results.

V DISCUSSION

From the results presented in this paper, it is known that the method of moments can be used to accurately predict the radiation characteristics of the quadrifilar helix antenna. However, the question of why neither program (NEC and Richmond's) can accurately predict the amplitude patterns when the bottom radials are shorted together, as in the experimental antenna, still remains.

The radiation patterns of the quadrifilar helix antenna are a sensitive function of how well the quadrature feed phasing relationship is maintained [5]. Any deviation from this quadrature phasing relationship, which results in a change of the current distributions along each helical arm, will seriously distort the antenna patterns. With the physical connection of the radial arms in the computer model, the resultant current distribution along the antenna structure does not represent the true antenna currents. The four wire arm connection may be causing the model to incorrectly account for the quadrature phase relationship.

Since the purpose of this paper was to present a usable and accurate model for the quadrifilar helix antenna, further investigation into the above problem will be left to future work.

Another problem that should be addressed is why does the Richmond code incorrectly predict the radiation patterns for the 1-turn volute at L1? Further investigation into the modelling of multi-turn volutes using NEC and Richmond's code may provide some insight into this problem.

VI CONCLUSIONS

An accurate moment method model, using an existing program (NEC), of the quadrifilar helix antenna was presented. With the use of this model, the amplitude and phase characteristics of this antenna can be easily and accurately determined. For high accuracy positioning systems, such as GPS, that require knowledge of these antenna characteristics, this model allows for quick determination of system errors that are a result of antenna performance.

VII REFERENCES

1. Kilgus, C. C., "Resonant Quadrifilar Helix Design," The Microwave Journal, December 1970, pp. 49-54.

2. Kilgus, C. C., "Shaped-Conical Radiation Pattern Performance of the Backfire Quadrifilar Helix," IEEE Transactions on Antennas and Propagation, Vol. AP-23, No. 3, May 1975, pp. 392-397.

3. Burke, G. J., and A. J. Poggio., "Numerical Electromagnetics Code (NEC) - Method of Moments," NOSC TD 116., Vols. 1, 2 and 3, Naval Ocean Systems Center, San Diego, CA, January 1981.

4. Richmond, J. H., "Computer Program for Thin-Wire Structures In a Homogeneous Conducting Medium," Contract Report NASA CR-2399., The Ohio State University Electroscience Laboratory, Columbus, Ohio, June 1974.

5. Best, S. R., "Amplitude, Phase and Phase Centre Model Performance for Antennas Used In Land and Satellite Based Positioning Systems," PhD Thesis, The University of New Brunswick, Fredericton, New Brunswick, April 1988.

6. Tranquilla, J. M., and S. R. Best., "Phase Center Considerations of the Monopole Antenna," IEEE Transactions on Antennas and Propagation., Vol. AP-34, No. 5, May 1986.

7. Tranquilla, J. M., and S. R. Best., "The Quadrifilar Helix as a GPS receiver Antenna," Symposium on Antenna Technology and Applied Electromagnetics., University of Manitoba, Winnipeg, Manitoba, August 1986.

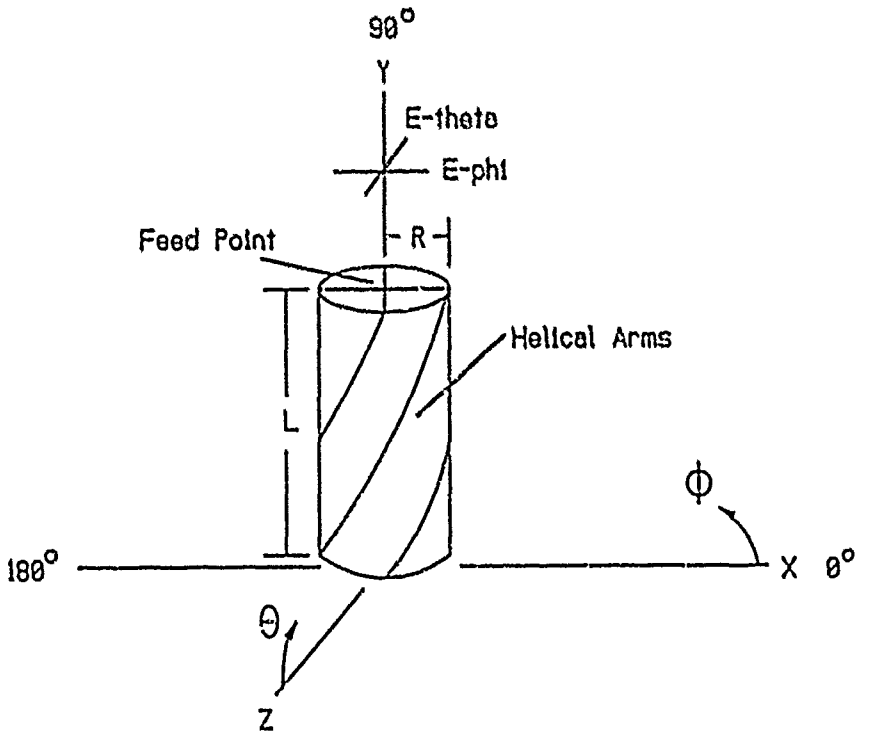


Figure 1. Geometry of the Quadrifilar Helix Antenna.

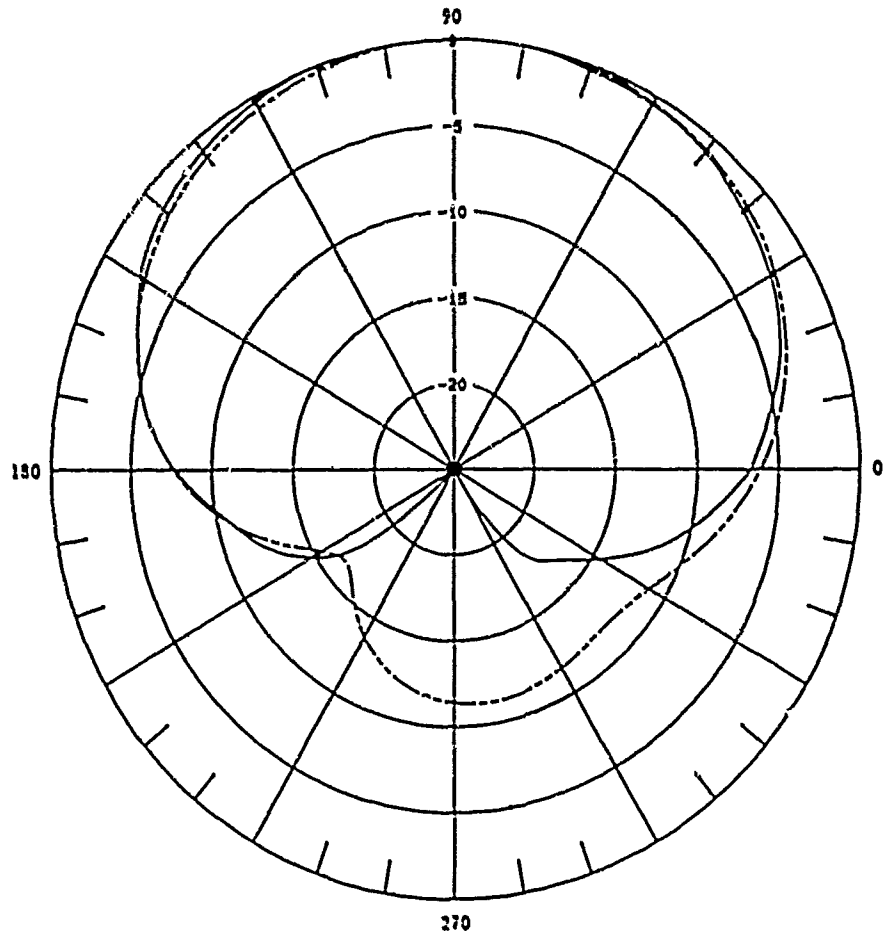


Figure 2a. Comparison of measured (———) and computed (— — —) results using Richmond's code for the 1/2-turn quadrifilar helix at L2. Bottom radials are short-circuited in the computed model.

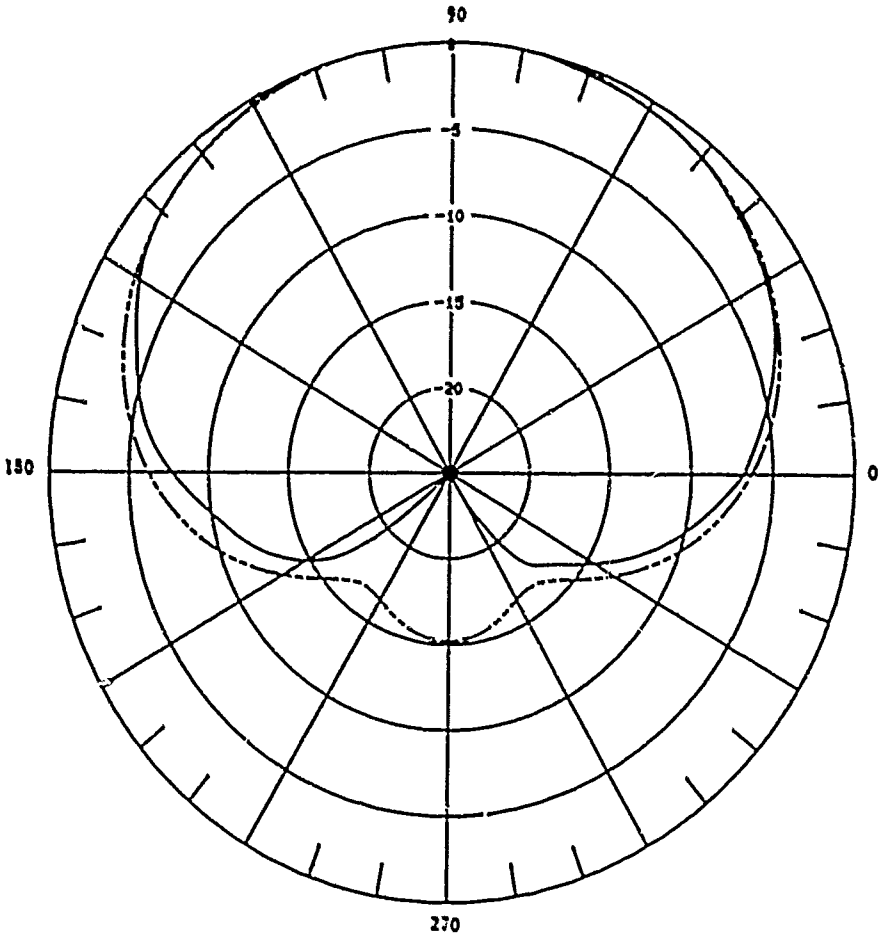


Figure 2b. Comparison of measured (———) and computed (— — —) results using NEC for the 1/2-turn quadrifilar helix at L2. Bottom radials are short-circuited in the computer model.

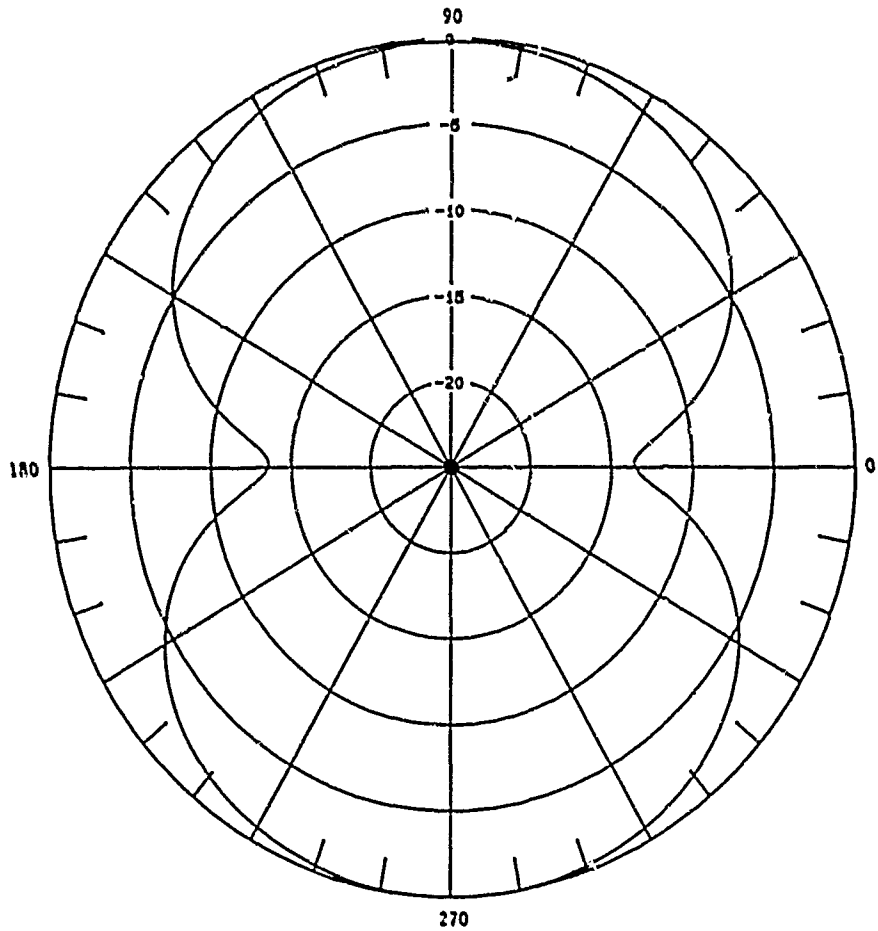


Figure 3. Computed radiation pattern for the bifilar helix at L2 using Richmond's code.

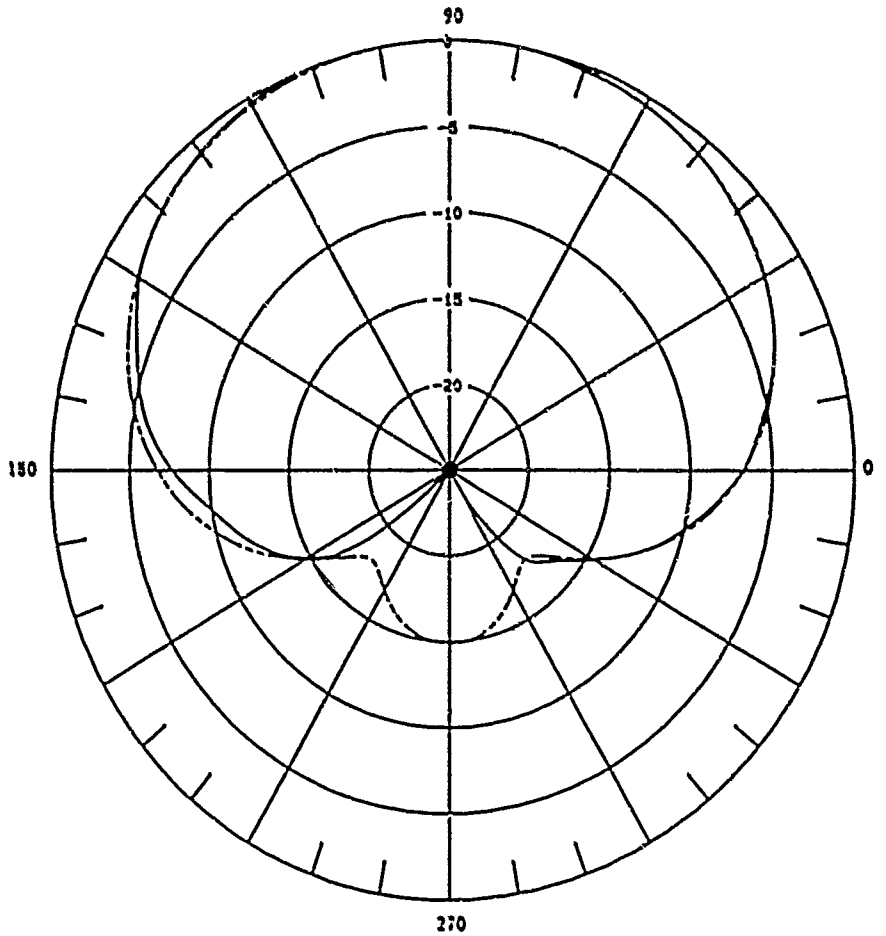


Figure 4a. Comparison of measured (———) and computed (— — —) results using Richmond's code for the 1/2-turn quadrifilar helix at L2. Bottom radials are not short-circuited in the computer model.

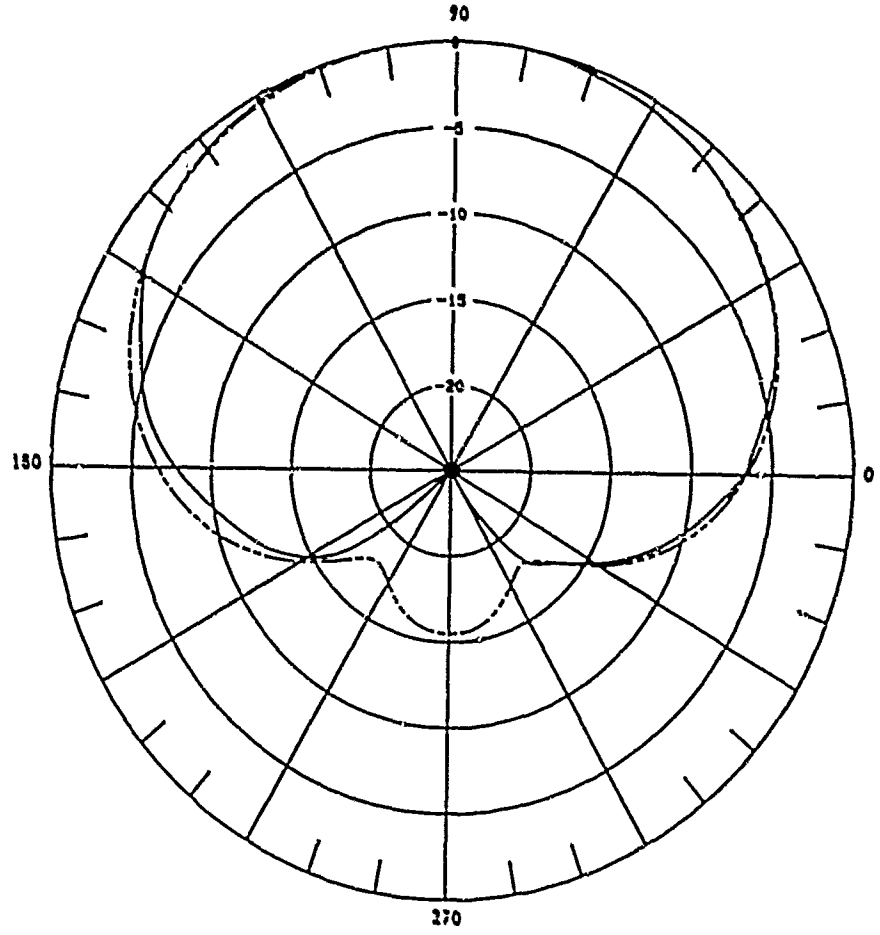


Figure 4b. Comparison of measured (———) and computed (— — —) results using NEC for the 1/2-turn quadrifilar helix at L2. Bottom radials are not short-circuited in the computer model.

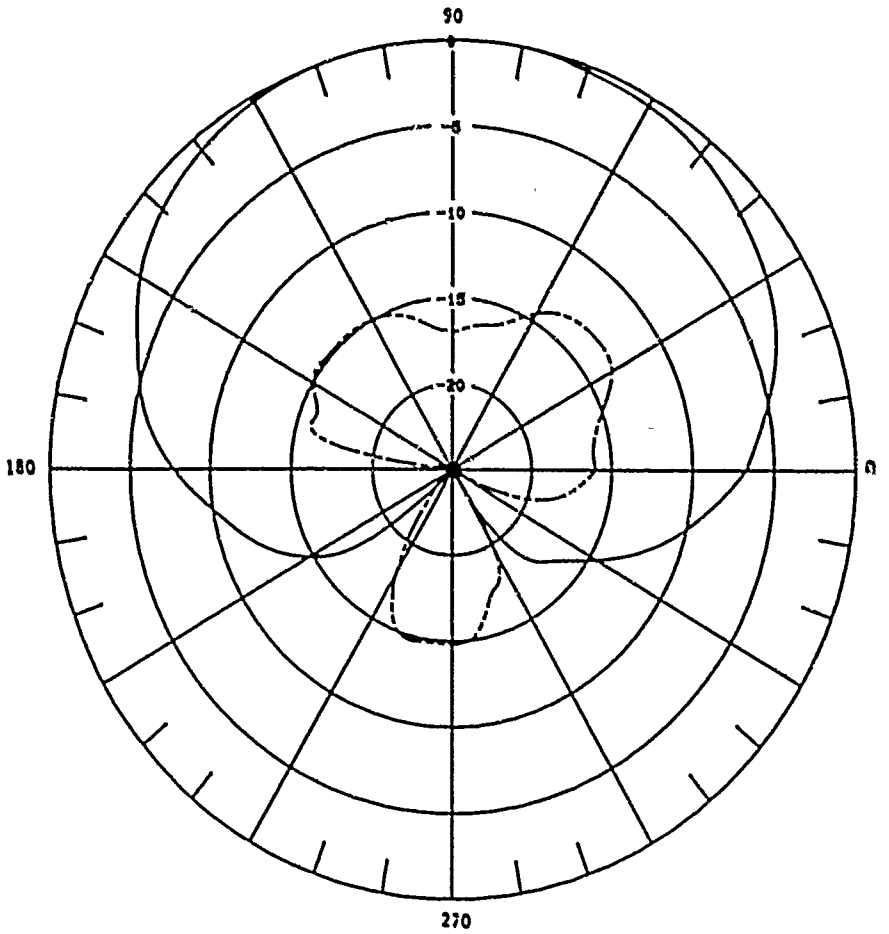


Figure 5. Measured RHCP (———) and LHCP (— — —) patterns for the 1/2-turn quadrifilar helix at L2.

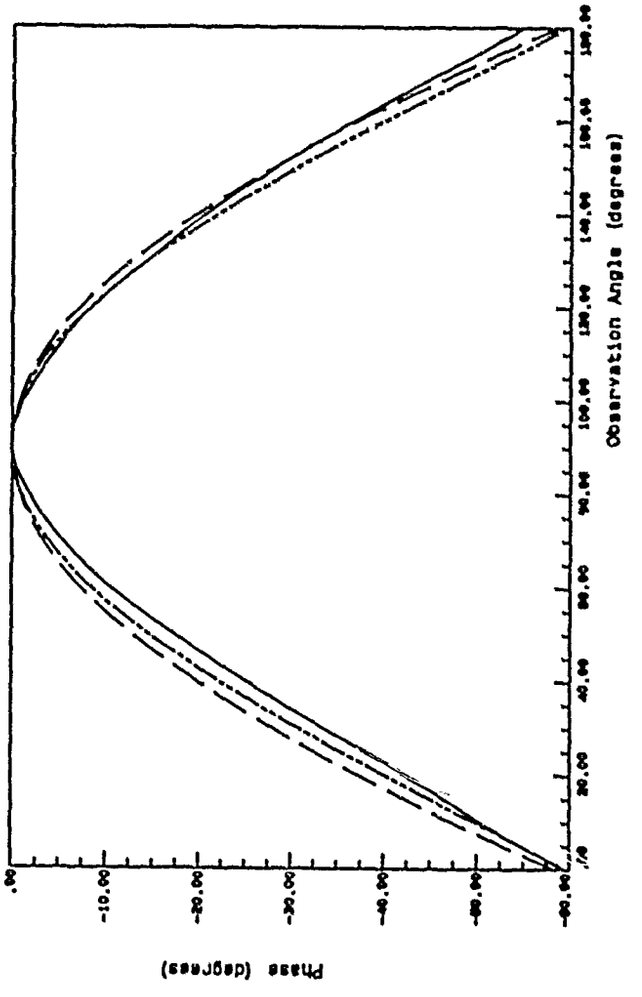


Figure 6a. Comparison of measured (———) and computed phase (E θ polarization) for both NEC (— —) and Richmond's code (— — —) for the 1/2-turn quadrifilar helix at L2.

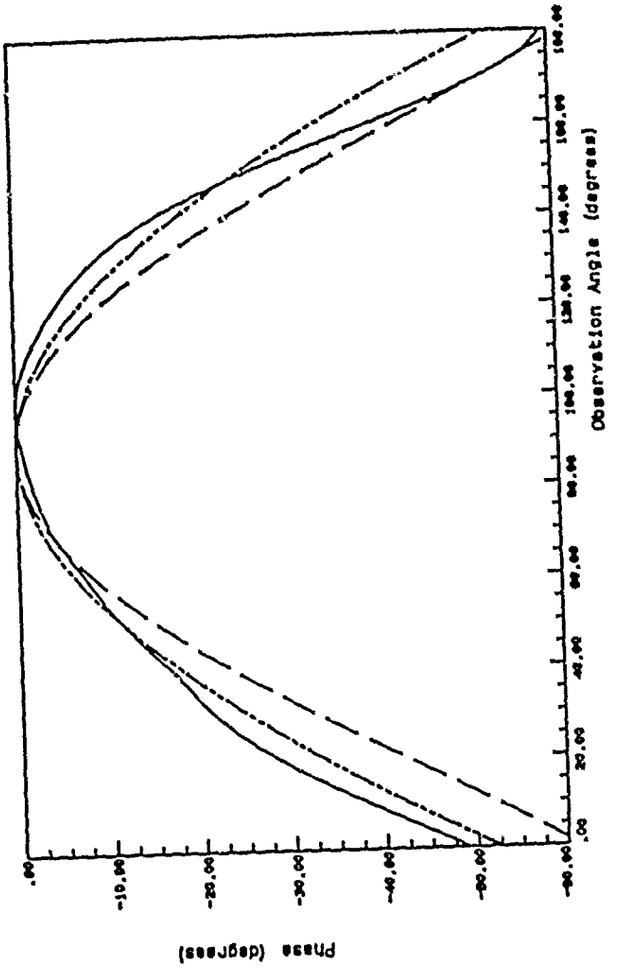


Figure 6b. Comparison of measured (———) and computed phase (E_ϕ polarization for both NEC (— — —) and Richmond's code (— · —) for the 1/2-turn quadrifilar helix at L2.

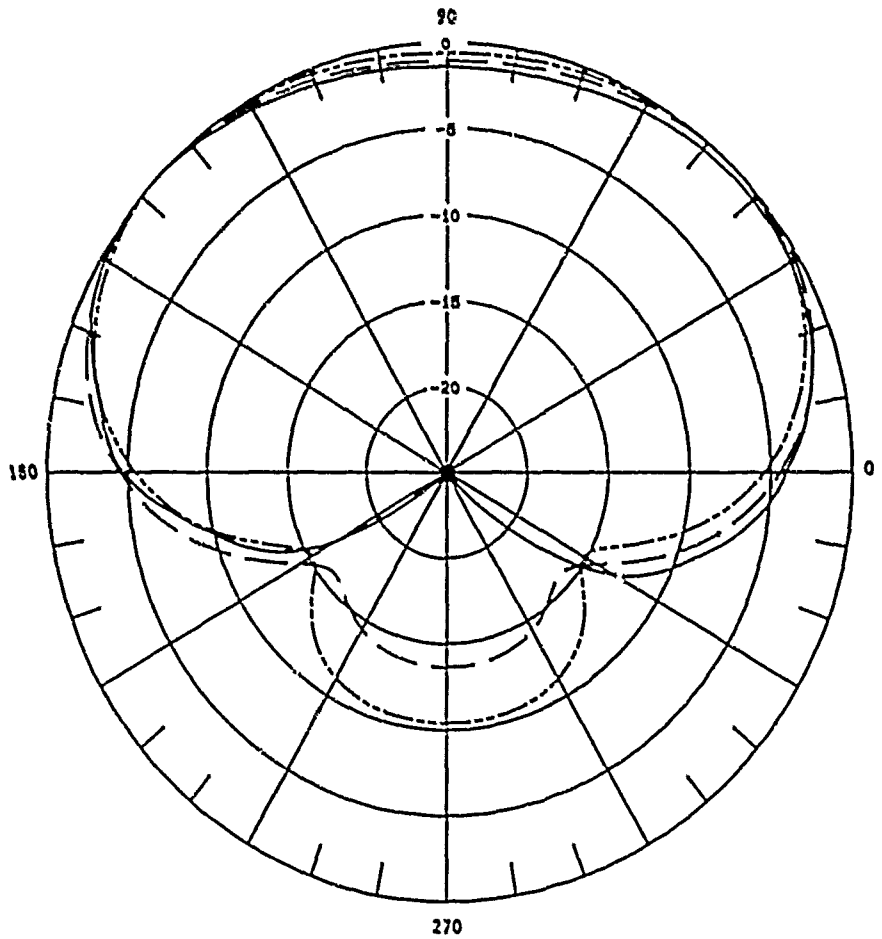


Figure 7. Comparison of measured (———) and computed amplitude patterns for both NEC (— — —) and Richmond's code (— — —) for the 1-turn quadrifilar helix at L2.

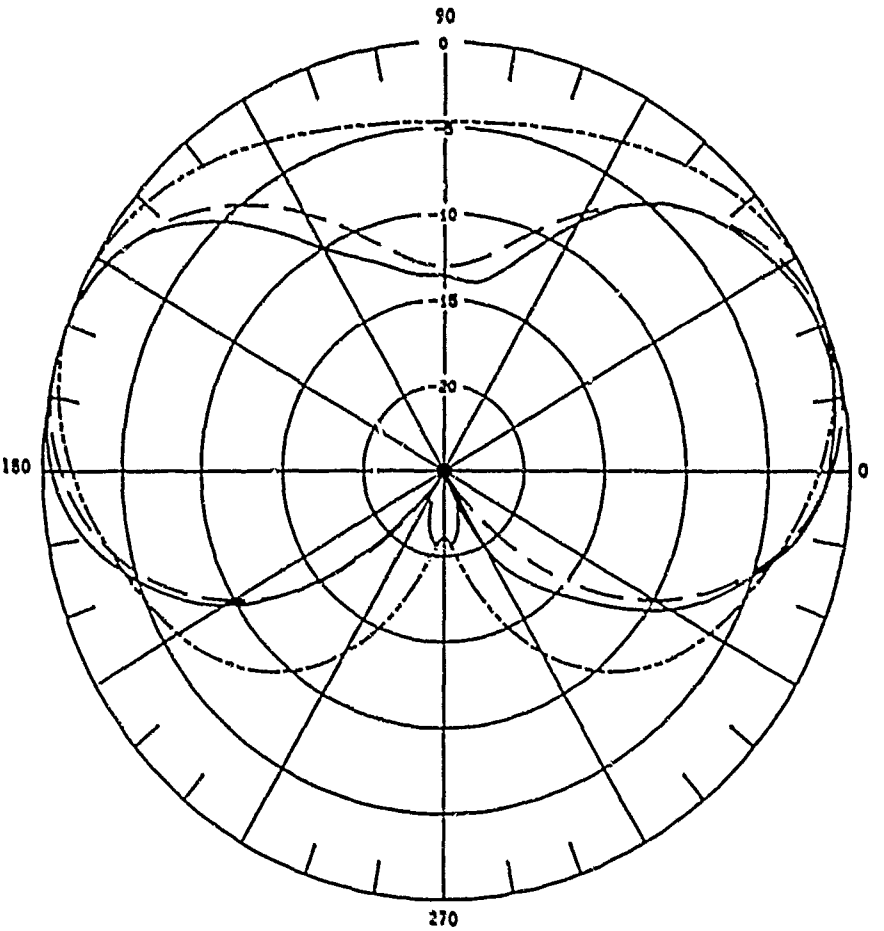


Figure 8. Comparison of measured (———) and computed amplitude patterns for both NEC (— —) and Richmond's code (— — —) for the 1-turn quadrifilar helix at L1.

ANALYSIS OF MICROSTRIP ANTENNAS USING THE TLM METHOD

F.J. German, G.K. Gothard , L.S. Riggs and M.E. Baginski
Department of Electrical Engineering
200 Broun Hall
Auburn University, AL 36849

The transmission line matrix, or modeling, (TLM) method of electromagnetic analysis provides a complete solution to the Maxwell equations in three space dimensions and time by simulating wave propagation on a mesh of orthogonally intersecting transmission lines. The complete electromagnetic field quantities are obtained at each node in the transmission line mesh from the voltages and currents entering the node. The model is conceptually simple and provides a general , efficient, and accurate algorithm for the calculation of electromagnetic fields in a complex three dimensional environment. The technique has found applications in diffusion, lumped network simulation, and lightning simulation. The largest area of application, however, remains in electromagnetic modeling where it has been used to model structures ranging from sub micron scale VLSI interconnects to the EMP analysis of a large satellite receiving complex.

The present study focuses on the analysis of microstrip antenna structures using the TLM technique. By using a pulse excitation in the time domain, one simulation yields data over a broad range of frequencies. The TLM technique models the microstrip antenna structures in three dimensions taking into account losses and inhomogeneities. Furthermore, because the TLM method provides a physical simulation of wave propagation, it is not necessary to deal with any complicated Green's functions. In addition, the algorithm need not be reformulated for each new geometry studied -- only the input data requires modification. This paper will give a brief review of the TLM method including mesh truncation conditions and present the results of the TLM analysis of several representative microstrip structures.

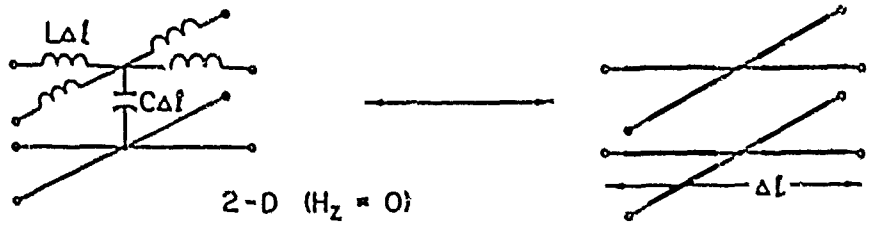
INTRODUCTION:

The transmission line matrix, or modeling, method is a time domain numerical simulation of Maxwell's equations in three dimensions [1] The basis of the technique lies in the circuit analogy to Maxwell's equations formulated by Kron in the mid 1940's [2]. In the TLM method, the equivalent circuit is modeled using a three dimensional mesh of interconnected transmission lines. The circuit/transmission line/field analogies are shown in Figure 1. In three dimensions, we have employed the three dimensional symmetrical condensed TLM node which was introduced recently by Johns [3] and is shown in Figure 2. The transmission line mesh is excited by initializing ideal impulses of voltage or current corresponding to desired field component. Following the initialization, time is stepped and the impulses are tracked as they propagate throughout the mesh. The output is then the impulse response of the transmission line mesh with all six field components available at the center of each node. This impulse response can then be either Fourier transformed to yield frequency domain information or convolved with any arbitrary excitation waveform.

The TLM method is not limited to regular meshes. Graded mesh techniques have been developed [4] which allow a fine mesh to be used in areas which require detailed geometric definition. The grading is achieved by adding or subtracting inductance or capacitance from a given node to model the shape of that node.

In order to model open structures such as antennas, a radiating boundary condition must be employed at the edges of the finite

CIRCUIT EQUIVALENT OF MAXWELL EQUATIONS - KRON (1944)



2-D ($H_z = 0$)

CIRCUIT	MAXWELL
$-\frac{\partial I_x}{\partial x} - \frac{\partial I_y}{\partial y} = C\frac{\partial V_z}{\partial t}$	$\frac{\partial H_y}{\partial x} - \frac{\partial H_x}{\partial y} = \epsilon\frac{\partial E_z}{\partial t}$
$\frac{\partial V_z}{\partial x} = -L\frac{\partial I_x}{\partial t}$	$\frac{\partial E_z}{\partial x} = -\mu\frac{\partial H_y}{\partial t}$
$\frac{\partial V_z}{\partial y} = -L\frac{\partial I_y}{\partial t}$	$\frac{\partial E_z}{\partial y} = -\mu\frac{\partial H_x}{\partial t}$

$E_z \equiv V_z$, $H_y \equiv -I_x$, $H_x \equiv I_y$, $C \equiv \epsilon$, $L \equiv \mu$

Figure 1. Relationship between Maxwell's Equations and Transmission Line Equivalent Circuit.

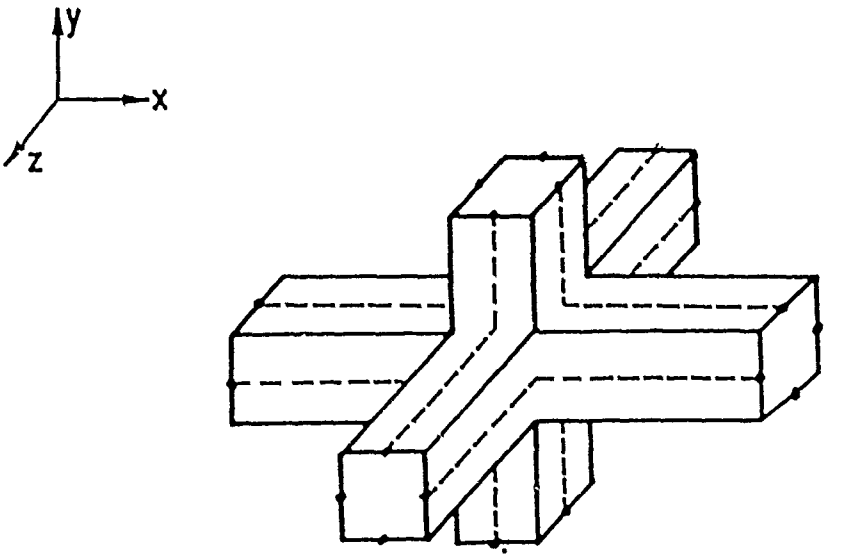


Figure 2. Symmetrical Condensed TLM Node.

computational space in order to prevent non physical reflections from occuring. For a uniformly graded TLM mesh, reflectionless truncation of the problem space is straightforward. For a graded, or anisotropic mesh, however, the mesh truncation is somewhat more involved. However, we have recently developed a very highly absorbing continuation boundary for use under these conditions. It is interesting to note that truncation boundaries require no more computer time or storage to calculate than any other type of boundaries in the TLM method.

In this paper, we present some preliminary results for the analysis of microstrip antennas using the TLM method. Usually, the substrate thickness for typical microstrip antennas is a small compared to the other dimensions of the antenna. For a regularly graded mesh, this presents a prohibitive computational burden since a mesh fine enough to obtain adequate resolution in the substrate would have to be used throughout the remainder of the geometry as well. To circumvent this difficulty, we have employed a three dimensional TLM program with graded mesh capabilities.

MICROSTRIP ANTENNA MODELING

The geometry of a general microstrip patch on a thin substrate is shown in Figure 3. The first configuration investigated was a square patch 3mm on a side with a substrate 2.4 thick with ϵ_r = 9.9.The patch was excited by initializing a voltage between the patch and ground plane at (x,y) = (1.5,0)mm. The output was taken at (x,y) = (1.5,0)mm at a point directly below the patch. The time domain impulse response at the output point was Fourier transformed to yield the frequency response at the output point. The output spectrum for this patch is shown in Figure 4. The peaks in the spectrum correspond to the resonances of the

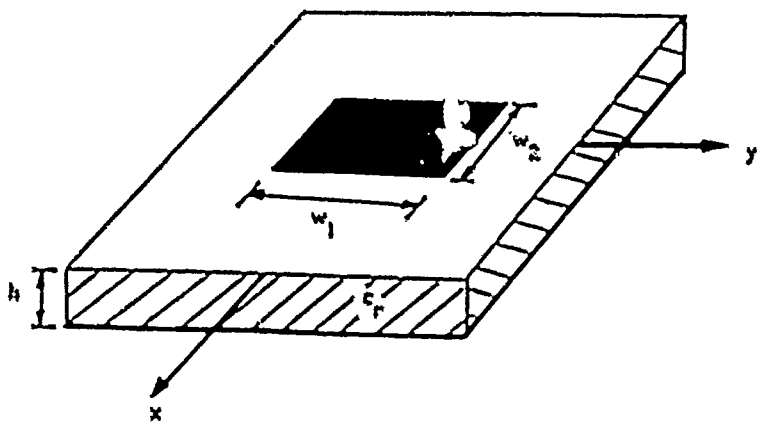


Figure 3. Geometry for Microstrip Patch.

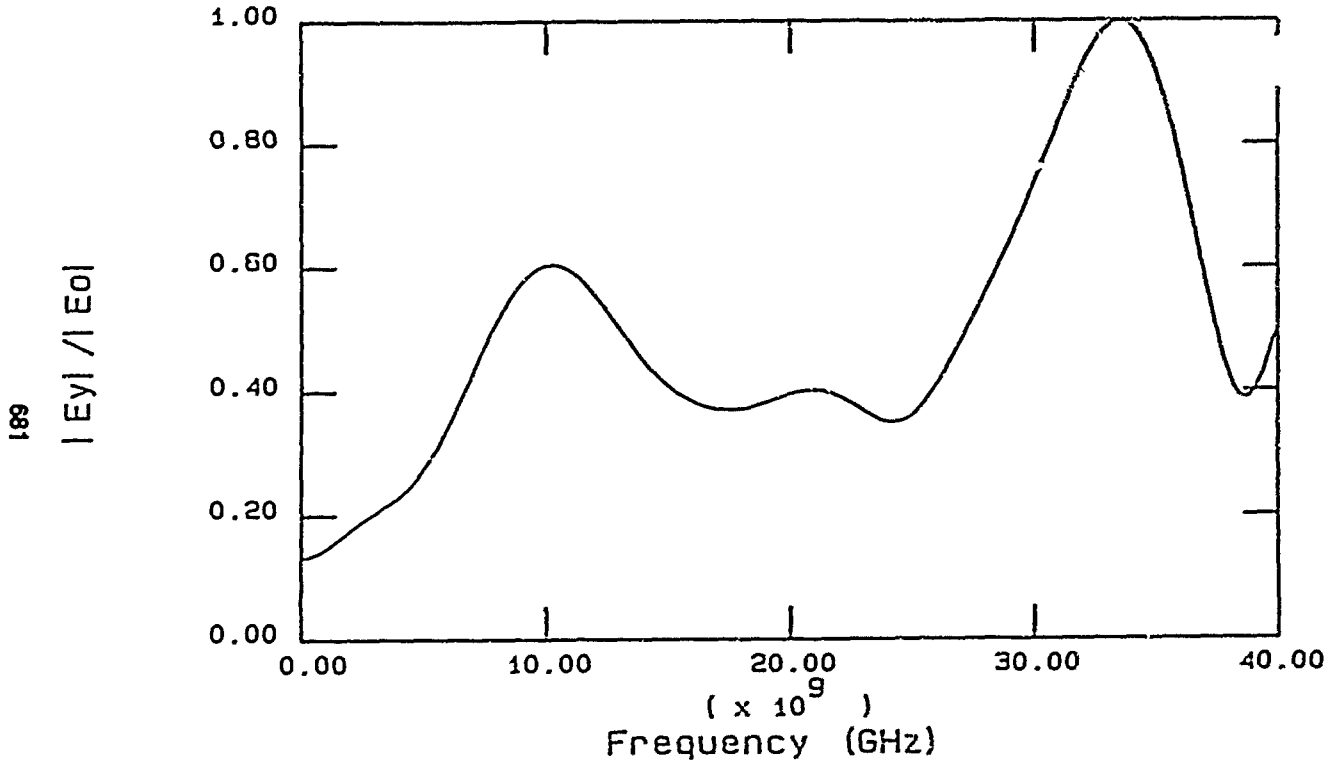


Figure 4. Frequency Spectrum For Square Patch

microstrip patch. To compare the resonant frequencies obtained with the TLM method, we have employed an empirical formula by Napoli and Hughes [5]. This formula is basically a first order correction to the magnetic walled cavity model and is given by:

$$f_r = f_{ro}\, c_r \,/\, [(1+\Delta)\sqrt{c_c(w_1)\, c_c(w_2)}]$$

where

$$\Delta = (h/w)\left[\, 0.692 + 0.164(c_r+1)/c_r^2 + \frac{(c_r+1)}{\pi c}\left(0.758 + \ln(1.88 + w/h)\right)\right]$$

and

$$c_c(w) = \frac{(c_r+1)}{2} + \frac{(c_r-1)}{2}\left[1 + \frac{10h}{w}\right]^{-1/2}$$

The resonant frequency of a magnetic walled cavity, f_{ro} is given by

$$f_{ro} = \frac{1}{\sqrt{\mu c}}\sqrt{(m/w_1)^2 + (n/w_2)^2}$$

Comparison with experimental data has shown that this formula yields resonant frequencies for the first resonant mode within approximately 3%. Comparisons of the TLM calculated resonant frequencies with those obtained form the above empirical formula are summarized in Table I.

TABLE I

Mode (m,n)	TLM (GHz)	Formula (GHz)
(1,0)	10.1	10.08
(3,0)	32.9	30.20

Next we examined a rectangular shaped patch of dimensions 1.3 mm by 0.44mm with a 0.66 mm thick substrate of $c_r = 9.9$. The TLM calculated resonant frequency for the first mode was found to be 28.72 GHZ. This compares very well with the the value of 28.97 GHz calculated from the empirical formula above.

In order to check the algorithm for a rectangular patch on a thin substrate we have calculated the resonant frequencies for a rectangular patch of dimensions 23.4 mm by 18.6 mm on a substrate 1.6 mm thick with $\varepsilon_r = 4.3$. The TLM calculated resonant frequency was 3.1 GHz as compared to 3.0 GHz from the empirical formula. TLM yields a resonance for the second mode of 6.1 GHz as compared to 6.0 GHz from the emprical formula. The frequency spectra is shown in Figure 5. Note that as the substrate thickness becomes thin, there is less fringing at the edges of the patch and the magnetic walled cavity model becomes more accurate as would be expected.

The next structure that we have examined is an electromagnetically coupled printed dipole that has been analyzed in [6]. The geometry for the structure is shown in Figure 6 along with the pertinent dimensions. The dipole was found to resonate at 29.88 GHz as compared to a theoretical resonance of 29.9 GHz. The surface current distributions on the top of the feed line and dipole are shown in Figure 7. These plots display the same characteristics as calculated in [6].

Finally, we have analyzed a microstrip fed rectangular patch. The geometry for this problem is shown in Figure 8. The Fourier transform for the electric field under the patch is shown in Figure 9. The resonant frequencies for the second and fourth modes occur at 48.0 GHz and 94.1 GHz. The theoretical values are 47.6 GHz and 95.2 GHz respectively. The Fourier transform of the voltage between the ground plane and microstrip feed line is shown in Figure 10. We are currently in the process of performing measurements to verify these results.

CONCLUSIONS

In this paper we have presented some preliminary results for the

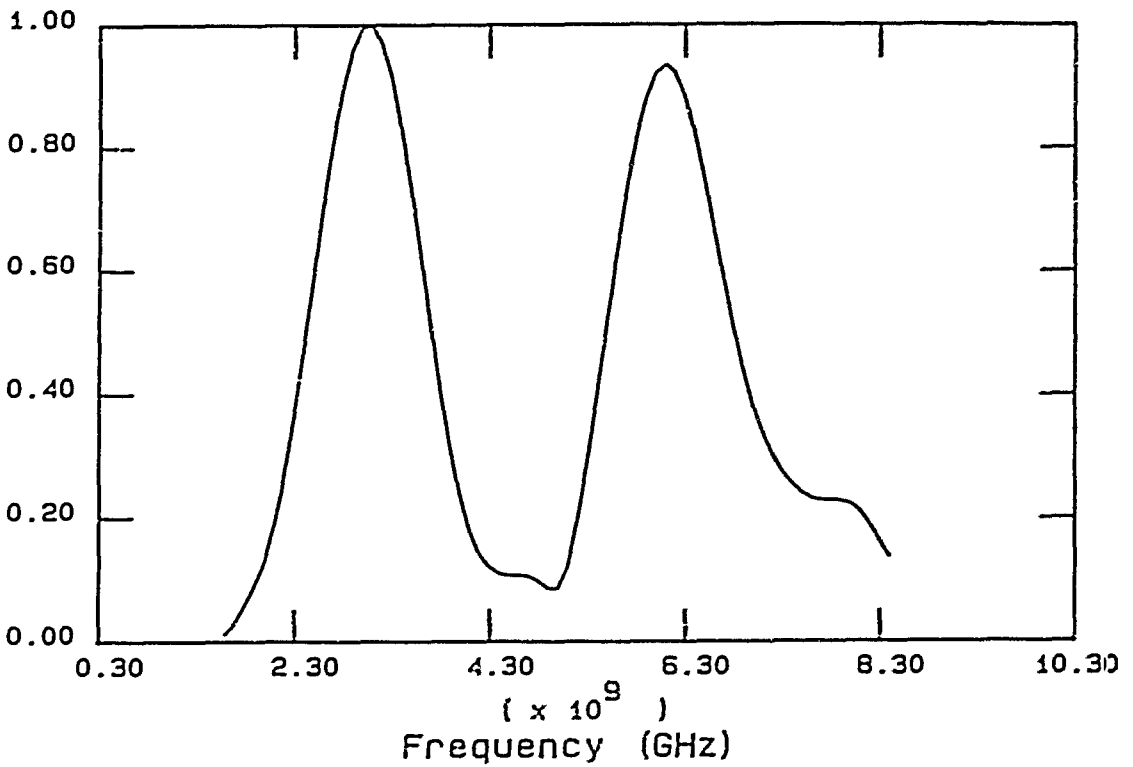


Figure 5. Frequency Spectrum For Rectangular Patch

l_1= 7.5 mm l_2= 3.0 mm

h_1= 0.24 mm

h_2= 0.84 mm

ϵ_r= 2.53

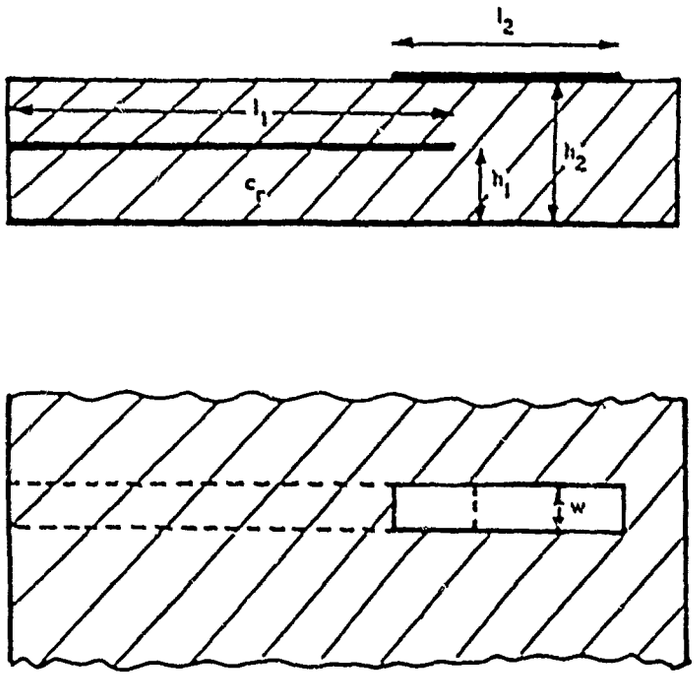


Figure 6. Microstrip Dipole Excited by a Strip Transmission Line .

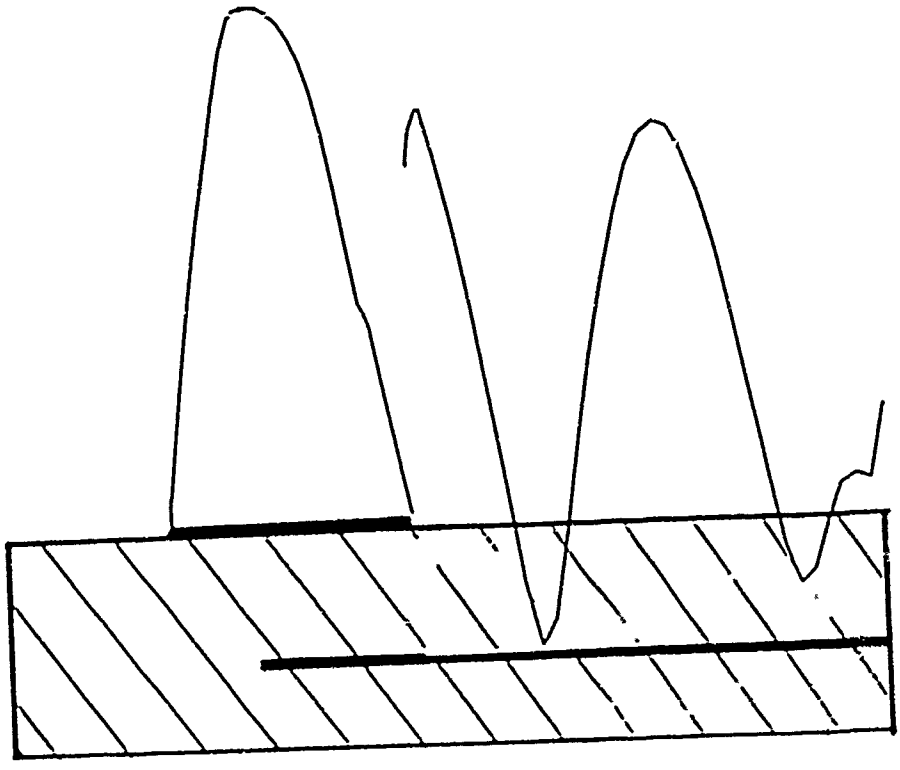


Figure 7. Current Distribution on Dipole and Feed

h = 0.326 mm
w_1 = 0.391 mm
w_2 = 0.7826 mm
l_2 = 3.13 mm
l_1 = 2.00 mm
ϵ_r = 3.8

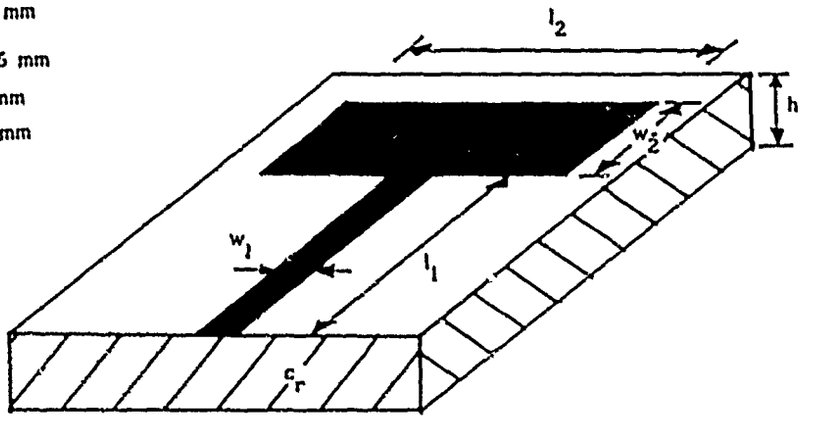


Figure 8. Rectangular Patch Fed by Microstrip Feed Line

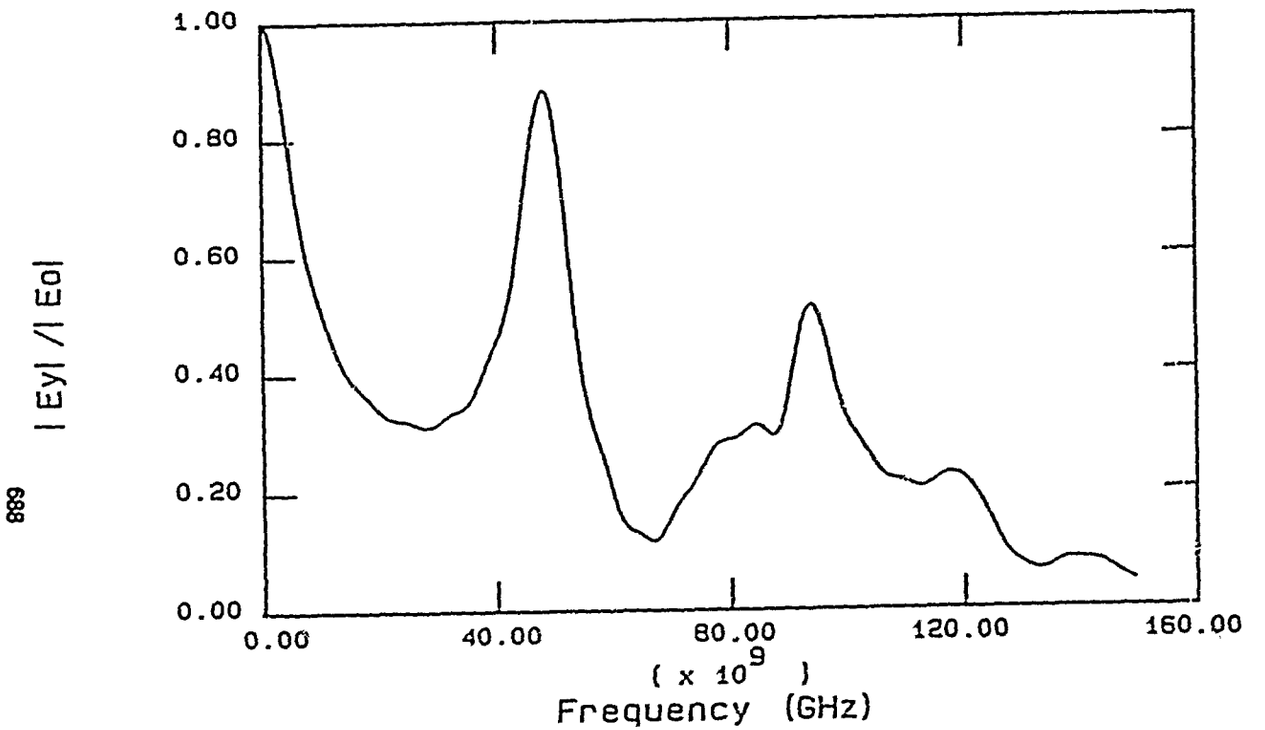


Figure 9. Frequency Spectrum Under Microstrip Fed Patch.

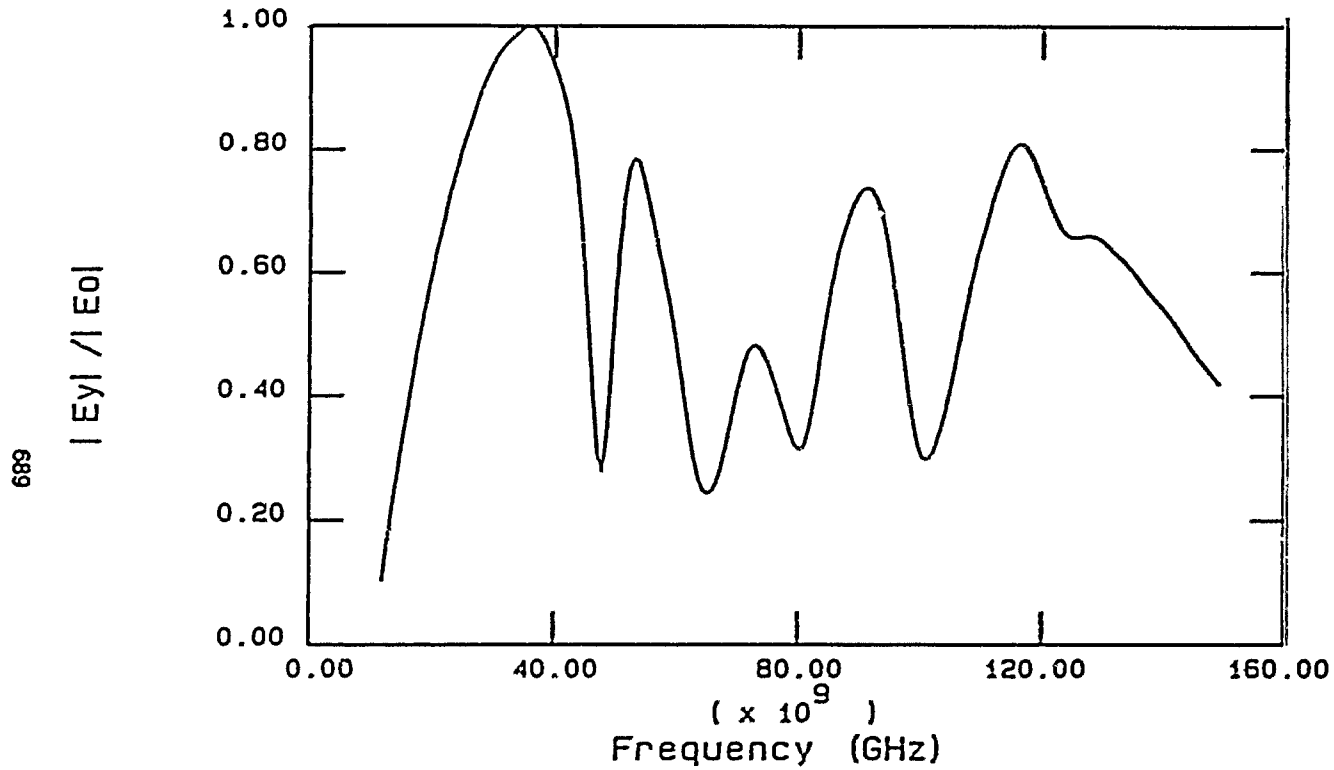


Figure 10. Fourier Transform of Feed Voltage.

analysis of microstrip antenna structures using the TLM method of electromagnetic modeling. While the data presented has been quite elementary, the results that we have obtained have been quite promising. The advantages of the TLM method for the analysis of microstrip antennas lies mainly in the simplicity and generality of the technique. No analytical formulation or computer coding is required form problem to problem as with some other techniques. A single formulation and computer code provides the capability to analyze microstrip antennas of arbitrary geometries. The use of a graded mesh makes the technique computationally feasible.

We are currently investigating further development of the TLM method for the analysis of microstrip antennas. Future work includes the calculation of input impedances and the effects of various feed geometries. Further validation via comparison with analytical techniques and measurements will be required and these comparisons are currently underway. In addition, a technique called diakoptics [7] can be used to analyze thin substrates independant of patch geometry. The results for a particular path are then obtained by connecting the separate patch solution with the pre-calculated substrate solution. Far field quantities are also available from TLM calculated near fields via a near-to-far field transformation.

REFERENCES

[1] P.B. Johns and R.L. Beurle, "Numerical Solution of 2-Dimensional Scattering Problems Using a Transmission Line Matrix," Proc. IEE, vol. 118, no. 9, 1971, 1203-1208.

[2] G. Kron, "Equivalent Circuit of the Field Equations of Maxwell - I," Proceedings IRE, May 1944, 289-299.

[3] P.B. Johns, "A Symmetrical Condensed Node for the TLM Method," IEEE Trans. Microwave Theory Tech., Vol. MTT-35, no. 4, April 1987, 370-382.

[4] D.A. Al-Mukhtar and J.E. Sitch, "Transmission Line Matrix Method with Irregularly Graded Space," Proc. IEE, Pt. H, Vol. 128, no. 6, 1981, 299-305.

[5] L. Napoli and J. Hughes, "Foreshortening of Microstrip Open Circuits on Alumina Substrate," IEEE Trans. Microwave Theory Tech., Vol. MTT-19, 1971, 559-561.

[6] P.B. Katehi and N.G. Alexopoulis, "On the Modeling of Electromagnetically Coupled Microstrip Antennas - The Printed Strip Dipole," IEEE Trans. Ant. Prop., Vol. AP-32, no. 11, 1984, 1179-1186.

[7] P.B. Johns and K. Akhtarzad, "The Use of Time DOmain Diakeptics in Time Discrete Models of Fields," Int. Journal for Numerical Methods in Eng., Vol. 17, 1981, 1-14

NUMERICAL & EXPERIMENTAL RESULTS OF MULTI-WIRE JUNCTION TRICOT KNIT MESH REFLECTORS BY FOURIER MOMENT METHODS*

W. Imbriale, V. Galindo-Israel, Y. Rahmat-Samii
Jet Propulsion Laboratory, California Institute of Technology, Pasadena, CA

ABSTRACT

Wire mesh knit reflecting surfaces are now frequently used on unfurlable type spacecraft reflector antennas (TDRSS, Galileo, etc.). The fineness of the wires and the complexity of the weave has made the problem of an exact numerical diffraction analysis quite formidable. In this paper this mesh is successfully analyzed by treating it as a flat weave of wire strips in a periodic array. The analysis is by moment methods using a piecewise triangular basis function with a Floquet mode analysis of the periodic structure. In particular, it is found that wire bends and junctions can be properly treated only if precise and careful attention is paid to the vector continuity of current through the wire strip bend or junction. It is common in some fine wire mesh grids to avoid soldering the junctions of wires and to depend upon contact pressure in order to obtain good electrical continuity at junction points. Under certain conditions, as has been found experimentally, poor electrical contact at the junction points can result in poor surface reflectivity and considerable transmission loss. Experimental validation of the theory is presented. In addition, a simple model of the tricot mesh which provides an understanding of the cause of the poor reflectivity is presented.

INTRODUCTION

The application of mesh surface provides a deployable capability which is very attractive from launch constraints for spacecraft requiring large antennas, e.g., TDRSS and Galileo spacecraft. These mesh surfaces are typically constructed from gold plated molybdenum wires which are woven in a particular pattern.

A commonly used knit is the tricot knit. The gold plated molybdenum wires of the knit are not welded where they cross at junction points. When a poor electrical contact is made at these junctions, such as when oxidation occurs on the surface, the reflection from the surface is poor and substantial power loss occurs by transmission through the mesh.

The mesh has been modeled as flat strips of wire on a plane surface. Since the tricot weave is essentially periodic, Floquet's theorem has been applied in the analysis of a plane wave incident upon the wire mesh. Currents induced along the wire were modeled as a series of triangular basis

*The research described in this paper was carried out at the Jet Propulsion Laboratory, California Institute of Technology, under contract with the National Aeronautics and Space Administration.

functions – the coefficients to be determined by inversion of the matrix obtained when tangential E is set to zero on the flat strips.

The multi-wire junction points were carefully modeled so that the currents were naturally continuous through the junctions with no additional conditions necessary to guarantee this (other than tangential E set to zero on the flat wire strips). Conditions of a good electrical contact, no contact, or partial contact at the junctions were readily controlled by this model. Finite wire conductivity was included as well.

The numerical results were compared to experimental results for various flat-strip meshes printed on a dielectric sheet. The theory permitted the inclusion of a dielectric sheet, although actual reflector antennas would not include this. Comparisons proved excellent over wide frequency ranges.

It was discovered that the particular character of the tricot knit weave made it susceptible to substantial losses when no electrical contact was made at the wire junctions. Thus, an improved knit is indicated for reflector surfaces so that electrical contact at the junctions is not critical.

THEORETICAL FORMULATION

In the past, the mesh surface problem has been solved using either Astrakhan [1] or Strip-Aperture formulations [2]. Both formulations have provided satisfactory results for cases of perfect contact and simple wire structure configurations. In order to formulate the problem for a complex wire structure as shown in Figure 1 for a tricot knit mesh, a moment method solution has been implemented. The mesh structure is modeled as planar wire strips instead of the actual round wire. Due to the fact that the wire diameter is very small in terms of the wavelength, this strip modelling has proven to be accurate. Additionally, it has been considered that the mesh configuration is periodic.

The methodology of the formulation is depicted in the block diagram shown in Figure 1. First, the complex wire strip structure in a given cell is broken into many linear segments by identifying the "node" points for the initial and the end points of the linear segment. If there is a wire intersect, or contact point, the same node point at the contact is used for all the branches intersecting at this point and making electrical contact there. Each linear segment is then subdivided in order to define the current basis element for the implementation of the method of moments. The method of moments formulation is then constructed utilizing the Floquet Expansion technique in conjunction with the enforcement of the total tangential electric field to be zero on the strip segment. Since the strip width is very narrow in terms of the wavelength, only current components in the wire strip direction are considered.

The theory exactly follows the development and notation given in [3], where the Floquet mode and method of moments theory is described. The major deviation is in the selection of the basis functions. Reference 3 used entire domain functions to represent the wires, whereas this treatment uses piecewise triangular functions. Portions of the development in [3] are repeated here for completeness.

Consider the printed wire array shown in Figure 2. The surface is periodic and is assumed infinite in the xy plane. This allows us to expand the fields in the three regions, i.e., inside the dielectric sheet and in the air on either side, into Floquet modes. The explicit expressions for scattered fields in the three regions may be found in [4] and hence are not repeated here. The incident field, i.e., the field produced by the incident plane wave in the absence of scatterers, is just the field produced by the incident wave in the presence of a dielectric sheet of thickness s. It therefore contains only the zero-order Floquet modes. Scattered fields, on the other hand, are produced by the current distribution $J(x,y)$ on the scatterers. If we denote the transverse components (in the xy plane) of the scattered fields by E_t^{scat}, H_t^{scat}, and those of the incident field by E_t^{inc}, H_t^{inc}, then each Floquet mode in the scattered field must satisfy the following boundary conditions:

1) E_t^{scat}, H_t^{scat} continuous at $z = s$,
2) E_t^{scat} continuous at $z = 0$,
3) H_t^{scat} discontinuity at $z = 0$ equals $J(x,y)$.

These boundary conditions, combined with the orthogonality of the Floquet modes over a single periodic cell, lead to an integral expression for E_t^{scat} at $z = 0$ in terms of $J(x,y)$.

Since the scattered field should cancel the incident field on the surface of the scattering dipoles, we have

$$E_t^{scat}(x,y,0) + E_t^{inc}(x,y,0) = 0, \quad \text{on a dipole} \tag{1}$$

This yields an integral equation for the unknown current distribution and is easily solved by the moment method if $J(x,y)$ is approximated as follows:

$$J(x,y) = \sum_{n=1}^{N} c_n h_n(x,y), \tag{2}$$

where the functions $h_n(x,y)$ are the basis functions and N is finite for computability. Substituting (2) into (1) and integrating over the scattering dipole contained in one periodic cell after multiplying both sides by $h_i^*(x,y)$, where the asterisk denotes the complex conjugate, the following system of equations is obtained [4]:

$$\sum_{m=1}^{2} (1 + R_{m00}^{\text{slab}})\, b_m \hat{\kappa}_{m00} \cdot g_l^*(k_{00})$$

$$= \sum_{n=1}^{N} c_n \frac{1}{d^2} \sum_{m=1}^{2} \sum_{p} {\sum_{q}}' \cdot \frac{\hat{\kappa}_{mpq} \cdot g_l^*(k_{pq}) \hat{\kappa}_{mpq} \cdot g_n(k_{pq})}{\eta_{mpq}^{eq}}, \quad l = 1, 2, \cdots, N, \tag{3}$$

where a time-dependence $\exp(j\omega t)$ is assumed, $m = 1$ corresponds to the TM mode and $m = 2$ to the TE mode, and

$$g_l(k_{pq}) = \int_{\text{dipole}} h_l(x,y) \exp(jk_{pq} \cdot \rho)\, dx\, dy,$$

d = array spacing,

$\rho = x\hat{x} + y\hat{y}$,

$$k_{pq} = \left(k_0 \sin\theta \cos\phi + \frac{\sqrt{2}\pi p}{d}\right)\hat{x} + \left(k_0 \sin\theta \sin\phi + \frac{\sqrt{2}\pi p}{d} + \frac{2\sqrt{2}\pi q}{d}\right)\hat{y}$$

$k_0 = 2\pi/\lambda_0$,

λ_0 = free-space wavelength,

(θ,ϕ) = direction of incidence,

b_m = incident field magnitude of mth mode,

$\hat{\kappa}_{1pq} = k_{pq}/|k_{pq}|$,

$\hat{\kappa}_{2pq} = \hat{z} \times \hat{\kappa}_{1pq}$,

$$\eta_{mpq}^{eq} = \eta_{mpq}^{\text{air}} + \eta_{mpq}^{\text{diel}} \left(\frac{1 - R_{mpq}}{1 + R_{mpq}}\right),$$

$$\eta_{1pq} = \frac{k\eta}{\gamma_{pq}},$$

$$\eta_{2pq} = \frac{\gamma_{pq}\eta}{k},$$

$$\eta = \sqrt{\alpha/\mu},$$

α, μ = the permittivity and permeability of medium,

k = propagation constant of the medium.

$$\gamma_{pq} = (k^2 - |k_{pq}|^2)^{1/2}, \quad k^2 > |k_{pq}|^2,$$

$$= -j(|k_{pq}|^2 - k^2)^{1/2}, \quad k^2 < |k_{pq}|^2,$$

$$R_{mpq} = \frac{\eta_{mpq}^{diel} - \eta_{mpq}^{air}}{\eta_{mpq}^{diel} + \eta_{mpq}^{air}} \exp(-j2\gamma_{pq}s),$$

$$R_{mpq}^{slab} = \frac{2\eta_{mpq}^{air} - \eta_{mpq}^{eq}}{\eta_{mpq}^{eq}}.$$

Once we select a suitable set of functions h_n, the unknown coefficients c_n can be easily obtained by solving (3).

Expressions for the reflected and transmitted fields can be found in [3] and are not repeated.

The wire will be modeled as being comprised of straight segments of wire. At the junction of two straight segments, special treatment is required. A discussion of this special treatment of the junction between straight segments is reserved until later. If there is no bend between straight 'segments' then no special treatment is required.

The currents are modeled as having a piecewise triangular variation in the longitudal direction and a constant in the transverse direction. The geometry is shown in Figure 3. In particular the currents on the nth segment are

$$h_n(x',y') = \hat{x}' \frac{(x' - \ell)}{w\ell} \qquad -\ell \le x' \le 0$$

$$-\frac{w}{2} \le y' \le \frac{w}{2}$$

$$h_n(x',y') = \hat{x}' \frac{(\ell - x')}{w\ell} \qquad 0 \le x' \le \ell$$

$$-\frac{w}{2} \le y' \le \frac{w}{2}$$

letting

$$x = x_n + x' \cos\psi - y' \sin\psi$$

$$y = y_n + x' \sin\psi + y' \cos\psi$$

we need to evaluate

$$g_{npq} = \int_{\text{dipole}} h_n(x,y)\, e^{jkpq \cdot \rho}\, dxdy = g^{-}_{npq} + g^{+}_{npq}$$

where

$$g^{-}_{npq} = \hat{x}'\, e^{jC} \left[\left(\frac{1}{Z^2} - \frac{j\ell}{Z} \right) e^{j\ell Z} - \frac{1}{Z^2} \right] \frac{\sin \frac{Vw}{2}}{\frac{Vw}{2}}$$

$$g^{+}_{npq} = \hat{x}'\, e^{jC} \left[\left(\frac{1}{Z^2} + \frac{j\ell}{Z} \right) e^{j\ell Z} + \frac{1}{Z^2} \right] \frac{\sin \frac{Vw}{2}}{\frac{Vw}{2}}$$

with

$$Z = k_x \cos\psi + k_y \sin\psi$$

$$V = -k_x \sin\psi + k_y \cos\psi$$

$$C = k_x x_n + k_y y_n$$

Bends and Junctions

Previous investigators have failed to be accurate in their treatment of bends and junctions. When the wires are orthogonal and wire contact is not significant, the treatment is not critical. In the present problem the treatment is critical and it is felt that a considerable breakthrough has been made in both the understanding of the problem and the treatment.

At the bend it is necessary to have both continuity of the magnitude of the current as well as its direction. The current representation of the bend is shown in Figure 4. For the bend we have

$$h_n = \frac{\bar{\psi}}{w} = \frac{-\hat{x}\sin\psi + \hat{y}\cos\psi}{w}$$

Again we need to evaluate g_{npq} for this segment, and the result is

$$g_{npq} = jC \int_{\psi_{n-1}}^{\psi_n} \frac{\bar{\psi}}{w} I_\rho \, d\psi$$

where the integration is carried out numerically and

$$I_\rho = \frac{e^{jZw} - jZwe^{jZw} - 1}{Z^2}$$

where Z is as described above.

At the junctions of more than one wire a superposition of all the possible bend currents is required.

EXPERIMENTAL VALIDATION

A considerable amount of numerical simulations have been performed to properly assess the convergent behavior of the resultant matrix equation. Results are shown for the contact and no-contact cases, and the numerical results are compared versus measured data.

A set of experiments were performed to provide a basis for comparing experimental results and theoretical predictions. The experimental setup consisted of measuring the transmission loss through a set of flat panels.. The flat panels were constructed by printing copper wires on a dielectric sheet (dielectric constant = 4.7) 70 mils thick. The wire patterns were selected to test the various aspects of the code, i.e., curved wires, contact and no-contact junctions, wire thickness, incident angle, etc. The simplest case was that of a straight wire grid. Figure 5 shows the normal incident (0 = 0.0) transmission loss for both incident polarizations on test sample 1 (TS-1). The data was taken over a 2 to 15-GHz frequency range and, as would be expected, the surface is virtually transparent to the polarization normal to the wire. Loss at the higher frequencies is due to the dielectric constant of the sheet. The circles are the theoretical predictions and agree very well with the experimental data. Figures 6 and 7 show the results for a 30 deg incident angle, one rotating in the phi = 0.0 deg plane and the other in the phi = 90 deg plane. Both amplitude and phase plots are shown. There appears to be a slight drift as a function of frequency in the experimental data in Figure 7 since the test results show gain at the lower frequencies.

The results for curved wires is shown in Figure 8. Observe that the curved wires (TS-2) have less reflectivity (lower transmission loss) than the straight wires. Also note that for TS-5 (contacting wires) the reflectivity is much greater than TS-1 or TS-2.

Figure 9 plots the transmission loss for the case of "perfect" and "broken" connections.

Note that for TS-3 the result, as would be expected, is the same as TS-1, and the most interesting result is from TS-4 (broken connection). Notice that although the wire pattern looks very similar to TS-3, there is no connection at the center and the reflectivity results are dramatically different. This result provides some understanding as to why the mesh can be leaky as well as providing a solid verification of the computer code.

Consider the actual trace of the mesh wire shown in Figure 10. Two independent strands of wire in the mesh were highlighted so that these two wires may be easily traced visually. Wire #1 is the heavily shaded line, and wire #2 is the dashed line. The entire mesh is made up of alternate strands of such wires. The connection between wire #1 and wire #2 inside of any periodic cell is what holds the mesh together physically. This connection also serves a significant electrical purpose as will be described shortly. Observe that the overall wire alignment is similar to the broken wire case of Figure 9.

This complex mesh example was analyzed for both the case of electrical contact and no electrical contact at the crossover points of the wires. The results are very similar to the cases in Figure 9, i.e., when there was electrical contact at the junctions the reflectivity was good (<0.5 dB for 5 mil wire at 8.0 GHz for example) and for the case of no electrical contact the reflectivity loss was large (>6 dB for the same parameters). Thus for good reflectivity, electrical contact is required at the junctions. A future paper will address the cases for non-perfect (impedance) junctions.

REFERENCES

[1] M. I. Astarkan, "Reflection and Screening Properties of Plane Wire Grids," *Radio Eng.* (Moscow), Vol. 23, pp. 76–83, 1968.

[2] Y. Rahmat-Samii and S. W. Lee, "Vector Diffraction Analysis of Reflector Antennas with Mesh Surfaces," *IEEE Trans. on Antennas Propagat.*, Vol. AP-33, pp. 76–90, Jan. 1985.

[3] V. D. Agrawal and W. A. Imbriale, "Design of a Dichroic Cassegrain Subreflection," *IEEE Trans on Antennas Propagat.*, Vol. AP-27, pp. 466–473, July 1979.

[4] J. P. Montgomery, "Scattering by an Infinite Periodic Array of Thin Conductors on a Dielectric Sheet," *IEEE Trans. Antennas Propagat.*, Vol. AP-23, pp. 70–75, Jan. 1975.

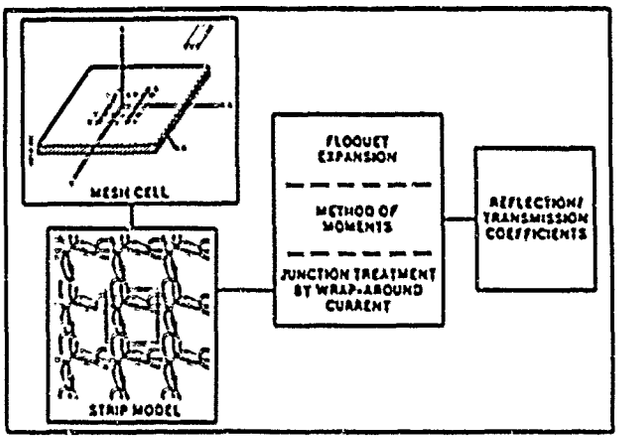


Figure 1. Computational Steps for Complex Mesh Structure

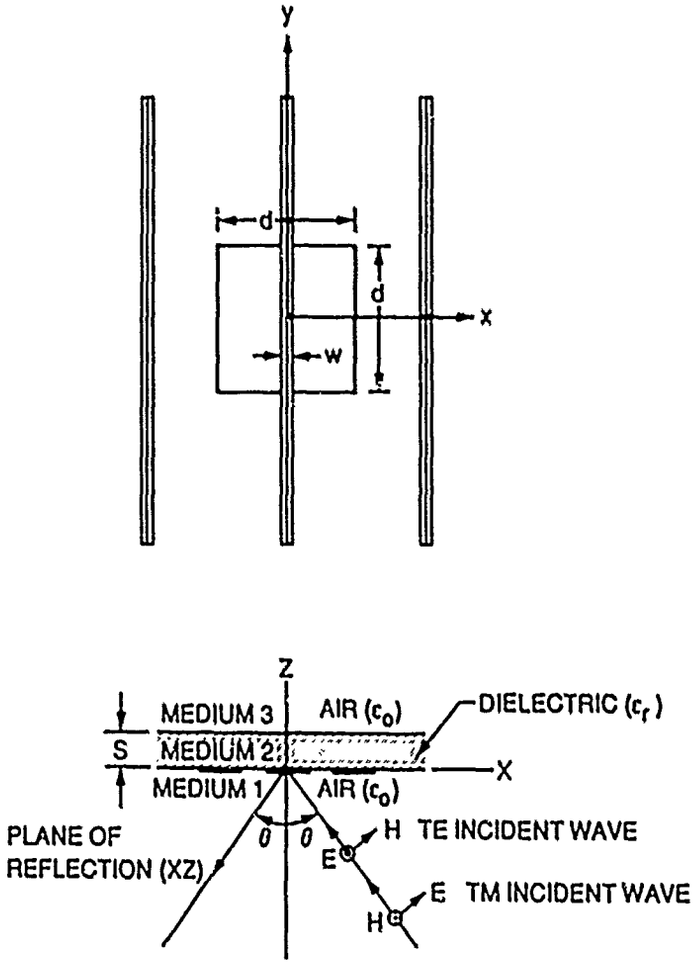
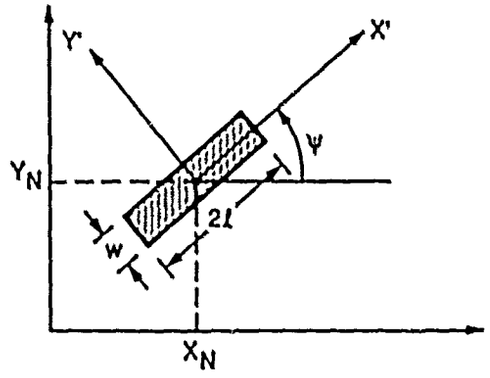
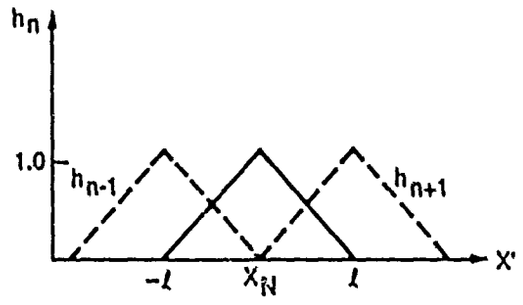


Figure 2. Geometry of Wire Surface



(a) GEOMETRY OF n^{th} SEGMENT



(b)

Figure 3. Basis Function Geometry

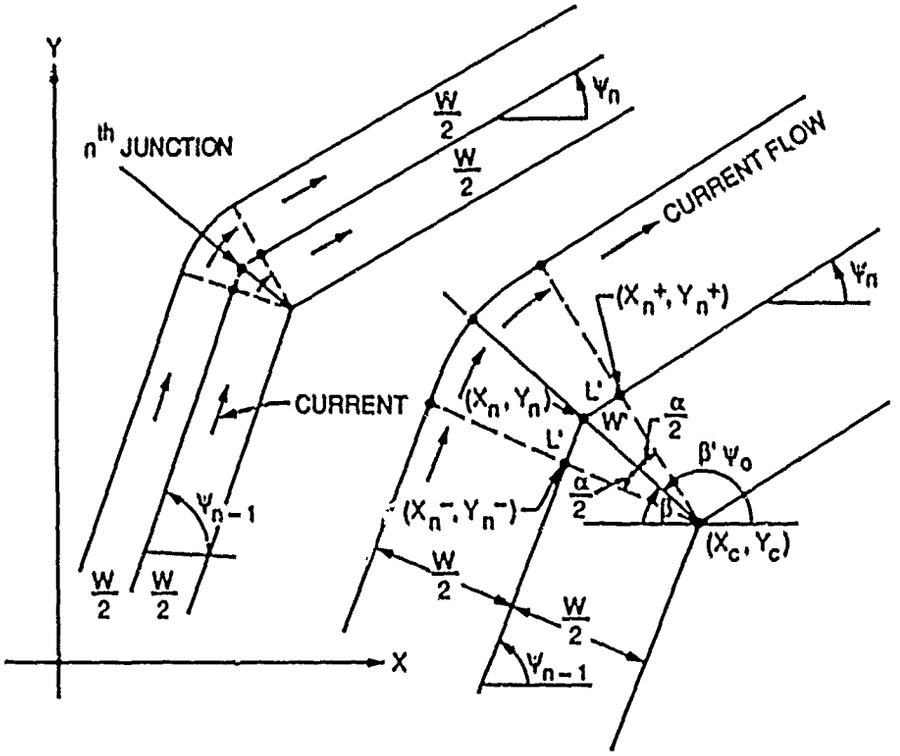


Figure 4. Wire Bend Geometry

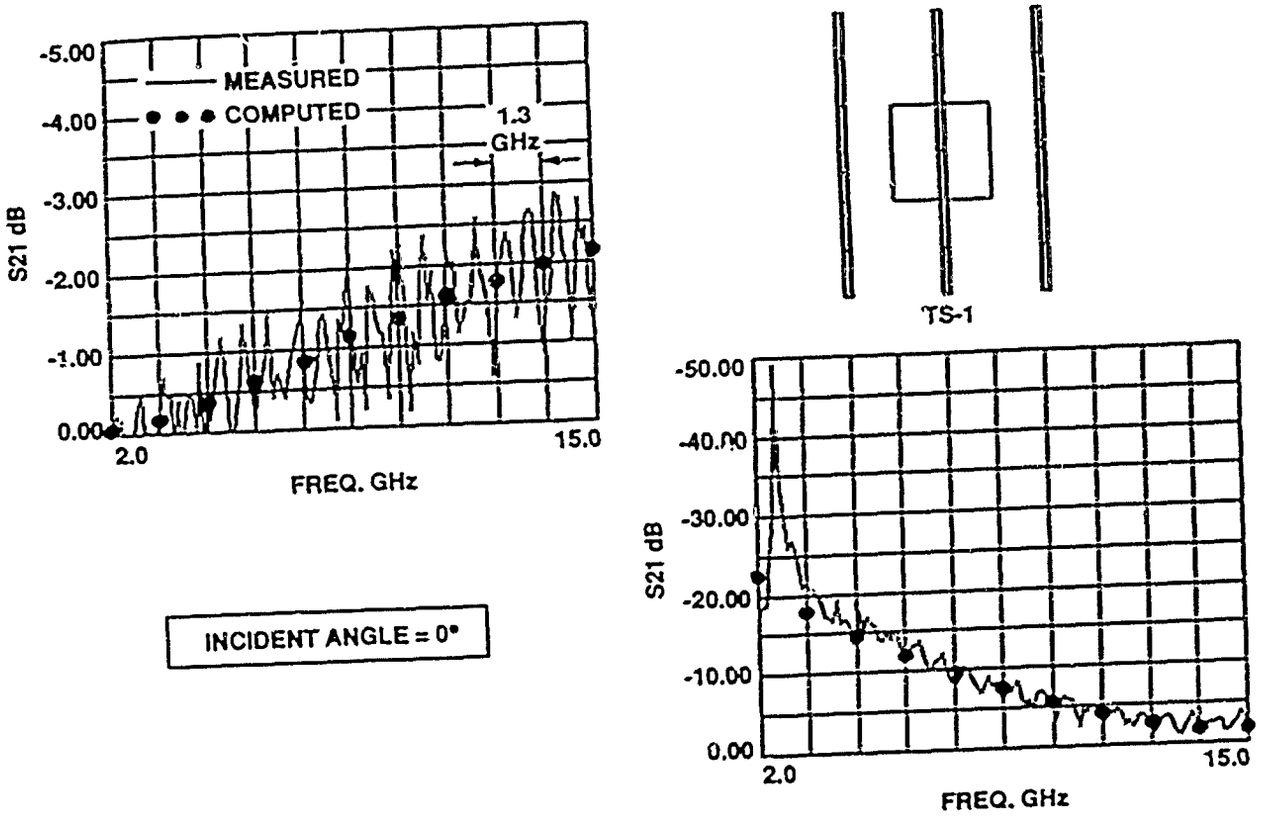


Figure 5. Transmission Loss Straight Wire Grid Normal Incidence

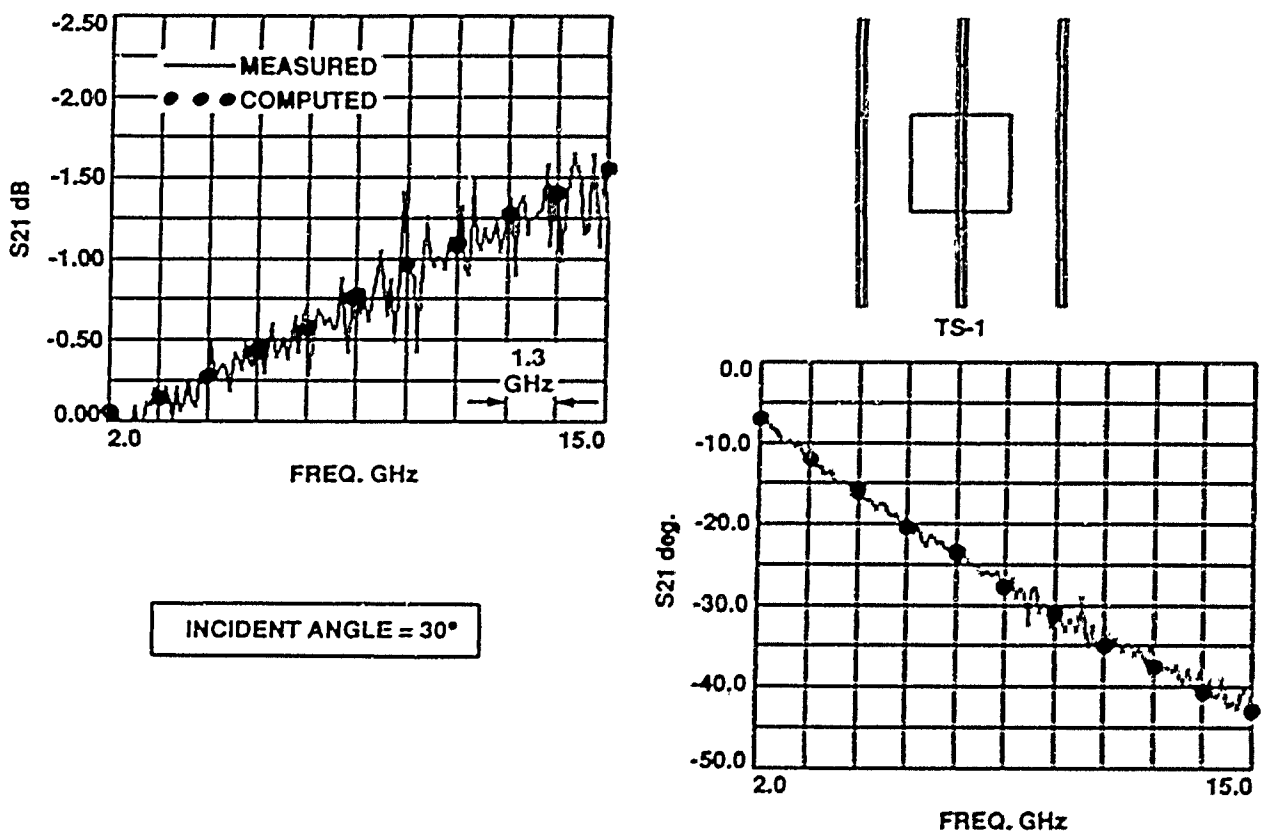


Figure 6. Transmission Loss for TS-1 with TE incident wave, E parallel to Wire and $\theta = 30°$

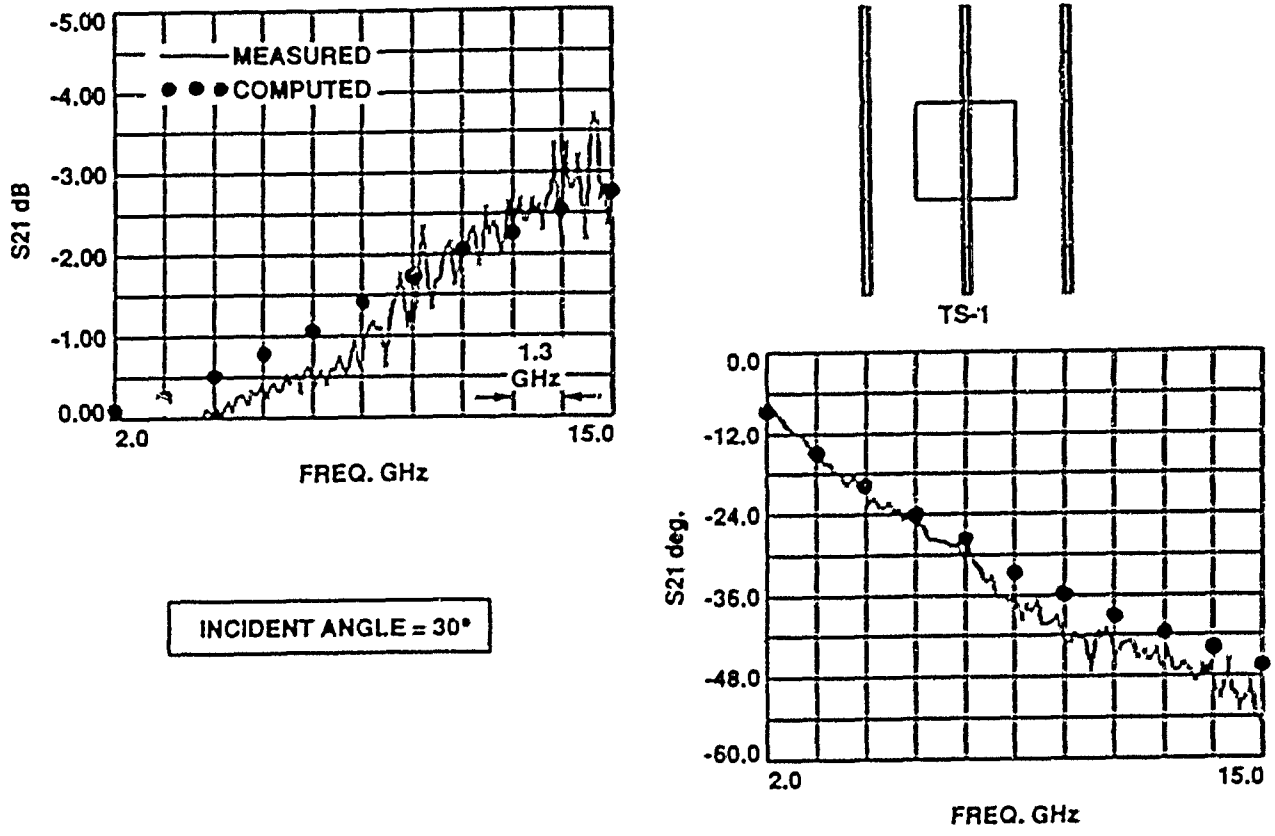


Figure 7. Transmission Loss for TS-1 with TM Incident Wave, E Parallel to Wire and θ = 30°

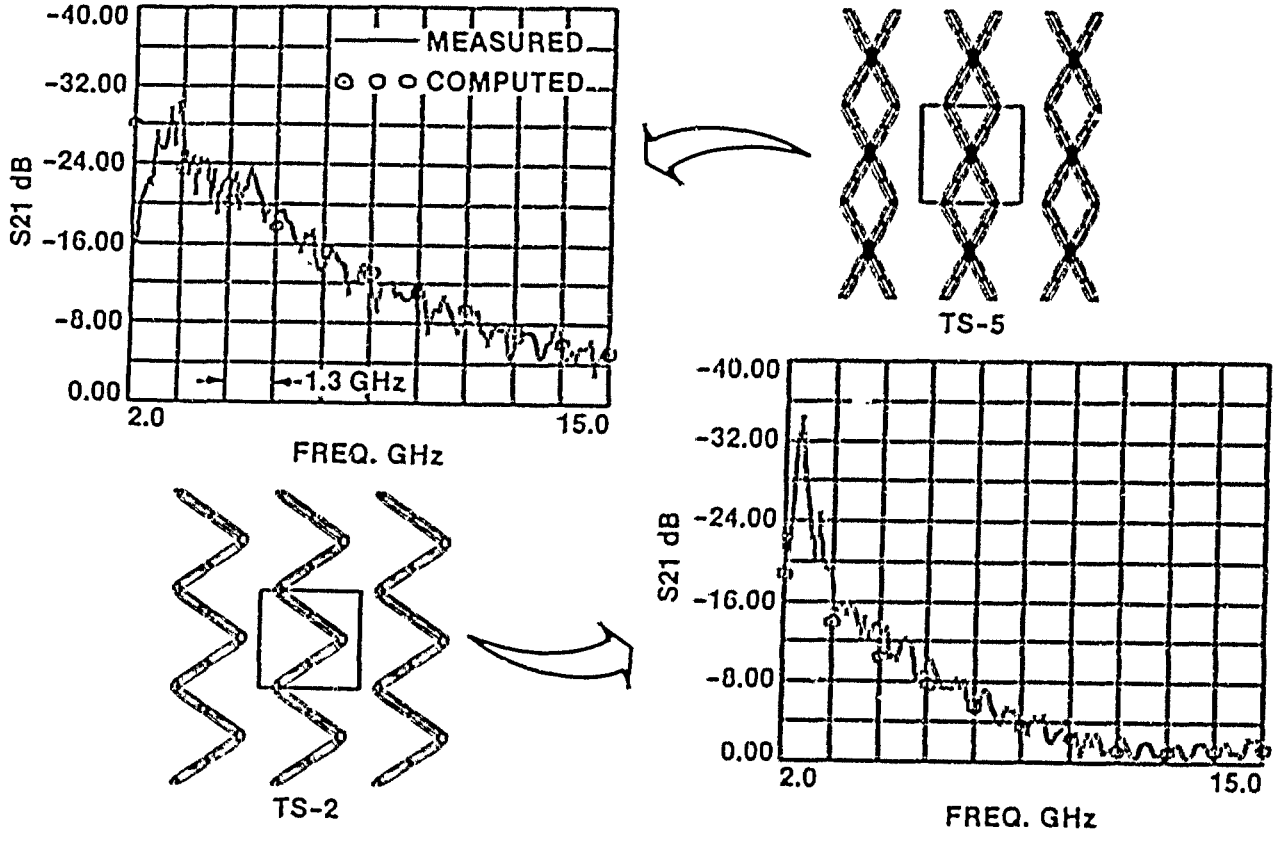


Figure 8. Computed and Measured Results for Wire Bend Cases – Normal Incidence

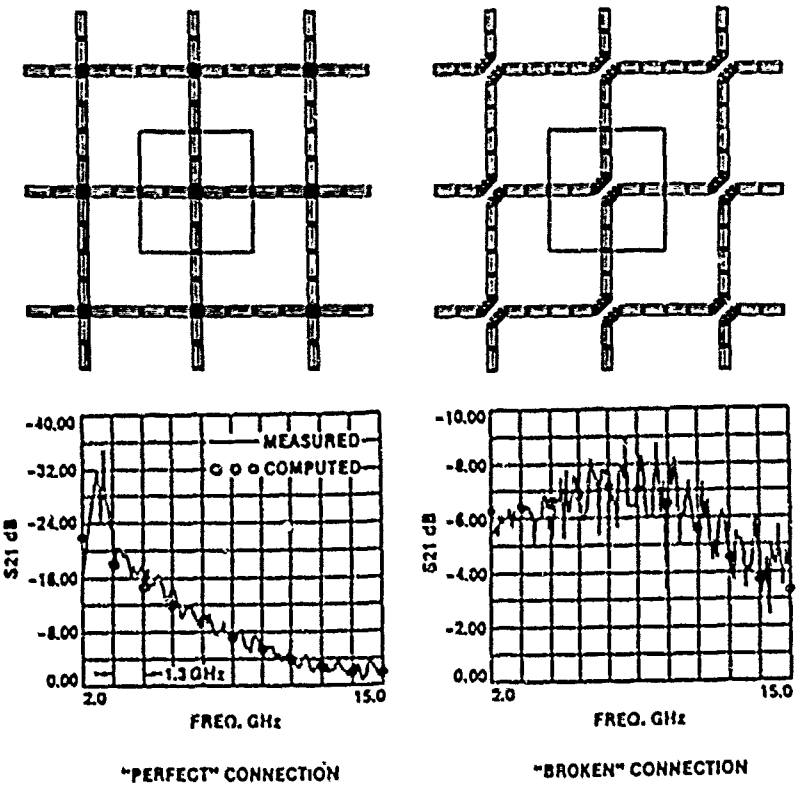


Figure 9. Transmission Loss for "Perfect" and "Broken" Connections

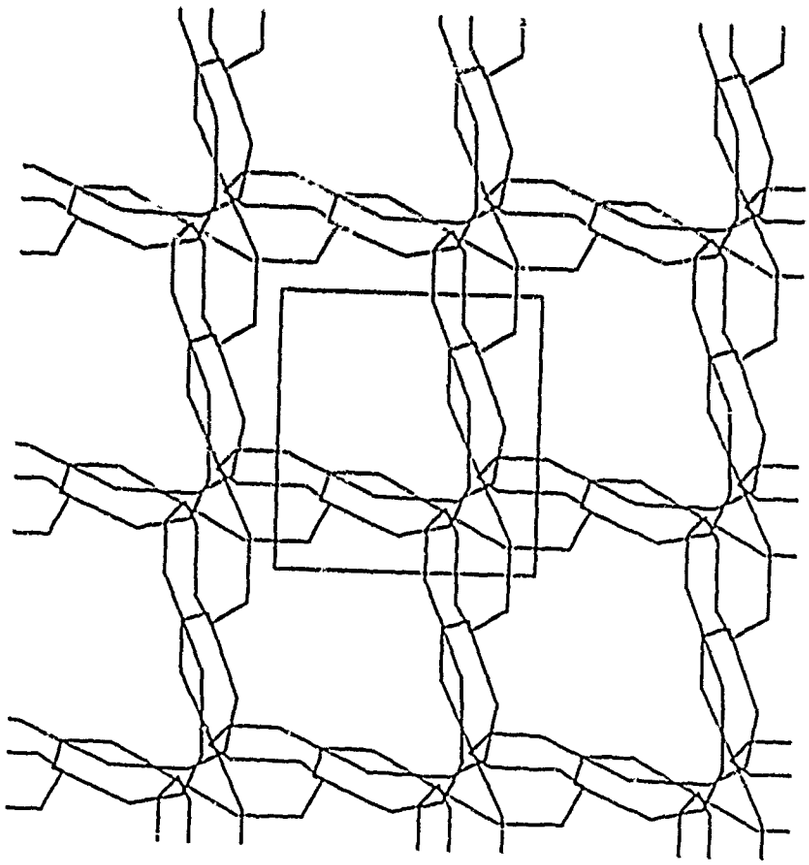


Figure 10. Complex Mesh Geometry

SESSION 9 - "COMPUTATIONAL ISSUES"

Chairman: Francis Canning

ASYMPTOTIC EVALUATION OF THE PHYSICAL OPTICS INTEGRAL FOR THE GENERALIZED ELLIPSOIDAL FRUSTA

R.L. Cravey, C.C. Cha
Syracuse Research Corporation
Merrill Lane
Syracuse, New York

ABSTRACT

To efficiently compute the bistatic high-frequency scattering responses of a complex target, a theory has been developed which employs asymptotic evaluation of the scattering integrals for a wide class of elliptical cross section shapes. This is a first-order theory which employs physical optics for smooth surface returns and edge equivalent currents for diffraction from surface discontinuities. The scattered field is obtained by integrating the surface and edge currents which have been induced by the incident field. Evaluation of the physical optics integral, a two-dimensional integral over the illuminated portion of the elliptical cross section surface, will be discussed here. The diffraction integral, which is a one-dimensional integral around elliptical ring discontinuities, is evaluated using the same type of asymptotic techniques.

PHYSICAL OPTICS INTEGRAL

The physical optics approximation assumes that the surface currents existing on the illuminated portion of the surface are equal to what would exist on an infinite planar structure tangent to the actual surface at the point of consideration. If the equivalent wave vector $\hat{k}_{eq}$ is defined as (see Figure 1)

$$\hat{k}_{eq} = \frac{\hat{k}_i + \hat{k}_r}{2 \cos \frac{\beta}{2}} , \qquad (1)$$

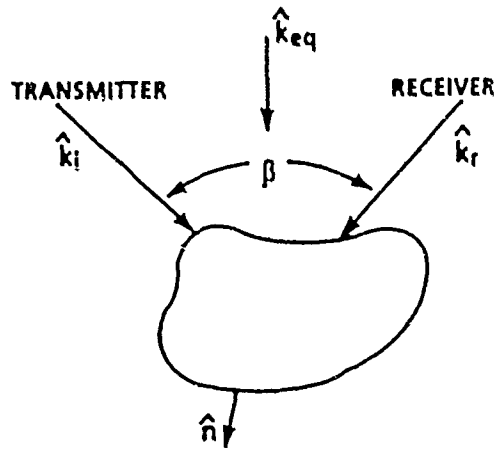


Figure 1. Bistatic Scattering Configuration

where $\hat{k}_i$ and $\hat{k}_r$ are the incident and reflected wave vectors, then the physical optics contribution to the scattered field may be written as

$$\iint_{\text{surface}} 2\,\hat{n} \times \underline{H}^i\, e^{-2j\,\underline{k}_{eq} \cdot \underline{r}'}\, da' \qquad (2)$$

This integral must be evaluated over the illuminated portion of the elliptical cross section surface.

The phase function of the equivalent wave vector (a combination of the transmitter and receiver wave vectors), is perhaps the most significant feature in an asymptotic scattering analysis. With the surface curvature and the wave frequency embedded in it, the phase function determines the location of the scattering centers and the "critical neighborhood" around such scattering centers. Often when analytically described surfaces are considered, "stationary points" in both surface dimensions can be found

analytically. These stationary points are then used in a general fashion to bring out either a specular return or contributions from a partial area of the critical neighborhood.

PARAMETERIZATION

The parameterization used to describe the elliptical cross section shapes can be thought of as a series of parallel ellipses whose semi-axes are allowed to vary along the axis of the body (Figure 2).

Analytically, the surface may be specified by

$$\underline{r}(\zeta,t) = r_0 + \Delta\underline{r} + [a(t)\cos\theta_0\cos\zeta - b(t)\sin\theta_0\sin\zeta]\,\hat{w} + [a(t)\sin\theta_0\cos\zeta + b(t)\cos\theta_0\sin\zeta]\,\hat{u} \qquad (3)$$

where $a(t) = \sqrt{a_1 t + b_1 t^2 + c_1}$ and $b(t) = \sqrt{a_2 t^2 + b_2 t + c_2}$. The geometry at a cross section is shown in Figure 3.

The angle ζ is nonlinearly proportional to θ and is given by

$$\frac{a\sin\alpha}{\sqrt{a^2\sin^2\alpha + b^2\cos^2\alpha}} = \sin\zeta \qquad (4a)$$

$$\frac{b\cos\alpha}{\sqrt{a^2\sin^2\alpha + b^2\cos^2\alpha}} = \cos\zeta \qquad (4b)$$

where $\alpha = \theta - \theta_0$. This is used to simplify the mathematical analysis. This simple analytical description allows for a surface normal to be written explicitly as a function of the parameters ζ and t.

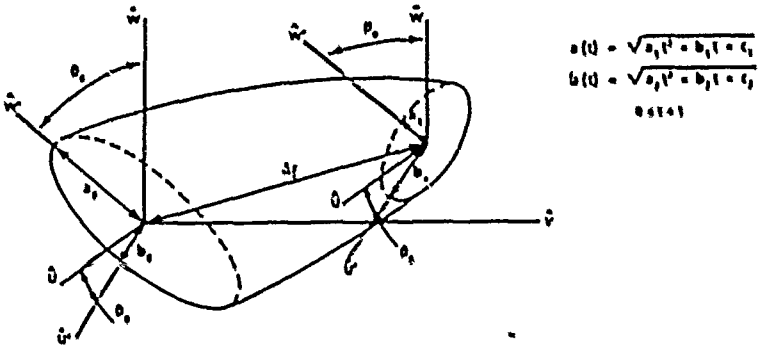


Figure 2. Elliptical Shape Parameterization

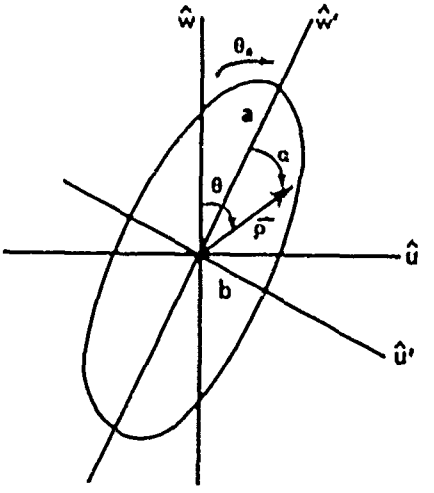


Figure 3. Geometry of Ellipses

EVALUATION OF THE PHYSICAL OPTICS INTEGRAL

Using the parameterization described above, the physical optics integral can be expressed as

$$\iint I(\zeta,t)\, e^{j\phi(\zeta,t)}\, d\zeta\, dt \tag{5}$$

The ζ integral is of the form

$$I(z) = \int_{x_o}^{x_1} f(x)\, e^{jz\phi(x)}\, dx \tag{6}$$

and, when evaluated, yields a t integral of the same form. This type of integral is known as a Fourier-type integral and can be solved using the asymptotic techniques discussed in the following paragraphs.

The first step in evaluating the integral above is to determine the stationary points, if they exist. A stationary point is a point x^* for which

$$\phi'(x)\Big|_{x=x^*} = 0 \tag{7}$$

If stationary points do not exist for the phase function of the integral, a change of variables is used to obtain a linear phase. If a stationary point does exist, a change of variables is used which yields a quadratic phase function. The change of variables is

$$\begin{cases} u = \dfrac{\phi(x) - \phi(x_o)}{\phi(x_1) - \phi(x_o)} & \text{for linear phase} \\ u^2 = \dfrac{\phi(x) - \phi(x^*)}{\phi(x^*) - \phi(x_o)} & \text{for quadratic phase} \end{cases} \tag{8}$$

With this variable change, we obtain an integral of the form

$$\begin{cases} \displaystyle\int_0^1 H(u)\, e^{j\pi u}\, du \;, \quad H(u) = \frac{f(x)}{\phi'(x)} & \text{if no stationary points exist} \\ \displaystyle\int_0^1 H(u)\, e^{j\pi u^2}\, du \;, \quad H(u) = \frac{u\, f(x)}{\phi'(x)} & \text{if stationary points exist} \end{cases} \tag{9}$$

The slow-varying part of the integrand is then approximated by a polynomial:

$$H(u) \approx H(0)\, p_1(u) + H(1)\, p_1(1-u) + H'(0)\, p_2(u) - H'(1)\, p_2(1-u) \tag{10}$$

where the functions p_1 and p_2 are given and illustrated in Figure 4.

$$p_1(w) = 1 - 3w^2 + 2w^3 \qquad p_1(1-w) = 3w^2 - 2w^3$$

$$p_2(w) = w - 2w^2 + w^3 \qquad p_2(1-w) = w^2 - w^3$$

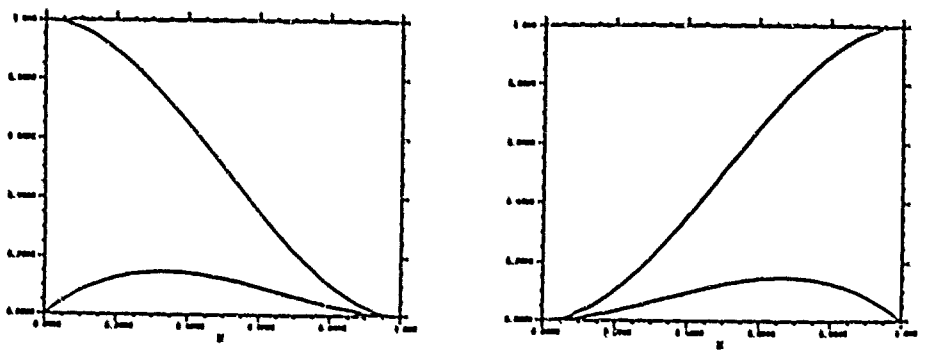


Figure 4. Fourier-Type Integrals

After approximation by the polynomial function, the integral reduces to a combination of integrals of the form:

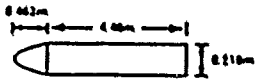
$$\begin{cases} \int_0^1 u^i \, e^{jzu} \, du & \text{if no stationary points exist} \\ \int_0^1 u^i \, e^{jzu^2} \, du & \text{if stationary points exist} \end{cases} \tag{11}$$

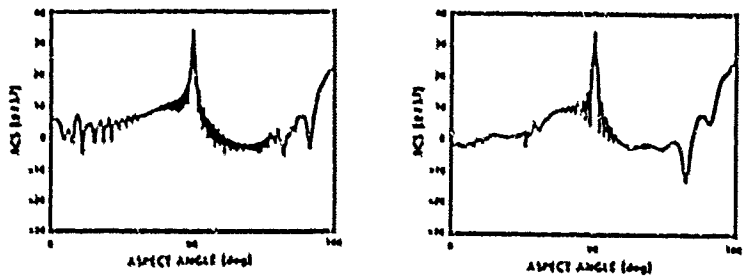
where $i = 0,1,2,$ or 3. The first type of integral can be evaluated exactly. The leading terms (from endpoint contributions) are proportional to $1/z$. The second type of integrals are either Fresnel or exact integrals (depending on whether i is even or odd) and the leading term (from the stationary point contribution) is proportional to $1/\sqrt{z}$.

CONCLUSIONS AND RESULTS

The solution to the physical optics integral described above uses a polynomial approximation to a slowly varying integrand and uses stationary points, when they exist, as phase origins. This results in analytical expressions of scattering center contributions, allowing for efficient computation of the scattered field for complex targets. The asymptotic solution also provides a uniform transition from discrete scattering centers to a continuum of them.

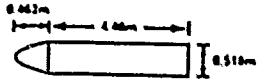
Some results are shown below. Figures 5 through 7 show comparison of measured data with results obtained using the techniques described in this paper. Figure 8 compares scattering from a flat plate and cylinders with elliptical cross sections of varying eccentricities.

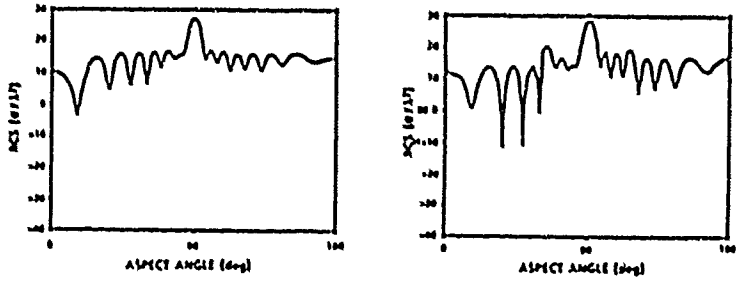




MEASURED PREDICTED

Figure 5. RCS of Delco Model 2A (β = 0°, VV Polarization, f = 1250 MHz)





MEASURED PREDICTED

Figure 6. RCS of Delco Model 2A (β = 160°, VV Polarization, f = 1250 MHz)

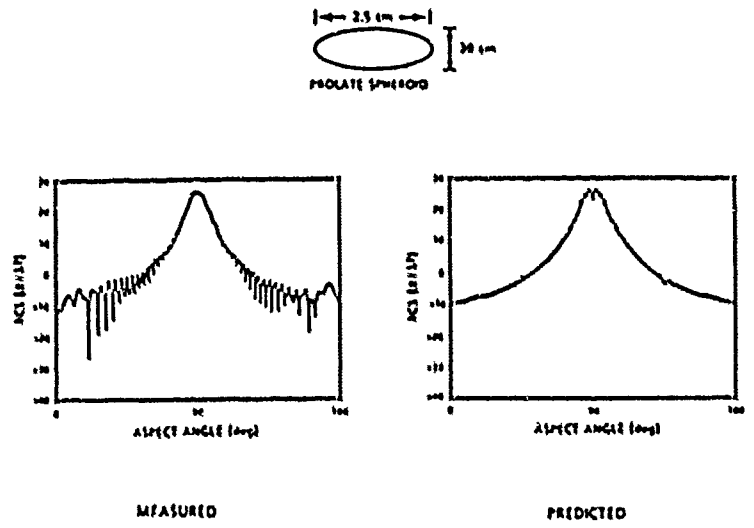


Figure 7. RCS of Delco Model 8A (β = 0°, VV Polarization, f = 35 GHz)

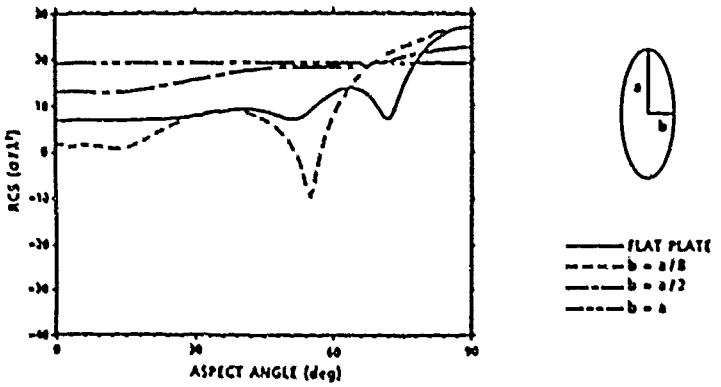


Figure 8. RCS of Cylinders of Varying Eccentricities (β = 0°, VV Polarization, f = 1000 MHz)

A NEW FAST FOURIER INTEGRAL TRANSFORM: REDISCOVERING THE SIGNIFICANCE OF LANCZOS SIGMA FACTORS

EARL L. DOMBROSKI
Science Applications International Corporation
2109 Air Park Road S.E.
Albuquerque, New Mexico 87106
(505) 247-8787

The Continuous Fourier Transform

The Fourier transform is defined by the integral expression

$$H(f) = \int_{-\infty}^{\infty} h(t)e^{-j2\pi ft}\,dt \tag{1}$$

and the inverse Fourier transform is

$$h(t) = \int_{-\infty}^{\infty} H(f)e^{j2\pi ft}\,df \tag{2}$$

where:

f	- frequency in Hertz
t	- time in seconds
j	- $\sqrt{-1}$

Together, these form a *continuous Fourier transform pair* (1).

The Discrete Fourier Transform

The transform of a discrete time impulse occurring at some time (t_n) is (2)

$$H(f) = h(t_n)\, e^{-j2\pi ft_n} \tag{3}$$

Substituting (3) into (1), using equidistant sampling of an event, leads to the *discrete Fourier transform (DFT)* pair. The DFT treats each sample as a discrete impulse, and sums the transformed impulses in the complex plane to obtain each point in the opposite domain. The result is a pair of records that provide a one to one mapping between the two domains. The DFT pair is shown in (4) and (5).

$$S_k = \sum_{n=0}^{N-1} s_n e^{-j2\pi f_k t_n} \tag{4}$$

$$s_n = \frac{1}{N}\sum_{k=0}^{N-1} S_k e^{j2\pi f_k t_n} \tag{5}$$

where:

s_n	- a sample from a time domain record (real or complex)
S_k	- a sample from a frequency domain record (complex)
t_n	- a discrete time chosen for the calculation
f_k	- a discrete frequency chosen for the calculation
N	- the number of samples
n	- 0, 1, ..., N-1
k	- 0, 1, ..., N-1

Note that because the samples are evenly spaced, that:

t_n	$= n\Delta_T$ (Δ_T is the time sampling interval)	(6)
f_k	$= k\Delta_F$ (Δ_F is the frequency sampling interval)	(7)

Sample spacing is determined by:

$$\Delta_f = \frac{1}{N\Delta_T} \tag{8}$$

or,

$$\Delta_f \Delta_T = \frac{1}{N} \tag{9}$$

Equation (8) follows intuitively by considering the first resolvable full wavelength in the sampled time record (f_1) above the DC component (f_0). Substituting (6), (7), and (9) into (4) and (5) yields the more familiar expressions for the DFT pair, shown in (10) and (11).

$$S_k = \sum_{n=0}^{N-1} s_n e^{-j2\pi kn/N} \tag{10}$$

$$s_n = \frac{1}{N}\sum_{k=0}^{N-1} S_k e^{j2\pi kn/N} \tag{11}$$

The DFT, by treating each sample as an impulse, assumes nothing between each sample; that is, to the DFT, the event did *not exist* where there were no samples. The DFT is satisfactory if the transform pair is used transparently to the user, as is common with convolutions.

The Approximate Fourier Transform

The *approximate Fourier transform (AFT)* pair follows straightforwardly from the rectangular rule applied to (1) and (2). Assuming equidistant samples,

$$S_k = \Delta_T \sum_{n=0}^{N-1} s_n e^{-j2\pi kn/N} \tag{12}$$

$$s_n = \Delta_f \sum_{k=0}^{N-1} S_k e^{j2\pi kn/N} \tag{13}$$

Close examination reveals that the AFT is merely a *scaled* DFT (2). Assuming adequate sampling, that is, assuming that the samples are closely spaced and sufficient in number to adequately characterize the event, results from the AFT pair (12) and (13) using known functions agree very closely with the continuous transform pair (1) and (2) at lower frequencies. While frequently confused with the DFT in common practice, the AFT exhibits one very important difference: the AFT assumes that the event *did* occur between the sampled points (although its unsampled activity is unknown). The AFT is used whenever the results of a discrete transform are to be evaluated independently. The AFT is performed by performing a DFT, then scaling the results.

The Fast Fourier Transform

A number of sophisticated techniques have been employed in the efficient encoding of equations (10) and (11) as computer algorithms. The significant reduction in execution time is underscored by the name given to the method(s), the *fast Fourier transform (FFT)*. Description of these techniques is beyond the scope of this paper. For analysis purposes, the reader may equate the DFT with the FFT. It should be noted, however, that the FFT is generally more accurate than a direct coding of the DFT because the FFT employs fewer intermediate calculations and therefore avoids potential floating point roundoff errors. The FFT is the preferred method of calculating the DFT.

Infinite Periodicity

The theorectical foundation of the DFT insists that the N samples in either domain constitutes a single cycle of an infinitely repeating periodic waveform. This is shown by

$$\frac{2\pi}{N}(qN + p) = q2\pi + \frac{2\pi p}{N} \tag{14}$$

therefore

$$e^{j2\pi(qN+p)/N} = e^{j2\pi p/N} \tag{15}$$

It is important to note that, in the frequency domain, using a similar analysis reveals that magnitude values reflect about frequency multiples of N/2.

$$\left|S_{q\frac{N}{2}+p}\right| = \left|S_{q\frac{N}{2}-p}\right| \tag{16}$$

Discrete Transform Aliasing

The DFT exhibits a severe problem called aliasing, where spectral components of one frequency are represented (aliased) by summing with components of a different frequency. This outcome is inherent in sampling. The more poorly an event is sampled, the greater the aliasing error. Common texts on the DFT suggest that higher sampling rates with longer sampled records (i.e., more points, closer together) reduces the aliasing error. In practice, there are two major problems with such reasoning: first, sampled time record limits are usually dictated by data acquisition instruments that cannot be replaced due to budgetary or technological constraints, and the second (and worst) problem is that the maximum frequency calculated by the DFT is done so using two samples/cycle, as implied by the *Nyquist sampling rate* (17).

$$\frac{1}{\Delta_T} = 2f_{max} \tag{17}$$

Rearranged, this leads to what is popularly referred to as the Nyquist cutoff frequency (18).

$$f_{max} = \frac{1}{2\Delta_T} \tag{18}$$

Using (7) and (8), (18) reveals that

$$f_{max} = f_{N/2} \tag{19}$$

Given a sampled time domain record, and using the DFT to calculate a frequency domain record, the level of confidence in calculated values decreases as the number of samples/cycle decreases. Restated, DFT errors increase as frequency increases.

The High Order Integral Fourier Transform

High order integral Fourier transform (IFT) techniques have been developed to remove the assumed infinite periodicity attributable to the discretization of a continuous event and reduce the aliasing errors. The essence of the technique is to assume that contiguous subsets of the sampled data are known values of a reasonably simple function of some assumed order, use the assumed function and perform piecewise analytic (continuous) Fourier transforms of the segments defined by the subsets. Assuming that the sampled points may be connected by straight lines leads to the first order, or linear, IFT; assuming second order curves fitted to the sampled points leads to the parabolic IFT, etc.

Removing the infinite periodicity characteristic is easily accomplished by brute force (20), where the proposition is made that the sampled event neither preceded nor succeeded the sample record.

$$\int_{-\infty}^{0} s(t)e^{-j2\pi ft}\,dt = \int_{t_{N-1}}^{\infty} s(t)e^{-j2\pi ft}\,dt = 0 \tag{20}$$

From (1) and (20), the IFT becomes:

$$S_k = \int_{0}^{t_{N-1}} s(t)e^{-j2\pi f_k t}\,dt \tag{21}$$

where:
s(t) = the assumed function fitted to the s sample set

Piecewise integration of (21) yields:

$$S_k = \sum_{\substack{n=r \\ s(ep\ r}}^{N-1} \int_{t_{n-r}}^{t_n} s(t)e^{-j2\pi f_k t}\,dt \tag{22}$$

where r is determined by the chosen assumed order of s(t).

Development of the Fast First Order IFT

The first order IFT defines the function

$$s(t) = mt + b \tag{23}$$

where m is the slope of the line fitted to two consecutive sample points and b is the Y-intercept along that line. Using Euler's definition, and (23), then (22) becomes

$$S_k = \sum_{n=1}^{N-1} \int_{t_{n-1}}^{t_n} (m_n t + b_n)\,[\cos(2\pi f_k t) - j \sin(2\pi f_k t)]\, dt \tag{24}$$

or,

$$S_k = \sum_{n=1}^{N-1} \int_{t_{n-1}}^{t_n} (m_n t + b_n) \cos(2\pi f_k t)\, dt - j \sum_{n=1}^{N-1} \int_{t_{n-1}}^{t_n} (m_n t + b_n) \sin(2\pi f_k t)\, dt \tag{25}$$

Considering the real component only, it follows that

$$S_{k(real)} = \sum_{n=1}^{N-1} \left[m_n \int_{t_{n-1}}^{t_n} t \cos(2\pi f_k t)\, dt + b_n \int_{t_{n-1}}^{t_n} \cos(2\pi f_k t)\, dt \right] \tag{26}$$

Restricting the evaluation to the sampling described in (9), (26) becomes

$$S_{k(real)} = \sum_{n=1}^{N-1} \left[\frac{m_n}{(2\pi k/N\Delta_T)^2} (-2\sin(\pi k/N)\sin(\pi k(2n-1)/N)) \right]$$

$$+ \frac{s_{N-1}}{2\pi k/N\Delta_T} \sin(2\pi k(N-1)/N) \tag{27}$$

Given

$$m_n = \frac{s_n - s_{n-1}}{\Delta_T} \tag{28}$$

and recognizing that the final term in (27) approaches zero, substitution obtains

$$S_{k(real)} = \frac{\sin(\pi k/N)}{(\pi k/N)^2} \Delta_T \sum_{n=1}^{N-1} \left[-\tfrac{1}{2}(s_n - s_{n-1}) \sin(\pi k(2n-1)/N) \right] \tag{29}$$

$$S_{k(real)} = \left[\frac{\sin(\pi k/N)}{(\pi k/N)} \right]^2 \Delta_T \sum_{n=0}^{N-1} s_n \cos(2\pi kn/N) \tag{30}$$

Similar analysis for the imaginary component yields

$$S_{k(\text{imaginary})} = -j\left[\frac{\sin(\pi k/N)}{(\pi k/N)}\right]^2 \Delta_T \sum_{n=0}^{N-1} s_n \sin(2\pi kn/N) \tag{31}$$

therefore,

$$S_k = \left[\frac{\sin(\pi k/N)}{(\pi k/N)}\right]^2 \Delta_T \sum_{n=0}^{N-1} s_n e^{-j2\pi kn/N} \tag{32}$$

$$L_k = \left[\frac{(\pi k/N)}{\sin(\pi k/N)}\right]^2 S_k \tag{33}$$

where k = 1, 2, ..., N/2 and

$L_{\frac{N}{2}-p}$ = complex conjugate of $L_{\frac{N}{2}-p}$

where p = 1, 2, ..., N/2 - 1 and

$$L_0 = S_0$$

so,

$$s_n = \Delta_f \sum_{k=0}^{N-1} L_k e^{j2\pi kn/N} \tag{34}$$

Note that equations (29) through (33) only hold for k not equal to 0, that is, evaluating the DC component. For that case, the complex exponential reduces to 1 and a simple rectangular integration is performed. Examination reveals that the first order IFT is an AFT with a triangular window applied; magnitude is affected, phase is not. The first order IFT, based on the AFT, can be performed using FFT techniques. Since the first order IFT is rooted in the DFT, then the Nyquist cutoff frequency still applies to the analysis. Further, infinite periodicity is still implied, despite the allegations made in equations (20) through (22). To reconstruct the N frequency domain samples to perform an inverse transform, the complex conjugate of the first half of the frequency domain record is used to reconstruct the second half; otherwise, practitioners would find themselves trying to resolve a signal from noise.

The technique described in equations (32) through (34) show that the first order IFT can be performed in an extremely efficient computation. Most importantly, note that the first order IFT results can now be inversed.

Lanczos Smoothing and the Zero Order IFT

Cornelius Lanczos devoted considerable effort to develop a function to remove the effects of the Gibbs phenomenon, that is, the rippling that is observed when a Fourier series is truncated. He argued that by averaging over the period of the first term neglected (or the last term kept) that the main effects of the rippling would be reduced. This development led to what are termed the sigma factors

$$\sigma(N,k) = \frac{\sin(\pi k/N)}{(\pi k/N)} \tag{35}$$

and were offered as a smoothing window to apply to the Fourier coefficients of the truncated series.

Note that this term squared is the term shown in equations (30) through (32). Following the reasoning applied to equations (23) through (34), except choosing a zero order function to fit to the samples, that is, each sample represents a step value that remains constant until modified by the next sample value, yields the sigma factors directly.

$$S_k = \left[\frac{\sin(\pi k/N)}{(\pi k/N)}\right]\Delta_T \sum_{n=0}^{N-1} s_n e^{-j2\pi kn/N} \tag{36}$$

$$L_k = \left[\frac{(\pi k/N)}{\sin(\pi k/N)}\right] S_k \tag{37}$$

again, where k = 1, 2, ..., N/2 and

$$L_{\frac{N}{2}+p} = \text{complex conjugate of } L_{\frac{N}{2}-p}$$

and again, where p = 1, 2, ..., N/2 - 1 and

$$L_0 = S_0$$

$$s_n = \Delta_F \sum_{k=0}^{N-1} L_k e^{j2\pi kn/N} \tag{38}$$

This development begs the question as to why a zero order IFT does not directly evaluate to the AFT, where the rectangular rule was applied to equations (1) and (2). The reason is twofold: first, the transform is accomplished by fitting complex exponentials to a given function, and a function of steps is not the same as a function of scaled points; second, because the DFT insists that it is summing impulses, and impulses are not band limited, then with very few exceptions, the results of summing transformed impulses will not be bandlimited. As equation (16) shows, frequency components that extend beyond the Nyquist cutoff frequency cannot be resolved, but as equations (10) and (11)

show, all frequency component information must be retained in order to develop a transform pair, therefore frequency components above the Nyquist cutoff frequency are aliased with the frequencies up to the Nyquist cutoff (often called *folding*).

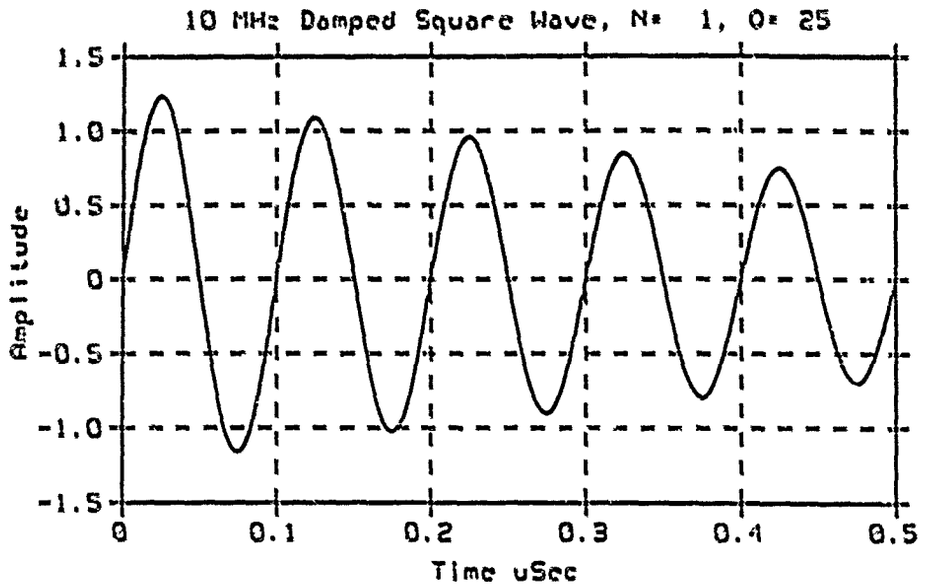
The sigma factors applied to a DFT of a square wave will result in a record whose magnitude agrees with the theoretical transform; the sigma factors squared applied to a DFT of a triangle will also result in agreement with analytic results. In a limited sense, the sigma factors can be thought of as helping to filter out the folding error inherent in the DFT. In broad terms, IFTs of any order may be thought of as filtered DFTs.

Comparison of the AFT, Fast IFT and Analytic Results

Damped square waves were used to assess the effectiveness of the fast first order IFT. The damped square waves were produced using a generating function that successively added terms to an infinite Fourier series of damped sines; the fundamental frequency was 10 MHz and low and high damping factors were applied (Q=25 and Q=5). The functions were sampled at 0.5 nanosecond intervals with a total record length of 16384 samples. Transforms were performed using the FFT based AFT, the fast first order IFT (using the same FFT routine) and also calculated analytically. Percentages of error for the AFT and fast IFT were calculated. The results are shown in Figures 1 through 9.

Figures 1 and 2 show the results of the transforms of a single damped sine term with a Q of 25. Figure 3 shows the error between the two transform methods. Note the difference in scale; the AFT exhibits folding errors approaching 150% at the Nyquist frequency, while the fast IFT never exceeds 0.025% error. Figure 6 shows the errors when the generating function is increased to seven terms; Figure 9 shows the errors for 25 terms with Q=5. In both cases the AFT errors approach 150% while the fast IFT folding errors are negligible.

Figures 6 and 9 also illustrate the aliasing error known as leakage, where missed resonance spectral information is retained by first overestimating the calculated values prior to a resonance then immediately underestimating the successive values. Just as these figures admirably show that the fast IFT virtually removes folding errors, they also admirably show that leakage, the natural outcome of the discretization of a continuous event, is absolutely incurable.


10 MHz Damped Square Wave, N= 1, Q= 25
1.5
1.0
0.5
0
-0.5
-1.0
-1.5
Amplitude
0
0.1
0.2
0.3
0.4
0.5
Time uSec

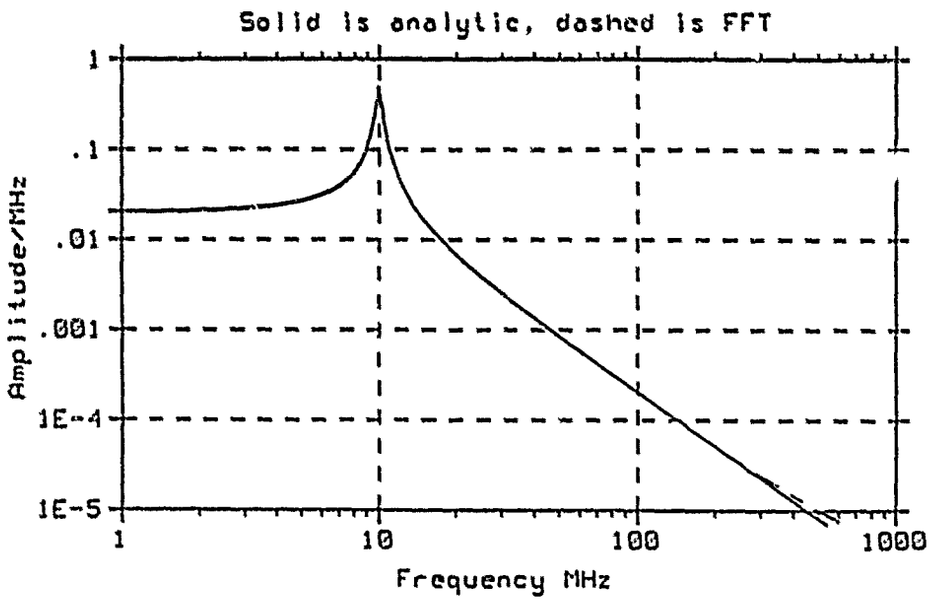
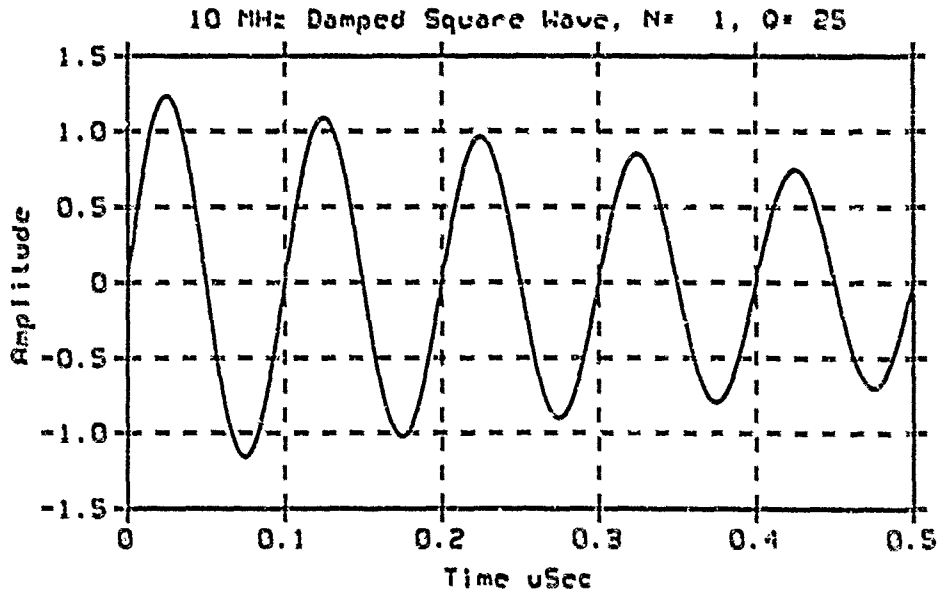

Solid is analytic, dashed is FFT
1
.1
.01
.001
1E-4
1E-5
Amplitude/MHz
1
10
100
1000
Frequency MHz

Figure 1.


10 MHz Damped Square Wave, N= 1, Q= 25
1.5
1.0
0.5
0
-0.5
-1.0
-1.5
Amplitude
0
0.1
0.2
0.3
0.4
0.5
Time uSec

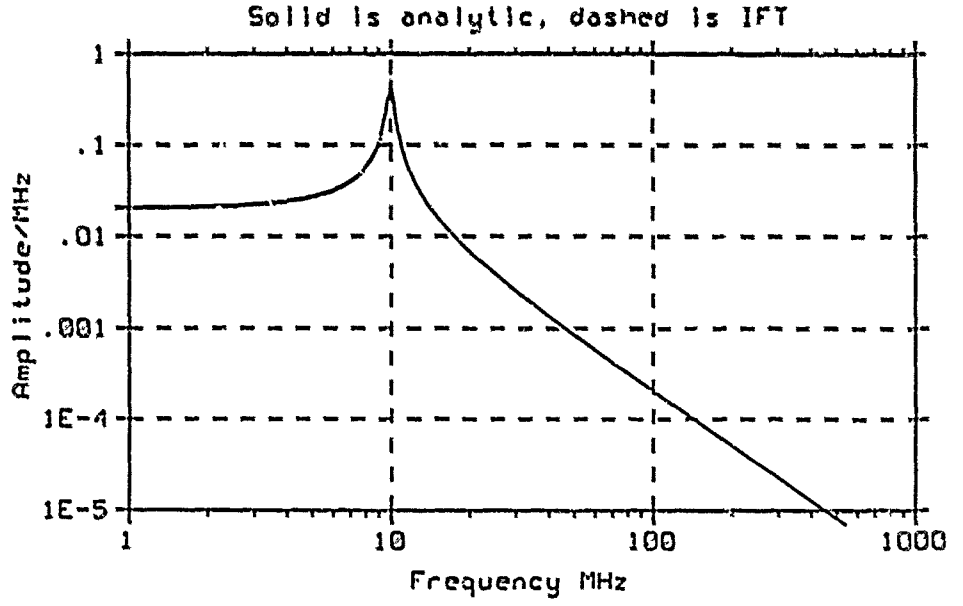
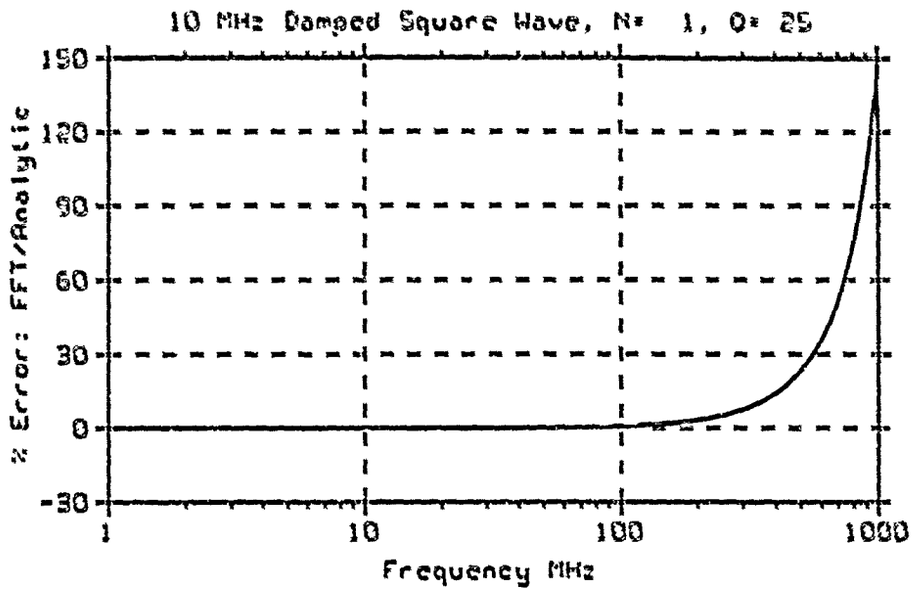

Solid is analytic, dashed is IFT
1
.1
.01
.001
1E-4
1E-5
Amplitude/MHz
1
10
100
1000
Frequency MHz

Figure 2.


10 MHz Damped Square Wave, N= 1, Q= 25
% Error: FFT/Analytic
150
120
90
60
30
0
-30
1
10
100
1000
Frequency MHz

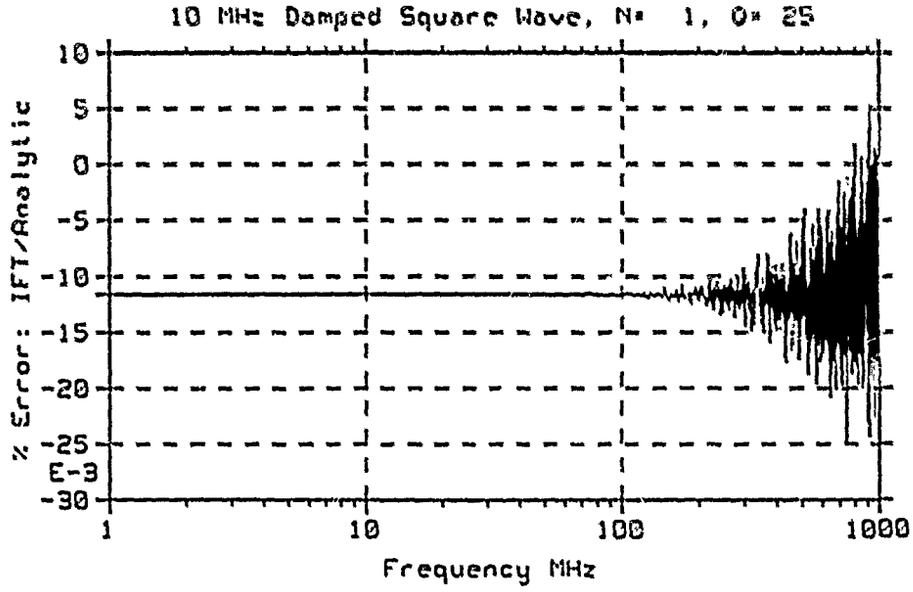
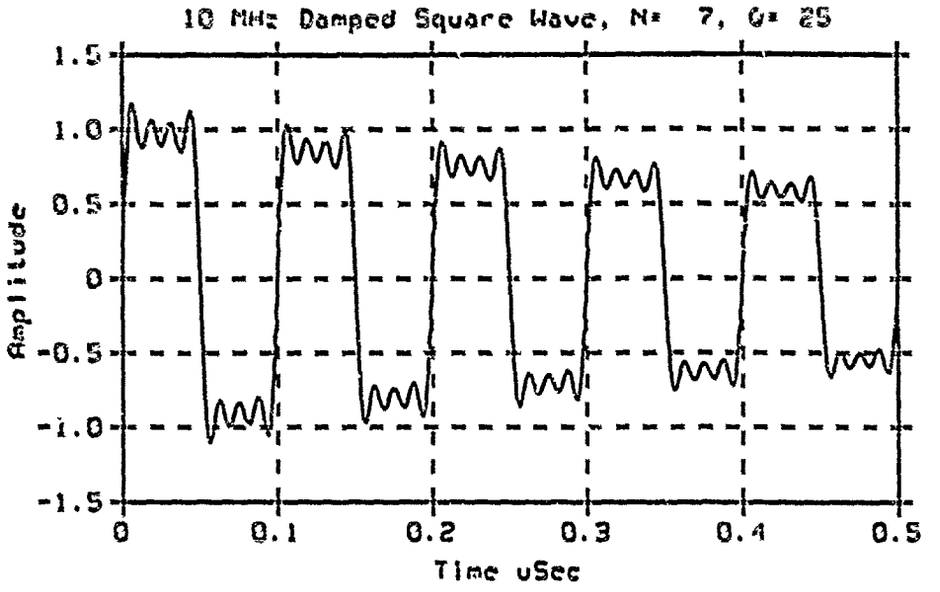

10 MHz Damped Square Wave, N= 1, Q= 25
% Error: IFT/Analytic
10
5
0
-5
-10
-15
-20
-25
E-3
-30
1
10
100
1000
Frequency MHz

Figure 3.


10 MHz Damped Square Wave, N= 7, Q= 25
1.5
1.0
0.5
0
-0.5
-1.0
-1.5
Amplitude
0
0.1
0.2
0.3
0.4
0.5
Time uSec

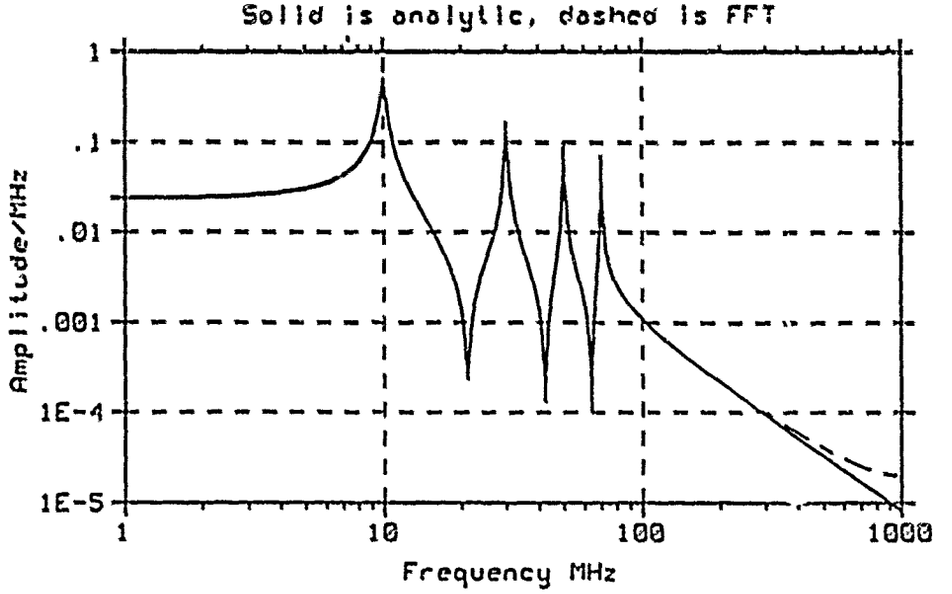
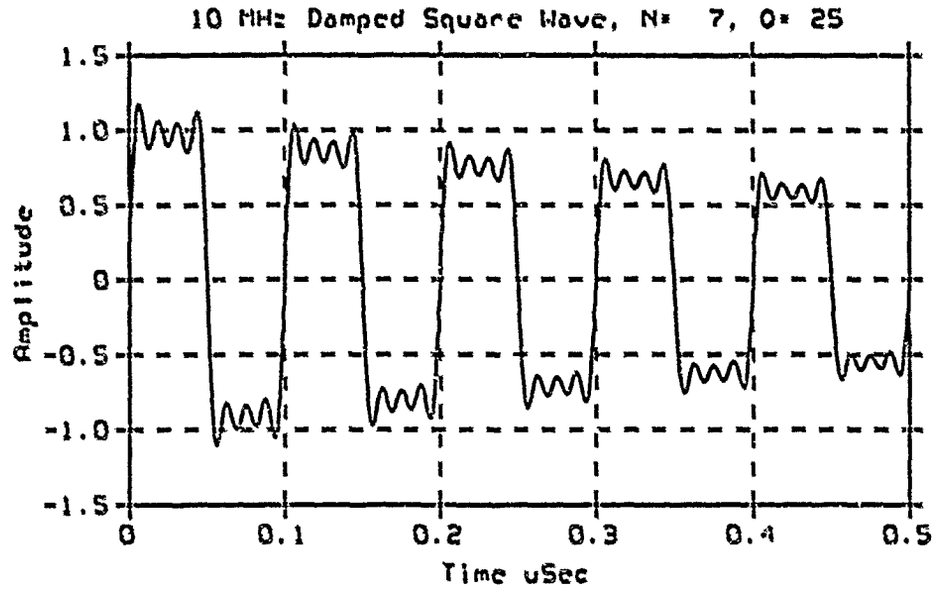

Solid is analytic, dashed is FFT
1
.1
.01
.001
1E-4
1E-5
Amplitude/MHz
1
10
100
1000
Frequency MHz

Figure 4.


10 MHz Damped Square Wave, N= 7, O= 25
1.5
1.0
0.5
0
-0.5
-1.0
-1.5
Amplitude
0
0.1
0.2
0.3
0.4
0.5
Time uSec

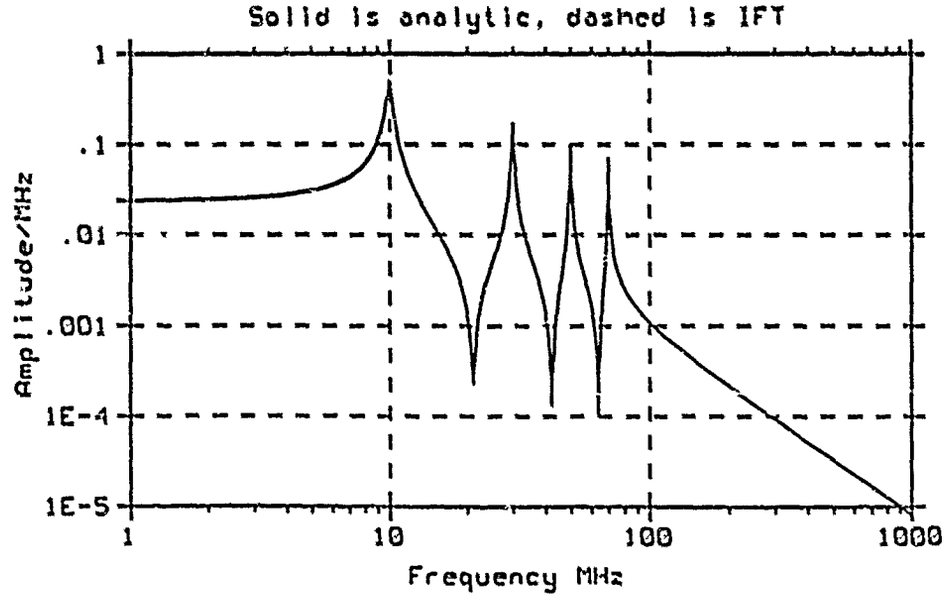
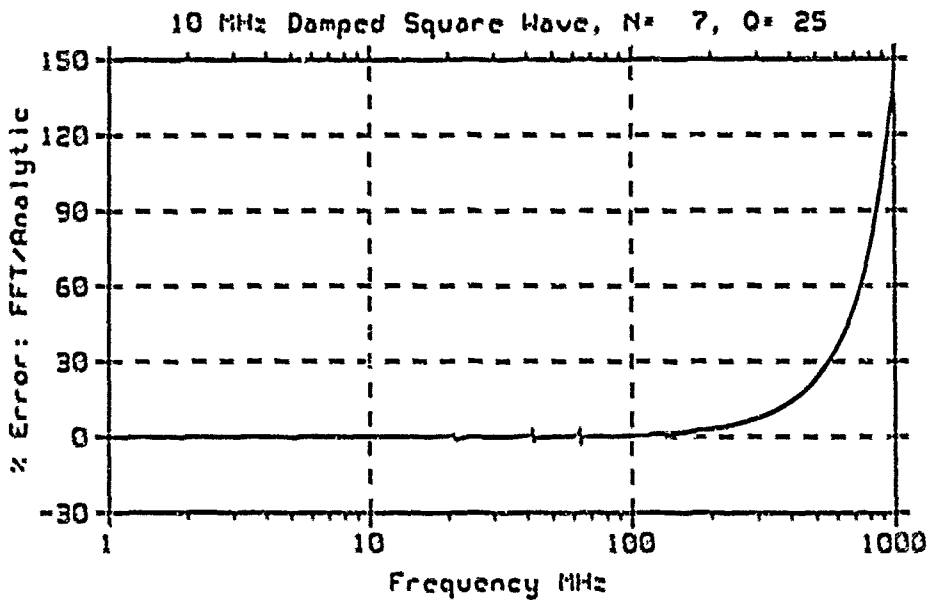

Solid is analytic, dashed is IFT
1
.1
.01
.001
1E-4
1E-5
Amplitude/MHz
1
10
100
1000
Frequency MHz

Figure 5.


10 MHz Damped Square Wave, N= 7, O= 25
% Error: FFT/Analytic
150
120
90
60
30
0
-30
1
10
100
1000
Frequency MHz

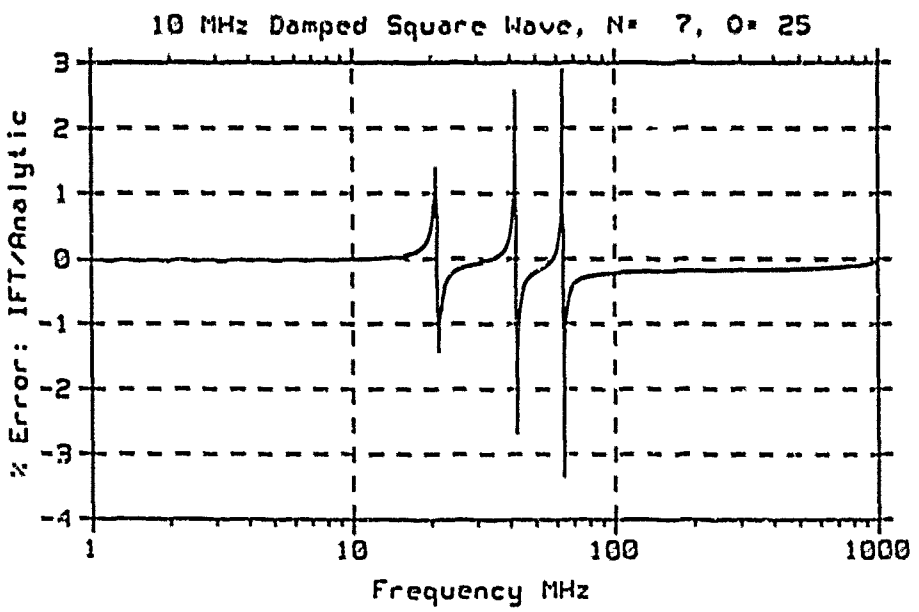
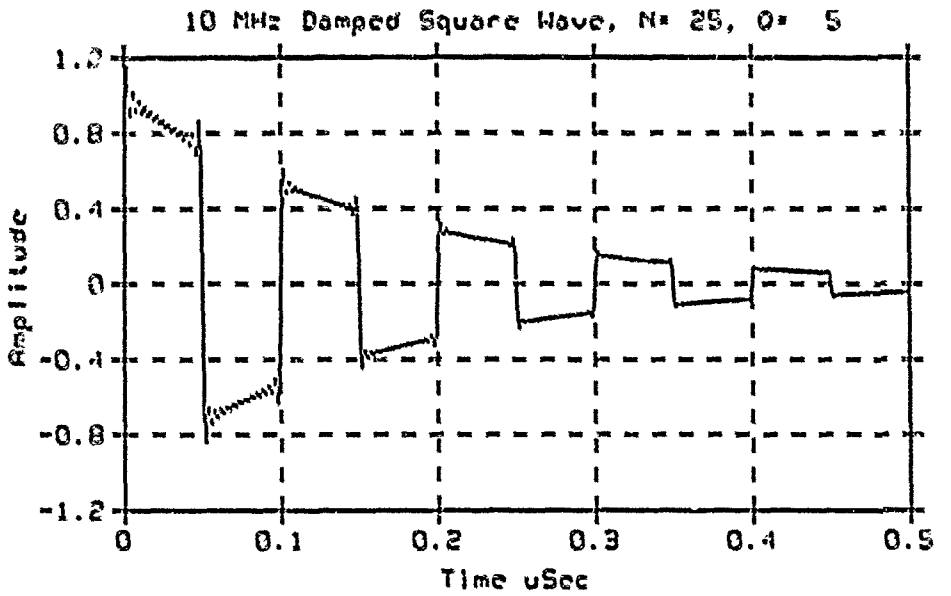

10 MHz Damped Square Wave, N= 7, O= 25
% Error: IFT/Analytic
3
2
1
0
-1
-2
-3
-4
1
10
100
1000
Frequency MHz

Figure 6.


10 MHz Damped Square Wave, N= 25, Q= 5
1.2
0.8
0.4
0
-0.4
-0.8
-1.2
Amplitude
0
0.1
0.2
0.3
0.4
0.5
Time uSec

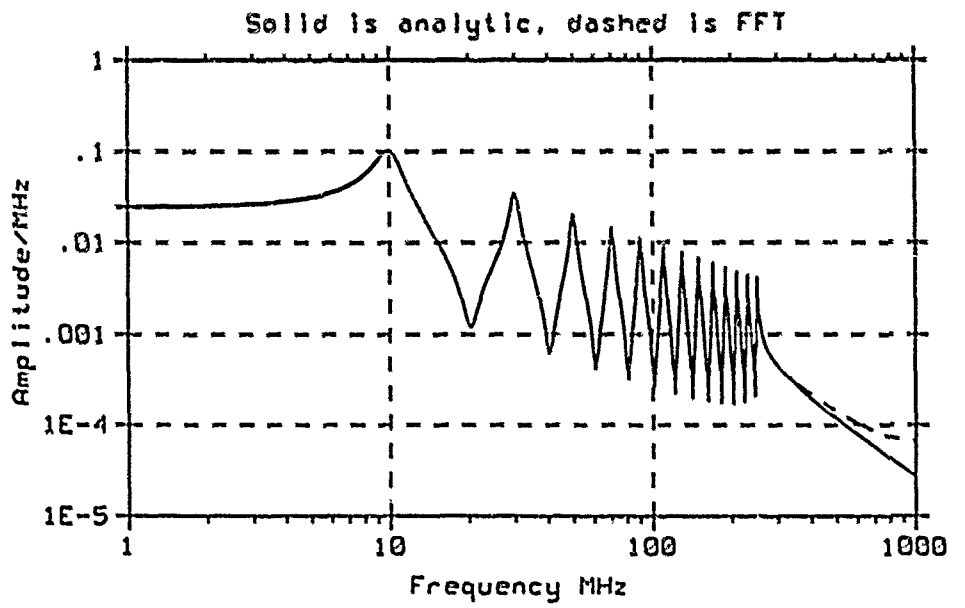
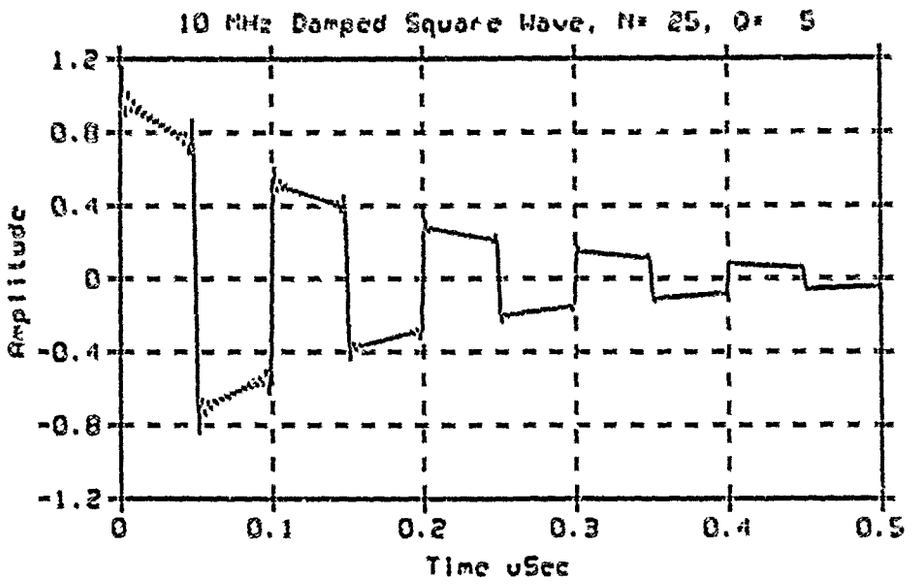

Solid is analytic, dashed is FFT
1
.1
.01
.001
1E-4
1E-5
Amplitude/MHz
1
10
100
1000
Frequency MHz

Figure 7.


10 MHz Damped Square Wave, N= 25, σ= 5
1.2
0.8
0.4
0
-0.4
-0.8
-1.2
Amplitude
0
0.1
0.2
0.3
0.4
0.5
Time uSec

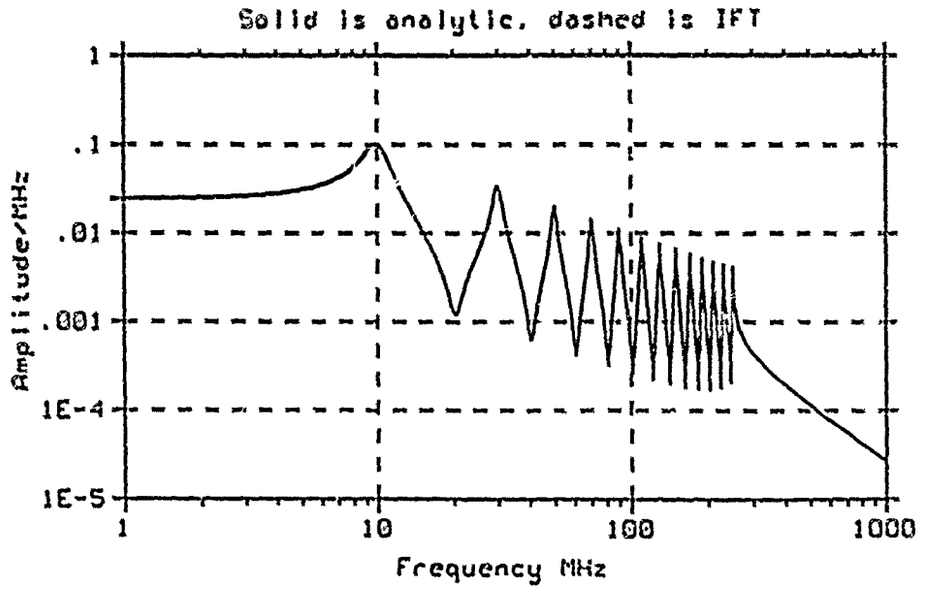
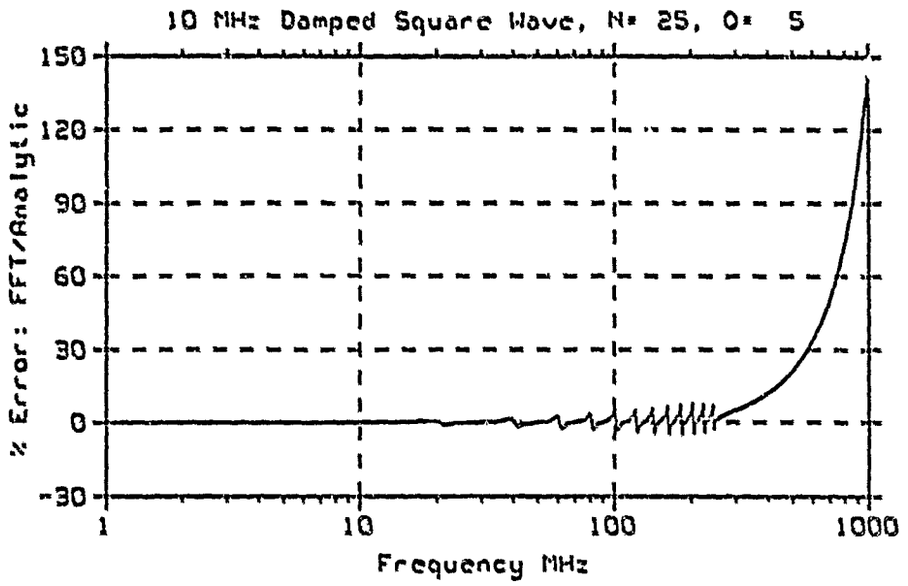

Solid is analytic, dashed is IFT
1
.1
.01
.001
1E-4
1E-5
Amplitude/MHz
1
10
100
1000
Frequency MHz

Figure 8.


10 MHz Damped Square Wave, N= 25, O= 5
% Error: FFT/Analytic
150
120
90
60
30
0
-30
1
10
100
1000
Frequency MHz

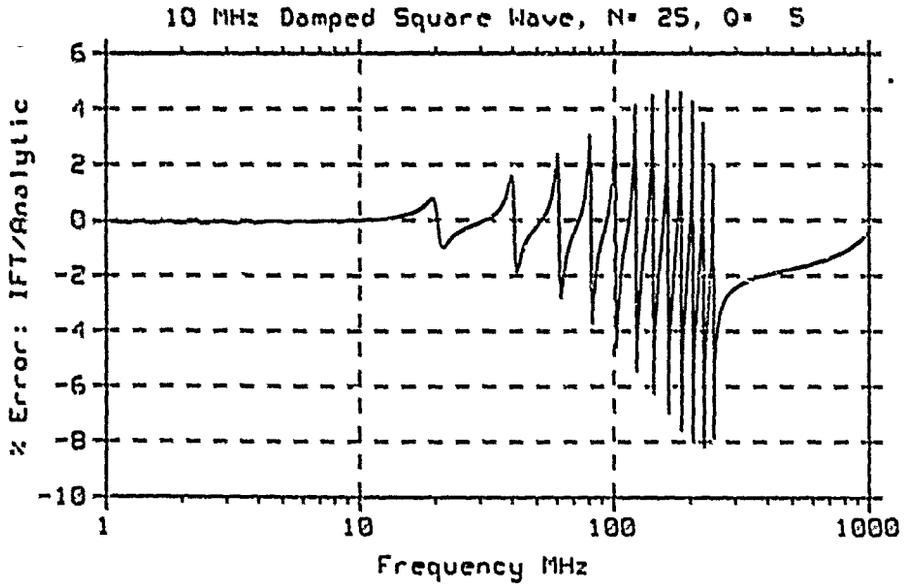

10 MHz Damped Square Wave, N= 25, O= 5
% Error: IFT/Analytic
6
4
2
0
-2
-4
-6
-8
-10
1
10
100
1000
Frequency MHz

Figure 9.

Conclusions and Applications

Practitioners of Fourier transforms have long realized that the AFT is highly erroneous for most functions above about half of the Nyquist cutoff frequency (and some would even argue for a lower limit). The choice has been to live with the error, or employ slower high order integral transforms without the ability to inverse the transform back to the original domain. The technique presented here offers a third alternative. Because of the proven inevitability of folding, at a minimum, a zero order correction should be applied. If one has sampled in the frequency domain directly, for example with a continuous wave test set, and can see that the function was not bandlimited but that test equipment impaired observability, then the inverse window should be applied if one wishes to obtain the inverse transform. In effect, this technique could be used to 'fool' the DFT, that is, to introduce the folding errors that would be present in the DFT spectrum (and required for construction of the time domain record), but were not present in the measured spectrum.

For those that would persist with the arguments that the current IFT techniques offer a host of advantages, such as utility with non-equidistant samples, the ability to choose frequencies of interest and the ability to resolve values above the Nyquist cutoff frequency, the following observations are made: 1) an IFT of some order applied to non-equidistant samples is equivalent to a curve fit of the IFT's order to generate equidistant samples; 2) if you can anticipate the frequencies of interest, why bother with transforms; and, 3) it is shown above that Nyquist was correct about sampling a continuous function, regardless of subsequent operations that one may hope for.

Further research should prove that all higher order IFTs reduce to a windowed AFT. Although a literature search did not reveal the prior existence of this technique, the author has no doubt but that some mathematician must have thought of it previously.

References

1. Brigham, E. O., *The Fast Fourier Transform*. Englewood Cliffs, NJ: Prentice-Hall, 1974.

2. Schwartz, M. and Shaw, L., *Signal Processing: Discrete Spectral Analysis, Detection and Estimation*. New York, NY: McGraw-Hill, 1975.

3. Hamming, R. W., *Digital Filters*. Englewood Cliffs, NJ: Prentice-Hall, 1977.

Acknowledgement

My thanks to Dr. Don Pierce, for generating the damped square waves and the corresponding analytic transforms.

IMPLEMENTATION AND PERFORMANCE OF MMP PROGRAMS ON TRANSPUTERS

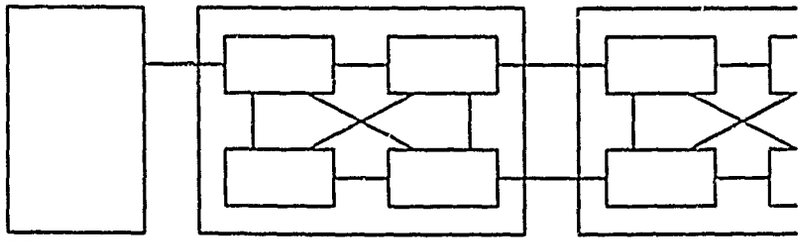
Christian Hafner, Lars Bomholt

Electromagnetics Group
Swiss Federal Institute of Technology
8092 Zurich, Switzerland

Abstract
Transputers are microprocessors designed for parallel computing in processor networks. They offer large computing power at a low price even when used as single processors. Standard languages like FORTRAN are available. Implementation of existing programs is easy. Depending on the program structure, parallelization may be more difficult.
We parallelized the MMP code and present details of implementation together which benchmark results.

IMS T800 Transputers and the PC

A T800 transputer is a 32-bit microprocessor with a 64-bit floating point unit and 4 Kbytes of RAM on a single chip. 4 link interfaces provide communication with neighbour processors. The name is a concatenation of 'transistor' and 'computer', which is suggesting the use of a single transputer as an element in a larger network only. One single transputer running with 20 MHz is for floating point operations typically as fast as a 20 MHz 80386 processor with 80387 coprocessor and Weitek 1167 floating point accelerator, but much cheaper [1].
A wide range of different PC compatible boards is offered by different companies,. Currently we use QUADPUTER boards from Microway, on which 4 Transputers with 4 Mbytes of memory each are combined. The boards can be connected with others to form networks of arbitrary size. Transputer networks are a coarse grained approach to parallel computing. Interprocessor communication and especially Input/Output to the host can slow down perfomance considerably and should be minimized.



Compilers

OCCAM is the best language for transputers, but also others are available. We are using the 3L Parallel FORTRAN 77 compiler. It is very standard, and it provides no Double Precision Complex (COMPLEX*16). For this reason we had to partially rewrite the program. Nevertheless it was worth the effort because also on SUN workstations it now runs twice to three times as fast as before. Implementation of standard FORTRAN programs on a single transputer is very simple and requires no change in the program. For parallelization the program has to be split up in several independant programs (tasks), which can run in parallel on a single or on several transputers. For communication between the tasks a library of FORTRAN callable subroutines is provided.

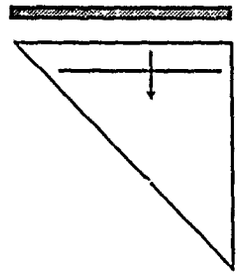
Implementation of the MMP Code

The structure of the MMP code is described in [2]. The small size of the program and its compact use of memory make it well suited for the implementation on small machines.

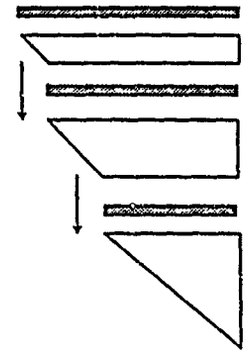
For a large number of unknowns practically all of the time is spent in the matrix updating while computation of the expansion functions and the equations become neglegible. Thus a high degree of parallelity with few effort can be reached by parallelizing only the updating routine and keeping the rest of the program on one single transputer.

A closer look at the updating routine reveals that the process of updating takes place in a front propagating from the top of the triangular matrix to the bottom. The matrix can therefore be split up in slices residing on different processors. Between the processors only the passing of simple vectors is necessary.

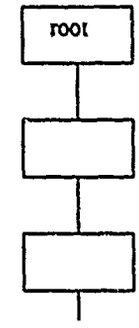
Therefore for this kind of algorithm a pipeline structure of the network is best suited. However, this utilization of the transputers is not perfect because computations on the different



A row (shaded) is updated into the matrix. The front of computation propagates down through the matrix.



The matrix is split up into several parts residing on different processors. The front is passed between the processors by vectors.



Network configuration. Each processor holds about the same number of matrix elements. The root transputer in addition computes the rows.

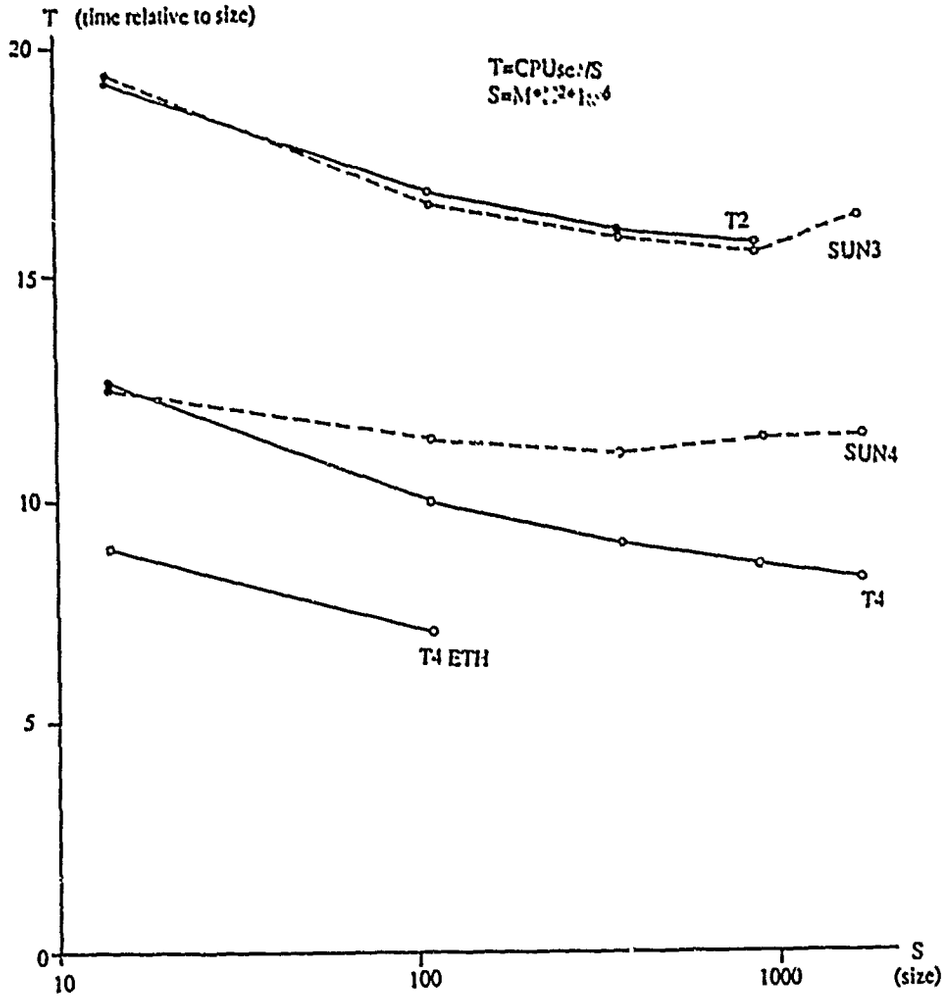


Fig.: Comparison of relative CPU time vs. problem size on different machines (see text). The size of problem is indicated by S which depends on the number of unknowns M and the number of equations N in an overdetermined system of equations. Relative time T is CPU time divided by problem size.

transputers never need exactly the same time and the triangle gets full only after M equations are updated, so the processors towards the end of the pipeline have less work to do than those at the beginning of the line.
An advantage of this pipeline configuration is that the number of processors used can easily be fit to the size of the problem calculated. The program does not have to be recompiled and additional transputers provide more memory as well as more computing power.

Benchmarks and Comparison with Other Machines

For comparison we ran an simple example with a varying number M of unknowns and N equations on the following machines:

- SUN3: SUN 3/260C workstation with a 25 MHz 68020 processor and WEITEK 1164/65 floating point accelerator and 8 Mbytes of memory
- SUN4: SUN 4/110 workstation with a MB86900 SPARC processor running at 14.28 MHz and Weitek 1164/65 floating point accelerator
- T2,T4: 2 or 4 T800 Transputers running at 20 MHz with 4Mbyte of memory each on a QUADPUTER board by Microway
- T4 ETH: 4 T800 transputers, 0 wait state, the root running at 30 MHz with 2 Mbytes of memory, the others at 20 MHz with 1 Mbyte of memory, on a PC board built at the ETH.

Unfortunately we didn't yet have access to larger networks, but results will soon be available.
With larger size of the problem the difference in use of capacity of the different transputers and the amount of communication between them gets relatively smaller and efficiency is increased compared to the one-processor-systems. This is especially obvious for very small problems and large networks [3].
For larger problems the CPU time of the SUN workstations is not representative because extensive paging increases turnaround time, which for single user operation is then about twice the CPU time. Performance of course also breaks down if more than one job is running at a time.

Conclusions

Transputers offer large power and a way into parallel processing at a very moderate price. Faster transputers are announced. We are looking forward to larger networks and to machines based entirely on transputers.

Literatur

[1] inmos, INMOS SPECTRUM, *March 1988*
[2] L. Bomholt, Ch. Hafner, "A MMP Program for Computation of 3D Electromagnetic fields oin PCs", *5th Annual Review of Progress in Applied Computational Electromagnetics (ACES), Conference Proceedings, March 1989*
[3] Ch. Hafner, R. Ballisti, "Electromagnetic Field Calculations on PCs and Workstations Using the MMP Method", *IEEE Trans. Magn., Vol MAG-25, July 1989*

EFFECT OF APPROXIMATIONS ON ACCURACY AND CONVERGENCE RATE IN THE MIXED-POTENTIAL INTEGRAL EQUATION

Allen W. Glisson
Department of Electrical Engineering
University of Mississippi
University, MS 38677

Abstract

The mixed-potential integral equation is widely used for the numerical solution of electromagnetic radiation and scattering problems. Various approximations are commonly made in the evaluation of the potentials and the moment method testing procedure for numerical implementation of the mixed-potential formulation. In this paper, we consider the effect on the accuracy and convergence rate of the numerical solution due to some of these approximations in the mixed-potential integral equation formulation. Results suggest that the usefulness of some approximations may diminish rapidly for larger structures, even though the number of unknowns per wavelength used in the numerical model remains constant.

Introduction

Surface integral equation formulations are currently used to model a wide variety of electromagnetic scattering problems involving perfectly conducting or homogeneous dielectric scatterers. The surface integral equations may expressed in one of several different forms for application of the method of moments numerical solution. The mixed-potential formulation, in which both the vector and scalar potentials appear explicitly, has been used very successfully for modeling strips, plates, and bodies of revolution [1], wires [2], and arbitrarily shaped bodies [3].

In the application of the mixed-potential approach, however, various approximations are commonly made in a effort to reduce computation time or for simplicity. In [1] and [2], the numerical solution procedure may be developed through the use of a pulse testing set and a triangle expansion set with subsequent approximations to both the testing integration and the basis function in the computation of vector potential terms. The numerical implementations in [1] and [2] employ pulse basis functions to represent both the current and the charge. This approach may be viewed as an approximation to the use of a triangle basis set for the current which, when differentiated, yields the same pulse basis set for the charge. Another commonly made approximation in the procedure is the evaluation of the testing integral in the vector potential contribution to a matrix element via a one-point rectangular rule integration.

The approximations employed in these procedures seem reasonable when a sufficient number of segments are used to represent the scattering structure. Comparisons of results obtained using such approximations, however, suggest that the usefulness of some of the approximations diminishes rapidly for larger structures, even when the number of unknowns per wavelength is constant in the numerical model. In this work we consider the effect on the solution accuracy and convergence rate of the use of some of these approximations in the mixed-potential integral equation formulation. The problem of electromagnetic scattering by a flat, two-dimensional infinite strip illuminated by a plane wave with electric field oriented transverse to the strip axis is employed as a base problem for testing these approximations.

Formulation

We use the simple strip geometry as a test case to provide a uniform means for evaluation the effects of various approximations. The perfect electric conductor (PEC) strip of width 2w is shown in Fig. 1. The strip is assumed to be illuminated by a normally incident transverse electric (TE) plane wave. The electric current (J_x) then flows only across the width of the strip. There is no current flow in the direction of the strip axis. The electric field integral equation (EFIE) for this geometry may be written in mixed-potential form as

$$-E_x^{inc}(x) = -j\omega A_x(x) - \frac{\partial}{\partial x}\Phi(x) \tag{1}$$

where

$$A_x(x) = \mu \int_{-w}^{w} J_x(x')\, G(x,x')\, dx' \tag{2}$$

$$\Phi(x) = \frac{1}{\epsilon} \int_{-w}^{w} \left[\frac{1}{\omega}\frac{\partial}{\partial x'} J_x(x')\right] G(x,x')\, dx' \tag{3}$$

$$G(x,x') = \frac{1}{4j} H_0^{(2)}(k|x-x'|) \tag{4}$$

and where k is the wavenumber. A harmonic time dependence $\exp(j\omega t)$ of the field is assumed and suppressed.

The method of moments [4] is employed to solve (1) using a triangle expansion set to represent the unknown induced current density J_x and a pulse testing procedure to generate the system of linear equations. The coordinates associated with the N triangle expansion functions are shown in Fig. 2a for a strip which has been subdivided into (N+1) segments. The pulse testing functions, which extend from the midpoint one segment

to the midpoint of an adjacent segment, are shown in Fig. 2b. Application of the method of moments then yields matrix elements formally defined by

$$z_{mn} = \frac{-k\eta}{4}\psi_{mn} - \frac{\eta}{4k}\left(\psi_{mn}^{+-} - \psi_{mn}^{++} - \psi_{mn}^{--} + \psi_{mn}^{-+}\right) \tag{5}$$

where

$$\psi_{mn} = \int_{x_{m-1/2}}^{x_{m+1/2}} \int_{x_{n-1}}^{x_{n+1}} \Lambda_n(x')\, H_0^{(2)}(k|x-x'|)dx'\, dx \tag{6}$$

$$\psi_{mn}^{\pm\mp} = \frac{\mp 1}{|x_n - x_{n\mp 1}|} \int_{x_n}^{x_{n\mp 1}} H_0^{(2)}(k|x_{m\pm 1/2} - x'|)dx' \tag{7}$$

where the $\pm$ symbol is used to denote the sign appearing above the m subscript in ψ_{mn} in (5) and the $\mp$ symbol denotes the sign above the n subscript, $x_{m\pm 1/2} = (x_m + x_{m\pm 1})/2$, $\Lambda_n(x')$ is the triangle basis function, and $\eta = \omega\sqrt{\mu\epsilon}$ is the impedance of the homogeneous medium surrounding the strip. The integrations over the source variable x' in (6) and (7) are generally evaluated numerically, except that when the observation coordinate is within the source region, the contribution due to the singular behavior of the Hankel function is extracted and evaluated analytically.

The approximations considered in this work all involve the vector potential contribution ψ_{mn} in (6). The scalar potential terms $\psi_{mn}^{\pm\mp}$ in (7) comprise only a single integration over the Hankel function which can be performed fairly efficiently. We also assume that the integration over the source region is performed accurately, since crude approximations of these integrations have previously been found to lead to poor results, particularly when the segments used to discretize the body are not equal in length. Several different approximations are commonly made in the evaluation of the vector potential term (6), however.

One approximation used to simplify (6) is to effectively evaluate the testing integration over the observation domain via a one-point rectangular rule integration. In this approximation, ψ_{mn} is evaluated at the observation point x_m and the result is multiplied by the length of the integration interval. Eq. (6) can then be written as

$$\psi_{mn} = \left(\frac{x_{m+1} - x_{m-1}}{2}\right) \int_{x_{n-1}}^{x_{n+1}} \Lambda_n(x')\, H_0^{(2)}(k|x_m - x'|)dx' \tag{8}$$

This approximation appears to be very efficient from a computational point of view since it eliminates the need for performing an additional numerical integration over the observation coordinates. One may further approximate (8) by replacing the triangle expansion function with a pulse expansion function of equivalent moment. This procedure simplifies the evaluation of the integral slightly, because the integrand is then of the same form as that of (7). The numerical integration procedure and the extraction of the singular behavior for self terms then becomes the same for both the vector and scalar potential terms. One may argue that the procedure is reasonable, because when the observation coordinate is outside the source region the integration in (8) should be relatively insensitive to the shape of the basis function, while for self terms the scalar potential contribution should be strongly dominant so that the shape of the basis function used in (8) is again relatively unimportant. When the triangle basis function is replaced by a pulse function, (8) becomes

$$\Psi_{mn} = \left(\frac{x_{n+1}-x_{n-1}}{2}\right) \int_{x_{n-1/2}}^{x_{n+1/2}} H_0^{(2)}(k|x_m-x'|)dx' \qquad (9)$$

A final approximation to be considered in this work is the replacement of the testing integration in (6) by a two-point evaluation procedure rather than the one-point evaluation used in (8). The two evaluation points used in this procedure are the points at the ends of the domain of each testing function. The motivation for this approach is that the observation coordinates used for the scalar potential and vector potential terms are then the same. The matrix computation procedure, thus, becomes slightly simpler and more efficient, because both contributions are evaluated more easily in the same source/observation loop. The computational advantages of this approach, as well as of the approximations described above, become more pronounced when three-dimensional scatterers are considered. The application of this approximation to (6) yields

$$\Psi_{mn} = (x_m-x_{m-1/2}) \int_{x_{n-1}}^{x_{n+1}} \Lambda_n(x')\, H_0^{(2)}(k|x_{m-1/2}-x'|)dx'$$

$$+ (x_{m+1/2}-x_m) \int_{x_{n-1}}^{x_{n+1}} \Lambda_n(x')\, H_0^{(2)}(k|x_{m+1/2}-x'|)dx' \qquad (10)$$

An approximation analogous to (10) is employed in the triangular patch code model for scattering by arbitrarily shaped objects [3].

Numerical Results

Numerical results have been obtained for the TE illuminated strip problem when each of the approximations indicated by (8)-(10) are used. In addition, a three-point "numerical integration" of the testing integration in (6) has been investigated for comparison. No higher order numerical integration was employed in the testing procedure because it was felt that the three-point integration could be implemented simply but could still provide an indication of the effect of a more accurate testing integration procedure.

Results are presented for several cases in Figs. 3 through 6 in the form of convergence plots for the current induced at the center of the PEC strip. In each plot the solution for the real and imaginary parts of the induced current at x=0 are plotted as a function of (1/N) where N is the number of unknown coefficients in the expansion for the current. The maximum number of unknowns used in each case is N=177. The curves may be extrapolated to (1/N)=0 to correspond to the expected solution if N were allowed to approach infinity. One generally expects to obtain reasonable results using equations (5)-(7) when about 7 unknowns per wavelength or more are used in the numerical model.

In Fig. 3 is shown convergence data for a strip of width 2w=1λ. The curve labeled "PA" (short dashes) refers to the use of (9) for Ψ_{mn} where the testing integration is replaced by a one-point evaluation and the triangle expansion functions have been approximated as pulses. The curves labeled "TE1" (solid lines) were obtained using (8) for Ψ_{mn} where the triangle expansion is retained, but a one-point approximation of the testing integration is performed. The curves labeled "TE2" (one long, two short dashes) in each case represent the use of (10) for Ψ_{mn} where the segment midpoints are employed in a two-point evaluation for the testing integration. The curves labeled "TE3" (dotted line) were obtained using the three-point "numerical integration" procedure to perform the testing integration in (6). For the 1λ strip we expect reasonable results for N≥7 (1/N≤0.143) and the convergence curves tend to confirm this expectation for each approach to the evaluation of (6). The dominant real part of the computed currents is almost the same for all methods for N≥7. The differences in the smaller imaginary part of the computed currents are more noticeable, but are still within reasonable limits.

Convergence data for a strip of width 2w=3λ is shown in Fig. 4. For this case reasonable results should be expected for N≥21 (1/N≤0.0476). One notes from the figure, however, that the deviations between results obtained with the various approximations are somewhat greater than those observed for the 1λ strip with the same number of unknowns per wavelength. Similar comments may be made for the 5λ-wide strip results of Fig. 5 and the 10λ-wide strip results of Fig. 6. For the 5λ strip accurate results would be expected for N≥35 (1/N≤0.0286), while for the 10λ strip the range would be N≥70 (1/N≤0.0143).

One may infer from the convergence data presented in Figs. 3-6 that, for a given number of unknowns per wavelength in the numerical model,

the use of (6) with numerical integration or of the approximation provided by (8) yields the most accurate numerical results, assuming that at least 7 unknowns per wavelength have been used. It should be noted that a specific "numerical integration" formula has been used with (6) to obtain the "TEJ" curves in the figures. Use of a different numerical integration scheme for the testing integration may produce either better or worse results. Furthermore, increasing the accuracy of the numerical integration by using a more complex formula may significantly increase the computation time required to obtain the solution for a given number of unknowns. On the other hand, if the triangle expansion function is retained and a one-point testing integration approximation is employed as in (8) one achieves a solution accuracy comparable to the direct use of (6), but without a significant increase in computation time.

References

[1] A.W. Glisson and D.R. Wilton, "Simple and efficient numerical methods for problems of electromagnetic radiation and scattering from surfaces," IEEE Trans. Antennas Propagat., Vol. AP-28, pp. 593-603, Sept. 1980.

[2] J.C. Logan and J.W. Rockway, "The new MININEC (Version 3): A mini-numerical electromagnetic code," Technical Document NOSC TD 938, Naval Ocean Systems Center, San Diego, CA, Sept. 1986.

[3] S.M Rao, D.R. Wilton, and A.W. Glisson, "Electromagnetic scattering by surfaces of arbitrary shape," IEEE Trans. Antennas Propagat., Vol. AP-30, pp. 409-418, May 1982.

[4] R.F. Harrington, Field Computation by Moment Methods, New York: Macmillan, 1968.

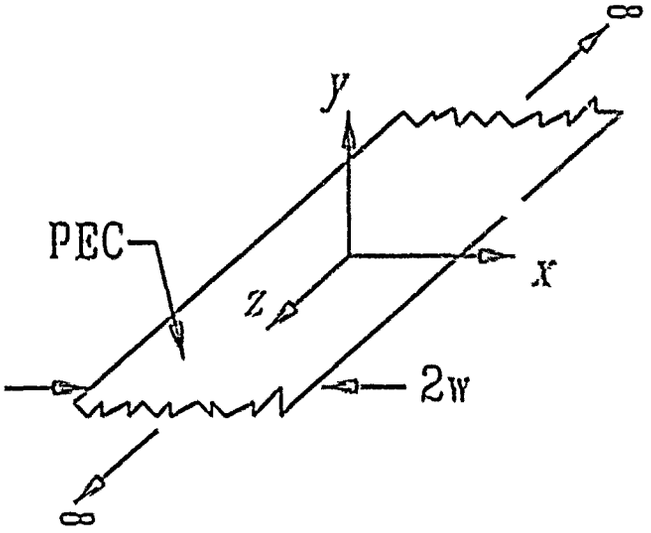


Fig. 1. Two-dimensional strip geometry.

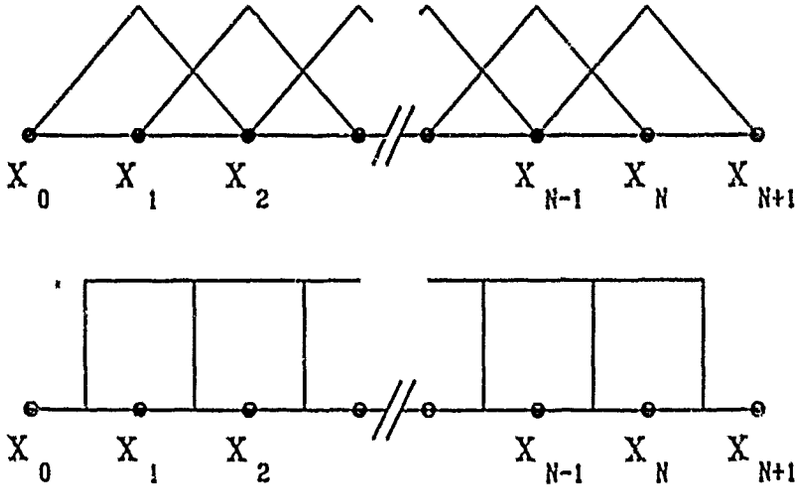


Fig. 2. Triangle expansion functions and pulse testing functions used in the mixed-potential integral equation.

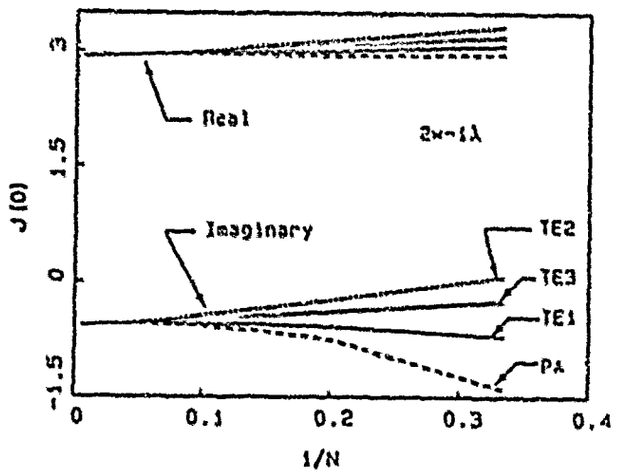


Fig. 3. Convergence of center current for a strip of width 1λ.

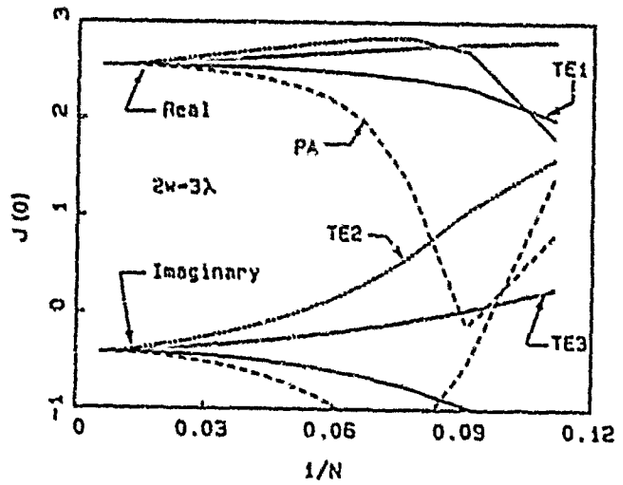


Fig. 4. Convergence of center current for a strip of width 3λ.

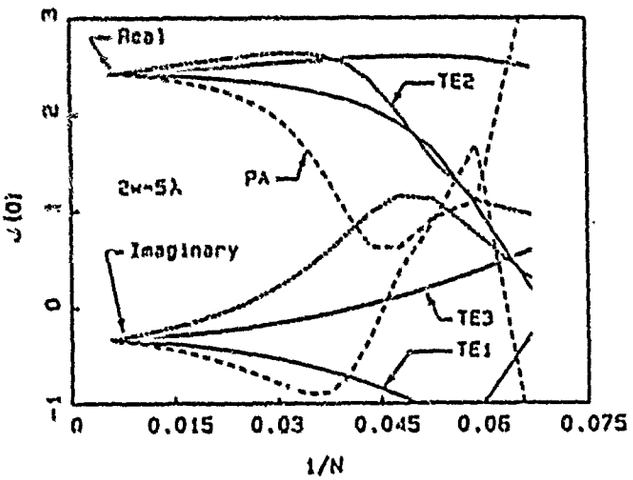


Fig. 5. Convergence of center current for a strip of width 5λ.

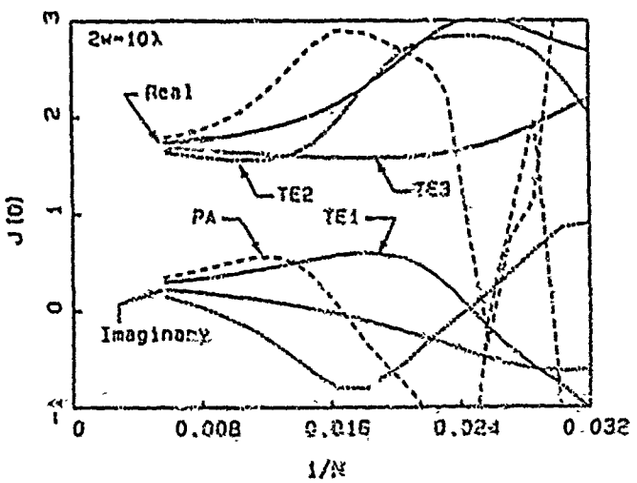


Fig. 6. Convergence of center current for a strip of width 10λ.

Exploitation of Structural Symmetries for the Solution of Huge Matrices

E. K. Miller*
General Research Corporation

K. Kalbasi
University of Kansas

K. R. Demarest
University of Kansas

The drawback of direct methods of solving a very large linear system of equations is the enormous computational cost involved. This limitation arises from the N^2 and N^3 fill and solve time requirements of these systems, where N is the number of unknowns in the problem. These requirements, especially the N^3 one, narrow the scope of geometries that can be modeled in many disciplines.

The ability to solve systems of equations with thousands of unknowns not only increases the range of geometries that can be analyzed in electromagnetic modeling, but extends further into areas such as investigation of effect of round-off for very large arithmatic operations, establishing benchmarks for certain applications, and observing the effect of forced sparsity into matrices resulting from EM modeling.

This paper describes an application of utilizing symmetry as a viable tool in the EM modeling of electrically large scatterers with certain symmetries. The three basic types of symmetries, i.e., reflection, translation and rotation exist singly or in combination in many geometries of interest. An example is a coaxial array of parallel regular polygons (or a cylindrical array of open-ended wires), which has all three types of symmetries. The resulting impedance matrix for this geometry, given the right numbering system, is block-circulant with Toeplitz blocks.

A Fourier transform technique making use of the rotational symmetry of this structure, in conjunction with a Toeplitz solver utilizing its translational symmetry, is implemented on this structure to show the huge amount of savings obtained. The analytical formulation of the problem as well as estimates of the number of operations involved for all three types of symmetries individually and combined, is presented. The algorithm developed is tested by solving a problem with thousands of unknowns and gains obtained are compared with predictions, as well as with cases where symmetries are not exploited. Finally, this geometry is used to investigate the effect of Near Neighbor Approximation (*NNA*) on a very large problem.

INTRODUCTION

The continuing revolution in microelectronics will decrease the cost of computing and increase the speed and memory available. These computer hardware improvements will increase current capabilities of available codes only to a limited extent. Additional capabilities must come from more efficient algorithms. Computational Electromagnetics, similar to many other disciplines, confronts a miriad of problems that, although analytically solvable, are not fit to be implemented on available computing machines because of their enourmous storage and CPU requirements. This paper adresses one of the many possible remedies that could be used towards developing more efficient codes by exploiting the underlying structural symmetries of a model. We will show that exploitation of any of three types of symmetries, namely rotation, translation and reflection, individually or combined, could decrease the computational burden drastically.

THE COST OF INTEGRAL EQUATION MODELING

In integral equation modeling (such as MoM), one eventually must solve a system of linear equations of the form:

$$[Z][I] = [V],$$

where Z is the matrix of interactions and I and V are the unknown and excitation vectors, resectively. The time for filling the matrix Z, of order N, and then solving this equation using direct solvers, such as Gaussian Elimination, is estimated in terms of number of arithmatic operations to be

$$T \approx A_{fill}N^2 + A_{solve}N^3,$$

with the N^3 requirement being the dominating factor. According to a study [1], inversion of a complex matrix of some 4000 coefficients per row takes about 120 hours of CPU time on a virtual memory machine (VAX-11/785).

TYPES OF SYMMETRY

The three types of symmetries mentioned above exist in a variety of structures [2]. Rotational symmetry exists when the object is created upon rotation through n (discrete) steps, each equal to $2\pi/n$ radians (loops, polygons, right circular cylinders,...). The resulting impedance matrix for a structure with this type of symmetry is circulant or block circulant and the corresponding time of filling and solving is

$$T \approx A_{fill}N^2/n + A_{solve}m(N/n)^3,$$

where m is the number of excited modes and varies as $1 \leq m \leq N$.

Similarly, translational symmetry can be defined as the rectilinear translation of some fixed shape (e.g., a straight wire). The matrix representation of structures of this type is Toeplitz, with the following time for filling and solving:

$$T \approx A_{fill}N + A_{solve}n_z^3[l((log_2 l)^2].$$

Here $n_s = N/t$ is the number of unknowns per t cross sections in the direction of translation, and the $t(log_2 t)$ term arises from transforming the Toeplitz matrix of order t into a circulant matrix of order $2t$ [2].

Finally, reflection of an object about one, two or three planes results in a source/image pair with similar self- and coupled-interaction blocks. The case of an object above a perfect conductor or ground plane is of this type. The direct matrix takes the form:

$$Z = \begin{bmatrix} Z_{ss} & Z_{si} \\ Z_{is} & Z_{ii} \end{bmatrix}$$

$$Z_{ii} = Z_{ss} \quad , \quad Z_{si} = Z_{is}$$

$$T \approx A_{fill} N^2/2^p + A_{solve} m(N/2^p)^3,$$

where p is the number of reflection planes and m is the number of excitation modes, varying according to $m = 1, 2, \ldots 2^p$. The subscripts s and i stand for source and its image, respectively.

To show the combined computational savings of exploiting all these symmetries, two structuctures possessing all three symmetries were studied. These structures were a right circular cylinder composed of open-ended wires, and a coaxial array of regular polygons, both shown in Figure 1. The goal was to develop a block circulant matrix with Toeplitz blocks so that full advantage of both symmetries could be taken. In both cases, a top-down numbering scheme was chosen in order to obtain the proposed matrix structure. Each individual wire (or loop) was excited in one segment via a voltage source.

THE ALGORITHM

In order to develop the algorithm, a fourier transform pair is introduced to transform Toeplitz block and corresponding excitation vector.

$$V_i = \sum_{k=1}^{m} S_{ik} \tilde{V}_k, \qquad \tilde{V}_i = \frac{1}{m} \sum_{k=1}^{m} S_{ik}^* V_k$$

$$Z_i = \sum_{k=1}^{m} S_{ik} \tilde{Z}_k, \qquad \tilde{Z}_i = \frac{1}{m} \sum_{k=1}^{m} S_{ik}^* Z_k,$$

where the transform operator S is defined as a function of indicies of blocks and m, the total number of rotational steps as

$$S_{ik} = \exp j2\pi(i-1)(k-1)/m.$$

Once all transformed blocks, $\tilde{Z}_i$ and $\tilde{V}_i$, have been obtained, the equation $\tilde{Z}_i = \tilde{I}_i \tilde{V}_i$ is solved using a Toeplitz solver and then transformed back to yield

$$I_i = \sum_{k=1}^{m} S_{ik} \tilde{I}_k \qquad i = 1, \ldots, m$$

The symmetric properties of original Z matrix are preserved in transformed domian, i.e., transformed blocks are still Toeplitz and reflection symmetry holds.

This algorithm decreases the total arithmatic operations as outlined in Figure 2. To see the implications, consider a case where $N_x \cong N_y$. Here, the costs are approximately $\sqrt{2}N^2, 2N^{\frac{1}{2}}$ and $N^{\frac{1}{2}}$ for rotation only, rotation + translation and all three symmetries combined, respectively (see Figure 3). These costs should be compared with those of direct solvers, which are on the order of N^2 operations.

The algorithm described above was implemented on a VAX-11/750 in conjunction with both the NEC [3] and Richmond [4] codes. In many respects, NEC was particularly well suited for this study. It requires fewer page faults because of the symmetry exploitation already built into it. However, due to its treatment of edges on thin wires, the matrix generated is not a "perfect" Toeplitz. For this reason, the Richmond code was used for cylindrical array of open-ended wires and NEC for the array of parallel loops.

The fill and solve times were recorded for different number of unknowns as shown in Figure 4. The CPU times were somehow higher than our predictions, due mainly to the paging required in and out of CPU in a virtual memory machine. The maximum number of unknowns that a VAX-11/780 (with limited page fault quota) could handle was 64000. This limitation was due to the increased memory required by these codes for other auxiliary functions as the number of unknowns is increased. If this page fault quota had not been in place, the solution of a system of equations in the order of 1000,000 would have been possible.

AN APPLICATION EXAMPLE

To show the usefulness of such an algorithm, a series of numerical experiments were conducted to determine the solution errors induced by systematically neglecting impedance couplings of distant subsections of the geometry. This can be termed a Near Neighbor Approximation (NNA). This algorithm is an ideal test-bed for tracing the effects of the NNA on extremely large structures, since the "exact" solutions are so easily calculated. We implemented three thinning strategies on a matrix with 10,000 coefficients per row and compared the resulting "approximate" solution with the exact one . These strategies were

1. NNA based on keeping only internal couplings within specified wires while other wire-wire couplings are ignored. The sparse matrix that is solved is then a singly block banded matrix. The resulting current distribution as well as mean square error as a function of window of interactions that are kept is shown in Figure 5.
2. NNA based on keeping interactions within a cylindrical window, which results in a multiply block-banded sparse matrix with equal bands. The corresponding current distribution, as well a mean square error (MSE) as a function of bandwith, is shown in Figure 6.
3. Finally, a NNA strategy based on keeping interactions that are within a distance threshold in a 3-D sense was examined. The resulting sparse matrix is again multiply-block-banded but with unequal bands. The error function and current distributions are shown in Figure 7.

SUMMARY

In this paper, we have shown that the exploitation of symmetry is a viable means worth considering, especially when large and dense matrices are to be solved . The amount of savings obtained depends on the degree and type of structural symmetries that exist in a given geometry. Furthermore, special symmetrical problems can be used as a test-bed to investigate other techniques that require the exact solutions of very large systems of equations for comparison. Finally, these special test-beds can be exploited to set benchmarks in areas such as study of round-off in extensive computations.

REFERENCES

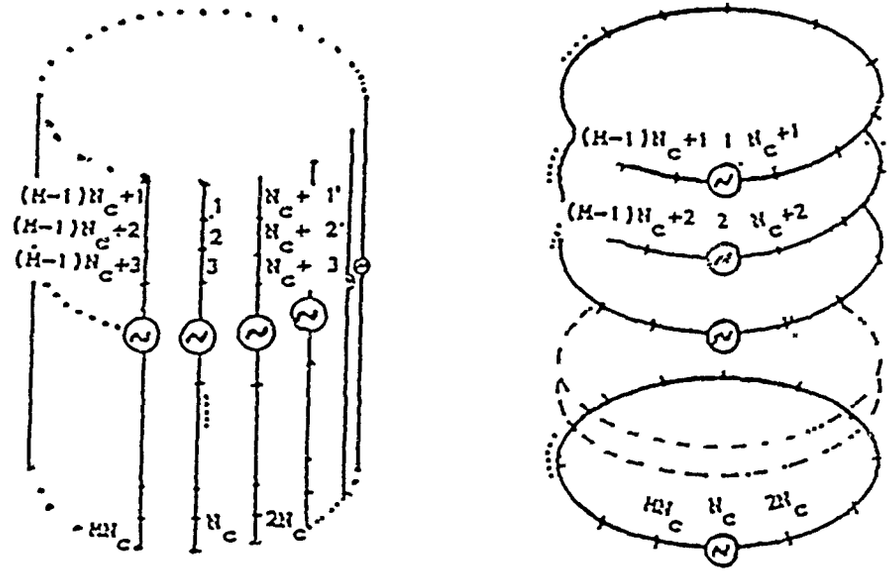
[1] J. L. Fath and A. J. Terzuoli : "Large Matrix Problems in the Computation of Electromagnetic Fields," *IEEE APS International Symposium Digest*, June 1987, pp. 502-504.

[2] E. K. Miller : "A Selective Survey of Computational Electromagnetics ," *IEEE Trans. Antennas Propagat., vol AP-36, pp.1281-1305, Sep. 1988.*

[3] G. J. Burke and A. J. Poggio : " Numerical Electromagnetic Code (NEC) ; Method of Moments, Part I, II, and III," *Technical Document No. 116.*, Lawrence Livermore National Laboratory, Livermore CA 94550.

[4] J. H. Richmond : " Computer Program for Thin Wire Structures in a Homogeneous Conducting Medium," NASA CR-2399 Report.

- A structure having all three types of symmetries would be a
  - Right circular cylander composed of open-ended wire or
  - Coaxial array of regular polygons



cylindrical wire array

parallel loops

Figure 1

Operation count

- Rotation Symmetry only :
  - For each $\tilde{Z}_i$ need $N_s N_p^2$ FLOPS
  - For each $\tilde{V}_i$ need $N_s N_p$ FLOPS
  - Solving for each $\tilde{I}_i$ requires N_p FLOPS
  - Inverse Transform for each I_i needs $N_s N_p$ FLOPS

$$Total = N_s^2 N_p^2 + 2N_s^2 N_p + N_s N_p^3$$

- Rotation+Translation Symmetries :

$$Total = 3N_s^2 N_p + N_s N_p^2$$

- Rotation+Translation+Reflection Symmetries :

$$Total = \frac{3}{4} N_s^2 N_p + \frac{1}{2} N_s N_p^2$$

Figure 2

- To see the implications, consider a case where

$$N_s = N_p$$

  - Direct solvers :

$$(N_s N_p)^3 = N_s^6 = N^3$$

  - Rotation symmetry only :

$$2(N_s^4 + N_s^3) \approx \sqrt{2} N^2$$

  - Rotation + Translation :

$$3N_s^2 N_p + N_s N_p^2 \approx 4N_s^3 = 2N^{\frac{3}{2}}$$

  - Rotation + Translation + Reflection :

$$2.5N_s^2 N_p + N_s N_p^2 \approx 3.5N_s^3 \approx N^{\frac{3}{2}}$$

Figure 3

RESULT

- Using above model a matrix of order 64000 was solved in less than half an hour

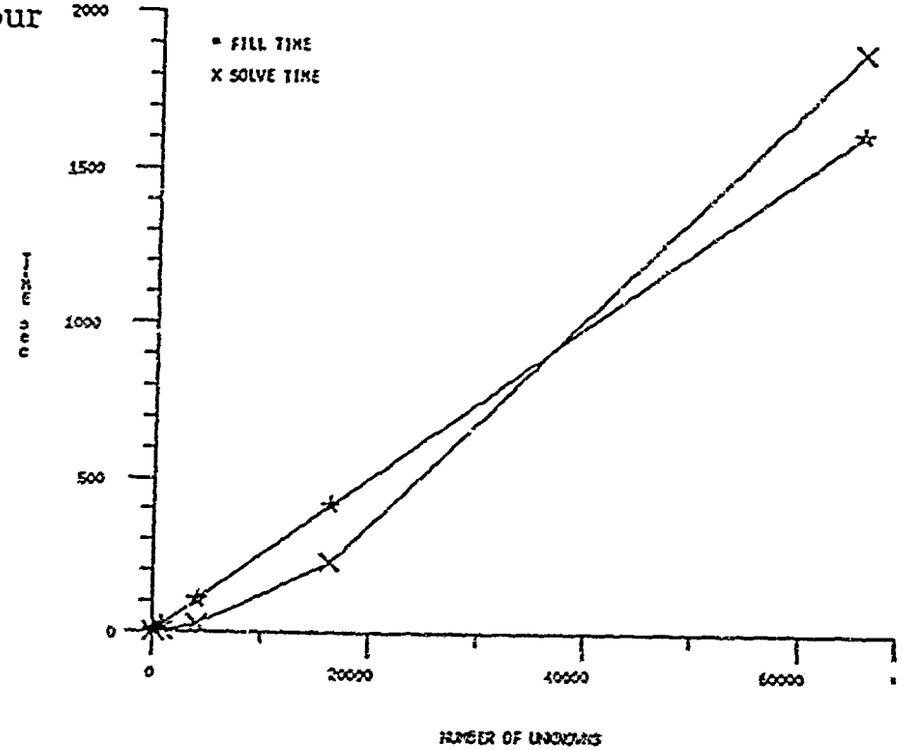


Figure 4

RESULTS

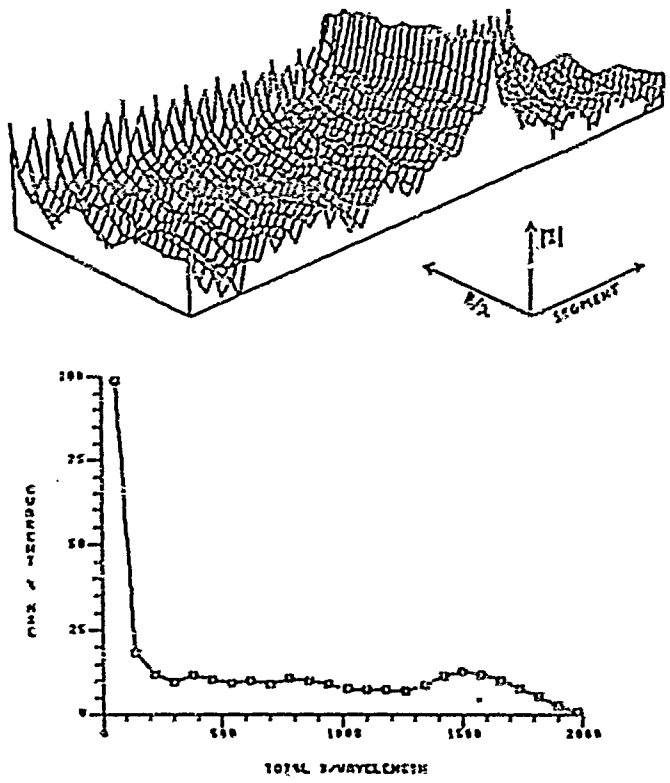


Figure 35. The Current Distribution (a) and MSE (b) of a Cylindrical Array of Wires as a Function of Window Size (Method One).

Figure 5

RESULTS

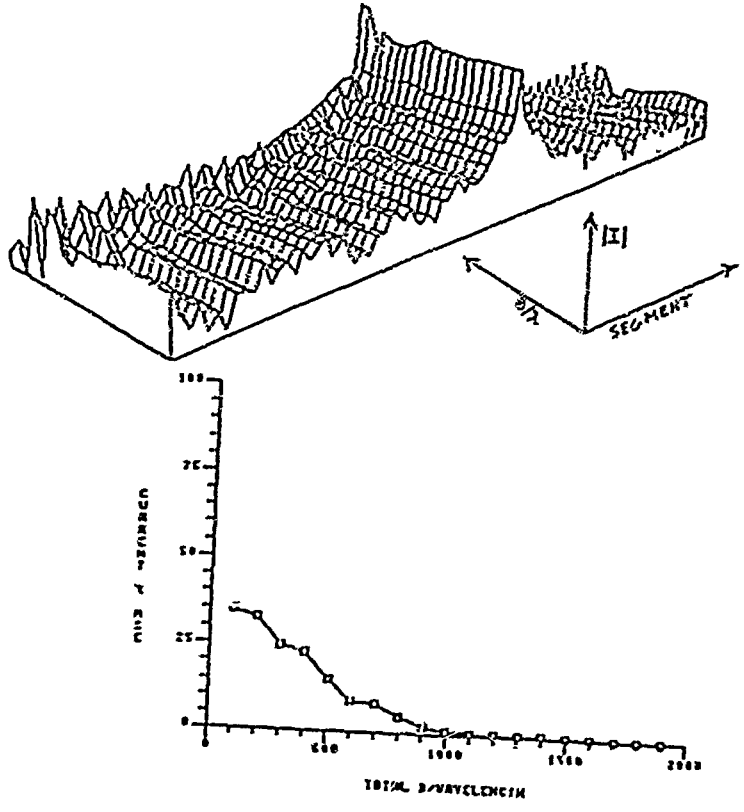


Figure 16. The Current Distribution (a) and MSE (b) of a Cylindrical Array of Wires as a Function of Window Size (Method Two).

Figure 8

RESULTS

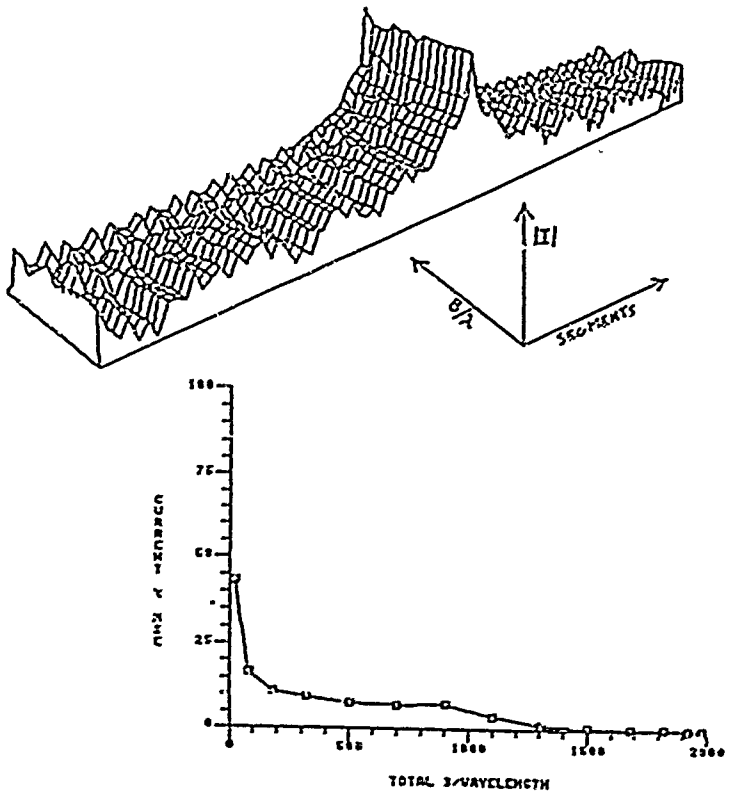


Figure 37. The Current Distribution (a) and MSE (b) of a Cylindrical Array of Wires as a Function of Window Size (Method Three).

Figure 7

HOW EFFICIENTLY TO CALCULATE MATRIX CONDITION NUMBERS AND THE ERROR BOUNDS THEY GENERATE

Francis X. Canning
Rockwell Science Center
1049 Camino Dos Rios
Thousand Oaks, CA 91360

ABSTRACT

It is suggested that when problems in electromagnetic field computation involving matrix equations are solved, it is appropriate to routinely calculate the matrix condition number, κ. The first reason given is that κ gives important information on both the desirability of the numerical formulation of the problem, and on the correctness of the geometrical specification of the scatterer. The second reason given is that any of several definitions of κ may be computed in a negligible additional time (say onepercent extra) once the matrix has been LU decomposed. Several well known methods for computing κ are given, as is the bound on accuracy of the answer that it provides. Finally, some considerations in programming these methods for computing κ are given.

I Definition of the condition number, κ

The paper begins by defining the condition number, κ, of a matrix and how its definition depends upon the matrix norm used. Throughout this paper, only consider square matrices composed of complex numbers will be considered. For a matrix Z, its condition number, $\kappa(Z)$, is defined as:

$$\kappa(Z) == ||Z|| \cdot ||Z^{-1}|| \qquad (1)$$

Clearly the definition of κ depends upon the matrix norm used. Often this is signified by writing the norm as a subscript to κ.

One class of matrix norms, the p-norms, are defined by

$$||Z||_p == \max_{(x)} \{||Zx||_p / ||x||_p\} \qquad (2)$$

The matrix p-norms are in turn defined in terms of the vector p-norms. The three vector p-norms of interest to us are:

$$||x||_1 = |x_1| + |x_2| + |x_3| + \ldots + |x_n| \quad (3)$$

$$||x||_2 = (|x_1|^2 + |x_2|^2 + \ldots + |x_n|^2)^{1/2} \quad (4)$$

$$||x||_{oo} = \max_m \{|x_m|\} \quad (5)$$

We note that it is easy to show that the matrix:

1-norm is the largest column-sum
2-norm is the largest singular value
oo-norm is the largest row-sum.

For example, the largest matrix column-sum is defined as follows. For each column of the matrix, one sums the absolute values of the elements in that column. The largest sum that one obtains, then gives the 1-norm of that matrix. Putting these definitions together, we find that the condition numbers in the one and infinity norms respectively are:

$$\kappa_1 = \text{largest col-sum}[Z] \cdot \text{largest col-sum}[Z^{-1}] \quad (6)$$

$$\kappa_{oo} = \text{largest rowsum}[Z] \cdot \text{largest rowsum}[Z^{-1}] \quad (7)$$

NOTE: This is easy to compute once Z^{-1} is found. However, calculating Z^{-1} takes 4 x as long as finding its LU decomposition. Thus, these formulas are appropriate as definitions, but not useful for efficient computation.

Consider now the two-norm. If λ_{max} is the maximum eigenvalue of Z, then we have:

$$\max_{\{x\}} ||Zx||_2/||x||_2 \quad \{ = \lambda_{max} \quad \text{If Z is Hermitian} \quad (8)$$

$$\{>= |\lambda_{max}| \quad \text{For all Z} \quad (9)$$

$$\{ = |\lambda_{max}| \quad \text{If Z is normal} \quad (10)$$

$$\{ = \sigma_{max} \quad \text{For all Z} \quad (11)$$

Where $\sigma_i^2(Z) == \lambda_i(Z^h Z)$

In the past, some authors have used the eigenvalues of matrices arising in electromagnetics as a guide to estimating the condition number of those matrices. There is really no need to do so, since the actual condition number can be calculated very easily and efficiently. In fact, this approximation of the singular values by the eigenvalues, for a non-Hermitian matrix, is unjustified and may lead to large errors. For example, consider the non-symmetric real matrix discussed by Moler [1]:

$$
Z = \begin{pmatrix} -149 & -50 & -154 \\ 537 & 180 & 546 \\ -27 & -9 & -25 \end{pmatrix} \quad \begin{matrix} \lambda_1 = 3 & \sigma_1 = 817.760 \\ \lambda_2 = 2 & \sigma_2 = 2.47497 \\ \lambda_3 = 1 & \sigma_3 = 0.0029645 \end{matrix} \qquad (12)
$$

The eigenvectors of this matrix are 1, 2, and 3. If one were to approximate the singular values of this matrix by its eigenvalues, then one would think its condition number, κ_2, was equal to three. The actual condition number of Z is almost five orders of magnitude larger! That means that Z is actually quite poorly conditioned. Moler also discussed the matrix:

$$
Z+\Delta Z = \begin{pmatrix} -149.00060 & -49.99807 & -154.00004 \\ 536.99980 & 180.00063 & 545.99998 \\ -27.00061 & -8.99803 & -25.00004 \end{pmatrix}
$$

$$
\lambda_3 = \sigma_3 = 0.00000... \qquad (13)
$$

Note that, within the accuracy of single precision, Z and Z+ΔZ are the same matrix. However, Z has eigenvalues of 1, 2, and 3 while Z+ΔZ is singular.

II Bounds generated by κ

Consider the matrix problem given by

$$
Z J = V \qquad (14)
$$

Due to errors in representing V and Z, one actually solves the matrix problem for a modified J, i.e. J+δJ, given as:

$$(Z + \delta Z)\,(J + \delta J) = V + \delta V \qquad (15)$$

A bound for the change in J due to the "errors" in V and Z is [2];

$$\frac{\|\delta J\|}{\|J\|} \le \kappa \frac{2\max\{\|\delta Z\|/\|Z\|,\ \|\delta V\|/\|V\|\}}{1 - \kappa\,\|\delta Z\|/\|Z\|} \qquad (16)$$

Eq.(16) applies for any of the norms mentioned, provided that κ is also given in that norm.

III How (efficiently) to calculate κ

A Strategy - {in the 1-Norm
{in the 00-Norm

a) Calculate {$\|Z\|_{00}$ as the largest rowsum
{$\|Z\|_1$ as the largest col-sum

b) Calculate $\|Z^{-1}\|$ by:
i) Choose x_0
ii) Solve $U^h L^h a = x_0$ for a ($Z=LU$; $Z^h=U^h L^h$) (17)
iii) Solve LU b = a (18)
iv) $\|Z^{-1}\| >= \|b\| / \|a\|$
v) Approximate: $\|Z^{-1}\| \sim \|b\| / \|a\|$
c) Calculate an approximation to κ by
$\kappa \sim \|Z\|\ \|b\| / \|a\|$

Linpack [3] uses this procedure in the one- norm for its condition number estimator. In addition, it has an algorithm for picking x_0 so that the inequality in b-iv will generally be close to an equality.

A Strategy in the 2-Norm

Let λ_m and e_m be eigenvalues and eigenvectors of Z^hZ

a) Choose x_0

b) Decompose x_0 as:

$$x_0 = \lambda_1 e_1 + \lambda_2 e_2 + \lambda_3 e_3 + \ldots + \lambda_n e_n$$

$$\text{where } \lambda_1 >= \lambda_2 >= \lambda_3 >= \ldots >= \lambda_n >= 0$$

c) Define $x_m = Z^hZ\, x_{m-1}$

$$= \lambda_1^m e_1 + \lambda_2^m e_2 + \ldots + \lambda_n^m e_n$$

$$\sim \lambda_1^m e_1$$

d) Choose $x'_0 = x_0$

e) Define $x'_m = (Z^hZ)^{-1}\, x'_{m-1}$

$$= \lambda_1^{-m} e_1 + \lambda_2^{-m} e_2 + \ldots + \lambda_n^{-m}$$

$$\sim \lambda_n^{-m} e_n$$

f) Approximate $\lambda_1 \sim ||x_m|| \,/\, ||x_{m-1}||$, in any norm

g) Calculate $||Z||_2 = \lambda_1^{1/2} \sim [||x_m|| \,/\, ||x_{m-1}||]^{1/2}$

h) Approximate $\lambda_n^{-1} \sim ||x'_m||/||x'_{m-1}||$, in any norm

i) Calc. $||Z^{-1}||_2 = \lambda_n^{-1/2} \sim [||x'_m||/||x'_{m-1}||]^{-1/2}$

j) Finally, $\kappa_2(Z) \sim ||Z||_2 \;\; ||Z^{-1}||_2$

IV Computational Issues

All of the methods given are $O(N^2)$. This means that they

require a negligible amount of computer time compared to the $O(N^3)$ time necessary for the LU decomposition of Z. Efficient subroutines already exist. For instance, Linpack uses the method given above for the one-norm (see: CGECO). It is attractive to simply use the subroutines in Linpack, unless one needs code that vectorizes on a given machine, or possibly if there are severe memory problems. All of the above methods are easy to program, so you may take your choice. My personal bias, is that the 2-Norm is the best. Also, by iterating, one can see when the estimate stabilizes, and thus control the error in the answer. Since this is only an $O(N^2)$ process, the extra time is not significant. One can further increase the convergence rate by using a sophisticated choice for x_0 as is done in Linpack [3]. For some related papers relating to condition numbers in electromagnetics and their computation, see [4] - [6].

There is one hint that will help in programming the calculation of any of the condition numbers mentioned above. Assuming that one already has routines for finding the LU decomposition of a matrix Z, he probably also has routines for solving for a in:

$$Z^h a = x_0 \qquad (19)$$

It also is necessary, however to solve:

$$Z b = a \qquad (20)$$

Actually, the equations given above (Eq. (17), (18)) were oversimplified, since when one uses partial pivoting (as is nearly universally done), the "LU decomposition of Z with partial pivoting" gives:

$$LU b = P a \qquad (21)$$

where P is a matrix that permutes rows. Since P is a unitary matrix, we also have

$$Z = P^h LU; \text{ and } Z^h = U^h L^h P \qquad (22)$$

If we first solve for the product (Pa) in

$$U^h L^h \ (Pa) = x_0 \qquad (23)$$

then we may solve for b in

$$LU\ b = Pa \qquad (24)$$

We never really need to find a since

$$||Pa|| = ||a|| \qquad (25)$$

for the norms considered above. Since U^h is lower triangular and L^h is upper triangular, $U^h L^h$ is the LU decomposition of $Z^h P^h$. Thus, in writing a routine for solving Eq. (23), one can copy the routine for solving Eq. (21). However, if L had ones on its diagonal, one must account for those ones being on the diagonal of the upper triangular matrix L^h in Eq. (23). Again, Linpack already has the subroutines for solving both Eq. (21) and (23). One either can use those as is, or as a model for writing a specialized version.

V Practical Issues

It has been shown that one can calculate the matrix condition number of the matrices arising in electromagnetics with little

effort and little computational cost whenever one already is calculating their LU decomposition. One should routinely calculate this condition number, since it can provide valuable information. A bound on the accuracy of the resulting calculation of the current was given earlier. On a more practical note, an abnormally large condition number in a routine calculation often signifies that the geometry was not specified in a desirable manner. This is especially important when a non-expert user is running a program. The program can automatically warn him that the results may not be reliable, and that further attention is advisable. Condition numbers are also helpful in code development, for a variety of reasons.

REFERENCES

1) Cleve B. Moler, "Three Research Problems in Numerical Linear Algebra," in "Proceedings of Symposia in Applied Mathematics," Vol XXII, American Mathematical Society, 1980.

2) G. H. Golub and C. F. Van Loan, " Matrix Computations," The Johns Hopkins Press, Baltimore, 1983.

3) J. J. Dongarra et al.,"Linpack Users Guide," SIAM, Philadelphia, 1979.

4) F. X. Canning, "Protecting Scattering Computations from Effects of Interior Resonances," Proceedings of the 4th Annual Review of Progress in Applied Computational Electromagnetics, March 1988.

5) F. X. Canning, "Singular Value Decomposition of Integral Equations of EM and Applications to the Cavity Resonance Problem," IEEE Transactions on Antennas and Propagation, September 1989.

6) F. X. Canning, "Protecting EFIE Based Scattering Computations from Effects of Interior Resonances," Submitted to IEEE Transactions on Antennas and Propagation.

SESSION 10 - "INPUT/ OUTPUT AND INTERFACE ISSUES"

Chairman: Frank Walker

TRIANGULATION OF ARBITRARILY SHAPED GEOMETRIC MODELS FOR METHOD-OF-MOMENTS APPLICATIONS

D.L. Wilkes, Dr. C.C. Cha

Syracuse Research Corporation
Merrill Lane
Syracuse, New York 13210

ABSTRACT

A number of CAD packages exist that allow for easy construction of objects composed of simple, canonical shapes which can be used by high-frequency scattering prediction software packages. One such modeling package will be considered here is the Syracuse Research Corporation Computer-Aided Modeling Package (SCAMP). These geometric models are usually not directly usable for low-frequency scattering prediction codes such as those using the method of moments. Method-of-moments packages generally require geometric models that are composed of a number of localized subdomains such as triangular patches that are connected in such a way as to ensure proper electrical continuity.

A software package has been written that can perform all of the appropriate conversions so that a model that was built using SCAMP can be used by a triangular patch method-of-moments software package. The model can be arbitrarily shaped; consisting of any number of generalized frusta and triangulated shapes. The operation of this model conversion package will be described.

Three basic steps must be performed to convert an arbitrarily shaped model into the appropriate triangular patch format: (1) to triangulate all of the objects, (2) the intersection between these triangulated objects must be found, and (3) to retriangulate the regions of intersection, taking care to ensure that the model satisfies the requirements imposed by the method-of-moments technique.

1.0 INTRODUCTION

This paper discusses a software package which converts an arbitrarily shaped computer-generated geometric model into a format that is suitable for applications which utilize the method of moments. The moment method formulation which we are using is based on the work done by Rao, Wilton, and Glisson, 1982. The surface of an object is modeled by triangular patches and the corresponding basis function is triangular.

The work presented here represents an extension of an existing CAD modeling package that was developed for use by a scattering prediction code which employs high-frequency, asymptotic techniques. This modeling package (SCAMP) allows for the creation of two types of geometric objects. The first is a surface that is represented by triangular patches, and is thus suitable for moment method applications. The second is a class of canonical shapes that are referred to as generalized ellipsoidal frusta. Furthermore, construction of an arbitrary geometric model is typically accomplished by modeling each component shape in a model separately. While this approach is suitable for high-frequency scattering predictions, it will yield inaccurate results in the low-frequency region.

Therefore, to convert an arbitrary model built with the SCAMP modeling package into a suitable triangular patch format, two general functions need to be performed. The first is the triangulation of any generalized ellipsoidal frusta shapes. The second is to find the intersection of any two objects and connect them appropriately.

2.0 TRIANGULATION OF GENERALIZED ELLIPSOIDAL FRUSTA

The first step in converting an arbitrary geometric model for use by a method-of-moments application is to triangulate any generalized frusta in the model. A generalized frusta can be described by two parametric variables, t and ζ, where the t variable is along the length of the object and the ζ is an angle around the circumference.

A generalized frusta can be triangulated by dividing it up into sections along its length and then breaking up each section into divisions around its circumference. Some examples of this process are shown in Figure 1.

3.0 CONNECTION OF TWO TRIANGULATED OBJECTS

Once a geometric model is comprised solely of triangular patch objects, it remains to connect any objects which are intersecting but not yet physically connected. As sketched in Figure 2, the nature of the intersection between two triangles is different for the coplanar and non-coplanar cases. For the non-coplanar case, the intersection is in the form of a line segment, while for the coplanar case, the general form of the region of intersection is a polygon. When two triangles intersect, we will use the notation "cutlines" to describe the line segment at the intersection and "cutpoints" to describe the two endpoints of this line segment.

The algorithms for both cases are comprised of two basic steps. The first step is to find and define all of the intersections between the two objects. This is done by comparing each triangle in one object with each triangle in the second object. Then, the second step is to retriangulate the triangular patches which contain these intersections.

3.1 Intersection of Two Non-Coplanar Triangles

To find these cutlines, an algorithm based on work done at the University of Missouri-Rolla and McDonnell Douglas Aircraft Company (Sabharwal and Nelson, 1988) was utilized. The two triangles and the line formed by the intersection of the planes which contain the two triangles are parameterized. Then ordinary differential equations are used to see if the two triangles intersect and, if they do, the two cutpoints are then found.

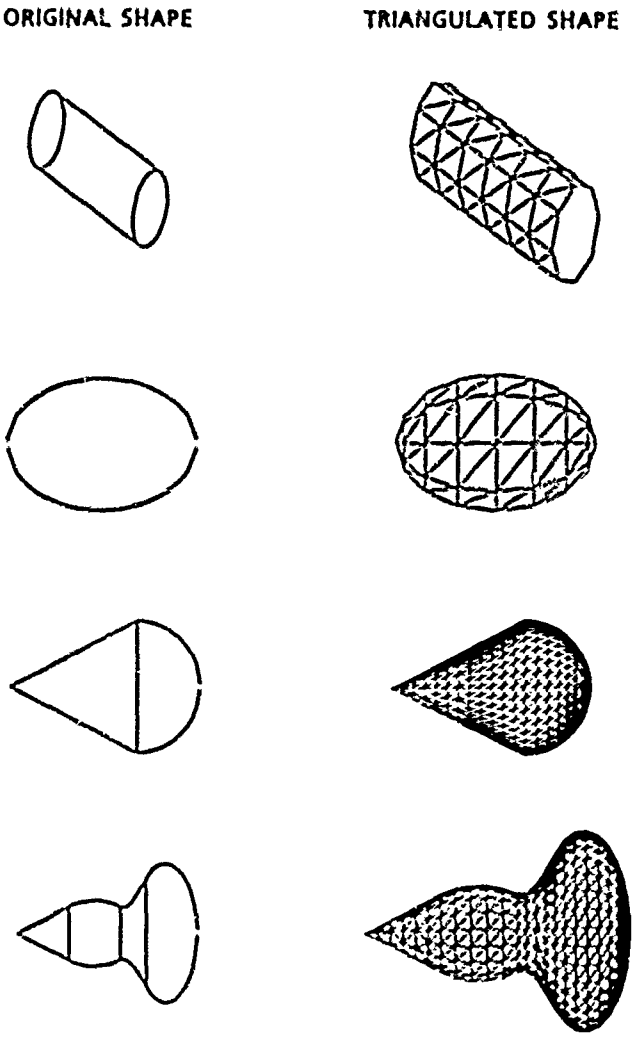
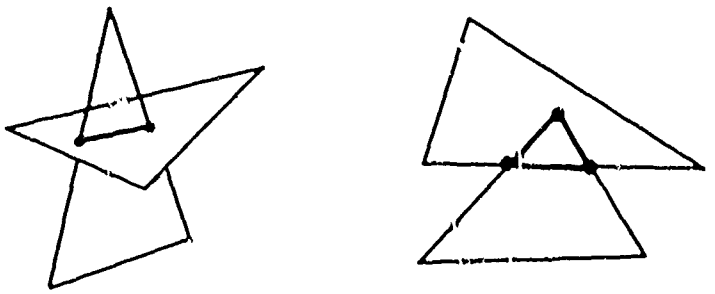


Figure 1. Triangulation of Generalized Frusta



(a) Non-Coplanar (b) Coplanar

Figure 2. Intersection of Two Triangles

For the vectors defined in Figure 3, the parametric equations of the two triangles can be written as follows:

$$\underline{R}_1(p,q) = \underline{A} + p\underline{P} + q\underline{Q} \qquad 0 \le p,q,p+q \le 1 \tag{3}$$

$$\underline{R}_2(u,v) = \underline{B} + u\underline{U} + v\underline{V} \qquad 0 \le u,v,u+v \le 1 \tag{4}$$

and the corresponding normal vectors can be defined as:

$$\underline{N}_1 = \underline{P} \times \underline{Q} \tag{5}$$

$$\underline{N}_2 = \underline{U} \times \underline{V} \tag{6}$$

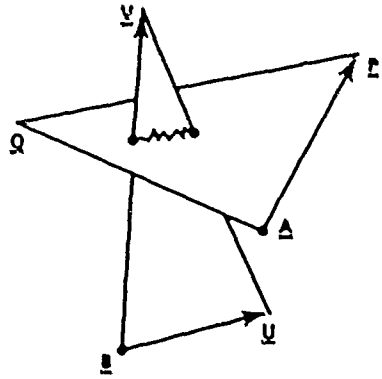


Figure 3. Intersection of Two Crossed Triangles

The requirement that the two triangles be non-coplanar ensures that $\underline{N}_1 \times \underline{N}_2 \neq 0$. Thus, the equation of the intersection of the planes which contain triangles A and B can be parametrically represented as

$$\underline{R}(t) = \underline{C} + t\, \underline{N}_1 \times \underline{N}_2 \tag{7}$$

The expressions for the triangle parameters p, q, u, and v, in terms of the parameter t, are found by differentiating the three parametric equations 3, 4, and 7. The resulting equations are found to be:

$$p(t) = -\underline{Q} \cdot \underline{N}_2\, t + C_p \tag{8}$$

$$q(t) = \underline{P} \cdot \underline{N}_2\, t + C_q \tag{9}$$

$$u(t) = \underline{V} \cdot \underline{N}_1\, t + C_u \tag{10}$$

$$v(t) = -\underline{U} \cdot \underline{N}_1\, t + C_v \tag{11}$$

where C_p, C_q, C_u, and C_v are constants of integration.

To determine whether the line of intersection passes through a triangle, the limits of the triangle parameters are enforced. Thus for triangle A, we must have $0 \leq p,q,p+q \leq 1$, or

$$0 \leq -\underline{Q} \cdot \underline{N}_2 \, t + C_p \leq 1 \tag{12}$$

$$0 \leq \underline{P} \cdot \underline{N}_2 \, t + C_q \leq 1 \tag{13}$$

$$0 \leq (\underline{P} \cdot \underline{N}_2 - \underline{Q} \cdot \underline{N}_2) \, t + C_p + C_q \leq 1 \tag{14}$$

which is illustrated in Figure 4. Similar inequalities can be written for triangle B. By enforcing the above inequalities at the limits of 0 and 1, corresponding values of t can be found. The final step, given that the line of intersection passes through both triangles, is to see if the resulting line segments overlap. The two possibilities are sketched in Figure 5. There is no intersection between the triangles if the two line segments do not intersect. However, if the two segments do overlap, then the outline is found by the region of the overlap.

3.2 Retriangulation of an Intersected Triangle

Once all of the outlines are found between each pair of triangles, it remains to retriangulate the triangular patches which contain outlines. The problem is illustrated in Figure 6. To do this, techniques such as those found in computational geometry will be utilized.

The edges and nodes of the original triangle, along with all of its outlines and outpoints form an edge set E and a vertex set V. Since none of these edges intersect, then the edge and vertex set form a planar straight

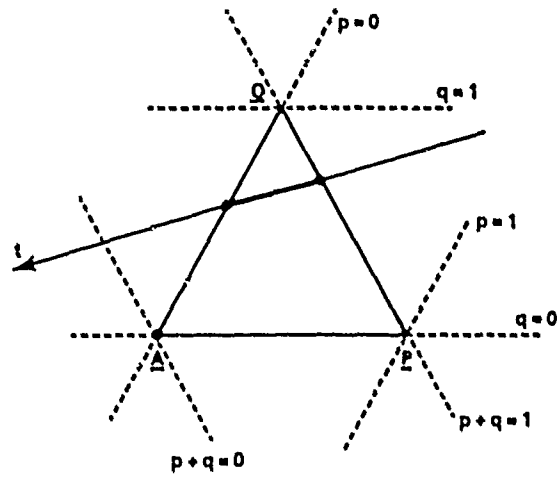


Figure 4. Intersection of Parametric Line and Triangle

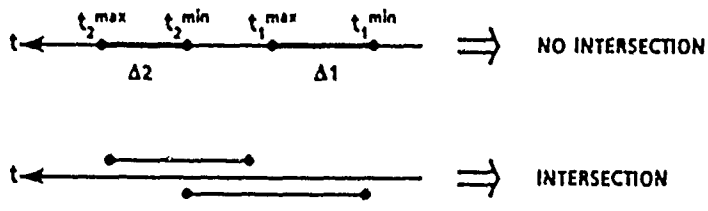


Figure 5. Intersection of Triangle Based on Limits of t

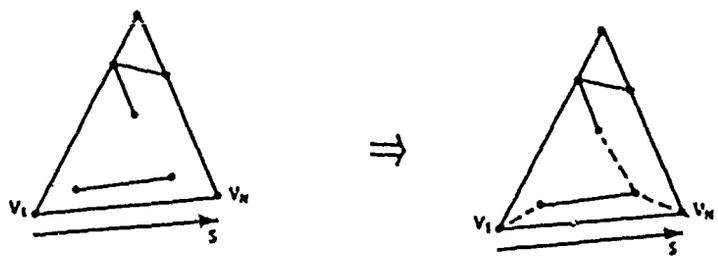


Figure 6. Regularization of a Triangle with Cutlines

line graph (PSLG). The algorithm used to form this graph into a set of triangles contains three steps:

1. Regularize the PSLG.
2. Find all of the monotone polygons in the regular PSLG by the use of chains.
3. Triangulate each monotone polygon.

For the first step, the vertices of the polygon must be ordered along some line s. As shown in Figure 6, the direction of the line s shall be chosen to be parallel to an edge of the original triangle. Thus, the first and last vertices v_1 and v_N are nodes of the original triangle. A vertex v_j is said to be regular if there are two integers $i < j < k$ such that (v_i, v_j) and (v_j, v_k) are edges of the graph G. The graph G is said to be regular if each vertex v_j is regular for $1 < j < N$.

The regularization procedure (Preparata and Shamos, 1985) adds edges to the PSLG which do not intersect with any other edge and make each vertex regular. An illustration of this procedure is shown in Figure 6.

At this point it can be recognized that the PSLG consists of f polygons, where

$$f = 1 + e - v$$

Furthermore, each of these polygons is monotone with respect to the line s. To find these polygons, the graph can be decomposed into a number of monotone chains.

Each chain will begin at vertex v_1 and end at vertex v_N. There will be f + 1 chains, which are ordered from lowest to highest. The lowest order chain, C_1, will always be defined as starting at v_1 and traveling straight along the "bottom" of the original triangle. The highest order chain will consist of the other two edges of the original triangle. An example is found in Figure 7. After all of the chains are found, the polygons can be formed by combining adjacent chains according to the following rule:

$$\text{polygon } i = C_i + C_{i+1} - C_i \cap C_{i+1} \qquad i = 1,\ldots f$$

The third, and final, step in the retriangularization process is to triangulate each monotone polygon. Although each polygon is monotone, and thus simple, they need not be convex. The triangularization of each polygon is accomplished by applying the algorithm as presented in Garey, Johnson, Preparata, and Tarjan, 1978. The vertices are stepped through from highest to lowest. As a vertex is processed, a number of diagonals may be added to the polygon. Each diagonal is added such that an n-sided polygon is divided up into a triangle and an n-1 sided polygon. An example of this process is given in Figure 8.

$P_1 = C_1 \cdot C_2$

$P_2 = C_2 \cdot C_3 - C_3 \cap C_2$

$P_3 = C_3 \cdot C_4 - C_3 \cap C_4$

$P_4 = C_4 \cdot C_5 - C_4 \cap C_5$

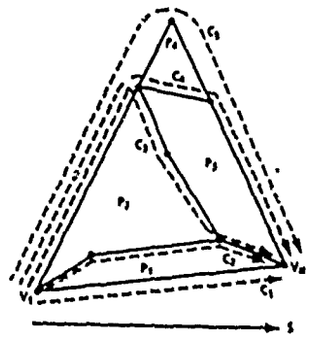


Figure 7. Decomposition into Monotone Chains

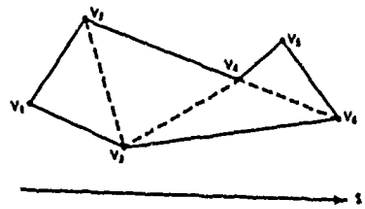


Figure 8. Triangulation of a Polygon

3.3 Intersection of Coplanar Triangles

If two triangles are coplanar, min-max boxes can be utilized to prescreen a set of two triangles. If the boxes do not overlap, then the triangles cannot overlap. However, if the two boxes overlap, then the two triangles may overlap.

The procedure for determining if two triangles, A and B, overlap involves two steps. The first is to see if any nodes of triangle A lie inside triangle B, and vice versa. The next step is to find all of the intersecting edges between the two triangles. Then, based on the number and location of the intersecting edges and interior nodes, an algorithm is exercised to find the corresponding cutlines and cutpoints.

As for the case of non-coplanar triangles, the resulting intersection must be retriangulated. The same procedure as described in Subsection 3.2 is followed. However, for intersecting coplanar triangles, the polygon formed by their intersection is treated separately.

3.4 Modification for Intersecting Surfaces

Recall that the basis functions which will be utilized were designed for an edge which is shared by one pair of triangles (N=2). Intersecting surfaces cause an edge to be shared by more than two triangles. If a line charge is not permitted along an edge, then the total current leaving an edge must vanish:

$$\sum_{i=1}^{N} I_i = 0 \tag{15}$$

Instead of modifying the basis function, the model geometry will be modified.

When an edge is shared by N triangles (where N > 2), N-2 "floating" pairs of triangles will be added. These triangles will be colocated with any two of the original triangles. Also, the interaction will be broken up in such a way so that only two triangles share a common edge. The current across the common edge of a floating pair is an added unknown. This procedure is illustrated in Figure 9.

4.0 RESULTS

Figures 10, 11, and 12 show some of the models which can be generated by this process. Figure 10 shows two crossed strips, both before and after being connected. Figure 11 shows an example of two coplanar plates. The combination of triangulated generalized frusta and connection of two triangular objects is illustrated in Figure 12 with a hemisphere sitting on a ground plane. The model is initially composed of two objects: the hemisphere was modeled as a generalized frusta and the ground plane as a triangulated plate. Then the hemisphere is triangulated. Once both objects are triangular patch models they are connected, resulting in additional triangular patches.

5.0 REFERENCES

Michael G. Garey, David S. Johnson, Franco P. Preparata, and Robert E. Tarjan, "Triangulating a Simple Polygon", Information Processing Letters, June 1978, pp 175-179.

Sadasiva M. Rao, Donald R. Wilton, and Allen W. Glisson, "Electromagnetic Scattering by Surfaces of Arbitrary Shape", IEEE Transactions on Antennas and Propagation, Vol. AP-30, May 1982, pp 409-418.

Franco P. Preparata and Michael Ian Shamos, Computational Geometry, An Introduction, Springer-Verlag, New York, 1985.

Chaman L. Sabharwal and Thomas G. Nelson, "Implementation of Cross Intersection Between Triangular Surfaces, Journal of the Association for Computing Machinery, 1988, pp 92-101.

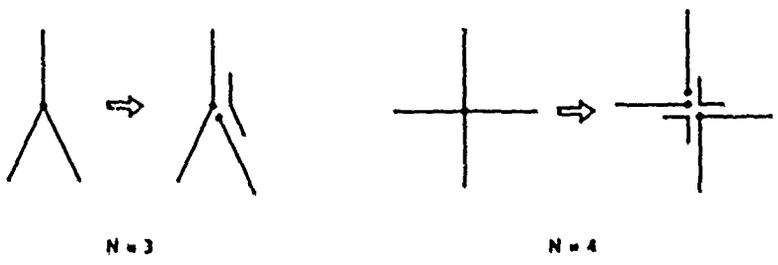


Figure 9. Addition of Floating Pairs at Intersecting Surfaces

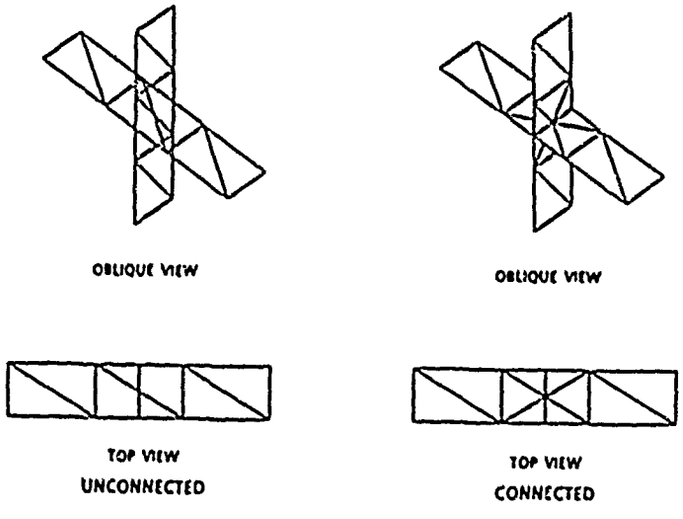


Figure 10. Intersecting Crossed Strips

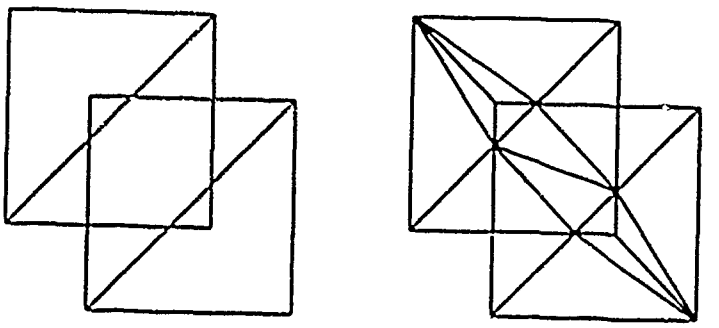


Figure 11. Intersecting Coplanar Plates

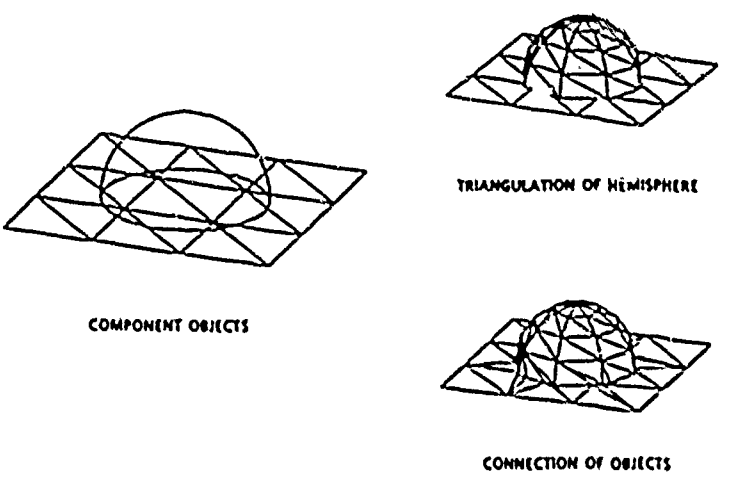


Figure 12. Hemisphere on a Ground Plane

GRAPHIC OUTPUT ROUTINES OF THE MMP PROGRAM PACKAGE ON PCs AND SUN WORKSTATIONS

Peter Regli, Christian Hafner and Niels Kuster

Electromagnetics Group
Swiss Federal Institute of Technology
8092 Zurich, Switzerland

Abstract

Fast and flexible output routines are essential for every numerical program, not only to plot the results but above all to control the simulation. The special aspects of the Multiple MultiPole (MMP) Program packages for the output techniques are described. The present output routines for dynamic electromagnetic fields are hereafter discussed and illustrated. These include plotting of scalar- and vectorfields in two- and threedimensional space as well as visualization of time dependence.

Introduction

A simple classification of different graphical techniques for field representations can be made with regard to their purpose:

- Analysis, error detection: Above all, research applications require efficient display of computed results. As much information as possible (and reasonable) should be viewable at one sight. The representation of residues combined with the geometry of the model is of great use for this purpose. Vector representations of the calculated fields especially around boundaries are also helpful to check the quality of the results.
- Education: In this area, clearness and comprehensiveness are more important than high information density. However, well designed vector charts make it possible to meet both of these requirements. Sequential display of plots from different time points are very well suited for educational demands.
- Illustration: Plots for illustrations should attract the attention of the reader. Good printing quality (high resolution output devices) is important.

The main reasons for difficulties associated with the graphical representation of electromagnetic data usually fall in one of the following categories:

- Properties of the data to be represented: quantity, dimensionality, range of values

- Properties of output devices: resolution, speed, two-dimensionality
- Properties of the human viewer: imagination, training

Aspects of the MMP-ProgramPackages for the output techniques

The Multiple Multipole (MMP) program packages are based on the - lately called - Generalized Multipole Technique (GMT) which has independently been developed by different groups worldwide [1]. The output routines presented in this paper were developed for the 2D and 3D Multiple MultiPole (MMP) Program packages which are implemented on PCs and SUN workstations. A detailed description of these packages are given by Bomholt and Hafner in this conference [2] [3].

The basis functions used in the present MMP-Program Packages are spherical or cylindrical multipole functions (Multipoles) which are analytical solutions of the time harmonic Maxwell equations for linear, homogeneous, isotropic media. Several (Multiple) of these Multipoles are used at different locations to expand the field in each domain. The unknowns are determined by using 3-10 times more points than necessary as a minimum to match the appropriate boundary conditions. The matrix is solved by a least squares technique. The following properties of the MMP Method facilitate the construction of output routines:

- The field inside the domains is always an exact Maxwell field (compared with FE, FD), even inside lossy materials (compared with MoM).
- No singularities at any point (compared with MoM).
- Smoothness of the field, even along the boundaries.
- In almost all cases the largest errors occur on the boundary and decrease with the distance (similar to MoM). Plotting the corresponding residue with every matching point is therefore a very efficient instrument for simulation control.
- The field vectors can be calculated at any point without interpolation. This allows zooming of details without loss of accuracy or need for remodeling the whole problem. (compared with FE, FD, MoM for lossy materials)
- The parameters of the basis functions require little memory and can therefore easily be stored in an ASCII File which also can be transferred to other computers for subsequent calculation of plot data.
- The basic data for the output routines are the complex amplitudes of the E- and H-field which are calculated with this parameter file for any configuration of points within a few minutes. This field values are temporarily saved and allow an instant plotting of a wide range of outputs for any timepoint (compared with time domain methods).

Graphical representation of the field

The representation of vector fields by arrays of arrows was found to be a fast and efficient technique which gives comprehensive plots with high information density. The flexibility of this vector plots depends much on how the geometric parameters of an arrow can be related to the field vector. Simple arrows varying only in length emphasize the directional aspect of the vector

field. Arrows varying in length and width extend the range and give a more realistic impression of amplitude distributions. To keep plots readable for large amplitude variations it is often necessary to limitate the maximum length and thickness of an arrow.

The representation of 3D vectors on a 2D sheet gives ambiguous pictures which are difficult to read. A solution to this problem is the separation of transverse and normal components relative to a clearly imaginable plane. The transverse component is then represented by an arrow while the normal component is displayed as a circle of varying diameter lying in the plane.

Equilines for scalar fields are easily plotted. With additional shading they become more readable. Sometimes a combination with the vector representation is useful.

Fieldlines are somewhat difficult to handle. They need considerable computation time and do not give more information than the simpler vector plots.

Fieldgraphics for 2D- and 3D applications

Cylinder model

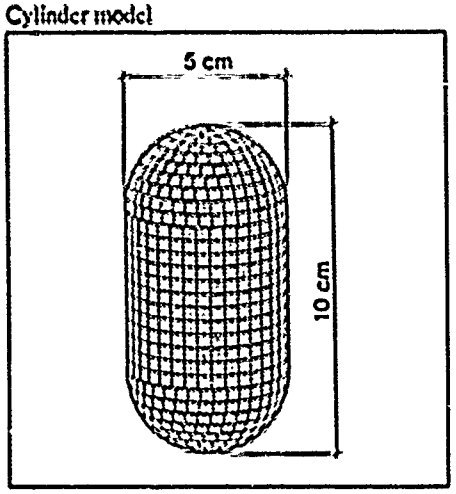


Figure 1: A full 3-dimensional cylinder model of muscle tissue (ε_r=50, σ=0.8 mho/m) is radiated by a plane wave of 2.45 GHz.

Human model

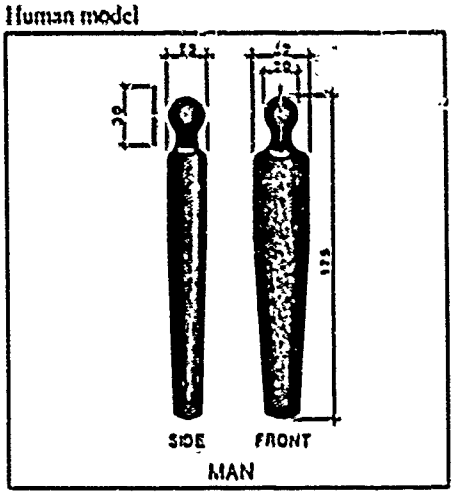


Figure 2: Full 3-dimensional model of a human using a portable radio held in front of the face. The antenna is made of perfectly conducting material and is driven in its center by a current source operating at 450 MHz. The body is built up of two parts: the head (ε_r=50, σ=0.8 mho/m) and the body (ε_r=60, σ=1.1 mho/m). More details are given in [4]

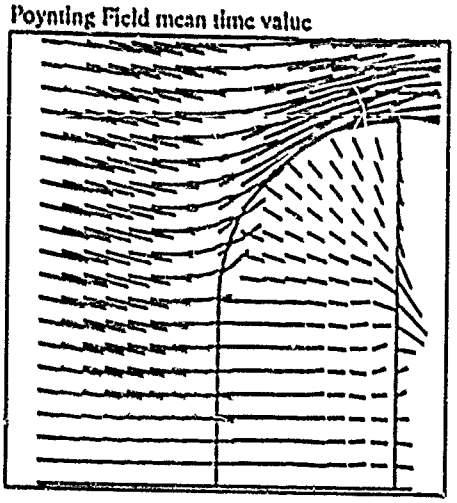


Figure 3: The simple vector plot emphasizes the directional aspect of the vector field. (see fig. 1)

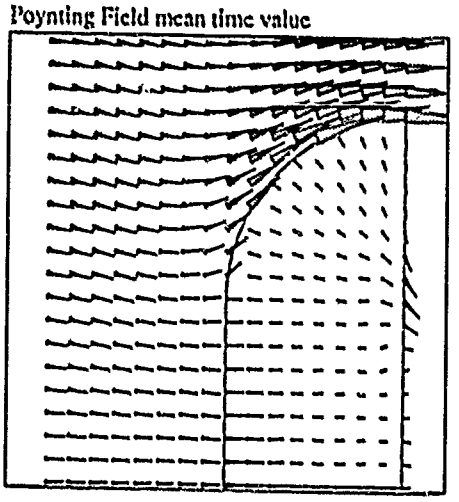


Figure 4: Filled arrows give a better impression of the amplitude distribution. (see fig. 1)

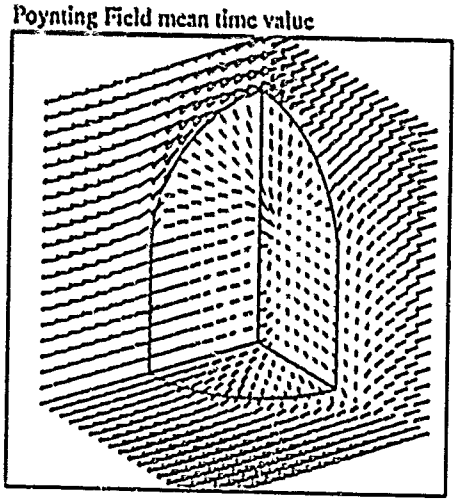


Figure 5: Three plane representation with 3D arrows. (see fig. 1)

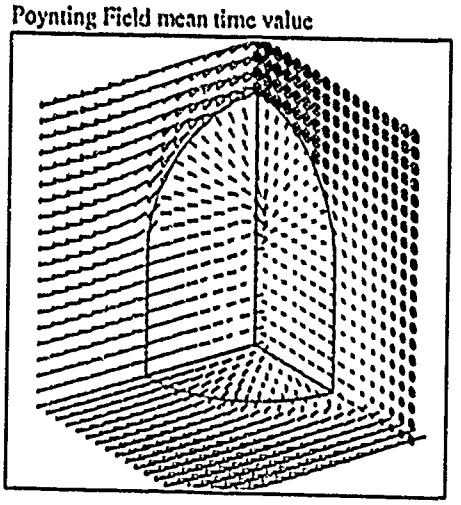


Figure 6: Three plane representation with 2D+1D representation. The normal component relative to each plane is shown as a circle lying in that plane. (see fig. 1)

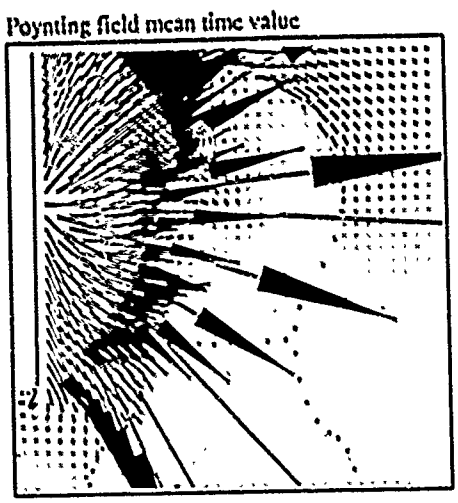


Figure 7: A linear scale display of near field problems often leads to bad plots. (see fig. 2)

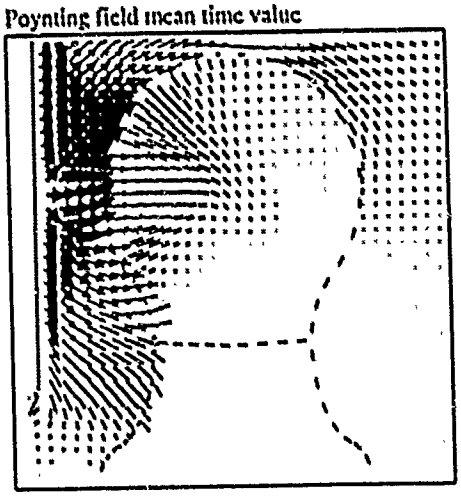


Figure 8: Limited arrows give comprehensive pictures and allow zoomed display of details.
(see fig. 2)

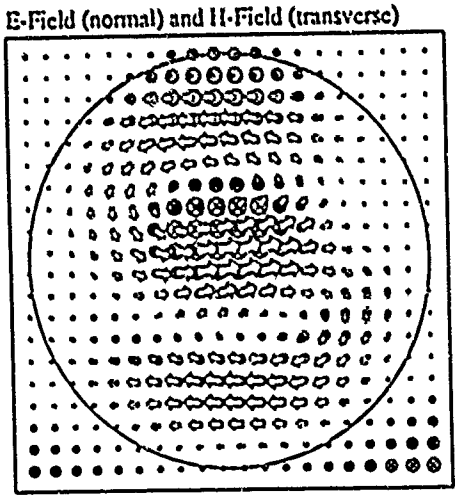


Figure 9: Combined display of E and H Field in a dielectric sphere (see figure 11). These plots are only reasonable if E and H are orthogonal.

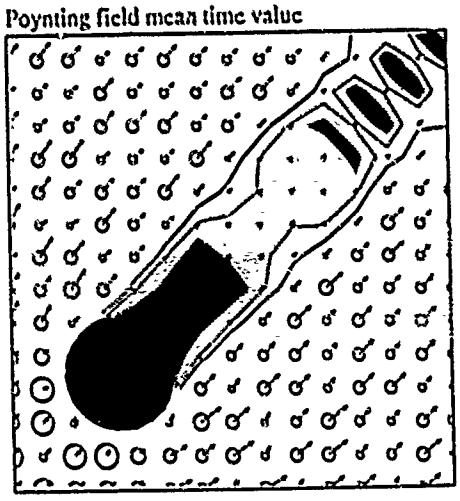


Figure 10: A 2D perfectly conducting cylinder is radiated by a plane wave (0.61,0.61,0.5), polarization of E (0.71,0.71,0). The combination of a vector plot and shaded logarithmical equilines highly extends the representable amplitude range.

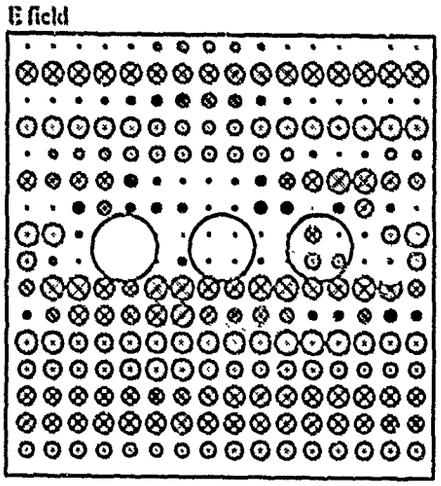


Figure 11: 3 spheres (from left to right: perfectly conducting, lossy, dielectric) radiated by a plane wave.

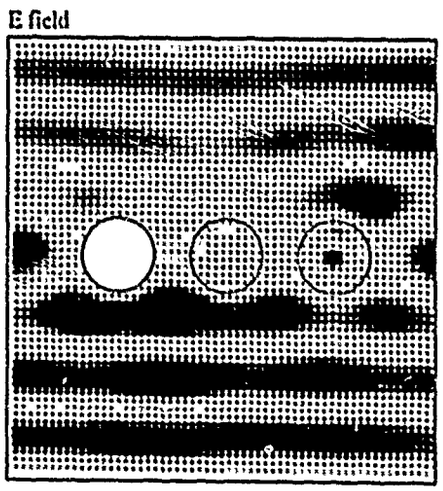


Figure 12: Same as picture 11 with higher density of field points.

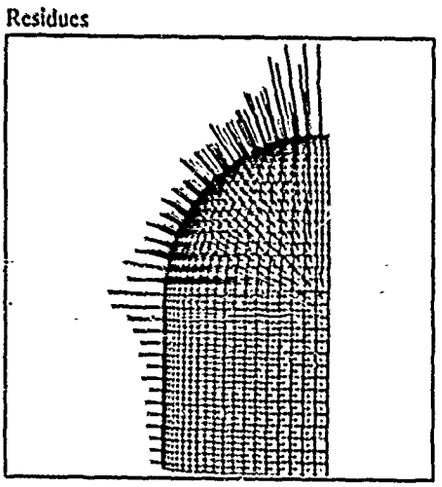


Figure 13: Error plot. The residues are indicated by the length of the surface normal vector. (see fig. 1)

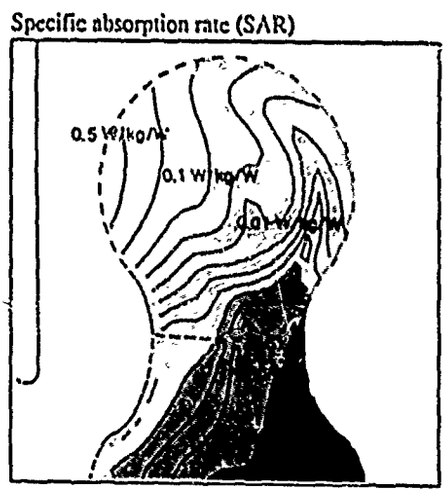


Figure 14: Man with radio. Shaded equilines give a clear and accurate representation of scalar quantities.

Representation of time-dependence

Since the General Multipole Technique (GMT) implies time-harmonic solutions, it is very simple to calculate plots for different time points from one set of complex E- and H- values. This plots are copied from the screen directly into the computer memory from where they can sequentially be read and displayed. Movies with about 30 pictures per second (500*500 pixels) are possible on SUN 3/50 workstations. This feature unfortunatly could not be implemented on Pesonal Computers until now.

Available Output Routines

A wide range of output routines is already written for SUN workstations and PCs:

- 2D and 3D error representation on every matching point
- Vector representation of E-, H- and Poynting field using planar arrows for transverse components and circles for normal components. The fields can be plotted on one or more rectangular planes simultanuously. A combination of E, H and S is also possible.
- Shaded equiline representation of the specific absorption rate or of the field amplitude, also in combination with vector representation.
- Farfield radiation pattern
- The sequential display of pre-stored pictures allows the representation of time dependence. Such "moving vector fields" are both attractive and useful for model validation, student training and presentations.

Conclusion

The present MMP Program packages include a wide range of rather sophisticated output routines. The 3D vector field plots still leave much to be desired. More stereoscopic representations are under study.

References

[1] A. Ludwig, "A new Technique for Numerical Electromagnetics", IEEE APS Newsletter (submitted)

[2] L. Bomholt, Ch. Hafner, "A MMP Program for Computation of 3D Electromagnetic Fields on PCs", 5th Annual Review of Progress in Applied Computational Electromagnetics (ACES), Conference Proceedings, March, 1989

[3] Ch. Hafner., L. Bomholt, "Implementation and Performance of MMP Programs on Transputers", 5th Annual Review of Progress in Applied Computational Electromagnetics (ACES), Conference Proceedings, March, 1989

[4] N. Kuster, R. Ballisti, "MMP Method Simulation of Antennae with Scattering Objects in the Closer Near Field", IEEE Trans. Magn., Vol. MAG-25, July, 1989

AN INTERACTIVE WAVEGUIDE PROGRAM

Granville Sewell
University of Texas at El Paso
Mathematics Department
El Paso, Texas 79968

WAVEGUIDE is an interactive program which, when used in conjunction with IMSL's finite element program PDE/PROTRAN, can solve cylindrical waveguide problems on arbitrary cross-sections, with variable permittivity and permeability (ε and μ may even be discontinuous, to model composite waveguides). The user only has to answer a series of basic questions about his problem, posed in engineering terms, and all propagating modes in a specified interval are calculated, and the corresponding electric and magnetic fields are plotted.

When the permittivity or permeability is variable, a nonlinear eigenvalue problem must be solved to find the (hybrid) modes. If random nonhomogeneous terms are added to the partial differential equations, the eigenvalues can be characterized (and hence located) as the parameter values which cause the norm of the solution to become infinite.

1. The Waveguide Problem

For a propagating wave in a cylindrical waveguide, Maxwell's equations for the electric and magnetic fields reduce to [see reference 1, Section 8.2]:

$$(1)\quad \frac{\partial}{\partial x}\left[\frac{-\beta E_y + \omega\mu H_x}{\omega^2\mu\varepsilon - \beta^2}\right] + \frac{\partial}{\partial y}\left[\frac{\beta E_x + \omega\mu H_y}{\omega^2\mu\varepsilon - \beta^2}\right] + \omega\mu H = 0$$

$$(2)\quad \frac{\partial}{\partial x}\left[\frac{\beta H_y + \omega\varepsilon E_x}{\omega^2\mu\varepsilon - \beta^2}\right] + \frac{\partial}{\partial y}\left[\frac{-\beta H_x + \omega\varepsilon E_y}{\omega^2\mu\varepsilon - \beta^2}\right] + \omega\varepsilon E = 0$$

where E and H are the electric and magnetic field components in the z direction, ω is equal to $2\pi f$ where f is the frequency, $\varepsilon(x,y)$ is the permittivity, $\mu(x,y)$ is the permeability, and β is the propagation constant (which is purely imaginary for propagating waves). Once E (usually denoted by E_z) and H ($=H_z$) are known, the other components of the electric and magnetic fields can be calculated directly from these two components. For a conducting boundary, the boundary conditions are

$$(3)\quad E = 0 \quad \text{and} \quad \partial H/\partial n = 0$$

For a given ω, the problem is to determine values of β for which nonzero solutions (eigenfunctions) of (1) and (2), with boundary conditions (3), exist.

When ε and μ are constants, equations (1-2) reduce to two simple uncoupled linear problems, whose eigenvalues are the transverse electric (TE) and transverse magnetic (TM) modes. However, in the general case where $\varepsilon(x,y)$ and $\mu(x,y)$ are variable (such as is usually the case for optical waveguides), we must solve the nonlinear eigenvalue equations 1-2 simultaneously, and the eigenvalues are called hybrid modes.

2. Solving the Nonlinear Eigenvalue Problem

PDE/PROTRAN [reference 2], a partial differential equation solver developed by the author and marketed by IMSL, Inc.,

solves very general systems of nonlinear partial differential equations in general two-dimensional regions, but it is not designed to solve nonlinear eigenvalue problems such as 1-2. However, if we introduce "random" non-zero right-hand sides to (1) and (2) and specify a value for β, PDE/PROTRAN can be used to solve this elliptic system. Since PDE/PROTRAN uses a Galerkin finite element method, it can handle composite media, where ϵ and/or μ are discontinuous at the interfaces between different materials, without the need for explicit interface conditions. Now if we vary β over a range of values (BMIN,BMAX), as β approaches an eigenvalue the solution becomes infinitely large in magnitude. Using this fact, we can attempt to locate all eigenvalues in a given β-range. If we are very unlucky in our choice of right hand sides, we could conceivably miss some eigenvalues, but the probability of such a unlucky choice is zero.

In order to make the power of PDE/PROTRAN easily available to engineers who want to solve cylindrical waveguide problems, the author has developed an interactive driver, called WAVEGIDE. This interactive program asks the user a few simple questions about his problem, phrased in engineering terms, and, based on the user's answers, it generates a PDE/PROTRAN input program to solve the PDE system 1-2 using the above-outlined approach.

WAVEGIDE asks the user to supply a frequency, f, ($\omega=2\pi f$) and limits (BMIN,BMAX) on β. For a given value of β, WAVEGIDE invokes PDE/PROTRAN to solve (1-2) with a nonzero right-hand side, returning a function value, $g(\beta)$, which represents the inverse of a norm of the solution. WAVEGIDE tries to locate all minima of $g(\beta)$ in (BMIN,BMAX) using the following procedure. $g(\beta)$ is evaluated at a user-specified number (NINTER) of uniformly-spaced values β_i between BMIN and

BMAX. When an index I is found such that $g(\beta_I)$ is less than both $g(\beta_{I-1})$ and $g(\beta_{I+1})$, it searches for a minimum of g in $(\beta_{I-1},\beta_{I+1})$, using a public domain subroutine FMIN [reference 3] to locate the minimum accurately. In our experience minima which do not correspond to eigenvalues are very rare, and they betray themselves by their shallowness ($g(\beta)$ does not go to zero near these minima). Thus WAVEGIDE is usually able to discard these pseudo-eigenvalues.

The user may, alternatively, supply a value of β and limits on f. In this case WAVEGIDE will find values of the frequency which correspond to propagating modes. If a value of $\beta=0$ is supplied, the frequencies thus found will be the cut-off frequencies.

3. An Example

WAVEGIDE was applied to the first problem in the "workshop problem set" of the Feb 5, 1989 "Workshop on Numerical Simulation and Analysis in Guided-Wave Optics and Optoelectronics" in Houston (Figure 1). The interactive WAVEGIDE session which generated the PDE/PROTRAN input program to solve this problem (for t=0.4 μm) is shown in Figure 2. Lines beginning with a "?" indicate a user response; the other lines are generated by the interactive program itself. Notice that the information which the user must supply is minimal. $\epsilon(x,y)$ and $\mu(x,y)$, which vary from subregion to subregion, are defined in a simple 15-line FORTRAN segment. If the region had been a more general, non-rectangular region, the amount of additional work required of the user would have been minor.

The contour plot of H (=H_z) generated by WAVEGIDE for the fundamental quasi-TE mode is shown in Figure 3, and Figure 4 shows the other two components of the magnetic field,

(H_x,H_y). Plots of the electric field components are also generated by WAVEGIDE. The calculated propagation constant was β=1.7627 E7, so that $n_{eff}=\lambda\beta/(2\pi)$=3.2262, in close agreement with the value calculated by other workshop contributors.

One difficulty encountered in solving this problem is that since PDE/PROTRAN cannot solve problems in unbounded regions, we have to truncate the substrate, guide and ribs to a finite length. Unfortunately, doing this introduces some "spurious" eigenvalues into the PDE system 1-2. These spurious modes are betrayed by their electric and magnetic field plots, which show rapid oscillation, but WAVEGIDE is not able to discard them automatically. In Figure 2, the β interval (BMIN,BMAX) is chosen so that only propagating waves with an n_{eff} in the narrow interval (3.2255,3.2275) will be found; this was done to avoid the spurious modes which showed up in previous WAVEGIDE runs where a larger search interval was used. When the guide cross section is bounded, these spurious modes are not a problem.

The author hopes to make WAVEGIDE available to the public within a few months, through the Advances in Engineering Software algorithms distribution service (reference 4).

References

1. Fields and Waves in Communication Electronics, S. Ramo, J.R. Whinnery and T. Van Duzer, John Wiley and Sons (second edition) 1984.

2. Analysis of a Finite Element Method: PDE/PROTRAN, G. Sewell, Springer Verlag, 1985.

3. Computer Methods for Mathematical Computations, G. Forsythe, M. Malcolm and C. Moler, Prentice-Hall, 1977.

4. "WAVEGIDE--An Interactive Waveguide Program". G. Sewell and S. Cvetkovic, submitted to Advances in Engineering Software.

Workshop on Numerical Simulation and Analysis in Guided-Wave Optics and Optoelectronics

Houston, TX, February 5, 1989

Workshop Problem Set - Problem Number 1

For the structure illustrated below, calculate the normalized propagation constant b of the fundamental quasi-TE mode for $t = 0.0$ μm, 0.2 μm, and 0.4 μm where b is defined as

$$b = (n_{eff}^2 - n_{sub}^2) / (n_{film}^2 - n_{sub}^2).$$

$\lambda = 1.15$ μm, and the propagation constant β of the fundamental quasi-TE mode is given by $\beta = 2\pi n_{eff}/\lambda$. The ribs should be chosen high enough so that they do not affect the fields.

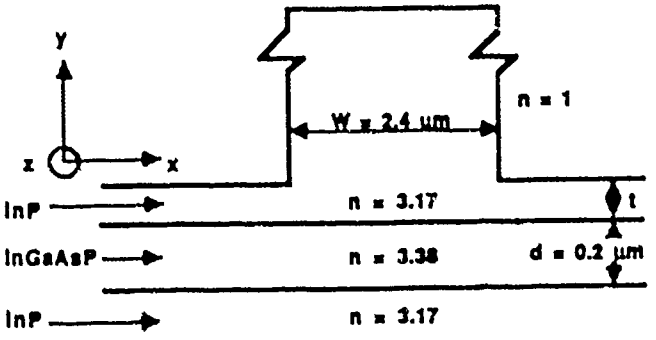


FIGURE 1 -- Houston Workshop Problem

```
                    ****************************
                    **** Welcome to WAVEGIDE ****
                    ****************************

   The WAVEGIDE program performs a modal analysis of a waveguide with
   arbitrary cross-section R, and bounded with perfectly conducting
   metallic walls.  The permittivity (EPS) and permeability (AMU) of
   the guiding media are real scalar quantities which can vary over
   the cross-section. The user may specify the frequency (F), and all
   propagating modes with propagation constants (BETA) in a specified
   BETA-range will (hopefully) be found.  Alternatively, the user may
   specify the propagation constant (BETA), and all propagating modes
   with frequencies (F) in a specified F-range will be found. In both
   cases, a full profile of each mode is also displayed graphically.

   Each question asked by WAVEGIDE has a short form and a long form.
   The long form is recommended for first time users.  Would you like
   to see the long form of each question?
***** Enter YES or NO
? NO

   If this is your first time using WAVEGIDE, you may want to work
   through an example problem before trying one of your own.  A simple
   example and a more complex one have been prepared.  Enter
        0 = if you do not want to see either example
        1 = if you want to work through the simple example problem
        2 = if you want to work through the more complex example
***** Enter an integer value in the range 0 to 2
? 0

   If you specify a value for the frequency (F), values of the
   propagation constant (BETA) for all propagating modes in a
   specified range BMIN < BETA < BMAX will be calculated.

   If you specify a value for the propagation constant (BETA), values
   of the frequency (F) for all modes in a specified range
   FMIN < F < FMAX will be calculated.  Thus if you want the cutoff
   frequencies, specify BETA=0.

   Do you want to specify a frequency (F)?
***** Enter YES or NO
? MAYBE

***** What?  YES or NO, starting in first column please.
? YES

   Enter the frequency (F).
***** Enter constant or FORTRAN expression **********************
? 2.9979 E8 / 1.15 E-6

   The interval (BMIN,BMAX) will be searched for values of BETA which
   correspond to propagating waves.  All propagating waves will have
   propagation constants in the interval (0 , 2*PI*F*SQRT(max(AMU*EPS)))
   where max(AMU*EPS) is the maximum value of the product AMU*EPS in
   R, so (BMIN,BMAX) should be a subinterval of this interval.

   Enter a value for BMIN.
```

FIGURE 2 -- Interactive Session

```
***** Enter constant or FORTRAN expression **********************
? 2*3.1415927 / 1.15 E-6 * 3.2255

   Now enter a value for BMAX.
***** Enter constant or FORTRAN expression **********************
? 2*3.1415927 / 1.15 E-6 * 3.2275

   NINTER values of BETA will be checked in the interval (BMIN,BMAX).
   The larger NINTER is chosen, the more likely the program is to find
   all modes in this interval, but also the more computer time will
   be required.  Enter a value for NINTER.  If no idea, enter 20.
***** Enter constant or FORTRAN expression **********************
? 10

   Do you want to generate plots of the Hz,Hr,(Ex,Ey) and (Hx,Hy)
   fields?  It is important to look at the eigenfunction plots
   before accepting the corresponding eigenvalue as valid.
***** Enter YES or NO
? YES

   Now you must construct an initial triangulation of the cross-
   section R.  This initial triangulation can later be refined and
   graded to your specifications.

   If the region R is a rectangle with sides parallel to the X and Y axes,
   then the initial triangulation can be defined in a special, easy,
   manner.  Is your region rectangular?
***** Enter YES or NO
? YES

   In that case, the initial triangulation of R is defined by a set of
   X and Y grid lines, with four equal area triangles in each grid square.

   List the X coordinates of the vertical grid lines, in the form:

            xgrid(1),xgrid(2),....xgrid(nxg)

   where xgrid(i) is the X coordinate of vertical grid line i.  It is
   assumed that xgrid(1) and xgrid(nxg) represent the values of X on the
   left and right sides of the rectangle R.
***** Enter first line of list ***********************************
?  -2.0E-6 , -0.7E-6 , 0.0E-6 , 1.2E-6 , 2.4E-6 , 3.1E-6 , 4.5E-6

***** Enter another line (press 'return' if no more) ************
? [RETURN]

   Now list the Y coordinates of the horizontal grid lines, in the form:

            ygrid(1),ygrid(2),....ygrid(nyg)

   where ygrid(i) is the Y coordinate of horizontal grid line i.  It is
   assumed that ygrid(1) and ygrid(nyg) represent the values of Y on the
   bottom and top sides of the rectangle R.
***** Enter first line of list ***********************************
?  -1.0E-6 , -0.3E-6 , 0.0E-6 , 0.1E-6 , 0.2E-6 , 0.6E-6 , 1.5E-6

***** Enter another line (press 'return' if no more) ************
```

```
? [RETURN]

   How many triangles are desired for the final triangulation?  If you
   enter 0, the number of triangles will default to 50 or the number
   of triangles in the initial triangulation, whichever is larger.
***** Enter an integer value in the range 0 to +INFINITY
? 0

   Now enter a FORTRAN expression for OBJECT(X,Y), which controls the
   grading of the triangulation.  OBJECT should be largest where the
   triangulation is to be most dense.  The default is OBJECT(X,Y)=1.0
   (a uniform triangulation).
***** Enter constant or FORTRAN expression ('return' is default)
? [RETURN]

   (The following keyword--SHAPE--is usually defaulted.)
***** Enter constant or FORTRAN expression ('return' is default)
? [RETURN]

   Which of the following linear equation solvers do you want to use?
   If you have no idea, use the band method.

   1. Band method
   2. Frontal method
   3. Conjugate gradient method

   Enter 1,2 or 3 to select a linear equation solver.
***** Enter an integer value in the range 1 to 3
? 1

   What element degree should be used? (2,3 or 4)  If no idea, enter 3.
***** Enter an integer value in the range 2 to 4
? 5

***** Illegal input.  Reenter integer in the range 2 to 4
? 3

   Now you must write a FORTRAN segment to define the permittivity
   (EPS) and the permeability (AMU).  These may be defined in terms of
   X and Y.  They may also reference the constants EPS0 (=8.854 E-12)
   and AMU0 (=12.566 E-7), which hold the permittivity and permeability
   in vacuum, in units of FARADS/METER and HENRIES/METER.

   The FORTRAN statements must obey the usual rules of FORTRAN--for
   example, statements must begin in column 7.
***** Enter first line of FORTRAN **********************************
?     IF (Y.LT.0.0) THEN
***** Enter another line (press 'return' if no more) ****************
?       RINDEX = 3.17
***** Enter another line (press 'return' if no more) ****************
?     ELSE IF (Y.GE.0.0 .AND. Y.LT.0.2E-6) THEN
***** Enter another line (press 'return' if no more) ****************
?       RINDEX = 3.36
***** Enter another line (press 'return' if no more) ****************
?     ELSE IF (Y.GE.0.2E-6 .AND. Y.LT.0.6E-6) THEN
***** Enter another line (press 'return' if no more) ****************
?       RINDEX = 3.17
```

```
***** Enter another lin  (press 'return' if no more) ********************
?     ELSE
***** Enter another line (press 'return' if no more) ********************
?        IF (X.GT.0.0 .AND. X.LE.2.4E-8) THEN
***** Enter another line (press 'return' if no more) ********************
?           RINDEX = 3.1
***** Enter another line (press 'return' if no more) ********************
?        ELSE
***** Enter another line (press 'return' if no more) ********************
?           RINDEX = 1.0
***** Enter another line (press 'return' if no more) ********************
?        ENDIF
***** Enter another line (press 'return' if no more) ********************
?     ENDIF
***** Enter another line (press 'return' if no more) ********************
?     AMU = AMUO
***** Enter another line (press 'return' if no more) ********************
?     EPS = EPSO*RINDEX**2
***** Enter another line (press 'return' if no more) ********************
? [RETURN]

   The solution is saved on an ns by ny rectangular grid of points,
   for postprocessing by the plotting routines.  Enter values for ns
   and ny in the form:

                     ns,ny

   ns and ny must each be between 3 and 51, inclusive.  If you have
   no idea, enter 21,21.
***** Enter answer as specified *********************************
? 26,26

              ****************************************
              ***** Input program is completed, *****
              ***** and should be executed using*****
              ***** IMSL's PDE/PROTRAN 1.0,     *****
              ****************************************
```

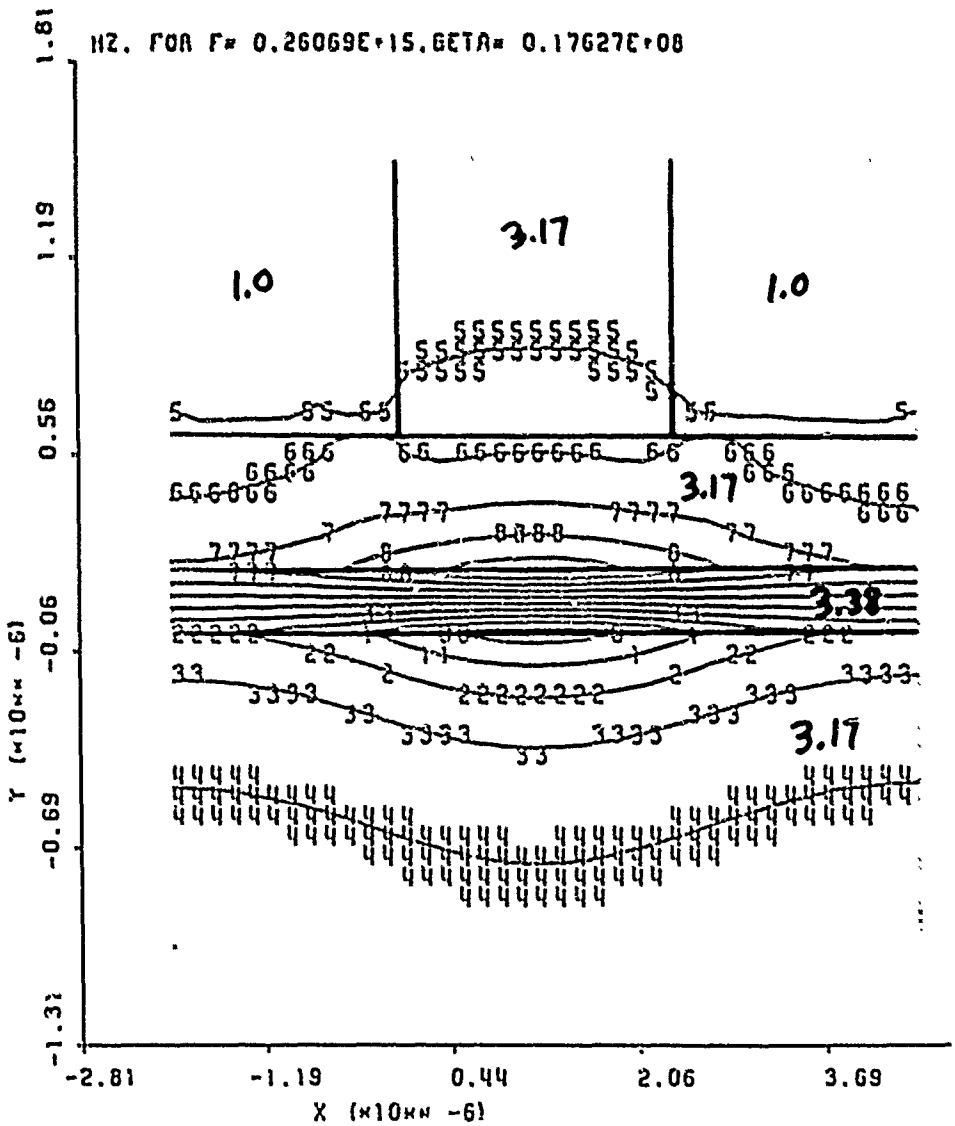


FIGURE 3 -- Contour Plot of Hz

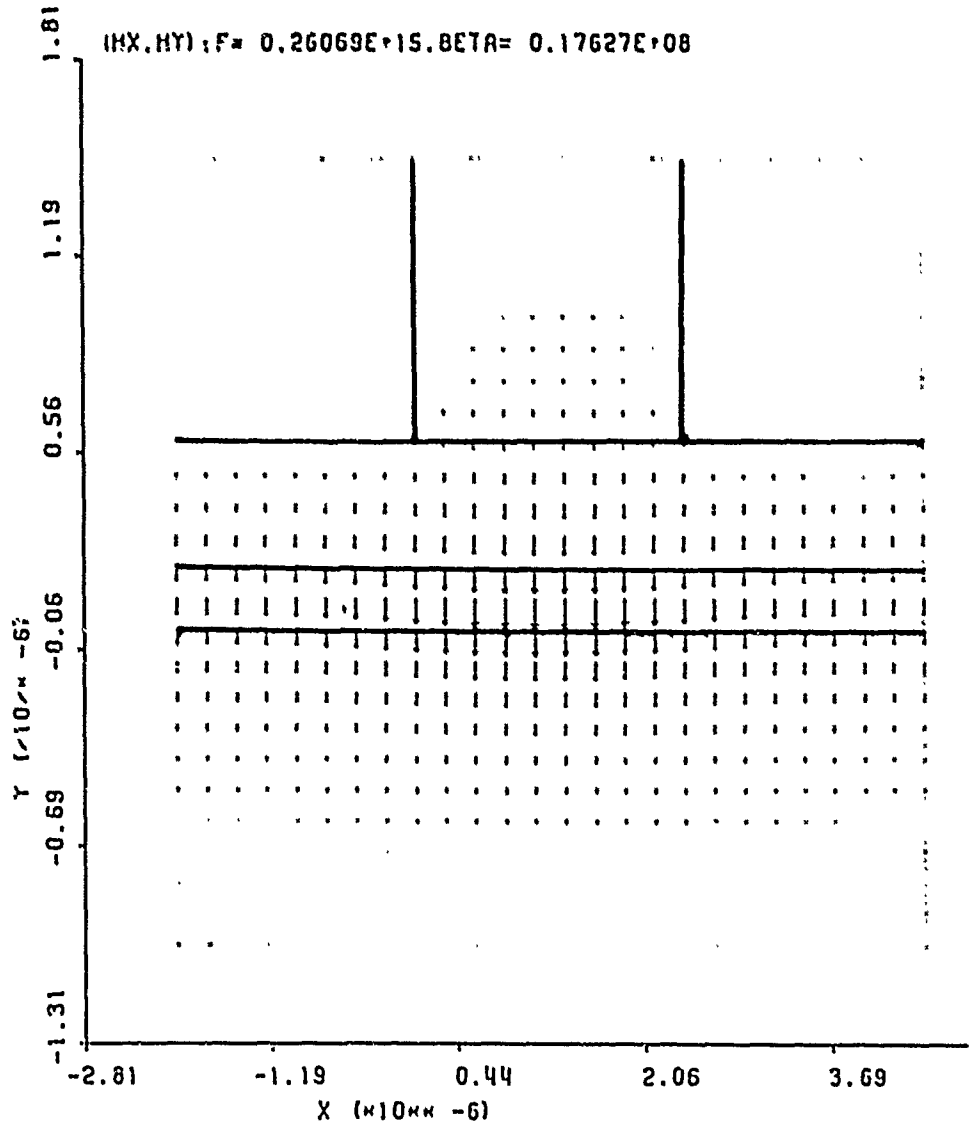


FIGURE 4 -- Plot of (Hx,Hy) Field

SUPERTAB INTERFACE FOR NEC

Frank E. Walker, Eugene A. Sorensen, And James S. Kenney
Boeing Aerospace; Seattle, Wa. 98124-2499

Key Words: Electromagnetic Analysis (EMA), Numerical Electromagnetic Code (NEC), SUPERTAB.

Abstract

A current topic of interest is the use of graphic interfaces to electromagnetic analysis (EMA) codes. Our effort was in response to an in-house request to provide a quick graphics interface development that would create geometry input files for several electromagnetic field analysis codes. Our solution was to employ the pre-processor in SUPERTAB* to generate and display three- dimensional finite element models. Conversion software was written to interface between the Universal Data File format of SDRC* and the input data format of the desired analysis code, in this case the Numerical Electromagnetics Code (NEC).

The SUPERTAB to NEC interface programs NECGEOM and NECONT allow the user to create a complete NEC input file from the geometry and topology information stored in a SUPERTAB Universal File. NECGEOM uses the Universal File and user input to generate comment cards, wire segment and surface patch generation cards, structure symmetry generation cards, an overall structure transformation card, and an end-of-geometry card. NECONT constructs the remainder of the NEC input file by obtaining user responses to prompts. It writes cards which control the generation of the method of moments interaction matrix, the solution for the current vector, and the calculation of radiated and scattered fields.

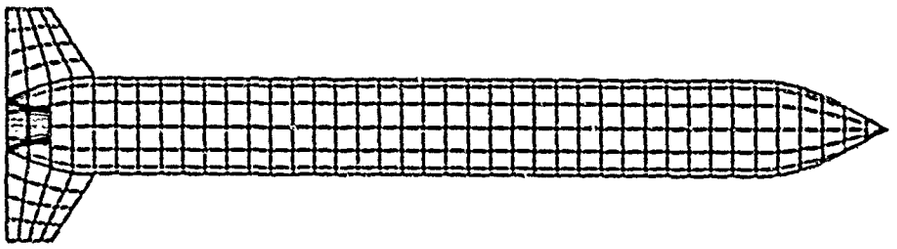
For NEC users who have access to the SDRC software SUPERTAB, this application can greatly simplify creation of the geometry to be evaluated and generation of an input file. This application has been successfully developed for use with other finite element analysis codes within Boeing.

Background

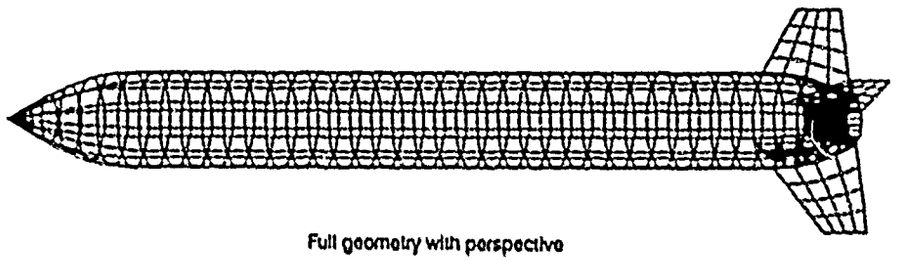
Electromagnetic (EM) fields analysis is currently performed using computers to calculate the solutions to large matrices. The problem matrix represents the geometry in question and the initial problem conditions. The solution matrix represents the resultant EM field. The methods used to solve the finite element calculations vary but the input and solution representations are most often in the form of extensive listings of point-by-point data. These data listings are cumbersome to generate and difficult to evaluate quickly. In order for an analyst to iterate to an acceptable solution using EM field analysis it is necessary to develop a more convenient method of representing the input data and the description of the resultant EM field.

The objective of this task was to find an approach that would provide a convenient method of generating input data for submission to an EM field analysis code. This was to be achieved with a minimum of required development using existing capabilities wherever possible. The most convenient method of depicting both input geometries and the resultant EM field are graphical representations. The old idiom that a picture is worth a thousand words (or data points) takes on new meaning to the electromagneticist faced with data reduction of a complex geometry. Geometries such as those illustrated in Figure 1 are commonly generated to graphically represent structural or aerodynamic features of a design. Computer generated geometries such as these can be modified with meshing techniques to serve as input data for finite element analysis. The results of these analysis can be quickly evaluated when viewed in a similar graphical format.

* SDRC is a service mark of Structural Dynamics Research Corporation
SUPERTAB is a part of the SDRC Integrated Design Engineering Analysis Software (I-DEAS).
SUPERTAB and I-DEAS are registered trademarks of SDRC.



Geometry with hidden line removal



Full geometry with perspective

Figure 1. Typical Structural Geometry

SUPERTAB

Our approach was to use the existing volumetric geometry meshing capability available in the SUPERTAB code and to develop the necessary interface to allow this data to be modified for submission to NEC and similar EMA codes. In addition, it was our desire that we be able to feed the analysis output data back into SUPERTAB where the resultant surface current distribution or radiated and scattered fields could be viewed. SUPERTAB is a software package which is intended for use in finite element modeling of mechanical systems (ref. 1). It is useful to this application because it allows for the automatic generation of a mesh of uniform or variable sized quadrilaterals or triangles over a surface. We can then interpret these polygons as either small surface patches or as multiple wire segments. The ability to vary the size of the mesh allows the analyst to emphasize regions where rapid variations in current occur. The following geometry entities are used in SUPERTAB for the creation of planar and volumetric geometries:

Point	defined by its coordinates in three dimensional space.
Line	defined by the two Points which it connects.
Arc	defined by three connected Points.
Spline	defined by four to twenty five connected Points.
Curve	a Curve is a Line, Arc, or Spline.
Edge	defined by one or more connected Curves.
Surface	defined as bounded by three or more connected Edges which contain it.

In addition the following entities are used in describing the meshing process of a surface geometry:

Subarea	defined by three or more connected Curves containing a Surface.
Node	defined by its coordinates in three dimensional space.
Element	defined by the two or more Nodes which it connects.

An Element connects some number of Nodes. For example a quadrilateral Element connects four Nodes whereas a beam Element connects two Nodes. There are five properties associated with every SUPERTAB Element. The Element properties of concern to us are:

Type	either Thin Shell (Linear Quadrilateral or Linear Triangle), Linear Beam, or Plate (Linear Quadrilateral)

Material Isotropic, Orthotropic, or Anisotropic
Type
Material such as Modulus of Elasticity
Values

Additional Element properties of Connectivity Type and Physical Property Values are used by SUPERTAB to perform mechanical analysis and are not used in this application. We will only use the Isotropic Material Type for the NEC input translation. SUPERTAB uses Material Values properties in mechanical finite element analysis, in this application NECGEOM can be instructed to interpret the Material Values Tables for radii of wire segments.

The ultimate goal in the use of SUPERTAB is to generate a set of nodes and elements which will be interpreted by the interface code, NECGEOM, as wire segments or surfaces patches.

Numerical Electromagnetic Code—NEC

NEC uses the method-of-moments technique to solve for the resultant EM field for a specified geometry and initial conditions (ref. 2). A NEC input data deck consists of three type of cards. These are 1) comment cards, containing a description of the problem to be analyzed; 2) geometry cards, containing geometry and structure data; and 3) control cards, to specify problem parameters and initial conditions.

The program geometry cards serve to identify the geometry of the problem and the structure to be analyzed. These cards contain point by point data of the geometry as well as model characteristics such as symmetry or the use of a ground plane. The geometry cards that are of interest to this application are:

GE	end of geometry card (this card also specifies the ground plane option)
GM	translate or duplicate structure
GR	generate cylindrical structure (rotational symmetry)
GW	generate wire
GX	reflect structure (planar symmetry)
SP	specify surface patch (also SC)

The geometry cards must be submitted to NEC in a specific order. The NECGEOM tutorial creates all of the needed geometry cards for submission of a NEC analysis.

The program control cards follow the structure geometry cards in a NEC input file. Their functions are to 1) set electrical parameters for the model; 2) select options for the solution procedure; and 3) request data computation. To carry out these control tasks, there are a number of different control cards, which are grouped into one of three categories. These control cards can be generated from within the NECCNT tutorial. The control cards that are of interest to this application are listed under their respective groups:

GROUP 1

EK	extended thin-wire kernel flag
FR	frequency specification
GN	ground parameter specification
KH	interaction approximation range
LD	structure impedance loading

GROUP 2

EX	structure excitation card
NT	two-part network specification
TL	transmission line between segments card

GROUP 3

CP	coupling calculation
EN	end of data card
NE	near electric field request
NH	near magnetic field request
PT	wire segment current print control
RP	radiation pattern request
WG	write Numerical Green's Function file
XQ	execute card

There is not a fixed order for the control input cards (a specified order is required for the geometry input cards). The parameters and options are set first, followed by the requests for calculation of currents, near fields, and radiated fields. Computation of currents may be requested with an XQ card. RP, NE, or NH cards cause calculation of the currents and radiated or near fields on the first occurrence. Subsequent RP, NE, or NH cards cause computation of fields using the previously calculated currents. Any number of near-field and radiation pattern requests can be grouped together, except when multiple frequencies have been specified by an FR card. If this is the case, then only a single NE or NH card and a single RP card will remain in effect for all frequencies. All parameters retain their values until changed by subsequent data cards. After the parameters have been set and currents/fields calculated, it is then possible to change selected parameter values and repeat the calculations.

Interface programs – SUPERNEC

The interface between SUPERTAB and NEC is achieved by a set of software programs collectively called SUPERNEC (SUPERtab to NEC). The SUPERNEC set of codes is comprised of the following computer programs:

NECTUTOR	A command procedure which performs the necessary assignments of files to logical names and runs the NECGEOM and NECONT tutorials.
NECGEOM	NEC geometry input tutorial program. Uses UNIFILE to read the SUPERTAB Universal File and generate a geometry data file (NECOUTEUNI). This data, in NEC absolute wire segment numbering format, is then used to create a patch and wire geometry NEC input file (NEC.DAT).
NECONT	NEC control input tutorial program. Creates the program control part of the NEC input file.
UNIFILE	Converts Universal File format data from SUPERTAB into an new data file (NECOUTEUNI) having the same Universal File format. Also returns geometry data to NECGEOM having the NE absolute wire segment numbering format.
MATHLIB	Vector and matrix math routines.
FLD	Performs output formatting for the NEC tutorials NECGEOM and NECONT.
ULIB	I/O routines.
DBNGEOM	I/O data base for NECGEOM. This code includes interactive query of user and stores user responses to prompts.
DBNEC	I/O data base for NECONT. This code includes interactive query of user and stores user responses to prompts. These codes are used to 1) translate SUPERTAB geometry data; 2) supplement data base with needed parameters by user query with prompts; and 3) generate geometry data files and control files for input to NEC.

Methodology

When a SUPERTAB Universal File is read by NECGEOM, the properties of a given element determine the way in which it is translated into NEC input cards (i.e. lines in the input file). The way in which the element properties control this interpretation is as follows:

- If an Element has type Thin Shell (Linear Quadrilateral or Linear Triangle) it is assumed that the bounding line segments are WIRE SEGMENTS.
- Every Linear Beam Element is assumed to represent a wire segment.
- An Element with Type Plate (Linear Quadrilateral or Linear Triangle) is assumed to represent a quadrilateral or triangular SURFACE PATCH.

These five Element types (TN_LQ, TN_LT, BM_LN, PLT_LQ, PLT_LT) are the only ones allowed by the NECGEOM program. The only other Element property which is used by NECGEOM is the first of the Material Values properties which NECGEOM may interpret as a wire segment radius. Note that even though we do not use all of the properties, SUPERTAB will associate them all with each Element.

The first step in a solution procedure is to calculate the interaction matrix, which determines a response from a geometry to an arbitrary excitation. The interaction matrix calculation depends solely on the structure geometry and the control cards from GROUP 1 created in the NECONT tutorial. Computation and factorization of the interaction matrix is not repeated if cards beyond GROUP 1 are changed. The second step is to solve the matrix equation for the currents due to a specified excitation. Finally, the near fields, radiated fields, or coupling effects between segments may be computed from the currents. NECONT requires the partially created data file NEC.DAT (constructed by running NECGEOM) as it's input file.

NECGEOM—The Translation of SUPERTAB Geometry to NEC Input Format

The SUPERTAB Universal File, NECGEOM, and DBNGEOM are used to modify the SUPERTAB volumetric geometry data for input to NEC. After the SUPERTAB data is read from the Universal File and assembled into a data file called NECOUTEUNI, the user is prompted to input the following information:

Comment line	Text entered in response to this prompt will appear as a single comment card in the NEC input file.
Wire segment radius	The user must choose between user entry or use of the

	SUPERTAB Material Values Tables for wire segment radii.
Planar symmetry	The user can identify reflection symmetry across one or more planes.
Rotational symmetry	The user must identify if the geometry has symmetry of rotation about the Z-axis.
Transformation	The user must identify additional overall transformation (i.e., rotation followed by translation) to the structure.
Ground plane	The user is asked if the x-y plane is to be used as a ground plane.

The wire segment radius prompt asks the user to choose between user defined wire segment radii and the use of the SUPERTAB Material Values tables. The user may choose to enter the global wire segment radius. In order to use the tables, the user must have taken steps in SUPERTAB to input the desired radii in the Material Values tables referenced by the corresponding Elements. NECGEOM will now write the GW, SP, and SC cards to the NEC input file NEC.DAT.

The planar symmetry prompt asks the user to identify when a structure has reflection symmetry across one or more planes. The computation time required by NEC may be reduced by using a smaller geometry and defining planar symmetry. This option will not work if the entire geometry was created in SUPERTAB. When a reflection is specified, NECGEOM checks to determine that no segment or surface patch lies in or crosses the reflection plane. If this condition is violated planar symmetry is not performed and the entire geometry will be evaluated but without the advantage of matrix reduction due to planar symmetry. With this input NECGEOM writes the GX card to the NEC input file NEC.DAT.

The rotational symmetry prompt asks the user to identify when the structure has symmetry of rotation about the Z-axis. The rules regarding rotational symmetry are similar to those for planar symmetry. NEC may take advantage of the symmetry in its computations but the GW, SP, SC, and GX cards may specify only the fundamental geometry to which rotational symmetry is to be applied. When rotational symmetry is specified, NECGEOM checks to determine that no segment lies on or crosses the Z-axis and that no surface patch is intersected by the Z-axis. If these conditions are violated then rotational symmetry will not be performed. Note that if both planar and rotational symmetry are specified (with planar symmetry specified first), NEC will perform the calculations for the structure having both types of symmetry but NEC will only take advantage of rotational symmetry (i.e., the last symmetry requested). In this latter case the entire geometry will be evaluated and matrix reduction will be based upon rotational symmetry. With this input NECGEOM writes the GR card to the NEC input file NEC.DAT.

The transformation prompt asks the user if an additional overall transformation (i.e., rotation followed by translation) is to be applied to the geometry. Such a transformation has no effect on previously generated symmetry. For example, to perform analysis on a structure with symmetry of rotation about the Y-axis, start with rotational symmetrical about the Z-axis and perform a ninety degrees rotation about the X-axis. It should be noted that such a transformation may later affect the use of symmetry in the analysis if a ground plan is specified. With this input NECGEOM writes the GM card to the NEC input file NEC.DAT.

The final NECGEOM prompt asks the user if the X-Y plane is to be used as a ground plane. The response to this query determines the integer which will follow the GE on the geometry end card. In order to use a ground plane in the NEC analysis it is necessary, but not sufficient, to specify a ground plan at this point in the geometry file creation process. Later, in NECONT, the properties of the ground plane must be specified. There is a provision to allow the user to cancel the ground plane specification in the NECGEOM tutorial procedure. When a ground plane is specified, NECGEOM checks to determine that no segment or patch lies below the X-Y plane. If this condition is violated the user is notified that a ground plane will not be allowed.

After completion of the NECGEOM tutorial there will be four new files in the user directory. These files are:

NEC.DAT	Partial NEC input file.
NECOUT.UNI	New Universal File created in NECGEOM with the UNIFILE program. This Universal File contains geometry data in NEC absolute wire segment numbering format.
FOR002.DAT	This file contains all user responses to NECGEOM prompts.
FOR003.DAT	This file contains both the NECGEOM prompts and the user responses.

The difference between the new Universal File (NECOUT.UNI) and the original SUPERTAB Universal File is that every NEC wire segment is represented in NECOUT.UNI by a single Linear Beam Element. In the original SUPERTAB file a single Element might represent several wire segments, and a single wire segment might be represented by two different Elements. The labels of the Linear Beams in NECOUT.UNI correspond to NEC absolute segment numbers.

The user can read NECOUT.UNI into SUPERTAB with the Universal File read option and obtain a three dimensional representation of the Linear Beam Elements which are labelled with the NEC wire segment numbers. It is worthwhile to do this if excitation or loading of individual wire segments is desired, or if networks or transmission lines are to be used in NEC. Viewing NECOUT.UNI in SUPERTAB allows the user to determine the order in which NECGEOM has numbered the wire segments. The capability to load NECOUT.UNI back into SUPERTAB allows convenient editing of the structure for iterative modification in the development of the model. Once the NECOUT.UNI geometry is edited in SUPERTAB it can be resubmitted to NECGEOM as a SUPERTAB Universal File and the process of NEC geometry file creation repeated.

NECONT—To Create the NEC Control Input File

NECONT has three main subroutines which correspondingly and exclusively write cards from each of the three groups. NECONT interfaces with the prompt database DBNEC and reads values input by the user. Based upon these input values, it then calls the appropriate WRITEGROUPxxx subroutine and writes the card or group of cards. Each card that is written is then appended onto the NEC input data file NEC.DAT.

The first prompt in the NECONT tutorial is the GROUP 1 menu. This menu allows the user to select optic s and input parameters needed to calculate the interaction matrix. The first option is for either Thin-wire Kernel or Extended Thin-wire Kernel. These approximations options are used for the kernel of the electric field integral equation. With the Thin-wire Kernel the current on the surface of a wire segment is reduced to a filament of current on the segment axis. With the Extended Thin-wire Kernel approximation, a current uniformly distributed around the segment surface is assumed. If the Extended Thin-wire Kernel option (EK) is chosen, the field of this current will be approximated with a higher degree of accuracy. The accuracy of the numerical solution for the currents on a wire segment depends on the wire segment length and the radius of the wire. If the ratio of segment length to radius (SL/A) is small (less than 8) then the possibility for solution error is increased. In this situation, it would be advantageous to use the Extended Thin-wire Kernel approximation as it allows for SL/A to be as small as 2 with computational error of less than 1%.

The Frequency Specification (FR) option allows the user to perform calculations at a single frequency or at multiple frequencies. If multiple frequency calculations are desired, the frequency increments can be linear or multiplicative. If no frequency is specified the default frequency of 299.8 MHz is assumed.

The Ground Type (GN) option allows the user to choose 1) free space (the absence of a ground plane); 2) a finite ground (using a reflection coefficient approximation); or 3) a perfectly conducting plane. If a ground plane is desired it must have been specified as a NECGEOM option.

The Interaction Approximation Range (KH) option allows the user to specify the minimum separation distance between segments. If this minimum separation distance is specified a time saving approximation can be used to fill the interaction matrix. The interaction field is computed using an impulse approximation whenever two segment are separated by more than RKH wavelengths.

The Structure Loading (LD) option allows the user to specify the impedance loading on one segment (or number of segments). The analyst may use the LD option to 1) specify complex impedance or lumped element parameters (R, L, and C that are fixed with frequency) on any number of elements; 2) specify wire conductivity on any number of elements; or 3) nullify any previous loads on all segments.

The second NECONT menu is for GROUP 2 control cards and allows the selection of parameters which will require NEC to factor the existing interaction matrix. The Structure Excitation Specification (EX) option allows the user to identify the excitation incident upon the structure. The excitation types can be 1) an applied E-field voltage source; 2) a linearly polarized incident plane wave; or 3) right or left hand elliptically polarized plane waves.

The Two Port Network Specification (NT) option allows the user to generate a two-port nonradiating network connected between any two segments in the

structure. The characteristics of the network are specified by its short-circuit admittance matrix elements.

The Transmission Line Between Segments (TL) option is similar to the Two Port Network Specification option in that the user is allowed to generate a structure between any two segments of a model. To define a transmission line the user must define the length of the line connecting the two segments, the line characteristic impedance, and shunt admittance.

Finally, the last NECONT menu, for GROUP 3 controls, allows the user to specify computation of segment currents, scattered or radiated fields, and coupling between segments. The first option, Compute Coupling Between Segments (CP), will solve for the maximum coupling that could occur between any of the segments that are used to make up the model. NEC can calculate the effects of coupling of five different segments upon each other.

The Compute Near Electric Field (NE) and Compute Near Magnetic Field (NH) options will calculate the total (incident plus scattered) electric or magnetic fields at some user specified distance from the object. Rectangular or spherical coordinates can be used for either of these two options.

The Compute Segment Currents Only and Compute Monostatic Field options are self explanatory. The possible excitation types for the monostatic source are 1) linearly polarized incident plane waves; 2) right or left hand elliptically polarized plane waves; or 3) an elementary current source. The Compute Monostatic Field option is a unique SUPERNEC feature that is not typically available to the NEC user.

After NECONT has written the control cards it returns with the GROUPSELECT menu to allow the user to return to any of the three groups. The options allows the analyst to change some of the parameter values. This action creates additional cards to be used in iterative calculations. When all desired control cards have been generated the user may choose to exit NECONT. Upon completion of the NECONT tutorial the NEC input file NEC.DAT is closed and is ready to be read into NEC to launch the analysis.

Examples:
Using SUPERTAB to Create Geometries for NEC

Most geometry modeling capabilities available with electromagnetic analysis codes are limited to stick figure approximations or crude cylindrical and polygon geometries. In some cases the geometry model options include a cone as a cylinder end cap. SUPERTAB allows the generation and meshing of complex shapes and intricate detail such as surface dimples or re-entrant cavities like an inlet duct. One such example can be found in the exhaust nozzle of the SUPERTAB model of a rocket in Figure 2.

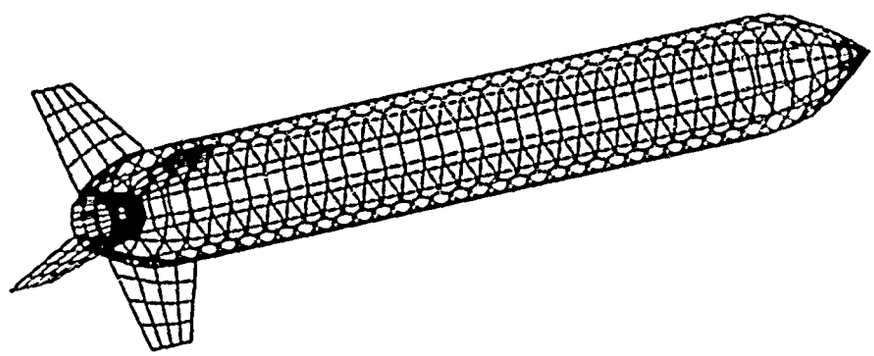


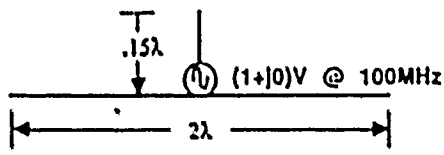
Figure 2. Rocket Shaped Geometry with Tail Fins

This model is a combination of cylindrical, conical and planar shapes with straight line and curved line plan forms. The spline option in SUPERTAB allows greater modeling accuracy, typically, than computational capability will permit. As computer processor speeds and working memory increase, computational analysis codes like NEC will be able to take greater advantage of the modeling accuracy of SUPERTAB.

Elementary EM analysis generally starts with planar modeling of simple geometries. Planar objects as well as attaching wires are easily modeled for NEC using the SUPERNEC concept. Figure 3 illustrates two and three dimensional views of a SUPERTAB model of a planar disk with a monopole antenna above the center of the disk. The disk has a diameter of two wavelengths. The monopole has a length of 0.1 wavelengths and the antenna is at a height of 0.05 wavelengths above the surface of the disk. The antenna is being driven by 1+j0 volts at 100 MHz. Using this geometry as an input to NEC, Figure 4 is a plot of the resultant NEC analysis showing the E-Plane pattern of the monopole above a disk.

The SUPERNEC interface between SUPERTAB and NEC allows modeling of geometries represented in spherical and cylindrical coordinates as well as cartesian coordinate geometries. A sphere can be modeled to any grid size depending on the desired accuracy. Overall grid size can be decreased quickly in SUPERTAB for cases where higher frequency data is desired. The SUPERTAB feature to generate variable sized grid spacing is illustrated in Figure 5 where free mesh generation was specified. Whenever variable meshing is employed in SUPERTAB the analyst should view the geometry prior to NEC input to verify model integrity.

Scattering can only be determined analytically for simple canonical shapes. SUPERNEC allows SUPERTAB modeling and NEC analysis of complex geometries that must be analyzed numerically. Figure 6 illustrates a complex volumetric star shaped



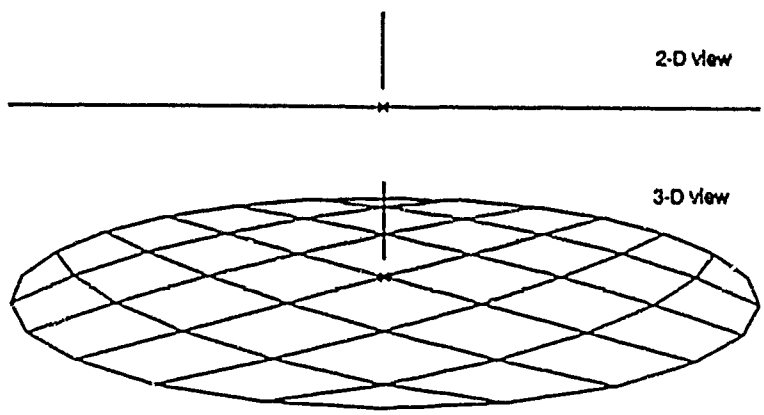


Figure 3. Monopole Above a Disk

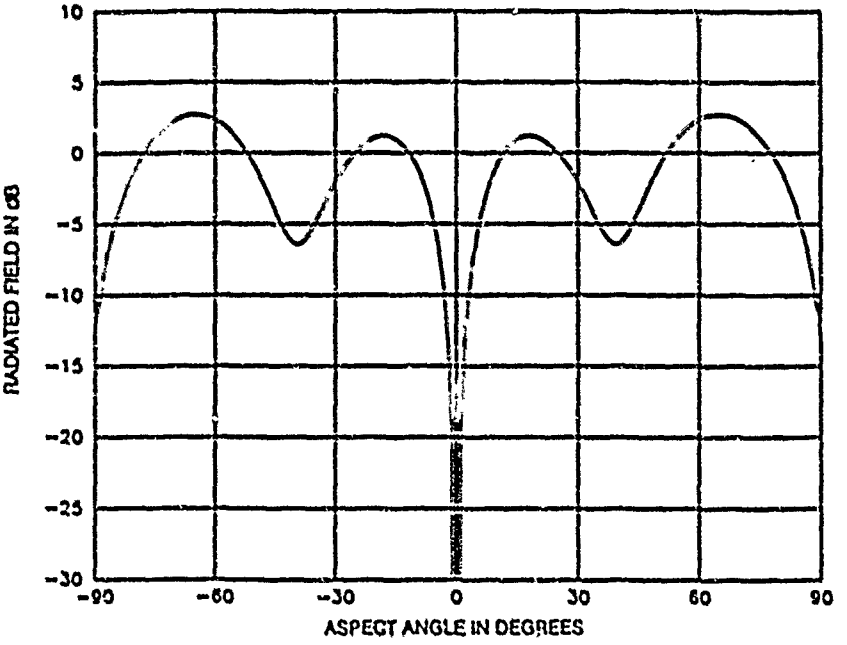


Figure 4. Radiation Pattern of a Monopole Above a Disk (E-Plane Pattern)

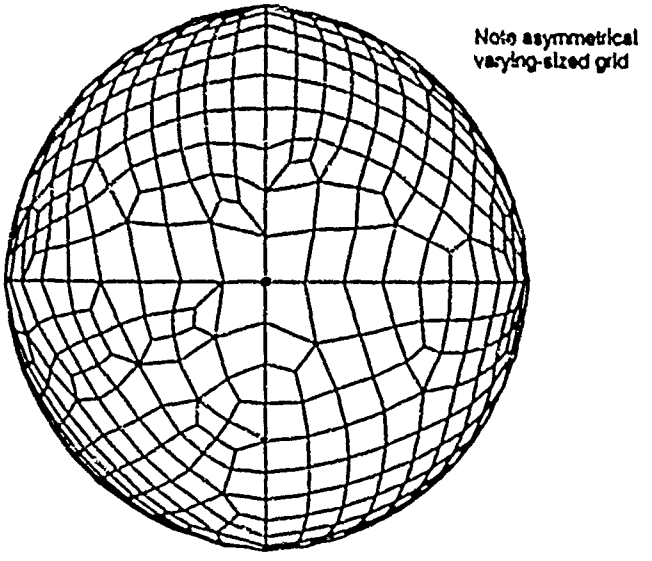


Figure 5. Sphere With Free Mesh Generation

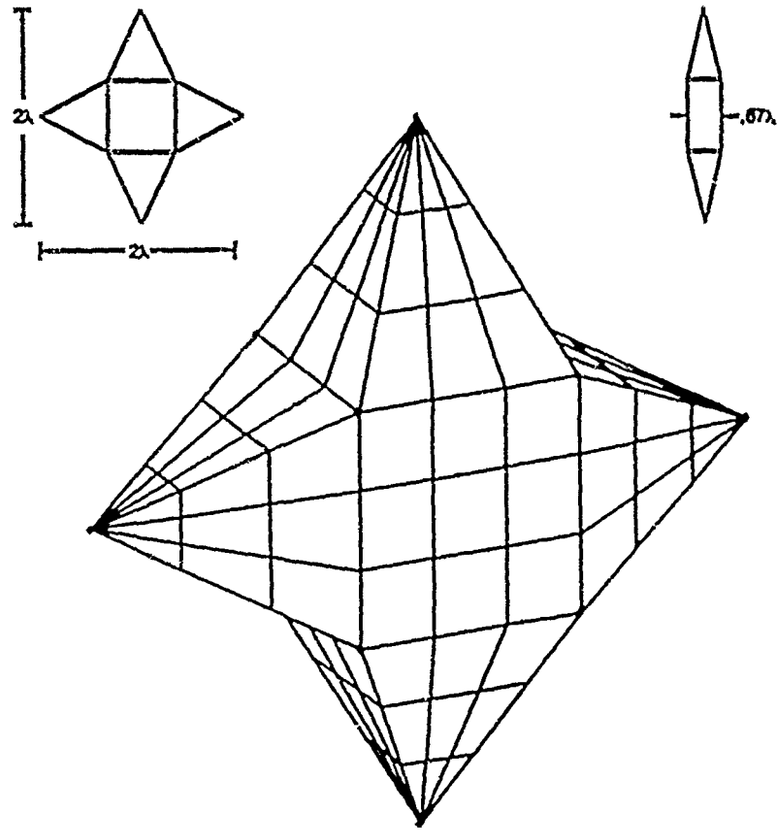


Figure 6. Volumetric Star Shaped Geometry

geometry created in SUPERTAB. The star has a height and width of two wavelengths and a depth of 0.67 wavelengths and is shown with course segmentation. Figure 7 is a plot of the NEC analysis of the scattering pattern of the same geometry.

Complex geometries can be modeled, analyzed and the resultant current distribution viewed using SUPERNEC. SUPERTAB in concert with NEC allows a graphic representation of a quantity that cannot be easily solved analytically nor experimentally. Our last example illustrates a volumetric triangular plate (Figure 8). The plate is a 30°, 120°, 30° triangle with a base length (longest dimension) of two wavelengths and a thickness of 0.05 wavelengths. Figure 9 contains several views of a contour plot of the induced surface current distribution on the triangular plate due to a broadside (normal to the plane of the plate) incident E-field. In this case the data results from the NEC analysis were fed back into SUPERTAB to create the induced surface current contour plots.

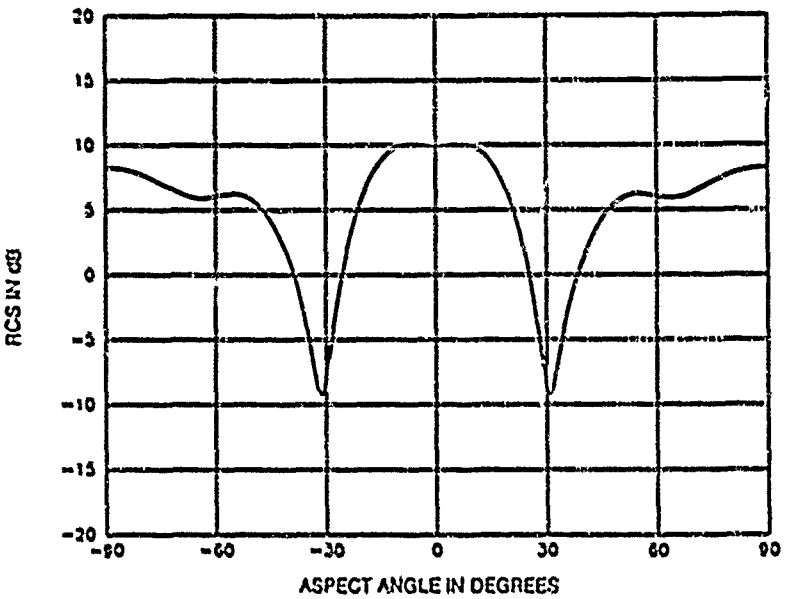


Figure 7. Monostatic Scattering Pattern of a Volumetric Star Shaped Geometry

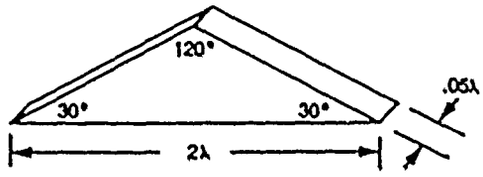
Summary

In general the SUPERTAB to NEC interface (SUPERNEC) offers modeling capabilities equivalent to any other modeling method currently available for use with an EM analysis code such as NEC. From a practical standpoint, the use of SUPERTAB has been successful in fulfilling the original criteria to use existing capabilities and produce the NEC I/O interface with minimal development. One possible drawback to this approach is the license requirement for the use of SUPERTAB. This can become prohibitive for individual users or in the event that the application is to reside in a classified area where it cannot be shared.

The specific advantages to the SUPERNEC concept include:

- The feature of automated mesh generation with either uniform or variable sized segmentation.
- The capability of creating either one, two, or three dimensional bodies with curved surfaces.
- The option of modeling in cartesian, spherical, or cylindrical coordinate systems.
- The ability to edit the structure geometry after it is created. Volumes, surfaces, and even individual wire elements can be edited, deleted or added to the model.
- The use of Splines to model complex curvatures with a high degree of accuracy.
- The option to compute monostatic fields in any plane.
- SUPERNEC insures that all segments are connected. NEC users may have experienced incorrect analysis results due to an input error that resulted in unconnected segments. This error is not detected by NEC.
- The ability to view NEC output as a SUPERTAB geometry. This has been demonstrated to be useful in the evaluation of the induced surface current distribution on a volumetric body (Figure 9).

Future application of the SUPERNEC concept include the development of I/O interfaces to other electromagnetic analysis codes. In particular, it is our desire to develop a convenient time domain analysis capability with a similar graphical user interface.



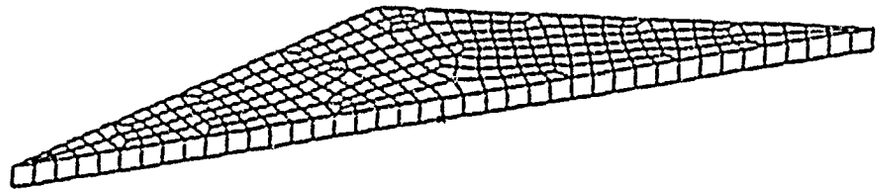


Figure 8. Meshed Triangular Plate Geometry



2-Dimensional (normal) view



3-Dimensional view



3-D View with mesh

Figure 9. Induced Surface Current Distribution on a Triagular Plate Due to a Broadside Incident E-Field

References

1. SUPERFAB User's Guide; Structural Dynamics Research Corp.; 5201.120 2M 4/86 printed in USA.

2. Numerical Electromagnetics Code (NEC)—Method of Moments; Technical Document 116, UCID-18834; Vol. 1, part 2: Program Description—Code, and Vol. 2, part 3: User's Guide; G.J. Burke and A.J. Poglo of Lawrence Livermore National Laboratory; Naval Ocean Systems Center, San Diego, CA. 92152.

Biography

Frank Ellis Walker
Boeing Aerospace (206) 773-5023
P.O. Box 3999, MS 85-84
Seattle, WA. 98124-2499, USA

Mr. Walker is a Senior Specialist Engineer and the principal investigator of the Electromagnetic Compatibility (EMC) research and development effort at Boeing Aerospace in Seattle, WA. He has been a member of the Electromagnetic Technology Staff at Boeing Aerospace for eleven years, participating in various elements of photovoltaic, electrical power, sneak circuit analysis, and electromagnetic compatibility research and development.

Prior to joining Boeing in 1978, Mr. Walker participated in automated process control development at IBM, in San Jose, CA. Mr. Walker holds Bachelor of Science degrees in Physics from Pacific Lutheran University, and in Electrical Engineering from the University of Idaho.

Eugene A. Sorensen
Boeing Aerospace (206) 773-2871
P.O. Box 3999, MS 8K-01
Seattle, WA. 98124-2499, USA

Mr. Sorensen is a Specialist Engineer in the Antenna Technology organization at Boeing Aerospace in Seattle, WA. He has been part of the Electromagnetics Technical Staff at Boeing Aerospace for five years devoted primarily to the development of analytical and computational techniques in support of performance optimization of small antenna arrays. His assignments have included computer modeling and analysis of antenna arrays and development and laboratory validation of optimization algorithms and interactive analysis graphic software. He has been a primary user of the SUPERFAB to NEC interface described in this paper.

Prior to joining Boeing in 1984, Mr. Sorensen was involved in power systems development at IBM, in San Jose, CA. Mr. Sorensen has received a Bachelor of Science degree in Electrical Engineering from Brigham Young University. He is currently enrolled in graduate studies, seeking a Master of Science degree specializing in electromagnetic theory, from the Electrical Engineering Department of the University of Washington.

James Scott Kenney (206) 527-4760
4732 18th Ave. N.E., Apt. 1A
Seattle, WA. 98105

Mr. Kenney is currently studying at the University of Washington School of Medicine. During his two year tenure in the Electromagnetic Technology organization at Boeing Aerospace he developed the SUPERFAB to NEC interface design and wrote much of the computer code to perform the data translations and user tutorials. While at Boeing Aerospace Mr. Kenney was also involved in the evaluation of materials effects on wave propagation.

Prior to joining Boeing Aerospace he served as a research assistant in the Physics departments of Pomona College and Stanford University and as a student researcher at Argonne National Laboratory. Mr. Kenney has earned a Bachelor of Arts degree in Physics from Pomona College and a Masters of Science degree in Applied Physics from Stanford University.

SESSION 11 - "COMPUTATIONAL ISSUES II"

Chairman: Michael Thorburn

RESULTS FROM A NEW THEORY OF LIGHT DIFFRACTION BY DIELECTRIC WEDGES†

by
Gregory L. Wojcik & John Mould, Jr.
Weidlinger Associates•

ABSTRACT

Dielectric wedge diffraction occurs whenever electromagnetic waves illuminate a sharp edge on an interface separating different dielectric media, e.g., air and glass. Such dielectric edges are often encountered in practice, for example, on prismatic and faceted transparent objects, or, more generally, on cylindrical and conical, nonconducting structures with polygonal cross-sections. Despite its importance in many applications, no mathematical solutions exist for dielectric edge diffraction since it is fundamentally a vector rather than scalar wave phenomenon.

This talk reviews a new vector theory for the canonical problem of two contiguous, semi-infinite, dielectric wedges, with a TM or TE polarized plane wave incident from the exterior wedge and parallel to the edge. The mathematical formulation, based on self-similar solutions of the vector wave equation in two space dimensions, yields a vector initial-boundary problem in connected complex half-planes. Solutions are presented as Cauchy-type integral representations on the boundaries. Boundary conditions yield a singular integral equation to be solved for the kernel of the boundary integral representation. The theory is discussed for an example problem that minimizes complexity while exhibiting all of the vector character. As a validation of the analysis, the solution is verified numerically.

† Supported under AFGL Contract F19628-84-C-0102 and NSF SBIR Grant SI-8760089
• 4410 El Camino Real, Suite 110, Los Altos, CA 94022 (415) 949-3010

INTRODUCTION

This talk describes some aspects of a new mathematical theory for the diffraction of electromagnetic waves by dielectric wedges. The canonical initial-boundary problem is formulated under the assumptions of classical field theory—appropriate provided the incident electromagnetic radiation is adequately represented by waves rather than quanta. The mathematical problem is one of generalized vector wave diffraction since it considers a generalized interface, i.e., an infinitely sharp edge on a plane interface, separating two different media supporting wave fields. This theory is relevant to computational electromagnetics since the canonical dielectric wedge solutions described below are fundamental to geometrical theories of diffraction, e.g, GTD, UTD. In addition, the theory provides a benchmark for testing accuracy of numerical approximations like time-domain finite differences or finite elements, since discrete meshes do not resolve sharp corners and the field singularities they produce without special attention.

The generalized two-wedge model consists of exterior and interior, two-dimensional, semi-infinite domains, with the larger wedge defining the exterior domain. It is assumed that a plane, polarized electromagnetic wave is incident on the edge and parallel to it, with either the electric component (TM polarization) or the magnetic component (TE polarization) directed along the edge. For simplicity it is also assumed that the wave is incident from the larger exterior wedge and does not reflect from the interface until it touches the edge. Clearly, since there is no spatial or temporal variation in the geometry or incident field along any line parallel to the edge, the problem's formulation may be confined to a plane perpendicular to the edge.

Some examples of generalized vector diffraction are illustrated in Fig. 1, showing incident, reflected, transmitted, and diffracted wavefronts. The four cases drawn are combinations of two interior wedge angles, 120° and 60°, and two relative wavespeeds, $c_1 < c_2$ and $c_1 > c_2$, where c_1 and c_2 are speeds in the interior and exterior wedges, respectively. To illustrate some limiting examples, the incident wavefronts are drawn nearly perpendicular to the line of symmetry in the

120° wedges, and parallel to the upper interface in the 60° wedges. Note, as a general rule all plane wavefronts propagating at c_1 or c_2 in the interior and exterior wedges, respectively, are tangent to their supporting wedge's diffracted wavefront or its "virtual" extension into the other wedge. Thus, it is relatively simple to draw wavefronts for any incidence angle by continuing tangentially off of the diffracted circles.

Referring to the figure, the circular wavefronts constitute the leading diffracted wave and the "triangular" wave fans are Mach waves excited in the slower wedge by the faster diffracted wave grazing the interface. For the case of $c_1 < c_2$, as the interior wedge angle decreases, the Mach wave fans will intersect, eventually reflecting between the interfaces. This yields the most complicated situation in terms of analysis. The case of $c_1 > c_2$ is generally simpler, although not as relevant to optical applications. Therefore, in order to simplify the presentation, this simpler case provides a model for much of the theory's development.

This canonical vector diffraction problem is well-known in applied mathematics, but has remained unsolved since its recognition in electromagnetism and elasticity perhaps a century ago. In contrast, effective analyses of the associated scalar diffraction problems have been well-developed. Diffraction by the degenerate scalar wedge (2π included angle), better known as the opaque screen, was first solved by Sommerfeld (1896). MacDonald (1902) formally solved the nondegenerate scalar problem of a single wave type in one wedge, with the first uniform asymptotic expansion, i.e., valid everywhere in the domain, obtained by Pauli (1938). A variety of scalar solution methods have subsequently been derived, in large part based on separation of variables, but also on the principle of self-similarity, e.g., Keller and Blank (1951).

Since vector diffraction involves two or more waves in one or more wedges, none of the available scalar methods work in the vector case. This is due to the essential nonseparability of coupled boundary conditions in wedge-shaped domains. To address this difficulty, many analysts (including mathematicians, physicists, and engineers, depending on the context of the problem) have attempted to extend the successful scalar methods to accommodate nonseparability, but without success. More recently, research by the present author, sponsored by the Air Force Geophysics Laboratory, has produced such an extension based on self-similarity, Wojcik (1989).

There are two essential parts to the analysis. First is transformation of the vector wave equation in the generalized diffractor via self-similarity. This yields d'Alembert's classic string equation (1-D wave equation) in characteristic coordinates, which is solved by inspection. The solution is mixed, that is, hyperbolic or elliptic over different parts of the domain. It follows that substitution of the boundary conditions yields a mixed boundary problem in semi-infinite strips. The second essential step is transformation of the mixed strips to two complex half-planes by the so-called characteristic mapping, essentially a Schwarz-Christoffel transformation, under which boundary conditions and the real characteristics are mapped entirely to the real axes. By eliminating the hyperbolic solutions on the axes, pure elliptic boundary conditions are prescribed. This reduces the boundary problem to a vector form of the Riemann-Hilbert problem on the real axes of two complex planes, which is reduced to a singular integral equation on the two axes.

The mathematical approach is elegant, and straightforward once certain key features are appreciated. It provides a consistent, constructive procedure for solving this most difficult diffraction phenomenon. Of course, the problem's long history of intractability proves that no formal analysis should be taken for granted, hence the need for numerical solution of the integral equation to ultimately confirm the theory. Therefore, to validate the solution, numerical results for the particular case of the canonical problem with $c_1 > c_2$ are described briefly at the end of the talk. Although an all-encompassing analysis, valid for every combination of geometry, input, and wavespeed is not presented, the techniques developed here are sufficient to analyze all such situations. However, these details must be left to future papers.

PROBLEM STATEMENT

The generalized, plane diffractor consists of two semi-infinite, contiguous dielectric wedges defined by lines $L^{(1)}$ and $L^{(2)}$ drawn from the origin. These lines define an interior domain with included angle $\omega_1 < \pi$ and an exterior domain with included angle $\omega_2 > \pi$, designated Ω_1 and Ω_2 respectively. Geometry, wedge numbering, and the polar coordinate system are illustrated in Fig. 2, where, for convenience, it is assumed that $L^{(1)}$ is on the x-axis.

The applied electromagnetic field is a TM or TE polarized plane wave incident from exterior wedge Ω_2 onto the vertex at time $t = 0$, with a unit step or jump across the wave front. More conventional time-harmonic response may be obtained by convolving a sinusoid with the solution to this step input. There is no need to specify a particular wave polarization at the outset since only constants in the boundary conditions differ.

Each wedge supports a scalar wave function, f_1 or f_2, in domains Ω_1 and Ω_2 respectively. Therefore, the two governing wave equations can be written in vector form as

$$(1) \qquad \Box \begin{bmatrix} f_1 \\ f_2 \end{bmatrix} \equiv \begin{bmatrix} c_1 & 0 \\ 0 & c_2 \end{bmatrix}^2 \Delta \begin{bmatrix} f_1 \\ f_2 \end{bmatrix} - \begin{bmatrix} f_1 \\ f_2 \end{bmatrix}_{tt} = \begin{bmatrix} 0 \\ 0 \end{bmatrix}$$

where $c_1 = 1/\sqrt{\epsilon_1\mu}$ and $c_2 = 1/\sqrt{\epsilon_2\mu}$ are wave speeds, scalar Laplacian $\Delta[\,] = [\,]_{rr} + [\,]_r/r + [\,]_{\theta\theta}/r^2$ operates on the elements of the vector and partial derivatives are indicated by r, θ, and t subscripts. For TM waves $f_n = (E_z)_n$ while for TE waves $f_n = (H_z)_n$, $n = 1, 2$. This equation is abbreviated as

$$(2) \qquad \Box f \equiv c^2 \Delta f - f_{tt} = 0$$

where definitions of matrix c and vector f are clear from (1).

The two wave functions are coupled by boundary conditions representing tangential field continuity on the wedge interface, $L \equiv L^{(1)} \cup L^{(2)}$, e.g., Stratton (1941). These can be written

$$(3) \qquad \begin{bmatrix} 0 & 0 \\ \nu_1 & -\nu_2 \end{bmatrix} \begin{bmatrix} f_1 \\ f_2 \end{bmatrix}_\theta + \begin{bmatrix} 1 & -1 \\ 0 & 0 \end{bmatrix} \begin{bmatrix} f_1 \\ f_2 \end{bmatrix}_t = \begin{bmatrix} 0 \\ 0 \end{bmatrix}$$

where for TM $\nu_n = 1/\mu_0$ and for TE $\nu_n = 1/\epsilon_n$.

Completion of the problem statement requires two initial conditions representing the incident plane wave, i.e., step function $f_2 = H(c_2 t - x\cos\phi - y\sin\phi)$, unity for positive argument and zero for negative. For the advantage of working with the same order of derivative, conditions on f_t and f_θ are preferred. Converting to polar coordinates and dividing the argument by r, taking derivatives and transforming the argument gives

$$(4) \qquad \frac{r}{c_2} f_t(r,\theta,0) = \pm f_\theta(r,\theta,0) = \delta(\theta - \phi - \pi \pm \pi/2) \begin{bmatrix} 0 \\ 1 \end{bmatrix}$$

with the (+) sign for vanishing argument at $\theta = \phi + \pi/2$, and the (-) sign at $\theta = \phi + 3\pi/2$.

WAVE SOLUTIONS AND THE INITIAL-BOUNDARY PROBLEM

Because the diffractor lacks a characteristic length scale, self-similar solutions of the governing equations are admissible. Such solutions are given by homogeneous functions of degree h, namely, functions satisfying $f(r,\theta,t) = t^h f(r/t,\theta)$. The most tractable and directly useful for the present case are functions of degree zero.

Defining scalar similarity variable $\rho \equiv r/t$ and transforming vector wave equation (2) using relation $rf_r = -tf_t = \rho f_\rho$ for homogeneous functions of degree zero, gives the reduced wave equation

$$(5) \qquad \rho^2(c^2 - \rho^2 I) f_{\rho\rho} + c^2 f_{\theta\theta} + \rho(c^2 - 2\rho^2 I) f_\rho = 0$$

where I is the 2x2 identity matrix. Observe that the leading coefficient vanishes at $\rho I = 0$ and $\rho I = c$, hence these yield a singular point and singular circle respectively. It follows that the equation is of mixed type across $\rho I = c$, i.e., hyperbolic outside the circle ($\rho I > c$) and elliptic inside ($\rho I < c$).

A direct solution of this self-similar form of the vector wave equation begins with the transformation to characteristic coordinates. The characteristic equation is readily found to be

$$(6) \qquad \rho^2(c^2 - \rho^2 I)(d\theta)^2 + c^2(d\rho)^2 = 0$$

and its solution is

(7) $$0\,I \pm \cos^{-1} c/\rho = w_\pm = u \pm v$$

where diagonal matrices $w_\pm = u \pm v$ are constants of integration defining the characteristic coordinates. Since $v = \cos^{-1}c/\rho \rightarrow i \cosh^{-1}c/\rho$, diagonal elements of v are real for $\rho I > c$ and imaginary for $\rho I < c$, hence, the characteristics are real outside the singular circles and complex inside.

Reduced vector wave equation (5) is transformed to characteristic coordinates by replacing derivatives via the chain rule, resulting in the normal vector form

(8) $$f_{w_+ w_-} = 0$$

which can of course be integrated directly giving d'Alembert's classic solution

(9) $$f(\rho,0) = F_+(w_+) + F_-(w_-)$$

where $F_\pm$ are two unknown vector functions. This solution is of mixed type, changing from hyperbolic (real characteristics) to elliptic (complex characteristics) across $v = 0$. Singular line $v = 0$ supports the diffracted wavefront and is itself characteristic since it satisfies characteristic equation (6), albeit degenerately. In the elliptic domain note that $F_\pm$ are complex conjugates. Asymptotic analysis shows that these solutions have a $\ln \rho$ singularity at the vertex for either polarization and are continuous across the singular circle.

The transformed wave domain for the vector initial-boundary problem is illustrated in Fig. 3 for a simple example that will be used later to demonstrate particular solutions. Each of the two mixed domains, Ω_n, $n = 1, 2$, drawn in the figure are spanned by diagonal coordinate matrices u_n and v_n, with hyperbolic Ω_{nH} and elliptic Ω_{nE} subdomains corresponding to real and imaginary v_n, respectively. The conjugate elliptic domains covered by complex variables w_{n+} and w_{n-} are drawn perpendicular to the hyperbolic domains covered by -45° and +45° lines, namely, $w_{n\pm} = u_n \pm v_n$. Limits on u_n are $\gamma^{(n)} \le u_n \le \gamma^{(n)} + \omega_n$, where $\gamma^{(n)}$ is the angle of $L^{(n)}$ and ω_n is the included angle of Ω_n. Real limits on v_n are $0 \le v_n \le \pi/2$ (hyperbolic subdomain), where $v_n = \pi/2$ corresponds to $t \rightarrow 0$ (or $r \rightarrow \infty$), the initial state; and $v_n = 0$ is the map of $r = c_n t$, the diffracted wave front. Imaginary limits on v_n are $i0 < v_n < i\infty$, where the upper limit is the map of limiting arcs surrounding the vertex. By virtue of the vector form of the problem, subsequent references to these domains, coordinates, and solutions will drop the subscript or superscript.

In order to proceed with a solution of the diffraction problem, particular solutions for $F_\pm$ must be found that satisfy the initial and boundary conditions on the transformed wave domain. Initial condition (4) is given on line $v = \pi/2$, corresponding to $\rho \rightarrow \infty$ (i.e., $t \rightarrow 0$ or $r \rightarrow \infty$), while boundary condition (3) is prescribed on lines $u = \gamma$ and $u = \gamma + \omega$. These conditions are readily transformed to their self-similar characteristic forms, to yield a complete statement of the mixed initial-boundary problem for $F_\pm$ in the semi-infinite strip domains. Since the problem involves coupled hyperbolic and elliptic subdomains, its solution requires analysis of each domain separately, as well as consideration of continuity across mixed interfaces.

Determining global elliptic solutions of the initial-boundary problem is complicated by geometry of the mixed vector wave domain, consisting of a semi-infinite strip in the u-v plane with real (hyperbolic) and complex (elliptic) characteristic coordinates changing across the diffracted front, $v = 0$, also a characteristic. Applying boundary conditions on the strip perimeter is inconvenient because the boundary parametrization changes at corners and the conditions are of mixed type.

Clearly, the problem would be better posed if it involved only elliptic conditions on a circle or half-plane, i.e., a single-parameter boundary. For a conventional scalar elliptic problem on a strip, it is natural to apply a conformal mapping to parametrize the boundary by a single variable. A similar approach is effective in the present case, although the transformation is on a characteristic variable rather than the conventional complex variable. This yields the so-called characteristic transformation

(10) $$z = [\cos(\pi\omega^{-1}(w_\pm - \gamma))]^{-1} = x + iy$$

mapping the elliptic w_+ subdomain to the upper half-plane, w_- to the lower, and the wedge vertex to the origin. The hyperbolic subdomain now maps to the real axis, on $-I \ge x \ge I$. This is the canonical domain for the vector initial-boundary problem. An example is shown in Fig. 4.

What remains is a boundary problem for the elliptic part of $F_{\pm}$ on the real axis, redefined for convenience as

$$F_1(w_1(z)) = W(z) = U(x,y) + i\,V(x,y) \tag{11}$$

where W(z) satisfies the reflection principle, i.e., $W(z^*) = W^*(z)$, since F_+' and F_-' are complex conjugates and map to the upper and lower half-planes respectively. The problem is to determine W(z) by continuation of the transformed boundary conditions on $y = 0$.

INTEGRAL REPRESENTATIONS AND SINGULAR SOLUTIONS

Boundary conditions on segments of the real axes in the complex half-planes relate real and/or imaginary parts of the unknown elliptic functions. These equations couple parts either between the two domains or within one domain only, defining respectively, vector or scalar boundary problems. The scalar problems may be solved in closed-form, establishing the fundamental structure of representations used to formulate the vector boundary problems.

Determination of an analytic function in the complex plane given a linear relation between its real and imaginary parts on a curve or contour has come to be called the Riemann-Hilbert (R-H) problem, e.g., see Carrier, Krook, and Pearson (1966). This is precisely the scalar problem mentioned above. The solution of R-H problems on the real axis follows a straightforward procedure based on factorization methods and Cauchy-type line integrals. Fundamental to this procedure is the representation of analytic functions in the half-plane by Cauchy-type line integrals over segments of the real axis. In particular, given the imaginary part of an analytic function on a segment of the real axis, then the function can be represented by a Cauchy-type line integral on this imaginary part over the segment. For example, if M(z) is analytic off the real axis, satisfies the reflection principle, and its imaginary part is known on $[x_a,x_b]$, then representations of the function and its boundary values are

$$M(z) = \frac{1}{\pi}\int_{x_a}^{x_b} \frac{\mathrm{Im}[M^+(s)]}{s-z}\,ds + N(z)$$

$$M^{\pm}(x) = \frac{1}{\pi}\int_{x_a}^{x_b} \frac{\mathrm{Im}[M^+(s)]}{s-x}\,ds + N(x) \pm i\,\mathrm{Im}[M^+(x)] \tag{12}$$

The integral is a particular solution of inhomogeneous equation $M^+ - M^- = i2\mathrm{Im}[M^+]$, while N(z) is a solution of homogeneous equation $N^+ - N^- = 0$, hence, N is real on $[x_a,x_b]$. This type of representation is a generalization of the Poisson integral formula on the half-plane, or equivalently, the Hilbert transform, and is readily mapped to arbitrary curves and contours. The second equation is the limit of the first as $z \to x$ from above (+) or below (−) the axis. The singular integral is evaluated as a Cauchy principal value and the imaginary part is the result of integrating around the Cauchy pole on an infinitesimal half-circle.

Solutions of the scalar Riemann-Hilbert problems yield global representations of analytic functions $W_1(z_1)$ and $W_2(z_2)$ that include unknown functions. To complete the solution, these unknowns are represented by Cauchy-type line integrals as

$$W_1(z_1) = B_1(z_1)G_1(z_1)\left[\frac{1}{\pi}\int_{-a}^{a} \frac{(B_1G_1)^{-1}\,K_1(s_1)}{s_1 - z_1}\,ds_1 + E_1(z_1) + P_1(z_1)\right] \tag{13}$$

$$W_2(z_2) = B_2(z_2)\left[\frac{1}{\pi}\int_{-b}^{b} \frac{(B_2)^{-1}\,K_2(s_2)}{s_2 - z_2}\,ds_2 + E_2(z_2) + P_2(z_2)\right] \tag{14}$$

where B, G, E, and P are known solutions of the scalar R-H problems, while K_1 and K_2 are unknown density functions to be determined. Taking the limit on the real axes and substituting into the vector R-H problems yields

$$(15)\qquad \mathrm{Re}\{B_1^+G_1^+\}\int_{-\infty}^{a}\frac{(B_1G_1Q)^{-1}K_2(x_2(s_1))}{s_1-x_1}ds_1 - B_2\int_{-1}^{1}\frac{(B_2)^{-1}K_2(s_2)}{s_2-x_2}ds_2 = S$$

where

$$(16)\qquad S = \pi(B_2\{\mathrm{Re}\{P_2^+\} + E_2\} - \frac{\nu_1}{\nu_2}\{\mathrm{Re}\{B_1^+G_1^+P_1^+\} + \mathrm{Re}\{B_1^+G_1^+\}E_1\})$$

$$+ \frac{\nu_1}{\nu_2}\frac{1}{2}(Q^{(1)}\zeta^{(1)}\delta(x_1 - z_1^{(1)}) + Q^{(2)}\zeta^{(2)}\delta(x_1 - z_1^{(2)}))$$

Therefore, solving the integral equations for $K_2 = (\nu_1/\nu_2)QK_1$ and substituting the result into representations (13) and (14) yields solutions for W_1 and W_2 satisfying the initial and boundary conditions of the problem.

SOLUTION OF AN EXAMPLE PROBLEM

The analysis described here is, in most part, formal since rigorous mathematical justification does not accompany each step. Therefore, in order to claim that this is in fact a solution to the generalized diffraction problem, extensive verification is necessary.

To begin the process of verification, an evaluation of the singular integral equation was performed for the following parameters, $c_1 = 1.$, $c_2 = .6854$, $\omega_1 = 120°$, $\omega_2 = 240°$, $\phi = 60°$, with both TE and TM polarizations. By subtracting out all singularities in the integral equation and applying a Gauss-Legendre quadrature rule, it reduces to a linear system for the unknown nodal values of the smooth residual function in the integral. This system may be solved uniquely, nodal values of K_2 determined, and integral representations (13) and (14) evaluated. It is readily verified by back substitution that the differential equations and all initial and boundary conditions are satisfied to the numerical accuracy of the linear system solution.

With $F(w(z)) = W(z)$ known, it must be integrated for $f(\rho,\theta)$. This is accomplished by integrating $F(w(z))$ along radial paths starting from known initial conditions and continuing along circumferential lines to fill in the complete diffracted solution in each wedge. Due consideration of the wavefront singularities is essential. Comparing the resulting analytical solution to a finite element solution, agreement was found to the numerical accuracy of the respective solutions, except near the vertex where the $\ln r/t$ behavior was not captured by the finite elements. Based on these evaluations it appears that the analysis described above does indeed provide a solution to the dielectric wedge diffraction problem. Further validation and extensions will be forthcoming.

REFERENCES

Carrier, G.F., M. Krook, and C.E. Pearson (1966). Functions of a Complex Variable, McGraw-Hill Book Company.

Keller, J. B. and A. Blank (1951). 'Diffraction and reflection of pulses by wedges and corners,' *Comm. Pure Appl. Math.*, 4.

MacDonald, H. M. (1902). Electric Waves, Cambridge University Press.

Pauli, W. (1938). 'On asymptotic series for functions in the theory of diffraction of light,' *Phys. Rev.*, 54, pp. 924-931.

Sommerfeld, A. (1896). 'Mathematische theorie der diffraction,' *Math. Ann.*, 47, pp. 317-374.

Stratton, J. A. (1941). Electromagnetic Theory, McGraw-Hill Book Company, New York.

Wojcik, G. W. (1989). Seismic Wave Propagation in Complex Geologic Structure, Air Force Geophysics Laboratory Report, Contract F19628-84-C-0102, Weidlinger Associates.

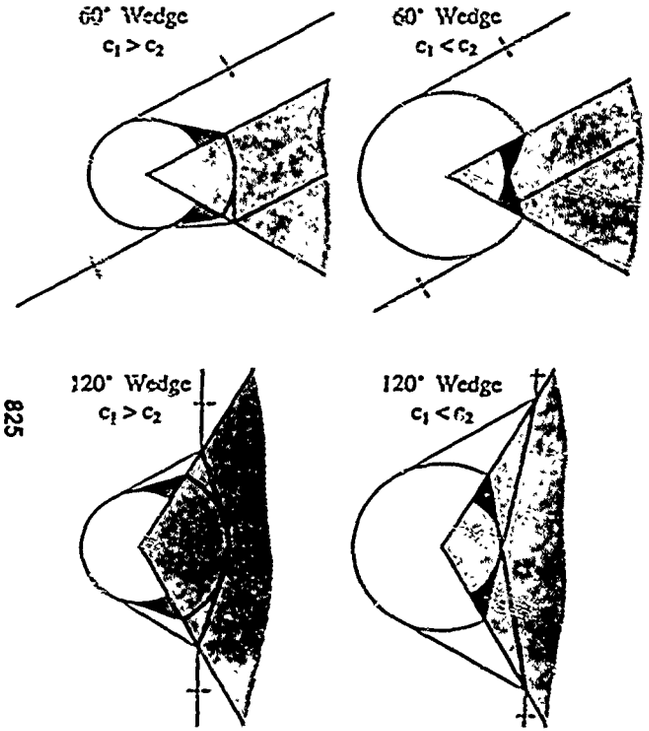


Figure 1. Examples of dielectric wedge diffraction for plane wave incident on 60° and 120° wedges.

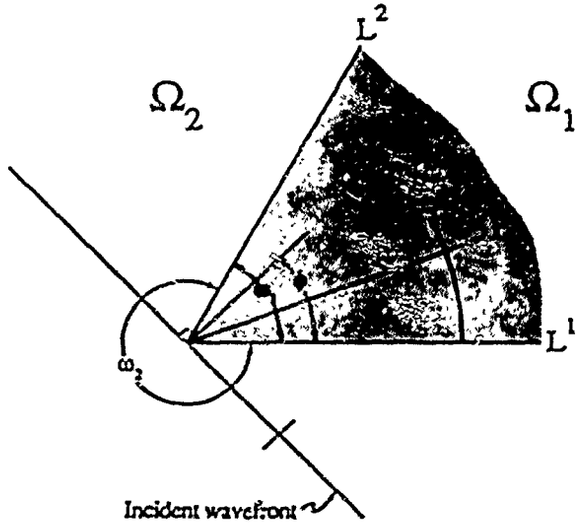


Figure 2. Geometry of the canonical diffraction problem.

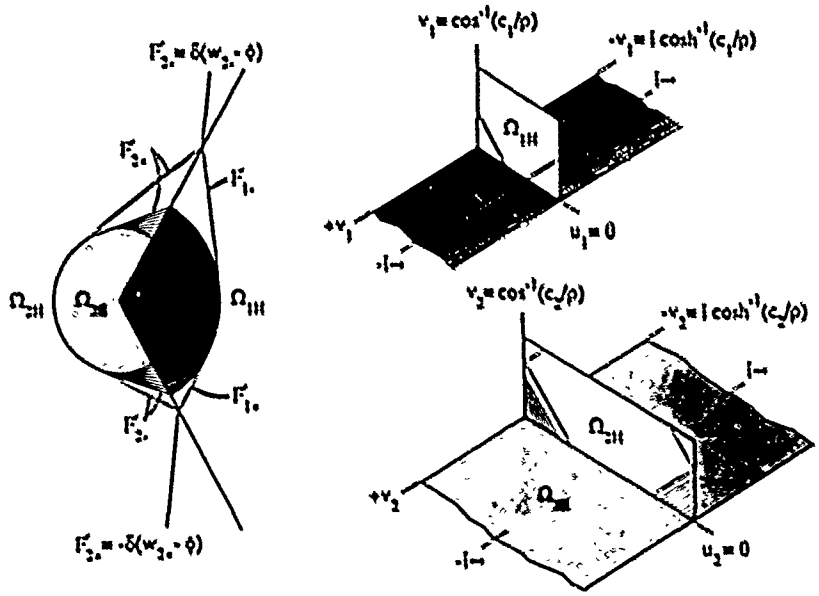


Figure 3. Transformation of the vector wave domain by the self-similar solution.

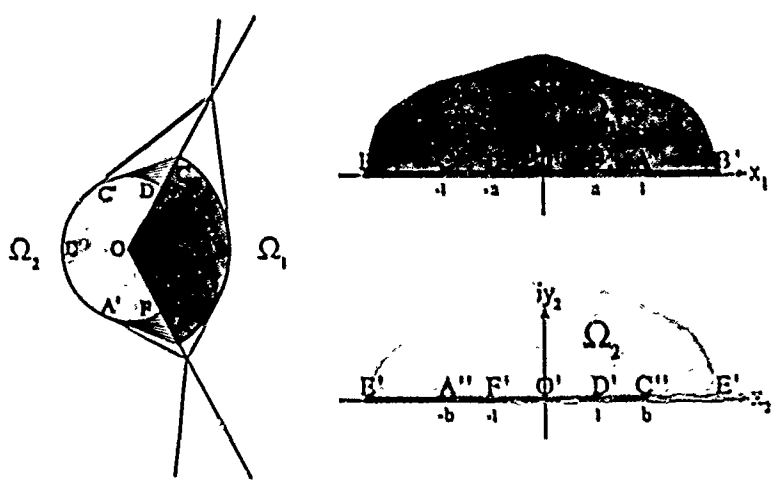


Figure 4. Transformation of the elliptic domains by the characteristic mapping.

SESSION 12 - "SCATTERING II"

Chairman: E L Fritz Rootman

A New FDTD Formulation for Materials with Frequency-Dependent Constitutive Parameters

R. J. Luebbers
F. P. Hunsberger
K. S. Kunz

Communications and Space Science Laboratory
Electrical Engineering Department
The Pennsylvania State University
University Park, PA 16802

March 1989

ABSTRACT

Current Finite Difference Time Domain (FDTD) formulations require the permittivity, permeability, and conductivity to be constant. However, for many materials these parameters vary significantly with frequency. This negates one of the primary advantages of the FDTD method, the ability to efficiently obtain results for a wide band of frequencies with a single computer run. Current practice for highly dispersive materials is to make separate FDTD computer runs for a multiplicity of narrow frequency bands of interest, using the appropriate values of the constitutive parameters. Thus, for dispersive materials, the FDTD method cannot compete effectively with the Method of Moments, except for situations where the Method of Moments cannot be readily applied.

The effects of constitutive parameters which vary with frequency are included in a new frequency-dependent FDTD formulation, $(FD)^2TD$, by extending the traditional Yee formulation to include discrete time-domain convolution. The accuracy of $(FD)^2TD$ is demonstrated by computing the reflection coefficient at an air-water interface over a wide frequency band including the effects of the frequency-dependent permittivity of water.

APPROACH

We begin the description by assuming familiarity with the classic FDTD paper by Yee [1]. His notation and positioning of field quantities about a rectangular "cell" is retained. Maxwell's curl equations for isotropic media are

$$\nabla \times \vec{E} = -\frac{\partial \vec{B}}{\partial t} \tag{1}$$

$$\nabla \times \vec{H} = \frac{\partial \vec{D}}{\partial t} - \vec{J} \tag{2}$$

$$\vec{B} = \mu \vec{H} \tag{3}$$

$$\vec{D} = \epsilon \vec{E} \tag{4}$$

where $\vec{E}$, $\vec{H}$, $\vec{D}$, and $\vec{B}$ are all instantaneous (time-domain) values. The above relation between D and E assumes a medium without memory of previous field values (a non-dispersive medium). In general, the present value of D will depend on the present value of E *and* all previous values of E [2]. Then, for a causal medium,

$$\vec{D}(t) = \epsilon_{\infty} \epsilon_0 \vec{E}(t) + \epsilon_0 \int_0^t \vec{E}(t-\tau)\chi(\tau)d\tau \tag{5}$$

where ϵ_0 is the permittivity of free space, ϵ_∞ is the relative permittivity of the material as $\omega \to \infty$, and where $\chi(\tau)$ is the electric susceptibility.

For this discussion, we will consider a plane wave travelling in the $+x$ direction. Then $\vec{E}$ will have only an E_y component and $\vec{H}$ will have only an H_z component. Then for conducting media equations (1) and (2) become

$$\frac{\partial B_z}{\partial t} = -\frac{\partial E_y}{\partial x} \tag{6}$$

$$\frac{\partial D_y}{\partial t} = -\frac{\partial H_z}{\partial x} \tag{7}$$

Discretizing space coordinates such that

$$(i, j, k) = (i\Delta x, j\Delta y, k\Delta z)$$

and time such that

$$D(t) \approx D(n\Delta t) = D^n$$

Yee's finite difference equations for this one-dimensional example become

$$\frac{B_z^{n+\frac{1}{2}}(i+\frac{1}{2}) - B_z^{n-\frac{1}{2}}(i+\frac{1}{2})}{\Delta t} = -\frac{E_y^n(i+1) - E_y^n(i)}{\Delta x} \tag{8}$$

$$\frac{D_y^{n+1}(i) - D_y^n(i)}{\Delta t} = -\frac{H_z^{n-\frac{1}{2}}(i+\frac{1}{2}) - H_z^{n-\frac{1}{2}}(i-\frac{1}{2})}{\Delta x} \tag{9}$$

To apply $(FD)^2TD$, the complex frequency-domain permittivity function of the material $\hat{\varepsilon}(\omega)$ is Fourier transformed into a time-domain electric susceptibility function $\chi(\tau)$. Using Yee's notation, we let $t = n\Delta t$ in (5) and so each vector component of $\vec{D}$ and $\vec{E}$ can be written as

$$D^n = \varepsilon_\infty \varepsilon_0 E^n + \varepsilon_0 \int_0^{n\Delta t} E(n\Delta t - \tau)\chi(\tau)d\tau \tag{10}$$

where the spatial index has been temporarily omitted. All field components are assumed to be constant over each time interval Δt. So, assuming E(t) is zero for $t < 0$,

$$D^n = \varepsilon_\infty \varepsilon_0 E^n + \varepsilon_0 \sum_{m=0}^{n-1} E^{n-m} \int_{m\Delta t}^{(m+1)\Delta t} \chi(\tau)d\tau \tag{11}$$

The value of D at the next time step is

$$D^{n+1} = \varepsilon_\infty \varepsilon_0 E^{n+1} + \varepsilon_0 \sum_{m=0}^{n} E^{n+1-m} \int_{m\Delta t}^{(m+1)\Delta t} \chi(\tau)d\tau \tag{12}$$

Now let

$$\chi_m = \int_{m\Delta t}^{(m+1)\Delta t} \chi(\tau)\,d\tau \tag{13}$$

and

$$\Delta\chi_m = \chi_m - \chi_{m+1} \tag{14}$$

Inserting the above equations into the difference equation for the $\nabla\times\vec{H}$ Maxwell equation and solving for E_y^{n+1}, we obtain (with the spatial index reinserted)

$$E_y^{n+1}(i) = \frac{\varepsilon_\infty(i)}{\varepsilon_\infty(i)+\chi_0(i)}\,E_y^n(i) + \frac{1}{\varepsilon_\infty(i)+\chi_0(i)}\sum_{m=0}^{n-1} E_y^{n-m}(i)\Delta\chi_m(i)$$

$$-\frac{\Delta t}{(\varepsilon_\infty(i)+\chi_0(i))\varepsilon_0\Delta x}\left[H_z^{n+\frac{1}{2}}(i+\tfrac{1}{2}) - H_z^{n+\frac{1}{2}}(i-\tfrac{1}{2})\right] \tag{15}$$

Note that if we assume the relative permittivity, ε_r, is independent of frequency (the usual FDTD assumption) then $\chi(\tau)=0$, $\varepsilon_\infty=\varepsilon_r$, $\chi_m=0$ for all m, and the above reduces to the Yee formulation. The Yee equation for H will be unchanged for nonmagnetic media,

$$H_z^{n+\frac{1}{2}}(i+\tfrac{1}{2}) = H_z^{n-\frac{1}{2}}(i+\tfrac{1}{2}) - \frac{\Delta t}{\mu\Delta x}\left[E_y^n(i+1) - E_y^n(i)\right] \tag{16}$$

While the summation term in (15) appears time-consuming, the mathematical nature of the time-domain susceptibility function can be utilized to convert this summation into a running sum that is updated at each time step and stored in one real variable per cell. In fact, an efficient algorithm can reduce the computation performed to update the sum to just two multiplications and one addition.

DEMONSTRATION

In order to demonstrate the validity and accuracy of the above formulation, the wide-band reflection coefficient of a plane wave normally incident at a planar air-water interface was calculated. The frequency band considered included frequencies where the complex permittivity of water is rapidly varying. A general expression for the complex frequency-domain relative permittivity of a polar dielectric is [3]

$$\varepsilon^*(\omega) - \varepsilon_\infty = \frac{\varepsilon_s - \varepsilon_\infty}{1 + j\omega t_0} \tag{17}$$

The corresponding time-domain relative susceptibility function is then

$$\chi(\tau) = \left(\frac{\varepsilon_s - \varepsilon_\infty}{t_0}\right) \cdot \exp(-\tau/t_0) \qquad \text{for } \tau > 0 \tag{18}$$

To demonstrate the $(FD)^2TD$ computation of wide-band reflections at an air-water interface we considered a one-dimensional problem space consisting of 1000 cells. 499 cells were used to model air (free-space) and 501 cells to model water. Each cell corresponded to a length of 37.5 μm and the time step was 0.0625 ps. The water parameters used were $\varepsilon_s = 81$, $\varepsilon_\infty = 1.8$, and $t_0 = 9.4 \times 10^{-12}$. Figure 1 shows the equivalent complex relative permittivity. The incident plane wave was a Gaussian pulse with a maximum electric field amplitude of 1 kV/m. The frequency content of the incident pulse is shown in Figure 2 while the electric-field amplitude vs. cell number at successive time intervals is shown in Figure 3 through Figure 8. The finite difference equations used for this example are equations (15) and (16).

In order to compare results using the $(FD)^2TD$ formulation with results from traditional FDTD algorithms, representative constant permittivity and conductivity values were required. The constant relative permittivity used was the real part of the complex permittivity of water at 20 GHz, 34.864. The constant conductivity value was calculated by transforming the imaginary part of the complex permittivity at 20 GHz into an equivalent conductivity of 43.43 S/m. These values of permittivity and conductivity were inserted in the FDTD algorithm presented

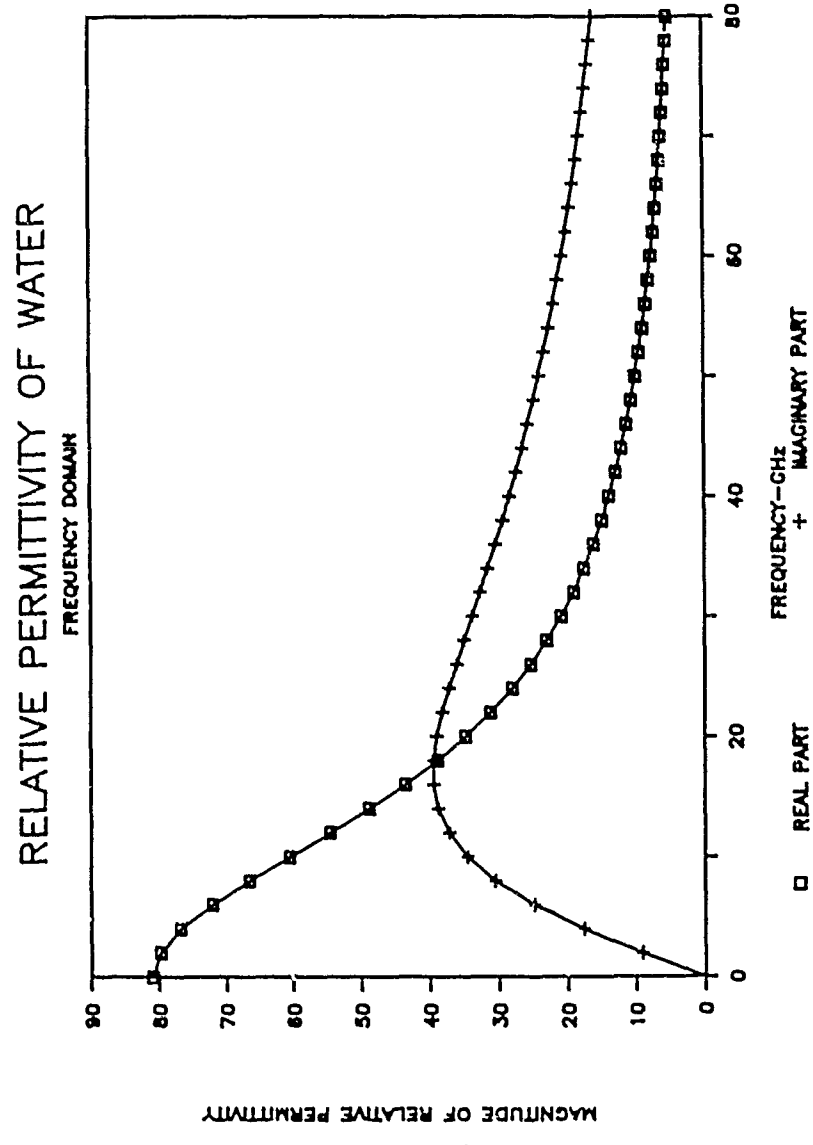


Figure 1: Complex Permittivity of Water

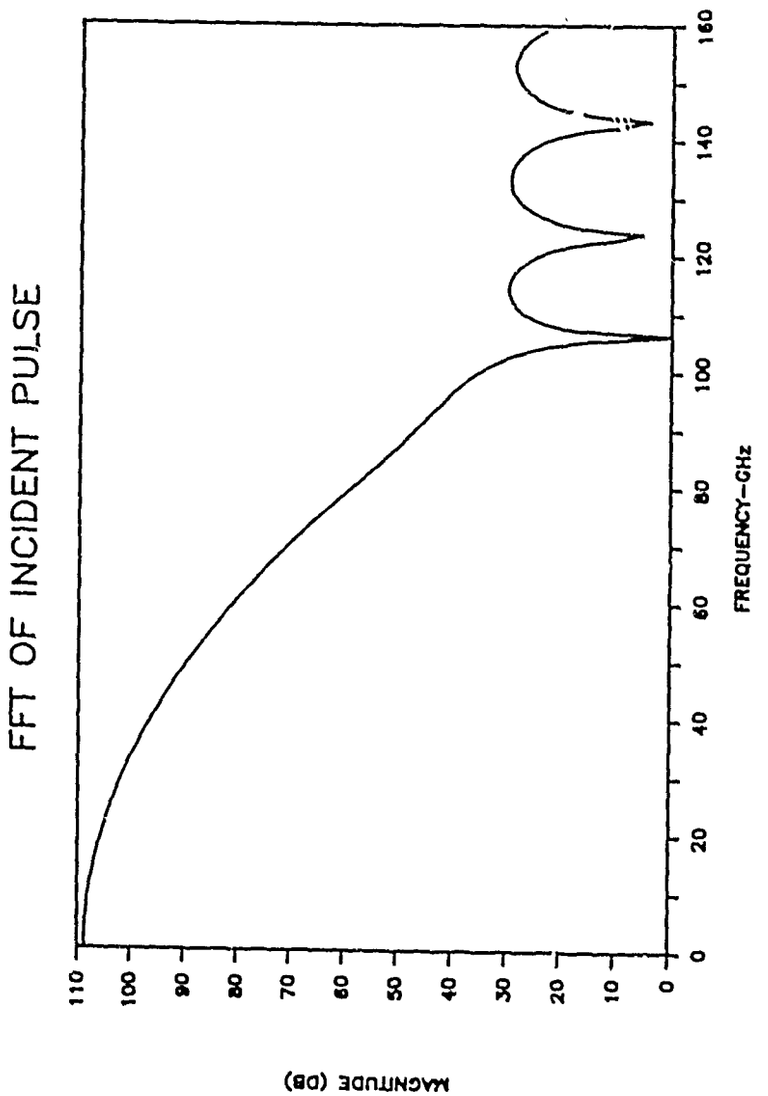


Figure 2: Incident Gaussian Pulse Spectrum

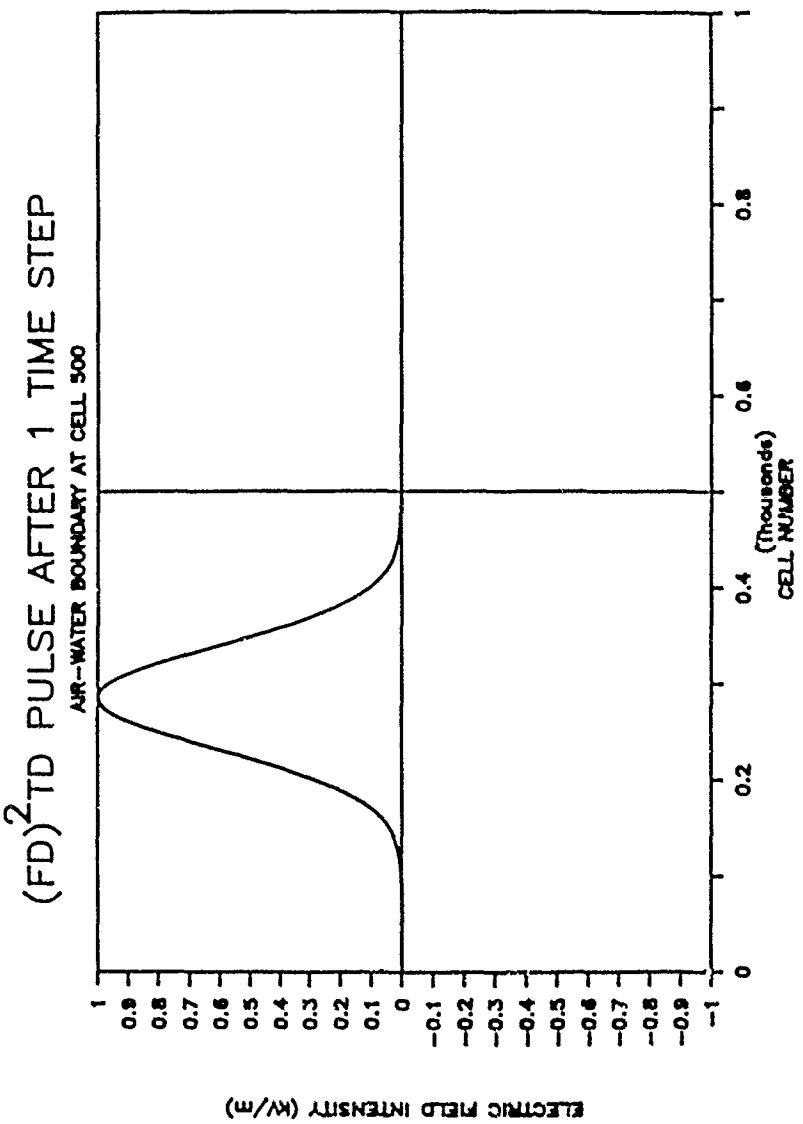


Figure 3: Initial Pulse

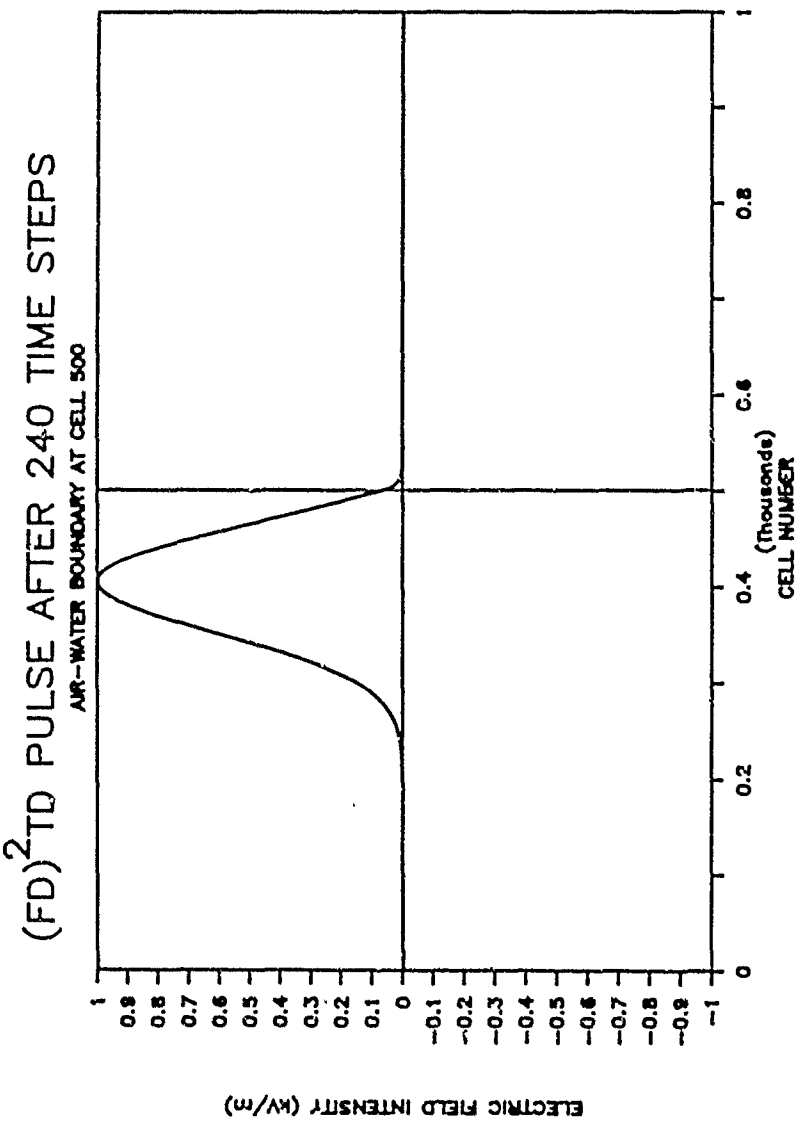


Figure 4: $(FD)^2TD$ Pulse at 240 Time Steps

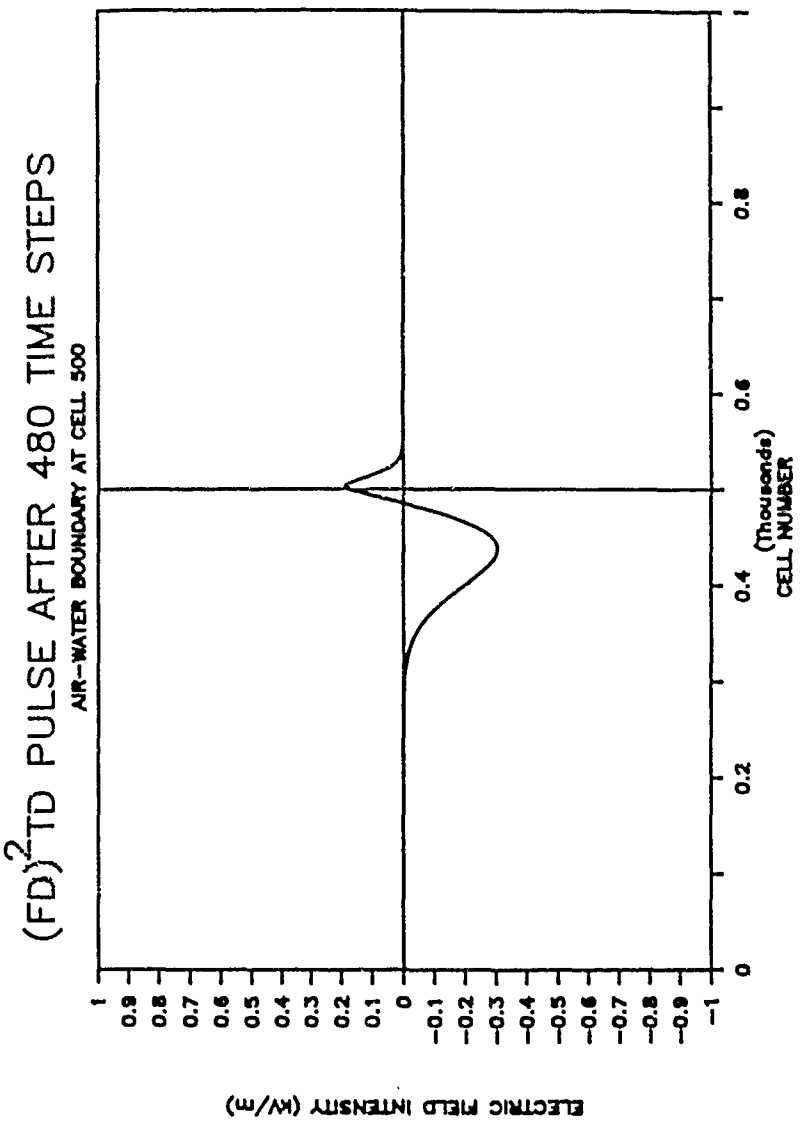


Figure 5: $(FD)^2TD$ Pulse at 480 Time Steps

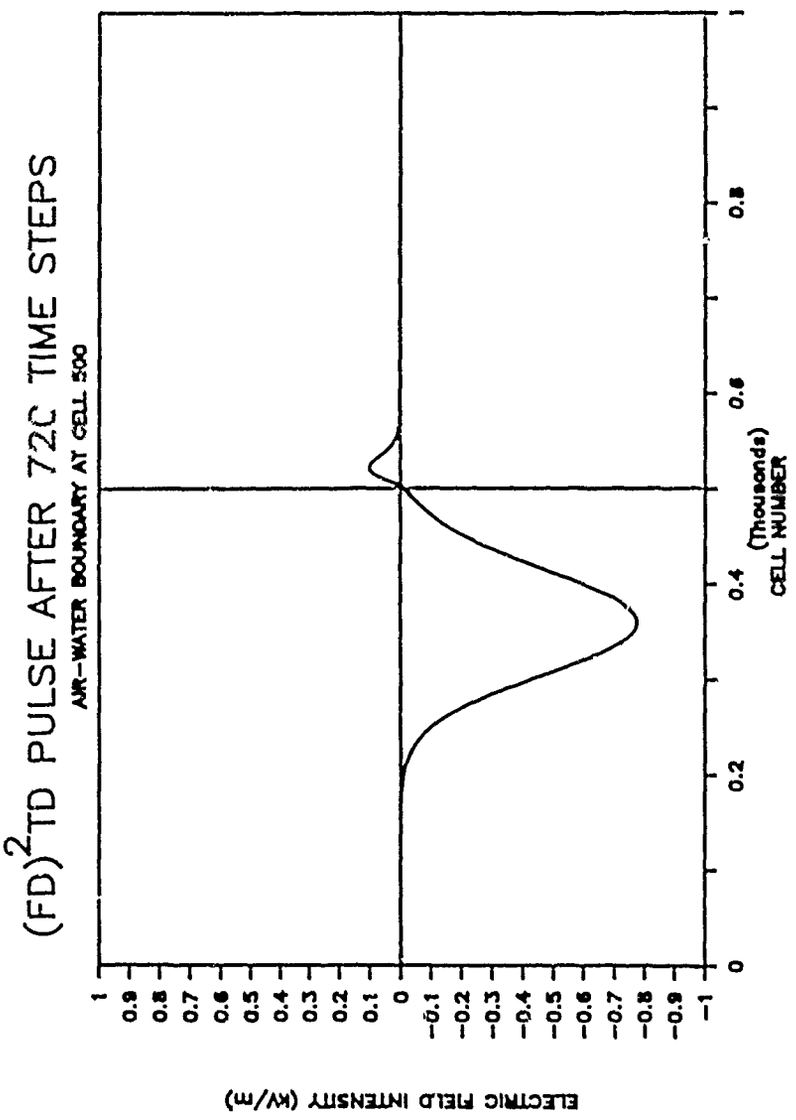


Figure 6: $(FD)^2TD$ Pulse at 720 Time Steps

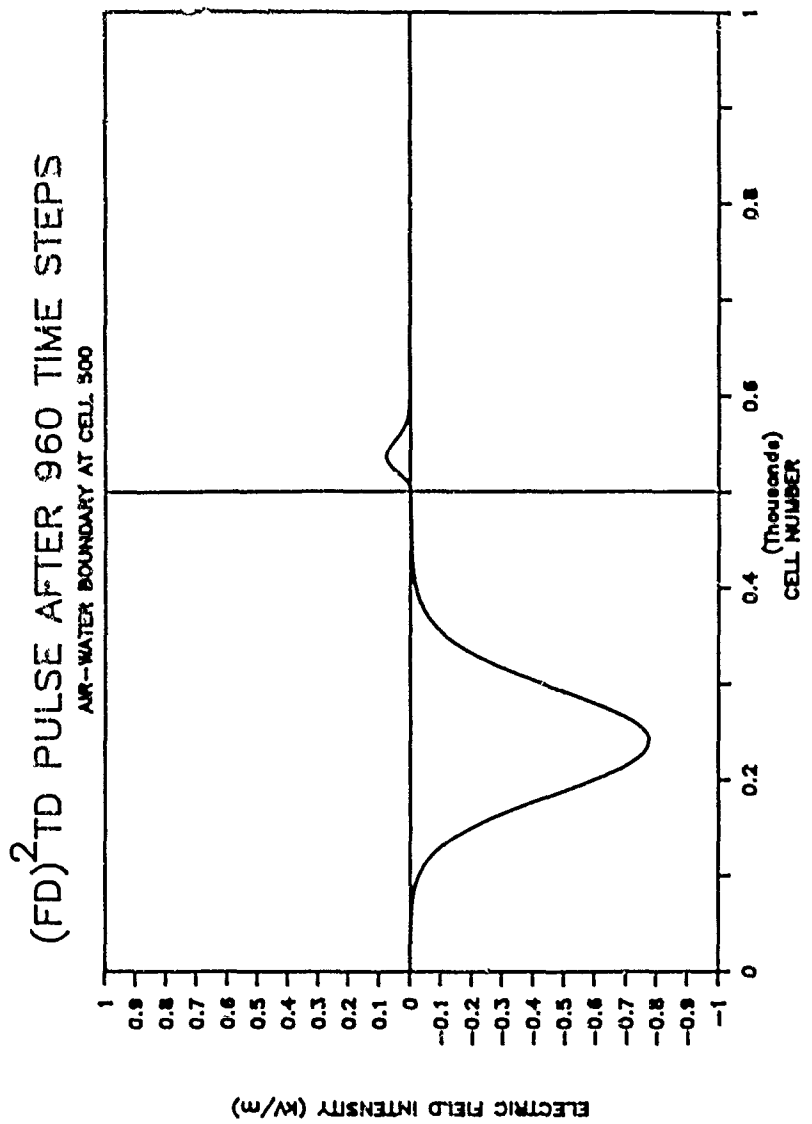


Figure 7: (FD)^{2}TD Pulse at 960 Time Steps

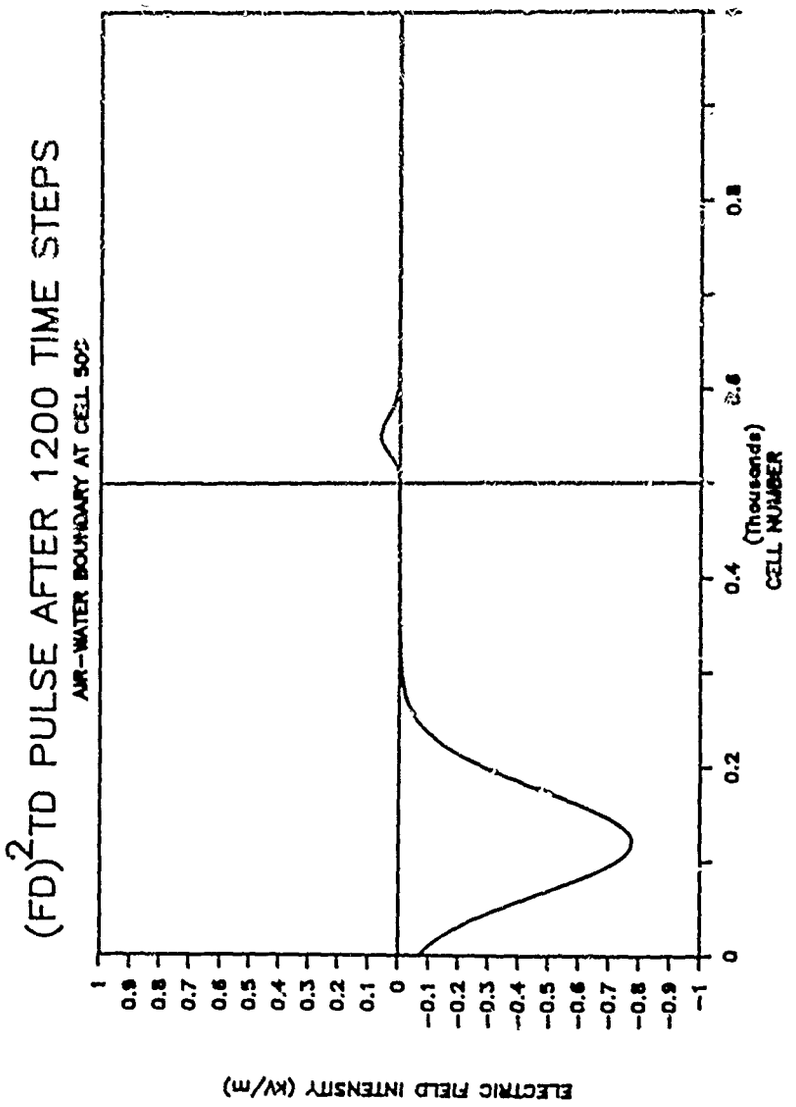


Figure 8: (FD)^{2}TD Pulse at 1200 Time Steps

in [4], and calculations were made for a pulse propagating through an air-water interface. The same parameters (cell size, time step, incident pulse, etc.) were used as in the $(FD)^2TD$ calculations. Figure 9 shows the pulse after 1200 time steps, computed by the traditional FDTD method.

Corresponding wide bandwidth reflection coefficients were determined by calculating the incident and reflected field strength vs. time one cell in front of the air-water interface. These electric field vs. time data were transformed to the frequency domain via the Discrete Fourier Transform. The reflection coefficient at each frequency was calculated by dividing the transform of the reflected field by the transform of the incident field. Figure 10 compares $(FD)^2TD$ results after 1200 time steps and FDTD results (with the 20 GHz permittivity and conductivity values) after 8000 time steps (to allow for the slower convergence of FDTD) with the exact frequency-domain result. The $(FD)^2TD$ result is clearly much more accurate than traditional FDTD. The FDTD result is correct at 20 GHz, as expected.

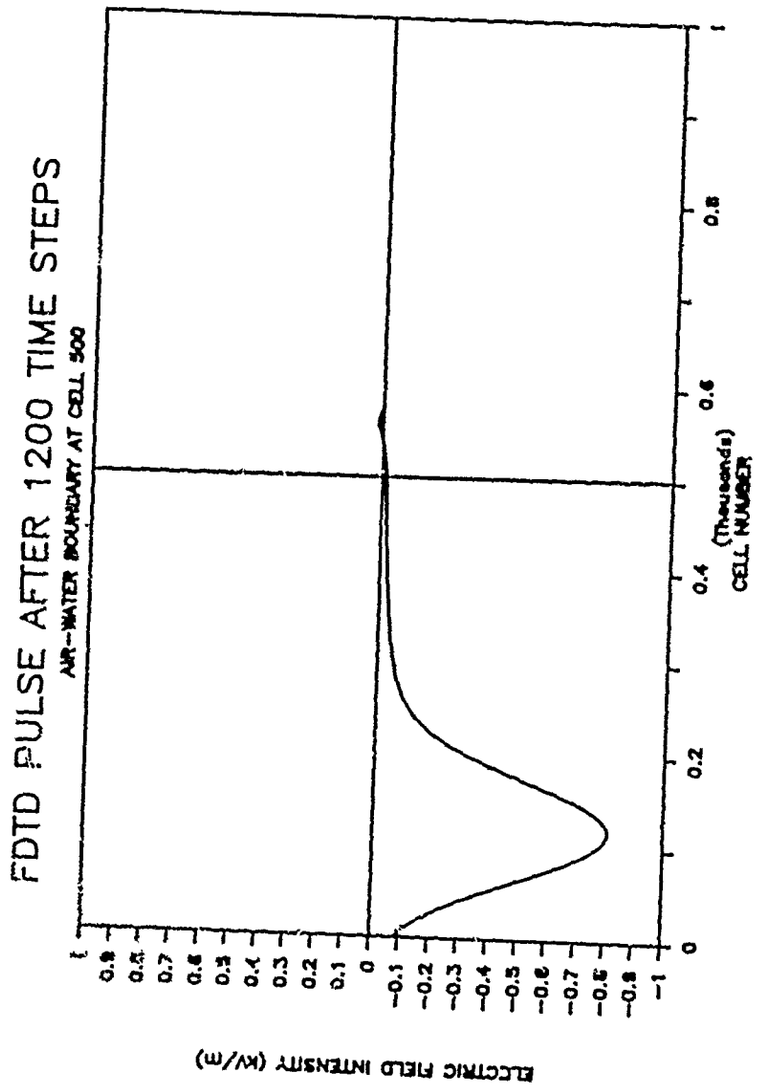


Figure 4. Traditional FDTD Pulse After 1200 Time Steps

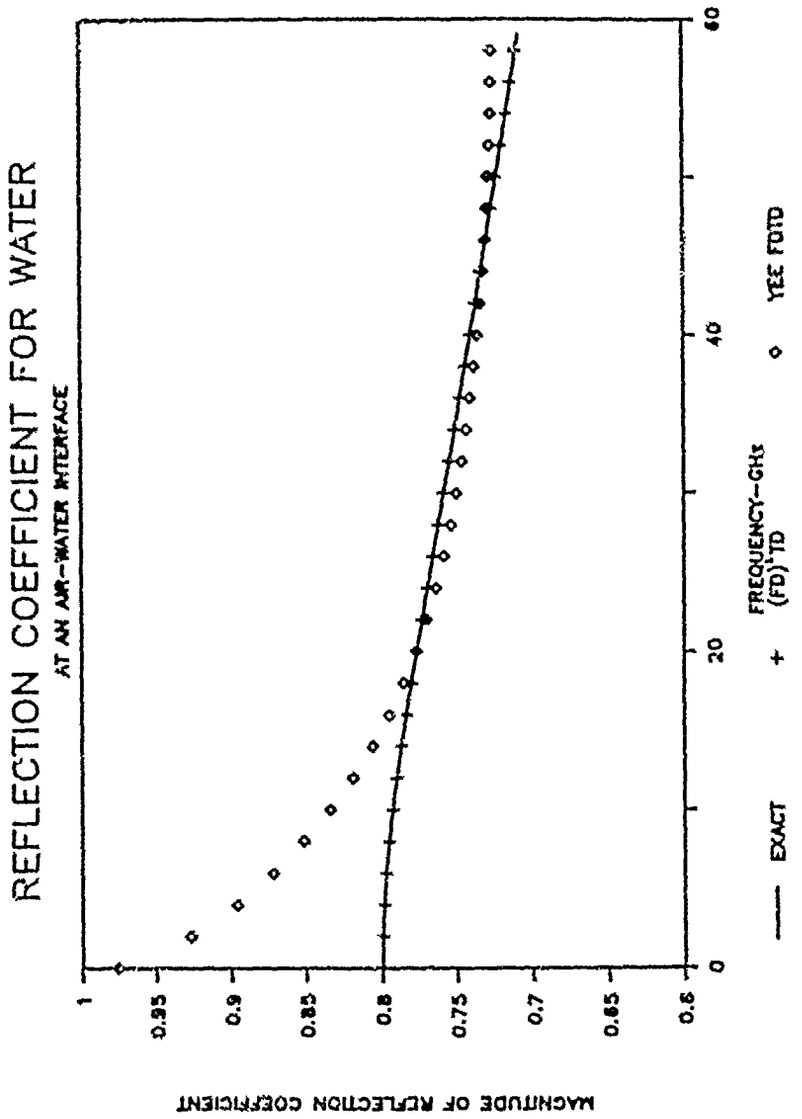


Figure 10: Reflection Coefficient vs. Frequency: Exact, FDTD, and $(FD)^2TD$

CONCLUSIONS

Modification of the basic FDTD algorithm to include electromagnetic wave interactions with materials characterized by dispersive permittivity and permeability has been presented. The validity of this method, called $(FD)^2TD$, has been demonstrated by computation of the reflection coefficient from an air-water interface over a wide frequency band using a single pulse. These results were in excellent agreement with exact values. Extension of $(FD)^2TD$ to include materials with dispersive permeability and anisotropic materials is straightforward.

BIBLIOGRAPHY

1. K. Yee, "Numerical Solution of Initial Boundary Value Problems Involving Maxwell's Equations in Isotropic Media", *IEEE Transactions on Antennas and Propagation*, vol. AP-14, no. 3, pp.302-307, 1966.
2. J. Jackson, *Classical Electrodynamics, 2nd ed.*. Wiley: New York, 1975.
3. K. Cole and R. Cole, "Dispersion and Absorption in Dielectrics", *J. Chemical Physics*, vol. 9, pp.341, 1941.
4. A. Taflove and M. Brodwin, "Numerical Solution of Steady-State Electromagnetic Scattering Problems Using the Time-Dependent Maxwell's Equations", *IEEE Transactions on Microwave Theory and Techniques*, vol. MTT-23, no. 8, pp. 623-630, 1975.

FAR FIELD PROJECTION

Dr. Marvin J. Barth and Dr. Richard W. Ziolkowski
Lawrence Livermore National Laboratory
P. O. Box 5504, L-156
Livermore, CA 94550

ABSTRACT

The FAR computer code, which post processes the results of a Finite Difference Time Domain (FDTD) code to produce far-field quantities from near-field values, is described. The integral equation and differential equation approaches are two methods of calculating the radiation and scattering effects of systems. Each method has practical limitations when used in general application codes. For instance, integral equation approaches such as the method of moments usually consider only perfectly conducting wires and patches in the frequency domain and the differential equation approaches such as FDTD, while applicable to multi-media and the time domain, are constrained to finite volumes determined by the specific computer memories. The FAR code allows the near-field details in the time domain modeled by FDTD codes to be extended to the far-field. This combined FDTD-FAR code set greatly extends the class of numerical electromagnetic modeling problems that can be treated with discrete differential equation methods.

The FAR code uses the equivalence principle. Specifically, the code utilizes the tangential electric and magnetic fields at a specified surface of the FDTD computational volume and calculates the resulting far-fields from the equivalent magnetic and electric sources. In this process the sources of errors are sampling density, the length of the excitation pulse, the total time history record length, the time step size, and the size of the FDTD volume. The FDTD-FAR approach will be illustrated with a pulse driven array of dipole elements. The far-field time histories and the resulting frequency domain antenna patterns will be presented. The sizes of the various errors in this approach will be discussed in detail. The efficacy of this approach will be contrasted with conventional methods.

I. INTRODUCTION

The finite difference time domain (FDTD) codes have several advantages including the ability to model very complex and elaborate systems, multi-media, and multiple frequencies (through Fourier inversion). The disadvantage of FDTD codes is that the problems they model are generally limited by the size of the available computer memory; hence, only the near-field may be modeled. The Lawrence Livermore National Laboratory (LLNL) developed code, FAR, will be described in this paper. It is a postprocessing code that uses the near-field results of discrete codes to determine the corresponding far-field in either the time or frequency domain.

The output of a FDTD code is the time domain $\vec{E}$ and $\vec{H}$ fields at the different grid points throughout the computational volume. With these $\vec{E}$ and $\vec{H}$ values we use the equivalence principle to define equivalent electrical and magnetic currents on a specified surface in this computational space. The projection of these dipole currents to the far-field is achieved with standard frequency and time domain dipole field formulas.

We assume zero sources outside the computational volume and use Maxwell's boundary conditions with a null field internal to the volume to determine the surface currents which would produce the same external field. For this condition, the magnetic($\vec{J}$) and electric($\vec{M}$) currents are:

$$\vec{J}_s = \hat{n} \times \vec{H} \tag{1}$$

$$\vec{M}_s = \vec{E} \times \hat{n} \tag{2}$$

It should be noted that we do not have the exact surfaces currents from the grid values given in the FDTD codes but only point values of these currents. This approximation will cause some error which we will discuss later.

Since exterior to this equivalent source surface the problem is linear (interior to the computational volume, the finite element methods allow some types of non-linearity), we assign the far-field of an equivalent infinitesimal dipole to each point of that surface and sum over all these surface points.

The field of an infinitesimal electric dipole may be determined by calculating the fields in the Fourier domain and transforming into the time domain. The equations for the dipole $\vec{e}$ field is [1]:

$$\vec{e} = \frac{-\mu}{4\pi r} e^{-jkr}(j\omega)\vec{p} \tag{3}$$

$$\vec{p} = p(\omega)(\hat{u}_x p^x + \hat{u}_y p^y + \hat{u}_z p^z) \tag{4}$$

where $\{p^x, p^y, p^z\}$ are components of a unit vector pointing in the direction of the point source and $p(\omega)$ is a scalar corresponding to dipole strength. For an array of N_J electric sources, equation (4) can be summed as:

$$\vec{E}_J(\omega, \vec{R}) = \frac{-\mu}{4\pi} \sum_{i=1}^{N_J} \frac{1}{r_i} e^{-jkr_i}(j\omega)p_i(\omega)\{\hat{u}_x p_i^x + \hat{u}_y p_i^y + \hat{u}_z p_i^z\} \tag{5}$$

$$r_i = |\vec{R} - \vec{r}_i'| \tag{6}$$

$$\vec{R} = \hat{u}_x X + \hat{u}_y Y + \hat{u}_z Z \tag{7}$$

$$\vec{r}_i' = \hat{u}_x x_i' + \hat{u}_y y_i' + \hat{u}_z z_i' \tag{8}$$

Capital letters will always designate total fields and the observer distance whereas primes will indicate the source coordinates. Since we are calculating the far-field, we follow the usual conventions and remove the inverse distance term $R = |\vec{R}|$ from the summation sign and treat the phase term as [1]:

$$r_i = R - \psi_i \tag{9}$$

$$\psi_i = x_i' \sin\theta\cos\phi + y_i' \sin\theta\sin\phi + z_i' \cos\theta \tag{10}$$

Transforming into spherical coordinates will result in:

$$E_{J\theta}(\omega, \vec{R}) = -K\mu(\cos\theta\cos\phi S_{J_x} + \cos\theta\sin\phi S_{J_y} - \sin\theta S_{J_z}) \tag{11}$$

$$E_{J\phi}(\omega, \vec{R}) = K\mu(\sin\phi S_{J_x} - \cos\phi S_{J_y}) \tag{12}$$

$$H_{J\theta} = \frac{-E_{J\phi}}{\eta} \tag{13}$$

$$H_{J\phi} = \frac{E_{J\theta}}{\eta} \tag{14}$$

$$K = \frac{e^{-jkR}}{4\pi R} \tag{15}$$

$$S_{J_x} = j\omega \sum_{i=1}^{N_J} e^{jk\xi_i} p_i(\omega) p_i^x \tag{16}$$

$$S_{J_y} = j\omega \sum_{i=1}^{N_J} e^{jk\xi_i} p_i(\omega) p_i^y \tag{17}$$

$$S_{J_z} = j\omega \sum_{i=1}^{N_J} e^{jk\xi_i} p_i(\omega) p_i^z \tag{18}$$

In equations (13) and (14) we have designated the medium impedance as $\eta = (\mu/\epsilon)^{1/2}$. The radiation field pattern is then a plot of RE_θ, or RE_ϕ. As R approaches infinity, the phase relation used in (14) is exact.

The time domain fields may be obtained from the inverse Fourier transform, i.e.,

$$E(t) = \frac{1}{2\pi} \int_{-\infty}^{\infty} E(\omega) e^{j\omega t} d\omega \tag{19}$$

To transform these into the time domain we will use the time shifting and time differentiation properties:

$$\text{for} \qquad f(t) \multimap F(\omega) \iff f(t - t_0) \multimap F(\omega) e^{-j\omega t_0} \tag{20}$$

$$\text{and for} \qquad f(t) \multimap F(\omega) \iff \frac{df}{dt} \multimap (j\omega) F(\omega) \tag{21}$$

The time domain fields from the electric sources can be written as:

$$E_{J\theta}(t, \bar{R}) = -K' \mu (\cos\theta \cos\phi S'_{J_x} + \cos\theta \sin\phi S'_{J_y} - \sin\theta S'_{J_z}) \tag{22}$$

$$E_{J\phi}(t, \bar{R}) = K' \mu (\sin\phi S'_{J_x} - \cos\phi S'_{J_y}) \tag{23}$$

$$K' = \frac{1}{4\pi R} \tag{24}$$

$$S'_{J_x} = \sum_{i=1}^{N_J} \frac{d}{dt'_i} p_i(t'_i) p_i^x \tag{25}$$

$$S'_{J_y} = \sum_{i=1}^{N_J} \frac{d}{dt'_i} p_i(t'_i) p_i^y \tag{26}$$

$$S'_{J_z} = \sum_{i=1}^{N_J} \frac{d}{dt'_i} p_i(t'_i) p_i^z \tag{27}$$

In these field expressions the retarded time is:

$$t'_i = t - \frac{R}{c} + \frac{\psi}{c} \tag{28}$$

The fields for magnetic sources are found by duality.

II. VALIDATION

We selected a problem involving two infinitesimal dipoles radiating in free space for our validations. The geometry is shown in Figure 1. The driving function and its Fourier transform are shown in Figures 2 and 3. We generally considered results at 1.0 GHz near the peak of the frequency spectrum.

We used four combinations of codes in our tests: TSAR-FAR, XNEAR-FAR, JOB, and NEC. TSAR is a LLNL developed FDTD code. XNEAR is a code which calculates the exact output of two infinitesimal dipoles and outputs the results in the same format as TSAR. JOB is a derivative of XNEAR which calculates the exact field at points on the specified equivalent current simulation surface. NEC is the LLNL developed Numerical Electromagnetics Code. The XNEAR-FAR comparison with NEC yields the errors due solely to FAR. The TSAR-FAR comparison with NEC yields the overall error. In computing the errors we made frequency plots of $\bar{E}_\theta$ in two planes: the horizonal plane ($\theta = 90; -90 \leq \phi \leq 90$) and the vertical plane ($\phi = 0; 0 \leq \theta \leq 180$). The error was then the maximum difference between the NEC and FAR plots. Figures 4 and 5 show a comparison between the TSAR-FAR and NEC predicted patterns at 1.0GHz in the horizonal and the vertical planes respectively when the dipoles are driven with the pulse shown in Fig. 2 and both a "10 cells and 20 cells per wavelength" discretization is used in TSARS.

Here we report on four types of errors we have uncovered and studied. We term these errors: discrete Fourier transform (DFT) errors, averaging errors, grid size errors, and frequency errors.

(1) *Discrete Fourier Transform Errors*

The FAR code has a subroutine which takes the DFT of the time domain TSAR (or XNEAR) output and then projects the DFT to the far-field. There are three types of errors inherit with the numerical DFT subroutines: aliasing, leakage, and picket-fence [2],[3].

Aliasing is caused by the sampling rate. It occurs when the high frequency components of the time signal impersonate a low frequency component. Since the time record is finite, the frequency transform will be infinite and there is no absolute cure for the error. The best that can be done is to design the excitation pulse as one which has most of the energy near the frequency of interest and to use a sampling frequency which is much higher.

Both leakage and the picket-fence errors are caused by using a time signal of finite duration. This is equivalent to multiplying (in the time domain) an infinite duration time signal by a window of amplitude one with the same duration as that of the time signal. In the frequency domain this is equivalent to a convolution of the time signal's Fourier transform and the "$\sin x/x$" Fourier transform of the window. The result is that each discrete frequency impulse of the time signal is replaced with the "$\sin x/x$" function and all "$\sin x/x$" functions summed.

Leakage refers to the error caused by the summation of the trailing ends of the "$\sin x/x$" functions. If there is a DC component to the time signal this error is exacerbated because the discontinuity of the signal at the record end will produce many more frequency points with each point convolved with the "$\sin x/x$" functions. The method of mitigation for

leakage errors is to multiply the time history by a window other than the rectangular window or to use a transit pulse (one which begins and ends at zero).

The picket-fence error is caused when the frequency of interest is not an exact multiple of the sampling frequency. (Here the series of "$\sin x/x$" functions act as filters in the frequency domain giving a picket-fence effect.) There are two cures which mitigate this effect. The first is to take the DFT at multiples of the sampling frequency and then to perform complex interpolation. The other is to "zero-pack" the time signal (i.e., add a large number of zero points to the time signal which creates a much longer time signal). The effect of zero-packing is to spread out the frequency components.

To mitigate the effects of aliasing, we use a pulse which has most of its energy at and below 1.0GHz and has continuous derivatives. One such pulse is termed the Z-pulse [4]. The equations describing this pulse for a period from zero to one are:

$$f(x) = 32x^3 - 48x^4 \quad \text{for} \quad 0 \leq x \leq 0.5 \tag{29}$$

$$f(x) = 32(1-x)^3 - 48(1-x)^4 \quad \text{for} \quad 0 \leq x \leq 0.5 \tag{30}$$

Although this pulse is good with reference to aliasing, it still has a poor characteristic with reference to leakage. In the near-field, the dipole is a sum of three terms, each proportional to the original excitation pulse, its derivative, and its integral. As is seen the integral term of the Z-pulse would have a DC term and thus a leakage problem. In order to mitigate the leakage effect, we have found that either a Half Hamming window or a Half Blackman window will give good results. The equations for these windows are:

$$W_H(x) = 0.54 - 0.56\cos\left(\frac{2\pi(x-1)}{M-1}\right) \tag{31}$$

$$W_B(x) = 0.42 - 0.5\cos\left(\frac{2\pi(x-1)}{M-1}\right) + 0.08\cos\left(\frac{4\pi(x-1)}{M-1}\right) \tag{32}$$

where M = the pulse length and the range is $M/2 \leq x \leq M$.

A better pulse (i.e., a transit pulse), with all the good characteristics of the Z-pulse is its derivative termed the DZ-pulse. It is described by the equations:

$$f(x) = 96x^2 - 192x^3 \quad \text{for} \quad 0 \leq x \leq 0.5 \tag{33}$$

$$f(x) = -96(1-x)^2 + 192(1-x)^3 \quad \text{for} \quad 0 \leq x \leq 0.5 \tag{34}$$

Figures 2 and 3 show this pulse for a time of 5.0e-11 sec. and a period of 120.0e-11 sec. It can be seen that most of the energy is below 2.0e9 Hz. and it has continuous derivatives.

We have found that a good choice of the excitation pulse will produce minimum aliasing and leakage errors. To account for the picket-fence error we have found that zero-packing to an order 12 yields results as good as any higher packing. (By zero-packing to an order 12 we mean to increase the time record by 2^{12} zeros. It should be pointed out that the time records are not actually increased by this amount, but with the proper choice of sampling frequency in the DFT subroutine, the DFT appears to add this order of zeros.)

(2) *Averaging Errors*

Another source of error is due to the staggered grid used in the FDTD calculations. The magnetic and electric fields are not recorded at the same spatial point in the FDTD

codes. We have chosen the measurement surface such that the the electric field calculation points exactly lie on it. Since the offsets for the magnetic fields are at half points on the grid cell, two sets of the magnetic field are computed, and then averaged to determine the magnetic field values on the measurement surface. This averaging process introduces an additional error.

To investigate the magnitude of the error introduced by this averaging two codes were used: XNEAR which calculates the magnetic fields at the half points (the same points as TSAR) and JOB. The other variables were set as follows:

(1) Frequency, f = 1.0GHz
(2) Grid size, Dx = λ 10
(3) Time sampling size, Dt = 5.0 e-11 sec.
(4) Time record length, NTOT = 201
(5) Zero packing order, ISTEP = 3
(6) Pulse = Z-Pulse
(7) Window = Half Hamming

Figure 6 shows the averaged (XNEAR) and exact (JOB) time records of the magnetic field H_y at the center of the front face of the measurement surface. The maximum percent error between these two curves is 3.53%. There are 2548 measurement points for the magnetic field over the six surfaces of this problem. When the horizonal pattern plot is compared with NEC the resulting errors are:

XNEAR error = 2.5793 %
JOB error = 0.6447 %

Thus, magnetic field averaging introduces an additional 1.8547% error in the far-field electric field patterns.

(3) *Grid Size Errors*

The grid size (Dx) is set in the FDTD code. In addition to wavelength sampling criterions, practical considerations such as the size of computer memory and near-field detail dictate the grid size. With decreasing grid size, more surface values of $\vec{E}$ and $\vec{H}$ are output and, from an information view, the more accurate the results of FAR will be. The objective of this part of our study was to quantify this effect.

We used the JOB code to investigate this error. This precluded FDTD or averaging errors and allowed us to concentrate on the grid size errors. In addition this choice premitted cost efficient code runs with grid sizes from $\lambda/6$ to $\lambda/20$ to be made.

When executing a FDTD code, the Courant condition sets a limit on the time sampling size (Dt). Therefore, as we varied Dx we correspondly varied Dt by the relation $Dt = Dx/c$ (where c is the velocity of light). Table 1 indicates the error associated with these variations. It is seen that major improvements occur with decreasing the grid size until $\lambda/10$ at which the rate of improvement decreases.

Dx	Dt	Final Error
λ/6	8.333333e-11	1.750
λ/8	6.250000e-11	0.949
λ/10	5.000000e-11	0.594
λ/12	4.166667e-11	0.402
λ/16	3.125000e-11	0.247
λ/20	2.500000e-11	0.159

TABLE 1.

Error Variation with respect to Dx

We also made code runs with variations of Dt while holding Dx constant to test the error effects of Dt variations. Throughout the Dx range of $\lambda/6$ to $\lambda/20$ we found negligible error.

(4) *Frequency Errors*

The last type of error we report on is the effect of varying the frequency while holding the geometry shown in Fig. 1 fixed. Figures 7 and 8 show horizonal plane plots at frequencies of 0.5GHz and 1.5GHz of TSAR-FAR and NEC. We made code runs at every 0.1GHz over this range at grid sizes of $\lambda/10$ and $\lambda/20$. In these code runs we have found maximum errors from 1.0% up to 20.0% when comparing the electric field pattern plots with NEC. (The average errors are on the order of up to 5.0%.) Figure 9 shows these pattern plot maximum errors as a function of frequency for XNEAR (which produces the exact dipole fields at the measurement surfaces) and TSAR-FAR (with a grid size of $\lambda/20$). With reference to the pattern plots shown in Figures 4, 7, and 8 it can be seen that these maximum errors occur at the nulls and peaks of the pattern near the endfire directions.

At this point we do not understand completely the causes of these errors. We do believe that a major factor of the error is associated with the sampling of the surface currents. That is, at lower frequencies (and longer wavelengths) our sampling density over the surface is greater, i.e., there are more samples per square wavelength. In contrast, at higher frequencies the sampling density decreases. Figure 10 shows a comparison of the sampling density (normalized to the error at 1.0GHz) and the XNEAR-FAR error over the range of frequencies. As can be seen the general trend of the curves support our contention. The fine structure remains to be investigated.

III. CONCLUSIONS

A limitation of FDTD codes has been the inability to model radiation and scattering effects of systems at distances far from their sources. At LLNL we have developed the code FAR which, using the equivalence principle, projects the computational surface time-domain $\vec{E}$ and $\vec{H}$ fields from a FDTD code to the far-field. The code output may be in either the frequency or time domain. This paper has described that code and its validation.

The major errors associated with this near-to-far-field procedure were identified and discussed. As noted above, we have tried to quantify these errors thoroughly. We grouped the errors as DFT, averaging, grid size, and frequency errors.

The aliasing, leakage, and picked-fence errors are always present whenever a DFT is used: thus, they are absent whenever time domain results are desired. The aliasing error may be mitigated with the proper choice of input pulse. We have found that the Z and DZ-pulses reduce aliasing to a negligible effect. Because the Z-pulse, when used as a dipole excitation, produces a DC term, windows must be used to mitigate the leakage effect. We have found the Half Hamming and Half Blackman windows to be adequate in these cases. The picked-fence error is negligible when "zero-packing" to the 12-th order is used. The averaging error is caused when the $\vec{H}$ field is averaged to make it coincident with the electric field values on the measurement surfaces. This error will account for approximately 2% of the total error. The grid size is set by the FDTD code parameters. The range of error is from slightly less than 0.16% to 2.0%. Although smaller grid sizes are desirable, we have found that a λ 10 choice is a good one. Here, λ corresponds to the frequency of interest. This choice is also appropiate when considering the FDTD parameters. Although we have not completed our investigation of frequency errors, we have found the error proportional to the surface sampling density (measurement points / square wavelengths). Choosing a grid size of $\lambda/10$ will produce good results (approximately 5% errors). The error is reduced at lower frequencies. It appears that when higher frequency results are required, the problem should be run with a grid spacing account for this fact.

ACKNOWLEDGMENTS

This work was performed by the Lawrence Livermore National Laboratory under the auspices of the U. S. Department of Energy under contract No. W-7405-ENG-48.

REFERENCES

[1] Roger F. Harrington, *Time-Harmonic Electromagnetic Fields*, (New York:McGraw-Hill,1961).

[2] G. D. Bergland, "A Guided Tour Of The Fast Fourier Transform", *IEEE Spectrum*, p. 41-52, July 1969.

[3] Fredric J. Harris, "On The Use Of Windows For Harmonic Analysis With The Discrete Fourier Transform", *Proc. IEEE*, Vol. 66, No. 1, p. 172-204, January 1978.

[4] Richard W. Ziolkowski, Niel K. Madsen, and Robert C. Carpenter, "Three-Dimensional Computer Modeling Of Electromagnetic Fields: A Global Lookback Lattice Truncation Scheme", *J. Comp. Phy.*, Vol. 50, No. 3, p. 360-408, June 1983.

FIGURE CAPTIONS

Figure 1. Geometry for the two pulsed dipole problem (Frequency = 1.0GHz, λ = 0.2997925m).

Figure 2. The input excitation pulse that drives each dipole. (Time Domain)

Figure 3. The Fourier transform of the input dipole excitation pulse. (Frequency Domain)

Figure 4. The horizontal pattern plot for $\theta = 90$, and $-90 \leq \phi \leq 90$ predicted at 1.0GHz by *NEC* (—), *TSAR-FAR* $\lambda/20$ (- - -), and *TSAR-FAR* $\lambda/10$ (···).

Figure 5. The vertical pattern plot for $\phi = 0$, and $0 \leq \theta \leq 180$ predicted at 1.0GHz

by *NEC* (—), *TSAR-FAR* $\lambda/20$ (- - -), and *TSAR-FAR* $\lambda/10$ (···).

Figure 6. The time record of the magnetic field for *JOB(exact)* (—) and *XNEAR(average)* (- - -) at a measurement point on the front face.

Figure 7. The horizonal pattern plot for $\theta = 90$, and $-90 \leq \phi \leq 90$ predicted at 0.5GHz by *NEC* (—), *TSAR-FAR* $\lambda/20$ (- - -), and *TSAR-FAR* $\lambda/10$ (···).

Figure 8. The horizonal pattern plot for $\theta = 90$, and $-90 \leq \phi \leq 90$ predicted at 1.5GHz by *NEC* (—), *TSAR-FAR* $\lambda/20$ (- - -), and *TSAR-FAR* $\lambda/10$ (···).

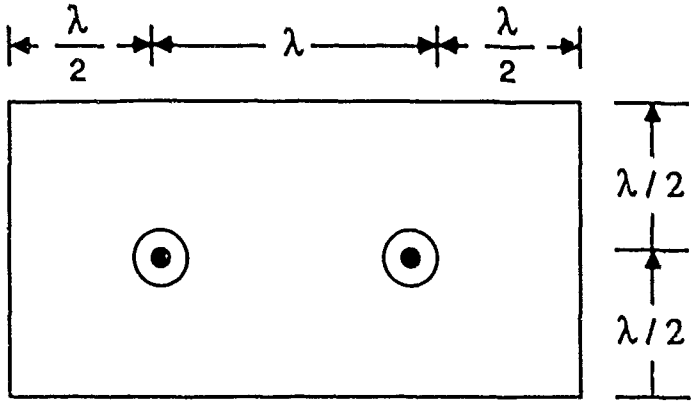
Figure 9. The maximum pattern plot error for *XNEAR* (—) and *TSAR-FAR* $\lambda/20$ (- - -) as a function of frequency.

Figure 10. A comparison of the *XNEAR* (—) maximum pattern plot error and the *NORMALIZED SAMPLING DENSITY* (- - -).

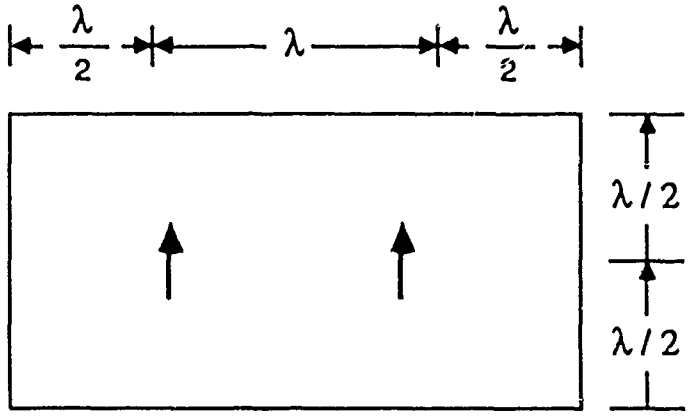
DISCLAIMER

This document was prepared as an account of work sponsored by an agency of the United States Government. Neither the United States Government nor the University of California nor any of their employees, makes any warranty, express or implied, or assumes any legal liability or responsibility for the accuracy, completeness, or usefulness of any information, apparatus, product, or process disclosed, or represents that its use would not infringe privately owned rights. Reference herein to any specific commercial products, process, or service by trade name, trademark, manufacturer, or otherwise, does not necessarily constitute or imply its endorsement, recommendation, or favoring by the United States Government or the University of California. The views and opinions of authors expressed herein do not necessarily state or reflect those of the United States Government or the University of California, and shall not be used for advertising or product endorsement purposes.

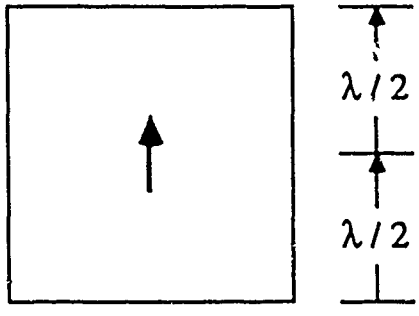
Top View



Side View



End View



854

Figure 1.

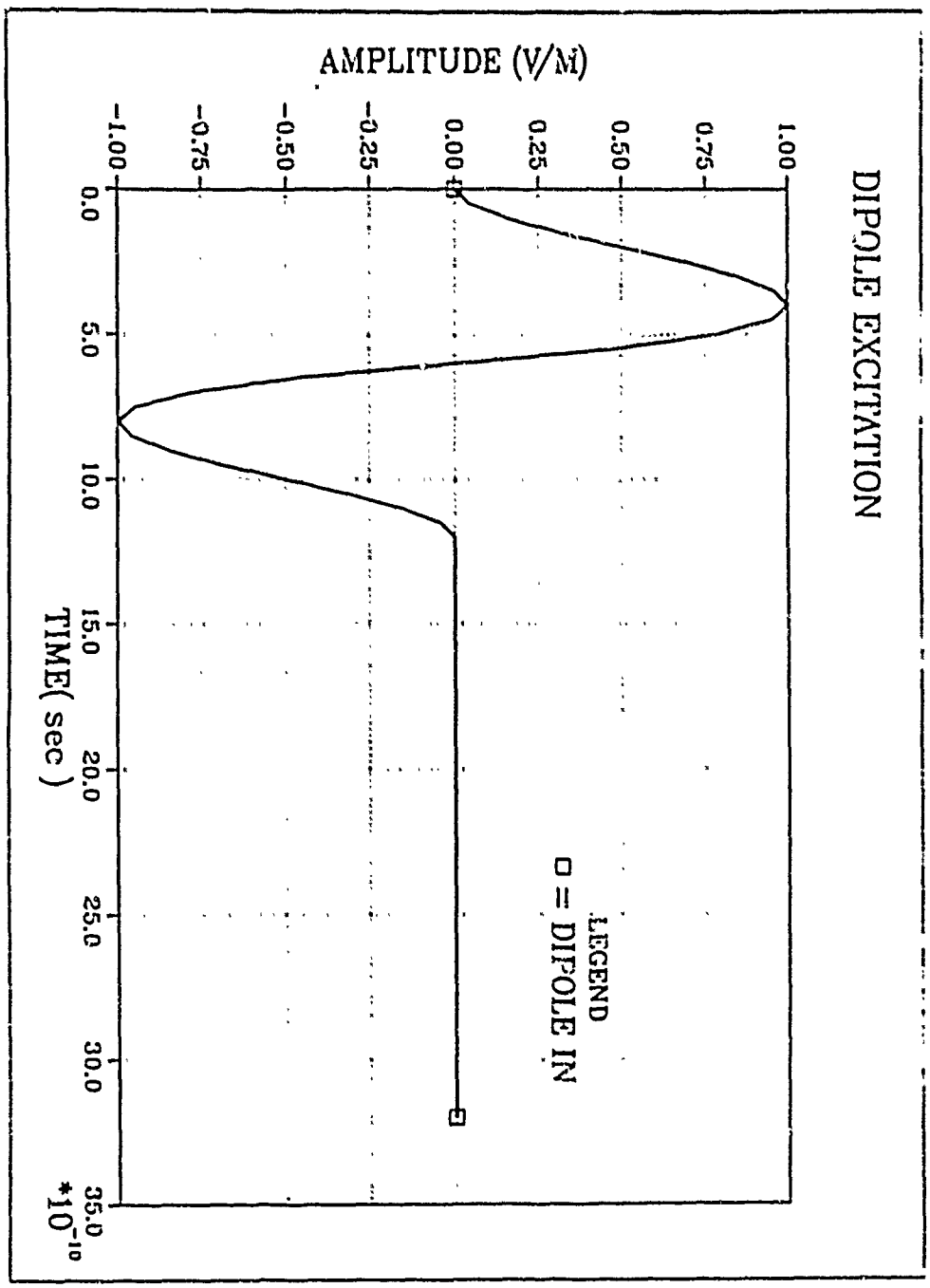

DIPOLE EXCITATION
AMPLITUDE (V/M)
-1.00
-0.75
-0.50
-0.25
0.00
0.25
0.50
0.75
1.00
0.0
5.0
10.0
15.0
20.0
25.0
30.0
35.0
TIME(sec)
*10^-10
LEGEND
□ = DIPOLE IN

Figure 2.

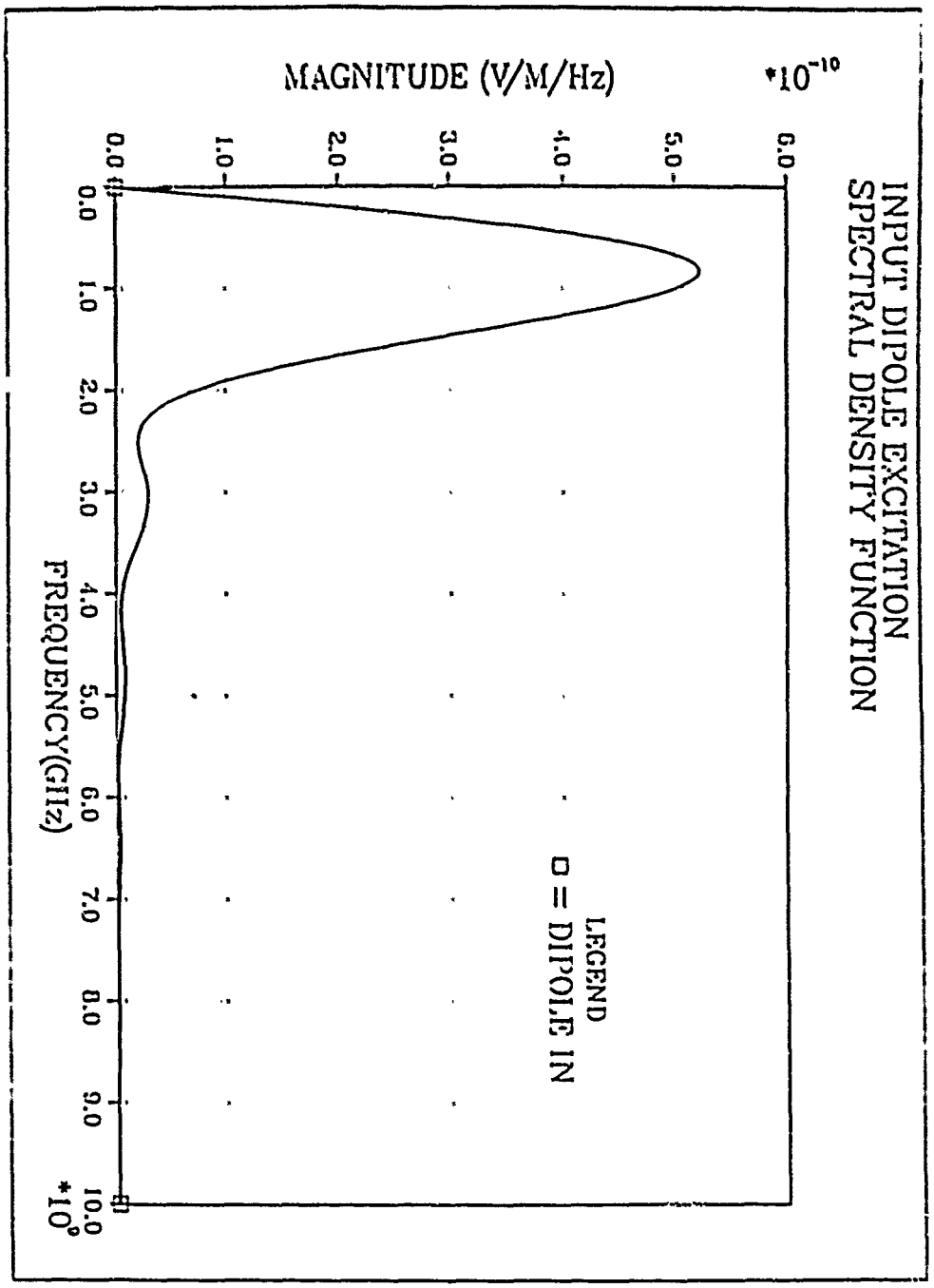

INPUT DIPOLE EXCITATION
SPECTRAL DENSITY FUNCTION
MAGNITUDE (V/M/Hz)
*10^-10
0.0
1.0
2.0
3.0
4.0
5.0
6.0
FREQUENCY(GHz)
*10^9
0.0
1.0
2.0
3.0
4.0
5.0
6.0
7.0
8.0
9.0
10.0
LEGEND
□ = DIPOLE IN

Figure 3.

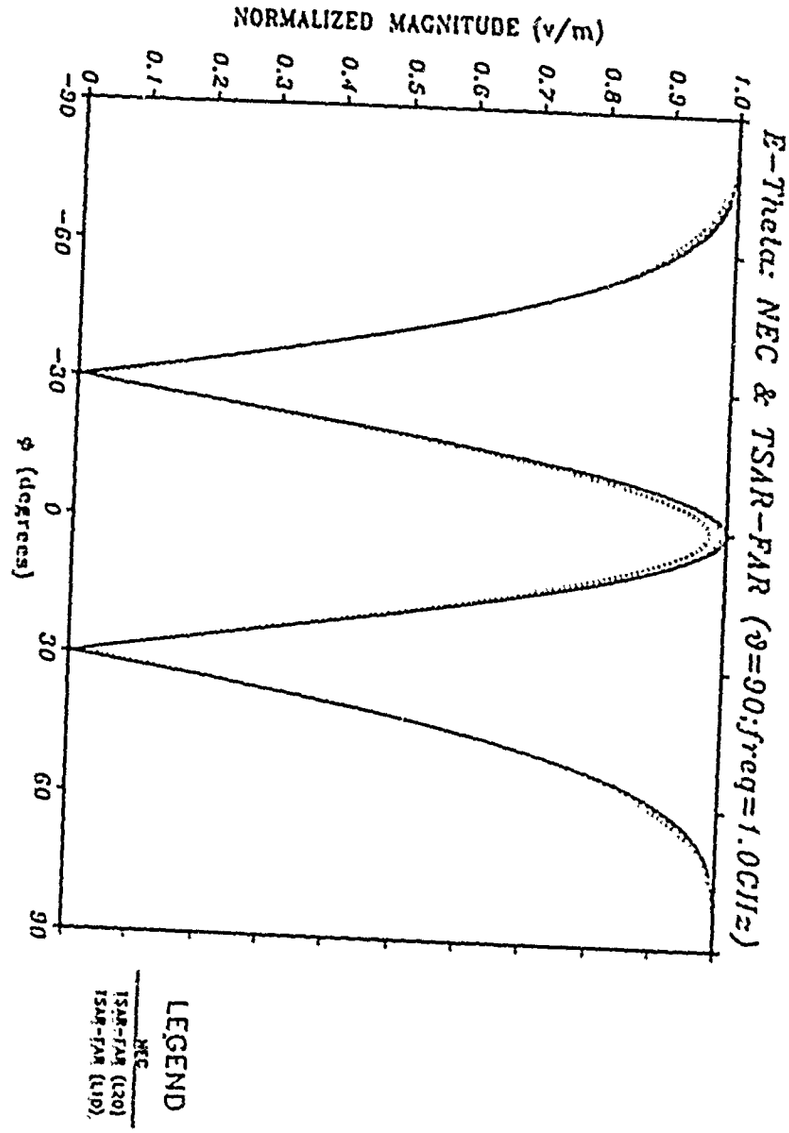

NORMALIZED MAGNITUDE (v/m)
0
0.1
0.2
0.3
0.4
0.5
0.6
0.7
0.8
0.9
1.0
-90
-60
-30
0
30
60
90
φ (degrees)
E-Theta: NEC & TSAR-FAR (θ=90;freq=1.0GHz)
LEGEND
NEC
TSAR-FAR (120)
TSAR-FAR (110)

Figure 4.

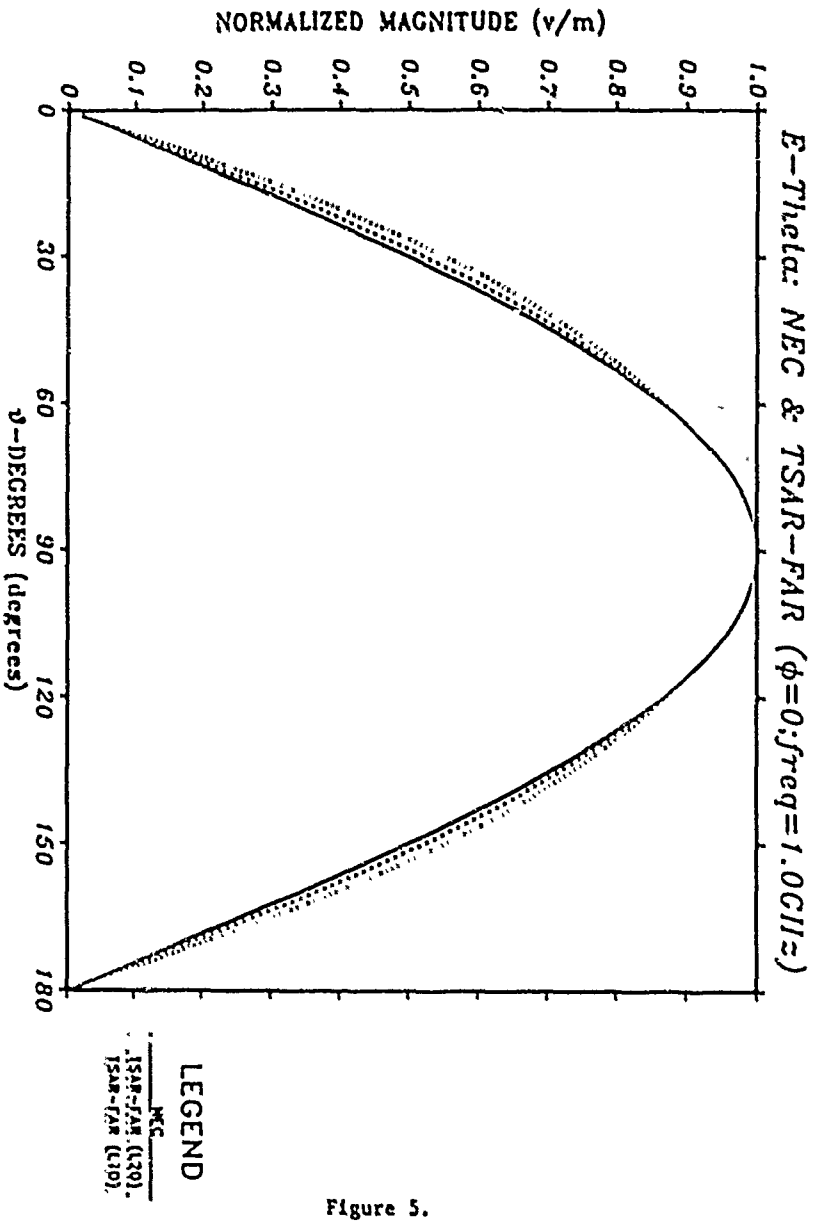

E-Theta: NEC & TSAR-FAR (φ=0;freq=1.0GHz)
NORMALIZED MAGNITUDE (v/m)
0
0.1
0.2
0.3
0.4
0.5
0.6
0.7
0.8
0.9
1.0
0
30
60
90
120
150
180
ϑ-DEGREES (degrees)
LEGEND
NEC
TSAR-FAR (L20).
TSAR-FAR (L10).

Figure 5.

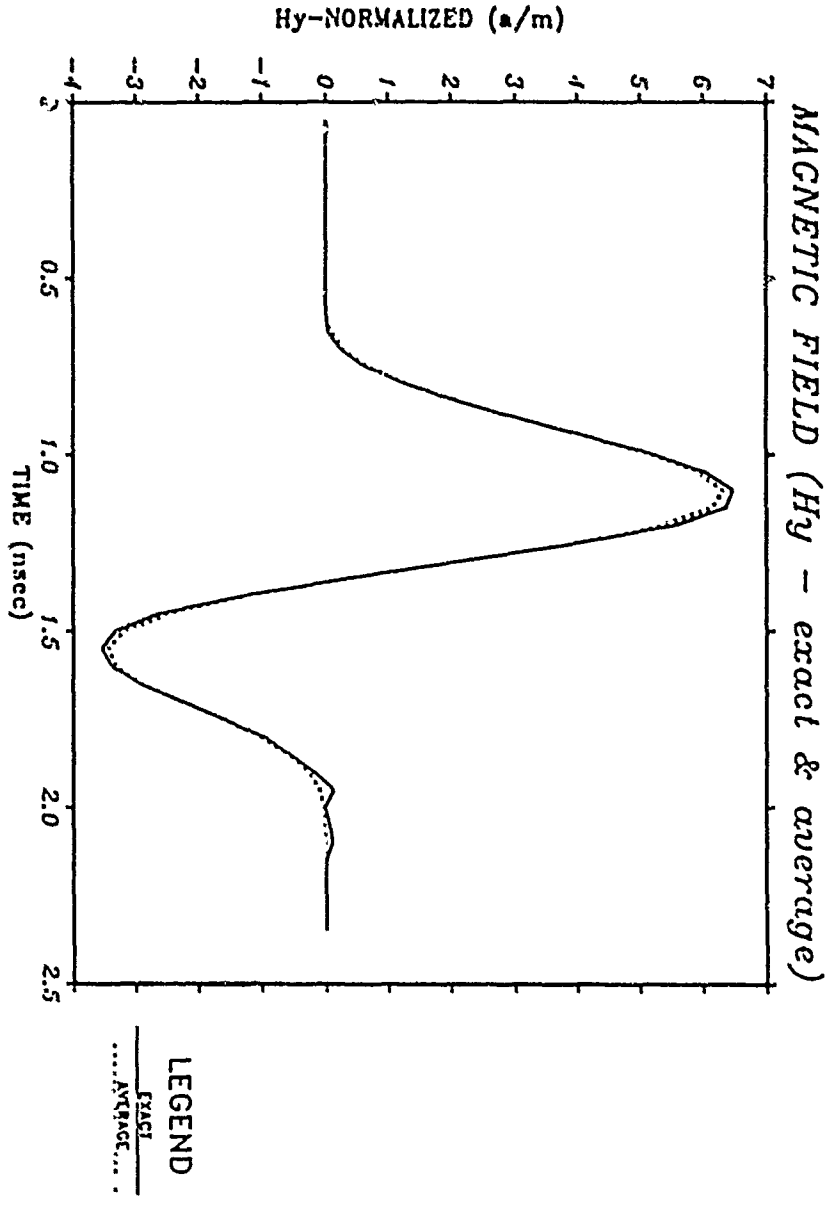

MAGNETIC FIELD (Hy - exact & average)
Hy-NORMALIZED (a/m)
TIME (nsec)
LEGEND
EXACT
AVERAGE

Figure 6.

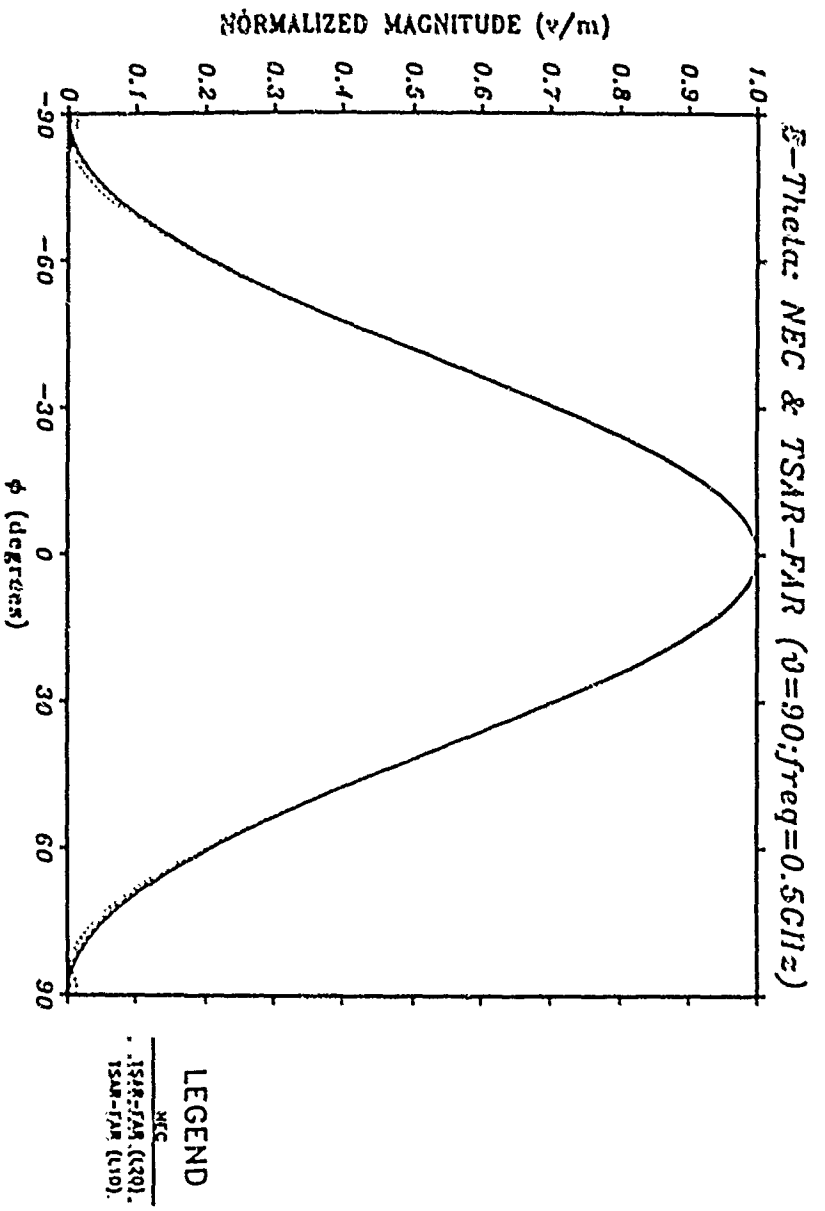

E-Theta: NEC & TSAR-FAR (θ=90;freq=0.5GHz)
NORMALIZED MAGNITUDE (v/m)
0
0.1
0.2
0.3
0.4
0.5
0.6
0.7
0.8
0.9
1.0
-90
-60
-30
0
30
60
90
φ (degrees)
LEGEND
NEC
TSAR-FAR (C20).
TSAR-FAR (L10).

Figure 7.

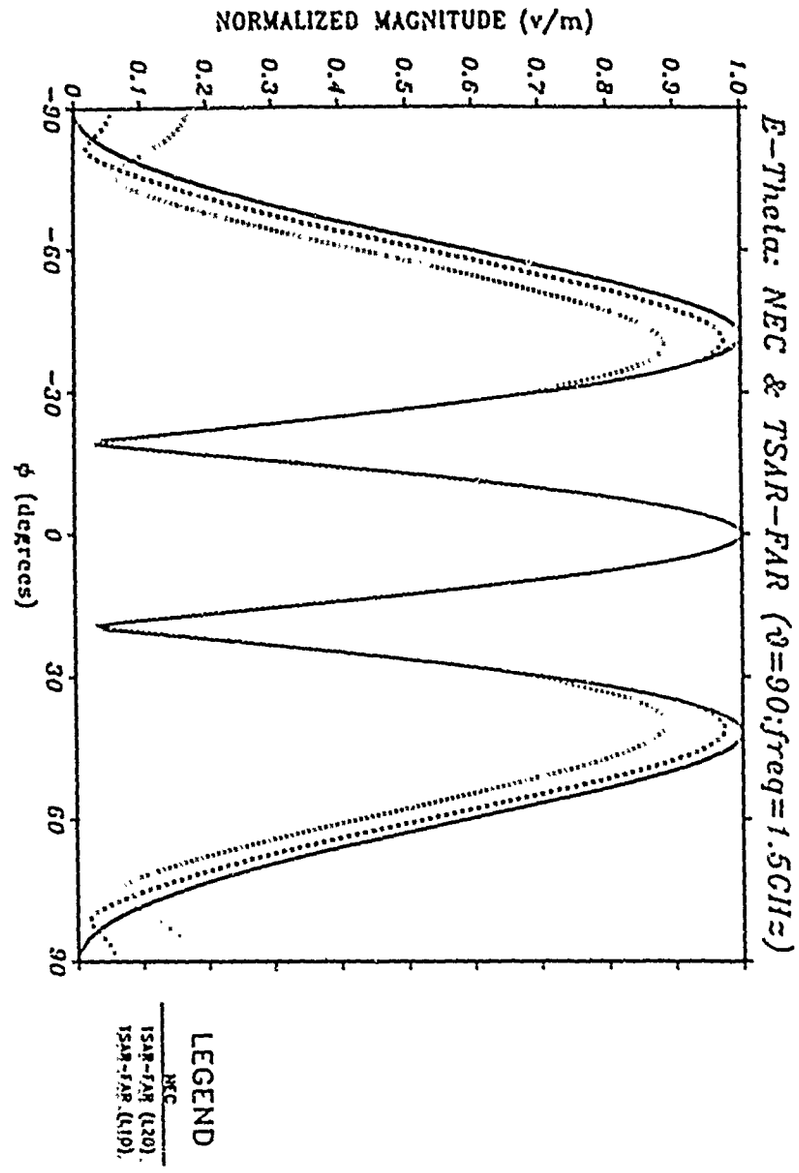

E-Theta: NEC & TSAR-FAR (θ=90;freq=1.5GHz)
NORMALIZED MAGNITUDE (v/m)
0
0.1
0.2
0.3
0.4
0.5
0.6
0.7
0.8
0.9
1.0
-90
-60
-30
0
30
60
90
φ (degrees)
LEGEND
NEC
TSAR-FAR (L20)
TSAR-FAR (L10)

Figure 8.

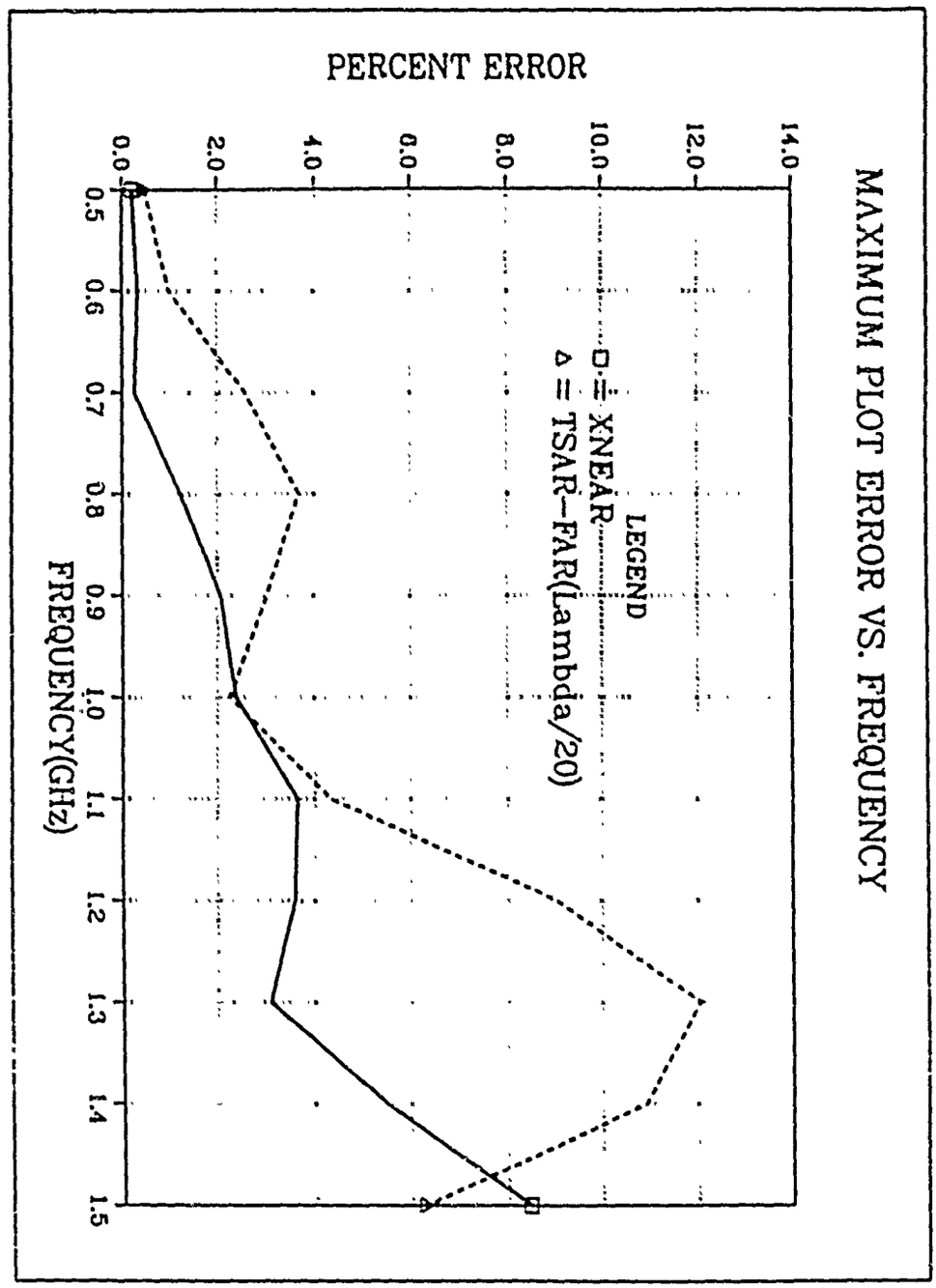

MAXIMUM PLOT ERROR VS. FREQUENCY
PERCENT ERROR
0.0
2.0
4.0
6.0
8.0
10.0
12.0
14.0
LEGEND
□ = XNEAR
Δ = TSAR-FAR(Lambda/20)
0.5
0.6
0.7
0.8
0.9
1.0
1.1
1.2
1.3
1.4
1.5
FREQUENCY(GHz)

Figure 9.

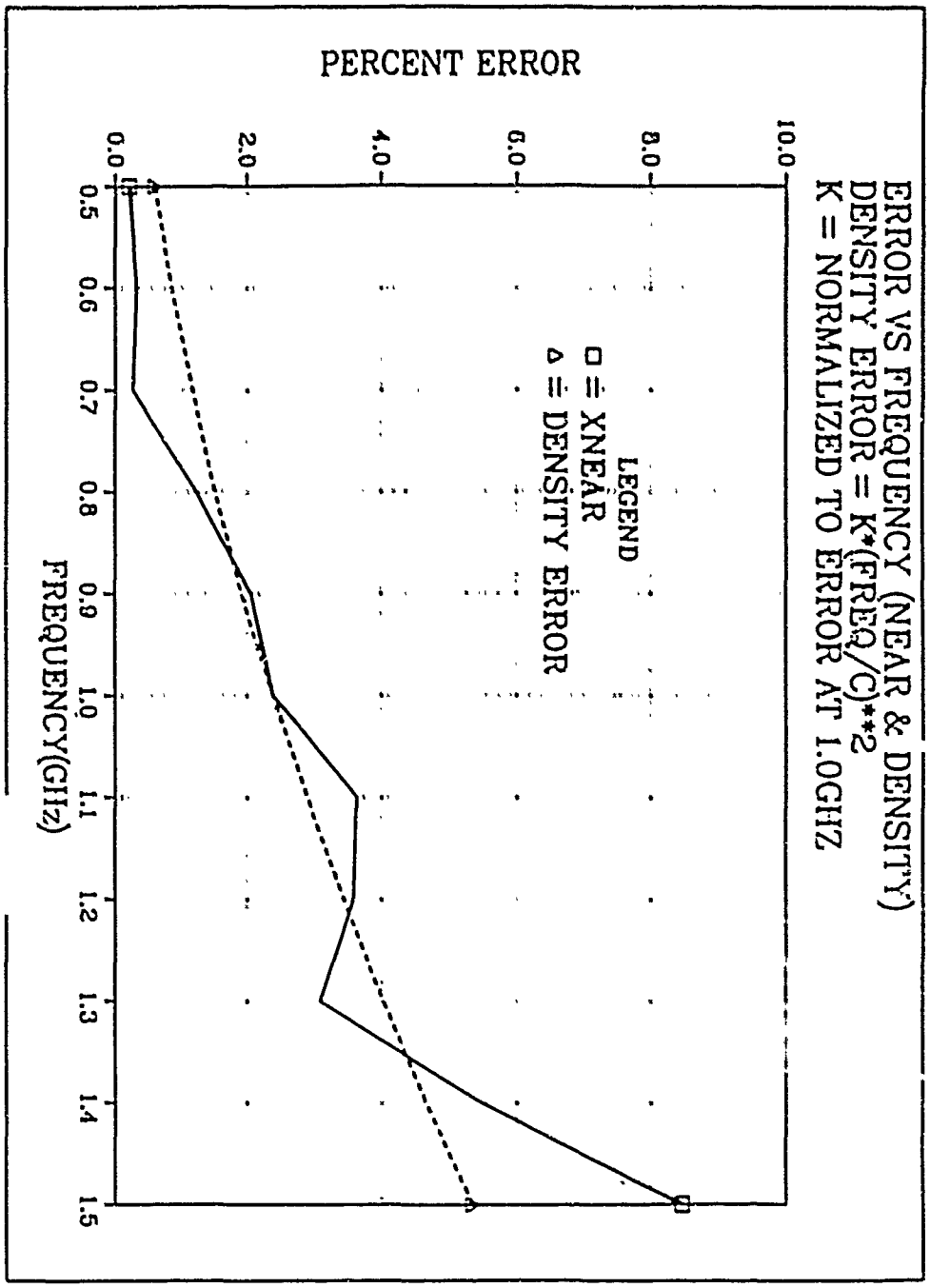

ERROR VS FREQUENCY (NEAR & DENSITY)
DENSITY ERROR = K*(FREQ/C)**2
K = NORMALIZED TO ERROR AT 1.0GHZ
PERCENT ERROR
0.0
2.0
4.0
6.0
8.0
10.0
0.5
0.6
0.7
0.8
0.9
1.0
1.1
1.2
1.3
1.4
1.5
FREQUENCY(GHz)
LEGEND
□ = XNEAR
Δ = DENSITY ERROR

Figure 10.

AUTHOR INDEX

Author	Page
Abouzahra, M	411
Adler, R W	22, 594
Akhter, N	374
Alexander, P	139
Au, R	281
Baginski, M	63, 260, 675
Balanis, C	1
Barth, M	845
Bartolucci, G	114, 195,
Barts, T,	9
Berrett, P	373
Berry, R	474
Best, S	657
Bomholt, L	245, 738
Breakall, J	22
Bridges, G	411, 584, 621
Browman, M	9
Burgio, J	474
Cable, G	474
Canning, F	763
Castaneda, J	81
Castillo, A	189
Castillo, S	550
Cha, C	710, 771
Chan, A	524
Chan, K	9
Chase, R	168
Chen, Y	532
Cheng, C	34
Choi, D	101
Chow, Y	78
Chui, C	524
Chute, F	251
Clancy, K	404
Clark, A	572, 584
Clemens, R	168
Conley, Jr, R	474
Cooper, R	9
Crowey, R	710
Daoud, N	95
Demarest, K	558, 751
Dombroski, E	719
Efiniadis, P	22
Fanning, M	609
Faust, D	373
Fourie, A	572, 584, 621
Fromme, D	461
Galindo-Israel, V	692
German, F	63, 260, 675
Giannini, F	114, 121, 195
Gilchrist, R	373
Givati, O	572
Gilsson, A	742
Gothard, G	675
Gross, B	373
Hafner, C	245, 738, 786
Hall, W	298
Happ, H	474
Hatfield, J	636
Heidler, F	159
Hensel, E	550
Hill, A	183
Hodges, R	464
Hoitzman, J	139
Howard, G	78
Hubing, T	153
Hudson, H	360
Hunsberger, F	328, 827
Hutchinson, S	550
Hwu, S	43
Iannecone, K	461
Imbriale, W	692
Janni, J	474,
Kalbasi, K	751
Kauffman, J	153
Kenney, J	806
King, M	373
Kishk, A	411
Knight, R	168
Kochhar, R	538
Kunz, K	328, 827
Kuster, N	786
Luebbers, R	316, 328, 827
Liu, K	1
Long, D	558
Lowe, T	536
Lutz, L	474
Mabrouk, M	95
Magis, P	139
Marhefka, R	374
McLeod, R	360
Metzger, D	461
Miller, E	751
Mohammadian, A	298
Mould, Jr, J	107, 819
Muller, K	159
Murphy, H	474
Nakatani, A	81
Norgard, J	461
O'Hara, T	594
Paoloni, C	114, 195
Pennock, S	328, 770

Author	Page
Peterson, A	189, 387
Phalliber, N	474
Pic, E	96
Radke, Jr, G	474
Rahmat-Samii, Y	692
Ranson, R G	53
Regil, P	786
Rengarajan, S	404
Riggs, L	63, 260, 675
Rogers, J	421
Sabatka, E	437
Schneider, N	316
Sega, R	461
Sewall, G	793
Shafai, L	411
Shankar, V	298
Sharpe, R	34
Sorensen, E	806
Spear, J	474
Speciale, R	200
Stach, J	457
Stubbs, M	78
Sumbar, E	251
Tam, D	139
Tedjini, S	95
Tirkas, P	558
Tripathi, V	114, 183
Vandament, C	649
Vermeulen, F	251
Villaseca, E	292
Walker, F	806
Wheeler, M	292
Wheless, Jr, W	609
Wilkes, D	771
Williams, H	63, 260
Wilton, D	43
Wojcik, G	107, 819
Wurm, M	159
Yesantharao, S	34
Yip, E	437
Zhong, X	532
Ziolkowski, R	845